

# **ATOMIC FORCE MICROSCOPY IN ADHESION STUDIES**

Edited by

JAROSLAW DRELICH and KASH L. MITTAL

VSP  
Leiden · Boston

2005

© Copyright 2005 by Koninklijke Brill NV, Leiden, The Netherlands.

Koninklijke Brill NV incorporates the imprints Brill Academic Publishers, Martinus Nijhoff Publishers and VSP.

All rights reserved. No part of this publication may be reproduced, translated, stored in a retrieval system, or transmitted in any form or by any means, electronic, mechanical, photocopying, recording or otherwise, without written permission by the publisher.

Authorization to photocopy items for internal or personal use is granted by Brill provided that the appropriate fees are paid directly to Copyright Clearance Center, 222 Rosewood Drive, Suite 910, Danvers, MA 01923, USA. Fees are subject to change.

ISBN 90 6764 434 X

Printed in the Netherlands by Ridderprint bv, Ridderkerk



## Preface

In recent years, atomic force microscopy (AFM) has become a technique of choice for non-destructive solid surface imaging and characterization with an atomic resolution. It is also the instrument that is commonly used in measurements of long-range and short-range surface forces for microscopic particles and nano-sized probes. With the AFM instrument, and other techniques classified under scanning probe microscopy, we are now capable of exploring the adhesion properties of materials from microscopic scale down to molecular level, which are required for developing micro-systems and nano-devices (where gravity does not matter and behaviour of systems is controlled by interactions between surfaces in contact or separated by only a few nanometers). The AFM has become established, therefore, as a problem-solving tool in the development of microsystems and nanotechnology. It has also become one of the basic analytical tools in applications relevant to particle-solid and particle-liquid interactions. It can deliver data on colloidal and molecular forces as well as local properties of materials that stimulate development of new and improved technologies in selective flotation of minerals, recovery of polymers from plastic waste, deinking of recycled paper, recovery of oil from mined oil sands, cleaning electronic materials from nanoparticles, design of new nanocomposites, fabrication of novel biosensors, and others.

This book provides a comprehensive review of AFM techniques and their application in adhesion studies. Over 100 authors have contributed to this book, and they provide a summary of current research on measurements and interpretation of particle-solid adhesion, capillary and molecular forces, solid surface imaging and mapping, and measurements of mechanical properties of materials at nanoscale. Also in this book, the contact mechanics models applicable to particle-substrate and particle-particle systems are discussed extensively. The process of compiling the technical papers presented in this book was initiated by us in the year 2000 during the preparation of a special issue of the *Journal of Adhesion Science and Technology* (JAST) on 'Application of Scanning Probe Microscopy in Interfacial Phenomena' (Vol. 14, No. 14). As we recognized that even with the present telecommunications revolution, it took time and effort to collect the published research articles on adhesion studies with the AFM technique, given their spread among numerous journals — not always easily accessible to many researchers — so we decided to compile information on this topic in an easily accessible source and this book is the result. The availability of focussed scientific information into a few accessible resources becomes attractive and gratifying to many researchers. The positive response that

we received from the readers of the first special issue of JAST motivated us to prepare and edit two other issues of this journal (Vol. 16, No. 7, 2002 and Vol. 19, No. 3-5, 2005) dedicated to the same topic. We have also noticed an increased submission of manuscripts on the use of the AFM technique and contact mechanics studies to JAST in the last five years, and concomitantly, several interesting technical reports have been published in regular JAST issues.

In this single volume, we offer all the papers that were published in JAST on AFM and contact mechanics studies during 2000–May 2005. This includes 30 papers published in the three special issues dedicated to ‘Application of Scanning Probe Microscopy in Interfacial Phenomena’ and 12 published in regular JAST issues. A few errors that appeared in some of the original papers have been corrected in this book. All these peer-reviewed papers, written by internationally-renowned researchers, have been arranged according to the following topics: Adhesion Force Measurements, Chemical Origins of Adhesion, Roughness Effects in Adhesion Force Measurements, Capillary Adhesion and Wetting Phenomena, Measurements of Colloidal Forces, Adhesion Mapping and Surface Imaging, and Examination of Interphases and Nano-indentation. This book not only highlights the current progress made in applications of the AFM techniques in adhesion studies and characterization and mapping of solid surfaces, but also provides useful guidelines for experimental methodologies used in measurements of adhesion, molecular, colloidal and capillary forces. Applicability of theoretical models in the interpretation of recorded forces as well as the controversy surrounding the selection of models in the analysis of the AFM results are also emphasized in this book. We hope this book will serve as a reference for both new and current users of the scanning probe microscopes, particularly those who are engaged in exploring both fundamental and practical aspects of adhesion phenomena. To our knowledge, this is the first book exclusively dedicated to this important and burgeoning topic.

This book could not materialize without contributions from the authors of included papers, time and effort that reviewers dedicated to the manuscripts during the review process, and help received from the publisher. We thank them all!

JAROSLAW DRELICH and KASH L. MITTAL  
June 2005

# Contents

## Preface

*J. Drelich and K. L. Mittal*

ix

## Adhesion Force Measurements

Application of atomic force spectroscopy (AFS) to studies of adhesion phenomena: a review

*F. L. Leite and P. S. P. Herrmann*

3

Interaction force measurements using atomic force microscopy for characterization and control of adhesion, dispersion and lubrication in particulate systems

*M. S. Esayanur, S. B. Yeruva, Y. I. Rabinovich and B. M. Moudgil*

45

Comparison of various adhesion contact theories and the influence of dimensionless load parameter

*X. Shi and Y.-P. Zhao*

61

Accounting for the JKR–DMT transition in adhesion and friction measurements with atomic force microscopy

*D. S. Grierson, E. E. Flater and R. W. Carpick*

75

Friction, adhesion, and deformation: dynamic measurements with the atomic force microscope

*P. Attard*

97

Direct adhesion measurements of pharmaceutical particles to gelatin capsule surfaces

*T. H. Ibrahim, T. R. Burk, F. M. Etzler and R. D. Neuman*

137

Analysis of atomic force microscopy data for deformable materials

*M. W. Rutland, J. W. G. Tyrrell and P. Attard*

155

Dynamic adhesion of grafted polymer surfaces as studied by surface force measurements

*M. A. Plunkett and M. W. Rutland*

173

## Chemical Origins of Adhesion

Chemical force microscopy: probing chemical origin of interfacial forces and adhesion

*D. V. Vezenov, A. Noy and P. Ashby*

189

Pull-off forces measured between hexadecanethiol self-assembled monolayers in air using an atomic force microscope: analysis of surface free energy

*E. R. Beach, G. W. Tormoen and J. Drelich*

241

Adhesion forces between functionalized probes and hydrophilic silica surfaces <i>D. Christendat, T. Abraham, Z. Xu and J. Masliyah</i>	265
Analysis of atomic force microscope pull-off forces for gold surfaces portraying nanoscale roughness and specific chemical functionality <i>G. W. Tormoen, J. Drelich and E. R. Beach, III</i>	281
A study of adhesion forces by atomic force microscopy <i>C. Jacquot and J. Takadoum</i>	299
<b>Roughness Effects in Adhesion Force Measurements</b>	
Microparticle adhesion studies by atomic force microscopy <i>L. H. G. J. Segeren, B. Siebum, F. G. Karssenberg, J. W. A. van den Berg and G. J. Vancso</i>	309
A distribution of AFM pull-off forces for glass microspheres on a symmetrically structured rough surface <i>G. W. Tormoen, J. Drelich and J. Nalaskowski</i>	345
Experimental analysis of the influence of surface topography on the adhesion force as measured by an AFM <i>A. Méndez-Vilas, M. L. González-Martín, L. Labajos-Broncano and M. J. Nuevo</i>	365
Adhesion forces between individual gold and polystyrene particles <i>L. O. Heim, S. Ecke, M. Preuss and H.-J. Butt</i>	377
Adhesion of carbonyl iron powder particles studied by atomic force microscopy <i>L. Heim, M. Farshchi, M. Morgeneyer, J. Schwedes, H.-J. Butt and M. Kappl</i>	393
Adhesion of rough surfaces with plastic deformation <i>L. Zhang and Y.-P. Zhao</i>	409
Deformation of soft colloidal probes during AFM pull-off force measurements: elimination of nano-roughness effects <i>G. W. Tormoen and J. Drelich</i>	425
<b>Capillary Adhesion and Wetting Phenomena</b>	
Role of surface roughness in capillary adhesion <i>A. Ata, Y. I. Rabinovich and R. K. Singh</i>	445
Direct measurements of the adhesion between a glass particle and a glass surface in a humid atmosphere <i>S. Biggs, R. G. Cain, R. R. Dagastine and N. W. Page</i>	455
Measurement of oil-mediated particle adhesion to a silica substrate by atomic force microscopy <i>Y. I. Rabinovich, M. S. Esayanur, K. D. Johanson, J. J. Adler and B. M. Moudgil</i>	473
Effect of relative humidity on adhesion and frictional properties of micro- and nano-scopic contacts <i>A. A. Feiler, P. Jenkins and M. W. Rutland</i>	491

Scanning force microscopy investigation of liquid structures and its application to fundamental wetting research <i>S. Herminghaus, T. Pompe and A. Fery</i>	507
Contact angles on hydrophobic microparticles at water–air and water–hexadecane interfaces <i>G. E. Yakubov, O. I. Vinogradova and H.-J. Butt</i>	523
Capillarity at the nanoscale: an AFM view <i>F. Mugele, T. Becker, R. Nikopoulos, M. Kohonen and S. Herminghaus</i>	541
<b>Measurements of Colloidal Forces</b>	
Surface forces between sphalerite and silica particles in aqueous solutions <i>Z. Xu, R. Chi, T. Difeo and J. A. Finch</i>	557
Long-range attractive forces and energy barriers in de-inking flotation: AFM studies of interactions between polyethylene and toner <i>J. Drelich, J. Nalaskowski, A. Gosiewska, E. Beach and J. D. Miller</i>	573
Surface forces and characterization of glass surfaces bearing grafted polymers: solvent dependence <i>M. A. Plunkett, S. Rödner, L. Bergström and M. W. Rutland</i>	589
<b>Adhesion Mapping and Surface Imaging</b>	
Design of a digitally controlled adhesion imaging mode using a scanning force microscope <i>Y. Zhang, A. Pungor, G. Jogikalmath and V. Hlady</i>	609
Mapping of adhesion forces on soil minerals in air and water by atomic force spectroscopy (AFS) <i>F. L. Leite, A. Riul, Jr. and P. S. P. Herrmann</i>	625
The investigation of sized cellulose surfaces with scanning probe microscopy techniques <i>L. E. Dickson and J. C. Berg</i>	641
Atomic force microscopy, X-ray diffraction, X-ray photoelectron spectroscopy and thermal studies of the new melamine fiber <i>R. S. Rajeev, S. K. De, A. K. Bhowmick, B. Gong and S. Bandyopadhyay</i>	657
Morphology and elasticity of waterborne acrylic pressure-sensitive adhesives investigated with atomic force microscopy <i>J. Malléol, O. Dupont and J. L. Keddie</i>	679
Relating material surface heterogeneity to protein adsorption: the effect of annealing of micro-contact-printed OTS patterns <i>G. Hodgkinson and V. Hlady</i>	697

**Examination of Interphases and Nano-Indentation**

Determining the interphase thickness and properties in polymer matrix composites using phase imaging atomic force microscopy and nanoindentation <i>T. D. Downing, R. Kumar, W. M. Cross, L. Kjerengtroen and J. J. Kellar</i>	721
Use of an atomic force microscope to measure surface deformations in polymeric systems <i>M. C. Roggemann and J. G. Williams</i>	733
Studies of the interphase in epoxy–aluminum joints using nano-indentation and atomic force microscopy <i>F. Li, J. G. Williams, B. S. Altan, I. Miskioglu and R. L. Whipple</i>	749
Interphase variation in silane-treated glass-fiber-reinforced epoxy composites <i>C. Griswold, W. M. Cross, L. Kjerengtroen and J. J. Kellar</i>	765
Characterization of the interphase in epoxy/aluminum bonds using atomic force microscopy and a nano-indenter <i>J. G. Williams, F. Li and I. Miskioglu</i>	777
Stiffness and adhesion characterization of nanolithographed poly(methyl methacrylate) by means of force–displacement curves <i>B. Cappella, H. Sturm and E. Schulz</i>	799

# Adhesion Force Measurements

## Application of atomic force spectroscopy (AFS) to studies of adhesion phenomena: a review

F. L. LEITE<sup>1,2</sup> and P. S. P. HERRMANN<sup>1,\*</sup>

<sup>1</sup> *Embrapa Agricultural Instrumentation, Rua XV de Novembro 1452, CEP 13560-970, São Carlos, São Paulo, Brazil*

<sup>2</sup> *Institute of Physics of São Carlos, University of São Paulo (USP), CEP 13560-970, São Carlos, São Paulo, Brazil*

**Abstract**—This review article describes the fundamental principles of atomic force spectroscopy (AFS) and how this technique became a useful tool to investigate adhesion forces. AFS is a technique derived from atomic force microscopy (AFM) and can determine, at every location of the sample surface, the dependence of the interaction on the probe–sample distance. AFS provides valuable information, at the nano-scale, such as, for example: (i) how the magnitude of the adhesion force depends on long- and short-range interactions and (ii) the tip–sample contact area. An overview about the theory and experiments with local force spectroscopy, force imaging spectroscopy, chemical force microscopy and colloidal probe technique is presented. The many applications of the AFS technique for probing surface interactions open up new possibilities to evaluate adhesion, an important characteristic of materials.

**Keywords:** Atomic force spectroscopy; adhesion phenomena; surface properties; atomic force microscopy; interfacial phenomena.

### 1. INTRODUCTION

In 1980–1981 Binnig and co-workers at the IBM Zürich Research Laboratory developed a new type of microscope which they called the scanning tunneling microscope (STM) [1], being the first one in the scanning probe microscopy (SPM) family, that allowed visualization of surfaces on an atomic scale. Although the STM technique is limited to electrically conducting samples, it led to the development of numerous devices that utilize a range of physico-chemical interactions between a tip and sample surface. Equally important, this family of techniques includes one

---

\*To whom correspondence should be addressed. Tel.: (55-16) 3374-2477. Fax: (55-16) 3372-5958.  
E-mail: herrmann@cnpdia.embrapa.br



of the most commonly used SPM systems, the atomic force microscope (AFM) [2], which can image surface topography of both insulating and conductive samples.

In general, the AFM studies can be divided into topographical applications (imaging mode) and force spectroscopy or so-called atomic force spectroscopy (AFS), i.e., measuring forces as a function of distance [3–6]. The former group generates an image of the sample surface to observe its structural or dynamic features and it has been employed very effectively on a wide variety of surfaces, including semiconductors [7], biological systems [8–11] and polymers [12–15], with resolution in the micrometer to subnanometer range, thus facilitating imaging at the submolecular level. The second group (AFS) is one of the most promising and interesting research areas related to SPM [16], allowing the study of inter- and intra-molecular forces. AFS has already been successfully applied to studies of biological systems [17–19], polymers (Refs [20–23] and data not shown) and interfacial phenomena [3, 24–28]. The aim of this review is to provide a glimpse of the potential and limitations of the application of AFS to studies of adhesion phenomena.

## 2. ATOMIC FORCE MICROSCOPY

### 2.1. Principle of operation

This section briefly introduces the basic elements of AFM and its principle of operation. The microscope scans over the sample surface with a sharp probe, or tip, situated at the apex of a flexible cantilever that is often diving board-shaped or V-shaped and normally made of silicon. AFM utilizes a piezoelectric scanner that moves the sample with a sub-nanometer displacement when a voltage is applied. This piezoelectric system is employed to move the sample in three dimensions relative to the tip (Fig. 1). To form an image, the tip is brought into contact with or close to the sample and raster-scanned over the surface, causing the cantilever to deflect because of a change in surface topography or in probe–sample forces. A line-by-line image of the sample is formed as a result of this deflection, which is detected using laser light reflected off the back surface of the cantilever onto a position-sensitive photodiode detector [29, 30].

Forces acting between the sharp probe (tip) placed in close contact with the sample result in a measurable deformation of the cantilever (console) to which the probe is attached. The cantilever bends vertically upwards or downwards because of a repulsive or attractive interaction. The forces acting on the tip vary, depending on the operating mode and the conditions used for imaging. A number of AFM imaging modes are available. The most widely used is the contact mode (C-AFM) [2, 31]; in this regime, the AFM tip is in intimate repulsive contact with a surface. Scanning can be done in two different ways: (1) in the ‘constant-force mode’ the cantilever deflection is kept constant by the extending and retracting piezoelectric scanner; in this method, a feedback loop adjusts the height of the sample (to

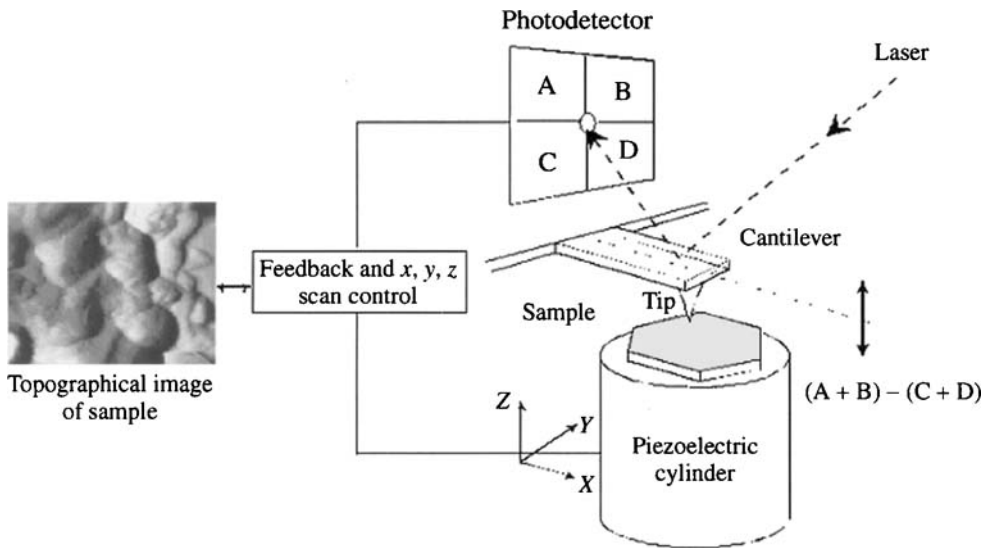


**Figure 1.** A schematic drawing of an atomic force microscope. A detector consisting of four photodiodes is shown. Scanning perpendicularly to the long cantilever axis, the  $(A + B) - (C + D)$  signal gives topographical data, while the  $(A + C) - (B + D)$  signal responds to friction due to torsion of the cantilever, providing lateral force information.

maintain constant deflection) by varying the voltage applied to the  $z$  portion of the  $xyz$  piezoelectric scanner. (2) In the 'variable-deflection mode' or 'constant height mode' the piezotube extension is constant and the cantilever deflection is recorded; in this method, the feedback loop is open, so that the cantilever undergoes a deflection proportional to the change in the tip-sample interaction.

'Friction force microscopy (FFM)' [32] is a variant of the contact mode, in which the laser beam detector is arranged so as to allow monitoring not only of the vertical component of the tip deflection (topography), but also the torsion deformation exerted by the lateral forces acting on the tip end. Yuan and Lenhoff [33] demonstrated clearly the versatility of the FFM technique. The authors measured surface mobility of colloidal latex particles adsorbed onto mica by moving the particles with an AFM tip in the lateral force microscopy mode. Their data showed that the mean lateral force was proportional to the particle diameter, while the effect of electrostatic interactions on the mobility of adsorbed particles was seen to be weak. The results were consistent with classical theories of friction in macroscopic systems. Recently Zamora *et al.* [34] showed that a water layer, adsorbed on the sample surface, affected both the normal force at the nanoasperity contacts by the effect of a meniscus loading force and the friction force. The influence of the water condensed at the tip-surface contact on the friction force was studied for hydrophilic, partially hydrophilic and hydrophobic surfaces. The results showed that surface wettability affected significantly the dependence of friction on the normal force and scan velocity.

The contact mode allows tracking of surface topography with a high precision and also provides a high lateral resolution of 0.2–0.3 nm (down to true atomic resolution under appropriate conditions [35]), but imposes a high local pressure as well as shear stresses on the surface. In contact-mode imaging, the deflection of the tip is mainly caused by the repulsive forces between the overlapping electron orbitals between the tip atoms and the sample atoms. The dominant attractive force is a van der Waals force arising primarily from the induced dipole interactions among atoms of the tip and specimen [36]. When the image is obtained in air, layers of water are adsorbed, producing an additional strong attractive force due to the liquid–air interfacial tension. While in liquids, contributions from electrostatic Coulomb interactions between charges on the specimen and tip (either occurring naturally or induced because of polarization), structural forces, such as hydration and solvation forces, and adhesion forces should be considered. However, in a fluid environment, the surface tension forces are abolished and van der Waals forces are typically also reduced due to screening of these forces by the intervening dielectric, resulting in a reduced imaging force.

Another way of avoiding the problems caused by the capillary layer is to use the longer-range attractive forces to monitor the tip–sample interaction. These attractive forces are weaker than the repulsive force detected in contact mode and, consequently, different techniques are required to utilize them. There are two main types of dynamic mode: the first is often known as the tapping or intermittent contact mode (IC–AFM) [37–39], whilst the second is usually called the non-contact mode (NC–AFM) [40–42]; the new techniques developed for the use of noncontact mode are achieving high lateral resolution (atomic resolution), and are showing new opportunities in sample analysis [43–45]. In the tapping mode, the cantilever is deliberately excited by an electrical oscillator to amplitudes of up to approximately 100 nm, so that it effectively bounces up and down (or taps) as it travels over the sample. The oscillation amplitude is measured as an RMS value of the deflection detector signal. The feedback system is set to detect the perturbation on the oscillation amplitude caused by intermittent contact with the surface [46, 47]. When the tapping mode is carried out in liquids, the tip of the cantilever taps the sample gently during part of the force curve; this mode is similar to the tapping mode operating in air, except that the sample is tapped against the tip instead of the cantilever being driven at resonance to tap the sample [48].

In the NC–AFM, the oscillating cantilever never actually touches the surface of the sample, the spacing between the tip and the sample for NC–AFM is on the order of tens to hundreds of Ångströms, with an oscillation amplitude of only about 5 nm. Non-contact mode usually involves a sinusoidal excitation of the cantilever with a frequency close to its main resonant frequency. In order to excite the vibration of the probe, in some applications, it is convenient to externally modulate the long-range probe–sample interactions. Therefore, the relatively long-range attractive forces induce changes in the amplitude, frequency and phase of the cantilever and maintain a constant distance during scanning [49]. These changes in amplitude or in phase

can be detected and used by the feedback loop to produce topographic data. Other forms will be to attach a bimorph piezoelectric to the cantilever, or if the sample can be excited by a suitable piezoelectric actuator.

The force modulation mode [50, 51] is an extension of the dynamic mode that uses very large vertical oscillations in which the AFM tip is actually pressed against the surface and the  $z$  feedback loop maintains a constant cantilever deflection (as for constant-force mode AFM). The tip moves laterally, point-by-point, over the surface and a complete distribution of the surface elastic properties (amplitude signal) and/or energy dissipation characteristics (phase signal) is collected concurrently with the topographical image [52]. The amplitude damping is determined by the elastic surface deformation against a hard tip. Usually, the elastic constant of the cantilever should be large to achieve reasonable contrast in the force modulation mode. In this mode experiments are typically conducted at the resonant frequency of the driving bimorph element (8–10 kHz) and oscillation amplitudes of 1 to 5 nm [53].

Figure 2 represents the tip-sample interaction force ( $F(D)$ ) with different AFM operation modes. At short distances, the cantilever mainly senses interatomic forces: the very short range ( $\approx 0.1$  nm) Born repulsive forces and the longer-range (up to 10 nm) van der Waals forces. At very small tip-sample distances, a strong repulsive force appears between the atoms of the tip and those of the sample. This repulsive force occurs between any two atoms or molecules that approach so closely

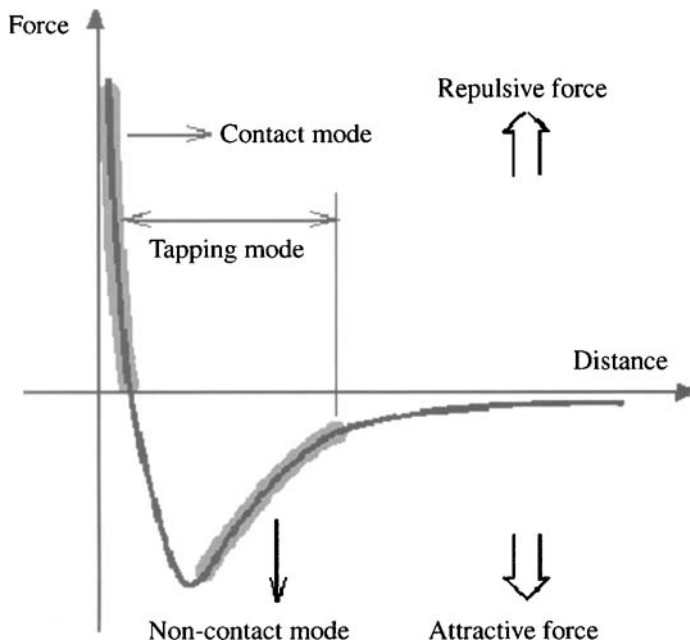


**Figure 2.** Empirical force vs distance curve that reflects the type of interaction between the scanning tip and sample during AFM measurements using specific imaging modes (adapted from Ref. [55]).

that their electron orbitals begin to overlap. It is thus a result of the so-called Pauli Exclusion Principle [54]. When this repulsive force is predominant in an AFM set-up, tip and sample are considered to be in ‘contact’ (regime of contact mode).

The total intermolecular pair potential is obtained by assuming an attractive potential,  $(-C_1/z^6)$  and a repulsive potential,  $(C_2/z^{12})$ . Superimposing the two gives an expression for the well-known Lennard–Jones potential:  $U = C_2/z^{12} - C_1/z^6$ , where  $C_1$  and  $C_2$  are the corresponding coefficients for the attractive and repulsive interactions, respectively, and  $z$  is the distance between the sample surface and rest position of the cantilever.

To describe the AFM tip and sample interactions, one needs to sum the attractive and repulsive potential pairs over all interacting atoms. A simple summation for all the atoms of the tip and sample is a good approximation for repulsive force (the first term of equation above). However, the van der Waals interaction (second term) is non-additive, i.e., the interaction of two bodies is affected by the presence of other bodies nearby, and a simple sum of the pair-wise interactions is usually greater than the actual force between the macro bodies of interest [55, 56]. To take into account non-additivity of the van der Waals part of the interaction, some methods can be used [57, 58]. Nevertheless, an additive approximation is used in many practical applications, including atomistic simulation of AFM [59]. In particular, the van der Waals interaction between the atoms at the end of the tip and in the surface is taken into account explicitly by summing the interactions of all pairs of atoms. However, a full tip contains billions of atoms and it is impossible to sum all the interactions; therefore, an approximation must be made based on the local geometry, material properties and structure of the tip [60, 61]. Hamaker [62] performed the integration of the interaction potential to calculate the total interaction between two macroscopic bodies using the following approximations: (1) the total interaction is obtained by the pair-wise summation of the individual contributions (additivity); (2) the summation can be replaced by an integration over the volumes of the interacting bodies assuming that each atom occupied a specific volume, with a density  $\rho$  (continuous medium); (3)  $\rho$  and  $C$  (interaction constant defined by London [63] and is specific to the identity of the interacting atoms) should be uniform over the volume of the bodies (uniform material properties).

However, for van der Waals interaction derived from second-order quantum perturbation theory [64] is only an approximation to reality, since the internal states of molecules,  $i$  and  $j$  will be modified by the presence of all other molecules of the system, which means that the assumption of pair-wise additivity is not completely correct, especially in condensed phases, where the mean distance between atoms is small and many-body effects cannot be ignored. This problem can be solved by a different approach, proposed by Lifshitz in 1956 [65]. Basically, the Lifshitz or macroscopic approach considers the interactions between electromagnetic waves emanating from macroscopic bodies. The detailed original treatment is very complicated [66] and requires sophisticated mathematics, but several more accessible accounts have subsequently been published [67, 68]. The Lifshitz approach has

the great advantage of automatically incorporating many-body effects and of being readily applicable to interactions in a third medium [69–71].

## 2.2. Atomic force spectroscopy

Atomic force microscopy (AFM) can be used to determine the dependence of the interaction on the probe–sample distance at every location [72]. To determine the spatial variation of the tip–sample interaction, force curves can be recorded at a large number of sample surface locations, using the technique of atomic force spectroscopy (AFS). With AFS it is possible to obtain the following information: (i) the magnitude of the force which depends on long-range attractive and adhesion forces, (ii) estimation of the point of tip–sample contact, (iii) the tip–sample contact area and (iv) the elastic modulus and plasticity of thin and thick films [73, 74].

The point of contact is defined as the intersection of the contact region of the force curve and the non-contact region of the force curve, i.e. the point of contact is that height where the tip would have touched the sample, if there was no attractive force resulting in a mechanical instability so that the tip jumps to the sample [75]. The contact area can be described and expressed by several continuum contact mechanics theories [74], besides modern molecular dynamics calculations that have been the source of many important insights into nano-scale mechanics [76]. The choice of the appropriate theory depends on the relative magnitudes of the materials properties and surface forces. Mechanical properties such as elastic modulus and hardness can be obtained from the corrected slope of the force curve after contact [77]; for more details, see Refs [78, 79]. One must choose the proper mechanical relationships with which to evaluate the data in order to determine the materials properties of the sample as well as the tip–sample contact area [80].

*2.2.1. Local force spectroscopy.* With commercially available cantilevers, AFM may be used to measure forces accurately down to approx. 10 pN [81]. It is possible to investigate the complex inter- and intra-molecular interactions, the ranges, magnitudes and time-dependence of rupture forces, the mechanical properties of molecules and the strength of individual bonds [82, 83]. There are several features of AFM that make it ideal for force sensing, such as the sensitivity of the displacement (around 0.01 nm), a small tip–sample contact area (about 10 nm<sup>2</sup>) and the ability to operate under physiological conditions [84]. In order to evaluate how the force mapping experiments are conducted, it is necessary to understand how single-point force–distance curves are obtained and what information they provide about tip–sample interaction.

In local force spectroscopy (LFS) (Fig. 3a), the force curve is determined at a particular location on the sample surface. At the start of the cycle, a large distance separates the tip and sample, there is no interaction between the tip and sample and the cantilever remains in a non-interacting equilibrium state (point (a)). As separation decreases, the tip is brought into contact with the sample at a constant velocity until it reaches a point close to the sample surface. As the sample moves

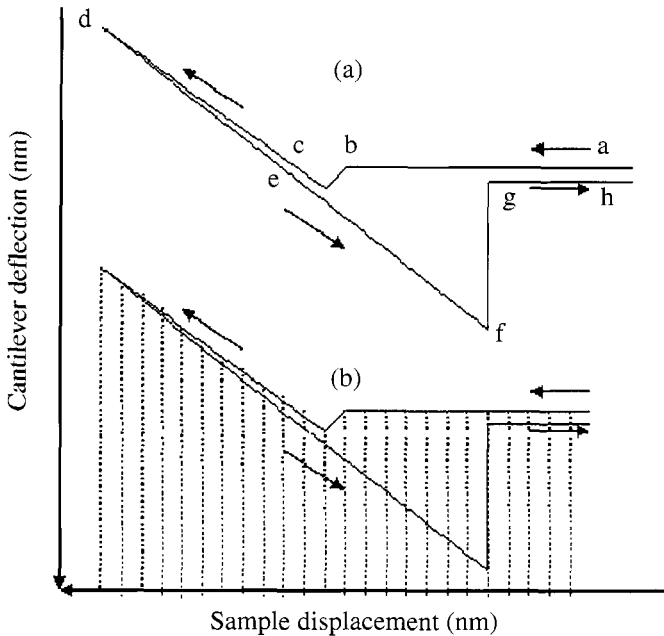


**Figure 3.** When performing force measurements, the AFM tip is brought into and out of contact with the sample at a fixed point. The effect that the sample has upon the deflection of the tip is plotted against the displacement of the sample in the  $z$ -direction. (a) Local force spectroscopy and (b) force imaging spectroscopy.

towards the tip various attractive forces pull on the tip (long- and short-range forces). Once the total force gradient acting on the tip exceeds the stiffness of the cantilever, the tip jumps into contact with the sample surface (jump-to-contact) ((b)→(c)). At point (d), the tip and sample are in contact and deflections are dominated by mutual electronic repulsions between overlapping molecular orbitals of the tip and sample atoms ((a)→(d)) is the approach curve. The shape of segment (c)→(d) indicates whether the sample is deforming in response to the force from the cantilever. The slope of the curve in contact region is a function of the elastic modulus and geometries of the tip and sample and will only approach unity for rigid systems [85–87]. This slope can be used to derive information about the hardness of the sample or to indicate differing sample responses at different loadings. The segment (d)→(e) is showing the opposite direction of the segment (c)→(d). The piezoscanner is travelling in the backward direction. If both segments are straight and parallel to each other, there is no additional information content. If they are not parallel, the hysteresis gives information on plastic deformation of the sample [88, 89].

During withdrawal curve (d)→(h), as the tip–sample surface distance decreases ((e)→(f)), adhesion or bonds formed during contact with the surface cause the tip to adhere to the sample up to some distance beyond the initial contact point on the approach curve. As the piezotube continues retracting, the spring force of the

bent cantilever overcomes the adhesion forces and the cantilever pulls off sharply, springing upwards to its undeflected or noncontact position ((f)→(g)). Finally, the tip-sample surface distance continues to decrease and the tip completely loses contact with the surface and returns to its starting equilibrium position ((g)→(h)). Figure 3b shows a force-volume data set, that contains an array of force curves and a so-called height image. Force-volume imaging is based on collecting arrays of force curves. Individual curves are transformed into force-distance curves and all the curves are assembled into a three-dimensional force-volume [3] (for more details, see Section 2.2.2).

Approach and withdrawal curves can be divided roughly into three regions: the contact line, the non-contact region and the zero line (Fig. 4). The zero line is obtained when the tip is far from the sample and the cantilever deflection is close to zero (when working in liquid, this line gives information on the viscosity of the liquid [74]). When the sample is pressed against the tip, the corresponding cantilever deflection plot is called the contact line and this line can provide information on sample stiffness. The most interesting regions of the force curve are two non-contact regions, containing the jump-to-contact and the jump-off-contact. The non-contact region in the approach curve gives information about attractive (van der Waals or Coulomb force) or repulsive forces (van der Waals in some liquids, double-layer, hydration and steric force) before contact; this discontinuity occurs when the gradient of the tip-sample force exceeds the spring constant of the cantilever (pull-on force). The non-contact region in the withdrawal curve contains the jump-off-contact, a discontinuity that occurs when the cantilever's spring constant is greater than the gradient of the tip-sample adhesion forces (pull-off force). A convenient way to measure forces with precision is to convert them into deflections of a spring, according to Hooke's law:

$$F = -k_c \delta_c, \quad (1)$$

where the cantilever deflection  $\delta_c$  is determined by the acting force  $F$  and the spring constant of the cantilever,  $k_c$ .

Although the manufacturer describes spring constants for the cantilevers, the actual spring constant may deviate from this value by an order of magnitude. It is, therefore, necessary to determine the spring constant experimentally. This may involve determining: (i) the resonant frequency of the cantilever before and after adding a small mass to the tip [90], (ii) ascertaining the unloaded resonant frequency with knowledge of the cantilever's density and dimensions [91], or (iii) thermal fluctuation of the cantilever [92, 93]. In equation (1), the acting force leads to a total bending  $\Delta z$  of the cantilever due interaction with the surface. The real probe-sample distance is then given by:

$$D = z - \Delta z, \quad (2)$$

where  $z$  is the distance between the sample surface and rest position of the cantilever and  $\Delta z$  is the sum of the cantilever deflection,  $\delta_c$ , and sample deformation,



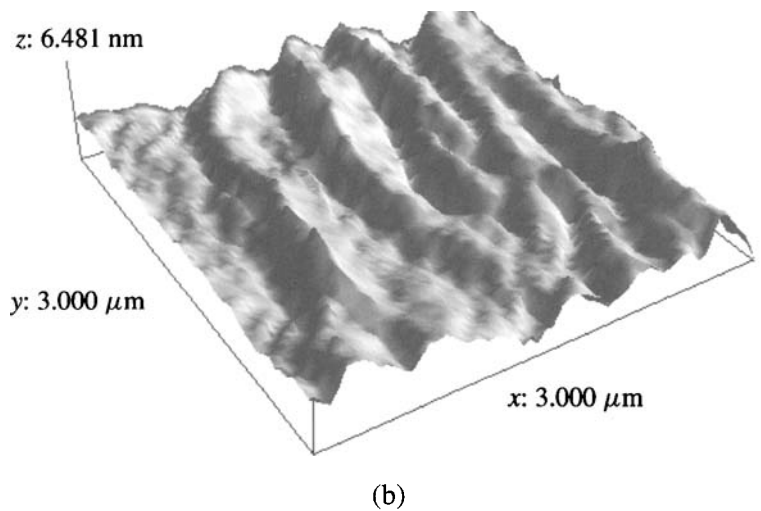
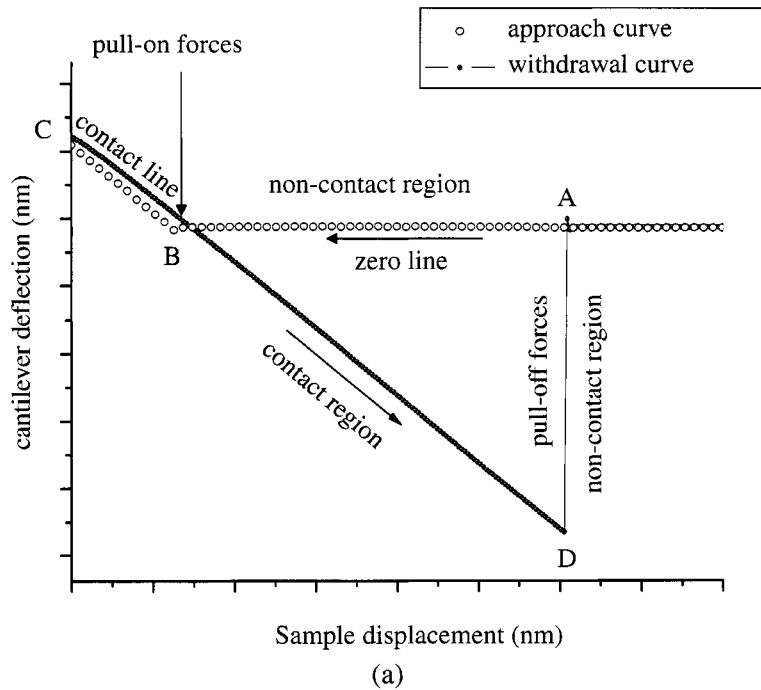


**Figure 4.** (a) Force curve on sisal fibers illustrating the points where jump-to-contact (approach) and jump-off-contact (withdrawal) occur and the maximum values of the attractive force (pull-on force and pull-off force); (b) contact mode topography image of sisal fiber.

$\delta_s$  [74]. Since we do not know in advance the cantilever deflection and the sample deformation, the distance that can be controlled is the displacement of the piezotube. Therefore, the raw curve obtained by AFM should be called ‘deflection–

displacement curve' rather than 'force–distance curve' [74]. This latter term should be employed only for curves in which the force is plotted vs. the true tip–sample distance (Fig. 2).

A complete force curve consists of two portions amounting to the movement of the probe towards the sample (approach) and its retraction back to its starting position (withdrawal). Figure 4a illustrates these two portions of the force curve for the case of measurements performed on a sisal fiber surface. The authors studied the surface chemistry by force spectroscopy and investigated the morphological changes caused by chemical treatments of sisal fibers. By AFM, it was possible to observe that the untreated sisal fiber (Fig. 4b) consisted of lengthwise macrofibrils oriented in the same direction. The adhesion force between the AFM tip and the surface of the fibers was found to increase after benzylation of the fibers, indicating a rise in their surface energy. The distribution of the measured adhesion force over an area of  $1\ \mu\text{m}^2$  was very nonuniform in all samples, but the low adhesion sites disappeared after benzylation. These results illustrate how the AFM can be used to detect heterogeneity in the wettability of fibers, such as sisal, with nanometer resolution and can be applied in the study of fiber-matrix adhesion in polymer composites.

The hysteresis apparent in Fig. 4a is due to the adhesion force between the probe and sample. For clean surfaces of probe and sample, adhesion can result from van der Waals interactions [94] or from covalent or metallic bonding between the probe and sample [95]. However, since the experiment was realized in ambient conditions, the pronounced hysteresis is due also to capillary forces [4, 96], as we will see in more detail in Section 3.3.

*2.2.2. Force imaging spectroscopy.* In the mid-1990s, the idea of collecting data from force–distance curves obtained from many points on a sample was introduced, effectively to produce a map of the tip–surface interactions [97, 98]. Layered imaging is an SPM technique in which several measurements of cantilever deflection are made at each image pixel. Each measurement of a deflection at a given displacement is recorded. When all measurements for the current pixel are completed, the process is repeated at the next pixel and so on through the scan area. The resulting spatial maps represent the lateral variation of adhesion force due to material inhomogeneities and the surface topography [22]. The resulting three-dimensional data set can be thought of as a stack of 'layers' of images (see Fig. 5b). Each horizontal layer is an image which represents measurements taken throughout the scan area at a specified height  $z$ . Since several measurements are made at each pixel, the data set can also be processed vertically to yield the force–distance curve at each pixel. This force imaging spectroscopy (FIS) mode of AFM can thus be used to measure adhesion [99], hardness, or deformability of samples. Many probe–sample interaction mechanisms can be studied.

For example, the spatial adhesion map for a  $5 \times 5\ \mu\text{m}^2$  mica surface contaminated by organic compounds is shown in Fig. 5a. The outward movement (withdrawal) of the cantilever (sections d–e, e–f and f–g of the force–distance curve shown in

Fig. 3a) was monitored and plotted. The pull-off force contrast in adhesion map images was adjusted to range between 0 nN (white pixel in the upper left corner of each image) and 20 nN (black pixel in the upper left corner of each image). For the cleaved mica surface, a mean pull-off force of 19 nN and a variance (i.e., squared standard deviation) of 3 nN<sup>2</sup> were calculated from the best fit of a normal distribution to the pull-off force histogram.

Adhesion maps can be constructed by measuring the vertical displacement of the sample, driven by the piezoscanner, with respect to its displacement when the cantilever is at rest position. Force curves can be digitally acquired at 100 or more points equally spaced from each other over the scanned area of the surface. Each force curve is comprised of a row of a maximum of 250 data points acquired during the vertical movements of approach and withdrawal of the cantilever; software is used to create the adhesion maps (Fig. 5b).

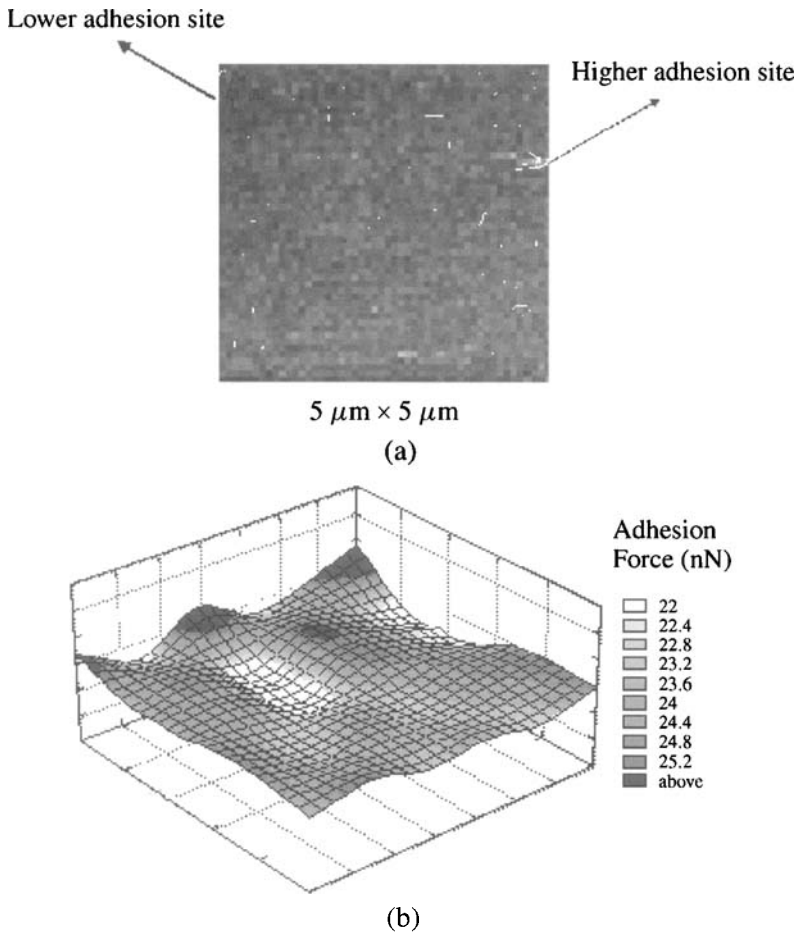


**Figure 5.** (a) A  $5 \times 5 \mu\text{m}$  map of the pull-off force recorded with a  $\text{Si}_3\text{N}_4$  AFM tip on a contaminated mica surface; (b) adhesion map plot illustrating the variability of the adhesion force on mica in air.

Tapping mode AFM (IC–AFM) has also been used to map tip–surface interactions [100, 101]. In this mode, the cantilever oscillates at its resonant frequency at a position just above the surface, so that the tip is in contact with the surface for only a very short time. A feedback loop ensures that the amplitude of the cantilever oscillation remains almost constant. It is possible to measure the phase difference between the driving oscillation and the detected cantilever oscillation, generating a phase difference map. An increase in the phase difference arises from a stronger tip–sample interaction, creating contrast in the phase map [102]. However, there are still problems associated with many of the alternative methods for determining tip–sample interactions. Although, the image contrast is very much under discussion [103].

Another possibility is to use the so-called dynamic mode AFM operated in the frequency modulation mode (FM–AFM). Schirmeisen *et al.* [104] measured metal–polymer adhesion properties by dynamic force spectroscopy with functionalisation of the tip by a thin layer of aluminum, while the polymer was plasma-etched. They found that plasma etching of the polymer resulted in strongly enhanced interactions, indicating a chemical activation of the polymer surface. Sokolov *et al.* [105] analyzed the possibility of using noncontact atomic force microscopy to detect variations in surface composition, i.e., to obtain a ‘spectroscopic image’ of the sample. The authors concluded that long-range forces acting between the AFM tip and the sample depended on the composition of both tip and sample. They showed theoretically how van der Waals forces could be utilized for force spectroscopy. Various results have been achieved in detecting the van der Waals interactions by use of molecular dynamics (MD) simulations and AFM measurements [106–108].

### 2.3. Chemical force microscopy

Adhesion is governed by short-range intermolecular forces which in many cases can be controlled by appropriate surface modification. This provides a specific chemical functionality on the probe surface. This technique is known as chemical force microscopy (CFM) [109–113] and it can be used to evaluate the strengths of specific forces of attraction directly and adds chemical interaction to a mechanical surface probe [114]. The AFM tip is first covered with an ordered monolayer of organic molecules (a self-assembled monolayer) to give it a specific chemical functionality. The force of interaction can be estimated from the excess force required to pull the tip free from the surface. The functionalization of the cantilever surface is a methodology that has been applied to biosensors [115].

Development of CFM has enabled investigation of the adhesion [116–118] and friction [119–121] between surfaces in close, molecular contact and the measurement of nanometer-scale tribological phenomena [122]. Starting around 1993, several papers have been published on the topic of CFM. The pull-off force, friction force measurements [123–125] and also simulations using molecular dynamics (MD) have been used to investigate the indentation and friction properties of SAMs and the rupture of films bonded to solid substrates [126–128]. CFM

is a newly emerging method introduced recently for probing surface chemical composition with high resolution [110, 129].

One of earliest examples used tungsten tips to perform force measurements on two chemical monolayers [85], demonstrating that it was possible to distinguish between two self-assembled monolayers (SAMs), one terminating in  $\text{CH}_3$  groups and the other in  $\text{CF}_3$ , simply by comparing the force–distance curves obtained from each surface. The investigation of force sensing has made rapid progress with the incorporation of surface chemistry techniques to bind specific chemical groups to the AFM tip [130]. An approach often employed is to produce gold-coated tips, which are modified with SAMs of thiol compounds terminated in a chosen functional group (Fig. 6). There is an extensive literature on the subject which should be referred for more detailed information on the formation and properties of self-assembled monolayers [131–133].

The functionalized tips can then be used in force–distance curve measurements. The general idea, in this case, is to probe the adhesion forces between the tip and the surface, both with well-defined chemical composition. This type of chemical functionalization is used in some research laboratories because of the well-defined surface properties of monolayers studied [134–137]. The most consistent pull-off force studies involving  $\text{CH}_3$ -terminated monolayers have been done in liquid environments [138–144].

It is important to understand and characterize the fundamental interactions between different tips and sample surfaces under different environmental conditions. Eastman and Zhu [145] measured the adhesion force between modified AFM tips and a mica substrate by atomic force spectroscopy. The results show that the ad-

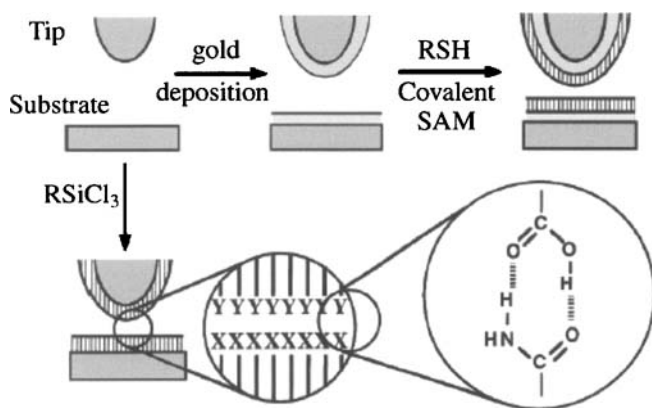


**Figure 6.** Scheme for chemical modification of tips and sample substrates. Tips and substrates are first coated with a thin layer of Au (50–100 nm) and then, upon immersion in a solution of organic thiol, a dense SAM is formed on the Au surface. Similarly, cleaned Si or  $\text{Si}_3\text{N}_4$  tips can be derivatized with reactive silanes. The functional groups comprise the outermost surface of the crystalline SAM, and the tip–sample interaction can be fine-tuned by varying the chemistry at the free SAM surfaces. The R in RSH and  $\text{RSiCl}_3$  represents an organic alkyl chain that ends with a functional group X ( $\text{X} = \text{CH}_3$ ,  $\text{COOH}$ ,  $\text{CH}_2\text{OH}$ ,  $\text{NH}_2$ , etc.) (reprinted with permission from Ref. [132]).

hesion force is sensitive to the surface energies of the materials coated on the tips, e.g., the adhesion force between a gold-coated tip and a mica surface is much larger than that between a paraffin-coated tip and a mica surface. The authors also show that both the van der Waals and capillary forces between the AFM tip and the substrate can account for this behavior of the adhesion forces. There have been only a limited number of attempts to correlate the measured adhesion forces and energies predicted by interfacial energy theories [123, 146, 147]. This is due to the difficulty in calculating the interfacial energy from the directly-measurable adhesion force, mainly because of the continuing uncertainty whether the Johnson–Kendall–Roberts (JKR) [148] or the Derjaguin–Muller–Toporov (DMT) [149] theory of the adhesion contact should be applied to analyze the adhesion forces between the tip and the substrate.

Beach *et al.* [150] measured pull-off forces between hexadecanethiol monolayers, self-assembled on gold-coated silicon nitride cantilever tip and silicon wafer, using AFM. The authors concluded that the AFM technique appeared to be a very useful tool in the examination of surface free energy of engineered materials. The surface energy of the self-assembled monolayer of hexadecanethiol was calculated to be in the range  $24.28 \pm 6.61$  to  $26.93 \pm 9.57$  mJ/m<sup>2</sup> using the measured pull-off force values. These values are between the values reported in the literature from contact angle and force curve measurements. Duwez and Nysten [136] used tips modified with methyl- and hydroxyl-terminated alkanethiols and showed that AFM tips functionalized with alkanethiol SAMs could be utilized to map the distribution of adhesion forces on polypropylene (PP) surfaces (Fig. 7). The image in Fig. 7 shows the lateral distribution of pull-off forces. The authors also found evidence for additives migrating toward the surface and modification of additive distribution on the surface due to material aging, utilizing laterally resolved adhesion force maps [151].

Recently, a study of the effect of topography on chemical force microscopy was carried out using adhesion force mapping [152]. The authors determined the distribution of adhesion forces measured in water by pulsed-force-mode atomic force microscopy (PFM–AFM). The peaks with the higher adhesion forces were attributed to the hydrophobic interactions between the CH<sub>3</sub>-terminated surfaces of the tip and the patterned sample in water. The results showed that variation in the grain sizes and in the multiplicity of contacts between the tip and convexities of the grains resulted in differences in the width of the distribution of the observed adhesion forces.

#### 2.4. AFM colloidal probe technique

A fundamental understanding of the factors controlling adhesion and the possible development of adhesion-free surfaces can potentially benefit greatly from direct measurements of the strength of adhesion interactions. A number of studies have been carried out using the surface force apparatus technique (SFA) [153]. However, SFA requires molecularly smooth crossed cylindrical samples with a radius of

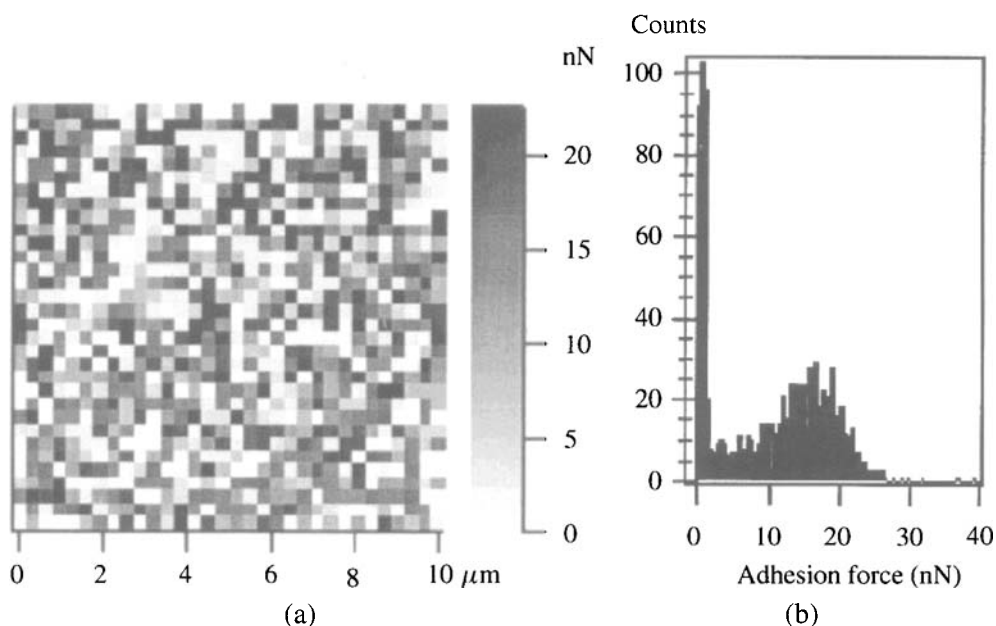


**Figure 7.** Typical adhesion map obtained on a few regions of the polypropylene surface with a  $\text{CH}_3$ -terminated tip in water (a); histogram of adhesion force distribution corresponding to the adhesion map (b) (reprinted with permission from Ref. [151]; copyright 2001 American Chemical Society).

the order of 1 cm. Thus, the development of the AFM has provided another experimental option for the measurement of surface forces which does not require a large smooth cross-section. Of special note is the use of colloidal probes, formed by attaching a single particle in the size range  $1\text{--}20\text{ }\mu\text{m}$  to the cantilever [154–158]. Examples of the cantilever with attached particle are shown in Fig. 8.

Bowen *et al.* [156] used AFM to quantify the adhesion interaction between a silica sphere and a planar silica surface. The authors found that the experimentally measured adhesion forces depended on sample preparation and solution pH and that the adhesion of such surfaces was a complex phenomenon in which non-DLVO (Derjaguin–Landau–Verwey–Overbeek) interactions probably played a substantial overall role. AFM tips with a well-defined silica colloidal particle have also been used to measure the adhesion of lactose carriers [159]. With this method, maps of adhesion between an individual lactose particle and gelatin capsules have been obtained [160].

Cho and Sigmund [161] suggested using a multi-walled carbon nanotube (MWNT) as a micrometer-length spacer and as a nanosized probe. This small-size probe is generally used for high-resolution imaging of topography of the sample. They proposed a systematic approach for data collection with a nanosize colloidal probe and an example of a directly measured surface force curve obtained with the MWNT probe was presented. Finally, the use of MWNT in the conventional liquid mode

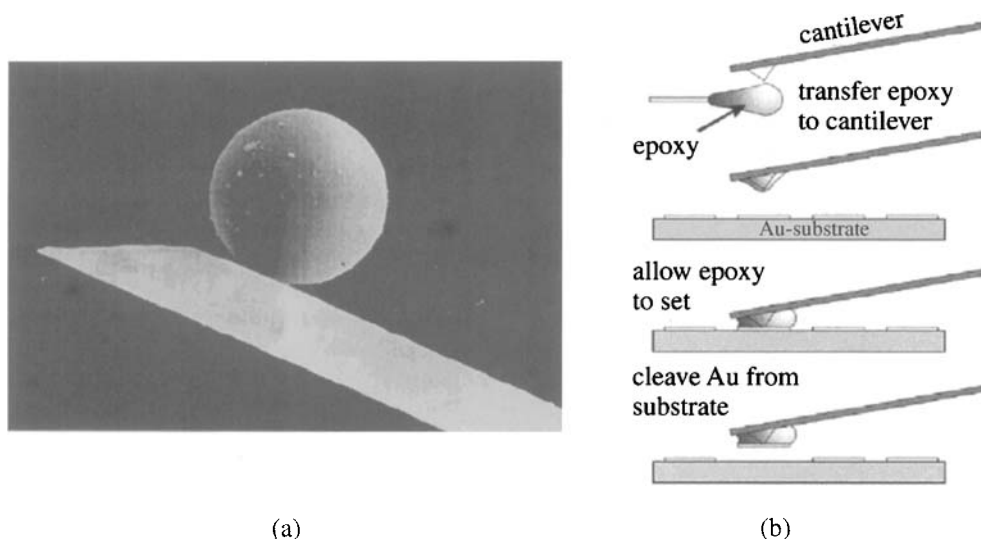


**Figure 8.** (a) Scanning electron micrograph of an 18  $\mu\text{m}$  polyethylene (PE) particle at the end of an AFM cantilever (2000  $\times$ ). (Reprinted with permission from Ref. [165]; Copyright 2003 American Chemical Society.) The particle was glued to the AFM cantilever with a small amount of epoxy resin using a procedure described in Ref. [158]. (b) Epoxy-based modification of cantilevers. Using commercially-available AFM cantilevers with integral tips, the free terminus of cantilever was coated with an epoxy resin. This epoxy-laden cantilever was then placed in direct contact with the sample. When the epoxy hardened, a portion of the sample was mechanically torn from the substrate to produce a cantilever-supported sample (reprinted with permission from Ref. [166]; copyright Elsevier).

of AFM opens the possibility of directly measuring the interaction force. Other authors have used a carbon nanotube as an STM or AFM probe [162–166].

### 3. APPLICATION OF ATOMIC FORCE SPECTROSCOPY TO THE STUDY OF ADHESION FORCES

#### 3.1. Adhesion mechanics

In general, the total adhesion force (pull-off force) between an AFM tip and a sample surface should include the capillary force ( $F_{\text{cap}}$ ), as well as the solid–solid interactions, which consist of van der Waals forces ( $F_{\text{vdw}}$ ), electrostatic forces ( $F_e$ ) and the chemical bonding forces ( $F_{\text{chem}}$ ).

If the measurement of the pull-off force is made in the presence of a ‘dry’ atmosphere, like nitrogen or vacuum, the adhesion force,  $F_{\text{adh}}$ , is due mainly to dispersion forces. Much of the present understanding of elastic adhesion mechanics (adhesion and deformation) of spheres on planar substrates is based on the theoretical work of Johnson, Kendall and Roberts (JKR) [148] and of Derjaguin, Muller and Toporov (DMT) [149]. Thus, studies of adhesion require application of either the JKR or the DMT theory. For a dissimilar sphere/flat system, in the



Derjaguin approximation, one can write:

$$F_{adh}^{DMT} = 2\pi R_t \varpi_{ikj}, \quad (3)$$

where  $\varpi_{ikj}$  is the work of adhesion between two surfaces  $i$  and  $j$  in a medium  $k$  and  $R_t$  is the tip radius.

In the JKR theory, separation will occur when the contact area between the surfaces is  $a_{adh} = 0.63a_0$ , where  $a_0$  is the contact area at zero applied load. This separation will occur when the pull-off force is:

$$F_{adh}^{JKR} = -\frac{3}{2}\pi R_t \varpi_{ikj}. \quad (4)$$

When plastic or elasto-plastic deformation occurs, both the DMT and JKR analyses do not hold. Instead, the Maugis and Pollock (MP) analysis [167] can be used, at least when full plasticity occurs. The MP analysis gives the pull-off force as [168]:

$$F_{adh}^{MP} = \frac{3\pi \varpi_{ikj} K}{2(\pi H)^{3/2}} P^{1/2}, \quad (5)$$

where  $H$  is the hardness of the yielding material,  $K$  is reduced Young's modulus and  $P$  is applied load. Generally, for ideally smooth surfaces the theoretically predicted  $F_{adh}^{DMT}$  and  $F_{adh}^{JKR}$  represent the lower and the upper limits of the experimentally measured  $F_{adh}$ , respectively. Hence, one can write [169]:

$$F_{adh} = -\alpha_a R_t \varpi_{ikj}, \quad (6)$$

where  $\alpha_a$  is a constant with values between  $(3/2)\pi$  (for soft materials) and  $2\pi$  (for hard surfaces). The JKR model should appropriately describe the adhesion for large spheres with high surface energies and low Young's moduli, while the DMT model should be appropriate for describing adhesion of small spheres of low surface energies and high Young's moduli.

To decide on which model to use, the parameter  $\mu$  is used, as suggested by Tabor [170]:

$$\mu = 2.92 \left( \frac{\varpi_{ikj}^2 R_t}{K^2 z_0^3} \right)^{1/3},$$

where  $z_0$  is the equilibrium size of the atoms at contact. Tabor suggested that when  $\mu$  exceeds unity, the JKR theory was applicable ( $\mu > 1$ ), otherwise the DMT model should be used ( $\mu < 1$ ).

Descriptions of the transition between these limits ( $\mu \approx 1$ ) are provided by Müller *et al.* [171], Maugis [172] and Johnson and Greenwood [173]. Contact area vs. load curves for each of the cases are shown in Fig. 9a [174]. The Maugis–Dugdale (M-D) theory can be expressed mainly in terms of a single non-dimensional parameter, the

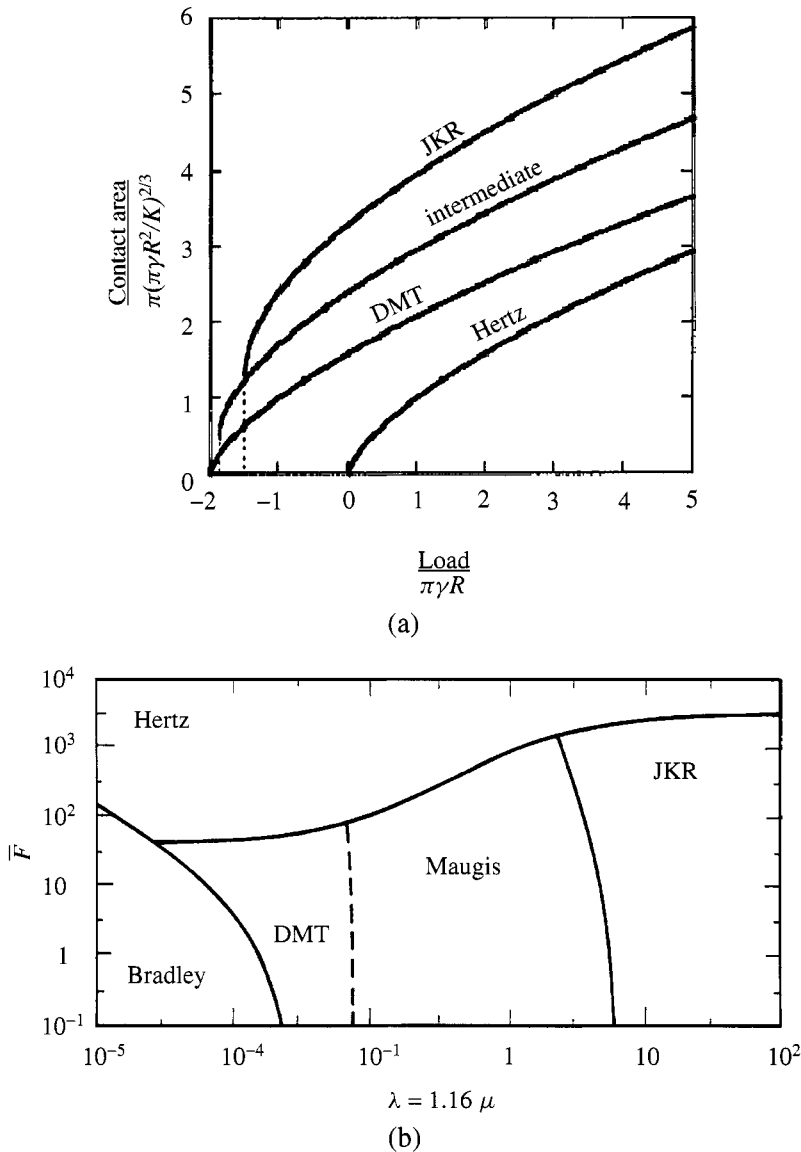


**Figure 9.** JKR–DMT transition. (a) The relationship between contact area and load for an elastic sphere contacting a plane depends upon the range of attractive surface forces. Area–load curves for the JKR limit (short-range adhesion), DMT limit (long-range adhesion), and an intermediate case are shown. All of these approach the Hertz curve in limit  $\gamma \rightarrow 0$  (no adhesion). Load and area are plotted in nondimensional units as indicated (reprinted with permission from Ref. [174]; copyright 1997 American Chemical Society). (b) Map of the elastic behavior of bodies. When the adhesion is negligible, deformations fall in the Hertz limit (approximately  $F > 10^3 \pi \omega R$ ); when the adhesion is small the behavior of materials is described by the DMT theory (approximately  $10^{-2} < \lambda < 10^{-1}$ ), whilst JKR theory predicts the behavior of bodies with high adhesion (approximately  $\lambda > 10^1$ ). The Maugis theory suits the intermediate region (approximately  $10^{-1} < \lambda < 10^1$ ) (adapted from Ref. [175]).

## **Interaction force measurements using atomic force microscopy for characterization and control of adhesion, dispersion and lubrication in particulate systems**

MADHAVAN S. ESAYANUR<sup>1</sup>, SURESH B. YERUVA<sup>1</sup>,  
YAKOV I. RABINOVICH<sup>2</sup> and BRIJ M. MOUDGIL<sup>1,2,\*</sup>

<sup>1</sup> *Department of Materials Science and Engineering, University of Florida, Gainesville, FL 32611, USA*

<sup>2</sup> *Particle Engineering Research Center, 205 Particle Science and Technology Building, University of Florida, Gainesville, P. O. Box 116135, FL 32611, USA*

**Abstract**—Atomic force microscopy is used as a vital tool in understanding the fundamental mechanisms of particulate processes in dry, humid and aqueous systems. Adhesion forces in both dry and humid systems were studied between surfaces of varying roughness, taking into account the capillary forces at high humidity conditions. Colloidal stability in aqueous systems due to non-DLVO forces and steric effects of surfactant aggregates formed on particle surfaces at varying pH and ionic strength conditions were investigated. The force–distance curves obtained by atomic force microscopy were used to determine the mechanical and thermodynamic properties of the self-assembled surfactant structures formed on the surface. Besides determining the repulsive force barrier provided by the surfactant aggregates in dispersion of slurries, the frictional interactions between surfactant adsorbed surfaces were measured using lateral force microscopy, providing valuable insights into the role of dispersants acting as lubricants. The range of interaction forces that can be explored using the Atomic Force Microscopy (AFM) can be utilized to predict, optimize and design a variety of industrially relevant processes such as chemical mechanical polishing (CMP), powder flow and handling and nano-dispersions, just to name a few.

**Keywords:** Adhesion; atomic force microscopy; nanoscale roughness; capillary force; friction force; nanotribology; surfactant; colloid stability.

### **1. INTRODUCTION**

Most industrial processes involve dry or aqueous colloidal systems, and the interaction forces in these systems need to be tuned according to the processing conditions

---

\*To whom correspondence should be addressed. Tel.: (1-352) 846-1194. Fax: (1-352) 846-1196.  
E-mail: [bmoudgil@erc.ufl.edu](mailto:bmoudgil@erc.ufl.edu)

for optimal performance. Controlling the process and product quality based on the interaction forces requires accurate measurement and modeling of the force laws in relation to the relevant process variables. Atomic force microscopy (AFM) has enabled direct measurement of nano- to pico-scale forces over atomic scale distances, which was inaccessible before. The interaction forces involved can be delineated using AFM to formulate precise theoretical expressions and manipulate the associated macroscopic properties to design and formulate optimally performing systems of practical relevance.

The interaction of two surfaces is usually dictated by the balance between the fundamental forces such as the van der Waals and the electrostatic forces (including ion-electrostatic and dispersion forces) as described by the Derjaguin–Landau–Verwey–Overbeek (DLVO) theory [1, 2]. In most cases, the interaction is not limited to these forces, alone and may include specific forces such as solvation, hydration, structural and hydrophobic forces, sometimes termed non-DLVO forces. Additionally, steric, hydrodynamic and frictional forces may also need to be considered in specific systems. The understanding of most industrially relevant phenomena such as particle adhesion and dispersion are based on the DLVO theory and other contact mechanics models such as the Hertz model [3], the Johnson–Kendall–Roberts (JKR) model [4] and the Derjaguin–Muller–Toporov (DMT) model [5]. The first systematic attempt at understanding the role of roughness in the interaction forces was made in terms of the Rumpf model [6]. The introduction of the AFM provided the capability of verifying the applicability of these theories to different length scales and revealed their limitations, thus necessitating the development of better models.

This paper presents highlights of the use of the AFM as a measurement tool, aiding in modeling and verification, at the Particle Engineering Research Center (PERC) for predicting and optimizing colloidal interactions for formulating optimal performing slurries and coatings. Specifically, the results presented focus on:

- (a) the effect of roughness on the adhesion force between surfaces in dry systems and the role of atmospheric moisture encountered in practice;
- (b) AFM studies on the measurement of non-DLVO forces in silica systems to delineate the role of surface hydration or formation of a surface gel layer;
- (c) finally, the importance of colloidal stability in concentrated aqueous systems, with an emphasis on the interplay between the dispersion and lubrication properties of surfactants, which are used to stabilize colloidal systems under extreme conditions such as those encountered in chemical mechanical planarization (CMP).

## 2. ADHESION FORCE IN DRY SYSTEMS

Most engineering surfaces, regardless of the method of preparation, exhibit some finite surface roughness. For many modern materials, particularly in the microelectronics industry, the requirement for highly polished surfaces with roughness on the

angstrom scale is becoming increasingly common. Particle adhesion to these surfaces is of critical importance due to the possibility of defects caused by adhered particles in applications such as micro-electro mechanical systems (MEMS) and nanotechnology. The existence of nanoscale roughness is known to dramatically reduce adhesion between surfaces due to decrease in the real area of contact and increase in the separation distance between the bulk surfaces [4, 7–10]. To understand the effect of surface roughness at the nanometer scale, the adhesion force must be accurately measured for very small deviations from ideally smooth surfaces. For this purpose, plates with controlled roughness were fabricated by deposition of aluminum thin films (10–100 nm thick) on silicon wafer substrates [11, 12]. The AFM was used to characterize these surfaces with regards to the local topography and the adhesion force. The root mean square (RMS) roughness of the substrates was measured using the AFM on a scan size of  $1.5 \mu\text{m}^2$ . Adhesion force measurements were made with either an AFM silicon nitride tip or a glass sphere attached to the cantilever. Since the radius of the glass sphere was much larger than the scale of the roughness, it was expected that contributions from both the contact and non-contact forces could be significant. In the case of the AFM tip, the radius of curvature of 10 nm as measured using scanning electron microscopy (SEM) was smaller than the scale of the surface roughness (10–20 nm). As a result, the contact force was expected to dominate the interaction, and the adhesion force values were expected to be much closer to those predicted for the interaction of smooth surfaces. Comparing these two geometries, the importance of the relative magnitude of the roughness compared to the size of the adhering particle can be revealed.

All the AFM force–distance curves were measured at a frequency of 1 Hz and the spring constant of the cantilevers was determined using the method of Cleveland *et al.* [13]. The force of adhesion between nanoscale rough surfaces was calculated from pull-off force measurements made with an AFM. The experiments were performed in ambient air at a relative humidity of 45% as measured using a Fisher Scientific hygrometer. The particle on the AFM tip was brought in contact with the substrate and the adhesion force was measured from the pull-off point on the force-distance curve. No additional loading force was applied during the point of contact. The results validated previous investigations at larger roughness, where a decrease of adhesion force as a function of roughness was reported [14, 15]. Measurement of adhesion force was also performed at lower roughness than previously reported. It was experimentally determined that a root mean square (RMS) roughness value of 1.6 nm was enough to significantly decrease the force of adhesion by nearly a factor of five compared to the theoretical adhesion force between two smooth surfaces as predicted by equation (1). The magnitude of reduction in the adhesion force was additionally found to have a strong dependence on the radius of the probe (sphere or tip) contacting the surface (Fig. 1). When the adhesion force was measured with an AFM tip, whose radius was of the same order or smaller than the peak-to-peak distance or radius of the asperities, the decrease in adhesion force of a surface with roughness of 1.6 nm RMS was only 1.5 times, thus

more closely approximating the contact of an ideally smooth sphere and flat surface. The observed effect of nanoscale surface roughness on the dramatic reduction of the adhesion force could have a significant implication in the design and modeling of many industrial processes such as particulate coatings and de-dusting, and this necessitated the development of a reliable predictive model for the adhesion force.

The key to predicting the adhesion force as a function of surface topography is to model the roughness in a manner that more closely resembles the true geometry of the surfaces. The PERC model was developed through a theoretical analysis of the surface topography measured experimentally using the AFM [11, 12]. The surface topography was described mathematically using both the height and breadth of the asperities, which were expressed as RMS roughness and peak-to-peak distance,  $\lambda$ , respectively. The force of adhesion,  $F$ , scaled by the particle radius,  $R$ , was expressed as:

$$\frac{F}{R} = \frac{A}{6H_0^2} \left[ \frac{1}{1 + \frac{58.14R \cdot RMS}{\lambda^2}} + \frac{1}{\left(1 + \frac{1.817RMS}{H_0}\right)^2} \right], \quad (1)$$

where  $A$  is the Hamaker constant and  $H_0$  is the minimum separation distance (0.3–0.4 nm). The local radius of the surface asperities determined by this method was much larger as compared to the previous models [10, 16]. The PERC model, using a van der Waals force based approach, predicts the force of adhesion within

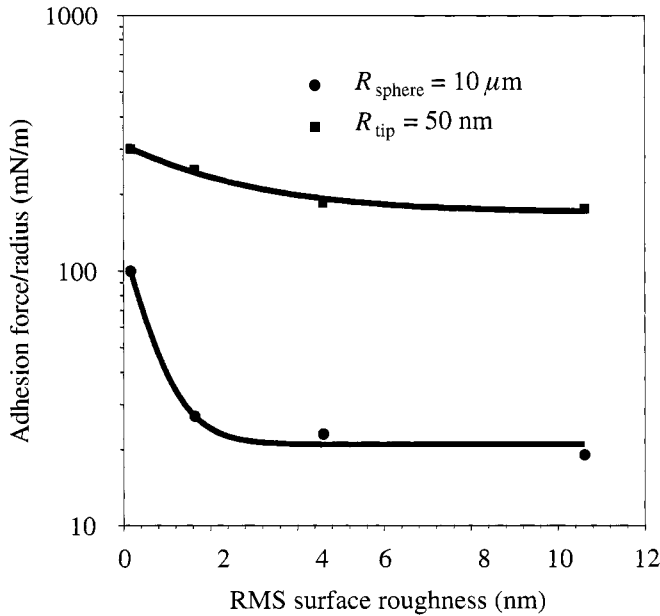


**Figure 1.** Experimentally measured normalized adhesion force between a glass sphere or AFM tip and model substrates as a function of increasing nanoscale roughness. The solid line is a graphic representation of the trend observed in the measured values.

50% of experimental values, whereas previous models, Rumpf model [6] and the modified Rumpf model [12], underestimated the adhesion force by 10–50 times. Application of the proposed roughness geometries with the JKR model was found to further reduce the discrepancy, although fitting values for the work of adhesion were used [17]. More recently, Beach *et al.* have used the AFM to determine the work of adhesion of rough solids [18] based on pull-off measurements and their results are in good agreement with the PERC model. The model can be further improved by including the polar interactions that can be significant during contact of low RMS roughness surfaces. The PERC model has been extended for the case of adhesion between surfaces in the presence of relative humidity and is used to develop equation (2) as discussed in the following section.

### 3. EFFECT OF RELATIVE HUMIDITY

Relative humidity is another practical parameter encountered in fine powder (approx. less than 100  $\mu\text{m}$ ) handling, and the resultant capillary forces contribute significantly to the adhesion force between the particles. A systematic investigation was conducted at the PERC to evaluate the role of humidity in adhesion between surfaces with nano-scale roughness. The simplified geometry of liquid bridges between an ideal smooth solid sphere and flat substrate for varying humidity conditions is shown in Fig. 2. At any given circumstance, depending on the relative humidity, only one of the two radii would exist and the bridge would be symmetric. This geometry was the basis for the theoretical framework developed to predict the onset and magnitude of capillary and dry adhesion forces in the presence of nanoscale roughness [19]. The force of adhesion ( $F$ ) of a particle of radius  $R$  to a flat surface as a function of separation distance,  $H$ , at a given relative humidity was expressed as:

$$\frac{F}{R} = 4\pi\gamma \cos\theta \left[ 1 - \frac{1.82 \cdot \text{RMS}}{2r \cos\theta} \right], \quad (2)$$

where  $\gamma$  is the surface tension of the liquid and  $\theta$  is the contact angle of the liquid on the particle surface. RMS is the root mean square roughness of the surface

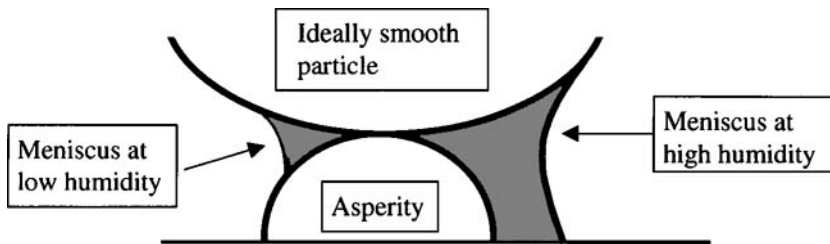


**Figure 2.** Schematic illustration of the meniscus formed in a capillary created by the adhesion of an ideally smooth particle to an asperity on a flat substrate for varying humidity conditions [19].

and  $r$  is the equilibrium radius of the liquid bridge at the given relative humidity as calculated by the Kelvin equation [20]. This basic framework was validated with direct measurement of surface forces using the AFM. Capillary adhesion was substantially lower in the presence of nanoscale roughness as shown in Fig 3. The points in the figure represent the experimental data and the solid black line is the theoretical estimate using equation (2). The values of RMS roughness shown in Fig. 3 were used as fitting parameters for equation (2) and these values were in good agreement with directly measured values of roughness of the substrates. In addition to the lowering in the magnitude of the adhesion force, the critical relative humidity, where capillary forces are first observed, increased with the nanoscale roughness. Although higher scales (micrometer level) of roughness may be present on real surfaces, it is suggested that the smallest scale (nanoscale) roughness contributes primarily to the reduction in adhesion between the surfaces [19]. The reduction in adhesion in the dry state is due to decrease in contact area and increase in the separation distance between the bulk surfaces. This phenomenon is of significant practical relevance when de-dusting or detachment of fine particles from surfaces is required, or where powder caking might occur.

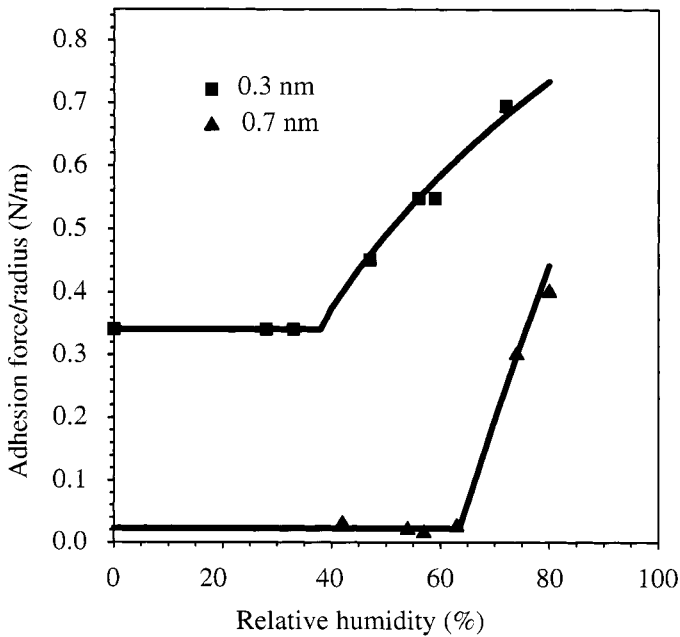


**Figure 3.** Adhesion force measured between a smooth glass sphere and silica surfaces of two different roughnesses as a function of relative humidity. The points in the figure represent the experimental data and the solid black line is the theoretical estimate using equation (2). The values of RMS roughness shown in the figure were used as fitting parameters for equation (2) and these values were in good agreement with directly measured values of roughness of the substrates.



## 4. AQUEOUS SYSTEMS

### 4.1. Silica gel layer

Traditional and advanced technologies, such as controlled drug-delivery systems, abrasives for precision polishing, multifunctional coatings and nanocomposite materials, are increasingly relying on nanoparticulate precursor materials to achieve the best performance. Simultaneously, environmental and safety issues have driven industrial processes toward synthesis and processing in aqueous media. Silica surfaces are known to exhibit large repulsion forces at relatively short distances ( $<10$  nm) in aqueous solutions, which result in unusual colloidal stability even at a pH around the point of zero charge (pzc). These forces are not in agreement with the conventional DLVO theory and are termed non-DLVO forces. Three leading hypotheses have been proposed. The first suggests that the non-DLVO forces are due to the structuring of water at the silica surface [21]. Due to the limited conformations available to water molecules (low entropy) in the region close to the surface, repulsion is observed when two oriented layers overlap. The second hypothesis suggests that the non-DLVO forces between hydrophilic surfaces in electrolyte solutions are due to the hydration of ions (hydration force and charge regulation mechanism) and their adsorption on the surface [22]. The third hypothesis suggests that the water molecules may dissolve or diffuse into and swell the silica surface (gel) layer, causing steric repulsion due to silicic acid chains constituting the gel layer [23, 24]. Depending on the operating mechanism, these non-DLVO forces may have significant implications in rheological properties, colloidal stability, filtration, and chemical mechanical polishing of silica both as a substrate and/or an abrasive.

Interparticle forces were measured at the PERC between a Fisher Scientific borosilicate glass microscope slide and a Duke Scientific soda-lime glass microsphere (30–40 nm) on a Digital Instruments AFM with Nanoscope IIIa controller, in a fused silica liquid cell according to the methods described by Ducker *et al.* [25]. All glass surfaces were cleaned by rinsing in acetone and methanol followed by repeated rinsing with concentrated nitric acid and deionized water. After that they were boiled in acidified (pH 2–4) water for 24 h. Such a treatment has been reported for the Fisher finest glass slides to result in a surface that is primarily silica [26]. After the boiling treatment, the surfaces were subsequently heat treated at 600°C for 24 h. This treatment is expected to eliminate any adsorbed water on or in the glass surface. Additionally, treatment at temperatures greater than 500°C has been shown to significantly decrease the density and change the type of silanol groups on the silica surface [27]. Hence, it is expected that a gel layer on the treated sample would be thinner or nonexistent. After heat treatment, the rehydration time was kept to a minimum (of about 1 h) and the samples were used immediately for measurement.

Particle-surface interaction forces were measured for various electrolyte concentrations in the pH range 2–9. Attractive van der Waals forces were observed for

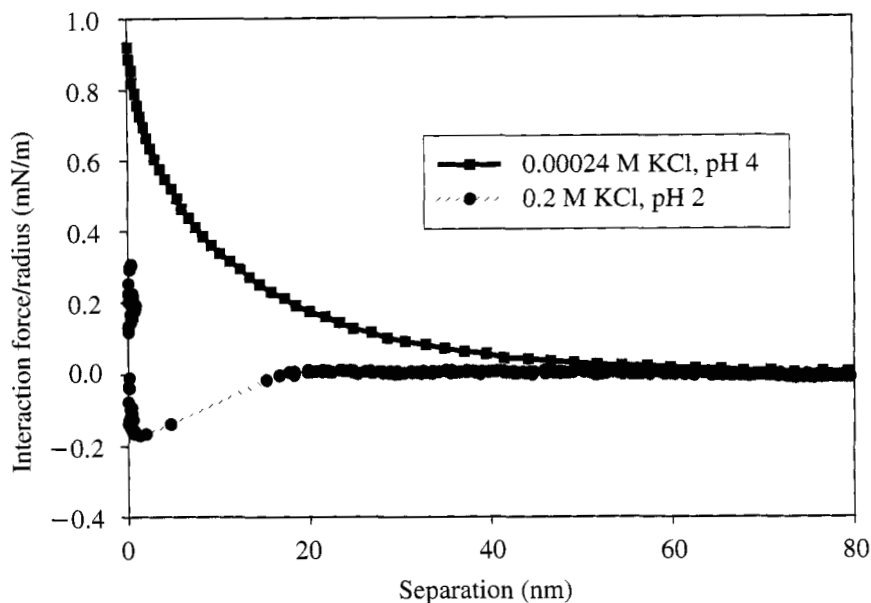


**Figure 4.** Experimentally measured force-distance profiles of the glass surfaces heated at 600°C. Only van der Waals attraction is measured between surfaces with low Stern potential and high electrolyte concentration (0.2 M KCl, pH 2).

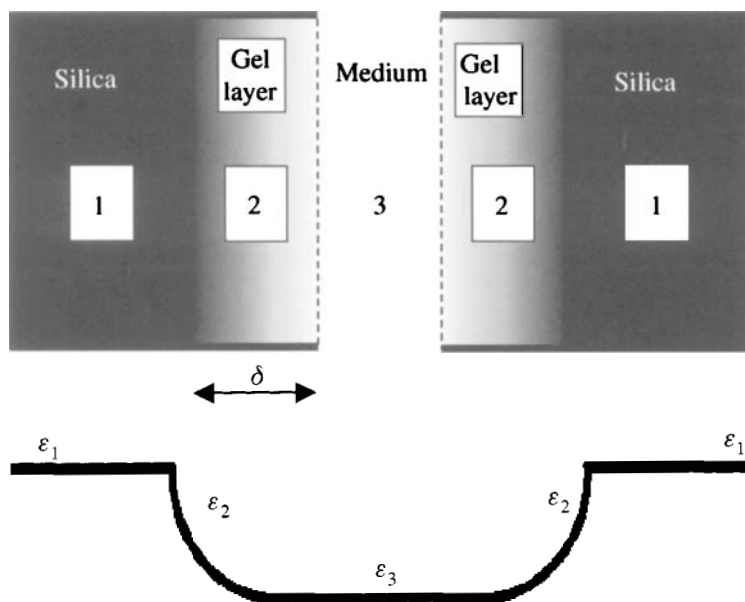


**Figure 5.** Schematic diagram of a five-layer model with smooth transition at each interface. The composition of the gel layer (layer 2) changes exponentially from bulk silica (layer 1) to bulk water (layer 3). The dielectric spectrum of layer 2 is not constant but varies between those of pure silica and pure water depending on position.

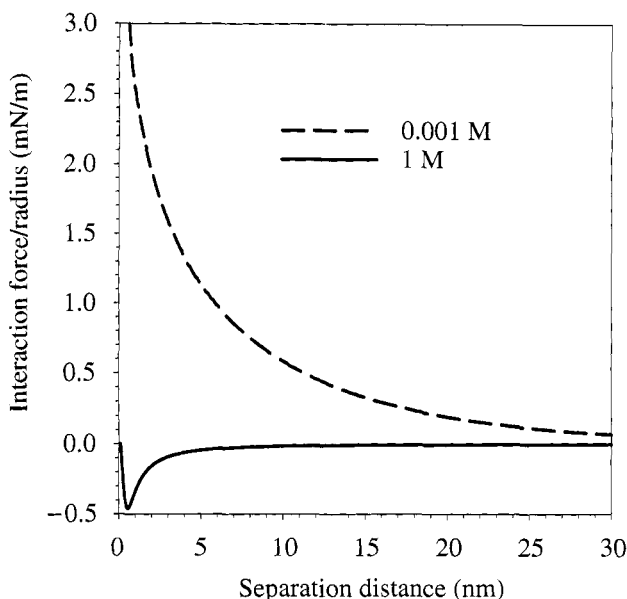


**Figure 6.** Theoretical force–distance profiles for a hypothetical silica surface with a gel layer of 2.0 nm thickness in a 1 : 1 electrolyte. The interaction conditions are 0.001 M and 1 M concentrations of 1 : 1 electrolyte, corresponding to surface potentials of  $-50$  mV (dotted line) and  $0$  mV (solid line), respectively. At low ionic strength and high surface charge the lack of attraction appears as an additional repulsive force. However, as ionic strength is increased van der Waals attraction begins to dominate and instability may occur.

surfaces with low Stern potential and high electrolyte concentration, whereas long-range repulsive forces were observed with no adhesion (van der Waals forces) for surfaces with high Stern potential and low electrolyte concentration (Fig. 4). The measured forces were attributed to the formation of a gel layer on silica, as a rigid surface swelled by water. The suggested hypothesis was modeled by calculating the decrease in van der Waals force that accompanies the formation of a gel layer as compared to the original silica surface. The method of Parsegian and Weiss [28] was modified to an exponential variation in the gel layer dielectric permittivity, as shown in Fig. 5. The modeling results are plotted in Fig. 6. Comparing the theoretical and experimental data using a Hamaker constant of  $14.2 \times 10^{-21}$  J, an average gel layer thickness, for the interaction of silica at pH 4, 6 and 9, was found to be approximately 2.0 nm [24].

#### 4.2. Surfactant-mediated suspension stability

The non-DLVO forces discussed so far are relevant in dispersion of selective systems only. But high performance industrial processes are leading towards dispersion of systems at extreme pH and electrolyte conditions. Electrostatic repulsion is often employed to stabilize homogeneous, low ionic strength suspensions where pH can be controlled in order to provide sufficient surface charge. However, with

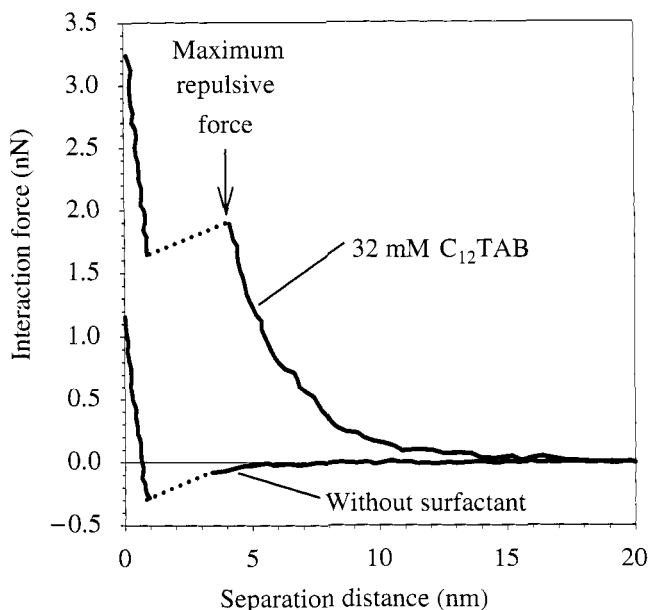


**Figure 7.** Measured interaction forces between an AFM tip and a mica surface in 0.1 M NaCl solution at pH 4, both with and without 32 mM of  $C_{12}$ TAB surfactant. The dotted line indicates the region of mechanical instability where the cantilever ‘jumps’ into contact with the surface.

all other forces being constant, the electrostatic repulsive energy between particles decreases proportionally with size, thereby necessitating an extraneous source to disperse nanoparticles. This requirement for a larger repulsive force may be too high to be achieved through pH adjustment. Addition of inorganic dispersants, such as sodium silicate, may not always lead to suspension stability under the given solid-loading conditions. Furthermore, many processes such as chemical mechanical polishing and crystallization must operate in extreme environments (high ionic strength, temperature, extreme pH, or high shear rate), where electrostatic stabilization alone may not be adequate to prevent agglomeration.

Adsorbed surfactant aggregates of alkyl trimethyl ammonium bromide ( $C_n$ TAB) at the solid–liquid interface were found to be effective dispersants under such conditions [29]. It was determined that the charge reversal process (due to the adsorption of oppositely charged surfactant) was not sufficient to produce a stable suspension in 0.1 M electrolyte solution. Instead, the steric repulsion due to elastic deformation of adsorbed surfactant aggregates was proposed as the primary stabilization mechanism at high ionic strength conditions. The repulsive force barrier measured using the AFM, as shown in Fig. 7 characterizes the steric repulsion encountered in these suspensions [29, 30]. Figure 8 demonstrates that the occurrence of the repulsive force correlates well with the stability of a suspension of 200 nm silica particles at pH 4. It confirms the critical role played by the force barrier in suspension stability. The formation of a repulsive barrier was found not

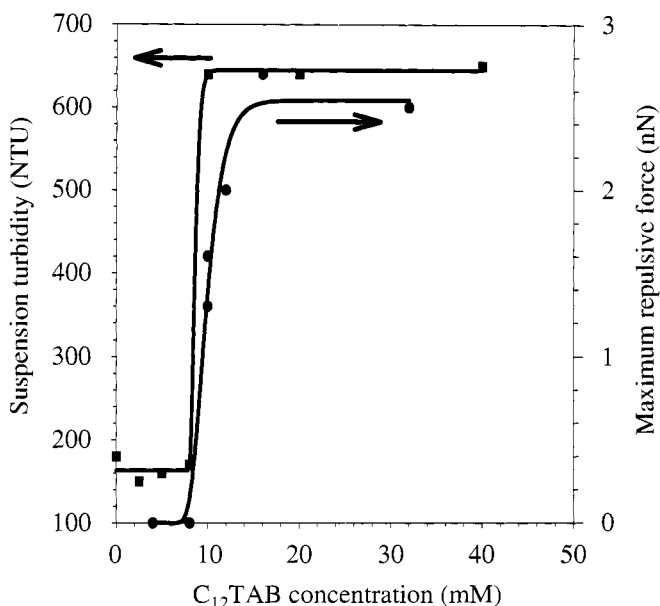


**Figure 8.** Turbidity in NTU (nephelometric turbidity units) of silica particles after 60 min in a solution of 0.1 M NaCl at pH 4 as a function of  $C_{12}TAB$  concentration, and the measured interaction forces between an AFM tip and silica substrate under identical solution conditions. A significant repulsive force arises upon a change in concentration from 8 to 10 mM  $C_{12}TAB$ , which directly corresponds to the formation of a stable suspension.

to correspond directly to the bulk critical micelle concentration (CMC). Instead, it appears at a concentration greater than the bulk critical hemi-micelle concentration but either below or just above the bulk cmc depending on the nature of the substrate as shown in Fig. 9. Possible mechanisms for this sudden appearance of repulsive forces include either a restructuring of the self-assembled surface surfactant layer, or a partial saturation of the surface resulting in limited mobility of the surfactant structures.

The AFM force–distance curves, as shown in Fig 10, were used to determine the mechanical and thermodynamic properties of micellar dispersant layers formed at the solid–liquid interface [31]. The elastic modulus and yield strength of these intervening steric layers significantly impact the particle–particle interactions during contact by modifying the mode and extent of deformation of the adsorbed surface layer under given loading conditions, such as those encountered in CMP. Similarly, the energy required for breaking these surface aggregates can be used to determine whether agglomeration will occur under a given applied pressure. The elastic modulus ( $E$ ) and the yield strength ( $Y$ ) were obtained through the use of a modified Hertz theory (Shull's method) that takes into account finite layer thickness effects [32]. Based on the Hertz model, the force,  $F$ , and the penetration depth,  $\delta$ ,

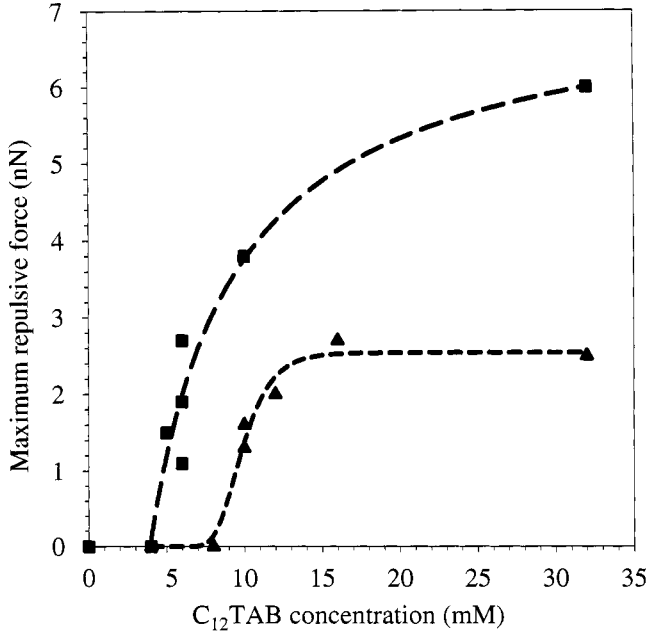


**Figure 9.** Maximum repulsive force as a function of C<sub>12</sub>TAB concentration in pH 4 solution between an AFM tip and a mica substrate with 0.1 M NaCl (squares and long dashed line), and a silica substrate with 0.1 M NaCl (triangles and short dashed line). The magnitude of the repulsive force and concentration at which they arise are dependent not only on solution conditions but also on the substrate material.

of the AFM tip are given, respectively, by equations (3) and (4) below.

$$F^H = \frac{3E}{2(1-\nu^2)} \frac{a^3}{R}, \quad (3)$$

$$\delta^H = \frac{a^2}{R}, \quad (4)$$

where the superscript H denotes the use of the Hertz theory,  $E$  is the elastic modulus,  $\nu$  is the Poisson ratio,  $R$  is the radius of the tip and  $a$  is the radius of the contact zone. For the case of a layer with a finite (small) thickness,  $h_o$ , Shull corrected the Hertz equations as follows:

$$\delta = \delta^H \left( 0.4 + 0.6 \exp \left( -\frac{1.8a}{h_o} \right) \right), \quad (5)$$

$$F = F^H \left( 1 + 0.15 \left( \frac{a}{h_o} \right)^3 \right). \quad (6)$$

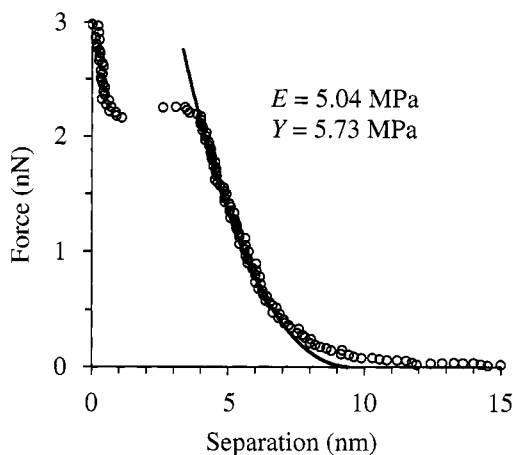


**Figure 10.** Experimental force–distance curve (circles) measured between an AFM tip and 1.8 mM C<sub>16</sub>TAB aggregates on a silica substrate at pH 5.8 in a 0.1 M NaCl solution. The theoretical (solid) curve is plotted using equations (5) and (6). The values of the elastic modulus,  $E$ , and yield strength,  $Y$ , of the aggregates based on the Shull method [32] were determined to be 5.04 MPa and 5.73 MPa, respectively.

The value of the yield stress,  $Y$ , was derived as:

$$Y = \frac{3F_m}{2\pi a_m^2} \quad (7)$$

where  $F_m$  and  $a_m$  represent, respectively, the force and contact radius at the point of rupture of the layer.

The derived values for the yield stress,  $Y$ , and the elastic modulus,  $E$ , increased linearly with chain length, i.e., the number of carbon atoms per chain for C<sub>10</sub>–C<sub>16</sub>TAB (alkyl trimethylammonium bromide) surfactants, and were comparable to those reported for elastomeric materials (e.g., poly(dimethylsiloxane) (PDMS)). It has been illustrated that using the classical form of the Hertz theory, without accounting for the underlying surface, the elastic modulus ( $E$ ) of these dispersant layers were overestimated by an order of magnitude. As a result, the values for the elastic modulus would be similar to that of more rigid polymeric materials (e.g., low-density polyethylene (LDPE)), which is unreasonable. The energy required to break a micelle was calculated by integrating the force–distance curves. These values were estimated to be of the same order of magnitude as the energy of micellization (or micelle breakage) for a single micelle in the bulk liquid.

The influence of intervening surfactant moieties on the frictional interactions between oxide surfaces was analyzed using lateral force microscopy (LFM) [33]. The extent of lubrication imparted by the quaternary amine surfactants was shown to increase to a maximum at the bulk CMC and plateaued at higher concentrations. It was illustrated that the reduction of friction imparted by the residual surfactant film depended predominantly on the number of strongly bound surfactant molecules at

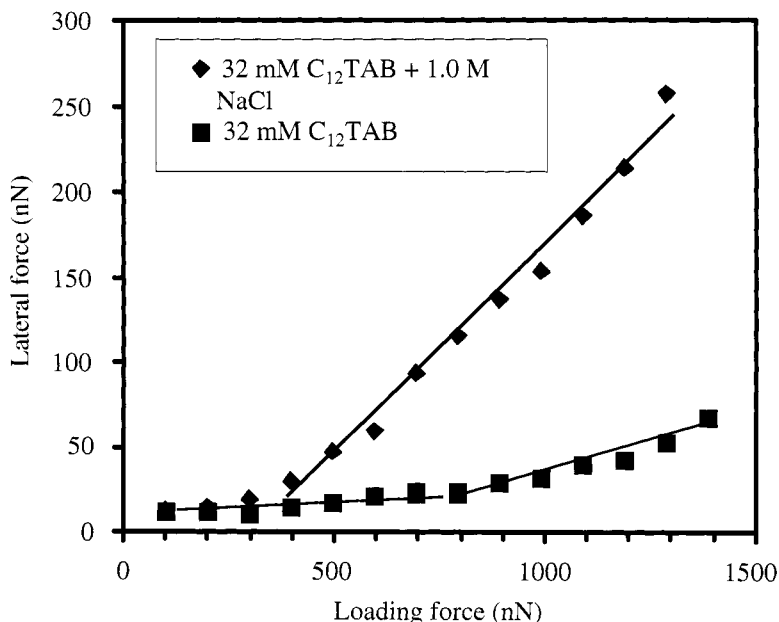


**Figure 11.** LFM measurement on a  $7.5\ \mu\text{m}$  diameter silica sphere interacting with a smooth silica surface in solutions of 32 mM of  $\text{C}_{12}\text{TAB}$  surfactant, in the presence and absence of 1 M NaCl.

the solid–liquid interface. Although these molecules may not exclusively take part in the reduction of friction force, they could serve as anchor points for adsorption of additional surfactant molecules (*via* hydrophobic chain–chain interaction), thereby governing the magnitude of lubrication that can be attained in the system.

By manipulating the extent of surfactant–surface affinity through change in the solution pH, ionic strength, or surfactant chain length, the extent of lubrication and the applied pressure above which the lubricating layer ceases to exist can be controlled as shown in Fig. 11. It was also demonstrated that the degree of lubrication exhibited by the surfactants could be manipulated without necessarily impacting their performance as dispersants through surface-affinity concepts [34]. The control of surfactant-mediated boundary lubrication as characterized by LFM was successfully implemented to devise optimal CMP slurry performance guidelines.

## 5. CONCLUSIONS

The advent of the AFM has facilitated the direct measurement of interaction forces and development of predictive models for determination of the adhesion force in the presence of nanoscale roughness. Surface roughness of the order of 2 nm RMS has been shown to result in an order of magnitude reduction in the force of adhesion. This has potential implications in the field of nanotechnology, in applications such as post-CMP cleaning, operation of micro-electro mechanical systems (MEMS),



where the scale of roughness is comparable to the size of the active components. The PERC roughness model can be used to accurately predict the force of adhesion in the presence of nanoscale roughness and humidity, thereby enabling reliable and robust design of industrial processes. In humid environments, increasing surface roughness increases the critical humidity required for the onset of capillary forces.

Colloidal stability in relatively high solids loading systems under extreme conditions can be achieved by creating a steric barrier due to the surfactant aggregate structures adsorbed at the solid-liquid interface. Guidelines for the design of robust and optimal performing dispersions were developed based on the repulsive force and friction force interactions. A typical application such as high performance slurry in the CMP process can be fine-tuned to provide stability (high repulsive force barrier) under extreme conditions (high ionic strength, pH), as well as optimal polishing performance (high friction force). All the results discussed in this study provide just a glimpse to the myriad of applications of the AFM in the field of colloid science.

### Acknowledgements

The authors acknowledge the financial support of the Engineering Research Center (ERC) for Particle Science and Technology at the University of Florida, The National Science Foundation (NSF) grant #EEC-94-02989, and the Industrial Partners of the ERC for support of this research. Any opinions, findings, and conclusions or recommendations expressed in this material are those of the author(s) and do not necessarily reflect those of the NSF.

### REFERENCES

1. B. V. Derjaguin and L. D. Landau, *Acta Physicochim. USSR* **14**, 633 (1941).
2. E. J. W. Verwey and J. Th. G. Overbeek, *Theory of the Stability of Lyophobic Colloids*. Elsevier, Amsterdam (1948).
3. H. Hertz, *Miscellaneous Papers*. McMillan, London (1896).
4. K. L. Johnson, K. Kendall and A. D. Roberts, *Proc. R. Soc. London, A* **324**, 301 (1971).
5. B. V. Derjaguin, V. M. Muller and Yu. P. Toporov, *J. Colloid Interf. Sci.* **53**, 314–326 (1975).
6. H. Rumpf, *Particle Technology*. Chapman and Hall, London (1990).
7. D. Tabor, *J. Colloid Interf. Sci.* **58**, 2–13 (1977).
8. B. J. Briscoe and S. S. Panesar, *J. Phys. D: Appl. Phys.* **25**, A20–A27 (1992).
9. H. Krupp, *Adv. Colloid Interf. Sci.* **1**, 111–239 (1967).
10. H. A. Mizes, in: *Advances in Particle Adhesion*, D. S. Rimai and L. S. Sharpe (Eds), p. 155. Gordon & Breach, Sydney (1996).
11. Y. I. Rabinovich, J. J. Adler, A. Ata, R. K. Singh and B. M. Moudgil, *J. Colloid Interf. Sci.* **232**, 10–16 (2000).
12. Y. I. Rabinovich, J. J. Adler, A. Ata, R. K. Singh and B. M. Moudgil, *J. Colloid Interf. Sci.* **232**, 17–24 (2000).
13. J. P. Cleveland, S. Manne, D. Bocek and P. K. Hansma, *Rev. Sci. Instrum.* **64**, 403–405 (1993).
14. K. Iida, A. Otsuka, K. Danjo and H. Sunada, *Chem. Pharm. Bull.* **41**, 1621–1625 (1993).
15. D. M. Schaefer, M. Carpenter, B. Gady, R. Reifemberger, L. P. DeMejo and D. S. Rimai, in: *Fundamentals of Adhesion and Interfaces*, D. S. Rimai, L. P. DeMejo and K. L. Mittal (Eds), p. 35. VSP, Utrecht (1995).

16. J. A. Greenwood and J. B. P. Williamson, *Proc. R. Soc. London, A* **295**, 300 (1966).
17. M. F. Ashby and D. R. H. Jones, *Engineering Materials I*. Pergamon, Oxford (1996).
18. E. R. Beach, G. W. Tormoen, J. Drelich and R. Han, *J. Colloid Interf. Sci.* **247**, 84–99 (2002).
19. Y. I. Rabinovich, J. J. Adler, M. S. Esayanur, A. Ata, R. K. Singh and B. M. Moudgil, *Adv. Colloid Interf. Sci.* **96**, 213–230 (2002).
20. A. W. Adamson, *Physical Chemistry of Surfaces*. Wiley-Interscience, New York, NY (1967).
21. B. V. Derjaguin and N. Churaev, *J. Colloid Interf. Sci.* **49**, 249–255 (1974).
22. J. N. Israelachvili and R. M. Pashley, *Nature* **306**, 249–250 (1983).
23. G. Vigil, X. Zhenghe, S. Steinberg and J. Israelachvili, *J. Colloid Interf. Sci.* **165**, 367–385 (1994).
24. J. J. Adler, Y. I. Rabinovich and B. M. Moudgil, *J. Colloid Interf. Sci.* **237**, 249–258 (2001).
25. W. Ducker, T. Senden and R. M. Pashley, *Nature* **353**, 239–241 (1991).
26. Z. Fu and M. Santore, *Colloid Surf. A* **135**, 63–75 (1998).
27. C. G. Armistead, A. J. Tyler, F. H. Hambleton, S. A. Mitchell and J. A. Hockey, *J. Phys. Chem.* **73**, 3947 (1969).
28. V. A. Parsegian and G. H. Weiss, *J. Colloid Interf. Sci.* **40**, 35 (1972).
29. J. J. Adler, P. K. Singh, A. Patist, Y. I. Rabinovich, D. O. Shah and B. M. Moudgil, *Langmuir* **16**, 7255–7262 (2000).
30. P. K. Singh, J. J. Adler, Y. I. Rabinovich and B. M. Moudgil, *Langmuir* **17**, 468–473 (2001).
31. Y. I. Rabinovich, I. U. Vakarelski, S. C. Brown, P. K. Singh and B. M. Moudgil, *J. Colloid Interf. Sci.* **270**, 29–36 (2004).
32. K. R. Shull, D. Ahn and C. L. Mowrey, *Langmuir* **13**, 1799–1804 (1997).
33. I. U. Vakarelski, S. C. Brown, Y. I. Rabinovich and B. M. Moudgil, *Langmuir* **20**, 1724–1731 (2004).
34. G. B. Basim, S. C. Brown, I. U. Vakarelski and B. M. Moudgil, *J. Dispers. Sci. Technol.* **24**, 499–515 (2003).

## Comparison of various adhesion contact theories and the influence of dimensionless load parameter

XINGHUA SHI and YA-PU ZHAO \*

*State Key Laboratory of Nonlinear Mechanics (LNM), Institute of Mechanics,  
Chinese Academy of Sciences, Beijing 100080, China*

**Abstract**—Three models, JKR (Johnson, Kendall and Roberts), DMT (Derjaguin, Muller, and Toporov) and MD (Maugis-Dugdale), are compared with the Hertz model in dealing with nano-contact problems. It has been shown that both the dimensionless load parameter,  $\bar{P} = P/(\pi \Delta \gamma R)$ , and the transition parameter have significant influences on the contact area at micro/nano-scale and should not be ignored in nano-indentation tests.

**Keywords:** Work of adhesion; elastic contact models; transition parameter; dimensionless load parameter.

### 1. INTRODUCTION

In recent years there has been considerable interest in the mechanical characterization of thin-film systems and small volumes of materials using depth-sensing indentation tests which utilize either spherical or pyramidal indenters [1, 2]. Usually, to obtain values for hardness and elastic modulus of the specimen material from the experimental values of indenter load and depth of penetration is the principal goal of such testing. The forces involved are usually in the millinewton ( $10^{-3}$  N) range and are measured with a resolution of a few nanonewtons ( $10^{-9}$  N), and the depths of penetration are in the order of nanometers, hence the term “nano-indentation” ( $10^{-9}$  m). As the experimental values of indenter load and depth of penetration give an indirect measure of the area of contact, from which the mean contact pressure, and thus hardness, can be estimated, the relationship between the contact area and the load is considerably important. Thus the appropriate use of the corresponding theoretical model will play a key role in the experimental investigation.

---

\*To whom correspondence should be addressed. Tel.: (86-10) 6265-8008. Fax: (86-10) 6256-1284.  
E-mail: yzhao@lnm.imech.ac.cn

Nano-contact mechanics refers to contact mechanics at nano-scales, which is fundamentally important for understanding of the force–distance curves from various scanning microscopies (atomic force microscopy (AFM), magnetic force microscopy (MFM), etc.) and of nano-indentation, the adhesion (or stiction) of microelectromechanical systems (MEMS) and nano-electromechanical systems (NEMS), nano-tribology and nano-wear. The emphasis of the present paper is to compare different adhesion contact mechanics models in their dimensionless form, and to discuss the influences of the governing dimensionless parameters.

## 2. MODELS OF CONTINUUM ADHESION CONTACT MECHANICS

Continuum models that predict the contact area for various geometries have a long history, dating back to the pioneering work of Hertz in 1881 [3]. Many of the most important contact problems are summarized in the book by Johnson in 1987 [4]. Hertz found that the radius of the circle of contact  $a_H$  was related to the indenter load  $P$ , the spherical indenter radius  $R$ , and the elastic properties of the contacting materials by:

$$a_H^3 = \frac{PR}{K}, \quad (1)$$

where  $K$  is the equivalent elastic modulus of the indenter tip and the sample, given by

$$K = \frac{4}{3} \left( \frac{1 - \nu_1^2}{E_1} + \frac{1 - \nu_2^2}{E_2} \right)^{-1},$$

where  $E$  and  $\nu$  are the Young's modulus and the Poisson's ratio, respectively, and subscripts 1 and 2 denote the indenter and the sample, respectively. If the contacting bodies are spheres with radii  $R_1$  and  $R_2$ , then  $R$  in the above equation is the equivalent radius given by:  $R = R_1 R_2 / (R_1 + R_2)$ . In the absence of adhesion, the Hertz model has been shown to accurately describe the contact area between elastic bodies [4]. However, a great many experimental and theoretical results show that the surface-to-bulk ratio becomes significant at small scales [5]. Therefore, adhesion arising from attractive surface forces is generally not negligible and must be included in any description of contact area. Actually, with the increasing popularity of nanoscale technology and the increasing sensitivity of nano-indentation instruments, experimental results increasingly show that the contact area of the bodies is much larger than estimated with the Hertz model; especially, when the load diminishes to zero, the contact area reaches a constant value [4–8]. It proves that the surface forces, especially the adhesion force, do play an important role in the contact of the indenter and the sample at sub-micro/nano-scale.

Considering the contact between two rigid spheres with radii  $R_1$  and  $R_2$ , the adhesion force,  $P_A$ , between them is given by the Bradley theory [9] as

$$P_A = 2\pi \Delta\gamma R, \quad (2)$$

where  $\Delta\gamma = \gamma_1 + \gamma_2 - \gamma_{12}$  is the work of adhesion,  $\gamma_1$  and  $\gamma_2$  are the surface energies of materials of spheres 1 and 2, respectively, and  $\gamma_{12}$ , is the interfacial energy. Equation (2) applies to the case of rigid spheres in contact, i.e., the contact radius is zero. In practice, the spheres deform when placed in contact due to their finite value of elastic modulus. Derjaguin, Muller and Toporov [10] considered the case of deformable bodies by adding the force given by equation (2) to the Hertz contact equation and the resulting contact theory is referred to as the DMT theory. The DMT model gives the contact radius  $a_{\text{DMT}}$  related to the work of adhesion,  $\Delta\gamma$ , by:

$$a_{\text{DMT}}^3 = \frac{R}{K}(P + 2\pi \Delta\gamma R). \quad (3)$$

It is obvious that upon application of a negative load,  $P_{\text{c(DMT)}}$  is given by:

$$P_{\text{c(DMT)}} = -2\pi \Delta\gamma R, \quad (4)$$

and the contact radius is zero, which means the two surfaces separate at that point. Therefore,  $P_{\text{c(DMT)}}$  is the critical force required to separate the two spheres, i.e. the pull-off force. The model also gives a particular value for the contact radius at a zero load as:

$$a_{0(\text{DMT})} = (2\pi \Delta\gamma R^2 / K)^{1/3}. \quad (5)$$

The adhesion contact between a solid rigid sphere and an elastic half space has been described by Johnson, Kendall and Roberts (JKR), which leads to the famous JKR theory [11]. They found that the contact radius,  $a_{\text{JKR}}$ , for a rigid sphere in contact with a compliant elastic half space, was related to the work of adhesion,  $\Delta\gamma$ , as:

$$a_{\text{JKR}}^3 = \frac{R}{K} \left\{ P + 3\pi \Delta\gamma R + [6\pi \Delta\gamma R P + (3\pi \Delta\gamma R)^2]^{1/2} \right\}. \quad (6)$$

According to the JKR theory, upon application of the negative load, separation of the surfaces would occur when the external force,  $P_{\text{c(JKR)}}$ , was applied such that

$$P_{\text{c(JKR)}} = -\frac{3}{2}\pi \Delta\gamma R. \quad (7)$$

The model also predicts a particular value for the contact radius at a zero load as:

$$a_{0(\text{JKR})} = \left( \frac{6\pi \Delta\gamma R^2}{K} \right)^{1/3}. \quad (8)$$

It should be noted that the pull-off force  $P_{\text{c(JKR)}}$  is independent of the elastic modulus and depends only on the equivalent radius of curvature and work of adhesion. So equation (7) should apply equally well to a rigid sphere, but this would be contradictory to equation (4). The apparent discrepancy led to a heated debate and later, following the analysis of Tabor [12], Muller *et al.* [13] pointed out that

the two theories represented the opposite extremes of a dimensionless parameter  $\mu$  given by

$$\mu = \left( \frac{R \Delta \gamma^2}{E^* \varepsilon^3} \right)^{1/3}, \quad (9)$$

where  $\varepsilon$  is the equilibrium spacing in the Lennard–Jones potential and

$$E^* = \left( \frac{1 - \nu_1^2}{E_1} + \frac{1 - \nu_2^2}{E_2} \right)^{-1}$$

is the combined elastic modulus. The significance of the Tabor number  $\mu$  in the contact theory, especially at the nanoscale, has attracted attention from many researchers (see Ref. [4]).  $\mu$  can be interpreted as the ratio of elastic deformation resulting from adhesion to the effective range of surface forces. Another dimensionless number, called transition parameter  $\lambda$ , was introduced by Maugis [14] and the transition parameter is related to  $\mu$  by  $\lambda = 1.157 \mu$ . For an appropriate use of the adhesion models, an adhesion map has been constructed by Johnson and Greenwood [15] using the Dugdale force-separation law with two parameters:  $\mu$  (or  $\lambda$ ) and  $\bar{P}$ , where the dimensionless load parameter  $\bar{P}$  is the ratio of the applied load to the adhesion force. The JKR theory is applicable to large radius, compliant solids ( $\mu > 5$ ) and the DMT theory applies to small radius, rigid solids ( $\mu < 0.1$ ). Physically, the JKR theory accounts for adhesion forces within the expanded area of contact only, whereas the DMT theory accounts for adhesion forces just outside the contact circle only, which are depicted in Fig. 1b and Fig. 1c, respectively. Table 1 presents the major assumptions and limitations inherent to each theory.

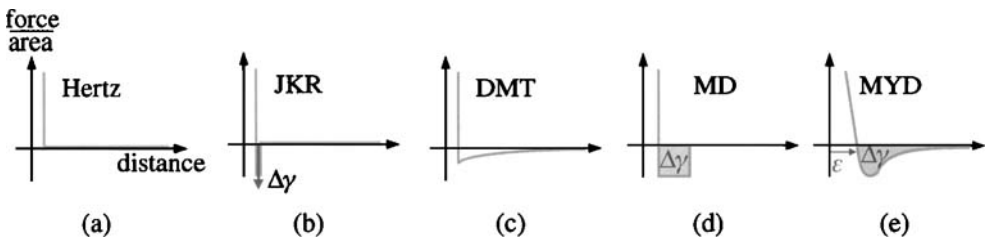


**Figure 1.** Interactive forces for the Hertz, JKR, DMT, MD and MYD models. The Hertz model does not consider the adhesion in contact. The JKR model includes only a short-range adhesion in the contact area, actually it is a  $\delta$  function with the work of adhesion  $\Delta\gamma$ . The DMT model shows a long-range surface force which acts outside the radius of the circle of contact. The MD model considers the Dugdale (square well) potential to describe attractive forces. The MYD model, however, includes both the short-range and long-range forces acting both inside and outside the circle of contact, just like the Lennard–Jones potential.

**Table 1.**

Comparison of the various contact theories

Theory	Assumptions	Limitations
Hertz (Fig. 1a)	No surface forces	Not valid for low loads if surface forces are present
JKR (Fig. 1b)	Short-ranged surface forces act only inside contact area Contact geometry allowed to deform	May underestimate loading due to surface forces Applies to high $\lambda$ systems only
DMT (Fig. 1c)	Long-ranged surface forces act only outside contact area	May underestimate contact area due to restricted geometry Applies to low $\lambda$ systems only
Maugis–Dugdale	Periphery of tip–sample interface modeled as a crack that fails at its theoretical strength	Analytical solution, but parametric equations Applies to all values of $\lambda$

### 3. COMPARISON OF THE DMT AND JKR MODELS WITH THE HERTZ MODEL

To compare the JKR model with the Hertz model, especially the influence of the adhesion force on the contact radius, it is convenient to make equation (6) dimensionless as

$$\frac{a_{\text{JKR}}}{a_{\text{H}}} = \left\{ 1 + \frac{3\pi \Delta\gamma R}{P} + \left[ \frac{6\pi \Delta\gamma R}{P} + \left( \frac{3\pi \Delta\gamma R}{P} \right)^2 \right]^{1/2} \right\}^{1/3}, \quad (10)$$

where the term on left-hand side is always larger than (or equal to) unity as expected, and can be expressed in the dimensionless load parameter  $\bar{P} = P/(\pi \Delta\gamma R)$  as

$$\frac{a_{\text{JKR}}}{a_{\text{H}}} = \left\{ 1 + \frac{3}{\bar{P}} + \left[ \frac{6}{\bar{P}} + \left( \frac{3}{\bar{P}} \right)^2 \right]^{1/2} \right\}^{1/3}.$$

It seems that the dimensionless load parameter  $\bar{P}$  dominates the change in the contact radius in the JKR model. The radius  $a_{\text{JKR}}$  increases with the work of adhesion  $\Delta\gamma$  and with decreasing applied load. This has been pointed out in Yang's work [16]. However, there has been no such analysis for the DMT model. Equations (3) and (1) give

$$\frac{a_{\text{DMT}}}{a_{\text{H}}} = \left( 1 + \frac{2}{\bar{P}} \right)^{1/3}. \quad (11)$$

From equation (11), it seems that the radius also increases with the work of adhesion and with decreasing applied load, as in the JKR model.

Figure 2 shows that the indentation radius is controlled by the work of adhesion when the load is less than  $10^{-3}$  mN. For a nano-indentation tip radius  $1 \mu\text{m}$ , and the work of adhesion between the tip and the thin film,  $100 \text{ mJ/m}^2$ , the ratio  $a_{\text{JKR}}/a_{\text{H}}$  in the JKR model decreases from 12.4 at the applied load of 1 nN to 1.5 at a load

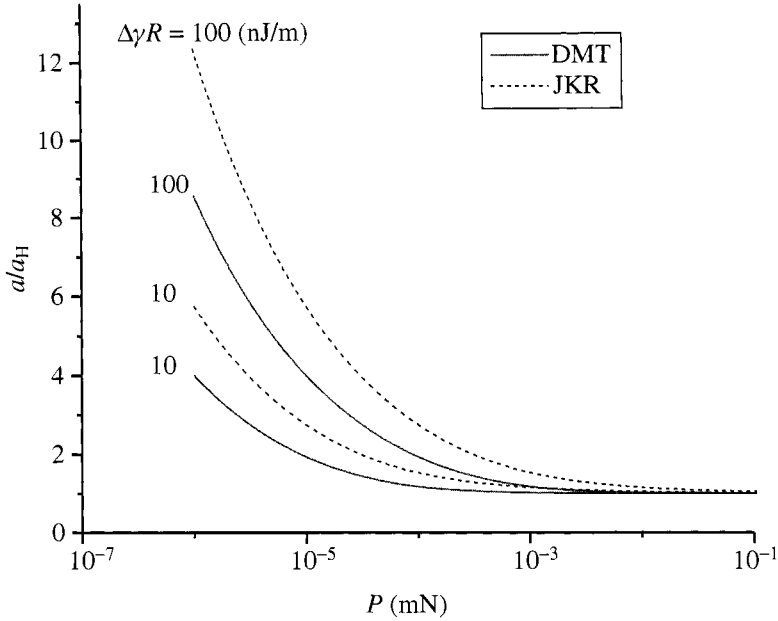


**Figure 2.** Influence of work of adhesion  $\Delta\gamma$  and applied load  $P$  on nano-indentation tip radius ratio in both JKR and DMT models.

of  $1 \mu\text{N}$ , and in the DMT model, the ratio  $a_{\text{DMT}}/a_{\text{H}}$  decreases also from 8.6 at a load of  $1 \text{ nN}$  to 1.2 at a load of  $1 \mu\text{N}$ . Gradually, the ratios for both models reach the value of 1 as the load approaches  $1 \text{ mN}$ . At small loads, the radius increases sharply with the work of adhesion. It proves that under small loads, the contact radius is dominated by the work of adhesion and the indenter tip radius  $R$ . Under large loads, the work of adhesion is negligible compared to the strain energy, which controls the deformation of the specimen surface. In conclusion, in both JKR and DMT models, for a small load and a large indenter size, the change in the work of adhesion controls the contact radius between the indenter and the substrate. In contrast, for a large load and small size of the indenter, the elastic deformation dominates.

Also, from equations (10) and (11), it can be seen that the dimensionless load parameter,  $\bar{P} = P/(\pi \Delta\gamma R)$ , independently controls the influence of the work of adhesion. In Fig. 3, when the value of  $\Delta\gamma R/P$  is less than 0.1, the influence of the work of adhesion is still insignificant. With the value of  $\Delta\gamma R/P$  increasing to  $10^2$ , the corresponding value of  $a/a_{\text{H}}$  is so large that the work of adhesion must not be ignored and would play the main role in the process of contact.

It should be noted that, in Figs 2 and 3, with the same parameter  $\Delta\gamma R$ , the values denoted by the dashed curve are always larger than that of the solid curve at most sites, which means that the influence of the work of adhesion in the JKR model is more prominent than in the DMT model. Actually, dividing equation (6) by



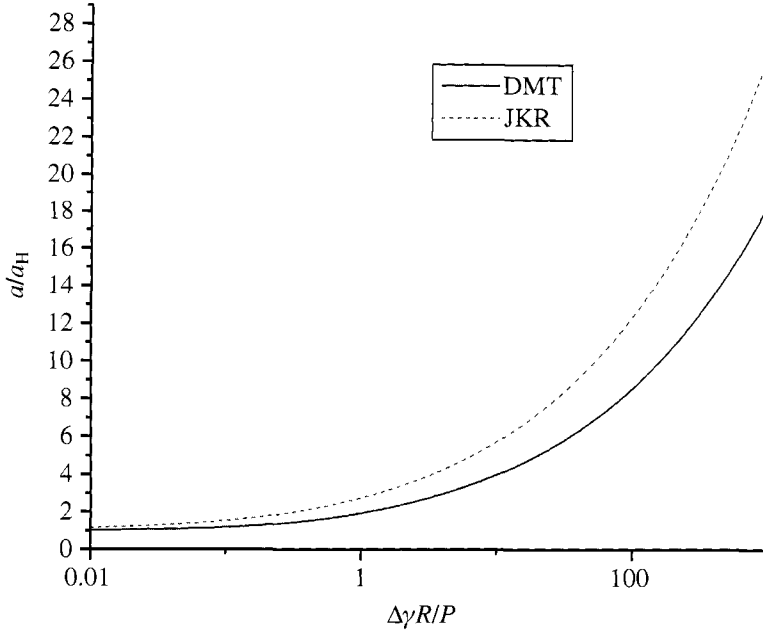


**Figure 3.** Influence of dimensionless number  $\Delta\gamma R/P$  on nano-indentation tip radius ratio in both JKR and DMT models.

equation (3), the ratio between  $a_{\text{JKR}}$  and  $a_{\text{DMT}}$  is given as:

$$\frac{a_{\text{JKR}}}{a_{\text{DMT}}} = \left\{ \frac{1 + 3/\bar{P} + [6/\bar{P} + (3/\bar{P})^2]^{1/2}}{1 + 2/\bar{P}} \right\}^{1/3}. \quad (12)$$

From equation (12) and Figs 4 and 5, it seems that with increasing work of adhesion, the JKR model has more influence on the contact radius. Also, an ultimate value of  $a_{\text{JKR}}/a_{\text{DMT}}$ ,  $\sqrt[3]{3}$ , can be deduced with the decrease of applied load.

In the above discussion about the difference in the JKR and DMT models, the effect of material properties such as the elastic modulus was not considered. Actually, equations (1), (3) and (6), respectively, can be recast into:

$$P_{\text{H}} = \frac{K a^3}{R}, \quad (13)$$

$$P_{\text{DMT}} = \frac{K a^3}{R} - 2\pi \Delta\gamma R, \quad (14)$$

$$P_{\text{JKR}} = \frac{K a^3}{R} - (6\pi \Delta\gamma K a^3)^{1/2}. \quad (15)$$

Then the additional terms  $P_{\text{A(DMT)}}$  and  $P_{\text{A(JKR)}}$  compared with the Hertz model in equation (13) are given by:

$$P_{\text{A(DMT)}} = 2\pi \Delta\gamma R, \quad (16)$$

$$P_{\text{A(JKR)}} = (6\pi \Delta\gamma K a^3)^{1/2}. \quad (17)$$

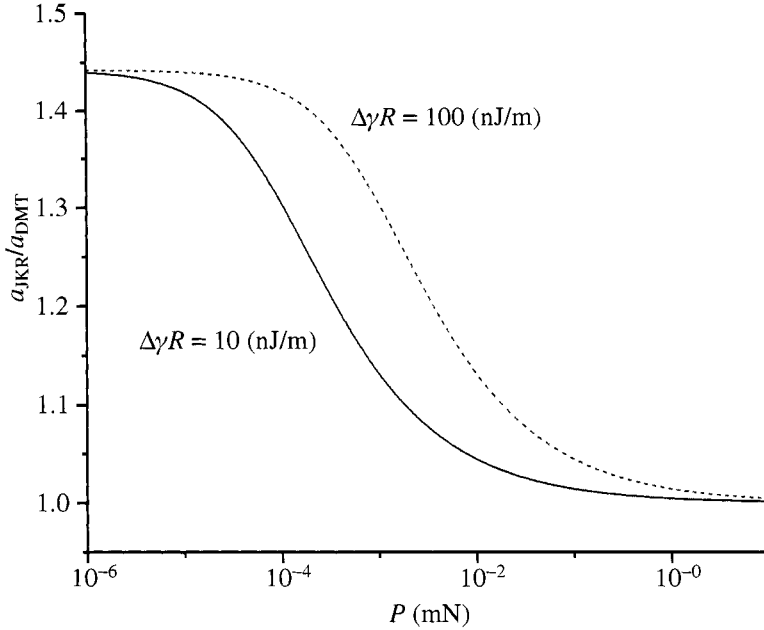


**Figure 4.** The ratio of  $a_{\text{JKR}}$  to  $a_{\text{DMT}}$  vs. the load  $P$ . Under the same load  $P$  and within the region  $10^{-4} - 10^{-1}$  mN, the ratio  $a_{\text{JKR}}/a_{\text{DMT}}$  increases appreciably when  $\Delta\gamma R$  changes from 10 nJ/m to 100 nJ/m, which shows that the work of adhesion has more influence on the JKR model.

Then the ratios between  $P_{\text{A(DMT)}}$  and  $P_{\text{H}}$ , as well as between  $P_{\text{A(JKR)}}$  and  $P_{\text{H}}$  are given by:

$$\frac{P_{\text{A(DMT)}}}{P_{\text{H}}} = \left(\frac{R}{a}\right)^2 \frac{2\pi \Delta\gamma}{aK}, \quad (18)$$

$$\frac{P_{\text{A(JKR)}}}{P_{\text{H}}} = \frac{R}{a} \left(\frac{6\pi \Delta\gamma}{aK}\right)^{1/2}. \quad (19)$$

Here, the quantity  $a/R$  is proportional to the indentation strain [1]. The value of  $aK$  determinates whether or not the adhesion force is significant for a particular contact. As  $aK$  becomes large, the additional term  $P_{\text{A}}$  becomes small. In the case of small  $K$ , the additional term is significant for very compliant surfaces even when the contact radius is large. Also, as the DMT model describes the contact by the Bradley theory [9], which considers that all contacting bodies were rigid, it is appropriate to use the DMT model if the modulus  $K$  is relatively large. In the case that the material is compliant, the JKR theory is suitable because the JKR model deals with the contact between a rigid sphere and an elastic compliant half space [11]. Actually, the JKR model is valid for low modulus, high surface energy materials and large indenters, whereas the DMT model is valid for more rigid materials with lower surface energies and for smaller indenters. It should be noted that in equations (18)

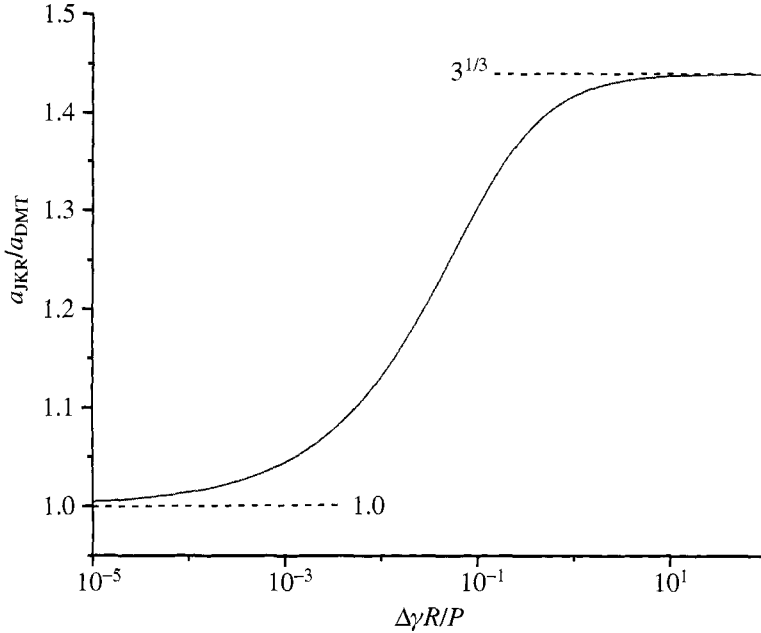


**Figure 5.** The ratio of  $a_{JKR}$  to  $a_{DMT}$  vs. the dimensionless number  $\Delta\gamma R/P$ . When the value of  $\Delta\gamma R/P$  increases, the ratio  $a_{JKR}/a_{DMT}$  increases from the lower critical value to the upper one. The lower critical value, 1.0, shows that when surface energy can be ignored, the contact radii in both JKR and DMT models are similar. Actually they are similar to what the Hertz model predicted. The upper critical value,  $3^{1/3}$ , however, shows the difference in contact radii between the JKR and the DMT models.

and (19), the ratios, in fact, express the ratios between the surface energy and the elastic energy, which has the similar scale as the Tabor parameter in equation (9).

#### 4. COMPARISON OF THE MD MODEL WITH THE HERTZ MODEL

The differences in the contact radii and separation forces between the JKR model and the DMT model which were denoted in equations (4), (5), (7) and (8) have caused some debate [17, 18]. As a result, Muller *et al.* proposed the Muller, Yushchenko and Derjaguin (MYD) model [13, 19] and described the adhesion force between the indenter tip and the sample by a pair-wise summation of the molecules *via* a Lennard–Jones potential. By using the Dugdale potential, Maugis [14] proposed the Maugis–Dugdale (MD) model in 1992. It was found that the MD model was the general case in describing the contact and both the JKR and DMT models were special cases. The transition between the JKR and DMT models was investigated by Maugis and Gauthier–Manuel [20], who used the ‘Dugdale’ (square well) potential to describe the attractive forces between contacting spheres

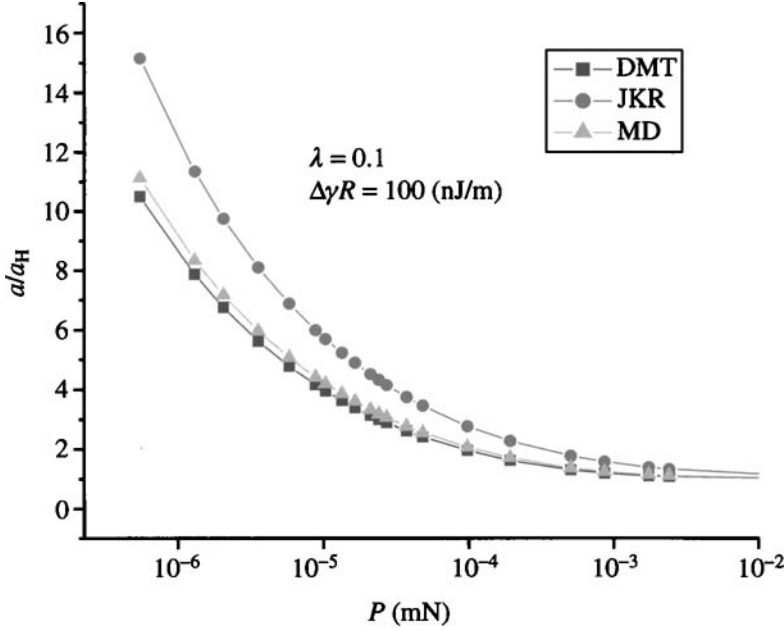


**Figure 6.** Effect of applied load  $P$  on nano-indentation tip radius ratio in JKR, DMT and MD models when  $\lambda = 0.1$  and  $\Delta\gamma R = 100$  nJ/m.

and obtained the following equations:

$$\begin{aligned} & \frac{1}{2}\lambda\bar{a}^2[\sqrt{m^2-1} + (m^2-2)\arccos(1/m)] \\ & + \frac{4}{3}\lambda^2\bar{a}^2[\sqrt{m^2-1}\arccos(1/m) - m + 1] = 1, \end{aligned} \quad (20)$$

$$\bar{P} = \bar{a}^3 - \lambda\bar{a}^2[\sqrt{m^2-1} + m^2\arccos(1/m)], \quad (21)$$

where  $\bar{a}/a = (K/\pi\Delta\gamma R^2)^{1/3}$ ,  $\bar{c}/c = (K/\pi\Delta\gamma R^2)^{1/3}$ ,  $m = c/a$ ,  $\bar{P} = P/(\pi\Delta\gamma R)$  and  $c$  is the outer radius given as  $c = a + 0.971\varepsilon$ , where  $a$  is the radius of the contact circle, and  $\varepsilon$  is the equilibrium spacing in the Lennard–Jones potential.

It is difficult in the MD model to obtain the expression relating only  $a$  and  $P$  as was the case in JKR and DMT models, because there is another parameter  $c$  that varies with  $\lambda$ . Therefore, it is necessary to use numerical calculations to obtain the solution. From Figs 6–8, the conclusion about the transition between the JKR model and the DMT model is verified. When  $\lambda = 0.1$ , the curve for the MD model approaches the curve due to the DMT model and in the case  $\lambda = 5$ , the curve for the MD model approximately coincides with that for the JKR model. With a value of  $\lambda$  between 0.1 and 5,  $\lambda = 1.5$ , the curve is in-between those for the other two. So, it can be clearly seen that the JKR and DMT models are two special cases of the MD model.

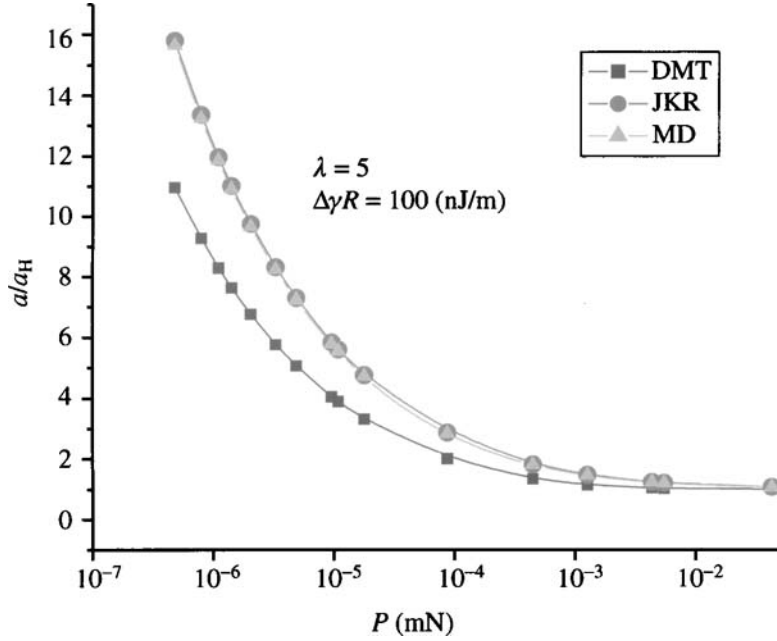


**Figure 7.** Effect of applied load  $P$  on nano-indentation tip radius ratio in JKR, DMT and MD models when  $\lambda = 5$  and  $\Delta\gamma R = 100$  nJ/m.

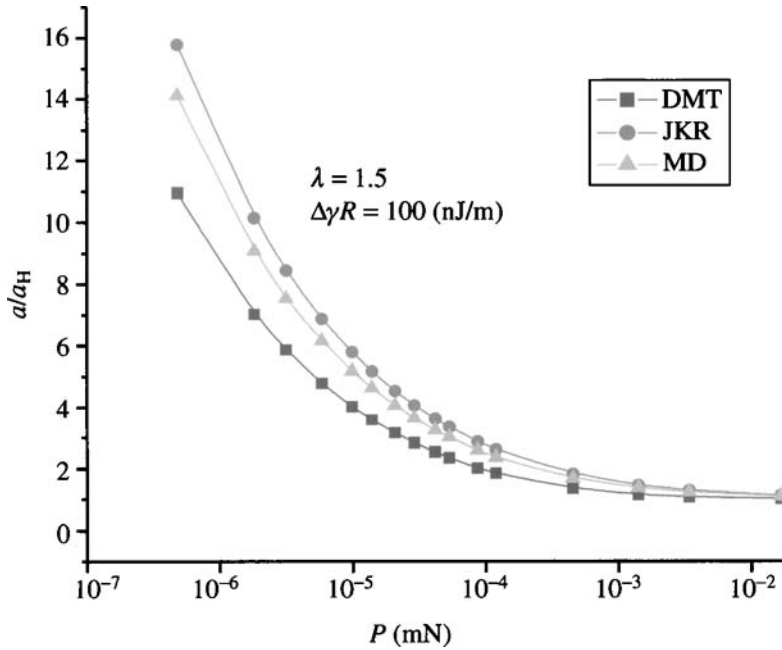


**Figure 8.** Effect of applied load  $P$  on nano-indentation tip radius ratio in JKR, DMT and MD models when  $\lambda = 1.5$  and  $\Delta\gamma R = 100$  nJ/m.

## 5. CONCLUSION

We analyzed the influences of the dimensionless load parameter,  $\bar{P} = P/(\pi \Delta \gamma R)$ , and the transition parameter,  $\lambda$ , on the nano-contact area, and we also validated the importance of the work of adhesion through comparison of the JKR, DMT and MD models with the Hertz model. The major conclusions drawn are given below:

- (1) With a small applied load, the work of adhesion does play a key role in the micro and/or nano-scale contact and must be taken into account. The difference between the JKR and DMT models is also discussed and the origin of the difference is analyzed in-depth.
- (2) The numerical examples show that both the JKR and DMT models are the upper and lower limits of the MD model, respectively. So, the MD model is the general case and can deal with most materials in contact. A large body of experiment results [21] showed that, in general, the AFM measurements were mostly located in the regime of the MD model. So considering the accuracy of the experiments, it is more suitable to use the MD model to deal with the problem. As the MD model is not so concise and the solutions of the equations are cumbersome, it would be much helpful to find some rapid and simple method to determine the parameters which describe the contact. Fortunately, some progress has been made [22, 23].

The influence of the work of adhesion on nano-scale plastic deformation has to be considered for a nano-indentation characterization and modeling. Considering the influence of the work of adhesion, the nano-indentation hardness for a fully plastic contact can be expressed as [24]:

$$H_{\text{adhesion}} = H \left( 1 + \frac{2}{\bar{P}} \right), \quad (22)$$

where  $H = P/\pi a^2$  is the hardness, and  $P$  again is the applied load and  $a$  is the plastic contact area. Equation (22) shows the influence of the dimensionless load parameter on the hardness. In other words, the influence of the work of adhesion is strong when the applied load is light. Surface roughness has also to be considered at the nano-scale in the future work.

## Acknowledgements

This research was sponsored by the Distinguished Young Scholar Fund of NSFC (Grant No. 10225209), key project from the Chinese Academy of Sciences (Grant No. KJCX2-SW-L2) and National '973' Project (No. G1999033103).

## REFERENCES

1. A. C. Fischer-Cripps, *Nano-indentation*. Springer, Berlin (2002).
2. N. A. Burnham, S. P. Baker and H. M. Pollock, *J. Mater. Res.* **15**, 2006 (2002).

3. H. Hertz, *J. Reine Angew. Math.* **92**, 156 (1881).
4. K. L. Johnson, *Contact Mechanics*. Cambridge University Press, Cambridge (1987).
5. Y.-P., Zhao, L. S. Wang and T. X. Yu, *J. Adhesion Sci. Technol.* **17**, 519 (2003).
6. D. S. Rimai, L. P. DeMejo and K. L. Mittal (Eds), *Fundamentals of Adhesion and Interfaces*. VSP, Utrecht (1995).
7. F. Restagno and J. Crassous, *Phys. Rev. E* **65**, 042301 (2002).
8. D. Erts, *Appl. Surface Sci.* **188**, 460 (2002).
9. R. S. Bradley, *Phil. Mag.* **13**, 853 (1932).
10. B. V. Derjaguin, V. M. Muller and Yu. P. Toporov, *J. Colloid Interface Sci.* **53**, 314 (1975).
11. K. L. Johnson, K. Kendall and A. D. Roberts, *Proc. R. Soc. London A* **324**, 301 (1971).
12. D. Tabor, *J. Colloid Interface Sci.* **58**, 2 (1977).
13. V. M. Muller, V. S. Yushchenko and B. V. Derjaguin, *J. Colloid Interface Sci.* **77**, 91 (1980).
14. D. Maugis, *J. Colloid Interface Sci.* **150**, 243 (1992).
15. K. L. Johnson and J. A. Greenwood, *J. Colloid Interface Sci.* **192**, 326 (1997).
16. F. Q. Yang, *Appl. Phys. Lett.* **80**, 959 (2002).
17. B. V. Derjaguin, V. M. Muller and Yu. P. Toporov, *J. Colloid Interface Sci.* **67**, 378 (1978).
18. D. Tabor, *J. Colloid Interface Sci.* **67**, 380 (1978).
19. V. M. Muller, V. S. Yushchenko and B. V. Derjaguin, *J. Colloids Interface Sci.* **92**, 92 (1983).
20. D. Maugis and B. Gauthier-Manuel, *J. Adhesion Sci. Technol.* **8**, 1311 (1994).
21. B. Cappella and G. Dietler, *Surface Sci. Rep.* **34**, 1 (1999).
22. R. W. Carpick, D. F. Ogletree and M. Salmeron, *J. Colloid Interface Sci.* **211**, 395 (1999).
23. E. Barthel, *J. Colloid Interface Sci.* **200**, 7 (1998).
24. S. K. R. Chowdhury and H. M. Pollock, *Wear* **66**, 307 (1981).

## APPENDIX

### List of symbols

$a$	contact radius
$\bar{a}$	$a(K/\pi\Delta\gamma R^2)^{1/3}$
$c$	outer contact radius
$\bar{c}$	$c(K/\pi\Delta\gamma R^2)^{1/3}$
$E$	Elastic modulus
$E^*$	$\left(\frac{1-\nu_1^2}{E_1} + \frac{1-\nu_2^2}{E_2}\right)^{-1}$ , combined elastic modulus
$K$	$\frac{4}{3}\left(\frac{1-\nu_1^2}{E_1} + \frac{1-\nu_2^2}{E_2}\right)^{-1}$ , equivalent elastic modulus
$m$	$c/a$
$P$	applied load
$P_A$	adhesion force
$P_c$	pull-off force
$\bar{P}$	$P/(\pi\Delta\gamma R)$ , dimensionless load parameter
$R$	radius of sphere
$\Delta\gamma$	work of adhesion
$\varepsilon$	intermolecular spacing
$\lambda$	$1.157\mu$ , transition parameter

$\mu$	$\left(\frac{R\Delta\gamma^2}{E^{*2}\varepsilon^3}\right)^{1/3}$ , Tabor number
$\nu$	Poisson's ratio



## **Accounting for the JKR–DMT transition in adhesion and friction measurements with atomic force microscopy**

D. S. GRIERSON, E. E. FLATER and R. W. CARPICK \*

*Department of Engineering Physics, University of Wisconsin-Madison, 1500 Engineering Drive, Madison, WI 53706, USA*

**Abstract**—Over the last 15 years, researchers have applied theories of continuum contact mechanics to nanotribology measurements to determine fundamental parameters and processes at play in nanometer-scale contacts. In this paper we discuss work using the atomic force microscope to determine nanoscale adhesion and friction properties between solids. Our focus is on the role that continuum contact mechanics plays in analyzing these measurements. In particular, we show how the JKR-to-DMT transition is taken into account, as well as limitations involved in using these models of contact in the presence of adhesion.

**Keywords:** Atomic force microscopy (AFM); adhesion; friction; nanotribology; contact mechanics.

### **1. INTRODUCTION**

With the rising interest in nanotechnology, new fields of research have emerged in the attempt to understand nanoscale science and engineering. One of these fields is nanotribology, the nanoscale analogue to the macroscale study of friction and wear [1, 2]. At the nanoscale, surface forces become dominant, and surface properties related to adhesion, friction and wear become critical design considerations. Of particular note are micro/nano-electromechanical systems (MEMS/NEMS). Because of the problematic effects of friction and wear [3, 4], there are currently no MEMS devices on the market that involve sliding interfaces in contact. Studies in this area are important not just for nanotechnology applications, but for fundamental science as well. Although many practical, macroscopic engineering applications involving tribology have been successfully addressed, relatively little is understood thus far about the underlying fundamental mechanisms of friction and energy dissipation between sliding surfaces.

---

\*To whom correspondence should be addressed. Tel.: (1-608) 263-4891. Fax: (1-608) 263-7451. E-mail: carpick@engr.wisc.edu

There are several experimental approaches to nanotribology, including the use of the atomic force microscope (AFM) [5] and the surface forces apparatus (SFA) [6]. In this paper we focus on work using the AFM to determine nanoscale adhesion and friction between solid surfaces. Our particular focus is on the role that contact mechanics plays in analyzing these measurements.

Over the last 15 years or so, researchers have applied theories of continuum contact mechanics to nanotribology measurements to determine fundamental parameters and processes at play in nanometer-scale contacts. In 1999, Unertl concisely discussed several of these issues [7]. An increasing amount of evidence supports the seemingly surprising conclusion that a continuum description of contact is accurate down to contacts as small as a few nanometers in size. Our primary focus will be on how to properly apply continuum mechanics theories to nanotribology measurements. The important question of where exactly continuum representations break down has yet to be addressed comprehensively. We will discuss this briefly at the conclusion of this paper. We will first briefly review contact mechanics, and then discuss its application to adhesion and friction measurements.

## 2. REVIEW OF CONTACT MECHANICS

Heinrich Hertz is said to be the pioneer of the field of contact mechanics as we know it today [8]. In 1882, part of his graduate work involved studying interference patterns between glass lenses when pressed together. One relation he determined was that contact between a flat plane and a sphere pressed together with a normal load  $P$  occurred within a circular contact area with contact radius  $a$  according to the following equation:

$$a = \left( \frac{PR}{K} \right)^{1/3}, \quad (1)$$

where  $R$  is the radius of the sphere,

$$K = \frac{4}{3} \left( \frac{1 - \nu_1^2}{E_1} + \frac{1 - \nu_2^2}{E_2} \right)^{-1},$$

$E_1$ ,  $E_2$  are the sphere and flat plane Young's moduli and  $\nu_1$ ,  $\nu_2$  are the sphere and flat-plane Poisson ratios, respectively. This theory describes the contact area for smooth macroscopic contacts, and is used to this day in many applications. It is applicable only to homogeneous, isotropic, linear elastic materials that exhibit no attractive surface forces (adhesion) and assumes that the contact radius is much smaller than the sphere radius, so that the sphere can be approximated as a paraboloid.

In 1971, Johnson, Kendall and Roberts (JKR) [9] proposed a new theory that accounted for adhesion between two elastic bodies. They were motivated by experimentally measured contact areas that were larger than predicted by the Hertz

theory at low loads, and by the observation of finite contact area at zero applied load. They derived the following equation to describe the contact radius between a sphere and a plane with adhesion acting:

$$a = \left( \frac{R}{K} (P + 3\gamma\pi R + \sqrt{6\gamma\pi R P + (3\gamma\pi R)^2}) \right)^{1/3}, \quad (2)$$

where  $\gamma$  is the Dupré energy of adhesion, or work of adhesion. It is, in fact, an energy per unit area and it represents the work done in completely separating a unit area of the interface. Characteristics of this theory include infinite tensile stress at the contact area perimeter, a non-zero contact area at zero load and a minimum stable normal load which still exhibits a non-zero contact area. This minimum load can be called the pull-off force or critical load  $P_c$ , and is given by:

$$P_{c(\text{JKR})} = -\frac{3}{2}\pi\gamma R. \quad (3)$$

Shortly thereafter, Derjaguin, Muller and Toporov (DMT) [10] derived a separate expression to include adhesion in the contact of elastic bodies. They assumed that the deformed contact profile remained the same as in the Hertz theory, but with an overall higher load due to adhesion. This is equivalent to attractive interactions acting at all separations between the sphere and the plane, like a dead weight, thus:

$$a = \left( \frac{R}{K} (P + 2\pi\gamma R) \right)^{1/3}, \quad (4)$$

and now the pull-off force is:

$$P_{c(\text{DMT})} = -2\pi\gamma R. \quad (5)$$

In the DMT model, the contact area goes to zero at the pull-off force, and there is no singularity in the contact stresses.

Although these two seemingly competing theories were the cause of much heated debate, the controversy was settled when it was determined that they were valid at opposite ends of the same spectrum of contact behavior. When surface forces are short range compared to the resulting elastic deformations (i.e. compliant materials, large sphere radii, and strong, short-range adhesion forces), the JKR model describes the contact area accurately. The opposite limit (i.e. stiff materials, small sphere radii and weak, long-range adhesion forces) corresponds to the DMT regime. The form of the contact area in the DMT model was, in fact, first presented in the work of Maugis [11] and is often referred to as the ‘Hertz-plus-offset’ model. The development of the theories is provided in a more detailed manner by Maugis in that paper.

It is convenient to utilize a non-dimensional physical parameter to quantify these limits and the cases in between. Often referred to as Tabor’s parameter  $\mu_T$ , this

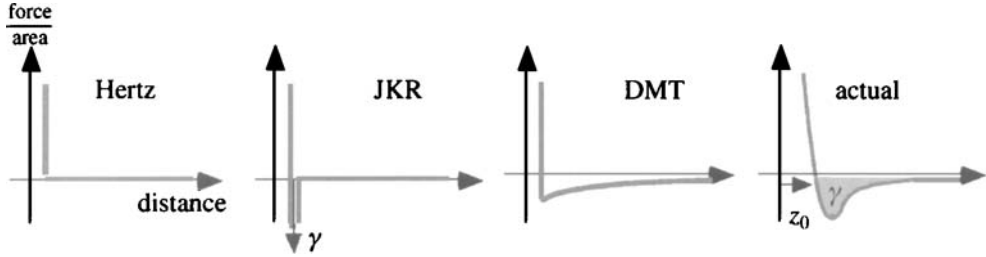


**Figure 1.** Interaction forces (per unit area) for the Hertz, JKR and DMT models, compared to an actual interaction. There is no attractive force in the Hertz model, only hard wall repulsion at contact. The JKR model includes short-range adhesion that is essentially a delta function with strength  $\gamma$ , and thus only acts within the contact zone. The DMT curve shown represents a long-range surface force. A volume integrated force, like the van der Waals force, can also lead to a DMT dependence, where the contact profile remains Hertzian and the attractive forces act like an additional external load. For an actual interaction force, the integral of the attractive well corresponds to the work of adhesion,  $\gamma$ .

transition parameter is defined as [12]:

$$\mu_T = \left( \frac{16R\gamma^2}{9K^2z_0^3} \right)^{1/3}, \quad (6)$$

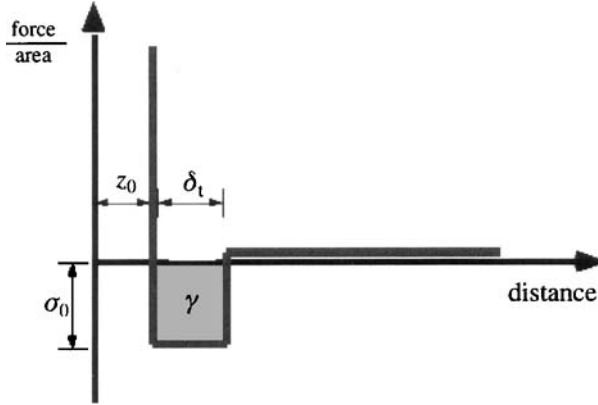
where  $z_0$  is the equilibrium separation of the surfaces. The spatial range of the adhesion forces is assumed to scale with  $z_0$ , as in the case of the Lennard–Jones potential, for example, where  $z_0$  is the only length scale in the definition of the potential. Tabor’s parameter is physically equivalent to the ratio between the normal elastic deformation caused by adhesion (i.e. in the absence of applied load) and the spatial range of the adhesion forces themselves.

Figure 1 illustrates the different interaction forces (per unit area) as a function of separation for the Hertz, JKR and DMT models, and a more ‘realistic’ interaction like a Lennard–Jones potential.

To approximate such an actual interaction, Maugis [11] elegantly showed that it was possible to connect the JKR and DMT limits and determine contact parameters for the entire range of materials parameters. He considered a ‘Dugdale’ (square-well) potential to describe attractive forces between contacting spheres, as is illustrated in Fig. 2. In this model, a constant adhesional stress  $\sigma_0$  acts over a range  $\delta_t$ . Thus, the work of adhesion is  $\gamma = \sigma_0 \cdot \delta_t$ . Maugis defines a parameter,  $\lambda$ , which is similar to  $\mu_T$ , given by:

$$\lambda = 2\sigma_0 \left( \frac{R}{\pi\gamma K^2} \right)^{1/3}. \quad (7)$$

By choosing  $\sigma_0$  to match the minimum adhesional stress for a Lennard–Jones potential (with equilibrium separation  $z_0$ ), it follows that  $\delta_t = 0.97z_0$ , and so  $\lambda = 1.1570\mu_T$ . Thus,  $\lambda$  and  $\mu_T$  are nearly equivalent. For convenience we shall refer to  $\lambda$  as the ‘transition parameter’. If  $\lambda > 5$ , the JKR model applies and if  $\lambda < 0.1$  the DMT model applies. Values between 0.1 and 5 correspond to the ‘transition



**Figure 2.** The force (per unit area)–distance relation for the Dugdale model used by Maugis. A constant adhesional stress (force per unit area)  $\sigma_0$  acts between the surfaces over a range  $\delta_t$ . At greater separations, the attractive force is zero. The work of adhesion is thus  $\gamma = \sigma_0 \delta_t$ .

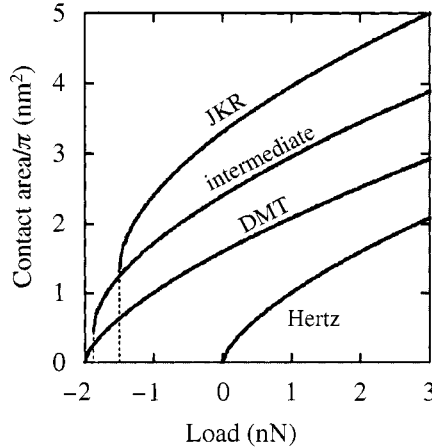


**Figure 3.** The Hertz area–load curve and the JKR–DMT transition, plotted by setting  $K = 1$  GPa,  $R = 1$  nm and  $\pi\gamma = 1$  J/m<sup>2</sup>. Area–load curves for the JKR limit, the DMT limit and an intermediate case are shown. These approach the Hertz curve in the limit  $\gamma \rightarrow 0$  (no adhesion). Adhesion increases the contact area from the Hertz case for a given load by an amount dependent upon the range of attractive forces.

regime’ between JKR and DMT models. A summary of different conventions used for defining this ‘transition parameter’ is provided by Greenwood [12]. When there are no attractive surface forces ( $\gamma = 0$ ), the Hertz theory applies. The variation of contact area with load in these cases is shown in Fig. 3.

The assumption of a square-well potential may seem somewhat limiting. However, Barthel has shown that the contact behavior is generally insensitive to the actual shape of the interaction potential, provided there is only one length scale involved [13]. However, the behavior can vary significantly if an additional length scale to the interaction is introduced [14]. It may be appropriate to describe, for ex-

ample, the simultaneous effect of short-range solid–solid adhesion and longer range electrostatic, van der Waals', or solvation forces.

The Maugis–Dugdale equations are somewhat difficult to utilize, since Maugis' formulation lacks a single expression relating only  $a$  and  $P$ . To plot the Maugis–Dugdale solution or fit it to data, one needs to simultaneously solve two equations by letting certain parameters vary between appropriate limits that depend upon  $\lambda$ . Furthermore, the relation for the pull-off force must be determined through iteration [15] if the value of  $\lambda$  is not known *a priori* (the usual case with experimental measurements). In practice, this is rather cumbersome to carry out with common software programs that utilize automated statistical fitting procedures.

In 1999, Carpick, Ogletree and Salmeron (COS) [16] provided an approximate general equation for easily describing the contact area. The general equation is amenable to conventional curve fitting software routines and provides a rapid method of determining the value of the transition parameter which describes the range of surface forces. They showed that the Maugis formulation could be approximated using the following formula to determine the contact radius:

$$a = a_{0(\alpha)} \left( \frac{\alpha + \sqrt{1 - P/P_{c(\alpha)}}}{1 + \alpha} \right)^{2/3}, \quad (8)$$

where  $\alpha$  is another transition parameter and  $a_0$  is the contact area at zero load. Note that  $\alpha = 1$  corresponds exactly to the JKR case, and  $\alpha = 0$  corresponds exactly to the DMT case. Included in equation (8) is the fact that  $P_c$  and  $a_0$  depend on  $\alpha$  as well. Equation (8) is referred to as the generalized transition equation or COS equation. For intermediate cases ( $0 < \alpha < 1$ ), the generalized transition equation corresponds very closely to Maugis' solution for the transition regime ( $0.1 < \lambda < 5$ ). An approximate relation is used to relate  $\alpha$  and  $\lambda$ :

$$\lambda = -0.924 \cdot \ln(1 - 1.02\alpha). \quad (9)$$

They also outlined a step-by-step procedure to fit this equation to determine the regime of contact for AFM or SFA experiments.

In an analogous fashion, Piétrement and Troyon subsequently presented approximate general equations for the elastic indentation depth and the normal contact stiffness [17] that are also easier to handle than the corresponding Maugis–Dugdale equations. Schwarz then showed that equation (8) could be derived from physically-based arguments by combining an infinitely short-range attractive interaction (essentially a JKR-type interaction) with a long-range force [18] of adjustable relative weight. This further supports the validity of the simple, approximate equations presented in Refs [16, 17].

All models described above assume homogeneous, isotropic, linear elastic contact between a sphere and a plane (or, equivalently, two spheres) where the contact radius is much smaller than the sphere radius (allowing it to be described mathematically as a paraboloid), and the loading is purely in the normal direction. In practice, there will be deviations from these assumptions that may be significant. Fortunately,

solutions for many of these cases have been worked out. Maugis worked out the adhesional contact problem for large contact radii (i.e. using spheres, not paraboloids) [19]. The solution for adhesional contact for an axisymmetric power-law indenter shape was presented by Carpick *et al.* [20, 21]. Johnson has discussed the effect that lateral forces may have on the contact [22]. Viscoelastic effects have been discussed in a number of cases [23–28] and were reviewed recently by Shull [29]. Plastic effects, while often dealt with through finite element modeling, have also been modeled analytically, including the effects of phase transitions [30] and adhesion [31]. However, the effects of anisotropy have been discussed in considerably less detail, see for example Refs [32, 33].

Some particularly interesting work has been performed in applying contact mechanics to the surface forces apparatus (SFA), which can be viewed as a single asperity contact of larger scale than the AFM, and with important capabilities including the direct measurement of the contact area [34, 35]. The SFA typically consists of thin mica layers on a compliant (glue) backing. The consequences of this geometry have been studied by Johnson and Sridhar [36]. They find that the JKR model works well for a sufficiently thick layer, as well as for a sufficiently thin layer, but layers of an intermediate thickness violate the conditions of the JKR theory. In between these limits the contact behavior is modeled by the numerical results. Violations of the JKR model were found to be due to the small size of the contact radius compared to the layer thickness.

Barthel and Roux have studied the velocity dependence of the work of adhesion when studying organic monolayers with the SFA [37]. They find that lower velocities produce consistent pull-off force values and, at higher velocities, viscoelastic effects give rise to higher pull-off force values. They derive analytical results by considering viscous dissipation, and they compare the results with numerical treatments. Stability of the system is significantly dependent on the chemical composition of the organic layer, and they highlight the importance of formulating generalized contact mechanics to intermediate ranges of interaction (i.e. between DMT and JKR regimes).

In summary, contact mechanics models can be powerful tools in extracting fundamental parameters from studies of surfaces in contact. However, they must be used cautiously, with attention paid to the appropriate limits and assumptions they entail. In what follows, we discuss how measurements of adhesion and friction with the AFM can be treated using contact mechanics approaches under conditions (as specified above) appropriate for behavior in the JKR-to-DMT range.

### 3. ADHESION MEASUREMENTS

Fundamental mechanisms of adhesion at the micro/nanoscale are a topic of substantial current interest. Much of this work is motivated by the ‘stiction’ problems seen in MEMS/NEMS devices [3, 38] and it is postulated that a fundamental understanding of adhesion at the nanoscale may give rise to guidelines for designing

and fabricating reliable NEMS/MEMS devices. In this regard, one can consider single-asperity adhesion to be at the smallest possible scale and, therefore, understanding single-asperity adhesion may be the key to understanding the true work of adhesion between two complex, multi-asperity surfaces at larger scales. The AFM is an ideal tool to quantitatively characterize the true work of adhesion at this length scale. Contact mechanics models are often used to analyze data, and considerable efforts have been made to enhance these models based on understanding how surface interactions can deviate from the ideal cases treated by DMT or JKR theories.

### *3.1. AFM methodology*

To use the AFM as a quantitative tool to investigate interfacial adhesion, cantilever calibration procedures and contact mechanics modeling need to be applied consistently. Adhesion data taken with the AFM can vary significantly due to seemingly subtle changes in the environmental conditions, AFM tip material and/or geometry, and surface contamination and/or modification. To ensure that calculated values for work of adhesion are intrinsic to the interface tested, rigorous characterization techniques of the tip and surface materials should be performed.

Typically, the pull-off forces are measured by AFM in the following way. A laser beam is focused onto the backside of the cantilever and reflected onto a position-sensitive photodetector. The cantilever is deflected by interaction with the surface material, which moves the reflected laser spot vertically on the photodetector. This motion is measured by the photodetector and is recorded in a so-called ‘force–distance’ plot. This plot is then analyzed to determine the magnitude of the pull-off force, which is subsequently converted into a value for the work of adhesion. The process of obtaining the data needed to calculate the work of adhesion generally involves three stages: acquiring reliable force–distance curves, calibrating force constants to obtain pull-off force values and compiling the necessary contact mechanics parameters.

### *3.2. Acquiring reliable force–distance curves*

The operation of an AFM is fairly straightforward, which is one reason why adhesion data are often reported without appreciation for the afore-mentioned subtleties. Assuming that the environmental conditions (temperature, relative humidity, atmospheric composition) are kept constant, several issues that often arise can prevent reliable, reproducible data from being collected. First, if the tip geometry is altered by contacting the surface (e.g. due to wear of the tip), pull-off force values can vary significantly. There are two primary techniques for measuring the shape of an AFM tip. One technique involves a tip reconstruction by analyzing AFM images with computer software [39, 40]. The other involves imaging the tip in a high-resolution scanning electron microscope (SEM) or transmission electron microscope (TEM). It is recommended that the AFM tips be analyzed both before and after scanning to check for tip modification.



Second, pull-off forces taken on a homogenous surface can vary if the surface chemical composition of the tip or sample is modified during the experiment. Even if geometrical changes of the tip do not occur, it is still possible that chemical changes may, due to surface contamination, material transfer, or modification involving surface treatments or coatings that are present. Contamination can be addressed by improving sample preparation procedures or conducting experiments in a clean, dry environment including ultrahigh vacuum. If the chemistry taking place is due to the presence of a surface coating, a more in-depth analysis of the surface interactions and chemical exchanges needs to be applied. Unfortunately, there is no technique for perfectly characterizing the chemical state of the tip, although measurements of contact conductance can at least be used to reveal changes that have occurred [41].

Third, when multiple pull-off measurements are taken at different locations on a heterogeneous surface, variations in both the surface roughness and surface chemistry can affect the interaction forces [42, 43]. If the surface topography and composition vary, the contact between the tip and sample changes based on local slope, curvature, elasticity, and adhesion. ‘Force-volume’ imaging is often performed, which involves acquiring a topography image and a pull-off force map simultaneously, to correlate pull-off force values with specific regions of a sample. In this way, high surface energy features can be observed (e.g. step edges, defects, other inhomogeneities). As well, regions of differing chemistry can be identified.

### *3.3. Extracting the pull-off force values from force–distance curves*

When it has been determined that the tip and sample are not being altered, the force–distance plots can then be analyzed to obtain quantitative pull-off force values using a cantilever calibration procedure. There are several methods in the literature, but two procedures have emerged as the most reliable. One method is Cleveland’s ‘added mass method’ [44] and the other is Sader’s ‘unloaded resonance technique’ [45]. For the added mass method, a known mass is attached to a cantilever, the resulting change in resonant frequency is measured, and this frequency shift is correlated with the normal stiffness of the cantilever. For the Sader method, the length, width, resonant frequency and quality factor of a cantilever are measured in ambient conditions. These measured properties are related to the cantilever’s normal stiffness through the hydrodynamic function due to the air damping of the cantilever. The Sader method is straightforward to apply *in situ* and is non-destructive. Therefore, this method is preferable for extracting calibrated pull-off force values from uncalibrated force–distance plots.

### *3.4. Compiling the necessary parameters for contact mechanics modeling*

Before work of adhesion values can be calculated from pull-off force data, several parameters must be either measured or determined from literature values. As discussed above, the contact between an AFM tip and the sample can range from

DMT-like to JKR-like, depending on the elastic properties (Young's modulus and Poisson's ratio) of the tip and sample, the tip radius, the work of adhesion and the equilibrium spacing (or range of attractive forces) between the tip and sample when in contact. The elastic properties can be determined from nanoindentation experiments or from literature values. However, the equilibrium spacing is not directly known. To handle this, upper and lower bounds can be used initially as described below.

### 3.5. Fitting adhesion data based on contact mechanics modeling

As mentioned above, the work of adhesion calculation depends upon the appropriate contact regime, which ranges from the JKR to the DMT regime. Equations (3) and (5) for the pull-off forces can be rearranged and then generalized as:

$$\gamma = \frac{-P_c}{\chi \pi R}, \quad (10)$$

where  $\chi$  ranges monotonically from 1.5 (for the JKR limit) to 2 (for the DMT limit), depending on Tabor's parameter,  $\mu_T$ . This full range of uncertainty in  $\chi$  corresponds to a possible error in  $\gamma$  of 33%. A plot, table and approximate formulae for  $\chi$  as a function of  $\mu_T$  are given in Ref. [16]. Still,  $\mu_T$  is not known without knowledge of  $z_0$  and  $\gamma$ . However,  $\gamma$  is not known without knowledge of  $\mu_T$ . This is the adhesion 'Catch-22'.

### 3.6. Experimental example

One way to get around this 'Catch-22' is to first check if upper (lower) bounds can be placed on  $\mu_T$  by assuming the smallest (largest) reasonable values of  $z_0$  and any other uncertain parameters in the experiment. This is best illustrated with an experimental example. An experiment was conducted using commercial AFM tips fabricated from silicon and coated with a partially oxidized tungsten carbide film. This presents an additional problem, since the elastic properties of the tungsten carbide are uncertain. Note that while the elastic constants do not enter into the calculation of the adhesion energy using equations (3) and (5), they do affect the value of  $\chi$ . We measured the pull-off force between these tips and a single crystal diamond sample (Diamond Innovations) with a (111) orientation, terminated with hydrogen by an RF microwave plasma treatment. X-ray photoelectron spectroscopy and near-edge X-ray absorption fine structure spectroscopy were used to verify the expected chemical composition and structure of the diamond surface. AFM measurements were carried out with two different cantilevers to check for reproducibility. We used the Sader method to calibrate each cantilever. The tip shape and radius were measured *in situ* by the inverse imaging method using a TipCheck calibration standard (Aurora Nanodevices) and deconvolution software. We reduced the possibility of modification of the AFM tip by taking pull-off force measurements directly without scanning the sample, and

**Table 1.**

Tip radii, normal force constants and average pull-off forces measured on different samples. Measurements taken using two separate AFM cantilevers are reported

Cantilever	$R$ (nm)	$k$ (N/m)	$P_c \pm \sigma$ (nN)
#1	$25 \pm 5$	$0.108 \pm 0.022$	$6.2 \pm 1.1$
#2	$30 \pm 6$	$0.146 \pm 0.029$	$9.2 \pm 5.0$

Errors are the standard deviations from each set of measurements.

took at least 35 measurements per tip. In another work (data not shown), we have successfully used a TEM to characterize AFM tips from the same wafer under the same experimental conditions to verify that the tips did remain unchanged while taking such measurements. Cantilever parameters and calculated values of the pull-off force for the two levers are presented in Table 1.

To determine the appropriate contact regime for these experiments, we used extreme (i.e. low) values for the elastic constants and equilibrium spacing ( $z_0$ ) to set an upper bound on Tabor's parameter. The test for an upper bound was chosen because it was likely that Tabor's parameter would be low given the stiffness and expected low interfacial energy of diamond and tungsten carbide. Our lower-bound 'test' value of  $z_0$  was chosen to be 0.154 nm, which is the C–C bond distance in diamond. We used a conservatively low modulus for the tip of 357 GPa (50% of the value of pure single-crystal tungsten carbide), and used the smallest possible value of  $\chi = 1.5$ . We used literature values for the modulus and Poisson's ratio of diamond. Poisson's ratio for tungsten carbide was also taken from the literature, which is a safe choice, since the dependence of Tabor's parameter on Poisson's ratio is rather weak. As stated above, the only other parameters in the problem, the pull-off force and the tip radius, are experimentally determined. Choosing the cases that exhibited the largest values of  $P_c$ , we determined 'test' adhesion energies from equation (10). These are then used in equation (6), where we find that even using the most extreme assumptions, Tabor's parameter does not exceed approx. 0.09. Thus, we are firmly in the DMT regime, i.e.  $\chi = 2$ , and the correct work of adhesion can now be directly determined from the pull-off force using equation (10). All values used in calculating  $\mu_T$  and the resulting work of adhesion values are given in Table 2. A significant error is associated with the measurement from cantilever #2. Despite the care taken with the measurement, there still exists some heterogeneity on the sample, and the possibility of tip changes may have also contributed. Nevertheless, the two values for the work of adhesion are comparable.

In the case of an interface expected to be in the JKR regime, an analogous procedure is used: assume  $\chi = 2$ , use the largest reasonable values for any uncertain elastic moduli and choose an upper bound for  $z_0$ . This upper bound for  $z_0$  could be extracted, for example, by examining the force-distance curve.  $z_0$  can be assumed to be no greater than the snap-in distance of the tip, which would be calculated by

**Table 2.**

Values used for determining the upper bound to Tabor's parameter and the subsequent work of adhesion values assuming the DMT model holds

Cantilever	$P_c \pm \sigma$ (nN)	$\chi$	$\gamma$ (test) (J/m <sup>2</sup> )	$E_{\text{tip}}$ (GPa)	$\nu_{\text{tip}}$	$E_{\text{sample}}$ (GPa)	$\nu_{\text{sample}}$	$K$ (GPa)	$z_0$ (nm)	$\mu_T$	$\gamma$ (actual, DMT) (J/m <sup>2</sup> )
#1	6.2 $\pm$ 1.1	1.5	0.053 $\pm$ 0.020	357	0.24	967	0.08	364	0.154	0.079	0.0397 $\pm$ 0.0072
#2	9.2 $\pm$ 5.0		0.065 $\pm$ 0.048							0.089	0.049 $\pm$ 0.027

converting the change in the normal load signal at snap-in to the distance the tip has moved. If one finds that  $\mu_T$ , even under these extreme assumptions, exceeds approx. 5, then one can safely assume that JKR limit applies.

Intermediate cases remain problematic without further information. At the very least, the methodology outlined above allows one to set upper and lower bounds for possible values of the work of adhesion. Also, as we show in the next section, if additional information about the contact area can be determined, such as from friction measurements, then Tabor's parameter can be determined.

The general methodology adopted here is well-suited for many tribological interfaces studied. This approach to characterization provides insight into why results can vary significantly between the DMT and JKR regimes, and offers guidelines on how to embody this understanding when analyzing AFM pull-off force data. If true work of adhesion values are to be trusted and are comparable between systems, experiments, and laboratories, this type of methodology needs to be applied consistently to AFM data and reported accordingly in publications and presentations.

#### 4. FRICTION MEASUREMENTS

As with adhesion measurements, friction measurements need to be carefully calibrated and analyzed, taking into account the necessary contact mechanics and the assumptions that go with them. The tip shape and the cantilever's normal force constant must be calibrated properly, as described above. In addition, the lever must be calibrated to quantitatively describe lateral forces. Frictional properties are also quite sensitive to tip and environmental conditions. The process for friction data takes a similar form as adhesion measurements: acquire reliable and reproducible friction data, calibrate the AFM lever to obtain quantitative values for normal load and friction during an experiment, and use known characteristics of the lever and sample along with contact mechanics fits, taking into account the JKR–DMT transition, to determine quantitatively the interfacial shear strength and adhesion energy.

An AFM cantilever can be scanned across a surface so that the direction of motion is perpendicular to the long axis of the cantilever. In this way the lever twists due to the frictional resistance of the tip and the laser spot reflected from the back of the cantilever moves laterally on the photodetector. Friction is determined by taking half the difference of the forward and backward scans along a given line on the surface. In topographic feedback control, the cantilever is scanned at a constant applied load. Alternately, the load can be varied in a specific way while scanning the tip across the sample as described below. We refer to this type of experiment as determining friction as a function of load, or more simply ‘friction *versus* load’.

Friction *versus* load curves can be obtained by the following procedure. First, the AFM control electronics must be able to vary the applied load on the cantilever while simultaneously monitoring and recording the normal and lateral signals while scanning across the surface. This can be accomplished in a number of different ways. Some software and controller packages, such as RHK’s SPM 100 controller and SPM 32 software (RHK Technology), allow the applied load to be automatically ramped in a stepwise fashion so that an image can be acquired with every scan line obtained at a different load. Some other AFM controller/software packages do not allow the user sufficient flexibility to complete such an experiment. In this case, the user may apply an external signal to the AFM itself. One way is to supply a voltage signal directly to the *z*-piezo of the AFM, thus altering the load on the cantilever. This may be accomplished by either modifying the electronics of the AFM controller, or by using an external connection, such as a breakout box. The downside to applying a signal directly to the *z*-piezo is that the feedback system needs to be turned off, so no line-by-line feedback can be maintained. A better method is to send a signal to the AFM that changes the feedback setpoint value, i.e. the applied normal load in feedback control. An external signal is sent directly into the AFM electronics to vary the setpoint, again either by modification of the AFM electronics or using a breakout box. This method allows for feedback control while the load is varied during scanning, which is beneficial for measurements on rough or sloped surfaces. Load and friction are continuously measured by monitoring the position of the laser spot on the photodetector in the normal and lateral directions, respectively. Usually it is easier to apply a continuously varying voltage, as opposed to the stepwise voltage ramp as in the RHK system for example. However, instead of each line being a separate load value, the load is continuously varied even during a single scan line. To account for this, the load and friction variations on a single line are averaged (excluding the edges of the image where the tip is sticking, and not sliding, with respect to the surface) to obtain a single data point of average load and friction for every scan line. This is reasonable to do if the variation in voltage (and, thus, force) during a single scan line is small compared to the range of voltage (force) applied during the experiment.

#### 4.1. Acquiring reliable friction versus load curves

To monitor the reproducibility of the data, the applied load may be started at a high value, ramped down until pull-off occurs and then increased back to the starting load. This way, the same normal applied load is measured twice within a short span of time, for both increasing and decreasing load (except for most of the negative load regime, which is only accessed during the decreasing load ramp). If the data overlap in these two cases, the data have been successfully reproduced. This can be checked by repeating the friction measurements at different locations on the sample surface to check for any variation. Note that for viscoelastic materials, hysteresis between loading and unloading portions may occur and is, in fact, a useful probe for the viscoelastic properties of the sample [23].

For consistent friction results one should obtain friction versus load data on a relatively small area of the sample to avoid topographic and chemical inhomogeneities, steps, grain boundaries, etc. However, to ensure that the AFM tip overcomes the static friction force and actually slides across the surface, the width of the line being scanned should be sufficiently large, which is easily verified by confirming that the friction loops contain a reasonable sliding portion. When analyzing the friction data, only the portion of the friction traces that corresponds to this steady sliding situation should be considered, thereby excluding the static friction regimes. In addition, it may be beneficial to scan the same line for the entire duration of the experiment, instead of rastering a square region on the surface. This allows for the sampling of the same region of the surface for all of the scan lines, except for a slight deviation from the region due to thermal drift and any in-plane translation of the tip due to the bending of the tilted lever. These effects can be compensated if desired [46].

#### 4.2. Relation between contact area and friction

Several studies have shown that the friction force in solid-solid nanocontacts below the wear threshold is proportional to the true contact area, i.e. number of interfacial atoms [1, 20, 47–50]. This was demonstrated by measuring both friction and the nano-scale contact area experimentally. In other words, friction force  $F_f$  for a single-asperity contact is given by:

$$F_f = \tau \cdot A, \quad (11)$$

where  $A$  is the interfacial contact area and  $\tau$  is the interfacial shear strength. As it represents the friction force per unit area of a pair of materials, one can also consider  $\tau$  as corresponding to the intrinsic frictional dissipation per interfacial atom.

The interfacial shear strength is not necessarily constant, and may, as a first attempt, be more generally described as a constant plus a pressure-dependent term:

$$\tau = \tau_0 + \zeta \cdot p, \quad (12)$$

where  $\tau_0$  is the constant interfacial shear strength term,  $p$  is the nominal contact pressure and  $\zeta$  is a dimensionless coefficient. The magnitude and pressure

dependence of the interfacial shear strength will depend on the materials and the sliding conditions (environment and temperature), and determining this behavior is a key goal in nanotribology, as is the determination of the general validity of equation (11), which may break down for sufficiently small contacts or under different sliding conditions (e.g. when wear takes place). Equation (12) has been shown to apply very well to systems involving molecular films in contact in the SFA [51], for some soft solids in macroscopic contact [52] and for some systems measured with the AFM [53]. For bare solid surfaces, the majority of studies report that  $\zeta$  is negligible [1, 15, 20, 22, 47–50, 53–60], but the range of materials for which this has been tested is limited. In any event, the determination of the contact area and how it relates to friction is a key challenge, and once again the JKR-to-DMT transition must be taken into account to properly describe the contact mechanics.

#### 4.3. Fitting friction versus load data to determine adhesion energy and interfacial shear strength

Although Carpick *et al.* outlined a procedure for applying equation (11) to a given set of contact area or friction data [16], the technique of determining a correct fit to data requires experience and knowledge of the characteristics of the different contact regimes. We have already discussed that the JKR and DMT limits represent two ends of the spectrum, but how does one determine from a given set of data whether it would obey the JKR model, the DMT model, or something in between, or neither? Figure 3 shows the contact area *versus* load relations for the various models, which again, we emphasize, are only truly valid under several assumptions including homogeneous, isotropic, linear elastic materials. One distinction of the JKR model is that the Hertz and DMT models predict zero contact area at pull-off, while the JKR, as well as the intermediate models, have a finite contact area at pull-off. This gives the experimentalist an easy way to make a qualitative estimate regarding the contact regime of the interface, and highlights the importance of acquiring a dense set of data in the adhesive regime (where the loads are negative).

As an example, a set of friction versus load data from an AFM experiment is shown in Fig. 4a. This set of data was taken using a Digital Instruments MultiMode AFM (Nanoscope IV controller) on a silicon substrate coated with a thin organic hydrocarbon monolayer film, using a silicon tip with native oxide termination. To be clear, the organic film will alter the contact mechanics substantially since the system is no longer homogeneous axially, it may be anisotropic, and the organic film may be somewhat non-linear and anelastic. This renders our example a case where no model in the JKR–DMT spectrum ought to apply quantitatively. However, for illustration purposes only, we carry out JKR–DMT analysis, assuming that the measured data are obtained for a homogeneous, isotropic, linear elastic system that obeys all the assumptions of the JKR–DMT models. A more complete and detailed analysis that goes beyond these assumptions will be presented elsewhere (data not shown).

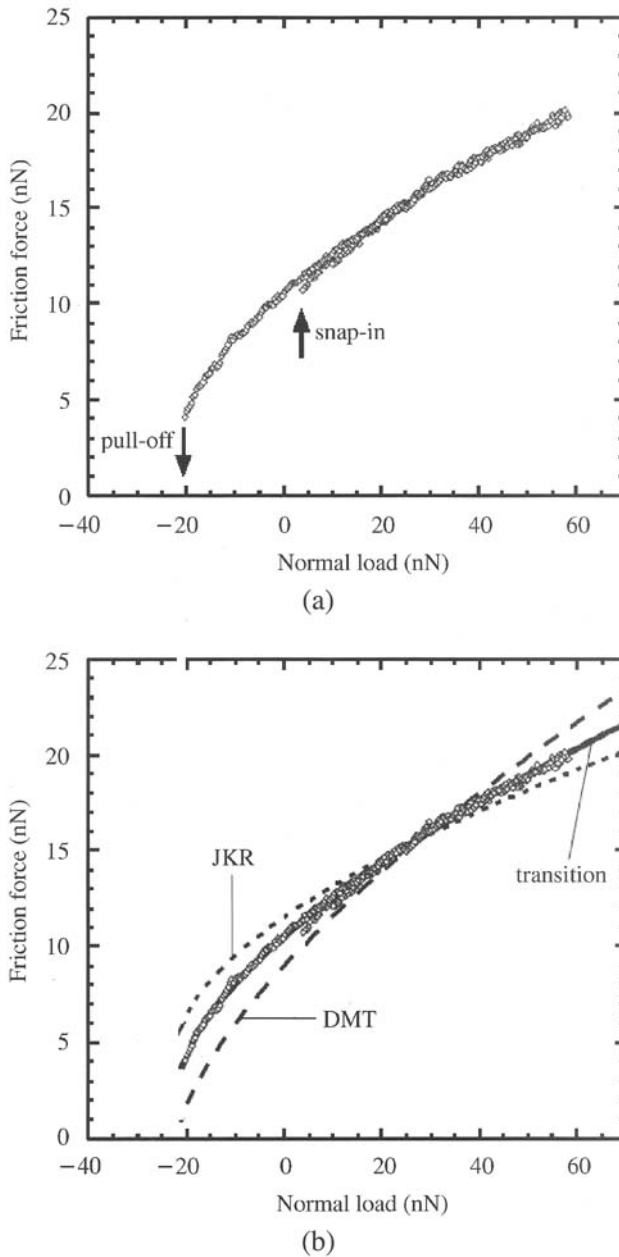


**Figure 4.** (a) An example set of AFM friction force *versus* load data, taken on a silicon substrate coated with a thin organic film, using a silicon tip with native oxide termination. This set of data is comprised of two overlapping traces, ramping from high load to low load, and then low load to high load. The instability points of pull-off and snap-in are shown on the graph. (b) Fit of data from (a) to the DMT, JKR and generalized transition equations, setting the same pull-off force for all fits. The two free parameters are the interfacial shear strength  $\tau$  and the transition parameter  $\alpha$ . (c) Fit of data from (a) to the DMT, JKR and generalized transition equations, where the pull-off force is a free parameter in addition to the interfacial shear strength  $\tau$  and the transition parameter  $\alpha$ .



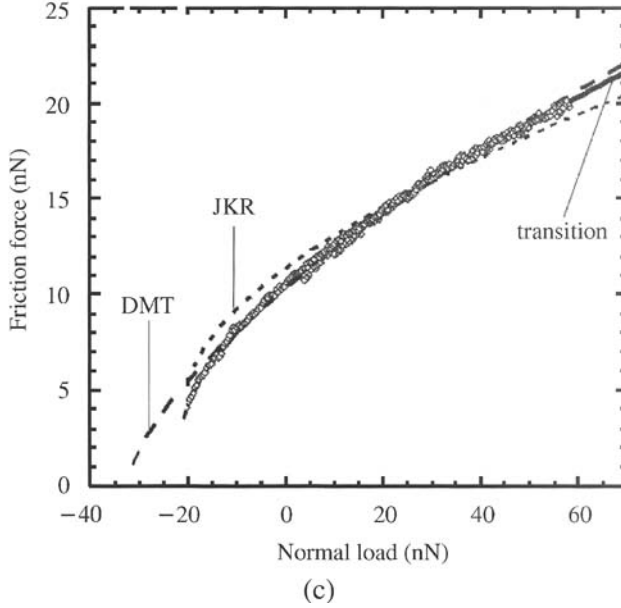


**Figure 4.** (Continued).

The data were acquired according to the procedure outlined above, where a ramped external voltage was applied to AFM electronics to continuously vary the normal force setpoint. There is minimal scatter in the data and no hysteresis other than a slight difference at the snap-in point.

Note that the normal load axis is defined such that zero corresponds to zero externally applied load. That is, a normal load of zero corresponds to the deflection of the lever when well out of contact with the sample, and no load is acting. This is the correct way to plot normal loads. The load axis then simply represents whether the lever is applying a tensile or compressive load to the sample. In some cases in the literature, researchers shift the normal load axis so that the pull-off force is at zero. This unfortunate practice is inappropriate and misleading, because it shifts the load axis by different amounts for different interfaces, and the unique amount of adhesion for each measurement cannot be determined from the graph as plotted.

The example data set has been fitted to the DMT, JKR, and generalized transition equation, as shown in Fig. 4b. The fit for the generalized transition equation is determined by letting the pull-off force  $P_c$ , friction at zero load  $F_{r0}$ , and transition parameter,  $\alpha$ , all be free parameters in a least squares minimization. The optimization was performed using KaleidaGraph (Synergy Software). The DMT and JKR fits were obtained by setting the pull-off force to be equal to that found from the transition fit. Equivalently, one could set this force equal to the pull-off force obtained from force–distance measurements, if one is confident that the adhesion measurements are consistent and uniform. Thus, there is only one free parameter, the friction force at zero load, for each of these two fits. Clearly, the JKR

and DMT fits are not appropriate. The transition fit is the most convincing, and the pull-off force from this fit is very close to that obtained directly from force-distance measurements.

The JKR and DMT fits can be improved somewhat by allowing the pull-off force to be a second free parameter. These fits are shown in Fig. 4c. The JKR fit is not substantially changed, but the DMT fit now matches the data better. However, this is at the expense of requiring a much larger adhesion force, whereby a portion of data at low loads appears to be ‘missing’. One could attribute the apparent ‘missing’ data to premature pull-off during friction scanning. However, as stated above, the pull-off force from the DMT fit does not match those from force-distance measurements. The transition fit, therefore, remains the most convincing.

The values from the transition fit are  $P_c = 22.3$  nN,  $F_{r0} = 10.4$  nN and  $\alpha = 0.42$ . From equation (6) and the relation  $\lambda = 1.1570\mu_T$ , this corresponds to  $\mu_T = 0.45$ , which indeed is in between the JKR and DMT limits.

Now that we know the value for  $\mu_T$ , the pull-off force and friction force at zero load can be converted into values for the work of adhesion and the interfacial shear strength by using the formulae in Ref. [16]. In this example,  $\gamma = 119$  mJ/m<sup>2</sup> and  $\tau = 550$  MPa. A pure two-parameter JKR fit would give  $\gamma = 123$  mJ/m<sup>2</sup> and  $\tau = 436$  MPa, and a pure two-parameter DMT fit would give  $\gamma = 148$  mJ/m<sup>2</sup> and  $\tau = 706$  MPa. Clearly, using the appropriate fit within the JKR–DMT spectrum makes a substantial difference, particularly for the interfacial shear strength.

The data can also be fitted by allowing  $\zeta$  to be non-zero. The fits are less accurate in this case, suggesting that  $\zeta$  is indeed zero for this system. However, the number of free parameters, four, is substantial. It, therefore, becomes desirable to measure the contact area independently of the friction force. This is done by measuring either the lateral contact stiffness [15, 48, 53, 57, 61] or the contact conductance [55, 62] as a function of load. Both of these quantities are related to the contact area, and analogous fitting procedures can be carried out to determine the transition parameter. These are important approaches that we strongly endorse, but do not discuss in detail in this publication.

## 5. FUTURE DIRECTIONS

It is remarkable that continuum mechanics is able to provide such a reasonable description of the contact properties at the nanometer scale. That is not to say that continuum mechanics tells the whole story; the system is, of course, made of atoms, and atomic-scale behavior like stick-slip friction is readily observed in many systems. Furthermore, recent work has indicated significant deviations from continuum behavior. Socoliuc *et al.*, for example, have found that the lateral contact stiffness at the lowest accessible loads for AFM tips with radii nominally below 15 nm cannot be accounted for by a continuum approach [63]. Specifically, the contact stiffness is load-independent, suggesting that a fixed number of atoms are interacting across the interface, and that this structure is not changing with the load.

Cha *et al.* have simulated single-asperity contact during loading and unloading using molecular dynamics [64]. The simulations and experiments both show that elastic contact mechanics should not be applied to describe asperity loading because the loading process involves generation and motion of dislocations. However, they find that the JKR model is applicable for unloading, where the deformation is almost completely elastic [64]. Luan and Robbins [65] have recently shown in simulations that the JKR model breaks down for sufficiently small contacts. The stress distribution no longer smoothly varies with location, and the contact area becomes difficult to determine. Wenning and Müser [66] have shown in simulations that for small contacts, atomic-scale contamination and lattice commensurability are determining factors, and the dependence of friction upon load is not necessarily monotonic nor strictly determined by the contact area.

These examples suggest that the description of the contact area, if it can even be defined in the atomistic limit, now poses the next set of challenges for researchers in nanotribology.

## 6. CONCLUSIONS

We have discussed the development of contact mechanics, from Hertz to the present day. In the case of homogeneous, isotropic, linear elastic normal adhesional contact between a sphere and a plane, the spectrum of interactions between the JKR and DMT limits can be applied to describe the contact area. We have shown how adhesion and friction measurements by AFM can be understood in light of the transition. We have also given examples of how the fits are performed, and how the fits significantly affect the calculations of fundamental interfacial parameters, namely the interfacial shear strength and the work of adhesion. Future challenges could encompass more complex contact mechanics situations, such as anisotropy, plasticity, viscoelasticity, inhomogeneity, the presence of thin films, and the breakdown of the continuum description of contact at the atomic scale.

### *Acknowledgements*

We thank Rachel J. Cannara and Dr. Anirudha V. Sumant for many fruitful interactions related to this work. We acknowledge Dr. William Robert Ashurst, Dr. Maarten P. de Boer and Dr. Alex D. Corwin for the organic-film-coated silicon sample. We gratefully acknowledge Prof. R. J. Hamers and Wensha Yang for use and assistance with the hydrogen plasma system. EEF acknowledges support from the National Science Foundation for a Graduate Research Fellowship. RWC acknowledges support from the National Science Foundation CAREER Program, grant #CMS-0134571, and from the Department of Energy, grant #DE-FG02-02ER46016.

## REFERENCES

1. R. W. Carpick and M. Salmeron, *Chem. Rev.* **97**, 1163–1194 (1997).
2. I. L. Singer and H. M. Pollock (Eds), *Fundamentals of Friction: Macroscopic and Microscopic Processes*. Kluwer, Dordrecht (1992).
3. R. Maboudian and R. T. Howe, *J. Vac. Sci. Technol. B* **15**, 1–20 (1997).
4. R. Maboudian, W. R. Ashurst and C. Carraro, *Tribol. Lett.* **12**, 95–100 (2002).
5. R. W. Carpick, PhD Thesis, Department of Physics, University of California at Berkeley, Berkeley, CA (1997).
6. A. M. Homola, J. N. Israelachvili, P. M. McGuiggan and M. L. Gee, *Wear* **136**, 65–83 (1990).
7. W. N. Unertl, *J. Vac. Sci. Technol. A* **17**, 1779–1786 (1999).
8. K. L. Johnson, *Contact Mechanics*. Cambridge University Press, Cambridge (1987).
9. K. L. Johnson, K. Kendall and A. D. Roberts, *Proc. R. Soc. Lond. A* **324**, 301–313 (1971).
10. B. V. Derjaguin, V. M. Muller and Yu. P. Toporov, *J. Colloid Interf. Sci.* **53**, 314–326 (1975).
11. D. Maugis, *J. Colloid Interf. Sci.* **150**, 243–269 (1992).
12. J. A. Greenwood, *Proc. R. Soc. Lond. A* **453**, 1277–1297 (1997).
13. E. Barthel, *J. Colloid Interf. Sci.* **200**, 7–18 (1998).
14. E. Barthel, *Colloid. Surf. A* **149**, 99–105 (1999).
15. M. A. Lantz, S. J. O'Shea, M. E. Welland and K. L. Johnson, *Phys. Rev. B* **55**, 10776–10785 (1997).
16. R. W. Carpick, D. F. Ogletree and M. Salmeron, *J. Colloid Interf. Sci.* **211**, 395–400 (1999).
17. O. Piétrement and M. Troyon, *J. Colloid Interf. Sci.* **226**, 166–171 (2000).
18. U. D. Schwarz, *J. Colloid Interf. Sci.* **261**, 99–106 (2003).
19. D. Maugis, *Langmuir* **11**, 679–682 (1995).
20. R. W. Carpick, N. Agrait, D. F. Ogletree and M. Salmeron, *J. Vac. Sci. Technol. B* **14**, 1289–1295 (1996).
21. R. W. Carpick, N. Agrait, D. F. Ogletree and M. Salmeron, *J. Vac. Sci. Technol. B* **14**, 2772 (1996).
22. K. L. Johnson, *Proc. R. Soc. Lond. A* **453**, 163–179 (1997).
23. K. J. Wahl, S. V. Stepnowski and W. N. Unertl, *Tribol. Lett.* **5**, 103–107 (1998).
24. D. Maugis and M. Barquins, *J. Phys. D* **11**, 1989–2023 (1978).
25. V. S. Mangipudi and M. Tirrell, *Rubber Chem. Technol.* **71**, 407–448 (1998).
26. W. N. Unertl, *J. Adhesion* **74**, 195–226 (2000).
27. M. Giri, D. B. Bousfield and W. N. Unertl, *Langmuir* **17**, 2973–2981 (2001).
28. E. Barthel, G. Haiat and M. C. Phan Huy, *J. Mech. Phys. Solids* **51**, 69–99 (2003).
29. K. R. Shull, *Mater. Sci. Eng. R* **36**, 1–45 (2002).
30. B. A. Galanov, V. Domnich and Y. Gogotsi, *Exp. Mech.* **43**, 303–308 (2003).
31. S. D. Mesarovic and K. L. Johnson, *J. Mech. Phys. Solids* **48**, 2009–2033 (2000).
32. D. Shi, Y. Lin and T. C. Ovaert, *J. Tribol.* **125**, 223–231 (2003).
33. V. I. Fabrikant, *J. Strain Anal. Eng. Design* **39**, 55–70 (2004).
34. J. N. Israelachvili and D. Tabor, *Proc. R. Soc. Lond. A* **331**, 19–38 (1972).
35. J. N. Israelachvili, in: *Fundamentals of Friction*, I. L. Singer and H. M. Pollock (Eds), p. 351. Kluwer, Dordrecht (1992).
36. K. L. Johnson and I. Sridhar, *J. Phys. D* **34**, 683–689 (2001).
37. E. Barthel and S. Roux, *Langmuir* **16**, 8134–8138 (2000).
38. M. P. de Boer and T. M. Mayer, *Mater. Res. Bull.* **26**, 302–304 (2001).
39. J. S. Villarrubia, *Surf. Sci.* **321**, 287–300 (1994).
40. J. S. Villarrubia, *J. Res. (Natl. Inst. Stand. Technol.)* **102**, 425–454 (1997).
41. M. Enachescu, R. W. Carpick, D. F. Ogletree and M. Salmeron, *J. Appl. Phys.* **95**, 7694–7700 (2004).
42. G. W. Tormoen, J. Drelich and E. R. Beach, III, *J. Adhesion Sci. Technol.* **18**, 1–17 (2004).

43. E. R. Beach, G. W. Tormoen, J. Drelich and R. Han, *J. Colloid Interf. Sci.* **247**, 84–99 (2002).
44. J. P. Cleveland, S. Manne, D. Bocek and P. K. Hansma, *Rev. Sci. Instrum.* **64**, 403–405 (1993).
45. J. E. Sader, J. W. M. Chon and P. Mulvaney, *Rev. Sci. Instrum.* **70**, 3967–3969 (1999).
46. R. J. Cannara and M. J. Brukman, *Rev. Sci. Instrum.* (submitted).
47. R. W. Carpick, N. Agrait, D. F. Ogletree and M. Salmeron, *Langmuir* **12**, 3334–3340 (1996).
48. R. W. Carpick, D. F. Ogletree and M. Salmeron, *Appl. Phys. Lett.* **70**, 1548–1550 (1997).
49. R. W. Carpick, M. Enachescu, D. F. Ogletree and M. Salmeron, in: *Fracture and Ductile vs. Brittle Behavior – Theory, Modeling and Experiment*, G. Beltz, K.-S. Kim and R. L. Selinger (Eds), pp. 93–103. Mater. Res. Soc., Warrendale, PA (1999).
50. M. Enachescu, R. J. A. van den Oetelaar, R. W. Carpick, D. F. Ogletree, C. F. J. Flipse and M. Salmeron, *Tribol. Lett.* **7**, 73–78 (1999).
51. B. J. Briscoe and D. C. B. Evans, *Proc. R. Soc. Lond. A* **380**, 389–407 (1982).
52. I. L. Singer, R. N. Bolster, J. Wegand, S. Fayeulle and B. C. Stupp, *Appl. Phys. Lett.* **57**, 995–997 (1990).
53. O. Piétrement and M. Troyon, *Langmuir* **17**, 6540–6546 (2001).
54. A. R. Burns, J. E. Houston, R. W. Carpick and T. A. Michalske, *Phys. Rev. Lett.* **82**, 1181–1184 (1999).
55. M. Enachescu, R. J. A. van den Oetelaar, R. W. Carpick, D. F. Ogletree, C. F. J. Flipse and M. Salmeron, *Phys. Rev. Lett.* **81**, 1877–1880 (1998).
56. R. Lüthi, E. Meyer, M. Bammmerlin, L. Howald, H. Haefke, T. Lehmann, C. Loppacher, H.-J. Güntherodt, T. Gyalog and H. Thomas, *J. Vac. Sci. Technol. B* **14**, 1280–1284 (1996).
57. M. A. Lantz, S. J. O’Shea, A. C. F. Hoole and M. E. Welland, *Appl. Phys. Lett.* **70**, 970–972 (1997).
58. O. Piétrement and M. Troyon, *Surf. Sci.* **490**, L592–596 (2001).
59. Z. Wei, C. Wang and C. Bai, *Langmuir* **17**, 3945–3951 (2001).
60. I. L. Singer, in: *Fundamentals of Friction*, I. L. Singer and H. M. Pollock (Eds), p. 237. Kluwer, Dordrecht (1992).
61. O. Piétrement, J. L. Beaudoin and M. Troyon, *Tribology Lett.* **7**, 213–220 (1999).
62. M. A. Lantz, S. J. O’Shea and M. E. Welland, *Phys. Rev. B* **56**, 15345–15352 (1997).
63. A. Socoliuc, R. Bennewitz, E. Gnecco and E. Meyer, *Phys. Rev. Lett.* **92**, 134301–134304 (2004).
64. P.-R. Cha, D. J. Srolovitz and T. K. Vanderlick, *Acta Mater.* **52**, 3983–3996 (2004).
65. B. Luan and M. O. Robbins, Personal Communication.
66. L. Wenning and M. H. Müser, *Europhys. Lett.* **54**, 693–699 (2001).

## **Friction, adhesion, and deformation: dynamic measurements with the atomic force microscope**

PHIL ATTARD \*

*Ian Wark Research Institute, University of South Australia, Mawson Lakes, SA 5095, Australia*

**Abstract**—A summary is given of the author's recent experimental and theoretical work involving the atomic force microscope, with the focus being upon dynamic measurements. Four topics are covered: calibration techniques for the friction force microscope, quantitative measurements of friction and the effect of adhesion, measurement and theory for the deformation and adhesion of viscoelastic particles, and the interaction and adhesion of hydrophobic surfaces due to bridging nanobubbles.

**Keywords:** Atomic force microscope; friction; adhesion; deformation; nanobubble.

### **1. INTRODUCTION**

The atomic force microscope (AFM) [1] is commonly used to image surfaces and to study the interaction and adhesion of particles. The widespread adoption of the AFM is due to its ease of use, the molecular-level information that it provides, and the variety of surfaces that can be studied in a broad range of environments. In addition, the computer interface allows flexible control of the device and the automated acquisition of large volumes of data; it facilitates multiple repeat experiments to check reproducibility and to minimize statistical error; and it enables detailed data analysis. This computer control opens up the possibility of real-time monitoring of experiments and the exploration of time-dependent effects. The AFM is well suited to studying the latter, whereas the original surface force apparatus [2] and its variants [3, 4] either lack automated data acquisition or suffer from inertial and other artefacts that must be taken into account in the quantitative interpretation of dynamic force measurements [5, 6].

The distinction between equilibrium and non-equilibrium forces is quite important. To some extent, the primary concern with the AFM has been (and should be) to ensure that the experiments are carried out slowly enough that equilibrium

---

\*Phone: +062 8 8302 3564. Fax: +062 8 8302 3683. E-mail: phil.attard@unisa.edu.au

is established at each instant, so that the measured forces are comparable to those measured statically. Beyond that, an exciting field of research exploits the dynamic capabilities of the AFM to measure non-equilibrium phenomena in a controlled fashion. We review two examples from our laboratory that show the utility of dynamic AFM measurements for non-equilibrium systems. Results and quantitative analyses are presented for the deformation, interaction, and adhesion of viscoelastic droplets (Section 4), and for the interaction and adhesion of surfaces via bridging nanobubbles during their spreading (Section 5).

The most obvious technique that utilizes the dynamic capability of the AFM is the measurement of friction, which is also called friction force microscopy or lateral force microscopy. Since the original work of Mate *et al.* [7], the fields of friction force mapping (sometimes called chemical imaging) and of nanotribology have grown greatly (see, for example, papers in Refs [8] and [9]). Although some progress has been made, this research has been limited by approximations or restrictions on the lateral calibration method for the AFM. This deficiency has been rectified quite recently by two techniques that yield the torsional spring constant of the cantilever and the voltage response of the lateral photodiode to cantilever twist [10–12]. This review begins by summarizing the limitations of previous calibration techniques and by detailing the procedures involved in the newer quantitative methods (Section 2). The results that we have obtained in our laboratory [13] for the quantitative dependence of friction on adhesion in a system with electrical double-layer interactions are then reviewed (Section 3).

## 2. CALIBRATION OF THE FRICTION FORCE MICROSCOPE

### 2.1. Critical review

In order to use the AFM, various calibrations have to be performed. The lateral movement of the piezo-crystal is often calibrated using model substrates. The expansion factor that relates the applied voltage to the distance that the piezo-crystal expands in the vertical direction normal to the substrate,  $\Delta z$ , can be measured from the interference fringes due to the reflection of the laser from both the cantilever and the substrate. The normal spring constant of the cantilever,  $k_x$ , can be obtained gravitationally, thermally, or by resonance techniques [14–16]. The normal photodiode sensitivity factor,  $\alpha_0$ , relates the measured vertical differential photodiode voltage,  $\Delta V_{\text{vert}}$ , to the vertical deflection of the cantilever,  $\Delta x$ , which in the constant compliance regime is equal to the piezo-drive movement,  $\Delta x = \Delta z$ . For the quantitative measurement of friction, in addition to these, one has to obtain the torsional spring constant of the cantilever,  $k_\theta$ , and the lateral photodiode sensitivity factor,  $\beta$ , which relates the measured lateral differential photodiode voltage,  $\Delta V_{\text{lat}}$ , to the twist angle of the cantilever,  $\Delta\theta$ .

Unfortunately, almost all lateral calibration techniques that have been used to date are approximate in one way or another, and the measurements of friction that

utilize them must be regarded as semi-quantitative. Briefly, a critical review of the literature reveals that in most cases [17–21], the torsional spring constant is calculated, not measured, using an analytic approximation [22] that idealizes the actual geometry of the cantilever. In addition, it ignores the effects of coatings and thickness variations, which in the case of the normal spring constant can alter the value by an order of magnitude. The lateral sensitivity factor, which relates the photodiode voltage to the twist angle, has also been obtained by assuming it to be proportional to the vertical sensitivity [18], by modelling the beam path and profile [19], and by assuming that the tip is pinned during the initial part of the friction loop [17, 23]. The assumed pinning does not take into account any slippage or deformation of the tip, which can make the method inaccurate, and others have attempted to improve the method by invoking certain simple models of friction and deformation [20, 21]. Measurements of friction parallel to the long axis of the cantilever using the normal spring constant and sensitivity [24, 25] erroneously neglect the bending moment of the cantilever [6, 21]. Toikka *et al.* [23] attempted to use gravity acting on an attached lever, but the torque that they applied was shown to give negligible cantilever twist [12], and it appears that what they measured was in fact photodiode saturation. And finally, the commonly used calibration method of Ogletree *et al.* [26] is restricted by the need for a specialized terraced substrate and an ultra-sharp tip. For the calibration, this method makes two assumptions about the friction law, namely that friction is a linear function of the applied load and that it vanishes when the applied load is the negative of the adhesion (i.e. the pull-off point). Counter-examples showing non-linear behaviour are known [13, 27] and one should check whether or not such a linear regime exists before using it for the calibration. That none of the previous calibration methods is entirely satisfactory is confirmed by the fact that many friction force microscopy (FFM) papers give friction in terms of volts rather than Newtons [27–29]. Almost all friction force maps are similarly uncalibrated and the images are given in terms of volts rather than the physical friction coefficient.

Feiler *et al.* [12] have developed a direct technique that simultaneously measures the cantilever spring constant and the lateral sensitivity of the photodiode. That particular method is discussed in detail below.

Meurk *et al.* [10] have given a method for directly calibrating the lateral sensitivity of the photodiode. Basically, the angle of a reflective substrate is varied with respect to the laser beam. In some AFM scanners, there is a stepper motor that facilitates the tilt of the head. From the geometry and the amount of movement, the degree of tilt,  $\Delta\theta$ , can be calculated. The change in the lateral photodiode voltage,  $\Delta V_{\text{lat}}$ , is linear in the tilt angle and the ratio of the two gives the lateral sensitivity of the AFM.

The torsional spring constant of the cantilever can be obtained directly by the technique developed by Bogdanovic *et al.* [11]. Here a protuberance (e.g. an upturned tipped cantilever) is glued to the substrate and force measurements are performed against it with the protuberance making contact off the central axis of



the tipless force measuring cantilever, which causes the latter to bend and to twist. Recording the normal and lateral photodiode voltages in the constant compliance regime at several different lateral off-sets allows the spring constant divided by the lateral sensitivity to be obtained. Combined with the method of Meurk *et al.* [10], this allows a full calibration of the AFM. (In principle, one can also obtain the lateral sensitivity with this method. However, the small leverage and high torsional spring constant make it impractical to do so.)

## 2.2. Quantitative calibration technique

We now describe in detail a one-step method that simultaneously measures both the lateral photodiode sensitivity and the torsional spring constant of the cantilever that has been developed in our laboratory [12]. A glass fibre 50–200  $\mu\text{m}$  in length is glued perpendicular to the long axis of the cantilever and parallel to the substrate. To ensure that the substrate pushes on the end of the fibre, a colloid sphere is attached at its tip (see Fig. 1). Using the well-known colloid probe attachment procedure of Ducker *et al.* [30], an epoxy resin is used to attach the sphere and a heat-setting adhesive is used to attach the fibre. This allows the fibre to be removed later and the cantilever used for friction measurements (i.e. the method is non-destructive). Attaching the sphere is convenient but not essential; other ways to ensure that it is the end of the fibre that touches the substrate include gluing the fibre to the cantilever at a slight angle, having a ledge or colloid probe on the substrate, or performing the measurement with the head or substrate tilted a small amount (e.g. by using the stepper motor).

The essence of the method is that pushing on the tip of the fibre with a force  $F$  produces a torque  $\tau = FL$ , where  $L$  is the length of the fibre. The cantilever simultaneously deflects,  $\Delta x = F/k_x$ , and twists,  $\Delta\theta = \tau/k_\theta$ . The deflection, and hence the force and torque, is obtained from the differential vertical photodiode voltage  $\Delta x = \alpha_0 \Delta V_{\text{vert}}$ , where the bare sensitivity factor,  $\alpha_0$ , is measured in the constant compliance regime *without the attached fibre*. The actual sensitivity factor with the attached fibre,  $\alpha_L$ , is greater than this because only part of the piezo-drive movement goes into deflecting the cantilever,  $\Delta x < \Delta z$  (the rest is soaked up by the twist). The bare vertical sensitivity factor has to be measured in a separate experiment and depends on the positions of the laser, the photodiode, and the cantilever mount. With practice, it is possible to obtain better than 10%

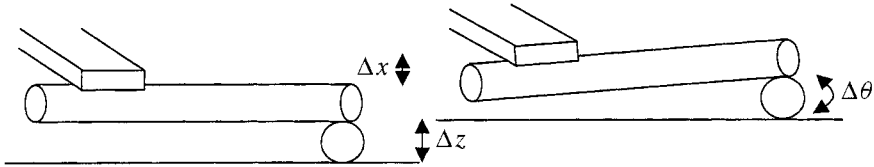


**Figure 1.** Rectangular cantilever with attached fibre and sphere. When the substrate is moved a distance  $\Delta z$ , the cantilever deflects a distance  $\Delta x$  and twists an amount  $\Delta\theta$ . The corresponding changes in the differential photodiode voltages,  $\Delta V_{\text{vert}}$  and  $\Delta V_{\text{lat}}$ , are measured.

reproducibility in this quantity between different experiments and after remounting the cantilever. The best way to ensure this is to maximize the total vertical signal and to minimize the differential lateral signal each time.

The calibration factor of primary interest is the one that relates the differential lateral photodiode voltage to an applied torque,  $\tau = \gamma \Delta V_{\text{lat}}$ . This is given by

$$\gamma = \frac{\tau}{\Delta V_{\text{lat}}} = \frac{k_x \Delta x L}{\Delta V_{\text{lat}}} = k_x \alpha_0 L \frac{\Delta V_{\text{vert}}}{\Delta V_{\text{lat}}}. \quad (1)$$

This equation predicts a linear relationship between the two photodiode signals, which, as can be seen in Fig. 2, is indeed the case. The slope of this line, combined with the measured values for the vertical spring constant, the bare vertical sensitivity factor, and the length of the fibre, gives the factor that converts the differential lateral photodiode voltage to the applied torque in general (i.e. independent of the attached fibre). Figure 3 shows the lateral sensitivity factor obtained using a number of different fibres. That the same value is obtained each time shows that it is an intrinsic property of the cantilever and AFM set-up. It also confirms that remounting the cantilever does not preclude reproducible results from being obtained.

We found that the calibration procedure was straightforward and relatively robust. The method was less successful whenever there was significant adhesion between the substrate and the tip of the fibre or the attached sphere. We minimized such adhesion by using silica surfaces and conducting the calibration in water at natural pH.

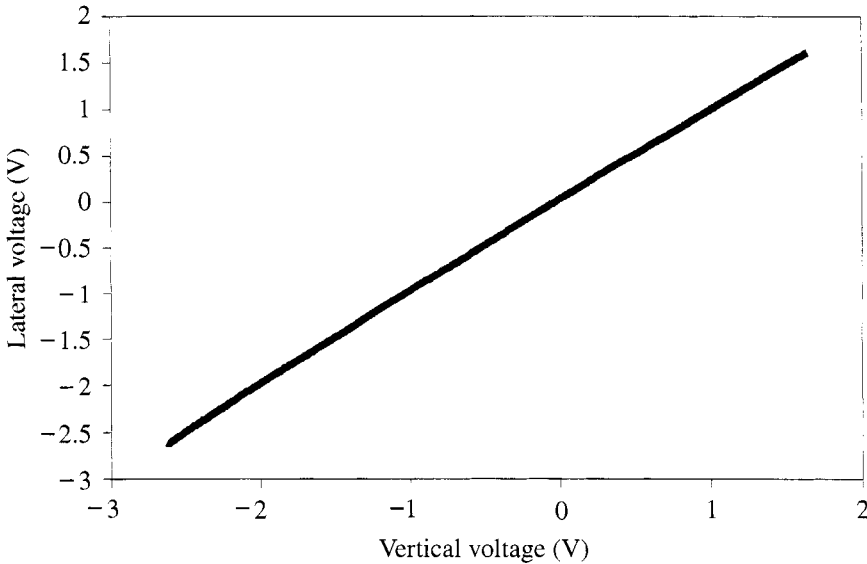


**Figure 2.** Lateral differential photodiode voltage as a function of the vertical voltage. Both were measured for a cantilever with an attached fibre over the whole approach regime of a single force measurement. The data are from Ref. [12].

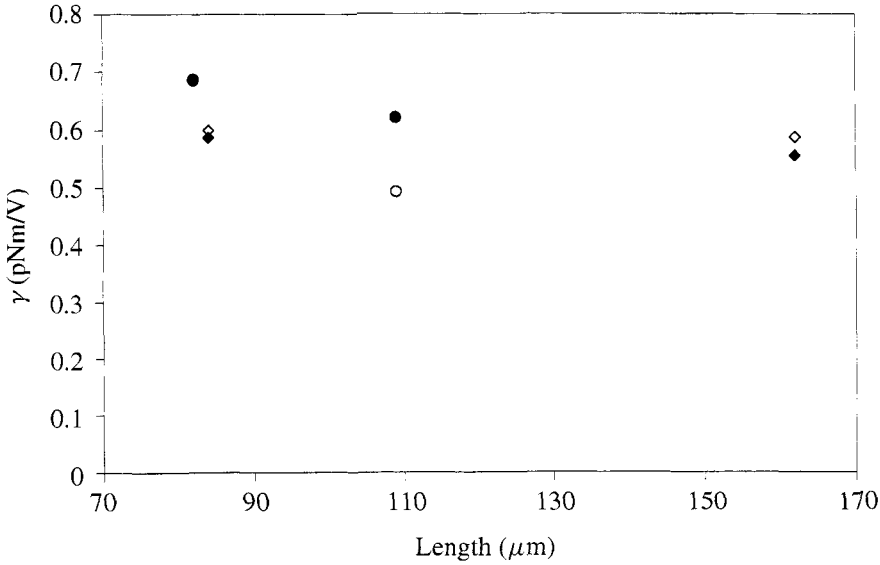


**Figure 3.** Lateral sensitivity factor for different fibres. The cantilevers were taken from the same batch. Circles indicate fibres with an end-attached sphere; diamonds indicate bare fibres; filled symbols are for approach; and open symbols are for retraction. The data are from Ref. [12].

It is possible to verify independently the procedure by obtaining the sensitivity factor that relates the change in angle to the change in the lateral photodiode signal, and comparing this with the value obtained by the method of Meurk *et al.* [10]. From the slope of the constant compliance region of the force curve with the attached fibre, one can obtain the constants

$$\alpha_L = \frac{\Delta z}{\Delta V_{\text{vert}}} \quad \text{and} \quad \beta_L = \frac{\Delta z}{\Delta V_{\text{lat}}}, \quad (2)$$

for the vertical and lateral deflections, respectively. With these, the lateral sensitivity can be shown to be given by [12]

$$\frac{\Delta \theta}{\Delta V_{\text{lat}}} = \frac{\beta_L(1 - \alpha_0/\alpha_L)}{L}. \quad (3)$$

A value of  $3 \times 10^{-4}$  rad/V was obtained using our method [12], compared with  $1.7 \times 10^{-4}$  rad/V using the method of Meurk *et al.* [10].

The torsional spring constant itself is given by [12]

$$k_\theta = \frac{-k_x L^2}{1 - \alpha_L/\alpha_0}. \quad (4)$$

A value of  $2 \times 10^{-9}$  N m was obtained using our method [12], compared with  $1.2 \times 10^{-9}$  N m calculated from the method of Neumeister and Ducker [22].

### 3. ADHESION AND FRICTION

#### 3.1. Intrinsic force

One of the oldest ideas concerning the nature of friction is embodied in Amontons' law, which states that the friction force  $f$  is proportional to the applied load  $L$ ,  $f = \mu L$ , where  $\mu$  is the coefficient of friction. For the case of adhering surfaces, where a negative load needs to be applied to separate them, it is known that there can be substantial friction even when the load is zero. Hence Amontons' law may be slightly modified:

$$f = \begin{cases} \mu(L + A), & L \geq -A \\ 0, & L < -A, \end{cases} \quad (5)$$

where  $A > 0$  is the adhesion, which is the greatest tension that the surfaces can sustain (i.e. it is equal to the absolute value of the force required to pull the surfaces apart). This modified version reflects the plausible idea that friction only occurs when the surfaces are in contact. Amontons' law raises several questions: Is friction a linear function of load? Is the role of adhesion only to shift the effective load? What is the law for non-adhering surfaces? Is friction zero for surfaces not in contact? And what does contact mean on a molecular scale?

The AFM is an ideal tool to test the fundamental nature of friction and we set out to answer quantitatively these and other questions [13]. We chose a system that would allow us to alter the adhesion in a controlled manner, so that as far as possible all other variables were kept constant. We used a titanium dioxide substrate (root mean square roughness of 0.3 nm) and a silicon dioxide colloid probe (root mean square roughness of 0.8 nm, 7  $\mu$ m diameter). The measurements were carried out in an aqueous electrolyte ( $10^{-3}$  M  $\text{KNO}_3$ ) as a function of pH. The  $\text{SiO}_2$  is negatively charged at practically all pHs (its point of zero charge is  $\approx$  pH 2), whereas  $\text{TiO}_2$  is positively charged at low pH and negatively charged at high pH (its point of zero charge is  $\approx$  pH 4.5). Hence at low pH the attractive double-layer interaction between the surfaces causes, them to adhere, and at high pH they repel each other and do not adhere.

There have been several other AFM studies of friction between surfaces with electrical double-layer interactions [27, 31, 32]. In some cases, an applied voltage has been used to modify the adhesion, but the friction coefficients and force laws have all been qualitative in the sense of the preceding section. A critical discussion of these results is given in Ref. [13].

The load, which is the applied normal force, is shown in Figs 4 and 5 as a function of the separation for various pHs. It can be seen that the surfaces do indeed interact with an electrical double-layer interaction and that the pH controls the sign and the magnitude of the force. For pH 4 and 5, the attractive double-layer interaction gives an adhesion of  $A = 10.5$  and 4.4 nN, respectively. However, at higher pH the surfaces do not adhere.

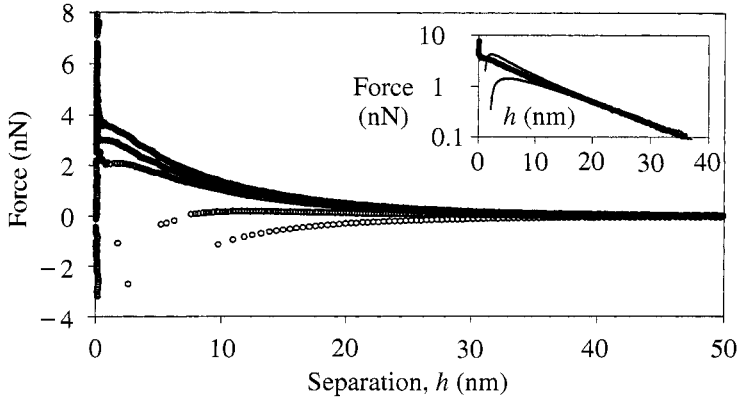


**Figure 4.** Force on approach as a function of the separation. The substrate is  $\text{TiO}_2$ , the  $7\ \mu\text{m}$  diameter colloid probe is  $\text{SiO}_2$ , and the background electrolyte is 1 mM  $\text{KNO}_3$ . From top to bottom, the curves correspond to pH 8, 7, 6, 5, and 4. The inset shows constant potential ( $\psi_{\text{SiO}_2} = -50\ \text{mV}$  and  $\psi_{\text{TiO}_2} = -43\ \text{mV}$ ) and constant charge fits to the pH 8 case on a log scale. Reprinted with permission from Ref. [13]. Copyright (2000) American Chemical Society.

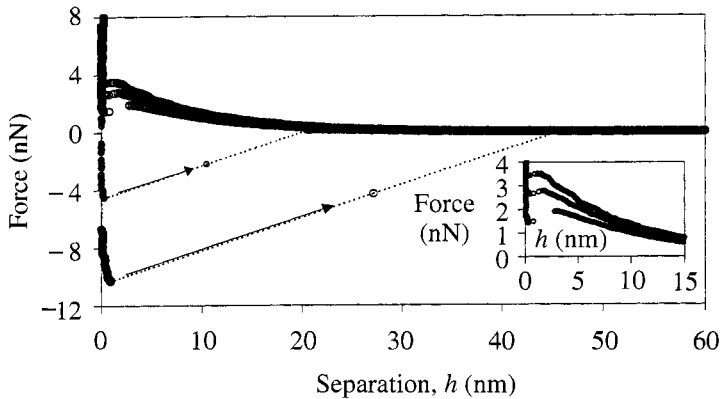


**Figure 5.** Same as Fig. 4 on retraction. The inset magnifies the three highest pHs at small separations. Reprinted with permission from Ref. [13]. Copyright (2000) American Chemical Society.

In view of equation (5), we are motivated to define the detachment force,  $F_{\text{detach}}$ , as the minimum applied force necessary to keep the surfaces in contact [13]. For non-adhering surfaces this is a positive quantity, and for adhering surfaces it is negative (in fact, it is the negative of the adhesion). The detachment force at pH 6, 7, and 8 was  $F_{\text{detach}} = 1.4, 2.6,$  and  $3.5\ \text{nN}$ , respectively (Fig. 5). In view of the close relationship between adhesion and the detachment force, one may define an intrinsic force,

$$F_{\text{intrinsic}} = L - F_{\text{detach}}, \quad (6)$$

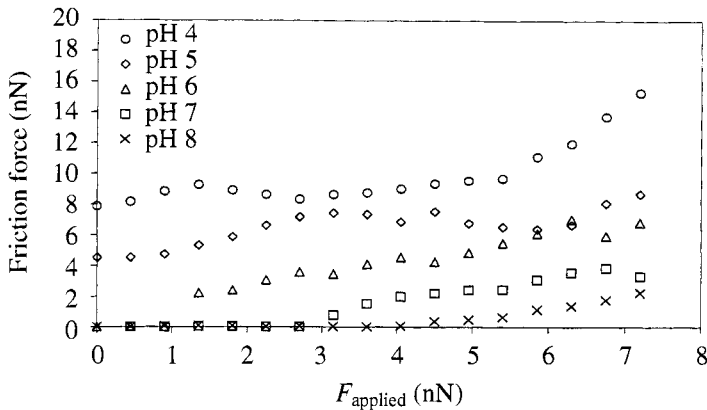


**Figure 6.** Friction force as a function of the applied load. Reprinted with permission from Ref. [13]. Copyright (2000) American Chemical Society.

which may be thought of as the force in excess of that when the surfaces are just in contact. In this language, Amontons' law generalized to non-adhering surfaces would read  $f = \mu F_{\text{intrinsic}}$ .

We measured friction as a function of the applied load at various pHs. This was done in the usual fashion [7] by moving the substrate back and forth in the direction perpendicular to the long axis of the cantilever and recording friction loops. The length of the scan in each direction was  $0.5 \mu\text{m}$  and the velocity was  $1 \mu\text{m/s}$ . The lateral calibration factor, obtained as detailed above [12], was used to convert (half) the voltage difference between the two arms of the friction loop to the applied torque  $\tau$ . The friction force was obtained as  $f = \tau/2r$ , where  $r = 7 \mu\text{m}$  is the radius of the colloid probe. The applied load was fixed by using the set-point feature of the AFM (i.e. the vertical deflection signal was held constant during the friction loop).

Friction is plotted as a function of the applied load in Fig. 6. In general, friction increases with increasing load. At a given applied load, friction is also larger, the lower the pH. Since the adhesion increases with decreasing pH, one may restate this fact as the higher the adhesion, the higher the friction at a given applied load. Moreover, friction is non-zero at zero loads for adhering surfaces. For non-adhering surfaces, friction is zero for small, but non-zero applied loads.

The quantitative behaviour of friction with pH is not obvious when plotted as a function of the applied load. But when plotted against intrinsic load, Fig. 7, the utility of the detachment force becomes evident. The functional form of the friction force law is fundamentally independent of pH and all the measurements lie on a single universal curve. In other words, the major role of pH is to determine the adhesion (or more precisely, the detachment force). Once this parameter has been experimentally determined from a normal force measurement at a given pH, the friction at that pH may be predicted from the friction measured at any other pH merely by shifting the load by the detachment force.

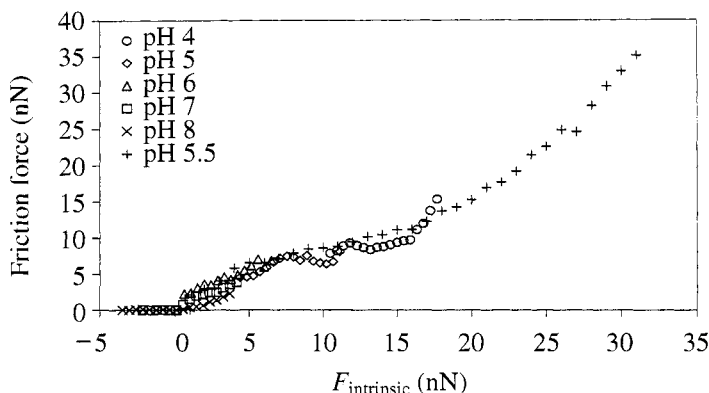


**Figure 7.** Friction force as a function of the intrinsic load. Reprinted with permission from Ref. [13]. Copyright (2000) American Chemical Society.

These experiments show that for this system friction is not a linear function of the load (i.e. the friction coefficient  $\mu = df/dL$  is not independent of load). There is a noticeable curvature in the plot, with friction increasing more rapidly at higher loads. The loads that have been applied here are relatively weak [the average pressure in the contact region (see below) is less than about 10 MPa and the peak pressure is less than about 100 MPa [13]] and it is not clear what will happen at higher loads than these.

Whilst it is not implausible that the friction should be zero for negative intrinsic forces in all cases (this corresponds to the surfaces being out of contact), it is a little surprising that for positive intrinsic forces the increase in friction is the same in all cases. After all, not only are the adhesion and the normal force laws different at different pHs, but also the surface chemistry varies due to the different amount of ion binding that occurs. The fact that the latter has almost no effect on friction is perhaps not unexpected, since over the range of pH studied, for  $\text{TiO}_2$  only about 1% of the surface sites are converted from  $\text{H}^+$  at low pH to  $\text{OH}^-$  at high pH, and for  $\text{SiO}_2$  the change is about 10% [33]. Nevertheless, it is not immediately obvious why surfaces with different adhesion display quantitatively the same friction for the same intrinsic force.

### 3.2. Elastic deformation

In order to investigate the above question further, we carried out elastic deformation calculations on the sphere and substrate under the experimental conditions [13]. Elastic deformation has long been thought to play a dominant role in the friction of macroscopic bodies, mainly in the context of using contact mechanics to account for asperity flattening [34, 35]. We, however, were in a position to go beyond contact theories such as that due to Johnson, Kendall, and Roberts (JKR) [36] or that due to Derjaguin, Muller, and Toporov (DMT) [37]. We used the soft-contact algorithm of Attard and Parker [38, 39] and invoked the actual experimentally measured force

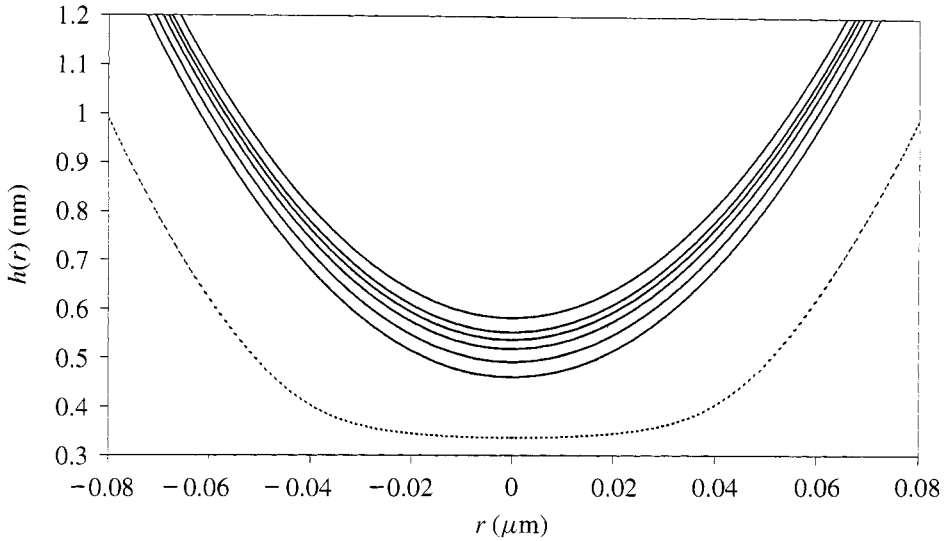


**Figure 8.** Calculated surface profiles for an applied load of 5 nN. From top to bottom, the pH is 8, 7, 6, 5, and 4, and in each case, the measured force law has been used in the calculations. Young's modulus and Poisson's ratio for SiO<sub>2</sub>,  $E/(1 - \nu^2) \approx 7.7 \times 10^{10}$  N/m<sup>2</sup>, have also been used. The bottom dashed curve is for an applied load of 720 nN for the pH 4 case. The abscissa is the distance from the central axis in micrometres and the ordinate is the local separation in nanometres. The data are from Ref. [13].

law, which has, of course, an extended range (i.e. it is not a contact force). The algorithm self-consistently calculates the surface shape of the elastically deformed bodies due to the local pressure, which, in turn, depends on the local separation of the deformed bodies. In this way, we obtain the actual surface shape and the actual pressure profile, whereas contact mechanics assumes simplified and non-physical forms for both. We fitted a smooth curve to the measured force law at different pHs and using the Derjaguin approximation, differentiated this to obtain the pressure as a function of the surface separation. The latter is required by the algorithm [38, 39], as discussed in the following. The calculations presented in Ref. [13] are the first elastic deformation calculations using an actual experimentally measured force law. For the present calculations, there was no hysteresis between the loading and unloading cycles. (The hysteresis observed in the original papers [38, 39] for soft adhering bodies has since been attributed to a non-equilibrium viscoelastic effect [40, 41]; see Section 4.)

Figure 8 shows the resultant surface shape at an applied load of 5 nN. This load is greater than all the detachment forces and in all cases, the surfaces showed non-zero friction. It can be seen that very little surface flattening has occurred and that the surfaces at different pHs are effectively displaced parallel to each other.

Also included in Fig. 8 is a high load (720 nN) case, which shows substantial flattening. However, there is no well-defined contact region and there is certainly



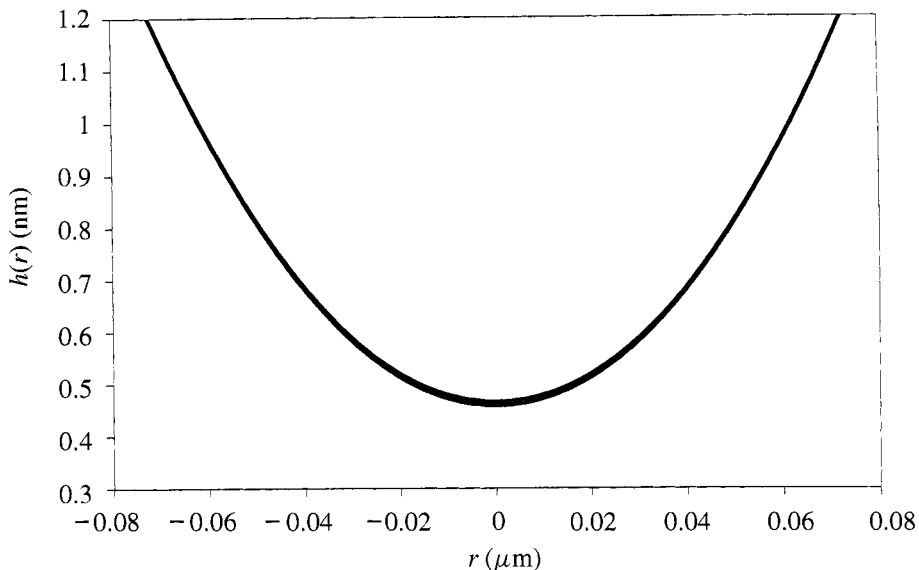


**Figure 9.** Calculated surface profiles for an intrinsic force of 15 nN. From top to bottom, the virtually indistinguishable curves correspond to pHs of 8, 7, 6, 5, and 4, respectively. The data are from Ref. [13].

no sharp change in the surface profile to demark contact, despite the fact that these calculations are for the adhering pH 4 surfaces.

The fitted force law includes a Lennard–Jones soft repulsion with length scale 0.5 nm [13] and one could define contact as local separations smaller than this. Such an arbitrary definition is somewhat problematic, particularly since the curves at 5 nN load, which are not in contact by the definition, display non-zero friction. In view of this discussion of the meaning of contact for systems with realistic surface forces of non-zero range, the inapplicability of simple contact theories such as Hertz, JKR, or DMT is clear. One might also conclude that the experimental verification or refutation of Amontons’ second law (for a given load, friction is independent of the contact area) at the molecular level will be difficult.

Figure 9 shows the surface shapes at different pHs at an intrinsic load of 15 nN, which corresponds to an applied load of 5 nN for the pH 4 case. The change from Fig. 8 is quite dramatic and one can see that the profiles have coalesced. In other words, surfaces at a given intrinsic load have the same shape and local surface separation. Given that friction is also a universal function of intrinsic load (Fig. 7), one may conclude that friction is a function of the local separation and independent of the force law. In so far as the short-range interactions between the atoms on the two surfaces can be expected to be independent of the pH, one can say that these are the interactions that determine friction. Friction occurs between two bodies when energy can be transferred from one to another, which means that they have to be close enough for the interaction between atoms on the two surfaces to be comparable to the thermal energy [13]. One concludes that the only role of

adhesion in friction is to decrease the amount of applied load that is necessary to bring the surfaces to a given separation.

#### 4. VISCOELASTIC DEFORMATION AND ADHESION

##### 4.1. Viscoelastic theory

The shapes of the deformed surfaces given above were obtained by solving the equations of continuum elasticity theory in the semi-infinite half-space approximation [38, 42]

$$u(r) = \frac{-2}{\pi E} \int ds \frac{p(h(s))}{|\mathbf{r} - \mathbf{s}|}. \quad (7)$$

Here the elasticity parameter  $E$  is given in terms of Young's moduli and Poisson's ratios of the two bodies,  $2/E = (1 - \nu_1^2)/E_1 + (1 - \nu_2^2)/E_2$ ;  $r = |\mathbf{r}|$  and  $s = |\mathbf{s}|$  are the lateral distances from the central axis connecting the centres of the bodies (the integration is over the two-dimensional plane bisecting the two bodies); and  $p(h)$  is the pressure between two infinite planar walls at a separation of  $h$ . The total deformation normal to the surfaces at each position is  $u(r)$  and hence the local separation between the two bodies is  $h(r) = h_0(r) - u(r)$ . Here the local separation of the undeformed surfaces is  $h_0(r) = h_0 + r^2/2R$ , where  $h_0$  is the separation on the axis, and where  $R^{-1} = R_1^{-1} + R_2^{-1}$  is the effective radius of the interacting bodies; in general, the  $R_i$  is related to the principal radius of curvature of each body [43].

For contact theories such as Hertz, JKR, or DMT, the local pressure  $p(h(r))$  that appears in the integrand of equation (7) is replaced by a contact pressure  $p_c(r)$  that is a specified function of radius which when integrated gives  $u(r) = r^2/2R$ , which corresponds to a flat contact region,  $h(r) = 0$ . In contrast, for realistic force laws that have an extended range, such as van der Waals, electrical double layer, or the actual measured  $p(h)$  discussed above, the integral must be evaluated numerically. Because in this case the local separation depends on the deformation, equation (7) represents a non-linear integral equation that must be solved by iteration for each nominal separation  $h_0$ .

An efficient algorithm for the solution of the non-contact elastic equation has been given by the Attard [38, 40] and it has been used to analyse a variety of force laws [13, 38–41]. Other workers have also calculated the elastic deformation of the solids using realistic surface forces of finite range [44–51]. There have, of course, been a large number of experimental studies to measure the interaction of deformable solids. These include AFM measurements [52–62], as well as results obtained with the surface force apparatus and the JKR device [63–72]. These studies, in general, show that the adhesion and interaction are hysteretic and time-dependent, particularly for highly deformable solids with high surface energies. Such behaviour is characteristic of viscoelastic materials. Maugis and Barquins have given a review of adhesion experiments on viscoelastic materials, which they

attempt to interpret in quasi-JKR terms, introducing a somewhat ill-defined time-dependent surface energy [73].

A proper theoretical treatment of the deformation and adhesion of viscoelastic materials involves replacing the elasticity parameter, which gives the instantaneous response to the pressure, by the creep compliance function, which gives the response to past pressure changes. In this way, the prior history of the sample is accounted for. Hence the generalization of the elastic half-space equation involves a time convolution integral [74, 75],

$$u(r, t) - u(r, t_0) = \int_{t_0}^t dt' \frac{-2}{\pi E(t - t')} \int ds \frac{\dot{p}(h(s, t'))}{|\mathbf{r} - \mathbf{s}|}. \quad (8)$$

Here  $\dot{p}(h(r, t))$  is the time rate of change of the local pressure at a distance  $r = |\mathbf{r}|$  from the axis and at time  $t$ . The bodies are assumed to be stationary up to time  $t_0$ , and if interacting or in contact, have at that time fixed deformation corresponding to static elastic equilibrium,  $u(r, t_0) = u_\infty(r)$ . This expression is essentially equivalent to that used by a number of authors [76–79], with the difference being that the latter have treated contact problems, with  $\dot{p}(h(s, t))$  replaced by a specified analytic  $\dot{p}_c(s, t)$ , whereas here  $\dot{p}(h(s, t))$  is determined by the physical force law and the rate of change of separation over earlier times.

An algorithm has been developed for solving the full non-contact problem for the case where the creep compliance function has an exponential form [74]:

$$\frac{1}{E(t)} = \frac{1}{E_\infty} + \frac{E_\infty - E_0}{E_\infty E_0} e^{-t/\tau}. \quad (9)$$

Here  $E_0$  and  $E_\infty$  are the short- and long-time elasticity parameters, respectively, and  $\tau$  is the relaxation time. The algorithm can be generalized to more complex materials with multiple relaxation times [74]. The present three-parameter model is perhaps the simplest model of viscoelastic materials, although an alternative three-parameter expression,  $E(t)^{-1} = C_0 + C_1 t^m$ ,  $0 < m < 1$ , has also been used to model liquid-like materials [78–80].

With the exponential creep compliance function, differentiation of the deformation yields [74]

$$\begin{aligned} \dot{u}(r, t) = & \frac{-1}{\tau} [u(r, t) - u_\infty(r, t)] \\ & - \frac{2}{\pi E_0} \int ds \frac{\dot{p}(h(s, t))}{|\mathbf{r} - \mathbf{s}|}, \end{aligned} \quad (10)$$

where  $u_\infty$  is the static deformation that would occur in the limit  $t \rightarrow \infty$  if the pressure profile were fixed at its current value,

$$u_\infty(r, t) = \frac{-2}{\pi E_\infty} \int ds \frac{p(h(s, t))}{|\mathbf{r} - \mathbf{s}|}. \quad (11)$$

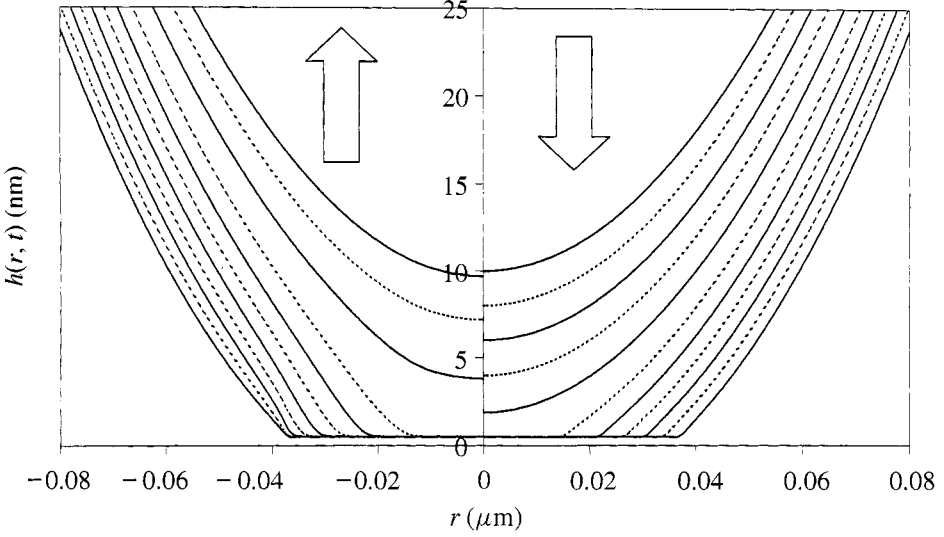


**Figure 10.** Surface profiles for adhering viscoelastic spheres. The profiles are plotted every millisecond, or every 2 nm from  $h_0 = 10$  nm (top) to  $-10$  nm (bottom). The drive speed is  $|\dot{h}_0| = 2 \mu\text{m/s}$  and the Hamaker constant is  $A = 10^{-19}$  J, with  $z_0 = 0.5$  nm and  $R = 10 \mu\text{m}$ . The viscoelastic parameters are  $E_0 = 10^{10}$  N/m<sup>2</sup>,  $E_\infty = 10^9$  N/m<sup>2</sup>, and  $\tau = 1$  ms. The right-hand panel is for loading and the left-hand panel is for unloading. The data are from Ref. [75].

The rate of change of the pressure is

$$\dot{p}(h(r, t)) = p'(h(r, t)) [\dot{h}_0(t) - \dot{u}(r, t)], \quad (12)$$

where  $\dot{h}_0(t)$  is the specified drive trajectory. Accordingly, equation (10) represents a linear integral equation for the rate of change of deformation. It can be solved using the same algorithm that has been developed for the elastic problem [38, 40]. It is then a simple matter to solve the differential equation for the deformation by simple time stepping along the trajectory,  $u(r, t + \Delta_t) = u(r, t) + \Delta_t \dot{u}(r, t)$ .

The algorithm has been used to obtain results for an electrical double-layer repulsion [74] and for a van der Waals attraction [75]. The latter is

$$p(h) = \frac{A}{6\pi h^3} \left[ \frac{z_0^6}{h^6} - 1 \right], \quad (13)$$

where  $A$  is the Hamaker constant and  $z_0$  characterizes the length scale of the soft-wall repulsion. Figure 10 shows the shape of viscoelastic spheres during their interaction. The total time spent on the loading branch is ten times the relaxation time, so that one expects to see viscoelastic effects. At the largest separation, prior to approach the surfaces are undeformed. Prior to contact, on approach they bulge towards each other under the influence of the van der Waals attraction. There is a relatively rapid jump into contact and initially a fast spreading of the flattened contact region, which continues to grow as the bodies are driven further together. At the edges of the contact region, there is a noticeable rounding of

the surface profiles on the approach branch. Following the reversal of the motion (unloading), the surfaces become extended as they are pulled apart and there is a sharper transition between contact and non-contact than on the loading branch. It should be noted, however, that even in this case the slopes at the edge of the contact region are not discontinuous, as predicted by the JKR theory. Following the turning point, the surfaces are effectively pinned in contact for a time and then the contact region begins to recede. After the surfaces jump apart, there remains a memory of the stretching that occurred during unloading and for a time comparable to the relaxation time of the material, the deformed separation is smaller on the unloading branch out of contact than at the corresponding position upon loading.

This hysteresis in surface shape is reflected in the difference in force versus nominal separation curves on the loading and unloading branches (Fig. 11). On approach, prior to contact a given attraction occurs at larger nominal separation, for slower driving speeds. In these cases, there is an increased bulge, leading to smaller actual separations, a consequence of the fact that viscoelastic materials soften over longer time-scales. The jump of the surfaces into contact is reflected in a sharp decrease in the force. Once in contact, the force increases and the nominal separation becomes negative, which is a reflection of the deformation and growth of the flattened contact region under increasing load. The faster the bodies are driven together, the steeper is the slope of the force curve, as one might expect, since this corresponds to materials that are in effect stiffer since they do not have time to relax.

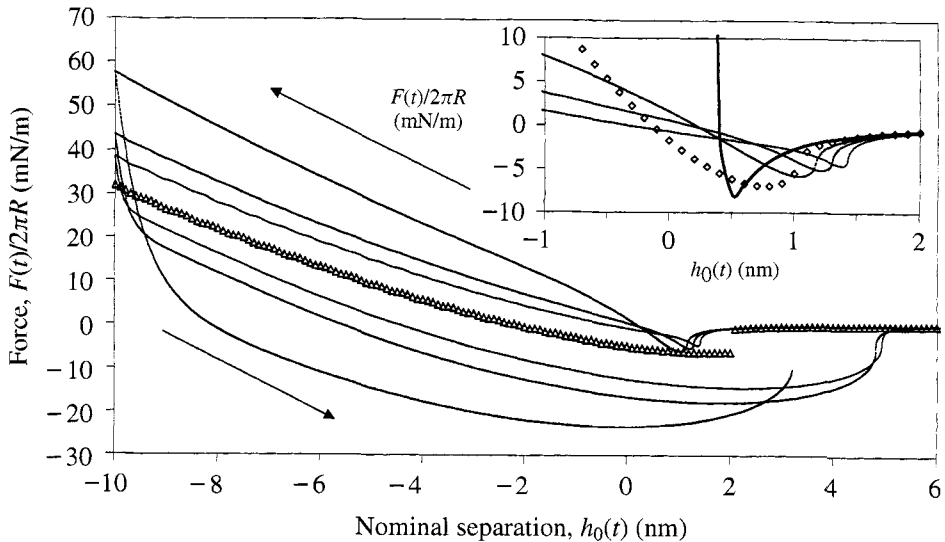


**Figure 11.** Interaction forces for adhering viscoelastic spheres. From small to large, the hysteresis loops correspond to driving velocities of  $|h_0| = 1, 2$ , and  $5 \mu\text{m/s}$ , using the viscoelastic parameters of Fig. 10. The crosses represent the static equilibrium elastic result for  $E_\infty = 10^9 \text{ N/m}^2$ . Inset: loading curves in the region near initial contact. The diamonds represent the static equilibrium elastic result for  $E_0 = 10^{10} \text{ N/m}^2$  and the bold curve is the force for rigid particles. The data are from Ref. [75].

Following the reversal of the direction of motion in Fig. 11, a small increase in the nominal separation gives a large decrease in the applied load, which causes the unloading branch to lie beneath the loading branch. This behaviour is reflected in the surface profiles (Fig. 10), where on the loading branch, increasing the load causes the contact area to grow. In contrast, immediately following the turning point, decreasing the load stretches the surfaces at a fixed contact area. The hysteresis in the force curves manifests the fact that a certain energy has to be put into the system to move the surfaces a nominal distance on loading, and less energy is recovered from the system in moving the same distance on unloading. This is precisely what one would expect from a viscoelastic system. The size of the hysteresis loop increases with the speed with which the bodies are driven together or pulled apart. As the speed is decreased, both loops appear to coalesce on the long-time elastic result, which corresponds to static equilibrium, equation (7).

Figure 11 also shows that the adhesion, which is the maximum tension on the force loop, increases with the drive velocity,  $\dot{h}_0$ . Because the position here is controlled, we are able to calculate the trajectory past the force minimum and beyond the out of contact jump. In an experiment that controlled the load, the force minimum would be the last point measured in contact. The position of the minimum force moves to smaller (more negative) nominal separations as the velocity is increased. It can be seen that the adhesion of the viscoelastic bodies is significantly greater than that of elastic bodies.

The velocity dependence of the adhesion is explored in more detail in Fig. 12. As the velocity is decreased, the curves asymptote to the static equilibrium elastic

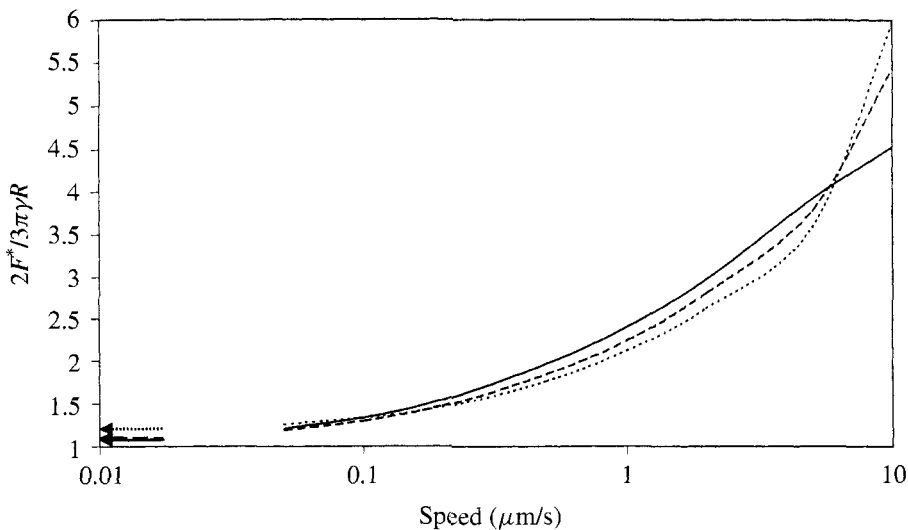


**Figure 12.** Adhesion force. The maximum tension normalized by the JKR elastic adhesion is plotted as a function of the drive velocity (logarithmic scale). The parameters are as in Fig. 10, except that the Hamaker constant is  $A = 1, 5, \text{ and } 10 \times 10^{-20} \text{ J}$  (the surface energy is  $\gamma \equiv A/16\pi z_0^2 = 0.80, 3.98, \text{ and } 7.96 \text{ mJ/m}^2$ ) for the dotted, dashed, and solid curves, respectively. The data are from Ref. [75].

## Direct adhesion measurements of pharmaceutical particles to gelatin capsule surfaces

T. H. IBRAHIM<sup>1,\*</sup>, T. R. BURK<sup>1</sup>, F. M. ETZLER<sup>2</sup> and R. D. NEUMAN<sup>1,†</sup>

<sup>1</sup> *Department of Chemical Engineering, Auburn University, Auburn, AL 36849-5127, USA*

<sup>2</sup> *Boehringer Ingelheim Pharmaceuticals, Inc., Research and Development Center,  
900 Ridgebury Road, Ridgefield, CT 06877-0368, USA*

**Abstract**—Scanning probe microscopy (SPM) was used to measure directly the adhesion of individual lactose particles to the surface of gelatin capsules employed in dry powder inhalant drug delivery systems. In this study, SPM shows that gelatin capsule surfaces with high surface heterogeneity and high-contrast friction exhibit high adhesion and that gelatin capsule surfaces with low surface heterogeneity and low-contrast friction exhibit low adhesion. The adhesion of lactose particles to gelatin capsules was also determined by measuring the retention of lactose particles in the capsules. The adhesion trend obtained with individual lactose particles using the colloidal probe technique agrees with the macroscopic retention results. The adhesion appears to be proportional to the particle size for homogeneous capsule surfaces. In dry powder inhalation products, the Lifshitz–van der Waals forces and acid–base interactions appear to be the principal forces contributing to particle–surface adhesion. The physicochemical nature of the capsule surface seems to dictate the spatial variation of adhesion across the surface. The SPM results clearly show that the surface physicochemical properties depend on the gelatin and mold release agent utilized in the manufacture of gelatin capsules. One of the practical implications of this study is that extraneous surface contamination of gelatin capsules by chemical processing aids such as mold release agents appears to be a key factor affecting the respirable fraction in dry powder inhalation products.

**Keywords:** Adhesion; atomic force microscopy; colloidal probe; friction imaging; lactose; gelatin capsule; particle–surface adhesion; pharmaceutical inhalation products; scanning probe microscopy.

### 1. INTRODUCTION

In a dry powder inhaler (DPI), an inhalation powder typically consisting of micronized drug and carrier particles (usually a sugar such as lactose) is inhaled

---

\*Present address: Department of Chemical Engineering, Tuskegee University, Tuskegee, AL 36088, USA.

†To whom correspondence should be addressed. E-mail: rdneuman@eng.auburn.edu

from a gelatin capsule in the form of a dry powder dispersion in air. The carrier is incorporated into the formulation because coarser carrier particles are typically more free flowing, thereby contributing to ease of handling during manufacture and improving emptying from the capsule during inhalation [1]. It has also been found that the use of carrier particles significantly improves the mass of drug particles in the respirable range (respirable fraction) in some inhaler devices [2].

In order for the full potential of DPIs to be realized, it is essential to obtain high performance in terms of the reproducibility and efficacy of the drug respirable fraction. In this type of drug delivery system, the surface properties of the various components of both the powder formulation and the gelatin capsules, as well as environmental conditions, govern the physical properties of the aerosol cloud during inhalation. An improved fundamental understanding of particle adhesion to solid surfaces and to other particles is essential for enhanced control of the aerosol properties and, therefore, the respirable fraction.

A significant amount of research attempting to evaluate the adhesion forces between particles and solid surfaces has been performed over the years [3, 4]. For example, a number of experimental techniques based on the detachment of particles from surfaces have been utilized for measuring adhesion: centrifugal [5–9], impact separation [10–12], aerodynamic [5, 13, 14], and cantilever beam [15] methods. While very useful, these methods provide only limited insight into microscopic details which are needed for an improved understanding of the factors influencing particle adhesion and removal.

More fundamental methods of evaluating adhesion have become available with the advent of new sophisticated techniques capable of investigating the physicochemical nature of surfaces. One powerful tool is scanning probe microscopy (SPM), which can be used to obtain nanoscale images of a surface, based on the physicochemical interaction of a scanning probe with a surface [16], and to measure directly the interaction (or adhesion) forces between an individual particle and a solid surface by using the colloidal probe technique [17–20]. In addition to topographic imaging, SPM can be operated in lateral force microscopy (LFM) mode to yield maps of surfaces that indicate the friction interactions with a scanning probe. If the magnitude of the friction force is compared only with that of the adhesion force (or energy), friction and adhesion are not generally related; however, recent experiments with the surface forces apparatus (SFA) technique have shown that the (kinetic) friction force correlates with the hysteretic or irreversible component of the adhesion energy [21, 22]. Furthermore, the humidity of the ambient environment can significantly influence both adhesion and friction forces [21], and therefore the relative humidity (RH) must be controlled in friction and adhesion measurements.

Recently, there has been considerable interest in the surface characterization of gelatin films. The topographic nanostructure of gelatin surfaces has been investigated using SPM [23–25]. The topographic and friction characteristics of gelatin films of different physicochemical and mechanical properties have also been examined by SPM [26–28]. The viscoelastic deformation induced by a cantilever



tip in a gelatin film has been studied by force modulation and LFM techniques [29]. In addition, microindentation measurements have been performed on gelatin films using a spherical indenter [30]. Furthermore, the adhesion of surface chemically characterized solids to gelatin surfaces has been evaluated by Lavielle *et al.* [31].

In this paper, we report direct adhesion measurements of individual lactose particles to gelatin capsule surfaces using SPM by employing the colloidal probe technique. Furthermore, the adhesion of lactose particles is correlated with the surface physicochemical variation observed by friction imaging of the capsule surfaces. To our knowledge, this is the first time that this approach has been used to characterize the adhesion of pharmaceutical particles to gelatin capsule surfaces under controlled conditions. Particle retention studies are also presented and reveal that the adhesion trend observed using the colloidal probe technique is in general agreement with the independently measured retention of lactose particles in gelatin capsules. This successful application of SPM techniques likely opens a new era of critical analysis of the performance of pharmaceutical dry powder inhalation products from the perspective of surface and colloid science.

## 2. EXPERIMENTAL

### 2.1. Materials

Pharmaceutical grade lactose monohydrate (Pharmatose 200M) was obtained from De Melkindustrie, Veghel, The Netherlands. Hard gelatin capsules of commercial origin were employed in this study. The capsule samples are designated as follows: 72601, 29625, and 29625ext, which was the same as 29625 but was subsequently extracted by a proprietary process.

### 2.2. Scanning probe microscopy

A Nanoscope III MultiMode™ SPM (Digital Instruments, Santa Barbara, CA, USA) with an extender electronics module was mounted on a pneumatic vibration isolation table. The sample chamber was enclosed with a Humplug (BioForce Laboratory, Santa Barbara, CA, USA) with accommodation for the cantilever holder handle and an internal humidity/temperature sensor with digital readout. The RH in the SPM sample chamber was controlled to within  $\pm 2\%$  using a humidity generator (Model RH1500, VTI, Miami, FL, USA).

The SPM was equipped with a J vertical scanner with scan size  $125 \times 125 \mu\text{m}$  and vertical range  $5 \mu\text{m}$ . Cantilevers (of nominal  $0.58 \text{ N/m}$  spring constant) with silicon nitride tips were used for both imaging and adhesion measurements. The force–distance measurements were performed at a vertical scan rate of  $6.5 \mu\text{m/s}$  and a loading force of approximately  $6 \text{ nN}$ . The scan rate employed in the colloidal probe measurements is about the same as that used by Hoh and Engel [32], which is significantly below the rate reported to cause oscillation in air at the pull-off point.

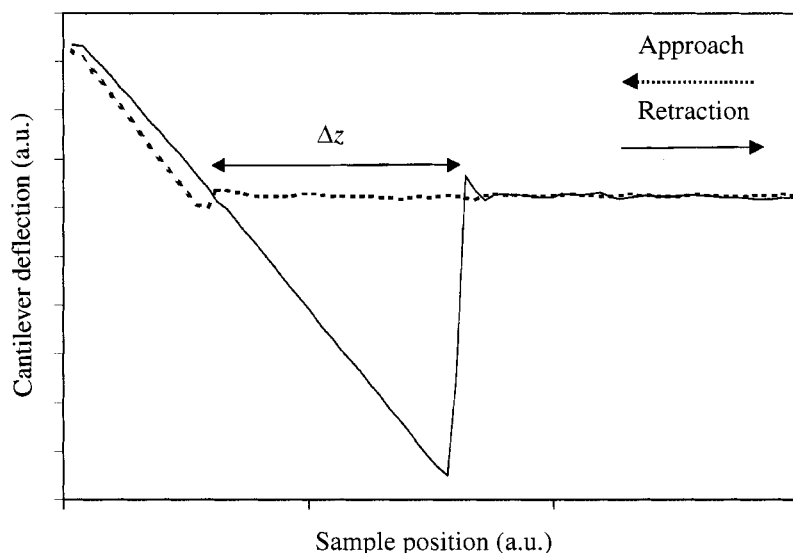


**Figure 1.** Typical lactose particle–gelatin capsule force curve.

All gelatin capsule samples and lactose colloidal probes were equilibrated for at least overnight at 50% RH in Pyrex containers and then in the humidity-controlled SPM sample chamber for at least 1 h before measurements. The contact force used for imaging was minimized to the extent ( $< 2$  nN) that the tip would not lose contact with the surface during scanning due to drift. Different areas on capsule samples prepared from multiple gelatin capsules were examined to verify that the surface physicochemical nature and adhesion characteristics presented are representative.

A typical force curve reflecting the interactions experienced between the lactose probe and the gelatin sample during approach, contact, and separation of the two surfaces is shown in Fig. 1. The change in cantilever deflection ( $\Delta d$ ) at pull-off may be used with the effective spring constant ( $k$ ) of the cantilever and Hooke's law ( $F = k \times \Delta d$ ) to calculate the adhesion force between the probe and the sample. However, when a large range of adhesion forces is obtained using a single cantilever, the complete deflection of the cantilever is often not evident. Therefore, the adhesion force was calculated based on the horizontal distance ( $\Delta z$ ) between the point at which the probe crosses the zero deflection line upon retraction and the point at which the probe pulls free of the surface. Essentially a right triangle forms between  $\Delta z$  and the negative portion of the force curve which results upon retraction, as can be seen in Fig. 1.

### 2.3. Capsule sample preparation

The preparation of the gelatin capsule samples was performed in a laminar flow hood to minimize extraneous contamination. The gelatin capsules were sectioned using a scalpel to obtain 5 mm  $\times$  5 mm samples. The inside surface of the capsule,

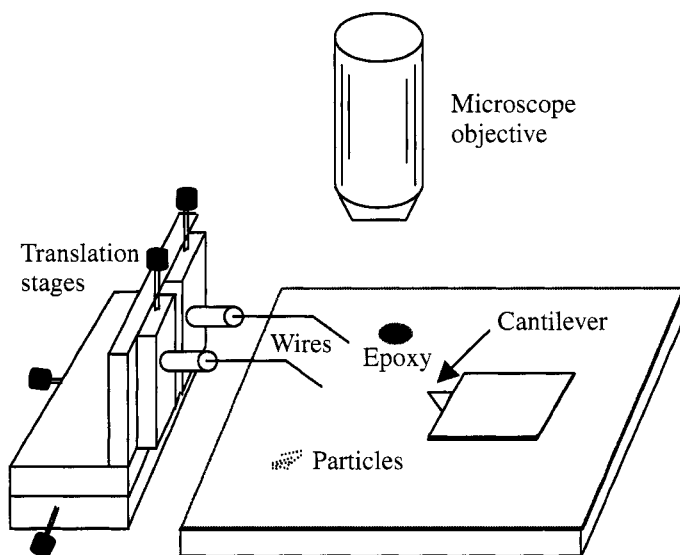


**Figure 2.** Apparatus for colloidal probe preparation.

which comes into contact with pharmaceutical formulations, was mounted face up on an epoxy adhesive-coated glass slide. While the epoxy adhesive was allowed to set, the capsule sample was maintained essentially flat using a custom-made Teflon clamp which avoided contact with the gelatin sample where imaging and adhesion measurements were to be performed.

#### *2.4. Colloidal probe preparation*

A lactose particle was attached to a silicon nitride tip as follows: briefly, two clean ultrafine wires were attached to an XYZ-translation stage for micromanipulation of the adhesive and colloidal particle as illustrated in Fig. 2. The first wire was used to obtain and deposit a small amount of adhesive onto the end of the cantilever tip where the probe particle was to be attached. The other wire was then used to pick up and attach a selected particle onto the cantilever tip. Figure 3 shows a typical lactose particle mounted onto a cantilever.

#### *2.5. Particle retention measurements*

The particle retention characteristics of gelatin capsules were assessed by two approaches. The first method measured the retention when a given amount of lactose particles was added to, mixed, and emptied from gelatin capsules. The second method was an attempt to simulate the re-dispersion of lactose particles from the gelatin capsule during usage of a DPI device.

Particle retention in gelatin capsules was evaluated under controlled humidity conditions. Each capsule was weighed before and after the addition of approximately 45 mg of lactose and shaken ten times each in the horizontal and vertical directions.

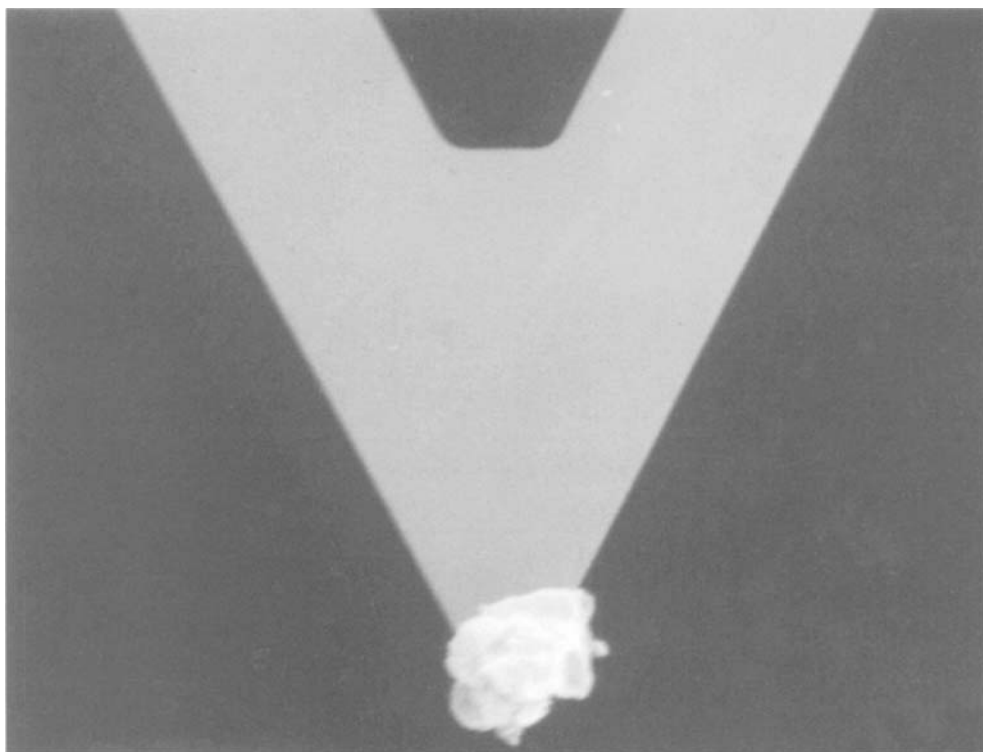


**Figure 3.** Lactose particle mounted onto a silicon nitride cantilever.

Next, the capsule was opened, vigorously emptied, and reweighed, and then the weight percentage of powder retained was determined.

Particle retention on planar capsule surfaces was investigated upon controlled application of a nitrogen gas stream. Lactose particles were dispersed on a capsule sample prepared as described previously; any loose particles were gently shaken from the capsule surface; and the particle distribution on the capsule sample was examined under the optical microscope of the SPM apparatus. The capsule sample was then mounted in front of a nozzle from which nitrogen gas flowed parallel to and across the capsule surface, resulting in a drag force on the particles. After each incremental increase of the gas flow rate, the retention of lactose particles on the capsule surface was evaluated by optical microscopy.

### 3. RESULTS AND DISCUSSION

Direct adhesion measurements of individual lactose particles to gelatin capsule surfaces were performed at 50% RH. This RH was selected for study as being representative of the 'water activity' that tends to be in the range of 40–60% RH in packaged (sealed) dry powder inhalation products (unpublished results). The adhesion of a lactose particle was measured 50 times at a single location on a

capsule surface to examine the reproducibility of the adhesion measurements. Next, the adhesion was measured ten times per location while the lactose particle was translated laterally across the surface at  $1\text{-}\mu\text{m}$  intervals to provide an indication of the intrinsic site-to-site variability of the adhesion characteristics. The ten adhesion measurements at each location were averaged to yield an adhesion profile over a  $50\text{-}\mu\text{m}$  scan length across the capsule surface. Figure 4 shows both the stationary and the scanned adhesion of a  $6\text{-}\mu\text{m}$  lactose particle to the surface of gelatin capsules 72601, 29625, and 29625ext plotted as a function of the contact number and distance. In addition, the adhesion forces for three different lactose (probe) particles on the three above-referenced capsule surfaces, as well as the overall average adhesion values, are summarized in Table 1.

The standard deviation associated with the direct measurement of the adhesion force between a lactose particle and a gelatin capsule surface is only about  $\pm 3\text{ nN}$  on the basis of the adhesion measurements at a single location. This is not too surprising since inspection of Fig. 4 reveals that there does not appear to be any appreciable change in the adhesion force with the number of contacts, thereby indicating that repetitive contact does not induce significant capsule sample (or lactose particle) alteration or damage. However, upon scanning, the scatter (standard deviation) in the adhesion force is observed to increase by a factor of *ca.* 2–30 depending on the particular combination of gelatin capsule and lactose particle, as can be seen from Table 1. The increased scatter is most likely due to spatial variations in the surface properties such as the chemical (composition), physical (topography), and mechanical (elasticity) properties of the gelatin capsule surfaces.

The adhesion profile can be markedly different depending on the source of commercial gelatin capsules, as can be seen in Fig. 4. For example, compare the adhesion profiles for gelatin capsules 72601 and 29625 which are illustrated in Figs 4a and 4b, respectively. In the case of gelatin capsule 72601, the adhesion of a lactose particle across the capsule surface is relatively uniform compared with the adhesion profile for capsule 29625. It can be seen that the adhesion force between a lactose particle and the surface of gelatin capsule 72601 is lower than that for capsule 29625. Furthermore, as shown in Fig. 4c, the adhesion characteristics, namely, the adhesion force and its spatial variation, for lactose particles on gelatin capsule 29625ext are very similar to those for lactose particles on capsule 72601. On the basis of Table 1, the apparent order of adhesion is as follows:  $29625\text{ext} \leq 72601 < 29625$ .

The adhesion force between a lactose particle and a gelatin capsule surface is affected by a number of factors, not the least of which are the surface properties of the two solids, the particle size, and the RH of the ambient environment. In practice, van der Waals, electrostatic, and capillary forces usually play an important role in the adhesion of particles to surfaces [33, 34]. Upon contact of a particle with a solid surface, deformation of the particle and/or surface occurs due to surface force-induced stresses, such that the contact area, and hence the particle–surface adhesion

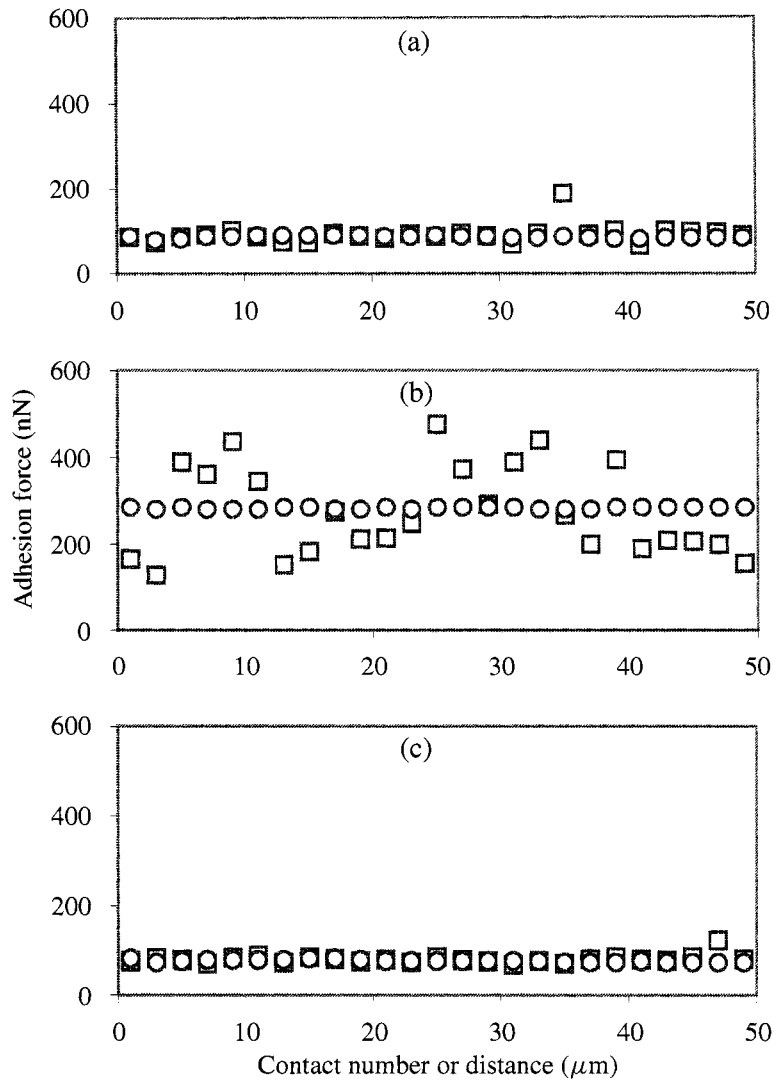


**Figure 4.** Adhesion of a single lactose particle ( $6\ \mu\text{m}$ ) to the surfaces of gelatin capsules (a) 72601, (b) 29625, and (c) 29625ext. ( $\circ$ ) Adhesion at a single location and ( $\square$ ) average adhesion of ten separate measurements at multiple locations.

force, increases [35, 36]. The extent and nature of the adhesion-induced (elastic, viscoelastic, and plastic) deformation depends on the strength of the interaction forces and the mechanical properties of the contacting materials [37, 38]. The adhesion and removal of particles to and from solid surfaces is further complicated by the shape and surface asperities of particles [11], the surface roughness of the substrate [12, 15], as well as the initial applied load [19], contact time [38], temperature [39], and cohesive strength of the particle and solid substrate.

**Table 1.**Adhesion of lactose particles to gelatin capsule surfaces<sup>a</sup>

Capsule	Probe 1 (5 $\mu\text{m}$ )	Probe 2 (15 $\mu\text{m}$ )	Probe 3 (6 $\mu\text{m}$ )	Average <sup>b</sup>
72601	46 $\pm$ 6	151 $\pm$ 25	91 $\pm$ 17	96 $\pm$ 47
29625	146 $\pm$ 42	287 $\pm$ 48	268 $\pm$ 95	234 $\pm$ 91
29625ext	43 $\pm$ 8	160 $\pm$ 43	80 $\pm$ 10	94 $\pm$ 55

<sup>a</sup> Adhesion force  $\pm$  standard deviation (nN). Measurements were performed at 50% RH.<sup>b</sup> Average of all measurements (1500 total) for the three probes.

The presence of water vapor in the ambient atmosphere can affect the adhesion of particles to solid surfaces in several ways. For example, it is well known that an adsorbed water film can aid in the dissipation of electrical charges on solid surfaces [40]. In the absence of electrical charge effects, however, there is usually an increase in the adhesion tendency of a particle to a surface with an increase in RH [15, 41, 42]. Under high humidity conditions, a liquid film can also form by capillary condensation of water around contacting surfaces [43], and the resulting capillary force can make a large contribution to the total force of adhesion [34]. The actual RH at which capillary bridges form also depends on the nature of the particle–surface system [44], but rather than considering the overall curvature of the particle in contact with a flat surface, the more relevant curvatures are the local radii of the contacting microasperities [45]. In addition, the presence of moisture may soften the surface of the particle and/or solid substrate due to water sorption, and the surface force-induced deformation, once again, increases the contact area and consequently the adhesion force [8].

In an attempt to identify the nature of the adhesion forces between lactose particles and gelatin capsule surfaces under the conditions of this study, direct adhesion measurements were performed with several lactose particles of different sizes. Figure 5 shows that the adhesion force appears to be directly proportional to the size (nominal diameter) of the lactose particle for gelatin capsule 72601. The observed linear trend is consistent with the view that the dominant component of the total adhesion force, on the basis of theoretical considerations for the interaction between a sphere and flat surface, arises from van der Waals forces [45]. However, when one considers the surface chemistry of the component materials in pharmaceutical products, it seems more appropriate that the principal forces contributing to particle–surface adhesion can be classified as Lifshitz–van der Waals forces [46, 47] and acid–base interactions [47–49]. The results of the adhesion force measurements can be explained by an increase in the molecular contact area with increasing particle size, since the number of real contacts will usually be proportional to the size of a rough particle [45]. On the other hand, if electrostatic forces of interaction were to predominate in the lactose particle–gelatin capsule system, the measured adhesion force likely would not exhibit a linear variation with particle size [45]. Furthermore, capillary interactions are not believed

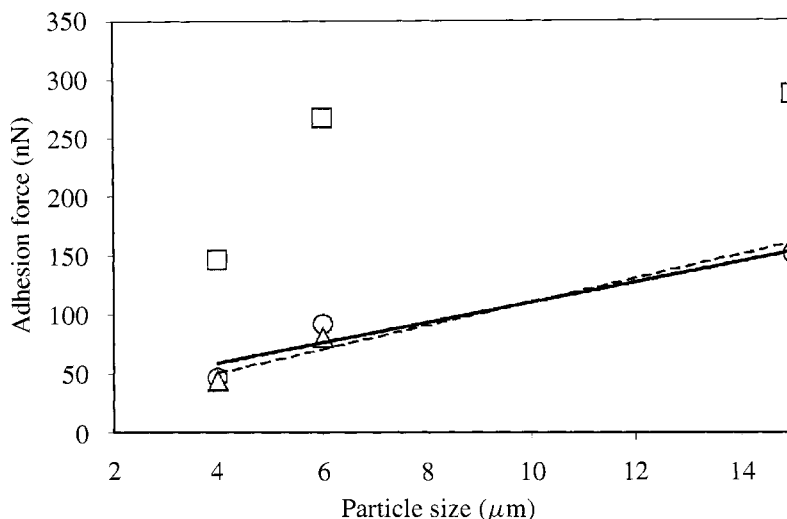


**Figure 5.** Adhesion force between lactose particles and the surfaces of gelatin capsules (○) 72601, (□) 29625, and (△) 29625ext as a function of the particle size. Least-squares fit for (—) 72601 and (---) 29625ext.

to play a significant role since the RH was below 65% [41]. This is supported by preliminary experiments of the effect of RH on the adhesion measurements of individual lactose particles to thin gelatin films which show that the adhesion force at 50% RH does not differ appreciably from that obtained under 'dry' conditions.

As shown in Fig. 5, however, the linear increase in adhesion force with respect to particle size was not observed for gelatin capsule 29625. One interpretation for the nonlinear trend is that the physicochemical nature of this capsule surface is not uniform. Indeed, the adhesion force measurements shown in Fig. 4b indicate that there is a significant surface heterogeneity associated with capsule 29625. This heterogeneity is probably due, in large part, to the presence of contaminants on the gelatin capsule surface. Therefore, gelatin capsule 29625 was extracted to learn to what extent the removal of (presumed) extraneous surface contaminants would impact the adhesion profile. As might be expected, the adhesion profile for capsule 29625ext, which is illustrated in Fig. 4c, shows that the surface heterogeneity is greatly reduced, and the plot of the adhesion force versus particle size is now linear as evident in Fig. 5.

The direct adhesion measurements of individual lactose particles to gelatin capsule surfaces clearly indicate the need for investigating the physicochemical nature of the capsule surfaces. Thus, the lateral force microscopy (LFM) mode was used to obtain simultaneously images of the gelatin capsules that show the topographic features and the friction interactions with the cantilever tip. LFM is an extension of contact mode imaging, and it identifies and maps relative differences in surface frictional characteristics in response to the torsion or twisting of the cantilever as the tip is scanned perpendicularly to the length of the cantilever. LFM



can be extremely useful for identifying surface composition differences and/or surface contamination where the materials have different friction characteristics and the topography is relatively invariant.

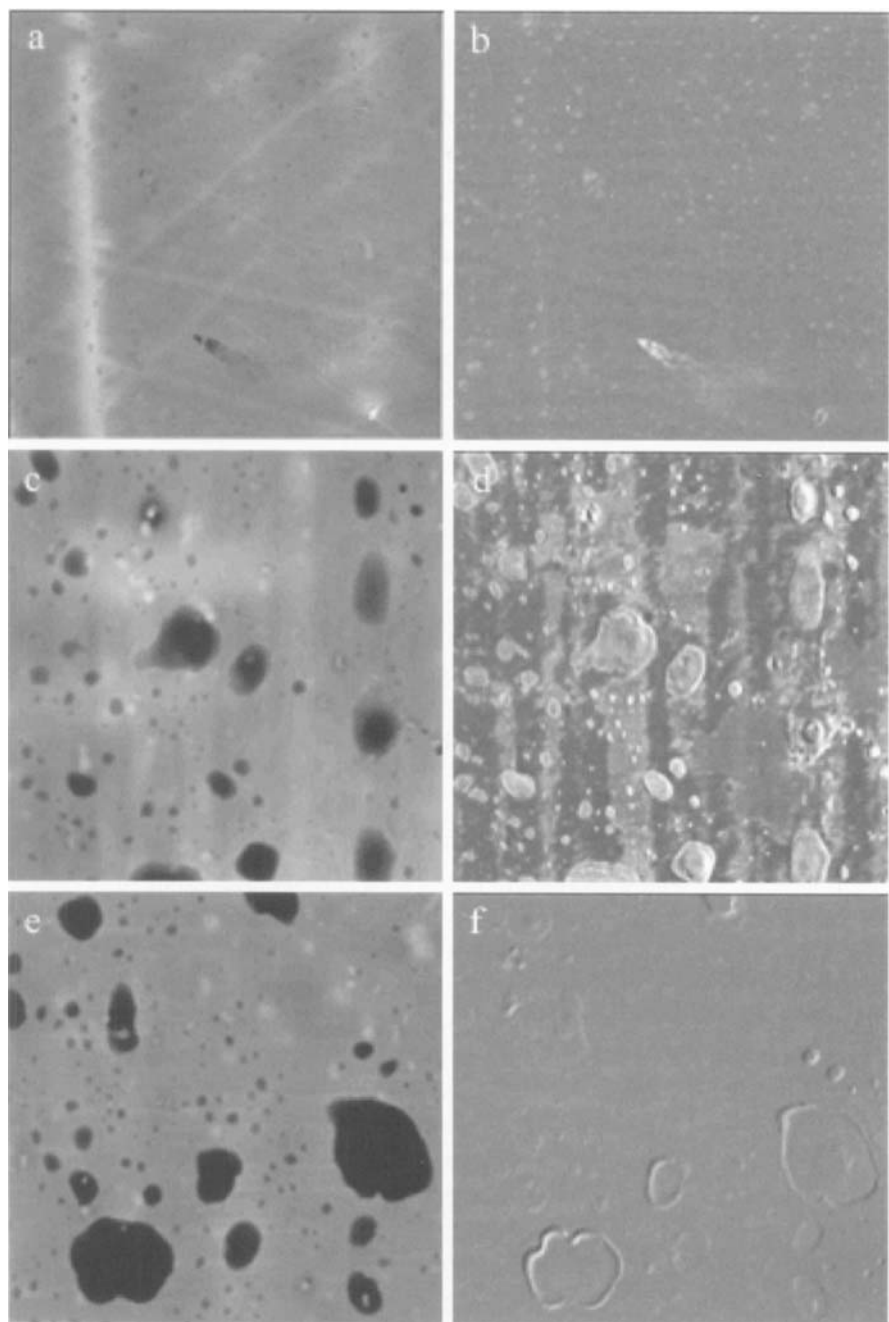
The representative SPM images which are presented in this paper illustrate the complexity and variability of the surface of gelatin capsules. Figure 6 shows height (constant force mode) and friction images of gelatin capsules 72601, 29625, and 29625ext. The friction image, which results upon subtraction of the re-trace scan image from the trace scan image, portrays the friction contrast more clearly by eliminating a large degree of friction artifacts arising from topographic effects. Both types of images are displayed in shades of gray. In the height images, the highest topographic features are the brightest. In the difference friction images (hereafter referred to as friction images), the areas where the greatest friction forces occur are the brightest.

Figure 6a shows that the surface topography of capsule 72601 consists of a complex network of fibrillar structures and many very small 'craters' of approximately 200 nm in diameter. The friction image, shown in Fig. 6b, reveals that the majority of the surface of capsule 72601 exhibits essentially uniform friction. The observed friction artifacts, which are identified by comparing areas of abrupt change in surface topography, are associated with the craters. These artifacts are the result of an increase (or decrease) in frictional drag on the cantilever tip upon ascending (or descending) a marked topographic slope [26]. A more detailed investigation is in progress to elucidate the physicochemical nature of the features of the craters. The SPM images shown in Figs 6a and 6b are significant in that topographically smooth areas of the capsule exhibit undifferentiated friction.

Figure 6c shows that the topography of the surface of gelatin capsule 29625 is extremely heterogeneous with respect to the size and occurrence of the craters. The craters range in size from approximately 0.2  $\mu\text{m}$  to 5  $\mu\text{m}$ . However, craters up to about 10  $\mu\text{m}$  in diameter have been observed in other height images of capsule 29625. Furthermore, the fibrillar structures observed in the height images of capsule 72601 are not present. The friction image shown in Fig. 6d reveals extremely nonuniform friction. Three relatively distinct levels of friction force can be seen in this image. The majority of the capsule surface exhibits low friction, which is presumably due to the mold release agent used in the capsule manufacturing process. One distinct region of intermediate friction is observed, and high friction areas are also present, many of which appear as streaks on the surface.

The height image of capsule 29625ext is topographically similar to that of capsule 29625 (unextracted), as can be seen in Fig. 6e. However, the friction image shown in Fig. 6f appears distinctly uniform compared with that of the unextracted capsule. There is no discernible friction contrast on the surface of the extracted capsule. This clearly indicates that extraction of the gelatin capsule has resulted in a significant change in the physicochemical nature of the capsule surface.

Capsules 72601 and 29625, as mentioned earlier, were obtained from different commercial sources. It is common practice in the manufacturing process of hard

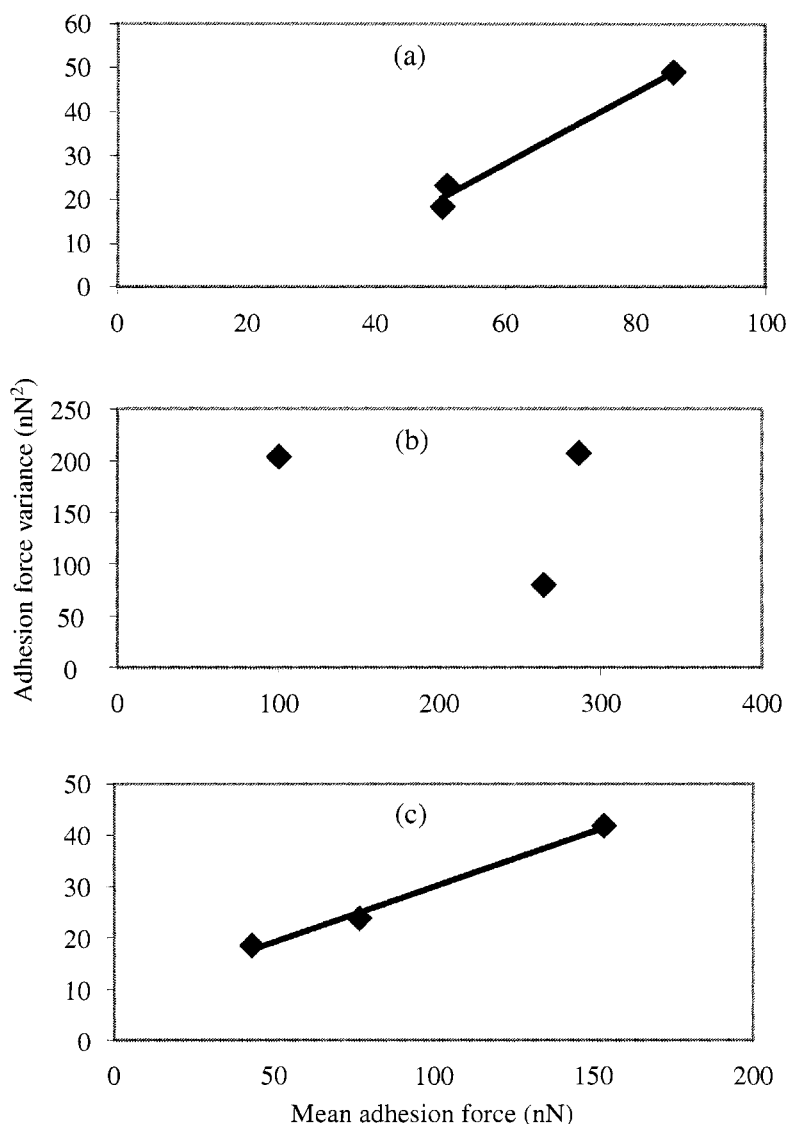


**Figure 6.** Height images of gelatin capsules (a) 72601, (c) 29625, and (e) 29625ext, and friction images of gelatin capsules (b) 72601, (d) 29625, and (f) 29625ext. The height and friction images were collected simultaneously. The scanning region is  $25 \times 25 \mu\text{m}$ , and the  $z$  contrast range is 400 nm. Higher pixel brightness corresponds to higher elevation or friction force.

gelatin capsules for a lubricant or release agent to be applied to stainless steel pins to enable the gelatin shells, which form after dipping and withdrawal of the pin bar from gelatin solutions, to be stripped from the mold pins [50]. ESCA analysis (data not shown) indicates that a small amount of mold release agent remains on the inner surface of the gelatin capsules after their manufacture. As can be seen in Fig. 6d, it appears that the mold release agent employed does not wet the entire surface of capsule 29625. The spatial variation in friction force correlates with that of the adhesion force as shown in Fig. 4b. In a separate preliminary study, an attempt was made to spread the mold release agent used for capsule 29625 on pure gelatin films. The mold release agent was observed to exhibit similar behavior; namely, it did not wet the gelatin surface and it exhibited a lower friction relative to the gelatin surface. On the other hand, the mold release agent utilized for capsule 72601 seems to wet the capsule surface, since an essentially uniform friction force (Fig. 6b) and a relatively constant adhesion force between the lactose particle and capsule surface (Fig. 4a) are observed. This suggests that the mold release agent used for capsule 72601 is not the same as that employed for capsule 29625. In addition, gelatin capsule 29625ext appears to exhibit uniform friction (Fig. 6f) and relatively constant adhesion between the lactose particle and capsule surface (Fig. 4c), thereby indicating that the extraction process has removed a significant amount of mold release agent. A more detailed SPM study is underway to examine the spatial distribution and physicochemical characteristics of the mold release agent that is present on the surface of gelatin capsules.

The statistical method developed by Beebe and co-workers [51, 52] for determining the force of a single chemical bond between a cantilever tip and a sample surface was extended to the analysis of the adhesion force between a lactose particle and a gelatin capsule surface. The method is based on the assumption that the total adhesion (pull-off) force is the sum of discrete bond or interaction forces. Multiple adhesion force measurements should then follow a Poisson distribution, so that a plot of the force variance versus the mean force should be linear with a slope which corresponds to the individual bond force and a zero intercept. If nonspecific long-range forces such as those which occur in colloidal systems are present, then the intercept will be negative. Furthermore, if the discrete bond force is not constant due to varying bond position and orientation or varying chemical composition, there will be curvature in the plot of the variance versus mean force. This method utilizes the natural variability in the tip (or colloidal particle) and sample surface asperities, and it does not require *a priori* assumptions of the tip (or particle) radius or knowledge of the tip (or particle)–sample surface contact area.

Figure 7 shows plots of the adhesion force variance versus the mean adhesion force obtained using the adhesion data for the three lactose particle–gelatin capsule systems employed in this study. For gelatin capsules 72601 and 29625ext, a linear relationship between the variance and mean force is observed, thereby suggesting a single bond-rupture process, rather than a sequential breakage of bonds between lactose particles and homogeneous capsule surfaces, which can also be inferred

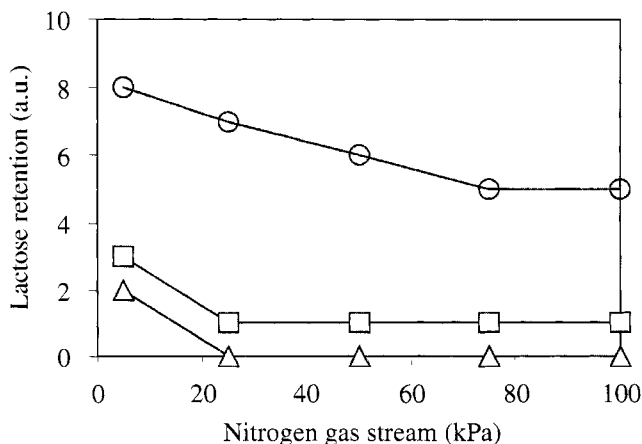


**Figure 7.** Adhesion force variance versus mean adhesion force for lactose particles of different sizes on the surfaces of gelatin capsules (a) 72601, (b) 29625, and (c) 29625ext.

from the sharp pull-off of the lactose particle from the solid surface as shown in Fig. 1. Furthermore, the linear plots of the variance versus the mean force indicate that the surfaces of gelatin capsules 72601 and 29625ext are homogeneous, or that the surface composition of the two gelatin capsules is uniform at the resolution of the colloidal probe measurements. In the case of capsule 29625, however, the nonlinear behavior of the variance versus mean force plot is simply a manifestation of the heterogeneous nature of the capsule surface, as can be seen

**Table 2.**Retention of lactose particles in gelatin capsules<sup>a</sup>

Capsule	Lot 1	Lot 2	Lot 3	Lot 4	Average <sup>b</sup>
72601	0.02 ± 0.02	0.16 ± 0.15	0.05 ± 0.05	0.24 ± 0.16	0.12 ± 0.35
29625	7.57 ± 0.85	5.76 ± 0.60	7.00 ± 0.61	5.88 ± 0.92	6.55 ± 2.19
29625ext	1.67 ± 0.76	0.22 ± 0.10	0.87 ± 0.27	0.92 ± 0.27	0.92 ± 1.40

<sup>a</sup> Weight percent ± standard deviation (wt%). Average of ten runs.<sup>b</sup> Average of all measurements (40 total) for the four lots.**Figure 8.** Retention of lactose particles on the surfaces of gelatin capsules (□) 72601, (○) 29625, and (△) 29625ext with pressure of the nitrogen gas stream.

from the scanning adhesion force measurements (Fig. 4b) and friction force image (Fig. 6d). Although the surfaces of gelatin capsules 72601 and 29625ext appear to be uniform, the question of the spatial variation of the surface-chemical composition at the nanometer scale of resolution remains for future study. These results show that the statistical method holds significant promise to obtain quantitative information on the nature and magnitude of bond-rupture forces (and ultimately bond energies) from *absolute* adhesion force measurements using colloidal particles of different sizes on homogeneous solid surfaces which are relevant to dry powder inhalation products.

The adhesion of lactose particles to gelatin capsule surfaces was also examined by measuring the retention of lactose particles. Two different approaches were employed. First, the retention was determined by measuring the retained amount of lactose particles in gelatin capsules. Table 2 shows that the order of retention is as follows: 72601 < 29625ext < 29625. The second approach was an attempt to simulate the re-dispersion of lactose particles from a gelatin capsule during the usage of a DPI device. Lactose particle retention on gelatin capsule samples was examined upon controlled application of a nitrogen gas stream. As can be seen from Fig. 8, the relative retention of lactose particles on the capsule surfaces is as follows:

29625ext < 72601 < 29625. Significantly, upon comparison of the results of both the microscopic adhesion and the macroscopic retention measurements, the same general trend was observed in the adhesion of lactose particles.

The SPM results show that gelatin capsule 29625, which exhibits high-contrast friction, tends to have high adhesion, whereas gelatin capsules 72601 and 29625ext, which exhibit low-contrast friction, have low adhesion. The surfaces of capsules 72601 and 29625ext also appear to be of relatively uniform friction, which is in accordance with the observed relatively constant adhesion. On the other hand, the nonuniform friction associated with capsule 29625 correlates with the observed spatial variation in adhesion. The implication is that the physicochemical nature of the capsule surface, which is dependent on the gelatin and mold release agent used in the capsule manufacturing process, is a crucial factor in the adhesion of lactose particles to gelatin capsule surfaces. Further systematic investigations are underway in our laboratory to provide a more complete basic understanding of the adhesion of pharmaceutical particles in dry powder inhalation products.

#### 4. CONCLUSIONS

The SPM results show that scanning probe techniques can provide unique information on the adhesion interactions and surface physicochemical nature of pharmaceutical materials. The direct measurement of adhesion by use of the colloidal probe technique has provided new insights into the mechanisms of particle–surface adhesion in dry powder inhalation products. The microscopic measurements of the adhesion of individual lactose particles to the surface of gelatin capsules not only have shown the effect of surface chemistry on adhesion, but also correlate well with the macroscopic performance of a large population of particles such as the retention of lactose particles in gelatin capsules. In addition, SPM shows that the physicochemical nature of the gelatin capsule surface, which depends on the gelatin and mold release agent utilized in the manufacture of commercial capsules, plays a critical role in the adhesion of pharmaceutical particles. By an appropriate choice of gelatin capsules, one can enhance and control the respirable fraction in dry powder inhalation products. Furthermore, one can conclude that the particle–surface adhesion in pharmaceutical systems can be advantageously modified by appropriate surface treatment of the gelatin capsules and/or lactose carrier particles.

#### REFERENCES

1. G. Buckton, *Interfacial Phenomena in Drug Delivery and Targeting*, pp. 165–196. Harwood Academic Publishers, Lausanne, Switzerland (1995).
2. J. Broadhead, S. K. Rouan and C. T. Rhodes, *Pharm. Acta Helv.* **70**, 125–131 (1995).
3. J. Visser, *Particulate Sci. Technol.* **13**, 169–196 (1995).
4. K. L. Mittal (Ed.), *Particles on Surfaces 5&6: Detection, Adhesion and Removal*. VSP, Utrecht, The Netherlands (1999).

5. M. Corn and F. Stein, *Am. Ind. Hyg. Assoc. J.* **26**, 325–336 (1965).
6. S. W. Booth and J. M. Newton, *J. Pharm. Pharmacol.* **39**, 679–684 (1987).
7. P. Kulvanich and P. J. Stewart, *J. Pharm. Pharmacol.* **40**, 453–458 (1988).
8. K. Iida, A. Otsuka, K. Danjo and H. Sunada, *Chem. Pharm. Bull.* **40**, 189–192 (1992).
9. F. Podczcek, J. M. Newton and M. B. James, *J. Adhesion Sci. Technol.* **8**, 1459–1472 (1994).
10. A. Otsuka, K. Iida, K. Danjo and H. Sunada, *Chem. Pharm. Bull.* **31**, 4483–4488 (1983).
11. A. Otsuka, K. Iida, K. Danjo and H. Sunada, *Chem. Pharm. Bull.* **36**, 741–749 (1988).
12. K. Iida, A. Otsuka, K. Danjo and H. Sunada, *Chem. Pharm. Bull.* **41**, 1621–1625 (1993).
13. R. I. Larsen, *Am. Ind. Hyg. Assoc. J.* **19**, 265–270 (1958).
14. S. Bhattacharya and K. L. Mittal, *Surface Technol.* **7**, 413–425 (1978).
15. M. Corn, *J. Air Pollution Control Assoc.* **11**, 566–584 (1961).
16. G. Binnig, C. F. Quate and C. Gerber, *Phys. Rev. Lett.* **56**, 930–933 (1986).
17. W. A. Ducker, T. J. Senden and R. M. Pashley, *Nature* **353**, 239–241 (1991).
18. M. L. Ott and H. A. Mizes, *Colloids Surfaces A* **87**, 245–256 (1994).
19. D. M. Schaefer, M. Carpenter, R. Reifengerger, L. P. DeMejo and D. S. Rimai, *J. Adhesion Sci. Technol.* **8**, 197–210 (1994).
20. U. Sindel, I. Zimmermann, D. Schaefer and R. Reifengerger, in: *Proc. 3rd World Congress Particle Technol.*, pp. 68–78. Institution of Chemical Engineers, Rugby, Warwickshire (1998).
21. H. Yoshizawa, Y.-L. Chen and J. Israelachvili, *J. Phys. Chem.* **97**, 4128–4140 (1993).
22. J. N. Israelachvili, Y.-L. Chen and H. Yoshizawa, *J. Adhesion Sci. Technol.* **8**, 1231–1249 (1994).
23. G. Haugstad, W. L. Gladfelter, M. P. Keyes and E. B. Weberg, *Langmuir* **9**, 1594–1600 (1993).
24. M. Radmacher, M. Fritz and P. K. Hansma, *Biophys. J.* **69**, 264–270 (1995).
25. M. Radmacher and P. K. Hansma, *Polym. Prepr.* **37**, 587–588 (1996).
26. G. Haugstad, W. L. Gladfelter and E. B. Weberg, *Langmuir* **9**, 3717–3721 (1993).
27. G. Haugstad, W. L. Gladfelter, E. B. Weberg, R. T. Weberg and T. D. Weatherill, *Langmuir* **10**, 4295–4306 (1994).
28. G. Haugstad, W. L. Gladfelter, E. B. Weberg, R. T. Weberg, T. D. Weatherill and R. R. Jones, *Mater. Sci. Eng.* **C3**, 85–89 (1995).
29. G. Haugstad, W. L. Gladfelter and R. R. Jones, *Langmuir* **14**, 3944–3953 (1998).
30. B. Y. Ni, G. R. Bisson and A. H. Tsou, *Mater. Res. Soc. Symp. Proc.* **308**, 489–494 (1993).
31. L. Lavielle, J. Schultz and K. Nakajima, *J. Appl. Polym. Sci.* **42**, 2825–2831 (1991).
32. J. H. Hoh and A. Engel, *Langmuir* **9**, 3310–3312 (1993).
33. H. Rumpf, in: *Agglomeration 77*, K.V.S. Sastri (Ed.), pp. 97–129. AIME, New York (1977).
34. R. A. Bowling, in: *Particles on Surfaces 1: Detection, Adhesion, and Removal*, K. L. Mittal (Ed.), pp. 129–142. Plenum Press, New York (1988).
35. V. B. Derjaguin, *Kolloid Z.* **69**, 155–164 (1934).
36. R. S. Bradley, *Trans. Faraday Soc.* **32**, 1088–1090 (1936).
37. D. S. Rimai, L. P. DeMejo and R. C. Bowen, *J. Adhesion Sci. Technol.* **8**, 1333–1355 (1994).
38. D. S. Rimai and A. A. Busnaina, *Particulate Sci. Technol.* **13**, 249–270 (1995).
39. K. K. Lam and J. M. Newton, *Powder Technol.* **73**, 267–274 (1992).
40. T. Nguyen and S. Nieh, *J. Electrostat.* **22**, 213–227 (1989).
41. A. D. Zimon, *Adhesion of Dust and Powder*, 2nd edn, pp. 108–119. Consultants Bureau, New York (1982).
42. F. Podczcek, J. M. Newton and M. B. James, *J. Colloid Interface Sci.* **187**, 484–491 (1997).
43. M. C. Coelho and N. Harnby, *Powder Technol.* **20**, 201–205 (1978).
44. M. C. Coelho and N. Harnby, *Powder Technol.* **20**, 197–200 (1978).
45. K. K. Lam and J. M. Newton, *Powder Technol.* **73**, 117–125 (1992).
46. C. J. van Oss, M. K. Chaudhury and R. J. Good, *Chem. Rev.* **88**, 927–941 (1988).
47. C. J. van Oss, *Interfacial Forces in Aqueous Media*. Marcel Dekker, New York (1994).
48. F. M. Fowkes, *J. Adhesion Sci. Technol.* **1**, 7–27 (1987).

49. K. L. Mittal and H. R. Anderson, Jr. (Eds), *Acid–Base Interactions: Relevance to Adhesion Science and Technology*. VSP, Utrecht, The Netherlands (1991).
50. B. E. Jones, in: *Hard Capsules — Development and Technology*, K. Ridgway (Ed.), pp. 68–79. The Pharmaceutical Press, London (1987).
51. J. M. Williams, T. Han and T. P. Beebe, Jr., *Langmuir* **12**, 1291–1295 (1996).
52. L. A. Wenzler, G. L. Moyes, L. G. Olson, J. M. Harris and T. P. Beebe, Jr., *Anal. Chem.* **69**, 2855–2861 (1997).



## Analysis of atomic force microscopy data for deformable materials

MARK W. RUTLAND\*, JAMES W. G. TYRRELL and PHIL ATTARD<sup>†</sup>

*School of Chemistry F11, University of Sydney, Sydney, NSW 2006, Australia*

**Abstract**—A protocol for measuring the interaction, deformation and adhesion of soft polymeric substrates with the atomic force microscope (AFM) is described. The technique obtains the photodiode response of the AFM (constant compliance factor) by independent calibration against the rigid substrate adjacent to the deformable particle or patchy film. The zero of separation is taken as the end-point of the jump into contact. A method is given for correcting the velocity dependence of the piezodrive expansion factor, the neglect of which will cause artefacts in dynamic viscoelastic measurements. It is emphasised that conventional force curve analysis, which uses the apparently linear large force region for calibration, will generate erroneous results for deformable substrates. Results are obtained for cellulose particles and for polystyrene films, and their Young's moduli are found to be 22 MPa and 100 MPa, respectively. The latter is about a factor of 30 less than for bulk polystyrene, which indicates that the polystyrene surface is in a less glassy state than the bulk.

*Keywords:* Polystyrene; cellulose; deformable materials; atomic force microscopy; piezo-calibration.

### 1. INTRODUCTION

The atomic force microscope and other surface force devices have long been used to measure forces between rigid particles and surfaces, and they are being increasingly applied to soft objects (a review of the former is given in Ref. [1] and of the latter in Refs [2, 3]). In the deformable case two experimental issues must be addressed for the quantitative interpretation of the data, namely the determination of the zero of separation and the calibration of the electronic force measurement device. Unlike rigid surfaces, the gradual increase in the repulsive force between the surfaces and the consequent gradual increase in the deformation of the surfaces

---

\*Permanent address: Department of Chemistry, Royal Institute of Technology, SE-100 44 Stockholm, Sweden, and Institute for Surface Chemistry, Box 5607, SE-114 86 Stockholm, Sweden.

<sup>†</sup>To whom correspondence should be addressed. Tel.: (61-2) 9352-5878. Fax: (61-2) 9351-3329. E-mail: attard@chem.usyd.edu.au

prior to their coming into intimate contact, and also the fact that intimate contact is not marked by a sharp discontinuity in the slope of the force curve, mean that the precise location of the surface cannot be deduced immediately from the force curve. Further, increasing deformation with increasing applied load means that the deflection of the force measuring spring in the contact region is not equal to the distance moved by the driving piezocrystal, and thus it is not possible to convert the electronic signal to deflection or force. Theoretical calculations [4–6] have shown that the deformation is negligible in the large separation, weak force regime, and if the force law is known for rigid particles, then this fact can be used to establish the zero of separation. This procedure has been used to analyse Atomic Force Microscopy (AFM) measurements on poly(dimethylsiloxane) emulsion droplets [7, 8] and oil droplets [9] that interact with an electric double layer repulsion. A number of other proposals for establishing the zero of separation are reviewed in Ref. [7].

This paper reports AFM force measurements on a cellulose particle and on a polystyrene film in air and presents results for their surface elasticity. We explore the utility of using the van der Waals attraction to establish the zero of separation. The steepness of the van der Waals force, in principle, presents an advantage over the relatively slowly decaying electric double-layer repulsion used previously to determine the zero of separation [7–9]. In practice we find that the presence of adsorbed water films in air creates some uncertainty in this quantity. The calibration of the force measuring photodiode is performed here *in situ* by moving the cantilever off the particle or film and pressing against the adjacent hard substrate, as has been done previously for droplets [8, 10]. The calibration is a significant issue in this context because both cellulose [11–14] and polystyrene [15–18] have previously been the subject of force measurement, and in all these cases the calibration factor was taken to be the rate of change of the force measuring voltage with piezocrystal movement in the pseudo-linear regime. This assumes not only that the force curve is linear, but also that the increase in deformation of the particle is negligible. Here, it will be shown that the apparent linearity of the force curve cannot be used as a guide to the magnitude of the deformation of these materials and that the calibration factor so deduced differs significantly from the actual calibration factor of the device. The force curves produced by such procedures can be in significant error. Furthermore, in those viscoelastic materials where dynamic effects are of interest [2, 3, 6, 8, 18–22], velocity-dependent artefacts in the piezodrive can also lead to a misinterpretation of the results unless they are accounted for, as will also be shown.

## 2. MATERIALS AND METHODS

The polystyrene surface was prepared under an optical microscope (Olympus BH2) equipped with a heating stage. Pieces of silicon wafer were washed with ethanol (analytical grade), rinsed thoroughly with high-purity MilliQ water (Elga UHQ

purification system) and left to dry in a clean-room environment. On the surface of the silicon wafer was a native oxide layer from exposure to the atmosphere, and henceforth it will be referred to as the silica substrate. A droplet of an aqueous suspension containing 3  $\mu\text{m}$  polystyrene spheres (Polysciences, USA) was placed on the silica substrate and subsequently heated. The liquid evaporated and the particles initially formed regions of crystalline arrays and subsequently melted to form smooth polystyrene films with well-defined borders. Scanning probe imaging of the film over an area of 1  $\mu\text{m}^2$  revealed a root mean square roughness of less than 0.4 nm. The force measurements on polystyrene were carried out under ambient conditions of 17°C and 78% relative humidity.

Cellulose particles [13] were attached to fragments of oxidised silicon wafer (approx. 1  $\text{cm}^2$ , supplied by Okmetic, Finland) with a high-melting-point adhesive (Epikote 100, Shell) as follows. The silica substrate was placed on a heating stage at a temperature above the adhesive melting point on the translation stage of a binocular microscope. Two etched tungsten wires were attached to an  $x$ - $y$ - $z$  micromanipulator (Narishige MN-151). With one of the wires tiny spots of adhesive (between  $10^{-15}$  and  $10^{-17}$  l) were applied to the substrate in a predetermined pattern to aid recognition in the AFM. With the other wire cellulose particles of about 20  $\mu\text{m}$  in diameter were placed onto the adhesive spots and the wafer was removed from the heating stage. For force measurements, particles were located under the AFM cantilever tip by manipulating the sample stage while monitoring it with a video microscope placed directly above the interaction zone. The force measurements on cellulose were carried out under ambient conditions of 26°C and 31% relative humidity.

Experimental data were acquired using a Nanoscope IIIa AFM (Digital Instruments) employing a V-shaped silicon nitride cantilever. The spring constant was taken to be 0.58 N/m, which is the manufacturer's nominal value, and no independent calibration was performed. A piezo-tube scanner (type E, Digital Instruments) with vertical ( $z$ ) range 2.5  $\mu\text{m}$  was used to drive the sample stage. Characterisation of the sample stage piezocrystal (i.e. movement *versus* applied voltage) was performed using an optical displacement sensor (model d20, Philtec, Annapolis, MD, USA) mounted directly above the sample piezocrystal [19]. The sensor utilises bundled optical fibres to transmit a divergent beam of light and to receive its reflection, the intensity of which is proportional to the distance between the tip of the fibre bundle and the reflecting substrate, which in this study was a clean, polished piece of oxidised silicon wafer placed on the piezodrive. Conversion of reflected intensity to distance moved was accomplished using the manufacturer's precalibrated response curve after the maximum response was set to the recommended value by means of the inbuilt gain adjustment. In these piezodrive characterisations, which were independent of the force measurements, the AFM optical head was physically removed to improve displacement sensor access to the piezodrive, although the electrical connections were maintained to facilitate software control of the piezocrystal. Signals from the displacement sensor were logged on an auxil-

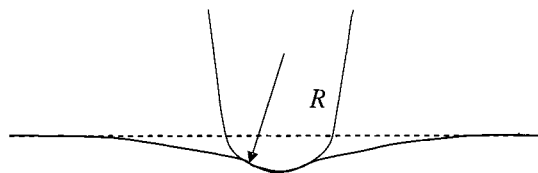


**Figure 1.** Sketch of the experimental geometry. The radius of the tip is  $R$ . The nominal separation is measured relative to the dashed line. The case of post-contact deformation due to a positive applied load is shown. For simplicity, the capillary condensate around the edge of the contact region is not shown.

ary PC via 16-bit data acquisition hardware and interrogated using a graphical user interface (LabVIEW R6.0 graphical programming environment, National Instruments, North Ryde, NSW, Australia). The AFM and displacement probe apparatus were placed on an anti-vibration stage to attenuate external noise.

A sketch of the experimental geometry is shown in Fig. 1 for the post-contact situation. Note that the radius of curvature of the end of the tip is much greater than the width of the tip. Note also that on this scale the undeformed cellulose particle and polystyrene film appear planar. In each experiment normal forces were obtained by ramping the lower surface towards the cantilever using a triangular wave without scanning in the lateral direction. Rates between 0.03 and 73  $\mu\text{m/s}$  were employed. In each experiment (cellulose particle and polystyrene), forces were first measured on a proximate region of the silica substrate, which enabled the photodiode voltage response to be calibrated as a cantilever deflection [8, 10]. For reasons discussed in detail below, this constant compliance calibration obtained from the tip-silica interactions was performed at the same rate as the subsequent force measurements on the soft substrate. In order to avoid nanoindentation, (irreversible plastic deformation), only small loads were applied so that the amount of flattening was less than 25 nm. It was confirmed that the forces measured upon approach and upon retraction were approximately coincident in the contact region, which indicates that the deformation was elastic and that no nanoindentation had occurred.

### 3. RESULTS

#### 3.1. Effect of piezodrive speed

The calibration factor, which converts the AFM photodiode output voltage to the cantilever deflection, is generally obtained in the so-called constant compliance regime, where the cantilever is in hard contact with the substrate that is being moved by the piezodrive. Figure 2 shows measurements of the calibration factor (V/nm) as a function of the drive speed ( $\mu\text{m/s}$ ) for a cantilever in hard contact with the silica substrate. Triangular waveforms for the drive signal were used with constant voltage amplitude and various frequencies. The drive speed was obtained by converting the voltage amplitude to a drive distance using the expansion coefficient obtained by

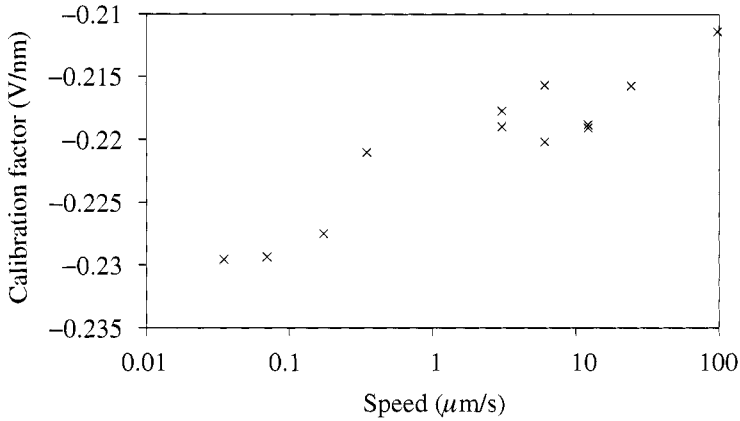


**Figure 2.** Speed dependence of the calibration factor for a tip in contact with a silica substrate. The same expansion coefficient has been used in all cases to convert the applied voltage to piezodrive displacement.

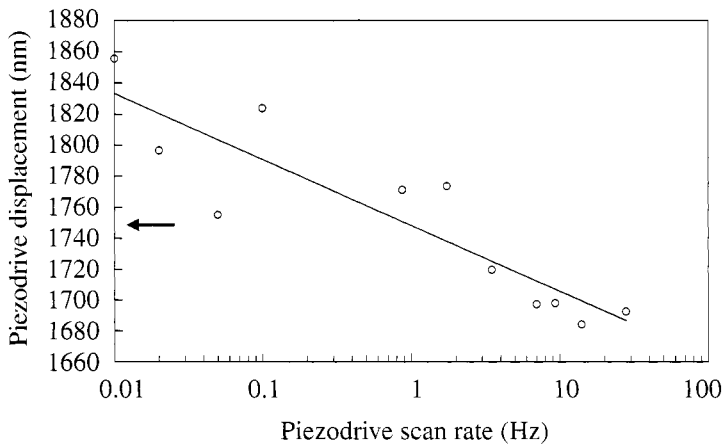


**Figure 3.** Measured total displacement of the piezodrive as a function of scan rate for a given applied voltage. The arrow indicates the nominal displacement expected from the original interferometric calibration. The straight line is a least-squares fit ( $R^2 = 0.80$ ).

a prior interferometric calibration (at a single velocity). It may be seen that the calibration factor depends upon the speed of the measurement, and that it decreases in magnitude monotonically by about 10% over the four decades increase in speed.

The displacement of the piezodrive was measured directly using the displacement sensor. Figure 3 shows displacement *versus* scan rate at constant applied voltage amplitude. It can be seen that the displacement depends upon the frequency (equivalently speed), and that it decreases monotonically with increasing frequency. The change was about 10% over the range of frequencies studied.

### 3.2. Interaction and deformation of cellulose

AFM measurements were performed for a cantilever tip interacting with a cellulose particle in air (Fig. 4). The particle was mounted on the silica substrate driven by the piezocrystal rather than the more common attachment to the cantilever tip. The force can be obtained by multiplying the deflection of the cantilever by the spring constant, 0.58 N/m. The AFM force measuring photodiode was calibrated by moving the cantilever off the particle and performing a force measurement for the cantilever tip interacting with the silica substrate. The calibration factor was found to be  $-0.191$  V/nm. This calibration factor makes the linear, constant compliance region of the voltage *versus* displacement curve for silica vertical in the force *versus* separation plane (Fig. 4B), and this vertical portion was taken to define the zero of separation for the tip-rigid substrate, as is usual.

The data for the tip interacting with the cellulose particle in Fig. 4 were obtained following the tip-silica measurements by aligning the particle beneath the cantilever using the lateral piezodrive and translator stage (i.e. without altering the optical path

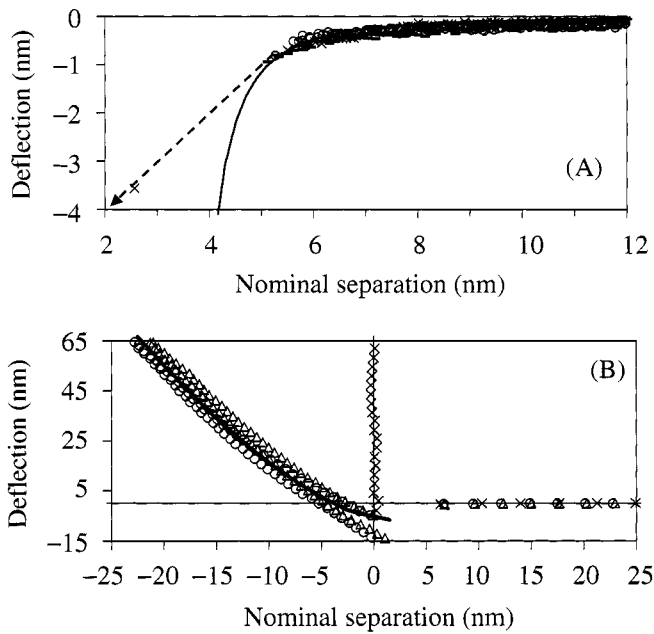


**Figure 4.** Deflection of a cantilever (spring constant 0.58 N/m) for a tip in air interacting with a rigid silica substrate (crosses, 0.7  $\mu\text{m/s}$  drive speed) or with a cellulose particle at driving speeds of 0.50 (circles) and 1.51 (triangles)  $\mu\text{m/s}$ . (A) Jump into contact (dashed arrow). The curve is the van der Waals force  $F$  as a function of separation  $h$ ,  $F(h) = AR/12(h-d)^2$ , using the water-air-water Hamaker constant,  $A = 3.7 \times 10^{-20}$  J [23], a fitted radius of curvature of the tip of 700 nm, and a fitted total water film thickness of  $d = 3.2$  nm. (B) Post-contact deformation. The curve is a JKR calculation using a fitted  $E/(1-\nu^2) = 2.2 \times 10^7$  Pa, the radius of curvature  $R = 700$  nm, and a fitted surface energy,  $\gamma = 1.2$  mJ/m<sup>2</sup>. The retract data lie slightly below the approach data in each case. For clarity, only every fiftieth datum is plotted.

in the AFM). The cellulose force data were converted from photodiode voltage to deflection, and from displacement to separation, using the tip–silica photodiode calibration factor obtained adjacent to the particle ( $-0.191$  V/nm). In Fig. 4B it can be seen for the cellulose that there is a well-defined constant compliance region (where deflection changes linearly with drive distance). This has a slope of  $-0.153$  V/nm. The zero of separation for the cellulose was defined by shifting horizontally the cellulose–tip force–separation curve so that the first measured datum after the jump-into-contact occurred at zero separation (Fig. 4B). At positive separations there is an attractive force that causes the cantilever to jump into contact (Fig. 4A). The negative nominal separations in Fig. 4B signify the amounts of deformation or flattening of the cellulose, since the nominal separation is the separation between the surfaces as if they were rigid [4, 6]. There is a small amount of hysteresis evident for cellulose in Fig. 4B, with the retract curve lying beneath the approach curve.

The adhesion (not shown), which is the maximum tension measured upon retraction, was 70 nN for both the tip–silica and the tip–cellulose cases. This was approximately independent of the speed of the retraction.

Figure 4A includes the calculated van der Waals attraction prior to contact,  $F(h) = AR/12(h-d)^2$ , where  $F$  is the force,  $h$  is the separation,  $A = 3.7 \times 10^{-20}$  J is the Hamaker constant for water–air–water [23] and  $R$  is the radius of curvature of the tip. Both  $R$  and  $d$  were used as fitting parameters. This equation assumes that there are water films present on the tip and the substrate of total thickness  $d$ . Figure 4B includes the JKR theory [24] for the force *versus* deformation. The radius obtained in the precontact data was used in the JKR theory, and the Young's modulus, which changes the slope, and the surface energy, which shifts the curve vertically, were used as fitting parameters. The influence of the capillary condensate, which would mainly shift the curve vertically, was not accounted for in the JKR theory (cf. Ref. [25]).

### 3.3. Interaction and deformation of polystyrene

AFM measurements were made on a tip interacting with a polystyrene film in air (Fig. 5). The photodiode calibration factor ( $-0.230$  V/nm) was measured by pressing the tip against the silica substrate on an adjacent bare patch in the film. This differs from the calibration factor used for cellulose ( $-0.191$  V/nm) due to the experiments being performed on different days with different mirror angles and hence optical paths. The same cantilever as for the data in Fig. 4 was used, and hence the spring constant was again 0.58 N/m. The zero of separation for the polystyrene film was established by horizontally shifting the curve so that the first point after the jump into contact coincided with the zero of separation for the tip–silica curve. Prior to contact an attractive force acts that either is smaller in magnitude or else is shifted to smaller separations for polystyrene than for silica. A linear constant compliance regime can be seen in the polystyrene post-contact data (Fig. 5B), with a slope of  $-0.212$  V/nm.

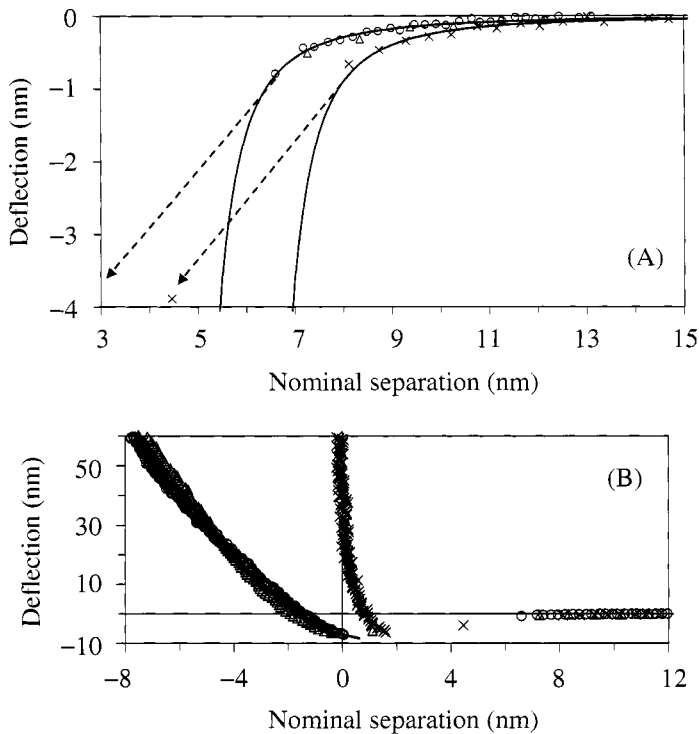


**Figure 5.** As Fig. 4, but for approach to silica (crosses,  $0.03 \mu\text{m/s}$  drive speed) and to a polystyrene film at a driving speed of  $0.09$  (circles) and of  $25.2$  (triangles)  $\mu\text{m/s}$ . (A) Jump into contact. The van der Waals curve has parameters  $A = 3.7 \times 10^{-20} \text{ J}$  [23], a fitted  $R = 700 \text{ nm}$ , and fitted  $d = 6 \text{ nm}$  (silica) and fitted  $d = 4.5 \text{ nm}$  (polystyrene). (B) Post-contact deformation. The JKR curve (obscured) has fitted  $E/(1 - \nu^2) = 1 \times 10^8 \text{ Pa}$ ,  $R = 700 \text{ nm}$  and fitted  $\gamma = 1.5 \text{ mJ/m}^2$ .

Van der Waals forces were fitted to the pre-contact attraction by fitting a total water film of  $d = 6 \text{ nm}$  for silica and  $d = 4.5 \text{ nm}$  for polystyrene. The same radius of curvature of the tip as found from the fit in Fig. 4 fitted the pre-contact data when the water–air–water Hamaker constant was used. A JKR fit was also made to the post-contact deformation in the case of polystyrene by fixing the radius of curvature of the tip and fitting Young's modulus and the surface energy.

In the contact region, the retract data for polystyrene were virtually coincident with the approach data and are not shown in Fig. 5. The adhesion was  $244 \text{ nN}$  for the tip–silica and  $203 \text{ nN}$  for the tip–polystyrene experiments.

## 4. INTERPRETATION AND DISCUSSION

### 4.1. Speed effects

The speed-dependence of the calibration factor measured in Fig. 2 arises from a change in the expansion (i.e. displacement) of the piezodrives with speed. This



follows because the change in photodiode voltage is linearly proportional to change in deflection of the cantilever tip, which, for the hard substrate, is equal to the distance the piezo-drive moves. Since the data in Fig. 2 were obtained using a constant amplitude voltage applied to the piezo-drive, this indicates that the expansion factor itself must be changing. This conclusion is confirmed and quantified by the direct measurements reported in Fig. 3, which show a change in the total expansion with scan rate (equivalently speed), again for a constant amplitude applied voltage. The speed dependence arises from the nonlinearities and hysteresis in the piezo-drive. In the absence of a displacement sensor such as the one used in Fig. 3, it is difficult to account for these artefacts, and commonly in AFM measurements a single expansion coefficient for the piezo-crystal is used to describe motion along the  $z$ -axis. Even when hysteresis effects are taken into account by the application of the manufacturer's preprogrammed polynomial curve, which attempts to describe the actual piezo-drive movement, the full expansion is overestimated at high speeds.

The speed dependence of the expansion factor can be substantial; neglecting it can introduce errors, particularly if one is seeking to measure the viscoelastic properties of soft samples. Depending on the stiffness of the sample, this change with speed can be of the same order as the change in slope due to deformation. In the present case of polystyrene, Fig. 5B shows that the results at a speed of  $0.09 \mu\text{m/s}$  are coincident with those obtained at  $25.2 \mu\text{m/s}$  when the correct calibration factor and expansion coefficients are used. From this, one can conclude that on this scale the polystyrene deformation is elastic rather than viscoelastic. However, if one were to use a single expansion factor, the force curves in contact would differ from each other and the apparent speed-dependence would be wrongly interpreted as viscoelastic deformation.

The quantitative measurements of the expansion of the piezocrystal in Fig. 3 shows that the amount of expansion decreases with increasing speed (scan rate, Hz). This is consistent with the results in Fig. 2, where the magnitude of the calibration factor decreases with increasing speed. In Fig. 3 the displacement is approximately linear on the logarithmic scale,  $(z - z_0)/z_0 = -r \log_{10}(v/v_0)$ , where  $z$  is the displacement,  $v$  is the speed, the subscript 0 denotes a canonical case and  $r$  is the proportionality constant. The decrease of about 45 nm for each order of magnitude change in speed corresponds to  $r = 2.4\%$  change in the displacement per decade. The data in Fig. 2 are also approximately linear on the logarithmic scale, corresponding to  $r = 2.7\%$  change in the calibration factor per decade of speed.

On the basis of these results, we have developed a practical protocol for performing dynamic measurements. Most AFM systems do not have a displacement sensor for directly measuring the expansion factor of the piezodrive on the  $z$ -axis. It may be both impractical and tedious to carry out an interferometric calibration as a function of drive speed. Instead the following protocol may be implemented. Let  $\alpha(v)$  be the expansion factor measured (interferometrically) at a single speed  $v$ , so that

$\Delta z(v) = \alpha(v)\Delta V_{pz}$  is the change in piezodrive position due to the change in applied voltage  $\Delta V_{pz}$ . Let  $\Delta z_{\text{nom}}(v') = \alpha(v)\Delta V_{pz}$  be the nominal expansion at a different speed  $v'$ , and let  $\beta_{\text{nom}}(v') = \Delta V_{pd}/\Delta z_{\text{nom}}(v')$  be the nominal photodiode calibration factor at this speed, which is measured in the usual way by pressing the cantilever tip against the hard substrate. Since the correct calibration factor must be independent of speed,  $\beta(v') = \beta(v)$ , the correct expansion factor at the relevant speed can be obtained from the ratio of the measured quantities

$$\alpha(v') = \alpha(v)\beta_{\text{nom}}(v')/\beta(v). \quad (1)$$

This expansion factor is used to obtain the correct displacement of the piezodrive at the speed of the measurement, and this should be used to analyse the data in conjunction with the correct calibration factor  $\beta(v') = \beta(v)$ . The nominal calibration factor that is required for this correction must be obtained by pressing the cantilever against the hard substrate adjacent to the soft particle or film and at the same nominal speed as each of the subsequent measurements on the soft matter.

#### 4.2. Water films

The van der Waals attractions fitted in Figs 4 and 5 included a parameter representing the total thickness of the water films assumed present on both surfaces. The data in Fig. 4 were obtained when the relative humidity was 31% and that in Fig. 5 when the relative humidity was 78%. In the case of Fig. 4A, the tip jumped into contact with the silica substrate from a separation of 5.5 nm to a separation of 0.82 nm, a jump of 4.7 nm. This distance is much larger than expected for a van der Waals jump between the solids. However, water is known to condense on hydrophilic substrates [26, 27], and contact with the tip has been shown to facilitate the deposition of water and to lead to long-lived, locally thickened films that can be measured on subsequent approaches; Xu *et al.* [26] report induced droplets 15 nm in height and 1  $\mu\text{m}$  in radius with lifetimes of the order of minutes. If it is assumed that there is a water film on both surfaces of total thickness 3.2 nm, then quite a good description of the prejump data can be obtained using the water–air–water Hamaker constant,  $A = 3.7 \times 10^{-20}$  J [23], and fitting a radius of curvature of the tip of 700 nm (if the Hamaker constant were doubled, on the grounds that the solids underlying the water films also contribute, then the radius of curvature would be reduced by a factor of two). The coincidence of the prejump data for the tip–silica and tip–cellulose interactions supports the assumption that the van der Waals force is due to the interaction of water films in both cases, since the van der Waals interaction of the bare solids would differ from each other.

A value of  $R = 700$  nm is not unreasonable for a worn tip, since there is no direct relation between the radius of curvature of the tip and the width of the tip itself. Provided that the interaction pressure becomes negligible by the edge of the curved region of the tip, the Derjaguin approximation will remain quantitatively accurate for the analysis of the forces. For an introduction to surface forces, Hamaker constants and the Derjaguin approximation, see Ref. [28].

The thickness of the water film is not unambiguously determined by the present method that varies the tip radius to make the calculated van der Waals attraction fit the pre-jump force data. A similarly good fit to the data in Fig. 4A can be obtained for a thickness of 2 nm by increasing the product  $AR$  by a factor of 2.5, and for a thickness of 4 nm by decreasing the product  $AR$  by a factor of 2. These are about the limits on the thickness that can be tolerated as greater or smaller values make it impossible to have both the correct tangent at the jump point and the correct magnitude of the van der Waals force at larger separations.

Following the jump of the tip into contact with the silica substrate, there is a small hook or soft compliance region of width 0.82 nm (Fig. 4B). Assuming a conical tip with bulk elastic properties, it can be shown that the deformation of the tip is negligible under these loads. If one assumes that the deformation of the silica substrate is negligible (JKR theory would give a deformation of 0.2 nm at zero load), then the most likely explanation of this soft compliance is the Reynolds drainage of the water film between the substrate and the approaching tip.

In the case of Fig. 4A, the same thickness water film was used for both silica and for cellulose. This is supported by the coincidence of the forces prior to the jump (i.e. the magnitude of the van der Waals force for the tip-silica and for the tip-cellulose would only be identical if both were coated with a water film) and the identical jump distances that were measured (see also the discussion of the zero of separation below).

For the measurements of the tip-silica interaction in Fig. 5A, the relative humidity at 78% was higher on that particular day than the 31% for the measurements in Fig. 4, which is consistent with the fact that a total water film thickness (tip plus silica) of 6 nm was required to fit the prejump van der Waals force, compared to a total thickness of 3.2 nm fitted in Fig. 4. This is also consistent with the fact that the postjump hydrodynamic drainage hook is larger in Fig. 5B (1.52 nm) than in Fig. 4B (0.82 nm). As discussed in connection with Fig. 4A, the data could still be fitted when the thickness of the film was varied by  $\pm 1$  nm.

For the tip-polystyrene data in Fig. 5A, a water film of total thickness 4.5 nm has been used in the fit to the van der Waals force. This water presumably adsorbs mainly on the tip, since polystyrene has a hydrophobic character (contact angle 83–89°) [17]. This is consistent with the smaller thickness used for the water film for these data than for the tip-silica data obtained in the same series of measurements.

The pull-off forces (not shown) were 70 nN for both the tip-silica and the tip-cellulose experiments reported in Fig. 4, when the relative humidity was 31%, and were 244 nN for the tip-silica and 203 nN for the tip-polystyrene data reported in Fig. 5, when the relative humidity was 78%. The force due to capillary condensation,  $F = 4\pi\gamma R$ , where  $\gamma = 72$  mN/m is the surface tension of water, and where zero contact angle on both surfaces has been assumed, is 633 nN for  $R = 700$  nm. The assumption that the pull-off force is due to capillary condensation is confirmed by the facts that the force is independent of the nature of the solids on any given day, that it is of the same order as the calculated capillary force (this

is much greater than the expected solid–solid adhesion, and roughness accounts for the fact that the measured values are less than the theoretical ones) and that it increases with increasing relative humidity. It has been shown theoretically [29], that going from less than 40% to greater than 60% relative humidity leads to a large increase in adhesion due to nanoscale roughness. These predictions have been broadly confirmed experimentally (Refs [26, 29, 30] and data not shown) and are consistent with the present results. That the measured pull-off forces are consistent with capillary adhesion confirms the conclusion based on the precontact van der Waals data that the surfaces are covered with water films.

#### *4.3. Zero of separation*

A crucial issue in AFM measurements is defining the zero of separation. For rigid substrates such as the present tip–silica measurements, the zero is found quite simply from the location at which the force curve becomes vertical when plotted against separation. For the case of deformable materials, such as the present cellulose particles and polystyrene films, determining the zero of separation is problematic. The zero of separation was here defined by shifting horizontally the force-separation curve for deformable surfaces, so that the first measured datum after the jump into contact occurred at zero separation (Figs 4B and 5B). This procedure ignores the flattening of the cellulose and polystyrene immediately following the jump. On the basis of the JKR theory [24], the amount of deformation in the case of cellulose is 2 nm, which suggests that the cellulose data ought to be shifted to more negative separations by this amount, and which implies that the water film is 2 nm thinner on cellulose than it is on silica. For polystyrene, the post-jump flattening is estimated as 0.3 nm.

The procedure for establishing the zero of separation also ignores the slow drainage of water following the jump, which added 0.82 nm to the separation for the tip–silica case. This was obtained from the separation relative to zero at the end of the jump in Fig. 4A. This drainage effect partially cancels the deformation effect.

The uncertainty in the thickness of the water film ( $\pm 1$  nm) creates uncertainty in the magnitude of the tip radius. It is the uncertainty in the amount of initial deformation and the film drainage that creates uncertainty in the zero of separation. We have taken the view that the best procedure is to set the zero of separation as the first data point after the jump into contact as this is a clearly defined protocol that avoids having to invoke a JKR fit to the data to obtain the amount of initial deformation.

#### *4.4. Deformation*

It can be seen from the finite slope in the cellulose force data in Fig. 4B that significant deformation of the cellulose occurs and that at no stage does it become rigid (i.e. have an elastic modulus comparable to that of the silica substrate). Rigidity in the cellulose, as for the silica, would be signified by a vertical region

in the force *versus* separation curve. The photodiode was found to change at a rate of  $-0.153$  V/nm at the largest force (46 nN) employed on the cellulose particle. It can be seen that the force curve appears linear in this regime and, hence, one concludes that linearity does not signify rigidity.

What we mean by this last remark is that the appearance of a constant compliance region in the force curve in which the photodiode signal appears to increase linearly with drive distance does not mean that the substrate has become rigid. The slope of such a region should not be used to calibrate the photo-diode because the substrate continues to flatten as the load is increased, and the deflection of the cantilever is less than the movement of the piezo-drive. The reason that a number of previous studies on deformable substrates [11–18] have used such erroneous calibration procedures is that they have assumed that it is only the curvature in the contact region that represents deformation. This is not true, as even JKR theory predicts a quasi-linear force curve at high enough loads. The data in Figs 4B and 5B, which use the calibration factor obtained for the silica substrate, confirm that one cannot use the deformable substrate to calibrate the system.

The negative nominal separations that occur for cellulose as the load is increased in Fig. 4B indicate the amount of flattening or deformation of the particle. The nominal separation is the separation that would occur between rigid particles that could interpenetrate; the actual separation (not shown for cellulose) is the physical separation of the surfaces, which is always positive [4]. For the loads shown the amount of deformation of the cellulose is as much as 25 nm. In the post-contact situation the JKR [24] theory can be fitted to the measured data using  $E/(1 - \nu^2) = 22$  MPa, where  $E$  is Young's modulus and  $\nu$  is Poisson's ratio. This rather low value is consistent with a wet surface layer of the amorphous cellulose II particle.

The hysteresis evident between the loading and unloading force curves in Fig. 4B, and the decrease in deformation with increase in speed indicate that the cellulose particle is slightly viscoelastic. We have not attempted to analyse the data using the viscoelastic theory of Attard [6, 31], because of the uncertainties regarding the tip curvature, the surface energy and the influence of the capillary adhesion (see Refs [8, 19] for quantitative analyses of AFM measurements on viscoelastic materials).

The polystyrene film appeared more elastic than viscoelastic, since there was little hysteresis between loading and unloading when in contact (force curves not shown). The slightly steeper loading force curve at the higher speed in Fig. 5B is consistent with the increased stiffness on short times scales of viscoelastic theory [6, 31]. The deformation following the jump into contact has been estimated by a fit to the JKR theory, which yields an elasticity parameter,  $E/(1 - \nu^2) = 0.1$  GPa. This fitted value depends on the value of the tip radius, but the latter is constrained by physically reasonable values of the Hamaker constant because the product  $AR$  must be constant to fit the van der Waals force. The lower bound, which was used here, corresponds to the water–air–water value  $A = 3.7 \times 10^{-20}$  J [23], which

gives  $R = 700$  nm and  $E/(1 - \nu^2) = 0.1$  GPa. The upper bound corresponds to the silica–air–silica value  $A = 7 \times 10^{-20}$  J [23], which gives  $R = 350$  nm and  $E/(1 - \nu^2) = 0.15$  GPa.

The value of Young's modulus found here, 0.1 GPa, is markedly less than the value of bulk polystyrene,  $E = 3$  GPa [32], and is consistent with the fact that the surface of polystyrene films is less glassy than the bulk [33–39]. It is also consistent with the value of 0.1 GPa found by Overney *et al.* [39] for the storage modulus of a polystyrene film in a poor solvent. Although not stated explicitly in Ref. [39], it appears that the AFM photodiode calibration factor was taken from the slope of the force curve at the highest applied load where the tip was thought to have fully penetrated the 5-nm-thick polystyrene film and to have been in contact with the underlying silica substrate. The zero of separation was taken to be the beginning of the saturation of the AC response, and was said to represent contact with the underlying silica substrate. The sample indentation was estimated by assuming that the polystyrene behaved as a simple spring, although it was noted that the spring constant changed with applied load. The value of the zero-shear rate storage modulus was deduced using a Maxwell rheological model from the AC measurements made in water, a poor solvent for polystyrene. The present measurements give the material properties of the surface of the film because the amount of deformation is only 10 nm, and deformation decays away from the point of contact. The thickness of the soft surface layer of polystyrene has been estimated to be greater than 4 nm [39]. Because of the small amount of deformation, the thickness of the film (order of  $\mu\text{m}$ ), the rigidity of the underlying substrate, or the bulk properties of the film do not have much influence on the measured data. Previous measurements on sub-micrometer polymer colloids revealed the effect of the substrate at high loads when the deformation was greater than about 10% of the radius of the colloid [8].

In contrast to the present results, the surface force measurements for polystyrene of Schmidt *et al.* [17] were apparently fitted with a value for the combination of Young's modulus and Poisson's ratio of  $E/(1 - \nu^2) = 2.2$  GPa. They analysed their surface force measurements with a deformation of 17 nm, which they state is consistent with the JKR theory. This is close to the bulk value but it corresponds to a material with a surface more than 20 times more rigid than is found here. The discrepancy appears due to the fact that Schmidt *et al.* [17] have calibrated the force measuring bimorph from the apparently linear region at the highest applied loads. It can be seen in Fig. 5B that the force data for polystyrene are quite linear at large applied loads, but that the slope,  $-0.212$  V/nm, is significantly less than the actual calibration factor of the AFM,  $-0.230$  V/nm in this case. Using the wrong calibration factor significantly overestimates the rigidity of the deformable material in any subsequent JKR analysis.

Biggs and Spinks [18] performed AFM force measurements on polystyrene spheres. However, the quantitative values reported by these authors have been vitiated by the experimental protocols employed. In those experiments the photodiode

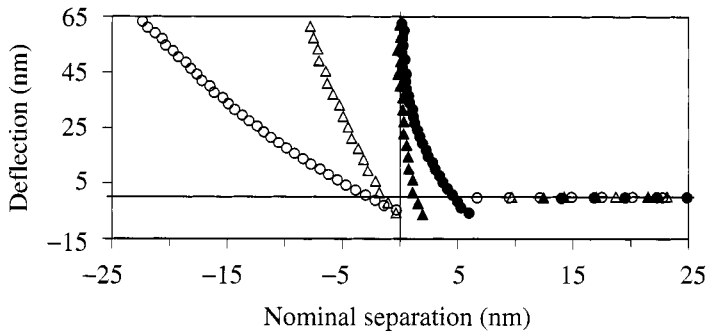


**Figure 6.** Cellulose (circles) and polystyrene (triangles) data from the slow speed cases of Figs 4 and 5. The open symbols represent data analysed using the protocol described in the text. The filled symbols are the conventional result obtained by calibrating the photodiode in the pseudolinear region at high loads and making this the zero of separation.

was calibrated from the slope of a pseudo-linear regime (and different slopes were used on the approach and on the retraction curves). As pointed out here, this neglects the flattening of the deformable particle with increasing load. The zero of separation was taken as the point where the calibration was made at the highest applied load. This again neglects the post-contact flattening of the particle. Finally, a single expansion coefficient was used for the piezo-drive for all the different drive speeds and the changes in the force curves were attributed to viscoelastic effects. As shown here, the expansion of the piezo-drive is speed dependent and this must be accounted for in a quantitative analysis of the data.

Using the wrong calibration procedure for deformable substrates has serious consequences, as is graphically illustrated in Fig. 6. Here the correct results obtained using the present method of calibration (open symbols) are contrasted with the erroneous results that use the apparently linear, high load part of the force curve to calibrate the electronic force measuring device and to set the zero of separation (filled symbols). This erroneous procedure has been used on a number of previous occasions [11–18]. It can be seen that it gives force curves with wrong shapes and wrong slopes and that it leads to a significant underestimate of the amount of deformation. The amount of error depends upon the relative stiffness of the force measuring spring and the deformable substrate.

## 5. CONCLUSIONS AND SUMMARY

This study has been concerned with force measurements on deformable particles and substrates using the atomic force microscope. The problem of establishing the zero of separation during force measurements in air was addressed. A common procedure in the past has been to take the zero of separation to be the separation corresponding to the position of largest load, but this is in substantial error for deformable materials. Instead we attempted to use the van der Waals force law

prior to contact. Whilst quite a good fit to the data could be obtained, the presence of water films diminished the utility of this method to establish unambiguously the zero of separation. We concluded that the best approach was to set the zero of separation at the end point of the jump. Whilst this ignores the competing effects of the initial post-jump flattening and the drainage of the water film, it does provide an unambiguous and reproducible protocol for analysing the force curves.

It was pointed out that for deformable materials the photodiode or other electronic force measuring devices must not be calibrated by fitting the linear regions of the force curves because part of the motion of the piezodrive goes into the deformation of the particle or film. Instead, the calibration has to be performed by pressing the cantilever against a rigid substrate.

It is necessary to recalibrate the photodiode for each experiment since the calibration factor varies with the positions of the cantilever and mirror, unless special care is taken in the setup [40]. The calibration must be performed *in situ* by moving the cantilever off the deformable particle or film and pressing it against a hard substrate. The calibration should also be performed at the same speed as the measurement unless a closed loop piezodrive is used. The expansion coefficient of the piezocrystal must be corrected for its dependence on speed using equation (1). This is particularly important for studies of viscoelastic materials where dynamic effects are of interest, because speed-dependent artefacts in the piezodrive will lead to a misinterpretation of the results unless they are accounted for. For measurement on deformable colloid particles, it is best to mount the deformable particle on the substrate rather than on the cantilever so that the calibration procedure described above can be used. For quantitative force measurements, a rigid colloid probe mounted on the cantilever can be used, and the apex of the two colloids can be located using the imaging facilities of the AFM. In cases where measurements of the interactions of two deformable colloids are required, it appears best to use the procedure of Feiler *et al.* [40] in which two calibrations are performed (pre- and post-mounting), with the optical path unchanged.

Specific results for the deformation of a cellulose particle and of a polystyrene film were obtained and elasticity parameters  $E/(1 - \nu^2) = 22$  and 100 MPa were obtained, respectively. In the case of the polystyrene film, the deformation corresponded to an elasticity parameter that was 30-times less than the bulk value, which indicated that the surface was in a less glassy state than the bulk.

### Acknowledgements

The Biofibre Materials Centre and the Australian Research Council are thanked for financial support.

### REFERENCES

1. P. M. Claesson, T. Ederth, V. Bergeron and M. W. Rutland, *Adv. Colloid Interface Sci.* **67**, 119–183 (1996).



2. P. Attard, *J. Adhesion Sci. Technol.* **16**, 753–791 (2002).
3. M. A. Plunkett and M. W. Rutland, *J. Adhesion Sci. Technol.* **16**, 983–996 (2002).
4. P. Attard and J. L. Parker, *Phys. Rev. A* **46**, 7959–7971 (1992).
5. P. Attard, *J. Phys. Chem. B* **104**, 10635–10641 (2000).
6. P. Attard, *Phys. Rev. E* **63**, 061604 (2001).
7. G. S. Gillies, C. A. Prestidge and P. Attard, *Langmuir* **17**, 7955–7956 (2001).
8. G. S. Gillies, C. A. Prestidge and P. Attard, *Langmuir* **18**, 1674–1679 (2002).
9. P. Attard and S. J. Miklavcic, *J. Colloid Interface Sci.* **247**, 255–257 (2002).
10. P. G. Hartley, F. Grieser, P. Mulvaney and G. W. Stevens, *Langmuir* **15**, 7282–7289 (1999).
11. M. W. Rutland, A. Carambassis, G. A. Willing and R. D. Neuman, *Colloids Surfaces A* **123**, 369–374 (1997).
12. M. Holmberg, J. Berg, S. Stemme, L. Ödberg, J. Rasmussen and P. M. Claesson, *J. Colloid Interface Sci.* **186**, 369–381 (1997).
13. A. Carambassis and M. W. Rutland, *Langmuir* **15**, 5584–5590 (1999).
14. S. Zauscher and D. J. Klingenberg, *J. Colloid Interface Sci.* **229**, 497–510 (2000).
15. Y. Q. Li, N. J. Tao, J. Pan, A. A. Garcia and S. M. Lindsay, *Langmuir* **9**, 637–641 (1993).
16. M. E. Karaman, L. Meagher and R. M. Pashley, *Langmuir* **9**, 1220–1227 (1993).
17. F.-J. Schmitt, T. Ederth, P. Weidenhammer, P. M. Claesson and H.-J. Jacobasch, *J. Adhesion Sci. Technol.* **13**, 79–96 (1999).
18. S. Biggs and G. Spinks, *J. Adhesion Sci. Technol.* **12**, 461–478 (1998).
19. J. W. G. Tyrrell and P. Attard, *Langmuir* **19**, 5254–5260 (2003).
20. J. Hammerschmidt, W. Gladfelter and G. Haugstad, *Macromolecules* **32**, 3360–3367 (1999).
21. H. van Melick, A. van Dijken, J. den Toonder, L. Govaert and H. Meijer, *Philos. Mag. A* **82**, 2093–2102 (2002).
22. S. Ge, Y. Pu, W. Zhang, M. Rafailovich, J. Sokolov, C. Buenviaje, R. Buckmaster and R. M. Overney, *Phys. Rev. Lett.* **85**, 2340–2343 (2000).
23. R. J. Hunter, *Foundations of Colloid Science*, Vol. I. Oxford University Press, Oxford (1986).
24. K. L. Johnson, K. Kendall and A. D. Roberts, *Proc. R. Soc. London Ser. A* **324**, 301–313 (1971).
25. A. Fogden and L. R. White, *J. Colloid Interface Sci.* **138**, 414–430 (1990).
26. L. Xu, A. Lio, J. Hu, D. F. Ogletree and M. Salmeron, *J. Phys. Chem. B* **102**, 540–548 (1998).
27. J. Colchero, A. Sorch, M. Luna, J. Gomez Herrero and A. M. Baro, *Langmuir* **14**, 2230–2234 (1998).
28. J. N. Israelachvili, *Intermolecular and Surface Forces*. Academic Press, New York, NY (1986).
29. Y. I. Rabinovitch, J. J. Adler, M. S. Esayanur, A. Ata, R. K. Singh and B. M. Moudgil, *Adv. Colloid Interface Sci.* **96**, 213–230 (2002).
30. S. Biggs, R. G. Cain, R. R. Dagastine and N. W. Page, *J. Adhesion Sci. Technol.* **16**, 869–885 (2002).
31. P. Attard, *Langmuir* **17**, 4322–4328 (2001).
32. D. R. Akeland, *The Science and Engineering of Materials*, 3rd edn. Chapman and Hall, London (1996).
33. G. F. Meyers, B. M. DeKoven and J. T. Seitz, *Langmuir* **8**, 2330–2335 (1992).
34. J. L. Keddie, R. A. L. Jones and R. A. Cory, *Europhysics Lett.* **27**, 59–64 (1994).
35. T. Kajiyama, K. Tanaka and A. Takahara, *Macromolecules* **28**, 3482–3484 (1995).
36. T. Kajiyama, K. Tanaka and A. Takahara, *Macromolecules* **30**, 280–285 (1997).
37. J. A. Forrest and K. Dalnoki-Veress, *Adv. Colloid Interface Sci.* **94**, 167–195 (2001).
38. J. H. Teichroeb and J. A. Forrest, *Phys. Rev. Lett.* **91**, 016104 (2003).
39. R. M. Overney, D. P. Leta, C. F. Pictroski, M. H. Rafailovitch, Y. Liu, J. Quinn, J. Sokolov, A. Eisenberg and G. Overney, *Phys. Rev. Lett.* **76**, 1272–1275 (1996).
40. A. Feiler, P. Attard and I. Larson, *Rev. Sci. Instrum.* **71**, 2746–2750 (2000).

## Dynamic adhesion of grafted polymer surfaces as studied by surface force measurements

M. A. PLUNKETT\* and M. W. RUTLAND

*Institute for Surface Chemistry, S-114 86 Stockholm, Sweden and Department of Chemistry, Surface Chemistry, Royal Institute of Technology, SE-100 44 Stockholm, Sweden*

**Abstract**—Surface force experiments have been carried out to investigate the dynamics of adhesion for grafted polymer-coated glass spheres in a solvent. The quality of solvent has been varied both by changing the relative concentrations in a mixed solvent system and by variations in temperature in order to investigate the effect on the measured adhesion. Under very poor solvent conditions (far from  $\theta$  conditions) there is a contact time dependence of the magnitude of the adhesion, that can be explained in terms of polymer interpenetration. This interpenetration is consistent with the diffusion following primitive path fluctuation dynamics. An increase in the maximum applied load leads to a decrease in adhesion which is attributed to a slower diffusion rate due to squeezing out of the solvent from the contact zone. Under slightly poor solvent conditions (near- $\theta$  conditions), any polymer interdiffusion is found to be rapid on the experimental time frame. In this case the adhesion is strongly dependent on the separation rate, which is interpreted in terms of viscoelastic losses at the crack tip.

**Keywords:** Dynamic adhesion; grafted polymer; viscoelasticity; poor solvent; polymer diffusion; surface forces.

### 1. INTRODUCTION

The process of adhesion is complex and may, on the molecular level, involve several different mechanisms. The combination of these individual contributions leads to the final adhesion strength, though individual mechanisms may dominate under specific conditions. At its simplest, adhesion is governed by the thermodynamic work of adhesion but becomes much more complex with the introduction of viscoelastic substrates and entanglement effects. In this study, we have investigated the dominant mechanisms of adhesion of two glass surfaces coated by a tethered

---

\*To whom correspondence should be addressed. Phone: +46 8 790 9900. Fax: +46 8 20 8998.  
E-mail: mark.plunkett@surfchem.kth.se

polymer layer, and how the relative contributions of different mechanisms change with the solvency conditions.

Various mechanisms related to the adhesion of polymers have been presented [1–4]. First, there is the thermodynamic work of adhesion, the magnitude of which is determined by intermolecular forces [1]. The types of interactions where the adhesion is dominated by the surface energy are often analyzed using contact mechanics theories such as those derived by Johnson, Kendall, and Roberts (JKR) [5], or by Derjaguin, Muller, and Toporov (DMT) [6], or various transitional models [7, 8]. These approaches predict the interaction area as a function of the load and differ in their assumptions of the deformations involved and the modeling of the interaction forces present. Due to the area relationship, any dynamics of the interaction is related to the rate of advancement of the contact zone.

For rough surfaces there may also be a relation between the applied load and the effective area of contact. In addition, there is an increase in adhesion due to any chemical bonding. It has also been argued that any electrostatic interactions present may have a significant influence on the adhesion (see Ref. [3]), though this argument seems to have gone out of favor [3]. Finally it is noted that acid–base interactions are also important in adhesion [9].

For polymer surfaces there is also an increase in adhesion due to polymer molecules diffusing across the boundary and thus leading to a broader more diffuse interface. This increase in adhesion can be attributed to an increase in the effective contact area, and thus in an increase in the work of separation compared to the work of adhesion between two smooth surfaces. Additionally, in dynamic situations increases in adhesion may also come from the frictional forces incurred in pulling the entangled molecules out from the opposing network, and thus in this case it is related to the polymer viscoelastic response. It is also possible for molecules that diffuse across the interface to be ‘torn’ apart during the separation process thus leading to an increase in adhesion which is related to both the type and number of the chemical bonds broken. Finally it has been shown that for viscoelastic materials, the bulk material may dissipate energy during separation and thus add to the adhesion force [10].

Polymer diffusion is usually more complex than that described by simple Fickian diffusion. This is particularly so if the polymer is tethered at any point, is highly branched, or if the molecular weight is high. For a polymer chain in which the distribution of the density of polymer from its center of mass can be described as Gaussian, the conformational relaxation to an equilibrium state is well described by the Rouse model [11]. For entangled polymers the relaxation becomes more complex. Entanglement in solution can occur when the polymer concentration becomes high enough to allow interactions between neighboring molecules [11]. Entanglement effects in the bulk are also seen to dramatically increase the viscosity in polymer melts when the molecular weight becomes larger than some critical value, which is dependent upon the particular polymer but is often in the range 5000–30 000 g/mol [12]. In the entangled state, the polymers may be considered

to be enclosed within 'tube-like' structures, in which the quickest relaxation mode is for the polymer to diffuse along the 'tube'. This type of diffusion process is called reptation. It is slower than ordinary diffusion but is the dominant relaxation mechanism for large molecular weight polymers as shown by de Gennes [13]. The relaxation process becomes even more complex if the polymer is pinned at a certain position, for example, a branch point or by being grafted to a surface. In this case the polymer's free end must diffuse along its 'tube', come back to the tethered position and then diffuse out again into an equilibrium position. This type of relaxation is referred to as 'primitive-path fluctuations' or 'breathing modes' [11].

Autoadhesion studies have been carried out for polymer systems, confirming diffusion across the interface [3, 14]. Theoretical work on the kinetics of penetration of a grafted polymer into a chemically identical, permanently cross-linked network has been carried out by, for example, O'Connor and McLeish [15, 16]. In addition to the mechanisms already discussed, they propose an additional mechanism for the grafted polymer to diffuse into the network. For the brush to be at equilibrium, they state that the grafted chain must enter the network directly above the grafting point. However, due to the quick Rouse penetration, the chains enter the network at a distribution of distances ( $R$ ) from the grafting point (related to the end-to-end distance of a polymer chain) to end up at local energy minima. Relaxation of  $R \rightarrow 0$  (and thus true equilibrium) thus occurs over a slower time frame, and this is referred to as  $R$ -hopping. This approach has been correlated with neutron reflection studies on similar systems [17], in which a slow approach to equilibrium is seen which correlates well to a logarithmic dependence with time. Related work has also been carried out on chemically different surfaces by Brown [18, 19], to investigate the effect of chain mobility.

This work on adhesion is the extension of a previous study [20], where we have characterized the system and investigated the effect of solvent quality on the surface forces. In that case we were primarily concerned with long range quasi-equilibrium interactions, above and below theta conditions, though small hydrodynamic contributions were discussed and accounted for. In the present work we are concerned with adhesion forces, which occur only in poor solvent conditions.

## 2. MATERIALS AND METHODS

The experiments were carried out on the same polymer coated surfaces characterized in our previous studies where we investigated the quasi-equilibrium interaction forces and the effect of hydrodynamic interactions, as a function of variation of the solvent-polymer interaction [20]. The force measuring technique and surface preparation procedure are described more fully in that work.

The polymer used was poly (12-hydroxystearic acid) (from ICI) which was grafted onto glass surfaces using the method of Pathmamanoharan [21]. Characterization of the polymer by gel permeation chromatography gave molecular weights (number and weight averages) of  $M_n = 2870$  g/mol and  $M_w = 4795$  g/mol leading

to a polydispersity ( $M_w/M_n$ ) of 1.67. The surfaces were approximately 4-mm diameter glass spheres prepared by flame melting 2-mm glass rods in a butane-oxygen flame. The surfaces were mounted in the MASIF<sup>1</sup> [22, 23] instrument, which is a non-interferometric surface force apparatus. Normal surface force measurements were carried out in a mixed solvent of ethanol (99.5%, Kemetyl) and heptane (p.a. Merck). Temperature was set by the use of Peltier units as discussed previously [20]. Forces are routinely normalized by  $2\pi R$  which according to the Derjaguin approximation [24], renders them equivalent to the interaction energy between two flat surfaces. For continuity, this normalization has also been applied to the adhesion measurements. In this case the radius  $R$ , is defined as  $R = R_1 \cdot R_2 / (R_1 + R_2)$ , where  $R_1$  and  $R_2$  are the radii of surfaces 1 and 2, respectively.

In these experiments we varied the contact time, maximum applied load and separation rate, which all influenced the measured adhesion. However, they cannot always be evaluated independently of one another. It is thus important to understand the operation of the instrument so that experimentally constrained links between different variables can be accounted for.

The MASIF instrument is designed to measure interaction forces between two surfaces. The most common surfaces employed are glass spheres. The force is obtained from the displacement of the lower surface, which is attached to a bimorph spring (a piezoelectric beam that produces a measurable charge when deflected). The position of the upper surface is controlled by a piezoelectric tube, and measured by the use of a linearly variable distance transducer (LVDT). In these experiments a triangular waveform was applied to the piezoelectric tube, such that the upper surface moved in an approximately linear expansion–retraction cycle. Figure 1 shows the measurement of the response from the bimorph in a typical experiment as a function of time. Point 1 in the figure shows the beginning of the run at time zero. Between points 1 and 2, the upper surface moves towards the lower one, which remains stationary due to the absence of any interaction. Around point 2 the bimorph responds to surface forces and thus moves from its equilibrium position. Between points 2 and 3, the bimorph is being linearly deflected with the movement of the upper surface indicating zero relative movement of the two surfaces, and defining zero separation. This region, usually referred to as constant compliance region, also calibrates the bimorph response (which can then, with the bimorph spring constant, be converted into a force). The upper surface then reverses direction at point 3. Point 4 indicates the point of separation expected for non-interacting surfaces; in this case there is a significant adhesion and the surfaces do not separate until considerably later where they jump out to point 5. Point 6 represents the end of the experimental run. The time of the run (time from point 1 to point 6) is a controlled variable. The last part of the curve shows a damped sinusoid, which is an artifact that occurs due to the spring jumping out from a large separation with a

---

<sup>1</sup>Measurement and Analysis of Surface Interaction Forces (MASIF), Australian Scientific Instruments, Canberra Australia (<http://www.anutech.com.au/asi/>).

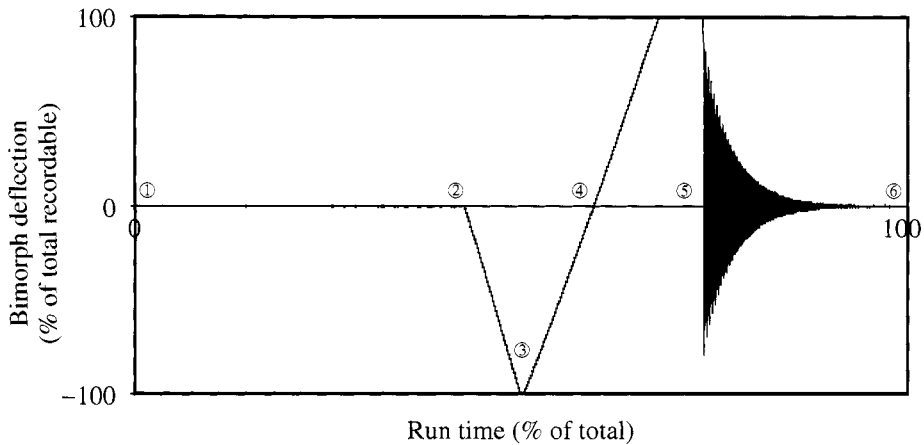


**Figure 1.** Bimorph response in a typical adhesion experiment. Between points 1 and 2 is the zero force regime. Surface forces detected at around point 2 prior to the onset of hard wall contact (points 2–3). At point 4 (zero applied force) the surfaces would have separated in the absence of an adhesion. Point 5 indicates the jump-out distance (the ringing is due to energy dissipation after the sudden release of the spring).

large potential energy. The sinusoidal part is damped as the energy is dissipated to the environment.

While the separation rate is simply given by the piezoelement movement divided by the period of the run (assuming linear piezoelement movement), the contact time of the two surfaces is much harder to control. It depends on the location of point 2 (i.e. on the initial separation of the surfaces) and on the strength of any adhesion (corresponding to the length of the constant compliance region after point 4 in Fig. 1). Thus one of the parameters potentially controlling the dynamic adhesion is itself a function of the adhesion.

### 3. RESULTS

We have investigated the adhesion of the same polymer bearing surfaces under two different solvency conditions. In a previous paper [20] we studied the surface forces measured on approach for a range of solvent conditions, and showed that they were purely attractive for the conditions employed, indicating that in both cases we were in poor solvent regimes. In the first case we have investigated the interaction under slightly poor solvent conditions (40% ethanol and 40°C). An increase in the temperature of 1°C in this situation had the effect of switching the force profile from attractive to repulsive, indicating that the system was close to  $\theta$  conditions. These conditions will be referred to as ‘bad’ solvent conditions. In the second case, which we will refer to as ‘worse’ solvency, the ethanol (poor solvent) concentration was increased to 43% and the experiment was performed at room temperature (21°C). The worse solvency conditions are illustrated by the change

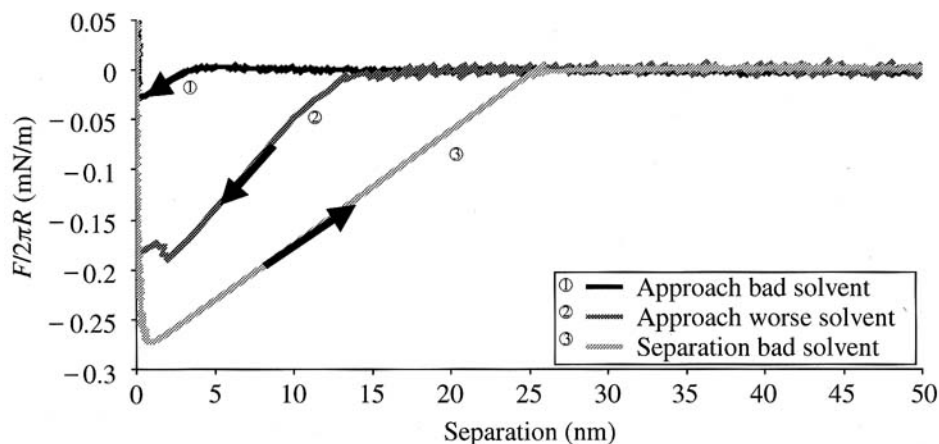


**Figure 2.** Force vs separation data. The upper curve (1) is the approach curve for slightly poor (bad) solvent conditions whilst the lower curve (3) is the separation data for the same conditions. The middle curve (2) is the approach run for the very poor (worse) solvent conditions.

in average adhesion (pull-off force/ $2\pi R$ ) from 0.48 mN/m (standard deviation of 0.13) under bad conditions to 15.7 mN/m (standard deviation of 2.3) under worse conditions, an increase well in excess of an order of magnitude.

A comparison of the surface forces between bad and worse solvency conditions is shown in Fig. 2. The approach runs for both solvency conditions are shown as the upper two curves. There is a significant increase in the range of the attractive force in going from bad to worse solvent conditions (approximately five-fold). Note that a stiffer spring is used in the worst solvent case and that the relative jump distances would be even larger if the same spring were used in both experiments. The jumps (both into and out of contact) are due to spring instability, which occurs when the rate of increase in the magnitude of the force with separation exceeds the spring constant and thus the linear regions of the curves do not reflect the 'true' force profiles.

For the bad solvent conditions, the jump-out is also shown, and can be seen to be approximately ten times the range of the jump-in. Strictly these values cannot be compared since the jump-in distance depends on the shape of the force curve whilst the jump-out depends on the depth of the adhesion minimum. The adhesion for the case of the worse solvent is larger than can be directly measured with the bimorph spring and is thus not included. Calculations based on the jump-out distance (point 4 in Fig. 1) show that the magnitude of the adhesion in this case is 25 mN/m, a ten-fold increase over the bad solvent conditions.

In both cases the adhesion is determined to be a dynamic quantity, the magnitude of which varies significantly with, for example, the length of time the two surfaces remain in contact — which we define as the 'contact time'. What is intriguing is that the dynamic adhesion behavior is completely different for the two cases, suggesting that the mechanisms behind the dynamic component of the adhesion are different.

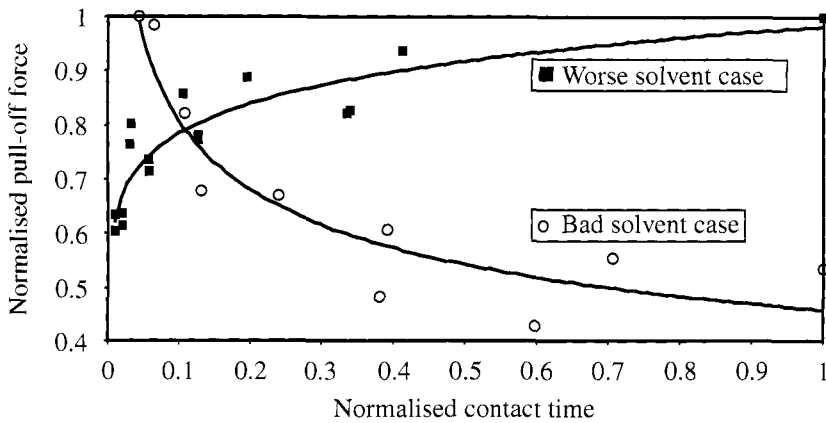


**Figure 3.** Pull-off-force vs contact time for the two solvent cases. (○ represents bad solvent conditions whilst (■) represents worst solvent conditions). Note that both sets of data are normalised to the maximum value in each case, giving a range from 0 to 1.

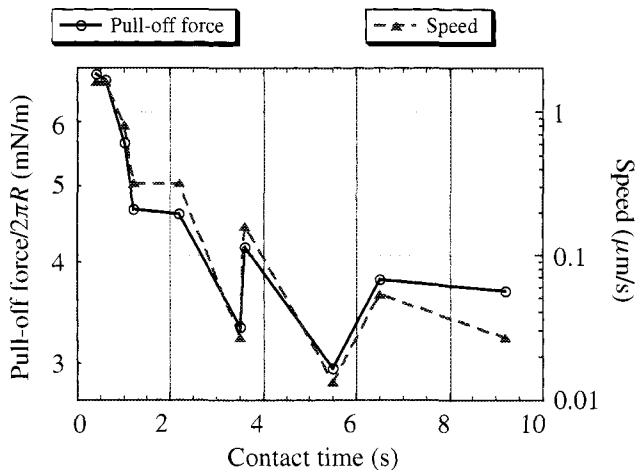


**Figure 4.** Pull-off force/2πR (mN/m) and speed (μm/s) vs contact time (s). Note log scales for both y-axes, which are scaled to clarify correlation between the two y-ordinates.

This is illustrated by Fig. 3 where we compare the normalized pull off-force vs contact time. The range of the magnitudes of the pull-off forces is so different, between the two different regimes, that they cannot be plotted on the same axes. We have, therefore, arbitrarily normalized the pull-off force by the maximum value in each regime. It can easily be seen that the two regimes display opposite responses to an increase in contact time.

In the previous section, we made clear that the contact time and the separation rate could not be varied entirely independently of each other. Thus it is important to investigate any correlation between these two variables. In Fig. 4, we have, therefore, plotted both the separation rate (speed) and the pull-off force vs the



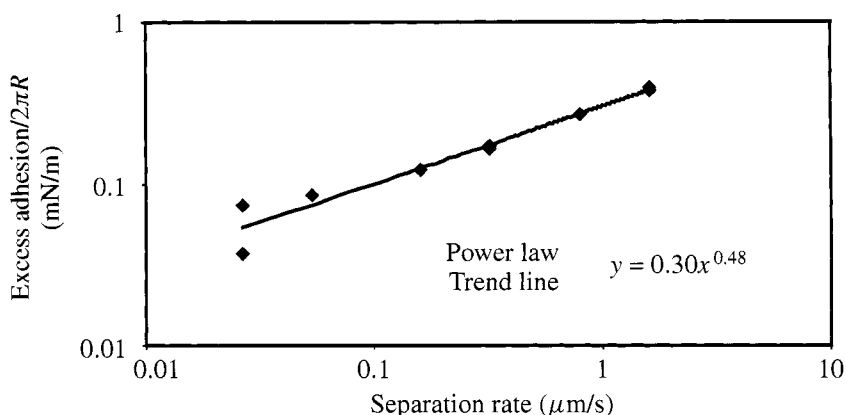


**Figure 5.** Double log plot of the excess adhesion/ $2\pi R$  (mN/m) vs separation rate ( $\mu\text{m/s}$ ) (power law trend line fitted giving exponent of 0.48).

contact time, for bad solvent conditions. Note that both the y-axes are logarithmic. In this case the maximum and minimum values of the y-axes have been set in order to best show any correlation. Fitting of the data to a correlation function [25] gives a value of 99%, which indicates a very high correlation, which is clearly apparent in the figure. Clearly the dynamic adhesion behavior can be interpreted as being a function of separation rate rather than contact time. As argued below, this is in fact the case under bad solvency conditions.

Both peel tests [26] and SFA experiments [27] indicate that under certain conditions, the pull-off force is related to the crack propagation rate. Ruths *et al.* [27] have suggested that the crack propagation rate is directly related to the separation rate, and hence we have displayed the excess pull-off force vs the separation rate on a log–log plot for the bad solvent conditions (Fig. 5). The excess pull-off force is the pull-off force for a specific separation rate, minus that for an infinitely slow separation rate. We have approximated the infinitely slow rate by our slowest separation rate (13 nm/s), and plotted the excess adhesion vs separation rate in Fig. 5. Fitting a power law to these data gives an exponent of 0.48.

For the worse solvency conditions, the increase in adhesion with increased separation rate is not apparent, and the dynamic adhesion behavior appears to be truly dependent on the contact time. This relation between the adhesion and the contact time is shown in Fig. 6 on a semi-log plot. As can be seen in the figure there are two different regimes, each of which is well fitted with a logarithmic trend line. The difference between these two data sets is the maximum load applied. The data in the upper curve are for small applied loads, whilst the data in the lower curve are for a relatively high applied load. The magnitudes of the mean maximum loads with standard deviations are 59.2 mN/m (standard deviation of 30.3 mN/m) for the low maximum load regime and 261 mN/m (standard deviation of 22 mN/m) for the high maximum load regime. Such behavior has not, to our knowledge, been seen before and we leave it to the discussion section to attempt to explain this behavior.

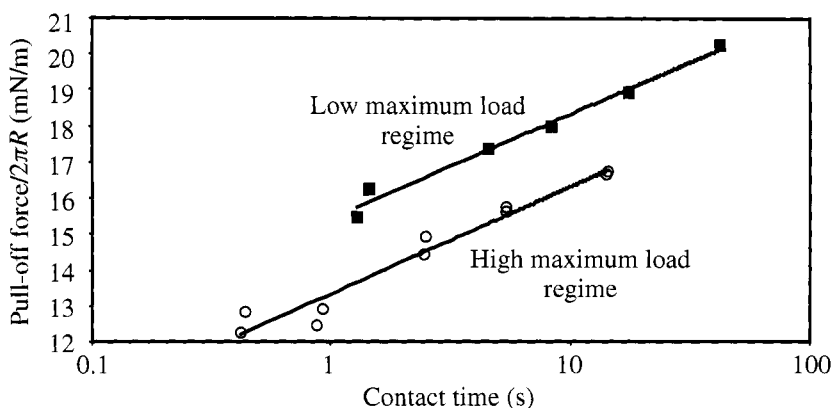


**Figure 6.** Pull-off force/ $2\pi R$  (mN/m) vs log contact time (s). High maximum load (261 mN/m  $\sigma = 22$  mN/m) is shown as (○) whilst the low maximum load (59 mN/m  $\sigma = 30$  mN/m) is shown as (■). Both sets of data are fitted with logarithmic fits (note  $\sigma$  is the standard deviation).

#### 4. DISCUSSION

It becomes obvious from the results that the two different solvent conditions lead to different mechanisms dominating the adhesion behavior. This is evident from Fig. 3, which clearly shows that the magnitude of the pull-off force as a function of the contact time is affected in opposite ways for the two solvent cases. The two independent cases, dealing with 'bad' solvent and 'worse' solvent are now dealt with.

##### 4.1. Bad solvency conditions

The results obtained under bad solvent conditions (poor solvent just below  $\theta$  conditions), can most easily be rationalized by considering the separation rate rather than the contact time (Fig. 5). The data suggest that the rate of inter-penetration is not a dominant mechanism for the adhesion. In fact, since the adhesion actually decreases with contact time (due to the speed/time relation), we assume that any diffusion that occurs is in effect complete even for the quickest investigated times (contact time of 0.4 s). Alternatively, it may just be that the effect on adhesion of any inter-penetration is low, since the polymer–polymer attraction in this case is so low. In any case we propose that the observed effect is solely due to the difference in separation rates.

The excess adhesion at a specific separation rate is the adhesion at this rate minus the adhesion at an infinitely slow separation rate. In Fig. 5 we show that the excess adhesion is a function of the separation rate to the power of 0.48. This is similar to that found by Ruths *et al.* [27] for the interaction of various polymer layers in air where their data were reasonably well fitted to a power law with an exponent of 0.5. Greenwood and Johnson [28] have previously shown theoretically that the excess adhesion should increase with the crack propagation rate to the power of 0.5.

This theory was based on bulk linear viscoelastic losses in the underlying polymer layer. Ruths *et al.* [27] state that this mechanical model, although developed for bulk materials, seems to be applicable to viscoelastic interfaces without violation of the theoretical assumptions. In addition, in their tests using the surface force apparatus (SFA), Ruths *et al.* suggest that the device separation rate is proportional to the crack velocity. Thus the fact that the current experiments give the same relationship as that of Ruths *et al.* [27], and the theory of Greenwood and Johnson [28] would seem to suggest that the separation rate dependence originates from viscoelastic losses at the interface. It should also be noted that our experiments were conducted in a liquid whilst those of Ruths *et al.* were conducted in air, yet both of these sets of experiments give the same 0.5 power law relationship.

The assumption of the direct relationship between the crack propagation rate and the device separation rate is, however, not apparent. First the magnitude of the excess adhesion at fast separation rates is very large in comparison to the adhesion at infinitely slow separation rates. For this reason, it is not apparent that the crack propagates in a similar manner, independent of the rate. Second, the assumption that the large increase in crack propagation rate near pull-off can be ignored is not necessarily correct. Private communication with E. Barthel [29], in reference to his re-analysis of the data of Ruths *et al.* [27], suggests that the intrinsic dissipation exponent is slightly larger than the 0.5 suggested by Ruths *et al.* One would expect a similar effect in the case of our experiments. If this is indeed correct, then the presented data may not agree with the theory of Greenwood and Johnson [28].

Maugis and Barquins [26] have carried out similar work on larger scale systems using three different geometries (adhesion of spheres, adhesion of punches, and peeling). In all cases they found a geometry independent exponent of 0.6 in the power law relation between the 'motive' (defined as  $(G - w)/w$  where  $w$  is the thermodynamic work of adhesion and  $G$  is the strain energy release rate) and the crack propagation rate. In this case viscoelastic losses at the crack tip are responsible for the excess adhesion. This work suggests a different exponent than that of Greenwood and Johnson (0.6 compared to 0.5). The fact that Maugis and Barquins have experimental evidence for their values tends to add more weight to the argument. However, more theoretical studies are required to relate the crack propagation rate to the device separation rate before any definitive statements can be made about which of the crack propagation models is most appropriate to describe the dynamic adhesion behavior measured in surface force devices. What is still unknown, however, is the effect that polymer interpenetration has on the excess adhesion.

#### 4.2. Worse solvency conditions

In the case of the worse solvent, there is a clear increase in adhesion with the contact time (Fig. 6). As discussed in the Materials and Methods section there is a link between the contact time and the separation rate that may alternatively explain this effect. In this case, though, the possibility of an effect due to separation rate can be

discounted, as it is hard to conceive of a mechanism that would explain an increase in the pull-off with a decrease in separation rate (such a mechanism would have to have the opposite effect on the adhesion strength to that operating in the bad solvent case).

The accepted interpretation for increases in adhesion with contact time is that there is polymer inter-penetration. At time frames that are generally much quicker than that at which diffusion processes occur, the wetting or joining of the polymer layers to each other could be responsible for an increase in adhesion (i.e. the rate of increase of the contact area between the two surfaces). (However, other measurements suggest that time frames for these processes on polymer or surfactant systems are outside the investigated period) [27]. In addition, this process, or other non-entanglement events, are unable to explain the observed maximum load effect seen in the current investigation (increase in maximum load leads to a decrease in adhesion).

In Fig. 6 we have shown two different regimes that both show an increase in adhesion with contact time. We conclude that this is the result of inter-penetration of the surface layers for reasons which are discussed later. In this case we cannot determine any separation rate dependence as, if there is any, it is overwhelmed by the inter-penetration effects. Thus the large increase in the adhesion is related to the increase in the effective contact area between the two surfaces as the polymer chains interpenetrate into the opposing polymer matrix (and are not related to the separation rate).

The relation between the pull-off force and the contact time is shown in Fig. 6 where the two regimes are fitted with logarithmic trend lines. Assuming that the adhesion increases linearly with diffusion distance into the polymer network, this relationship suggests that the mechanism of the diffusion is dominated by primitive path fluctuations or 'breathing modes'. Although reptation relaxation is expected in situations such as this, with high polymer concentrations, it is ruled out here since the polymer chains are terminally attached. Primitive path fluctuations are reptation style diffusion where a polymer chain is pinned at a section and follows the relationship [17]:

$$\tau(x) = \tau_0(x) \exp\left[\frac{3M}{2M_e}(1-x)^2\right], \quad (1)$$

where  $\tau(x)$  is the relaxation time for a chain segment at a fractional distance  $x$  from the tether point,  $\tau_0$  is a time scale that, in principle, is dependent on  $x$  but due to its weak dependence is often roughly estimated as the Rouse relaxation time of the chain,  $M_e$  is the molecular weight between entanglements, and  $M$  is the molecular weight.

Under poor solvent conditions polymer molecules adopt a less extended configuration than that predicted purely due to a random walk configuration. This is due to the unfavorable polymer-solvent interactions in a poor solvent. Reptation occurs as the polymer layer on each surface is deformed upon contact with the opposing

surface and then relaxes back into an equilibrium configuration. The new equilibrium position for each polymer chain after the two surfaces come into contact also differs from the pre-contact configuration, as the polymer chains are able to extend further from the surface they are grafted onto without increasing the amount of unfavorable polymer–solvent interactions. On compression, the chains are, however, entangled amongst themselves and must diffuse back towards their grafting point along their primitive path before quickly interpenetrating back into the network via normal Rouse dynamics. It should be noted that the reptation diffusion is similar to *R*-coordinate hopping [15] which also gives an exponential relationship [15], and may be an alternative explanation. *R*-coordinate hopping is, however, expected more for larger molecular weight polymers than those in the current study.

The two regimes depicted in Fig. 6, are due to the difference in maximum applied load. Contrary to intuition, a higher pull-off force is actually seen with a lower maximum applied load. One would usually assume that a higher applied load would lead to both a more intimate surface contact and an increased surface area, and both these effects would be expected to increase the pull-off force between viscoelastic materials. Our results, however, are in the opposite direction. The results are also different from the bad solvent situation where we have seen no appreciable effect of the applied load. There are two possible explanations. First, it has been shown that an increase in pressure leads to a small increase in relaxation times [30, 31]. Second, the increase in maximum applied load could be enough to squeeze out additional solvent from the layers and hence further reduce the relaxation rates. Without a measurement of the compressed layer thickness (an instrumental drawback of the non-interferometric techniques such as the MASIF in bimorph sensing mode) we cannot unconditionally distinguish between these two possibilities. This result does allow us to conclude that the contact time effect is, in fact, due to entanglement effects as opposed to a mechanism such as a gradual relaxation of the surface leading to an increase in the contact area (and thus the measured adhesion). In that case, the mechanism would be expected to be favored rather than hindered by increased pressure. Entanglement is generally expected for polymers with molecular weights in excess of 5000 g/mol (at least in polymer melts) and thus our polymer would appear to be a borderline case. However, it must be remembered that we have a thin film of tethered polymer molecules, which, due to polydispersity, has a significant fraction well in excess of the average molecular weight, and that such numbers are very dependent on polymer structure and are thus no more than a guide.

A decrease in solvent quality is known to decrease the radius of gyration in a polymer–solvent system [32]. Similarly, a decrease in solvent quality will lead to a decrease in layer thickness for a grafted polymer layer. In each case this leads to a lower solvent concentration within the polymer matrix. This causes a slowing down in the mobility of the polymer and an increase in its relaxation times. Thus as the solvent conditions become worse, inter-penetration becomes slower, which also explains why we see an effect due to the contact time in the worse solvent case but not in the bad solvent case.

## 5. SUMMARY

We have shown that the polymer relaxation time is dependent upon the solvent quality. In the case of a bad solvent (poor solvent close to  $\theta$  conditions), the polymer diffusion reaches equilibrium even in the quickest experimental runs. Under worse solvent conditions, however, (poor solvent far from  $\theta$  conditions), the polymer does not achieve this equilibrium, even for the slowest experimental runs (minutes). Pushing the surfaces together with a greater force squeezes out the solvent and thus further reduces the rate of diffusion. In the worse solvency conditions, the pull-off force increases as a logarithmic function of the contact time. This is suggestive of reptation based primitive path fluctuations as the dominant mechanism of inter-diffusion.

For the bad solvent conditions, there is a large effect of the separation rate on the measured pull-off force. The observed power law dependence of the adhesion on the separation rate, with exponent 0.5, does agree with studies on monolayers in air [27]. However, in view of the lack of linearity between the crack propagation and the separation rates it seems possible that the apparent agreement with the theory of Greenwood and Johnson [28] is coincidental.

The correlations between surface force measurements and fracture mechanics models seem to be a promising means to investigate adhesion systems. The current difficulty, however, lies in determining the contact radius as a function of time in our surface force experiments. At present, studies with the JKR instrument, such as those by Maugis and Barquins [26], seem better suited to the problem, though they are limited both in experimental time frames and in the systems they can investigate. With the use of video imaging and interferometry, SFA experiments may also yield valuable information, and extend the range of systems that can be investigated. Alternatively, the current theoretical developments to describe the peeling of viscoelastic layers may render MASIF and AFM even more valuable tools in this area.

### *Acknowledgement*

M. A. Plunkett thanks the Swedish Foundation for Strategic Research 'Colloid and Interface Technology' for funding. Thanks to S. Rödner for surface preparation and Per Claesson for valuable discussions.

## REFERENCES

1. S. Wu, *Polymer Interface and Adhesion*. Marcel Dekker, New York (1982).
2. R. A. L. Jones and R. W. Richards, *Polymers at Surfaces and Interfaces*. Cambridge University Press, Cambridge (1999).
3. S. S. Voyutskii, *Adhesives Age* **5**, 30 (April 1962).
4. K. L. Johnson, *Langmuir* **12**, 4510 (1996).
5. K. L. Johnson, K. Kendall and A. D. Roberts, *Proc. R. Soc. Lond.* **A324**, 301 (1971).

6. B. V. Derjaguin, V. M. Muller and Y. P. Toporov, *J. Colloid Interface Sci.* **53**, 314 (1975).
7. V. M. Muller, V. S. Yushchenko and B. V. Derjaguin, *J. Colloid Interface Sci.* **92**, 92 (1983).
8. D. Maugis, *J. Colloid Interface Sci.* **150**, 243 (1992).
9. K. L. Mittal (Ed.), *Acid–Base Interactions: Relevance to Adhesion Science Technology*, Vol. 2. VSP, Utrecht (2000).
10. A. N. Gent, *Langmuir* **12**, 4492 (1996).
11. R. G. Larson, *The Structure and Rheology of Complex Fluids*. Oxford University Press, New York (1999).
12. J. D. Ferry, *Viscoelastic Properties of Polymers*. Wiley, New York (1980).
13. P. G. de Gennes, in: *Microscopic Aspects of Adhesion and Lubrication*, J. M. Georges (Ed.), pp. 355–367. Elsevier, Amsterdam (1982).
14. S. S. Voyutskii and V. M. Zamazii, *Rubber Chem. Technol.* **30**, 544 (1957).
15. K. O'Connor and T. C. B. McLeish, *Faraday Discuss.* **98**, 67 (1994).
16. K. P. O'Connor and T. C. B. McLeish, *Macromolecules* **26**, 7322 (1993).
17. M. Geoghegan, C. J. Clarke, F. Boue, A. Menelle, T. Russ and D. G. Bucknall, *Macromolecules* **32**, 5106 (1999).
18. H. R. Brown, *Macromolecules* **26**, 1666 (1993).
19. H. R. Brown, *Faraday Discuss.* **98**, 47 (1994).
20. M. A. Plunkett, S. Rödner, L. Bergström and M. W. Rutland, *J. Adhesion Sci. Technol.* **16**, 965 (2002).
21. C. Pathmamanoharan, *Colloids Surfaces* **50**, 1 (1990).
22. J. L. Parker, *Prog. Surf. Sci.* **47**, 205 (1994).
23. J. L. Parker, *Langmuir* **8**, 551 (1992).
24. B. V. Derjaguin, *Kolloid Z* **69**, 155 (1934).
25. R. V. Hogg and E. A. Tanis, *Probability and Statistical Inference*. Prentice Hall, New York (1988).
26. D. Maugis and M. Barquins, *J. Phys. D: Appl. Phys.* **11**, 1989 (1978).
27. M. Ruths, H. Yoshizawa, L. J. Fetters and J. Israelachvili, *Macromolecules* **29**, 7193 (1996).
28. J. A. Greenwood and K. L. Johnson, *Phil. Mag. B* **43**, 697 (1981).
29. E. Barthel, Private Communication (2000).
30. J. E. McKinney and H. V. Belcher, *J. Res. (Nat. Bur. Stand.)* **67a**, 43 (1963).
31. H. Singh and A. W. Nolle, *J. Appl. Phys.* **30**, 337 (1959).
32. P. G. de Gennes, *Scaling Concepts in Polymer Physics*. Cornell University Press, Ithaca, NY (1979).

# Chemical Origins of Adhesion



## **Chemical force microscopy: probing chemical origin of interfacial forces and adhesion**

DMITRI V. VEZENOV<sup>1,\*</sup>, ALEKSANDR NOY<sup>2</sup> and PAUL ASHBY<sup>3</sup>

<sup>1</sup> *Department of Chemistry and Chemical Biology, Harvard University, 12 Oxford Street, Cambridge, MA 02138, USA*

<sup>2</sup> *Chemistry and Materials Sciences, Lawrence Livermore National Laboratory, L-234, Livermore, CA 94550, USA*

<sup>3</sup> *Materials Sciences Division, Mail Stop 66R0200-8256, Lawrence Berkeley National Laboratory, 1 Cyclotron Road, Berkeley, CA 94720, USA*

**Abstract**—Intermolecular interactions between distinct chemical functionalities define a multitude of adhesion events in chemistry, biology and materials science. Modern techniques for measuring molecular level forces have allowed direct quantitative characterization of these interactions. In particular, chemical force microscopy (CFM), which uses the probe tip of a force microscope covalently modified with specific organic functional groups, provides a flexible approach for studying interactions between specific chemical functionalities. In this review, we survey the progress in CFM in recent years as it applies to adhesion of soft materials. We show how new developments in the experimental and theoretical approaches continue to build a realistic and detailed picture of adhesion interaction in condensed phases. We specifically highlight the importance of the kinetics of the unbinding processes and solvation effects in determining the strength of intermolecular interactions. We also describe some recent new directions in CFM, such as high-throughput adhesion measurements and mapping of full intermolecular potentials.

**Keywords:** Chemical force microscopy; force titrations; self-assembled monolayers; dynamic force spectroscopy.

### **1. INTRODUCTION. CHEMICAL FORCE MICROSCOPY: MOTIVATION AND APPLICATION TO ADHESION SCIENCE**

Solid–fluid interfaces occupy a prominent place in condensed matter sciences, since many of the important molecular events in chemistry, physics and biology are interfacial in nature [1]. Examples of such processes span length scales of many

---

\*To whom correspondence should be addressed. Tel.: (1-617) 495-9436. Fax: (1-617) 495-2500.  
E-mail: dvezenov@gmwgroup.harvard.edu

orders of magnitude: from the fracture of materials, wetting and lubrication on a macroscopic scale, to self-assembly and colloidal interactions on the mesoscopic scale and to molecular recognition, protein folding and membrane interactions at the nanoscopic scale. This vast array of phenomena initially appears complex and diverse; yet their outcomes are largely determined by the adhesion interactions among molecular assemblies that comprise the surfaces and surrounding fluid phase.

Adhesion forces are mediated by both specific and non-specific interactions. Potential technological and scientific benefits, which stem from gaining control over these interactions, are enormous. For instance, much of the current progress in nanotechnology hinges upon the bottom-up approaches that utilize precisely tailored intermolecular interactions to form higher-order structures [2]. The molecular-level organization of the interfaces and their binding of solvent play an important role in shaping the strength and distance scale of adhesion forces. Although often poorly understood, adhesion, in general, influences a widely diverse set of industrial applications from airplanes to paints to biosensors [3].

Understanding adhesion phenomena requires an intimate knowledge of the intermolecular forces from which they arise. Historically, these forces have been inferred from macroscopic measurements such as adsorption calorimetry, surface tension studies, pressure induced chemical or vibrational line shifts, equilibrium constants, virial coefficients and elastic moduli [1, 3–5]. Although indirect measurements have provided significant information, the true nanoscopic nature of the interaction is accessible only through a direct measurement. At present, our progress in understanding adhesion interactions at the interfaces is closely linked to the development of physical techniques for measuring such interactions. Typical chemical bond strength ranges from 10 pN for a very weak van der Waals bond to 2–10 nN for a strong covalent bond [4]. The interaction strength also varies significantly, depending on the properties of the surrounding medium. Therefore, an ideal technique for measuring interactions at the interfaces must be capable of measuring forces in the pN to nN range with a sub-nanometer distance resolution under a variety of environmental conditions and solvent media.

Only in recent decades have techniques for elucidating the molecular origin of forces been developed. Specifically, chemical force microscopy (CFM) [6] uses the high precision and nanometer scale probe of atomic force microscopy (AFM) [7] to measure molecular and interfacial interactions. AFM uses nanometer-size probe tips mounted on flexible cantilevers with spring constants ranging from 0.01 N/m to 100 N/m. These springs, coupled with Ångström-level positioning precision of the microscope, provide a natural ability to measure forces in the 50 pN – 100 nN range. However, the use of standard commercial AFM tips as force probes is quite limited, since a generic chemical composition of a silicon nitride or a silicon (common materials in the microfabrication process) tip does not allow researchers to measure specific interactions such as, for example, molecular recognition forces involving organic functional groups. Thus, the tip-sample interaction is typically not well-

defined, and even though image contrast is observed, most AFM images are devoid of chemical information.

Chemical force microscopy addresses these problems by introducing chemical modification of the AFM probes [6, 8]. Well-defined chemical interactions are created by coating the interacting surfaces with self-assembled monolayers (SAMs) terminated with specific organic functional groups. Such modification transforms AFM from a tool for measuring interactions of silicon probes with surfaces to a tool for measuring specific well-defined chemical interactions [9]. Careful design of the probe coating can also help deal with contamination, control the number of interacting molecules, and even separate different types of interactions spatially. This review presents the progress in applying CFM techniques for measuring equilibrium and time-dependent force profiles of molecular interactions, which has led to a greater understanding of the origin of interfacial forces in adhesion. Measurements of force profiles with chemically modified probes are more appropriately termed 'chemical force spectroscopy' (CFS) (where the spectrum represents 'force versus probe-surface distance' dependence), while the term 'chemical force microscopy' (CFM) implies chemically sensitive imaging with such probes. While both names have been used interchangeably in the literature to describe the force-distance experiments, we will use the above nomenclature to make the distinction.

## 2. PROBING POTENTIAL ENERGY SURFACES WITH CHEMICAL FORCE SPECTROSCOPY

Before we discuss probe modification strategies, we need to review the basic physics of interaction force measurements with a force microscope. AFM can provide critical information about potential energy surfaces through the measurement of force profiles. An equilibrium force profile is a derivative of a one-dimensional slice of the potential energy surface, where the reaction coordinate is defined by the pulling direction. The potential energy surface, which determines both energetics and dynamics of the interaction, can then be reconstructed by integration. The force acting on a modified AFM cantilever consists of the cantilever restoring (spring) force and the force originating from the interactions between the functional groups of the tip and the sample. In the simplest case, we can represent the tip-sample interaction with a single-well potential and assume a parabolic potential of a Hookean spring for the cantilever. The overall potential of the system, which determines equilibrium position of the cantilever, is a sum of these two potentials (Fig. 1). A simple analysis shows that depending on the cantilever stiffness the system can behave in two very different ways: (1) for stiff cantilevers, the spring potential is so steep that it prevents formation of secondary minima at all separations. Therefore, as the cantilever approaches and retracts from the surface, the forward and reverse curves coincide, and the probe can trace the entire potential energy well (Fig. 1A–C). (2) When the cantilever spring is

soft, the parabolic potential is shallow and secondary minima can emerge at certain separations, leading to sudden jumps of the cantilever towards the surface during approach and away from the surface during retraction (Fig. 1D–F). These instabilities cause hysteresis in the approach–retraction cycle and preclude the probe tip from sampling a large part of the energy well where the force gradient exceeds the cantilever spring stiffness. As the result, a force microscopy experiment can only map the regions close to the very top and very bottom of the energy well. Unfortunately, the second situation is overwhelmingly prevalent in CFM measurements due to steep potential energy gradients typical of the surface forces and the limitations imposed by AFM sensitivity and noise levels. Practically, it means that a large portion of CFM measurements is restricted to characterization of maximum interaction force, or the pull-off force, which is manifested by a sharp jump in the retraction portion of the force–distance curve. Fortunately, as we will show, these measurements can still offer a wealth of information about intermolecular interactions.

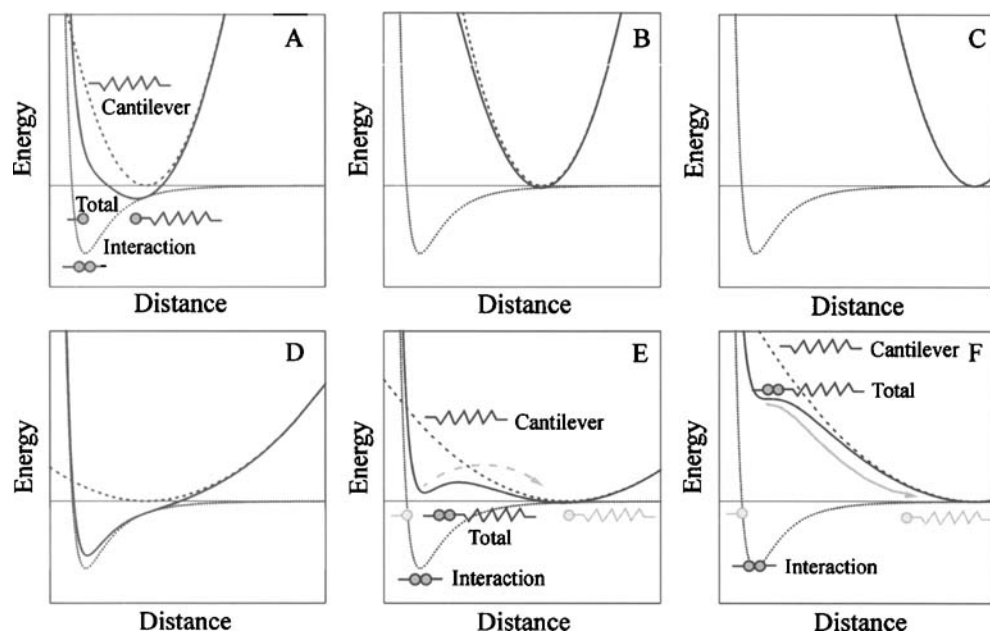


**Figure 1.** Schematic potential energy surface diagram showing loading of a chemical bond (dotted curve potential) by an external spring (dashed curve potential). The total energy profile of the system is a sum of the two potentials (shown as a solid curve). Measurements with soft springs result in the system being trapped in a secondary minimum (E), whereas transition to the global minimum (as indicated by the gray line in F) does not allow to probe the potential profile in a quasi-equilibrium manner. When several local minima are present (soft spring loading shown in D–F), thermal fluctuations can drive the system over the barrier separating these two minima (as indicated by the gray dashed line in E).

### 3. CFM STUDIES OF FUNDAMENTAL NON-COVALENT INTERACTIONS

The fundamental CFM results obtained in the Lieber group were detailed in our earlier review article [9], which is a good starting point on the basics of the CFM technique; therefore, only a brief summary will be given here. Lieber and co-workers showed that CFM could discriminate interactions between apolar and polar (hydrogen-bonding) groups, such as  $-\text{CH}_3$  and  $\text{COOH}$  [6, 8]. Histograms of adhesion forces observed in repeated pull-off measurements in ethanol for the tips and samples terminating with these groups clearly showed that probe functionalization influences the interaction strength. The trends observed in these experiments followed our intuitive expectations; hydrogen-bonding  $\text{COOH}$  groups show stronger adhesion than the  $\text{CH}_3$  groups that can interact only through van der Waals interactions. Further studies extended this approach to a large number of different functionalities and solvents [9]. The advantage of direct force measurements with CFS was demonstrated for high-energy interfaces (such as  $\text{COOH}$  or  $\text{OH}$  groups in ethanol or water), where surface energies are not available by conventional contact-angle measurements because of complete wetting. The most striking feature of these CFS results is that they clearly showed that a simplistic model based solely on the predominant type of chemically specific forces, that act between the functional groups attached to surfaces of the tip and sample, cannot adequately describe the trends that govern the interaction strength. Instead, if we want to rationalize and quantitatively predict these trends, a detailed analysis of the thermodynamics and kinetics of the interactions is necessary. We will outline the main approaches to this analysis in Section 5 of this review.

The CFM approach was also useful for investigating double-layer interactions in aqueous solutions. Water is by far the most important solvent due to its role in biological and colloidal systems. A large number of surface functional groups can ionize in water giving rise to electrochemical interactions. Charging of the surface functional groups is accompanied by the redistribution of the counterions in solution, giving rise to double layer forces. Vezenov *et al.* showed that chemically-modified AFM tips and samples can probe the changes in solid-liquid interfacial free energies with pH [10]. By monitoring the adhesion force with an ionizable AFM probe, the authors detected changes in surface charge induced by the dissociation of acidic ( $\text{COOH}$ ) or basic ( $\text{NH}_2$ ) groups on the surface. Variations in the sign and magnitude of the force indicated changes in the surface charge. Importantly, this work showed that an abrupt transition in the tip-sample force, from attractive to repulsive, occurred at a certain pH, attributed to the  $\text{p}K_a$  of the functional groups on the surface. Researchers have termed such data ‘force titration curves’. As expected, non-ionizable functional groups did not produce force titration curves. Instead, they showed an approximately constant, finite adhesion interaction throughout the whole pH range. The use of probes terminating in hydrophilic non-ionizing groups (such as  $\text{OH}$  groups) as  $\text{p}K$  probes for unknown surface functionalities was also demonstrated. This new method of ‘chemical force

titration' (CFT) provided a convenient way to determine the  $pK_a$  of the surface groups, potentially with a nanometer scale lateral resolution.

Contact angles (CAs), measured using buffered solution droplets on the same surfaces, also showed a sharp transition (an increase in wettability) as the droplet pH was varied. Both local force microscopy measurements using a modified probe tip and macroscopic wetting studies provided very similar values for the  $pK_{1/2}$  (i.e., the pH at which adhesion or CA changes by a factor of two) of the surface amine group for disordered amine-terminated siloxane SAMs, although these values were 6 pK units lower than the typical bulk solution values. Vezenov *et al.* also used CFT to determine pK values for COOH-terminated surfaces and found that the  $pK_{1/2}$  of the surface-confined carboxylic acid was approx. 5.5, very similar to the  $pK_a$  of the COOH functionality in aqueous solution. Similar results for these groups were obtained by van der Vegte and Hadziioannou [11] and by He *et al.* [12].

Noy *et al.* also demonstrated that CFS was well suited to probe single molecule forces and elasticity of synthetic DNA oligomers [13]. While adhesion interactions between biological molecules is an important topic in the force spectroscopy literature, we will, for the most part, leave this subject out of the scope of this review and focus on simpler organic, or 'soft matter', systems of SAMs. Applications of CFM to polymers also deserve a separate summary (see, e.g., the work by the Vancso group [14–21]). In addition, while CFM uses chemical sensitivity of friction forces to map the distribution of the chemical functionality on the surface [9], we will only mention relevant studies in the context of adhesive contact between functionalized tips and samples.

#### 4. CHEMICAL FUNCTIONALIZATION OF FORCE PROBES

Formation of thiol self-assembled monolayers on gold-coated tips has become the most widely used method for chemical modification of AFM tips since the introduction of chemical force microscopy by the Lieber group [6, 8, 22]. Several other methods for covalent attachment of functionalized monolayers have been investigated in detail since then (Table 1): (1) formation of siloxane self-assembled monolayers on silicon nitride AFM probes with [23] and without [24] surface oxide layer and on tungsten probes [25]; (2) attachment of alkyl monolayers on silicon probes with direct Si–C bond [26], and (3) functionalization of carbon nanotube (NT) probes [27, 28]. We found that the use of silver instead of gold produces similar results in CFS [29]. Fresh thiol SAM can be prepared on regenerated Au-coated tips after removal of organic monolayer in plasma oxidation followed by reduction of the Au surface in hot (65°C) ethanol [30]. CFM was further advanced in the Lieber laboratory using carbon nanotubes as AFM probes [27] and a review of this work is available [31]. The small size of the probe and the capability of chemical functionalization make nanotube tips ideal for trying to achieve the ultimate lateral resolution in CFM; however, the commercial availability and mass production of such probes remain a problem.

**Table 1.**

Methods for chemical modification of the AFM probes

Probe material	Treatment	Attached molecule/group	Conditions	Reference
Si or SiN <sub>x</sub>	Cr(Ti)/Au	HS-(CH <sub>2</sub> ) <sub>n</sub> -X	1 mM in ethanol, 1–24 h	[6, 9]
Si or SiN <sub>x</sub>	Cr(Ti)/Ag	HS-(CH <sub>2</sub> ) <sub>n</sub> -X	1 mM in ethanol, 1–24 h	[29]
SiN <sub>x</sub>	O <sub>3</sub> 30 min, 0.5 M NaOH 20 min, 0.1 M HCl 10 min, 0.5 M NaOH 10 min Dry 120°C, 10 min	Cl <sub>3</sub> Si-(CH <sub>2</sub> ) <sub>n</sub> -CH=CH <sub>2</sub>	1 mM in dehydrated toluene, 4 h 10–30 min at 120°C	[9, 23]
SiN <sub>x</sub>	Piranha solution (H <sub>2</sub> SO <sub>4</sub> /30% H <sub>2</sub> O <sub>2</sub> , 7:3), 110°C, 15–20 min 49% HF, 1 min	Cl <sub>3</sub> Si-(CH <sub>2</sub> ) <sub>17</sub> -CH <sub>3</sub> Cl <sub>3</sub> Si-(CH <sub>2</sub> ) <sub>11</sub> -Br	2–5 mM in hexadecane/chloroform (4:1, v), approx. 12 h	[24]
Si	8% NH <sub>4</sub> F 1 min	CH <sub>2</sub> =CH-(CH <sub>2</sub> ) <sub>9</sub> -CH CH <sub>2</sub> =CH-(CF <sub>2</sub> ) <sub>9</sub> -CF <sub>3</sub>	neat, UV light, 2 h	[26]
Si	Piranha solution (H <sub>2</sub> SO <sub>4</sub> /30% H <sub>2</sub> O <sub>2</sub> , 7:3), 80°C 2% HF, 1 min	CH <sub>3</sub> O(CH <sub>2</sub> CH <sub>2</sub> O) <sub>3</sub> - -(CH <sub>2</sub> ) <sub>9</sub> -CH=CH <sub>2</sub>	degassed 0.1 M in freshly distilled mesitylene under N <sub>2</sub> , reflux, 2 h	[62]
W	Electrochemical etch, 2 M KOH, 6 V <sub>ac</sub> Preheat 1600°C	Cl <sub>3</sub> Si-(CH <sub>2</sub> ) <sub>17</sub> -CH <sub>3</sub>	0.2–0.5% in hexadecane (70%)/chloroform (30%), 18 h	[25]
Carbon nanotube (NT)	Bias voltage between NT and Nb substrate in O <sub>2</sub> atmosphere	-COOH -CONH-C <sub>6</sub> H <sub>5</sub> -CONHCH <sub>2</sub> CH <sub>2</sub> NH <sub>2</sub>	Shortened NT, as is NT + 5 mM benzylamine NT + 5 mM ethylenediamine in pH 6 buffer containing 50 mM carbodiimide, 2 h	[27, 28, 31]
	N <sub>2</sub> atmosphere	-NH <sub>2</sub>	Shortened NT as is	
	H <sub>2</sub> atmosphere	=CH <sub>2</sub> , -CH <sub>3</sub>	Shortened NT as is	

## 5. THEORETICAL MODELS OF CFS

### 5.1. Thermodynamic model of quasi-static CFS

*5.1.1. Contact mechanics approach to tip-surface contact in CFM.* Although force microscopy with sharp probes approaches the limit of point contact, in actual CFM experiments the number of interacting molecular species remains on the order of tens to hundreds, unless carbon nanotube probes are used. An attempt to estimate

the number of molecular contacts found that continuum contact mechanics theories provided a surprisingly reasonable framework for interpretation of CFM data even at the nanoscopic level. Limitations to contact mechanics models could still be encountered in the lower range of the nanoscopic regime or when the interaction was specific.

When coming into contact, two elastic bodies of radii of curvature,  $R_1$  and  $R_2$ , and effective radius  $R$ :

$$R = (1/R_1 + 1/R_2)^{-1}, \quad (1)$$

deform due both to repulsive forces (Born repulsion) within the area of contact and attractive forces near the edge of the contact zone as well as outside of it. Since the Born repulsion is extremely steep, the interatomic distances within the contact zone differ little and, thus, this area can be considered to be a flat circle of radius  $a$ . For repulsive-only interactions (Hertz model), the dependence of the contact area size on an external load,  $P$ , is well known:

$$a^3 = \frac{RP}{K}, \quad (2)$$

where

$$K = \frac{4}{3} \left( \frac{1 - \nu_1^2}{E_1} + \frac{1 - \nu_2^2}{E_2} \right)^{-1}, \quad (3)$$

is the effective elastic constant of the system ( $\nu$  is the Poisson ratio and  $E$  is the Young's modulus). Inclusion of more realistic potentials is not straightforward, because interaction force depends on the intermolecular separation; in other words, it is defined by the surface profile of the deformed sphere, which, in turn, depends on the interaction force. One can decouple the force-surface profile dependency by assuming that (1) the profile does not change because of the presence of attractive forces outside the contact zone, or (2) attractive forces act only within the contact area (zero range forces). The first option means that the forces are based on the Hertz result and it leads to the DMT (Derjaguin, Muller and Toporov) model of adhesion [32]: the radius  $a$  and the stress distribution are given by Hertz equations with external load substituted by the total force, which includes adhesion  $F_a$ ,  $P + F_a$ . The force of adhesion is then given by  $F_a = 2\pi RW_{132}$ , where  $W_{132}$  is the thermodynamic work of adhesion, given by a balance of interfacial free energies  $W_{132} = \gamma_{13} + \gamma_{23} - \gamma_{12}$ .

The second choice, implemented in the JKR (Johnson, Kendall and Roberts) model [33], results in a different stress distribution: compressive in the center of the contact zone, changing to tensile when approaching the boundary (and zero outside the contact circle). Using the energy minimization approach, JKR predicted that the contact radius can be derived from Hertz equation when the external load  $P$  is substituted by an apparent load  $P_1$ :

$$a^3 = \frac{RP_1}{K}, \quad P_1 = P + 3\pi W_{132}R + \sqrt{6\pi W_{132}RP + (3\pi W_{132}R)^2}. \quad (4)$$



Alternatively, the problem of separation of the two surfaces can be treated within the formalism of the linear fracture mechanics: the mechanical energy made available through the crack growth, the energy release rate  $G$  (i.e. rate of change in strain energy with area), is used to overcome the surface energy of newly created surfaces (so-called Griffith criterion for stability of the crack:  $G = W_{132}$ ). This leads to an equation for the energy release rate equivalent to the energy minimization result above [34]:

$$W_{132} = G = \frac{(P_1 - P)^2}{6\pi R P_1} = \frac{(K a^3 / R - P)^2}{6\pi K a^3}. \quad (5)$$

The requirement for  $P_1$  to remain real results in the JKR expression for the force of adhesion:

$$F_a = \frac{3}{2}\pi R W_{132} \quad (6)$$

The JKR theory predicts a finite radius of contact under zero external load and when surfaces separate:

$$a_{0(\text{JKR})} = \left( \frac{6\pi W_{132} R^2}{K} \right)^{1/3} \quad \text{and} \quad a_{s(\text{JKR})} = \frac{a_{0(\text{JKR})}}{4^{1/3}} \approx 0.63 a_{0(\text{JKR})},$$

respectively. Dividing the contact area at pull-off,  $a_s$ , by the area occupied by a single functional group allows an estimate of the number of molecular contacts to be made. The corresponding quantities for the DMT theory are

$$a_{0(\text{DMT})} = \left( \frac{2\pi W_{132} R^2}{K} \right)^{1/3} \quad \text{and} \quad a_{s(\text{DMT})} = 0.$$

The estimate of the number of molecular contacts must consider the range of intermolecular forces,  $z_0$ .

The two models differ substantially in predicted contact area, force of adhesion and surface profile. After some heated debate in the literature, numerical calculations based on the Lennard–Jones potential showed [35] that the DMT and JKR results corresponded to the opposite ends of a spectrum of a non-dimensional parameter (so-called Tabor elasticity parameter):

$$\mu = \left( \frac{16}{9} \frac{R W^2}{K^2 z_0^3} \right)^{1/3}, \quad (7)$$

where  $z_0$  is the equilibrium distance in the Lennard–Jones potential. This parameter asserts the relative importance of the deformation under surface forces: for  $\mu < 0.1$  the DMT model is appropriate, for  $\mu > 5$  the JKR model applies. Although the JKR model predicts infinite stresses at the perimeter of the contact zone, whereas the DMT model predicts discontinuous stress, no discontinuity was observed in the numerical results.

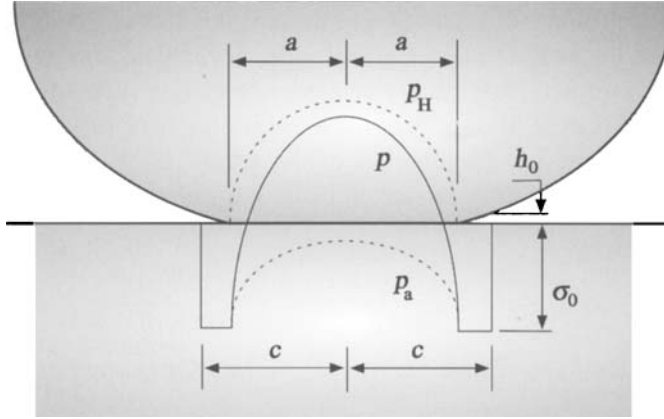


**Figure 2.** The Maugis–Dugdale stress distribution is a sum of two terms: the Hertz pressure  $p_H$  acting on the area of radius  $a$  and adhesion tension  $p_a$  acting on the area confined by radius  $c$ .

To avoid self-consistent calculations based on a specific potential, Maugis produced an analytical solution to this problem [34] using the Dugdale approximation that the adhesion stress has a constant value  $\sigma_0$  (theoretical stress) until a separation  $h_0 = W/\sigma_0$  is reached at radius  $c$ , whereupon it falls to zero (Fig. 2). The external load is given by ( $m = c/a$ ):

$$\bar{P} = \bar{a}^3 - \lambda \bar{a}^2 \left( \sqrt{m^2 - 1} + m^2 \arccos(1/m) \right), \quad (8)$$

where  $\lambda$  is a measure of the ratio of the elastic deformation to the range of surface forces and  $\bar{a}$  and  $\bar{P}$  are, respectively, the scaled radius of the contact zone and external load:

$$\lambda = 2\sigma_0 \left( \frac{RK^2}{\pi W} \right)^{1/3} = 1.16\mu, \quad \bar{a} = \frac{a}{(\pi WR^2/K)^{1/3}}, \quad \bar{P} = \frac{P}{\pi WR}. \quad (9)$$

The elasticity parameter  $\lambda$  is related to  $m$  through:

$$\begin{aligned} & \frac{1}{2} \lambda \bar{a}^2 \left[ (m^2 - 2) \arccos(1/m) + \sqrt{m^2 - 1} \right] \\ & + \frac{4}{3} \lambda^2 \bar{a} \left[ \sqrt{m^2 - 1} \arccos(1/m) - m + 1 \right] = 1. \end{aligned} \quad (10)$$

When  $\lambda$  is increased,  $m \rightarrow 1$  and the JKR limit is recovered:

$$\bar{P} = \bar{a}^3 - \sqrt{6\bar{a}^3} = \bar{P}_1 - \sqrt{6\bar{P}_1}. \quad (11)$$

When  $\lambda$  is decreased,  $m \rightarrow \infty$  and the DMT limit is achieved:

$$\bar{P} = \bar{a}^3 - 2. \quad (12)$$

The Maugis–Dugdale (MD) model is an accurate representation of the adhesion in the presence of a liquid meniscus (constant pressure inside the meniscus).

Knowing the functional form of the contact area dependence on the load is crucial to interpretation of friction data, which will depend on both shear strength of the contact and its size. The difficulty with the MD theory is that it does not easily lend itself to fitting experimental data. This issue was addressed by Carpick *et al.* [36] who demonstrated that a simple general equation,

$$\frac{a}{a_{0(\alpha)}} = \left( \frac{\alpha + \sqrt{1 - P/F_{a(\alpha)}}}{1 + \alpha} \right)^{2/3}, \quad (13)$$

closely approximates Maugis' solution and can be used to fit experimental data on contact area (friction). Numerical results are then used to obtain the Tabor parameter from the fitting parameter  $\alpha$  ( $\alpha = 0$  corresponds exactly to the DMT case,  $\alpha = 1$  corresponds exactly to the JKR case).

The development of contact mechanics models and adhesion measurement techniques over the past few years prompted Johnson to construct an 'adhesion map' of the applicability of particular models depending on the parameter  $\mu$  and applied forces [37]. In the CFM, high-modulus materials ( $\approx 100$  GPa) and tip radii  $\approx 100$  nm result in  $\mu < 1$ ; thus, CFM experiments fall into a 'transition' zone. Johnson notes, however, that from comparison with numerical calculations for  $\mu < 0.3$  the compliance of an adhesive contact (external load *versus* compression) and computed contact radii are well represented by the JKR equations. Therefore, it appears that JKR equations give good predictions, even under conditions well outside the expected JKR zone. We note that it is impossible to place a given system in the respective contact mechanics regime based on adhesion force measurement alone, since contact area is not measured independently. An estimate of the Tabor elasticity parameter is preferred in this case, although this approach still needs to make assumptions about effective elastic constant of the monolayer/substrate system.

*5.1.2. Intermolecular force components theory.* The sphere-on-flat tip-sample geometry of AFM does not correspond to the interaction between two atoms. The Lennard-Jones potential typically used to represent interaction between molecular species (with minimum energy  $\varepsilon_0$ ),

$$\frac{F_{\text{molec}}(z)}{\varepsilon_0/r_0} = 12 \left[ -\left( \frac{z}{z_0} \right)^{-7} + \left( \frac{z}{z_0} \right)^{-13} \right], \quad (14)$$

has to be modified for the CFM geometry to account for multiple intermolecular pairs. The fundamental  $1/z^7$  law of attraction for dispersion forces between molecules was first derived by London based on second-order perturbation theory. An alternative approach by Dzyaloshinskii, Lifshitz and Pitaevskii (DLP) [38] relates van der Waals (vdW) forces to bulk spectroscopic properties of materials. However, quantum field theory of DLP produces an analytically useful result only in the case of vdW pressure between two semi-infinite dielectric slabs separated by

a third medium:

$$f(z) = -\frac{A}{6\pi} \frac{1}{z^3}, \quad (15)$$

where  $A$  is the (non-retarded) Hamaker constant, which is related to detailed dielectric behavior through a complete electromagnetic spectrum.

The two methods (macro and microscopic) converge in Hamaker's approach: from the power law for intermolecular interactions,  $F_{\text{molec}}(z) = -C/z^7$ , the macroscopic vdW force, between bodies 1 and 2 with molecular densities  $\rho_1$  and  $\rho_2$ , can be obtained by volume integration of the pairwise interactions:

$$f(z) = -\frac{\pi\rho_1\rho_2 C}{36z^3}, \quad \text{where } \rho_1\rho_2 C = 6A/\pi^2. \quad (16)$$

Thus, London's result for energy of interactions across vacuum ( $h$  is Planck's constant,  $\alpha$  is atomic polarizability and  $\nu_e$  is characteristic electronic absorption frequency) [39]:

$$U_{\text{molec}}(12) = -\frac{3}{4\pi} h \frac{\nu_{e1}\nu_{e2}}{\nu_{e1} + \nu_{e2}} \frac{\alpha_1\alpha_2}{z^6}, \quad (17)$$

leads to a geometrical mean combining rule for the corresponding Hamaker constants ( $\nu_{e1} \approx \nu_{e2}$ ) and surface free energies for bodies interacting *via* Lifshitz–van der Waals (LW) forces:

$$A_{132} = \pm\sqrt{A_{131}A_{232}} \quad \text{and} \quad \gamma_{12}^{\text{LW}} = \sqrt{\gamma_1^{\text{LW}}\gamma_2^{\text{LW}}}. \quad (18)$$

The pull-off forces, as described in the contact mechanics models, depend on the surface energetics through the thermodynamic work of adhesion. In associating solvents and for polar surfaces, it is important to take a proper account of both additive (symmetric) van der Waals interactions and complimentary (asymmetric) electron donor–acceptor interactions (hydrogen bonding). Donor–acceptor or Lewis acid–base interactions are short-ranged (contact) forces and are not accounted for in London or Lifshitz treatment of weak intermolecular forces. These interactions, however, influence thermodynamic data and, thus, must be included in computational models for analysis and prediction of physico-chemical properties; for example, in solvation models and the linear free energy relationship approaches.

Hydrogen bonding interactions operate over the background of omnipresent dispersion forces. While the dispersion forces for dielectrics are often very similar in magnitude, the hydrogen bonding interaction differentiates various classes of organic functional groups quite dramatically. One can compare, for example, boiling points of homologous hydrocarbons and alcohols or adhesion forces between  $\text{CH}_3/\text{CH}_3$  and  $\text{COOH}/\text{COOH}$  pairs.

Various scales for acidity exist. Acid–base interactions (or hydrogen bonding) can be treated as the formation of a complex (however weak) and one can draw parallels with Klopman's theory of chemical reactivity based on the concept of charge and frontier-controlled reactions [40]. Perturbation theory predicts that the energy of

the two systems R and S, interacting through atoms r and s, is given by the sum of (1) the contribution  $\alpha_{RS}$  from the total electronic charge density,  $\sum_i (c_i^r)^2$ , or charge-controlled effects and (2) the contribution  $\beta_{RS}$  from the frontier (lowest unoccupied and highest occupied molecular orbitals) electron density,  $(c_i^k)^2$ , or covalent-type effects:

$$\Delta E = \Delta E_{\text{charge}} + \Delta E_{\text{frontier}} = \left( \sum_m^{\text{occupied}} (c_r^m)^2 \sum_n^{\text{unoccupied}} (c_s^n)^2 \right) \alpha_{RS} + (c_r^m)^2 (c_s^n)^2 \beta_{RS}. \quad (19)$$

Therefore, this approach argues for separation of interactions at interfaces into two terms, due to total electron density and due to more localized interactions. The form of the equation also suggests that each term can be represented as a product of the parameters corresponding to individual interacting molecular species. Drago has proposed and successfully used an equation of this type to quantitatively predict enthalpies of formation for weak acid–base complexes in solution [41].

A successful scale of the same type for the strength of acid–base interactions was included in the theory of surface free energy proposed by Fowkes, van Oss, Chaudhury and Good (F-vOCG) [5]. They recognized that two values of polar surface tension components were needed to represent electron accepting and electron donating abilities in combining relations. In this model, the total surface tension of a polar system is separated into Lifshitz–van der Waals,  $\gamma^{\text{LW}}$ , and Lewis acid,  $\gamma^+$ , and Lewis base,  $\gamma^-$ , components:

$$\gamma_{\text{total}} = \gamma^{\text{LW}} + \gamma^{\text{AB}}, \quad (20)$$

where  $\gamma^{\text{AB}} = 2\sqrt{\gamma^+ \gamma^-}$ . For cross-interactions, combining rules apply:

$$\gamma_{12} = \sqrt{\gamma_1^{\text{LW}} \gamma_2^{\text{LW}}} + \sqrt{\gamma_1^+ \gamma_2^-} + \sqrt{\gamma_2^+ \gamma_1^-}, \quad (21)$$

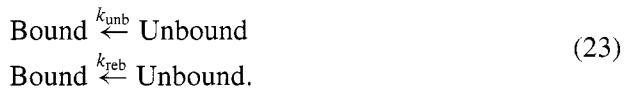
and the solid–liquid interfacial tension is then given by:

$$\begin{aligned} \gamma_{\text{SL}} &= \gamma_{\text{SV}} + \gamma_{\text{LV}} - 2 \left( \sqrt{\gamma_{\text{SV}}^{\text{LW}} \gamma_{\text{LV}}^{\text{LW}}} + \sqrt{\gamma_{\text{LV}}^+ \gamma_{\text{SV}}^-} + \sqrt{\gamma_{\text{SV}}^+ \gamma_{\text{LV}}^-} \right) \\ &= \left( \sqrt{\gamma_{\text{SV}}^{\text{LW}}} - \sqrt{\gamma_{\text{LV}}^{\text{LW}}} \right)^2 + 2 \left( \sqrt{\gamma_{\text{LV}}^+ \gamma_{\text{SV}}^-} + \sqrt{\gamma_{\text{LV}}^- \gamma_{\text{SV}}^+} - \sqrt{\gamma_{\text{SV}}^+ \gamma_{\text{LV}}^-} - \sqrt{\gamma_{\text{SV}}^- \gamma_{\text{LV}}^+} \right). \end{aligned} \quad (22)$$

The interpretation of adhesion measurements in liquids can be complicated if all components are involved in acid–base interactions. Although there is no solid fundamental theoretical basis for applying the geometric mean combining rule for interactions of the acid–base type (unlike for LW interactions), the F-vOCG model has been successfully used in examining surface energies in polymer systems and organic liquids using CFM.

## 5.2. Kinetic model of CFS

**5.2.1. Dynamics of tip-sample interactions.** The thermodynamic models summarized in the previous section clearly show that we expect CFM measurements to be sensitive to the interfacial free energy, i.e., to specific types of intermolecular interactions. A detailed analysis of these measurements, however, is more complicated, because they involve multiple chemical bonds, which are not always loaded by macroscopic springs in an equilibrium manner. To extract quantitative information about intermolecular interactions from these measurements, we need to provide a rigorous time-dependent model description of the CFM experiment. In Section 1 we have briefly touched on the dynamics of the cantilever-sample system. We now need to consider how loading by an AFM cantilever changes the tip-sample interactions. We assume that the tip-sample interaction is described by a single potential well (which we will call a ‘bond potential’), and the cantilever behaves as an ideal Hookean spring represented by a parabolic potential. Addition of the cantilever potential to the bond potential leads to the emergence of a secondary minimum on the potential energy surface, which typically represents the unbound state (Fig. 1E). The dynamics of the system is then determined by the transition from the primary minimum to this secondary minimum. Let us consider how external loading force changes the thermodynamics and kinetics of the transition between bound and unbound states. In the most general case, the dynamics of this two-well system involves two elementary first-order processes, unbinding and rebinding, with each process characterized by a rate constant.



As Bell showed in his pioneering work [42], loading the system in the direction of unbound state lowers the barrier to unbinding and simultaneously raises the barrier to rebinding. Consequently, loading by tensile force  $F$  leads to amplification of unbinding rate constant,  $k_{\text{unb}}$ , and retardation of the rebinding rate constant,  $k_{\text{reb}}$  ( $k_B$  is Boltzmann’s constant,  $T$  is the temperature):

$$k_{\text{unb}} = k_{\text{unb}}^0 \cdot e^{\frac{F \cdot x_{\beta}^{\rightarrow}}{k_B T}}, \quad (24)$$

$$k_{\text{reb}} = k_{\text{reb}}^0 \cdot e^{\frac{-F \cdot x_{\beta}^{\leftarrow}}{k_B T}}, \quad (25)$$

where  $x_{\beta}^{\rightarrow}$  denotes the distance to the transition state from the bottom of the primary well and  $x_{\beta}^{\leftarrow}$  is the corresponding distance from the bottom of the secondary, cantilever-induced potential well. One of the key points is that the distance  $x_{\beta}^{\leftarrow}$  is mostly determined by the cantilever potential (Fig. 1), which can cause surprising variations in unbinding dynamics. Stiff springs place the secondary well relatively close to the transition barrier, while shallow potentials of weak springs place the secondary minimum far away. Equation (25) then predicts that the rebinding process

becomes extremely slow when the bond is stretched by a soft spring. Another key point is that in most CFM experiments the loading force rarely stays constant during the loading process and almost always ramps up linearly, as the piezoelectric scanner retracts from the surface at a constant speed.

A simple qualitative analysis shows that the unbinding transition can happen in two different regimes, determined by the rate of bond loading. Under slow loading of the bond, the unbinding proceeds as an equilibrium process and the force necessary to break the adhesive junction is simply determined by the energy balance between bound and unbound states. Alternatively, if the loading rate is comparable with the rate of at least one of the processes described by equations (23), the system never reaches equilibrium and the unbinding proceeds under kinetic control. One direct consequence of this conclusion is that the unbinding force becomes very dependent on how the bond is loaded; in other words, the loading history starts to play a critical role. Before we consider these regimes in more details, we note that equilibrium unbinding imposes extremely restrictive conditions on the system. In particular, to achieve equilibrium we need to load the bond slower than the rebinding rate, a situation which does not happen often due to the exponential retardation of the rebinding rate by the external load. Equation (25) indicates that for realistic loading rates the best chance to observe the equilibrium unbinding is with the systems that feature deep bond potentials (i.e. large  $k_{\text{reb}}^0$ ) and short distances from the secondary well to the transition state. In practical terms, it means that we can observe equilibrium unbinding only in multi-bond systems stretched slowly by stiff springs, although even in this case the system would transition into the non-equilibrium unbinding regime with increase of the loading rate. As a general rule, most of the single-molecule bond measurements always happen in non-equilibrium regime. Tethering interacting molecules to the AFM tip with long flexible linkers, which is a popular technique for studying biological interactions, also leads to non-equilibrium unbinding [43, 44]. In this case the bond is effectively stretched by the entropic elasticity of the polymer tether, which is equivalent to a very weak spring.

*5.2.2. Non-equilibrium unbinding: kinetic model of bond strength.* As mentioned in Section 5.2.1, we typically encounter non-equilibrium unbinding when strong chemical bonds are stretched with soft springs which place the probe-induced energy minimum far away from the transition state. This situation is common for routine CFM adhesion measurements; therefore, we will consider it in detail. Figure 3 shows the energy diagram for this case, which is somewhat simpler than the generalized energy diagram presented in Fig. 1. In this case, the spring potential is so shallow that any significant movement along the reaction coordinate does not change the applied force appreciably. Therefore, we can approximate the potential of the cantilever by a linear function instead of a parabola. In this case, the external force lowers the energy barrier simply by tilting the interaction potential (Fig. 3).

Evans and Ritchie [45] developed a detailed description of the unbinding process in this regime based on Kramers' theory of thermally-assisted barrier crossing in

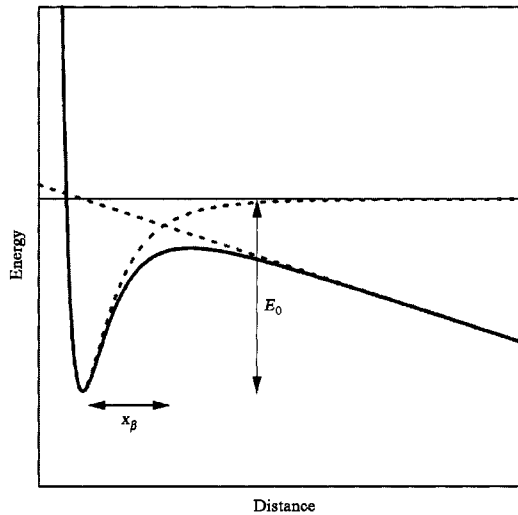


**Figure 3.** An energy diagram illustrating the effect of the external loading force on the interaction potential in the case of loading a sharp barrier with a weak spring.  $E_0$  is the depth of potential energy well and  $x_\beta$  is the distance to the transition state along the bond-stretching direction.

liquids [46]. Evans' model describes an irreversible escape from the bound state as the potential tilts under the influence of the external loading force. This model completely neglects rebinding; therefore, the magnitude of thermal fluctuations and the interaction parameters define a finite lifetime of the adhesive bond in the absence of loading force. Loading the bond amplifies the escape rate exponentially, according to equation (24), and as the result, the system has a higher probability to reach the top of the barrier and escape from the well. The loading force increases linearly with time during a typical CFM experiment; therefore, the potential landscape is constantly changing as the loading force keeps tilting the barrier. Qualitatively, at lower applied forces the barrier is still too high for the thermally-activated transition to happen and at higher applied forces the transition has most likely happened already. In other words, the unbinding of a chemical bond under external load does happen in a fairly narrow range of the applied forces, which ultimately defines the bond strength that we register in the experiment.

Quantitative analysis verifies this intuitive picture. Evans and Ritchie [45] solved the kinetic equations for the case of linear loading at constant rate,  $r_f$ , to find the most probable detachment force. They obtained the following expression for the pull-off force [47]:

$$f_{\text{pull-off}} = \frac{k_B T}{x_\beta} \ln\left(\frac{r_f}{r_0}\right), \quad (26)$$

where  $r_0$  is defined as:

$$r_0 = \frac{k_B T}{x_\beta} \cdot \frac{1}{\tau_D \exp\left(\frac{E_0}{k_B T}\right)}. \quad (27)$$



Here  $\tau_D$  represents the inverse of the diffusion-limited attempt frequency,  $E_0$  is the depth of energy well and  $x_\beta$  is the distance to the transition state. Immediately, we can see from equation (26) that the pull-off force increases logarithmically as the loading rate  $r_f$  increases. Thus, bond strength can vary quite significantly over a wide range of loading rates. Moreover, the slope of this dependence provides the value of the distance to the potential barrier,  $x_\beta$ . Evans and co-workers [48] demonstrated this behavior in a dynamic force spectroscopy experiment by measuring the interaction between biotin ligands and avidin or streptavidin proteins over many decades of loading rate (Fig. 4). Subsequently, researchers used dynamic force spectroscopy to study energy landscapes of single bonds for a number of interactions between biological and chemical species, such as DNA [49, 50], RNA [51], proteins and ligands [52, 53] and enzymes and drugs [54]. Table 2 summarizes some of these results.

CFM often involves studying multiple individual bonds connected in parallel. Evans and Williams considered the kinetics of the bond rupture in such systems [43, 44]. We can simplify the analysis by assuming that all the bonds are correlated, i.e. they share a single reaction coordinate. Then the system can be analyzed as a single ‘macro-bond’ with the total potential equal to the sum of the potentials of individual components [44]. For the serial loading of  $N$  identical bonds, Evans and Williams obtained the following expression for the unbinding force:

$$f_{\text{pull-off}} = \frac{k_B T}{x_\beta} \ln \left( \frac{r_f}{r_0} N \exp \left( \frac{(N-1)E_0}{k_B T} \right) \right). \quad (28)$$

Qualitatively, in case of parallel loading of  $N$  bonds the binding force is only slightly smaller than  $N$  times single-bond strength. One of the most important features of this case is that the distance scale of the interactions is unchanged, i.e., the width of the potential for the ‘macro-bond’ is still equal to the width of the potential for a single bond. Moreover, the scaling of the bond strength with the loading rate predicted by the kinetic model for a single bond case is still valid.

We can use the dynamic force spectroscopy measurement to determine the width of the interaction potential using CFM experiments that provide an almost ideal parallel loading case due to the configuration constraints imposed by the rigid self-assembled monolayers. Noy and co-workers [55] demonstrated such measurement for the interactions of COOH-terminated surfaces (Fig. 5) and for interactions of mica surface with  $\text{Si}_3\text{N}_4$ -terminated probe. Remarkably, both cases show the distinctive behavior predicted by our analysis. When the tip-sample junction was loaded slowly, the unbinding force was virtually independent of the loading rate, indicating unbinding in the equilibrium regime. As the loading rate increased further, the system transitioned to the non-equilibrium unbinding, leading to a characteristic exponential increase in the binding force with the loading rate. The measured slope of this increase provides the distance to the transition state of 0.6 Å for the interactions between COOH functionalities. The distance to the transition state is significantly shorter than the values typically observed for

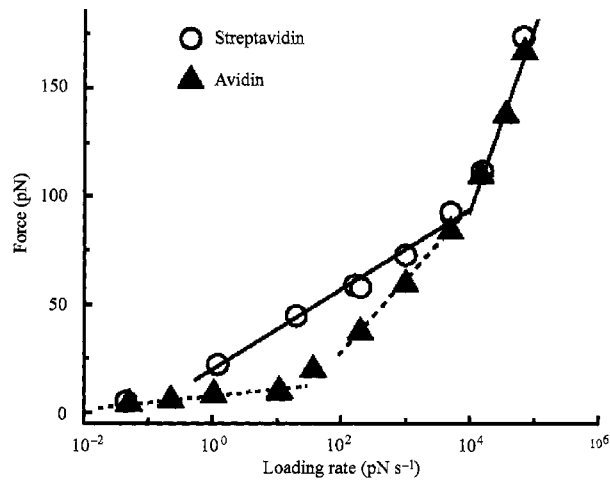


**Figure 4.** Dynamic force spectroscopy measurements of the strength of biotin–streptavidin (circles) and biotin–avidin (triangles) bonds. Biotin–streptavidin data show activation barriers at 0.5 nm and 0.12 nm (derived from the corresponding slopes using equation (26)). Biotin–avidin pair also shows an inner barrier at 0.12 nm; but the outer barrier shifts to 0.3 nm (dashed line). In addition, at very low loading rates the biotin–avidin force spectrum exhibits a low-strength regime (dashed line) that corresponds to a barrier at 3 nm. Preprinted from Ref. [101] with permission.

**Table 2.** Interaction potential parameters for various single bond systems determined using dynamic force spectroscopy

Experimental system	$x_\beta$ (nm)	$k_{\text{unb}}$ (s <sup>-1</sup> )	Reference
12-mer DNA	0.58		[49]
12-mer RNA	0.67	0.39	[51]
12-mer RNA with UCU bulge	0.37	7.94	[51]
10, 20 and 30-base pair DNA	$0.7 + 0.07 \cdot n^a$	$10^{3-0.5 \cdot n}$	[50]
Titin I27 domains	0.32	$2.9 \times 10^{-4}$	[52]
Immunobiotin–Streptavidin	0.57	0.2	[53]
	0.13	69	
Dihydrofolate reductase/methotrexate	0.3		[54]

<sup>a</sup>  $n$  = number of bp.

interactions between biological macromolecules (Table 2), which is reasonable to expect considering the size difference. Interestingly, this value is comparable to the barrier width per base pair (0.7 Å) obtained by Strunz *et al.* in the DNA unbinding experiments [50]. It is tempting to assign the value obtained in the CFM experiment to the hydrogen bond potential, but, as we will show in Section 7, the interpretation is more complicated.

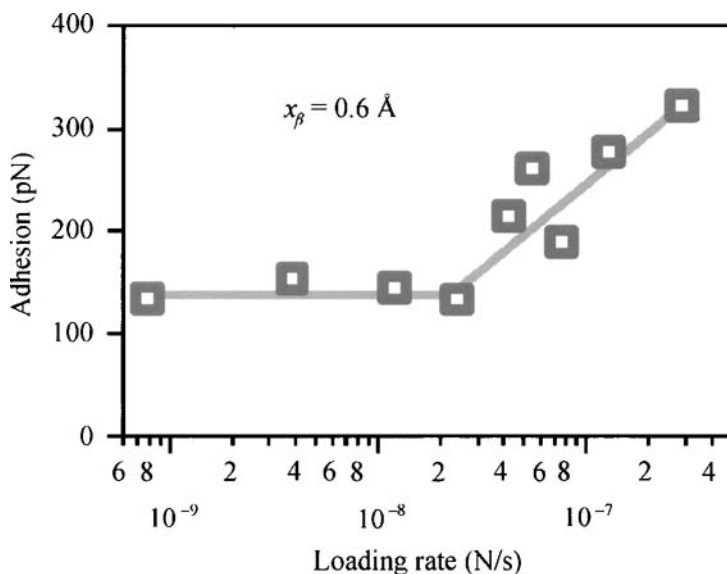


**Figure 5.** Binding forces (adhesion) between COOH-modified probe and sample in ethanol plotted as a function of loading rate. Lines indicate fits according to equation (25) in the equilibrium (slow loading,  $<10^{-8}$  N/s) and non-equilibrium (fast loading,  $>10^{-8}$  N/s) unbinding regimes.

## 6. VALIDITY OF CONTACT MECHANICS DESCRIPTION OF CFM EXPERIMENTS

Although the theoretical framework of contact mechanics has been applied to interpret CFS results since its original report [6], it is remarkable that one can even turn to continuum models as a valid approach for interpretation of experiments conducted at the nanometer scale, when only a limited number (tens to hundreds) of molecular species participate in the formation of the contact. Several issues can cast doubt on applicability of continuum mechanics down to the nanometer scale regime. Do SAM-coated tips and samples follow the JKR model of adhesion? How significant is the idealization of the tip and sample shapes? Can one accurately determine effective radius of the CFM probes? What is the effective elastic constant in the system? Do the relationships and trends predicted by the contact mechanics model hold in experimental observations? Several experiments reported in the last few years confirmed, in a systematic manner, the general validity of the contact mechanics description of the CFM experiments.

### 6.1. Determination of the tip radius

Three methods for tip characterization have been applied in CFM: (1) tip imaging using scanning electron microscopy provides a direct measure of the radius and is the most common approach [9, 56–58]; (2) ‘standard’ system (e.g.,  $\text{CH}_3\text{—H}_2\text{O—CH}_3$ ) provides the benchmarked work of adhesion to define effective tip radius from adhesion force measurements and selected contact mechanics model,

e.g.,  $R = F_a / (3\pi W_{132})$  [59, 60]; (3) tip characterizers, such as sharp Si spikes [58] on a flat surface, atomically sharp features on the (305) face of  $\text{SrTiO}_3$  [61], or the sample itself [62], are used to image tip shape with a scanning probe microscope, and tip radius is found with blind tip reconstruction algorithms based on image morphology operations. The results from the last method were compared with the estimates from the direct SEM imaging of the tips by Tormoen *et al.* [58], who found an excellent agreement between the two techniques.

### 6.2. Effect of the substrate and tip curvatures: scaling of adhesion with effective tip radius

One of the advantages of using point probe experiments in adhesion studies is that the requirements to the surface quality in order to achieve molecularly smooth contact are reduced by virtue of nanometer size dimensions of the contact. Contact mechanics predicts that pull-off forces in CFS are directly proportional to effective radius defined by equation (1). One can immediately recognize, however, that substrate roughness, e.g., local variations in the substrate radius of curvature will affect the magnitude of adhesion. For example, analysis of force and topography maps from AFM measurements on a chemically homogeneous, hydrophobic sample, silanized etched silicon [63], showed unambiguous direct correlation between substrate's local curvature and the force of adhesion (Fig. 6). Performing CFS on a  $\text{HS}(\text{CH}_2)_{15}\text{COOH}/\text{HS}(\text{CH}_2)_{15}\text{COOH}$  pair in ethanol, McKendry *et al.* observed [64] a greater than a factor of two reduction in the width of adhesion force distribution when they switched from polycrystalline Au substrates to predominantly single crystalline annealed Au on mica substrates. A similar observation was made in the work of Fujihira and co-workers [65], who measured adhesion in water and used

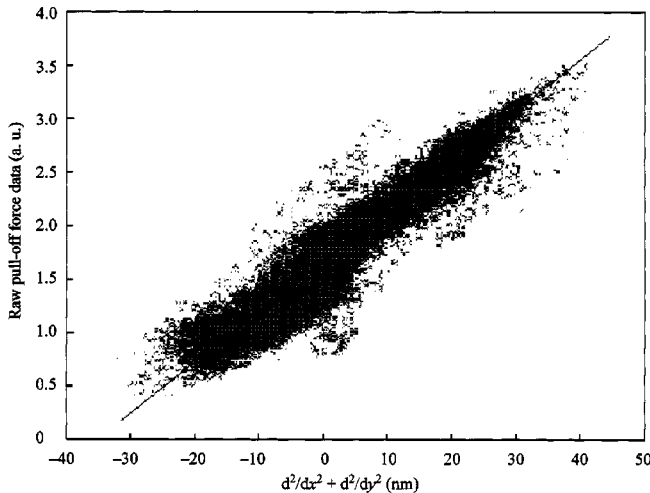


**Figure 6.** Relationships between adhesion (pull-off force) and the second derivative of substrate topography (silanized etched Si). Reproduced from Ref. [63].

the same  $\text{HS}(\text{CH}_2)_{19}\text{CH}_3$  terminated tip on several  $\text{HS}(\text{CH}_2)_{15}\text{CH}_3$ -modified substrates: (1) 11-nm sputtered Au film, (2) 110-nm sputtered Au film and (3) annealed Au(111) on mica (Fig. 7). A direct correlation was observed in cross sections taken from topography and adhesion maps. The width of the distribution ( $\sigma_F$ ) and mean force were dramatically affected by the nature and quality of the Au layer:  $\sigma_F$  values were 2 nN, 3 nN and 0.45 nN for substrates (1)–(3), respectively. Au substrates presenting large areas of the (111) face had the same mean value of adhesion, while having a factor of five smaller standard deviation. This finding demonstrates that the width of local curvature distribution of the substrate is a primary factor responsible for the width of adhesion force distributions for chemically identical tip–sample combinations. Thus, one needs to exercise caution in statistical treatments of force fluctuations in CFS, a significant contribution to  $\sigma_F$  could arise from the distribution of asperity curvature at pull-off.

Skulason and Frisbie probed systematically [56] the relationship between the tip radius and force of adhesion,  $F_a$ , measured in CFS of hydrophobic contacts ( $\text{CH}_3/\text{CH}_3$ ) in water. For tip radii ranging from  $R = 15$  nm to 125 nm, they observed a remarkably good linear correlation between mean  $F_a$  and  $R$ . Moreover, when they also considered substrate roughness (radius of curvature of Au grains) in defining effective radius (equation (1)), the linear fit had a zero intercept, as expected from the predictions of contact mechanics models (Fig. 8). From the slope of the least-squares linear fit,  $0.52 \pm 0.05$  N/m, and value for thermodynamic work of adhesion in the  $\text{CH}_3\text{--H}_2\text{O--CH}_3$  system,  $103$  mJ/m<sup>2</sup>, one can derive the value of the coefficient in the equation for the force of adhesion,  $(1.59 \pm 0.15)\pi$ , very close to the  $1.5\pi$  value of the JKR model.

### 6.3. Scaling of adhesion force with interfacial free energy

To preserve geometrical parameters of the system, researchers have used the same tip–sample pair both terminating in  $\text{CH}_3$  groups and determined the force of adhesion in a series of methanol water mixtures, where interfacial free energy could be varied by changing the composition of the solvent [29]. Combining results from the adhesion force measurements with the contact angle data on these low surface energy  $\text{CH}_3$  monolayers, Vezenov *et al.* [29] observed that there was a direct, linear correlation between adhesion forces and corresponding interfacial free energy values determined with contact angles (Fig. 9). The interfacial free energy for identical non-polar surface groups was found not to exceed 2 mJ/m<sup>2</sup> in these experiments.

### 6.4. Change of contact area with applied load

The main weakness of CFS in deriving adhesion values is its inability to obtain independent measure of the contact area. Frequently, a tip–sample friction force is assumed to provide a simultaneous measurement of the contact area on the assumption that friction is proportional to the actual contact area and interfacial

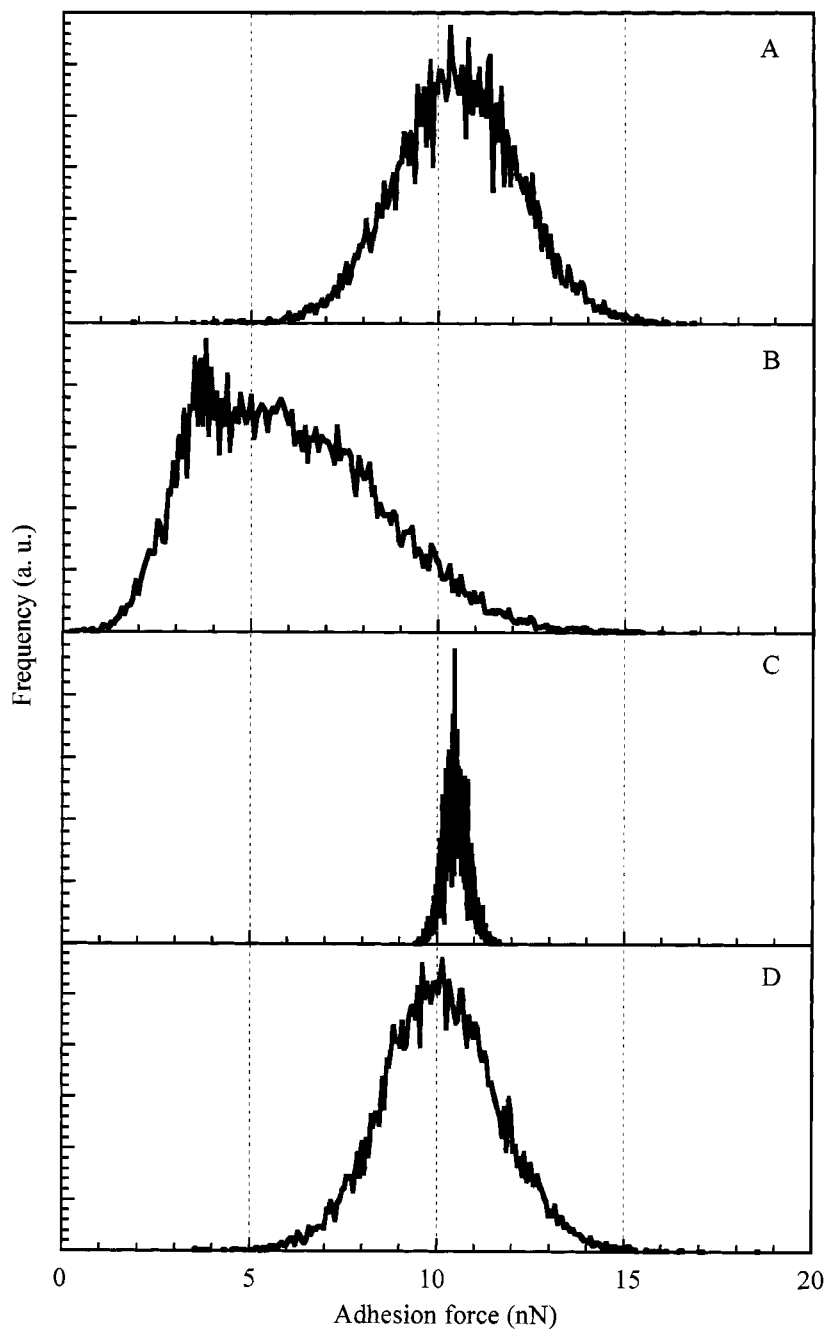


**Figure 7.** Histograms of adhesion force mappings using the same  $\text{CH}_3$ -terminated tip on  $\text{HS}(\text{CH}_2)_{19}\text{CH}_3$  SAMs formed on: (A) 11-nm-thick sputtered gold, (B) 110-nm-thick sputtered gold, (C) 100-nm-thick thermally-evaporated Au(1 1 1) on mica and (D) same as (A). The sequence of CFS measurements was (A)–(B)–(C)–(D). Reproduced from Ref. [65] with permission.

## **Pull-off forces measured between hexadecanethiol self-assembled monolayers in air using an atomic force microscope: analysis of surface free energy**

E. R. BEACH, G. W. TORMOEN and J. DRELICH \*

*Department of Materials Science and Engineering, Michigan Technological University, Houghton, MI 49931, USA*

**Abstract**—The pull-off forces were measured between hexadecanethiol monolayers, self-assembled on gold-coated silicon nitride cantilever tip and silicon wafer, using atomic force microscopy (AFM). The blind tip reconstruction technique was used for determination of the curvature of the AFM tip. The measured pull-off force value remained practically unaffected by a variation of the maximum applied load in a range of 5–80 nN. This result suggests that the use of continuum elastic contact mechanics in the analysis of AFM pull-off force measurements is not as straightforward as usually assumed in the literature reports on similar systems. The surface free energy of hexadecanethiol monolayer on a gold film of  $\gamma = 24\text{--}27\text{ mJ/m}^2$  was calculated based on the pull-off forces ( $F$ ), measured using  $R = 60\text{--}80\text{ nm}$  radius tips, and next applying the Derjaguin approximation:  $F = 4\pi R\gamma$ . These  $\gamma$ -values were found to match the surface free energy value calculated from contact angle data and using Lewis acid–base interfacial free energy theory.

**Keywords:** Adhesion; atomic force microscopy; blind tip reconstruction; pull-off force; self-assembled monolayer; surface free energy.

### **1. INTRODUCTION**

Force measurements made with an atomic force microscope (AFM) using surfaces modified with a chemically-linked self-assembled monolayer (SAM), categorized as chemical force microscopy (CFM), have become an area of intensive fundamental research [1]. SAMs of organic molecules form very regular, close-packed structures on selected inorganic solids by reacting one end group with a solid surface whereas the other end group is exposed to the environment [2]. Generally, SAMs are fabricated using thiols adsorbed from solution onto a gold-coated AFM probe

---

\*To whom correspondence should be addressed. Phone: (906)487-2932. Fax: (906)487-2934. E-mail: jwdrelic@mtu.edu

and flat gold-coated substrate because of the relatively smooth surfaces that can be prepared via gold deposition and rapid self-assembly kinetics of monolayer formation, with reproducible molecular structure. Utilizing the CFM method, chemical functionality and surface roughness can be controlled and quantitative information is much simpler to extract from the experimental data.

Starting around 1995, several papers have been published discussing the topic of CFM pull-off force and friction force measurements [1, 3–16]. In the present research, SAMs terminated with a  $\text{CH}_3$ -end group were used due to well-defined surface properties of monolayers studied in many laboratories around the world.

The most consistent pull-off force studies involving  $\text{CH}_3$ -terminated monolayers have been done in liquid environments. Several studies have reported pull-off forces ranging from 0.5 to 5 nN in ethanol solution [1, 3, 6, 12]. The variation in the measured forces was attributed to the size of the interacting probe. The SAM-ethanol interfacial free energy was calculated according to the Johnson–Kendall–Roberts (JKR) theory [17] to be in the range of 1.0–3.0  $\text{mJ/m}^2$  in these studies.

The pull-off force values measured between  $\text{CH}_3$ -terminated surfaces in water were much less reproducible [1, 12, 16]. Complications in pull-off force measurements arise in an aqueous environment due to capillary effects associated with formation of gas bridges between hydrophobic surfaces. Submicroscopic air bubbles can nucleate on hydrophobic surfaces, which then form air bridges between the probe and the substrate [16].

The surface free energy of a solid–vapor interface,  $\gamma_{\text{SV}}$ , is a key parameter in both adhesion and friction [18]. The common method to characterize  $\gamma_{\text{SV}}$  of low energy surfaces is through contact angle measurements [19, 20]. For example, the  $\gamma_{\text{SV}}$  value for  $\text{CH}_3$ -terminated monolayers was calculated based on measured contact angles to be 18–21  $\text{mJ/m}^2$  [7, 21]. On the other hand, direct measurements of the pull-off force in air (or in dry  $\text{N}_2$ ) using AFM, or other scanning probe microscopy techniques, for  $\text{CH}_3$ -terminated monolayers indicate values for  $\gamma_{\text{SV}}$  ranging from 28 to 30  $\text{mJ/m}^2$  [4, 7]. The error in the AFM measurements is often significant, up to 50% of the reported value. Therefore, a more detailed study into the reason for the discrepancy between solid–vapor surface free energy values from contact angle and adhesion measurements is of great fundamental and practical importance. For example, research into which of the contact mechanics models, described in the next section, best represents the SAM–SAM systems is needed. Both JKR [17] and Derjaguin–Muller–Toporov (DMT) [22] models are often used in the interpretation of the pull-off forces measured by AFM without any clear justification.

The goal of this AFM study was to measure the pull-off forces between a hexadecanethiol (HDT),  $\text{CH}_3(\text{CH}_2)_{15}\text{SH}$ , adsorbed onto a gold-coated AFM probe, and gold-coated silicon wafer substrate in ambient air with a low relative humidity level ( $\text{RH} < 20\%$ ). This system was treated as a homogeneous system with a spherical particle-to-smooth surface geometry. The blind tip reconstruction technique to characterize the radius of curvature of the AFM tips used in pull-off



force measurements was evaluated. Next, the effect of increasing the maximum applied load during SAM–SAM pull-off force measurements was investigated. An attempt was made to analyze the deformation of the SAM caused by loading and to determine if there was any effect of deformation on the measured pull-off force. Both the JKR and DMT models were used to discuss the pull-off force data.

## 2. BACKGROUND: CONTINUUM ELASTIC CONTACT MECHANICS

### 2.1. Hertz model

Hertz was the first scientist to formulate a model for mechanics of contact between a spherical body on a planar surface [23]. There are several assumptions made in this classical model that dates back to 1881. The spherical particle is considered to be elastic with a smooth surface, and the substrate is assumed to be smooth and rigid. The geometry of the deformation would resemble that shown in Fig. 1b. Surface forces are not taken into consideration in Hertzian mechanics. Equations (1)–(4) summarize the relationships from the Hertz model:

$$F_{ad} = 0, \quad (1)$$

$$a = \left( \frac{RP}{K} \right)^{1/3}, \quad (2)$$

$$a_0 = 0, \quad (3)$$

$$\delta = \frac{a^2}{R}, \quad (4)$$

where  $F_{ad}$  is the pull-off force,  $P$  is the load applied to a particle normal to the plane of the surfaces it is in contact with,  $R$  is the radius of the particle,  $K$  is the elastic modulus for the particle-substrate system,  $a$  is the radius of contact after

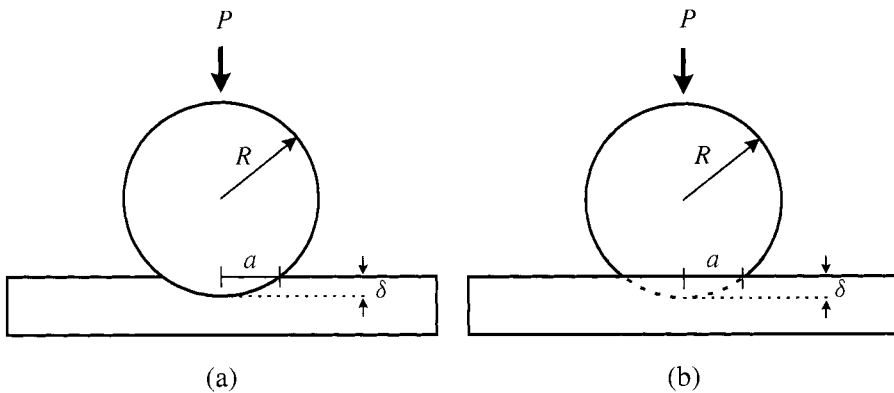


**Figure 1.** Schematic representation of the effect of an applied load ( $P$ ) normal to the plane of the surface on a system with a rigid particle and compliant substrate (a) and a compliant particle on a rigid substrate (b).

deformation,  $a_0$  is the contact radius at zero load, and  $\delta$  is the deformation of the compliant portion of the system (geometrical parameters are shown in Fig. 1).

The Hertzian mechanics is applicable to systems with very low surface forces and where high loads are applied to the particle. Most real systems do not have negligible surface forces and in these circumstances one of the following models is a better representation of particle to surface contact mechanics.

## 2.2. DMT model

The DMT model was published in 1975 [22]. In contrast to the Hertz model, in the DMT model surface forces in both the particle–surface contact area and just outside this region are taken into account. The equations describing the DMT model are given in equation (5)–(8).

$$F_{\text{ad}} = 2\pi RW, \quad (5)$$

$$a = \left\{ \frac{R}{K} (P + 2\pi RW) \right\}^{1/3}, \quad (6)$$

$$a_0 = \left\{ \frac{R}{K} (2\pi RW) \right\}^{1/3}, \quad (7)$$

$$\delta = \frac{a^2}{R}, \quad (8)$$

where  $W$  is the work of adhesion. Other terms are the same as in the Hertz model.

The DMT model has been most successfully applied to systems with small particle radii, low surface forces (although this is not well agreed upon in the literature), and when rigid materials are involved. This theory may underestimate the true area of contact since the geometry is constrained to be Hertzian. Regardless of these limitations, the DMT theory has been shown to fit the experimental data in many studies [24].

Both the Hertz and DMT models suggest that loading and unloading is a smooth process and that there is no adhesion hysteresis during these processes. This is a physically unrealistic situation for many elastic systems and has led to the formulation of more complex models.

## 2.3. JKR model

The JKR theory [17] is one of the most popular contact mechanics models used today. In contrast to the smooth process of loading and unloading described by the Hertz and DMT models, the JKR model is more abrupt and allows for adhesion hysteresis. The assumptions made in this model are that the long-range forces outside the contact area can be neglected and only short range forces within the contact range are important. The equations describing the JKR model are given as

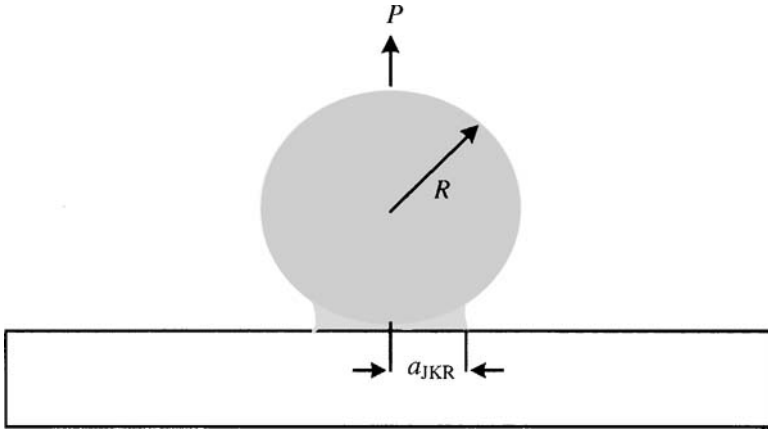


**Figure 2.** Schematic representation of the formation of a neck between the particle and sample as described by the JKR theory.

follows:

$$F_{ad} = \frac{3}{2}\pi RW, \quad (9)$$

$$a = \left[ \frac{R}{K} \left\{ P + 3\pi RW + \sqrt{6\pi RW P + (3\pi RW)^2} \right\} \right]^{1/3}, \quad (10)$$

$$a_0 = \left\{ \frac{R}{K} (6\pi RW) \right\}^{1/3}, \quad (11)$$

$$\delta = \frac{a^2}{R} - \frac{2}{3} \sqrt{\frac{6\pi W a}{R}}. \quad (12)$$

The hysteresis observed in the JKR model is due to the formation of a neck that links the particle and the surface when a negative load is applied, as shown in Fig. 2.

The contact is ruptured abruptly at high negative loads, and separation occurs when the radius of the contact area is reduced to the value given by equation (13):

$$a_s = 0.63a_0, \quad (13)$$

where  $a_s$  is the radius of the contact area at separation.

The JKR theory works well for systems that involve high surface energies, large particle radii and compliant materials. One problem associated with the JKR theory is that it predicts an infinite stress at the edge of the contact area since it only accounts for forces inside the contact region.

#### 2.4. Maugis model

There has been much debate since the introduction of DMT and JKR models as to which one is valid. It has been recognized that each model applies to very different particle–surface systems and this issue has been addressed by Maugis [25]. Maugis

proposed to use a dimensionless parameter,  $\lambda$ , to determine whether DMT or JKR model was more appropriate.

The theory of contact mechanics formulated by Maugis in 1991 [25] is said to be one of the most versatile descriptions because it does not assume any specific limit on material properties. The range of material properties is given by the dimensionless parameter  $\lambda$  in equation (14).

$$\lambda = \frac{2.06}{z_0} \left( \frac{RW^2}{\pi K^2} \right)^{1/3}, \quad (14)$$

where  $z_0$  is a typical atomic dimension.

A large value of  $\lambda$  characterizes larger particle radii, and compliant materials with high surface free energies. Small values of  $\lambda$  are indicative of smaller particles that are more rigid with low surface free energies. At the extreme values of  $\lambda$ :

$$\begin{aligned} \lambda \rightarrow 0, \quad F_{\text{ad}} &= 2\pi RW \text{ (DMT model),} \\ \lambda \rightarrow \infty, \quad F_{\text{ad}} &= \frac{3}{2}\pi RW \text{ (JKR model).} \end{aligned}$$

### 3. EXPERIMENTAL METHODS

#### 3.1. HDT SAM-coated sample preparation

1-Hexadecanethiol ( $\text{CH}_3(\text{CH}_2)_{15}\text{SH}$ ), henceforth referred to as HDT, was obtained from Aldrich Chemical Co. (Milwaukee, WI, USA). 1500 mm diameter silicon wafers (100 orientation) were obtained from MEMS Corporation (St. Louis, MO, USA). Pieces of silicon were cut into approximately 2 cm  $\times$  2 cm sections and cleaned in acetone, methanol and deionized water followed by exposure to UV light. Silicon nitride ( $\text{Si}_3\text{N}_4$ ) V-frame cantilevers, with spring constants ranging from 0.06 to 0.58 N/m, were purchased from Digital Instruments (Santa Barbara, CA, USA). Cantilevers were cleaned in ethanol followed by UV light exposure.

Silicon substrates and cantilevers were then coated with gold in a Polaron Equipment Limited SEM Coating Unit E5000. The gold target was set to a fixed distance from the samples during all gold coating sessions. The parameters of operation for the gold-coater were as follows: a pressure of 0.05–0.07 torr was obtained, a sputtering current of 5 mA, and the coating time was 10 min.

Immediately after application of the gold coating, the substrates and cantilevers were rinsed with absolute ethanol (200 proof) and immersed in a solution of 1–2 mM HDT in absolute ethanol that was prepared at least 2 h prior to placing the samples in solution. The substrates and cantilevers were left in the HDT solution for a period of 2–12 h to allow a complete self-assembled monolayer to form. The silicon wafers and cantilevers were rinsed extensively with absolute ethanol upon removal from solution to remove any excess thiol components on the surface. In order to ensure that no ethanol remained on the surfaces, the samples were placed in an oven at 80°C for 20–30 min.

### 3.2. Gold surface imaging

The TappingMode™ etched silicon probes (TESP) cantilevers were purchased from Digital Instruments. Intermittent contact mode (TappingMode™) was used to image the gold surfaces of the coated silicon substrates using a Dimension 3000 AFM (Digital Instruments). Scan sizes of  $500\text{ nm} \times 500\text{ nm}$ ,  $1\text{ }\mu\text{m} \times 1\text{ }\mu\text{m}$  and  $2.5\text{ }\mu\text{m} \times 2.5\text{ }\mu\text{m}$  were taken at a scan rate in the range of 0.75–1 Hz. The ratio of the setpoints,  $r_{\text{sp}}$ , was set to no lower than 0.8 to minimize sample damage caused by the AFM tip.

### 3.3. Pull-off force measurements

All pull-off force measurements were made in air under ambient conditions. The relative humidity (RH) level during measurements ranged from less than 5 up to 15%. The RH level was continuously monitored during all experiments with a digital thermo/hygrometer (Cole Palmer Instrument Company, Vernon Hills, IL, USA). Pull-off force measurements were made using a Dimension 3000 AFM equipped with Nanoscope Software version 4.43 from Digital Instruments. Cantilevers with a spring constant of 0.12 N/m were selected for the SAM-coated sample measurements. The pull-off force measurements were made in the force mode. The  $x$ – $y$  lateral motion of the piezoelectric element is suspended in this operating mode and deflections of the cantilever in response to movements along the  $z$ -axis are recorded as deflection vs  $z$ -position curves. The operating parameters of the AFM were as follows: the ramp size was in the range of 500–900 nm with 750 nm being the most common ramp size; a scan rate of 0.996 Hz; 512 samples per deflection vs  $z$ -position curve were recorded; and the setpoint, or zero deflection position in the non-touching regime, was set as the 0 voltage position for all curves.

One hundred to five hundred deflection versus  $z$ -position curves were collected per cantilever per experiment. The deflection versus  $z$ -position curves were converted into force–separation, more commonly referred to as force–distance curves, using Scanning Probe Image Processor (SPIP) software from Image Metrology (Lyngby, Denmark). The corrected spring constant was entered into the data prior to any force curve analysis.

### 3.4. Determination of cantilever tip radius using blind tip reconstruction

Images of a grating consisting of an array of sharp silicon spikes were made using a Nanoscope II AFM (Digital Instruments) in contact mode. Scan sizes of  $1500\text{ nm} \times 1500\text{ nm}$ , or  $1750\text{ nm} \times 1750\text{ nm}$  depending on the dimensions of the particular tip, were captured. Scan rates between 0.25 and 0.5 Hz were used. The images were divided into  $512 \times 512$  pixels resulting in lateral resolutions of 2.93 and 3.42 nm/pixel at scan sizes of 1500 and 1750 nm, respectively. The AFM was mounted on a platform hanging from bungee cords to minimize noise in the images. Blind tip reconstruction (BTR) was performed using Deconvo version 1.1 Software (Silicon

MDT, Ltd., Moscow, Russia) on tips that were coated with the SAM. This software uses the method of J. S. Villarrubia to calculate the shape of the AFM probe from an image taken with the tip [26]. Noise thresholds from 5 up to 500 nm were used in the BTR process.

### 3.5. Contact angle measurements

Contact angles were measured with a Krüss G10 contact angle goniometer. The shape of the liquid drop on the sample is fitted automatically with the Drop Shape Analysis software (Krüss) that calculates the contact angle. Three probe liquids of various polarities, namely, deionized water filtered through a Barnstead E-pure system, ethylene glycol (99.9%, Fisher Scientific) and diiodomethane (99%, Aldrich Chemical Co., Inc.), were used for these measurements. Measurements were made in a covered cell to avoid evaporation of the probe liquid. A small liquid drop was placed on a substrate. The size of the drop was increased to a base diameter of 5–8 mm. A relaxation of advancing contact angle was recorded at 30-s intervals over a period of 30-min.

## 4. RESULTS AND DISCUSSION

### 4.1. Gold surface roughness analysis

The gold-coated silicon wafer substrates were characterized using intermittent contact mode, more commonly referred to as TappingMode™ atomic force microscopy (TMAFM). The surface roughness was quantified using three parameters of roughness: root-mean-square roughness (RMS), average roughness ( $R_a$ ) and percent surface area difference (%SAD). These parameters are defined in equations (15)–(17).

$$\text{RMS} = \sqrt{\frac{\sum (Z_i - Z_{\text{ave}})^2}{N}}, \quad (15)$$

where  $Z_{\text{ave}}$  is the average of the  $Z$  values ( $Z$ -axis representing topographical height features) within the given area,  $Z_i$  is the current  $Z$  value and  $N$  is the number of points within the given area.

$$R_a = \frac{1}{L_x L_y} \int_0^{L_y} \int_0^{L_x} |f(x, y)| dx dy. \quad (16)$$

In the equation for  $R_a$ ,  $f(x, y)$  is the surface relative to the center plane, and  $L_x$  and  $L_y$  are the dimensions of the surface.

$$\% \text{ SAD} = \left[ \frac{\sum (\text{surface area of the sample})_i}{\sum (\text{projected surface area})_i} - 1 \right] \times 100\%. \quad (17)$$

Table 1 shows the results of the roughness analysis for three areas of the gold-coated substrate at various scan sizes. The RMS and  $R_a$  values are consistent for

**Table 1.**

Roughness analysis of the gold surface used in pull-off force measurements (see equations (15)–(17) for definitions of the roughness parameters)

Scan size	RMS (nm)	$R_a$ (nm)	%SAD
$500 \times 500 \text{ nm}^2$	0.332	0.260	0.230
$1000 \times 1000 \text{ nm}^2$	0.350	0.277	0.215
$2500 \times 2500 \text{ nm}^2$	0.333	0.270	0.300

the three scales of images here. Therefore, the surface roughness is reproducible over a wide area of the sample used in this study. Since the roughness is less than 0.4 nm, it is expected that the pull-off forces should be negligibly affected by the topography of the substrate.

#### 4.2. Determination of cantilever tip radius of curvature

The radius of curvature for a gold coated AFM cantilever tip is less than 100 nm for the coating procedure used in our laboratory (uncoated tips have radii ranging from 20 to 60 nm). Standard thermionic emission scanning electron microscopy cannot resolve the edges of such small features without reducing the signal-to-noise ratio to the point that the object is indistinguishable from the background. Scanning transmission electron microscopy (STEM) is capable of much better resolution, but in the case of the pyramidal geometry of the AFM tips, STEM did not provide satisfactory depth of focus on the edges of the tip. The sample preparation for STEM imaging renders the AFM tips useless thereafter and is an experimentally difficult process, not worth the time invested, for the resulting images. These problems eliminated both standard thermionic emission SEM and STEM as methods to characterize the AFM tip shape.

A suitable alternative method was used in this study to determine the size and shape of the cantilever tip. This approach utilized the blind tip reconstruction method developed by Villarrubia [26].

Gold-coated AFM tips were scanned over a specially fabricated array of sharp silicon spikes. The spikes must have a higher aspect ratio than the pyramidal shape of the AFM tip in order to produce an inverted image of the tip instead of the spike. Using software based on mathematical morphology operations, described in detail elsewhere [26], the radius of curvature of the tip was determined. Figure 3 shows examples of images made by scanning the gold-coated AFM tips over the array of spikes.

The resolution of the images increases from (a) to (c) in Fig. 3. Images on the size scale of the image shown in Fig. 3c were used for all BTR work done in this study. The resolution of the image in Fig. 3c is 3.42 nm/pixel and this value is consistent with the value recommended by Villarrubia [27].

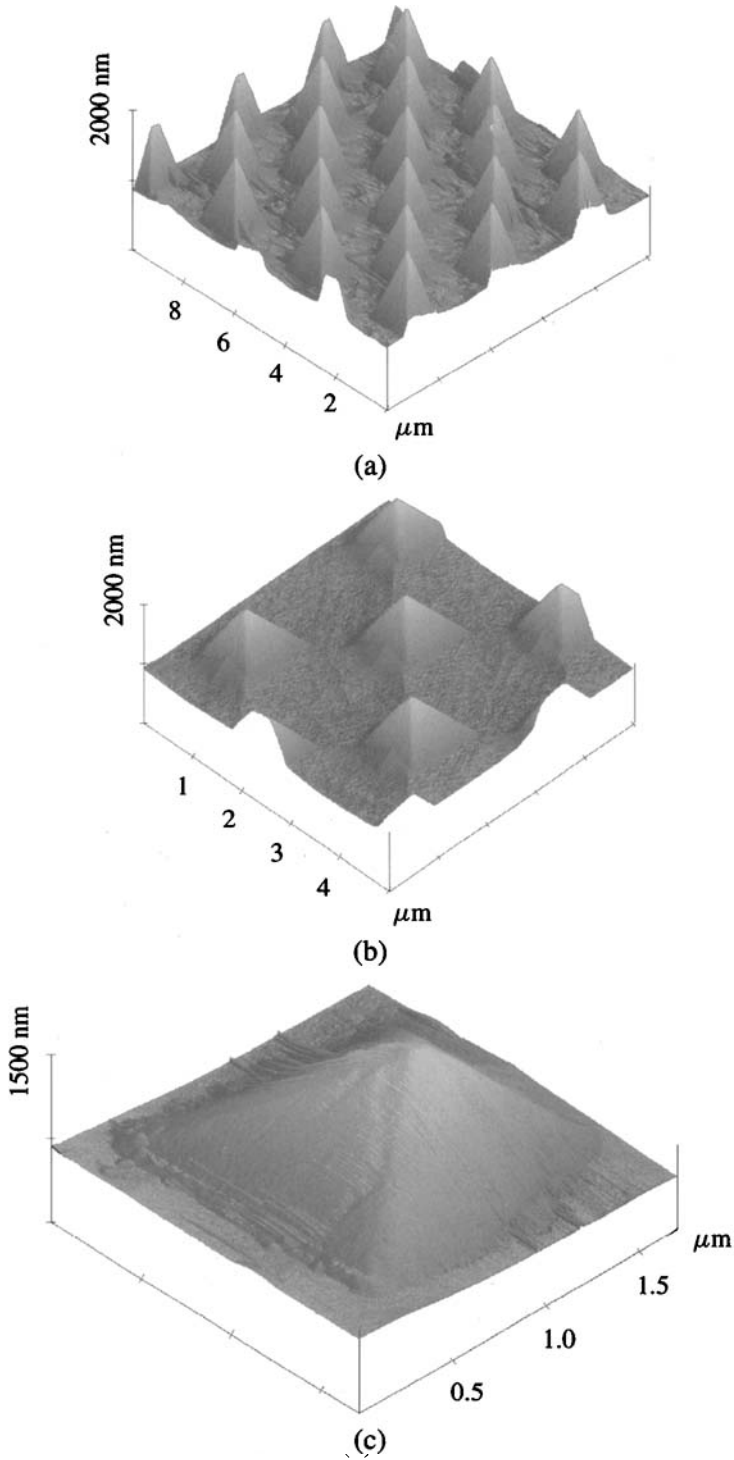


**Figure 3.** Contact mode AFM images of silicon spikes taken with gold-coated AFM tips. Scan sizes are: (a) 10  $\mu\text{m}$ ; (b) 5  $\mu\text{m}$ ; and (c) 1.75  $\mu\text{m}$ .



The noise artifacts in the image have a large influence on the results of BTR experiments. Therefore, scan rates were reduced as much as possible and the AFM was placed on a special stage suspended by bungee cords to help eliminate vibrations. Even after taking such precautions, sharp changes in the heights of the spikes produced noise in the image, as can be seen in Fig. 3c. An additional complication to consider is the material property differences between the gold-coated tip and the silicon spike. The noise in these images may be caused by scratching of the gold layer due to the hard, very sharp peak (diameter less than 10 nm) of the silicon spikes [28]. Contact forces during imaging were minimized to reduce this effect; nevertheless, some damage to the gold surface is probable and cannot be overlooked as an additional source of noise. Small errors such as this can cause considerable changes in values when working with nanoscale systems. However, a proper threshold value selection insures that the tip size estimate is not an erroneous value. The threshold parameter determines how large of an area containing noise will be included in a blind tip reconstruction calculation. When a high quality image, such as those used in this research, is used for tip size analysis a small noise threshold of approximately 5 to 10 nm is selected. A threshold of 5 nm indicates that any group of pixels containing noise for an area larger than  $5\text{ nm} \times 5\text{ nm}$  are not included in the tip reconstruction calculation by the software. The Deconvo 1.1 software has a built-in function to insure that a threshold value in the proper range is selected. When the threshold is too low (excludes too much of the image), the cantilever is reconstructed as a sharp needle with a radius of curvature much smaller than the tip radius specified by the manufacturer. Additionally if the threshold is too high (includes too much of the image containing noise artifacts), the tip is reconstructed with a nearly flat end and a large radius of curvature value.

The radii of the cantilever tips used in this research were determined with the BTR technique to be 79.7 and 60.2 nm for the cantilevers labeled # 1 and # 2, respectively. The values of the tip radii are reasonable despite the possible small error noise artifacts. We estimate the error associated with any noise artifacts in the images to be approximately 8.43 and 6.34 nm for cantilevers #1 and # 2, respectively, and the calculation of this error is discussed later in this paper. Another independent method for determining the tip radius of curvature is still necessary for comparison and validation of the blind tip reconstruction results.

#### *4.3. Pull-off forces measurements at various applied loads*

Figure 4 shows the pull-off force measurement results for various maximum applied loads. The data from the region of small loading, less than 20 nN, have a significantly larger scatter in values than at applied loads larger than 20 nN. The reason for this is not clear at this point. For the applied loading regime larger than 20 nN, the pull-off force data become more consistent. The increase in pull-off force consistency as the load is increased suggests that the contact in the low loading region might not be adequate. Incomplete contact could lead to a reduced,

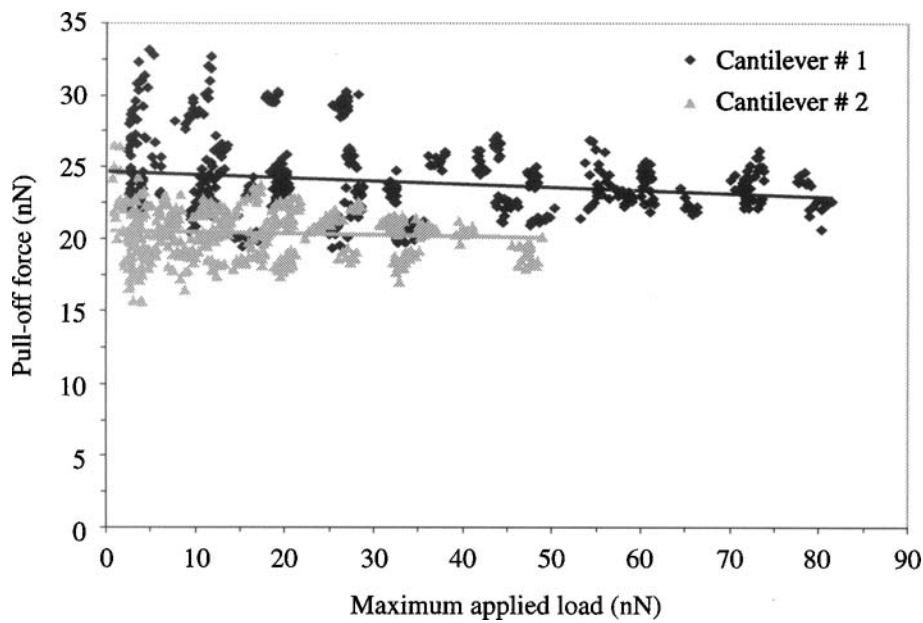


**Figure 4.** Pull-off force vs maximum applied load for HDT self-assembled monolayer coated cantilever tip and substrate.

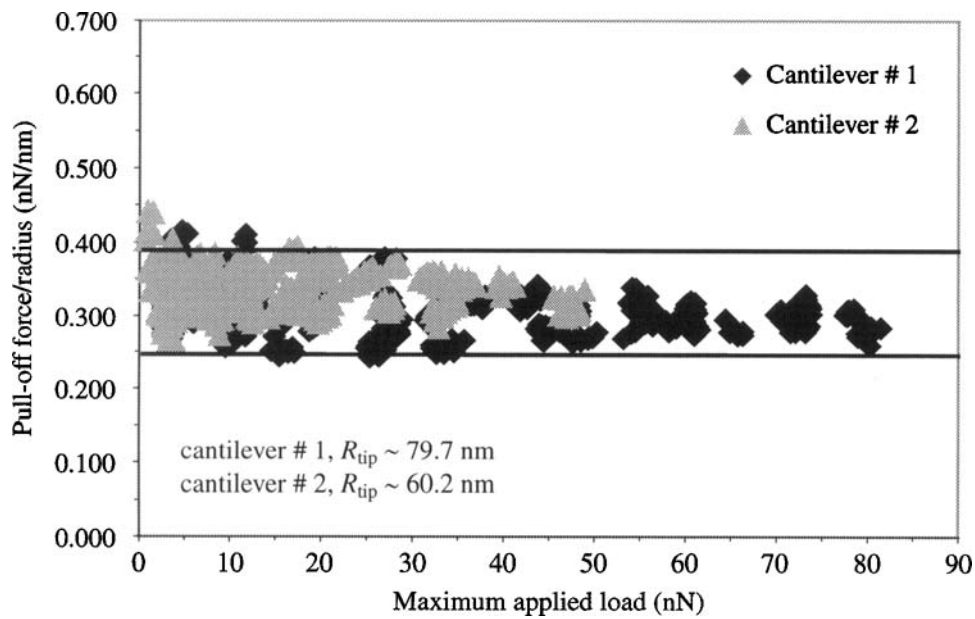


**Figure 5.** Normalized pull-off force vs maximum applied load from data presented in Fig. 4. Lines were drawn to highlight the range of pull-off force values.

inconsistent contact area and possible lateral deflections of the cantilever. Both of these factors introduce error into the pull-off force measurements.

As shown in Fig. 4, no significant effect of loading, other than a decrease in the scatter of data on the measured pull-off forces was observed in the SAM–SAM system. The average values of the pull-off force measured for cantilevers # 1 and # 2 are  $24.3 \pm 4.1$  and  $20.4 \pm 3.4$  nN, respectively. The difference between the results of pull-off forces for the two cantilevers is due to a difference in the radii of curvature of the cantilever tips, 79.7 and 60.2 nm for cantilever # 1 and # 2, respectively, as determined by the BTR methodology described in Section 3.2.

Normalization of the data presented in Fig. 4 was performed using the cantilever tip radii determined with the BTR technique. The correlation between the normalized pull-off force/radius versus maximum applied load is shown in Fig. 5.

The normalized pull-off forces for cantilever # 1 and cantilever # 2 are in very good agreement with average values of 0.305 and 0.338 nN/nm, respectively.

#### 4.4. Contact angle measurements

Contact angle measurements on a gold-coated silicon wafer with chemically adsorbed SAM on the surface were made with water, diiodomethane and ethylene glycol for calculation of the three surface energy parameters ( $\gamma^{\text{LW}}$ ,  $\gamma^-$ , and  $\gamma^+$ ) in the Lewis acid–base interfacial free energy (LABIFE) theory. The advancing contact angle and its changes were measured over a period of thirty minutes. Figure 6 is a plot of the advancing contact angle,  $\theta$ , versus time for the three probe liquids.

The behavior of the contact angle for each of the three liquids was different over the allowed time period. Contact angles for water relaxed from a value of approximately  $112^\circ$  to  $110^\circ$  over the 30-min time period. Contact angles of  $110^\circ$  to

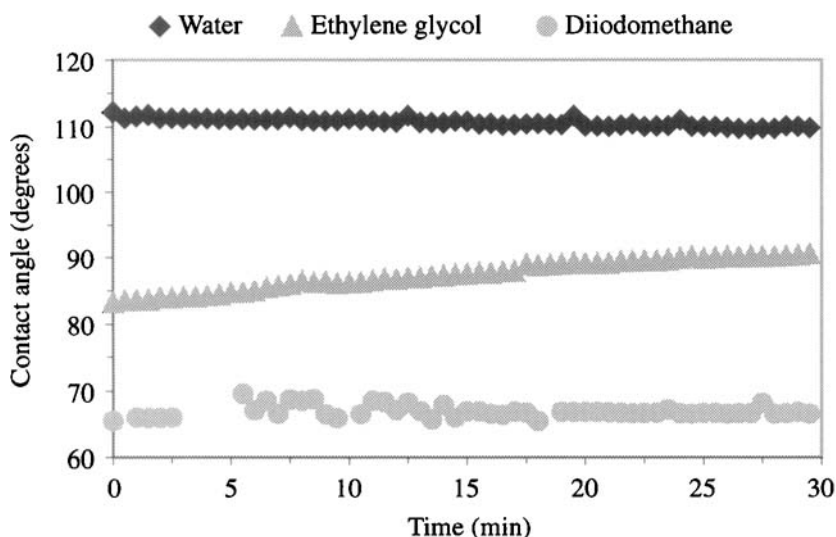


**Figure 6.** Contact angle vs time for three liquids of different polarities on a HDT-SAM monolayer.

**Table 2.**

Surface free energy components of probe liquids and contact angles measured on CH<sub>3</sub>-terminated self-assembled monolayers (see text for discussion)

Probe liquid	$\gamma_L$ (mJ/m <sup>2</sup> )	$\gamma_L^{LW}$ (mJ/m <sup>2</sup> )	$\gamma^+$ (mJ/m <sup>2</sup> )	$\gamma^-$ (mJ/m <sup>2</sup> )	$\theta$ (°)
Water	72.8	21.8	25.5	25.5	111.7
Diiodomethane	50.8	50.8	0	0	66.9
Ethylene glycol	48.0	29	3.0	31.0	83.0

112° for water on a CH<sub>3</sub>-terminated SAM are commonly reported in the literature [21, 29, 30]. An advancing contact angle of 112° was selected for water for the surface free energy component calculations.

As shown in Fig. 6, the contact angle for the diiodomethane was virtually unchanged with an average value of 66.9° during these measurements. A 68° to 72° advancing contact angle was measured on a similar monolayer in previous research [31].

Ethylene glycol showed an increase in the contact angle from 83° at the beginning of the time period to approximately 89° at 30-min. Slightly lower contact angles of 76° to 79° were measured on a similar monolayer by Drelich *et al.* [31]. The measurements were repeated, and the same trend with approximately the same contact angles was found on three HDT-SAM samples prepared in the same manner. We speculate that the increasing contact angle might be a result of absorption of moisture by the ethylene glycol. Further research into the cause of this phenomenon is needed. A contact angle of 83° for ethylene glycol was selected for the LABIFE theory calculation of the surface free energy.

The components of the surface free energies of the probe liquids must be known in order to make the solid surface free energy calculation using the LABIFE theory. The components for the three liquids used here are shown in Table 2 [19], along with the measured contact angles on a HDT-SAM.

In Table 2,  $\gamma_L$  is the liquid surface tension (surface energy and surface tension are used interchangeably when discussing a liquid),  $\gamma_L^{LW}$ , is the Lifshitz–van der Waals component of the liquid surface tension, and  $\gamma^+$ ,  $\gamma^-$  are the Lewis-acid and Lewis-base components of the surface tension, respectively. The well-established values of  $\gamma_L$ ,  $\gamma_L^{LW}$ ,  $\gamma^+$ , and  $\gamma^-$  for water, diiodomethane, and ethylene glycol reported in the literature are used in these calculations [19].

The equation for relating the measured contact angle, for a particular liquid, to the Lifshitz–van der Waals component of the LABIFE theory of the solid surface free energy was written by van Oss, Chaudhury, and Good and is given below in equation (18) [32]:

$$\gamma_L(1 + \cos \theta) = 2\sqrt{(\gamma_S^{LW}\gamma_L^{LW})} + 2\sqrt{(\gamma_S^+\gamma_L^-)} + 2\sqrt{(\gamma_S^-\gamma_L^+)}, \quad (18)$$

**Table 3.**

Lifshitz–van der Waals and Lewis acid–base components of HDT-SAM solid surface free energy (see text for discussion)

$\gamma_S^{LW}$ (mJ/m <sup>2</sup> )	$\gamma_S^+$ (mJ/m <sup>2</sup> )	$\gamma_S^-$ (mJ/m <sup>2</sup> )
24.6	0.0464	0.0009

where the subscripts S and L represent the solid and liquid, respectively, and the superscripts LW, +, and – are the Lifshitz–van der Waals, Lewis-acid, and Lewis-base components, respectively.

The terms  $\gamma_S^{LW}$ ,  $\gamma_S^+$ , and  $\gamma_S^-$  must be found from these equations, and then the surface free energy of the solid ( $\gamma_{SV}$ ) can be calculated according to equation (19):

$$\gamma_{SV} = \gamma_S^{LW} + 2\sqrt{(\gamma_S^+ \gamma_S^-)}. \quad (19)$$

The Lifshitz–van der Waals component of the solid surface free energy,  $\gamma_S^{LW}$ , is the first term solved by using the contact angle value measured for diiodomethane drops (Table 2). The last two terms on the right hand side of equation (18) drop out in this case and the equation can be rearranged to solve for  $\gamma_S^{LW}$  as shown in equation (20):

$$\gamma_S^{LW} = \frac{\gamma_L^2 \{1 + \cos(\theta)\}^2}{4\gamma_L^{LW}}, \quad (20)$$

for diiodomethane,  $\gamma_L$  is equal to  $\gamma_L^{LW}$  reducing equation (20) to:

$$\gamma_S^{LW} = \frac{\gamma_L \{1 + \cos(\theta)\}^2}{4}. \quad (21)$$

Using the value for  $\gamma_S^{LW}$  from equation (21) a system of equations for water and ethylene glycol is written using equation (18). The variables  $\gamma_S^+$ , and  $\gamma_S^-$  can be isolated and solved for one at a time in this way. Once all the components are known they are substituted back into equation (19) to calculate the solid surface free energy. The values  $\gamma_S^{LW}$ ,  $\gamma_S^+$ , and  $\gamma_S^-$  for the HDT-SAM are shown in Table 3.

As indicated by the data in Table 3, the Lifshitz–van der Waals component of the surface free energy is the only significant term that contributes to the calculated solid–vapor surface free energy of the HDT-SAM. The significant figures in the liquid surface tension are only reported to one decimal place in the literature, therefore, the  $\gamma_S^+$ , and  $\gamma_S^-$  components can be neglected for the HDT monolayer on gold. The solid surface free energy calculated using the values from Table 3 is  $24.6 \pm 2.0$  mJ/m<sup>2</sup>, approximately equal to the Lifshitz–van der Waals component,  $\gamma_S^{LW}$ .

The value of  $\gamma_{SV} = 24.6$  mJ/m<sup>2</sup> is higher than reported previously in the literature [21, 33]. The fabrication process for SAMs is slightly different in every laboratory. The differences in fabrication might slightly alter the SAMs with regard to defects

caused by different qualities of gold-coating and molecular arrangements for thiols on the surface. It should also be recognized that the gold film might interact with the probe liquids placed on top of SAMs through van der Waals interactions and this depends on the length of the bonded thiol [5]. In any case, as shown in the next section, our contact angle results are consistent with our pull-off force measurements showing that the AFM technique can produce accurate measures of the solid–vapor surface free energy when the operating conditions of the AFM are set up properly.

#### 4.5. Surface free energy calculation for $\text{CH}_3$ -terminated self-assembled monolayers

The surface free energy for the SAMs can be calculated from the AFM pull-off forces using either the DMT or JKR model for adhesion of a particle to a flat surface. In the literature there is no clear consensus, at this point in time, which of these models should be used for surface free energy calculation. This problem will be examined here. Table 4 shows the calculated surface free energy values from the measured adhesion between  $\text{CH}_3$ -terminated SAMs used in this study according to the DMT and JKR models. The surface free energy values determined from the AFM measurements are also compared to the values calculated from contact angle measurements using the LABIFE theory and surface free energy values from the literature.

The values of the surface free energy calculated according to the DMT theory match the values calculated using the LABIFE theory very closely. The values calculated according to the JKR theory, as well as values from pull-off forces reported in the literature, seem to overestimate the value of the surface free energy substantially. The DMT model is expected to be more appropriate for this system because it appears to be a rigid system within the range of experimental conditions used in this study. As shown in Figs 4 and 5, the pull-off forces were not sensitive

**Table 4.**

Surface free energy of  $\text{CH}_3$ -terminated self-assembled monolayers (see text for discussion)

Calculated values from experimental measurements			
Cantilever	$\gamma_{\text{SV}}$ (mJ/m <sup>2</sup> ) DMT	$\gamma_{\text{SV}}$ (mJ/m <sup>2</sup> ) JKR	$\gamma_{\text{SV}}$ (mJ/m <sup>2</sup> ) LABIFE theory
Cantilever # 1	24.28 ± 9.28	32.37 ± 21.18	24.6 ± 0.9
Cantilever # 2	26.93 ± 9.57	35.91 ± 22.45	
Literature values			
$\gamma_{\text{SV}}$ (mJ/m <sup>2</sup> ) DMT	$\gamma_{\text{SV}}$ (mJ/m <sup>2</sup> ) JKR	$\gamma_{\text{SV}}$ (mJ/m <sup>2</sup> ) (contact angle)	
30 ± 16 [4]	40 ± 21 [13]	18.9 [33]	
	25 ± 11.5 [13]	19.3 [21]	

to the applied loads suggesting the absence of deformation of the interacting tip and substrate. The deformation of this system is discussed later in this paper.

#### 4.6. Experimental certainty in $\gamma_{SV}$ determination from AFM pull-off force measurements

The error in the pull-off force measurements comes from two sources, namely the error associated with force measurements and the error associated with the determination of the cantilever tip radius of curvature. The error can be derived starting with the DMT equation written in terms of the surface free energy component,  $\gamma_{SV}$ , given in equation (22):

$$F_{ad} = 4\pi R\gamma_{SV}. \quad (22)$$

Rewriting this equation in terms of  $\gamma_{SV}$  and taking the derivative with respect to the force component results in the following equation:

$$\partial\gamma_{SV} = \frac{\partial F_{ad}}{4\pi R}. \quad (23)$$

The error in the pull-off force measurements,  $\partial F_{ad}$ , is a result of the scatter of data points, as shown in Fig. 4, and the calibration of the spring constant of the cantilever. The error in  $F_{ad}$  is found by differentiating Hooke's law ( $F = k \times \Delta z$ ) with respect to the spring constant,  $k$ , adding the error contributed by the scatter in the data, and writing in terms of  $\partial F_{ad}$  as shown in equation (24):

$$\partial F_{ad} = \Delta z \partial k + k \partial(\Delta z), \quad (24)$$

where  $\Delta z$  is the deflection of the cantilever beam during a pull-off force measurement. The first term is the error associated with the spring constant calculation and the second term represents the scatter in the data. We assume that the second term of equation (24) is simply the standard deviation of the measured pull-off forces. The average value of  $\partial F_{ad}$  was used for the calculation of the error associated with the pull-off force measurements. Rewriting equation (23) in terms of the error in the surface free energy from the force component results in:

$$\partial\gamma_{SV} = \frac{\Delta z}{4\pi R} \partial k + \frac{k}{4\pi R} \partial(\Delta z). \quad (25)$$

The error associated with determination of the tip radius of curvature is found by differentiating equation (8) with respect to  $R$  and writing in terms of  $\partial\gamma_{SV}$  as shown in equation (26).

$$\partial\gamma_{SV} = \frac{F_{ad}}{4\pi R^2} \partial R. \quad (26)$$

For the blind tip reconstruction technique, the error associated with the tip radius of curvature determination is associated with the quality of the image. If there is significant noise in the image, the calculation of the radius is less reliable than that

**Table 5.**

Error components in AFM pull-off force measurements ( $\Delta\gamma_F$  refers to the first two terms in equation (27) accounting for the error due to the spring constant calibration and scatter in the AFM pull-off data,  $\Delta\gamma_R$  refers to the third term in equation (27), and  $\Delta\gamma_{SV} = \Delta\gamma_F + \Delta\gamma_R$ )

Cantilever	$\Delta\gamma_F$ (DMT) (mJ/m <sup>2</sup> )	$\Delta\gamma_R$ (DMT) (mJ/m <sup>2</sup> )	$\Delta\gamma_{SV}$ (DMT) (mJ/m <sup>2</sup> )
# 1	$\pm 6.71$	$\pm 2.57$	$\pm 9.28$
# 2	$\pm 6.68$	$\pm 2.89$	$\pm 9.57$

from a noise-free image. The BTR software used for these experiments contains a function called a certainty map. This determines the number of pixels that have noise in them and provides the user with this information as a percentage of the total pixels.

To the best of our knowledge no reports on error in BTR measurements have been presented in the literature. Therefore, it was decided that using the certainty map was the best method to quantify the error associated with BTR measurements since multiple images with the same or nearly the same amount of noise gave the exact same radius of curvature. The certainty map reports the percent of pixels that contain noise, and this percent is taken as the percent error in the tip radius of curvature determination.

The total error in the surface free energy of the self-assembled monolayer is the sum of the error from the force component and the radius component of equations (25) and (26), respectively and is given below in equation (27) (written in  $\Delta$  notation):

$$\Delta\gamma_{SV} = \frac{\Delta z}{4\pi R} \Delta k + \frac{k}{4\pi R} \Delta(\Delta z) + \frac{F_{ad}}{4\pi R^2} \Delta R. \quad (27)$$

This equation was used to calculate the errors in the surface free energy calculated from AFM pull-off force measurements shown in Table 5 for the DMT model. The error is derived in the same manner for the JKR model, the only change in equation (27) is that the constant in the denominator is changed to a value of 3. Table 5 shows the error contribution from each term in equation (27) for the DMT model for each cantilever. In Table 5, the notation  $\Delta\gamma_F$  refers to the first two terms in equation (27) accounting for the error due to the spring constant calibration and scatter in the data, and  $\Delta\gamma_R$  refers to the third term in equation (27) accounting for the error due to uncertainty in the radius of curvature determination.

The error in the surface free energy calculation from contact angle measurements using the LABIFE theory for quantitative analysis is determined in a similar manner. The contact angle values are used to calculate the three parameters of the surface free energy,  $\gamma_S^{LW}$ ,  $\gamma_S^+$ ,  $\gamma_S^-$  in the LABIFE theory and there is an error associated with this procedure. The terms  $\gamma_S^+$  and  $\gamma_S^-$  drop out of the surface free energy calculation for the HDT-SAM because the values are very small. Therefore, only the error associated with the term  $\gamma_S^{LW}$  contributes to the error in the calculation of



the surface free energy.  $\gamma_S^{LW}$  is calculated from the contact angle measurements of diiodomethane on the HDT monolayer, and the error is found by taking the derivative of equation (21) with respect to  $\theta$  and  $\gamma_L$ :

$$\frac{\partial \gamma_S^{LW}}{\partial \theta} = \frac{\gamma_L}{4} (\sin \theta + 2 \cos \theta), \quad (28)$$

$$\frac{\partial \gamma_S^{LW}}{\partial \gamma_L} = \frac{(1 + \cos \theta)^2}{4}. \quad (29)$$

Rewriting equations (28) and (29) to solve for the error in  $\gamma_S^{LW}$ , and adding the two error components together results in (written in  $\Delta$  notation):

$$\Delta \gamma_S^{LW} = \left[ \frac{\gamma_L}{4} (\sin \theta + 2 \cos \theta) \right] \Delta \theta + \left[ \frac{(1 + \cos \theta)^2}{4} \right] \Delta \gamma_L. \quad (30)$$

The scatter in the data for the experimentally determined contact angle values of diiodomethane on the HDT-SAM surface taken from Fig. 6 was used as  $\Delta \theta$  (approximately  $2^\circ$ ). The error in the liquid surface tension,  $\gamma_L$ , is known to be approximately  $0.5 \text{ mJ/m}^2$  from previous work in our laboratory. The total error,  $\Delta \gamma_{SV}^{\text{total}}$ , which is equal to the error in determination of the solid surface free energy from the diiodomethane contact angle measurements,  $\Delta \gamma_{SV}^{\text{diiodomethane}}$  (equal to the error from the Lifshitz–van der Waals component,  $\Delta \gamma_S^{LW}$  found in equation (30)):

$$\Delta \gamma_{SV}^{\text{total}} \cong \Delta \gamma_{SV}^{\text{diiodomethane}} = \Delta \gamma_S^{LW}. \quad (31)$$

The error in the first term in equation (30) is about  $\pm 0.67 \text{ mJ/m}^2$  and the error in the second term is about  $\pm 0.25 \text{ mJ/m}^2$  making the total error  $\pm 0.92 \text{ mJ/m}^2$  for the calculated surface free energy.

#### 4.7. Predicted deformation of the system

All of the contact mechanics theories described in the Introduction predict that there will be some deformation when a particle and surface come into contact. The mechanical properties and AFM operating conditions of the system control the amount of deformation observed for a given system. The effect of maximum applied loading was specifically studied in this research to examine the deformation of the system. The loading and unloading rate was shown in preliminary experiments not to have any noticeable effect (not shown) and all the experiments here were done at a constant loading/unloading rate. The contact time was not controlled in this part of the study due to limitations in the AFM controller software at the time of this study but the contact time is not expected to have any significant effect on the results in Figs 4 and 5.

The mechanical properties of the self-assembled monolayer on a gold-coated AFM cantilever tip are generally reported in the literature to be equal to the mechanical properties of the gold [1, 3, 6, 7, 12, 14]. The mechanical properties of gold were used in the aforementioned studies because the elastic modulus of the

**Table 6.**

Mechanical properties and physical constants ( $E$  is the Young's modulus,  $\nu$  is the Poisson's ratio,  $K$  is the reduced elastic modulus,  $W$  is the work of adhesion,  $d$  is the thickness of self-assembled monolayer, and subscripts 'gold' and 'SAM' refer to gold substrate and self-assembled monolayer, respectively)

$E_{\text{gold}}$ (GPa)	78.0	$E_{\text{SAM}}$ (GPa)	20.0
$\nu_{\text{gold}}$	0.42	$\nu_{\text{SAM}}$	0.45
$K_{\text{gold-gold}}$ (GPa)	63.1	$K_{\text{gold-SAM}}$ (GPa)	26.4
$W_{\text{SAM-SAM}} = 40.0 \text{ mJ/m}^2$			
$d_{\text{SAM}} = 2.26 \text{ nm}$			

SAM was believed to be at least one order of magnitude smaller than the elastic modulus of the gold. Therefore, the contribution of the SAM to the mechanical behavior of the system is expected to be negligible.

Recently it has been proposed that the elastic modulus of the SAM is higher than previously thought [13, 34, 35]. The methods used to determine the elastic modulus values are very different. Leng and Jiang used molecular simulations to determine the value of the elastic modulus for thiol type  $\text{CH}_3(\text{CH}_2)_m \text{SH}$  SAMs (where  $m = 8$  or 15) to be  $20 \pm 10$  GPa [34]. Work by Burns *et al.* [13] and Joyce *et al.* [35] using an interfacial force microscope (IFM), which is laterally more stable than the AFM, showed that SAMs relaxed when a load was applied [13]. They deduced from these data that the elastic modulus of the film was not negligible compared to that of the gold, although they did not provide a quantitative value.

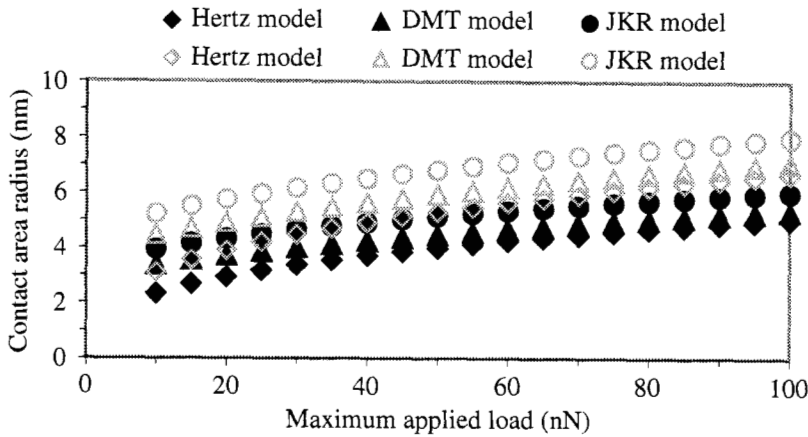
Since no general consensus on which set of mechanical properties is more appropriate, we will investigate the predicted deformation using the mechanical properties of gold and a combination of gold and SAM mechanical properties.

Table 6 lists the mechanical properties and physical constants used in the calculations that follow. The values for gold are taken from Callister [36]. The modulus of the SAM ( $E_{\text{SAM}}$ ) is taken from Leng and Jiang [34]. Poisson's ratio for the SAM ( $\nu_{\text{SAM}}$ ) is estimated to be approximately that of a typical polymer (since no value is reported in the literature). The work of adhesion is estimated to be a simple value that falls in between our measurements and those reported in the literature from contact angle measurements (see Table 6). Finally, the thickness of the SAM,  $d_{\text{SAM}}$ , is calculated as follows [5]:

$$d_{\text{SAM}} = 1.37m + 2.07, \quad (32)$$

in which  $m$  is the number of  $\text{CH}_2$  groups present in the monolayer ( $m = 15$  for HDT-SAM).

The contact area radius,  $a$ , and deformation,  $\delta$ , predicted for cantilever # 1 (radius of curvature = 79.7 nm) are shown in Figs 7 and 8, respectively, for the Hertz, DMT, and JKR models as a function of the maximum applied load. In these figures only the calculated values for cantilever # 1 are shown.



**Figure 7.** Contact area radius ( $a$ ) versus maximum applied load ( $P$ ) for cantilever # 1. The filled data points represent calculations based on the mechanical properties of gold only, while the open data points represent calculations based on the combined mechanical properties of gold and HDT-SAM from Table 6.

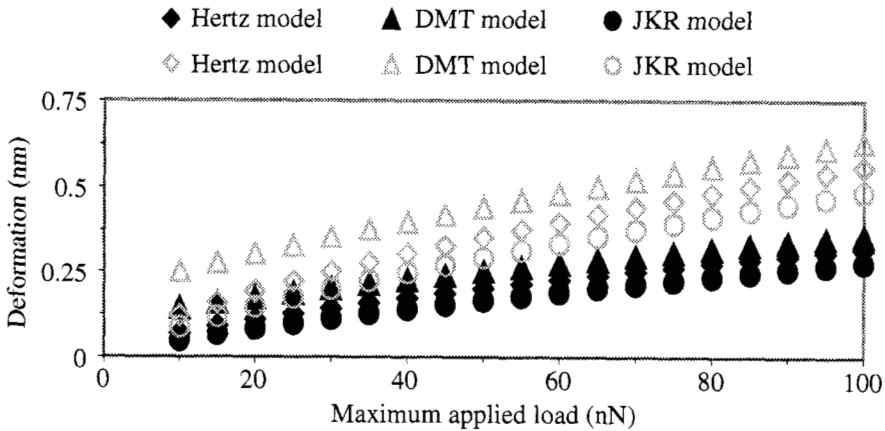


**Figure 8.** Deformation ( $\delta$ ) vs maximum applied load ( $P$ ) for cantilever # 1. The filled data points represent calculations based on the mechanical properties of gold only, while the open data points represent calculations based on the combined mechanical properties of gold and HDT-SAM from Table 6.

The Maugis parameters for the system (equation (14)) using the reduced elastic modulus of gold and gold-SAM system using a  $z_0$  value of 0.2 nm are 0.15 and 0.27, respectively. These are a near zero values, and according to Maugis mechanics the DMT model is more appropriate to describe this system than the JKR model (note that more accurate analysis requires the use of the Maugis–Dugdale model) [25].

All three theories (Hertz, DMT, JKR) predict that both the contact area and the deformation increase as the maximum applied load increases. The calculations that consider the combined gold-SAM mechanical properties predict both larger contact

areas and deformation. The data collected in our research and shown in Figs 4 and 5 indicate that there is no significant increase in the measured pull-off force due to increasing applied load. Accordingly, our results suggest that no increase in the contact area or deformation occurs at the moment of pulling the tip off the substrate. The data using only the mechanical properties of gold seem to be more appropriate because the predicted response to the applied load is smaller. Predicted values using only the mechanical properties of gold will be used in the following discussion.

The predicted increase in contact area radius may seem small, increasing from 3.36 nm for a load of 10 nN to 4.93 nm for an applied load of 75 nN but this is significant on the molecular scale. The contact area is approximately  $3,547 \text{ \AA}^2$  for a load of 10 nN while it increases to approximately  $7,636 \text{ \AA}^2$  for a load of 75 nN. The HDT-SAM molecules are known to occupy about  $20 \text{ \AA}^2$  [6]. This means that at a load of 10 nN, approximately 177 self-assembled molecules are interacting while at 75 nN, 382 self-assembled molecules are predicted to be in contact with molecules located at the tip. At the higher applied load the number of molecules predicted to be in contact is more than twice the value at 10 nN. This increase in the number of interacting molecules would clearly increase the pull-off force and would be noticable in the experimental results.

The contact area and deformation predictions of the three contact mechanics models presented here do not seem appropriate to the HDT-SAM on a gold-coated tip and substrate system in atomic force microscopy studies of pull-off forces. No noticable deformation occurs in the specified loading range according to the results presented in this paper. None of the three common contact mechanics theories (Hertz, DMT, JKR) accurately describes the contact interactions of this system. However, from the result of this research it appears that the pull-off force values measured by AFM techniques for SAMs in air, at low loading values are best described by equation (5) of the DMT model relating the adhesion force with surface free energy. This equation has exactly the same form as the equation describing the adhesion force between a rigid sphere and a rigid flat substrate in term of the work of adhesion between two flat surfaces, and is a direct consequence of the Derjaguin approximation [20, 37].

## 5. CONCLUSIONS

The AFM technique combined with a precise determination of the AFM cantilever tip curvature appears to be a very useful tool in the examination of surface free energy of engineered materials.

High quality images captured using the blind tip reconstruction technique provided reasonable values of the AFM tip size with a radius from 60 to 80 nm. A method for estimating the error in the blind tip reconstruction technique using the certainty map function was proposed in this paper.

The pull-off force measurements between hexadecanethiol monolayers, chemically adsorbed onto gold-coated AFM cantilever tips and substrates, in an ambient

environment presented here were reproducible within 10–20%. It was shown that the pull-off forces were not very sensitive to the maximum applied load in the range of 5–80 nN. This result suggests that the use of continuum elastic contact mechanics in the analysis of AFM pull-off force measurements is not as straightforward as usually assumed in the literature reports on similar systems.

The surface free energy of the self-assembled monolayer of hexadecanethiol was calculated to be in the range of  $24.28 \pm 6.61$  to  $26.93 \pm 9.57$  mJ/m<sup>2</sup> using the measured pull-off force values. The surface free energy values calculated from AFM pull-off force measurements matched our calculated values from the Lewis acid–base interfacial free energy theory using the contact angle measurements made in our laboratory ( $24.6 \pm 0.9$  mJ/m<sup>2</sup>). The experimentally determined surface free energy values were in between the literature values reported from contact angle measurements (18–19 mJ/m<sup>2</sup>) and direct pull-off force measurements (25–30 mJ/m<sup>2</sup>).

The results of this research indicate that the 6–10 mJ/m<sup>2</sup> error in determination of the surface free energy value using the AFM technique was reduced by as much as 40–50% when the pull-off force measurements were carried out at 30–80 nN maximum applied loads. This suggests that the accuracy of surface free energy determination can be substantially improved when appropriate operating parameters of measurement are set up for the atomic force microscope.

### Acknowledgements

The financial support for the research presented in this paper was received from the US National Science Foundation through subcontract with the University of Utah and Dura Pharmaceuticals Inc. in San Diego and is greatly appreciated. The authors also thank Dr. Rao Yalamanchili for silicon wafers.

### REFERENCES

1. A. Noy, D. V. Vezhenov and C. M. Lieber, *Annual Rev. Mater. Sci.* **27**, 381–421 (1997).
2. A. Ulman, *An Introduction to Ultrathin Organic Films from Langmuir-Blodgett to Self-Assembly*. Academic Press, Boston, MA (1991).
3. A. Noy, C. D. Frisbie, L. F. Rozsnyai, M. S. Wrighton and C. M. Lieber, *J. Am. Chem. Soc.* **117**, 7943–7951 (1995).
4. R. C. Thomas, J. E. Houston, R. M. Crooks, T. Kim and T. A. Michalske, *J. Am. Chem. Soc.* **117**, 3880–3884 (1995).
5. W. J. Miller and N. L. Abbott, *Langmuir* **13**, 7106–7114 (1997).
6. E. W. van der Vegte and G. Hadzioannou, *Langmuir* **13**, 4357–4356 (1997).
7. J. E. Houston, T. A. Michalske, R. M. Crooks and H. P. Schreiber, in: *Proceedings of the 20th Annual Meeting of the Adhesion Society*, pp. 31–33 (1997).
8. E. Kokkoli and C. F. Zukoski, *Langmuir* **14**, 1189–1195 (1998).
9. R. McKendry, M.-E. Theoclitou, C. Abell and T. Rayment, *Langmuir* **14**, 2846–2849 (1998).
10. V. V. Tsukruk and V. N. Bliznyuk, *Langmuir* **14**, 446–455 (1998).
11. M. Hartig, L. F. Chi, X. D. Liu and H. Fuchs, *Thin Solid Films* **327/329**, 262–267 (1998).

12. S. C. Clear and P. F. Nealy, *J. Colloid Interface Sci.* **213**, 238–250 (1999).
13. A. R. Burns, J. E. Houston, R. W. Carpick and T. A. Michalske, *Langmuir* **15**, 2922–2930 (1999).
14. H. Skulason and C. D. Frisbie, *Langmuir* **16**, 6294–6297 (2000).
15. S. Ohnishi, V. V. Yaminsky and H. Christenson, *Langmuir* **16**, 8360–8367 (2000).
16. G. Papastavrou, S. Akari and H. Mohwald, *Europhys. Lett.* **52**, 551–556 (2000).
17. K. L. Johnson, K. Kendall and A. D. Roberts, *Proc. R. Soc. London, A* **324**, 301–313 (1971).
18. B. Bhushan (Ed.), *Handbook of Micro/Nano Tribology*, 2nd edn. CRC Press, Boca Raton, FL (1999).
19. R. J. Good, *J. Adhesion Sci. Technol.* **6**, 1269–1302 (1992).
20. J. N. Israelachvili, *Intermolecular and Surface Forces*, 2nd edn. Academic Press, London (1992).
21. C. D. Bain, E. B. Troughton, Y.-T. Tao, J. Evall, G. M. Whitesides and R. G. Nuzzo, *J. Am. Chem. Soc.* **111**, 321–335 (1989).
22. D. V. Derjaguin, V. M. Muller and Yu. P. Toporov, *J. Colloid Interface Sci.* **53**, 314–326 (1975).
23. J. Hertz, *Reine Angew. Math.* **92**, 156–171 (1881).
24. M. Enachescu, R. J. A. van den Oetelaar, R. W. Carpick, D. F. Ogletree, C. F. J. Flise and M. Salmeron, *Phys. Rev. Lett.* **81**, 1877–1880 (1998).
25. D. Maugis, *J. Colloid Interface Sci.* **150**, 243–269 (1991).
26. J. S. Villarrubia, *J. Res. (NIST)* **102**, 425–453 (1997).
27. J. S. Villarrubia, Internet discussion over the Digital Instruments SPM Chat Group (2000).
28. V. Bykov, A. Gologanov and V. Shevyakov, *Appl. Phys. A* **66**, 499–502 (1998).
29. E. B. Troughton, C. D. Bain, G. M. Whitesides, R. G. Nuzzo, D. L. Allara and M. D. Porter, *Langmuir* **4**, 365–385 (1988).
30. J. Drelich, J. D. Miller and R. J. Good, *J. Colloid Interface Sci.* **179**, 37–50 (1996).
31. J. Drelich, J. L. Wilbur, J. D. Miller and G. M. Whitesides, *Langmuir* **12**, 1912–1922 (1996).
32. C. J. van Oss, M. K. Chaudhury and R. J. Good, *Adv. Colloid Interface Sci.* **28**, 35–64 (1987).
33. D. V. Vezenov, A. Noy, Ch. M. Lieber, L. T. Drzal and H. P. Schreiber, in: *Proceedings of the 20th Annual Meeting of the Adhesion Society*, pp. 23–25 (1997).
34. Y. Leng and S. Jiang, *J. Chem. Phys.* **113**, 8800–8806 (2000).
35. S. A. Joyce, R. C. Thomas, J. E. Houston, T. A. Michalske and R. M. Crooks, *Phys. Rev. Lett.* **68**, 2790–2793 (1992).
36. W. D. Callister, Jr., *Materials Science and Engineering: An Introduction*, 4th edn. John Wiley, New York (1997).
37. B. V. Derjaguin, *Kolloid Zeit.* **69**, 155–164 (1934).

## **Adhesion forces between functionalized probes and hydrophilic silica surfaces**

D. CHRISTENDAT, T. ABRAHAM, Z. XU\* and J. MASLIYAH

*Department of Chemical and Materials Engineering, University of Alberta, Edmonton, Alberta T6G 2G6, Canada*

**Abstract**—Adhesion forces between functionalized colloidal polymer spheres and a hydrophilic silica surface under different solution conditions were measured using an atomic force microscope (AFM). The measured force profiles show that the adhesion forces are sensitive to surface functional groups, pH, salt concentrations and the valency of cationic species. At pH below 8, the adhesion force between the surfaces of carboxylate functionality and hydrophilic silica wafer is about one order of magnitude greater than that between the surfaces of amine functionality and hydrophilic silica wafer. The strong adhesion interactions observed between the carboxylic-acid-functionalized probe and the hydrophilic silica surfaces are mainly attributed to hydrogen bonding between the surfaces. Our results suggest that hydrogen-bonding interactions can be mediated by the addition of divalent species as demonstrated by the addition of calcium ions at 0.1 and 1.0 mM concentration.

**Keywords:** Adhesion forces; amine; carboxylate; functionalized surfaces; hydrogen bonding; calcium ion.

### **1. INTRODUCTION**

The knowledge and accurate determination of adhesion forces between colloidal particles and surfaces at a molecular resolution is of vital importance in many disciplines of science and engineering [1]. The atomic force microscope (AFM) has been extensively used in studying various surface forces, such as DLVO colloidal forces [2], hydrophobic force [3], hydration force [4], depletion force [5], bridging force [6], chiral force [7] and even single-bond rupture force [8]. In addition, AFM provides a straightforward and precise means of determining the adhesion forces with a high degree of spatial resolution [9, 10]. There are several reports on adhesion force measurements between modified AFM tips bearing various surface

---

\*To whom correspondence should be addressed. Tel.: (1-780) 492-7667. Fax: (1-780) 492-2881.  
E-mail: zhenghe.xu@ualberta.ca

functional groups, such as  $\text{CH}_3$ ,  $\text{COOH}$ ,  $\text{CH}_2\text{OH}$ ,  $\text{CO}_2\text{CH}_3$ ,  $\text{CH}_2\text{Br}$  and  $\text{NH}_2$ , and the substrate bearing self-assembled monolayers (SAM) of similar surface groups [11–14]. In these studies, the surface terminal group was found to control the adhesion behavior between the two surfaces. As a result, the AFM, commonly referred to as chemical force microscope in this field of applications [11, 12], can be used effectively to probe surface chemical composition at a molecular resolution. The effect of ionic strength and pH of the solution on ionization of terminal groups and the role of electrostatic interactions between those ionized terminal groups were studied. Direct surface modification of silicon wafers or silicon nitride tips by silanes is also reported as a powerful means to mediate surface forces [15]. In the present work, we report on adhesion interactions between hydrophilic silica wafers and microsphere probes of carboxylate and amine surface functionalities under various aqueous environments, such as pH and varying mono- and divalent salt concentrations. In contrast to the modified AFM tips as molecular probes in earlier studies [11, 12], the use of micrometer spheres as probe, as used in our study, improves detection sensitivity of interaction forces, which allows probing weaker interactions, as will be illustrated later in this communication. The purpose of this study was to better understand the role of molecular interactions in protein foldings of amino-acid building blocks in biological systems under different pH and electrolyte concentrations with emphasis on the role of divalent calcium ions. Various pH-dependent interactions between amino-acid building blocks in proteins, mediated by the presence of various types of electrolytes, are anticipated to control molecular folding and hence their functions in biological systems. In addition to van der Waals and electrostatic forces, hydrogen bonding between acrylic acid and/or amine groups plays a critical role in such conception.

## 2. EXPERIMENTAL

### 2.1. Materials

Silicon wafers of [100] crystal planes were purchased from MEMC Electronic Materials (Italy). Ultrahigh purity potassium chloride (99.999%) and sodium hydroxide (99.996%) were purchased from Aldrich, while calcium chloride (99.996%) and hydrochloric acid (99.999%) were obtained from Alfer Aser (USA). These chemicals were used as received without further purification. Spectra grade ethanol, chloroform, ammonium hydroxide, sodium hydroxide (for cleaning glassware) and hydrogen peroxide were also purchased from Aldrich. Carboxylate- and amine-terminated polymer microspheres were obtained from Bangs Laboratories (USA) and used without further modification. For comparison, micrometer-size silica spheres with carboxylic functionality, also obtained from Bangs Laboratories, were tested. In some cases, silica wafer and micrometer-size glass beads were silanized in our laboratory to obtain amine-terminated surfaces for comparative studies.

All glassware was cleaned using a 10% by weight sodium hydroxide aqueous solution containing 5% by volume ethanol and rinsed thoroughly with Millipore



water. Millipore water was obtained from an Elix-5 coupled to a Millipore-UV plus unit (Millipore, Canada).

## 2.2. Hydrophilic silica wafers

A sheet of silicon wafer was cut into rectangular pieces of  $2 \times 1.5$  cm dimensions. After cleaning the cut wafers with chloroform in an ultrasonic bath for 10 min to remove any possible organic surface contaminants, they were rinsed thoroughly with absolute ethanol followed by Millipore water. The wafers cleaned by this procedure were immediately oxidized with a mixture of  $\text{H}_2\text{O}_2$ ,  $\text{NH}_3$  and Millipore water at a volume ratio of 1 : 1 : 5 and heated to a temperature of about  $70^\circ\text{C}$  for about 45 min. The resulting hydrophilic surfaces, referred to as silica wafer in this paper, were rinsed with ample amount of Millipore water and blow-dried with ultrahigh purity nitrogen. The hydrophilic nature of the surfaces was maintained by storing the wafers in absolute ethanol. The silica wafers were rinsed with Millipore water and blow-dried with a stream of ultrahigh purity nitrogen prior to each use.

## 2.3. Adhesion force measurement

A Nanoscope-E atomic force microscope (Digital Instruments, USA) equipped with an AS-12 E scanner was used to measure the adhesion forces between the hydrophilic silica wafers and the functionalized polymer spheres under a controlled aqueous environment (Fig. 1). For each set of experiments, a single polymer sphere of *ca.*  $10\ \mu\text{m}$  in diameter was carefully glued onto a short cantilever (with a spring constant of  $0.58\ \text{N/m}$ ) at positions as close to the cantilever apex as possible by means of a micromanipulator under an optical microscope and using a two-component Master Bond epoxy polymer (EP21LV, Master Bond, USA). Figure 2 shows a typical scanning electron micrograph of a  $10.4\ \mu\text{m}$  polymer sphere mounted onto a rectangular cantilever.

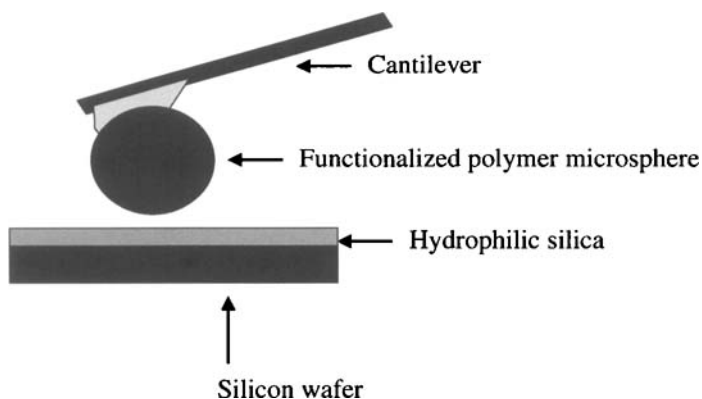


**Figure 1.** Schematic of force measurement between a functionalized polymer microsphere and hydrophilic silica wafer using an atomic force microscope (AFM).

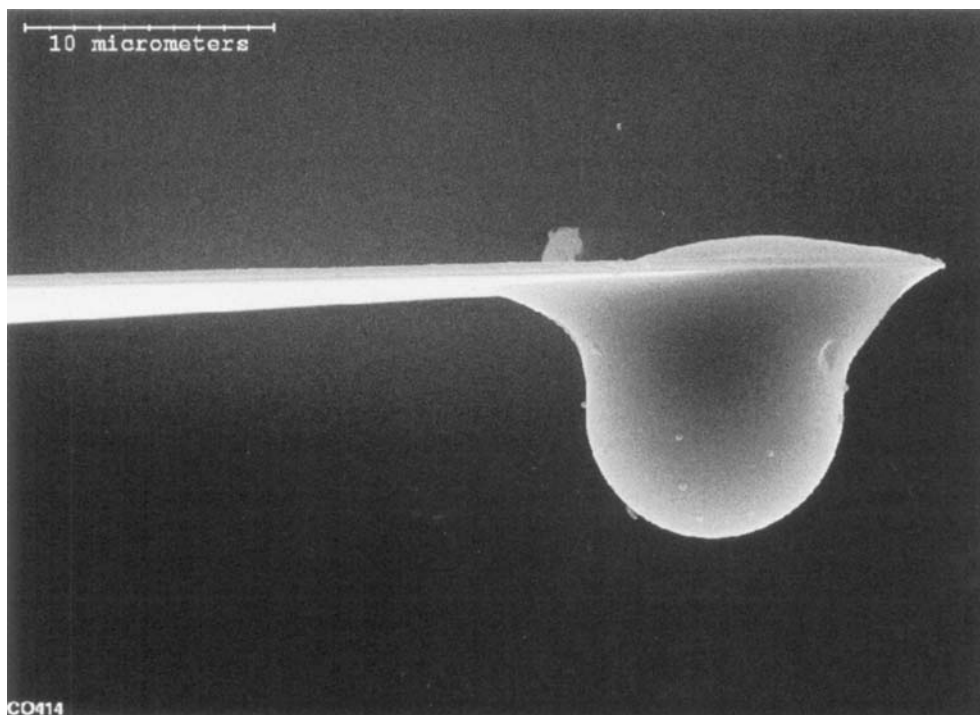


**Figure 2.** Scanning electron microscope (SEM) micrograph of polymer microsphere glued onto the cantilever.

The cleaned silica wafer and the solution cell assembly, obtained from Digital Instruments, were placed under an ultraviolet light in a horizontal laminar flow hood for 3 h prior to assembly. This procedure helps to destroy any organic contaminant that may adhere onto the surfaces of the substrate and the solution cell. After the cantilever assembly was carefully mounted into the solution cell and the solution cell mounted onto the AFM, the apparatus was then finally assembled, all accomplished in a horizontal laminar flow hood. The probe particle and silica wafer were incubated in Millipore water for 6 h prior to adhesion force measurements. At least 18 force–displacement profiles at three different locations on a given substrate were collected in each freshly prepared electrolyte solution after an equilibrium period of 15 min at room temperature. After each set of measurements at a given solution pH, the liquid cell was flushed with ample amount of freshly prepared solutions of progressively increasing or decreasing solution pH, depending on whether it was going from neutral to basic or acidic solution conditions. For each set of measurements, the adhesion force between the polymer microspheres and the silica wafer surfaces was determined from the deflection of the AFM cantilever as it retracted from the surface using the Hooke's law given below:

$$\Delta F = \frac{1}{n} \sum_{i=1}^n -k_S D_i, \quad (1)$$

where  $D$  represents the deflection and  $k_s$  is the spring constant of the cantilever, typically 0.58 N/m. For comparison from one experiment to another, the measured pull-off force was normalized by the radius ( $R$ ) of the probe to obtain the adhesion force ( $F/R$ ). Under a given set of conditions, the measurements were made with two independently prepared pairs of samples, each at five different locations. At each location, at least five representative force profiles were captured for analysis. The calculation of adhesion forces from these 50 force profiles resulted in a maximum relative standard deviation of about 10%. This magnitude of relative standard deviation is not uncommon as shown by Lieber and co-workers [11, 12].

### 3. RESULTS AND DISCUSSION

#### 3.1. Adhesion forces between amine-terminated probe and silica

The normalized pull-off forces between amine ( $\text{NH}_2$ )-terminated polymer sphere and hydrophilic silica surface in KCl electrolyte solutions as a function of pH are shown in Fig. 3. In a 1 mM KCl solution, the adhesion forces between the amine-terminated probe and silica surfaces decreased monotonically from 11 mN/m at pH 3 to 1 mN/m with increasing solution pH to 10. The adhesion forces at pH below 8 were found to decrease with increasing supporting electrolyte concentration. At pH 6, for example, the adhesion force decreased from 11 mN/m to 6 and 2 mN/m with increasing ionic strength from 1 mM to 10 and 100 mM, respectively. At pH > 8 there is little or no effect on the adhesion forces with increasing KCl concentration.

The effects of different types of electrolytes on the adhesion forces between amine-functionalized polymer and silica wafer were also examined. The results in Fig. 4 show a significant impact of divalent ion addition. The addition of 0.1 mM calcium ions at a solution pH of 6, for example, reduced the measured pull-off force by half. At higher pH, the measured adhesion forces followed the same trend as in the case of without divalent cation addition. A further increase in calcium ion concentration to 1 mM caused the adhesion forces to disappear, irrespective of solution pH.

Considering the presence of multiple isoelectric points with different  $\text{p}K_a$  values on the interacting surfaces, the pH dependence of adhesion forces between amine-terminated probe spheres and silica can be qualitatively explained by interplay of electrostatic and van der Waals forces between the surfaces. Within the contact area, van der Waals forces and other relevant adhesion interactions such as ionic binding, hydrogen bonding, etc. make up overall adhesion forces that can be calculated according to the JKR theory [16]. Outside the contact area, the van der Waals interactions and electrical double layer forces between a truncated sphere and a flat surface add an additional contribution to total adhesion forces. The balance of all these contributions can result in from predominantly adhesional to non-adhesional contact, depending on the nature of interfacial bonding, charge on the surfaces and solution conditions.

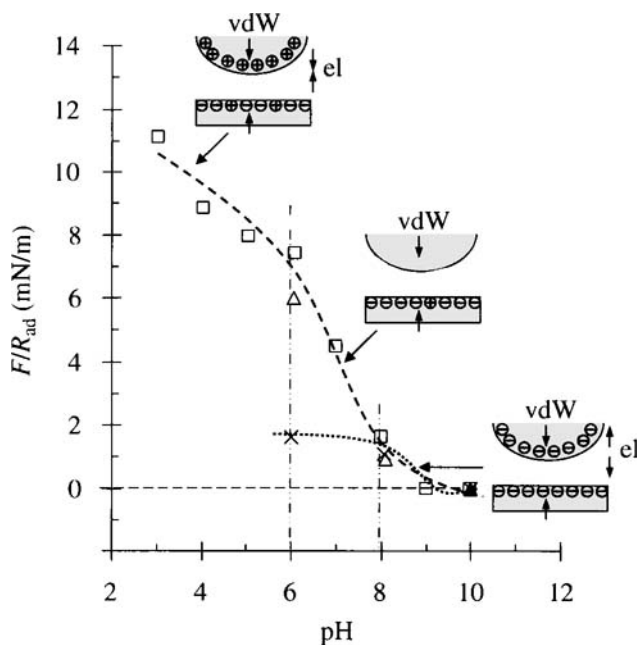


**Figure 3.** Normalized adhesion force ( $F_{ad}/R$ ) measured between amino functionalized polymer sphere and hydrophilized silicon wafer as a function of pH under different ionic conditions. (□) 1.0 mM KCl; (Δ) 10 mM KCl; (×) 100 mM KCl.

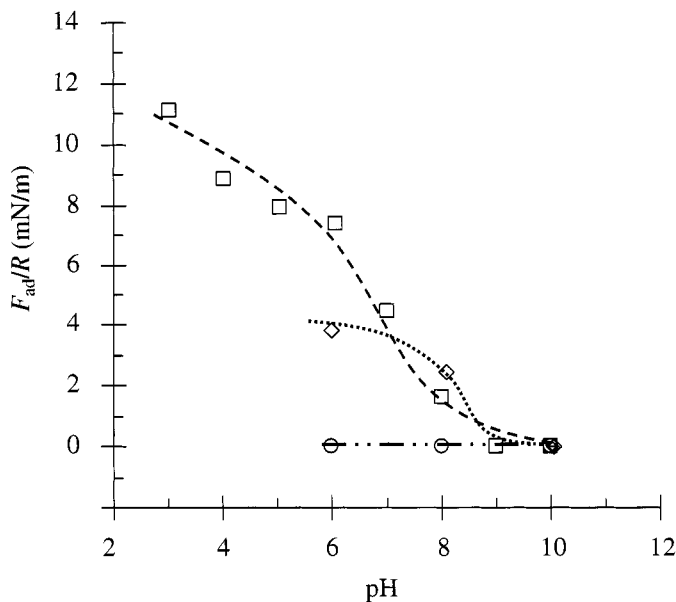


**Figure 4.** Normalized adhesion force ( $F_{ad}/R$ ) measured between amino functionalized polymer sphere and hydrophilized silicon wafer as a function of pH under different ionic conditions. (□) 1.0 mM KCl; (◇) 1.0 mM KCl/0.1 mM  $CaCl_2$ ; (○) 1.0 mM KCl/1.0 mM  $CaCl_2$ .

It is well established that the change of van der Waals forces can be considered negligible with changing solution pH and supporting electrolyte concentration [17, 18]. The measured adhesion forces in this study do not scale with ionic strength, suggesting that the electrostatic double layer forces were not the sole contributor to the observed reduction of adhesion forces with electrolyte addition.

In addition to contact adhesion from van der Waals attraction and hydrogen bonding, the electrostatic forces acting between surfaces outside contact area can be understood by taking into account the complex chemical compositions of surfaces. The usual  $pK_a$  value for amine surfaces is in the range of 7–8 [19]. The hydrophilized silicon wafer in water is, in fact, composed of a relatively thin layer of silicon dioxide ( $\text{SiO}_2$  bonds,  $pK_a = 2\text{--}3$ ), some of them being hydrolyzed to become silanol groups ( $\text{Si}\text{--}\text{OH}$ ,  $pK_a$  approx. 6). As a result, silica wafer surfaces exhibit essentially zwitterionic behavior due to significant changes of electrostatic interactions caused by shifts of acid–base equilibria of different types of surface groups [20]. It is, however, known that the actual  $pK_a$  values for chemical groups on surfaces are, usually, lower compared with  $pK_a$  values of the same groups in solution [21]. The difference is attributed to the difficulty in forming charged state of the ionizable groups at constrained surfaces due to the influence of nearby charged sites. Considering the  $pK_a$  values and adhesion forces, it can be inferred that the amine surface bears strong positive charges in the pH range from 3 to 6, and becomes predominantly neutral over solution pH between 8 and 10. In contrast, the silica surface, which exhibits zwitterionic behavior due to the presence of  $\text{SiO}_2$  and  $\text{Si}\text{--}\text{OH}$ , is predominantly negatively charged in the solution of pH from 3 to 6, and becomes increasingly more negative at pH 7–8 and fully negatively charged in solutions of pH from 8 to 10. The pH dependence of surface charging mechanism interpreted here is in line with the observations of zeta potential measurements using corresponding surfaces [22]. Thus, the variation of both amine and silica surface charges can be considered as the reason for the observed variation of adhesion forces with solution pH. The charging states of amine-terminated probe and silica surfaces at various pH values are shown schematically in Fig. 3. At very low pH, the probe surface is strongly positively charged due to protonation of amine groups, while silica surface carries negative charges. In addition to the non-compensated strong van der Waals forces within the contact area, the opposite charges on the two interacting surfaces result in an electrostatic attraction. As a result, a maximum adhesion force was measured. An increase in pH causes a steady decrease in adhesion forces due to a gradual decrease in protonation of surface amine groups at an intermediate solution pH. The reduced protonation translates into a reduced positive surface charge density on the probe particle, diminishing the attractive electrostatic contribution which, in turn, leads to a decrease in adhesion forces. At higher pH, above 10, both amine-terminated probe and silica surfaces bear strong negative charges due to ionization of both silanol and amine groups, inducing a strong electrostatic repulsion between highly negatively charged surfaces, which compensates attractive van der Waals forces. More importantly, such ionization

at high pH on silica and amine-terminated probe reduces the potency of hydrogen bonding within the contact area, resulting in a decrease of adhesion eventually to zero.

The effect of monovalent and divalent cations addition on adhesion interactions can be rationalized as follows. For KCl concentration at 100 mM, a significant reduction in pull-off force is observed at pH around 6. Over this pH range, the amine surface bears partial positive charges and the silica surface predominantly carries negative charge. The addition of 100 mM KCl causes screening of these charges, which, in turn, diminishes electrostatic attraction between the surfaces and contributes to the reduction of net adhesion. At high pH values (from 8 to 10), where both surfaces carry negative charges, the electrostatic screening is expected to enhance the adhesion interactions. Contrary to expectation, the pull-off force remains the same. In these cases, the electrostatic contribution is possibly suppressed by hydration effects resulting from the adsorption of counterions on the surfaces. The addition of divalent cations showed a much more drastic effect on adhesion interactions. The addition of 0.1 mM  $\text{CaCl}_2$ , for example, caused an equivalent depression of adhesion as the addition of 100 mM KCl. This large difference cannot be accounted for by simple electric double layer compression. It appears that calcium cations specifically adsorbed on negatively charged silica surface reduce its negative surface charge. This reduction of surface charge contributed to a significant reduction in electrostatic attraction between positively charged probe particle and negatively charged silica surfaces. Moreover, the specific adsorption of positively charged calcium on silica may reduce the potential for hydrogen bonding within the contact region, which significantly impacts the adhesion interactions. By increasing  $\text{CaCl}_2$  concentration to 1 mM, the adhesion disappeared, which supports the above explanation of specific adsorption of calcium on silica. The specific adsorption of calcium on silica not only reduces electrostatic attraction or even reverses from attraction to repulsion, should silica surfaces become charge-reversed, but also induces a strong repulsive hydration force to prevent intimate contact where van der Waals forces prevail.

### *3.2. Adhesion forces between carboxylate-terminated probe and silica*

The pull-off forces between carboxylate-terminated colloidal probe and hydrophilic silica as a function of solution pH at different KCl and  $\text{CaCl}_2$  concentrations are shown in Figs 5 and 6. In the presence of 1 mM KCl, the adhesion force shows little or no variation with solution pH below 8. However, the measured adhesion force decreased drastically from 66 mN/m to 2 mN/m as the solution pH increased from 8 to 10. The adhesion force profile obtained in this case study closely resembles those measured using a molecular force microscope for a similar system (Fig. 2 in Ref. [11]). However, the forces measured in our study using microsphere are an order of magnitude larger than those reported in the literature where AFM tips were used. A slight shift of our force profile to a slightly higher pH direction reflects a slightly different dissociation environment of carboxylic groups on AFM

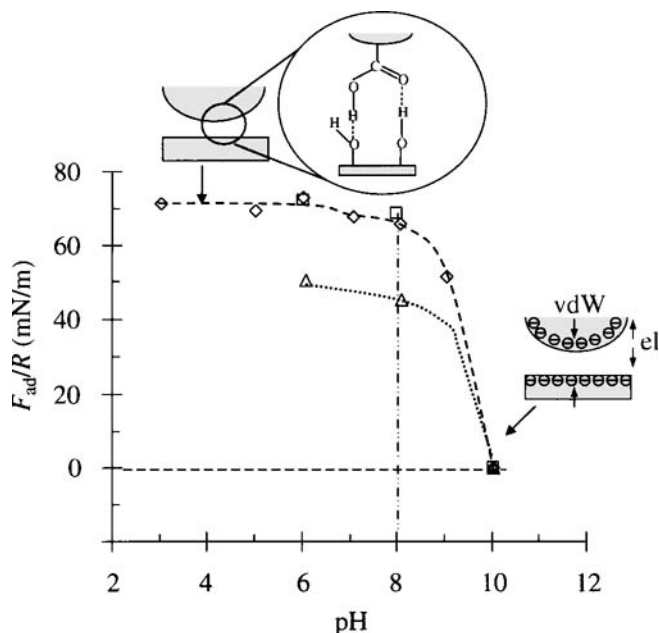


**Figure 5.** Normalized adhesion force ( $F_{ad}/R$ ) measured between carboxylate-functionalized polymer sphere and hydrophilic silica wafer as a function of pH under different ionic conditions. ( $\square$ ) 1.0 mM KCl; ( $\diamond$ ) 10 mM KCl; ( $\Delta$ ) 100 mM KCl.

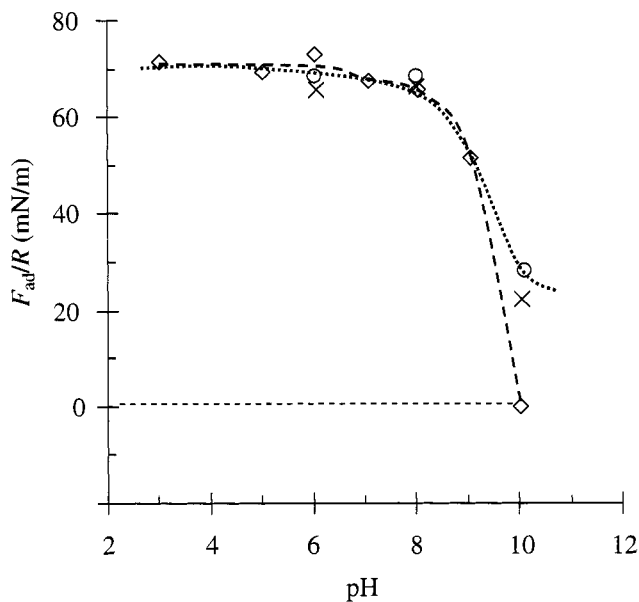


**Figure 6.** Normalized adhesion force ( $F_{ad}/R$ ) measured between carboxylate-functionalized polymer sphere and hydrophilic silica wafer as a function of pH under different ionic conditions. ( $\diamond$ ) 1.0 mM KCl; ( $\times$ ) 1.0 mM KCl/0.1 mM  $\text{CaCl}_2$ ; ( $\circ$ ) 1.0 mM KCl/1.0 mM  $\text{CaCl}_2$ .

tip from those on a microsphere, possibly arisen from surface density difference of carboxylic groups on these two different probes. It is also interesting to note that the adhesion force showed little variation as the concentration of KCl increased from 1 mM to 10 mM. A further increase of KCl concentration to 100 mM caused a significant reduction in the pull-off forces over the pH range of 6–8. The addition of 0.1 mM divalent calcium ions showed only a little effect on the pull-off force at pH below 8. At pH 10, however, an increase in pull-off force from 2 mN/m to 25 mN/m was observed. A similar effect of calcium addition on pull-off forces was observed when calcium ion concentration was increased to 1 mM.

The interactions between the carboxylate-terminated probe and silica surface cannot be explained by considering only the electrostatic force, van der Waals forces and the ionic binding mechanism, all compounded in the JKR theory. Considering the  $pK$  values for the carboxylate-terminated microsphere and hydrophilic silica surface, one would expect similar or weaker pull-off forces than that of the amine-terminated microsphere interacting with silica surface. However, the pull-off forces are almost an order of magnitude higher for hydrophilic silica interacting with carboxylate-terminated than with amine-terminated sphere under the similar conditions. Hydrogen bonding appears to be a controlling factor in determining adhesion between the carboxylate-terminated probe and the hydrophilic silica wafer [23]. The  $pK_a$  value of carboxylate-terminated surfaces ( $pK_a$  around 8) has been determined to be several units higher than that of carboxylate in solution [24]. The increase in adhesion force below pH 8 is attributed to hydrogen bonding between the proton of the carboxylic acid group [ $\text{RC(O)OH}$ ] on the sphere and the oxygen atom on the silica wafer [ $\text{SiO}$ ], and between proton of silanol group on silica wafer [ $\text{SiOH}$ ] and oxygen of both carboxylate [ $\text{COO}^-$ ] and carboxylic acid [ $\text{RC(O)OH}$ ] groups on the sphere. Symbol  $\parallel$  in this paper emphasizes the species on a surface. Evidence of hydrogen bonding was further substantiated by a rapid decrease in pull-off forces at pH above 8 where the carboxylic groups and hydrolyzed silica surfaces are substantially deprotonated to become  $\text{C(O)O}^-$  and  $\text{SiO}^-$ , respectively, a system with diminishing hydrogen bonding potency. Further increase in solution pH to 10 results in a strong electrostatic repulsion between highly negatively charged surfaces without hydrogen bonding and hence a zero adhesion force. It is clear that the adhesion between carboxylate-terminated sphere and hydrophilic silica surfaces in an electrolyte solution is controlled collectively by electrostatic interactions, van der Waals forces and hydrogen bonding. Because of this nature, the adhesion forces between the carboxylate-terminated probe and silica surfaces (Figs 5 and 6) were determined to be much stronger than that between the amine-terminated probe and silica surfaces (Figs 3 and 4).

Ionic binding appears to be the main controlling factor in determining adhesion, as shown in Fig. 3 between the amine-terminated probe and silica surfaces. At pH below 6 the amine probe is fully protonated, whereas the silica surface is predominantly negatively charged and hence an ion pair is formed, resulting in an adhesion interaction. It appears that this type of ionic interaction is almost an



order of magnitude smaller than that of hydrogen bonding. The constant decrease in adhesion force above pH 6 is attributed to deprotonation of the amine group and a constant increase in negative charge on the silica surface, i.e., repulsion between the amine lone pair electrons and the negatively charged silica surface. At pH above 8, the silica surface is fully negatively charged and the amine probe is substantially deprotonated, resulting in a zero adhesion force between these two surfaces.

After establishing hydrogen bonding as an important factor in controlling the adhesion between a carboxylate-terminated sphere and a flat hydrophilic silica surface, it is reasonable to envision a less sensitive effect of KCl concentration on the measured adhesion forces between a carboxylate-terminated sphere and a flat hydrophilic silica surface than between an amine-terminated sphere and a flat hydrophilic silica surface, as shown in Figs 5 and 3, respectively. The screening effect of electrostatic interaction by concentrated electrolyte appears to account for the observed decrease in adhesion forces between a carboxylate-terminated sphere and a flat hydrophilic silica wafer by increasing KCl concentration to 100 mM, which diminishes the electrostatic contribution to adhesion between the surfaces. At pH values higher than 8, both surfaces are highly charged as such that hydrogen bonding is minimized to cause non-adhesional contact. In this case, screening of electrostatic double layer repulsion does not really help in inducing adhesional contact due to the lack of attractive nature. It is interesting to note the minimal effect of calcium addition on the measured adhesion. Considering specific adsorption of calcium on both carboxylate-terminated sphere and highly hydrophilic silica, the loss of hydrogen bonding by calcium adsorption is anticipated to be well compensated by bridging of calcium ions. Overall, the adhesion shows a minimal response to calcium addition at pH below 8. At pH higher than 8, calcium bridging ( $\text{||COO}-\text{Ca}-\text{OSi||}$ ) due to its specific adsorption induces adhesion for a system absent of adhesional contact due to hydrophilic nature of interacting surfaces and a lack of hydrogen bonding.

### 3.3. Adhesion forces between amine-terminated probe and amine-terminated silica flat

The adhesion forces were also measured using an amine-terminated polymer sphere and amine-terminated silica flat. The amine-terminated silica wafer was prepared by direct silanation with 3-aminopropyltriethoxysilane, following the procedures given by Xu *et al.* [25]. The results in Fig. 7 show that at pH below 5, the surfaces are not in adhesional contact in 1 mM KCl solutions. At this pH, the amine-terminated surfaces can be considered to be highly protonated to carry strong positive surface charges and hydrated to prevent proximate contact in such a way that van der Waals forces are not sufficient to cause adhesional contact. As pH increases above 5, the surfaces become less protonated, although remain positively charged overall. Under such conditions, one expects a reduction in both hydration and electrostatic repulsive interactions with increasing solution pH. As a result, a relatively small adhesional contact is anticipated due to attractive van der Waals forces at small

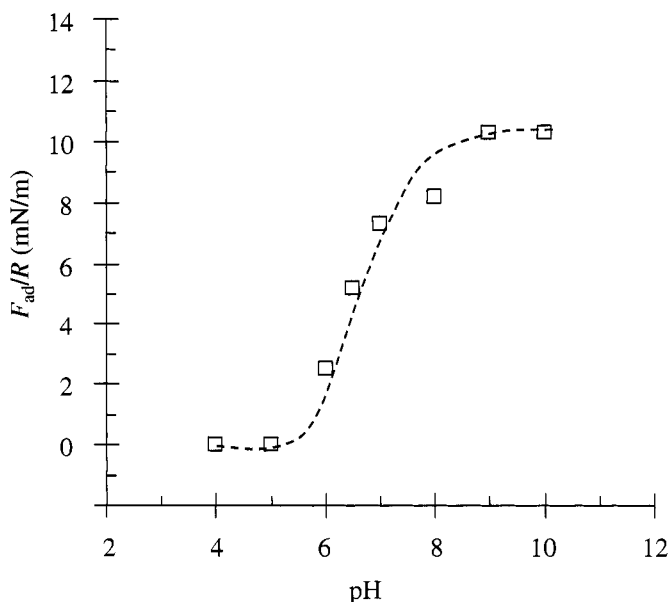


**Figure 7.** Normalized adhesion force ( $F_{ad}/R$ ) measured between amine-functionalized polymer sphere and amine-functionalized silica wafer in 1 mM KCl solution as a function of pH.

separation distances. At pH above 10, the amine groups are anticipated to be fully deprotonated to become neutral amine groups. Under such condition, a minimum hydration of a neutral surface is anticipated to cause a maximum adhesion of 10 mN/m, which is significantly smaller than the case where hydrogen bonding is available such as shown in Figs 5 and 6. A similar adhesion force profile between an amine-terminated AFM tip and an amine-terminated flat surface was reported in Ref. [11] (Fig. 1). Vezenov *et al.* attributed the strong adhesion at pH above 6 to hydrophobic nature of surface, although it is hard to comprehend the hydrophobic nature of amine-terminated surfaces. The presence of defects in their surface modification might have led to modified surfaces with considerable hydrophobicity.

### 3.4. Adhesion forces between carboxylate-terminated probe and amine-terminated silica flat

To relate adhesion forces to protein folding, it is instructive to measure adhesion forces between carboxylate-terminated probe and amine-terminated silica flat, as these two functional groups are major constituents of amino acid building blocks for proteins. The measured adhesion forces in Fig. 8 show only a little effect of changing solution pH. In general, the measured adhesion forces are 6-times weaker than those measured between carboxylate-terminated silica and hydrophilic silica surfaces. The weaker adhesion between carboxylate-terminated probe and amine-terminated silica flat is attributed to the absence of hydrogen bonding between the

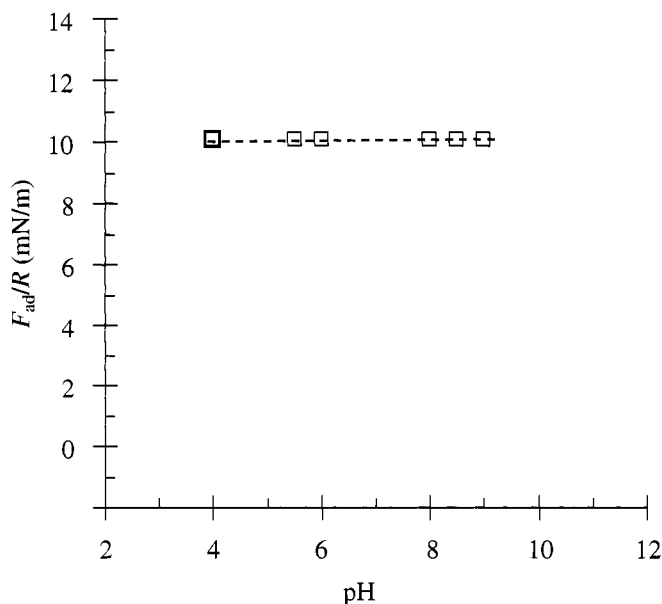


**Figure 8.** Normalized adhesion force ( $F_{ad}/R$ ) measured between carboxylate-functionalized polymer sphere and amine-functionalized silica wafer in 1 mM KCl solution as a function of pH.

two interacting surfaces at  $\text{pH} < 8$ . At  $\text{pH} > 8$  one would expect a decrease in adhesion force between the probe and amine-terminated surface due to the presence of repulsion between the lone pair electrons of neutral amine groups and negatively charged carboxylic surface. Although intriguing, it remains unclear as to why the adhesion force between two oppositely charged surfaces is independent of solution pH within the pH range studied. Nevertheless, this behavior appears to be related to the opposite directions of surface charge density changes with increasing solution pH, with amine groups becoming less positively charged by deprotonation, while carboxylic acid groups being gradually ionized to become progressively more negatively charged with increasing solution pH. The implication of this study is that one would expect folding of polymeric protein molecules in aqueous solutions due to a substantial adhesion (11 mN/m) between the amine and carboxylic acid groups of amino-acid moieties which are building blocks of proteins. Considering a weak adhesion varying from 0 to 10 mN/m with pH from 5 to 10, however, only a weak pH dependence of polymeric protein folding is anticipated. Recognizing hydrogen bonding as a major contributor to adhesion as revealed from this study, one would expect a strong pH dependence of protein folding, arising from intra-hydrogen bonds between carboxylic acid moieties on amino acids. At a solution pH below the  $\text{pK}_a$ , carboxylic acid groups dominate and strong hydrogen bonding between nearby carboxylic acid groups would result in a strong adhesion. At a pH higher than the  $\text{pK}_a$ , on the other hand, the surfaces become dominated by carboxylate groups, not only reducing hydrogen bonding potency, but also

inducing a strong electrostatic repulsion between anionic carboxylate groups. In this case, adhesion interaction may well disappear. Unfortunately, the measurement of adhesion between carboxylate-terminated probe and carboxylate-terminated silica wafer was not performed due to technical difficulties in preparing robust and smooth carboxylate-terminated silica surfaces in our laboratory, that would be used in our AFM force measurements. However, our expectation is in line with a recent report by Vezenov *et al.*, who showed a much stronger adhesion of the carboxylic acid-terminated AFM tips with the carboxylic acid terminated flat surface than with the hydroxyl-terminated flat surface [11].

#### 4. CONCLUSIONS

The adhesion force measurement reported in this study clearly demonstrates an important role of hydrogen bonding in adhesion interactions. Whenever there is a potential for hydrogen bonding, a strong adhesional contact is observed, although long-range electrostatic and short-range hydration repulsion also play vital roles. Translating these insights into folding of protein molecules in a biological system, it is desirable to eliminate intra-chain hydrogen bonding and to maximize hydration and electrostatic repulsion. This can be accomplished collectively by increasing surface charge densities of carboxylic acid groups, for example, with increasing solution pH or protonation of amine groups with decreasing solution pH.

#### REFERENCES

1. B. Capella and G. Dietler, *Surf. Sci. Rep.* **34**, 1–105 (1999).
2. W. A. Ducker, T. J. Senden and R. M. Pashley, *Nature* **353**, 239–241 (1991).
3. Y. Tsao, D. F. Evans and H. Wennerstrom, *Science* **262**, 547–550 (1993).
4. C. D. Frisbie, L. F. Rozsnyai, A. Noy, M. S. Wrighton and C. M. Lieber, *Science* **265**, 2071–2074 (1994).
5. A. Milling and S. Biggs, *J. Colloid Interf. Sci.* **170**, 604–606 (1995).
6. T. Abraham, D. Christendat, J. F. Gohy, R. Jérôme, Z. Xu and J. Masliyah, *AIChE J.* **50**, 2613–2626 (2005).
7. R. McKendry, M. Theoclitou, T. Rayment and C. Abell, *Nature* **391**, 566–5687 (1998).
8. J. M. Williams, T. Han and T. P. Beebe, *Langmuir* **12**, 1291–1295 (1996).
9. C. B. Prater, P. G. Maivald, K. J. Kjoller and M. G. Heaton, *Digital Instruments Application Note* (1995).
10. P. Samori, *J. Mater. Chem.* **14**, 1353–1366 (2004).
11. D. V. Vezenov, A. Noy, L. F. Rozsnyai and C. M. Lieber, *J. Am. Chem. Soc.* **119**, 2006–2015 (1997).
12. D. V. Vezenov, A. V. Zhuk, G. M. Whitesides and C. M. Lieber, *J. Am. Chem. Soc.* **124**, 10578–10588 (2002).
13. S. Akari, D. Horn, H. Keller and W. Schrepp, *Adv. Mater.* **7**, 549 (1995).
14. S. K. Sinniah, A. B. Steel, C. J. Miller and J. E. Reutt-Robey, *J. Am. Chem. Soc.* **118**, 8925–8931 (1996).
15. C. A. Johnson and A. M. Lenhoff, *J. Colloid Interf. Sci.* **179**, 587–599 (1996).

16. K. L. Johnson, K. Kendall and A. D. Roberts, *Proc. Roy. Soc.* **A324**, 301–320 (1971).
17. J. D. Green, M. T. McDermott and M. D. Porter, *J. Phys. Chem.* **97**, 10960–10965 (1995).
18. X. Y. Lin, F. Creuzet and H. Arribart, *J. Phys. Chem.* **99**, 7272–7276 (1995).
19. D. R. Lide (Ed.), in: *CRC Handbook of Chemistry and Physics*, 80th edn, pp. 6–147. CRC Press, Boca Raton, FL (1972).
20. T. J. Senden and C. J. Drummond, *Colloid. Surf. A* **94**, 29–51 (1995).
21. C. D. Bain, J. Evall and G. M. Whitesides, *J. Am. Chem. Soc.* **111**, 7155–7164 (1989).
22. V. M. Gun'ko, E. F. Voronin, E. M. Pakhlov, V. I. Zarko, V. V. Turov, N. V. Guzenko, R. Leboda and E. Chibowski, *Colloid. Surf. A* **166**, 187–201 (2000).
23. A. Noy, C. D. Frisbie, L. F. Rosznyi, M. S. Wrighton and C. M. Lieber, *J. Am. Chem. Soc.* **117**, 7943–7951 (1995).
24. K. Hu and A. J. Bard, *Langmuir* **13**, 5114–5119 (1997).
25. Z. Xu, Q. Liu and J. A. Finch, *Appl. Surf. Sci.* **120**, 269–278 (1997).

## Analysis of atomic force microscope pull-off forces for gold surfaces portraying nanoscale roughness and specific chemical functionality

GARTH W. TORMOEN<sup>1</sup>, JAROSLAW DRELICH<sup>1,\*</sup>  
and ELVIN R. BEACH, III<sup>2</sup>,

<sup>1</sup> *Department of Materials Science and Engineering, Michigan Technological University,  
Houghton, MI 49931-1295, USA*

<sup>2</sup> *Dow Chemical Company, Midland, MI 48667, USA*

**Abstract**—Pull-off force measurements were carried out between gold-coated atomic force microscope (AFM) cantilever tips modified with self-assembled monolayers (SAMs) of thiols and similar SAMs prepared on gold-coated silicon wafer surfaces in air with a relative humidity level less than 15%. The gold sputtered silicon wafer substrate formed a granular morphology with dimensions of 30–50 nm. The radii of curvatures for the two different cantilever tips used in this study were 32 nm and 53 nm. Pull-off force results were analyzed using the Derjaguin–Muller–Toporov (DMT) contact mechanics theory to determine both surface free energy ( $\gamma$ ) for OH, CH<sub>3</sub>, CO<sub>2</sub>H and NH<sub>2</sub>-terminated monolayers and the resultant work of adhesion ( $W_A$ ) between SAMs. The analysis took into account the coarse morphology of the gold coating. It was found that the  $\gamma$  and  $W_A$  values determined with the AFM technique approached similar thermodynamic parameters as calculated from the Lifshitz–van der Waals/Lewis acid–base interaction theory using advancing contact angles; however, the high ends of the adhesion force distributions significantly exceeded the predicted values. This discrepancy is discussed in terms of multiple contact points experienced by a probe penetrating into the grain structure of the gold coating.

**Keywords:** Adhesion; atomic force microscopy; chemical force microscopy; contact angles; pull-off forces; surface free energy; surface tension.

### 1. INTRODUCTION

Pull-off (adhesion) force measurements carried out by atomic force microscopy (AFM) techniques have shown promise for determining solid surface free energy ( $\gamma$ ) values at a sub-micrometer scale [1–22]. The mechanics of an AFM force mea-

---

\*To whom correspondence should be addressed. Tel.: (1-906) 487-2932. Fax: (1-906) 487-2934.  
E-mail: jwdrelic@mtu.edu

surement have been described extensively elsewhere [23] and are not discussed here. The calculation of  $\gamma$  from adhesion force measurements is quite straightforward and involves normalization of the measured adhesion forces by the contact area to yield the work of adhesion ( $W_A$ ). The inability to directly measure the contact area for most AFM measurements is circumvented by applying one of a number of theoretical contact mechanics models. The models derived by Derjaguin, Muller and Toporov (DMT model) for very small, rigid probes interacting with smooth, rigid substrates of low  $\gamma$  [24] and Johnson–Kendall–Roberts (JKR model) for larger probes in systems with rather high surface energies [25], are the most frequently used in the analysis of pull-off forces [17, 26]. According to these two models, the correlation between the measured adhesion force ( $F$ ) and the work of adhesion ( $W_A$ ) is as follows:

$$F = x\pi RW_A, \quad (1)$$

where the constant  $x$  equals 2 for the DMT model and 1.5 for the JKR model, and  $R$  is the probe apex radius of curvature. The work of adhesion per unit contact area is related to  $\gamma$  values by the Dupré equation [27]:

$$W_A = \gamma_{13} + \gamma_{23} - \gamma_{12}, \quad (2)$$

where  $\gamma_{13}$  is the solid 1–medium (substrate–air) interfacial energy,  $\gamma_{23}$  is the solid 2–medium (probe–air) interfacial energy and  $\gamma_{12}$  is the solid 1–solid 2 (substrate–probe) interfacial energy.

In reality, no surface is perfect, and representation of the true contact area between the AFM cantilever probe and a substrate by one of the contact mechanics model is difficult. Surface asperities of rough surfaces can either reduce or increase the contact area of interacting surfaces, and often various contact areas are encountered between successive measurements for the same system [28]. This phenomenon is evident in reporting data as a distribution of adhesion force values [28, 29]. Similarly, heterogeneities in surface composition lead to a collection of adhesion force values for a single system that actually encompasses a myriad of local surface compositions [30]. This is especially true for pull-off force measurements with submicroscopic probes, whose responses are sensitive to molecular and nanoscale variations in substrate composition, changes in molecular conformations, boundaries between molecular domains and compositional defects of the substrate. Contamination may also alter a solid's  $\gamma$ , and, therefore, affect the adhesion force measurement.

The measurement of adhesion force itself is not foolproof either. For measurements in ambient air, a number of precautions must be taken. Capillary bridging has been shown to significantly alter the magnitude of adhesion force measured [31, 32]. This is due to condensation of water in nanoscale separations formed around the probe–substrate contact area. The subsequent meniscus force often dominates the measured pull-off force. The size of the condensed water bridge and, therefore, the operating capillary forces, depend on the humidity level and the wetting characteris-

tic of the interacting surfaces. Operation in liquids or, conversely, dry environments, has been shown to reduce or eliminate the capillary bridging effect [4, 21, 31–36].

Additionally, contacting surfaces in dry atmospheres are prone to static charging for non-conducting surfaces. Static charges may result in an attractive or repulsive force between the probe and the substrate, depending upon charge similarity [37].

In this research, adhesion force measurements were conducted between standard isotropic AFM cantilever tips and surfaces portraying nanoscale roughness and heterogeneity, both coated with a gold film and then modified with self-assembled monolayers of thiols. Nanoscale imperfections of substrates are common features of real-world materials, and their effects on measured AFM pull-off forces require investigation.

## 2. EXPERIMENTAL

### 2.1. Reagents and materials

1-Hexadecanethiol, 16-mercaptohexadecanoic acid, and 11-mercapto-1-undecanol were obtained from Sigma-Aldrich (Milwaukee, WI, USA). 11-amino-1-undecanethiol hydrochloride was received from Dojindo Labs (Kumamoto, Japan). Thiols were dissolved in histological grade methanol to concentrations of 1 mM. Solutions were shaken for complete dissolution, except for 16-mercaptohexadecanoic acid, which needed to be ultrasonicated for 10 min. Solutions were sealed and stored at 5°C.

Pieces of silicon (Si) were cut from a single (100) wafer obtained from MEMC Corporation (St. Peters, MO, USA). Si pieces were held in a stream of air to remove all Si shards, and then inserted into a UV cleaner (Bioforce Labs, Ames, IA, USA) for 1 h. The Si pieces were next coated with 10–12 nm of Au in a Polaron SEM Limited 5000 type sputter coater. Coated pieces were reinserted into the UV cleaner for one hour, before immersion into the thiol solutions for 16 h. Upon removal from the solutions, the Si pieces were individually placed in a beaker containing methanol and ultrasonicated for 2 min to remove any secondary layers of thiol molecules. The Si pieces were then rinsed in methanol for 10 s, and dried at 70–80°C for 30 min prior to testing.

AFM cantilever tips were Olympus TR800PSA-1 contact mode cantilevers with spring constant calibrated at Asylum Research (Santa Barbara, CA, USA) using the thermal noise method. All probes were placed in the above stated UV cleaner for 2 h prior to immersion in thiol solutions for 16 h. Upon removal, all probes were given a methanol bath for one minute, and then dried in a 70–80°C oven for 30 min. Immediately after drying, pull-off force measurements were made to ensure only fresh thiol monolayers on the probe surface were tested. For the second round of functionalities, the initial SAMs were removed by placing again in the UV cleaner for 90 min. The cleaned probes were then placed in the thiol solutions following the procedures for the initial monolayer application. To ensure monolayer integrity, samples were kept sealed in dry conditions between monolayer applications.



In the next part of the report, the substrates (and probes) modified with the self-assembled monolayers of 1-hexadecanethiol, 16-mercaptohexadecanoic acid, 11-mercapto-1-undecanol and 11-amino-1-undecanethiol are referred to as CH<sub>3</sub>, CO<sub>2</sub>H, OH and NH<sub>2</sub> surfaces (probes), respectively.

## 2.2. Scanning electron microscopy (SEM) imaging

An FEI Dual-Beam Strata 235 Focused Ion Beam-Scanning Electron Microscope (FIB-SEM) was used for all SEM imaging. The DB235 is equipped with a field emission gun SEM. All images were captured using a 2 kV electron accelerating voltage, a 30  $\mu\text{m}$  objective aperture, spot size of 3 and working distance between 3–5 mm. Images were captured using the through-lens detector (TLD) in secondary electron mode. Ultra-high resolution (UHR) imaging mode available on this system was used to capture all images.

## 2.3. Blind tip reconstruction of the AFM tip

Upon completion of adhesion force measurements (described below), the cantilever tips were characterized using the technique of blind tip reconstruction (BTR). Here, each probe was scanned over a TGT01 grating (NT-MDT, Moscow, Russia). Scan sizes ranged from 2  $\mu\text{m} \times 2 \mu\text{m}$  to 5  $\mu\text{m} \times 5 \mu\text{m}$  in the lateral directions, with  $z$ -scale (height) of either 2  $\mu\text{m}$  or 3  $\mu\text{m}$ . A height image was captured, and next analyzed using Deconvo 1.1 software (Silicon-MDT, Moscow, Russia). This software performs a tip reconstruction algorithm according to the technique of Villarubia [38].

## 2.4. Tapping-mode AFM

Topographical images were obtained for each surface using the intermittent contact mode operation on a Digital Instruments Dimension 3000 AFM (Santa Barbara, CA, USA). 2  $\mu\text{m} \times 2 \mu\text{m}$  images with 256  $\times$  256 resolution were captured for each surface, using a scan rate of 1 Hz. All images showed a similar ‘coarse’ topography with characteristic 30–50 nm grains. Next, 2  $\mu\text{m} \times 2 \mu\text{m}$  images with 512  $\times$  512 resolution were obtained for surface asperity measurements at a scan rate of 0.75 Hz for the CH<sub>3</sub> surface. Since all surfaces showed similar topography at the 2  $\mu\text{m}$  scan size, the asperity data from the CH<sub>3</sub> surface were assumed for all surfaces tested.

## 2.5. Contact angle measurements and analysis

Advancing and receding contact angles were measured with a Krüss G10 contact angle goniometer. Three probe liquids with different surface tensions and surface tension components ((deionized water (15–18 M $\Omega$ ), ethylene glycol (99.9%, Fisher Scientific) and diiodomethane (99%, Sigma-Aldrich)), were used for these measurements. The contact angles were measured for at least 5 liquid drops having a base diameter from 6 to 10 mm. Measurements were carried out 10–20 s after

adding/withdrawing enough liquid to/from the drop in order to visually observe a change in the drop size, ensuring measurement of the drop's equilibrium shape. All measurements were conducted at room temperature, 20–22°C.

The surface free energy and surface free energy components of substrates were calculated using the Lifshitz–van der Waals/Lewis acid–base interaction model developed by van Oss, Chaudhury and Good [39, 40]. The model assumes that the surface free energy,  $\gamma$ , of a solid or a liquid can be divided into the Lifshitz–van der Waals surface free energy component ( $\gamma^{\text{LW}}$ ) and the acid–base component ( $\gamma^{\text{AB}}$ ), which is related to the acidic (electron acceptor) parameter ( $\gamma^-$ ), and the basic (electron donor) parameter ( $\gamma^+$ ), as:

$$\gamma_{\text{S}} = \gamma_{\text{S}}^{\text{LW}} + \gamma_{\text{S}}^{\text{AB}}, \quad (3)$$

$$\gamma_{\text{S}}^{\text{AB}} = 2\sqrt{\gamma_{\text{S}}^+ \gamma_{\text{S}}^-}. \quad (4)$$

The model also assumes that the interfacial free energy can be calculated based on the geometric mean approach:

$$\gamma_{\text{SL}} \cong (\sqrt{\gamma_{\text{S}}} - \sqrt{\gamma_{\text{L}}})^2. \quad (5)$$

Combining this equation with Young's equation results (equation (6)), which is commonly used to calculate the surface free energy and surface free energy components of a solid surface, based on contact angle measurements:

$$\gamma_{\text{LV}}(1 + \cos \theta) = 2\left(\sqrt{\gamma_{\text{S}}^{\text{LW}} \gamma_{\text{L}}^{\text{LW}}} + \sqrt{\gamma_{\text{S}}^+ \gamma_{\text{L}}^-} + \sqrt{\gamma_{\text{S}}^- \gamma_{\text{L}}^+}\right). \quad (6)$$

Equation (6) contains three unknowns ( $\gamma_{\text{S}}^{\text{LW}}$ ,  $\gamma_{\text{S}}^-$ ,  $\gamma_{\text{S}}^+$ ); therefore, three liquids of known components must be used for contact angle measurements. The measured contact angle ( $\theta$ ) for each liquid, along with its known surface tension components ( $\gamma_{\text{L}}^{\text{LW}}$ ,  $\gamma_{\text{L}}^-$ ,  $\gamma_{\text{L}}^+$ ) can be inserted into equation (6). The three equations may then be solved simultaneously to obtain values for the unknown surface free energy components of the measured solid surface. The liquids used in contact angle measurements and their surface tension components are shown in Table 1.

**Table 1.**

Surface tension components (in mN/m) of the liquids used in contact angle measurements

Liquid	$\gamma_{\text{L}}$	$\gamma_{\text{L}}^{\text{LW}}$	$\gamma_{\text{L}}^-$	$\gamma_{\text{L}}^+$
Diiodomethane	50.8	50.8	~0	0
Ethylene glycol	48.0	29.0	3.0	30.1
Water	72.8	21.8	25.5*	25.5*

\* Values assumed by van Oss, Chaudhury and Good.

## 2.6. Adhesion force measurements

This study presents pull-off force measurements performed in ambient air. Sub-15% relative humidity levels were maintained during measurements, well below the bulk water condensation level, and thus adsorbed water layer effects are considered secondary. Adhesion force measurements were performed on a Dimension 3000 AFM with a NanoScope IIIa controller (Digital Instruments, Santa Barbara, CA, USA). Pull-off force ( $F$ ) measurements were performed at a scan rate of 0.498 Hz, with a ramp size of 750 nm for cantilever A (spring constant  $k = 0.189$  N/m) and 350 nm for cantilever B ( $k = 0.691$  N/m), and captured with a resolution of 256 points/measurement. Ten random spots per surface, with ten measurements per spot, were captured for each tip-substrate system. The force measurements were then analyzed with SPIP software (Image Metrology, Lyngby, Denmark), which translates the force–distance data to force–load curves.

A Zerostat® 3 Anti-Static Instrument (Aldrich, Milwaukee, WI, USA), that produces a stream of positive and negative ions, was applied to all surfaces prior to adhesion force measurements. In addition, slow scan rates (0.5 Hz) and light loads ( $<20$  nN) were implemented to eliminate air damping of the cantilever, and to minimize probe deformation upon contact, respectively [17].

## 3. RESULTS AND DISCUSSION

### 3.1. Tip characterization

Representative Field Emission Gun (FEG)-SEM images of two gold-coated probes used in this study are shown in Fig. 1. It is apparent from these pictures that the two probes have different apex shapes and sizes. To estimate tip radius of curvature, a ‘zoomed-in’ section of each image that included the probe apex and scale bar was

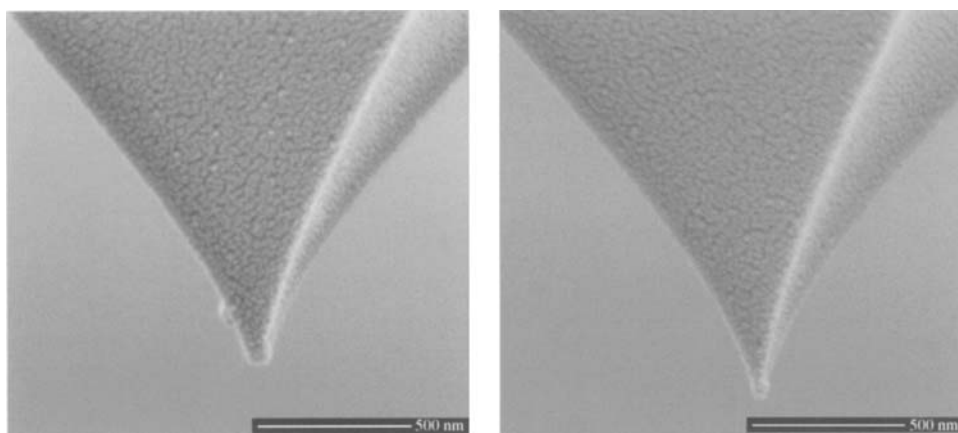


**Figure 1.** FEG-SEM images of probe tips used in adhesion force measurements. Tips are classified, from left to right, as A and B.

**Table 2.**

Estimates of tip radii from BTR and SEM techniques

Probe	Scan size ( $l \times w \times h$ ) ( $\mu\text{m}$ )	Tip radius determined by BTR (nm)	Tip radius determined from SEM micrographs (nm)
A	$5 \times 5 \times 2$	48.1	$52.5 \pm 4$
	$2 \times 2 \times 2$	59.5	
B	$5 \times 5 \times 2$	31.5	$32.0 \pm 2$
	$5 \times 5 \times 2$	35.3	

printed out. Next, three different circles were fitted to the image. These circles were then calibrated against the scale bar. The intermediate circle was selected to be the approximate tip radius, while the smaller and larger circles were used to create a range of radii values, which undeniably encompassed the true radius. This technique yielded the following tip radii:  $R = 52.5 \pm 4$  nm for A and  $R = 32.0 \pm 2$  nm for B (Table 2).

Upon completion of adhesion force measurements, the tips were re-characterized using the BTR technique. The results from this analysis are shown in Table 2.

As shown in Table 2, the BTR and SEM radii estimates correlate well. This suggests that the probe apex was not plastically deformed during adhesion force measurements. Therefore, normalization of adhesion force data presented in the next part of the paper was performed with the tip radii estimated from the FEG-SEM images.

### 3.2. Sample surface characterization: topographical analysis

A Tapping-Mode image of the  $\text{CH}_3$ -functionalized surface used in performing adhesion force measurements is shown in Fig. 2. Topographical analysis involved taking high magnification AFM Tapping-Mode images, and analyzing cross sections of these surfaces in order to obtain quantitative information on surface morphologies. Three 300-nm dimension images of the  $\text{CH}_3$  surface were captured, and three different cross sections were analyzed for each image yielding a total of nine cross sections for analysis of surface topography. A typical cross-section is shown in Fig. 3 along with a high magnification Tapping-Mode image representative of all surfaces used.

Each cross section produced several asperities that were clearly defined, and were subsequently used for analysis. To simplify the analysis, all asperities were assumed to be spherical caps. The average length ( $l$ ) of an asperity was measured, along with its height ( $h$ ), and the asperity radius ( $R$ ) was determined using the following equation:

$$R = (h^2 + (l/2)^2)/(2h). \quad (7)$$

The surfaces displayed an array of asperities with radii  $40 \pm 8$  nm. In addition, peak-to-peak distances were measured to be approx. 50 nm, and heights were  $< 10$  nm.

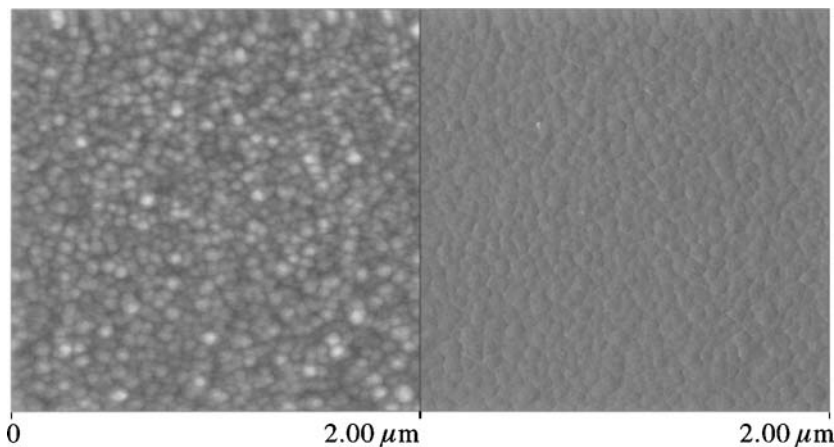


**Figure 2.** Tapping Mode image of a gold-coated Si wafer surface used in adhesion force measurements, which is representative of all samples tested.

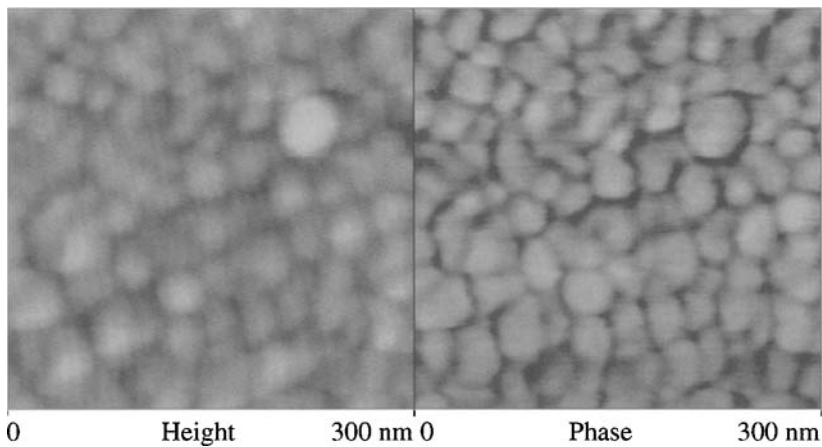


**Figure 3.** High-magnification Tapping Mode image (top) and cross-section of surface (bottom).

From the AFM images of substrates, the distance between gold islands was estimated to be  $<5$  nm. We expect that this spacing could be the area of silicon wafer surface that is uncoated with gold and, therefore, may remain unmodified with self-assembled monolayers and affect contact angles (see next section). The space between gold islands was assigned to be  $<10\%$  of the total surface area of the substrate.

### 3.3. Sample surface characterization: contact angle analysis

Advancing and receding contact angles measured on SAMs are shown in Table 3. Our samples had different wetting characteristics than previously reported for similar substrates [9, 41, 42]. For example, advancing water contact angles close to a zero value were reported for  $\text{CO}_2\text{H}$  terminated SAMs [41, 42], whereas the SAMs used in this study had advancing contact angles of about 84 degrees (Table 3). The cause(s) of such significant discrepancy between advancing contact angles is not clear to us. Possible causes include a limited purity of thiol commercial products used in this study, contamination of the substrates with air- and liquid-borne contaminants [43] and aging effects. Several repeated measurements with different samples provided reproducible data comparable to those shown in Table 3. Some of the results are also close to contact angle values that we reported earlier for  $\text{CO}_2\text{H}$  terminated SAMs prepared in Prof. Whitesides' laboratory at Harvard University [43]. A small difference is of no surprise and is attributed to a rough and heterogeneous nature of the samples studied in this program (see previous section). Because the major goal of this program is to compare the solid surface free energy values as determined by contact angle technique with those determined based on pull-off force measurements for substrates of different wetting characteristics, the discrepancy between wetting properties of our samples and similar substrates used by other groups should have no impact on the outcome of this study.

Contact angle hystereses as large as 51, 43 and 30 degrees for water, ethylene glycol and diiodomethane, respectively, were recorded (Table 3). Large hystereses indicate a rough and/or heterogeneous nature for the substrates. We expect that intergranular areas are probably not well modified with SAMs, and may be

**Table 3.**

Advancing (Adv.) and receding (Rec.) contact angles and contact angle hysteresis (Hyst.) measured on self-assembled monolayers

Surface	Contact angle (deg)								
	Water			Ethylene glycol			Diiodomethane		
	Adv.	Rec.	Hyst.	Adv.	Rec.	Hyst.	Adv.	Rec.	Hyst.
$\text{CH}_3$	$106.8 \pm 2.8$	$78.1 \pm 2.4$	28.7	$85.7 \pm 0.3$	$52.4 \pm 0.7$	33.3	$63.7 \pm 2.3$	$38.3 \pm 2.2$	25.4
$\text{CO}_2\text{H}$	$84.4 \pm 3.1$	$40.4 \pm 1.0$	44.0	$53.5 \pm 0.2$	$16.4 \pm 3.5$	37.1	$42.9 \pm 1.3$	$12.9 \pm 0.8$	30.0
OH	$65.4 \pm 2.8$	$28.6 \pm 1.3$	36.8	$41.7 \pm 1.5$	$7.6 \pm 1.9$	34.1	$18.5 \pm 2.8$	$7.8 \pm 0.8$	10.7
$\text{NH}_2$	$70.3 \pm 3.1$	$19.3 \pm 2.0$	51.0	$49.8 \pm 1.4$	$6.8 \pm 0.2$	43.0	$20.4 \pm 2.4$	$6.2 \pm 2.4$	14.2

**Table 4.**

Surface free energy and its components from contact angle analysis

Surface	Surface free energy components (mJ/m <sup>2</sup> )			Surface free energy (mJ/m <sup>2</sup> )
	$\gamma_S^{LW}$	$\gamma_S^+$	$\gamma_S^-$	$\gamma_S$
CH <sub>3</sub>	26.4	0.5*	1.1*	27.9 (26.4)*
CO <sub>2</sub> H	38.1	0.1	3.5	39.3
OH	48.2	0.3	18.8	52.9
NH <sub>2</sub>	47.7	0.8	17.1	55.0

\* Non-zero values for the electron-acceptor and electron-donor components of the CH<sub>3</sub> terminated SAM result from imperfect substrates used in this study. After assumption that  $\gamma_S^+ = \gamma_S^- = 0$ , the surface free energy is reduced to the value of the Lifshitz–van der Waals component.

responsible for pinning of the three-phase contact line during the contact angle measurements.

The surface free energy components for self-assembled monolayers used in this study, estimated through the Lifshitz–van der Waals/Lewis acid–base interaction model using average advancing contact angles from Table 3 are shown in Table 4.

Using the surface free energy and surface free energy components from Table 4, the adhesion values between symmetrical and asymmetrical self-assembled monolayers were estimated in terms of work of adhesion ( $W_A$ ) or work of cohesion ( $W_C$ ) using the following equations:

$$W_C = 2\gamma_S, \quad (8)$$

and

$$W_A = 2 \left( \sqrt{\gamma_S^{LW} \gamma_P^{LW}} + \sqrt{\gamma_S^+ \gamma_P^-} + \sqrt{\gamma_S^- \gamma_P^+} \right), \quad (9)$$

where subscripts S and P refer to SAMs on the surface and probe, respectively. The results of calculations are shown in Table 5 (last column).

### 3.4. Adhesion force measurements

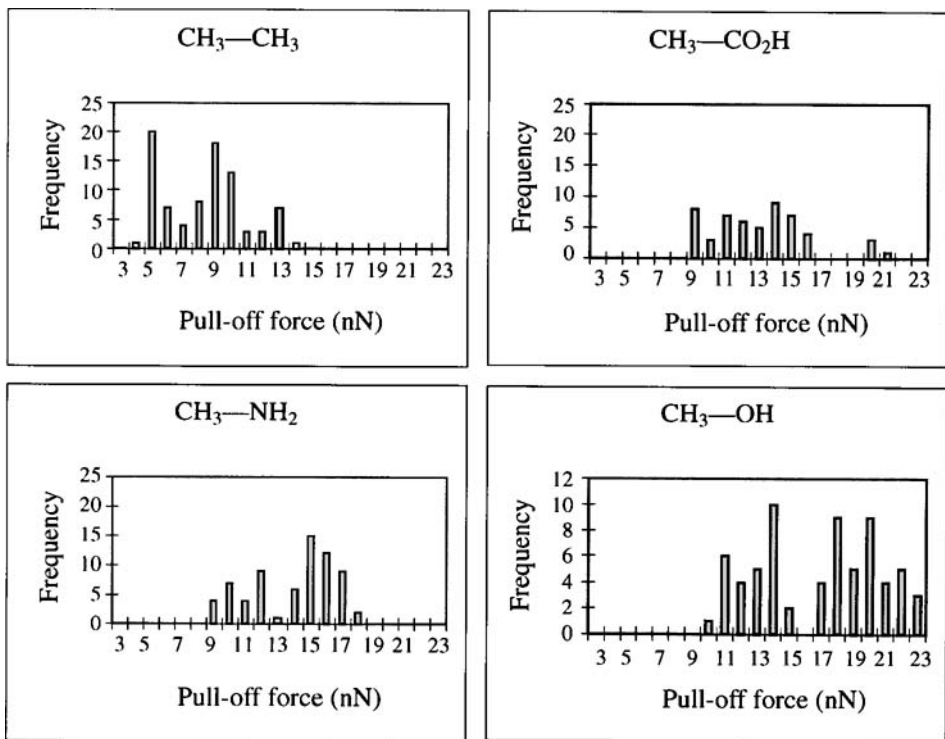
Histograms displaying adhesion forces ( $F$ ) for all systems tested are shown in Figs 4 to 6. Based on these results, the following observations were made:

- (1) A wide range of pull-off force (POF) values was recorded for each system.
- (2) The distribution of adhesion forces varied characteristically between the probes, as well as between surface functionalities.
- (3) Several systems showed multi-modal distributions, instead of commonly reported Gaussian distributions for adhesion force measurement studies.

The first step in data analysis was to normalize the adhesion force measurement values using the probe tip radius of curvature (ROC). For measurements on a flat

**Table 5.**Calculated  $W_A$  values from adhesion force (DMT) measurements and contact angle analysis (CAA)

System	Probe	$F$ (mean) (nN)	$F/R^*$ (N/m)	$W_A$ -DMT (mJ/m <sup>2</sup> )	$W_A$ -CAA (mJ/m <sup>2</sup> )
CH <sub>3</sub> -CH <sub>3</sub>	A	7.8	0.27-0.46	43.7-73.0	55.8 (52.8)*
CH <sub>3</sub> -CO <sub>2</sub> H	A	12.5	0.44-0.74	70.0-117.0	66.7
CH <sub>3</sub> -NH <sub>2</sub>	A	13.4	0.47-0.79	75.1-125.4	78.7
CH <sub>3</sub> -OH	A	16.3	0.57-0.96	91.3-152.6	78.6
OH-CH <sub>3</sub>	B	8.1	0.37-0.60	58.6-94.8	78.6
OH-CO <sub>2</sub> H	B	11.7	0.53-0.86	84.6-136.9	90.5
OH-NH <sub>2</sub>	B	14.2	0.65-1.04	102.7-166.2	108.2
OH-OH	B	15.1	0.69-1.11	109.2-176.7	105.8
NH <sub>2</sub> -CH <sub>3</sub>	B	10.2	0.46-0.75	73.8-127.5	78.7
NH <sub>2</sub> -CO <sub>2</sub> H	B	10.9	0.50-0.80	78.8-127.5	91.2
NH <sub>2</sub> -NH <sub>2</sub>	B	13	0.59-0.96	94.0-152.1	110.0
NH <sub>2</sub> -OH	B	14.8	0.67-1.09	107.1-173.2	108.2

\* After assumption that  $\gamma_S = \gamma_S^{LW}$ .**Figure 4.** Histograms of adhesion forces between different surfaces and probe A modified with CH<sub>3</sub> functionality.



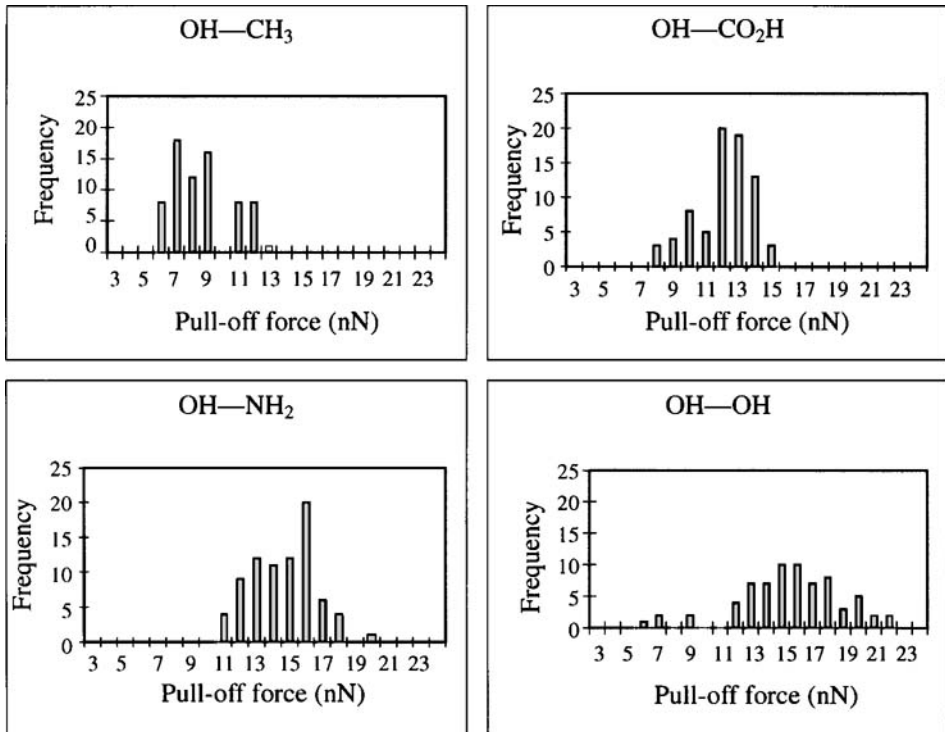


**Figure 5.** Histograms of adhesion forces between different surfaces and probe B modified with OH functionality.

surface, the tip's ROC is the correct normalizing factor, however, as can be seen in the three-dimensional representation of the CH<sub>3</sub> surface in Fig. 7, the tested sample surfaces were not flat. For sample systems displaying similar surface topographies, it is appropriate to normalize the adhesion data with the reduced radius,  $R^*$ :

$$R^* = R_{\text{tip}} R_{\text{surface}} / (R_{\text{tip}} + R_{\text{surface}}). \quad (10)$$

This technique produced the following reduced radii:  $R^* = 22.7 \pm 5.7$  nm for cantilever A and  $R^* = 17.8 \pm 4.2$  nm for cantilever B.

Table 5 displays the adhesion force measurement results normalized by  $R^*$ . Also, the values of work of adhesion ( $W_A$ ) were calculated using the DMT contact mechanics model. To validate the use of DMT mechanics to describe the adhesion contact in the AFM experiment, the Maugis parameter was calculated [44]. The dimensionless parameter ( $\lambda$ ) was calculated using the following formula [44]:

$$\lambda = 2.06/z_0(RW_A^2/\pi K^2)^{1/3}, \quad (11)$$

where  $z_0$  is the equilibrium separation distance between the probe and the substrate,  $R$  is the radius of the probe, and  $K$  is the reduced elastic modulus of the contacting system.

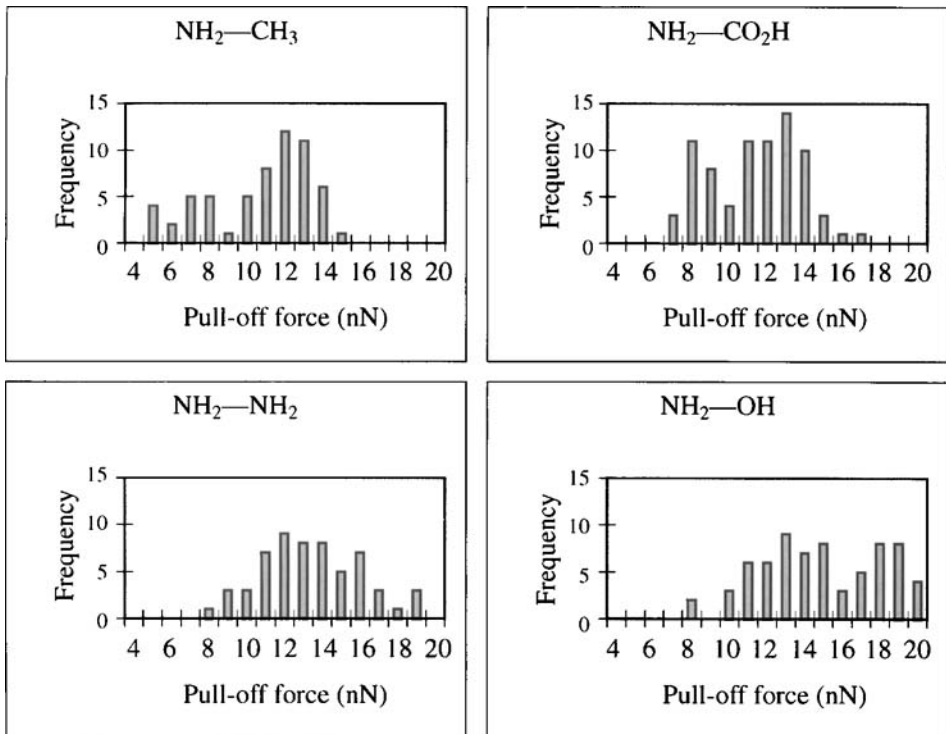


**Figure 6.** Histograms of adhesion forces between different surfaces and probe B modified with NH<sub>2</sub> functionality.

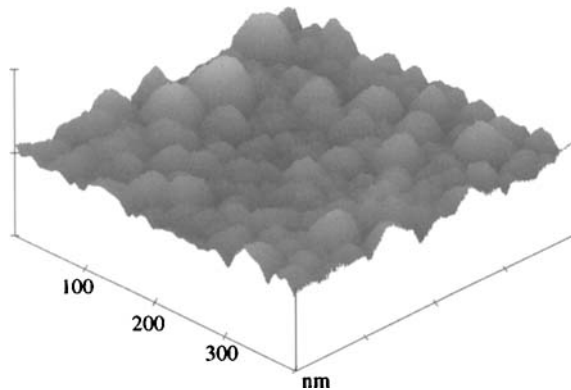


**Figure 7.** Three-dimensional representation of the CH<sub>3</sub> surface used in measuring adhesion forces ( $z$ -scale = 25 nm). Topography typical for all surfaces tested.

If  $\lambda < 0.1$ , DMT mechanics would apply. A large parameter,  $\lambda > 5$ , is indicative of JKR mechanics for describing the contact. In general, for low-energy (low  $W$ ) surfaces and rigid (high  $K$ ) materials, the lower the calculated parameter  $\lambda$ , the more accurate the DMT description of the deformation. To verify the use of DMT

mechanics in this work, the ‘least’ DMT-like system was analyzed. That is, of all surfaces tested in this research, the highest energy surface with the largest probe radius was calculated. Therefore, probe A ( $R = 53$  nm) with a  $\text{NH}_2$  functionality ( $W_A = 110$  mJ/m<sup>2</sup>) was analyzed. In order to simplify our analysis, deformation of gold instead of gold-monolayer was considered (see Ref. [17] for more detailed analysis of the gold–SAM system). The reduced elastic modulus ( $K$ ) for this system was calculated from elastic modulus ( $E = 78$  GPa) and Poisson’s ratio ( $\nu = 0.42$ ) values for gold taken from Callister [45] using the following equation for a symmetrical particle–surface contact.

$$1/K = 1.5(1 - \nu^2)/E. \quad (12)$$

Equation (12) yields  $K = 63.1$  GPa. The Maugis parameter was then calculated using  $z_0 = 0.2$  nm, and was found to be small ( $\lambda = 0.17$ ). The  $\lambda$  value is only slightly larger than 0.1, and therefore, we do not make any significant error selecting the DMT mechanics model to analysis of the cantilever tip–substrate systems used in this study. Note that in our previous paper [17] we assumed  $z_0$  incorrectly to be 2.5 nm instead of 0.2–0.4 nm. This mistake, however, does not influence any of the general conclusions reached in the previous study.

For reference, the theoretical  $W_A$  from contact angle analysis ( $W_A$ -CAA) is also included in the last column of Table 5. The results in Table 5 show that most of the calculated  $W_A$  values approach those predicted from advancing contact angle analysis. The only significant inconsistency was noted for the  $\text{CH}_3$ –OH system with cantilever A. However, it was also noted that much of the high-end distribution of  $W_A$  values determined through pull-off force measurements significantly exceeded the values calculated from the advancing contact angle data. These discrepancies suggest either limitations of the model used in this study, or effects of surface imperfections on pull-off forces. Although the inter-grain area of the substrates probably served as higher energy regions, the small dimensions of the crevices could not allow the cantilever tip to penetrate them deep enough to sense the high  $\gamma$  of unmodified silicon. Instead, penetration of the tip into crevices likely caused the formation of multiple contact points between the tip and the modified gold grains in pull-off force measurements. Figure 8 shows a schematic representation of how multiple contact points could be made between the probe and the spherical caps making up the topography of the sample surfaces.

Additional support for multiple contact points between the tip and the substrate is the multi-modal distributions of some of the pull-off forces shown in Figs 4–6. For example, consider the force data for the  $\text{CH}_3$ –OH system with probe A in Fig. 4. The data show two distinct frequencies at approx. 12 and 20 nN, likely resulting from one and two contact points, respectively. Similar bimodal force distributions can be distinguished for  $\text{CH}_3$ – $\text{NH}_2$ ,  $\text{NH}_2$ – $\text{CH}_3$ ,  $\text{NH}_2$ – $\text{CO}_2\text{H}$ , and  $\text{NH}_2$ –OH systems. Other data are less distinguishable regarding bi-modal distributions of the results.

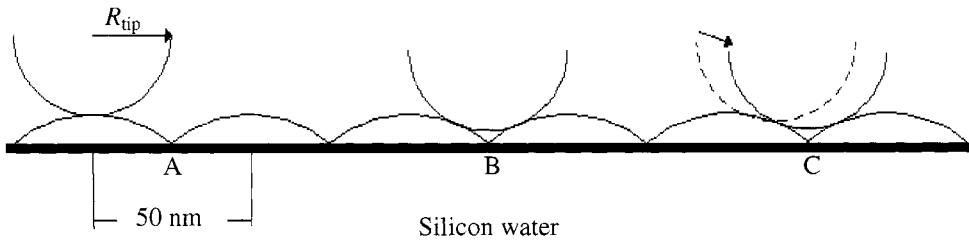


**Figure 8.** Schematic illustration of multiple contact scenarios during an adhesion force measurement. (A) a single contact point can be made, (B) multiple contact points can be obtained, and (C) shows how an initial single contact point may slide to yield multiple contact points.

The hypothesis developed from this research only suggests one possibility for the ranges of reported POF values in this and similar reports. In a work by McKendry *et al.* [46], POF distributions were examined for both single-crystal (atomically flat) gold substrates and polycrystalline gold substrates, similar to those studied in this paper. The surfaces were modified with a  $\text{CO}_2\text{H}$ -terminated SAM. For the single-crystal gold, a narrow distribution was reported for POF measurements, where the polycrystalline gold yielded a broader distribution of POF values, which also showed a multi-modal character. The authors hypothesized that different orientations of the SAM between gold domains for the polycrystalline substrate was the cause for the broad distribution of reported data. The authors also commented on the possibility for angled contacts on the polycrystalline surface to touch different areas of the probe, representing different contacting surfaces between successive measurements. This phenomenon would certainly have an effect on the spread of the POF values recorded in our study.

#### 4. CONCLUSIONS

Adhesion force values between isotropic gold-coated AFM probes and wafer surfaces sputtered with a coarse gold coating and subsequently modified with self-assembled monolayers of thiol molecules terminated with  $\text{CH}_3$ ,  $\text{CO}_2\text{H}$ ,  $\text{OH}$  and  $\text{NH}_2$  functionalities were measured. The magnitude and distribution characteristics of the measured adhesion forces varied between tips and surface functionalities. Also, as expected for sharp probes (approx. 60–100 nm in diameter) interacting with imperfect substrates having a rough topography with dimensions of asperities varying from about 30 to 50 nm, broad distributions of adhesion forces were measured for all systems. The adhesion force frequency distributions often had a bimodal character.

Work of adhesion values calculated from DMT contact mechanics theory approached those predicted from the Lifshitz–van der Waals/Lewis acid–base interaction theory calculated from the advancing contact angles. However, the largest

$W_A$  distribution values, determined with AFM, deviated up to almost 100% from the  $W_A$  values estimated from the wetting characteristics of the SAMs. The results along with the analysis of the substrate surface roughness characteristics indicate the possibility for multiple contact points of similar character, dependent on tip and surface asperity curvatures. If this hypothesis is correct, the resultant adhesion force measurements may, therefore, vary by over 100% for the same surface and still represent characteristic adhesion properties between the probe and sample surface. A study with model rough surfaces is under way and results will justify if indeed the roughness is the primary cause for a bimodal variation of the POF values. It may be infeasible for AFM studies to provide characteristic surface free energy characterizations through adhesion force measurements if geometrical configurations in the probe–rough surface interactions are not well defined.

### Acknowledgements

Financial support provided by the Petroleum Research Fund administrated by the American Chemical Society is gratefully acknowledged.

### REFERENCES

1. N. A. Burnham, D. D. Dominguez, R. L. Mowery and R. J. Colton, *Phys. Rev. Lett.* **64**, 1931–1934 (1990).
2. R. C. Thomas, J. E. Houston, R. M. Crooks, T. Kim and T. A. Michalske, *J. Am. Chem. Soc.* **117**, 3830–3834 (1995).
3. A. Noy, C. D. Frisbie, L. F. Rozsnyai, M. S. Wrighton and C. M. Lieber, *J. Am. Chem. Soc.* **117**, 7943–7951 (1995).
4. A. Noy, D. Vezenov and C. M. Lieber, *Ann. Rev. Mater. Sci.* **27**, 381–421 (1997).
5. T. Ito, M. Namba, P. Bühlmann and T. Umezawa, *Langmuir* **13**, 4323–4332 (1997).
6. E. W. Van der Vegte and G. Hadzioannou, *Langmuir* **13**, 4357–4368 (1997).
7. J. E. Houston, T. A. Michalske and R. M. Crooks, in: *Proc. 20th Ann. Meeting Adhesion Soc.*, pp. 31–33 (1997).
8. D. V. Vezenov, A. Noy and C. M. Lieber, in: *Proc. 20th Ann. Meeting Adhesion Soc.*, pp. 23–25 (1997).
9. V. V. Tsukruk and V. N. Bliznyuk, *Langmuir* **14**, 446–455 (1998).
10. A. E. Ghzaoui, *J. Appl. Phys.* **85**, 1231–1233 (1999).
11. S. C. Clear and P. F. Nealey, *J. Colloid Interface Sci.* **213**, 238–250 (1999).
12. H. Y. Nie, M. J. Walzak, B. Berno and N. S. McIntyre, *Langmuir* **15**, 6484–6489 (1999).
13. G. Papastavrou, S. Akari and H. Möhwald, *Europhys. Lett.* **52**, 551–556 (2000).
14. H. Skulason and C. D. Frisbie, *Langmuir* **16**, 6294–6297 (2000).
15. D. S. Rimai, D. J. Quesnel and A. A. Busnaina, *Colloids Surfaces A* **165**, 3–10 (2000).
16. C. Jacquot and J. Takadom, *J. Adhesion Sci. Technol.* **15**, 681–687 (2001).
17. E. R. Beach, G. W. Tormoen and J. Drelich, *J. Adhesion Sci. Technol.* **16**, 845–868 (2002).
18. M. Giesbers, M. Kleijn and M. A. Cohen Stuart, *J. Colloid Interface Sci.* **252**, 138–148 (2002).
19. P. Warszyński, G. Papastavrou, K.-D. Wantke and H. Möhwald, *Colloids Surfaces A* **214**, 61–75 (2003).
20. Y. Leng and S. Jiang, *J. Am. Chem. Soc.* **124**, 11764–11770 (2002).
21. R. Jones, H. M. Pollock, J. A. S. Cleaver and C. S. Hodges, *Langmuir* **18**, 8045–8055 (2002).

22. A. Relini, S. Sottini, S. Zuccotti, M. Bolognesi, A. Gliozzi and R. Rolandi, *Langmuir* **19**, 2908–2912 (2003).
23. C. B. Prater, P. G. Maivald, K. J. Kjoller and M. G. Heaton, *Probing Nano-Scale Forces with the Atomic Force Microscope*. Digital Instruments Application Note. [http://www.veeco.com/appnotes/AN08\\_ForceCurve.pdf](http://www.veeco.com/appnotes/AN08_ForceCurve.pdf)
24. B. V. Derjaguin, V. M. Muller and Yu. P. Toporov, *J. Colloid Interface Sci.* **53**, 314–326 (1975).
25. K. L. Johnson, K. Kendall and A. D. Roberts, *Proc. Royal Soc. London A* **324**, 301–313 (1971).
26. J. Nalaskowski, J. Drelich, J. Hupka and J. D. Miller, *Langmuir* **19**, 5311–5317 (2003).
27. J. Israelachvili, *Intermolecular and Surface Forces*, 2nd edn. Academic Press, London (1992).
28. E. R. Beach, G. W. Tormoen, J. Drelich and R. Han, *J. Colloid Interface Sci.* **247**, 84–99 (2002).
29. A. Méndez-Vilas, M. L. González-Martín, L. Labajos-Broncano and M. J. Nuevo, *J. Adhesion Sci. Technol.* **16**, 1737–1747 (2002).
30. J. Schneider, W. Barger and G. U. Lee, *Langmuir* **19**, 1899–1907 (2003).
31. E. Beach and J. Drelich, in: *Functional Fillers and Nanoscale Minerals*, J. J. Kellar, M. A. Herpfer and B. M. Moudgil (Eds), pp. 177–193. SME, Littleton, CO (2003).
32. M. He, A. Szuchmacher Blum, D. E. Aston and C. Buenviaje, *J. Chem. Phys.* **114**, 1355–1360 (2001).
33. N. A. Burnham and A. J. Kulik, in: *Handbook of Micro/Nano Tribology*, B. Bhushan (Ed.), 2nd edn, pp. 247–271. CRC Press, Boca Raton, FL (1999).
34. B. Cappella and G. Dietler, *Surface Sci. Reports* **34**, 1–104 (1999).
35. T. Stifter, O. Marti and B. Bhushan, *Phys. Rev. B* **62**, 667–673 (2000).
36. A. Ata, Y. I. Rabinovich and R. K. Singh, *J. Adhesion Sci. Technol.* **16**, 337–346 (2002).
37. F. Podczek, *Particle–Particle Adhesion in Pharmaceutical Powder Handling*. Imperial College Press, London (1998).
38. J. S. Villarubia, *J. Res. (NIST)* **102**, 425–453 (1997).
39. C. J. van Oss, R. J. Good and M. K. Chaudhury, *J. Colloid Interface Sci.* **111**, 378–390 (1986).
40. C. J. van Oss, *Interfacial Forces in Aqueous Media*. Marcel Dekker, New York, NY (1994).
41. C. D. Bain, E. B. Troughton, Y.-T. Tao, J. Evall, G. M. Whitesides and R. G. Nuzzo, *J. Am. Chem. Soc.* **111**, 321–335 (1989).
42. S. C. Clear and P. F. Nealy, *J. Colloid Interface Sci.* **213**, 238–250 (1999).
43. J. Drelich, J. L. Wilbur, J. D. Miller and G. M. Whitesides, *Langmuir* **12**, 1913–1922 (1996).
44. D. Maugis, *J. Colloid Interface Sci.* **150**, 243–269 (1991).
45. W. D. Callister, Jr., *Materials Science and Engineering: An Introduction*, 4th edn. John Wiley, New York, NY (1997).
46. R. McKendry, M.-E. Theoclitou, C. Abell and T. Rayment, *Langmuir* **14**, 2846–2849 (1998).

## A study of adhesion forces by atomic force microscopy

C. JACQUOT and J. TAKADOUM\*

*Laboratoire de Microanalyse des Surfaces, ENSMM, 26 Chemin de l'Épitaphe,  
25030 Besançon Cedex, France*

**Abstract**—An atomic force microscope (AFM) was used to investigate  $\text{Si}_3\text{N}_4$  tip interactions with various materials in four different liquid media (water, ethanol, ethylene glycol, and formamide). The adhesion forces calculated using surface energies and the values measured experimentally were compared. For all materials, the calculated adhesion force closely correlated with AFM measurements, except in water. In the case of water, the AFM experiments showed strong adhesion, whereas theoretically (van Oss–Chaudhury–Good model) repulsion is predicted. The difference observed is discussed in terms of the chemical interactions between  $\text{Si}_3\text{N}_4$  and water.

**Keywords:** Adhesion force; AFM; surface energy; electron-acceptor parameter; electron-donor parameter.

### 1. INTRODUCTION

High-resolution topographic images of a wide variety of material surfaces can be recorded with an atomic force microscope (AFM). These topographic images can be made with several modes of operation (contact mode AFM [1], non-contact mode AFM [2], and tapping mode AFM [3]).

An AFM can also be used to measure the forces between a tip attached to the cantilever and the surface of a sample in air or in an electrolyte. Previous studies have used the AFM to probe the interactions between surfaces in liquids. Weisenhorn *et al.* measured the adhesion forces between an insulating tip on an insulating sample (silicon nitride tip on mica) and a conducting tip on a conducting sample (tungsten carbide tip on a gold or platinum foil) in water, ethanol, and different concentrations of aqueous KCl solution [4]. Meurk *et al.* measured the attractive and repulsive interactions between inorganic materials in diiodomethane and 1-bromonaphthalene. They compared their measurements with theoretical

---

\*To whom correspondence should be addressed. Phone: 33-3-81-40-28-57. Fax: 33-3-81-40-28-52.  
E-mail: Jamal.Takadoun@ens2m.fr

Lifshitz calculations, taking into account the Hamaker constants for the different materials tested [5].

The aim of the work reported here was to investigate the adhesion between a  $\text{Si}_3\text{N}_4$  probe tip and several flat surfaces in different liquid media. We measured the pull-off force between the tip and the sample surface in water, ethanol, ethylene glycol, and formamide, by studying the force versus displacement curves. The adhesion forces were compared with the van der Waals forces calculated for a sphere approaching a flat surface. The Derjaguin–Muller–Toporov (DMT) adhesion theory was used to analyse the adhesion forces.

## 2. MATERIALS AND METHODS

The AFM experiments were conducted in four liquid media: water (Chromanorm, Prolabo, France), absolute ethanol (Prolabo, France), ethylene glycol (anhydrous, Aldrich), and formamide (Prolabo, France), using a  $\text{Si}_3\text{N}_4$  tip (Digital Instruments) attached to a V-shaped cantilever against five different flat surfaces.

The following materials were tested: Si(100), Si(111), silica glass, 3  $\mu\text{m}$  thick titanium nitride (TiN), and diamond-like carbon (DLC) films deposited, respectively, by physical vapor deposition and plasma-enhanced chemical vapor deposition on a steel substrate. The surface roughness of the samples was determined using the AFM by scanning over an area of 3  $\mu\text{m}^2$ . The mean surface roughness ( $R_a$ ) for the five samples is given in Table 1.

A Nanoscope III (Digital Instruments) including electronic control and software was used to record the force versus displacement curves, revealing the interaction between the surface of the sample and the tip. The principle of operation for the AFM is shown in Fig. 1. Each liquid was introduced between the sample and the glass cantilever mount with a micropipette. After each experiment, the sample and the glass cantilever mount were rinsed with absolute ethanol and dried in air. A new cantilever was used for each experiment.

The average radius  $R$  of the  $\text{Si}_3\text{N}_4$  tip was 200 nm and the spring constant  $k$  was 0.3 N/m. This value was determined from the tip dimensions and Young's modulus. The forces were estimated using a split photodiode to measure deflections

**Table 1.**  
Mean surface roughness ( $R_a$ ) for the five samples used

Sample	Roughness $R_a$ (nm)
Silica glass	1
TiN	13
DLC	12
Si(111)	0.5
Si(100)	0.7



of the cantilever. Extension–retraction cycles of the piezoelectric crystal in the Z direction and the corresponding response of the cantilever were recorded as force versus displacement. A low scan rate of 0.3 Hz was used for all cycles.

Figure 2 shows a force versus displacement curve for  $\text{Si}_3\text{N}_4/\text{Si}(100)$  in water. According to Ducker *et al.* [6], the surface of the sample is considered to be in contact with the tip when the output of the photodiode becomes a linear function of the sample displacement. The force is equal to zero when the displacement of the surface causes zero deflection of the cantilever.

For each experiment, the AFM software allows us to measure directly the pull-off force between the AFM tip and the sample surface, taking into account the cantilever stiffness. As shown in Fig. 2, the separation distance AB is a measure of the adhesion force.

For each specimen, 20 force curves were recorded in different areas on the surface, leading to the determination of the average adhesion force.

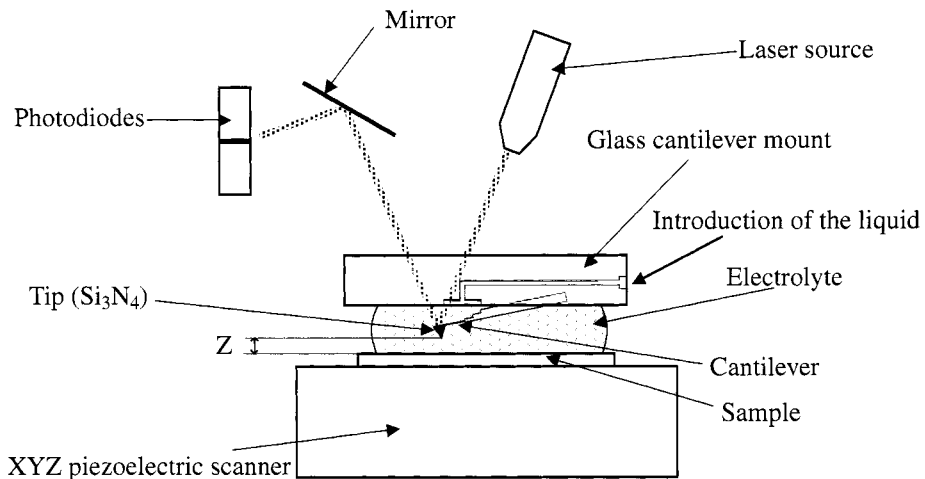


**Figure 1.** Schematic representation of the AFM operating principle.

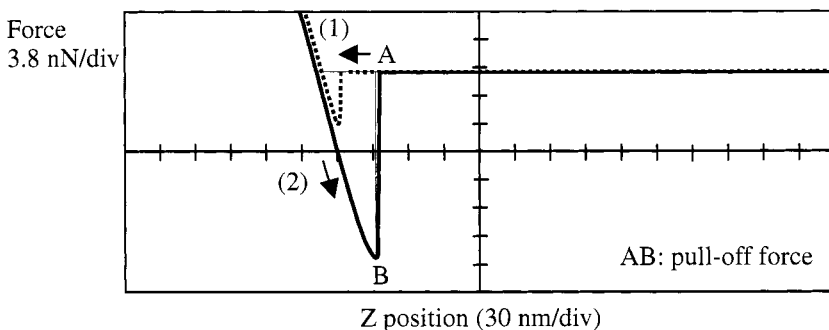


**Figure 2.** Experimental force versus displacement curve for  $\text{Si}_3\text{N}_4/\text{Si}(100)$  in water. Curve (1): piezoelectric crystal extension; curve (2): retraction.

**Table 2.**

Contact angles of different liquids on the materials tested

	Contact angle ( $\theta$ , degrees) in air				
	Bromonaphthalene	Diiodomethane	Water	Ethylene glycol	Formamide
Silica glass	$38.4 \pm 0.5$	$57.2 \pm 0.8$	$48.2 \pm 1.2$	$39.6 \pm 1.6$	$40.4 \pm 2.4$
TiN	$35.1 \pm 2.0$	$58.6 \pm 2.4$	$63.0 \pm 3.8$	$52.6 \pm 3.3$	$54.1 \pm 3.1$
DLC	$29.3 \pm 3.0$	$47.3 \pm 1.5$	$63.3 \pm 2.6$	$42.8 \pm 3.8$	$51.8 \pm 1.8$
Si(111)	$22.3 \pm 2.1$	$39.3 \pm 0.9$	$38.2 \pm 2.2$	$21.2 \pm 2.1$	$20.0 \pm 1.1$
Si(100)	$31.3 \pm 1.3$	$49.0 \pm 1.0$	$50.3 \pm 0.6$	$31.0 \pm 3.0$	$35.6 \pm 1.3$
Si <sub>3</sub> N <sub>4</sub>	$26.1 \pm 2.0$	$48.1 \pm 1.8$	$23.0 \pm 0.5$	$17.1 \pm 3.8$	$18.6 \pm 3.0$

According to the Derjaguin–Muller–Toporov (DMT) theory [7], the adhesion force measured by an AFM cantilever can be expressed by

$$F_{\text{ad}} = 2\pi R W_{132}, \quad (1)$$

where  $R$  is the tip radius and  $W_{132}$  is the work of adhesion per unit area between the Si<sub>3</sub>N<sub>4</sub> tip of the AFM (subscript 2), with the material tested (subscript 1), under a liquid (subscript 3).

Equation (1) is correct for contact between a hard sphere and a flat surface and it is applicable for a system with low adhesion and a small tip radius.  $W_{132}$  can be expressed as a function of the works of adhesion  $W_{12}$ ,  $W_{13}$ ,  $W_{23}$  and the cohesive energy  $W_{33}$  of the liquid:

$$W_{132} = W_{12} + W_{33} - W_{13} - W_{23}. \quad (2)$$

In agreement with the van Oss–Chaudhury–Good theory [8, 9], the work of adhesion  $W_{ij}$  is related to the different components of the surface energy as

$$W_{ij} = 2 \left( \sqrt{\gamma_i^{\text{LW}} \gamma_j^{\text{LW}}} + \sqrt{\gamma_i^+ \gamma_j^-} + \sqrt{\gamma_i^- \gamma_j^+} \right), \quad (3)$$

where  $\gamma^{\text{LW}}$  is the apolar (Lifshitz–van der Waals) surface energy component,  $\gamma^+$  is the electron-acceptor surface energy parameter, and  $\gamma^-$  is the electron-donor surface energy parameter.

The different surface energy components were measured with a video camera equipped with a contact angle goniometer. Five liquids were used (bromonaphthalene, diiodomethane, water, ethylene glycol, and formamide). The surface energy components for the Si<sub>3</sub>N<sub>4</sub> tip were determined experimentally with a Si<sub>3</sub>N<sub>4</sub> flat substrate. Table 2 shows the experimental values of the contact angles,  $\theta$ , for each material.

The surface energy components were obtained from the contact angle values according to the following expression:

$$\left( \gamma_1^{\text{LW}} + 2\sqrt{\gamma_1^+ \gamma_1^-} \right) (1 + \cos \theta) = 2 \left( \sqrt{\gamma_s^{\text{LW}} \gamma_1^{\text{LW}}} + \sqrt{\gamma_s^+ \gamma_1^-} + \sqrt{\gamma_s^- \gamma_1^+} \right). \quad (4)$$

**Table 3.**

Surface energy components of the materials and the liquid media used for the AFM and contact angle experiments. For liquids, the values of the surface energy components were taken from Ref. [10]; the other values were derived from the contact angle measurements

Materials and liquid	$\gamma^{LW}$ (mJ/m <sup>2</sup> )	$\gamma^+$ (mJ/m <sup>2</sup> )	$\gamma^-$ (mJ/m <sup>2</sup> )
Silica glass	32.9 ± 0.4	0.40 ± 0.30	37.4 ± 0.5
TiN	33.2 ± 0.4	0.04 ± 0.03	24.8 ± 0.5
DLC	37.4 ± 0.4	0.12 ± 0.10	19.7 ± 0.5
Si(111)	40.8 ± 0.4	0.47 ± 0.40	40.0 ± 0.5
Si(100)	36.5 ± 0.4	0.60 ± 0.50	29.0 ± 0.5
Si <sub>3</sub> N <sub>4</sub> (tip)	38.0 ± 0.4	0.47 ± 0.40	56.5 ± 0.5
Bromonaphthalene	44.4	0	0
Diiodomethane	50.8	0	0
Water	21.8	25.5	25.5
Ethylene glycol	29	47	1.92
Formamide	39	39.6	2.28
Ethanol	18.8	0.019	68

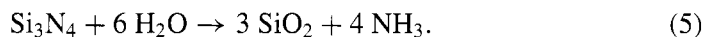
Table 3 shows the surface energy components deduced from the contact angle measurements. These values were obtained by solving the system of equations formed with expression (4) for the five liquids tested.

### 3. RESULTS AND DISCUSSION

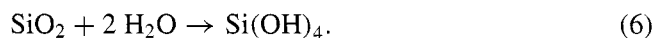
The results of the AFM experiments were averaged and are reported in Table 4. The adhesion force calculated using equation (1) is also reported in Table 4.

Table 4 shows that the adhesion forces deduced from equation (1) are quite similar to those measured experimentally for all the liquids except water. In the case of water, the experimental values indicate that strong adhesion takes place, whereas theoretically repulsion is predicted.

It is well known that silicon nitride interacts with water with the following reaction:



SiO<sub>2</sub> may also react with water to form Si(OH)<sub>4</sub>:



Reactions (5) and (6) show clearly that in water the chemical nature of the tip changes at the surface and, consequently, the surface energy components will change [SiO<sub>2</sub> and Si(OH)<sub>4</sub> instead of Si<sub>3</sub>N<sub>4</sub>]. In addition, NH<sub>3</sub> formed from reaction (5) can alter the water pH and thus the electron donor and acceptor surface energy parameters will also change.

**Table 4.**

Adhesion force calculated using equation (1) and measured experimentally between the  $\text{Si}_3\text{N}_4$  tip and the samples immersed in water, ethanol, ethylene glycol, and formamide

Specimen	Adhesion force calculated with equation (1) (nN)				Adhesion force measured by AFM (nN)			
	Water	Ethanol	Ethylene glycol	Formamide	Water	Ethanol	Ethylene glycol	Formamide
Silica glass	$-35.0 \pm 5$	$2.6 \pm 4$	$0.7 \pm 3$	$-2.3 \pm 3$	$38 \pm 4$	$3.5 \pm 2$	$14 \pm 3$	$1.6 \pm 2$
TiN	$-25.2 \pm 5$	$1.9 \pm 4$	$2.0 \pm 3$	$-1.2 \pm 3$	$23 \pm 4$	$3 \pm 2$	$3 \pm 2$	$2 \pm 2$
DLC	$-17.0 \pm 5$	$2.5 \pm 4$	$3.9 \pm 3$	$0.2 \pm 3$	$15 \pm 3$	$3 \pm 2$	$2.5 \pm 2$	$2 \pm 2$
Si(111)	$-34.5 \pm 5$	$5.7 \pm 4$	$1.7 \pm 3$	$-2.7 \pm 3$	$53 \pm 5$	$8 \pm 2$	$0.8 \pm 2$	$4 \pm 2$
Si(100)	$-25.0 \pm 5$	$2.7 \pm 4$	$2.8 \pm 3$	$-0.4 \pm 3$	$30 \pm 4$	$5 \pm 2$	$0 \pm 1$	$0 \pm 1$

The chemical modifications which take place either at the surface of the tip or in the liquid medium may explain the strong difference observed, in the case of water, between the adhesion forces measured and those deduced from the theory (Table 4).

#### 4. CONCLUSION

We have shown that it is possible to measure the adhesion forces between an AFM tip and several types of samples in various liquid media. It is possible to correlate these adhesion forces with the different surface energy components of liquid media and materials obtained from contact angle measurements.

This correlation is obtained using the van Oss–Chaudhury–Good theory, which determines in a given liquid medium the work of adhesion between the tip and the material tested, and the Derjaguin–Muller–Toporov theory, which relates the work of adhesion to the adhesion force.

In pure water, due to chemical reactions between the  $\text{Si}_3\text{N}_4$  tip and the water, a large difference between the calculated and measurement forces was observed.

The results presented in this preliminary work show that the van Oss–Chaudhury–Good model allows us to calculate easily the adhesion forces in liquid media. This study is currently continuing in our laboratory with other materials and liquid media.

#### REFERENCES

1. G. Binnig, C. F. Quate and C. Gerber, *Phys. Rev. Lett.* **56**, 930 (1986).
2. Y. Martin, C. C. Williams and H. K. Wickramasinghe, *J. Appl. Phys.* **61**, 4723 (1997).
3. C. A. J. Putman, K. O. Van der Werf, B. G. De Grooth, N. F. Van Hulst and J. Greve, *Appl. Phys. Lett.* **64**, 2454 (1984).
4. A. L. Weisenhorn, P. Maivald, H. J. Butt and P. K. Hansma, *Phys. Rev. B* **45**, 11226 (1992).
5. A. Meurk, P. F. Luckham and L. Bergstrom, *Langmuir* **13**, 3896 (1997).
6. W. A. Ducker, T. J. Senden and R. M. Pashley, *Langmuir* **8**, 1831 (1992).
7. B. V. Derjaguin, V. M. Muller and Yu. P. Toporov, *J. Colloid Interface Sci.* **53**, 314 (1975).
8. C. J. van Oss, M. K. Chaudhury and R. J. Good, *Adv. Colloid Interface Sci.* **28**, 35 (1987).
9. C. J. van Oss, M. K. Chaudhury and R. J. Good, *Chem. Rev.* **88**, 927 (1988).
10. C. J. van Oss, *Interfacial Forces in Aqueous Media*. Marcel Dekker, New York (1994).

# Roughness Effects in Adhesion Force Measurements

## Microparticle adhesion studies by atomic force microscopy

L. H. G. J. SEGEREN<sup>1,2</sup>, B. SIEBUM<sup>1</sup>, F. G. KARSSENBERG<sup>2</sup>,  
J. W. A. VAN DEN BERG<sup>1</sup> and G. J. VANC SO<sup>1,2,\*</sup>

<sup>1</sup> *Department of Materials Science and Technology of Polymers and MESA<sup>+</sup> Research Institute,  
University of Twente, P.O. Box 217, 7500 AE Enschede, The Netherlands*

<sup>2</sup> *Dutch Polymer Institute, P.O. Box 902, 5600 AX Eindhoven, The Netherlands*

**Abstract**—Atomic force microscopy (AFM) is one of the most flexible and simple techniques for probing surface interactions. This article reviews AFM studies on particle adhesion. Special attention is paid to the characterization of roughness and its effect on adhesion. This is of importance when comparing the measured adhesion forces to theoretical values, as the contact area is included in the contact mechanics theories. Even though adhesion models for time-independent adhesion are reasonably well developed, it remains difficult to connect the measured values to model predictions, especially because of the unknown value of the true contact area. The true area of contact depends on both the roughness of the probe as well as of the substrate. Our studies on the interactions between smooth silica particles, or rougher toner particles, and silicon substrates as a function of the surface roughness of the latter has shown the utility of AFM for measuring both roughness and particle adhesion.

**Keywords:** Particle adhesion; practical adhesion; particle attachment; roughness; toner; force microscopy; AFM.

### 1. INTRODUCTION

Physical interactions between macroscopic bodies or molecules are usually described by interaction energies. Another possibility is to express interactions in terms of forces, which can be measured directly, e.g. by sensitive force transducers in contact mechanics [1] or by the surface forces apparatus (SFA) [2]. The forces considered in this review act between a microparticle and a surface. The discussion will be confined to pairwise additive interatomic (intermolecular) forces, represented by the so-called Hamaker constant [3]. By adding up these pairwise interaction forces of interacting macroscopic bodies for various geometries, such as

---

\*To whom correspondence should be addressed. Phone: (+31) 53 489 2974. Fax: (+31) 53 489 3823. E-mail: g.j.vancso@ct.utwente.nl

flat parallel surfaces, spheres, cylinders, or the combinations of these geometries [2], the net interaction energies and the corresponding forces can be expressed in a closed form, using geometrical parameters such as radius, and separation distance. However, the form of the (intermolecular) potential and the number density of the interacting molecules (atoms) must be known.

Atomic force microscopy (AFM) was invented in the 1980s [4] as a technique for imaging surface topography from micrometer to nanometer length scales. At the same time, AFM allows one to measure forces, precisely and accurately, in gaseous and various liquid media, and at controlled temperatures. Thus, AFM is an excellent method to characterize surface topography of various surfaces *and* to quantitatively study microparticle adhesion forces for these surfaces. In this paper we first review the theoretical and experimental basics of this approach and then review selected papers to illustrate the added value of AFM investigations when applied to particle adhesion. We complement this review with original results obtained in our laboratory for the adhesion of photocopy toner and silica particles on silicon substrates.

AFM experiments are based on measuring the forces between a sharp pyramidal tip and the sample surface. The tip is attached to a cantilever spring and can be raster scanned over the sample surface using e.g. a piezoelectric scanner. Based on the interaction forces the topography can be imaged with an ultimate resolution in the sub-nanometer range as a function of lateral tip position. In adhesion measurements, the sample is moved by the scanner in the vertical direction (i.e. perpendicular to the sample surface) and the deflection (force) of the cantilever spring is monitored as a function of the piezoelectric actuator displacement (force–displacement curves). The details of the various imaging modes, structure visualization, surface properties by AFM, and examples of force–displacement studies have been reviewed in the literature [5–9]. We shall focus here on force–displacement studies using microparticles attached to AFM cantilever springs to illustrate the use of this approach to study particle adhesion.

As mentioned, force–displacement experiments carried out by an AFM monitor the deflection of the cantilever, and thus the force between the tip at the end of the cantilever as a function of the displacement of the surface in the sample-normal direction is measured [10]. The characteristic points of force–displacement curves, such as snap-on and pull-off upon approach and withdrawal, will be discussed later. The pull-off forces can be used for measuring adhesion. Various approaches have been developed to measure pull-off forces and calculate the work of adhesion with an AFM using microparticles, following the first report on AFM force–distance measurements using silica particles attached to AFM cantilevers in 1991 [11]. The knowledge of adhesion obtained in subsequent studies is very useful for numerous products and applications, for example adhesives, binders, coatings etc. [12], pharmaceuticals [13, 14], paint, and inks [15]. In particular, many industrial processes often deal with particle adhesion, such as in membrane



filtration [16], xerography [17, 18], and removal of particles in the semiconductor industry [19–22].

AFM measures adhesion over small contact areas with typical radii on the order of several tens of nanometers at the sample surface [12]. This advantage is important because local surface mechanical characteristics, such as hardness, and loss and storage moduli, often differ from those in the bulk, hence the AFM yields complementary surface-related information. A second advantage is the ability of AFM to determine both adhesion and topography, i.e. to observe local nanoscale variations in chemical and physical constitution (e.g. roughness) of the surfaces involved. Some experimental setups allow one to measure particle adhesion, as well as substrate topography, during the same experimental run [23].

## 2. THEORY

### 2.1. Different forms of adhesion

In AFM measurements based on the particle-on-cantilever technique one should distinguish between the concepts of ‘fundamental or thermodynamic adhesion’ and ‘practical adhesion’ [24]. Fundamental, or thermodynamic, adhesion refers to the force based on the thermodynamic work of adhesion between two ‘ideal’, smooth surfaces. Practical adhesion, or adherence, incorporates other factors as well, including the rate of applied force, viscous energy dissipation, mechanical properties of both contacting materials, and also roughness. In this paper we mainly focus on practical adhesion and analyze its dependence on surface roughness.

The aim of microparticle adhesion measurements by an AFM is to determine the ‘practical’ work of adhesion,  $W_{\text{adh}}$ , between the particle and the substrate, and to relate this quantity to molecular and material properties of the microparticle and the substrate, the so-called ‘fundamental’ work of adhesion,  $W$ . The adhesion quantity resulting from an AFM experiment is not immediately the value of  $W_{\text{adh}}$ , but rather the pull-off force,  $F_{\text{pull-off}}$  (Section 3.1.1). As its value is essentially a measure of practical adhesion, we define that the adhesion force  $F_{\text{adh}}$  between the microparticle and the substrate equals the pull-off force:

$$F_{\text{adh}} = F_{\text{pull-off}}. \quad (1)$$

The adhesion force is not related in a simple way to the practical work of adhesion: relating the one to the other involves the appropriate choice of one of the two following approximations as limiting cases [8]:

$$F_{\text{adh}} = 1.5\pi R W_{\text{adh}}, \quad (2)$$

for compliant materials with high surface energy, and large microparticles ( $R$  in the  $\mu\text{m}$  range) or

$$F_{\text{adh}} = 2\pi R W_{\text{adh}}, \quad (3)$$

for stiff materials with low surface energies, and small particles ( $R$  in the low nm range).

The first equation is derived from the contact mechanics theory developed in 1971 by Johnson, Kendall, and Roberts (JKR) [25], and equation (3) is the result of the contact mechanics theory by Derjaguin, Müller, and Toporov (DMT), published in 1975 [26]. In these theories no distinction is made between practical adhesion  $W_{\text{adh}}$  and fundamental adhesion  $W$ . The contacting bodies in both JKR and DMT theories are in adhesional contact, with interaction energy  $W$ , and are considered elastic. Viscoelasticity is not taken into account. This limits the applicability of  $W_{\text{adh}}$  derived from (2) or (3) for e.g. polymers.

The applicability of equation (3) to small particles with low surface energy can be illustrated by considering equation (3) as a special case of the ‘Derjaguin approximation’. This approximation results in an equation [27] for the van der Waals attraction between two hard macroscopic spheres, with radii  $R_1$  and  $R_2$  at a separation  $D$  ( $D \ll R_1$  and  $D \ll R_2$ ). The contacting area is assumed to be locally flat and the bodies under consideration interact with a van der Waals potential,  $W(D)$ . The Derjaguin approximation relates the force,  $F(D)$ , to the interaction free energy,  $W(D)$ :

$$F(D) = 2\pi W(D)R_1R_2/(R_1 + R_2). \quad (4)$$

$W(D)$  is defined as the interaction potential between two flat surfaces of the same material [8]. Note that (3) has the same form as (4) for  $R_2 \rightarrow \infty$ , and in this case  $W_{\text{adh}}$  in (3) is equal to the  $W(D)$  in (4).

Let us consider an example for the theoretical values of the interaction forces between an AFM-tip, and a silica sphere, as a function of distance from a silicon plane. The plane–plane potential is equal to  $-(A/(12\pi D^2))$  [2] which results in  $F(D) = -(AR)/(6D^2)$  in the Derjaguin approximation. The Hamaker constant  $A$  used for silicon nitride/silicon has a value of  $2.13 \times 10^{-19}$  J and for silica/silicon equals  $1.31 \times 10^{-19}$  J [28]. The corresponding force–distance relations are shown in Fig. 1.

Maugis showed that equations (2) and (3) could be considered as two extremes, so that they could be denoted as the JKR-limit and the DMT-limit, respectively [29]. He derived a general contact mechanics expression for the force  $F$  between an elastic sphere and an elastic flat substrate as a function of the contact area and the penetration depth. The value of the parameter  $\Lambda$ , which determines the choice between the DMT and JKR models, is relevant for the present discussion:

$$\Lambda = \frac{2.06}{z_0} \left( \frac{RW^2}{\pi K^2} \right)^{1/3}, \quad (5)$$

in which  $z_0$  is the equilibrium separation, 0.3 nm [28], and  $K$  is defined as:

$$\frac{1}{K} = \frac{3}{4} \left( \frac{1 - \nu_1^2}{E_1} + \frac{1 - \nu_2^2}{E_2} \right), \quad (6)$$

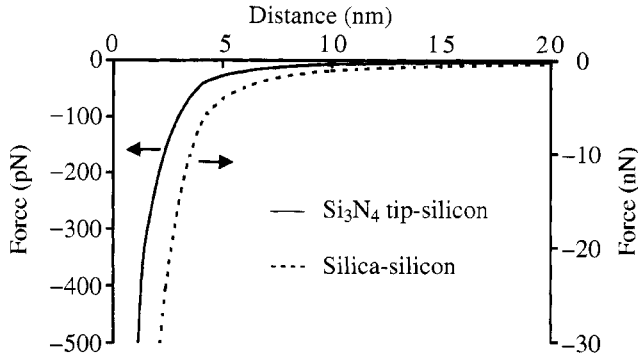


**Figure 1.** Theoretical force–distance curves for a silicon nitride tip ( $R = 20$  nm) and a silica sphere ( $5\text{ }\mu\text{m}$ ) on a plane silicon surface.

in which  $E$  is the Young's modulus and  $\nu$  the Poisson's ratio for the two contacting materials '1' and '2'.

In (5) we have used  $W$ , and not  $W_{\text{adh}}$ , since the original literature referred explicitly to the thermodynamic work of adhesion. The DMT- and JKR-limits are the  $\Lambda \rightarrow 0$  and  $\Lambda \rightarrow \infty$  limiting cases, respectively.

Johnson and Greenwood [30] considered another quantity, the so-called reduced load  $F_{\text{red}} = F/(\pi WR)$ , in order to compare forces between spheres having different radii, and constructed a map of  $F_{\text{red}}$  in terms of  $\Lambda$ . The AFM measurements usually fall in the Maugis region, though the DMT limit is a good approximation for  $10^{-2} < \Lambda < 10^{-1}$ , while the JKR limit can be used for  $\Lambda > 10$  [8]. Thus, by inserting appropriate estimates for  $W$ ,  $K$ , and  $R$  in (5), a choice between (2) and (3) can be made. For adhesional interactions between a small, hard, smooth sphere (e.g. the apex of an AFM tip) and a hard, smooth, flat (e.g. a clean Si surface of several  $\mu\text{m}^2$  in size) equation (3) should be used.

In standard AFM only pull-off forces are determined, and there is usually no direct way to deduce contact area or indentation depth. This means that one cannot benefit from the full Maugis expression (and its special cases: the JKR and the DMT theory), to extract (by curve fitting) a more reliable value for  $W_{\text{adh}}$  than that obtained from the AFM pull-off force only. For the same reason, the improvements of these theories [31–34] taking viscoelastic phenomena into account cannot directly be applied in AFM data analysis. The first experimental study relating contact area, deformation depth and adhesion force for viscoelastic bodies measured the changes of the shape of adhered particles using scanning electron microscopy [35]. Recently, such contact mechanics relations have been studied experimentally using AFM and other techniques for viscoelastic particle-substrate systems [32, 36, 37].

Studies by the surface force apparatus [38, 39], nano- and micrometer indentation tests [40], and particle deformation experiments [41] have shown that the practical adhesion of plastically or viscoelastically deformable macroscopic bodies, or particles, to a substrate exceeds the thermodynamic adhesion as measured by pull-

off experiments. The value of  $W_{\text{adh}}$  as determined from peel, shear tests etc. is also often much higher than the thermodynamic work of adhesion [42–44]. In fact  $W_{\text{adh}} = W_{\text{thermo}}(1 + \phi)$  with  $\phi$  as a dissipation function depending on test parameters (e.g. crack propagation, temperature and rate) and bulk parameters (e.g. thickness, interdigitation, and viscoelasticity). As far as we know, no systematic studies have been published regarding the practical adhesion of plastically or viscoelastically deformable particles attached to an AFM cantilever to substrates as a function of substrate hardness or roughness. One might anticipate from the evidence presented by the aforementioned experimental studies [32, 35–37] using different techniques that the pull-off force of such particles from soft surfaces would be at least equal to the value calculated from the thermodynamic adhesion. In such cases the substrate would ‘engulf’ the particle [41]. The same would hold true for the pull-off force of a plastically or viscoelastically deformable particle from a hard, rough, surface: the particle could fill the space between the microasperities of the rough surface. Such phenomena could explain why in some cases the practical adhesion values were found close to the thermodynamic adhesion, for instance in references [14, 18, 41, 45].

The discrepancy between  $W_{\text{adh}}$  and numerical results obtained from theoretical expressions for the fundamental adhesion  $W$  (for the systems and the materials studied up to now) is usually so large that it often does not make sense to apply the full Maugis, JKR or DMT equations to obtain the best possible values for  $W_{\text{adh}}$ . This discrepancy can be attributed not only to uncertainties in the choice of the model (i.e. equation (2) or (3)), or the applicability of (2) and (3) in view of plastic or viscoelastic effects, but also to surface roughness. The effects of surface roughness will be considered in more detail in Section 2.3 [38, 46, 47].

We conclude this section with a short review of the fundamental work of adhesion. According to Cappella and Dietler [8] there are several different theoretical expressions for the form of  $W(D)$  in the Derjaguin approximation, equation (4). Hence, it is possible to interpret the  $W_{\text{adh}}$  derived from (2) or (3) in terms of one of the theoretical expressions for  $W$  reviewed by Cappella and Dietler [8] e.g. expressions for the three types of van der Waals interactions, and for electrostatic interactions.

A simple expression often used for the thermodynamic work of adhesion  $W$  was proposed by Tabor [48].

$$W = 2(\gamma_1 \gamma_2)^{1/2}, \quad (7)$$

where  $\gamma_1$  represents the particle surface free energy, and  $\gamma_2$  that of the substrate.  $W$  can be separated into dispersion and acid–base components [49, 50]. Other authors split up  $W$  in dispersive (d), and polar (p) parts resulting in the adhesion force  $F_A$ , [51, 52].

$$F_A = 2\pi R W = 4\pi R (\gamma_{\text{probe}} \gamma_{\text{substrate}})^{1/2} = 4\pi R \{ (\gamma_{\text{probe}}^{\text{d}} \gamma_{\text{substrate}}^{\text{d}})^{1/2} + (\gamma_{\text{probe}}^{\text{p}} \gamma_{\text{substrate}}^{\text{p}})^{1/2} \}. \quad (8)$$

In several applications e.g. toner particles for xerographic purposes, electrostatic forces must also be considered. In these cases surface charges may be created by triboelectricity. Hays presented a so-called charge patch model for toner, which assumes a highly non-uniform surface charge distribution on irregularly-shaped toner caused by triboelectricity [53]. We do not go into detail here, but from practical and fundamental points of view one should be aware of this additional possible interaction.

## 2.2. Roughness

Various parameters related to roughness are frequently used for describing and explaining adhesion of particles to surfaces. The large number of parameters and functions available to describe roughness have not been extensively reviewed in the adhesion research literature. Hence we will summarize and describe the most important and frequently used roughness terminology. Applications and practical points of consideration are described in Section 4.1.

The adhesion theories as described in Section 2.1 do not explicitly take into account the roughness of either the probe or the substrate. Roughness can be defined as ‘the finer irregularities of the surface texture that usually result from the inherent action of the production process or material conditions’ [54]. Such definition of roughness suggests that roughness is an unintentionally present aspect of minor importance. Roughness, however, can also be ‘added’ and exploited. In some cases it can improve the material properties, e.g. by enhancing its coatability, or bonding to another surface.

For roughness on a larger scale, the term waviness is commonly used, but the transition to this regime is not sharply defined. Normally, roughness and waviness are both present. Which one is the more important depends on the application of interest.

The history of the quantification of roughness and waviness has led to the introduction of many different characteristic parameters. The choice for the most useful parameter depends on the purpose of the specific model. For microparticle adhesion, the scale of waviness is too large, as only finer irregularities will influence such adhesion.

The equations, which will be presented for the roughness parameters in this section, are given in discrete representation. These equations can be applied to 3D-images ( $x$ ,  $y$  and  $z(x, y)$ ) only, and are based on two references [54, 55]. Many of the parameters discussed are accessible by most commercial AFM software packages.

The *roughness average* or *mean-line-average* ( $R_a$ ) is defined as:

$$R_a = \frac{1}{MN} \sum_{i=1}^M \sum_{j=1}^N |z(i, j)|. \quad (9)$$

The roughness average represents the mean of the absolute values of the altitudes within a  $M \times N$  matrix containing height data,  $z(i, j)$ .

The *root mean square (RMS) roughness* ( $R_q$ ) of a surface represents the standard deviation of the heights:

$$R_q = \sqrt{\frac{1}{MN} \sum_{i=1}^M \sum_{j=1}^N (z(i, j))^2}. \quad (10)$$

Both  $R_a$  and  $R_q$  parameters depend on the reference plane as all the heights are relative. The extreme properties of a surface can be expressed in terms of the following two parameters,  $R_t$  and  $R_z$ . The *peak-valley height* ( $R_t$ ) is defined as the height difference with respect to a centerline between the highest,  $z_p$ , and lowest,  $z_v$ , pixels in the image, respectively:

$$R_t = z_p - z_v. \quad (11)$$

System errors — such as spikes — have an enormous influence on this roughness parameter and therefore the *ten point height* ( $R_z$ ) was introduced. This value is equal to the average height of the five highest local maxima and five lowest local minima.

$$R_z = \frac{\sum_{n=1}^5 |z_{p(n)}| + \sum_{n=1}^5 |z_{v(n)}|}{5}. \quad (12)$$

In a digitized image a local maximum is defined as a pixel surrounded by eight neighbor points which are all lower in height. A local minimum is the lowest point of a local  $3 \times 3$  submatrix.

The asymmetry of the height distribution histogram is expressed by the so-called *surface skewness* ( $R_{sk}$ ).

$$R_{sk} = \frac{1}{MN R_q^3} \sum_{i=1}^M \sum_{j=1}^N (z(i, j))^3. \quad (13)$$

This parameter was introduced to discriminate between different surfaces with the same  $R_a$  and  $R_q$  values. A zero value of the surface skewness indicates a symmetric height distribution, e.g. a Gaussian-like distribution.

The *surface kurtosis* ( $R_{ku}$ ) is equal to the normalized fourth moment of the height distribution.

$$R_{ku} = \frac{1}{MN R_q^4} \sum_{i=1}^M \sum_{j=1}^N (z(i, j))^4. \quad (14)$$

For Gaussian height distributions the surface kurtosis approaches 3.0 when the number of pixels is increasing. Skewness and kurtosis are introduced as they provide more insight in the distribution of height around the height average.

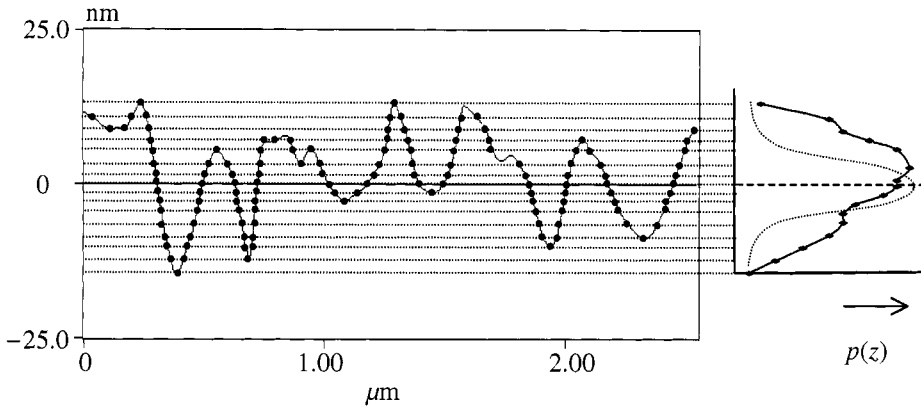


**Figure 2.** Height data of a cross section of  $\text{SF}_6$  plasma-etched silicon and the corresponding probability density function. The dotted line corresponds to a symmetrical Gaussian distribution.

The *probability function*  $P(z)$  associated with the surface height ( $z$ ) is defined as the fraction of the surface having height  $\leq z$ , with  $P(-\infty) = 0$  and  $P(\infty) = 1$  and is equal to the integral of the *probability density function*  $p(\xi)$ :

$$P(z) = \int_{-\infty}^z p(\xi) d\xi. \quad (15)$$

The value of  $p(\xi)$  represents the fraction of the surface with height between  $\xi$  and  $\xi + d\xi$ . A well-known example of a probability density function is the Gaussian distribution, which is defined in terms of the mean height  $\mu$ , and the standard deviation of the height values  $\sigma$ :

$$p(z) = \frac{1}{\sigma\sqrt{2\pi}} \exp \left\{ -\frac{(z - \mu)^2}{2\sigma^2} \right\}. \quad (16)$$

An illustration of a probability density function obtained from AFM height information is given in Fig. 2.

The probability and amplitude roughness parameters as defined in equations (9)–(16) become comparable if the original data  $z(i, j)$  are lowered by the average of the height values  $\bar{R}$  to arrive at a converted height data set  $z'(i, j)$ :

$$z'(i, j) = z(i, j) - \bar{R} = z(i, j) - \frac{1}{MN} \sum_{i=1}^M \sum_{j=1}^N z(i, j). \quad (17)$$

After this operation, each element in the  $M \times N$  height matrix in equation (17) will have a new value, and the following expressions hold:  $\bar{R} = \mu = 0$  (mean) and  $R_q = \sigma$  (standard deviation).

Another set of functions describing a surface profile result from *bearing analysis* [54] which is often used in AFM studies. An imaginary line parallel to the average is lowered in steps, starting at e.g. the highest point. The ratio of the cumulative intercept lengths compared to the total considered length is called the bearing length ratio. In the same way, the analysis can be carried out with a plane instead of a line. The determination of the bearing length for every height level results in a bearing area curve, also called the Abbott–Firestone curve [54]. The lowering of the line or plane can also be performed relative to the mean height.

The rate of change of the profile height is in mathematical terms equal to the slope gradient. The *root mean square slope* ( $\Delta_q$  or  $S_{dq}$ ) is the RMS-value of the surface slope.

$$\Delta_q = \sqrt{\frac{1}{(M-1)(N-1)} \sum_{i=2}^M \sum_{j=2}^N \left( \frac{z(i, j) - z(i-1, j)}{\delta x} \right)^2 + \left( \frac{z(i, j) - z(i, j-1)}{\delta y} \right)^2}. \quad (18)$$

In some cases it could even be useful to define a hybrid roughness parameter based on a second-order derivative, i.e. a Hessian instead of a gradient.

One of the most useful applications of Fourier transformations in the characterization of rough surfaces is called *power spectrum* or *area power spectral density* (APSD) *function*. This three-dimensional function is capable of identifying the nature of periodic features of the measured topography of a quadratic ( $M = N$ ) image with spacing intervals  $\delta x = \delta y$ . In a discrete form, it is defined as the square of the amplitude of the Fourier transform:

$$APSD(f_x, f_y) = \left( \frac{\delta x}{M} \right)^2 \left| \sum_{k=1}^M \sum_{j=1}^M z(j, k) \exp \{ -i2\pi [f_x(j-1) + f_y(k-1)]\delta x \} \right|^2. \quad (19)$$

Information about the characteristic wavelengths, amplitudes and phases can be extracted from the power spectra, even though the result of an APSD analysis is always an approximation, as the summation is finite. The Fourier-based roughness parameters are very useful for the determination of texture orientation and the (an)isotropic character of the surface.

In addition to the concepts and definitions described above, roughness parameters based on the *contact area* concept were also developed, for example, by Brown *et al.* in 1993 [56]. These authors covered rough, digitized surfaces with equilateral triangles of a certain dimension (patch size), counting the number of triangles needed for this operation. In such case, the slope of the total area as a function of the specific patch size is a fractal-like roughness parameter. An area-based roughness description provides complementary information to the study of adhesion, which strongly depends on contact area.



### 2.3. Adhesion as a function of topography

Several recent studies have attempted to incorporate roughness into adhesion theories. Rabinovich *et al.* recently considered the adhesion between a smooth particle and a rough surface [28, 57]. The authors model roughness as a distribution of closely packed hemispheres with equal radius (the asperity radius)  $r$  having their origin below the average surface, each protruding from this surface to a maximum peak height  $y_{\max}$ . According to the authors, two experimentally accessible roughness parameters, the root-mean-square roughness (equation (10)), and the mean peak-to-peak distance  $\lambda$ , determine the asperity radius  $r$  as follows:

$$r = \frac{\lambda^2}{58 \text{ rms}}. \quad (20)$$

It has been shown experimentally that the force to remove a smooth particle from a smooth flat substrate is higher than the force to remove it from a rough surface of the same chemical composition [28, 57]. Rabinovich *et al.* have calculated the value of this reduced force using the aforementioned asperity radius  $r$  [28, 57]. As a refinement, Rabinovich *et al.* describe a rough surface with two asperities, one with a short wavelength  $\lambda_2$  and a small asperity radius  $r_2$  superimposed over another surface with a long-range roughness  $\lambda_1$  and a large asperity radius  $r_1$ . The parameters  $\lambda_2$  and  $r_2$  could be considered as referring to ‘roughness’ whereas  $\lambda_1$  and  $r_1$  refer to ‘waviness’. The surface with roughness values on short- and long-length scales is characterized by  $\text{rms}_1$  and  $\text{rms}_2$ , respectively. The corresponding values must be determined, together with  $\lambda_1$  and  $\lambda_2$ , from experimental roughness profiles and peak-to-peak distances in order to estimate the reduced adhesion force. These parameters are schematically shown in Fig. 3.

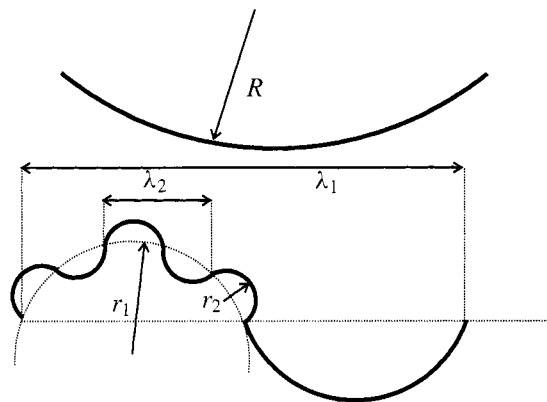


**Figure 3.** Important parameters used in the roughness model proposed by Rabinovich *et al.* [28, 57] for a smooth sphere in close contact with a rough substrate. The origins of the asperities are positioned below the respective average surfaces. The parameters  $\lambda_2$  and  $r_2$  indicate ‘roughness’ whereas  $\lambda_1$  and  $r_1$  refer to ‘waviness’.

As mentioned before, the adhesion force predicted by equation (2) or (3) for a rough substrate is higher than the anticipated value for smooth surfaces. The first term in equation (21), the equation proposed by Rabinovich *et al.* [28], takes this into account by introducing a Derjaguin-like factor (equation (4)) in the original JKR equation. This modified JKR-term describes the lowering of the direct contact interaction between the sphere with a radius  $R$  and the small asperities with radii  $r_2$ . The non-contact interactions between  $R$  and the surface close to and around the contacting asperities are included in the second term in equation (21) (described as a van der Waals interaction):

$$F_{\text{adh}} = \frac{3\pi W R r_2}{2(r_2 + R)} + \frac{(AR/6H_0^2)}{\left(1 + \frac{58R \text{ rms}_1}{\lambda_1^2}\right) \left(1 + \frac{1.82 \text{ rms}_2}{H_0}\right)^2}, \quad (21)$$

where  $A$  and  $H_0$  are van der Waals parameters (the Hamaker constant and the distance of closest approach, respectively).

Rabinovich *et al.* derived values for  $W$ , close to the theoretical value for some systems by fitting equation (21) to experimental data for  $F_{\text{adh}}$  and roughness data for model surfaces. The agreement was good, though the authors mention that it is difficult to obtain realistic and reliable values for the crucial parameter  $r_2$ . In addition to their ‘surface energy approach’ described by equation (21), the authors introduced the universal molecular ‘van der Waals approach’ as well, in order to have an expression for  $F_{\text{adh}}$  that does not depend on the thermodynamic macroscopic parameter  $W$ . It differs from equation (21) in the first term, with  $A/6H_0^2$  replacing  $(3/2)\pi W$ . In this approach, the model will be independent of an estimation, or experimental fit, of the value of  $W$ .

A smooth particle interacting with a rough flat surface was studied earlier by Fuller and Tabor [58], using Bowden and Tabor’s characterization of surface roughness by means of asperities [59]. Fuller and Tabor modelled the interaction between the smooth particle and the rough surface using the simpler case of a smooth flat surface in contact with a rough flat surface. As such, their theory can be seen as one of the precursors of the more general theory proposed by Rabinovich *et al.* [28, 57].

In contrast, Schaefer and coworkers [60, 61] studied the case of a rough particle interacting with a smooth flat surface. The absolute values of the measured pull-off forces were approximately fifty times smaller than expected from the JKR approximation (equation (2)) using the radius  $R$  of the particle. Using instead the roughness characteristic of the particle, i.e. its mean radius of asperity, the measured pull-off forces were only three times smaller than the value calculated from the JKR approximation.

Mizes [62] studied the adhesion of a toner used for xerographic applications by measuring forces between the toner particles (attached to the AFM cantilever) and various surfaces. Instead of measuring  $W_{\text{adh}}$ , the author measured adhesion forces and topography in one AFM run, and related the changes in adhesion to changes in

topography. This is an alternative useful approach to study  $W_{\text{adh}}$  and its comparison with a theoretical  $W$ . In our model study of the interaction between smooth silica particles and silicon substrates as a function of roughness (Section 6) we essentially follow Mizes' approach.

When the fluctuation in the value of the measured force is plotted as a function of the curvature variation of the surface topography of different materials, the slope of the least squares fit corresponds to the Derjaguin approximation ( $dF/F = R_{\text{tip}}dC$ , with surface curvature  $C = 1/R_{\text{surface}}$  in which the slope is the radius of the tip) [20]. This was observed experimentally for four different materials by Mizes [62]. The line through the data points  $dF/F$  (fluctuation in the local adhesion force) and  $dC$  (fluctuation in the surface curvature) passes through the origin, verifying that the adhesion should be uniform on a flat surface. The Derjaguin approximation, however, is valid only if no deformation occurs, neither plastic nor elastic. In conclusion, both the surface and the particle have to be sufficiently hard and the forces must be small to ensure the applicability of this model.

### 3. MEASURING PARTICLE ADHESION BY AFM AND OTHER METHODS

#### 3.1. AFM experimental procedures

**3.1.1. Force–displacement curve.** When an AFM is used to study adhesion, the force acting on the tip is usually monitored as a function of the relative displacement of the substrate. A schematic of a so-called force–displacement curve, capturing the main characteristics typically observed, is shown in Fig. 4.

At the point where the gradient of the intermolecular forces exceeds the spring constant, defined as  $dF/dz \geq k$  [63–65], the spring becomes unstable and the tip

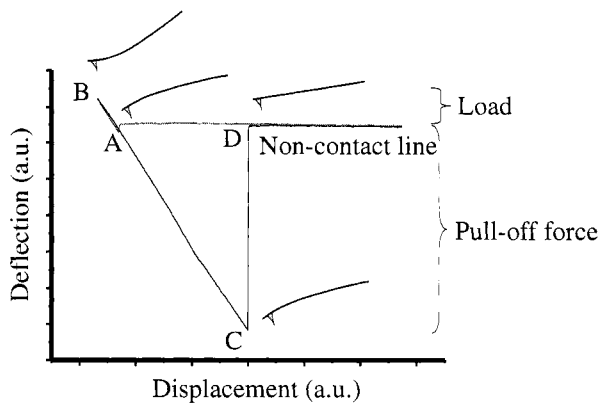


**Figure 4.** AFM force–displacement curve of an AFM silicon nitride tip on a gold substrate.

jumps in contact with the surface (snap-on shown by (A) in Fig. 4). The force acting on the tip, which deforms the spring, is increasing up to a certain value as the piezoelectric actuator continues moving upward. This upward movement is followed by the retraction of the sample in the force curve cycle. The tip stays in contact until the snap-off occurs when the spring constant exceeds the gradient of intermolecular forces between the tip and the sample. The force monitored during such an approach and retraction cycle, plotted as a function of the substrate position, is called a force–displacement curve. In contrast to force–displacement curves, which are usually measured in AFM experiments, force–distance curves show the forces as a function of the real separation distance between the tip and the sample. Force–displacement curve experiments have been described extensively in the literature [8]. We want to recapitulate that the vertical distance  $A-B$  indicates the ‘load’ and  $C-D$  the ‘pull-off force’. Willing *et al.* suggested using the substrate displacement  $A-D$  for the adhesion force determination [66].

The force acting on the AFM tip bends the cantilever which is usually measured by an optical lever technique. A laser light beam is usually used to measure cantilever bending. The position of the light beam reflected from the back of the cantilever is monitored by four closely spaced photodiodes. The four photodiode signals are fed into a differential amplifier and the two resulting signals are proportional to the bending in vertical and lateral directions. Subsequently, the vertical deflection signal must be related to the cantilever bending, which can be done by pressing the tip onto a stiff substrate. Assuming hard-wall contact, the bending of the cantilever follows exactly the displacement of the substrate. The degree of bending can now be expressed as calibrated length value (e.g. nanometers) and multiplication with the cantilever spring constant (assuming Hooke’s Law) results in the corresponding force.

The force–displacement curve shown in Fig. 4 represents an idealized situation for a smooth substrate interacting with the tip via short-range forces. Depending on the interactions between the tip and the substrate, more complicated force–displacement curves have been reported, for example, with a shoulder or with multiple snap-offs. The shoulder upon snap-off was found in force–displacement studies of AFM tips on compliant samples, e.g. [67]. Multiple snap-offs in force–displacement curves were first described in 1992 by Hoh *et al.* [68] for a silicon nitride tip on glass. Such multiple snap-offs were also observed in other systems including supramolecular host–guest interactions [69] and on latex particles [70]. If repulsive electrostatic forces are present, the force–displacement curve will have an upward curvature, as the distance between the tip and the substrate is reduced due to electrostatic repulsion (non-contact).

For the correct interpretation of a force–displacement curve the possible occurrence of two artifacts should be taken into account. The first one is the response of the piezoelectric device, which shows creep and hysteresis effects [71]. The second artifact is caused by the non-linear detector response [72].

*3.1.2. Force–volume surface scan.* Force–displacement experiments provide a quantitative measure for practical adhesion forces at a specific  $(x, y)$  coordinate over a small contact area (tip-sample contact). A so-called force–volume surface scan consists of a series of force–displacement experiments at given  $(x, y)$ -grid positions (pixels) on the surface of the substrate. For every chosen  $(x, y)$ -coordinate one or multiple force–displacement curves are stored. Parallel to this force–displacement data acquisition the accessory height profile is captured and stored. In force–volume analysis, the measured force values with respect to a reference force, obtained from the force–displacement curves, are plotted as a function of  $(x, y)$ . The qualitative and quantitative analyses of the force–displacement curves, in combination with the corresponding topographic data, offer the opportunity to correlate the measured adhesion forces with the surface structure, as will be described further in Section 5.

This AFM method requires long data acquisition times. Moreover, large data sets are generated, and consequently the lateral height resolution is limited by commercial software.

*3.1.3. Spring constant.* As mentioned in Section 3.1.1, the cantilever spring constant must be known in order to obtain adhesion force values. A good review on spring constant calibration procedures is given by Gibson *et al.* [73], hence we only briefly recapitulate here the main aspects of spring constant determination. If a microparticle is attached to the spring, it does not influence the spring stiffness (as long as the induced pre-bending is within the harmonic range), whereas the applied adhesive may have an influence if it spreads over the spring surface. Considering this, one should determine the spring constant after particle attachment. There are several methods to measure spring constants, including: (a) the thermal resonance method [74]; (b) via reference cantilevers [75]; (c) relating the cantilever resonance frequency to its dimensions and mass [76, 77]; and (d) fastening particles differing in mass and measuring the resonance frequency [78]. The last method is destructive and has the disadvantage that the amount of adhesive is unknown. However, this method cannot be used when the cantilever already contains a particle. The exact value of the spring constant is considered to be crucial for many AFM applications and new or modified approaches are still being discussed in literature e.g. the hydrodynamic drag method [79]. The value of the spring constant is considered to be the main source of uncertainty in the values of the measured forces [8, 23].

### *3.2. Attaching microparticles to AFM cantilevers with adhesives*

For microparticle adhesion studies by AFM the particles of interest must be attached to the AFM cantilever. Commercial cantilevers can be employed provided that the particle is larger than the tip. In other cases expensive tipless cantilevers should be used. Cantilevers with optimum spring constants must be chosen depending on the actual experiments in order to ensure a high signal-to-noise ratio in the force curves.

A reference for a detailed fastening procedure for a microparticle to an AFM cantilever is given by Claesson *et al.* [80]. Essentially, a micromanipulator, or an XYZ-translation stage, is used to attach particles to cantilevers. First, a small amount of heat-sensitive adhesive is warmed up. The end of a small wire is brought into contact with the adhesive by means of the XYZ-translation stage. The amount of adhesive is then reduced by bringing the end of the wire repeatedly into contact with a dry part of a microscope slide. In a subsequent step the adhesive is transferred to the end of a cantilever which is heated up on a hot plate. Finally, a second wire covered with particles to be fastened is brought into contact with the cantilever. Rolling of the particle in the adhesive should be prevented in this step and the cantilever should be removed from the hot plate immediately. These operations take place with a suitable optical microscope. A gentle nitrogen stream can be used to ensure that the particle is held by the adhesive, and not by e.g. electrostatic forces.

A different method, which we employed in our laboratory, is described by Raiteri *et al.* [81]. These authors place particles onto a microscope glass cover slip which is subsequently fixed in the focus of an optical microscope. The cantilever is brought into contact with the adhesive via an XYZ-translation stage. The adhesive is melted by passing a current through an aluminum wire, which was sputtered previously onto the glass cover slip. The molten adhesive is picked up by the cantilever and is smeared out on the glass, for the same reasons as described in the first method. Finally, the cantilever with a small amount of adhesive at the end is translated to one of the particles on the cover slip (i.e. a single, isolated particle). If the particles are heat sensitive, this method cannot be used. In this case, a two-component epoxy resin with a short curing time can be employed.

Depending on the particle and method used, several different adhesives are reported in the literature dating back to 1991 [18, 45, 60, 64, 82–84]. The choice of the adhesive depends, among other things, on the nature of particle material, the experimental medium (liquid or air), the cantilever material, and on the method of fastening.

### 3.3. Other methods for the determination of adhesion of particles

The force required to remove adhered particles from a substrate can be measured with other techniques, as well. Corresponding methods have been described by Mullins *et al.* [85], by Corn [86], and by van Duijvenbode and Koper [87]. In toner studies Mizes *et al.* have described and applied one of these methods, the centrifugal detachment method, in more detail [88]. The authors introduced also the electric field detachment method for particles for which electric charges e.g. caused by triboelectricity, play a role during transfer in xerographic applications [88].

At this point we would like to point out the differences between AFM studies on particle adhesion and the aforementioned methods. In the former approach the adhesion of one isolated particle to a substrate is studied, whereas the latter technique results in average values and distributions of adhesion values for a large number of particles. In addition, in the latter approach the particles are free to rotate

and find an equilibrium position, whereas they are fixed in AFM particle studies. Finally, the application of most of these other methods is limited to micrometer-size particles, since for smaller particles (typically  $< 5 \mu\text{m}$ ) the centrifugal force is not high enough to exceed the adhesion forces between the particles and the surface.

## 4. MEASURING ROUGHNESS BY AFM AND OTHER METHODS

### 4.1. Choice of roughness parameters

Topography is of importance in many research fields, e.g. mechanical, chemical and medical engineering, since it influences adhesion, wetting, mechanical properties, catalytic reactivity, etc. In the literature numerous roughness parameters have been reported [55]. Basically, these parameters simplify an extensive data set regarding height,  $z$ , as a function of lateral coordinates  $(x, y)$  to a few numbers or height distribution functions. This simplifies comparison and further calculations. The choice of a specific roughness parameter depends on the phenomenon studied, and on the applied model. In this review, we focus on roughness measured by AFM. It should be noted that roughness, in general, depends on the sampling area, i.e. it is scan-size dependent. In general, it approaches a plateau value as a function of increasing scan-size, depending on the nature of the roughness and the size of the scanning probe [89–92]. We cannot be conclusive about which roughness parameter is suitable for a given phenomenon. However, we can summarize the practical meaning of some roughness parameters as follows: the power spectral density is a measure of wavelengths of periodic features; the statistical roughness parameters such as root-mean-square roughness, skewness and kurtosis are measures of the height variation; and the autocovariance is a measure of the spatial correlation of heights [90].

AFM can not only provide adhesion forces, it also measures the surface topography in three dimensions. Naturally, an AFM as an imaging tool provides the  $z(x, y)$  height information, which is needed to calculate various roughness parameters. Another possibility is to use the full height data set in contact mechanics simulation studies [20] to avoid oversimplification and fully utilize the experimental data available.

### 4.2. Direct and inverse imaging

The local topography of a single particle can be analyzed by fixation of the particle onto an arbitrary substrate and by imaging using standard AFM procedures with a low contact force. Imaging can also be performed in an inverse manner by means of a so-called array of tips [93]. For inverse imaging a silicon substrate with sharp tips pointing upwards, placed next to each other in the  $x$ - and  $y$ -directions, is usually employed. Such tip arrays are usually used to check tip geometry and tip contamination. This non-destructive way can provide topographic information

about the particle fastened onto a cantilever. For example, Neto and Craig recently showed that the particle dimensions obtained by this method were comparable to SEM data [93]. Further examples will be shown in Section 6.4.

#### 4.3. Other methods for roughness determination

White-light interferometry uses the reflection and interference of light from a surface to produce a topographic surface profile [54, 94–96]. In the so-called phase measuring interferometric microscope, light is emitted from a source — through filters and stops — to a beam splitter. One part of the light directly goes to a camera, while another part is first transmitted to, and reflected by, the surface of interest. By moving the sample which is placed on a piezoelectric element in the  $z$ -direction while measuring the interference of light between these two beams, the topography of a surface can be determined with an area ranging from the micrometer to the millimeter range.

Some disadvantages of this technique should be mentioned here. To measure the roughness of a material that is poorly reflective, such as carbon-black filled rubber with a rough surface, the surface must be treated (e.g. by metal sputtering) to prevent complete absorption of the light. Another disadvantage of white light interferometry is found in the maximum detectable local slope of the height as a function of the  $(x, y)$ -position. When this slope of a local peak or valley in the surface profile passes a critical value, the light is no longer reflected back to the camera, i.e. certain regions will not contribute to the topographic data.

A so-called stylus profilometer can also be employed to profile a surface and is often used in mechanical engineering purposes [97]. It measures the displacement of a stylus, which has a radius typically between 1 and 20  $\mu\text{m}$ , while moving with respect to the substrate of interest within several  $\text{mm}^2$  [98].

### 5. REVIEW OF LITERATURE RESULTS ON PARTICLE ADHESION STUDIES BY AFM

During the last decade a considerable number of publications and review articles concerning particle adhesion studies by AFM have been published. The invention of attaching particles to AFM cantilevers [11] enabled the verification of the contact mechanics models [25, 26, 99] also by the use of AFM.

In 1991 Mizes and coworkers showed that an AFM could be used to map tip-surface adhesion as a function of substrate topography and material inhomogeneities [100]. Both topography and adhesion forces were determined with an AFM using cantilevers with an integrated  $\text{Si}_3\text{N}_4$  tip having a radius of curvature of the order of 10 nm (as determined with scanning electron microscopy (SEM)). Spatial correlations between areas differing in topography or material properties and adhesion forces were shown. In later work Mizes *et al.* also applied the technique of fastening particles to an AFM cantilever and determined both topography and



adhesion simultaneously [23, 84, 88, 101, 102]. The purpose of these studies was to gain insight into the effect of particle-surface contact area and the non-uniform particle charging on the adhesion of toner particles. Empirical relations were found between adhesion and treatment of substrate or toner, variations in chemical or physical surface constitution (e.g. roughness), contact number and loading force, contact time, and particle shape. For example, the authors found qualitative relations between: (i) the degree of modification of the toner surfaces using nanoparticles; and (ii) adhesion and xerographic performance. In some cases the Derjaguin approximation (Section 2.1, equation (4)) was applied to determine the work of adhesion  $W$ , and the results were usually not in agreement with what was expected theoretically due to roughness and other (e.g. electrostatic tribocharge) contributions.

A new method of scanning, the jump mode, has been recently described by Schaefer and Gomez [61]. Instead of saving all force and displacement data, only the height and pull-off force values are saved in this approach before moving to the next position in an AFM scan. The cantilever is moved to the next position when it is at the largest distance from the surface. This method allows ‘force–volume’ measurements, as mentioned in Section 3.1.2, without the need of extensive data storage, and can be applied for acquiring adhesion maps of surfaces within a short period of time.

Adhesion of highly charged toner particles can be studied by AFM [53, 88]. For AFM measurements in electric fields, a cantilever is employed which is not coated with a metallic layer (which is usually done to improve reflection of laser light in AFM measurements). However, the cantilever still remains slightly conductive because of adsorbed water [102]. Whenever measurements without charge were aimed at, Ott and Mizes used  $\alpha$ -radiation to remove residual charges [101]. To perform AFM measurements in an electric field, the AFM must be modified, i.e. by positioning a transparent electrode above the cantilever. An electric field is applied between this electrode and the conducting surface used in the experiment [102]. The effect of charge on particles has also been studied under moderate vacuum [103]. Gady *et al.* [103] studied the individual contributions of electrostatic and van der Waals forces on the interaction between a micrometer-sized polystyrene sphere and highly oriented pyrolytic graphite. It was found that for distances smaller than 30 nm the van der Waals interactions dominated, and for distances larger than 30 nm the interactions were controlled by electrostatic forces due to charges trapped on the polystyrene sphere.

A disadvantage of the AFM is that it studies just a single particle at a time, while the two detachment techniques, i.e. centrifugal and electric field detachments, provide information on a large amount of particles. Even though Mizes *et al.* showed that the strength of the expected electrostatic interaction between neighboring particles was limited, further research on the adhesion of larger numbers of particles is still essential [88]. Crowding of particles on a surface causes different adhesion behavior as recently studied with an AFM by Portigliatti

*et al.* [70]. The authors investigated the interaction between a tip and a single latex particle. It was discovered that upon retraction of the tip, viscoelastic and plastic energies were dissipated in a volume, which could extend to several neighboring particles, if present. If the stress cannot propagate to the neighboring particles, it is dissipated by pulling out filaments from the particle, which is indicated by multiple snap-offs in the force–displacement curves.

Another AFM application is the mapping of the chemical composition of a surface by high-resolution adhesion measurements [6, 104–108]. In our group Schönherr *et al.* recently investigated the spatial distribution of ionizable functional groups in surface treated polymers with chemically modified tips (‘chemical force microscopy’) [108]. Silicon nitride tips were coated with Ti and Au in high vacuum and functionalized with 11-hydroxyundecanol and used to probe oxyfluorinated polypropylene films in solution as a function of pH. The study of the distribution of pull-off forces revealed the sub-50 nm variation in chemical composition. In addition, the influence of roughness on adhesion of chemically treated polyethylene was studied. It was found that roughness introduced by using chromic acid treatment reversed the trends in pull-off forces, which was anticipated due to the introduction of polar groups at the polymer surface during the treatment [109].

Paiva *et al.* employed an AFM on a polymer blend and tracked both the lateral and vertical deflections of the cantilever in order to determine adhesion on ‘pressure sensitive adhesives’ [12]. The material showed areas with different local adhesion characteristics. Many commercial AFMs are equipped with a quadrant photodetector, which implies that lateral and vertical deflections of the cantilever are monitored. These AFMs can generate both AFM and lateral force microscopy (LFM) data simultaneously [110]. Paiva *et al.* in Ref. [12] combined LFM data with the force–displacement curves obtained by indentation and found that the higher, tackifier-rich, domains exhibited viscoelastic behavior and that the polymer matrix showed a viscous response [12].

The study by Hariadi *et al.* presents another application of LFM [111]. These authors did not attach a particle to an AFM cantilever, but used the tip of a scanning force microscope as a well-characterized single asperity to rub nanometer scale single crystal NaCl particles from a soda lime glass substrate under controlled atmospheres with known humidity. The strength of the particle-substrate bond decreased dramatically when the humidity was raised from low values. They interpreted their results in terms of detachment by ‘chemically assisted crack growth’ along the NaCl-glass interface. Rolling-friction forces between silica microspheres were also measured by combining AFM and optical microscopy. The forces were approximately 100 times lower than the corresponding adhesion forces [112].

Schaefer *et al.* measured the adhesion between glass, polystyrene, and tin particles of 8  $\mu\text{m}$  in diameter with a roughness of 10–20 nm on atomically smooth surfaces with an AFM under dry nitrogen gas [60]. The pull-off forces were about 50 times smaller than the theoretical values calculated with the JKR theory. A water

layer on the surfaces cannot be the origin of this difference, because the presence of water on a surface would increase adhesion via capillary forces. Oxidation of the surfaces or the presence of hydrocarbon contamination does not decrease adhesion enough to account for this difference. The roughness of the substrate was considered to account for the discrepancy between experimental and theoretical values. A quantitative assessment of the role of roughness was performed by using an estimated asperity radius in the calculations. After this adjustment, the adhesion values were about three times smaller, which were within the experimental error as stated by the authors. Thus, particle and substrate roughnesses cause practical adhesion values as measured by AFM to be lower than thermodynamic adhesion, but humidity and plastic or viscoelastic deformability tend to bring practical and fundamental adhesion closer together [18, 113].

The adhesion between microparticles (in general) attached onto an AFM cantilever and a liquid interface, e.g. oil/water or air/water, has been theoretically studied by Chan *et al.* [114]. Cooper *et al.* [115] employed AFM to monitor, *in situ*, variations in adhesional interactions induced by chemical reactions in  $\text{KNO}_3$  at the surfaces of a latex particle to a silicon substrate. In addition, these authors studied the role of surface morphology, and roughness in particular, on the adhesion. The interaction forces changed by nearly 90% by changes in the roughness of the silicon substrate. Sirghi *et al.* explained the increased adhesion at the concave parts of ridge walls by capillary and interfacial tension forces [116]. In ambient humidity conditions these two forces 'greatly affect' the tip to substrate adhesion in AFM measurements, due to the water meniscus in the tip-substrate region. These authors modeled the effect of surface asperities on the curvature of a symmetrical water meniscus. For the convex asperities a lower adhesion was found. Thus, asperities affect both van der Waals forces and capillary forces.

A promising approach to deal with the contact of rough surfaces is included in simulations as described by Bhushan [117] and for particles on surfaces, in particular, by Mizes *et al.* [84] and recently by Cooper *et al.* [20]. Cooper *et al.* extended the van der Waals approach by Rabinovich *et al.* [57] (discussed in Section 2.3) for modeling adhesion on rough surfaces [20]. Random surfaces were generated based upon parameters relevant in AFM studies including a common asperity shape for the surface with a given average asperity size, the variance in asperity size and the fractional coverage of the surface by asperities. The surfaces were brought together until a single contact point was reached. The asperities on the softer surface were compressed if an external load was present, until equilibrium was reached. With this model it was possible to calculate the average adhesion force and the adhesion force distribution for rough surfaces. The authors calculated the pull-off forces for polystyrene spheres on both rough and smooth silicon surfaces in water. These theoretical values were in good agreement with the range of experimental data [20].

# 6. A MODEL STUDY OF TONER AND SILICA PARTICLES ON SILICON SUBSTRATES

## 6.1. Introduction

In this section a typical case study, carried out in our laboratory, is presented to illustrate particle–surface adhesion. The dependence of microparticle adhesion on roughness was studied on a series of surfaces with increasing roughness. Silicon surfaces covered with a native oxide layer were chosen as model substrates, since the material is stiff and easy to roughen by etching. All AFM experiments were carried out using a NanoScope III system (Digital Instruments, Santa Barbara, CA, USA), equipped with a custom-made data acquisition and control unit, as described elsewhere [18]. A  $1 \times 1 \mu\text{m}^2$  ( $x, y$ )-calibration grid (Digital Instruments) was used as a substrate for the adhesion mapping. A silicon grating (TGT01, manufactured by NT-MDT Russia) was used to image particles. This array consists of reversed tips of  $0.7 \mu\text{m}$  height and the tip–tip spacing is about  $2 \mu\text{m}$ .

## 6.2. Preparation of silicon model surfaces

Oxygen plasma cleaned silicon samples were roughened by a controlled  $\text{SF}_6$  plasma treatment. The roughness of the samples (denoted as  $\text{SF}_6\text{s}0 \dots \text{SF}_6\text{s}10$ , in the text abbreviated as  $\text{s}0 \dots \text{s}10$ ) was measured by AFM (Table 1).

The surface treatment did not alter the surface chemistry significantly. X-ray photoelectron spectroscopy (XPS) showed that the atom% distribution was unchanged for the different samples. In order to reduce the hydrophilic character of oxidized silicon [118] and to exclude the possible influence of lateral chemical heterogeneity, silane surface modification was performed on the roughened substrates [119].

**Table 1.**

Total etching time and roughness data on the  $\text{SF}_6$  plasma etched silicon samples ( $10 \times 10 \mu\text{m}^2$  scan size). In the text the samples are denoted as  $\text{s}1 \dots \text{s}10$ . Since the etching was performed in steps and the individual periods in the plasma chamber influence the roughness, the individual etching times are reported as well

Sample	Etching time (s)	Cumulative time (s)	$R_q$ (nm)	$R_t$ (nm)
$\text{SF}_6\text{s}0$	0	0	0.10	1.0
$\text{SF}_6\text{s}1$	45	45	1.16	9.8
$\text{SF}_6\text{s}2$	45 + 75	120	1.44	11.5
$\text{SF}_6\text{s}3$	45 + 75 + 60	180	1.54	21.5
$\text{SF}_6\text{s}4$	45 + 75 + 60 + 75	255	2.77	38.7
$\text{SF}_6\text{s}5$	45 + 75 + 60 + 75 + 60	315	5.39	59.8
$\text{SF}_6\text{s}6$	45 + 75 + 60 + 75 + 60 + 75	390	12.00	119.3
$\text{SF}_6\text{s}7$	45 + 75 + 90	210	3.14	37.1
$\text{SF}_6\text{s}8$	45 + 75 + 90 + 105	315	10.53	89.9
$\text{SF}_6\text{s}9$	45 + 75 + 90 + 105 + 90	405	15.56	127.4
$\text{SF}_6\text{s}10$	45 + 75 + 90 + 105 + 90 + 105	510	17.27	159.4

The silicon surface was cleaned using a 'piranha' solution (a 2 : 1 mixture of 97% sulfuric acid and 30% hydrogen peroxide) for 10 min. (Caution: piranha reacts violently with organic compounds and should not be stored in closed containers.) Octadecyltrichlorosilane was used to form a monolayer on the surface according to the literature [120].

### 6.3. Adhesion measurement with an $\text{Si}_3\text{N}_4$ AFM tip

An ordinary  $\text{Si}_3\text{N}_4$  AFM tip can be seen as a small particle with a radius value equal to the tip radius, as the apex of the pyramidal tip can be approximated by a spherical shape. The influence of roughness and heterogeneity of the substrate on the adhesion of this 'particle' was studied by AFM (force–volume measurements).

**6.3.1. Topography and adhesion by AFM force–volume experiments.** Using a commercial  $\text{Si}_3\text{N}_4$  contact mode AFM tip, force–volume measurements were performed on three different samples. These samples included a  $1 \times 1 \mu\text{m}^2$  ( $x, y$ )-calibration grid, the sample s10b (etched silicon surface) and the sample s10a (silane treated silicon), respectively. The data were used as input for a custom-made Matlab program. The flow diagram of this program is shown in Fig. 5.

In the program, the height matrix is first filtered using a Gaussian filter and then used to determine the local second derivative in the  $x$ - and  $y$ -directions based on eight neighboring points (Fig. 6).

The derivative of point  $h_{i,j}$  is equal to the value of point  $h_{i+1,j}$  minus point  $h_{i-1,j}$  for the  $x$ -direction and is equal to the value of point  $h_{i,j+1}$  minus point  $h_{i,j-1}$  for the

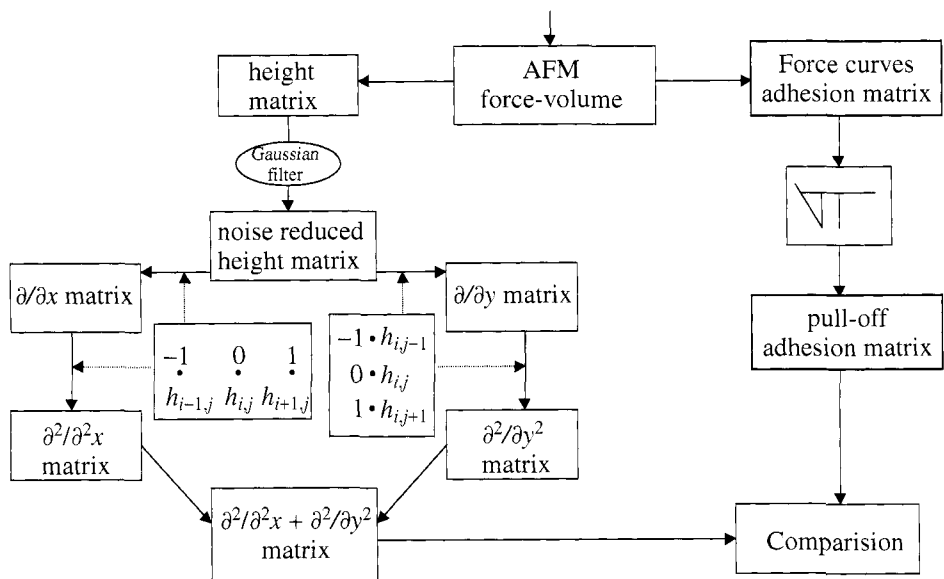


**Figure 5.** Flow diagram of the custom-made Matlab program to calculate the first and second derivatives of height profiles.

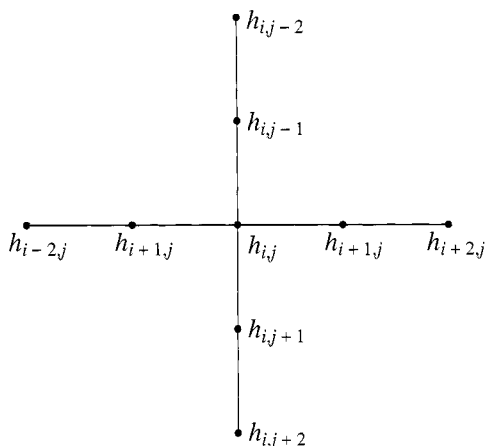


**Figure 6.** The eight points used for the determination of the second derivatives in the  $x$  and  $y$  directions.

$y$ -direction. Here it is not necessary to divide by two times the step-size in the  $x$ - and  $y$ -directions, respectively, since these are both constant and only influence correlations by a fixed factor. The first derivative is constructed from its four and the second derivative from its eight neighboring points. The pull-off force was now compared with the roughness, represented by the second partial derivative of the local height matrix with respect to  $x$  and  $y$ , respectively ( $\partial^2/\partial x^2 + \partial^2/\partial y^2$ ). Every individual value  $(i, j)$  in the pull-off force matrix was plotted as a function of its respective value in the second derivative of the height matrix. The results are shown in Fig. 7.

**6.3.2. Discussion.** For the hydrophobized sample s10a, a correlation between the second derivative and the tip adhesion was found. If the second derivative of the local height increases from the negative (peaks) to the positive (valleys) regime, the adhesion increases. The other two samples, i.e. the calibration grid and sample s10b, do not show such a correlation. These observations could be explained by the heterogeneous character of these surfaces. Locally, the adhesion of the tip is influenced by both the roughness and the chemical nature, but in the case of sample s10a the latter is uniform all over the surface, as it is functionalized. All three surfaces show a relatively large percentage of flat regimes, as the density of the points with a second derivative equal to zero is high.

#### 6.4. Toner and silica particles

The influence of roughness on the adhesion of microparticles was investigated by AFM, using the above mentioned silicon surfaces as substrates with different surface roughnesses. Two different kinds of particles were selected for this study. First, toner particles were studied. These particles consist of a polyester matrix filled with magnetic iron-containing particles. Second, silica particles were investigated because of their smooth surface. Commercial contact mode cantilevers were altered

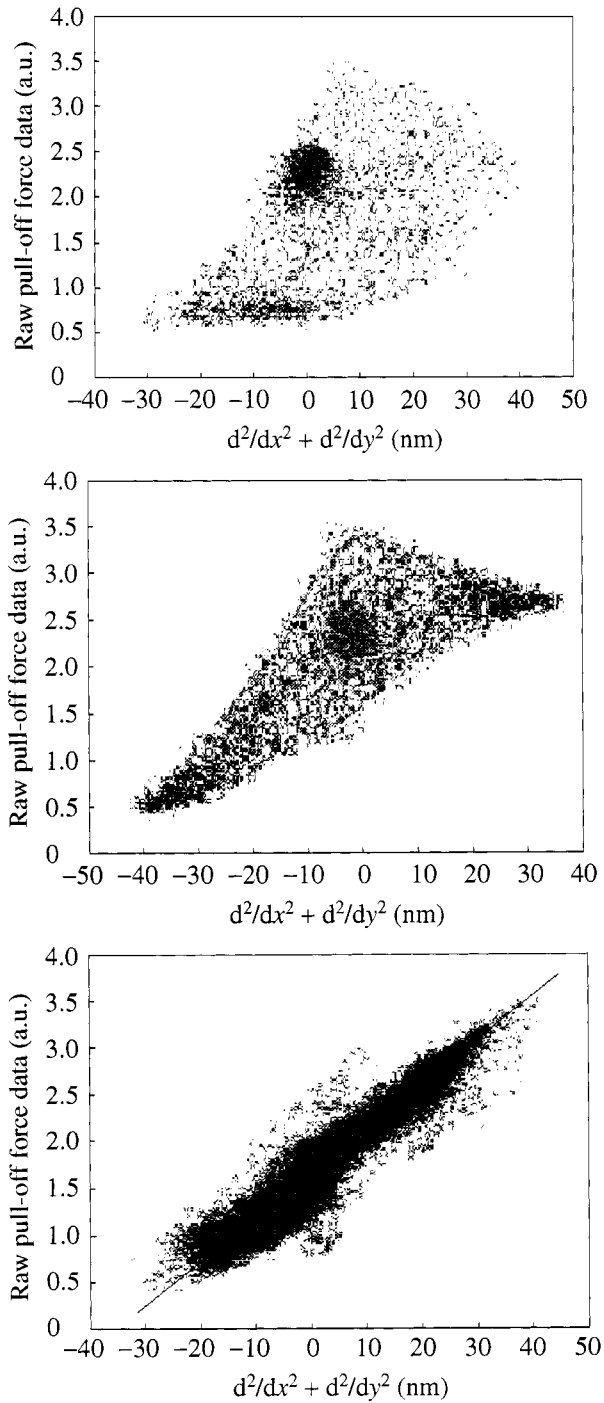


**Figure 7.** Relationships between adhesion (y-axis) and the second derivative (x-axis) for the grid (top), sample s10b (middle) and sample s10a (bottom).

by fastening toner particles next to the pyramidal tip at the end of the cantilevers, according to the method described in Section 3.2. Since the silica particles were as small or smaller than the tip-height ( $\sim 3\text{ }\mu\text{m}$ ), tipless cantilevers were used. A scanning electron micrograph of a toner particle attached to an AFM contact mode cantilever is shown in Fig. 8.

First, the roughness of the particles was determined. In Fig. 9a and b the local topographies of a smooth silica particle and a rough F10 toner particle are shown, respectively, as obtained from direct imaging by AFM in the contact mode. The top parts of the images exhibit the actual particle topography, and the bottom parts correspond to surfaces after removing the sphere curvature.

The values of the radii of the toner and silica particles were 7.8 and 2.5  $\mu\text{m}$ , respectively, as determined from the analysis of the topographic data obtained from AFM. In order to determine the roughness parameters, first the curvature of the sphere must be excluded. The simplest way to perform this specific operation is by using the two-dimensional second-order flattening procedure, which is available in the commercial AFM software used (Digital Instruments, Santa Barbara, CA, USA).

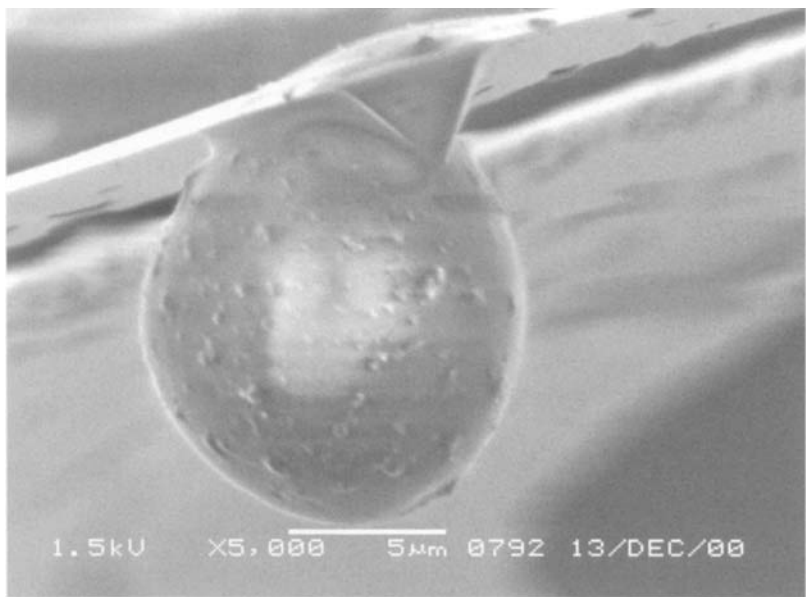


**Figure 8.** Scanning electron micrograph of a toner particle fastened onto an AFM contact mode cantilever.

**Table 2.**  
 $R_q$  and  $R_t$  roughness parameters of a silica and a toner particle

Particle	Particle radius ( $\mu\text{m}$ )	Scan size (nm)	$R_q$ (nm)	$R_t$ (nm)
Toner	7.8	2500	4.7	50
Silica	2.5	350	0.18	2.3



This procedure calculates a polynomial least-squares fit in the  $x$ - and  $y$ -directions. After performing this operation, the curved backgrounds of the images change to flat surfaces (see Fig. 9). The  $R_q$  and  $R_t$  roughness parameters were calculated and are reported in Table 2.

In Fig. 10 silica particles are depicted as measured with an array of sharp tips as a substrate. The data obtained from this image can be used as an alternative way

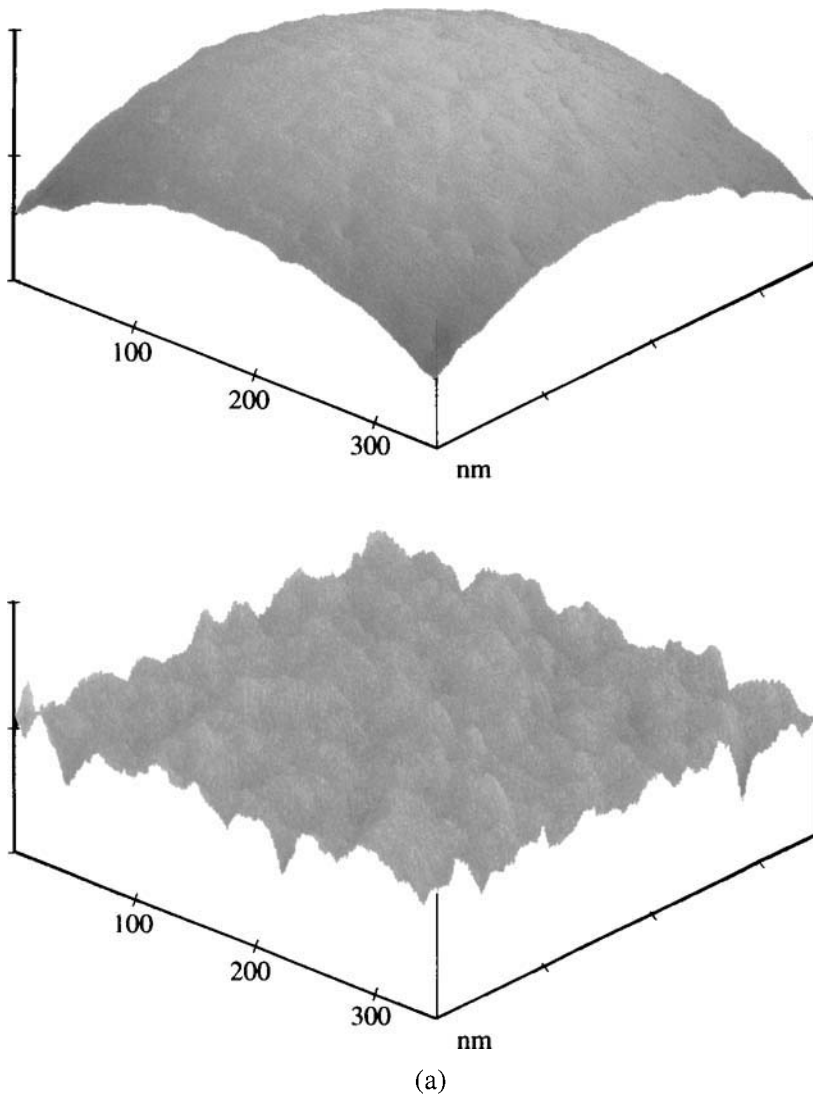


**Figure 9.** Topographic data obtained by contact-mode AFM at low contact force of (a) silica particle before ( $z$ -scale 12 nm/division) and after ( $z$ -scale 2 nm/division) a second order flattening procedure and (b) toner particle before ( $z$ -scale 180 nm/division) and after ( $z$ -scale 80 nm/division) a second order flattening procedure. The micrographs at the top and bottom are obtained before and after the second order flattening, respectively.

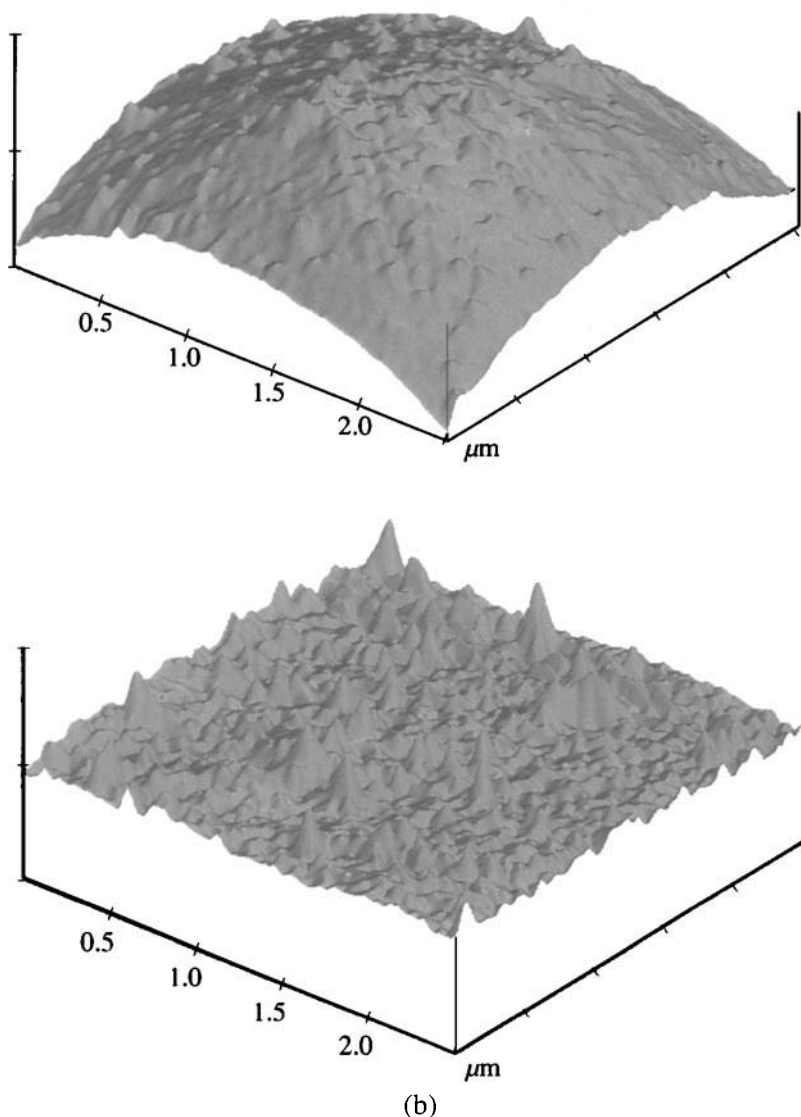


**Figure 9.** (Continued).

of determining the dimension and the surface roughness of a particle attached to an AFM cantilever.

As will be shown in the next section, the adhesion decreases with increasing surface roughness, due to the effects of a less 'intimate' contact. The height profiles of the toner and silica particles, as well as of a  $\text{SF}_6$  plasma treated silicon are depicted in Fig. 11 in order to visualize the topography of the contacting surfaces.

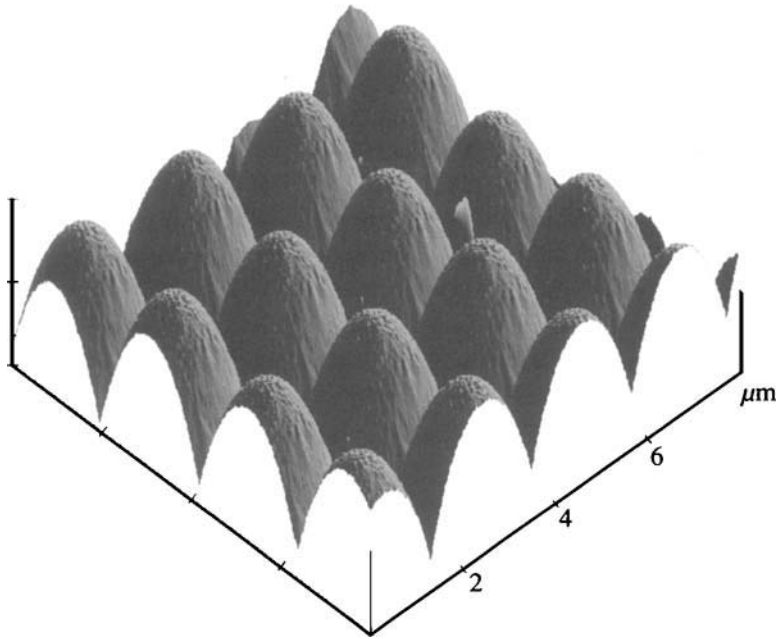


**Figure 10.** Local topography of a silica particle, which was fastened onto an AFM cantilever, as obtained by 'reverse imaging' on an array of tips (z-scale 200 nm/division).

### 6.5. Adhesion of toner and silica microparticles

Modified cantilevers were used to acquire force curves on the various silicon surfaces, as described earlier. More than one thousand force curves were accumulated per sample at ambient conditions. During the measurements the load was kept small and constant. The large number of force curves was processed by a computer program [18] in order to determine the average pull-off force. In Fig. 12 the average pull-off forces for a toner and a silica particle are plotted as a function of the  $R_q$  roughness of the silicon surfaces. The adhesion forces in these systems are increased at humidity values higher than typical ambient conditions (40% in our laboratory), as is described and discussed elsewhere [18].

From Table 2 it can be derived that the silica particle is smoother ( $R_q = 0.18$ ) compared to the rough silicon substrates (Table 1). Thus, the theoretical adhesion force proposed by Rabinovich *et al.*, described in Section 2.3, can in principle be calculated. We will show this for sample s5b. As mentioned in Section 4.1, roughness, in general, depends on the sampling area. The roughness of sample s5b has been determined as a function of AFM scan-size. The  $R_q$  roughness,  $\text{rms}_2$  (see equation (21)), had a value of approximately 0.5 nm at the scan-size of  $250 \times 250 \text{ nm}^2$ , which approximately corresponds to the contact area between the particle and the silicon substrate. From Fig. 11c we estimated that  $\lambda_2 \approx 300 \text{ nm}$ , which results, according to equation (20), in an asperity radius of the substrate  $r_2 \approx 3.1 \mu\text{m}$ . Roughness over larger scales was ignored, i.e.  $\text{rms}_1 \rightarrow 0$  and

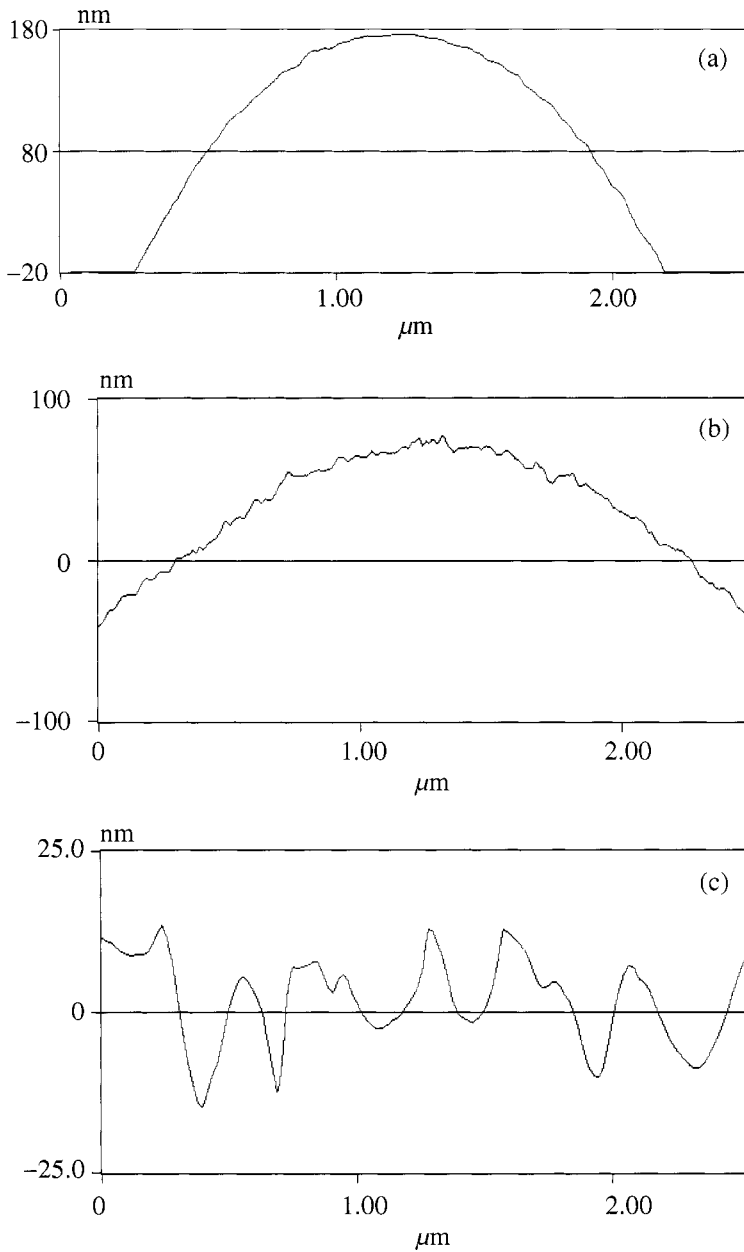


**Figure 11.** Cross-sections of the height images of AFM contact mode scans on (a) silica particle, (b) toner particle, and (c) plasma treated silicon.

$\lambda_1 \rightarrow \infty$ . The values taken in the van der Waals approach of Rabinovich *et al.* for silica/silicon ( $A = 1.31 \times 10^{-19}$  J and  $H_0 = 0.3$  nm) combined with the particle radius  $R = 2.5 \mu\text{m}$  and the roughness parameter  $r_2 \approx 3.1 \mu\text{m}$  result

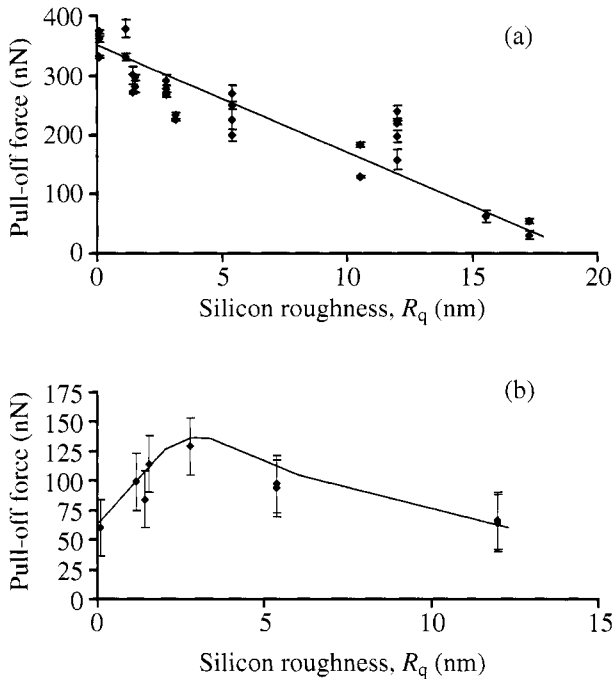


**Figure 12.** Adhesion (pull-off) force of (a) a silica and (b) a toner particle as a function of silicon substrate roughness.

in  $F_{adh} \approx 370$  nN. This is in reasonable agreement with the value measured in the AFM pull-off experiments, which showed a pull-off force for sample s5b of approximately 250 nN. In the case of a smooth substrate ( $rms_2 \rightarrow 0$ , and  $r_2 \rightarrow \infty$ ), the calculated pull-off force would be 560 nN, whereas the experimental value is 360 nN (see Fig. 12).

Both graphs in Fig. 12 show a maximum in adhesion force at the point where the substrate roughness is approximately equal to the roughness of the particle, i.e. at the place where the two roughnesses match. For toner, the adhesion is low for both flat and relatively rough surfaces, as the effective contact area is small in both cases. The adhesion reaches a maximum at a  $R_q$  roughness of about 3 nm, where the dimensions of the asperities of particle and substrate are approximately equal. The smooth silica particles demonstrate a monotonically decreasing adhesion force as a function of substrate roughness. The largest (maximum) adhesion was found for the silica particle in contact with the flattest silicon surface (i.e.  $R_q \sim 0$  nm), where the contact area is highest.

## 7. CONCLUSIONS

Micrometer-sized particles can be attached to AFM cantilevers and by means of force–displacement experiments with such a modified cantilever the force required

to remove a single particle from a substrate can be directly measured. Other particle detachment methods result in adhesion force distributions as determined by the removal of a large number of particles. In addition, AFM force–displacement experiments can be carried out over the entire surface of a substrate resulting in adhesion maps, which can be correlated to surface chemistry and topography.

Practical adhesion cannot be predicted from the value of theoretical adhesion in a simple way. Many interrelated effects play a role in particle to surface adhesion, in particular roughness of both the particle and the substrate, viscoelastic or plastic properties of the particle as well as the substrate, triboelectric charges on particle and surface, and environmental effects including temperature and relative humidity.

Unambiguous experimental results, free from artifacts, could and should be obtained from systematic studies regarding the practical adhesion of plastically or viscoelastically deformable particles, preferably attached to an AFM cantilever, on polymeric substrates as a function of substrate hardness or roughness, or the combination of both.

Atomic force microscopy is a flexible and simple surface force measurement technique for probing surface interactions. In addition to information regarding adhesion, AFM yields roughness data, or more generally, surface topography, if used as imaging tool. The latter is of importance when measured adhesion data are compared with theoretical values, as the contact area is included explicitly in the contact mechanics theories. The true area of contact, however, depends on both the roughness of the particle as well as of the substrate.

The discrepancies encountered during the past ten years between experimental and theoretical work of adhesion by AFM can be anticipated to be resolved. This anticipation is based on promising theories which are currently being developed to account for surface roughness (of both the substrate and the particle) as well as for plastic and viscoelastic effects, either as separate phenomena [39, 40], or in combination [31, 121]. At present, it remains difficult to exactly relate the measured values to the model predictions, especially because of the unknown true contact area resulting from surface roughness.

### *Acknowledgements*

We would like to thank Océ-Technologies B. V. for supply of materials, and especially R. J. W. Lugtenberg for the many in-depth discussions, H.-J. Butt and S. Ecke (University of Mainz) for particle attachment training. J. Brugger and B. Kim are acknowledged for their assistance and supply of plastic tipless cantilevers. R. G. H. Lammertink is thanked for his contribution to the plasma etching, J. P. Pickering for the development of the automated extended AFM setup, H. Schönherr for discussions and suggestions regarding the manuscript. We thank C. J. Padberg for acquiring the SEM micrographs. We are grateful to Y. I. Rabinovich for his comments and help with roughness calculations.

## REFERENCES

1. A. Falsafi, M. Tirrell and A. Pocius, *Langmuir* **16**, 1816–1824 (2000).
2. J. N. Israelachvili, *Intermolecular and Surface Forces*. Academic Press, London (1991).
3. H. C. Hamaker, *Physica* **4**, 1058–1072 (1937).
4. G. Binnig, C. F. Quate and C. H. Gerber, *Phys. Rev. Lett.* **56**, 930–933 (1986).
5. S. N. Magonov and M.-H. Whangbo, *Surface Analysis with STM and AFM*. VCH, Weinheim (1996).
6. A. Noy, D. V. Vezhenov and C. M. Lieber, *Ann. Rev. Mater. Sci.* **27**, 381–422 (1997).
7. R. J. Colton, A. Engel, J. E. Frommer, H. E. Gaub, A. A. Gewirth, R. Guckenberger, J. Rabe, W. M. Heckl and B. E. Parkinson (Eds), *Procedures in Scanning Probe Microscopies*, Wiley, Chichester (1998).
8. B. Cappella and G. Dietler, *Surf. Sci. Rep.* **34**, 1–104 (1999).
9. T. J. Senden, *Curr. Opinion Colloid Interface Sci.* **6**, 95–101 (2001).
10. A. L. Weisenhorn, P. K. Hansma, T. R. Albrecht and C. F. Quate, *Appl. Phys. Lett.* **54**, 2651–2653 (1989).
11. W. A. Ducker and T. J. Senden, *Nature* **353**, 239–241 (1991).
12. A. Paiva, N. Sheller, M. D. Foster, A. J. Crosby and K. R. Shull, *Macromolecules* **33**, 1878–1881 (2000).
13. K. K. Lam and J. M. Newton, *Powder Technol.* **73**, 267–274 (1992).
14. B. P. Frank and G. Belfort, *Langmuir* **17**, 1905–1912 (2001).
15. M. L. Hair and M. D. Croucher, in: *Colloids and Surfaces in Reprographic Technology*, ACS Symposium Series 200, M. Hair and M. D. Croucher (Eds). Washington, DC (1982).
16. W. R. Bowen and T. A. Doneva, *J. Colloid Interface Sci.* **229**, 544–549 (2000).
17. L. B. Schein, *Electrophotography and Development Physics*. Springer, Berlin (1988).
18. L. H. G. J. Segeren, F. G. Karssenberg, J. P. Pickering, J. W. A. van den Berg and G. J. Vancso, in: *Particles on Surfaces 7: Detection, Adhesion and Removal*, K. L. Mittal (Ed.), VSP, Utrecht (in press).
19. A. Busnaina, J. Taylor and I. Kashkoush, *J. Adhesion Sci. Technol.* **7**, 441–455 (1993).
20. K. Cooper, A. Gupta and S. Beaudoin, *J. Colloid Interface Sci.* **234**, 284–292 (2001).
21. S. Biggs and G. Spinks, *J. Adhesion Sci. Technol.* **12**, 461–478 (1998).
22. K. L. Mittal (Ed.), *Particles on Surfaces 5&6: Detection, Adhesion and Removal*. VSP, Utrecht (1999).
23. H. Mizes, M. L. Ott, K.-G. Loh and R. J. D. Miller, in: *Particles on Surfaces: Detection, Adhesion and Removal*, K. L. Mittal (Ed.), pp. 47–59. Marcel Dekker, New York (1995).
24. K. L. Mittal, in: *Adhesion Measurement of Films and Coatings*, K. L. Mittal (Ed.), pp. 1–13. VSP, Utrecht (1995).
25. K. L. Johnson, K. Kendall and A. D. Roberts, *Proc. R. Soc. Lond. Ser. A* **324**, 301–313 (1971).
26. B. V. Derjaguin, V. M. Müller and Yu. P. Toporov, *J. Colloid Interface Sci.* **53**, 314–326 (1975).
27. B. V. Derjaguin, *Kolloid Z.* **69**, 155–164 (1934).
28. Y. I. Rabinovich, J. J. Adler, A. Ata, R. K. Singh and B. M. Moudgil, *J. Colloid Interface Sci.* **232**, 17–24 (2000).
29. D. Maugis, *J. Colloid Interface Sci.* **150**, 243–269 (1992).
30. K. L. Johnson and J. A. Greenwood, *J. Colloid Interface Sci.* **192**, 326–333 (1997).
31. C. Y. Hui, Y. Y. Lin, J. M. Baney and A. Jagota, *J. Adhesion Sci. Technol.* **14**, 1297–1319 (2000).
32. W. N. Unertl, *J. Adhesion* **74**, 195–226 (2000).
33. P. Attard, *Langmuir* **17**, 4322–4328 (2001).
34. J. Q. Feng, *J. Colloid Interface Sci.* **238**, 318–323 (2001).
35. D. S. Rimai, L. P. DeMejo and R. C. Bowen, *J. Appl. Phys.* **66**, 3574–3578 (1989).

36. I. U. Vakarelski, A. Toritani, M. Nakayama and K. Higashitani, *Langmuir* **17**, 4739–4745 (2001).
37. C.-Y. Hui, J. M. Baney and E. J. Kramer, *Langmuir* **14**, 6570–6578 (1998).
38. G. Luengo, J. Pan, M. Heuberger and J. N. Israelachvili, *Langmuir* **14**, 3873–3881 (1998).
39. E. Barthel and S. Roux, *Langmuir* **16**, 8134–8138 (2000).
40. M. Giri, D. B. Bousfield and W. N. Unertl, *Langmuir* **17**, 2973–2981 (2001).
41. D. S. Rimai, D. J. Quesnel and A. A. Busnaina, *Colloids Surfaces A* **165**, 3–10 (2000).
42. A. N. Gent and J. Schultz, *J. Adhesion* **3**, 281–294 (1972).
43. E. H. Andrews and A. J. Kinloch, *Proc. R. Soc. Lond. Ser. A* **332**, 385–399 (1973).
44. M. Ruths and S. Granick, *J. Phys. Chem. B* **102**, 6056–6063 (1998).
45. B. Gady, R. Reifengerger, D. M. Schaefer, R. C. Bowen, D. S. Rimai, L. P. DeMejo and W. Vreeland, *J. Adhesion* **67**, 19–36 (1998).
46. C. Y. Hui, Y. Y. Lin and J. M. Baney, *J. Polym. Sci., Part B: Polym. Phys.* **38**, 1485–1495 (2000).
47. J. A. Greenwood and K. L. Johnson, *Phil. Mag. A* **43**, 697–711 (1981).
48. D. Tabor, *J. Colloid Interface Sci.* **58**, 2–13 (1977).
49. K. L. Mittal and H. R. Anderson, Jr. (Eds), *Acid–Base Interactions: Relevance to Adhesion Science and Technology*. VSP, Utrecht (1991).
50. K. L. Mittal (Ed.), *Acid–Base Interactions: Relevance to Adhesion Science and Technology*, Vol. 2. VSP, Utrecht (2000).
51. N. A. Burnham, D. D. Dominguez, R. L. Mowery and R. J. Colton, *Phys. Rev. Lett.* **64**, 1931–1934 (1990).
52. A. Kawai, K. Shimada and E. Andoh, *Solid State Phenom.* **65–66**, 191–194 (1999).
53. D. A. Hays, *J. Adhesion* **51**, 41–48 (1995).
54. J. Raja, M. B. Grant and P. Stumpf, *Surface Texture (Surface Roughness, Waviness, and Lay)*, An American National Standard. ASME, New York (1996).
55. International Norm ISO 4287/1, Surface Roughness — Terminology, Part 1: Surface and its Parameters (1984).
56. C. A. Brown, P. D. Charles, W. A. Johnsen and S. Chesters, *Wear* **161**, 61–67 (1993).
57. Y. I. Rabinovich, J. J. Adler, A. Ata, R. K. Singh and B. M. Moudgil, *J. Colloid Interface Sci.* **232**, 10–16 (2000).
58. K. N. G. Fuller and D. Tabor, *Proc. R. Soc. Lond. Ser. A* **345**, 327–342 (1975).
59. F. P. Bowden and D. Tabor, *Br. J. Appl. Phys.* **17**, 1521–1544 (1966).
60. D. M. Schaefer, M. Carpenter, B. Gady, R. Reifengerger, L. P. DeMejo and D. S. Rimai, *J. Adhesion Sci. Technol.* **9**, 1049–1062 (1995).
61. D. M. Schaefer and J. Gomez, *J. Adhesion* **74**, 341–359 (2000).
62. H. A. Mizes, *J. Adhesion* **51**, 155–165 (1995).
63. D. Sarid, *Scanning Force Microscopy with Applications to Electric, Magnetic and Atomic Forces*. Oxford University Press, New York (1994).
64. C. J. Drummond and T. J. Senden, *Colloids Surfaces A* **87**, 217–234 (1994).
65. D. Tabor and R. H. S. Winterton, *Proc. R. Soc. Lond. Ser. A* **312**, 435–450 (1969).
66. G. A. Willing, T. H. Ibrahim, F. M. Etzler and R. D. Neuman, *J. Colloid Interface Sci.* **226**, 185–188 (2000).
67. J. P. Pickering, D. Krüger, B. Anczykowski, H. Fuchs and G. J. Vancso, *Polym. Prepr. Am. Chem. Soc. Div. Polym. Chem.* **41**, 1478–1479 (2000).
68. J. H. Hoh, J. P. Cleveland, C. B. Prater, J.-P. Revel and P. K. Hansma, *J. Am. Chem. Soc.* **114**, 4917–4918 (1992).
69. H. Schönherr, M. W. J. Beulen, J. Bügler, J. Huskens, F. C. J. M. van Veggel, D. N. Reinhoudt and G. J. Vancso, *J. Am. Chem. Soc.* **122**, 4963–4967 (2000).
70. M. Portigliatti, V. Koutsos, H. Hervet and L. Léger, *Langmuir* **16**, 6374–6376 (2000).
71. H. Jung and D.-G. Gweon, *Rev. Sci. Instrum.* **71**, 1896–1900 (2000).



72. L. H. G. J. Segeren, S. Zapotoczny and G. J. Vancso, (in preparation).
73. C. T. Gibson, G. S. Watson and S. Myhra, *Scanning* **19**, 564–581 (1997).
74. J. L. Hutter and J. Bechhoefer, *Rev. Sci. Instrum.* **64**, 1868–1873 (1993).
75. T. Akihiro, S. Minoru, H. Kazuhiro and O. Shigeru, *Measurement Sci. Technol.* **7**, 179–184 (1996).
76. J. E. Sader, J. W. M. Chon and P. Mulvaney, *Rev. Sci. Instrum.* **70**, 3967–3969 (1999).
77. M. Tortonese and M. Kirk, *Proc. SPIE* **3009**, 53–60 (1997).
78. J. P. Cleveland, S. Manne, D. Bocek and P. K. Hansma, *Rev. Sci. Instrum.* **64**, 403–405 (1993).
79. N. Maeda and T. J. Senden, *Langmuir* **16**, 9282–9286 (2000).
80. P. M. Claesson, T. Ederth, V. Bergeron and M. W. Rutland, *Adv. Colloid Interface Sci.* **67**, 119–183 (1996).
81. R. Raiteri, M. Preuss, M. Grattarola and H.-J. Butt, *Colloids Surfaces A* **136**, 191–197 (1998).
82. Attaching particles to cantilevers (Online) (2000). Available: <http://www.digmbh.de/servsupp/gluing/gluing.html> (June 2001).
83. M. R. Yalamanchili, S. Veerasuneni, M. A. D. Azevedo and J. D. Miller, *Colloids Surfaces A* **133**, 77–88 (1998).
84. H. A. Mizes, M. L. Ott, E. A. Eklund and D. A. Hays, in: *Proc. 18th Ann. Meet. Adhesion Soc.*, pp. 240–242 (1995).
85. M. E. Mullins, L. P. Michaels, V. Menon, B. Locke and M. B. Ranade, *Aerosol Sci. Technol.* **17**, 105–118 (1992).
86. M. Corn, in: *Aerosol Science*, C. N. Davies (Ed.), pp. 359–392. Academic Press, New York, (1966).
87. R. C. v. Duijvenbode and G. J. M. Koper, *J. Colloid Interface Sci.* **239**, 581–583 (2001).
88. H. Mizes, M. Ott, E. Eklund and D. Hays, *Colloids Surfaces A* **165**, 11–23 (2000).
89. P. F. Smith, I. Chun, G. Liu, D. Dimitrievich, J. Rasburn and G. J. Vancso, *Polym. Eng. Sci.* **36**, 2129–2134 (1996).
90. J. D. Kiely and D. A. Bonnell, *J. Vac. Sci. Technol. B* **15**, 1483–1493 (1997).
91. G. J. Simpson, D. L. Sedin and K. L. Rowlen, *Langmuir* **15**, 1429–1434 (1999).
92. D. L. Sedin and K. L. Rowlen, *Appl. Surface Sci.* **182**, 40–48 (2001).
93. C. Neto and V. S. J. Craig, *Langmuir* **17**, 2097–2099 (2001).
94. P. Hariharan and M. Roy, *J. Mod. Optics* **41**, 2197–2202 (1994).
95. S. Tolansky, *Multiple-Beam Interference Microscopy of Metals*. Academic Press, New York (1970).
96. S. Tolansky, *Philos. Mag. A* **36**, 225–236 (1945).
97. T. Provder and B. Kunz, *Progr. Org. Coatings* **27**, 219–226 (1996).
98. K. J. E. Stout (Ed.), *Development of Methods for the Characterisation of Roughness in Three Dimensions*. Penton Press, London (Rev. repr. 2000).
99. H. Hertz, *J. Reine Angew. Math.* **92**, 156–171 (1881).
100. H. A. Mizes, K.-G. Loh, R. J. D. Miller, S. K. Ahuja and E. F. Grabowski, *Appl. Phys. Lett.* **59**, 2901–2903 (1991).
101. M. L. Ott and H. A. Mizes, *Colloids Surfaces A* **87**, 245–256 (1994).
102. H. A. Mizes, *J. Adhesion Sci. Technol.* **8**, 937–951 (1994).
103. B. Gady, D. Schleef, R. Reifengerger, D. Rimai and L. P. DeMejo, *Phys. Rev. B* **53**, 8065–8070 (1996).
104. C. D. Frisbie, L. F. Rozsnyal, A. Noy, M. S. Wrighton and C. M. Lieber, *Science* **265**, 2071–2074 (1994).
105. H. Schönherr, Z. Hruska and G. J. Vancso, *Macromolecules* **31**, 3679–3685 (1998).
106. D. Trifonova-van Haeringen, H. Schönherr, G. J. Vancso, L. van der Does, J. W. M. Noordermeer and P. J. P. Janssen, *Rubber Chem. Technol.* **72**, 862–875 (1999).
107. H. Schönherr, M. T. van Os, Z. Hruska, J. Kurdi, R. Förch, F. Arefi-Khonsari, W. Knoll and G. J. Vancso, *Chem. Commun.*, 1303–1304 (2000).

108. H. Schönherr, Z. Hruska and G. J. Vancso, *Macromolecules* **33**, 4532–4537 (2000).
109. H. Schönherr and G. J. Vancso, *J. Polym. Sci.: Part B: Polym. Phys.* **36**, 2483–2492 (1998).
110. R. Howland and L. Benatar, *A Practical Guide to Scanning Probe Microscopy*. Park Scientific Instruments, Sunnyvale, CA (1997).
111. R. F. Hariadi, S. C. Langford and J. T. Dickinson, *J. Appl. Phys.* **86**, 4885–4891 (1999).
112. L.-O. Heim, J. Blum, M. Preuss and H.-J. Butt, *Phys. Rev. Lett.* **83**, 3328–3331 (1999).
113. R. A. Quon, A. Ulman and T. K. Vanderlick, *Langmuir* **16**, 8912–8916 (2000).
114. D. Y. C. Chan, R. R. Dagastine and L. R. White, *J. Colloid Interface Sci.* **236**, 141–154 (2001).
115. K. Cooper, A. Gupta and S. Beaudoin, *J. Colloid Interface Sci.* **228**, 213–219 (2000).
116. L. Sirghi, N. Nakagiri, K. Sugisaki, H. Sugimura and O. Takai, *Langmuir* **16**, 7796–7800 (2000).
117. B. Bhushan, *Tribology Lett.* **4**, 1–35 (1998).
118. T. Baum and D. J. Schiffrin, *J. Chem. Soc., Faraday Trans.* **94**, 691–694 (1998).
119. A. Ulman, *An Introduction to Ultrathin Organic Films: From Langmuir-Blodgett to Self-assembly*. Academic Press, Boston, MA (1991).
120. S. C. Clear and P. F. Nealey, *Langmuir* **17**, 720–732 (2001).
121. F. Yang, X. Zhang and J. C. M. Li, *Langmuir* **17**, 716–719 (2001).

## **A distribution of AFM pull-off forces for glass microspheres on a symmetrically structured rough surface**

GARTH W. TORMOEN<sup>1</sup>, JAROSLAW DRELICH<sup>1,\*</sup>  
and JAKUB NALASKOWSKI<sup>2</sup>

<sup>1</sup> *Department of Materials Science and Engineering, Michigan Technological University, Houghton, MI 49931, USA*

<sup>2</sup> *Department of Metallurgical Engineering, University of Utah, Salt Lake City, UT 84112, USA*

**Abstract**—The adhesional contact between a particle and a substrate is a fundamental parameter for analyzing pull-off force data generated by atomic force microscopy (AFM). Roughness, present at some scale for all real materials, complicates this task by introducing asperity-controlled contact. Roughness also causes pull-off force data scatter, a well-known phenomenon that is usually neglected in analysis of the AFM pull-off results. This paper presents the first systematic study of roughness effect on the pull-off force magnitude and its distribution characteristics. The results indicate that the scatter in the data decreases with increasing diameter of the probe as compared to the dimension of surface irregularities, but the magnitude of the pull-off force is more severely altered by roughness. The results also show that when particle size is at the same scale as surface roughness, multiple contact points may be made yielding increased adhesion.

**Keywords:** Adhesion; atomic force microscopy; pull-off forces; roughness; structured surfaces; surface free energy; surface tension; work of adhesion.

### **1. INTRODUCTION**

The adhesional contact area between a particle (probe) and a substrate is a fundamental parameter for analyzing AFM (atomic force microscopy) pull-off force data in terms of the work of adhesion, or solid surface energy [1]. This is done conveniently by using an appropriate contact mechanics model such as the JKR [2], DMT [3], or MD [4] model. However, these models were developed by assuming a spherical particle in contact with a smooth surface, two ideal geometries. In the real world, particles are not perfect spheres and surfaces of both particles and substrates

---

\*To whom correspondence should be addressed. Tel.: (1-906) 487-2932. Fax: (1-906) 487-2934.  
E-mail: jwdrelic@mtu.edu

are almost always rough at either a micro- or nano-scale or both. Surface roughness can significantly alter the true contact area between the probe and the substrate from that predicted by contact mechanics models, making analysis of the measured pull-off forces very difficult.

Roughness often yields irreproducible probe-substrate contact areas when sampling different locations on the substrate, resulting in scattered data from which representative information is difficult to obtain [5–8]. The effect of submicroscopic roughness on measured pull-off forces needs to be understood and controlled in order to adopt the AFM technique for characterization of engineered materials. Although the literature reports often speculate that the roughness plays an important role in irreproducibility of and scatter in reported pull-off forces obtained from an experiment, systematic experimental studies on the effect of surface roughness on AFM pull-off forces are lacking.

The pull-off force value of a particle at different regions on a substrate will change as a result of substrate surface roughness and variation in particle-substrate contact area [5, 9]. In extreme scenarios, when the particle is in contact with the top of asperity the pull-off force is much lower than when particle touches the sides of the asperities or entirely penetrates an inter-asperity valley. Recent experimental results on pull-off forces for sharp tips (30–50 nm radius of curvature) on substrates of granular morphology provide experimental support for this hypothesis [10].

A variation in the pull-off force ( $F$ ) for a rigid particle on a rough and rigid substrate can be predicted theoretically using the Derjaguin approximation [9]:

$$F = 2\pi \left( \frac{1}{C_P + C_S} \right) W_A, \quad (1)$$

where  $C_P = 1/R_P$  and  $C_S = 1/R_S$  are the radii of curvature of the particle and substrate irregularities (asperities and grooves), respectively;  $R_P$  and  $R_S$  are the radii of the particle and substrate irregularities, respectively; and  $W_A$  is the interaction energy per unit area of two flat surfaces, or simply the work of adhesion. As  $C_S$  changes for surfaces of random roughness characteristics, the pull-off force changes as predicted by equation (1).

The concept of predicting adhesion from roughness considerations was analyzed by Cooper *et al.* [11, 12]. In their first contribution [11], a model for contact analysis between a rough deformable particle and a smooth substrate was derived. The model predicts the effects of varying surface asperity size and asperities distribution on measured pull-off force. In the second paper [12], a computer simulation was used to predict adhesion of arbitrarily shaped particles on rough surfaces. The simulation predicted a range of values to account for topographical irregularities, mechanical behavior and environmental effects, rather than a single, representative value. The computer simulation was tested for a latex particle on a smooth silicon wafer in water, for an alumina particle on a silicon wafer as well as on a rougher copper surface. Collected data fell within the predicted range, thus validating this approach to predicting particle adhesion.

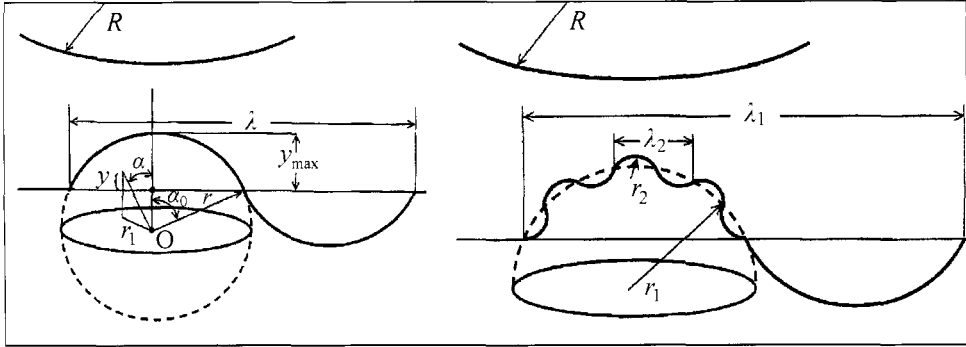


Figure 1. Model geometry for the Rabinovich model.

Also recently, Rabinovich *et al.* [13, 14] suggested that by measuring the root mean square (RMS) roughness parameters along with asperity sizes and distribution for both the probe and substrate, one could predict the adhesional contact and ultimately account for lower adhesion forces than what is expected from ideal geometries. The Rabinovich model states:

$$W_A = \left( \frac{F}{R} - B \right) \frac{58 R R M S_2}{c \pi \lambda_2^2}, \quad (2)$$

where:

$$B = \frac{A}{6 z_0^2} \frac{1}{\left( 1 + \frac{58 R R M S_1}{\lambda_1^2} \right) \left( 1 + \frac{1.82 R M S_2}{z_0} \right)^2} \quad (3)$$

and:

$$R M S = \sqrt{\frac{32 \int_0^r y^2 r_1 dr_1}{\lambda^2}} k_p. \quad (4)$$

$c$  is a constant (JKR  $c = 1.5$ , DMT  $c = 2$ );  $k_p$  is the surface packing density for close-packed spheres ( $k_p = 0.907$ );  $A$  is the Hamaker constant;  $z_0$  is the distance of closest approach between the two surfaces. All other variables, as well as the model geometry, are illustrated in Fig. 1.

In this paper, we present experimental results of pull-off forces measured for rigid microprobes on silicon-based surfaces structured at a micro-scale. For comparison, the pull-off forces were also measured between the same microprobes and 'smooth' silicon surfaces having RMS roughness 0.3 and 1 nm. Glass beads with diameters 5  $\mu\text{m}$ , 10  $\mu\text{m}$  and 40  $\mu\text{m}$  were attached to AFM cantilevers and used as microprobes in our experiments. The substrate was composed of a regular array of triangular ridges with an approximate spacing of 3  $\mu\text{m}$  and ridge peak radii <10 nm. This is the first attempt to measure the pull-off forces on symmetrically rough structures. The results show that increasing the ratio of the probe diameter to the

size of roughness features reduces the scatter in the measured pull-off forces. The measurements of pull-off forces performed with the array of microscopic ridges also demonstrate that the value of adhesion depends on the position of the probe over the location of ridges. In accordance with what was often speculated in the past, smallest pull-off force is noted when the probe is located on the top of individual ridges and the maximum pull-off force is recorded when the probe is in contact with two ridges.

## 2. EXPERIMENTAL

### 2.1. AFM probes

Four AFM probes with attached glass beads were used in this study. A 5  $\mu\text{m}$  glass sphere attached to a tipless cantilever with nominal spring constant  $k = 17.0 \text{ N/m}$  was purchased from Thermomicroscopes (Sunnyvale, CA, USA). One 40  $\mu\text{m}$  and two 10  $\mu\text{m}$  glass spheres were glued to tipless triangular silicon nitride cantilevers with nominal spring constants of 0.58 N/m (Digital Instruments, Santa Barbara, CA, USA). Gluing was performed using Epon 1001F thermoplastic resin (Shell, Houston, TX, USA) and a micromanipulator. Special care was taken to assure that the surface contacting area of the particle was not contaminated with the glue.

AFM probes were cleaned prior to testing by immersing into a 10 vol% Micro 90 cleaning solution (International Products, Burlington, NJ, USA) for approx. 20 min. The probes were then removed and rinsed for approx. 60 s with deionized water and allowed to air-dry in a covered Petri dish. Neither UV cleaning nor organic solvents were used to clean glass bead probes in order to avoid any possibility of degradation of the glue attaching the glass beads to the AFM cantilever.

Silanization was performed on the 5  $\mu\text{m}$  probe after the wet cleaning. In this case, the probe was additionally cleaned by placing it for approximately 5 min in a UV cleaner (Bioforce Labs, Ames, IA, USA). The probe was then placed on a crucible platform with 1–2 drops of chlorotrimethylsilane (99+%) obtained from Aldrich (Milwaukee, WI, USA) and covered with a beaker. The chlorotrimethylsilane immediately evaporated, and the probe was left in the silane vapor-filled chamber for 10 min.

The probes were scanned over a TGT01 grating (NT-MDT, Moscow, Russia) to obtain probe surface roughness information. Scan sizes of 10  $\mu\text{m} \times 10 \mu\text{m}$  were used for this purpose.

Scanning electron microscopy (SEM) images of the probes were obtained with a JEOL JSM-6400 Scanning Electron Microscope operated with an accelerating voltage of 20 kV.

### 2.2. Model rough surface

Silicon wafer pieces were cut from a single wafer (Polishing Corporation of America, Santa Clara, CA, USA) and used as a model smooth surface. The

model rough, or ‘microrough’ substrate was a TGG calibration grating (NT-MDT). The TGG grating contains a regular array of triangular ridges with a spacing of  $3.0 \pm 0.3 \mu\text{m}$  and ridge peak radii of  $<10 \text{ nm}$ . Additionally, the TGG substrate contains flat areas outside the grid areas, which were also used in pull-off force measurements. TappingMode images at scan sizes of  $5 \times 5 \mu\text{m}$  and  $50 \times 50 \mu\text{m}$  were taken to verify the pitch spacings. A  $1 \times 1 \mu\text{m}$  AFM image was also analyzed to gain insight into the roughness properties of the grating features themselves. A  $5 \times 5 \mu\text{m}$  AFM image was also obtained from the flat area outside of the grid area on the TGG substrate to characterize roughness parameters.

The TGG grating was cleaned prior to testing by ultrasonicing in the 10 vol% Micro 90 cleaning solution for approx. 20 min. The samples were next rinsed for approx. 60 s in deionized water. The samples were then placed in a covered Petri dish and inserted in an oven at  $105^\circ\text{C}$  for 10–15 min.

### 2.3. Adhesion force measurements

All force measurements were performed using a Dimension 3000 AFM (Digital Instruments). A scan rate of 0.5 Hz was used for all pull-off force measurements. Force measurements were performed in air with relative humidity levels ranging from  $<5$  to 26.5%. It was confirmed before that such humidity did not lead to capillary condensation between the probe and the substrate during the conditions of pull-off force measurements used in this study. A ZeroStat 3 Anti-Static Instrument (Aldrich) was applied to surfaces before measurements to eliminate any static charge buildup on the silicon substrates.

For measurements on the TGG flat areas, or smooth substrate, 4–10 spots were chosen randomly, with 10–20 measurements made at each spot. Measurements on the grid areas of the TGG substrate were performed in two ways. First, 10–20 random spots were tested with 10–20 measurements made at each spot. Second, for the  $10 \mu\text{m}$  beads only, from 6 to 55 spots were tested with 10–20 measurements made at each spot. Here, the spots were successively offset from each other in a direction perpendicular to the ridge peaks by 50 to 400 nm.

## 3. RESULTS AND DISCUSSION

### 3.1. Surface characterization

**3.1.1. TGG grating.** A  $5 \times 5 \mu\text{m}$  topographical AFM image along with a cross-sectional profile of the TGG grating is shown in Fig. 2. Figure 2 shows that the sidewalls of the features appear smooth at this scale. The peak-to-peak distance was measured from the cross-sectional profile of a  $50 \mu\text{m}$  AFM scan shown in Fig. 3. From Fig. 3, the distance spanning 15 ridge peaks was measured to be  $45.9 \mu\text{m}$ , which gives an average peak-to-peak distance of  $3.06 \mu\text{m}$ , within the manufacturer’s quoted value of  $3.0 \pm 0.3 \mu\text{m}$ . Also the RMS roughness parameter was determined for the image presented in Fig. 3 and found to be 577 nm.

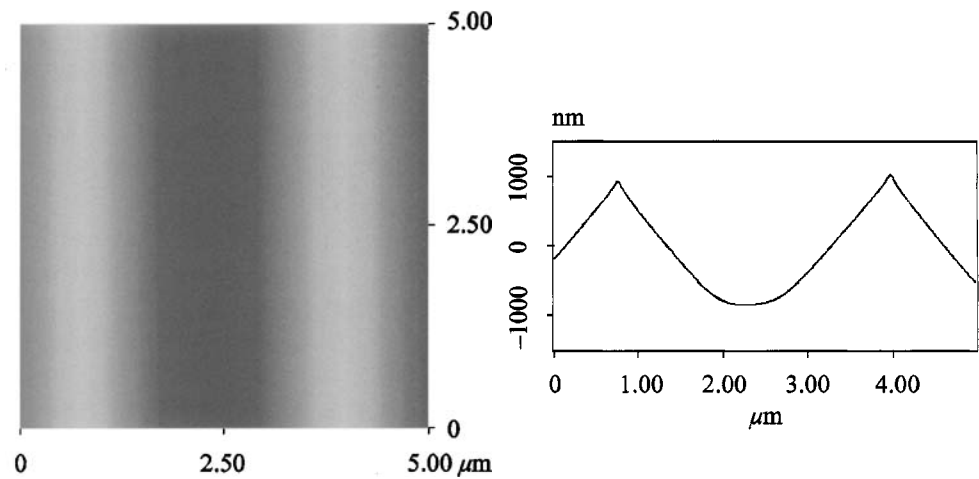


**Figure 2.** 5 × 5 μm AFM tapping mode image of TGG substrate grid (left) and its cross-sectional profile (right).

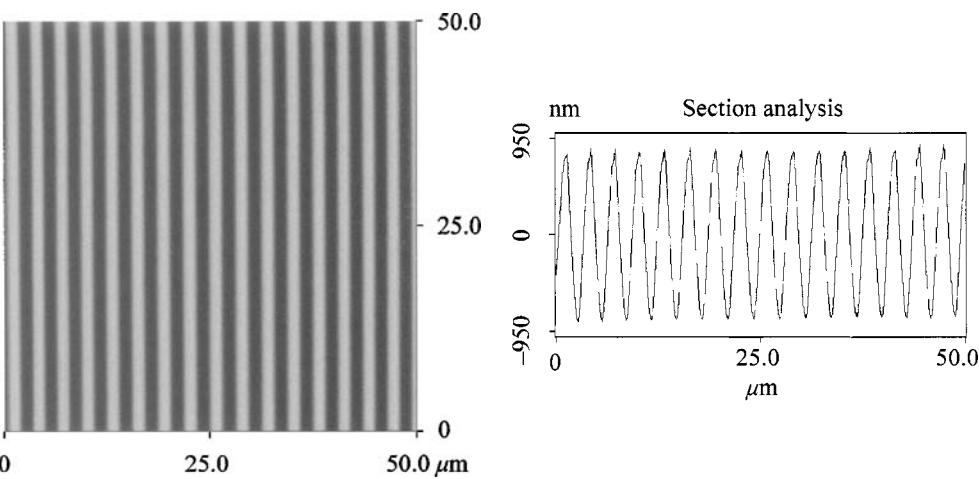


**Figure 3.** 50 × 50 μm AFM tapping mode image of TGG substrate grid (left) and its cross-sectional profile (right).

A 1 × 1 μm AFM scan was taken over a single ridge peak to gain insight into the roughness characteristics of the peaks and the sidewalls of the TGG grid. This images are shown in Fig. 4A and 4B. To better characterize irregularities of the asperity and perceive the scale of this roughness, a cross-sectional profile, parallel to the peak, cutting through the irregularities is also shown in Fig. 4C. It was found that the height of nano-scaled irregularities varied from less than 10 nm to about 50 nm. Approximately 20–30% of the total length of the cross section deviated from an expected straight line. It was found that the ridge itself contained a significant number of irregularities with protruding heights up to 5 nm. These elevations on the



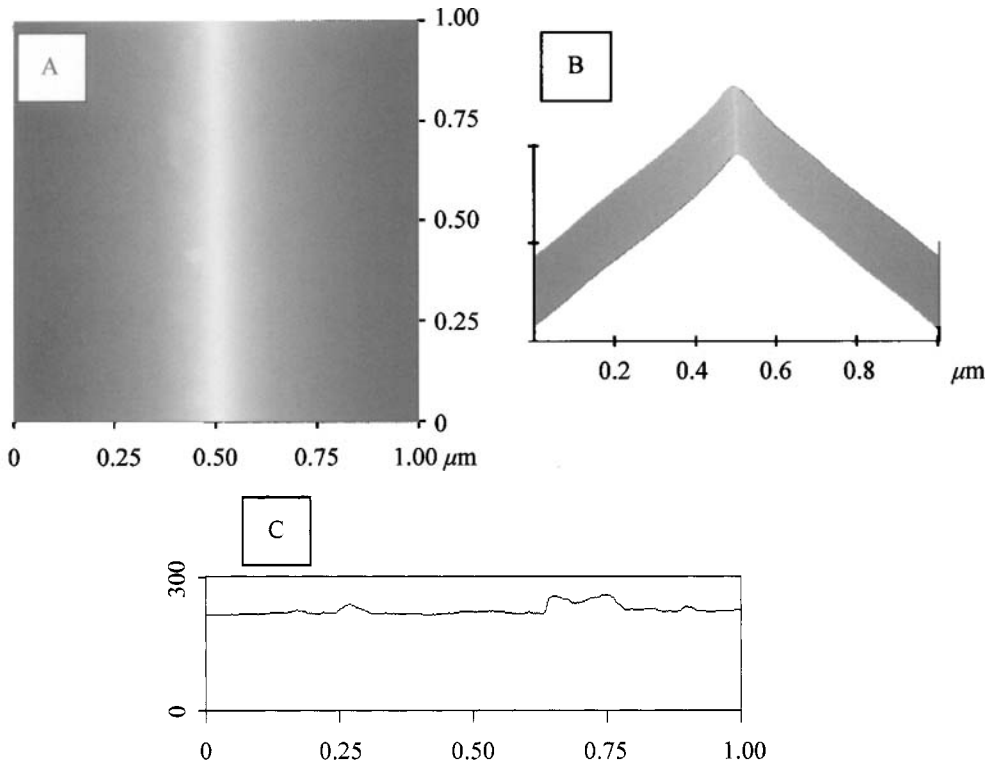


**Figure 4.** (A)  $1 \times 1 \mu\text{m}$  AFM tapping mode image of a single ridge of the TGG grid. (B) 3-Dimensional view of the ridge. (C)  $1 \mu\text{m}$  cross-sectional profile of the ridge taken along the ridge side wall.

sidewall or top of asperity, if contacted by the glass sphere probes during pull-off force measurements, could significantly alter the probe-substrate contact area.

**3.1.2. Flat area of the TGG grating.** An AFM image of the flat part of the TGG grating is shown in Fig. 5. The surface shows the grainy texture indicative of a lower grade finish for silicon wafers. The RMS roughness value from this  $5 \times 5 \mu\text{m}$  scan was 1.015 nm. An analysis was performed for the surface shown in Fig. 5 in order to determine the radii of the surface asperities from cross-sectional profiles. The peak-to-peak distance was also analyzed from the cross sections. An example of one of these cross sections is shown in Fig. 5.

53 asperities were analyzed, yielding surface asperity radius ( $r_{\text{asp}}$ ) varying from about 55 to 200 nm with an average value and standard deviation of  $122 \pm 52$  nm. The peak-to-peak distance between asperities varied from 35 to 127 nm with an average value of  $64 \pm 21$  nm.

**3.1.3. Silicon wafer.** Images of the 'smooth' silicon substrate were also captured at scan sizes of  $2 \times 2 \mu\text{m}$  and  $5 \times 5 \mu\text{m}$ . A representative topographical image is shown in Fig. 6, along with a cross-sectional profile.

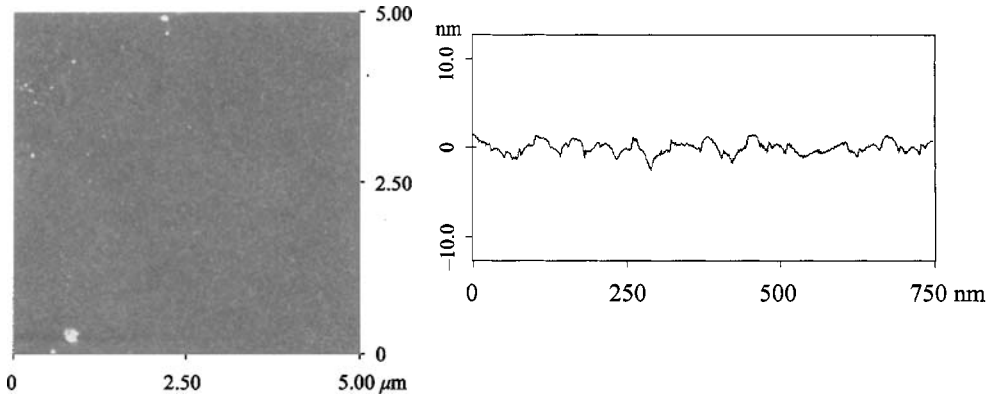


**Figure 5.**  $5 \times 5 \mu\text{m}$  AFM tapping mode image (left) and cross-sectional profile (right) of the flat TGG substrate outside grating.

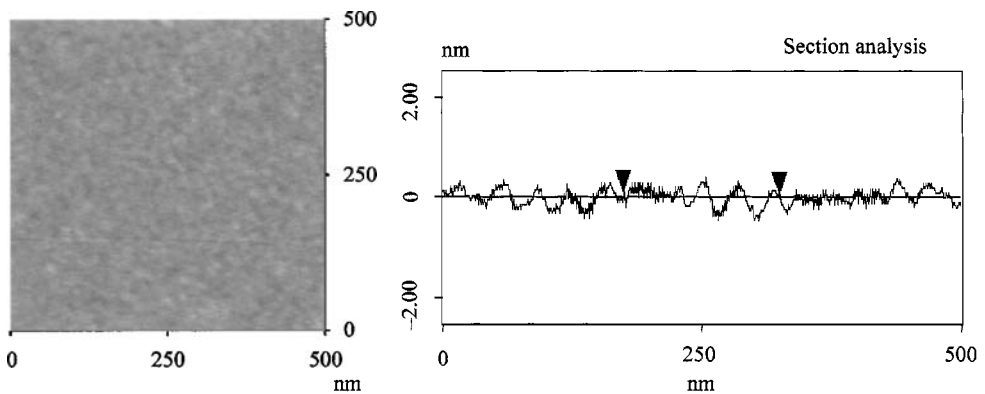


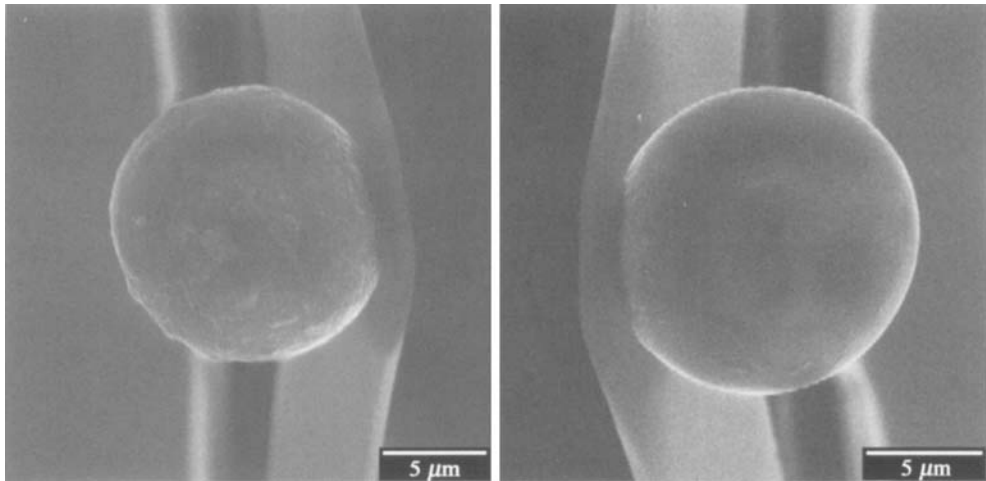
**Figure 6.**  $500 \times 500 \text{ nm}$  tapping mode AFM image of smooth silicon wafer (left) and its cross-sectional profile (right).

This silicon wafer does show a smoother surface than the flat area of the TGG grating discussed in the previous paragraph. The RMS roughness value was found to be a fraction of a nanometer,  $\text{RMS} = 0.305 \text{ nm}$ . Surface asperity radius ( $r_{\text{asp}}$ ) was found to vary from 48 to  $>400 \text{ nm}$  with an average value and standard deviation of  $142 \pm 84 \text{ nm}$ . The peak-to-peak distance between asperities ranged from 20 to 42 nm with an average value of  $31 \pm 5 \text{ nm}$ .

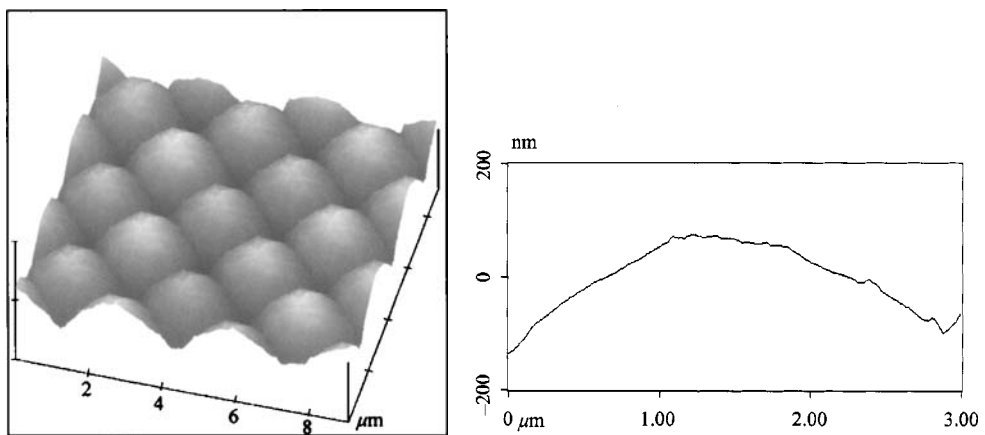
### 3.2. Probe characterization

Figure 7 shows SEM images of the  $10 \mu\text{m}$  probe before cleaning and after cleaning. The glass probes required cleaning before their use in pull-off force measurements. Similar contamination of probes as shown in Fig. 7 was also observed for a number of other probes in their ‘as-received’ condition (not reported here).

The recorded SEM images also suggested that the glass probes were not inherently smooth and nano-scale imperfections in the probe surface topography were



**Figure 7.** SEM images of the 10  $\mu\text{m}$  probe before (left) and after its cleaning (right).



**Figure 8.** AFM image (left) of the 10  $\mu\text{m}$  probe and its cross-sectional profile (right).

observed. Due to limited resolution of the SEM micrographs, an AFM image of the probe after its cleaning was recorded to confirm the nanoroughness of the probe, and this image is shown in Fig. 8. A number of tests performed on other glass probes (not shown) confirmed that the nano-scale surface roughness was a common feature of the borosilicate glass microspheres used in our laboratory.

Figure 8 reveals surface roughness on the bead surface, concurrent with observations made from the SEM images. The asperities on 10  $\mu\text{m}$  probe are regular in shape and almost symmetrical, indicating the roughness is inherent to the probe surface. The cross-section of the glass probe in Fig. 8 showed that surface asperities protruded as high as 12 nm. These small asperities had radii of curvature of 50–70 nm. This is an important observation, which suggests that approximating such probes as spheres can be inaccurate. As is commonly believed, the surface

roughness of the probes causes difficulties in predicting probe-substrate contact areas during pull-off force measurements.

### 3.3. Pull-off force measurement results

Figure 9 shows histograms for the 5  $\mu\text{m}$ , 10  $\mu\text{m}$  and 40  $\mu\text{m}$  probes, showing the measured force distribution changes. The 5  $\mu\text{m}$  probe (silanization of this probe was necessary to reduce the pull-off forces measured on the grid) yielded a pull-off force of  $34.3 \pm 2.2$  nN on the flat area of the TGG grating and  $53.2 \pm 28.9$  nN on the grid area. The force measurements on the grid yield force values that are both larger and smaller than those on the flat area, and the scatter in the data is significantly increased as well.

The 10  $\mu\text{m}$  probe yielded a pull-off force of  $35.9 \pm 5.3$  nN on the smooth silicon wafer, and  $31.8 \pm 15.6$  nN on the grid area of the TGG grating. The force measurements on the grid yielded force values that are close to those on the flat area, although the scatter in the pull-off force data for the probe-grid system was still significant.

The 40  $\mu\text{m}$  probe yielded a pull-off force of  $51.2 \pm 3.1$  nN on the flat area and  $16.1 \pm 6.5$  nN on the grid area. The force measurements recorded on the grid are

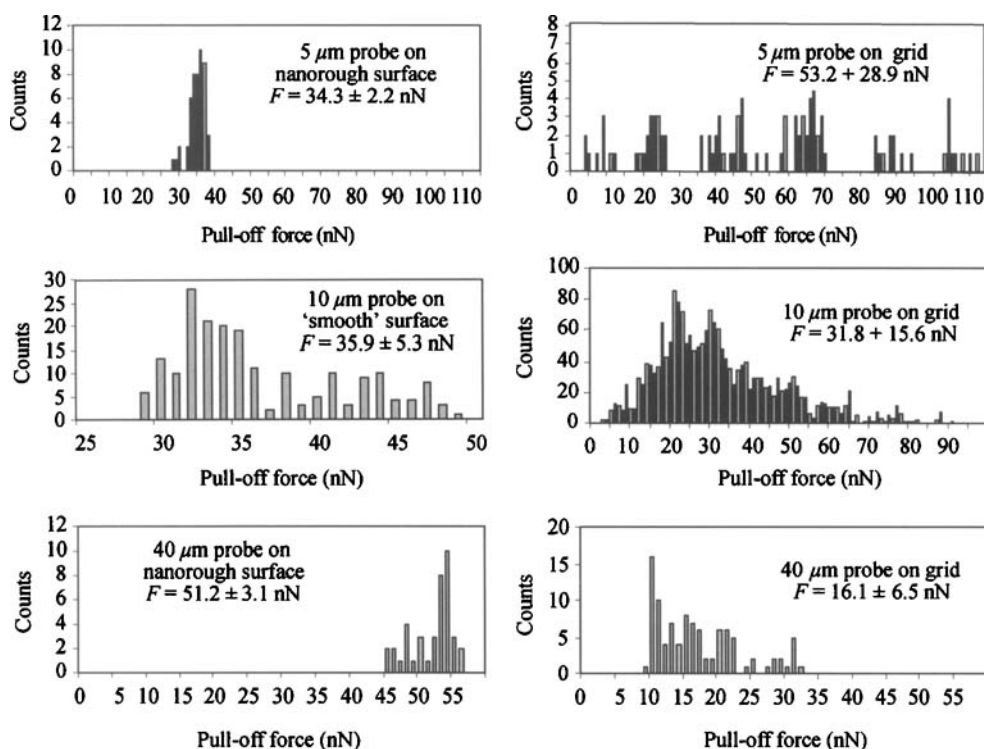


**Figure 9.** Histograms of force measurements for the 5  $\mu\text{m}$ , 10  $\mu\text{m}$  and 40  $\mu\text{m}$  probes.

now significantly smaller than those on the flat area. The scatter in the data for the 40  $\mu\text{m}$  probe does not increase as much as for the 5  $\mu\text{m}$  and 10  $\mu\text{m}$  probes when moving from the flat area to the grid area.

For all three probes, a uni-modal distribution is observed for force data recorded from the flat area of the TGG grating (for 5  $\mu\text{m}$  and 40  $\mu\text{m}$  probes) and smooth silicon wafer (for 10  $\mu\text{m}$  probe). Force data for 5  $\mu\text{m}$  probe yield multi-modal distributions for measurements performed on the TGG grid with distinct groupings at values of approximately 10, 25, 45, 70, 90 and 105 nN. The results for the 10  $\mu\text{m}$  and 40  $\mu\text{m}$  probes on the TGG grid can be interpreted as uni-modal.

Figure 9 provides a direct evidence that micro-scale roughness or, in other words, roughness with features whose dimensions are close to the size of the probe, increases the scatter in the data for AFM pull-off force measurements. For the 5  $\mu\text{m}$  probe, its diameter is close to the peak-to-peak distance (3  $\mu\text{m}$ ) for the grating, and as a result the roughness increased the scatter in the pull-off force results due to numerous possible scenarios for the contact between the probe and one or two asperities. The roughness of the glass probe surface (Fig. 8), coupled with the apparent surface irregularities of the TGG ridge peaks (Fig. 4) gives rise to data scatter due to roughness effects, as well as multi-modal distribution characteristics. For example, this probe is able to contact an individual ridge not only at its apex but also at its side, just below the top of the ridge. As discussed in Section 3.1, the sides of the ridge are more irregular than the ridge's apex, so this probe-ridge side contact scenario provides the opportunity for a variety of different probe-substrate contact areas and, therefore, a variety of pull-off force values. Discussion on the multiple contact scenarios will be given in the later part of this paper.

As can be deduced from Fig. 8, the probe surfaces are not perfectly spherical. In fact, the 10  $\mu\text{m}$  probe showed the most distinct roughness characteristics (observation primarily made based on the SEM imaging of the probes) and coincidentally yielded much smaller force magnitude on the smooth surface as compared to 40  $\mu\text{m}$  probe.

### *3.4. Data scatter due to surface roughness*

The appearance of a continuous distribution of forces over a wide range of values for probes measured on the TGG grid may seem a bit odd. There are essentially three different contact scenarios available between the probe and substrate (Fig. 10): probe in contact with the apex of one ridge (Fig. 10A), contact of the probe with two ridges (Fig. 10C) and contact of the probe with one ridge and long range-interaction with the second ridge (Fig. 10B).

The probe-ridge two-contact or non-contact interaction scenarios are quite restricted, due to size limitations and specific orientations of the probe over the ridges. The double contact scenario can only occur if the probe is positioned exactly between two adjacent peaks (because of torsional elasticity of the cantilever, double point contact can also be forced during loading, however intuitively only one point will be detached first during retraction). Any slight variation from this, barring the

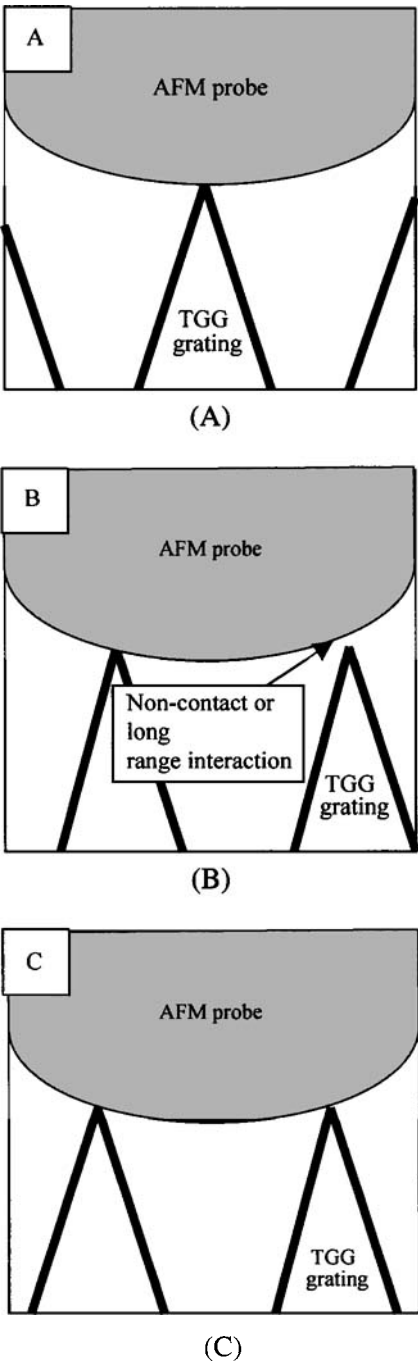


**Figure 10.** Schematics of possible contact scenarios for glass probes on TGG substrate. (A) Single contact point, (B) a single contact point with a non-contact interaction felt by a second asperity and (C) a double-contact point scenario.

occurrence of sliding, would result in the intermediate scenario in Fig. 10. This scenario is also limited due to size constraints as it can occur only if the probe is close enough to the second peak to experience a measurable attraction from surface forces, typically  $<10$  nm in air. More serious complication for the two-contact scenarios comes from the nano-scale roughness of the asperities demonstrated in Fig. 4. The nano-irregularities of micro-ridges will hinder a full contact between the probe and the ridge.

The single contact point scenario may occur at any point over a rather large area on the probe surface. In fact, anywhere between the two contact points shown in scenario (C) in Fig. 10 the probe may experience contact. As the probe may have any arbitrary orientation with respect to the direction of the ridges, the possible contact areas for the different scenarios are illustrated in Fig. 11.

Since the probes were found to have some inherent surface roughness, along with some surface irregularities on the ridge peaks of the TGG grid, a data scatter is to be expected from the force measurements captured from single contact point scenario. Also, there is a range of forces possible for the non-contact attraction scenario. This non-contact force increases the closer the probe is to the second contact with another ridge (from a zero non-contact force for single-contact point scenario when the distance between the probe and another ridge exceeds the range of surface forces to a maximum force characteristic for a double contact point scenario). Therefore, it is physically possible to capture representative data with continuous values between the two extreme contact point scenarios (single and double contact points), even for ridges having perfectly smooth surfaces. The occurrence of surface roughness simply adds to the likelihood of data scatter.

The statistical data from the systems studied in this research are presented in Table 1 and Fig. 12. These data illustrate how the scatter in the force values changes as the probe size to surface roughness ratio changes ( $D/\lambda \equiv$  probe diameter divided by the peak-to-peak distance). The  $\Delta F/F$  parameter, which is the standard deviation for the measured pull-off forces normalized by the mean value, is used in this study to directly compare different systems with regards to their distribution characteristics. A plot of  $\Delta F/F$  versus  $D/\lambda$  is shown in Fig. 12.

It is clear from the results in Table 1 and Fig. 12 that scatter in the experimental pull-off force values decreases as the ratio of surface irregularities size (expressed by  $\lambda$  parameter) to probe size ( $D$ ) decreases.  $\Delta F/F$  increases from 4.4–14.8%, calculated for smooth surfaces, to 40.4–64.3% for microrough surfaces. It is difficult to discern between probes of different sizes on the microrough surface, as all probes are prone due to geometric limitations to the same contact scenario. It appears from the results in Table 1 that the microrough surface features may have an impact on the contact area between any of the probes used and give rise to data scatter. The probe surfaces also showed some surface roughness that could alter the contact areas, a problem compounded by the possibility for contact to be made over a substantial portion of the probe surface (Fig. 11).

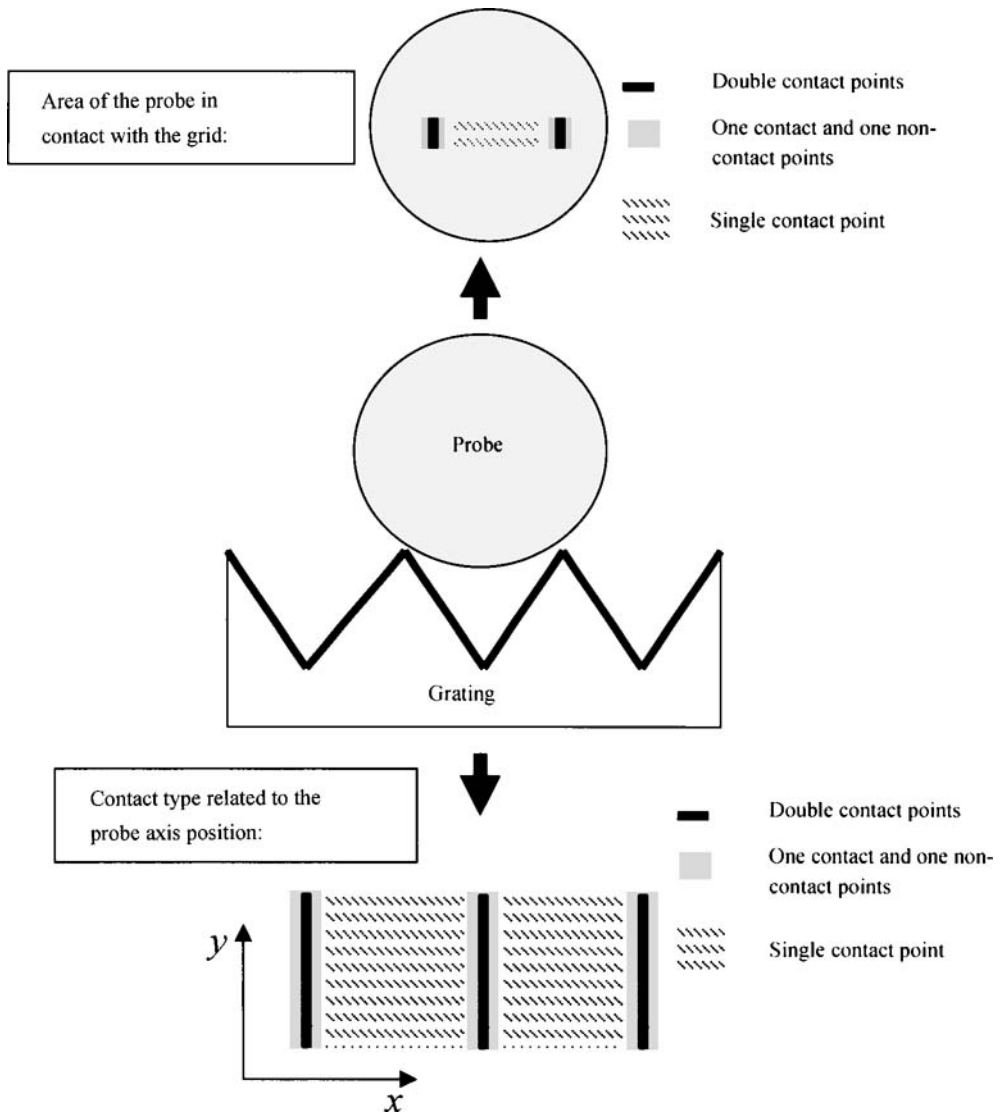


**Figure 11.** Areas of possible contact points between the probe and the TGG grid.

### 3.5. Probe-ridge geometry effects

To further support the occurrence of data scatter from different contact scenarios, pull-off forces were captured for different locations, separated by an operator-controlled offset distance. The offsets were positioned so that probe was translated perpendicular to the ridges. Any variations in force measurement as the probe was cycled systematically between a single ridge and double ridges could then be easily discerned. An example of the results obtained from these experiments is shown in Fig. 13.



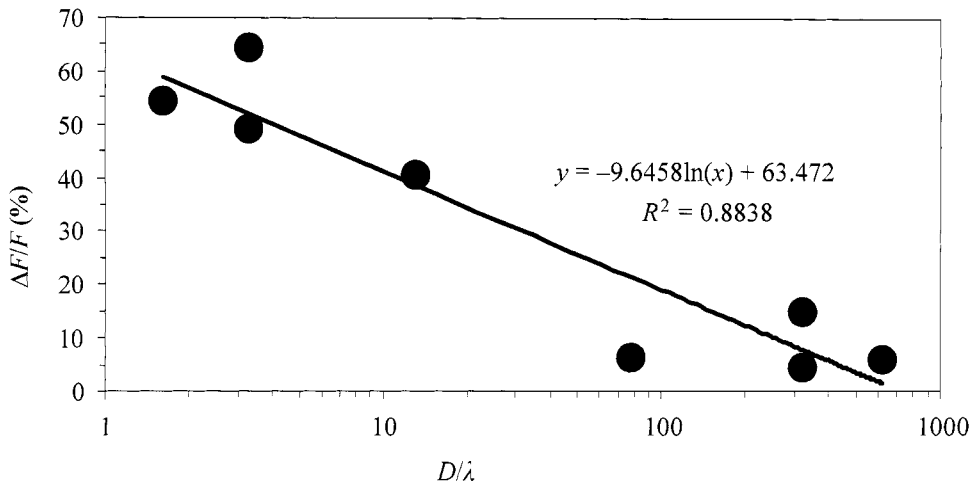


**Figure 12.** Standard deviation *versus* ratio of the probe diameter ( $D$ ) to the peak-to-peak distance ( $\lambda$ ) for all systems studied. A trend line is included as a means to guide the eye.

**Table 1.**

Statistical force data for all systems studied

Probe diameter ( $\mu\text{m}$ )	Surface	$D/\lambda$ (m/m)	$F \pm \Delta F$ (nN)	$\Delta F/F$ (%)
5	nanorough (flat TGG)	78.1	$34.3 \pm 2.2$	6.4
	microrough (TGG grid)	1.6	$53.2 \pm 28.9$	54.3
40	nanorough (flat TGG)	625	$51.2 \pm 3.1$	6.1
	microrough (TGG grid)	13.1	$16.1 \pm 6.5$	40.4
10 (a)	smooth (Si wafer)	323	$110.4 \pm 4.9$	4.4
	microrough (TGG grid)	3.3	$57.4 \pm 36.9$	64.3
10 (b)	smooth (Si wafer)	323	$35.9 \pm 5.3$	14.8
	microrough (TGG grid)	3.3	$31.8 \pm 15.6$	49.1

(a) and (b) represent two different probes of the same diameter but possible different surface nano-roughness characteristic.

The plot in Fig. 13 shows vast differences in pull-off force values as the probe is positioned differently over the grating ridges. Force values approached a maximum of about 50 nN and a minimum of about 10 nN. The data follow a pattern, which mirrors the structure of the TGG grid, as shown by the guideline in Fig. 13. If this hypothesis is correct, the larger force values would correspond to double-contact

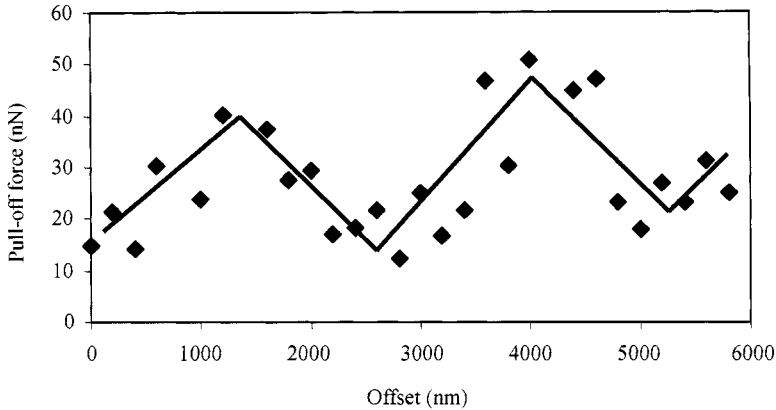


**Figure 13.** Averaged pull-off force vs.  $x$ -offset for the 10  $\mu\text{m}$  probe on TGG grating. A guideline is included in the plot to aid the eye in following the data trend.

points, or the occurrence of a second non-contact attraction. The low force values would correspond to single contact point scenario. This trend was not always clearly seen, however, possibly since the force value is so sensitive to positioning of the probe over the ridge peak. Due to surface roughness of the probe, and more important due to variation in the size and distribution of nano-scale irregularities on the asperities' surfaces, the possibilities for entering different contact scenarios are practically endless. In addition, creep of the piezoelectric crystals that drive the offset translations, makes it unlikely that the same area of the probe is contacted with successive ridge peaks, even if offsets are scaled to the peak spacings of the grating itself.

Figure 13 shows how sensitive the force measurement was to location of the probe over the model grating. The value of the measured pull-off force changed significantly at different locations of the substrate and this effect was noticeable even when sampling areas of the grating (represented by step size for offsets shown on the  $x$ -axis) were only a few hundred nanometers apart.

### 3.6. Work of adhesion

In an effort to convert the measured pull-off forces to the work of adhesion, contact mechanics theoretical models for idealized sphere–flat systems and those taking into account the topography of the substrate roughness effects were used. The work of adhesion values are shown in Table 2 and explanation for theoretical equations used along with the discussion of results are provided in the following paragraphs.

In the first approach, the work of adhesion between a probe and a 'smooth' substrate or flat area of the TGG grating was calculated from the following equation:

$$W_A = \frac{F}{c\pi R_P}, \quad (5)$$

where  $F$  is pull-off force (average value from experimentation),  $R_P$  is the radius of the probe (or radius of asperity located at the apex of the probe) and  $c$  is a constant

**Table 2.**

Calculated work of adhesion values for probes and substrates used based on the experimental pull-off forces and theoretical models presented in the text

Probe ( $\mu\text{m}$ )	Substrate	Work of adhesion ( $\text{mJ/m}^2$ )			
		equation (5)	equation (9)	equation (10)	equation (11)
5 (silanized)	Flat TGG	2.7 ( $c = 1.6$ )	<b>53</b> ( $c = 1.7$ )	NA	<b>98</b> ( $c = 1.6$ )
	TGG grid	NA	NA	<b>60</b> ( $c = 1.8$ )	NA
10 (a)	Si wafer	4.4 ( $c = 1.6$ )	<b>147</b> ( $c = 1.7$ )	NA	415 ( $c = 1.6$ )
	TGG grid	NA	NA	45 ( $c = 1.8$ )	NA
10 (b)	Si wafer	1.4 ( $c = 1.6$ ) <b>96–135</b> ( $R_p = 50\text{--}70\text{ nm}$ , $c = 1.7$ )	47 ( $c = 1.7$ ) <b>135–172</b> ( $R_p = 50\text{--}70\text{ nm}$ , $c = 1.8$ )	NA	<b>135</b> ( $c = 1.6$ )
	TGG grid	NA	NA	25 ( $c = 1.8$ )	NA
40	Flat TGG	0.5 ( $c = 1.6$ )	<b>79</b> ( $c = 1.7$ )	NA	<b>146</b> ( $c = 1.6$ )
	TGG grid	NA	NA	6 ( $c = 1.8$ )	NA

Numbers in bold indicate the values of the work of adhesion which are close to those predicted from the surface energy consideration, see text. (a) and (b) represent two different probes of the same diameter but possible different surface nano-roughness characteristic.

and can vary from 1.5 to 2.0. In extreme cases, the  $c$  value can be 2 if equation (5) represents the Derjaguin approximation [15] for the sphere–flat interactions or represents the DMT contact mechanics model [3] (for  $\lambda \geq 5$ ), whereas  $c = 1.5$  if the JKR contact mechanics model [2] applies (for  $\lambda \leq 0.1$ ).

The value of constant  $c$  in equation (5) (for  $0.1 < \lambda < 5$ ) can be calculated from the expression derived by Carpick *et al.* [16]:

$$c = \frac{7}{4} - \frac{1}{4} \left( \frac{4.04\lambda^{1.4} - 1}{4.04\lambda^{1.4} + 1} \right), \quad (6)$$

where  $\lambda$  is the Maugis parameter that can be calculated from [4]:

$$\lambda = \frac{2.06}{z_0} \sqrt[3]{\frac{R_p W_A}{\pi K^2}}, \quad (7)$$

$z_0$  is the equilibrium separation distance between the probe and substrate during adhesional contact, usually assumed in the range of values from 0.2 to 0.4 nm and

$K$  is the reduced elastic modulus:

$$\frac{1}{K} = \frac{3}{4} \left( \frac{1 - \nu_P^2}{E_P} + \frac{1 - \nu_S^2}{E_S} \right), \quad (8)$$

$E$  denotes Young's modulus and  $\nu$  is the Poisson's ratio; subscripts P and S refer to probe and substrate, respectively. Assuming  $E_P = 64$  GPa and  $\nu_P = 0.2$  for borosilicate glass and  $E_S = 129$  GPa and  $\nu_S = 0.28$  for silicon wafer [17], the reduced elastic modulus is  $K = 60.2$  GPa for our systems.

The third column in Table 2 shows  $W_A$  values calculated using equation (5). The values vary from 0.5 to 4.4 mJ/m<sup>2</sup>, which appears to be 1–2 orders of magnitude smaller than what we could expect. For example, Sharma and Freitas [18] determined the surface energy of both silicon wafer and glass using contact angle measurements to be 60–65 mJ/m<sup>2</sup>. Surface energy of both silicon wafer and glass depend on the surface cleaning procedure and degree of surface contamination. It is well known that water will spread to form a film on well-cleaned surfaces of both silicon wafer and glass, which indicates that the surface energy of these materials can be even larger than reported by Sharma and Freitas [18], i.e.,  $\gamma_S > 72$  mJ/m<sup>2</sup>. These, silicon wafer and glass are difficult to maintain clean in the laboratory environment during the AFM experiments for a long time. Certain amount of contaminants from the air will adsorb at the surfaces of both silicon wafer and glass during the AFM experiment, reducing the surface energy to less than 72 mJ/m<sup>2</sup>, but usually not less than what was reported in Ref. [18]: 60–65 mJ/m<sup>2</sup>. As the surface energies for both silicon wafer and glass are similar, we can assume that the work of adhesion between glass and silicon wafer will be close to the twice the surface energy of one of these materials, i.e.,  $W_A \approx 120$ – $150$  mJ/m<sup>2</sup> (this value is reduced to  $<100$  mJ/m<sup>2</sup> for the 5  $\mu$ m probe whose surface was partially silanized). The results of our calculations shown in the third column of Table 2 are two orders of magnitude smaller than could be expected. This discrepancy clearly indicates that analysis of the  $W_A$  value cannot be done based on the microscopic dimensions of the probe and substrate, and nanoroughness significantly reduces the contact between the probe and substrate during the pull-off force measurements. If instead, the radius of curvature of nano-irregularity located on the 10  $\mu$ m probe apex (probe 10b, Table 2) is used, the calculated  $W_A$  value is much closer to our estimate. The danger with this approach is that it does not take into account the roughness of the substrate and this result can be coincidental.

Because 'smooth' substrates used in this research still possessed roughness characteristic at the nano-scale, the adhesion between the probe and individual asperities of the substrate with the radius of curvature of  $R_A$  could be estimated from the following equation:

$$W_A = \frac{F}{c\pi} \frac{(R_P + R_A)}{R_P R_A}. \quad (9)$$

Here asperity shape is assumed to be spherical, for simplicity of our analysis. In our calculations we used average value of asperity size instead of radii distribution.

As can be seen from the data shown in the fourth column of Table 2, much more reasonable values of the work of adhesion were obtained, an order of magnitude or more larger values than the values calculated with equation (5) ( $W_A = 47\text{--}172 \text{ mJ/m}^2$ ).

Equation (9) cannot be used for analysis of the work of adhesion between spherical probes and ridges of the TGG gratings. The geometry of this system can be approximated as a sphere in contact with a cylinder. The expression for  $W_A$  for this geometry was taken from the work by Kirsch [19]:

$$W_A = \frac{F}{c\pi R_P} \sqrt{1 + \frac{R_P}{R_A}}. \quad (10)$$

The radius of the ridges in the TGG grating ( $R_A$ ) is assumed to be 10 nm, according to the manufacturer's specification. As shown by the data in the fifth column of Table 2, the calculated work of adhesion decreased from 60 to 6 mJ/m<sup>2</sup> for increasing probe sizes from 5 to 40  $\mu\text{m}$ . Although we recognize that the 5  $\mu\text{m}$  probe was silanized (providing reduced probe's adhesion to the substrate) and the data generated with this probe cannot be used for direct comparison with other unmodified probes, the effect of increasing dimension of the probe on calculated work of adhesion is remarkable. This clearly indicates that larger probes are more sensitive to nano-scale imperfections of the standard grating noted in the previous discussion (Fig. 4).

Finally, the model of Rabinovich *et al.* [13, 14] (equations (2)–(4)) was used to analyze the data. Because in our systems  $F/R \gg B$ , equation (2) was reduced to:

$$W_A = \frac{58FRMS}{c\pi\lambda^2}. \quad (11)$$

The results of calculations are shown in the last column of Table 2. With the exception of the result for the probe 10a, the work of adhesion values calculated for other probes in contact with flat silicon substrates are in the range of our estimates.

#### 4. CONCLUSIONS

Roughness has typically been held responsible for decreasing the pull-off force magnitude on account of asperity contact rather than intimate contact of the spherical body with the flat substrate (idealized geometries). We show here that when the probe size is close to the scale of roughness, the magnitude of the force measured may actually increase or decrease. The explanation for this comes from the possibility of multiple contact points (double contact points in the case of our systems with the TGG grating) with asperity sidewalls when the probe is able to penetrate inter-asperity spacing.

In addition, roughness effect was studied systematically by varying the probe size to the scale of substrate roughness features, and controlling the orientation of the probe over the substrate features to induce different contact scenarios. The experimental results showed that the scatter in the pull-off forces decreases with increasing ratio of the probe diameter to the dimension of the surface asperity, but on the contrary, the magnitude of the pull-off force is more severely altered by roughness.

The analysis of pull-off forces measured for rough (rigid) substrates and probes in terms of the work of adhesion still seems possible if the probe diameter is much larger than the size of roughness features of interacting surfaces. In order to succeed in interpreting such complex systems, a detailed surface analysis in terms of roughness parameters, asperity size and shape, and spacing between asperities is required. Then, analysis of the experimental data should be done with one of the theoretical models applicable to rough surfaces.

### Acknowledgements

Financial support provided by the Petroleum Research Fund administered by the American Chemical Society is gratefully acknowledged.

### REFERENCES

1. J. Drelich, G. W. Tormoen and E. R. Beach, *J. Colloid Interf. Sci.* **280**, 484–497 (2004).
2. K. L. Johnson, K. Kendall and A. D. Roberts, *Proc. Roy. Soc. London* **A324**, 301–313 (1971).
3. B. V. Derjaguin, V. M. Muller and Yu. P. Toporov, *J. Colloid Interf. Sci.* **53**, 314–326 (1975).
4. D. Maugis, *J. Colloid Interf. Sci.* **150**, 243–269 (1992).
5. A. D. Zimon, *Adhesion of Dust and Powder*. Plenum Press, New York, NY (1969).
6. R. McKendry, M.-E. Theoclitou, C. Abell and T. Rayment, *Langmuir* **14**, 2846–2849 (1998).
7. E. R. Beach, G. W. Tormoen, J. Drelich and R. Han, *J. Colloid Interf. Sci.* **247**, 84–99 (2002).
8. F. L. Leite, A. Riul, Jr. and P. S. P. Herrmann, *J. Adhesion Sci. Technol.* **17**, 2141–2156 (2003).
9. H. A. Mizes, *J. Adhesion* **51**, 155–165 (1995).
10. G. W. Tormoen, J. Drelich and E. R. Beach, *J. Adhesion Sci. Technol.* **18**, 1–17 (2004).
11. K. Cooper, N. Ohler, A. Gupta and S. Beaudoin, *J. Colloid Interf. Sci.* **222**, 63–74 (2000).
12. K. Cooper, A. Gupta and S. Beaudoin, *J. Colloid Interf. Sci.* **234**, 284–292 (2001).
13. Y. I. Rabinovich, J. J. Adler, A. Ata, R. K. Singh and B. M. Moudgil, *J. Colloid Interf. Sci.* **232**, 10–16 (2000).
14. Y. I. Rabinovich, J. J. Adler, A. Ata, R. K. Singh and B. M. Moudgil, *J. Colloid Interf. Sci.* **232**, 17–24 (2000).
15. J. Israelachvili, *Intermolecular and Surface Forces*, 2nd edn. Academic Press, London (1992).
16. R. W. Carpick, D. F. Ogletree and M. Salmeron, *J. Colloid Interf. Sci.* **211**, 395–400 (1999).
17. W. D. Callister, Jr., *Materials Science and Engineering: An Introduction*, 4th edn. John Wiley, New York, NY (1997).
18. M. M. Sharma and A. M. Freitas, in: *Particles on Surfaces 7: Detection, Adhesion and Removal*, K. L. Mittal (Ed.), pp. 171–187. VSP, Utrecht (2002).
19. V. A. Kirsch, *Adv. Colloid Interf. Sci.* **104**, 311–324 (2003).

## Experimental analysis of the influence of surface topography on the adhesion force as measured by an AFM

A. MÉNDEZ-VILAS, M. L. GONZÁLEZ-MARTÍN,  
L. LABAJOS-BRONCANO and M. J. NUEVO \*

*Departamento de Física, Facultad de Ciencias, Universidad de Extremadura, Avda. de Elvas s/n,  
06071 Badajoz, Spain*

**Abstract**—Force curves have been acquired using an atomic force microscope (AFM) on homogeneous microspheres of three different materials (latex, glass and yttria), in order to study the possible influence of the surface topography/geometry on the adhesion force as measured by an AFM. Forces were measured in regions at the top of the spheres ( $\theta \approx 90^\circ$ ), at half-heights ( $\theta \approx 0^\circ$ ) and in an intermediate region between these two ( $\theta \approx 45^\circ$ ), where the angle  $\theta$  is measured from the equatorial plane of the sphere to its polar axis. A very irregular and non-reproducible behaviour was found at  $\theta \approx 0^\circ$ , so only the other two regions were quantitatively analysed. For all the three materials, a much smaller adhesion force was obtained in the region corresponding to  $\theta \approx 45^\circ$  as compared to  $\theta \approx 90^\circ$ . Moreover, a quite similar adhesion decrease ratio of about  $1.60 \pm 0.5$  was obtained for all the three materials, which may suggest that the observed behavior might be due to geometrical factors. This observed influence could, in part, explain the observed heterogeneity in adhesion maps of microbial cells reported in the literature. The influence of the surface roughness is also discussed and it seems to result in a poor reproducibility of force curves.

**Keywords:** Atomic force microscopy; adhesion force; force curve mapping; surface roughness.

### 1. INTRODUCTION

The adhesion property of surfaces is of great interest in many scientific and industrial fields. In industry, for example, adhesive tapes require a high gluing/adhesive property irrespective of the other material. On the contrary, magnetic tapes and hard disks work better if the adhesion between the read and write heads is minimal. Also, adhesion is of great importance in biology and medicine because of specific and non-specific interactions of microorganisms with biomaterials, biofilm forma-

---

\*To whom correspondence should be addressed. Phone: +34 924 289 533. Fax: +34 924 289 651.  
E-mail: maria@unex.es

tion and biofouling. Moreover, approaching surfaces are more conveniently treated in terms of surface energy rather than forces so, since adhesion is directly related to surface energy, it becomes a very useful parameter in practical problems [1].

Since its invention in 1986, Atomic Force Microscopy (AFM), also known as Scanning Force Microscopy (SFM), is being increasingly used in the analysis of adhesion. AFM features include high lateral resolution and versatility. This technique is capable of performing adhesion measurements under different environmental conditions and without special sample preparation. Force curves obtained by AFM are force-distance plots measured by monitoring the deflection of a cantilever as the tip attached at its end approaches or retracts from the sample. Physico-chemical surface properties of the sample such as friction, adhesion and elasticity can be derived from the analysis of force curves taken at extremely high lateral resolution [2–4]. This technique has been applied to many industrial [5–8] and biological fields [9–13].

In general, the surface area of an object is proportional to the square of its linear dimension, while the volume is proportional to its cube. Surface forces such as friction and adhesion are proportional to the surface contact area, while inertial forces are proportional to the volume. In micrometer and sub-micrometer-sized systems such as microbial cells and microelectromechanical systems (MEMS), the decreased size of features means that the influence of the surface forces exceeds that of the inertial forces. Therefore, tribological phenomena and adhesion play an extremely important role in these types of systems [14, 15]. A recent and excellent review about application of SFM in biological systems can be found in Ref. [16]. See also Refs. [17, 18] for good overviews of theoretical and experimental aspects of modern nanotribology.

Despite the advantages, problems arise due to the finite size of the AFM tip, when an AFM is used for imaging surface features with dimensions smaller or comparable to that of the radius of curvature of the tip. In this situation, since the image is dominated by the shape of the tip, several tip-related artifacts can be introduced [19], which distort the topographical images and lead to wrong quantification of surface parameters such as surface roughness [20]. Because the adhesion force depends on the contact area between the tip and the sample, these tip-artifacts will affect it. There are some publications dealing with the influence of nanometre-sized surface features on adhesion as measured by an AFM, from both theoretical [21] and experimental [22] points of view.

However, some authors have reported an influence of the surface topography on the adhesion forces when acquiring adhesion maps on micrometer-sized sphere-like cells, whose origin is not clear to date. The results from the published literature show a general tendency of the force values and related properties to decrease from the central areas to the periphery. For instance, the force maps obtained by Auerbach *et al.* [23] on unsaturated *Pseudomonas putida* biofilms showed less adhesion on the periphery than on the central areas (upper part of the cells). In this work, the authors assumed that this result could be caused by a minor moisture content



or a minor quantity of extracellular polymeric substances (EPS) on the interstitial areas than in the central regions. Similar results were obtained by Penegar *et al.* [24] regarding the Young's modulus, which was determined from the force curves, for the marine bacteria *Sphingomonas paucimobilis*. These authors did not take account the most peripheral regions because they could be affected by lateral displacements of the sample, as well as being influenced by the underlying substratum. In a previous study on yeast *Candida parapsilosis*, analogous results were obtained by our group [25]. In these types of systems, it is not easy to confirm the origin of such behaviour of the adhesion force, since cells can be quite heterogeneous at a molecular level, so it could be due to a complex interplay of topographical/geometrical, chemical and mechanical factors. In the present work, the influence of the topography/geometry on the adhesion force is analysed. To do so, three different systems with identical (spherical) geometry have been chosen: homogeneous microspheres of latex, glass and yttria, and adhesion force curves have been acquired in three chosen regions on each system, using an atomic force microscope.

## 2. MATERIALS AND METHODS

Three different kinds of homogeneous microspheres differing in their chemical nature and size were used: (a) latex (3.0  $\mu\text{m}$  microspheres), (b) glass (Glass beads, 3–10  $\mu\text{m}$ ), both supplied by Polysciences, Inc., and (c) yttria (10–100  $\mu\text{m}$ ) from Goodfellows GmbH. Concentrated aqueous dispersions of these particles were prepared and drops of them were placed on glass slides. By gently heating the glass slide with the drop, beads were partially fixed and the water evaporated. The samples were stored in a desiccator overnight. Water for preparing dispersions was deionized (from a Milli-Q Plus, Millipore). Figure 1a shows an AFM image taken in the topography mode, showing the surface of a glass microsphere. The corresponding 3D image is shown in Fig. 1b. From both images it is clear that the surface is quite homogeneous from a topographical point of view. The absence of highly irregular surface features can also be seen from the surface line profile recorded over a microsphere (Fig. 1c). Very similar images (not shown) were obtained for the latex microspheres, showing also a quite regular surface.

All AFM experiments were performed with an Autoprobe CP atomic force microscope (Park Scientific Instruments, Geneva, Switzerland), equipped with a scanner with a maximum range 100  $\mu\text{m}$  in the  $x$  and  $y$  directions and 7  $\mu\text{m}$  in the  $z$  direction. This instrument has an optical microscope to locate the region of interest in an easy way by monitoring the sample on a TV screen. Images were acquired using V-shaped cantilevers with conical silicon tips (Ultralevers, Park Scientific Instruments). The nominal force constant of the cantilevers is  $0.4 \text{ N m}^{-1}$ . Tips have a nominal radius of curvature of 10 nm according to manufacturer's specifications, and an aspect ratio (length-to-width ratio) of 3. The scanner speed ranged between 1 and 5  $\mu\text{m s}^{-1}$  and the images were acquired at a resolution of  $512 \times 512$  pixels

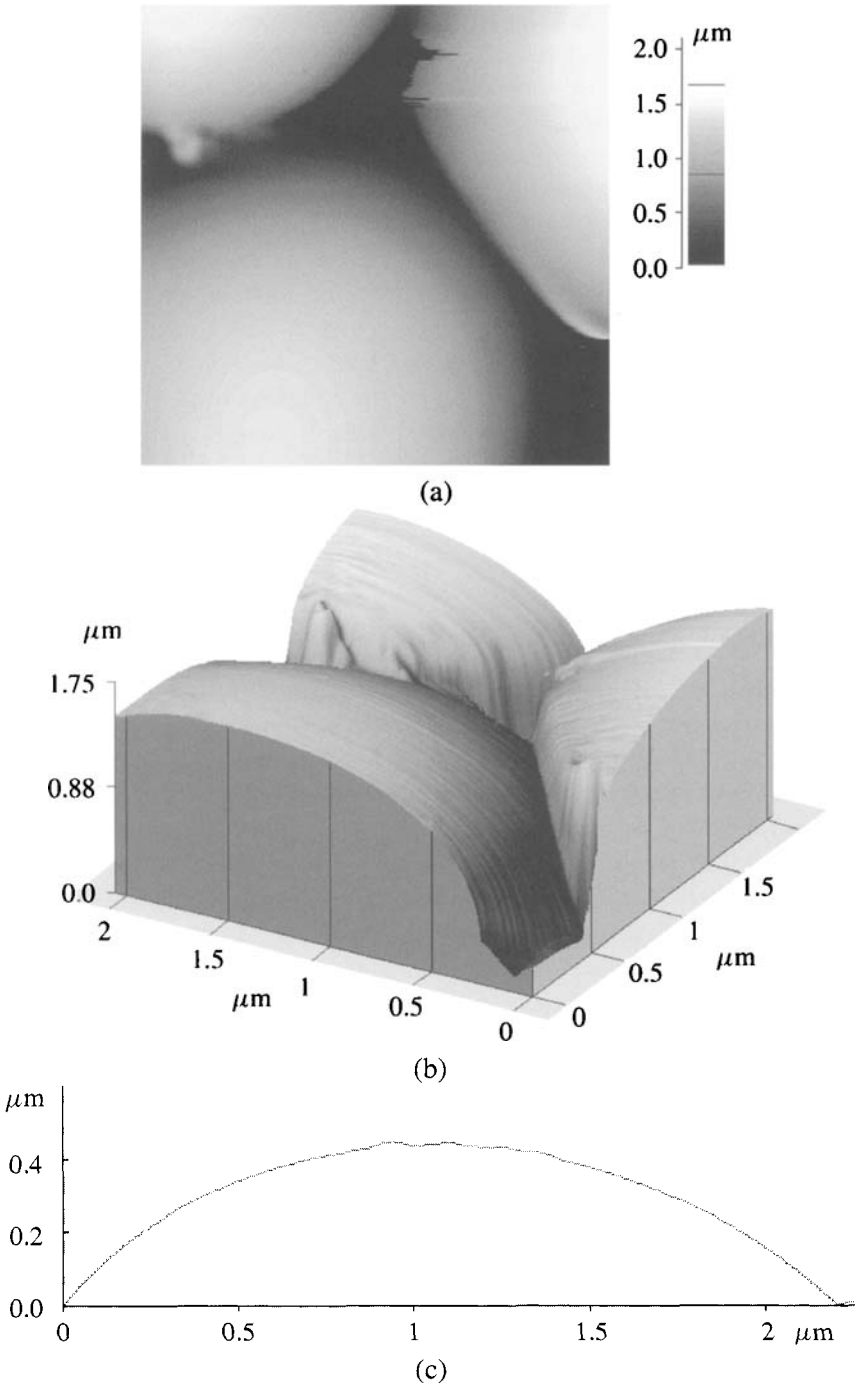


**Figure 1.** (a) Topographical AFM image ( $2.0 \times 2.0 \mu\text{m}^2$ ) of the surface of a set of latex microspheres. (b) 3D image of the topography of the microspheres shown in (a). (c) Line profile recorded over the latex microspheres, showing the topographical surface homogeneity of these beads.

and processed by applying a flattening routine. The maximum applied force was  $\approx 17$  nN.

Force vs. distance curves were acquired in three different areas of the surface of each microsphere as described in the next section.

### 3. RESULTS AND DISCUSSION

An AFM adhesion study was performed on microspheres of very different materials which are commonly used in scientific research. In order to show the influence of topography on adhesion forces as measured by an AFM, a set of force curves was obtained in different zones of the microsphere surface. A schematic diagram of these regions is shown in Fig. 2, where A, B and C denote regions whose average angles  $\theta$  are approximately  $90^\circ$ ,  $45^\circ$  and  $0^\circ$ , respectively. The area of each region was about  $0.2 \mu\text{m}^2$ .

A first observation in the adhesion measurement process on the microspheres was that force curves taken in region C were often extremely irregular and hardly reproducible since the force curves acquired consecutively on the same point were very different. This makes the characterization of adhesion in this region quite difficult or impossible. For this reason, data in regions A and B only will be compared for these materials.

In the case of latex microspheres, the mean value of the adhesion force was  $F_A = 39.3 \pm 9$  nN, with a number of trials  $N = 57$ , in region A, while in region B it was  $F_B = 23.5 \pm 9$  nN ( $N = 56$ ). Thus, a notable decrease in adhesion force is obtained when the surface is sloped with respect to the horizontal, even when no surface composition variation is present. This general behaviour was obtained irrespective of where the surface was selected around the sphere polar axis, at an angle of  $\theta \approx 45^\circ$ , giving a decrease ratio value of  $F_A/F_B = 1.67 \pm 0.50$ . Besides, it is interesting to note how the data reproducibility becomes poorer as the considered regions are more peripheral, as it can be seen by acquiring several consecutive force curves on the same point of a given area. These results are shown in Figs 3a and 3b

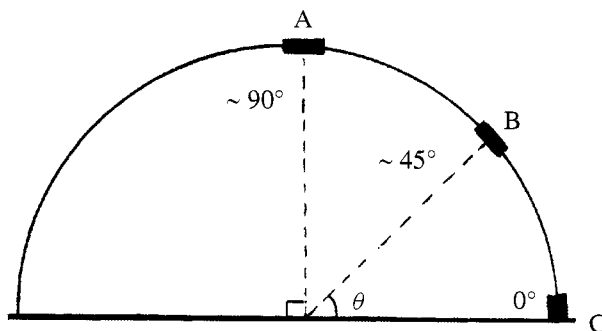


**Figure 2.** Schematic diagram of the three regions of the microspheres in which force curves have been recorded:  $\theta \approx 90^\circ$  (region A);  $\theta \approx 45^\circ$  (region B); and  $\theta \approx 0^\circ$  (region C).

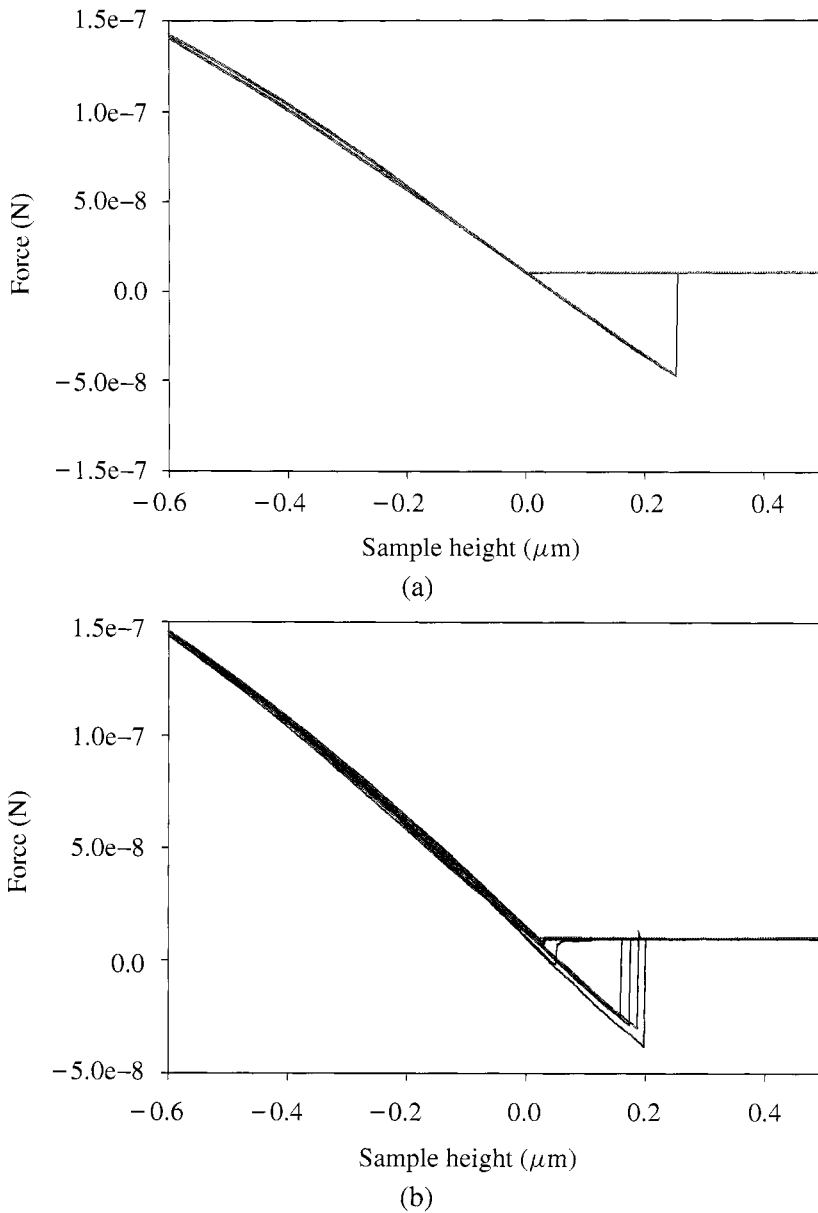


**Figure 3.** Five consecutive force curves taken at the same points of (a) region A and (b) region B, on latex microspheres.

where five force curves on the same point in regions A and B, respectively, have been plotted. From these pictures it is clear how adhesion becomes more difficult to characterize as more tilted the regions are.

For glass microspheres, a quite analogous behaviour is found. In this case, the measured adhesion force mean value was  $F_A = 18.4 \pm 6$  nN ( $N = 64$ ) in

the nearly horizontal region A, while the corresponding value in region B was  $F_B = 11.5 \pm 2$  nN ( $N = 64$ ). Again, a decrease in adhesion from region A to B is obtained, in spite of the fact that glass microspheres also represent a homogeneous system. In this case, the adhesion ratio was  $F_A/F_B = 1.60 \pm 0.50$ , comparable to that obtained for latex ( $1.67 \pm 0.50$ ). The similar ratios obtained for such different materials suggest that the observed decrease may be due to geometrical factors, probably related to a decrease in the contact area between the tip and the surface, as some authors have suggested [23], and not to the nature of the microsphere material. In order to test this assumption, analogous measurements were carried out on such a different material as yttria. From these additional sets of force curves on yttria microspheres with a diameter  $\phi \approx 10$   $\mu$ m, the adhesion forces were  $F_A = 30 \pm 4$  ( $N = 71$ ) and  $F_B = 18.2 \pm 7.5$  ( $N = 80$ ), in zones A and B, respectively. In this case, the adhesion ratio is  $1.65 \pm 0.5$ , which is in agreement with the above results, conferring some plausibility to the hypothesis of the topographical/geometrical effects in the adhesion measurements.

On the other hand, the behavior of force curves of glass microspheres in regions A and B are shown in Figs 4a and 4b, respectively. As can be derived from the comparison of forces curves in region B for latex (Fig. 3b) and glass (Fig. 4b), a better data reproducibility is achieved when force curves are acquired on glass beads (although a lateral off-set is observed amongst them). As in both latex and glass microspheres a quite homogeneous composition has been considered, so it must be some particular feature of each material that influences the data reproducibility. As is well known, since the surface roughness is quite different in glassy and polymeric materials and, thus, it could be responsible for the difference in data reproducibility between these two materials. In order to test this premise, surface roughness measurements were performed on both kinds of microspheres. Although several parameters have been proposed for characterizing surface roughness, the most commonly used is the root mean squared roughness,  $R_{rms}$ , defined as the standard deviation of height data in a chosen area. Since this parameter depends on the scale in which it is measured, its dependence with scale must be obtained to fully characterize the surface roughness of the materials. The results are presented in Fig. 5 showing that latex has a higher surface roughness than glass, at all the scales in which it has been measured.

The possible influence of surface roughness on data reproducibility can be qualitatively understood by making use of a simple model. Figures 6a and 6b show schematic diagrams of an AFM tip approaching horizontal and tilted rough surfaces, respectively. In the case of a normal approach, the tip-surface contact is made through the tip apex which will be the point where the force is applied during the complete force curve acquisition process. However, if a tilted surface is approached, the initial contact could be made at a lateral point of the tip. In this case, while the tip is being pushed against the surface, the tip-surface contact point could be varying during the force curve acquisition process, giving rise to a non-comparable set of force values and, consequently, to very irregular force curves.

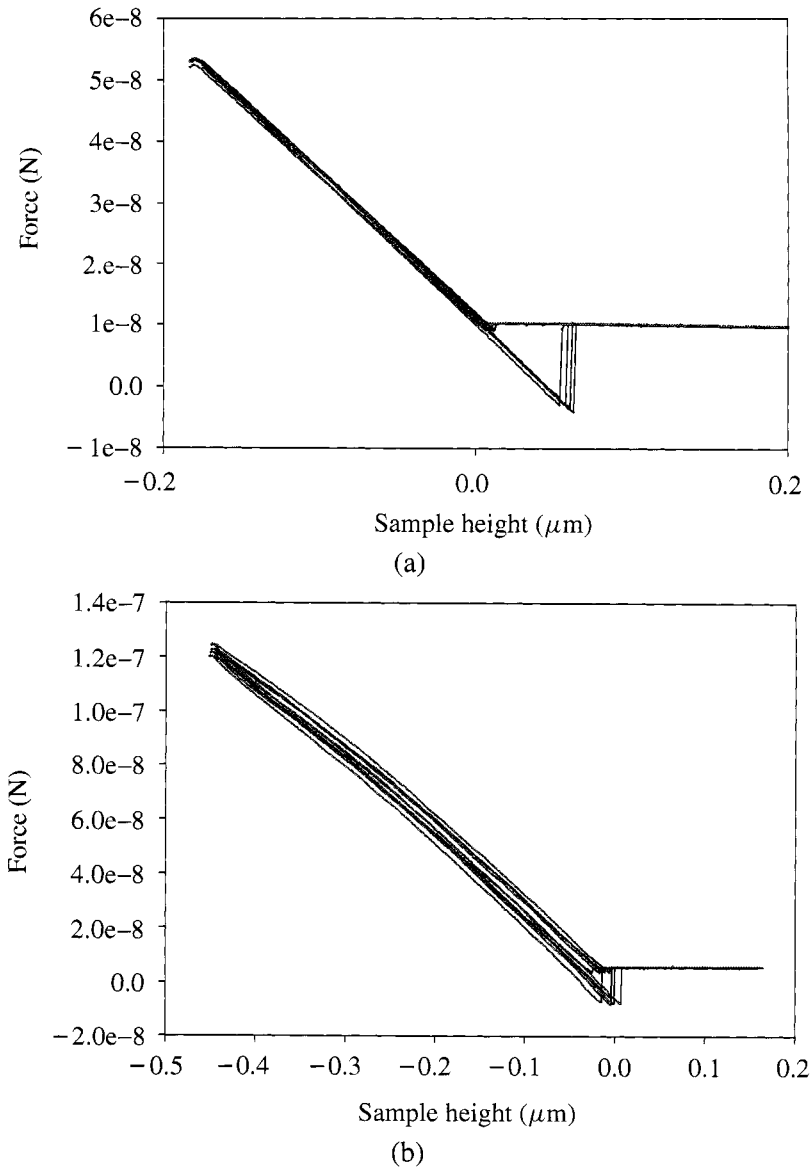


**Figure 4.** Five consecutive force curves taken at the same points of (a) region A and (b) region B, on the glass beads.

Moreover, an additional effect could occur when a lateral interaction takes place between the tip and the surface. It is quite possible that pushing against a tilted surface causes the tip to twist a little, in such a way that the laser spot could be moved not only from side to side on the photodiode, but also up and down, resulting in artificial force data at that point.

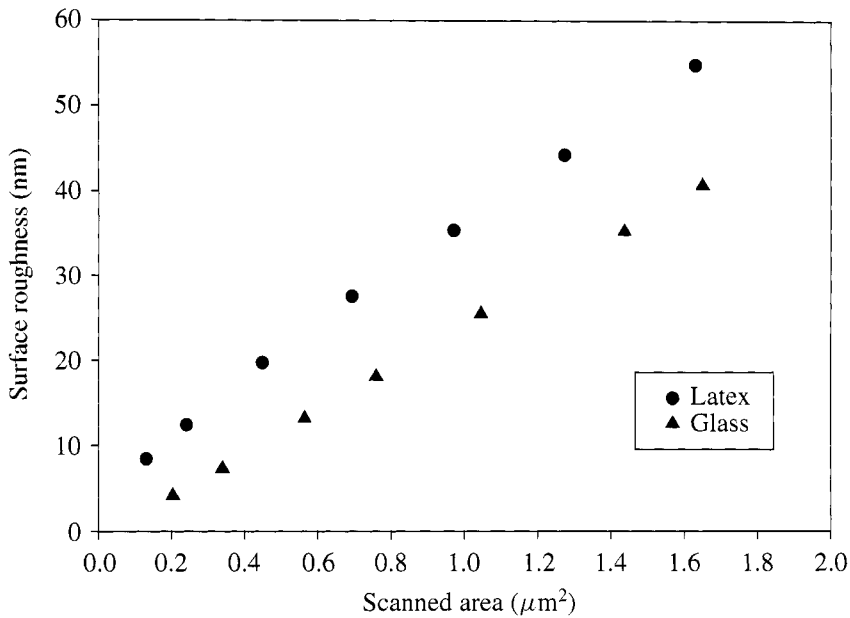


**Figure 5.** Surface roughness values ( $R_{rms}$ ) as a function of scanned area for (●) latex and (▲) glass microspheres.

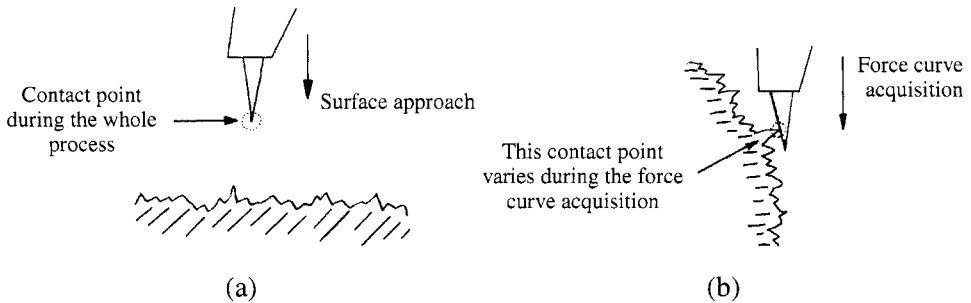


**Figure 6.** Schematic pictures of an AFM tip approaching (a) horizontal and (b) tilted rough surfaces.

Finally, it is interesting to note that lateral interactions are also the cause of *tip artifacts*, as some authors have reported [26, 27] and as it was mentioned in the Introduction. Usually, these types of artifacts produce very particular distortions of the image (line profiles over affected images usually display straight lines when obtained on curved surface features). However, we have to emphasize that we did not find these types of artifacts in our images, which suggests that although all these effects could have the same origin, the adhesion measurement is probably more sensitive to this lateral interaction than *tip artifacts*.

#### 4. CONCLUSIONS

In this study, a significant decrease in the adhesion force when force curves are taken in regions far from the top of the spheres (nearly horizontal region) is shown, even when homogeneous systems are considered. The observed decrease seems to be nearly independent of the size and material, suggesting that it could be due to the geometry of the sample. This effect must be taken into account when adhesion force maps of microbial cells are obtained. The influence of surface roughness on force curves has been analyzed. Although surface roughness does not seem to have a significant influence on decrease ratio of adhesion force between the two zones studied, it seems to cause a greater scatter in the data and a poorer reproducibility of force curves.

#### Acknowledgements

Thanks are due to the Consejería de Educación, Ciencia y Tecnología (Junta de Extremadura) for financial support through Project IPR00A083.

#### REFERENCES

1. J. N. Israelachvili, *Intermolecular and Surface Forces*. Academic Press, London (1991).
2. A. L. Weisenhorn, P. Maivald, H. J. Butt and P. K. Hansma, *Phys. Rev. B* **45**, 1126 (1992).
3. N. A. Burnham and R. J. Colton, *J. Vac. Sci. Technol. A* **7**, 2906–2913 (1989).
4. E. A. Hassan, W. F. Heinz, M. D. Antonik, N. P. D'Costa, S. Nageswaran, C. A. Schoenenberger and J. H. Hoh, *Biophys. J.* **74**, 1564–1578 (1998).
5. R. Kaneko, K. Nonaka and K. Yasuda, *J. Vac. Sci. Technol. A* **6**, 291–292 (1988).
6. H. A. Mizes, K. G. Loh, R. J. D. Miller, S. K. Ahuja and E. F. Grabowski, *Appl. Phys. Lett.* **59**, 2901–2903 (1991).
7. A. Torii, M. Sasaki, K. Hane and S. Okuma, *Sensors Actuators A* **44**, 153–158 (1994).
8. K. O. van der Werf, C. A. J. Putman, B. G. de Grooth and J. Greve, *Appl. Phys. Lett.* **65**, 1195–1197 (1994).
9. M. Radmacher, J. P. Cleveland, M. Fritz, H. G. Hansma and P. K. Hansma, *Biophys. J.* **66**, 2159–2165 (1994).
10. M. Radmacher, M. Fritz, J. P. Cleveland, D. A. Walters and P. K. Hansma, *Langmuir* **10**, 3809–3814 (1994).
11. D. R. Baselt and J. D. Baldeschwieler, *J. Appl. Phys.* **76**, 33 (1994).
12. M. Radmacher, M. Fritz, C. M. Kacher, J. P. Cleveland and P. K. Hansma, *Biophys. J.* **70**, 556–567 (1996).
13. D. E. Laney, R. A. Garcia, S. M. Parsons and H. G. Hansma, *Biophys. J.* **72**, 806–813 (1997).
14. H. Fujita, in: *Proc. IEEE Micro Electro Mechanical Systems*, IEEE, New York, pp. 1–8 (1997).
15. Y. Ando, *Wear* **238**, 12–19 (2000).
16. Z. Reich, R. Kapon, R. Nevo, Y. Pilpel, S. Zmora and Y. Scolnik, *Biotechnol. Adv.* **19** (6), 451–485 (2001).
17. G. V. Dedkov, *Physics-Uspekhi* **43** (6), 541–572 (2000).
18. R. W. Carpick and M. Salmeron, *Chem. Rev.* **97**, 1163–1194 (1997).
19. M. O'Reilly, L. McDonnell and J. O'Mullane, *Ultramicroscopy* **86**, 107–112 (2001).
20. K. Westra, *J. Vac. Sci. Technol. B* **13**, 344 (1995).
21. T. Stifter, E. Weilandt, S. Hild and O. Marti, *Appl. Phys. A* **66**, 597–605 (1998).



22. K. Komvopoulos and W. Yan, *Trans. ASME J. Tribology* **119**, 391–400 (1997).
23. I. D. Auerbach, C. Sorensen, H. G. Hansma and P. A. Holden, *J Bacteriol.* **182**, 3809–3815 (2000).
24. I. Penegar, C. Toque, S. D. A. Connell, J. R. Smith and S. A. Campbell, in: *Proc. 10th International Congress on Marine Corrosion and Biofouling*, DSTO, Victoria, Australia, pp. 5–15 (1999).
25. A. Méndez-Vilas, A. M. Gallardo, C. Pérez-Giraldo, M. L. González-Martín and M. J. Nuevo, *Surf. Interface Anal.* **31**, 2027–2030 (2001).
26. P. Dietz, P. K. Hansma, O. Inacker, H.-D. Lehmann and K.-H. Herrmann, *J. Membrane Sci.* **65**, 101–111 (1992).
27. A. W. Marczewski and K. Higashitani, *Computers & Chemistry* **21**, 129–142 (1997).

## Adhesion forces between individual gold and polystyrene particles

LARS O. HEIM, STEFAN ECKE, MARKUS PREUSS  
and HANS-JÜRGEN BUTT\*

*Physical Chemistry II, University of Siegen, D-57068 Siegen, Germany*

**Abstract**—Using the particle interaction apparatus, adhesion forces between individual pairs of spherical polystyrene and gold particles ( $\varnothing$  2–20  $\mu\text{m}$ ) were measured. With the particle interaction apparatus the contact time and load can be adjusted keeping all other parameters constant. Adhesion forces between different pairs of particles varied by a factor of five even for similar particle sizes. Adhesion forces were significantly lower than expected from the JKR or DMT theory. AFM images confirmed that one reason was probably the surface roughness on the nanometer scale. For both materials the adhesion force did not depend on the load (at least up to loads of 1  $\mu\text{N}$ ). Thus plastic deformation is probably negligible. The adhesion force increased with contact time. We interpret this increase as being at least partially caused by squeezing out of surface films. By removing the surface film a closer contact between the particle surfaces is established.

**Keywords:** Atomic force microscope; adhesion; fine particles; powder; pull-off.

### 1. INTRODUCTION

Adhesion between small particles or particles and surfaces is important for a variety of natural phenomena and industrial processes [1]. One example is the aggregation, flow, and mixing of powders. Friction phenomena are strongly influenced by the adhesion between microcontacts [2, 3]. In order to understand and predict the aggregation of small particles, the forces between two particles in contact need to be known. When two particles in a vacuum or in a gaseous environment come close, they usually experience attractive forces such as van der Waals forces or the capillary force. Once in contact, they are inevitably deformed due to their finite elasticity.

---

\*To whom correspondence should be addressed. Phone: 0049-271-740 4125. Fax: 0049-271-740 3198. E-mail: butt@chemie.uni-siegen.de

The contact between two solid spheres is usually described by the model of Johnson, Kendall and Roberts (JKR) [4] or by the model of Derjaguin, Muller, and Toporov (DMT) [5]. Both models are based on an earlier analysis by Hertz, who considered two elastic bodies in contact under an external load but ignored the attractive interparticle forces [6]. In the JKR approach, the effective steady-state pressure in the contact circle is assumed to be the superposition of elastic Hertzian pressure and attractive surface forces which act only over the contact area. As a result, a tensile force is necessary to separate the adhering particles. This pull-off force between two spherical particles is given by

$$F_{\text{JKR}} = 3\pi R\gamma, \quad (1)$$

where,  $\gamma$  is the effective solid surface energy and  $R$  is the reduced radius of curvature of the two surfaces,  $R = R_1 R_2 / (R_1 + R_2)$ , with  $R_1$  and  $R_2$  being the individual particle radii.

DMT published an alternative theory which also accounts for non-contact forces in the vicinity of the contact area. It predicts a slightly higher pull-off force, i.e.

$$F_{\text{DMT}} = 4\pi R\gamma. \quad (2)$$

In both JKR and DMT models, the separation force between two spherical particles is independent of the elastic material properties but is a linear function of the particle size and the surface energy. It turned out that both models were limiting cases of a more general description [7]. The JKR model is appropriate for large, soft bodies with high surface energies. For small, hard solid particles with low surface energy, the DMT model should be applied [8, 9].

Adhesion forces for individual particles have been measured with a variety of methods [10–12]. The two most direct and precise methods are the centrifuge method [13–17] and atomic force microscope (AFM) based-techniques. The centrifuge method is based on the detachment of particles from a substrate due to a centrifugal force. The particles are deposited onto the substrate, the substrate is placed into a centrifuge, and the number of particles which detach at a certain angular velocity is measured. From the size of the particles and the angular velocity, the centrifugal force can be calculated. This centrifugal force equals the adhesion force when the particles detach from the surface. In this way adhesion forces for a large number of particles can be determined.

With the invention of AFM and the development of suitable microfabricated cantilevers as force sensors it became possible to measure repeatedly the adhesion force between individual particles. In a typical AFM force experiment the interaction between a spherical particle of 1–15  $\mu\text{m}$  radius attached to the end of a cantilever and a plane is measured [18–22]. The advantage is that with an individual well-characterized particle several experiments can be done [23–26].

For surfaces which are perfectly smooth and clean, equations (1) and (2) have been verified. In normal circumstances, however, the adhesion observed between hard solids is smaller. This may be due either to surface films or surface roughness [27].

Much theoretical [28] and experimental [23, 29] effort is devoted to find out to which degree in a specific system roughness or surface films influence adhesion.

Here we present results of adhesion measurements with an AFM related setup called the particle interaction apparatus (PIA). In contrast to most experiments in which the force between a particle and a planar surface is determined and Derjaguin's approximation [30] is used to calculate the corresponding particle-particle interaction we really measured the adhesion force between two particles. Mainly four questions were addressed:

- (1) Is the first contact different from subsequent contacts? This question is relevant with respect to the methodology of AFM force measurements. In an AFM experiment the first contact is usually not recorded. The first few contacts are used to adjust the instrumental parameters. Only after several contacts, force curves are recorded and the adhesion (pull-off) force is measured. An implicit assumption is that the adhesion force does not change from contact to contact. With PIA we could verify this assumption.
- (2) How does the adhesion force depend on the particle size? Does the adhesion force increase linearly with the particle radius as predicted by equation (1) and (2)?
- (3) Does the adhesion force depend on the maximal load? Irreversible changes like plastic deformation are expected to depend on the load.
- (4) Does the adhesion force depend on the contact time? If a surface film (e.g. hydrocarbon, water contamination layer) influences adhesion this is expected to change with time due to a thinning of the film. In addition, viscoelastic processes or the formation of bonds might depend on the contact time.

These questions were already addressed for spherical silica ( $\text{SiO}_2$ ) particles [31]. Silica particles are rigid, usually show an elastic response, and have a smooth surface. In this sense they are an ideal model system to verify theories of elastic contact. Here we describe results obtained with spherical polystyrene and gold particles. Gold and especially polystyrene are significantly less rigid. Their surfaces are rougher and probably less homogeneous. One advantage of PIA is that the contact time can be varied keeping the load constant or the load can be varied keeping the contact time constant.

## 2. MATERIALS AND METHODS

Gold spheres with appropriate diameters were produced using two gold wires connected to a power supply and briefly creating a short circuit (30 V, max 0.2 A). This was done under argon atmosphere to avoid chemical reactions and contamination. A small aerosol cloud was produced in the spark. It was captured in a small container and consisted of gold spheres with a wide size distribution in the micrometer range. Gold spheres were glued onto tipless cantilevers (Veeco Instruments, Santa Barbara, CA, USA: V-shaped, 190  $\mu\text{m}$  long and 0.6  $\mu\text{m}$

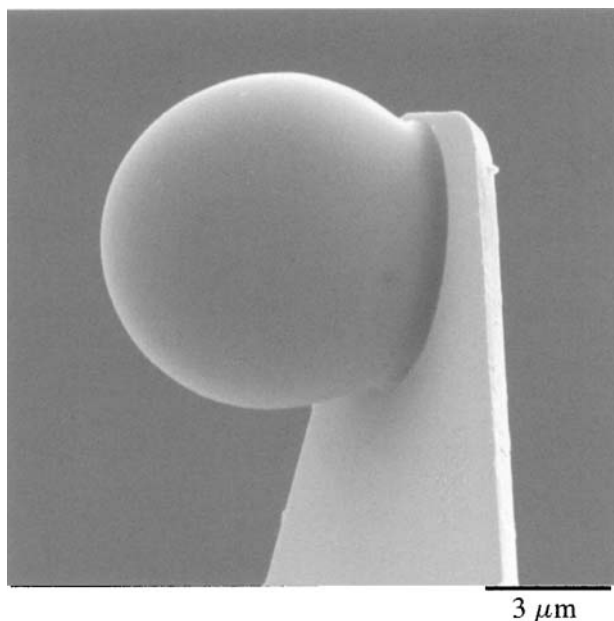


**Figure 1.** Scanning electron micrograph of a polystyrene particle at the end of a cantilever. The particle was melted onto the cantilever by heating for a few minutes at 120°C.

thick, spring constant 0.04–0.17 N/m) using a small amount of epoxy resin (Epikote 1004, Shell). Polystyrene spheres of different radii (Bangs Labs Inc., Carmel, IN, USA) were first rinsed with excessive amounts of water to get rid of adsorbed surfactants which were present to stabilize the polystyrene dispersion during synthesis as described earlier [32]. The particles were glued or melted onto silicon nitride cantilevers (Fig. 1).

The particle interaction apparatus (Fig. 2) was described in detail before [33]. Briefly, cantilevers are fixed in a cantilever holder. The sample, consisting of a row of particles (Fig. 3), was placed on top of the piezoelectric translator. The particle on the cantilever was then positioned a few micrometers above a particle on the sample with three micrometer screws. This was done under optical control of a microscope with a long-distance lens (magnification 120) and a binocular. Using these microscopes and also being able to detect a twisting of the cantilever (since we used a two-dimensional photosensor, see below) we were able to position the particle on the cantilever with a lateral accuracy of roughly 0.5 μm with respect to the particle on the sample. All experiments were done at room temperature, the relative humidity was 40–50%. Humidity influences the adhesion force usually only above 40–50% [34, 35].

To measure force-vs-position curves the sample was moved towards the particle with a 15-μm range piezoelectric translator (Physik Instrumente, Germany). ‘Sample’ in our case is the row of particles mounted on a substrate on top of the piezoelectric translator. This translator was equipped with an integrated position

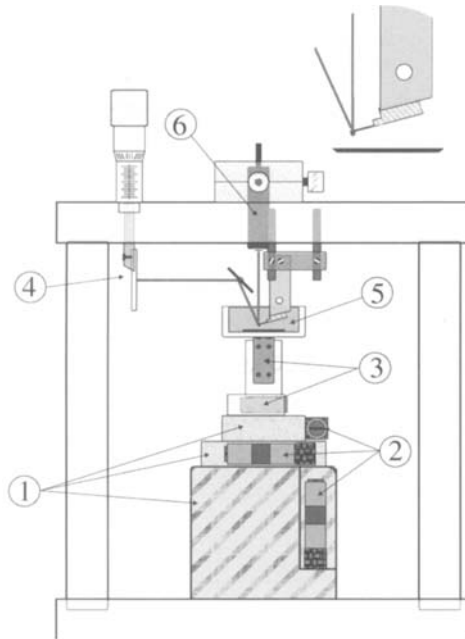


**Figure 2.** Schematic diagram of the particle interaction apparatus: (1)  $x$ - $y$ - $z$  translation stage; (2) stepper motors; (3) piezoelectric translator for horizontal and vertical displacements; (4) position sensitive device for monitoring the cantilever deflection; (5) liquid cell with sample on the bottom, cantilever with particle fixed on a holder coming from above; and (6) laser light source (movable in  $x$ - $y$  directions for focusing on the cantilever end). The cantilever holder and the light path are shown in detail in the insert.

sensors, which provides the position with an accuracy of 1 nm in a closed-loop operation. During the movement the deflection of the cantilever was measured with an optical lever technique. Therefore, the light of a laser diode (1.5 mW, 670 nm wavelength) was focussed onto the back of the gold coated cantilever. Via a mirror, the position of the reflected laser spot was measured with a two-dimensional position sensitive device (SiTek Electro Optics, Sweden, active area  $20 \times 20 \text{ mm}^2$ ). Using a position-sensitive device instead of a split photodiode increases the dynamic range for deflection and hence force detection.

In contrast to normal AFM force experiments the sample was not moved up and down periodically with constant speed (triangular position curve) but moved fast towards the particle on the cantilever, then held at a fixed position. After a certain contact time it was retracted again. In this way, during contact the load was constant. Approaching and retracting speeds for all experiments were  $0.7 \mu\text{m/s}$ . Both the height position of the sample and the deflection of the cantilever were recorded directly with an AD-board in a personal computer or with a digital oscilloscope (12 bit effective resolution). The computer also controlled the movement of the sample. The adhesion force is the force required to separate the two particles after

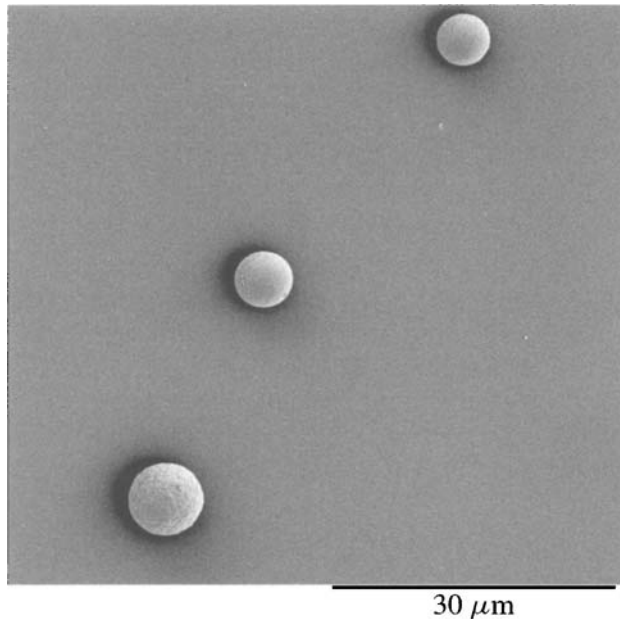


**Figure 3.** Scanning electron micrograph of three gold particles glued to a silicon wafer.

contact. It was obtained by multiplying the maximal negative deflection of the cantilever with its spring constant.

Spring constants of each individual spring used were determined by moving them against a reference cantilever as described before [36]. The reference cantilever was calibrated with a method described by Cleveland *et al.* [37] by measuring its resonance frequency with attached spheres.

To determine surface roughness of particles the particles were imaged with a commercial AFM (Multimode, NanoScope 3 controller, Veeco Instruments, CA Santa Barbara, USA) in contact mode using oxide sharpened V-shaped silicon nitride cantilevers (Veeco Instruments, 110 μm long and 0.6 μm thick, spring constant  $\approx 0.15$  N/m). The scan size is limited by the radius of the particle. When imaging steeply inclined surfaces often the images become distorted and surface roughness cannot quantitatively be measured anymore. To avoid imaging steep regions the scan size was limited to typically 20–30% of the radius. For surface areas between (100 nm<sup>2</sup>) and (1 μm<sup>2</sup>) the roughness did not depend significantly on the scan area.

### 3. RESULTS AND DISCUSSION

#### 3.1. Dependence of adhesion force on the number of contacts

When carrying out experiments with individual particles one important question is whether the adhesion after the first contact is different from the adhesion after the

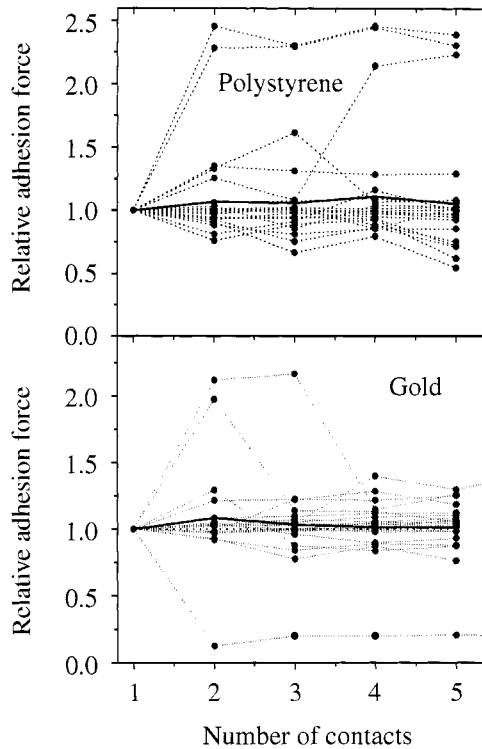


**Figure 4.** Adhesion forces measured between many pairs of particles depending on the number of contacts. For a better comparison all adhesion forces were divided by the adhesion force measured at the first contact. Only results obtained from the first five force curves are shown. Each symbol represents the result of one measurement with one pair of particles. The continuous line corresponds to the mean value. Dashed lines connect adhesion forces measured with one pair of particles. The contact time was roughly 1 s and the external load was 20–80 nN.

second or subsequent contacts. Therefore, we recorded force curves for the first five contacts, and the adhesion force did not depend on the number of the contact (Fig. 4). Although in some experiments a significant difference between first and subsequent contacts was detected no systematic variation could be observed. The average adhesion force remained the same within an accuracy of 10%. Hence, under normal conditions we could safely adjust all device parameters and then start recording the force curves.

Reitsma *et al.* [38] detected an increase in the adhesion force when studying the interaction of a 27- $\mu\text{m}$  diameter polystyrene particle and a flat silica surface. In contrast to our experiments they applied a high load of 95  $\mu\text{N}$ . In our experiments the load was only 20–80 nN.

### 3.2. Absolute adhesion forces and their dependence on particle radius

Figure 5 shows the measured adhesion force vs the reduced particle radius determined for many pairs of particles. The mean normalized adhesion forces ( $F_{\text{ad}}/R$ )



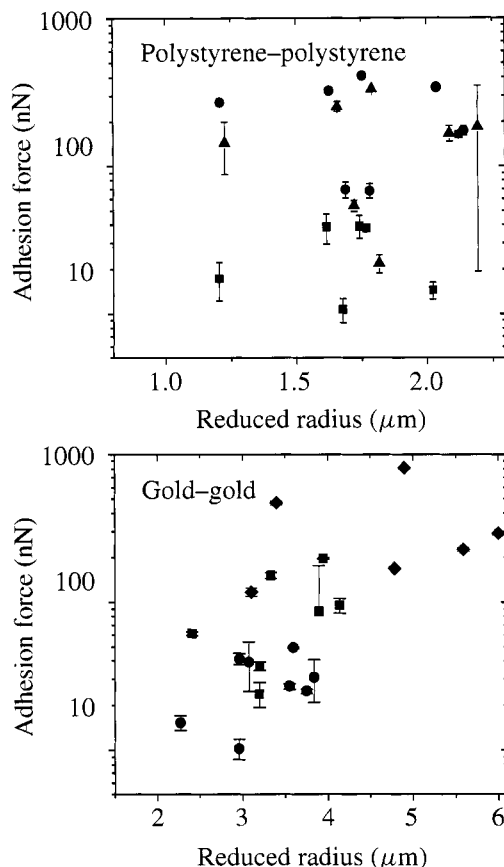


**Figure 5.** Adhesion forces measured for many pairs of particles vs the reduced radius. Results are shown for three different particles on cantilevers (indicated by different symbols) interacting with 8 particles on the substrate. The error bars indicate the standard deviation determined from many force measurements for a certain pair of particles. The contact time was 1 s and the maximal load roughly 50 nN.

were 0.087 N/m for polystyrene and 0.038 N/m for gold. There was a general tendency for the adhesion force to increase with increasing particle radius. A precise verification of equation (1) or (2) is, however, principally impossible because the results were widely scattered. Adhesion forces for different pairs of particles differ by a factor of 5–10 even when comparing similar reduced radii.

At this point it is necessary to distinguish different sources of variation in the adhesion force. First, when doing adhesion measurements with one pair of particles the adhesion varies slightly from force curve to force curve. This variation is indicated by the error bars in Fig. 5. A significantly higher variation occurs when comparing adhesion forces obtained with different pairs of particles. This wide distribution of adhesion forces is well known from centrifuge studies [16, 17]. In AFM studies often relatively precise adhesion forces are reported. This, however, is

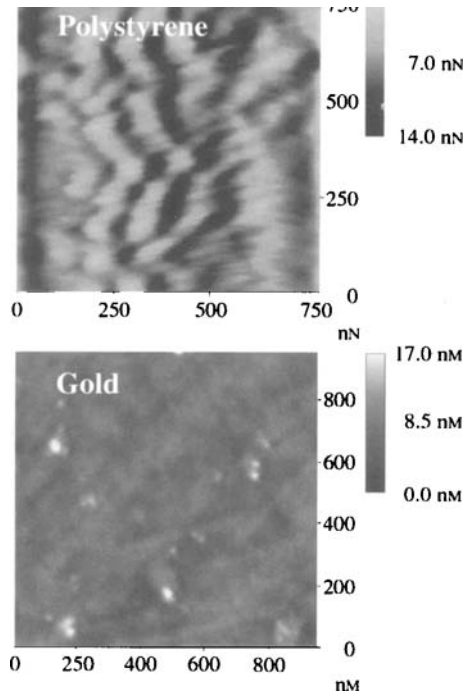


**Figure 6.** Atomic force microscope images of the surfaces of a polystyrene ( $\varnothing 5 \mu\text{m}$ ) and a gold particle ( $\varnothing 20 \mu\text{m}$ ). The images were flattened to remove the overall spherical curvature. Flattening partially caused the appearance of vertical stripes.

misleading. It merely reflects the fact that it is time consuming to measure adhesion forces with many particles since each particle has to be attached to a cantilever and the spring constant needs to be determined.

Adhesion forces measured were lower than expected from equation (1) or (2). For polystyrene surface energies around  $40 \text{ mJ/m}^2$  are reported [39–42]. Hence, we expected adhesion forces of  $0.8 \mu\text{N}$  for  $R = 2 \mu\text{m}$ . For clean gold surface energies are above  $1000 \text{ mJ/m}^2$  [43, 44]. Under ambient conditions this is reduced by at least an order of magnitude [45] and the surface energy is of the order of  $100 \text{ mJ/m}^2$  [46].

These two observations — the scatter in adhesion force and the low average adhesion force — can be explained in terms of surface roughness. Surface roughness decreases the actual area of contact and, as a consequence, the adhesion is not as high as expected from equation (1) or (2) [23, 27, 47]. To estimate surface roughness several particles were imaged with an AFM in contact mode. The surface roughness was of the order of  $\text{rms} = 3\text{--}5 \text{ nm}$  for polystyrene (those that were melted onto the cantilever) and  $6\text{--}15 \text{ nm}$  for gold particles (Fig. 6).

Compared to the results of other AFM studies our adhesion forces were relatively high (Table 1). One reason might be the small reduced radii. For small radii the influence of surface roughness is reduced. The adhesion force between gold particles is slightly lower than the adhesion force determined earlier with the

**Table 1.**

Normalized adhesion force (adhesion force  $F_{ad}$  divided by the reduced radius  $R$ ) for the interaction of polystyrene particles with different materials. Results were obtained with an AFM, or a bimorph surface forces apparatus (*Measurement and Analysis of Surface Interaction Forces* (MASIF))

$R(\mu\text{m})$	Material	$F_{ad}/R$ (N/m)	Ref.
8	Graphite/mica	0.0025/0.0038	[23]
6	Rigid elastomer	0.017	[53]
27	Silica	0.04	[38]
5	Steel	0.01–0.015	[54]
1...2	Polystyrene	0.1	This work
$\approx 1000$	Polystyrene	0.15	[42]

centrifuge method [15, 16, 48, 49]. Instead of roughly  $0.1 \mu\text{N}$  at a radius of  $4 \mu\text{m}$  they measured  $\approx 1 \mu\text{N}$  at  $R = 5\text{--}15 \mu\text{m}$ . One possible explanation is the longer contact time of 1–24 h which is required when using the centrifuge method.

It is also instructive to compare these results to adhesion forces determined earlier with silica particles. Adhesion forces between silica particles were only two or three times lower than expected from equation (1) or (2) [31]. In addition, adhesion forces varied only by a factor of two from particle to particle. Both observations probably reflect the smoothness of the silica surface; the roughness was  $\text{rms} \approx 0.2 \text{ nm}$  as determined by AFM.

### 3.3. Dependence of adhesion forces on external load

Within the range of our experiments the adhesion force did not depend significantly on the externally applied load and this was valid for both polystyrene and gold particles for contact times of roughly 1 s. As one example, results obtained with six pairs of gold particles are shown in Fig. 7. For a better comparison the normalized forces (force divided by the reduced radius) are plotted. The range of loads accessible is limited by the spring constant of the cantilever used and by the fact that we avoided large deflections of the cantilever. Large deflections were avoided to reduce a lateral movement of the particles on top of each other which is inevitable at large deflections. The deflection was always kept below roughly 2% of the cantilever length ( $200 \mu\text{m}$ ). Hence, we did not apply loads above  $\approx 1 \mu\text{N}$ .

That for loads up to  $1 \mu\text{N}$  no change in the adhesion force was observed is in agreement with earlier reports. Only for much higher loads the adhesion force increased. Reitsma *et al.* observed a 50% increase in the adhesion force between a polystyrene particle and a flat silica surface when applying loads up to  $95 \mu\text{N}$  [38].

An increase in the adhesion force with load is usually interpreted as resulting from plastic or viscoelastic deformation. Plastic deformations can be estimated based

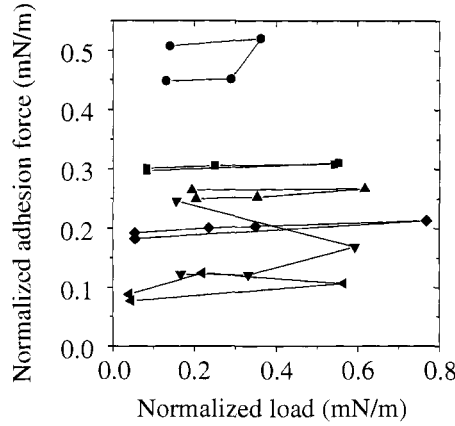


**Figure 7.** Normalized adhesion forces ( $F_{ad}/R$ ) vs the normalized applied load (load/ $R$ ) measured for a gold particle on the cantilever with respect to six gold particles on the sample. In this case the reduced radius ranged from 0.86 to 9.3  $\mu\text{m}$ .

on Maugis–Pollock theory [46]. According to their analysis, the load at which elasto-plastic deformation is induced ( $F_{ep}$ ) and the load for the onset of full plastic deformation ( $F_{fp}$ ) are given as [46]:

$$F_{ep} = 118 \frac{R^2 Y^3}{K^2}, \quad (3)$$

$$F_{fp} = 33900 \frac{R^2 Y^3}{E^2}, \quad (4)$$

where,  $Y$  is the yield strength,  $K$  the modulus of compression, and  $E$  is the elastic modulus. For gold these values are  $Y \approx 400$  MPa,  $K = 180$  GPa, and  $E = 80$  GPa. For polystyrene the material properties are  $Y = 10.8$  MPa,  $K = 4$  GPa, and  $E = 2.6$  GPa [50]. For our particles with typically  $R = 2$   $\mu\text{m}$  we obtain  $F_{ep} \approx 1$   $\mu\text{N}$  and  $F_{fp} \approx 1$  mN for gold and  $F_{ep} \approx 40$  nN and  $F_{fp} \approx 25$   $\mu\text{N}$  for polystyrene. Thus, at least for polystyrene some contribution of elasto-plastic contact was to be expected. We have no explanation why no indication for plastic deformation was found in these experiments.

In addition, we take into account that due to surface roughness a plastic deformation at single asperities might occur. The radius of an asperity can be much smaller than the radius of the whole sphere. In fact, Quon *et al.* measured the adhesion force between a gold coated mica surface and bare mica with the surface forces apparatus [51]. With increasing load they indeed found an increasing adhesion force caused by a reduction of the surface roughness of the gold and hence a larger contact area. They, however, used higher normalized loads than applied in our study. Using equation (4) we can calculate the maximal radius of curvature of an asperity which is expected to deform plastically under a certain load, say 200 nN. For gold

this radius of curvature is 24 nm. Thus, even for gold a plastic deformation cannot be excluded if contact is established via a single asperity of  $R < 24$  nm.

Still, in our experiments plastic or viscoelastic deformation was probably negligible because the adhesion force did not increase after the first contact and it did not depend on the applied load.

### 3.4. Dependence of adhesion force on contact time

The influence of the contact time on the adhesion forces at constant load was studied in a range of 1 to 100 s. Despite the large scatter in the results (Fig. 8a) a general increase in the adhesion force with contact time was observed. Increasing the contact time from 1 to 100 s leads to an increase of the average adhesion force by roughly 30% for both gold and polystyrene.

The time span of 100 s is too short for all processes summarized as 'time consolidation' which lead to the formation of solid bridges between particles [52]. Further, for gold plastic deformation or viscoelastic processes are highly unlikely. Thus we believe that the increase in the adhesion force with time at constant load reflects a thinning of surface films. Gold surfaces are usually coated with a layer of organic contamination, unless prepared and kept in UHV. This surface layer drastically reduces the surface energy of gold and, as a consequence, the adhesion.

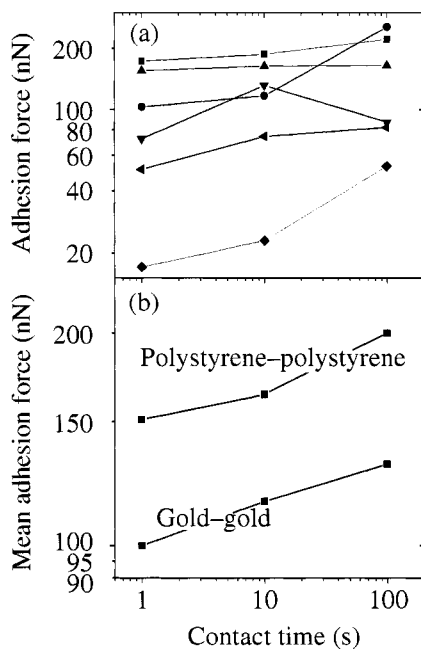


**Figure 8.** (a) Representative example of the adhesion force versus contact time for six pairs of gold particles. (b) Mean adhesion force versus the contact time averaged over all experiments. The load was roughly 50 nN in all experiments.

When two gold surfaces are pressed together the film is squeezed out of the gap and the adhesion increases.

For polystyrene, viscoelastic processes might be responsible for the increase in adhesion force with time; though we did not observe a dependence of the adhesion force on load. The calculations using equation (3) indicate that such a deformation is expected. The increase in the adhesion force with time is similar to the one observed with gold. This might indicate that the same process is also responsible and we believe that also for polystyrene surface films influence the adhesion significantly. More elaborate studies covering a longer time span and higher loads are necessary to be able to discriminate between viscoelastic processes or a possible effect of a surface layer.

#### 4. CONCLUSIONS

Dry adhesion between small particles is much lower than predicted from JKR and DMT theories. Surface roughness, heterogeneity, and surface films reduce the adhesion force and also cause a wide scatter in adhesion forces between different pairs of particles. The adhesion force between polystyrene particles and between gold particles does not depend on the load as long as the load is comparable to the adhesion force itself. It does not change from first to subsequent contacts; hence, a plastic deformation is probably negligible. The adhesion force does increase with time over a time span of 1–100 s. We believe this is due to a thinning of the surface films between the particles.

#### Acknowledgement

We acknowledge the financial support of the Deutsche Forschungsgemeinschaft under grant Bu 701/14 within the priority program 'Handhabung hochdispenser Pulver'. We further thank Manfred Ruppl, Universität Frankfurt, for the scanning electron images.

#### REFERENCES

1. K. L. Mittal (Ed.), *Particles on Surfaces 546, Detection, Adhesion and Removal*. VSP, Utrecht (1999).
2. K. C. Ludema, *Friction, Wear, and Lubrication. A Textbook in Tribology*. CRC Press, Boca Raton, FL (1996).
3. B. N. J. Persson, *Sliding Friction. Physical Principles and Applications*. Springer, Berlin (1998).
4. K. L. Johnson, K. Kendall and A. D. Roberts, *Proc. R. Soc. London A* **324**, 301 (1971).
5. B. V. Derjaguin, V. M. Muller and Yu. P. Toporov, *J. Colloid Interface Sci.* **53**, 314 (1975).
6. H. Hertz, *J. Reine Angewandte Mathematik* **92**, 156 (1882).
7. D. Maugis, *J. Colloid Interface Sci.* **150**, 243 (1992).
8. D. Tabor, *J. Colloid Interface Sci.* **58**, 2 (1977).
9. V. M. Muller, V. S. Yushchenko and B. V. Derjaguin, *J. Colloid Interface Sci.* **92**, 92 (1983).

10. M. Corn, in: *Aerosol Science*, C. N. Davies (Ed.), p. 359. Academic Press, New York (1966).
11. H. Krupp, *Adv. Colloid Interface Sci.* **1**, 111 (1967).
12. H. Mizes, M. Ott, E. Eklund and D. Hays, *Colloids Surfaces A* **165**, 11 (2000).
13. R. I. Larsen, *Am. Ind. Hyg. Assoc. J.* **19**, 265 (1958).
14. M. C. Kordecki and C. Orr, *Arch. Environmental Health* **1**, 13 (1960).
15. G. Böhme, W. Kling, H. Krupp, H. Lange and G. Sandstede, *Z. Angew. Physik* **6**, 486 (1964).
16. R. Polke, *Bull. Soc. Special Chim. France* **A3241**, 51 (1969).
17. F. Podczeczek and J. M. Newton, *J. Pharm. Sci.* **84**, 1067 (1995).
18. W. A. Ducker, T. J. Senden and R. M. Pashley, *Nature* **353**, 239 (1991).
19. H.-J. Butt, *Biophys. J.* **60**, 1438 (1991).
20. B. Cappella and G. Dietler, *Surface Sci. Reports* **34**, 1 (1999).
21. H.-J. Butt, M. Jaschke and W. Ducker, *Bioelectrochem. Bioenergetics* **38**, 191 (1995).
22. A. Jansoff, M. Neitzert, Y. Oberdörfer and H. Fuchs, *Angew. Chemie* **112**, 3346 (2000).
23. D. M. Schaefer, M. Carpenter, B. Gady, R. Reifengerger, L. P. DeMejo and D. S. Rimai, *J. Adhesion Sci. Technol.* **9**, 1049 (1995).
24. R. W. Stark, T. Drobek, M. Weth, J. Fricke and W. M. Heckl, *Ultramicroscopy* **75**, 161 (1998).
25. M. Enachescu, R. J. A. van den Oetelaar, R. W. Carpick, D. F. Ogletree, C. F. J. Flipse and M. Salmeron, *Phys. Rev. Lett.* **81**, 1877 (1998).
26. Y. Ando and J. Ino, *Wear* **216**, 115 (1998).
27. K. N. G. Fuller and D. Tabor, *Proc. R. Soc. London A* **345**, 327 (1975).
28. K. Cooper, A. Gupta and S. Beaudoin, *J. Colloid Interface Sci.* **234**, 284 (2001).
29. F. Podczeczek, J. M. Newton and M. B. James, *J. Appl. Phys.* **79**, 1458 (1996).
30. B. Derjaguin, *Kolloid Zeits.* **69**, 155 (1934).
31. L. O. Heim, J. Blum, M. Preuss and H.-J. Butt, *Phys. Rev. Lett.* **83**, 3328 (1999).
32. G. E. Yakubov, O. I. Vinogradova and H.-J. Butt, *J. Adhesion Sci. Technol.* **14**, 1783 (2000).
33. M. Preuss and H.-J. Butt, *Langmuir* **14**, 3164 (1998).
34. F. Podczeczek, J. M. Newton and M. B. James, *J. Colloid Interface Sci.* **187**, 484 (1997).
35. Y. Sugawara, M. Ohta, T. Konishi, S. Morita, M. Suzuki and Y. Enomoto, *Wear* **168**, 13 (1993).
36. M. Preuss and H.-J. Butt, *J. Colloid Interface Sci.* **208**, 468 (1998).
37. J. P. Cleveland, S. Manne, D. Bocek and P. K. Hansma, *Rev. Sci. Instrum.* **64**, 403 (1993).
38. M. Reitsma, V. Craig and S. Biggs, *Int. J. Adhesion Adhesives* **20**, 445 (2000).
39. D. K. Owens and R. C. Wendt, *J. Appl. Polym. Sci.* **13**, 1741 (1969).
40. H. J. Busscher, A. W. J. van Pelt, H. P. de Jong and J. Arends, *J. Colloid Interface Sci.* **95**, 23 (1983).
41. V. S. Mangipudi, E. Huang and M. Tirrell, *Macromol. Symp.* **102**, 131 (1996).
42. F. J. Schmitt, T. Ederth, P. Weidenhammer, P. Claesson and H. J. Jacobasch, *J. Adhesion Sci. Technol.* **13**, 79 (1999).
43. B. H. Alexander, M. H. Dawson and H. P. Kling, *J. Appl. Phys.* **22**, 439 (1951).
44. J. S. Vermaak and D. Kuhlmann-Wilsdorf, *J. Phys. Chem.* **72**, 4150 (1968).
45. H.-J. Butt and R. Raiteri, in: *Surface Characterization Methods, Surfactant Science Series*, A. Milling (Ed.), Vol. 87, p. 1. Marcel Dekker, New York (1999).
46. D. Maugis and H. M. Pollock, *Acta Metall.* **32**, 1323 (1984).
47. Y. I. Rabinovich, J. J. Adler, A. Ata and B. M. Moudgil, *J. Colloid Interface Sci.* **232**, 17 (2000).
48. D. F. S. John and D. J. Montgomery, *J. Appl. Phys.* **42**, 663 (1971).
49. R. Polke, H. Krupp and H. Rumpf, in: *Proc. VIth International Congress on Surface Active Substances*, Carl Hanser Verlag, München (1973).
50. D. S. Rimai, R. S. Moore, R. C. Bowen, V. K. Smith and P. E. Woodgate, *J. Mater. Res.* **8**, 662 (1993).
51. R. A. Quon, R. F. Knarr and T. K. Vanderlick, *J. Phys. Chem. B* **103**, 5320 (1999).
52. J. Tomas, *Chemie Ingenieur Technik* **69**, 455 (1997).

53. B. Gady, R. Riefenberger, D. M. Schaefer, R. C. Bowen, D. S. Rimai, L. P. DeMejo and W. Vreeland, *J. Adhesion* **67**, 19 (1998).
54. W. R. Bowen, R. W. Lovitt and C. J. Wright, *J. Mater. Sci.* **36**, 623 (2001).



## Adhesion of carbonyl iron powder particles studied by atomic force microscopy

LARS HEIM<sup>1</sup>, MAHDI FARSHCHI<sup>1</sup>, MARTIN MORGENEYER<sup>2</sup>,  
JÖRG SCHWEDES<sup>2</sup>, HANS-JÜRGEN BUTT<sup>1</sup> and MICHAEL KAPPL<sup>1,\*</sup>

<sup>1</sup>Max Planck Institute for Polymer Research, Ackermannweg 10, 55128 Mainz, Germany

<sup>2</sup>Institute of Mechanical Process Engineering, University of Braunschweig, Volkmaroder Straße 4/5, 38104 Braunschweig, Germany

**Abstract**—Adhesion forces between individual micrometer-sized carbonyl iron powder (CIP) particles were measured with an atomic force microscope (AFM) using the colloid probe technique. The effective normalized adhesion force  $F_{\text{adh}}/R$  was  $14 \pm 10$  mN/m ( $R$  is the reduced radius of two particles), which is much smaller than expected from the surface energy of iron oxide. This is mainly due to the pronounced surface roughness of the particles. The spatial variation of adhesion and the influence of surface contamination could be visualized from the adhesion maps of the particle surface using the force volume AFM mode. Adhesion between CIP particles and a silicon surface increased by 160% when increasing the external load from 21 to 204  $\mu\text{N}$  and remained high afterwards, indicating plastic deformation of the particles. Residual magnetization after exposure of the particles to a magnetic field of 0.8 T did not influence the adhesion force.

**Keywords:** Adhesion; carbonyl iron powder; atomic force microscope; colloid probe; magnetization.

### 1. INTRODUCTION

The behavior of highly dispersive powders is governed by the surface forces between individual particles. For a fundamental understanding of the handling and processing of such powders, studying the individual particle interaction is a prerequisite. A classical method to study the interaction of fine particles with surfaces is the centrifuge technique [1–6]. Here, the centrifugal force required to detach a particle from a surface is determined. Usually the detachment force for many particles is recorded in a single experiment, yielding statistics on the distribution of adhesion forces. The maximum rotational speed achievable in an

---

\*To whom correspondence should be addressed. Tel.: (49-6131) 379-114. Fax: (49-6131) 379-100.  
E-mail: kappl@mpip-mainz.mpg.de

ultracentrifuge is dictated by the material strength of the rotor. This leads to the limitation that only particles larger than a few micrometers can be detached.

With the invention of the atomic force microscope (AFM) in 1986 [7] and the introduction of the so-called 'colloid probe' technique [8, 9], a direct measurement of interaction between individual micrometer-sized particles became possible. The advantage of this method is that it allows studying the adhesion of a specific particle with a surface or another particle. The surface of this particle can be examined, e.g. by SEM, after the experiment. Particle sizes in the range of 1–50  $\mu\text{m}$  can be studied; the lower limit is given by the fact that the particles have to be mounted under optical control, the upper limit is given by the size of the cantilevers. Therefore, the colloid probe technique has become a well established tool for studying particle adhesion and particle–particle interaction [10].

The iron particles used in this study were from carbonyl iron powder (CIP). The prefix 'carbonyl' is due only to the production process of this powder by thermal decomposition of iron pentacarbonyl to pure iron (with a thin iron oxide layer at the surface) and is not related to the composition of the final product. The decomposition process generates spherical particles by formation of shell-like layers around the nuclei. Carbonyl iron powders have found a broad range of applications in industry in electronic components (e.g., for plastic encapsulated inductor cores); for production of magnetorheological fluids, magnetic inks and toners; as supplements for food and pharmaceuticals; and for metal injection molding (MIM) and powder metallurgy.

## 2. MATERIALS AND METHODS

The carbonyl iron powders used in this study were CIP EL ( $d_{50} = 6 \mu\text{m}$ ), CIP HQ ( $d_{50} = 1.1 \mu\text{m}$ , used for electric components) and CIP OM ( $d_{50} = 4 \mu\text{m}$ , used for MIM) manufactured by BASF (Ludwigshafen, Germany). According to the manufacturer the three powders differ in their mean particle size (characterized by the median  $d_{50}$  of the particle diameters) and width of the size distribution. In our study, individual particles were used and their sizes measured. The use of the different powders offered us a wider range of particle sizes. Figure 1 is a scanning electron micrograph of the CIP particles. It shows a reasonably spherical shape and a pronounced surface roughness of the particles.

The particles were glued onto tipless cantilevers using a small amount of epoxy resin (Epikote 1004, Shell) by means of a micromanipulator (model MMO 203, Narishige, Japan) under an optical microscope. Particles were deposited on a glass slide placed on a heating stage. A small amount of resin was placed near the particles. After heating the stage above the melting temperature of the resin a small amount of glue was taken up by touching the molten resin with the end of a tipless AFM cantilever. The selected particle could be picked up with the resin-coated end of the cantilever by gently touching it from above. We used two types of cantilevers: polycrystalline silicon cantilevers that were designed and manufactured

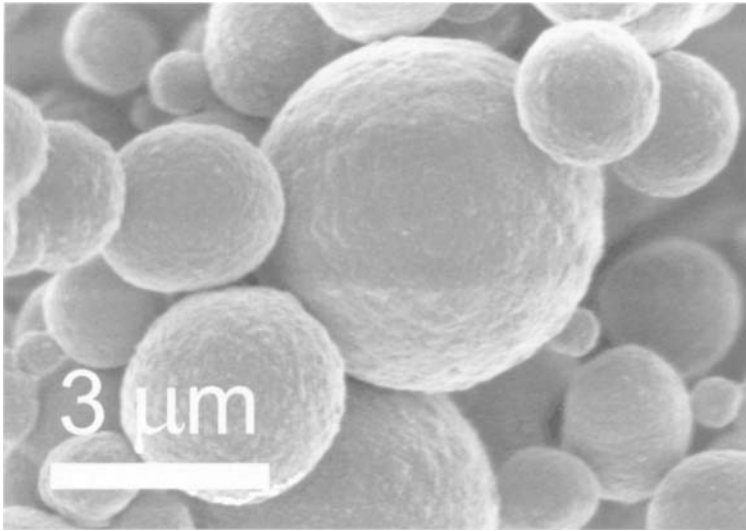


**Figure 1.** SEM image of CIP particles. Particles are reasonably spherical but have a pronounced surface roughness and a broad size distribution. For our study the size distribution was not critical since we measured the diameter of each particle used by SEM.

at the Institute for Microtechnology Mainz (IMM) and silicon cantilevers from Mikromasch (Tallinn, Estonia). Spring constants were determined with a reference cantilever as described before [11]. The reference cantilever itself was calibrated with a method described by Sader *et al.* [12]. Measured spring constants ranged between 0.0015 and 0.0224 N/m for the IMM cantilevers and between 3.8 N/m and 18.6 N/m for the Mikromasch cantilevers.

To measure particle-particle interaction, a set of CIP particles were mounted on a glass slide. The glass slide was covered with a thin ( $<0.5$  mm) film of the Epikote epoxy resin. The particles were arranged on this glass slide individually by picking them up with an AFM cantilever (just using the adhesion between the particle and cantilever) and depositing them at defined positions close to a mark in the epoxy film. The slide was heated to 80°C for 30 min to sinter the particles to the resin layer. By this procedure we were later able to find again each individual particle in the SEM to check its shape and measure its radius.

The silicon wafer (Si-mat, Landsberg, Germany) used for the measurements of the load dependence of adhesion forces was cleaned by sonication in ethanol and ultrapure water (MilliQ water filtration system, Millipore, Schwalbach, Germany).

The relative humidity in the laboratory was controlled to 35–40%. It has been shown that below this level of humidity, meniscus forces do not contribute significantly to the adhesion between the particles [13, 14].

All particles were inspected by scanning electron microscopy (LEO Gemini 1530) after the experiments to measure individual radii. The microscope was operated at a voltage of 1 or 3 kV so that it was not necessary to coat the samples with a conductive layer.

Force versus distance profiles ('force curves') were recorded as described earlier [10] at approach speeds of typically  $3 \mu\text{m/s}$ . Self-written software was used to convert the recorded detector signal versus piezo position profiles to force *versus* distance curves and extract the adhesion forces. Force curves for individual particles were recorded using a Bioscope AFM (Veeco, Santa Barbara, CA, USA) that allowed a fast alignment of the particles under the control of the inverted optical microscope which is part of the instrument. Force curves between CIP particles and a silicon surface were recorded using our custom-made Particle Interaction Apparatus [11]. One advantage of this instrument compared to the commercial AFMs is the higher dynamic range which allows us to apply larger forces.

AFM images of particle surfaces and force volume measurements were carried out with a Multimode AFM (Veeco) and a Nanowizard AFM (JPK Instruments, Berlin, Germany) using contact mode silicon AFM probes with a tip radius of  $<10 \text{ nm}$  (according to the manufacturer's data sheet) and a measured spring constant of  $0.27 \text{ N/m}$  (type CONT-W from Nanosensors, NanoAndMore, Wetzlar, Germany). AFM probes were treated in an argon plasma (Harrick PDC-002 Plasma Cleaner) for 1 min before use. For the Force Volume measurements, the JPK Nanowizard AFM allowed a higher resolution ( $64 \times 64$  force curves per image, 1024 points per curve) compared to the Multimode ( $32 \times 32$ , 256 points per curve) AFM.

### 3. RESULTS

#### 3.1. Dependence of adhesion on particle radius

For spherical particles, the classical theories of contact mechanics such as the theory of Johnson, Kendall and Roberts (JKR) [15] or Derjaguin, Muller and Toporov (DMT) [16] predict a linear increase of the adhesion force  $F_{\text{adh}}$  with the reduced radius  $R$ :

$$F_{\text{adh}} = \text{const} \cdot \gamma \cdot R \quad \text{with} \quad R = \frac{R_1 \cdot R_2}{R_1 + R_2},$$

where  $\gamma$  is the surface energy of the particle material and  $R_1$  and  $R_2$  are the radii of the two particles. The proportionality factor 'const' is  $3\pi$  for the JKR theory and  $4\pi$  for the DMT theory. The DMT model is usually applied for harder materials, whereas the JKR model is used for the limiting case of softer materials.

Adhesion forces were measured for reduced radii  $R$  between  $0.16 \mu\text{m}$  and  $1.13 \mu\text{m}$  (Fig. 2). The maximum applied load was 20–40 nN and contact times ranged from 0.15 to 0.40 s. Adhesion showed a tendency to increase with increasing value of  $R$ , but the scatter in the data was too large to verify the linear dependence. The mean normalized adhesion force  $F_{\text{adh}}/R$  had a value of  $14 \pm 10 \text{ mN/m}$ .

#### 3.2. Influence of load on adhesion

To study the load dependence of the adhesion force, particles were mounted on stiffer cantilevers to significantly increase the accessible range of loading forces.

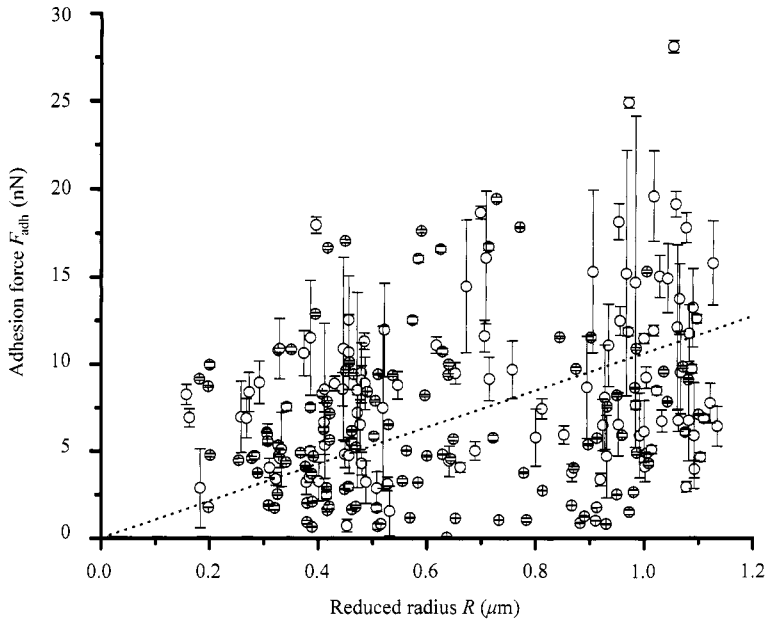


**Figure 2.** Dependence of the adhesion force  $F_{adh}$  between individual CIP particles on the reduced radius  $R = (R_1 \cdot R_2)/(R_1 + R_2)$ . Single data points are the mean of at least 5 force measurements between each individual pair of particles. The mean normalized adhesion force  $F_{adh}/R$  was  $14 \pm 10$  mN/m.

A clean silicon wafer was used as a flat substrate. This avoids the complication of aligning the two particles under the optical microscope and serves as a reference surface with minimum roughness. In Fig. 3 the dependence of adhesion force on loading force is plotted for two different particles which were mounted on cantilevers with spring constants of 3.8 N/m (left) and 18.6 N/m (right), respectively. In each of the six plots a series of adhesion force measurements at the same spot on the silicon wafer are shown where the load was first increased (full squares) and then decreased (open circles). Data in the plots denoted with A are from the first series of force curves with the corresponding particle, plots B and C are from consecutive series taken at other spots on the silicon wafer. For the softer cantilever, an increase of about 50% in adhesion is observed (plot A, left) when the loading force is increased from 2.5 to 43  $\mu$ N and this increased adhesion level remains even when the loading force is reduced again. In the subsequent series (plots B and C, left) the adhesion does not change any more. For the stiffer cantilever, that allowed higher loading forces, adhesion increased by about 160% during the first cycle when increasing the loading force from 21 to 204  $\mu$ N (plot A, right). For the third series (plot C, right) no significant change in adhesion with load is observed and the value is about the same as the maximum reached during the first series. The second series (plot B, right) with this particle shows strong fluctuations which may indicate a surface irregularity at this spot.

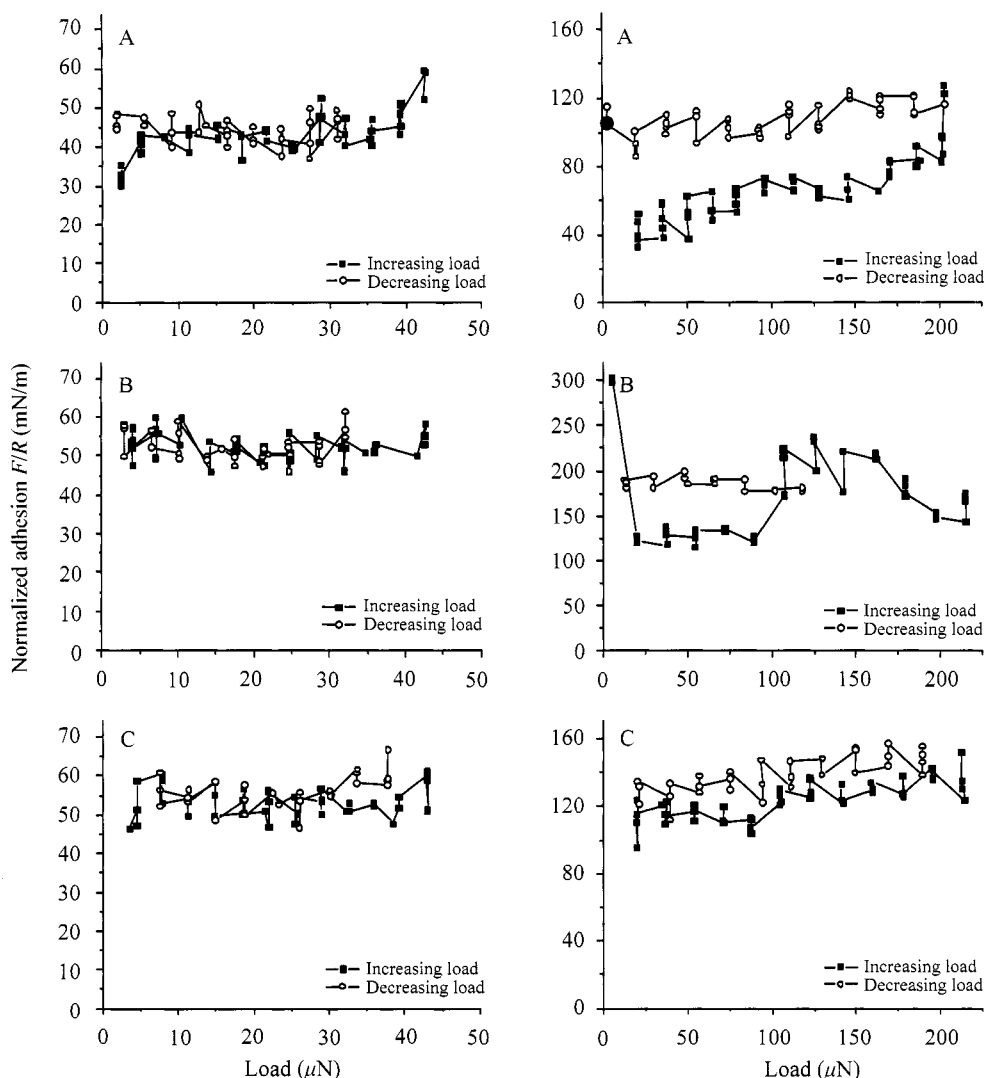


**Figure 3.** Normalized adhesion force  $F/R$  between CIP particles and a silicon wafer *versus* applied load for two different particles. Plots A show the first cycle for each particle, where the load was increased stepwise to the maximum value and then decreased stepwise. The maximum applied load was limited by the spring constant of the cantilevers (3.8 and 18.6 N/m). An increase of the loading force from 2.5 to 43  $\mu\text{N}$  for the first particle (left,  $R = 3.0 \mu\text{m}$ ) lead to increase in adhesion of 50%. For the second particle (right,  $R = 8.3 \mu\text{m}$ ) adhesion increased by 160% when the load was increased from 21  $\mu\text{N}$  to 204  $\mu\text{N}$ . In subsequent cycles B and C, the load had no significant influence on the adhesion force, indicating plastic deformation of the particle.

### 3.3. Distribution of adhesion forces

The observed variations of adhesion forces may be due to local variations in surface topography as well as in chemical composition of the surface. To gain more insight

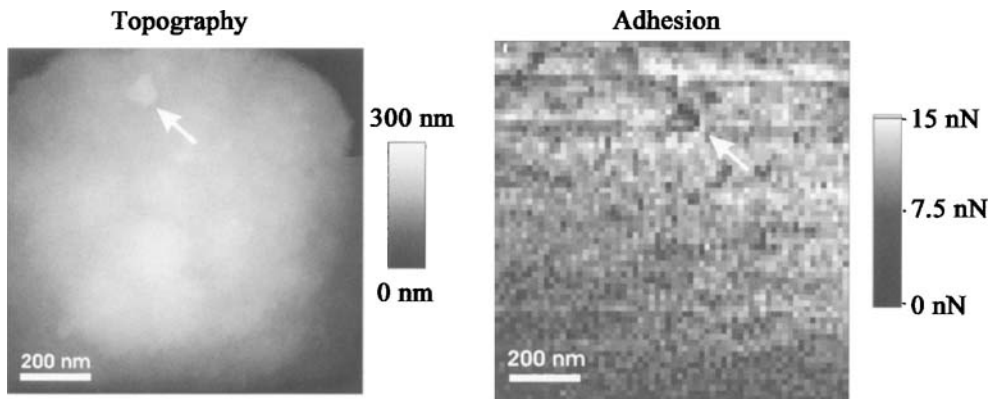


**Figure 4.** AFM height image (left) and adhesion map (right) of a CIP particle. A silicon AFM tip with a nominal radius of approx. 10 nm was used to image the particle and measure the adhesion on the same area. The arrows indicate the same spot in the two images (the offset between the two images is due to thermal drift during acquisition time of 3 h), where possibly a contamination is adsorbed that exhibits lower adhesion.

in the cause for the variations, we used the so-called ‘force volume’ mode. In this mode a surface area is scanned with the AFM tip and force–distance curves are taken in equidistant points on the surface [17, 18]. To analyze the 4096 force curves (from a raster of  $64 \times 64$  points) from such a scan efficiently, self-written Lab View software was used that automatically converts all curves, extracts the adhesion data and displays the result as a color-coded adhesion map of the surface. In Fig. 4 an example of such an adhesion map is given. On the left side, an AFM image of the topography of a CIP particle with a diameter of  $2 \mu\text{m}$  is shown. On the right-hand side, the corresponding adhesion map is drawn. The arrow in each picture denotes a protrusion on the surface of the particle that is visible in the topography as well as in the adhesion image. The small lateral offset of this spot in the adhesion map is due to thermal drift of the instrument during data acquisition which takes almost 3 h for one  $64 \times 64$  map. An adhesion map was taken between two CIP powder particles (Fig. 5). The upper left-hand corner of the scan area consisted of the glue that was used to fix the particle. Only a small variation in the adhesion force is observed on this smooth substrate. In the remaining part of the adhesion force map that corresponds to particle–particle contact, a large variation in the adhesion force is observed. Figure 6 shows adhesion force histograms from the adhesion maps in Figs 4 and 5. The mean adhesion force between the particle and the AFM tip was  $10.5 \pm 2.0$  nN, whereas between the two particles a mean adhesion force of  $12.7 \pm 4.7$  nN was obtained.

### 3.4. Influence of magnetization on particle adhesion

Magnetorheological (MR) fluids are suspensions of ferromagnetic or ferrimagnetic particles with sizes of some micrometers [19] (in contrast to ferrofluids, where ferromagnetic nanoparticles are used [20]). The viscosity of such suspensions can

be altered by an external magnetic field, making them attractive for applications such as a magnetic clutch or active damping elements [21–23]. With their high purity iron composition, CIP particles are especially well suited for this purpose due to their high saturation magnetization [24].

To check for a possible effect of the residual magnetization on the adhesion force we magnetized CIP particles outside the AFM by exposing them to the field of a permanent magnet of 0.8 T. The particle fixed to the surface was magnetized by exposing it to a magnetic field oriented perpendicular to the surface. The particle mounted on the cantilever was alternately magnetized in the same direction or in the opposite direction. Both particles were mounted in the AFM and 5 force–distance cycles were taken in one place. Then the relative lateral position of the two particles was slightly changed and again 5 cycles were conducted. This was repeated 10 times to obtain enough statistics for the adhesion force. After that the particle on the cantilever was magnetized in the opposite direction and the same cycle of  $5 \times 10$  measurements was carried out. This was continued for three complete sets of the different orientations (parallel/antiparallel) of the magnetic field. Figure 7 shows the adhesion force between the two iron particles. Open symbols denote results for parallel orientation of the magnetization of the two spheres, full symbols denote results from antiparallel orientation. All values plotted are averages from five force–distance cycles and the error bars denote the corresponding standard deviations. The measured adhesion was equal for both orientations: total average adhesion

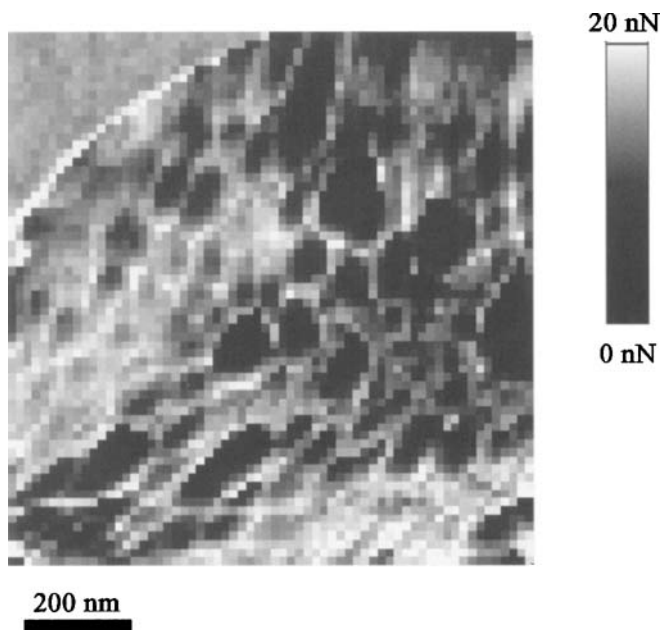


**Figure 5.** Adhesion map ( $64 \times 64$  force curves) for the interaction between two carbonyl iron particles. The flat area in the upper left corner consists of cured epoxy glue used to mount the particles onto the surface.



forces were  $11.7 \pm 6.5$  nN for the parallel and  $11.7 \pm 5.3$  nN for the antiparallel magnetization.

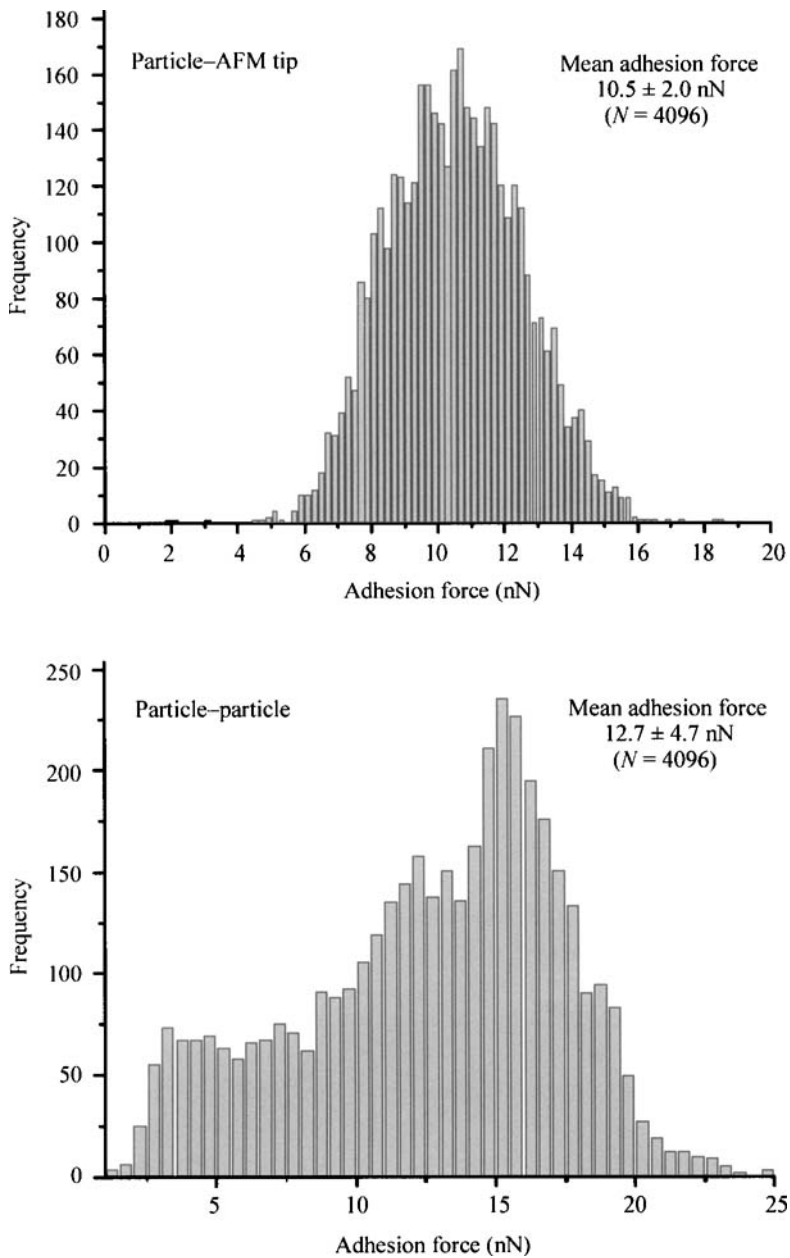


**Figure 6.** Histograms of the adhesion forces from the adhesion maps in Figs 4 and 5.

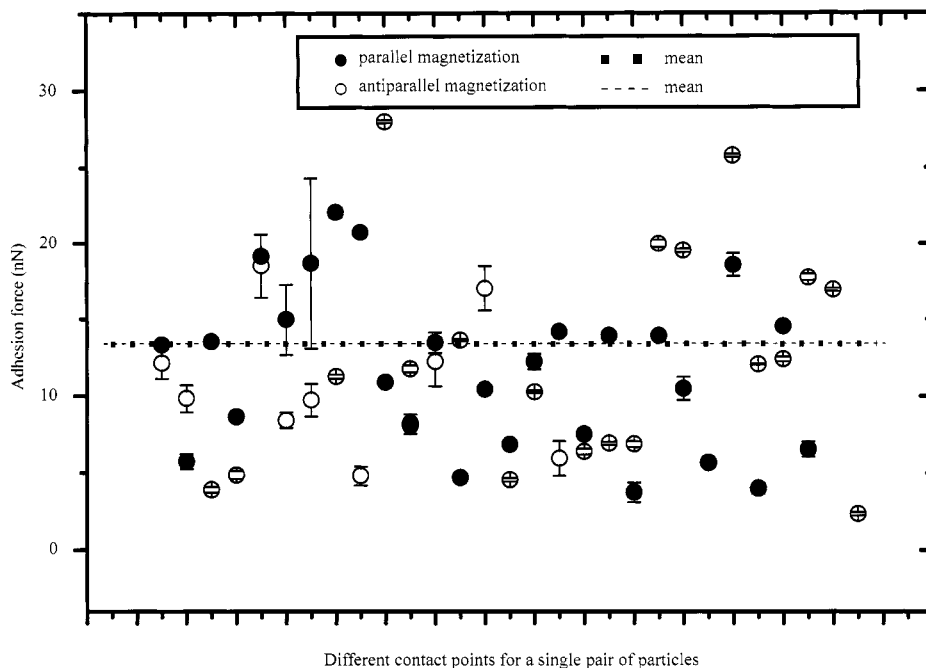


**Figure 7.** Adhesion force between an individual pair of CIP particles after temporary exposure to an external magnetic field of 0.8 T. Open symbols denote antiparallel magnetization of the two particles, full symbols denote parallel orientation. The residual magnetization of the particles has no influence on the adhesion force. Each data point is an average of at least 5 force measurements. The mean adhesion forces (plotted as dashed and dotted horizontal lines that overlap) are  $11.7 \pm 6.5$  nN for the parallel and  $11.7 \pm 5.3$  nN for the antiparallel magnetization.

## 4. DISCUSSION

### 4.1. Adhesion forces and surface energy: influence of surface roughness

Adhesion forces between iron particles have been measured for reduced radii between  $0.16 \mu\text{m}$  and  $1.13 \mu\text{m}$ . The scatter in the data in Fig. 2 was too large to confirm the linear dependence of adhesion force on reduced radius or for determining the surface energy of the iron powder. This is not a limitation of the method but is due to the natural variation of adhesion for individual particles within a powder sample. Therefore, adhesion of powder particles should be described by at least two parameters: ‘mean adhesion’ and ‘width of the distribution’. At this point one should also specify more clearly the term ‘surface energy’, since for a solid the creation of a new surface can be done either plastically or elastically. In the case of an adhesion force experiment, both effects contribute. Therefore, the surface energy obtained from adhesion experiments should be considered as an ‘effective’ surface energy that may be different from values obtained by other methods.

Another problem in this type of experiments is the influence of surface roughness. Considering the pronounced surface roughness of the iron particles (as apparent

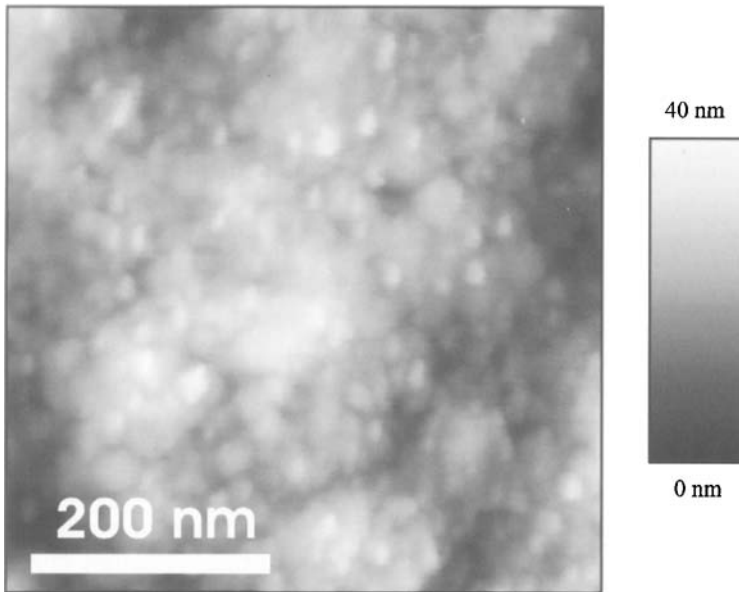


**Figure 8.** AFM height image of a CIP particle at a scan size of  $500 \times 500 \text{ nm}^2$ . The curvature of the sphere was subtracted from the height profile to better visualize the surface structure and determine the surface roughness. The surface exhibits a grain-like structure with typical grain diameters of 10–25 nm. The RMS roughness for this particle was 17 nm.

from Fig. 8) it is obvious that the true contact area between two iron particles can be very different from the value estimated from the JKR or DMT theory using the particle radius. Even for very smooth model systems (RMS roughness  $< 1 \text{ nm}$ ), effective surface energies only half as large as theoretically expected and with standard deviations  $> 25\%$  have been obtained [14]. Experiments by other groups on adhesion of small particles of other materials commonly showed large scatter in the data and deviations from predicted surface energies [25–35]. Both effects were attributed to the roughness of the interacting surfaces. Rabinovich *et al.* [33, 34] have developed a model based on suggestions of Rumpf [36] that explicitly takes into account the surface roughness and predicts lower effective surface energies than the classical models. In our study, both probe and surface have the same pronounced roughness which should result in even larger deviations. The mean of the normalized adhesion values  $F_{\text{adh}}/R$  of  $14 \pm 10 \text{ mN/m}$  corresponds to very low surface energies of the order of  $1.1 \pm 0.8 \text{ mJ/m}^2$  as calculated according to the DMT theory. A linear fit of the data in Fig. 2 that is forced through zero (dotted line) results in a slope of  $10.5 \pm 0.5 \text{ mN/m}$ , corresponding to a surface energy of  $0.84 \pm 0.04 \text{ mJ/m}^2$ . For clean metals, surface energies of 2000–2500  $\text{mJ/m}^2$  are reported [37, 38]. In our situation the particles are expected to be covered with an iron oxide layer and no metallic bonds will be formed during contact. Therefore, it should be more appropriate to calculate the contribution of the van der Waals forces

only. This can be done in good approximation using the equation [38]:

$$\gamma \approx \frac{A}{24\pi(\sigma/2.5)^2},$$

where  $A$  is the Hamaker constant of the material and  $\sigma$  is the interatomic distance at the surface. With  $A = 2.1 \times 10^{-19}$  J for iron oxide [38] and an inter-atomic distance of approx. 0.2 nm, the resulting surface energy is of the order of

$$\gamma \approx \frac{A}{24\pi(\sigma/2.5)^2} = \frac{2.1 \times 10^{-19} \text{ J}}{75.4 \times 0.0064 \text{ nm}^2} = 435 \text{ mJ/m}^2.$$

This is still roughly 500-times larger than our experimental values. RMS roughness values determined for 4 different particles from AFM images (after subtraction of the curvature of the particle surface) ranged from 8 to 17 nm on an area of  $1 \times 1 \mu\text{m}^2$ . If we take a closer look at the CIP particle surface as imaged by AFM (Fig. 8), the surface reveals a grain-like structure with a grain diameter of typically 10–25 nm. Since the CIP particle will mainly contact these surface asperities during adhesion force measurements, values for the reduced radii could be as small as 2–25 nm. Using these much smaller contact radii, one calculates a mean value of the surface energy in the order of  $F/4\pi R = 14 \text{ nN}/4\pi \times 13 \text{ nm} = 85 \text{ mJ/m}^2$ . This is still much smaller than the theoretical value for iron oxide but in the range of typical values for lower energy surfaces. This might indicate the presence of a contamination layer at the surface or that impurities of the CIP particles (0.6–0.9% carbon, 0.6–0.9% nitrogen, according to manufacturer's data sheets) are concentrated at the surface. The assumption of such small contact areas is, however, not realistic since the contact pressures under such conditions will lead to plastic yielding of the surfaces, as we will see in the next section. Therefore, the value of  $85 \text{ mJ/m}^2$  for the effective surface energy calculated before should be seen as an upper limit.

#### 4.2. Load dependence of adhesion

The observed increase of adhesion force with applied load during the first cycle and only small changes in further cycles indicate that the particles undergo plastic deformation. A simple estimation of the contact pressure can be made using the Hertz model [39]. If two spheres made of materials with Young's moduli  $E_1$  and  $E_2$  and Poisson ratios  $\nu_1$  and  $\nu_2$  are pressed together with an external force  $F_L$ , the contact radius  $a$  is given by:

$$a = \sqrt[3]{\frac{3RF_L}{4E^*}}, \text{ where } \frac{1}{E^*} = \frac{1-\nu_1^2}{E_1} + \frac{1-\nu_2^2}{E_2}.$$

The average contact pressure is then simply given by:

$$P_{\text{avg}} = \frac{F}{\pi a^2}.$$

With the Young's modulus of 205 GPa, a Poisson ratio of 0.29 for iron [40], 130 GPa and 0.279 for a silicon <100> surface [41], an effective modulus of  $E^* = 87$  GPa is calculated. For values of  $R = 1 \mu\text{m}$  and  $F_L = 50 \mu\text{N}$ , this results in a contact radius of  $a = 76$  nm and an average contact pressure of  $P_{\text{avg}} = 2.8$  GPa. Since the yield stress of iron is below 350 MPa [40], plastic deformation will readily occur under these conditions. Since the yield stress of silicon is  $>1$  GPa [42], the particles are mainly expected to deform. This is strongly supported by the fact that after the particle adhesion has increased due to high load, adhesion force measurements at a different location on the wafer with low loads result in the same magnitude of the adhesion force. An analogous calculation can be done for the contact between two CIP powder particles. If we assume that the contact between the particles occurs at single asperities with a reduced radius of  $R = 10$  nm and an adhesion force of  $F_{\text{adh}} = 10$  nN, we obtain a contact radius of  $a = 0.9$  nm and a mean contact pressure of  $P = 4.2$  GPa, which is much higher than the yield stress. Therefore, one expects the effective contact areas to be substantially larger due to plastic deformation.

#### 4.3. Distribution of adhesion values

Quantitative adhesion maps of the surface of a CIP particle were obtained. This enables us to compare surface topography and adhesion and allows identification of inhomogeneities in surface composition. In Fig. 4 the comparison of topography and adhesion image (right) shows that the protrusion visible in the topography (arrow in the left image) exhibits lower adhesion values than the surrounding surface (arrow in the right image), indicating a different surface chemistry of this part of the surface. In Fig. 5 the upper left corner shows the adhesion between the CIP powder particle colloid probe and the epoxy glue around the opposing particle. The interaction of the particle with the smooth epoxy surface leads to a relatively small variation of adhesion. In the rest of this adhesion map, the adhesion between the particle mounted on the cantilever and the particle fixed to the surface have been recorded. Here the variation is much higher due to the interaction of the two rough particle surfaces.

It is striking that the absolute value of the adhesion force measured with an AFM tip (nominal tip radius of approx. 10 nm) is nearly of the same magnitude as adhesion force between the particles with approx.  $1 \mu\text{m}$  radius. This further supports the idea that the rough, grainy surface structure of the particles is responsible for the small adhesion forces between the particles.

The distribution of adhesion forces between the particle and the AFM tip shows a single peak. The adhesion force between the two particles showed a bimodal distribution (the third peak at approx. 12 nN arises from the adhesion between the particle and the glue in the upper left corner). This is in agreement with the expected influence of surface roughness on adhesion distribution [35]. The interaction geometry for such a force volume experiment between two particles is expected to change as the colloid probe moves from the glue onto the edge of the lower particle and across to its centre. Interestingly, this seems to have a pronounced

effect only at the points where the colloid probe is moving from the glue onto the particle and probably has contact with both surfaces at the same time, creating a bright rim (indicating higher adhesion) in the adhesion map. For the other parts of the particle, the variations seem to be dominated by local surface roughness rather than by overall particle curvature.

#### 4.4. Influence of magnetization on adhesion

For high purity iron particles it is expected that the residual magnetization should be small due to the low magnetic coercivity of the material. However, Genç and Phulé [43] found that the coercivity of CIP particles could be up to 30-times higher than the bulk value. A possible reason is the presence of defects and impurities in the particles. Therefore, an influence of the residual magnetization on the adhesion could be envisioned. From our results (Fig. 7) we can conclude that the residual magnetization is too small to have a significant influence on the adhesion between the CIP particles.

## 5. CONCLUSIONS

Adhesion forces between individual micrometer-sized CIP particles showed strong fluctuations due to the pronounced surface roughness (RMS roughness of 17 nm on an area of  $0.5 \times 0.5 \mu\text{m}^2$ ). The mean normalized adhesion force  $F_{\text{adh}}/R$  was  $14 \pm 10 \text{ mN/m}$ . From estimations of the contact pressure and the measured load dependence of the adhesion force we can speculate that plastic deformation occurred at the contact point. The residual magnetization of the particles after exposure to a magnetic field of 0.8 T was too small to have an influence on the adhesion force.

#### Acknowledgements

We thank the DFG Projektgruppe ‘Vom Molekül zum Material’, ‘Initiative Verhalten Granularer Medien’ for funding (grants Bu 701/19 and SCHW 233/29-3).

## REFERENCES

1. R. I. Larsen, *Am. Ind. Hyg. J.* **19**, 265–270 (1958).
2. G. Böhme, H. Krupp, H. Rabenhorst and G. Sandstede, *Trans. Inst. Chem. Eng. (London)* **40**, 252–259 (1962).
3. H. Krupp, *Adv. Colloid Interf. Sci.* **1**, 111–239 (1967).
4. R. Polke, *Chem. Ing. Techn.* **40** 1057–1060 (1968).
5. F. Podczeck and J. M. Newton, *J. Pharm. Sci.* **84**, 1067–1071 (1995).
6. D. S. Rimai, D. J. Quesnel and R. Reifenberger, *J. Adhesion* **74**, 283–299 (2000).
7. G. Binnig, C. F. Quate and C. Gerber, *Phys. Rev. Lett.* **56**, 930–933 (1986).
8. W. A. Ducker, T. J. Senden and R. M. Pashley, *Nature* **353**, 239–241 (1991).

9. H.-J. Butt, *Biophys. J.* **60**, 1438–1444 (1991).
10. M. Kappl and H.-J. Butt, *Particle Particle System Charact.* **19**, 129–143 (2002).
11. M. Preuss and H.-J. Butt, *Langmuir* **14**, 3164–3174 (1998).
12. J. E. Sader, J. W. M. Chon and P. Mulvaney, *Rev. Sci. Instrum.* **70**, 3967–3969 (1999).
13. F. Podczeck, J. M. Newton and M. B. James, *J. Colloid Interf. Sci.* **187**, 484–491 (1997).
14. L. O. Heim, J. Blum, M. Preuss and H. J. Butt, *Phys. Rev. Lett.* **83**, 3328–3331 (1999).
15. K. L. Johnson, K. Kendall and A. D. Roberts, *Proc. R. Soc. London Ser. A* **324**, 301–313 (1971).
16. B. V. Derjaguin, V. M. Muller and Yu. J. Toporov, *Colloid Surf. A* **53**, 314–326 (1975).
17. M. Radmacher, J. P. Cleveland, M. Fritz, H. G. Hansma and P. K. Hansma, *Biophys. J.* **66**, 2159–2165 (1994).
18. E. Hassan, W. F. Heinz, M. D. Antonik, N. P. D'Costa, S. Nageswaran, C.-A. Schoenenberger and J. H. Hoh, *Biophys. J.* **74**, 1564–1578 (1998).
19. J. Rabinow, *AIEE Trans.* **67**, 1308–1315 (1948).
20. S. Odenbach, *Colloid Surf. A* **217**, 171–178 (2003).
21. F. Gandhi, K. W. Wang and L. B. Xia, *Smart Mater. Struct.* **10**, 96–103 (2001).
22. H. J. Jung, B. F. Spencer and I. W. Lee, *J. Struct. Eng. ASCE* **129**, 873–883 (2003).
23. S. B. Choi, H. J. Song, H. H. Lee, S. C. Lim, J. H. Kim and H. J. Choi, *Int. J. Vehicle Des.* **33**, 2–16 (2003).
24. P. Phulle and J. Ginder, *Int. J. Mod. Phys. B* **13**, 2019–2027 (1999).
25. B. Gady, R. Reifengerger, D. M. Schaefer, R. C. Bowen, D. S. Rimai, L. P. Demejo and W. Vreeland, *J. Adhesion* **67**, 19–36 (1998).
26. J. Y. Walz, *Adv. Colloid Interf. Sci.* **74**, 119–168 (1998).
27. G. Toikka, R. A. Hayes and J. Ralston, *J. Colloid Interf. Sci.* **180**, 329–338 (1996).
28. G. Toikka, G. M. Spinks and H. R. Brown, *Langmuir* **17**, 6207–6212 (2001).
29. R. W. Bowen and T. A. Doneva, *J. Colloid Interf. Sci.* **229**, 544–549 (2000).
30. K. Cooper, A. Gupta and S. Beaudoin, *J. Colloid Interf. Sci.* **228**, 213–219 (2000).
31. K. Cooper, A. Gupta and S. Beaudoin, *J. Colloid Interf. Sci.* **234**, 284–292 (2001).
32. K. Cooper, N. Ohler, A. Gupta and S. Beaudoin, *J. Colloid Interf. Sci.* **222**, 63–74 (2000).
33. Y. I. Rabinovich, J. J. Adler, A. Ata, R. K. Singh and B. M. Moudgil, *J. Colloid Interf. Sci.* **232**, 10–16 (2000).
34. Y. I. Rabinovich, J. J. Adler, A. Ata, R. K. Singh and B. M. Moudgil, *J. Colloid Interf. Sci.* **232**, 17–24 (2000).
35. M. Göttinger and W. Peukert, *Langmuir* **20**, 5298–5303 (2004).
36. H. Rumpf (Ed.), *Particle Technology*. Chapman & Hall, London (1990).
37. V. K. Kumikov and K. B. Khokonov, *J. Appl. Phys.* **54**, 1346–1350 (1983).
38. J. Israelachvili, *Intermolecular and Surfaces Forces*, 2nd edn. Academic Press, London (1992).
39. H. Hertz, *J. Reine Angew. Math.* **92**, 156–171 (1882).
40. D. R. Lide (Ed.), *Handbook of Chemistry and Physics*, 76th edn. CRC Press, Boca Raton, FL (1995).
41. W. A. Brantley, *J. Appl. Phys.* **44**, 534–535 (1973).
42. J. Rabier and J. L. Demenet, *Phys. Stat. Solid. B* **222**, 63–74 (2000).
43. S. Genç and P. P. Phulé, *Smart Mater. Struct.* **11**, 140–146 (2002).

## Adhesion of rough surfaces with plastic deformation

LIXIAN ZHANG and YA-PU ZHAO \*

*State Key Laboratory of Nonlinear Mechanics (LNM), Institute of Mechanics,  
Chinese Academy of Sciences, Beijing 100080, China*

**Abstract**—Adhesion is attractive and has a close relation to many modern problems of contacts between plastically deformable surfaces on the micro/nano-scale (such as microelectromechanical systems (MEMS) and nanotechnology). In the present paper a theoretical model is developed to obtain a better understanding of the adhesion of rough surfaces with plastic deformation. The present research goes beyond the Gaussian and exponential distributions of microasperity heights by introducing the description of self-affine fractal surfaces. General expressions for real contact area, total load and required separation force are derived. Two new dimensionless parameters are derived, which are used in further analysis of adhesion together with the existing roughness exponent and plastic adhesion index, giving a quantitative understanding about adhesion with plastic deformation and the relevant phenomenon.

**Keywords:** Adhesion; plastic deformation; self-affine fractal surface; surface roughness; distribution of microasperity heights.

### NOMENCLATURE

$A_r$	actual contact area
$A'_r$	real area of contact per unit area
$a'$	contact radius of an individual microasperity
$a_p$	contact radius during plastic loading
$d$	separation between the mean plane and the flat surface during loading
$E$	Young's modulus
$E^*$	effective modulus
$H$	hardness of material

---

\*To whom correspondence should be addressed. Tel.: (86-10) 6265-8008. Fax: (86-10) 6256-1284.  
E-mail: yzhao@lnm.imech.ac.cn



$N$	number of asperities per unit area of rough surface
$n$	number of asperities per unit area that are able to make contact
$P$	force that pressed surfaces together
$P'$	load per unit area to compress the microasperities
$P_{\text{ad}}$	adhesion force, also separation force
$P'_{\text{ad}}$	adhesion force per unit area
$R$	equivalent radius of smooth sphere
$r$	radius of a perfectly plastic hemispherical tip
$r_a$	radius of curvature of an asperity
$U_d$	energy absorbed in plastic deformation of a perfectly plastic hemispherical tip
$U_p$	work done by the applied load
$U_s$	contribution due to work of adhesion
$U_t$	total energy of system
$Y$	yield stress of material
$z$	peak height above the mean line
$\alpha$	roughness exponent
$\Gamma(x)$	gamma function, $\Gamma(x) = \int_0^\infty e^{-t} t^{x-1} dt$
$\Gamma(x, d)$	incomplete gamma function, $\Gamma(x, d) = \int_d^\infty e^{-t} t^{x-1} dt$
$\Delta\gamma$	Dupré adhesion or work of adhesion
$\gamma_i$ ( $i = 1, 2$ )	surface energy of material
$\gamma_{12}$	interface energy of contacting materials 1 and 2
$\delta$	vertical displacement of a perfectly plastic hemispherical tip
$\zeta$	length scale for the Gaussian distributed rough surface
$\zeta_\alpha$	length scale of the fractal surface
$\eta$	ratio of the separation between the mean plane and the flat surface during loading to the standard deviation of the peak heights
$\theta$	adhesion parameter for Gaussian distributed rough surface
$\theta_\alpha$	generalized adhesion parameter for a self-affine fractal surface
$\lambda$	plastic adhesion index
$\mu$	ratio of the work of adhesion to the product of the standard deviation of the peak heights and the hardness
$\nu$	Poisson's ratio
$\xi$	correlation length of the self-affine fractal surface parallel to the surface
$\sigma$	standard deviation of peak heights

## 1. INTRODUCTION

The interaction between deformable solids, which is derived from physical attractive and repulsive forces, has a close relevance to contact problem, friction and wear of contacting surfaces [1, 2]. Larger-scale systems are more influenced by inertia effects, while smaller-scale systems are more influenced by surface effects. In microelectromechanical systems (MEMS) and nanotechnology fields, the adhesion becomes more significant [3]. Developing a sophisticated understanding of adhesion between solid–solid surfaces will help controlling processes such as bonding and debonding [4] that are essential to fabrication of MEMS. It has been known for a long time that the surface roughness is very important in determining the interaction force between the contacting surfaces. Since the actual contacting surfaces are rough, the effect of the roughness will lead to the scenario that the actual contact area occurs at the peaks of the inevitable surface irregularities where the local contact pressure is very high. Furthermore, the details of the distribution of asperities can also affect the adhesion.

Greenwood and Williamson, assuming the asperity heights distribution to be Gaussian, discovered that many important properties of the contact were almost independent of the details of the local asperity behavior [5]. A dimensionless parameter, plasticity index, was proposed in Ref. [5] to predict the plastic deformation of asperities. Johnson *et al.* [6] studied the adhesion between two elastic spheres with radii  $R_1$  and  $R_2$ , and concluded that the adhesion force or force required to separate the bodies  $P_{ad}$ , was independent of both the applied load and the elastic constants of the materials, i.e.

$$P_{ad} = -\frac{3}{2}\pi \Delta\gamma R, \quad (1)$$

where  $R = R_1 R_2 / (R_1 + R_2)$  is the equivalent radius, and  $\Delta\gamma = \gamma_1 + \gamma_2 - \gamma_{12}$  is the Dupré adhesion or work of adhesion, with  $\gamma_1$  and  $\gamma_2$  being the surface energies of the two spheres and  $\gamma_{12}$  being the interface energy. It should be noted that there is no consistent term for  $P_{ad}$  in equation (1) in the literature, separation force and pull-off force are also used [7]. Subsequently, Fuller and Tabor [8] investigated the effect of surface roughness with Gaussian distribution on the adhesion of elastic solids and introduced an adhesion parameter  $\theta$  given by

$$\theta = \frac{E\sigma^{3/2}}{r_a^{1/2}\Delta\gamma}, \quad (2)$$

where  $E$  is Young's modulus,  $\sigma$  the standard deviation of the peak heights and  $r_a$  the radius of curvature of an asperity. This dimensionless parameter represents the relative importance of surface roughness and adhesion, and is the ratio between the elastic energy and the work of adhesion, assuming that complete contact has occurred. When  $\theta \gg 1$  only partial contact occurs, where the elastic solids make contact only at the tops of the highest asperities, while a complete contact occurs when  $\theta \ll 1$ .

It was during the 1950s that experiments showed plastic deformation of particles caused by adhesion forces [9]. Krupp [10] originally proposed that the adhesion forces could rise to such large values that they would exceed the elastic limit of the material and induce irreversible, plastic flow. Experiments on gold spheres were carried out and showed that only small particles exhibited plastic deformation due to adhesion force. Easterling and Tholen [11] and Tholen [12] showed plastic deformation in electron micrographs of metal particles sticking together. They observed dislocations and plastic twins emanating from the highly stressed contact region. Scanning electron microscope (SEM) studies were performed on polystyrene spheres sitting on polished silicon surfaces by Rimai *et al.* [13], and plastic deformation was observed due to adhesion forces.

Johnson [14] derived both elastic adhesion index and plastic adhesion index. The latter is given as

$$\lambda = \frac{\pi^2 H^4 r_a \sigma}{8 \Delta \gamma^2 E^{*2}}, \quad (3)$$

where  $H$  is the material hardness, and

$$E^* = \left( \frac{1 - \nu_1^2}{E_1} + \frac{1 - \nu_2^2}{E_2} \right)^{-1}$$

is the effective modulus, where  $E_{1,2}$  and  $\nu_{1,2}$  are Young's moduli and Poisson's ratios of the two bodies, respectively. According to the von Mises flow rule, the hardness,  $H$ , is related to yield stress,  $Y$ , by the Tabor relation [15]:  $H = 3Y$ . Also, Johnson investigated the adhesion problem for both elastic and plastic deformations assuming an exponential distribution of asperity heights. For plastic deformation, the ratio of the force that separated the surfaces,  $P_{ad}$ , to the force that pressed them together,  $P$ , was obtained as

$$\frac{P_{ad}}{P} = -1 + \frac{1 + \lambda}{\lambda} \exp\left(-\frac{1}{\lambda}\right). \quad (4)$$

With the same assumed heights distribution Chowdhury and Pollock [16] studied adhesion between metal surfaces with plastic deformation. Considering multi-asperities, the total real area of contact per unit area is given as

$$A'_r = 2\pi n r_a \sigma, \quad (5)$$

where  $n$  denotes the number of asperities per unit contact area. And the adhesion coefficient or ratio of total adhesion force to the total compression force is expressed as

$$\frac{P_{ad}}{P} = \frac{1}{1 - \Delta \gamma / (H \sigma)} \left\{ -1 + \frac{1 + \lambda}{\lambda} \exp\left(-\frac{1}{\lambda}\right) \right\}. \quad (6)$$

For plastic adhesion index  $\lambda > 2$ , very small adhesion is predicted [14].

Recently, considering the influence of the microstructure of self-affine fractal surfaces, Chow studied the adhesion between elastic deformable fractal surfaces

[17, 18]. Persson studied the contact mechanics between solids on all roughness length scales, discussed the relation of adhesion parameter to different roughness length scales [19, 20] and derived the generalized adhesion parameter  $\theta_\alpha$  for a self-affine fractal surface as

$$\theta_\alpha = \theta \left( \frac{\zeta_\alpha}{\zeta} \right)^{2\alpha-1}, \quad (7)$$

where  $\theta$  and  $\zeta$  are the adhesion parameter and length scale for the Gaussian-distributed rough surface, respectively,  $\alpha$  is the dimension of the self-affine fractal surface and  $0 < \alpha < 1$ ,  $\zeta_\alpha$  is the length scale of the fractal surface. It should be noted that the generalized adhesion parameter in equation (7) is reduced to the adhesion parameter for Gaussian distribution in equation (2) when  $\alpha = 1/2$ . It should be noted that the generalized adhesion parameter in equation (7) is valid for surface roughness on a wide distribution of length scales.

Under ideal equilibrium conditions, the work of adhesion is considered to be a well-defined reversible thermodynamic quantity, i.e. the work done on bringing two unit areas of surfaces together and the work needed to separate two unit areas of surfaces from contact are the same. But under most realistic conditions there is adhesion hysteresis: the work needed to separate two unit areas of surfaces is always greater than that originally gained on bringing them together; in other words, the approach/separation cycles are thermodynamically irreversible [21] and, therefore, energy is dissipated. Adhesion contact with plastic deformation is one of the mechanisms of adhesion hysteresis [21, 22]. The research on adhesion in case of plastic deformation has been in the past mainly restricted to the Gaussian or exponential distribution of asperity heights. The present research studied the adhesion of rough surfaces with plastic deformation. Furthermore, the effects of relevant parameters, such as roughness exponent, plastic adhesion index and two new dimensionless terms introduced in this theoretical model are analyzed.

## 2. PLASTIC DEFORMATION THEORY OF A SINGLE ASPERITY

Contact happens between surfaces of two bodies when they are pressed together. When the applied load exceeds a critical value, an irreversible curve will be obtained in the loading-unloading experiment, which indicates that the applied load has compressed the microasperity plastically. When a perfect plastic contact due to adhesion is assumed, i.e. when a perfectly plastic hemispherical tip of radius  $r$  is pressed against a perfectly horizontal rigid plane, the vertical displacement  $\delta$  is given by the geometric relationship as [16]:

$$a_p^2 \approx 2r\delta, \quad (8)$$

where  $a_p$  represents the contact radius during plastic loading, and equation (8) holds provided that the change in contact geometry due to the material flow is

neglected [16]. The work done by the applied load,  $U_p$ , is given as [16]

$$U_p = -P\delta. \quad (9)$$

The energy absorbed in plastic deformation,  $U_d$ , is given by

$$U_d = \int_0^\delta \pi a_p^2 H d\delta, \quad (10)$$

and the contribution due to the work of adhesion is

$$U_s = -\pi a_p^2 \Delta\gamma. \quad (11)$$

Thus the total energy of this system is obtained as

$$U_t = U_p + U_d + U_s. \quad (12)$$

Considering the energy equilibrium condition  $\partial U_t / \partial \delta = 0$ , one has

$$P = \pi a_p^2 H - 2\pi r \Delta\gamma. \quad (13)$$

Without the effect of work of adhesion, the applied load is

$$P = \pi a_p^2 H, \quad (14)$$

which is adopted in Johnson's analysis of adhesion in case of perfectly plastic deformation [14]. Therefore, if a single area of contact is assumed, the contact size can be derived from the resistance measurements by varying the applied load [16], and values of both  $\Delta\gamma$  and  $H$  can be derived from equation (13).

During unloading, adhesion forces play an important role. Adhesion contact established during loading is capable of appreciable plastic extension before fracture, especially for materials with high modulus and low hardness. If we take into account the condition that plastic deformation of the material during loading is followed by ductile extension of the contact, then a criterion for ductile extension is given by [14]

$$H^2 < 4 \frac{\Delta\gamma E^*}{\pi a_p}. \quad (15)$$

Here it is assumed that the tip of microasperity will extend in a ductile manner when the contact pressure just exceeds the hardness  $H$  of the material during unloading. Generally, the softer the material, the greater the possibility of plastic extension before fracture [14].

### 3. THEORETICAL MODEL OF ADHESION OF ROUGH SURFACES WITH PLASTIC DEFORMATION

A theoretical formulation of applied load by assuming a single area of contact was shown above, but in fact the real surfaces at the nano/micro-level are rough. The surface profile of single crystal silicon ( $8 \mu\text{m} \times 8 \mu\text{m}$ ) obtained using an atomic

force microscope (AFM) is shown in Fig. 1. Figure 1 shows that a multi-asperity structure at microscopic scale exists in the real surface. For simplicity and without loss of generality, we consider a randomly rough deformable surface and a perfectly rigid smooth surface in contact as depicted in Fig. 2 [23], where the separation between the mean plane and the flat surface during loading is  $d$ , the asperity peaks are assumed to have a radius of curvature  $r_a$  and the peak height above the mean line is  $z$ .

Fractals present a natural language for describing the scaling behavior of roughness on all length scales [18]. Self-affine fractals are invariant under an anisotropic dilation. A general distribution of microasperity heights derived from the description of fractal surfaces is introduced into the present analysis of adhesion. The distribution of asperity heights is expressed as [17]:

$$\Psi(z) = \Psi_0 \exp \left[ -\alpha \left( \frac{z}{\sigma} \right)^{1/\alpha} \right], \quad 0 < \alpha \leq 1, \quad (16)$$

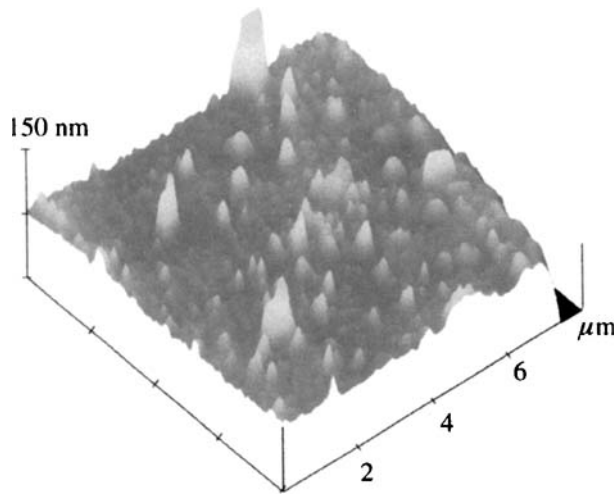


**Figure 1.** Surface roughness profile of single crystal silicon ( $8 \mu\text{m} \times 8 \mu\text{m}$ ) obtained by an atomic force microscope (AFM).

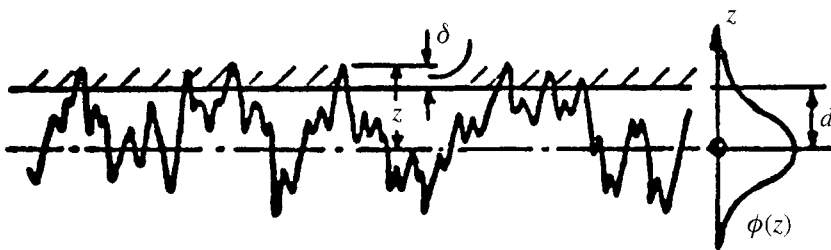


**Figure 2.** Contact of a random rough deformable surface with a rigid plane.

where

$$\Psi_0 = \left[ \sigma \int_0^\infty \exp(-\alpha u^{1/\alpha}) du \right]^{-1} = \frac{1}{\sigma \alpha^{1-\alpha} \Gamma(\alpha)}, \quad (17)$$

where  $\Gamma$  is the gamma function and is defined as  $\Gamma(x) = \int_0^\infty e^{-t} t^{x-1} dt$ ,  $\sigma$  is the standard deviation of the peak asperity heights and  $\alpha$  is the roughness exponent which can be calculated using digital data obtained from AFM [24]. For a given domain size of short-range surface profile, the smaller the exponent  $\alpha$ , the rougher the local variation of the surface structure, and smoother hills and valleys are expected as  $\alpha$  approaches 1 [25]. When  $\alpha = 1/2$ , we obtain the Gaussian distribution function from the above two equations, and when  $\alpha = 1$ , we obtain the exponential distribution function. The radius of curvature of asperities  $r_a$  is given as [17]:

$$\frac{1}{r_a} = \frac{2\sigma}{\xi^2}, \quad (18)$$

where  $\xi$  is the correlation length of the self-affine fractal surface parallel to the surface. The vertical deformation  $\delta$  is defined as

$$\delta = z - d. \quad (19)$$

If the rough surface has  $N$  asperities per unit area, the number of asperities,  $n$ , per unit area that are able to make contact is given by

$$n = N \int_d^\infty \Psi(z) dz = N \Gamma^{-1}(\alpha) \Gamma(\alpha, \alpha(d/\sigma)^{1/\alpha}), \quad (20)$$

where the two-argument gamma function  $\Gamma(x, d)$  is also called incomplete gamma function and is defined as  $\Gamma(x, d) = \int_d^\infty e^{-t} t^{x-1} dt$ . As shown by Archard [26], the quantities  $r_a$ ,  $\sigma$  and  $N$  are not independent of each other but are related, i.e.  $r_a \sigma N = \text{constant}$ . The value of this constant is between 0.05 and 0.1 [4].

The total real area of contact per unit area is given by [16]

$$A'_r = N \int_d^\infty \pi a'^2 \Psi(z) dz, \quad (21)$$

where  $a'$  is the contact radius of an individual microasperity. Replacing the contact radius of a microasperity by  $(2r_a \delta)^{1/2}$  derived simply from geometric considerations and integrating the former expression, one has

$$A'_r = 2\pi n r_a \sigma \alpha^{-\alpha} \left[ \frac{\Gamma(2\alpha, \alpha(d/\sigma)^{1/\alpha})}{\Gamma(\alpha, \alpha(d/\sigma)^{1/\alpha})} - \frac{\alpha^\alpha d}{\sigma} \right]. \quad (22)$$

For a roughness exponent of 1, this equation is reduced to equation (5). Considering the microasperities that are deformed plastically at an applied load, the total load per

unit area to compress the microasperities is given by

$$P' = N \int_d^\infty (\pi a'^2 H - 2\pi r_a \Delta\gamma) \Psi(z) dz. \quad (23)$$

Similarly substituting the contact radius of a microasperity by  $(2r_a \delta)^{1/2}$ , we have

$$P' = 2\pi n r_a H \sigma \alpha^{-\alpha} \left[ \frac{\Gamma(2\alpha, \alpha(d/\sigma)^{1/\alpha})}{\Gamma(\alpha, \alpha(d/\sigma)^{1/\alpha})} - \frac{\alpha^\alpha d}{\sigma} \right] - 2\pi n r_a \Delta\gamma. \quad (24)$$

Combining equation (24) with equation (22) gives

$$P = A_r \frac{H[\sigma \Gamma(2\alpha, \alpha(d/\sigma)^{1/\alpha}) - \alpha^\alpha d \Gamma(\alpha, \alpha(d/\sigma)^{1/\alpha})] - \Delta\gamma \alpha^\alpha \Gamma(\alpha, \alpha(d/\sigma)^{1/\alpha})}{\sigma \Gamma(2\alpha, \alpha(d/\sigma)^{1/\alpha}) - d \alpha^\alpha \Gamma(\alpha, \alpha(d/\sigma)^{1/\alpha})}, \quad (25)$$

where  $A_r$  is the actual contact area and  $P$  the real applied load.

From equation (25) we make an interesting observation that the microasperities can be plastically deformed, even at zero load, when the following condition is satisfied:

$$\frac{H[\sigma \Gamma(2\alpha, \alpha(d/\sigma)^{1/\alpha}) - \alpha^\alpha d \Gamma(\alpha, \alpha(d/\sigma)^{1/\alpha})] - \Delta\gamma \alpha^\alpha \Gamma(\alpha, \alpha(d/\sigma)^{1/\alpha})}{\sigma \Gamma(2\alpha, \alpha(d/\sigma)^{1/\alpha}) - d \alpha^\alpha \Gamma(\alpha, \alpha(d/\sigma)^{1/\alpha})} = 0. \quad (26)$$

The above equation can be rewritten as follows:

$$\frac{\Delta\gamma}{H} = \frac{\sigma \Gamma(2\alpha, \alpha(d/\sigma)^{1/\alpha}) - \alpha^\alpha d \Gamma(\alpha, \alpha(d/\sigma)^{1/\alpha})}{\alpha^\alpha \Gamma(\alpha, \alpha(d/\sigma)^{1/\alpha})}. \quad (27)$$

If the roughness exponent is taken as 1 ( $\alpha = 1$ ), viz., the distribution of microasperity heights conforms to exponential distribution, equations (24) and (27) can be rewritten as

$$P' = 2\pi n r_a \sigma [H - (\Delta\gamma/\sigma)] \quad (28)$$

and

$$\sigma = \frac{\Delta\gamma}{H}, \quad (29)$$

which are the same as equations (12) and (14) in Ref. [16], respectively.

The force required to separate the contacting surfaces during ductile extension, or the adhesion force, can be determined by considering those asperities that are plastically deformed in such an extension. Only those microasperities that satisfy the condition of ductile extension described as equation (15) would extend in a ductile manner. Considering the criterion of ductile extension, we can rewrite the condition of equation (15) as  $\delta < \delta_a \equiv 8\Delta\gamma^2 E^{*2}/(\pi^2 r_a H^4)$ . Then Johnson's plastic adhesion index,  $\lambda$ , can be formulated as  $\lambda \equiv \sigma/\delta_a$  which is the same as equation (3). The adhesion force per unit area is given by

$$P'_{ad} = N \int_d^{d+\delta_a} H \pi a'^2 \Psi(z) dz. \quad (30)$$



And integration of the above equation yields

$$\begin{aligned}
 P'_{\text{ad}} = & 2\pi n H r \alpha^{-\alpha} \sigma \Gamma^{-1} \left( \alpha, \alpha \left( \frac{d}{\sigma} \right)^{1/\alpha} \right) \left[ \Gamma \left( 2\alpha, \alpha \left( \frac{d}{\sigma} \right)^{1/\alpha} \right) \right. \\
 & - \Gamma \left( 2\alpha, \alpha \left( \frac{\delta_a}{\sigma} + \frac{d}{\sigma} \right)^{1/\alpha} \right) - \frac{\alpha^\alpha d}{\sigma} \Gamma \left( \alpha, \alpha \left( \frac{d}{\sigma} \right)^{1/\alpha} \right) \\
 & \left. + \frac{\alpha^\alpha d}{\sigma} \Gamma \left( \alpha, \alpha \left( \frac{\delta_a}{\sigma} + \frac{d}{\sigma} \right)^{1/\alpha} \right) \right]. \quad (31)
 \end{aligned}$$

#### 4. DISCUSSION

Considering the expressions derived above, in addition to the plastic adhesion index  $\lambda$  and the roughness exponent  $\alpha$ , there are two new dimensionless terms,  $\Delta\gamma/(\sigma H)$  and  $d/\sigma$ , which play important roles in the adhesion of rough surfaces with plastic deformation. Therefore, two dimensionless parameters are introduced as

$$\mu \equiv \frac{\Delta\gamma}{\sigma H}, \quad (32)$$

and

$$\eta \equiv \frac{d}{\sigma}, \quad (33)$$

where  $\mu$  is the ratio of the work of adhesion to the product of the standard deviation of the peak heights and the hardness. The larger the  $\mu$ , the easier the plastic deformation becomes. The dimensionless parameter  $\eta$  is the ratio of the separation between the mean plane and the flat surface during loading to the standard deviation of the peak heights. Considering equations (27) and (29), one can see that  $\mu = 1$  represents the condition of plastic deformation at zero load for exponential distribution of asperity heights.

Using these dimensionless parameters, equation (22) is rewritten as

$$\frac{A'_r}{2\pi n r_a \sigma} = \alpha^{-\alpha} \frac{\Gamma(2\alpha, \alpha \eta^{1/\alpha})}{\Gamma(\alpha, \alpha \eta^{1/\alpha})} - \eta. \quad (34)$$

The term on the left-hand side of the above equation is normalized by  $2\pi n r_a \sigma$  which is the actual contact area per unit area for exponential distribution of asperity heights. The influence of the parameters  $\alpha$  and  $\eta$  on the dimensionless form of real contact area is shown in Fig. 3. Figure 3 illustrates that the real contact area is directly proportional to the roughness exponent, i.e. the rougher the surface, the smaller the real contact area. However, the actual contact area decreases with the increment of the parameter  $\eta$ .

Equation (24) is rewritten as

$$\frac{P'}{2\pi n r_a \sigma H} = \alpha^{-\alpha} \frac{\Gamma(2\alpha, \alpha \eta^{1/\alpha})}{\Gamma(\alpha, \alpha \eta^{1/\alpha})} - \eta - \mu, \quad (35)$$

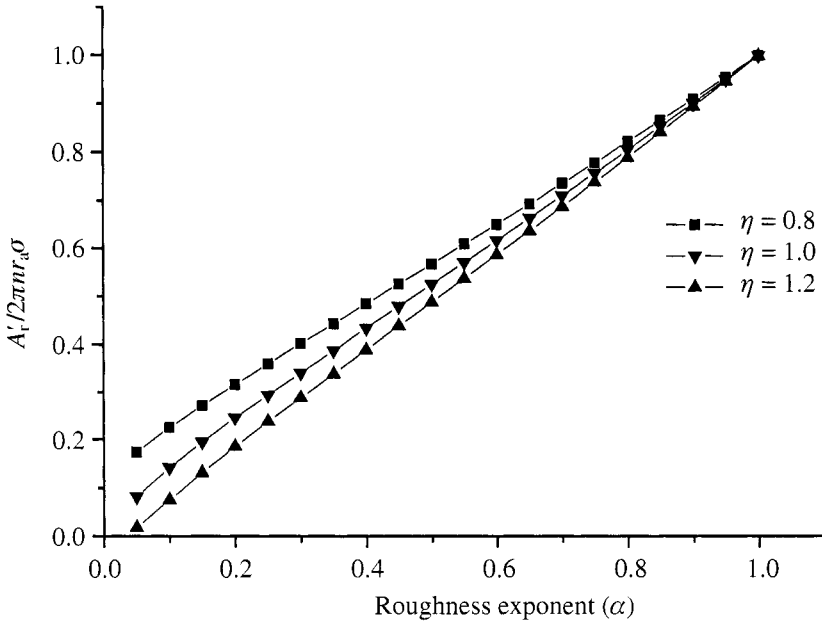


**Figure 3.** Variation of the dimensionless term  $A'_t/2\pi n r_a \sigma$  with roughness exponent  $\alpha$  for  $\eta = 0.8$ , 1.0 and 1.2.

and similarly the influence of  $\alpha$ ,  $\mu$  and  $\eta$  on the ratio  $P'/2\pi n r_a \sigma H$  is shown in Fig. 4. The dimensionless load is directly proportional to the roughness exponent  $\alpha$ ; in addition, both smaller parameter  $\eta$  and smaller parameter  $\mu$  correspond to a larger value of the dimensionless load. An interesting phenomenon is observed that the dimensionless load term becomes negative in a certain  $\alpha$  range, for example, when  $\alpha$  approaches zero,  $\eta$  equals 1.2 and  $\mu$  equals 0.1.

By using equation (32), equation (27) is rewritten as

$$\mu = \alpha^{-\alpha} \frac{\Gamma(2\alpha, \alpha\eta^{1/\alpha})}{\Gamma(\alpha, \alpha\eta^{1/\alpha})} - \eta, \quad (36)$$

and the influence of  $\alpha$  and  $\eta$  on the required condition of plastic deformation at zero load is shown in Fig. 5. One can see that the parameter  $\mu$  is directly proportional to the roughness exponent  $\alpha$ , but it is inversely proportional to the parameter  $\eta$ . When  $\alpha = 1$ , the condition is the same as equation (29), i.e.  $\mu$  equals 1 and is independent of the parameter  $\eta$ . The parameter  $\mu$  decreases with decreasing  $\alpha$ . For  $\alpha < 1$ , a smaller  $\eta$  corresponds to a larger  $\mu$ .

Considering equations (24) and (31), the ratio between the force to separate the contacting surfaces and the force that presses them together is expressed as

$$\frac{P'_{ad}}{P'} = \frac{\Gamma(2\alpha, \alpha\eta^{1/\alpha}) - \Gamma(2\alpha, \alpha(1/\lambda + \eta)^{1/\alpha}) - \alpha^\alpha \eta \Gamma(\alpha, \alpha\eta^{1/\alpha}) + \alpha^\alpha \eta \Gamma(\alpha, \alpha(1/\lambda + \eta)^{1/\alpha})}{\Gamma(2\alpha, \alpha\eta^{1/\alpha}) - \alpha^\alpha \eta \Gamma(\alpha, \alpha\eta^{1/\alpha}) - \mu \alpha^\alpha \Gamma(\alpha, \alpha\eta^{1/\alpha})}, \quad (37)$$

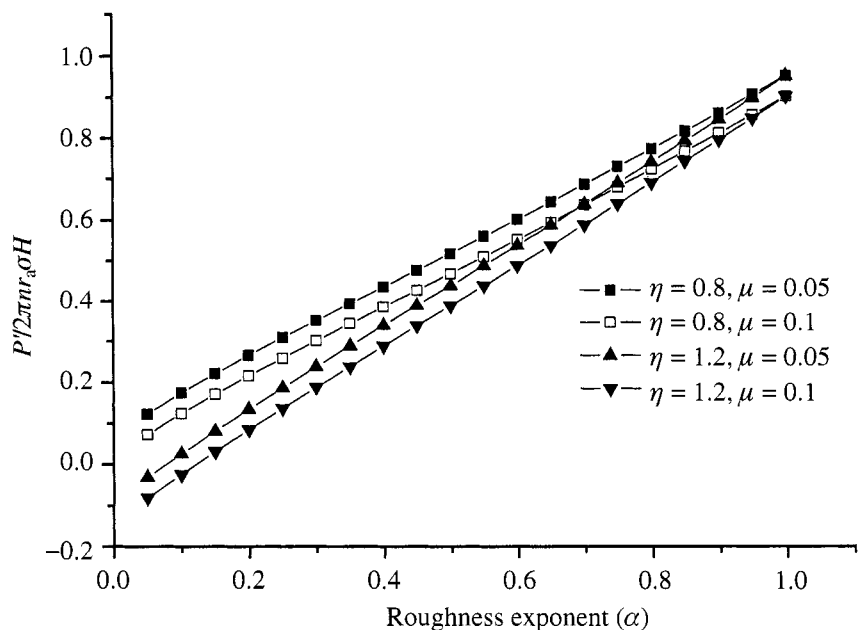


**Figure 4.** Variation of the dimensionless term  $P'/(2\pi nr_a \sigma H)$  with roughness exponent  $\alpha$  for various  $\eta$  and  $\mu$ .

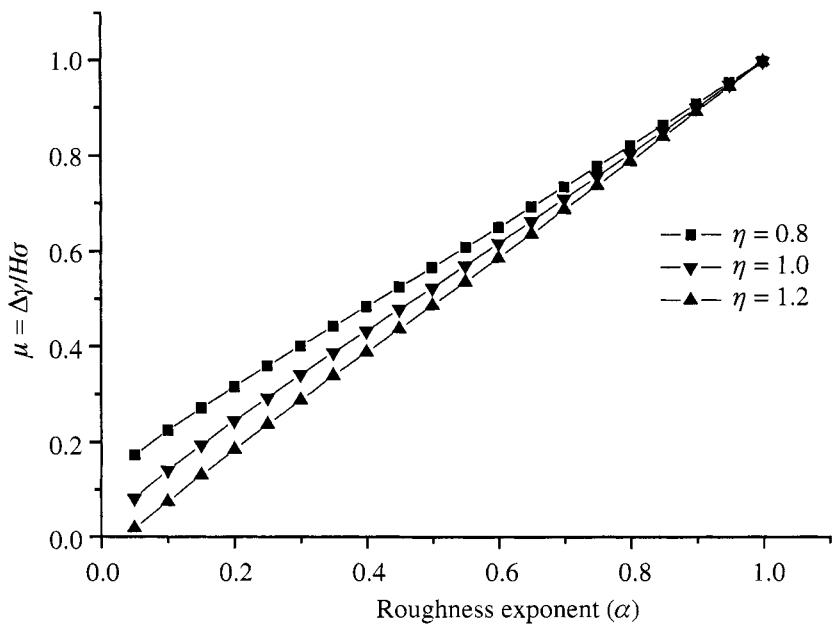


**Figure 5.** Variation of  $\mu = \Delta\gamma/(H\sigma)$  with roughness exponent  $\alpha$  for  $\eta = 0.8, 1.0$  and  $1.2$  which represents the condition for plastic deformation at zero load.

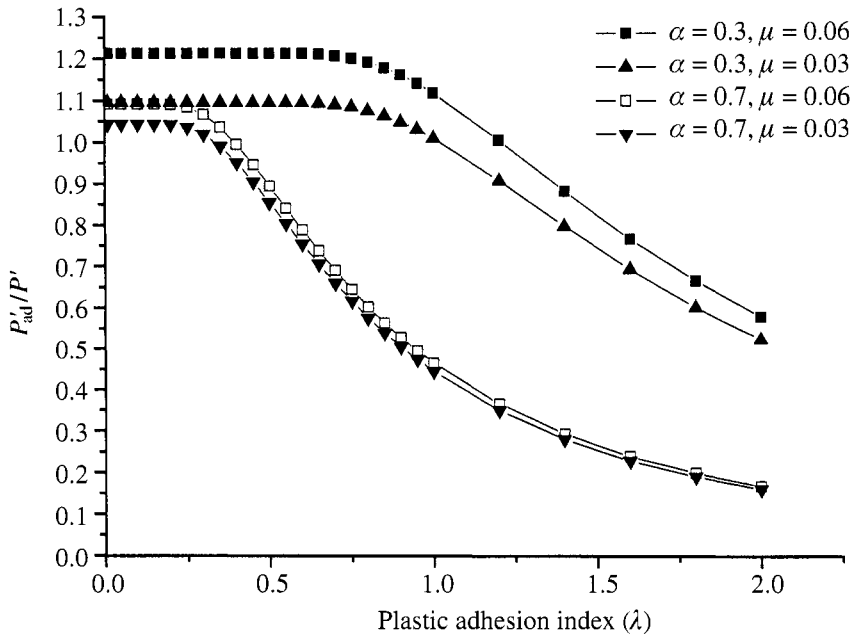


**Figure 6.** Variation of ratio of adhesion force to total load with plastic adhesion index  $\lambda$  for  $\eta = 1.0$  and various  $\alpha$  and  $\mu$ .

which is shown in Figs 6 and 7 as functions of the plastic adhesion index  $\lambda$  for various  $\alpha$ ,  $\eta$  and  $\mu$ . If the roughness exponent is taken as 1, equation (37) can be reduced to equation (6). These figures show that the ratio  $P'_{ad}/P'$  is inversely proportional to both the plastic adhesion index  $\lambda$  and to the roughness exponent  $\alpha$ . The ratio is approximately constant when  $\lambda$  is less than a limiting value which is sensitive to  $\alpha$ . For example, this limiting value is about 0.25 for  $\alpha = 0.7$  and about 0.75 for  $\alpha = 0.3$ . Then it drops rapidly with increasing  $\lambda$ . It is seen from Fig. 6 that for constant  $\alpha$ , a larger  $\mu$  corresponds to a larger  $P'_{ad}/P'$  ratio. It is also seen from Fig. 7 that a larger  $\eta$  corresponds to a larger  $P'_{ad}/P'$  ratio. An unusual phenomenon appears that the upper limit of the ratio  $P'_{ad}/P'$  is more than unity. With the present assumption of perfectly plastic adhesion contact, the effect of the work of adhesion explains this behavior.

## 5. CONCLUSIONS

A theoretical model is developed to describe the adhesion between plastically-deformable fractal surfaces whose asperity heights conform to a general distribution. General expressions for real contact area, total load and the required separation force are obtained. In special cases, for  $\alpha = 1/2$ , the results obtained in this study can be reduced to those of Gaussian distribution of surface asperities and for  $\alpha = 1$  they can be reduced to those of exponential distribution of surface asperities.

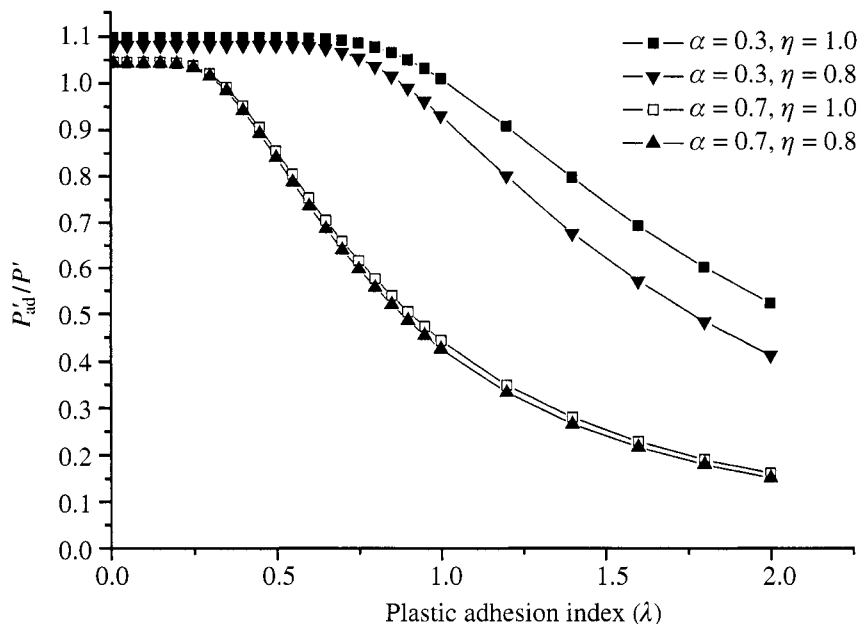


**Figure 7.** Variation of ratio of adhesion force to total load with plastic adhesion index  $\lambda$  for  $\mu = 0.03$  and various  $\alpha$  and  $\eta$ .

The condition has been determined for interface plastic deformation due to the work of adhesion at zero external load for asperities with fractal distribution. For exponential distribution ( $\alpha = 1$ ), this condition reduces to  $\mu = 1$ , or equivalently  $\sigma = \Delta\gamma/H$  [16].

In addition to the roughness exponent  $\alpha$  and the plastic adhesion index  $\lambda$ , two new dimensionless parameters,  $\eta = d/\sigma$  and  $\mu = \Delta\gamma/(\sigma H)$ , are derived. The influences of these dimensionless parameters on adhesion with plastic deformation are studied.

### Acknowledgements

This research was supported by the Distinguished Young Scholar Fund of the National Natural Science Foundation of China (NSFC) (Grant No. 10225209 and No. 90305020), key project from the Chinese Academy of Sciences (Grant No. KJCX2-SW-L2) and NSFC-RGC Joint Project (Grant No. 50131160739).

### REFERENCES

1. D. Tabor, in: *Surface Physics of Materials*, J. M. Blakely (Ed.), Volume 2, Chapter 10. Academic Press, New York, NY (1975).
2. W. C. Wake, *Adhesion and the Formulation of Adhesives*, 2nd edn. Applied Science, London (1982).
3. Y. P. Zhao, L. S. Wang and T. X. Yu, *J. Adhesion Sci. Technol.* **17**, 519 (2003).

4. C. Gui, M. Elwenspoek, N. Tas and J. G. E. Gardeniers, *J. Appl. Phys.* **85**, 7448 (1999).
5. J. A. Greenwood and J. B. P. Williamson, *Proc. R. Soc. Lond.* **A295**, 300 (1966).
6. K. L. Johnson, K. Kendall and A. D. Roberts, *Proc. R. Soc. Lond.* **A324**, 301 (1971).
7. X. H. Shi and Y. P. Zhao, *J. Adhesion Sci. Technol.* **18**, 55 (2004).
8. K. N. G. Fuller and D. Tabor, *Proc. R. Soc. Lond.* **A345**, 327 (1975).
9. K. Kendall, *Molecular Adhesion and Its Applications*. Kluwer Academic/Plenum Publishers, New York, NY (2001).
10. E. Krupp, *Adv. Colloid Interface Sci.* **1**, 111 (1967).
11. K. E. Easterling and A. R. Tholen, *Acta Metall.* **20**, 1001 (1972).
12. A. R. Tholen, in: *Microscopic Aspects of Adhesion and Lubrication*, J. M. Georges (Ed.), p. 263. Elsevier, Amsterdam (1982).
13. D. S. Rimai, L. P. DeMejo and R. C. Bowen, in: *Fundamentals of Adhesion and Interfaces*, D. S. Rimai, L. P. DeMejo and K. L. Mittal (Eds), p. 1. VSP, Utrecht (1995).
14. K. L. Johnson, in: *Theoretical and Applied Mechanics*, W. T. Koiter (Ed.), p. 133. North-Holland, Amsterdam (1976).
15. D. Tabor, *Hardness of Metals*. Clarendon Press, Oxford (1951).
16. S. K. R. Chowdhury and H. M. Pollock, *Wear* **66**, 307 (1981).
17. T. S. Chow, *Phys. Rev. Lett.* **86**, 4592 (2001).
18. T. S. Chow, *J. Phys.: Condens. Matter* **15**, L83 (2003).
19. B. N. J. Persson, *Phys. Rev. Lett.* **87**, 116101 (2001).
20. B. N. J. Persson, *Phys. Rev. Lett.* **88**, 129601 (2002).
21. J. N. Israelachvili, in: *Fundamentals of Friction: Macroscopic and Microscopic Processes*, I. L. Singer and H. M. Pollock (Eds), p. 351. Kluwer, Dordrecht (1992).
22. K. L. Johnson, *Tribol. Int.* **31**, 413 (1998).
23. K. L. Johnson, *Contact Mechanics*. Cambridge University Press, Cambridge (1985).
24. K. R. Morris, S. L. Nail, G. E. Peck, S. R. Byrn, U. J. Griesser, J. G. Stowell, S. J. Hwang and K. Park, *Pharm. Sci. Technol. Today* **1**, 235 (1998).
25. R. Chiarello, V. Panella, J. Krim and C. Thompson, *Phys. Rev. Lett.* **67**, 3408 (1991).
26. J. F. Archard, *Tribol. Int.* **7**, 213 (1974).

## **Deformation of soft colloidal probes during AFM pull-off force measurements: elimination of nano-roughness effects**

GARTH W. TORMOEN and JAROSLAW DRELICH\*

*Department of Materials Science and Engineering, Michigan Technological University, Houghton, MI 49931, USA*

**Abstract**—The forces needed to remove polystyrene (PS) and polyethylene (PE) particles from silicon wafers were measured using the atomic force microscopy colloidal probe technique. The polymeric probes had surfaces with nano-sized asperities. The ability to deform these asperities and conform to the topography of the substrate surface allowed the soft probes to mitigate roughness effects on the measured pull-off forces. Adequate deformations for surface asperities on PS and PE probes that resulted in reproducible probe-substrate contact area required loads of approx.  $0.8\text{--}4\ \mu\text{N}$ . For these applied loads the standard deviation in measured pull-off forces was reduced to 0.5–2.7%.

**Keywords:** Adhesion; atomic force microscopy; colloidal probe technique; deformable probes; pull-off forces; roughness.

### **1. INTRODUCTION**

Atomic force microscopy (AFM) force measurements on soft materials require unique analytical approaches, as the adhesion force has been shown to strongly depend on the applied load [1–7]. For rigid materials, the compressive stress due to loading is typically kept below the yield strength of the probe material to keep all probe deformation elastic. Elastic deformation is recoverable immediately upon retraction of the AFM probe and, therefore, does not affect the final contact area between the probe and substrate. This condition does not hold for soft probes, typically made from polymeric materials, which may undergo viscoelastic and/or plastic deformation. Even light loads on soft probes, below those causing plastic deformation, show a heavy influence on the measured pull-off force.

This paper focuses on utilizing the deformability of soft materials to overcome roughness effects on AFM force measurements. Based on the results reported earlier

---

\*To whom correspondence should be addressed. Tel.: (1-906) 487-2932. Fax: (1-906) 487-2934. E-mail: jwdrelch@mtu.edu

[5–8], it is hypothesized, and studied in this paper, that under adequate loading conditions, surface asperities on the probe may be ‘squeezed-out’, and the probe may conform to substrate surface asperities to yield consistent, reproducible contact areas.

## 2. EXPERIMENTAL

### 2.1. Colloidal probes

Two polystyrene (PS) probes, and one polyethylene (PE) probe were used in this study. The PS probes consisted of  $10 \pm 1 \mu\text{m}$  diameter PS beads glued to regular v-frame ContactMode cantilevers (Digital Instruments, Santa Barbara, CA, USA) with a nominal spring constant ( $k$ ) of 0.58 N/m. The PE probe consisted of a  $14 \pm 2 \mu\text{m}$  diameter bead glued to a stiffer v-frame (pre-calibrated) cantilever having a nominal  $k$  value of 17.0 N/m, and was provided by Bioforce Nanosciences (Ames, IA, USA). Spring constants provided by the suppliers of the cantilevers were used in analysis of the data, and no measurement to confirm the accuracy of claimed values was performed in this research.

Polymeric probes used in our laboratory had rough surfaces with nano-sized asperities as shown in Fig. 1. The dimensions of these asperities can vary from several to a few tenths of nanometers. Such nano-roughness, the character of which may differ from one probe to another, is inherent to practically all polymeric colloidal probes as it cannot be eliminated or controlled during the fabrication processes of the particles.

All probes were cleaned prior to testing by immersing in a bath of surfactant solution composed of approximately 10% by volume Micro 90 cleaning solution (International Products, Burlington, NJ, USA) in deionized water (15–18 M $\Omega$ ), for 1 to 2 min (care must be taken when attempting to clean glued colloidal probes, as

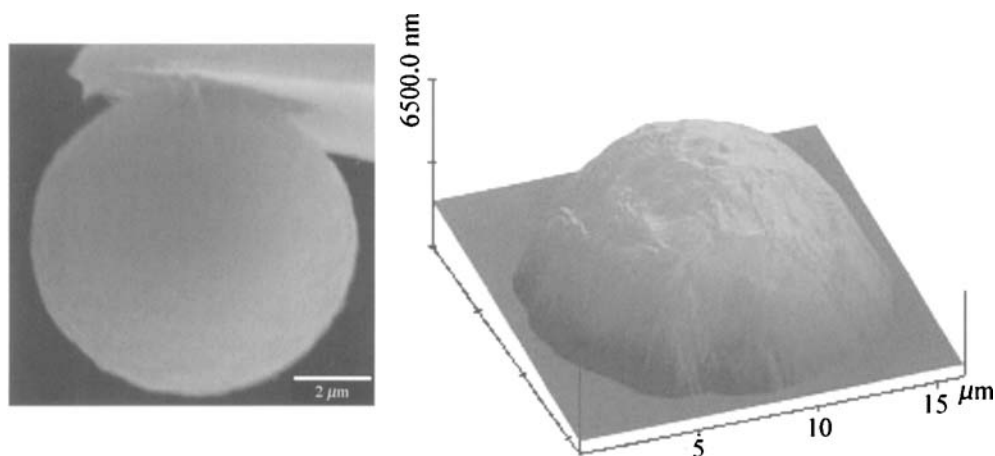


**Figure 1.** SEM micrograph (left) of a PS probe and AFM image (right) of a PE probe [9].



they can be washed off of from the cantilever). The probes were then removed from the bath and either rinsed in a stream of deionized water for 60 s or immersed in a bath of deionized water and swirled for 1–2 min. Probes were allowed to air dry for 2 min in a covered container prior to use.

## 2.2. Substrates

Substrates used in this research were pieces of silicon wafers obtained from either MEMS (St. Louis, MO, USA), or Polishing Corporation of America (Santa Clara, CA, USA), having either a ‘nano-rough’ or ‘smooth’ finish, respectively (Fig. 2). Substrate surfaces were ultrasonicated in a bath of Micro 90 surfactant solution for 20 min, followed by another 20 min ultrasonication in a bath of deionized water. Silicon wafer samples were then inserted into a covered glass Petri dish, and placed in an oven at 105–120°C for 5 to 20 min. Substrates were allowed to cool in the covered Petri dish prior to experimentation.

## 2.3. Adhesion force measurements

The initial experiment with the PS probes involved measuring 100 force curves sequentially on a single spot. This was performed with a scan rate of 0.5 Hz in a sub-5% relative humidity (RH) environment using a Dimension 3000 AFM

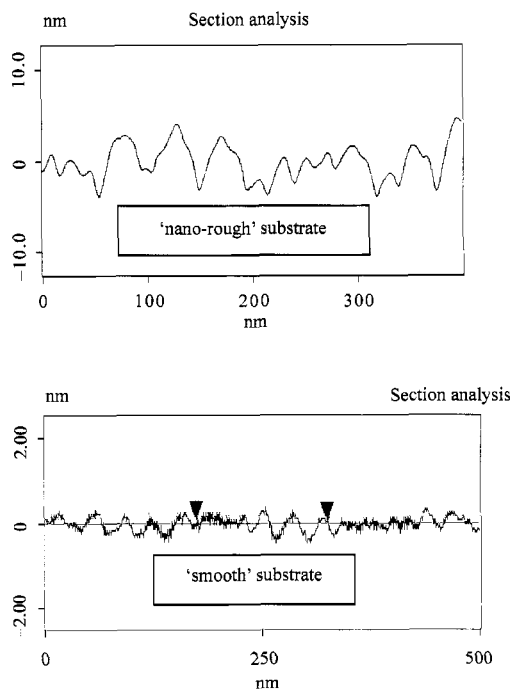


**Figure 2.** Cross-sectional profiles of surface topography for silicon wafers with ‘nano-rough’ and ‘smooth’ finishes.

(Digital Instruments). The purpose of this test was to see if the probe underwent any plastic deformation during normal experimentation conditions. If this occurred, the adhesion forces would increase over time. The second round of experiments with the PS probes involved measuring 60–200 force curves at 3–10 random locations (20 measurements on each spot) on the ‘smooth’ silicon surfaces. Experiments were performed in air with sub-5% RH levels, using a scan rate of 0.5 Hz.

The PE probe was tested on both ‘smooth’ and ‘nano-rough’ substrates. Here, the loading conditions were varied between three regimes, referred to as low, mid and high. The loading conditions varied between regimes, but were kept approximately equal within the regimes. The purpose of this experiment was to see how the scatter in the data varied at different loading conditions on the same substrate. Ten random locations were chosen with 20 measurements recorded per spot for each loading regime. Measurements were performed in air with sub-7% RH levels at a scan rate of 0.5 Hz.

### 3. RESULTS AND DISCUSSION

#### 3.1. Pull-off forces for PS probes

Figure 3 shows a plot of pull-off force *vs.* measurement number for one of the PS probes, hereafter called PS probe 1. The maximum applied load used in this experiment was held virtually constant at  $184.8 \pm 10.4$  nN. As indicated by the results in Fig. 3, the scatter in the data for measurements taken at a single location is about 10%. Force measurement values were recorded between 302 and 336 nN, with the average value and standard deviation equal to  $314.5 \pm 8.0$  nN. No characteristic trend was seen as the measurements were recorded sequentially. However, even in the small range of loads used (about 167 nN to 207 nN) a linear dependence in the measured force measurement on applied load is observed (Fig. 4).

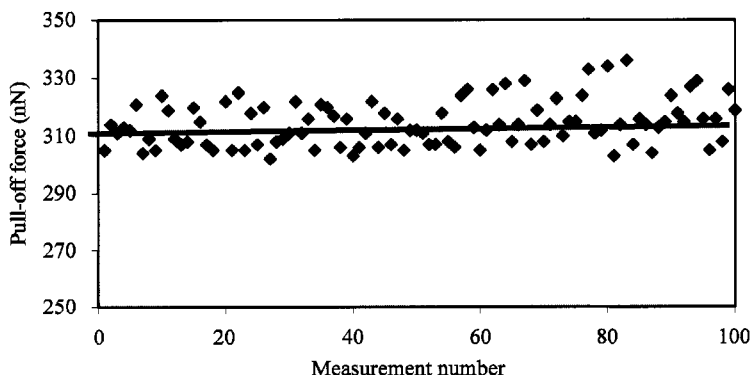


**Figure 3.** Pull-off force *vs.* sequential measurement number for PS probe 1 on the ‘smooth’ silicon wafer. The trend line is included to guide the eye.

It appears from Figs 3 and 4 that the measured pull-off forces relied on the applied loads, but with no lasting effect between measurements. This is assumed to be indicative of viscoelastic deformation of the probe [10], and no permanent (plastic) deformation occurred for the PS probe. Applied loads and the adhesion energy between the probe and substrate were sufficient to maintain the expanded contact area induced by viscoelastic deformation, but this deformation was recovered once the probe was removed from the substrate, before the next measurement was made. However, plastic deformation of nano-irregularities, present on the probe, cannot be ruled out, particularly in view of the previous report [6]. The deformation of single asperities is discussed further in Section 3.4.

Figure 5 shows how the pull-off force data vary during measurements on random spots for PS probe 1 on the 'smooth' silicon surface. The trend line in Fig. 5 is included only to show the consistency in the average force measured between spots on the 'smooth' substrate.

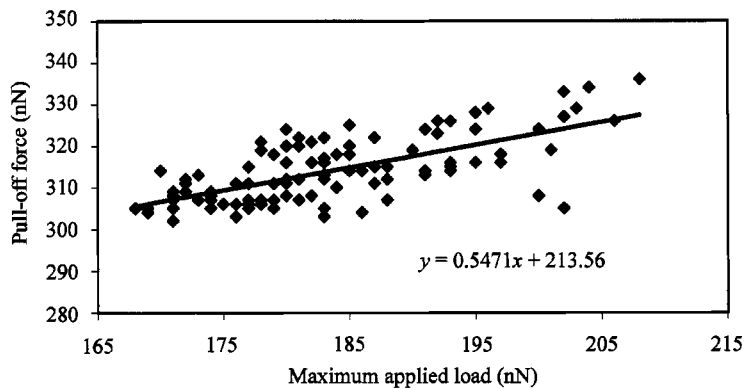


**Figure 4.** Pull-off force vs. load for PS probe 1 in a single location on the 'smooth' silicon wafer. The trend line is included to guide the eye.

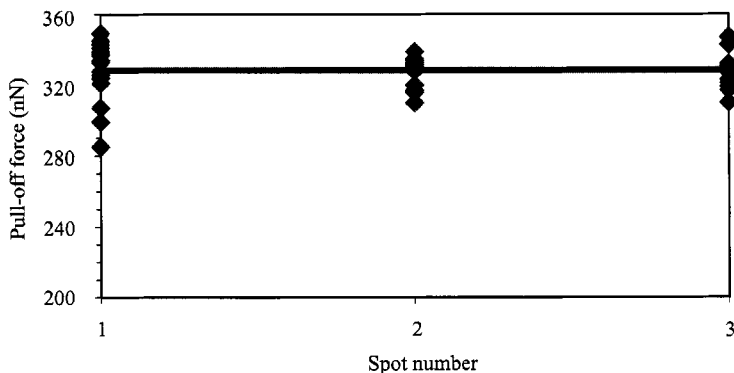


**Figure 5.** Pull-off forces measured for PS probe 1 on three different spots on the 'smooth' silicon wafer. The trend line is included to guide the eye.

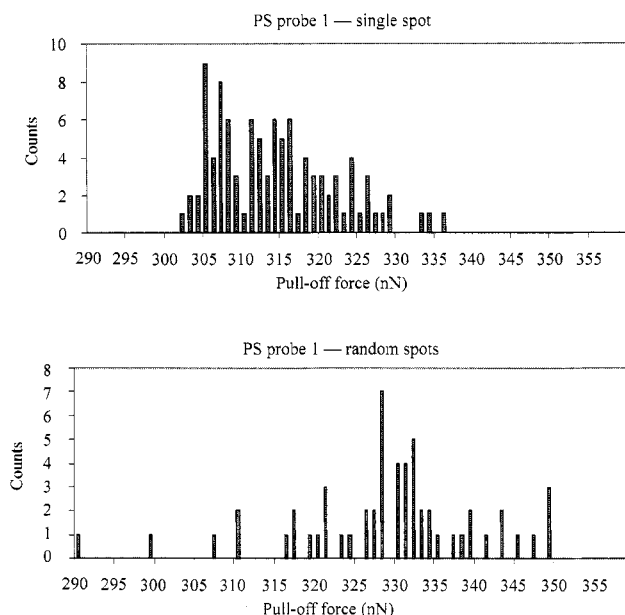


**Figure 6.** Histograms of force data for PS probe 1.

Although only three locations were tested in this experiment, Fig. 5 indicates that using soft probes may yield very consistent force measurements between random locations on a surface, in contradiction to rigid probes discussed in another paper [11]. The mean force value from Fig. 5 is  $328.6 \pm 11.9$  nN at loads within  $202.6 \pm 25.7$  nN. To aid in comparing distributions between the single spot recordings (Fig. 3) and the random spot recordings (Fig. 5), histograms of the force data from each of these experiments are included in Fig. 6.

The histograms in Fig. 6 indicate a tighter grouping of force data for the single location, with forces recorded between 302 and 336 nN ( $314.5 \pm 8.0$  nN), a result that is consistent with previous observations [12]. For random locations, forces were recorded from 290 to 341 nN ( $328.6 \pm 11.9$  nN).

PS probe 2 was tested against the 'smooth' silicon wafer, measuring pull-off forces at 10 random locations. The maximum applied loads for this experiment ranged from 78 to 101 nN, with the average and standard deviation values of  $89.9 \pm 4.9$  nN. Figure 7 shows the force data collected for PS probe 2 against the applied load.

As shown in Fig. 7, even at small loads, a strong dependence of measured force on applied load is observed. The forces recorded for PS probe 2 were significantly weaker and more scattered ( $F = 88.6 \pm 17.2$  nN) than for PS probe 1 ( $F = 328.6 \pm 11.9$  nN) at random locations. Presumably, this probe had a different number, size and distribution of nano-asperities in the probe's apex area, where the contact with the substrate is established during the pull-off force measurements. It is also probable that the lower forces experienced by the probe were insufficient

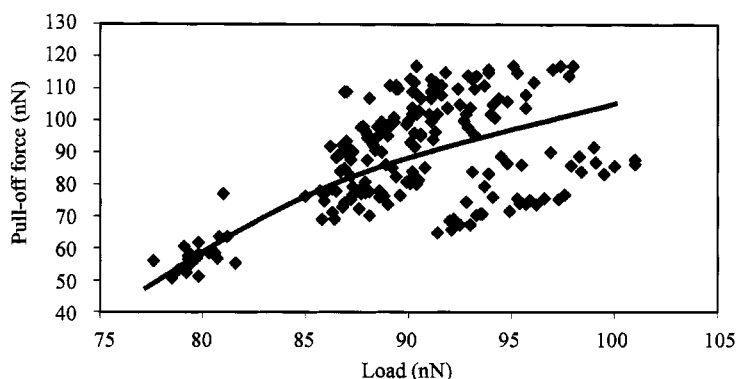


**Figure 7.** Force vs. load for PS probe 2 on 'smooth' silicon wafer at 10 random locations. The trend line is included to guide the eye.

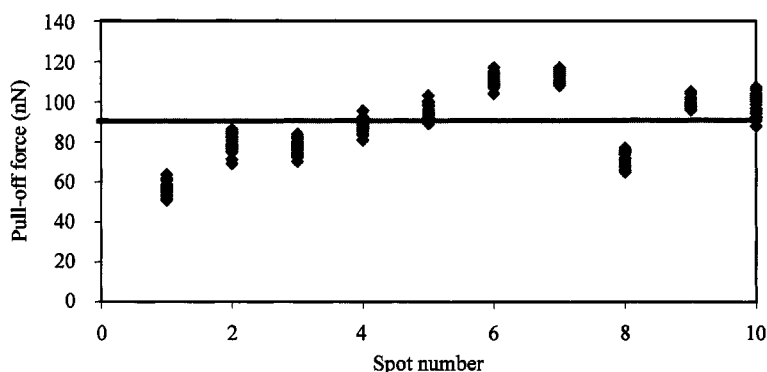


**Figure 8.** Force measured vs. spot number for PS probe 2 on 'smooth' silicon wafer. The trend line is included to guide the eye.

to consistently squeeze out the probe surface's asperities, and/or conform to the inherent asperities of the substrate surface. This would prevent intimate contact between the probe and substrate, accounting for the decrease in average force value. It would also explain the increased scatter, as random asperities contacted at different surface locations would yield random contact points, and effectively cause scatter in recorded force data. To support this hypothesis, Figs 8 and 9 show the variation in force data collected at random spots.

Force values were recorded between 52 and 118 nN for all ten locations (Fig. 9). Figure 8 indicates no distinct trend in the force data at the different locations, but a significant, random variation is observed. For example, an average force of approx. 60 nN was measured at spot #1, while spot #7 averaged approx. 115 nN.

The average pull-off forces measured for PS probes 1 and 2 on 'smooth' silicon wafer were  $328.6 \pm 11.9$  and  $88.6 \pm 17.2$  nN, respectively. These force ( $F$ ) values were used to calculate the work of adhesion ( $W_A$ ) between polystyrene and silicon

using the JKR contact mechanics model [13, 14],

$$W_A = \frac{F}{1.5\pi R}, \quad (1)$$

where  $R$  is the radius of the probe, approx.  $5 \mu\text{m}$ .

The JKR model is used here because of the large value for the Maugis number ( $\lambda \approx 92$ ) calculated by the following equation [15]:

$$\lambda = \frac{2.06}{z_0} \sqrt[3]{\frac{R_P W_A}{\pi K^2}}, \quad (2)$$

where  $z_0$  is the equilibrium separation distance between the probe and substrate during adhesional contact ( $z_0 \approx 0.2 \text{ nm}$ ) and  $K$  is the reduced elastic modulus:

$$\frac{1}{K} = \frac{3}{4} \left( \frac{1 - \nu_P^2}{E_P} + \frac{1 - \nu_S^2}{E_S} \right). \quad (3)$$

$E$  denotes Young's modulus and  $\nu$  is the Poisson's ratio; subscripts P and S refer to probe and substrate, respectively. Because polystyrene is a much softer material than silicon wafer, equation (3) can be reduced to:

$$K \approx \frac{4E_P}{3(1 - \nu_P^2)}. \quad (4)$$

For polystyrene  $K \approx 4 \text{ GPa}$  [6]. The work of adhesion  $W_A = 200 \text{ mJ/m}^2$  was assumed for calculation of the  $\lambda$  value using equation (2). The value of  $W_A = 200 \text{ mJ/m}^2$  for the polyethylene-silicon system is reported in Section 3.2. Because of similar surface energy values for polystyrene ( $40\text{--}42 \text{ mJ/m}^2$ ) and polyethylene ( $30\text{--}35 \text{ mJ/m}^2$ ) [16],  $W_A$  for the polystyrene-silicon should be of similar magnitude as for the polyethylene-silicon, or somewhat larger.

Based on the measured pull-off forces and using equation (1), the work of adhesion between polystyrene and a silicon wafer was calculated to be 14 and  $4 \text{ mJ/m}^2$  for PS probes 1 and 2, respectively. These values are at least an order of magnitude too small from expected values, and indicate strong surface roughness

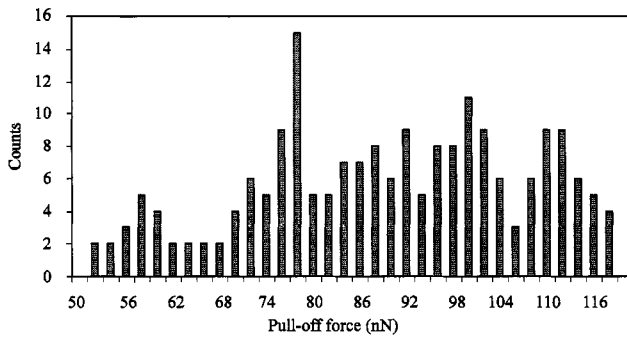


**Figure 9.** Histogram of force data for PS probe 2 on 'smooth' silicon wafer.

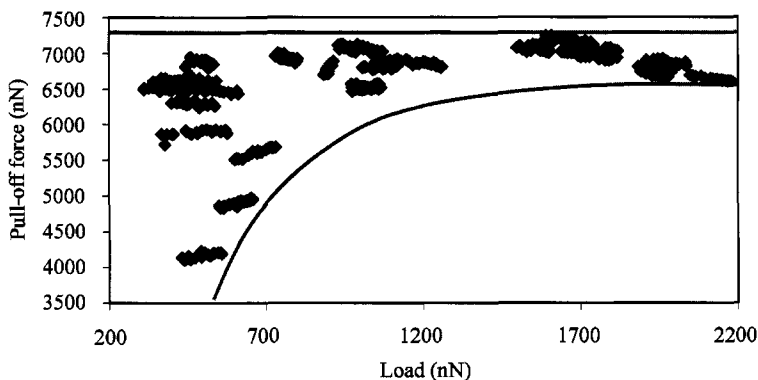
effects in pull-off force measurements. In other words, the contact area between the probe and the substrate was smaller than expected for an approx.  $10\text{ }\mu\text{m}$  sphere in adhesive contact with a flat substrate. Since fabrication of colloidal spheres and substrates that are free of roughness seems improbable for most materials, the effects of roughness during the AFM pull-off force measurements should be taken into account during interpretation of the results. This can be done through the use of appropriate theoretical models for systems with rough surfaces [14]. Another approach, which is a primary focus of this study, is elimination, or rather minimization, of the roughness effects through intentional deformation of surface asperities. In order to succeed with deformation of surface asperities, stiffer cantilevers (with higher spring constant) than used in this part of our study are required [5, 7, 8, 14].

### 3.2. Pull-off forces for PE probe

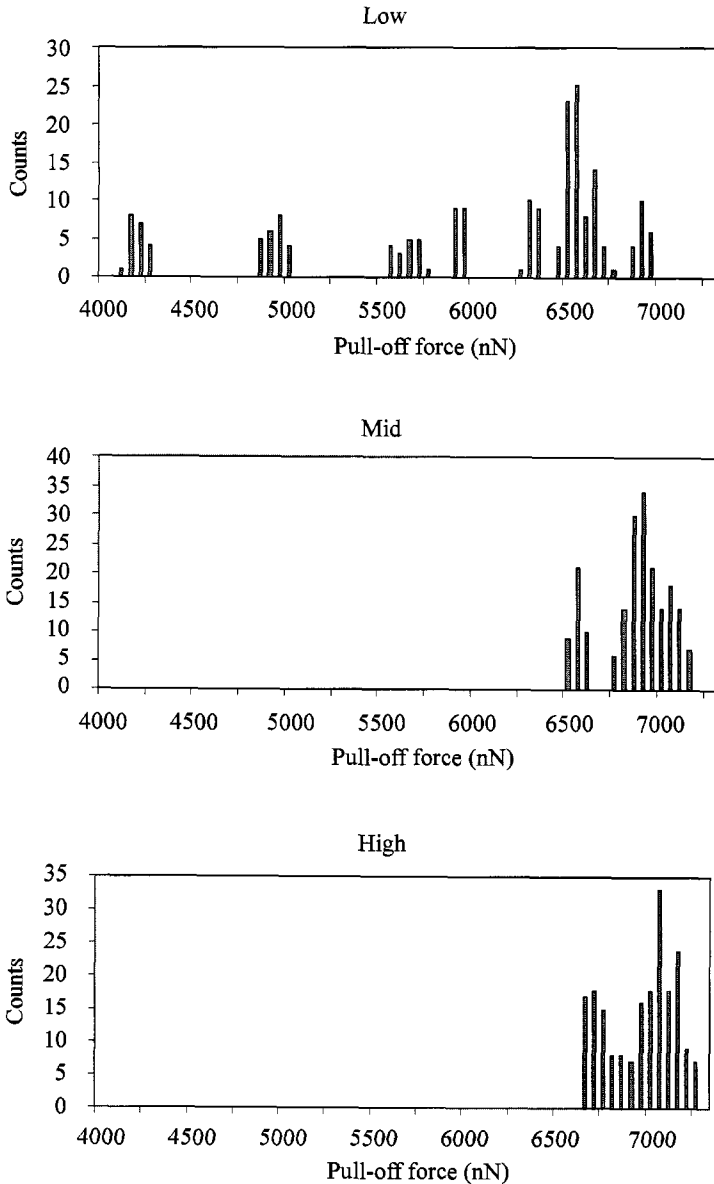
The PE probe was pressed against both ‘smooth’ and ‘nano-rough’ silicon substrates. A plot of the recorded pull-off force data on the ‘nano-rough’ substrate is shown in Fig. 10.

Figure 10 contains data from all three loading regimes. The loads varied from approx. 300 to approx. 2180 nN, in the low- and high-loading regimes, respectively. Figure 10 shows that at low loads, force data are widely scattered, varying from approx. 4100 to approx. 6800 nN, whereas the data are much more tightly grouped at the high loads, varying from approx. 6600 to approx. 7200 nN. Conceivably, as hypothesized for the PS probes, the low-loading regime did not supply an adequate compressive stress to either ‘squeeze-out’ the probe’s own asperities, or to conform to the surface asperities.

To gain a more comprehensive understanding of the data scatter in the different loading regimes, Fig. 11 contains histograms of the force measured in each of the loading regimes with average values and their standard deviations:  $497 \pm 95$ ,



**Figure 10.** Plot of force data for PE probe on ‘nano-rough’ silicon substrate. Trend lines are included to demonstrate how the scatter in the pull-off forces diminishes with increasing maximum applied loads.



**Figure 11.** Histograms of measured force data for PE probe in different loading regimes.

$980 \pm 134$  and  $1792 \pm 183$  nN for the low-, mid- and high-loading regimes, respectively.

The forces recorded in the low-, mid- and high-loading regimes were  $5974 \pm 838$ ,  $6837 \pm 183$  and  $6931 \pm 180$  nN, respectively (Fig. 11). The average pull-off force value increased with applied load, indicating deformation of the probe and increased contact area. This increase in pull-off force diminishes between the mid- and high-



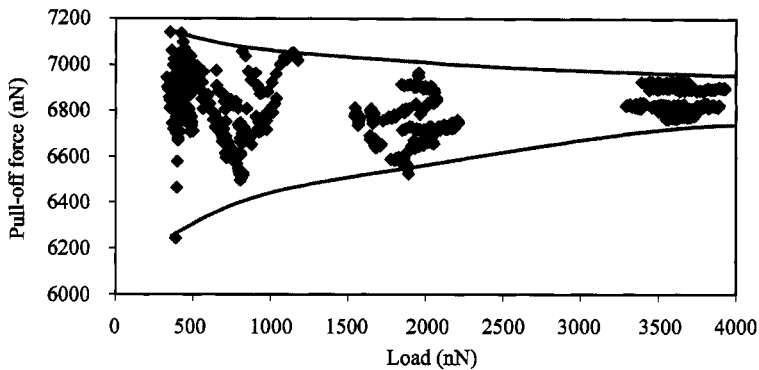


**Figure 12.** Force data collected for PE probe on 'smooth' silicon wafer. Trend lines are included to demonstrate how the scatter in the pull-off forces diminishes with increasing maximum applied loads.

loading regimes (Fig. 10). This was interpreted as 'saturation' of the contact area between the probe and surface, meaning that for the 'nano-rough' surface, the load required to squeeze-out the probe's asperities as well as to conform to the asperities of the 'nano-rough' surface is sufficient in the mid-loading regime. The increase in force measured between the mid- and high-loading regimes can be explained as a result of further deformation outside the 'saturated' contact area, although the differences between these forces are nearly insignificant. The range of forces measured between these two regimes is indistinguishable.

Force data collected from the same PE probe on the 'smooth' silicon substrate are shown in Fig. 12. Concurrent with the observations from the force measurements on 'nano-rough' surfaces, as the loading regimes increase from low to high, the scatter in the data decreases. The loads for this experiment ranged from approx. 330 to approx. 3900 nN, with force values recorded between 6242 and 7141 nN. Figure 13 contains individual histograms of the force measured in each of the loading regimes. The average applied loads were  $580 \pm 198$ ,  $1871 \pm 186$  and  $3606 \pm 160$  nN for these low-, mid- and high-loading regimes, respectively. The measured pull-off force values for three regimes were  $6829 \pm 150$ ,  $6739 \pm 95$  and  $6840 \pm 46$  nN, respectively. The average force value did not vary much between the regimes, indicating that squeezing out of the probe's asperities occurred in all loading regimes, and an intimate contact between the probe and substrate was evident, even in the low-loading regime. As this substrate was as smooth as we could achieve in the laboratory, there were no significant surface asperities to conform to, and contact areas were almost consistent across all regimes, with reduction of data scatter as the loading increased.

As shown in Figs 10 and 12, similar pull-off forces were measured in the mid- and high-loading regimes for 'nano-rough' substrate ( $6837 \pm 183$  nN and  $6931 \pm 180$  nN, respectively) and in low- to high-loading regimes for 'smooth' silicon surface ( $6804 \pm 117$  nN). The proximity of these values, coupled with the knowledge that the same probe was used which underwent an identical cleaning

procedure, and the substrate was the same material but different surface roughness characteristic (Fig. 2), indicates that similar contact areas were achieved in the high-loading regime for both ‘nano-rough’ and ‘smooth’ substrates. This shows that the roughness effects on AFM pull-off force data, coming from both probe and substrate, may be eliminated by using soft probes and adequate loads.

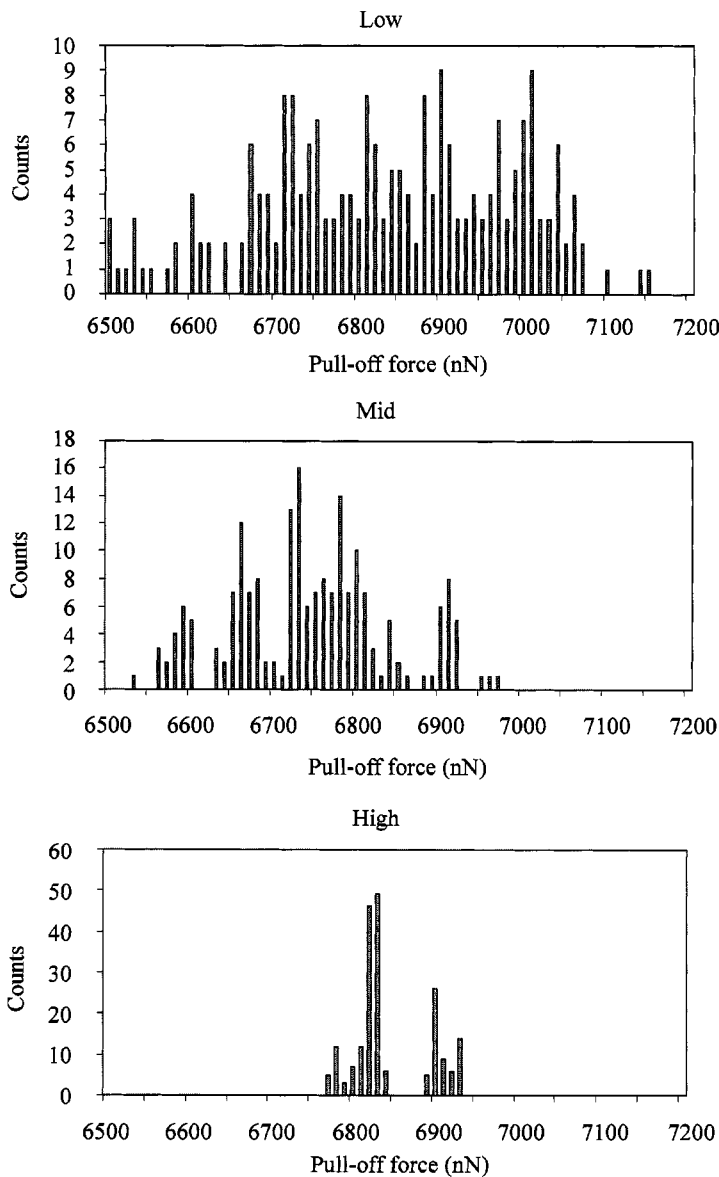


**Figure 13.** Individual histograms of force data for different loading regimes for PE probe on smooth silicon wafer.

The work of adhesion between polyethylene and silicon wafer, calculated from the measured pull-off forces and using the JKR model (equation (1)), is  $W_A = 200\text{--}210 \text{ mJ/m}^2$ . Since no accurate measurements of both spring constant and probe size were made in this study, the  $W_A$  value should be treated as a crude estimate.

### 3.3. Standard deviation for measured pull-off forces

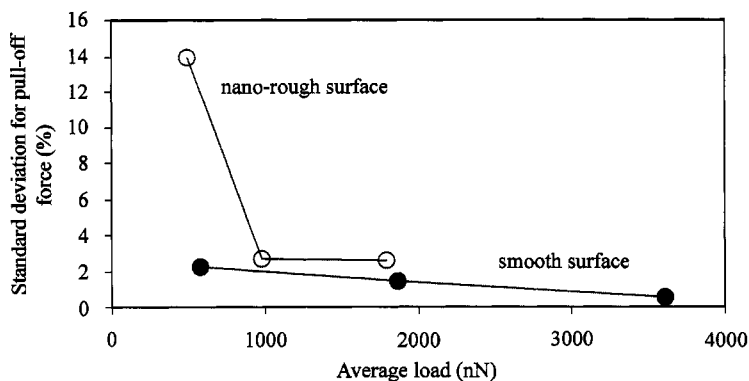
The results from the study with soft probes are displayed in Table 1. The ability to deform asperities on the probe surface, and conform to the asperities present on the substrate surface allowed soft probes to mitigate roughness effects. This idea is supported by the correlation between standard deviation for measured pull-off forces and applied maximum loads, as shown in Fig. 14.

Figure 14 shows a marked decrease from 14 to 2.6 in the standard deviation (% SD) for the PE probe on the 'nano-rough' substrate as the applied load increased from approx. 500 to approx. 1000 nN. The reduced % SD holds steady for increased loads up to approx. 1800 nN, approx. 2.6–2.7% SD, indicating a saturated contact area. The % SD for the 'nano-rough' surface approaches the values obtained from the 'smooth' surface, which was shown to be as little as 0.5% SD at loads of about

**Table 1.**

Pull-off force data for soft probe systems

Probe	Radius ( $\mu\text{m}$ )	Substrate surface	Average load (nN)	Pull-off force (nN)
PS1	approx. 5	Smooth	185	$319.5 \pm 11.7$
PS2	approx. 5	Smooth	90	$88.6 \pm 17.2$
PE	approx. 7	Smooth	580	$6829 \pm 150$
			1870	$6739 \pm 95$
			3606	$6840 \pm 46$
		Nano-rough	497	$5974 \pm 838$
			980	$6837 \pm 183$
			1792	$6931 \pm 180$



**Figure 14.** Standard deviation for the measured pull-off force vs. maximum applied load for PE probe on substrates with different finishes.

3600 nN. It is doubtful that the rougher surface could ever match the smooth surface as sizes and shapes of surface roughness features on 'nano-rough' surface vary from location to location. The surface asperities present a myriad of true surface areas at different locations on a surface, and even saturated contact areas may differ slightly in magnitude for these surfaces. However, the results show a possible way to sufficiently mitigate roughness effects. For this to occur, adequate loads need to be applied.

### 3.4. Analysis of asperity deformation

**3.4.1. Elastic (viscoelastic) deformation.** It was speculated in Sections 3.1 and 3.2 that at least some of the nano-sized asperities on a polymeric probe surface deform elastically to such a degree that the colloidal probe establishes its full contact area with the substrate during loading, without interference from the substrate surface roughness. The elastic deformation of the probe recovers soon after the probe-substrate contact is broken. However, the recovery of elastic deformation usually requires more time than the period from release of the applied load to the moment of detachment of the probe from the substrate is (this time in our experiments was estimated to be usually less than 10 ms). The delay in full recovery of the original probe shape is caused by viscoelastic properties for polymers (viscoelastic deformation exhibits the mechanical characteristics of elastic deformation coupled with viscous flow).

It is possible to estimate the size of roughness irregularities, which can be squeezed out during the probe's elastic deformation, using one of the contact mechanics models [14]. The JKR model [13] seems the most appropriate for the colloidal probes used in this study, see discussion in Section 3.1. According to the JKR model, the elastic deformation of the probe ( $\delta$ ) can be calculated by the following equation [13]:

$$\delta = \frac{a^2}{R} - \frac{2}{3} \sqrt{\frac{6\pi a W_A}{K}}, \quad (5)$$

where:

$$a = \sqrt[3]{\frac{R}{K} \left[ P + 3\pi R W_A + \sqrt{6\pi R W_A P + (3\pi R W_A)^2} \right]}. \quad (6)$$

Figure 15 shows a dependence of  $\delta$  on  $P$  for two probes with  $R = 4$  and  $7 \mu\text{m}$ .  $W_A = 200 \text{ mJ/m}^2$  and  $K = 4 \text{ GPa}$  were used in calculations, as per our discussion in Sections 3.1 and 3.2.

As shown in Fig. 15,  $\delta$  changes from about 5 to 10 nm when the applied load increases from 0 to  $4 \mu\text{N}$ . It is expected that all asperities present on the surface of the colloidal probe with a height equal or smaller than  $\delta$  would be squeezed out completely during deformation of the probe. Since most of the irregularities that have been observed on our polystyrene and polyethylene probes are several nanometers tall, they most likely are deformed during the pull-off force

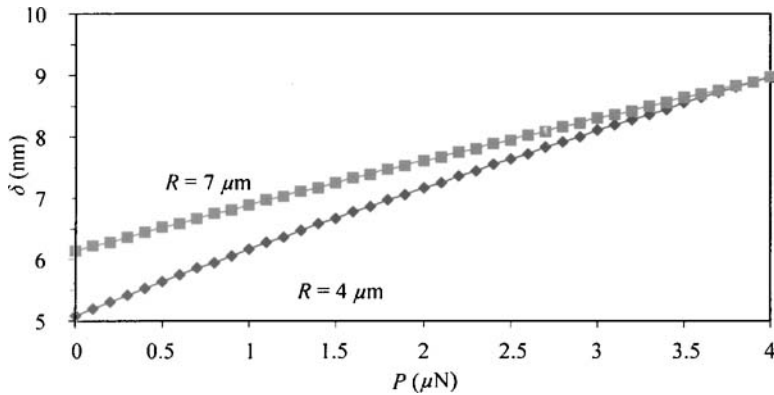


**Figure 15.** Vertical deformation of the probe ( $\delta$ ) with the radius  $R = 4$  and  $7 \mu\text{m}$  under different loads  $P$ . The deformation was calculated using the JKR model assuming  $W_A = 200 \text{ mJ/m}^2$  and  $K = 4 \text{ GPa}$ .

**Table 2.**

Mechanical properties of probes and critical loads for elasto-plastic ( $P_e$ ) and full plastic ( $P_p$ ) deformations

Probe	$R$ ( $\mu\text{m}$ )	$Y$ (MPa)	$\nu$	$E$ (GPa)	$P_e$ ( $\mu\text{N}$ )	$P_p$ (mN)
PS	$5.0 \pm 0.5$	82.8–89.7*	0.38	2.8–3.5	71–87	39–78
PE	$7.0 \pm 1.0$	6.9–14	0.49	0.14–0.28	23–86	5–30

All values taken from Fried [18], except \*, which is the compressive strength of the material [19].

measurements and, therefore, have no effect on contact area between the probe and the substrate. Some of these asperities can undergo a plastic deformation, as observed by Reitsma *et al.* [6].

**3.4.2. Plastic Deformation.** In this part of our discussion, we refer to an analysis by Maugis and Pollock [17], who indicated that the applied load for inducing elasto-plastic ( $P_e$ , term that refers to plastic deformation in peripheral zone of contact, which begins much earlier than full plastic deformation of materials) and full plastic deformation ( $P_p$ ) of a probe with radius  $R$  could be calculated from the following equations:

$$P_e = \frac{118R^2Y^3}{K^3}, \quad (7)$$

$$P_p = 10800\pi \frac{R^2Y^3}{E^2}, \quad (8)$$

where  $Y$  is the material's yield strength.

To apply this analysis to our probes, Table 2 shows the material properties for PS and PE, along with the calculated  $P_e$  and  $P_p$  values. Note that ranges of properties for polymers are expected, based upon different processing procedures resulting

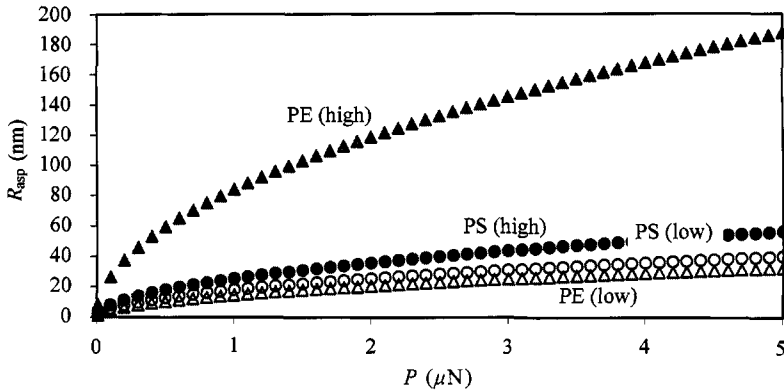


**Figure 16.** Deformable asperity size *vs.* applied load for both probe materials.

in different molecular weights. The specific properties of the probe polymers are not known, so the low and high limits for the ranges are used in calculations using equations (7) and (8).

Table 2 shows that for full plastic deformation of the probe body to occur, loads on the order of 5–78 mN need to be applied. In order to generate elasto–plastic deformation, on the other hand, loads at a level of 23–87  $\mu\text{N}$  must be applied to our probes. The largest load applied in this research was roughly 4  $\mu\text{N}$ . This indicates that the microscopic probe remained in the elastic/viscoelastic regime during the pull-off force measurements. However, this might not be the case for individual nano-asperities, present on the probe surface (Fig. 1), which can deform permanently under loads much smaller than 4  $\mu\text{N}$  as demonstrated by Reitsma *et al.* [6]. To analyze the deformation of asperities we limit our analysis to the fully plastic deformation regime.

To determine the size of the asperity ( $R_{\text{asp}}$ ) that may be squeezed-out by plastic deformation, equation (8) is rearranged as:

$$R_{\text{asp}} = \sqrt{\frac{PE^2}{10800\pi Y^3}}, \quad (9)$$

where  $P$  is now the applied load. To see how this varies for the range of loads used ( $<4 \mu\text{N}$ ), Fig. 16 shows a plot of size of the deformable asperity ( $R_{\text{asp}}$ ) *vs.* the applied load ( $P$ ). Again, two values are listed for each material, reflecting the low and high extremes for the range of mechanical properties reported.

Figure 16 shows that the largest deformable asperity size is possible with soft PE. At a load of 4  $\mu\text{N}$ , an asperity with radius  $r$  approx. 170 nm would be plastically deformed. It is unknown how much error is introduced by utilizing the compressive strength of PS rather than yield strength, but the results seem reasonable in calculating that an approximately 40 nm asperity would be flattened at a 4  $\mu\text{N}$  load.

PS probe 1 experienced loads of approximately 200 nN (Fig. 4) and such loads could permanently deform asperities with radii of  $r \leq 25\text{--}36$  nm. PS probe 2, which only experienced loads of approx. 90 nN, would only deform asperity of  $r \leq 18\text{--}25$  nm. The vast difference in the magnitude of the forces recorded between the two probes (approx. 320 nN and approx. 100 nN) indicates that asperities with  $r < 30$  nm were present on the 'active' part of the PS surface. At the light loads experienced by probe 2, these asperities would not be deformed and an intimate contact between the probe body and the substrate would not be achieved, yielding a low pull-off force magnitude. However, the spring constant of cantilevers used were not calibrated, and although the differences in force magnitudes are larger than can be explained by the errors in spring constants (up to 20% error for each cantilever), some caution should be used in this type of analysis.

The PE probe showed different force magnitudes on the same 'nano-rough' substrate for different applied loads (Fig. 10). In the low-loading regime for this cantilever, with an applied load of approx. 500 nN and yielding forces ranging from about 4.1 to 6.8  $\mu\text{N}$ , asperity of  $r = 10\text{--}59$  nm would deform plastically. In the mid-loading regime, which included loads of approx. 1  $\mu\text{N}$  and recorded pull-off forces of 6.6–7.2  $\mu\text{N}$ , asperities with  $r \leq 15\text{--}84$  nm would be deformed.

It should be noted that, since the substrate is much harder than the probe materials, all deformation is restricted to the probes and no permanent deformation could occur on the substrate. When referring to Figs 1 and 2, asperities from a few to about 50 nm were recorded for surfaces of both PS and PE probes. Some of these asperities could be deformed plastically according to the calculations presented in this section. It should be recognized, however, that our calculations were limited to a simple geometry where a single asperity was in contact with the substrate. It is more likely that more than one asperity is under pressure during the adhesion contact between the probe and substrate, and theoretical analysis should take such complex geometry into account. Such analysis is, however, beyond the scope of this contribution.

#### 4. CONCLUSIONS

We have presented here a unique approach to overcome pull-off force data scatter in the AFM measurements caused by the substrate roughness. If what is shown in this paper for the PE probe on a substrate with the nano-rough finish is applicable to all systems, it may be possible to overcome the roughness effect at any scale by selecting a soft probe, operating at adequate loads to conform to the substrate surface irregularities, and consistently yielding saturated contact areas at different locations of the surface. Pull-off force measurements would then yield data for consistent contact areas, leaving only heterogeneity as a cause for pull-off force data scatter.

### Acknowledgements

Financial support provided by the Petroleum Research Fund administered by the American Chemical Society is gratefully acknowledged.

### REFERENCES

1. J. P. Amié, Z. Elkaakour, C. Odin, T. Bouhacina, D. Michel, J. Curely and A. Dautant, *J. Appl. Phys.* **76**, 754 (1994).
2. V. Mangipudi, M. Tirrell and A. V. Pocius, *J. Adhesion Sci. Technol.* **8**, 1251 (1994).
3. F.-J. Schmitt, T. Ederth, P. Weidenhammer, P. Claesson and H.-J. Jacobasch, *J. Adhesion Sci. Technol.* **13**, 79 (1999).
4. G. Luengo, J. Pan, M. Heuberger and J. N. Israelachvili, *Langmuir* **14**, 3873 (1998).
5. S. Biggs and G. Spinks, *J. Adhesion Sci. Technol.* **12**, 461 (1998).
6. M. Reitsma, V. Craig and S. Biggs, *Int. J. Adhesion Adhesives* **20**, 445 (2000).
7. E. R. Beach, III and J. Drelich, in: *Functional Fillers and Nanoscale Minerals*, J. J. Kellar, M. A. Herpfer and B. M. Moudgil (Eds), pp. 177–193. Society for Mining, Metallurgy, and Exploration, Littleton, CO (2003).
8. J. Nalaskowski, J. Drelich, J. Hupka and J. D. Miller, *Langmuir* **19**, 5311 (2003).
9. E. R. Beach, III, MS Thesis, Michigan Technological University, Houghton, MI (2001).
10. P. Attard, *J. Adhesion Sci. Technol.* **16**, 753 (2002).
11. G. W. Tormoen, J. Drelich and J. Nalaskowski, *J. Adhesion Sci. Technol.* **19** JAST 2525.
12. F. L. Leite, A. Riul, Jr. and P. S. P. Herrmann, *J. Adhesion Sci. Technol.* **17**, 2141 (2003).
13. K. L. Johnson, K. Kendall and A. D. Roberts, *Proc. Roy. Soc. London* **A324**, 301 (1971).
14. J. Drelich, G. W. Tormoen and E. R. Beach, *J. Colloid Interf. Sci.* **280**, 484 (2004).
15. D. Maugis, *J. Colloid Interf. Sci.* **150**, 243 (1992).
16. S. Wu, *Polymer Interface and Adhesion*. Marcel Dekker, New York, NY (1982).
17. D. Maugis and H. M. Pollock, *Acta Metall.* **9**, 1323 (1984).
18. J. R. Fried, *Polymer Science and Technology*. Prentice Hall, Englewood Cliffs, NJ (1995).
19. R. D. Corneliussen, available online at [http://www.maropolymeronline.com/Properties/ps\\_properties.asp#Compressive%20Strenght](http://www.maropolymeronline.com/Properties/ps_properties.asp#Compressive%20Strenght) (2002).



# Capillary Adhesion and Wetting Phenomena

## Role of surface roughness in capillary adhesion

ALI ATA<sup>1,\*</sup>, YAKOV I. RABINOVICH<sup>2</sup> and RAJIV K. SINGH<sup>2</sup>

<sup>1</sup> *Department of Materials Science, Gebze Institute of Technology, P.O. Box 141, Gebze 41400, Kocaeli, Turkey*

<sup>2</sup> *Department of Materials Science and Engineering and Engineering Research Center for Particle Science and Technology, University of Florida, Gainesville, FL 32611, USA*

**Abstract**—The adhesion forces between a smooth spherical particle and flat surfaces of alumina, silver, and titanium-coated Si wafers were measured with an atomic force microscope (AFM) under various humidity conditions. The results showed that there is a discrepancy between the experimentally observed and the theoretically predicted values of capillary adhesion forces. The reason for the discrepancy is explained considering the relative humidity of the surrounding atmosphere and the surface roughness profiles of the contacting surfaces. Two geometrical configurations to define the contact region profile are suggested. The equations to calculate the capillary adhesion forces were modified using the new geometries. The discrepancy was largely eliminated using the modified equations.

**Keywords:** Capillary force; surface roughness; adhesion force; humidity; atomic force microscope.

### 1. INTRODUCTION

The behavior of a particle mixture in air, whether it shows a free or sticky flow, depends on the inter-particle forces, such as van der Waals (VdW), electrostatic attraction and repulsion, and capillary forces. Many factors contribute to the total inter-particle force experienced by an assembly of particles and most are difficult to evaluate in either absolute or relative terms [1].

The flow becomes more sensitive to capillary forces in the presence of moisture. The contribution of capillary forces to the total inter-particle force increases after a certain critical humidity level. The determination of the critical humidity is crucial in the transport, filtration, and separation of powders, because the magnitude of the capillary force can exceed the VdW force unless the surface is hydrophobic [2].

---

\*To whom correspondence should be addressed. Fax: (90) 262 653 8490. E-mail: aliata@gyte.edu.tr

There is evidence that a capillary force may remain even after baking for over 24 h [3].

A small change in the relative humidity, particularly in the transition region around the critical humidity, can produce substantial changes in the processing characteristics of powders. It can even lead to a loss of process control. Hartholt *et al.* [4] reported that when the humidity increased from 45% to about 65%, the particle (glass particles) mobility decreased. When the humidity increased above 65%, the particles became immobile. Harnby *et al.* [5] have given a good review of the literature for the effect of moisture on the structural strength and, hence, the flow characteristics of powders.

A theoretical explanation for the absence of capillary force at low humidity was first given by Coelho and Harnby [6], where the moisture associated with the particles of a powder was adsorbed water vapor. The critical humidity was found from the equilibrium between the thin liquid film, meniscus, and humid atmosphere. Sedin and Rowlen [7] studied the nature of the transition on mica and quartz surfaces and observed a clear transition in the adhesion force at relative humidities around 20%. Thundat *et al.* [8] and Salmeron and co-workers [9] obtained a flat response in force at relative humidities less than 20%. The reason for adhesion after reaching the critical humidity is the capillary force acting due to the liquid meniscus formed near the contact area. The pressure difference across the curved meniscus creates an attractive force, bonding the two surfaces. The water film is in a state of tension, meaning that its pressure is below atmospheric pressure. The total adhesion force can be divided into a capillary force and an interfacial tension force originating from the surface tension acting tangentially to the interface along the contact line with the solid body [10].

A simple approximation has been used to describe the capillary adhesion,  $F_{ad}$ , due to a liquid bridge between a spherical particle and a flat surface:

$$F_{ad} = \Delta P \times S, \quad (1)$$

where  $\Delta P$  is the Laplace pressure due to the meniscus and  $S$  is the area of the flat surface coated by condensed water.  $\Delta P$  is given by the Laplace–Young equation:

$$\Delta P = \gamma \left[ \frac{1}{r} + \frac{1}{x} \right], \quad (2)$$

where  $\gamma$  is the surface tension of the liquid and  $r$  and  $x$  are the radii of curvature of the meniscus measured in two planes at right angles to each other. Since  $x \gg r$ ,  $\Delta P = \gamma/r$ .

‘ $S$ ’ can be calculated by the formula

$$S = 2\pi Rr(\cos \theta_1 + \cos \theta_2), \quad (3)$$

where  $R$  is the radius of the particle and  $\theta_1$  and  $\theta_2$  are the contact angles that the liquid is supposed to form with the particle and the flat substrate, respectively.

Substituting equations (2) and (3) into equation (1), the capillary adhesion force is obtained as

$$F_{\text{ad}} = 2\pi\gamma R(\cos\theta_1 + \cos\theta_2). \quad (4)$$

The values reported in the literature regarding the determination of critical humidity are mainly based on tensile test measurements, centrifuge or optical observations [11]. The measurements were generally performed on smooth surfaces and the effect of surface roughness has not yet been explained to a sufficient extent, particularly for nanometer size regimes. The complications probably arise from the difficulty in characterizing or properly defining geometrical models for the surface roughness based on experimentally measurable parameters. Recently, Colbeck [12] has proposed a two-dimensional geometrical model with four variables and concluded that the effect of surface roughness on the capillary adhesion force was very complicated.

The novel usage of an atomic force microscope (AFM) provides an opportunity to obtain experimental data for adhesion force measurements on a variety of surfaces as a function of the humidity, thus enabling a more in-depth investigation of the subject even in nanometer scale regimes.

In this study, direct adhesion force measurements were performed to determine the critical humidity range more precisely and to quantify the magnitude of capillary forces at different relative humidity levels considering the role of surface roughness. Attention is focused on the calculation of the capillary force on a single particle using the AFM.

## 2. EXPERIMENTAL

The surface forces were measured under varying humidity conditions using an atomic force microscope (AFM), Nanoscope III (Digital Instruments). For this purpose, an AFM piezoelectric unit was placed into a special humidity chamber and all the force measurements were performed under controlled humidity levels. Humidity was measured in both upper and lower parts of the chamber to ensure a uniform humidity throughout the volume of the chamber by an electronic hygrometer.

A relatively smooth glass sphere of 10  $\mu\text{m}$  in radius and 0.2 nm in roughness (RMS) was attached to the AFM cantilever tip with epoxy-type glue. The effect of the glue on the adhesion strength is negligible due to its very small thickness ( $<2$  nm). The glass sphere was brought into contact with alumina and silver flat surfaces having 0.2 and 1.2 nm surface roughnesses, respectively. The samples were kept at a chosen humidity for 1 h to provide equilibrium conditions between the surfaces and the surrounding atmosphere. The change in the adhesion force at different humidity levels was measured as a function of the loading force using the AFM in contact mode. The adhesion and loading forces were normalized by the radius of the adhering particle, to eliminate radius effects on the results.

The load/radius ( $L/R$ ) and adhesion force/radius ( $F_{ad}/R$ ) values were used in the graphs.

The effect of humidity on the adhesion force for rough surfaces was investigated on silicon wafer samples having controlled surface roughnesses from 0.2 to 10 nm. The roughness was characterized by the AFM in root mean square (RMS) values; this has been described in detail elsewhere [13]. Rough samples were obtained by depositing titanium on the wafers obtained from Motorola by the chemical vapor deposition (CVD) technique. Before starting adhesion force measurements, the samples were cleaned by rinsing with ethanol, methanol, and de-ionized water, and dried by blowing dry tetrafluoroethane gas. The titanium-coated wafer surface was allowed to interact with the silica sphere attached to the AFM cantilever tip. Adhesion measurements were conducted in both low [25–30% relative humidity (RH)] and high humidity (65% RH) regimes.

### 3. RESULTS AND DISCUSSION

Figure 1 shows that the normalized force value on the alumina flat surface increases from 320 to 550 mN/m at around 40% RH. In the low humidity range (<40% RH), the adhesion force is relatively weak,  $F/R = 320$  mN/m; this can be related to dry contact resulting from van der Waals forces. Assuming this force to be van der Waals type, the experimental value of the Hamaker constant was calculated as  $A = 1.6 \times 10^{-19}$  J. This value is overestimated compared with theoretical and experimental values obtained from the literature,  $A = (0.7-1) \times 10^{-19}$  J [14, 15]. The higher value of  $A$  found in the experimental data indicates the action of some additional forces besides dispersion forces. Short-range polar forces suggesting the

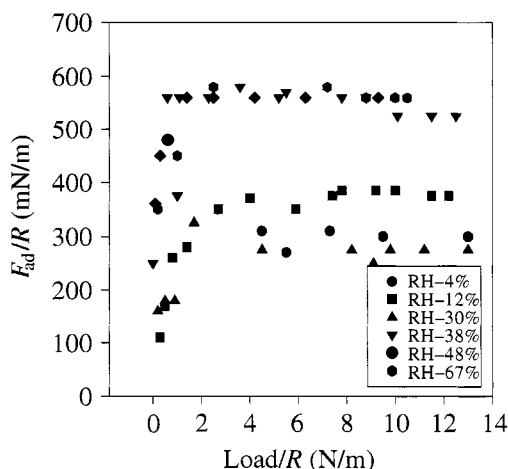


**Figure 1.** Experimentally measured normalized adhesion force between the glass sphere attached to the AFM tip and the alumina substrate at various humidity levels as a function of increasing loading force ( $R_{sphere} = 10 \mu\text{m}$ ).

existence of an adsorbed water layer can be the reason why the total adhesion force is larger than the theoretical van der Waals value. Even at very low humidity levels, a single or double layer of water molecules is adsorbed, which is different from the bulk water. It could also be attributed to an electrostatic charge build-up at the examined surfaces; however, the Coulomb force has been found to be two orders larger than the van der Waals force [16], while in the present study the additional force was approximately of the same order as the van der Waals force. Similarly, Chikazawa *et al.* [17] observed the same type of behavior at a humidity as low as 20% RH, using porous glass particles. It was presumed that this was due to the formation of hydrogen bonds between the particle and the glass substrate.

In the higher humidity regime ( $>40\%$  RH), a sharp increase of the adhesion force to 550 mN/m was observed, whereas the theoretical value for capillary forces is 790 mN/m. This result is an indication of meniscus or liquid bridge formation; however, the difference between the two values is very large and can be attributed to the existence of surface roughness. An in-depth investigation of the effect of surface roughness on the capillary force was thus performed to account for the discrepancy between the theory and the experimental results considering the geometry of the contact region.

There are two possible geometrical configurations for the meniscus existing between a rough flat surface and a smooth sphere. Figure 2a shows the first case, where the diameter,  $2r$ , of the meniscus is larger than the height of the asperity,  $H$  ( $2r > H$ ). In the second case (Fig. 2b), where  $2r < H$ , the meniscus forms between the roughness peak and the sphere, rather than between the sphere and the flat surface.

In the first case where  $2r > H$ , one may think that the same force acts as in the case of a smooth surface and that the asperity does not alter the force appreciably. However, the asperity peak will certainly increase the separation distance between the smooth sphere and the flat surface, thus altering the area of the condensed vapor phase ( $S$ ). Thus, the adhesion force in equation (1) ( $F_{ad} = \Delta P \times S$ ) will also change. The Laplace pressure term  $\Delta P$  in the equation does not change because according to the Young–Laplace equation (2),  $\Delta P$  depends on the radius of the meniscus and the radius of the meniscus depends only on the relative humidity of the surrounding atmosphere and the surface energies of the interacting bodies. In order to calculate the adhesion force for this configuration, the area of the bridge

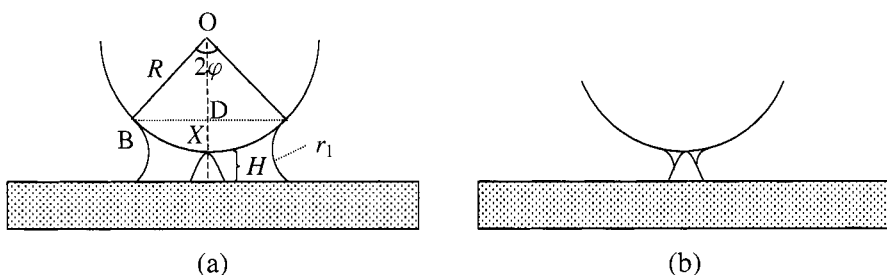


**Figure 2.** Schematic diagram of a meniscus. (a)  $2r > H$ ; (b)  $2r < H$ .

under the smooth sphere must be calculated. For simplicity, the thickness of the adsorbed layer was neglected. From Fig. 2a

$$[\text{OA}] = R + H \text{ (height of the asperity)} = (R + r) \cos \phi + r,$$

where  $\phi$  is the angle embracing the meniscus. Assuming that  $R \gg r$  and  $\cos \phi \ll 1$ , the following expression is obtained:

$$\phi \text{ (rad)} = \sqrt{\frac{2(2r - H)}{R}}. \quad (5)$$

The area of the condensed vapor phase considering the triangle ODB is

$$S = \pi [\text{DB}]^2 \text{ and } [\text{DB}] = R \sin \phi = R\phi. \quad (6)$$

Substituting  $\phi$  from equation (5) into equation (6), the area  $S = 2\pi R(2r - H)$  is obtained. Thus, using equation (1), where  $F_{\text{ad}} = \Delta P \times S$ , we obtain a formula to calculate the capillary adhesion force in the presence of a surface asperity which is smaller than the diameter of the meniscus:

$$F_{\text{ad}} = 4\pi\gamma R[(1 - H)/2r]. \quad (7)$$

The theoretical value of the capillary force between smooth surfaces of alumina and glass was obtained from equation (4) as 790 mN/m for contact angles  $\theta_1 = 0^\circ$  for glass and  $\theta_2 = 41^\circ$  for alumina surfaces. The contact angle measurements were done by placing a small amount of water (1  $\mu\text{l}$ ) on the related substrate with a micro-syringe and the contact angle was determined in a standard way by an NRL goniometer. The discrepancy between the observed (550 mN/m) and the theoretical (790 mN/m) values of capillary adhesion forces can be minimized using equation (7). The numerical values of  $H$ ,  $\gamma$ , and  $r$  can be calculated. The surface roughness of alumina can be used as the  $H$  value, which was measured to be around 0.3 nm using the AFM. The radius of the meniscus  $r$  can be calculated from the Kelvin equation as

$$r = \frac{-V\gamma}{RT \log(p/p_s)} = \frac{-V\gamma}{kT \log \psi}, \quad (8)$$

where  $V$  is the molar volume of water;  $kT$  is the product of the Boltzmann constant and absolute temperature;  $p$  and  $p_s$  are the condensation vapor pressure and saturated vapor pressure, respectively; and  $\psi$  is % relative humidity. The liquid–vapor interface at the meniscus is concave, causing condensation at pressure smaller than the saturation pressure. For 40% relative humidity,  $r$  is calculated as 0.78 nm. Substituting the data in equation (7), the adhesion force was found to be  $F_{\text{ad}} = 406$  mN/m. This value is much closer to the experimentally observed 550 mN/m. Therefore the discrepancy was largely eliminated using a correct geometrical configuration to consider the surface roughness profile.

For the second geometrical configuration where  $2r < H$ , the asperity separates the two contacting surfaces by more than the diameter of the meniscus. The

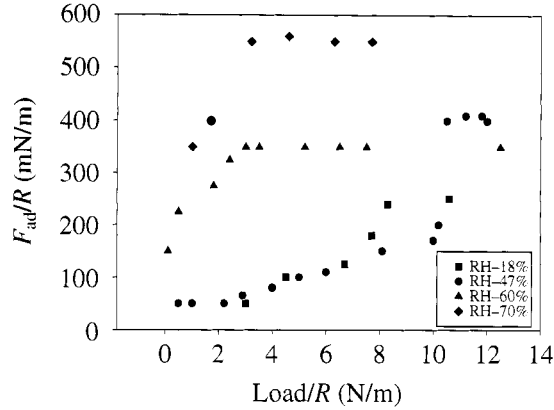


**Figure 3.** Experimentally measured normalized adhesion force between the glass sphere attached to the AFM tip and the silver substrate at various humidity levels as a function of increasing loading force ( $R_{\text{sphere}} = 10 \mu\text{m}$ ).

adhesion force can be calculated using equation (4), but the radius of the asperity peak ( $r_p$ ) should be used instead of the radius of the interacting sphere,  $R$ , as follows:

$$F_{\text{ad}} = 2\pi\gamma r_p(\cos\theta_1 + \cos\theta_2). \quad (9)$$

Note that in Fig. 1 the adhesion force levels off at around 40% relative humidity, showing a type IV adsorption isotherm described by Brunauer [18] which is considered to reflect a capillary condensation phenomenon before the saturation pressure is reached [19].

The AFM force measurements in the contact mode were conducted on a soft silver flat surface, under the same conditions as those used for the alumina surface in order to examine the effect of the substrate's physical properties on the results. The critical humidity range for the silver substrate was observed around 60%, as shown in Fig. 3. The adhesion force behavior as a function of the humidity was different from the alumina flat surface for the same range of applied force.

The adhesion force at low loading forces,  $L/R < 4 \text{ mN/m}$ , where  $L$  is the load applied to the cantilever and  $R$  is the radius of the particle, and in the high humidity range of 60–70% RH steadily increases and reaches a plateau value. The increase for the silver substrate is more gradual than that observed for the alumina substrate.

At a very low loading force,  $L/R \approx 0$ , since the roughness of silver is high (3 nm as measured with the AFM), the meniscus forms between the asperity and the sphere as explained in the geometrical configuration in Fig. 2b. Below the critical humidity range, the force was dependent on the loading force and no plateau region was observed. The increase in the adhesion force by increasing the loading force is caused by the plastic deformation of silver, which is mainly the deformation of the asperity.



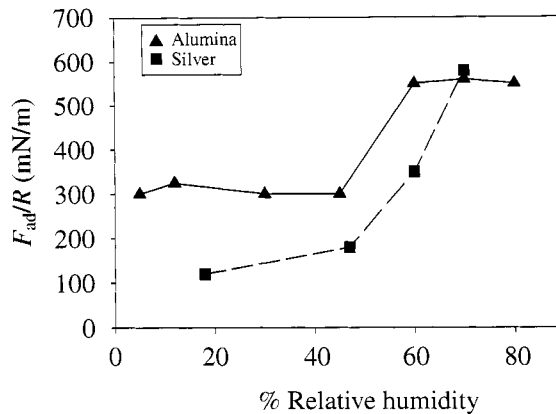


**Figure 4.** Experimentally measured normalized adhesion force as a function of the humidity on alumina and silver substrates using a 10  $\mu\text{m}$  glass sphere attached to the AFM tip.

Lower adhesion forces were observed in the range  $< 47\%$  RH for the silver substrate. These low forces should be related to the interaction of ‘dry’ surfaces without the formation of a liquid meniscus. Not enough molecules of water are present at the surface to form a bulk water phase at low humidity levels. Using scanning polarization force microscopy, Salmeron and co-workers [20] studied the structure of the water layer on mica as a function of the relative humidity. The authors described two distinct structural phases of the water film, phase I being an ice-like film and phase II a more liquid-like island structure. They attributed the transition in the adhesion force as a function of the relative humidity to the transition from a tightly bound ice-like layer of water on mica to more liquid-like islands which lead to capillary condensation during contact.

For humidities greater than 47% RH and at a high loading force,  $L/R > 12$  mN/m, the capillary force appears, which can be explained by the plastic deformation of silver causing a decrease in the gap between the substrate and the sphere. Thus, the formation of a meniscus becomes easier.

A comparison of the adhesion behavior of silver and alumina substrates to humidity changes is shown in Fig. 4. A sharp transition in the adhesion force is observed for alumina in the critical range. The silver surface, on the other hand, having a higher surface roughness, did not show any sharp transition. Instead, a gradual increase was observed.

Figure 5 shows the adhesion force measurements on silicon wafer samples having controlled roughness for dry (25–30% RH) and for humid (RH = 65%) atmospheric conditions. In this case, flat silicon wafers were coated with titanium by the CVD technique. A surface roughness with peaks of regular shape and reproducible height was obtained. There is a significant difference in the adhesion force values measured in dry and in humid atmospheres at low roughness levels (RMS = 1–2 nm). The adhesion forces at 0.2 nm roughness were measured as 130 and 100 mN/m for humid and dry air conditions, respectively. Since the surface roughness for this

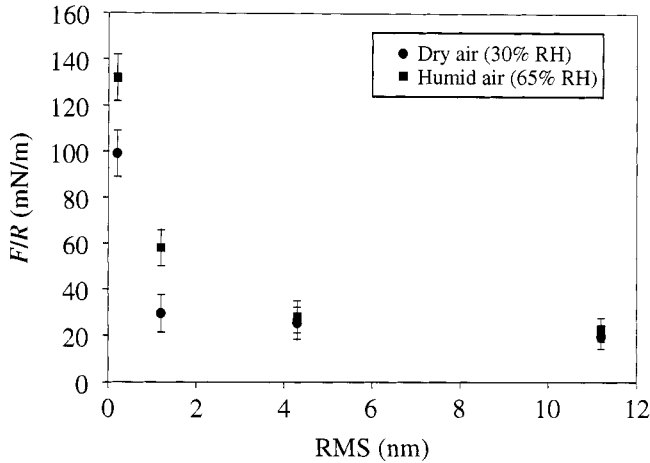


**Figure 5.** Normalized adhesion force measured in dry and in humid atmospheres between the glass sphere attached to the AFM tip and the Si wafer surface as a function of increasing surface roughness (RMS) ( $R_{\text{sphere}} = 10 \mu\text{m}$ ).

case is very low, i.e. showing a very small deviation from an ideal surface, the difference should be arising from the action of capillary forces, but not to the extent of bulk meniscus formation. Otherwise, the experimental value should be close to the predicted theoretical value of 540 mN/m, using a water contact angle  $\theta = 40^\circ$  for the Ti-coated wafer surface. Capillary patches may be formed rather than a bulk bridge, indicating that the meniscus had not yet reached the critical radius to grow. The absence of a meniscus between the surfaces can be attributed to poor wetting of the wafer surface.

At high roughness levels, however, both the dry and the humid adhesion force values approach each other within an average of 10% standard deviation. This can be explained by considering the geometrical configuration in Fig. 2b, where the meniscus is formed between the asperity and the particle rather than between the wafer surface and the particle. Since the meniscus formed in this way is very thin, it does not affect the adhesion force.

#### 4. CONCLUSIONS

The adhesion force measured in the presence of moisture depends strongly on the size of the meniscus, which is a function of the roughness profile of the surface as well as the relative humidity of the air. Therefore, for an accurate and precise measurement of the total adhesion force, the geometry of the asperity peak should be taken into account. Two geometrical configurations that might commonly be encountered were proposed for the asperities. The adhesion force was expressed as a function of the relative sizes of the separation gap ( $H$ ) and the radius of the meniscus ( $r$ ) for the two proposed geometries. The experimental data calculated using the

proposed formulae were seen to be closer to the predicted theoretical calculations. It is expected that this study will not only establish a deeper understanding of the capillary adhesion of a particle to a surface, but also contribute, in general, to the understanding of the role of roughness on a nanometer scale in any type of technology involving contacts.

### Acknowledgement

We acknowledge the financial support of the Gebze Institute of Technology Research Foundation grant 99-A-03-01-07 and Engineering Research Center (ERC) for Particle Science and Technology at the University of Florida, supported by the National Science Foundation (NSF) (Grant EEC-94-02989).

### REFERENCES

1. H. Y. Xie, *Powder Technol.* **94**, 99–108 (1997).
2. R. A. Bowling, *J. Electrochem. Soc.* **132**, 2208–2219 (1985).
3. S. Bhattacharya and K. L. Mittal, *Surface Technol.* **7**, 413–425 (1978).
4. G. P. Hartholt, A. C. Hoffmann and L. P. B. M. Janssen, *Powder Technol.* **88**, 341–345 (1996).
5. N. Harnby, A. E. Hawkins and I. Opalinski, *Trans. Inst. Chem. Eng.* **74**, 605–615 (1996).
6. M. C. Coelho and N. Harnby, *Powder Technol.* **20**, 197–200 (1978).
7. D. L. Sedin and K. L. Rowlen, *Anal. Chem.* **72**, 2183–2189 (2000).
8. T. Thundat, X. Y. Zheng, G. Y. Chen and R. J. Warmack, *Surface Sci. Lett.* **294**, L939–L943 (1993).
9. L. Xu, A. Lio, J. Hu, D. F. Ogletree and M. Salmeron, *J. Phys. Chem. B* **102**, 540–548 (1998).
10. A. de Lazzer, M. Dreyer and H. J. Rath, *Langmuir* **15**, 4551–4559 (1999).
11. G. Jimbo and R. Yamazaki, in: *Proc. Eur. Symp. Particle Technol.*, Amsterdam, pp. 1064–1074 (1980).
12. S. C. Colbeck, *J. Adhesion Sci. Technol.* **11**, 359–371 (1997).
13. Y. I. Rabinovich, J. J. Adler, A. Ata, R. K. Singh and B. M. Moudgil, *J. Colloid Interface Sci.* **232**, 17–24 (2000).
14. B. V. Derjaguin, N. V. Churaev and Y. I. Rabinovich, *Adv. Colloid Interface Sci.* **28**, 197 (1988).
15. Y. I. Rabinovich and N. V. Churaev, *Colloid J. USSR* **52**, 256 (1990).
16. R. G. Horn and D. T. Smith, *Science* **256**, 362 (1992).
17. M. Chikazawa, T. Kanazawa and T. Yamaguchi, *Kona* **2**, 54–61 (1984).
18. S. Brunauer, *The Adsorption of Gases and Vapors*. Princeton University Press, Princeton (1943).
19. A. Adamson, *Physical Chemistry of Surfaces*. John Wiley, New York (1976).
20. J. Hu, X. D. Xiao, D. F. Ogletree and M. Salmeron, *Science* **268**, 267–269 (1995).

## Direct measurements of the adhesion between a glass particle and a glass surface in a humid atmosphere

SIMON BIGGS<sup>1,\*</sup>, ROBERT G. CAIN<sup>2</sup>, RAYMOND R. DAGASTINE<sup>3</sup>  
and NEIL W. PAGE<sup>2</sup>

<sup>1</sup> *School of Biological and Chemical Sciences, The University of Newcastle, Callaghan, NSW 2308, Australia*

<sup>2</sup> *Department of Mechanical Engineering, The Centre for Bulk Solids and Particle Technology, The University of Newcastle, Callaghan, NSW 2308, Australia*

<sup>3</sup> *Department of Chemical Engineering, Carnegie-Mellon University, Pittsburgh, PA 15213, USA*

**Abstract**—An atomic force microscope has been used to measure the adhesion between individual silica-glass particles and a glass substrate in the presence of water vapour. It was found that the adhesion between the surfaces was not significantly altered, when compared with the dry case, at relative water vapour pressures of less than 0.6. Above this level of water vapour, the magnitude of the adhesion between the surfaces increased by approximately an order of magnitude. The transition of behaviour at a relative water vapour pressure of 0.6 corresponds to the formation of a capillary annulus having a critical Kelvin radius of approximately 2 nm. These findings are in good agreement with previous research data for the interaction of mica surfaces in water vapour. Force–distance data recorded as the particle and surface are separated from one another indicate the presence of a capillary neck between the surfaces. The form of these force–distance data indicates that the separation occurs under non-equilibrium conditions that more closely resemble the expected interaction under constant volume conditions (for the capillary neck). The results of this study also indicate the important role of equilibration time for the surfaces when not in contact. Successive force scans with only short equilibration times when the surfaces are separated result in the development of larger than expected capillary interaction forces. The results are relevant to the interactions between particles in a powder bed under flow.

**Keywords:** Silica-glass; adhesion; capillary forces; atomic force microscope.

---

\*To whom correspondence should be addressed. Discipline of Chemistry, School of Biological and Chemical Sciences, The University of Newcastle, Callaghan, NSW 2308, Australia. Phone: +61 2 4921 5481. Fax: +61 2 4921 5472. E-mail: [simon.biggs@newcastle.edu.au](mailto:simon.biggs@newcastle.edu.au)

## 1. INTRODUCTION

The adhesion between particles in a powder bed is increased as a result of the capillary condensation of water from a humid atmosphere. The adhesion of particles to surfaces is also affected by the same mechanism. The importance of this capillary condensation to processes such as dust suppression or the contamination of 'clean' surfaces is obvious [1]. More recently, the role of capillary condensation on the stick-slip motion of a particulate assembly has been reported [2]. It was postulated that the critical parameter of interest in controlling the motion of such an assembly were the forces operating between particles in stress chains throughout the powder bed. Motion of the powder can only be induced when the stress chains weaken sufficiently, as a result of dilation, under the action of a shear stress. Since dilation of the stress chains is a critical stage in the control of powder flow, the forces between particles in these stress chains that resist this dilation are clearly of interest. For elastic particles, the adhesion between particles in a dry atmosphere is controlled by the action of surface forces, primarily the intermolecular dispersion or van der Waals forces [3]. In a humid atmosphere, any capillary condensation between particles will result in an increased attractive interaction. Depending on the geometry of interaction, the relative humidity and the strength of the surface forces, the interaction pull-off force between the two surfaces can be predicted (see below).

The fundamental investigation of capillary condensation between well-characterized surfaces has received much attention in the scientific literature, both from theoretical and from experimental standpoints [4–10]. For perfectly clean and smooth surfaces, theoretical treatments are very well developed [11]. Unfortunately, in real particulate systems the idealized smooth clean surfaces are rarely found. For example, the use of techniques such as the surface forces apparatus (SFA) has highlighted the important role of surface contaminants in mediating any capillary condensation between surfaces [9, 10]. Such studies have shown that the presence of ions or other contaminants on silica or mica can lead to the condensation of water at partial vapour pressures well below those predicted from the Kelvin equation.

The advent of scanning probe microscopy (SPM) has led to renewed interest in the role of surface adsorbed water films on particulate adhesion. Capillary forces have received considerable attention within the SPM literature as a result of their importance in imaging applications [12–21]. The presence of capillary adsorbed moisture between an imaging probe and the surface of interest can lead to the development of large interaction forces that result in significant elastic deformation of the imaging tip. Such deformations have been shown to significantly reduce the resolution available from the SPM technique. On a more fundamental level, it was quickly realized by researchers that the small size of SPM probe tips and the high sensitivity of the cantilever springs could lead to important fundamental knowledge about the adhesion and friction between single asperity contacts in a humid atmosphere [12]. The role of variables such as contact angle and relative humidity has been extensively investigated. For hydrophilic surfaces, the force

of adhesion is seen to increase dramatically at between 30% and 40% relative humidity (RH) [12, 17–20]. The increase is interpreted as occurring when capillary forces first become significant with respect to surface forces in the contact region. Although there is some debate about the exact position of the transition point, it is clear that a critical value of RH is needed to ensure that adequate capillary condensation can occur. After this point, the effect of the capillary neck is quickly maximized and no further increase in pull-off force is observed as RH is increased further.

In the present study, our aim was to investigate the role of capillary condensation in mediating the interaction between micrometre-sized elastic particles in a humid environment. As noted above, this is relevant to the understanding of the strength of stress chains in particulate systems [2]. This, in turn, affects the resistance of particulate networks to applied shear and the motion of the particle system. In a previous investigation [2], shear test cell measurements were used to investigate the motion of glass particles under a given series of applied normal loads and relative humidities. Careful measurements of the dilation of the particle system during the application of a shear stress indicated that the slip event during stick–slip motion of the particle bed was accompanied by rapid collapse of a dilated material. The dilation of the material was seen to occur during a plastic strain step immediately prior to slip. This mechanism is contrary to predicted models of the stick–slip behaviour of particulate systems such as that of Thomson and Grest [22]. In this model, the material dilation is predicted to occur during the slip phase and collapse occurs immediately the material comes to rest. In this model, the dilation is likened to fluidization of the material.

Colloidal sized particles may be attached to standard SPM cantilevers. The use of SPM techniques to investigate the interactions between particles and surfaces has developed rapidly since the first reported use of a colloid probe [23]. In the study of adhesion, measurements have been reported between particles and surfaces for systems as diverse as tin [24], polystyrene [25, 26], glass [27], cross-linked poly(dimethyl siloxane) [28], and metal oxides [29]. In most cases, the authors have gone to great lengths to prevent capillary condensation and to ensure a dry atmosphere. Despite the obvious importance of capillary condensation in particle adhesion, there is, to our knowledge, only one previous report of direct measurements using colloid probes and an SPM [13]. This is the purpose of the current investigation.

### *1.1. Capillary forces*

The origin of capillary forces is the condensed neck of water that can form in asperities at RH values below saturation. This condensation can occur because of the pressure difference that exists across the surface of a curved interface, as

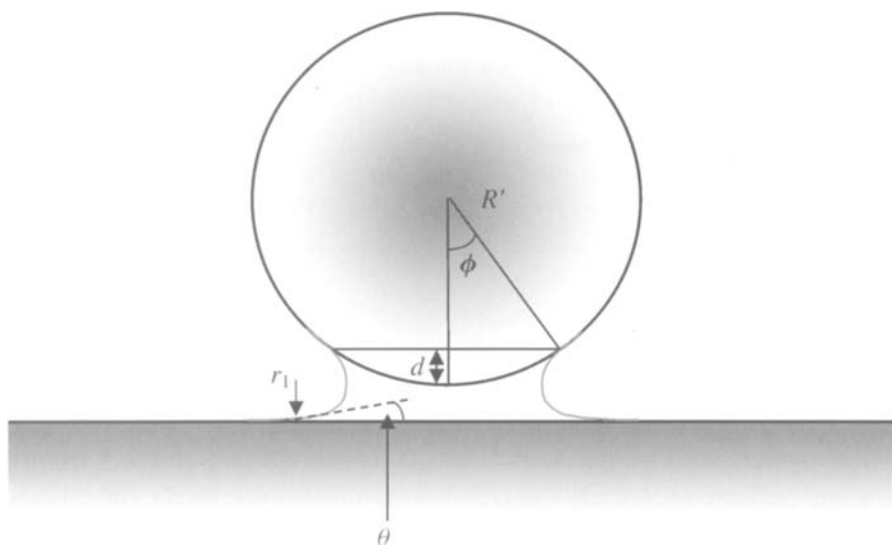


**Figure 1.** Schematic representation of the capillary neck between a sphere and a flat plate in a humid atmosphere.  $\theta$  is the contact angle at the air–water–glass interface,  $R'$  is the sphere radius,  $r_1$  is the capillary Kelvin radius, and  $d$  is the distance indicated.

described by the Young–Laplace equation [30]:

$$p = \gamma_{LV} \left( \frac{1}{r_1} + \frac{1}{r_2} \right), \quad (1)$$

where  $\gamma_{LV}$  is the surface tension of the liquid of interest and  $r_1$  and  $r_2$  are the principal radii of curvature for the liquid surface. The Young–Laplace equation leads directly to the Kelvin equation, which relates the curvature of the interface to the relative vapour pressure acting over that interface according to

$$\frac{1}{r_K} = \left( \frac{1}{r_1} + \frac{1}{r_2} \right) = \frac{RT}{\gamma_{LV} V} \ln \left( \frac{p'}{p''} \right), \quad (2)$$

where  $r_K$  is the equilibrium radius,  $R$  is the universal gas constant,  $T$  is the absolute temperature,  $V$  is the molar volume of the liquid,  $p''$  is the normal vapour pressure, and  $p'$  is the vapour pressure acting above the curved interface. From this equation, it is apparent that the vapour pressure above a curved interface is reduced and thus, condensation can occur in an asperity well below the saturated vapour pressure of the liquid.

The typical sphere–flat geometry used in our experiments is shown in Fig. 1. When the two surfaces are hydrophilic, as in our experiments, the meniscus that forms between the sphere and flat is expected to be concave and will lead to an attractive capillary pressure between the surfaces. When the two surfaces are in contact, the capillary pressure is greatest and is given by [11]

$$F_{\text{cap}} = 4\pi R' \gamma_{LV} \cos \theta, \quad (3)$$

where  $R'$  is the sphere radius and  $\theta$  is the equilibrium contact angle of the liquid with the surfaces. The total adhesion force between the surfaces must also include any contributions from the solid–solid contact inside the meniscus. Thus, the final result for a capillary, as shown in Fig. 1, is given by

$$F_{\text{ad}} = 4\pi R'(\gamma_{\text{LV}} \cos \theta + \gamma_{\text{SL}}), \quad (4)$$

where  $\gamma_{\text{SL}}$  is the solid–liquid interfacial tension. This value is frequently much smaller than the value of  $\gamma_{\text{LV}}$  and, in these cases, the capillary bridge dominates the adhesion between the two surfaces.

It should be noted that the above equation contains no capillary radius parameter. The value of this capillary radius will obviously increase with increasing RH [see equation (2)] and so it is important to know at what point the RH is sufficient to allow application of equation (4). Several authors have investigated this point [8, 10]. The largest and most quantitative body of research available has been performed using the surface forces apparatus (SFA). In this device, the adhesion between two crossed hemispherical sheets of mica is directly measured as a function of the atmospheric humidity. Using this technique, liquids such as cyclohexane and benzene have been investigated. For organic liquids, it has been shown that capillary condensation is sufficient to allow the use of equation (4) at RHs as low as 10% [8]. The meniscus has a radius of only 0.5 nm under this condition. In water vapour, it appears that a higher vapour pressure of around 0.6, corresponding to a radius of 2 nm, is required [10]. This point will be discussed in more detail below after presentation of the results from this study.

In addition to the adhesion force at contact, the force of attraction between the surfaces as they are separated from one another will also be affected by the presence of condensed water vapour. At a given surface–surface separation distance, the presence of a capillary neck will result in an attractive force between the surfaces. If the surfaces are separated from each other infinitely slowly, the capillary neck will always be at equilibrium with the surrounding atmosphere. Under these conditions, a constant capillary radius will be maintained and the capillary neck will persist until the separation is such that the central annular radius approaches zero. Under these conditions, the force as a function of the surface–surface separation,  $D$ , is given by [8]

$$F_{\text{eq}} = 4\pi R' \gamma_{\text{LV}} \cos \theta \left( 1 - \frac{D}{2r_1 \cos \theta} \right). \quad (5)$$

Clearly, if the surfaces are separated under the conditions of equilibrium, the force will vary linearly with distance. An alternative solution for the force–separation relationship arises if we separate the surfaces rapidly such that the volume of liquid between them remains constant. In this case, the force as a function of the separation distance is given as [11]

$$F_{\text{eq}} = \frac{4\pi R' \gamma_{\text{LV}} \cos \theta}{(1 + D/d)}, \quad (6)$$



where  $d$  defines the area over which the capillary acts. In this case, the force is inversely related to distance.

## 2. MATERIALS AND METHODS

### 2.1. Chemicals

Where used, all water was of Millipore Milli-Q grade. High-purity nitrogen was used as supplied (BDH Gases).

### 2.2. Glass beads

The beads used in this study were soda-lime glass spheres obtained from Polysciences (Warrington, PA, USA). Spheres for use in the AFM experiments were individually selected from a sample with nominal diameters in the range 10–30  $\mu\text{m}$ .

### 2.3. Glass flats

Silica plates were made from Suprasil silica and were polished to optical smoothness (H. A. Groiss, Melbourne). Roughness information for the surfaces was obtained directly using AFM images. The standard deviation in the mean height was found to be  $0.6 \pm 0.2$  nm over a scan area of  $2.5 \times 2.5$   $\mu\text{m}$  and  $1.2 \pm 0.4$  nm over the larger area of  $10 \times 10$   $\mu\text{m}$ .

### 2.4. Surface preparation

All surfaces were used in AFM experiments immediately after cleaning. The glass surfaces used in the AFM experiments were cleaned in sulphochromic acid and then rinsed in Milli-Q filtered water. Contact angle measurements on the cleaned surfaces revealed that water formed a wetting film. After 30 min exposure to the atmosphere, the contact angle rose to  $25 \pm 5^\circ$ . Care was therefore taken to control the environment for the preparation and testing of all samples in the AFM experiments.

### 2.5. Colloid probes

The colloid probes used here were prepared in-house by gluing a glass bead to a single beam TESP cantilever (Digital Instruments, Santa Barbara, CA, USA) using an epoxy adhesive (Araldite). Prior to use, hydrophilic probes were cleaned by exposure to UV radiation for 5–10 min.

### 2.6. Colloid probe microscopy

A Nanoscope III lateral force microscope (Digital Instruments, Santa Barbara, CA, USA) was used in all AFM experiments described here. Here, as with most

commercially available systems, the scanner moves the sample while the probe remains fixed. To achieve the precision required, a piezoelectric tube scanner (Scanner E, Digital Instruments) was used which could be controlled to provide sub-angstrom motion increments.

The colloid probe of interest was mounted in a commercial fluid cell (Digital Instruments, Santa Barbara, CA, USA) in a clean laminar flow cupboard and the assembly was then mounted in the AFM. High-purity nitrogen (nitrogen > 99.99%, moisture < 12 ppm, oxygen < 10 ppm; BOC gas code #034) was passed through the fluid cell for approximately 30 min prior to an experiment. The RH was then varied by bubbling a proportion of the incoming nitrogen through Milli-Q filtered water. The system was then allowed to equilibrate for 30 min at the given RH. The RH was determined at the outlet of the fluid cell using a Thermo-Hygrometer (Hanna Instruments, HI 91610-C). A slight positive pressure was maintained throughout the experiment to ensure no ingress of atmospheric air. Experiments were conducted in an air-conditioned room and the temperature did not vary significantly over the course of the testing programme.

### 2.7. Spring constant calibration

The value of the normal spring constant was determined using the method of Cleveland *et al.* [31]. For the cantilevers used here, a value of  $k = 27 \pm 0.5$  N/m was determined.

### 2.8. Data analysis

Raw data for the normal interaction between the surfaces were converted into force–separation data using standard analysis protocols. Photodiode response in the normal direction is calibrated directly when the surfaces are in contact: a unit movement of the piezoelectric crystal will cause a corresponding movement of the probe; this results in a measured voltage change in the photodiode output. Thus, if the piezoelectric crystal is calibrated correctly, the photodiode output can be easily obtained. The piezoelectric crystal was calibrated here by imaging a grating with known  $x$ ,  $y$ , and  $z$  dimensions.

## 3. RESULTS AND DISCUSSION

Force–separation data for the interaction of a glass sphere with a glass surface under conditions of zero humidity are shown in Fig. 2. These data will serve as a control for all the subsequent discussion regarding interaction forces in a humid environment. The form of these data is typical for the interaction between two clean dry surfaces in air. As the surfaces approach one another, there is no interaction until the surface separation is very small. An attractive van der Waals interaction between the surfaces then results in a short-range jump-to-contact. The small oscillations in

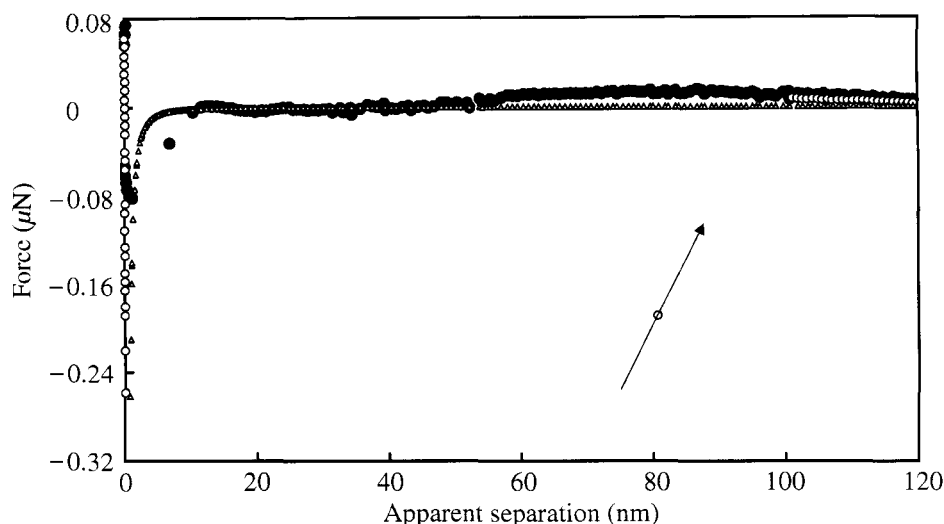


**Figure 2.** Force–separation data for the interaction between a 10  $\mu\text{m}$  radius glass sphere and a flat glass surface. The data were collected at RH = 0. Data are shown for both the approach (●) and the retraction (○) of the sphere and the surface. Calculated data points for the van der Waals interaction between a dry glass surface and a dry glass sphere across air are also shown ( $\Delta$ ). A value of  $1 \times 10^{-19}$  J was used for the Hamaker constant of glass in this case [11]. The arrow indicates the direction of return for the pull-off data.

the baseline data result from optical interference caused by reflections from the surface. Such interference can lead to erroneous calculations of interaction forces, although they are expected not to have a large effect on the jump-to-contact distance. Using an appropriate value of the Hamaker constant for glass surfaces in dry air [11], a predicted interaction was calculated and is shown in Fig. 2. The qualitative agreement between the measured and the predicted interaction suggests that the surfaces were clean and dry. The retraction data can be used to determine the pull-off force for these surfaces. The adhesion force between a sphere and a flat is predicted to be

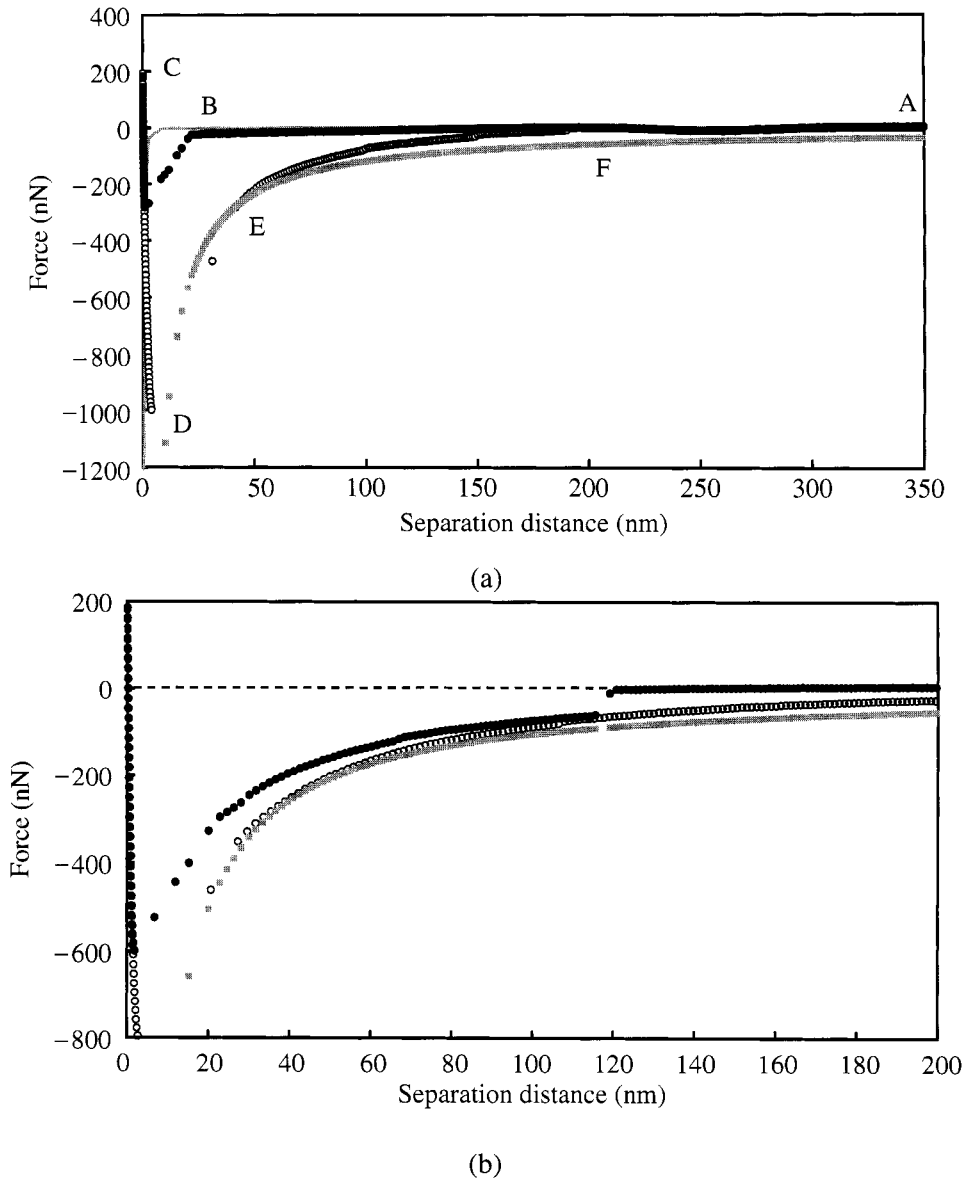
$$F_{\text{adh}} = 4\pi R' \gamma_{\text{SV}}, \quad (7)$$

which for a silica glass sphere with  $R' = 10 \mu\text{m}$ , and using a typical value of  $\gamma_{\text{SV}} = 150 \text{ mN/m}$  [32], should have a value of  $18 \mu\text{N}$ . The measured value here is  $1 \pm 0.1 \mu\text{N}$ . The difference between these values is commonly attributed to asperities on either the particle or the surface. The role of surface asperities on solid–solid adhesion measurements is well documented and has been discussed by many authors [23–29]. In general, a reduction of between 1 and 2 orders of magnitude between the predicted and the measured values is observed. In this study, the important features of the data in Fig. 2 are the van der Waals type interaction as the surfaces approach, and on retraction the jump-out in the surface separation after the adhesion force is overcome.

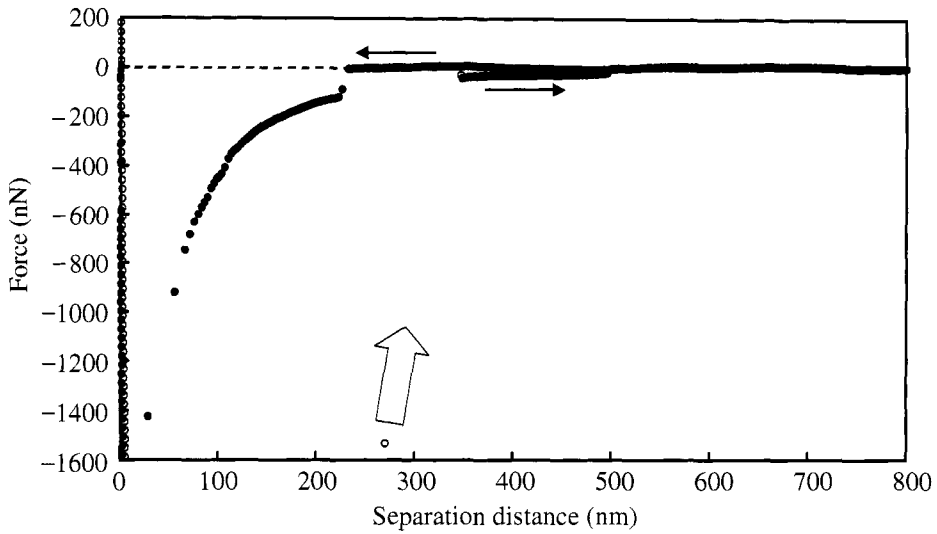
Force–separation data collected at three different values of the RH, 14%, 30% and 95%, are shown in Fig. 3. The data collected at the lowest RH value, 14%, shown in Fig. 3a will be discussed first. Using the lettering given in this figure, it is obvious that starting at the maximum separation, A, there is initially no interaction between the probe and the surface and the probe shows no detectable force. As the surface separation is reduced, no interaction between the surfaces is observed until point B, where a sudden instability in the probe results in a jump-to-contact from a separation of about 25 nm. Further movement of the piezoelectric drive results in a loading of the surfaces whilst in contact until the drive voltage is reversed at point C. At this point, the flat surface motion is reversed. Initially, the surfaces remain in contact until the restoring force of the spring is sufficient to overcome the adhesion interaction force at point D. The hysteresis between the two data sets is a consequence of both the mechanical construction of the measurement device and capillary condensation of liquid at the sphere–flat junction during contact. The breaking of the adhesion interaction at point D is followed by rapid relaxation of the spring to point E, although it does not immediately return to the baseline, as is typically seen for clean dry systems. Instead, from point E to point F, the attraction between the surfaces gradually relaxes as the surface separation increases. Finally, at point F there is a very small jump back to the baseline, whereupon further separation of the surfaces has no effect on the probe.

The main features described above are also seen in both Fig. 3b and 3c collected at higher RHs, although certain specific differences should be noted. At the higher humidity values shown, the initial contact between the surfaces as they come together occurs at larger separation distances with greater values of the RH. The ‘jump’ to initial contact is relatively small and is followed by a region of increasing attractive force with decreasing separation distance until at some point a final jump-to-contact is observed. The form of the data in this attractive zone, after the initial contact is made, closely resembles that of the retraction data, although there is some clear hysteresis between the data sets. At the highest humidity value tested, 97%, the pull-off data show a large adhesion and a rapid return to the baseline after this adhesion is overcome. As a result, little information about the form of the pull-off data is evident.

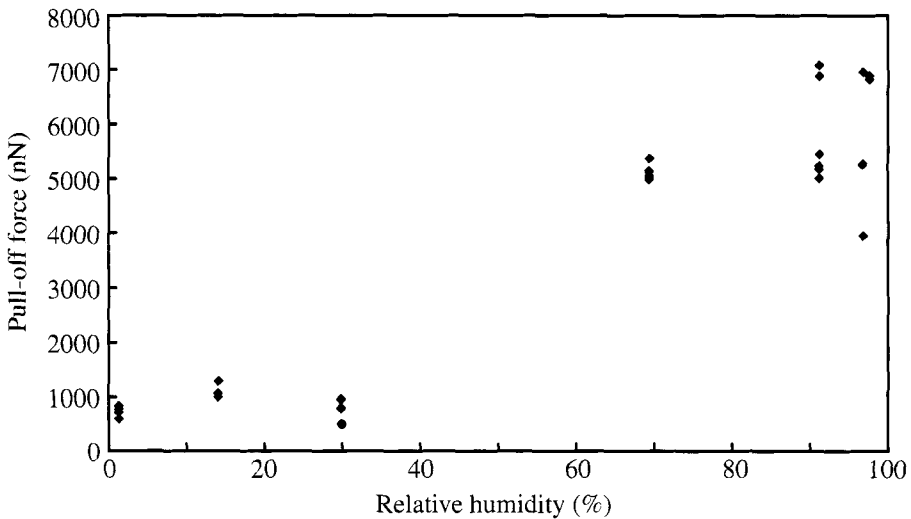
We first consider the data set collected at a RH of 14%. At this RH, the predicted capillary radius for water on glass, if we assume a contact angle of  $0^\circ$ , is approximately 0.5 nm. This is below the expected value of 2 nm at which point capillary forces become important with respect to the pull-off force, as predicted by equation (4). If we assume that the contact angle of water on glass is  $0^\circ$ , then for a glass probe with a radius of  $15.5\ \mu\text{m}$  as used here, the predicted capillary adhesion (at contact) from equation (3) is approximately  $14\ \mu\text{N}$ . This is more than one order of magnitude greater than the measured value of  $\sim 1\ \mu\text{N}$  from Fig. 3a. The pull-off forces as a function of the RH for all the experiments performed in this study are shown in Fig. 4. It is clear from these data that there is a shift in behaviour between the data collected at a RH value of 30% and those at 69%. As noted previously,



**Figure 3.** Force–separation data recorded between a  $15.5\ \mu\text{m}$  glass sphere and a flat glass surface at three values of the relative humidity: (a) RH = 14%; (b) RH = 30%; and (c) RH = 97%. Data are shown for both the approach ( $\bullet$ ) and the retraction ( $\circ$ ) of the sphere and the surface. The lettering in a refers to information which can be obtained from each force curve and is explained fully in the text. The solid grey line in a is the van der Waals fit used in Fig. 2. Fits to the retraction data using the constant volume capillary model [equation (6)] are shown in a and b as solid grey squares. The parameters used were (a)  $\theta = 0^\circ$  and  $d = 0.8\ \text{nm}$  and (b)  $\theta = 0^\circ$  and  $d = 0.9\ \text{nm}$ . The arrow indicates the direction of return for the pull-off data in c.



(c)

**Figure 3.** (Continued).

**Figure 4.** The measured pull-off forces as a function of the relative humidity. All experiments were performed using a single glass sphere (radius =  $15.5 \mu\text{m}$ ). The points at each value of RH are for repeat runs and indicate the errors involved in this type of experiment. A transition in behaviour is observed between the data collected at or below RH = 30% and those collected at or above RH = 69%.

Christenson determined that a capillary radius of 2 nm was required before capillary adhesion became significant in the pull-off force [10]. This occurs at a RH of about 60%. The data collected here support this earlier finding. The pull-off forces

collected at RH values below 60% were of a similar magnitude to that collected for a bare dry probe (Fig. 2). This suggests that the ‘surface–surface’ adhesion is the dominant contribution to the measured pull-off forces under these conditions. Above the limiting condition for RH of 60%, the pull-off data have values that range between 5 and 7  $\mu\text{N}$ . Whilst significantly higher than the dry case, these values are clearly not as large as the predicted value of 14  $\mu\text{N}$ . The difference between the predicted value and the measured values is most probably due to the surface asperity problems discussed above. The contact region must therefore consist of multiple liquid bridges that cover approximately half the expected area.

Returning to the force–distance data shown in Fig. 3a, what are the origins of the attractive force as the surfaces are brought together? Using a value of the Hamaker constant for quartz surfaces in vacuum, the maximum predicted van der Waals interaction between the sphere and the plate can be calculated. These data are shown in Fig. 3a. The magnitude of the measured attraction is clearly much greater than this predicted interaction. A possible source of the interaction seen in this and the other data sets comes from locally adsorbed water that is present as a result of the broken capillary neck from the previous force cycle. It should be noted here that the data were usually collected in a constant scan cycle such that an inward force curve immediately followed the end of an outward cycle. The data here correspond to the equilibrium case observed after many scans at the given set of conditions, i.e. scan rate and scan size. If we examine the pull-off data in Fig. 3a, we observe that the surfaces remain attractive until a separation of around 180 nm is achieved. This attractive force varies non-linearly with separation. The fact that the surfaces remain ‘connected’ out to a separation of 180 nm indicates that there is a capillary neck between the surfaces after contact. The non-linear form of these data indicate that the system is not at equilibrium during the separation process. The pull-off data can be fitted using equation (6). Once again, we assume a contact angle of  $0^\circ$ . It is clear that whilst not perfect, there is general agreement between the measured and the fitted data. The discrepancy between the two may be due to some evaporation as the surfaces are separated. At such low RH, the assumption of constant volume is clearly problematic. We will return to this point when we consider the data in Figs 3b and 3c below. The best fit to the data are obtained using a value of  $d = 0.8$  nm. If  $d \approx 2r_1 \cos \theta$ , then this implies a value of  $r_1 = 0.4$  nm. This corresponds to a RH of 8%. Allowing for the relatively poor fit and the crude nature of the calculations, this is an acceptable agreement with the measured value of 14% for the RH.

It seems likely that as the surfaces are separated, the velocity is too great to allow the system to equilibrate and the interaction tends towards that predicted for a constant volume system [11]. When the capillary neck breaks, the water is concentrated between the surfaces and it seems likely that a droplet of the water persists on both surfaces immediately after the breakage. This is illustrated schematically in Fig. 5. Under equilibrium conditions, it is expected that at a RH of 14% this water would evaporate, leaving the contact region effectively dry. In

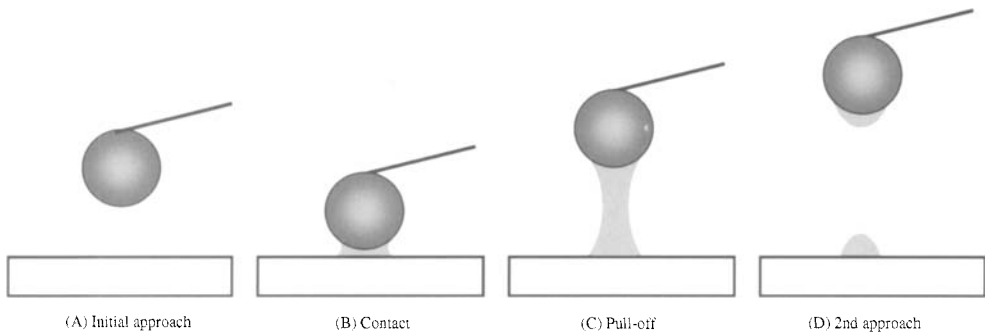


**Figure 5.** Schematic representation of the pooling of liquid between the surfaces after the initial formation of a capillary bridge. The retraction of the surfaces results in the extension of the capillary bridge. Eventually, the restoring force of the cantilever spring causes the bridge to rupture. Under equilibrium conditions, the fluid between the surfaces would evaporate, leaving only a thin film on both surfaces. The data collected here indicate that upon subsequent approaches, the surfaces form a capillary neck at large separation distances. Such a neck can form only if there is substantial liquid between the surfaces at the contact point as indicated in this schematic figure.

our case, immediately after the capillary neck is broken a new scan is started. The attraction seen when the surfaces are brought together is then caused by the coming together of these liquid drops. The large hysteresis between the data indicates that substantial evaporation does occur, as expected at this low RH. The pooling of liquid in the contact region between a probe and surface immediately after pull-off has been observed previously by others [19–21]. Salmeron and co-workers have even succeeded in imaging the ‘pooled’ water immediately after pull-off [19]. The results of their investigations suggest that this water does not immediately dissipate, but remains in the contact region for a finite time. A further complication of the system chosen here is the possible presence of a surface gel layer on the glass. Such layers, caused by the formation of poly(silicic acid), have been reported by many authors [33]. The presence of gel layers is known to affect the condensation of water vapour at these surfaces.

The importance of the data collected at these low RH values is that there is definitely a capillary neck present, but it does not significantly enhance the ‘contact’ adhesion between the particle and the surface. However, this capillary neck does influence the long-range pull-off behaviour, in that it results in an attachment between the surfaces out to significant separation distances. This attachment may be important in granular systems, under dynamic flow conditions, when the breaking of stress chains is required to initiate motion.

Further evidence of the pooling of liquid between the surfaces in the contact region is seen in the data collected at the higher humidity values, Figs 3b and 3c. In Fig. 3b, collected at a RH of 30%, the data show clearly the presence of a capillary neck in both the attraction and the separation data sets. Once again, the retraction data can be fitted using equation (6). The results of such a fit are shown in Fig. 3b. The agreement between the data and the fit are excellent. Once again,



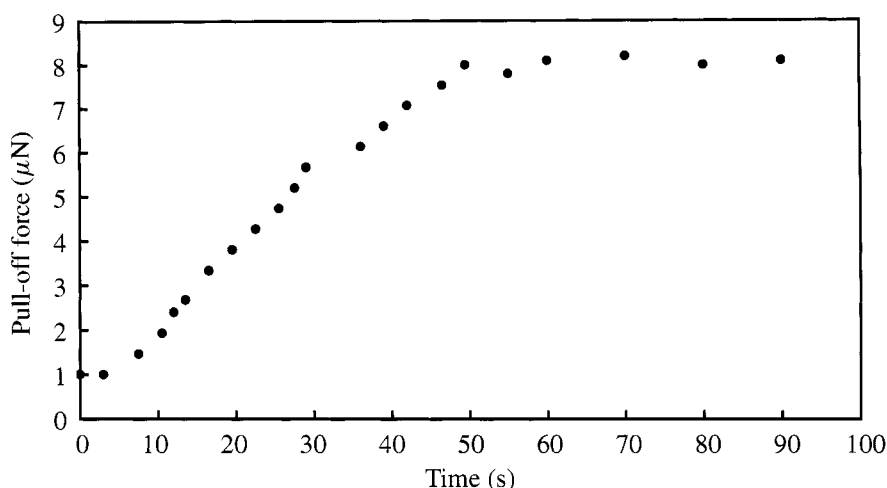


**Figure 6.** The pull-off force as a function of time for the interaction between a glass sphere (radius  $10\ \mu\text{m}$ ) and a flat glass surface. Time zero corresponds to the point in the experiment when the  $\text{RH} = 0$  air stream was replaced with humid air of  $\text{RH} = 72\%$ . Force–distance data were recorded continuously at this time. The data points shown were determined from force curves chosen at random from this set.

the hysteresis between the two data sets is most probably explained by evaporation during the finite time between capillary neck breakage and contact during the next compression cycle. Another possible complication in the fitting procedure could arise if the interaction area of the capillary bridge alters during retraction. As an example, the pull-off data in Fig. 3b can be well fitted using the constant volume model at either small separation distances (as shown) or larger separations simply by adjusting the  $d$  parameter. The possibility that the area of interaction alters during this dynamic pull-off event should not be discounted. A similar result is seen at the highest RH tested, Fig. 3c. In this case, however, the adhesion is sufficiently strong that upon pull-off the restoring force of the spring results in a loss of all detail during the retraction. It should be noted that at this value of the RH, the pull-off force has a significant contribution from the capillary force.

The role of non-equilibrium effects in the capillary condensation observed above was probed further by performing a series of experiments where the system was initially dried under a constant stream of dry nitrogen over a 2 h period. After collecting the resultant force–separation data under these conditions, humid air at a relative vapour pressure of 0.76 was allowed to enter the cell. Force–separation data were then collected continuously over a 5 min period. The scan size used here was  $\pm 300\ \text{nm}$  and the data were recorded at a scan rate of 1 Hz. The approximate time that the surfaces were in contact was 0.2 s. The resultant values of the pull-off force, as a function of time, are plotted in Fig. 6. The pull-off force is seen to increase steadily from the dry system value towards the ‘equilibrium’ value of  $8\ \mu\text{N}$  over the first minute of measurement. Thereafter, a constant value was seen.

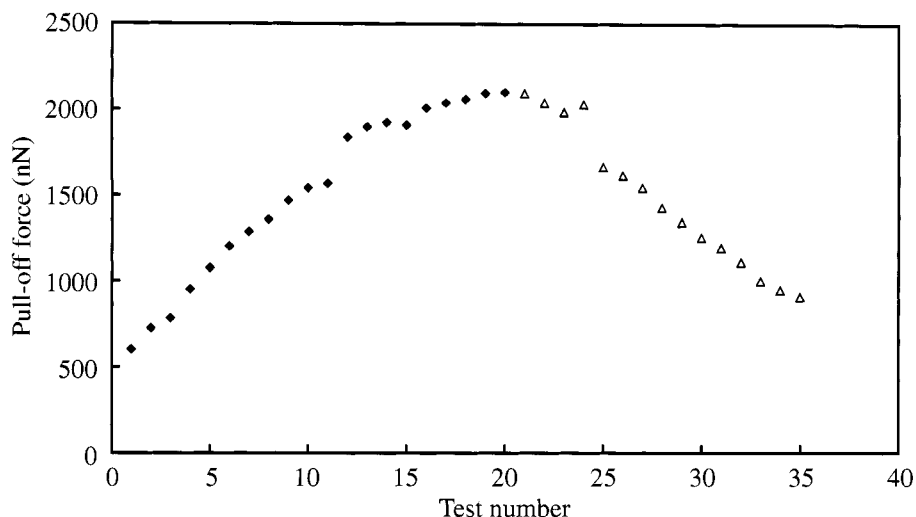


**Figure 7.** The pull-off force determined from a series of consecutive scans at RH = 14% and at two different scan sizes and a constant scan rate (1 Hz). The two scan sizes used were (a)  $\pm 300$  nm (◆) and (b)  $\pm 600$  nm (△). In both cases, the size of the constant compliance region was kept approximately constant at  $\pm 100$  nm. An approximate calculation indicates that the time from breakage of the capillary bridge to reformation (see Fig. 5) takes approximately 0.3 s at a scan size of  $\pm 300$  nm and 0.6 s at a scan size of  $\pm 600$  nm.

Under the conditions of the experiment, it is clear that a finite time is required for the system to reach an equilibrium state.

Further information about the non-equilibrium nature of the forces recorded in this study was obtained by varying the length of time between capillary breakage and reattachment in a single experiment. This was achieved by maintaining an approximately constant contact period between the surfaces using the commercial software but increasing the scan size. In this way, the distance travelled by the surfaces out of contact is increased. At a constant scan rate, this is directly related to the time. The results of such an experiment performed at a RH of 1.3% are shown in Fig. 7. The pull-off force values quoted were collected in a series of consecutive scans. It is clear that the apparent 'equilibrium' value of the pull-off force is strongly dependent on the conditions of measurement. In the case where the time between scans was the shortest, the measured pull-off force values increased towards a limiting value of  $2.1 \mu\text{N}$ . This result suggests that there is an increased contribution of the capillary force under these conditions. When the time out-of-contact was increased during the second half of the experiment, the pull-off forces decreased to a limiting value of approximately  $1 \mu\text{N}$ . The increase seen at small out-of-contact times reinforces the idea of a water 'pool' between the surfaces immediately after the capillary neck is broken. If the surfaces are brought together again rapidly and not held in contact too long, this can result in an excess of water being present at the contact junction at the moment of pull-off. The net result of this is a capillary force that is too large with respect to the expected value at the same

RH. As a result of this observation, all the pull-off force data reported in Fig. 4 were collected at scan sizes where any further increases in the scan size had no effect on the measured pull-off force value.

#### 4. CONCLUSIONS

The results of this study highlight the significant role that capillary forces may play in the interactions between particles in a granular body. A limiting value of RH = 60% was observed. Below this value, adsorbed water at the contact junction did not have a significant effect on the pull-off force. Above this value, the capillary forces were seen to result in an increase of the pull-off force by a factor of between 5 and 7. In all cases, the pull-off forces were smaller than predicted from theory. The differences are attributed to the effects of surface roughness at the contact point. The dynamic nature of the measurement when using a standard AFM is highlighted by the long-range force data that indicate that the surfaces remain connected through a capillary neck at large separations and that the extension of this neck occurs under conditions of constant volume.

#### Acknowledgements

Funding from the Australian Research Council Large Grants Scheme, the Centre for Multiphase Processes, and the Centre for Bulk Solids and Particle Technology is gratefully acknowledged.

#### REFERENCES

1. J. Visser, *Surface Colloid Sci.* **8**, 3–79 (1976); K. L. Mittal (Ed.) *Particles on Surfaces 5 & 6: Detection, Adhesion and Removal*. VSP, Utrecht (1999).
2. R. G. Cain, S. Biggs and N. W. Page, *Phys. Rev. E*. (in press).
3. K. L. Johnson, K. Kendall and A. D. Roberts, *Proc. R. Soc. London, Ser. A* **324**, 301 (1971); B. V. Derjaguin, V. M. Muller and Y. P. Toporov, *J. Colloid Interface Sci.* **53**, 314 (1975).
4. A. Zimon, *Adhesion of Dust and Particles*. Plenum Press, New York (1982).
5. E. Barthel, X. Y. Lin and J. L. Loubet, *J. Colloid Interface Sci.* **177**, 401 (1996).
6. M. M. Kohonen and H. K. Christenson, *Langmuir* **16**, 7285 (2000).
7. L. R. Fisher, *Adv. Colloid Interface Sci.* **16**, 117 (1982).
8. L. R. Fisher and J. N. Israelachvili, *Colloids Surfaces* **3**, 303 (1981).
9. H. K. Christenson, *J. Colloid Interface Sci.* **104**, 234 (1985).
10. H. K. Christenson, *J. Colloid Interface Sci.* **121**, 170 (1988).
11. J. N. Israelachvili, *Intermolecular and Surface Forces*, 2nd edn. Academic Press, San Diego (1992).
12. T. Stifter, O. Marti and B. Bhushan, *Phys. Rev. B* **62**, 13667 (2000).
13. D. L. Sedin and K. L. Rowlen, *Anal. Chem.* **72**, 2183 (2000).
14. M. He, A. Blum, D. E. Aston, C. Buenviaje, R. M. Overney and R. Luginbuhl, *J. Chem. Phys.* **114**, 1355 (2001).
15. L. Sirghi, N. Nakagiri, K. Sugisaki, H. Sugimura and O. Takai, *Langmuir* **16**, 7796 (2000).

16. A. de Laazer, M. Dreyer and H. J. Rath, *Langmuir* **15**, 4551 (1999).
17. N. A. Burnham, R. J. Colton and H. M. Pollock, *J. Vac. Sci. Technol. A* **9**, 2548 (1991).
18. T. Thundat, X.-Y. Zheng, G. Y. Chen and R. J. Warmack, *Surface Sci.* **294**, 939 (1993).
19. L. Xu, A. Lio, J. Hu, D. F. Ogletree and M. Salmeron, *J. Phys. Chem. B* **102**, 540 (1998).
20. J. Hu, X.-D. Xiao, D. F. Ogletree and M. Salmeron, *Science* **268**, 267 (1995).
21. P. B. Miranda, L. Xu, Y. R. Shen and M. Salmeron, *Phys. Rev. Lett.* **81**, 5876 (1998).
22. P. A. Thompson and G. S. Grest, *Phys. Rev. Lett.* **67**, 1751 (1991).
23. W. A. Ducker, T. J. Senden and R. Pashley *Nature* **353**, 239 (1991).
24. D. M. Schaefer, M. Carpenter, B. Gady, R. Reifengerger, L. P. DeMejo and D. S. Rimai, in: *Fundamentals of Adhesion and Interfaces*, D. S. Rimai, L. P. DeMejo and K. L. Mittal (Eds), pp. 1–23. VSP, Utrecht (1995).
25. S. Biggs and G. Spinks, *J. Adhesion Sci. Technol.* **12**, 461 (1998).
26. M. Reitsma, V. S. J. Craig and S. Biggs, *J. Adhesion* **74**, 125 (2000).
27. D. M. Schaefer, M. Carpenter, B. Gady, R. Reifengerger, L. P. DeMejo and D. S. Rimai, *J. Adhesion Sci. Technol.* **9**, 1049 (1995).
28. M. K. Chaudhury, T. Weaver, C. Y. Hui and E. J. Kramer, *J. Appl. Phys.* **80**, 30 (1996).
29. H. A. Mizes, *J. Adhesion* **51**, 155 (1995).
30. A. W. Adamson and A. P. Gast, *Physical Chemistry of Surfaces*, 6th edn. Wiley, New York (1997).
31. J. P. Cleveland, S. Manne, D. Bocek and P. Hansma, *Rev. Sci. Instrum.* **64**, 403 (1993).
32. W. N. Unertl, *Langmuir* **14**, 2201 (1998).
33. G. Vigil, Z. Xu, S. Steinberg and J. Israelachvili, *J. Colloid Interface Sci.* **165**, 367 (1994).

## Measurement of oil-mediated particle adhesion to a silica substrate by atomic force microscopy

YAKOV I. RABINOVICH<sup>1</sup>, MADHAVAN S. ESAYANUR<sup>1,2</sup>,  
KERRY D. JOHANSON<sup>1</sup>, JOSHUA J. ADLER<sup>1,2</sup> and BRIJ M. MOUDGIL<sup>1,2,\*</sup>

<sup>1</sup> *Engineering Research Center for Particle Science and Technology, University of Florida, Gainesville, Florida, USA*

<sup>2</sup> *Department of Materials Science and Engineering, University of Florida, Gainesville, Florida, USA*

**Abstract**—Preventing particle segregation while maintaining flow is critical to enable processing in a variety of industries. Where segregation or dusting is particularly troublesome, oil may be added to the powder to increase cohesion between particles or to attach flow-aids to the particle surface. In this investigation, the role of the capillary force produced by an oil annulus between surfaces and its influence on adhesion are explored. The results of direct measurement by atomic force microscopy are compared with ensemble powder properties, as well as a simple theoretical expression that predicts the magnitude of the adhesion force as a function of the separation distance. Agreement is achieved between theory and experimental data using only the volume of the oil annulus and its surface tension as variables.

**Keywords:** Capillary force; adhesion; atomic force microscopy; powder mechanics; particles.

### 1. INTRODUCTION

The addition of liquid binders to bulk solids has been employed to increase the cohesive properties of the bulk material. This technique is often used to decrease the dustiness of a bulk material, to enhance agglomeration processes, to increase green strength during tablet and mold production, and to prevent segregation tendencies [1]. For example, roofing tile production companies may occasionally add oil to the roofing granules to prevent segregation of fine and coarse granules as they are deposited on the asphalt shingle. Food industries, chemical producers,

---

\*To whom correspondence should be addressed. 205 Particle Science and Technology Bldg., P.O. Box 116135, Gainesville, FL 32611-6135, USA. Phone: (352) 846-1194. Fax: (352) 846-1196. E-mail: [bmoudgil@erc.ufl.edu](mailto:bmoudgil@erc.ufl.edu)

and even wood manufactures add liquid binders to their briquetted or extruded products to produce a more robust particulate ensemble. Conversely, the presence of liquid in bulk powder materials can significantly increase the unconfined yield strength of the bulk and create significant arching and rathole tendencies in process equipment. These flow problems are responsible for many billions of dollars in lost revenue, additional operator involvement, and high maintenance cost to powder manufacturers. The mechanism behind increasing cohesiveness through the addition of liquid binders is not well understood but, in part, arises from the capillary forces between the individual particles. Understanding of these capillary forces will help prediction of the cohesive properties acting within a bulk material.

The bulk property of a particulate ensemble system that characterizes segregation tendencies, agglomerate production, and tablet integrity is the unconfined yield strength. This term is defined as the major principal stress acting on an unconfined sample of material, which causes shear failure. The actual failure of the bulk sample occurs at some angle relative to the major principal stress direction. At the failure surface, an individual particle must rise past the peak of an adjacent particle during shear, resulting in an expansion (dilation) of the bulk material. This expanding shear motion causes separation and reforming of liquid bridges between particles in the bulk assembly. Consequently, the force required to shear bulk particulate material depends on the sum of all the individual forces acting at the contact points between particles in the bulk. This implies that adhesion forces due to local inter-particle capillary forces should play an important role in increasing the bulk unconfined yield strength of a bulk assembly of particles.

Figure 1 shows the increase in unconfined yield strength as measured by the Schulze Cell technique for fine quartz powder (Novacite from Malvern Mineral Co., Hot springs, AR, USA) as a function of increasing oil content. White mineral oil (Norton Co., Littleton, NH, USA) was added to the powder as a fine mist and mixed thoroughly before measurements. An increase in bulk strength of up to 150% is found to occur with the addition of only 1–2% oil by weight, depending on the consolidation pressure. Understanding the adhesion mechanisms, the particle topography, and the distribution of particle sizes in the bulk will allow us to predict the cohesive properties of bulk assemblies of particles with a knowledge of basic forces acting between them. The objective of this investigation was to develop a model that predicted capillary force as a function of the separation distance between particles in order to form the basis of a methodology to estimate the unconfined yield strength of the bulk assembly of particles.

There is a significant body of literature concerning the adhesion of films and particles to surfaces in the absence of capillary forces [2–4]. Direct measurements of adhesion have been performed with most modern instrumentation including the surface force apparatus [5], atomic force microscope [6, 7], and interfacial gauge [8, 9]. There have also been a number of theoretical and experimental descriptions of the force of adhesion due to liquid in a capillary. That the amount of liquid (meniscus radius) condensed from such a system may be adequately described by

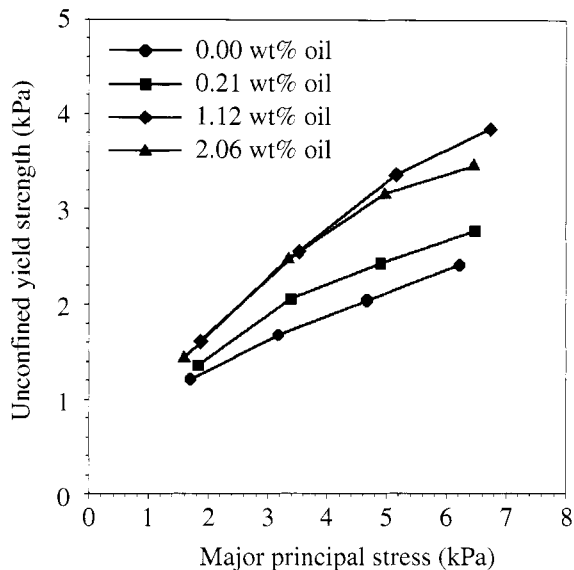


**Figure 1.** Dependence of unconfined yield strength on major principal stress for ground quartz (Novacite from Malvern Mineral Co.) in a Schulze cell as a function of the weight percent of added white mineral oil. Oil droplets between the particles are observed to greatly increase the cohesiveness between particles and thus the overall yield strength of the bulk powder.

the Kelvin equation has been confirmed by a number of authors [10–14]. An early discussion of capillary phenomena related to particle adhesion was presented by Coelho and Harnby [15, 16]. Through Kelvin's description of the lesser radius of curvature of the meniscus [17], the Laplace prediction of the pressure inside the meniscus [17], and inclusion of the adhesion component produced by the surface tension, a description of capillary adhesion was developed.

More recently, Marmur [18] and de Lazzer *et al.* [19] have extended these basic theories for other geometries, environmental conditions, and separation distances, while more accurately describing the meniscus and its effect on adhesion. de Lazzer *et al.* additionally incorporated surface tension in their model and have discussed capillary adhesion for a variety of probe geometries.

A direct measurement of capillary forces has been primarily performed in systems where liquid in a capillary is in thermodynamic equilibrium with the environment. Fisher and Israelachvili [20] investigated the adhesion between smooth mica surfaces in the presence of water and cyclohexane vapors and directly measured the relative contributions of solid–solid interactions and the capillary effect to the total adhesion force. Rabinovich *et al.* [21] further explored this area through direct measurement of the force of adhesion between fused quartz filaments in various semi-miscible liquids. Forces have also been measured in gaseous atmospheres saturated to various levels with water or an organic solvent [11, 22–24]. Capillary forces have also been measured between two oil droplets as they consolidate using the micropipette technique developed by Masliyah and co-workers [25].

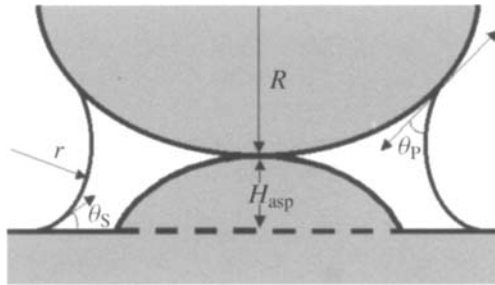


**Figure 2.** Illustration of the geometry of a liquid annulus formed in a capillary between a smooth spherical adhering particle and a rough substrate. The flat substrate is modeled as a single contacting asperity with the other surface features assumed to be equivalent to a plane representing the average of the surface profile. This geometry corresponds to equation (1) derived by Rabinovich *et al.* [22] and ignores the contribution of liquid surface tension.

As described above, the formation of capillary bonds between particles is known to have a significant effect on the mechanical properties and transport of powders [1]. In a previous investigation [22], the role of nanoscale surface roughness in the capillary adhesion forces between silica and other systems in both dry and humid atmospheres was explored. Corresponding to Fig. 2 and based on the equations of Marmur [18] and de Lazzer *et al.* [19], a simplified expression was developed for the capillary adhesion force,  $F_{ad}$ , between a smooth spherical particle and a flat substrate with nanoscale roughness:

$$F_{ad} = -4\pi\gamma R \cos\theta \left(1 - \frac{H_{asp}}{2r \cos\theta}\right). \quad (1)$$

In this relationship,  $\gamma$  is the surface tension of the liquid,  $R$  is the radius of the adhering particle,  $H_{asp}$  is the maximum height of the asperities above the average surface plane,  $r$  is the lesser radius of meniscus, and  $\cos\theta = (\cos\theta_p + \cos\theta_s)/2$ , where  $\theta_p$  and  $\theta_s$  are the contact angles of the liquid on the adhering particle and substrate, respectively. It should be noted that equation (1) is applicable only when the meniscus is large enough to span the distance between the adhering particle and the average surface plane, i.e.  $H_{asp} < 2r \cos\theta$ , and when the radius of the meniscus is small compared with the adhering particle.

Although derived in Ref. [22] for rough surfaces, equation (1) is also valid for the capillary adhesion of a smooth particle and a smooth substrate separated by a distance  $H$  [20]. However, the radius of the meniscus in the above formula is fixed because  $r$  is determined solely by the relative humidity through Kelvin's equation. Once the surfaces begin to separate, the liquid annulus rapidly decreases in size (evaporates) in order to maintain this radius. Hence, in cases such as condensed gases in thermodynamic equilibrium with vapors in surrounding media, the capillary adhesion should rapidly decrease as the surfaces separate. Due to the jump-out of the sphere on the cantilever, observed during the retraction of the tip, equilibrium is not maintained and the force measured corresponds to just the maximum adhesion



force. However, during powder transport the actual attachment/detachment process may occur rapidly and may not allow the radius of the capillary to reach equilibrium. Additionally, for the case of an oil annulus or other non-volatile liquid, the volume of the liquid would actually be conserved. In this case, the magnitude of the adhesion force is expected to decrease as a function of the separation distance but remain measurable.

The present investigation demonstrates the significance of capillary force in the mechanical properties of bulk powders and presents direct measurements of the capillary adhesion force acting between surfaces separated by oil droplets of various sizes. However, theoretical expressions first need to be developed, to correlate experimental and predicted values.

## 2. THEORETICAL FORCE OF CAPILLARY ADHESION FOR ANNULI OF CONSTANT VOLUME OR RADIUS

### 2.1. Capillary force

As mentioned above, equation (1) is expected to be valid for smooth surfaces, taking  $H$  as the shortest distance between the adhering particle and the flat substrate. For detachment rates faster than the evaporation time or for non-volatile liquids, such as oil, the radius of meniscus will be dependent on the initial volume of the liquid annulus rather than on the partial pressure of vapor around the annulus. Figure 3 shows schematically the liquid annulus formed between a particle and a flat surface separated by a distance  $H$  and Fig. 4 shows the same system at contact. Corresponding to Figs 3 and 4 and according to Marmur [18] and de Lazzer *et al.* [19], the adhesion force,  $F_{ad}$ , between a spherical particle of radius  $R$  and a flat substrate, connected by a liquid annulus, is the sum of two forces. We do not consider the classical DLVO forces here, as they would be much smaller than capillary forces that act at much larger distances. The first force,  $F_{\Delta P}$ , is the result of the pressure difference,  $\Delta P$ , across the meniscus due to its curvature and the second force,  $F_{\gamma}$ , is the vertical component of the surface tension acting tangentially to the liquid/air interface, given as

$$F_{ad} = F_{\Delta P} + F_{\gamma} = \pi x^2 \Delta P - 2\pi x \gamma \sin(\theta_p + \alpha), \quad (2)$$

where  $x$  is the horizontal distance from the center of the annulus to its intersection with the adhering particle,  $\gamma$  is the surface tension of the liquid,  $\theta_p$  is the contact angle between the liquid and the particle, and  $\alpha$  is the angle formed between the axis of interaction and the line of intersection between the meniscus and the particle. If  $r$  is the lesser radius of the capillary,  $\Delta P$  may be substituted from the Laplace equation [17]

$$\Delta P = \gamma(1/x - 1/r), \quad (3)$$

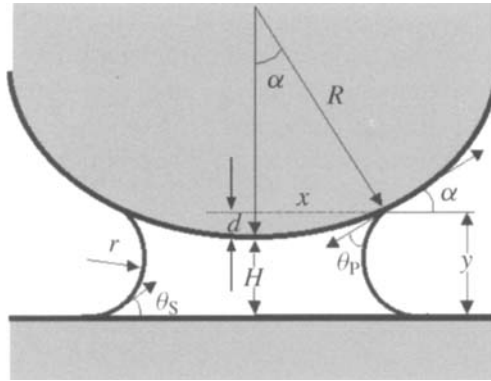


**Figure 3.** Illustration of the geometry of a liquid annulus formed in a capillary between a smooth spherical adhering particle and a smooth substrate when the particle and substrate are separated by a distance  $H$ . Note that if  $H$  is equal to  $H_{asp}$ , Fig. 2, for the same size particle and annulus, then the capillary forces would be equivalent.

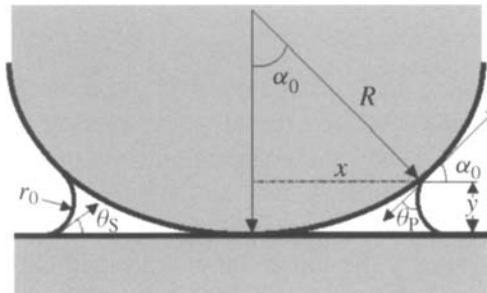


**Figure 4.** Illustration of the geometry of a liquid annulus formed in a capillary between a smooth spherical adhering particle and a smooth substrate when the separation distance,  $H$ , is zero.

to obtain

$$\frac{F_{ad}}{R} = \pi \gamma x' \left\{ 1 - \frac{x' [\cos(\theta_p + \alpha) + \cos \theta_s]}{H' + 1 - \sqrt{1 - x'^2}} - 2 \sin(\theta_p + \alpha) \right\}, \quad (4)$$

where  $R$  is the radius of the adhering particle,  $\theta_s$  is the contact angle between the liquid and the substrate,  $x'$  is the scaled annulus size ( $x' = x/R$ ),  $H'$  is the scaled separation distance ( $H' = H/R$ ), and  $H$  is the separation distance between the adhering particle and the flat substrate. The angle  $\alpha$  can be calculated by the following equation:

$$\alpha = \arctan\left(\frac{x'}{\sqrt{1 - x'^2}}\right). \quad (5)$$

It should be noted that de Lazzer *et al.* [19] graphically present the theoretical dependence of adhesion force as a function of  $x'$ , but do not develop the analytical expression for this dependence.

Israelachvili [26] also suggested a simple expression for capillary force as a function of distance, which should be valid for a small and constant volume of liquid annulus. However, this expression includes the value of  $d$ , shown in Fig. 3, which, in turn, depends on the distance  $H$ . Thus, the expression given by him requires knowledge of the relationship between  $d$  and  $H$ . In the limit of a small liquid annulus compared with adhered particle radius ( $x' \ll 1$ ) and contact between the particle and substrate, it is possible to obtain the classic approximate equation of capillary adhesion force:

$$\frac{F_{\text{ad}}}{R} = -4\pi\gamma \cos(\theta) - 2\pi\gamma x' \sin(\theta + \alpha). \quad (6)$$

Using the above approximation, for non-zero separation distances (and neglecting the second term, the force due to surface tension, which is relatively small for small contact angles) equation (1) is obtained.

The principal difficulty in using equation (4) or (6) to predict the adhesion force is that the experimental scaled size of the annulus,  $x'$ , is often unknown. Furthermore, de Lazzer *et al.* [19] suggest that the variables  $x'$  and the scaled separation distance,  $H'$ , are independent of each other. For many systems this is not the case. The relationship between  $x'$  and  $H'$  in reality will depend on boundary conditions necessitated by a particular experimental system. As mentioned previously, if the detachment process is much faster than evaporation, then the volume of liquid in the annulus will remain relatively constant as the two surfaces are separated. This limiting case should be applicable also to non-volatile systems such as oil droplets. The alternative limiting case, related to thermodynamic equilibrium between the annulus and media, is more common for systems of volatile liquids (such as water) when detachment rates are slower. For these systems, the maximum stable radius of the meniscus is determined by the Kelvin equation and a boundary condition of a constant radius should be employed. Note that the constant volume or constant radius boundary conditions are not only possible in gaseous atmospheres, but should also be valid in semi-miscible liquid mixtures [21]. The next two sections describe methodologies to implement these different boundary conditions.

## 2.2. Relationship between $x'$ and $H'$ for constant volume annulus

According to Fig. 3, the volume,  $V$ , of a non-volatile liquid annulus can be approximately calculated through geometrical methods [27] as

$$V = \pi x^2 y - (1/3)\pi(y - H)^2(3R - y + H), \quad (7)$$

where  $y$  is the vertical distance from the flat substrate to the intersection of the meniscus with the particle,  $x$  is the horizontal distance between the interaction axis  $y$  and the intersection of the meniscus with the particle,  $H$  is the minimum vertical distance between the sphere and the flat substrate, and  $R$  is the radius of the adhering

particle. For a spherical particle,  $x$  and  $y$  can be related as

$$\frac{y}{R} = \frac{H}{R} + 1 - \sqrt{1 - \left(\frac{x}{R}\right)^2}. \quad (8)$$

Substituting equation (8) in to equation (7) and assuming that  $x' = x/R \ll 1$  (in order to limit the series expansion), the following bi-quadratic equation is obtained:

$$x'^4 + 4H'x'^2 - \frac{4V}{\pi R^3} = 0, \quad (9)$$

whose solution relative to  $x'$  is

$$x' = \sqrt{-2H' + 2\sqrt{H'^2 + \frac{V}{\pi R^3}}}. \quad (10)$$

With this relationship, the dependence of the capillary force of adhesion,  $F_{ad}$ , on the scaled separation distance,  $H'$ , given by equation (4) can be solved, using  $\alpha$  calculated by equation (5) and  $x'$  from equation (10).

### 2.3. Relationship between $x'$ and $H'$ for constant radius annulus

According to Fig. 3 or 4, the following relationship is obtained:

$$\frac{y}{R} = \frac{r}{R} [\cos(\theta_S) + \cos(\theta_P + \alpha)], \quad (11)$$

where  $y$  is the vertical distance from the flat substrate to the intersection of the meniscus with the particle,  $R$  is the radius of the adhering particle,  $r$  is the lesser radius of the meniscus,  $\theta_S$  is the contact angle between the liquid and the substrate,  $\theta_P$  is the contact angle between the liquid and the particle, and  $\alpha$  is the angle formed between the axis of interaction and the line of intersection between the meniscus and the particle. Using equation (8) for small values of the scaled capillary size,  $x'$ , and equation (11), the capillary radius is derived as

$$\frac{r}{R} = \frac{H' + 0.5x'^2}{\cos(\theta_S) + \cos(\theta_P + \alpha)}. \quad (12)$$

For contact between the surfaces, Fig. 4 ( $H = 0$  and hence  $H' = 0$ ), it follows from equation (10) that

$$x'_0 = \sqrt[4]{\frac{4V_0}{\pi R^3}}, \quad (13)$$

where the subscript 0 indicates zero separation distance. Substituting equation (13) in to equation (12), the following expression for the capillary radius at zero separation distance,  $r_0$ , is obtained:

$$\frac{r_0}{R} = \sqrt{\frac{V_0/\pi R^3}{\cos(\theta_S) + \cos(\theta_P + \alpha_0)}}, \quad (14)$$

where

$$\alpha_0 = \arctan\left(\frac{x'_0}{\sqrt{1 - x'^2_0}}\right), \quad (15)$$

and  $V_0$  is original volume of the annulus at contact. Note that for this boundary condition the radius is constant, so for all separation distances  $r = r_0$ . Therefore, equation (14) is equivalent to equation (12) and the relationship between  $x'$  and  $H'$  becomes

$$x' = \sqrt{\frac{2\sqrt{V_0/\pi R^3}[\cos(\theta_S) + \cos(\theta_P + \alpha)]}{\cos(\theta_S) + \cos(\theta_P + \alpha_0)} - 2H'^2}. \quad (16)$$

Hence, as for the constant volume annulus boundary condition, the adhesion force for an annulus of constant radius can be predicted from equations (4) and (5) but with the value of  $x'$  from equation (16) instead of equation (10). Note that the capillary force of adhesion as a function of the separation distance can also be calculated for a constant meniscus radius boundary condition using equation (1) in combination with equation (14) for the radius. It should be noted that this equation does not account for the surface tension component of the capillary force. A comparison between these two approaches for a fixed radius of meniscus will be presented below.

### 3. EXPERIMENTAL

#### 3.1. Materials

Adhesion force was measured between 20–50  $\mu\text{m}$  glass microspheres from Duke Scientific Corp. and silica substrates. The spheres were found to have a root mean square (RMS) roughness of less than 0.2 nm. Silica substrates were provided by Dr. Arwin (Linköping University, Sweden) and were fabricated from 180 nm thick oxidized silicon wafers of 0.2 nm RMS roughness. All silica surfaces were cleaned by rinsing in acetone, methanol, and DI water. Cleaning was performed immediately prior to experimentation. Also, before each experiment, particles were glued to tapping mode TESP rectangular atomic force microscopy (AFM) cantilevers, supplied by Digital Instruments Inc., using a low melting temperature resin, Epon R 1004f from Shell Chemical Company. White mineral oil of 'Sharpening Stone' grade was obtained from Norton Co., Littleton, NH, USA and was used to form the liquid interlayer between the particle and the substrate. The viscosity of the oil was 25 cP as measured by a capillary viscometer. The contact angle of oil on the silica surfaces ranged from 0° to 10°. These very low contact angles suggest that the oil may be partially hydrophilic.

### 3.2. Methods

Surface forces were measured on a Digital Instruments Nanoscope IIIa AFM according to the methods described by Ducker and Senden [28]. The spring constant ' $k$ ' for each cantilever was calibrated by the frequency method, suggested by Cleveland *et al.* [29]. The average value of ' $k$ ' was close to 27 mN/m; however, individual values of ' $k$ ' were used for each cantilever. The sphere, attached to a cantilever of known spring constant, was positioned close to the flat substrate. Then as the substrate was moved towards and away from the particle by a piezoelectric scanner, the deflection of the cantilever was monitored by a laser that reflected from the top of the cantilever onto a position-sensitive photodiode. In this manner, the force between the two surfaces as a function of the separation distance was obtained. The force–distance profiles were normalized by dividing the measured force by the radius of the sphere. In other words, the data are presented in terms of energy per unit area of flat surfaces. This enables determination of the force for different geometries and sizes of particles as long as the range of the forces is much smaller than the radius of curvature of the particles.

To create the oil droplets, several larger drops of the order of a few millimeters were placed on the flat silica substrate. These drops were then disrupted by a gas jet that left many small droplets a few micrometers in size. In order to predict the adhesion force for either boundary condition described above, the initial volume of the capillary must be known. For the case of condensation of vapor or a semi-miscible liquid in a capillary, this can be derived from the geometry of the capillary and Kelvin's equation. For non-volatile liquids (oil), the volume is dependent on the size of the oil droplets present on the surface and cannot be predicted from theory.

Fortunately, in the present experimental system, the oil volume can be estimated from the experimentally observed distance at which the oil drops present on the substrate and the particle first touch. At this separation distance,  $H_c$ , there is a sudden jump in the force–distance profile as the two oil drops begin to coalesce. The geometry of the liquid drop on a flat surface is shown in Fig. 5. Based on this geometry, the volume of the drop,  $V_d$ , can be calculated as

$$V_d = \frac{\pi H_d^3}{3} \left( 1 + \frac{1}{1 - \cos \theta} \right), \quad (17)$$

where  $H_d$  is the height of the oil droplet on each of the surfaces and  $\theta$  is the contact angle. Note that in this approach the thickness of any wetting film is considered to be significantly smaller than  $H_d$ . However, spreading of the oil film and its thickness are described, for example, in Ref. [30].

Assuming that the radius of the liquid annulus is small compared with the radius of the particle and that the size of the droplets on the substrate and the particle is identical, the annulus volume  $V$  can be calculated using the experimental value of

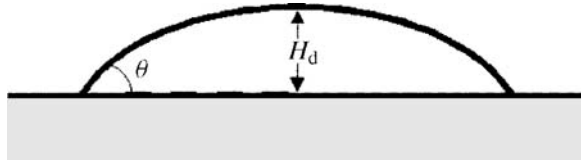


**Figure 5.** Illustration of the geometry of a liquid droplet on a surface. The distance at which two drops on opposing surfaces interact is  $2H_d$  and may be observed on the approaching force profile as  $H_c$ .

$H_c$ , where  $H_c$  is twice the individual droplet size:

$$V = 2V_d = \frac{\pi H_c^3}{12} \left( 1 + \frac{1}{1 - \cos \theta} \right). \quad (18)$$

#### 4. RESULTS AND DISCUSSION

Force–distance profiles were obtained upon approach and retraction of the two surfaces. If the viscosity of the oil is too large, then a hydrodynamic term should be included in the force–distance profile. To make sure that this is not the case, the detachment of the surfaces was measured at different rates (0.1, 0.75, 1.9, and 10 Hz). The detachment velocity can be calculated from twice the scan size ( $2.5 \mu\text{m}$ ) multiplied by rate, which yields velocities of 0.500, 3.75, 9.5, and  $50 \mu\text{m/s}$ , respectively, for the four scanning rates. These results are presented in Fig. 6. The differences between the measurements are small compared with the noise inherent in the system. This conclusion is also supported by theoretical calculation. For example, for a sphere in oil (with a dynamic viscosity 25 cP) at a maximal velocity of  $50 \mu\text{m/s}$ , Stokes' formula yields a normalized viscous resistance force equal to 0.024 mN/m, which is much smaller than the experimentally measured value. Hence it can be concluded that the hydrodynamic force is significantly smaller than the magnitude of the capillary force. Therefore, ignoring the hydrodynamic force in the above-mentioned equations for capillary force is correct for our experiments.

Force curves were obtained for different samples, drop sizes, cantilevers, and even using two different AFM instruments. The force–distance profiles presented in Figs 7–9 were measured at a rate of 0.75–1 Hz. Each example curve was taken on a different day with fresh samples. Note also that the particle size ( $14\text{--}25 \mu\text{m}$  radius) and the oil droplet volume (approximately  $7 \times 10^8$  to  $180 \times 10^8 \text{ nm}^3$ ) are significantly different. The example in Fig. 9 was obtained from a second AFM. In Fig. 7, both the approaching and the retracting curves are shown. As can be clearly seen in Fig. 7, at some separation distance, corresponding to  $H_c$ , there is a jump in the approaching force–distance profile. This jump corresponds to the formation of a stable liquid annulus between the particle on the AFM tip and the substrate. After the jump, the approaching curve follows an equilibrium path until contact. Upon retraction of the two surfaces, the adhesion force is observed to have the same

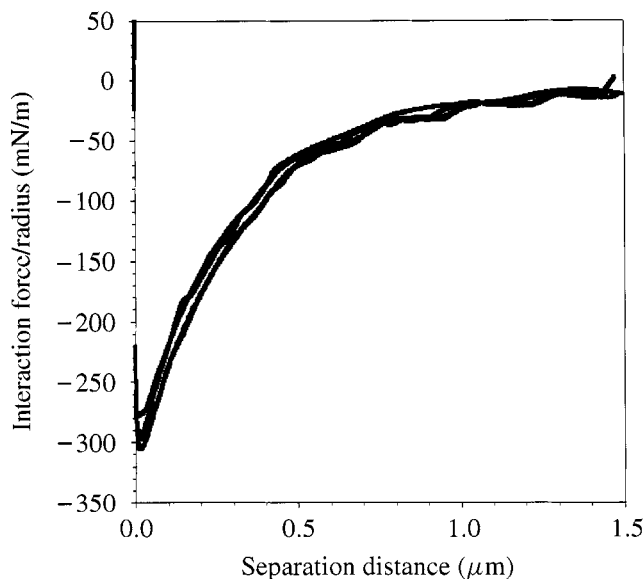


**Figure 6.** Retracting (detaching) interaction force profiles normalized by particle radius as a function of the separation distance for a particle radius of  $14\ \mu\text{m}$ . The four detachment rates shown (0.1, 0.75, 1.9, and 10 Hz) correspond to velocities of 0.500, 3.75, 9.5, and  $50\ \mu\text{m/s}$ , respectively, and are identical within the resolution of the technique. This indicates that effects from the viscosity of the oil (25 cP) are small compared with the equilibrium capillary forces.

form as the approaching curve. This suggests that the forces being measured are indeed primarily due to a capillary force at a near mechanical equilibrium state for a given separation distance. It can also be seen that the process whereby the capillary first forms is much faster than the approach rate. It should also be noted that upon retraction the annulus does not break at  $H_c$ ; rather, the liquid continues to stretch to larger separation distances. Usually the force at which the meniscus broke in the retracting curve was too small to be observed, compared with the background noise. However, on some curves a distinct jump back to zero interaction force was observed. The distance at which these breaks occurred was not always consistent.

Also shown in Figs 7–9 are the theoretical predictions assuming an annulus with a constant volume boundary condition [from equations (4), (5), and (10): curves 1 in Figs 7–9], a line suggesting a constant capillary radius without the surface tension component [from equations (1) and (14): curves 2 in Figs 7–9], and a line suggesting a constant capillary radius with the surface tension component [from equations (4), (5), and (16): curves 3 in Figs 7–9]. As expected for the case of an oil droplet, although the lines representing the constant annulus radius condition (lines 2 and 3) adequately predict the maximum adhesion force (at contact), they do not describe the adhesion force profile as a function of the separation distance well. Furthermore, a significantly lower energy of adhesion (integral of the force profile) would be predicted for this case than from the theory for constant annulus volume. The relatively small difference between these two curves 2 and 3 should be related



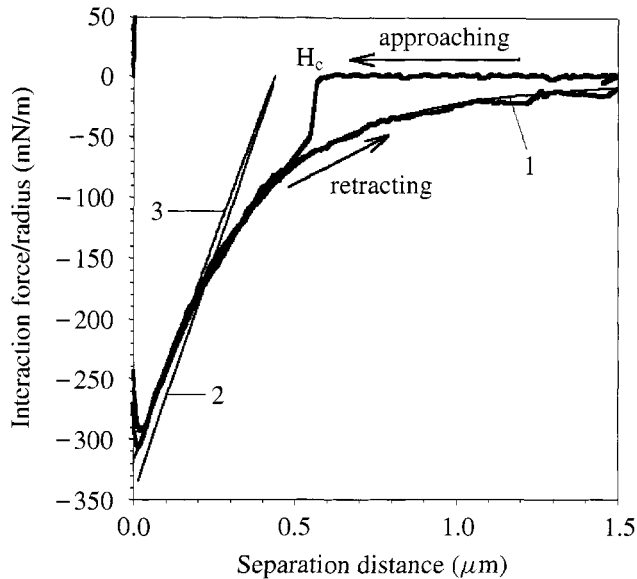


**Figure 7.** The thick profiles are the approaching and retracting interaction forces normalized by particle radius as a function of the separation distance for a particle radius of  $14\ \mu\text{m}$ . Curve 1 is the predicted capillary adhesion force profile derived under a constant annulus volume boundary condition from equations (4), (5), and (10). Line 2 is derived from equations (1) and (14) for a constant meniscus radius boundary condition where the surface tension component is neglected. Line 3 is derived from equations (4), (5), and (16) for a constant meniscus radius boundary condition where the surface tension component is taken into account. The fitting value of the volume of the liquid annulus is equal to  $80 \times 10^8\ \text{nm}^3$  and surface tension to  $27.5\ \text{mN/m}$ . Contact angle  $\theta_s = \theta_p = 10^\circ$ .

to different approximations made in equations (1) and (4) and to the surface tension component of the capillary adhesion force. As shown in Fig. 9, this difference disappears for contact angle  $\theta_s = \theta_p = 0^\circ$ .

In Figs 7–9, the theoretical predictions arising from the constant annulus volume boundary condition (curve 1) seem to fit the experimental data better. This indicates that the approximations made in the above derivations are appropriate for this system and that the principal origin of the adhesion is the annulus formed between the two surfaces by the oil. Furthermore, it seems that the rate of detachment is slow enough that at non-zero separation distances the liquid annulus is able to form a meniscus defined by the geometry of the capillary, the volume of the oil, and its surface tension. We can also note that the calculation on the basis of the expression suggested by Israelachvili [26] is in good agreement for the constant volume case as shown in curve 1.

As observed in the presented graphs, there is a large difference in behavior for the constant volume (curve 1) or constant radius (curve 2 or 3) boundary conditions as a function of the separation distance. This difference may be especially important in the modeling of powder flow or adhered particles. For powder flow, it should be the energy (integral of the force profile) of adhesion during the detachment process that

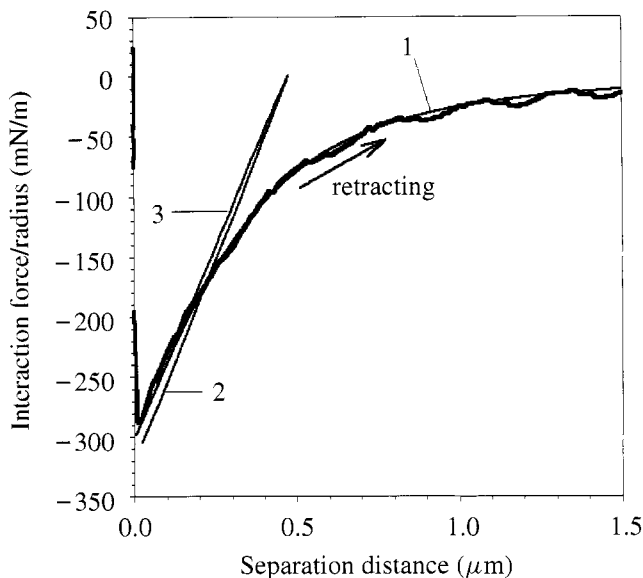


**Figure 8.** The thick profile is the retracting interaction force normalized by particle radius as a function of the separation distance for a particle radius of  $25\ \mu\text{m}$ . Curve 1 is the predicted capillary adhesion force profile derived from equations (4), (5), and (10) under a constant annulus volume boundary condition. Line 2 is derived from equations (1) and (14) under a constant meniscus radius boundary condition where the surface tension component is neglected. Line 3 is derived from equations (4), (5), and (16) under a constant meniscus radius boundary condition where the surface tension component is taken into account. The fitting value of the volume of the liquid annulus is equal to  $170 \times 10^8\ \text{nm}^3$  and surface tension to  $25.5\ \text{mN/m}$ . Contact angle  $\theta_s = \theta_p = 10^\circ$ .

controls the bulk behavior. For example, a water-filled capillary and an oil-filled capillary may provide a similar maximum adhesion force, but the energy needed to separate the two could be quite different and lead to dramatic differences in handling characteristics such as flow of powders. Also, to initiate powder flow or remove particles from a surface, different forces would have to be applied. For example, not only would a mechanical oscillation have to be applied which is enough to overcome the capillary adhesion, but also the duration must be long enough (or amplitude large enough) to allow the liquid annulus between the two surfaces to be broken. These concepts as they relate to powder flow in the presence of capillary forces will be explored further in an upcoming article.

The theoretical predictions described above depend on two variables: the volume of the liquid annulus and the surface tension of the liquid; and the former is not known experimentally. Each measured capillary adhesion profile and the ones presented in Figs 7–9 were fitted using the various values of these two variables. For all the measured adhesion profiles, the fitting value of surface tension used was  $26.5 \pm 2\ \text{mN/m}$ . However, using the Wilhelmy plate technique [17] with a platinum blade, the surface tension was found to be  $30 \pm 0.5\ \text{mN/m}$ . Although these values are

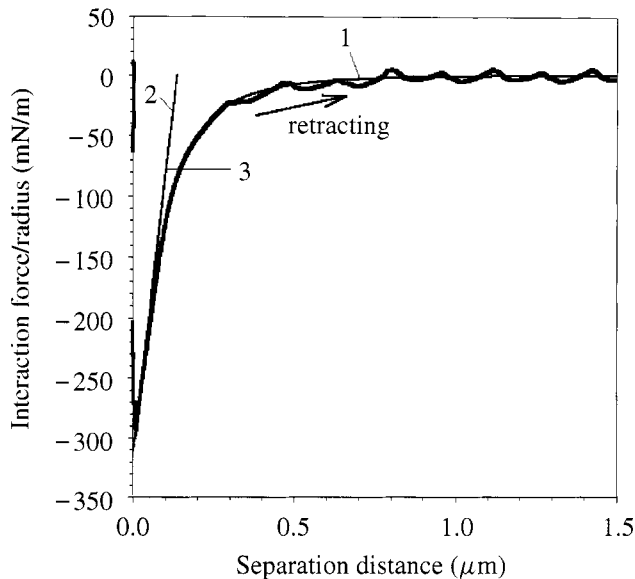


**Figure 9.** The thick profile is the experimental retracting interaction force normalized by particle radius as a function of the separation distance for a  $14\ \mu\text{m}$  particle. Curve 1 is the predicted capillary adhesion force profile derived under a constant annulus volume boundary condition from equations (4), (5), and (10). Line 2 is derived from equations (1) and (14) under a constant meniscus radius boundary condition where the surface tension component is neglected. Line 3 is derived from equations (4), (5), and (16) under a constant meniscus radius boundary condition where the surface tension component is taken into account. The fitting value of the volume of the liquid annulus is equal to  $7 \times 10^8\ \text{nm}^3$  and surface tension to  $26.0\ \text{mN/m}$ . Contact angle  $\theta_S = \theta_P = 0^\circ$ .

close, the difference may represent a systematic error associated with the calibration of the cantilever.

The volume of the liquid annulus was also used as a fitting parameter in the prediction of the adhesion force curves. However, as described earlier, equation (18), this volume can also be calculated from the distance upon which the liquid droplets on the two surfaces first make contact,  $H_c$ . A comparison of the fitted annulus volume and  $H_c$  using equation (18) should show a cubic dependence and can be used to extract a value for the contact angle. Figure 10 shows this correlation (on a log/log scale) for a number of experimentally measured force profiles. The straight line has a slope of 3, indicating a cubic dependence and an adequate correlation. Moreover, the intersection of the correlation line with the ordinate axis can be used to calculate the contact angle from equation (18). The calculated value of  $3.7^\circ$  fits well with the measured values which fell between  $0^\circ$  and  $10^\circ$  for oil on the silica surface. Hence, it appears that the approximations developed in this investigation are appropriate for modeling capillary adhesion forces between surfaces mediated with oil.

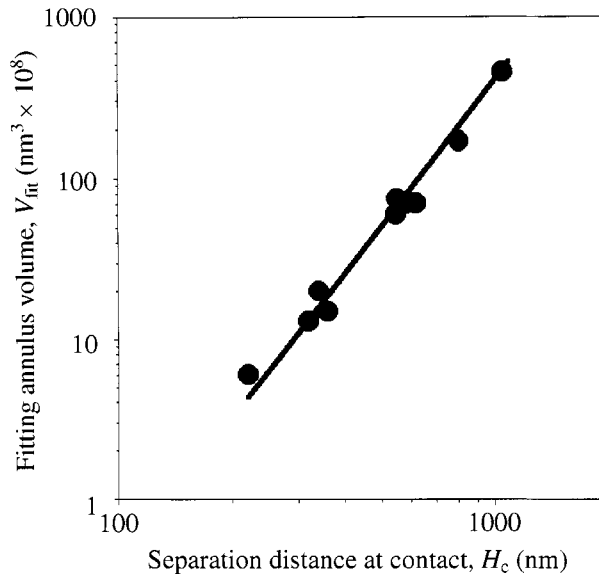


**Figure 10.** Fitting value of the volume of liquid annulus (from constant annulus volume boundary condition) as a function of the separation distance at which contact is first made,  $H_c$ , as determined from the approaching interaction force profiles. The symbols are experimental values and the line is the best fit with a slope of 3 on the log scale. That  $H_c$  and the fitting annulus volume have a cubic dependence indicates that equation (18) is valid. Furthermore, from the line's intercept at the ordinate axis and equation (18), the contact angle of the oil on glass is found to be  $3.7^\circ$ , which correlates well with the measured values, which ranged from  $0^\circ$  to  $10^\circ$ .

## 5. CONCLUSIONS

In this investigation, the role of the capillary force produced by an oil annulus between surfaces and its influence on adhesion and powder mechanics was explored. Although the maximum adhesion force has been investigated in the literature for a number of systems, the distance-dependent nature of the capillary force has not been verified experimentally. In order to interpret this behavior, a simplified theoretical model of the capillary force of adhesion as a function of the separation distance was developed with boundary conditions for a constant annulus volume and for a constant annulus radius. For surfaces with intervening oil droplets, the boundary condition of a constant annulus volume was found to correspond to the experiment. Furthermore, it was found for this system that the oil droplet during detachment approximated the mechanical equilibrium state for surfaces separated by a specific distance. The calculation of the distance-dependent capillary force of adhesion is expected to be important in the prediction of adhesion energy required to significantly control the flow behavior of powder systems, or in removal of particles from a polished surface.

## Acknowledgements

We acknowledge the financial support of the Engineering Research Center (ERC) for Particle Science and Technology at the University of Florida, The National Science Foundation (NSF) grant #EEC-94-02989, and the Industrial Partners of the ERC.

## REFERENCES

1. J. S. Reed, *Principles of Ceramic Processing*, 2nd edn. John Wiley, New York (1995).
2. K. L. Mittal (Ed.), *Adhesion Measurement of Films and Coatings*. VSP, Utrecht (1995).
3. D. S. Rimai and L. H. Sharpe (Eds), *Advances in Particle Adhesion*. Gordon and Breach, Amsterdam (1996).
4. K. L. Mittal (Ed.), *Particles on Surfaces 5 & 6: Detection, Adhesion and Removal*. VSP, Utrecht (1999).
5. J. N. Israelachvili and G. E. Adams, *J. Chem. Soc. Faraday Trans. 1* **74**, 975 (1978).
6. Y. I. Rabinovich, J. J. Adler, B. M. Moudgil and R. K. Singh, *J. Colloid Interface Sci.* **232**, 10 (2000).
7. Y. I. Rabinovich, J. J. Adler, B. M. Moudgil and R. K. Singh, *J. Colloid Interface Sci.* **232**, 17 (2000).
8. V. V. Yaminsky, R. K. Yusupov, E. A. Amelina, V. A. Pchelin and E. D. Shchukin, *Colloid J. USSR* **37**, 918 (1975).
9. V. V. Yaminsky, B. W. Ninham and R. M. Pashley, *Langmuir* **14**, 3223 (1998).
10. L. M. Skinner and J. R. Sambles, *Aerosol Sci.* **3**, 199 (1972).
11. L. R. Fisher and J. N. Israelachvili, *J. Colloid Interface Sci.* **80**, 528 (1981).
12. L. R. Fisher, R. A. Gamble and J. Middlehurst, *Nature* **290**, 575 (1981).
13. J. C. Melrose, *Langmuir* **5**, 293 (1989).
14. W. Pietsch and H. Rumpf, *Chemie-Ing. Techn.* **39**, 885 (1967).
15. M. C. Coelho and N. Harnby, *Powder Technol.* **20**, 197 (1978).
16. M. C. Coelho and N. Harnby, *Powder Technol.* **20**, 201 (1978).
17. A. W. Adamson, *Physical Chemistry of Surfaces*, 2nd edn. Interscience, New York (1967).
18. A. Marmur, *Langmuir* **9**, 1922 (1993).
19. A. de Lazzer, M. Dreyer and H. R. Rath, *Langmuir* **15**, 4551 (1999).
20. L. R. Fisher and J. N. Israelachvili, *Colloids Surfaces* **3**, 303 (1981).
21. Y. I. Rabinovich, T. G. Movchan, N. V. Churaev and P. G. Ten, *Langmuir* **7**, 817 (1991).
22. Y. I. Rabinovich, J. J. Adler, M. S. Esayanur, A. Ata, R. K. Singh and B. M. Moudgil, *Adv. Colloid Interface Sci.* **96**, 213 (2002).
23. R. A. Quon, A. Ulman and T. K. Vanderlick, *Langmuir* **16**, 8912 (2000).
24. M. M. Kohonen and H. K. Christenson, *Langmuir* **16**, 7285 (2000).
25. A. Yeung, T. Dabros, J. Masliyah and J. Czarnecki, *Colloids Surfaces A* **174**, 169 (2000).
26. J. Israelachvili, *Intermolecular and Surface Forces*, 2nd edn. Academic Press, San Diego (1992).
27. M. R. Spiegel, *Mathematical Handbook of Formulas and Tables*. McGraw-Hill, New York (1994).
28. W. A. Ducker and T. J. Senden, *Langmuir* **8**, 1831 (1992).
29. J. P. Cleveland, S. Manne, D. Bocek and P. K. Hansma, *Rev. Sci. Instrum.* **64**, 403 (1993).
30. J. Drelich, D. Lelinski and J. D. Miller, *Colloids Surfaces A* **116**, 211 (1996).

## Effect of relative humidity on adhesion and frictional properties of micro- and nano-scopic contacts

ADAM A. FEILER <sup>1,\*</sup>, PAUL JENKINS <sup>2</sup> and MARK W. RUTLAND <sup>1,†</sup>

<sup>1</sup> *Department of Chemistry, Surface Chemistry, Drottning Kristinasväg 51,  
Royal Institute of Technology, SE-100 44 Stockholm, Sweden*

<sup>2</sup> *Unilever Research, Port Sunlight, Quarry Road East, Bebington, Wirral CH63 3JW, UK*

**Abstract**—The effect of relative humidity (RH) on the interactions of AFM tips and colloidal probes with hydrophilic silica substrates is investigated. Both friction and adhesion are studied. For the case of a colloidal probe the interaction is characteristic of a multiasperity contact, the adhesion increased with increasing RH and above a certain threshold relative humidity a large increase in adhesion was measured. This behaviour is explained in terms of a recent model where the Kelvin radius of the condensate becomes larger than some characteristic roughness on the surface. The interaction between the tip and the substrate also exhibited an increase in adhesion above a threshold RH although the increase was much less marked than with the colloid probe. The friction decreased with increasing humidity for both tip and colloid probe although the friction force was much less sensitive than adhesion to changes in RH. Stick-slip behaviour was observed between tip and substrate for all humidities at high loads, but only at the lowest RH (about 5%) it was observed at all loads. At higher humidity the behaviour became increasingly continuum on the experimental timescale, presumably due to viscous contributions from the water. Stick-slip was not observed for the colloidal probe friction measurements.

**Keywords:** Friction; adhesion; capillary condensation; atomic force microscope; surface force.

### 1. INTRODUCTION

Local adhesion and rheological properties of dry powders or biofibre networks are the determining parameters for the behaviour of these materials at the macroscopic scale, and the effect of relative humidity on the formation of capillary condensates between contact points has long been known to play a key role. Direct measurement of the forces between particles or fibres, however, has only rather recently been

---

\*Current Address: Centre for Surface Biotechnology, Uppsala Biomedical Centre (BMC), SE-75123 Uppsala, Sweden.

†To whom correspondence should be addressed. E-mail: mark.rutland@surfchem.kth.se

feasible, since the development of the colloid probe technique [1], and so the quantification of these parameters has been lacking.

The development of the Surface Force Apparatus [2] in the early 1970s made the first measurement of capillary condensation adhesion possible and Kelvin's equation was verified down to rather low vapour pressures [3, 4]. Subsequent measurements [5] with an improved experimental setup showed a clear trend in the variation in the measured pull-off force between mica sheets interacting in undersaturated vapours of water and nonpolar solvents. A discussion of capillary condensation and the consequent adhesion which arises between two bodies in contact can be obtained from a now biblical reference work on surface forces [6]. We will confine ourselves here to reproducing the Kelvin equation, and the expression for the adhesion force ( $F_c$ ) due to capillary condensate between two perfect spheres with a combined interaction radius  $R_s$  assuming that the liquid has a contact angle of zero (the *combined* radius can be thought of as the radius of the equivalent sphere-flat interaction). The Kelvin equation relates the mean radius of curvature  $r_K$  of the condensate meniscus to the relative vapour pressure  $p/p_0$ , surface tension of the liquid  $\gamma$ , gas constant  $R$ , temperature  $T$  and molar volume,  $V$ , of the condensing fluid (Fig. 1).

$$r_K = \frac{\gamma V}{RT \ln(p/p_0)}, \quad (1)$$

$$F_c = 4\pi R_s \gamma. \quad (2)$$

The pull-off force,  $F_c$ , is obtained from considering the area over which the Laplace pressure operates and it so happens that the area and Laplace pressure have inverse dependencies on the Kelvin radius, which implies that  $F_c$  is independent of the Kelvin radius and thus the relative humidity. This is contradicted by common experience which tends to suggest that the adhesion increases with increasing humidity. Recently, a spate of articles have addressed the humidity issue [7–20]. The picture is by no means unified and the adhesion has been shown to increase [10, 17, 18, 20] or decrease [19, 21] with relative humidity, depending on the work in question. Inevitably though, the surface roughness of the samples proves to be a critical factor in determining the magnitude of the surface forces. This is particularly relevant for AFM studies when the surface roughness, which typically is of the order of a few nanometres, is comparable in size to the Kelvin radius [6]. This is shown schematically in Fig. 2. Ata *et al.* [7] recently showed that the discrepancies between measured adhesion and theoretical predictions could be largely eliminated using Rabinovich's model [22, 23] of asperity contacts to explicitly account for surface roughness.

Another issue with, for example, dry powders is that their rheological properties are dependent both on lateral forces as well as adhesion forces. Certainly plug flow of powders is influenced by particle-wall friction, and the role of particle friction in mechanisms for bed fluidising (a requirement for flow) is still the subject of debate. It is, therefore, instructive to attempt to understand the influence

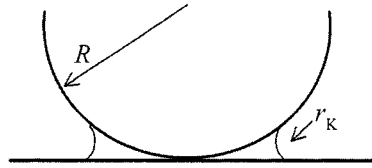


**Figure 1.** Schematic representation of capillary condensation between a smooth sphere and a flat surface.  $R$  is the radius of the sphere,  $r_K$  is the Kelvin radius. A contact angle of  $0^\circ$  is assumed on both surfaces.

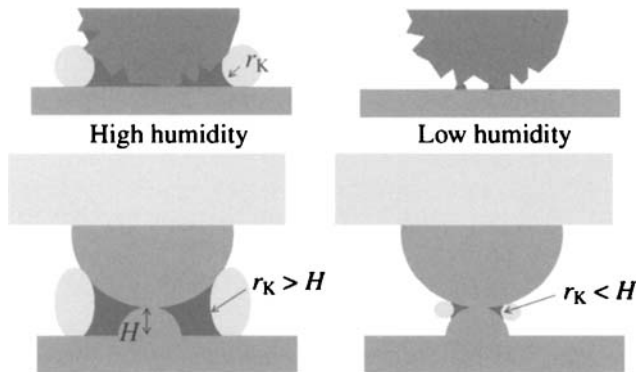


**Figure 2.** Schematic diagram to show how the surface roughness and the RH influence capillary condensation. The surfaces with associated surface roughness can be thought of as the contact of a smooth sphere with a surface bearing asperities of height  $H$  (which is characteristic of the roughness of the two surfaces). Only when the Kelvin radius is larger than  $H$  can a large capillary condensate form with commensurate increase in adhesion.

of capillary condensation on frictional forces. It is worth noting that, although intuitively expected, there is as yet no unambiguous relationship between adhesion (or pull-off) measurements and observed frictional behaviour, even for what might be considered the ‘simplest’ case of interfacial friction. This confusion may be due to the generally overlooked effect of capillary condensation, since a capillary condensate will tend to raise the measured adhesion and possibly change the sliding regime from ‘interfacial’ to ‘lubricated’. Again, the current literature presents diverse results with observations of friction decreasing [11, 13, 24, 25], increasing [15, 26] or being largely insensitive to changes in relative humidity [14]. The role that water plays during interfacial sliding remains a source of contention: on the one hand, lubrication by a liquid water layer is credited as reducing friction as humidity increases, whilst, on the other hand, the opposite phenomenon of increased friction with humidity is attributed to viscous drag due to a water meniscus.

In this work we present measurements of both the adhesion and frictional behaviour of silica surfaces as a function of relative humidity. Using similar substrates for measurements with both sharp tips and macroscopic spherical probes allows us to evaluate the influence of interaction geometry on capillary condensation and its effect on adhesion and friction.



## 2. EXPERIMENTAL

### 2.1. Substrates

The substrates used throughout the work were polished silicon wafers, thermally oxidized to produce a  $\text{SiO}_2$  layer of 170 nm (kindly provided by Dr. Stefan Klintström, University of Linköping, Sweden). AFM imaging revealed an rms roughness of 1–2 nm over a scan size of  $1\ \mu\text{m}^2$ . The silica substrates were cut into  $1\text{-cm}^2$  squares and cleaned by thorough rinsing in water then in ethanol and followed by plasma treatment (PDG-32G Plasma Cleaner, Harrick Scientific, USA) on medium setting for 1 min and placed immediately into the AFM. A water droplet was seen to perfectly wet the substrate after cleaning.

### 2.2. Control of relative humidity

A simple humidity chamber consisting of an air-tight Perspex box was built to house the AFM. Initially the chamber was dried to 0% RH using containers of  $\text{P}_2\text{O}_5$  powder to remove moisture for typically 2 h whilst using a fan to ensure thorough circulation. The humidity was varied by placing containers of various concentrated salt solutions or silica gel inside the chamber and monitored continuously with a humidity probe (Vaisala, Helsinki, Finland). The chamber atmosphere was equilibrated for 1 h, after which the fan was turned off prior to conducting measurements. The temperature remained constant throughout at  $22 \pm 0.2^\circ\text{C}$ .

### 2.3. Colloidal probe preparation

Colloidal probes were prepared and used according to the standardized methodology [27]. Tipless rectangular cantilevers (NSC12, Mikromasch, Tallinn, Estonia) were functionalised by attachment of glass beads ( $R \approx 10\ \mu\text{m}$ ) (Duke Scientific, USA) using a very small amount (pl) of quick setting two-part epoxy resin (Araldite<sup>TM</sup>). Two etched tungsten wires attached to a micromanipulator arm were used to position first a tiny quantity of epoxy and then a glass bead at the tip of the cantilever under microscopic control (Nikon, Japan). The cantilever was left for at least 12 h to allow the glue to fully cure. The functionalised cantilever comprises the so-called colloid probe. The radius of the attached sphere was determined by optical microscopy and this value was used both for normalising adhesion values and in the calculation of frictional forces. Immediately prior to measurement the AFM cantilever was cleaned by rinsing in Milli-Q water then in ethanol then blown dry under nitrogen and finally plasma treated (PDG-32G Plasma Cleaner, Harrick Scientific) on medium setting for 1 min. AFM cantilevers with sharp integrated tips were cleaned in the same way as for the colloid probes. Reverse imaging of a standard spiked calibration sample (Mikromasch) was used to determine the radius of curvature and ensure that the tip had no obvious defects. The tip radii were determined to be around 10–25 nm.

## 2.4. Force measurements

AFM force and friction measurements were carried out using a Nanoscope IIIa Multimode atomic force microscope (Digital Instruments, USA). The normal spring constant of the cantilever was determined from the change in resonant frequency after attachment of a series of tungsten spheres to the end of the cantilever [28]. The normal spring constants were determined to be  $14.5 \pm 0.6$  N/m for the tipless cantilevers and 40 N/m for the cantilevers with tips. A linear correlation was observed between the resonant frequency of the unloaded cantilever and the calculated normal spring constant for 20 cantilevers from the same batch. This indicated a consistent material property of the cantilevers with the slight variation in spring constant being attributed to a difference in the thickness, most likely from the thickness of the reflective coating.

Quantitative measurements of the friction force are possible once the torsional spring constant of the AFM cantilever is known. The cantilever torsional spring constant was determined according to two recently developed calibration protocols. In the method of Feiler *et al.* [29], a glass fibre attached orthogonally to the end of the cantilever provides torque as the cantilever is brought into contact with a flat silicon substrate. The second calibration procedure was a method proposed by Bogdanovic *et al.* [30], in which a second cantilever with integrated tip glued upside on the lower surface acts as a pivot which twists the cantilever as it is brought into contact with the pivot. The procedure was simplified by pressing the cantilever at three contact points only, one in the centre line of the cantilever (where the probe was to be mounted) and one at either side as close as possible to the outer edge. Since the width of the cantilever could be determined accurately using optical microscopy, this avoided the use of the piezo movement to measure the distance. Both calibration methods were in quantitative agreement and yielded values for the torsional spring constant varying between 2.7 and  $4.1 \times 10^{-8}$  N m/rad. There was a linear correlation between the normal and torsional spring constants.

## 2.5. Friction measurements

The friction force was calculated from so-called friction force loops by taking the average friction force between the forward and reverse scan directions as the substrate was moved under the colloidal probe [31]. In all measurements a scan length of 1  $\mu\text{m}$  was used. The friction force was measured as a function of increasing then decreasing load and in some cases as a function of scan rate at constant load.

# 3. RESULTS

The variation in adhesion between a silica sphere and a silica wafer is shown in Fig. 3. The adhesion pull-off force is plotted as a function of relative humidity.

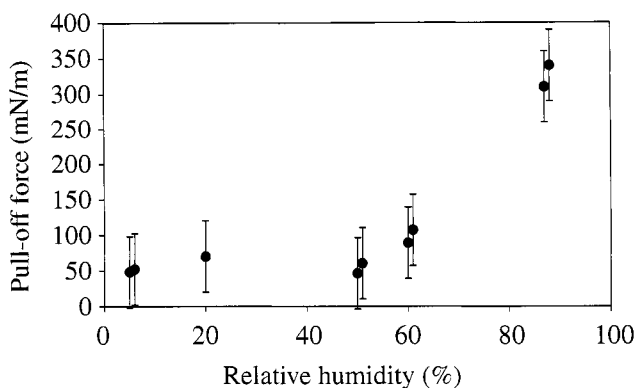


**Figure 3.** Variation of pull-off force (normalized by radius  $R = 10 \mu\text{m}$ ) with RH between silica spheres and a silica substrate. A clear threshold is observed at RH value above 60%.

A clear threshold is observed at about 60% RH above which there is a significant increase in the adhesion. The observation of a marked increase in adhesion above a critical threshold RH has been observed previously in a number of other studies [7, 16, 20]. As discussed earlier, this is in contravention with the predictions from the simplest theory of the capillary adhesion between smooth surfaces in which the adhesion is independent of the Kelvin radius and, hence, the relative humidity. The reported critical RH% threshold varies considerably between different studies which reflects the differences in both surface chemistry and geometry of the substrates employed. However, for measurements on silica substrates (most commonly used for AFM measurements) there is a general consensus of a critical threshold of  $60 \pm 10\%$ . The main reason for discrepancies between measured adhesion forces and theoretical predictions, and indeed a major contributor to variation between AFM studies in general, is inevitably due to surface roughness [7, 8]. If the models of McFarlane and Tabor [32] and, more recently, Rabinovich [22, 23] are applied to account for surface roughness then the resulting observed threshold can be understood in terms of the relative magnitudes of the Kelvin radius and the surface roughness [7].

The variation in pull-off force for the case of a tip interacting with a silica substrate is shown in Fig. 4. Similarly a transition to larger adhesion is observed at relative humidities above 60% though the increase is less dramatic than that observed for the spherical particles, presumably because the number of asperities is smaller. This transition, which is consistent with some other AFM studies of tip–substrate interactions, is again indicative of the critical relationship between the Kelvin radius and asperity height.

The friction force as a function of load between a colloid probe interacting with a silica substrate at various RH is shown in Fig. 5. The main graph shows the friction behaviour as the load is increased, the inset shows the unloading behaviour. Classically, friction–load relationships are linear and intersect the origin, and are characterised by a slope which is defined as the friction coefficient (Amontons law).

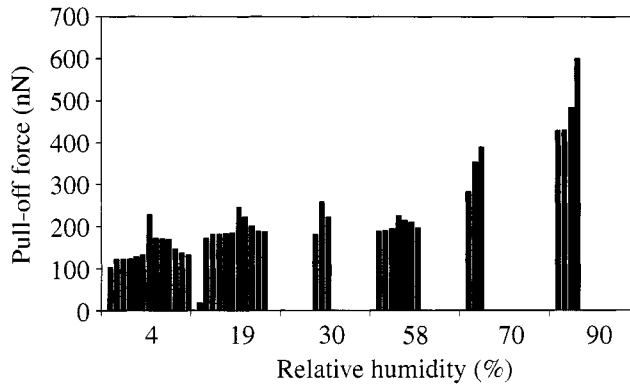


**Figure 4.** Pull-off force for the case of a tip interacting with a silica surface as a function of RH. Once again a threshold is observed at high RH above 60% RH, though the increase is less dramatic than that observed in Fig. 3.

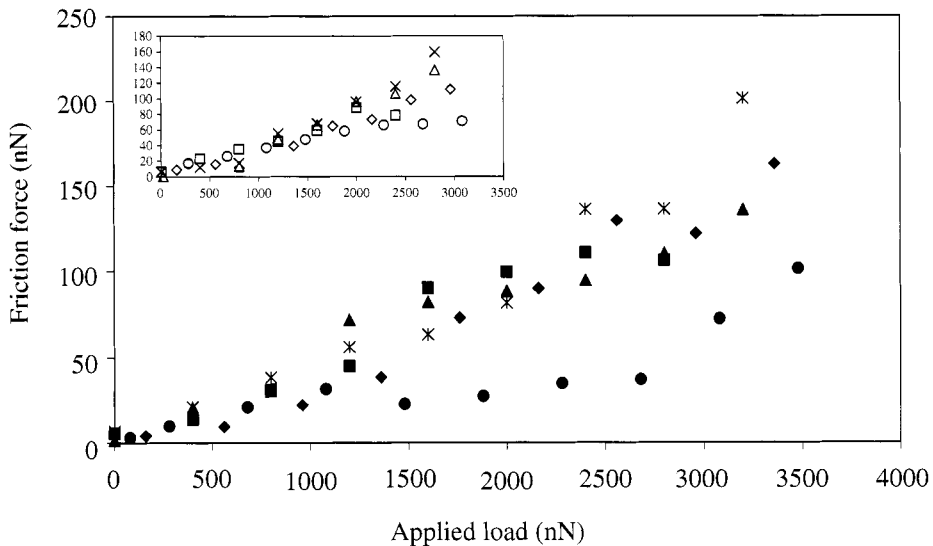


**Figure 5.** Friction force–load relationship of a glass sphere against a silica substrate as a function of RH. The main graph shows the loading data, the inset shows the unloading data. The symbols refer to RH 88% (circles), 70% (diamonds), 60% (triangles), 20% (squares), 5% (crosses). The friction coefficient decreases with increasing humidity with a dramatic decrease above 60% RH. The hysteresis in the friction loops also increases with humidity.

This type of behaviour is indeed observed (except that the lines do not quite intersect the origin, due to the adhesion modifying the effective load) and is qualitatively similar for all RH values. The general trend for the data is a decreasing friction coefficient with increasing humidity. The friction force measured at the highest relative humidity has a significantly lower friction coefficient than at the other relative humidities over most of the loading range but displays an increase in friction

force above applied loads of 3000 nN. The capillary condensate thus appears to act as a lubricant, a point we will address in the Discussion. It is interesting to note that the common association of a higher friction coefficient with a higher adhesion force

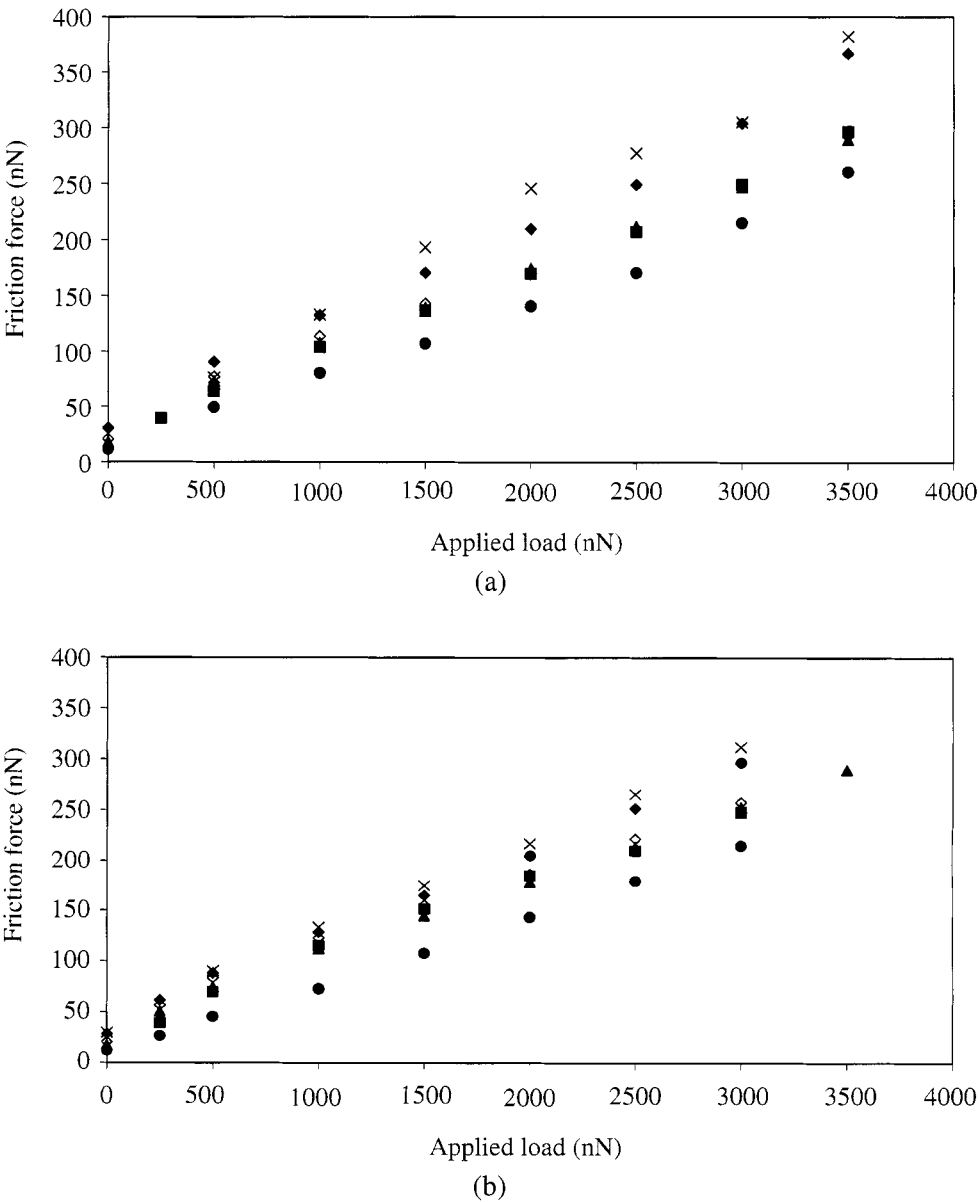


**Figure 6.** Friction force–load relationships for various relative humidities between a tip and a silica substrate during increasing load (a) and decreasing load (b). The symbols refer to RH 88% (circles), 70% (open diamonds), 58% (triangles), 31% (filled diamonds), 20% (squares), 5% (crosses). There is a decrease in the friction coefficient with increasing RH.

is clearly not borne out here since the friction coefficient decreased significantly above the critical RH threshold whereas the adhesion increased dramatically in this RH regime (Fig. 3). In this case though the adhesion is not associated with the surface contact but rather with the surrounding condensate whereas friction occurs as usual at the surface contact.

The case of an AFM tip interacting with an oxidized silicon wafer is shown in Figs 6 and 7. Figure 6a shows the friction–load relationship at different humidities as the load is increased, and Fig. 6b shows the equivalent curves for unloading. The conclusions are the same in each case; the friction force decreases with increasing humidity, though by no means as dramatically as the adhesion changes. Friction coefficients obtained from linear fits to the data vary from 0.087 for 4% RH to 0.063 for 80% (loading curve).

The friction–load relationships were reproducible for all humidities except for those conducted at 4% RH. As seen in Fig. 7 there is a time effect for the case of 4% RH. On the very first friction loading cycle the friction coefficient is initially much lower, but at higher loads it increases dramatically to a higher friction regime in which it remains for subsequent measurements. Note that this effect is obtained again for the same tips if the ambient air is dried again to 0% RH using  $P_2O_5$  and then the system is equilibrated as before; thus, we can rule out the possibility of tip blunting during the first measurement as the cause of the increase in friction force. Instead, we attribute this effect to a harvesting of water as the tip continues to slide across the surface and builds up a water trail along the surface.

The effect of the rate at which the friction force measurements are performed has also been studied. If the capillary condensate was sufficiently developed

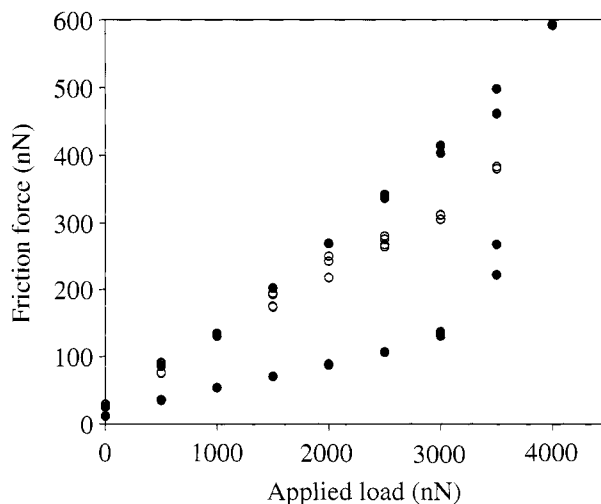


**Figure 7.** Friction force–load relationship between a tip and a silica substrate at a RH of 4% showing the first loading and unloading measurement (filled symbols) and then a subsequent measurement (open symbols) after which the friction coefficient remains fairly constant.

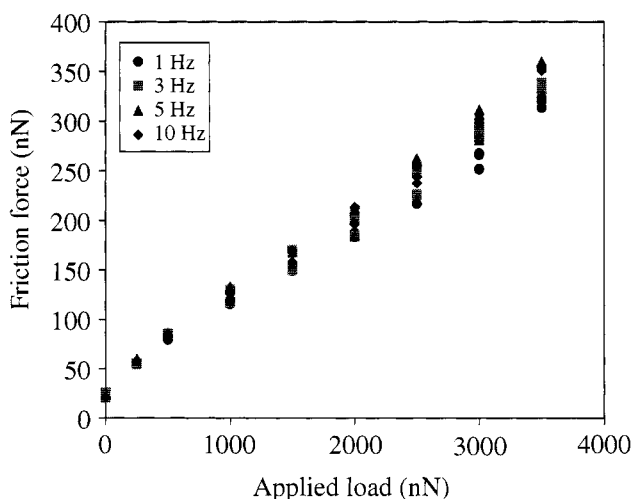


**Figure 8.** Friction force–load relationships between a tip and a silica substrate at 70% RH as a function of scan rate from 1 to 10 Hz.

to behave as a hydrodynamic lubricant then the friction force should decrease with increasing scan rate as predicted by the Stribeck model, and as observed previously [33]. However, for this to occur the capillary condensate would have to be either physically dragged along by the tip or condense rapidly on the timescale of the experiments. Figure 8 shows the friction–load behaviour at 70% RH at scan rates varying from 1 Hz to 10 Hz, i.e., a 10-fold increase in scan speed from  $10\ \mu\text{m/s}$  to  $100\ \mu\text{m/s}$ . There is virtually no variation in the friction over this range of rates whereas in an earlier work involving two silica surfaces immersed in water [33] the friction coefficient was reduced by 25% over the same span. We note that at the lowest humidity studied there is a small increase in the friction coefficient with increasing scan rate which may be attributed to an insufficient amount of liquid in the condensed drop to provide effective lubrication. Evidence that both the scan rate and the amount of liquid in the contact region influence the sliding mechanism is seen clearly in the friction traces with the onset of stick-slip. Generally stick-slip behaviour during sliding is not observed with colloid probe measurements of friction. A notable exception is the work of Cain *et al.* [9] who did measure stick-slip between colloid probes and silica substrates. We did not observe stick-slip motion using colloid probes at any humidity; however, stick-slip phenomenon was observed for measurements using AFM tips over the full range of humidities, though it was most pronounced at the lowest case of 4% RH where stick-slip was observed at all loads. At high humidities the stick-slip behaviour was observed only at high loads. Figure 9 shows a periodic artefact which changes its spatial frequency as the scan rate is stepwise increased from top to bottom at a fixed applied load. Spectral analysis of the different regions of the images indicates that the wavelength changes linearly with scan rate which indicates that the spatial wavelength is the manifestation of a constant temporal frequency. The fact that stick-slip is not

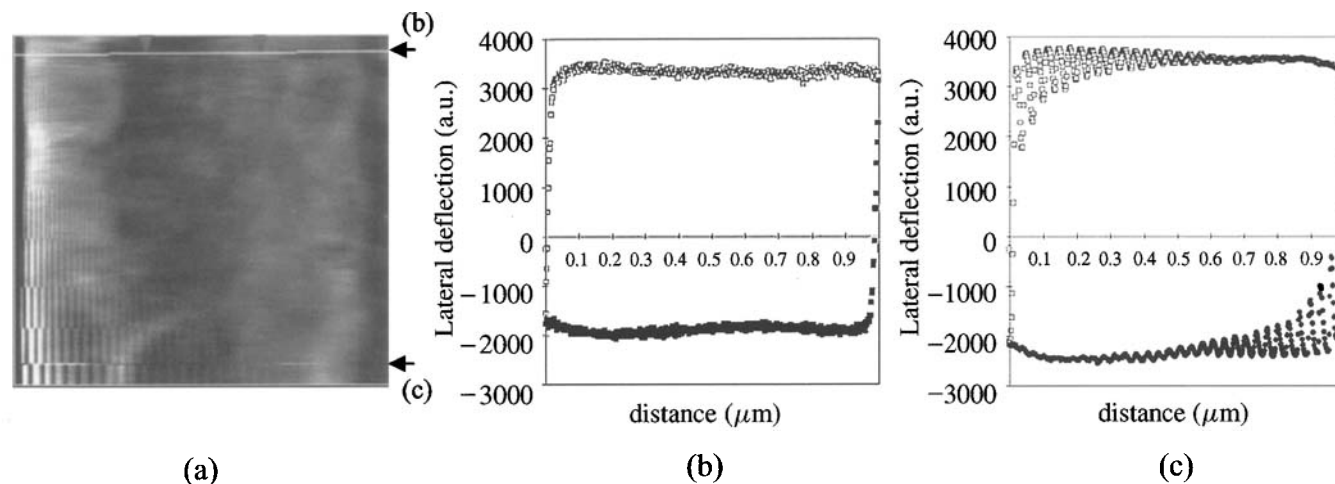


**Figure 9.** (a) A  $1 \times 1 \mu\text{m}$  scan in friction mode (scan angle  $90^\circ$ ) of a silica substrate using a sharp tip at a relative humidity of 60%. The load is unchanged but the scan rate is stepwise increased down the image starting at 1 Hz and increased to 5 Hz in 0.5-Hz steps. The changing spatial frequency corresponds to a constant temporal frequency. (b) and (c) show friction loops taken at 1 Hz and 5 Hz, as indicated by the arrows in (a), plotted as friction deflection signal (arbitrary units) against distance travelled showing no stick-slip behaviour at low scan rates and clear stick-slip behaviour at higher scan rates.



as pronounced at higher humidities is strong evidence for the presence of bound water which modifies the frictional properties somewhat and presumably renders the contact as ‘boundary lubricated’, rather than interfacial friction. The presence of a thin (approximately monolayer) layer of water on silica at atmospheric pressures is hardly controversial and has been described often in the past.

#### 4. DISCUSSION

The results of both Ando [15] (where a truncated tip interacted with rather large artificial asperities) and Optiz *et al.* [34] (a tip interacting with both hydrophilic and hydrophobic silicon under UHV conditions as well as in air) indicate that at low humidity the friction force is lower than at higher humidities. Optiz *et al.* showed that under UHV a layer thickness corresponding to a water molecule was present whereas in ambient conditions this was closer to 10 molecular layers. These authors have argued that the increase in friction force is due to viscous effects in the water surrounding the contact point (Optiz *et al.* tend to the view that the contact itself is solid–solid, though the evidence for this is unclear). These observations are supported by the fact that our ‘first contact’ friction run in Fig. 6 was initially at low friction, but on increased time in contact the friction behaviour rapidly translated into a more reproducible higher friction regime. We interpret this as a form of harvesting, any condensate which is formed and deposited in the sliding trail is gradually harvested by the sliding tip [35]. Despite the low relative humidity, any deposits therefore appear not to evaporate spontaneously but to be stable [35–37]. The increased friction is thus due to the same viscous dissipation as inferred by Optiz *et al.* and Ando. At higher RH values, however, we clearly observe a decrease in friction, which we ascribe to lubrication. That is to say:

- at very low RH and short contact times only a thin, rigidly adsorbed water layer is present on the surface with a solid (elastic)-like response so the surfaces slide with little dissipative loss;
- as the contact time is increased or the relative humidity is raised, liquid-like water is present around the contact and leads to increased dissipation and commensurately higher friction;
- at high relative humidities the contact can be considered to be immersed in water, a thicker water film will be adsorbed onto the (isolated) surfaces and while friction appears not to be reduced due to hydrodynamic lubrication, the separation of the surfaces is likely to be larger for a given load and the water layer thickness may be sufficient to act as a boundary layer lubricant.

The fact that at low humidity we observe stick-slip behaviour at all loads gives further support to the idea that the thin layer of adsorbed water behaves like a rigid film. At higher humidities, however, when the volume of the capillary condensate increases significantly, the viscosity of the liquid layer ‘damps out’ the stick-slip. At high loads, the stick-slip behaviour returns, suggesting that at the higher loads

bound water is increasingly displaced until the surfaces reach a separation of only a few water molecules. We note that Salmeron and co-workers [21, 36, 38], backed by spectroscopic evidence, invoke the concept of a structural change in the water adsorbed onto mica in going from a tightly bound rigid ice-like structure 'phase I' at low humidities to a fluid-like island layer 'phase II' at higher humidities.

It is interesting that for a tip interacting with a surface, which might be considered a good model for a single asperity contact, the adhesion is not constant with RH, as would be predicted by the simple model in equation (2), which is appropriate for smooth bodies (or single asperity contacts). Since the trend is the same as for a glass sphere we assume that the explanation for this is the same, i.e., there is a surface roughness effect even at that scale and when the Kelvin radius exceeds the typical asperity size, the contact is flooded with water and an increased adhesion is observed. We note that irrespective of which experimental geometry is employed, there is an additional effect i.e., the amount of adsorbed (as distinguished from capillary condensed) water on each surface will also increase with increasing humidity, even at large separations (see friction force discussion above) which will also affect the adhesion.

An interesting aspect of the friction-load relationships is their apparent linearity despite adhesion due to capillary condensation. Previously, it has been shown that friction measurements of adhesive contacts show a contact area dependence rather than a load dependence (at least at low loads) see, e.g., Refs [39, 40] and that the area can be described well by contact mechanics theories. Such friction-load relationships are characterised by a decreasing gradient with increasing load, eventually becoming linear at higher applied loads as the contact area asymptotes. Such observations have provided the hitherto absent proof that the dissipative frictional mechanism is directly related to the true area of contact, a fact that Amontons law, with its apparent area independence had long disguised. In this case we do not see a strong deviation from linearity and this can be easily explained in the following way: while the interaction between the surfaces as a whole is adhesive (the Laplace pressure acts over the area covered by the condensate), the actual contact of the surfaces themselves is not necessarily adhesive. Two glass or silica surfaces, for example, interacting in pure water do not adhere due to the presence of hydration forces [41–48]. It is thus inappropriate to invoke contact mechanics theories for adhesive bodies (which necessarily involve a single asperity contact) to describe the area of contact; rather the friction is expected to continue to follow the multi-asperity contact behaviour where increasing load leads to increasing numbers of asperity contacts. This, of course, is the Amontonsian regime of linear relationship between load and friction, and is indeed observed, except at the very highest humidity. Note that both the multi-asperity contact model of friction [49] and the single asperity contact model predict a linear friction-load relationship at high loads, in the former case due to increased asperity contacts, and in the latter case due to the increased work of separating the surfaces to permit sliding as predicted by the cobblestone model [50–52].

## 5. CONCLUSIONS

The behaviour of an AFM tip and a glass sphere with curvature in the micrometer range is qualitatively similar both in terms of friction and adhesion for their variation with relative humidity. This raises the question as to whether an AFM tip can be treated as a model for a single asperity interacting with a surface. We find it implicit in this result that, for example, the non-linear adhesion behaviour is determined by the same mechanism in each case. If the mechanism is correct, i.e., a marked increase in adhesion is associated with the Kelvin capillary radius exceeding the surface roughness and permitting contact flooding, then a direct consequence must be that even the tip-surface contact is multiasperity in nature.

The fact that the frictional behaviour also follows the same trend for both tip and sphere implies that although the volumes of capillary condensates must be very different, the influence that the condensed water has on the sliding mechanisms is similar in the two cases.

At a fundamental level we also note for the benefit of the continuing debate as to the relationship between friction and adhesion, that while the adhesion increases dramatically above a threshold value of RH, the friction decreases albeit less dramatically. This raises an important distinction between the global and local adhesion, the net interaction between the probes and surface is attractive due to the presence of a capillary condensate, but the interaction between the contacts themselves is net repulsive, rendering any treatment by contact mechanics theory irrelevant.

## Acknowledgements

A. F. gratefully acknowledges Unilever Research, Port Sunlight, UK for partial funding during 2001–2002 when this work was conducted. M. R. acknowledges support from BiMac, the Biofibre Materials Centre at KTH.

## REFERENCES

1. W. A. Ducker, T. J. Senden and R. M. Pashley, *Nature* **353**, 239–241 (1991).
2. J. N. Israelachvili and D. Tabor, *Progr. Surf. Membr. Sci.* **7**, 1–55 (1973).
3. L. R. Fisher and J. N. Israelachvili, *Nature* **277**, 548–549 (1979).
4. L. R. Fisher and J. N. Israelachvili, *J. Colloid Interf. Sci.* **80**, 528–541 (1981).
5. H. K. Christenson, *J. Colloid Interf. Sci.* **121**, 170–178 (1987).
6. J. Israelachvili, *Intermolecular and Surface Forces*. Academic Press, London (1991).
7. A. Ata, Y. I. Rabinovich and R. K. Singh, *J. Adhesion Sci. Technol* **16**, 337–346 (2002).
8. E. R. Beach, G. W. Tormoen, J. Drelich and R. Han, *J. Colloid Interf. Sci.* **247**, 84–99 (2002).
9. R. G. Cain, N. W. Page and S. Biggs, *Phys. Rev. E* **64**, 016413 (2001).
10. X. Xiao and L. Qian, *Langmuir* **16**, 8153–8158 (2000).
11. M. Binggeli and C. M. Mate, *Appl. Phys. Lett.* **65**, 415–417 (1994).
12. R. Price, P. M. Young, S. Edge and J. N. Staniforth, *Int. J. Pharm.* **246**, 47–59 (2002).
13. F. Tian, X. Xiao, M. M. T. Loy, C. Wang and C. Bai, *Langmuir* **15**, 244–249 (1999).

14. L. Sirghi, *Appl. Phys. Lett.* **82**, 3755–3757 (2003).
15. Y. Ando, *Wear* **238**, 12–19 (2000).
16. S. Biggs, R. G. Cain, R. R. Dagastine and N. W. Page, *J. Adhesion Sci. Technol.* **16**, 869–885 (2002).
17. T. Thundat, X.-Y. Zheng, G. Y. Chen, S. L. Sharp, R. J. Warmack and L. J. Schowalter, *Appl. Phys. Lett.* **63**, 2150–2152 (1993).
18. D. L. Sedin and K. L. Rowlen, *Anal. Chem.* **72**, 2183–2189 (2000).
19. T. Eastman and D.-M. Zhu, *Langmuir* **12**, 2859–2862 (1996).
20. R. Jones, H. M. Pollock, J. A. S. Cleaver and C. S. Hodges, *Langmuir* **18**, 8045–8055 (2002).
21. J. Hu, X. D. Xiao, D. F. Ogletree and M. Salmeron, *Science* **268**, 267–269 (1995).
22. Y. I. Rabinovich, J. J. Adler, A. Ata, R. K. Singh and B. M. Moudgil, *J. Colloid Interf. Sci.* **232**, 17–24 (2000).
23. Y. I. Rabinovich, J. J. Adler, A. Ata, R. K. Singh and B. M. Moudgil, *J. Colloid Interf. Sci.* **232**, 10–16 (2000).
24. J. Hu, X. D. Xiao, D. F. Ogletree and M. Salmeron, *Surf. Sci.* **327**, 358–370 (1995).
25. M. Binggeli and C. M. Mate, *J. Vac. Sci. Technol. B* **13**, 1312–1315 (1995).
26. E. Riedo, F. Levy and H. Brune, *Phys. Rev. Lett.* **88**, 185505 (2002).
27. J. Ralston, I. Larson, M. W. Rutland, A. Feiler and M. Kleijn, *Pure Appl. Chem.* (2005) (in press).
28. J. P. Cleveland, S. Manne, D. Bocek and P. K. Hansma, *Rev. Sci. Instrum.* **64**, 403–405 (1993).
29. A. Feiler, P. Attard and I. Larson, *Rev. Sci. Instrum.* **71**, 2746–2750 (2000).
30. G. Bogdanovic, A. Meurk and M. W. Rutland, *Colloid. Surf. B: Biointerf.* **19**, 397–405 (2000).
31. A. Feiler, I. Larson, P. Jenkins and P. Attard, *Langmuir* **16**, 10269–10277 (2000).
32. J. McFarlane and D. Tabor, *Proc. Roy. Soc. Lond. Ser. A* **202**, 224–243 (1950).
33. A. Feiler, M. A. Plunkett and M. W. Rutland, *Langmuir* **19**, 4173–4179 (2003).
34. A. Opitz, S. I. U. Ahmed, J. A. Schaefer and M. Scherge, *Surf. Sci.* **504**, 199–207 (2002).
35. R. D. Piner and C. A. Mirkin, *Langmuir* **13**, 6864–6868 (1997).
36. J. Hu, X. D. Xiao, D. F. Ogletree and M. Salmeron, *Surf. Sci.* **344**, 221–236 (1995).
37. S. Rozhok, P. Sun, R. Piner, M. Lieberman and C. A. Mirkin, *J. Phys. Chem. B* **108**, 7814–7819 (2004).
38. L. Xu, A. Lio, J. Hu, D. F. Ogletree and M. Salmeron, *J. Phys. Chem. B* **102**, 540–548 (1998).
39. G. Bogdanovic, F. Tiberg and M. W. Rutland, *Langmuir* **17**, 5911–5916 (2001).
40. A. Homola, J. N. Israelachvili, P. M. McGuiggan and M. L. Gee, *Wear* **136**, 65–83 (1990).
41. P. Hartley, in: *Atomic Force Microscopy*, R. S. Farinato and P. L. Dubin (Eds), pp. 253–286. John Wiley, New York, NY (1999).
42. P. Hartley, I. Larson and P. Scales, *Langmuir* **13**, 2207 (1997).
43. R. Horn, D. Smith and W. Haller, *Chem. Phys. Lett.* **162**, 404 (1989).
44. I. Larson, C. Drummond, D. Chan and F. Grieser, *Langmuir* **13**, 2109 (1997).
45. G. Vigil, Z. Xu, S. Steinberg and J. Israelachvili, *J. Colloid Interf. Sci.* **165**, 367–385 (1994).
46. W. A. Ducker, T. J. Senden and R. M. Pashley, *Langmuir* **8**, 1831–1836 (1992).
47. M. W. Rutland and T. J. Senden, *Langmuir* **9**, 412–418 (1993).
48. M. W. Rutland and J. L. Parker, *Langmuir* **10**, 1110–1121 (1994).
49. F. Bowden and D. Tabor, *The Friction and Lubrication of Solids*. Oxford University Press, Oxford (1950).
50. G. M. McClelland, *Adhesion and Friction*. Springer, Berlin (1989).
51. G. A. Tomlinson, *Philos. Magn.* **7**, 905–939 (1929).
52. J. Israelachvili, in: *Handbook of Micro/Nanotribology*, B. Bhushan (Ed.), p. 309. CRC Press, Boca Raton, FL (1995).

## Scanning force microscopy investigation of liquid structures and its application to fundamental wetting research

S. HERMINGHAUS<sup>1,\*</sup> T. POMPE<sup>2</sup> and A. FERY<sup>2</sup>

<sup>1</sup>*Abt. Angewandte Physik, Universität Ulm, D-89069 Ulm, Germany*

<sup>2</sup>*Max-Planck-Institut für Kolloid- und Grenzflächenforschung, D-14424 Potsdam-Golm, Germany*

**Abstract**—The possibility of determining the topography of liquid profiles by scanning force microscopy (SFM) in tapping mode is discussed in detail as to its possible mechanism and accuracy. Applications of this technique to the investigation of contact line tensions and effective interface potentials are presented. Two complementary methods, both based on SFM of the liquid topography, are demonstrated for determining contact line tensions. The values obtained are within the theoretically expected range.

**Keywords:** Scanning force microscopy; wetting; line tension.

### 1. INTRODUCTION

We are all accustomed to liquid droplets being spherical, due to the tendency of the surface tension to minimize the surface area at fixed volume. In some contrast, Fig. 1 shows a number of macroscopic sessile droplets sharing the striking feature of being faceted along the vertical direction. This is because the substrate, a standard silicon wafer with a native oxide layer, has been structured chemically by microcontact printing. It bears vertical hydrophobic stripes about 200 nm in width, separated by hydrophilic domains of similar width. The whole sample is thus stripewise patterned as to its wettability and the spatial period of the pattern is 400 nm, well below the optical resolution of a standard optical microscope. Nevertheless, the impact of this

---

\*To whom correspondence should be addressed. Phone: +49-731-502-2950; Fax: +49-731-502-2958; E-mail: stephan.herminghaus@physik.uni-ulm.de

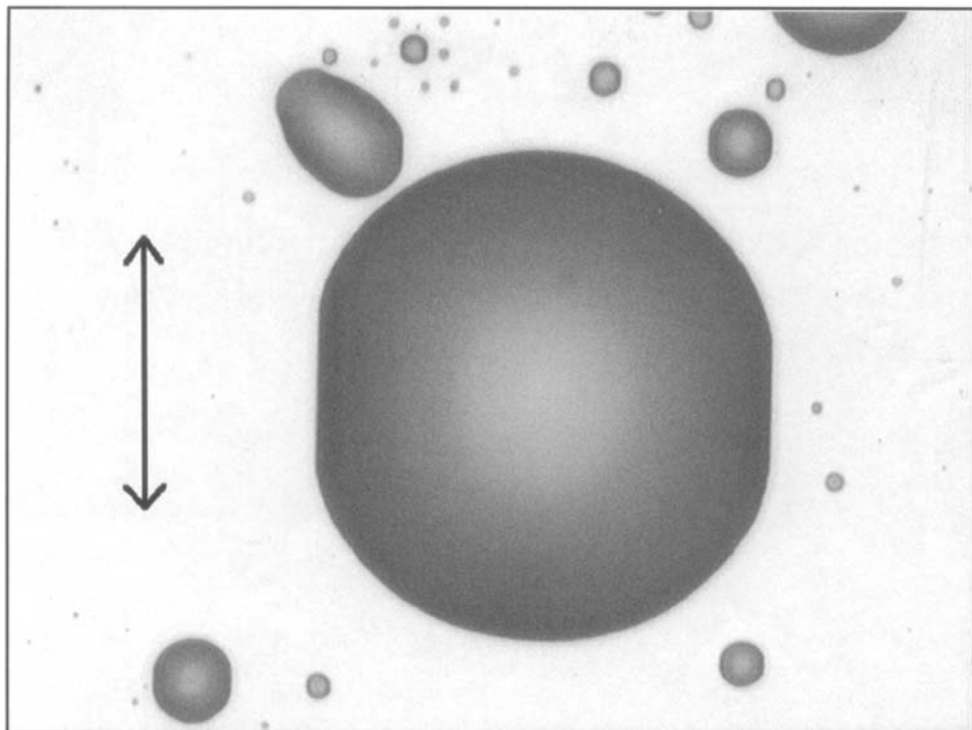


**Figure 1.** Optical micrograph ( $150\ \mu\text{m} \times 110\ \mu\text{m}$ ) of hexaethylene glycol droplets deposited on a substrate bearing wettability stripes (periodicity: 400 nm) in the direction of the arrow.

chemical structure on the substrate (which is almost perfectly flat) on the shape of the drops is quite obvious and easily visible. This simple experiment shows that in order to understand wetting even on a macroscopic scale, it is indispensable to study it on very small scales, down to those governed by, and comparable to, the typical range of wetting forces. It is therefore natural to consider modern techniques of submicrometer scale microscopy, such as scanning probe or electron microscopy, as important methods for investigating the fundamentals of wetting phenomena.

Wetting is a rather general concept and applies whenever one asks for the stability and morphology of small amounts of a substance at a given interface. It is most significant, and has thus mostly been studied, with liquid rather than with solid substances. Consequently, if one sets out to study wetting phenomena in detail, one is faced with the substantial problem of imaging objects as delicate as liquid surface profiles on molecular scales. While solid samples are usually sturdy enough to withstand the assault of a scanning probe tip or a many-kilovolt electron beam, this is not the case with liquid structures. Our first concern must therefore be to find an imaging technique of sufficient spatial resolution which is soft enough to leave the liquid surface profile to be imaged unchanged.

## 2. FORCE MICROSCOPY INVESTIGATION OF LIQUIDS

### 2.1. Imaging in 'tapping mode'

Let us discuss in some detail the applicability of scanning force microscopy (SFM) to our problem. Since its development in 1986 [1], SFM has found applications in many different branches of science. The common feature of classic SFM techniques is a tip with a small radius of curvature (usually a few nanometers) probing the sample, which is mounted on a cantilever with a typical spring constant in the N/m range. The forces of interaction of the sample with the tip result in a deflection of the cantilever, which is measured and controlled with Ångstrom accuracy.

The necessity of imaging particularly soft samples, for example in biology and biophysics, led to the development of non-contact [2] and tapping mode imaging [3–5]. In tapping mode, the tip is vibrated by exciting the cantilever near its resonance frequency (typically 100–300 kHz). Typical amplitudes are 10–100 nm and the interaction of the tip with the sample surface results in a characteristic damping of the cantilever. The tip touches the sample only close to the turning point of its vibration. As a consequence, the interaction of the tip with the sample in tapping mode is particularly soft, which enables the imaging of particularly soft surfaces [3, 6–17]. In addition, it was shown that the phase shift between the signal exciting the cantilever and the motion actually carried out by the cantilever could provide valuable information about the mechanical properties of the sample [18]. However, the details of the damping mechanism in tapping mode are still controversial and much work has been dedicated to its understanding [19–30].

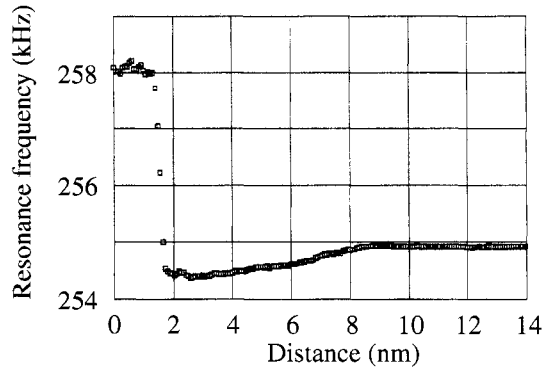
For SFM of liquid surfaces, we have carried out a number of experiments to elucidate the nature of the interaction of the tip with the sample in tapping mode and to evaluate this technique for its applicability to quantitative investigations of liquid surface topographies. It is observed that when the tip approaches the liquid surface, the resonance frequency of the cantilever changes in a characteristic way. If the drive frequency is chosen as the resonance frequency of the free cantilever (at a large distance between the tip and the sample), the shift of the resonance frequency of the system can be calculated from the measured amplitude of vibration and phase according to

$$\omega_{\text{res,d}} = \sqrt{\omega_{0,\text{d}}^2 + \frac{(\omega_{\text{res,f}}^2 - \omega_{0,\text{d}}^2)^2}{2\omega_{\text{res,f}}^2} \left(1 - \frac{1}{\cos^2 \phi_{\text{d}}}\right)} \quad (1)$$

with

$$\omega_{0,\text{d}} = \omega_{\text{res,f}} \sqrt{1 + \frac{A_{\text{f}}}{A_{\text{d}}} \frac{\sqrt{4Q_{\text{f}}^2 - 1}}{2Q_{\text{f}}^2 - 1} \cos \phi_{\text{d}}}, \quad (2)$$

where  $A_{\text{f}}$ ,  $Q_{\text{f}}$ , and  $\omega_{\text{res,f}}$  denote the amplitude, quality factor, and resonance frequency of the free cantilever, while  $A_{\text{d}}$  and  $\phi_{\text{d}}$  denote the amplitude and phase shift of the damped cantilever, respectively.



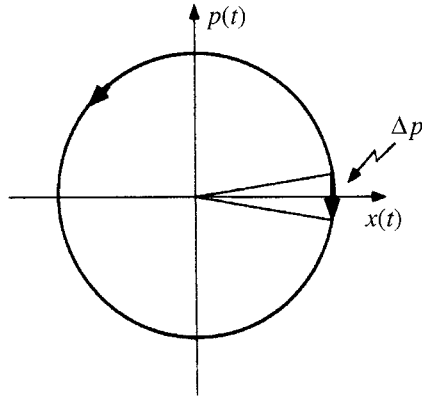
**Figure 2.** Resonance frequency  $\omega_{\text{res}}$  of the cantilever as a function of the distance between the tip and the liquid surface. It has been calculated from the measured quantities, as explained in the text.  $\omega_{\text{res}}$  first decreases with decreasing distance and then increases abruptly (within the accuracy of the measurement) to a higher resonance frequency which then remains constant. For distances in this latter regime, the amplitude of the tip is still measurable ( $\approx 2$  nm), but strongly reduced ( $A_f = 12$  nm).

Figure 2 shows a typical data set obtained on an aqueous solution of  $\text{P}_2\text{O}_5$  [15], with cantilever parameters  $Q_f = 166$ ,  $k \approx 20$  N/m (the spring constant of the cantilever), and  $\omega_{\text{res},f} = 254.9$  kHz. Qualitatively, one finds a regime of shift towards lower resonance frequencies at large distances and a sharp transition towards a higher resonance frequency regime at smaller distances. The first regime is used for imaging and is the one to be discussed in more detail. At amplitudes used for imaging, one finds typical resonance frequency shifts up to 500 Hz. From these data, it is possible to derive the momentum transfer from the tip onto the sample. In phase space, the trajectory of the freely oscillating cantilever can be described by a circle, as sketched in Fig. 3. When the tip interacts with the sample, the trajectory experiences a slight displacement, parallel to the momentum axis of the phase plot. Since the interaction takes place at the turning point of the cantilever, this displacement is tangential to the trajectory. Consequently, there is a direct relationship between the shift,  $\Delta\omega = \omega_{\text{res},f} - \omega_{\text{res},d}$ , of the resonance frequency of the system and the momentum transfer per cycle,  $\Delta p$ :

$$\frac{\Delta\omega}{\omega_{\text{res}}} = \frac{\Delta p}{2\pi p_{\text{max}}}, \quad (3)$$

where  $p_{\text{max}} = kA_d/\omega_{\text{res}}$  is the maximum momentum of the cantilever. It is now possible to calculate the average force,  $\bar{F}$ , that the tip exerts on the liquid surface. Since this is given by the average momentum transfer per cycle, we have  $\bar{F} = \frac{\omega_{\text{res}}}{2\pi} \Delta p = kA_d \frac{\Delta\omega}{\omega_{\text{res}}}$ . Inserting the system characteristics above, we see that for the experiment represented by Fig. 2, the maximum average force was about  $3 \times 10^{-10}$  N. The fact that the resonance frequency is reduced by the proximity of the sample tells us that the force must be attractive, not repulsive.





**Figure 3.** Phase space representation of the cantilever motion. The momentum transfer between the tip and the sample takes place at the turning point, such that the corresponding translation is collinear to the trajectory.

Let us see how this is expected to affect the liquid topography to be investigated. Assuming that the liquid adjusts slowly to the average force to yield a zero mean curvature surface, the latter will be described rather well by a logarithmic profile,  $f(r) = \frac{\bar{F}}{2\pi\sigma} \ln \frac{r}{R}$ , where  $r$  denotes the lateral distance from the tip,  $\sigma$  is the surface tension of the liquid, and  $R$  is the dimension of the liquid object to be imaged, which may be a few micrometers. Inserting the above numbers, one sees that if one is working at a small detuning of, say,  $\Delta\omega < 100$  Hz, the distortion of the liquid surface is less than 5 nm.

Up to now, we have not specified what type of forces gives rise to the momentum transfer and to the detuning of the tip; all we know is that they must be attractive. If these forces are merely the van der Waals forces between the tip and the substrate, no noticeable dissipation would be expected. To check this, we performed phase shift measurements during imaging. As is well known, the average power,  $\bar{P}$ , dissipated in the sample during imaging can be calculated from these data. Provided that the cantilever motion is sinusoidal, it can be shown that [27]

$$\bar{P} = \frac{1}{2} \frac{k A_d^2 \omega}{Q_f} \left[ \left( \frac{A_d}{A_f} \right) \sin \phi_d - 1 \right]. \quad (4)$$

$A_d$ ,  $A_f$ ,  $\omega$ ,  $Q_f$ , and  $\phi_d$  can be measured, and thus the energy dissipated in the sample during a tapping cycle can be determined.

Figure 4 shows the measured topography of a liquid drop on a flat surface, along with the energy dissipation by the interaction of the tip with the sample. The average dissipated power  $\bar{P}$  equals  $9.2 \times 10^{-13}$  W, which gives an energy dissipation per cycle of  $3.3 \times 10^{-18}$  J ( $\approx 20$  eV). We thus indeed have substantial dissipation, which shows that the reduction in amplitude, which is used by the feedback loop in the imaging process, is not just due to the detuning of the cantilever resonance, but also to its damping.

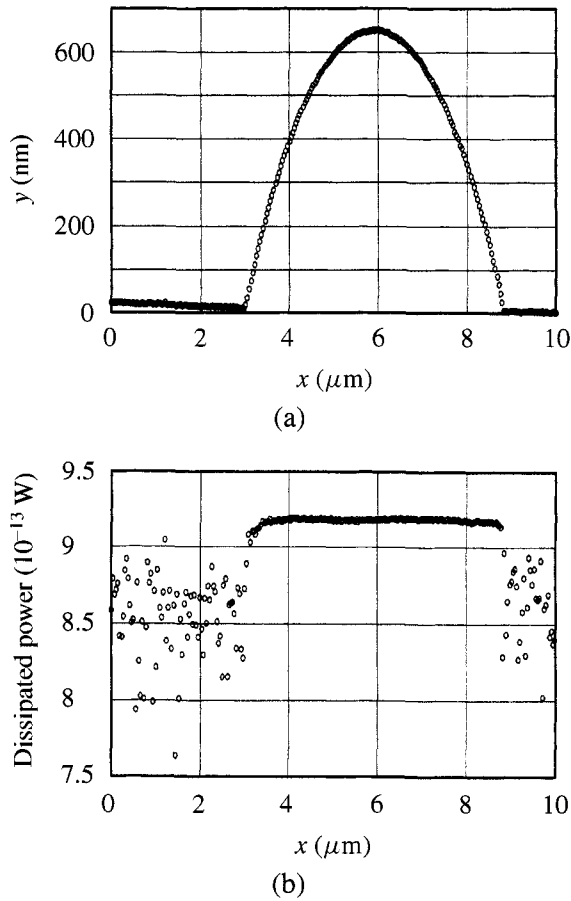


**Figure 4.** (a) Cross-section of the topography of a triethylene glycol drop on a silicon wafer substrate. (b) Dissipated power for each point of the cross-section. It was obtained from the phase shift measured simultaneously with the topography, as explained in the text.

## 2.2. Capillary force model

The presence of an attractive force which is connected to noticeable damping leads us to believe that the forces, which give rise to these effects are capillary forces and that a nanoscopic liquid neck forms whenever the tip comes close to the liquid surface [17]. Let us elaborate on this model in some detail, in order to check whether its predictions are in accordance with our findings. The change in energy upon formation of a liquid neck between a liquid surface and an SFM tip may be estimated using the simplified picture sketched in Fig. 5. The tip is approximated by a paraboloid with a minimal radius of curvature,  $\rho$ , and a distance  $D$  from the flat liquid surface, and the liquid neck is approximated by a cylinder of liquid with

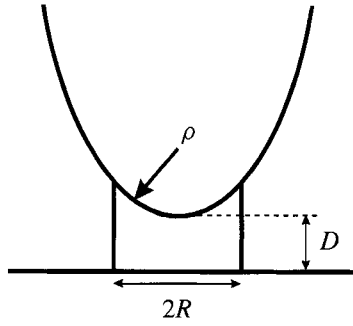


**Figure 5.** Schematic drawing of capillary formation in the model described in the text. The tip is approximated by a paraboloid of radius of curvature  $\rho$ ; at a distance  $D$  from the surface, the capillary is approximated by a cylindrical column of liquid with radius  $R$ .

radius  $R$ . The excess energy  $\Delta E$  required to form the liquid neck can be written as

$$\frac{\Delta E}{\pi \rho^2 \sigma} = -R^2 - 2 \cos \Theta \int_0^R r \sqrt{1 + r^2} dr + 2R(D + R^2/2), \quad (5)$$

where  $r$  is the lateral distance from the center of the neck and  $\Theta$  is the contact angle of the liquid with the tip material. All quantities are taken in units of  $\rho$ . The first term on the right-hand side of equation (5) describes the reduction of the liquid/air interfacial area at the base of the neck. The second term represents the energy contribution of the interface between the tip and the neck and the third term describes the energy to be expended for the creation of the outer surface of the neck. It is clear that equation (5) represents a simplified model of the liquid neck formation between the tip and the sample, since in reality the neck surface certainly has a non-vanishing 'vertical' curvature [31, 32]. However, we found that refinement of the model neck geometry, or taking into account the effects of a contact line tension, did not change the results appreciably. This suggests that equation (5) captures the essential physics involved.

What is the typical size of a liquid neck forming within the gap between the sample and the tip? This can be estimated by considering the first derivative of  $\Delta E$  with respect to the neck radius,  $R$ , which is given by

$$\frac{1}{2\pi \rho^2 \sigma} \frac{d\Delta E}{dR} = D - R \left( 1 + \sqrt{1 + R^2} \cos \Theta - \frac{3}{2} R \right). \quad (6)$$

Its zeros for positive  $R$  reveal the size of the neck which will form. For  $D = 0$ , it is readily seen that the neck radius will be at most 2.4, and for  $\cos \Theta = 0$ ,  $R = 2/3$ . When the tip is removed again from the surface in the course of its oscillation, the neck will break off again at a certain distance,  $D_c$ . This is reached when the two zeros of the right-hand side of equation (6) with  $R > 0$  merge to one degenerate zero, since at this point there is no longer a local minimum in the neck energy at finite  $R$ . This is the case when  $D_c = \max[R(1 + \sqrt{1 + R^2} \cos \Theta - \frac{3}{2} R)]$ , which is smaller than 0.92 for all values of  $\Theta$ .

The surface energy of a liquid object of these dimensions is of the order of a few tens of an electron-volt, if a radius of curvature of 10 nm (manufacturer's specification) is assumed. This is in good agreement with the experimentally determined dissipation of about 20 eV per cycle. The capillary force of this neck is a few nanonewtons, which is consistent with an average force of the order of a tenth of a nanonewton. Finally, it should be noted that the lateral resolution that we could obtain with this technique was between 2 and 10 nm, in qualitative accordance with the lateral extension of the neck.

In order to demonstrate that the liquid profiles obtained by imaging in tapping mode are physically reasonable, we had already shown that the image profiles of liquid droplets small enough for gravity to be negligible were perfectly spherical within experimental accuracy [15]. A final ambiguity within this test is that the contact angle had to be used as a fitting parameter, since the droplet was necessarily too small to be simultaneously imaged with optical equipment. To close this gap, we have performed measurements of the contact angle at the contact line of a larger drop, both optically and by SFM. With SFM, we measured a contact angle of  $\Theta_{\text{SFM}} = 46.2 \pm 0.5^\circ$ ; the value from the optical measurement was  $\Theta_{\text{opt}} = 46 \pm 1^\circ$ . Hence there is perfect agreement between the optical and SFM profiles.

### 3. APPLICATION OF SFM TO LIQUID CONTACT LINES

#### 3.1. The contact line tension

Let us now apply this technique to liquid structures appearing in wetting science in order to gain insight into the microscopic details of wetting forces and their impact on macroscopic wetting phenomena. In particular, we want to tackle the problem of determining the contact line tension, i.e. the excess free energy of a three-phase contact line. This is probably the most controversial quantity in wetting science, which is mainly due to its poor accessibility. Theory predicts that typical values of the contact line tension,  $\tau$ , should be in the range of a few tens of piconewtons [33–39]. The characteristic length scale,  $l$ , at which these forces become important can readily be obtained by comparison with typical values of interfacial tensions,  $\sigma$ , yielding  $l = \tau/\sigma \approx 10^{-10} \text{ N}/10^{-2} \text{ N m}^{-1} = 10 \text{ nm}$ . At much larger scales, interfacial tensions are expected to dominate all measurements of line tension effects and particular care must be taken in the experiments. The classical approach for tackling the problem is to investigate the dependence of the contact angle of small sessile droplets on their size. The smaller a droplet becomes, the larger the effect of the contact line tension on its shape. For a positive line tension, the droplet base is contracted, which gives rise to an increased value of the contact angle. This is expressed by the modified Young equation for a liquid droplet on a plane solid surface, which reads

$$\cos(\Theta) = \cos(\Theta_{\text{Young}}) - \frac{1}{\sigma} \frac{\tau}{R}, \quad (7)$$

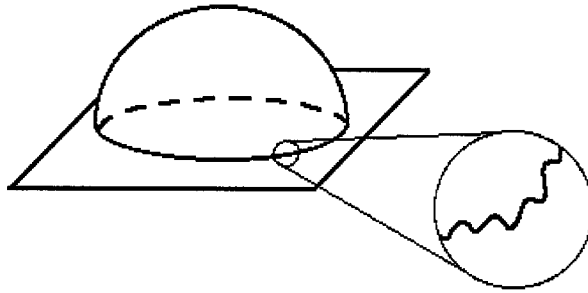


**Figure 6.** Sketch of a macroscopic liquid droplet on a microscopically heterogeneous surface. Optical techniques would yield an apparent radius of curvature of the contact line from the base of the macroscopic droplet. The real radius of curvature of the contact line (from the local corrugations) is beyond their resolution.

where  $\Theta$  is the actual contact angle that the droplet forms with the substrate and  $\Theta_{\text{Young}}$  is the contact angle which would be derived from Young's equation, i.e. for a straight contact line, or infinitely large drop.  $R$  is the radius of curvature of the (circular) contact line.

Assuming the theoretically predicted values of contact line tension to be true, one is faced with the necessity of investigating extremely small droplets in order for the change in contact angle to be measurable. For instance, for a water droplet, a radius of contact line curvature of 20 nm on a substrate with Young's contact angle of  $30^\circ$  gives rise to a change in the contact angle (with respect to its value for a straight contact line) of only  $1^\circ$  when a contact line tension of  $10^{-11}$  N is assumed. In marked contrast, experiments have been performed for a long time using optical techniques on droplets with typical sizes of at least several tens of micrometers. The results show an exceptionally large scatter in the magnitude of the contact line tensions obtained: values ranging from  $10^{-5}$  to  $10^{-12}$  N, both positive and negative, are reported in the literature [40–44].

From the sketch presented in Fig. 6, it is quite straightforward to imagine how such a large scatter in the experimental values of the contact line tension may come about, since every surface is, as far as its surface energy is concerned, inhomogeneous at least at a very small scale. Thus, the contact line is expected to exhibit a corrugation as shown in the figure, which is not accessible with optical imaging techniques. As a consequence, the total free energy of the contact line, which is measured using a coarse-graining experimental technique (such as optical microscopy), consists not only of the genuine contact line tension, or its sum over the corrugations [45], but also of the excess free energy connected to the increased total surface near this line. This may at least explain large positive apparent line tensions.

### 3.2. Imaging corrugated contact lines

It follows directly that high-resolution imaging of the three-phase contact line and the local liquid surface is crucial for the determination of the contact line tension.

In order to achieve nanometer spatial resolution, SFM has been used as described in the previous sections.

Typical working conditions were cantilever oscillation amplitudes of 10–20 nm with very small damping values of 1–5%. Commercial silicon cantilevers were used with typical resonance frequencies of 200–400 kHz and spring constants of 20–40 N/m. The tip radius was  $\approx 10$  nm, as specified by the manufacturer (Nanoprobe). The liquid structures were prepared by depositing liquid (hexaethylene glycol) droplets on a substrate which was provided with a pattern of stripewise wettability, as already shown in Fig. 1 [46]. In order to achieve liquid structures in thermal equilibrium with the solid substrate, the droplets were created by means of an atomizer (Fisher Scientific) and were deposited on the substrate out of the aerosol phase.

The patterned substrates were created by microcontact printing [47–55] of perfluorinated alkylsilanes [(heptadecafluoro-1,1,2,2-tetrahydrodecyl)dimethylchlorosilane] from hexane solution onto silicon wafers. The roughness of the substrates was 0.25 nm, as revealed by SFM. The printing process leads to stripes of self-assembled monolayers with a typical thickness of 0.5 nm. Hence, the topography of this structure and of the solid substrate in general can be neglected in comparison with the larger liquid structures that are investigated. The spatial period of the stripes ranged from 400 to 1000 nm. A typical image of a structure of this kind is presented in Fig. 7. Due to the printing process, the hydrophilic regions are not as hydrophilic as the freshly prepared silicon dioxide surfaces. However, the wettability contrast between the stripes is large enough to generate pronounced periodic structures in the contact lines of the sessile droplets on these surfaces, as may be anticipated by the strong influence of the wettability pattern on the macroscopic shape demonstrated in Fig. 1.

By imaging smaller droplets with SFM, images of the liquid profile at the three-phase boundary, i.e. the contact line region, were obtained with a resolution in the nanometer range. A typical image of a small droplet is shown in Fig. 8, while in Fig. 9 the contact line region of a slightly larger droplet is shown in detail. Images like Fig. 9 can be used to determine the local value of the contact angle and the local radius of curvature of the contact line. The latter was obtained by a second-order polynomial fit in the vicinity of the point of interest along the contact line. The local contact angles were directly determined from sections of the topography, perpendicular to the local direction of the contact line.

In order to connect our data to equation (7), we have plotted the cosine of the local contact angle versus the local curvature of the contact line,  $1/R$ , in Fig. 10. As is clearly seen, the data group into two distinct clusters, one at higher and the other at lower cosines of the contact angle. They correspond to the hydrophilic and hydrophobic domains, respectively.

Quite obviously, the cosine of the contact angle varies linearly with the curvature of the contact line for both the hydrophilic and the hydrophobic domains. This dependence is expected from equation (7). It is now straightforward to determine

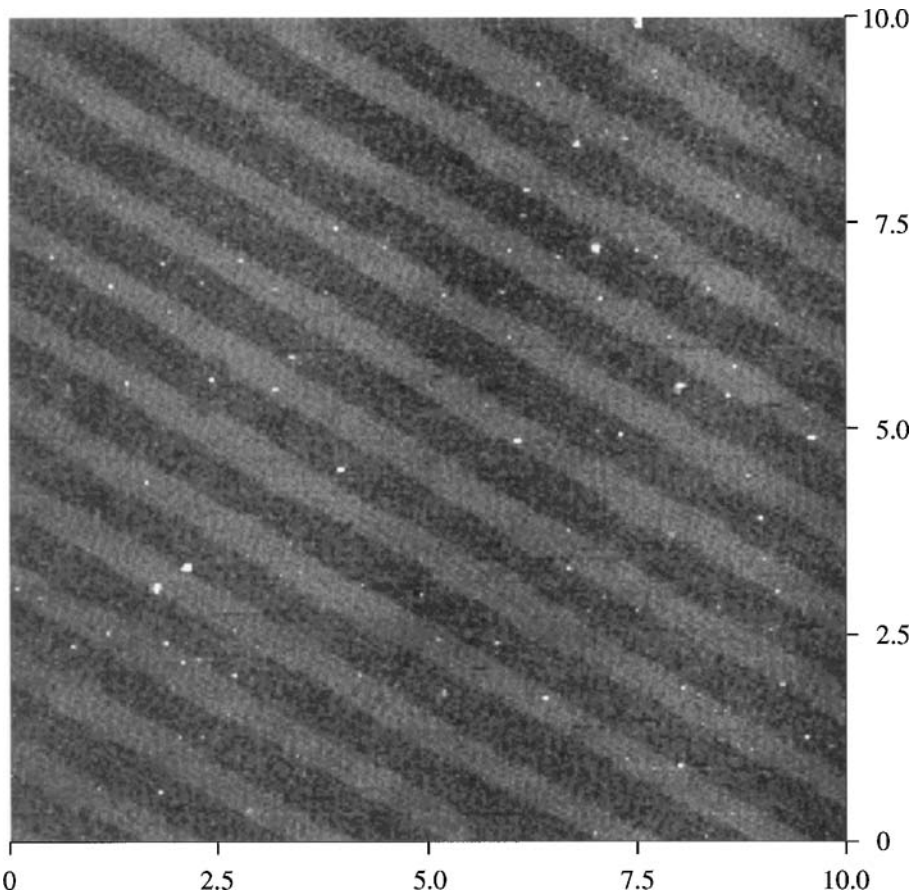


**Figure 7.** SFM topography image of a silicon wafer chemically patterned by microcontact printing, similar to the one used for Fig. 4. A patterned self assembled monolayer of perfluorinated monochloroalkylsilane, molecules provides a wettability contrast of hydrophilic and hydrophobic stripes (periodicity: 900 nm).

the contact line tension by a linear fit, which is then found to be  $-6 \times 10^{-11}$  N for the hydrophilic domains ( $\Theta_{\text{Young}} = 18^\circ$ ) and  $-3.5 \times 10^{-10}$  N for the hydrophobic domains ( $\Theta_{\text{Young}} = 34^\circ$ ). As the substrates used are patterned in wettability, the observed local contact angle  $\Theta$  is a function of both the local wettability of the substrate and the local curvature of the contact line. Ideally,  $\Theta_{\text{Young}}$  has one distinct value on hydrophilic and another (higher) on the hydrophobic stripes. Due to inherent problems of the preparation process, this could not be perfectly achieved. The change in wettability from hydrophobic to hydrophilic is not discontinuous, but slightly smeared out over a finite region with intermediate values of  $\Theta_{\text{Young}}$ . Therefore, data closer than 15 nm to the boundary were not taken into account.

A comparison of our results with those of other experiments [40, 41] reveals that the absolute values of the contact line tension found here are much lower and within the theoretically predicted range. In theoretical simulations of the contact

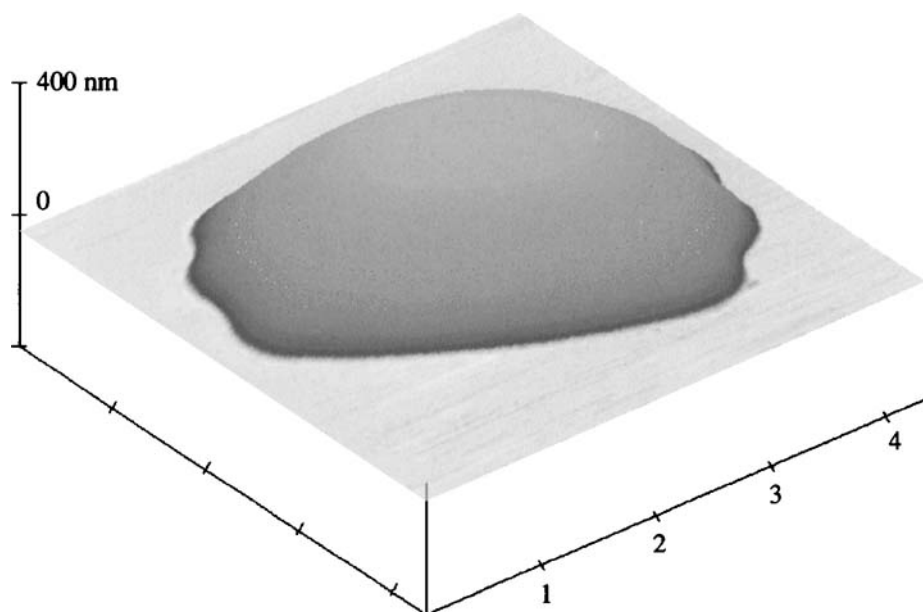


**Figure 8.** SFM topography image of a small droplet on a patterned substrate (spatial period: 800 nm). The elongation of the droplet in the direction of the stripes and the distinct corrugation of the contact line perpendicular to the stripes can be clearly seen.

line tension for a similar system by Dietrich and co-workers [34, 51], negative values were obtained, too, which compare favorably with our results. Furthermore, the dependence of the contact line tension on Young's contact angle is similar to theoretical predictions [52–54], indicating an increasing contact line tension with decreasing Young's contact angle.

It should be pointed out that naively one could expect a negative line tension to give rise to spontaneous contact line undulations, at least at small enough scales. However, Dobbs has recently shown by a quite ingenious argument [55] that the contact line always experiences a restoring force and is thus straight in equilibrium, despite its negative tension.

### 3.3. Imaging contact line profiles

It is also informative to study the liquid profile very close to the contact line. As Fig. 11 clearly shows, the profile may be distinctly different from the mere intersection of two planes. Instead, there is a smooth transition from the substrate surface to the tilted liquid surface. The shape of this transition reflects the long-range interaction of the solid/liquid and liquid/vapor interfaces with each other. From these profiles, it is straightforward to obtain the effective interface potential [56]. The details of the effective interface potentials derived from the contact line tails for several systems will be the subject of a forthcoming paper. Here we want to exploit these measurements only insofar as the contact line tension



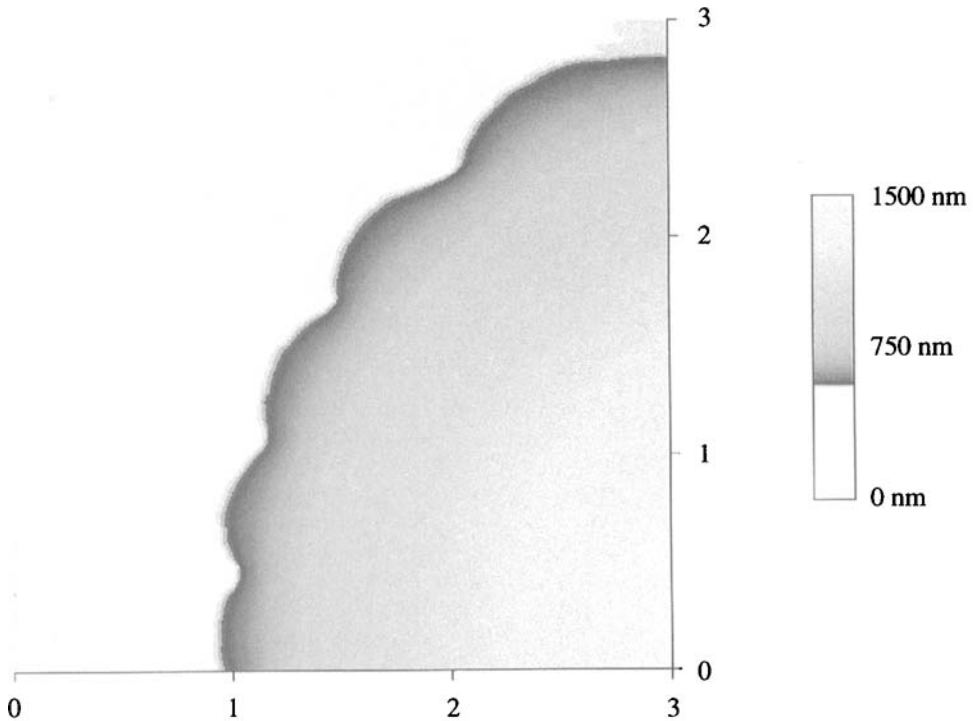


**Figure 9.** High-resolution ( $\approx 10$  nm per pixel) SFM topography image of the contact line region of a large hexaethylene glycol droplet. The corrugation of the contact line due to the stripewise wettability contrast of the substrate is used to determine the dependence of the local contact angle on the local curvature of the contact line. The direction of the stripes is from left to right in this image.

can be computed from the effective interface potential [52]. The liquid profile close to the contact line, which does not have to be curved, thus provides us with a completely complementary method of determining the line tension.

In order to compare these results with those obtained from the modified Young equation, one has to do both analyses with the same drop, since there is some scatter in the results, due to imperfections in the sample preparation. We have done this only for hexaethylene glycol. For the hydrophilic domains, we obtained a line tension of  $-1 \times 10^{-10}$  N from both the modified Young equation and the effective interface potential approach. So, there is agreement of the two methods, within the (yet substantial) experimental errors, which indicates that the values that we obtained are quite reliable. For the hydrophobic domains, the modified Young equation approach yielded a line tension of  $-4 \times 10^{-10}$  N, while we extracted from the effective interface potential a line tension of  $-2 \times 10^{-10}$  N. A discrepancy by a factor of 2 is satisfactory in view of the large experimental scatter and the fact that the numbers reported in the literature disagree by several orders of magnitude.

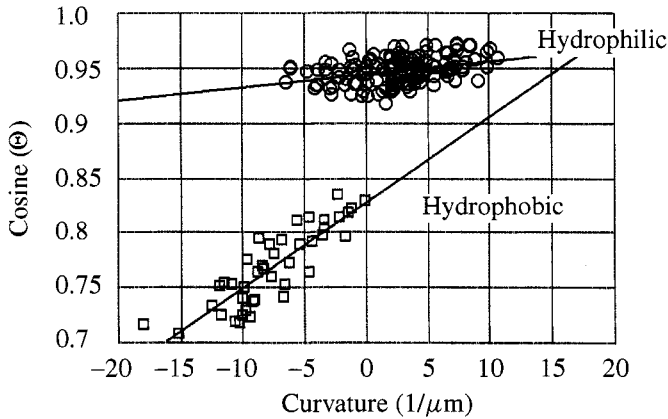


**Figure 10.** Experimental values of the cosine of the local contact angle are plotted versus the local curvature of the contact line. The local contact angle was obtained from a section of the measured profile, taken perpendicular to the contact line at the point of interest. Two distinct clusters of data are clearly seen, corresponding to the hydrophilic and hydrophobic domains. A linear dependence of the cosine of the contact angle on the curvature of the contact line is observed, as expected from the modified Young equation [equation (7)]. With a linear fit to the data, contact line tensions of  $-6 \times 10^{-11}$  and  $-3.5 \times 10^{-10}$  N for hydrophilic and hydrophobic surfaces, respectively, are determined.

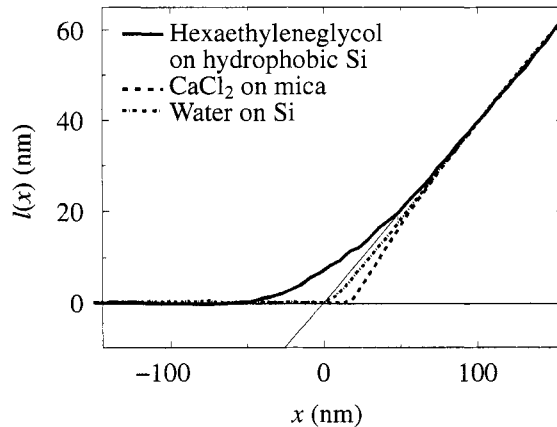


**Figure 11.** Topographic microstructure of the profile,  $l(x)$ , close to the contact line for water on silicon, hexaethylene glycol on silicon and an aqueous solution of calcium chloride on mica. A characteristic deviation from the straight line (thin solid line) is clearly visible, which is due to the finite range of the effective potential acting between the interfaces involved.

#### 4. CONCLUSIONS

We have demonstrated that it is possible to obtain the topography of liquid profiles by SFM in tapping mode with remarkable accuracy. We applied this technique to the investigation of fundamental quantities in wetting science, such as the contact line tension and the effective interface potential. We determined the contact line

tension and found values of the same order of magnitude as expected from theory. Despite the poor accuracy that we have achieved to date, the data may be considered as particularly reliable since they were obtained with two complementary methods, both based on SFM investigation of the liquid topography. We are currently tackling more sophisticated problems in these systems, such as the functional dependence of the line tension on the contact angle.

### Acknowledgements

We gratefully acknowledge generous funding by the Deutsche Forschungsgemeinschaft under grant He 2016/5 within the Priority Program 'Wetting and Structure Formation at Interfaces'.

### REFERENCES

1. G. Binnig, C. Quate and C. Gerber, *Phys. Rev. Lett.* **56**, 930 (1986).
2. U. Hartmann, *Ultramicroscopy* **42**, 59 (1992).
3. Q. Zhong, D. Inniss, K. Kjoller and V. Elings, *Surface Sci. Lett.* **290**, 688 (1993).
4. P. K. Hansma, J. P. Cleveland, M. Radmacher, D. A. Walters, P. E. Hillner, M. Bezanilla, M. Fritz, D. Vie, H. Hansma, C. Prater, J. Massie, L. Fukunaga, J. Gurley and V. Elings, *Appl. Phys. Lett.* **64**, 1738 (1994).
5. C. A. J. Putman, K. O. Van der Werf, B. G. De Grooth and N. F. Van Hulst, *Appl. Phys. Lett.* **64**, 2454 (1994).
6. M. Radmacher, R. W. Tillmann and H. E. Gaub, *Biophys. J.* **64**, 735 (1993).
7. R. Hoerper, R. K. Workman, D. Chen, D. Sarid, T. Yadav, J. C. Withers and R. O. Loutfy, *Surface Sci.* **311**, L731 (1994).
8. K. Umemura, H. Arakawa and A. Ikai, *J. Vac. Sci. Technol. B* **12**, 1470 (1994).
9. K. Umemura, H. Arakawa and A. Ikai, *Jpn. J. Appl. Phys. Part 2* **32**, 1711 (1993).
10. T. Shibata-Seki, W. Watanabe and J. Masai, *J. Vac. Sci. Technol. B* **12**, 1530 (1994).
11. S. S. Sheiko, G. Eckert, G. Ignateva, A. M. Muzafarov, J. Spickermann, H. J. Räder and M. Möller, *Makromol. Rapid Commun.* **17**, 283 (1996).
12. S. S. Sheiko, A. Muzafarov, R. G. Winkler, E. V. Getmanova, G. Eckert and P. Reinecker, *Langmuir* **13**, 4172 (1991).
13. J. Tamayo and R. Garcia, *Langmuir* **12**, 4430 (1996).
14. S. Bardon, M. P. Valignat, A. M. Cazabat, W. Stocker and J. P. Rabe, *Langmuir* **14**, 2916 (1998).
15. S. Herminghaus, A. Fery and D. Reim, *Ultramicroscopy* **69**, 211 (1997).
16. T. Pompe, A. Fery and S. Herminghaus, *Langmuir* **14**, 2585 (1998).
17. A. Fery, T. Pompe and S. Herminghaus, *J. Adhesion Sci. Technol.* **13**, 1071 (1999).
18. R. Hoerper, T. Gesang, W. Possard, O.-D. Hennemann and S. Boseck, *Ultramicroscopy* **60**, 17 (1995).
19. R. Brandsch, G. Bar and M.-H. Whangbo, *Langmuir* **13**, 6349 (1997).
20. S. J. T. Van Noort, K. O. Van der Werf, B. G. De Grooth, N. F. Van Hulst and J. Greve, *Ultramicroscopy* **69**, 117 (1997).
21. B. Anczykowski, D. Krüger and H. Fuchs, *Phys. Rev. B* **53**, 15 485 (1996).
22. B. Anczykowski, D. Krüger, K. L. Babcock and H. Fuchs, *Ultramicroscopy* **66**, 251 (1996).
23. A. Kühle, A. H. Soerensen, J. B. Zandbergen and J. Bohr, *Appl. Phys. A* **66**, 329 (1998).
24. A. Kuehle, A. H. Soerensen and J. Bohr, *J. Appl. Phys.* **81**, 6562 (1997).

25. R. G. Winkler, J. P. Spatz, S. Sheiko, M. Möller, P. Reineker and O. Marti, *Phys. Rev. B* **54**, 8908 (1996).
26. N. A. Burnham, O. P. Behrend, F. Oulevey, G. Gremaud, P.-J. Gallo, D. Gourdon, E. Dupas, H. M. Pollock and G. A. D. Briggs, *Nanotechnology* **8**, 67 (1997).
27. J. P. Cleveland, B. Anczykowski, A. E. Schmid and V. B. Elings, *Appl. Phys. Lett.* **72**, 2613 (1998).
28. A. Noy, C. H. Sanders, D. V. Veznov, S. S. Wong and C. M. Lieber, *Langmuir* **14**, 1508 (1998).
29. J. Tamayo and R. Garcia, *Appl. Phys. Lett.* **71**, 2394 (1997).
30. M. Luna, J. Colchero and A. M. Baro, *Appl. Phys. Lett.* **72**, 3461 (1998).
31. J. N. Israelachvili, *Intermolecular and Surface Forces*, 2nd edn. Academic Press, London (1992).
32. F. M. Orr, L. E. Scriven and A. P. Rivas, *J. Fluid Mech.* **67**, 723 (1975).
33. A. Marmur, *J. Colloid Interface Sci.* **186**, 462 (1997).
34. T. Getta and S. Dietrich, *Phys. Rev. E* **57**, 655 (1998).
35. J. A. de Feijter and A. Vrij, *J. Electroanal. Chem.* **37**, 9 (1972).
36. W. D. Harkins, *J. Chem. Phys.* **5**, 135 (1937).
37. F. Bresme and N. Quirke, *Phys. Rev. Lett.* **80**, 3791 (1998).
38. J. S. Rowlinson and B. Widom, *Molecular Theory of Capillarity*, p. 240. Oxford University Press, New York (1984).
39. N. V. Churaev, V. M. Starov and B. V. Derjaguin, *J. Colloid Interface Sci.* **89**, 16 (1982).
40. D. Li and A. W. Neumann, *Colloids Surfaces* **43**, 195 (1990).
41. J. Drelich, J. L. Wilbur, J. D. Miller and G. M. Whitesides, *Langmuir* **12**, 1913 (1996).
42. J. Drelich, *Pol. J. Chem.* **71**, 525 (1997).
43. R. Aveyard, J. H. Clint and D. Nees, *J. Chem. Soc., Faraday Trans.* **93**, 4409 (1997).
44. A. Amirfazli, D. Y. Kwok, J. Gaydos and A. W. Neumann, *J. Colloid Interface Sci.* **205**, 1 (1998).
45. D. Li, F. Y. H. Lin and A. W. Neumann, *J. Colloid Interface Sci.* **142**, 224 (1991).
46. L. Boruvka, J. Gaydos and A. W. Neumann, *Colloids Surfaces* **43**, 307 (1990).
47. P. F. Nealey, A. J. Black, J. L. Wilbur and G. M. Whitesides, in: *Molecular Electronics*, J. Jortner and M. Ratner (Eds), p. 343. Blackwell Science, Oxford (1997).
48. A. R. Bishop and R. G. Nuzzo, *Curr. Opin. Colloid Interface Sci.* **1**, 127 (1996).
49. P. M. S. John and H. G. Craighead, *Appl. Phys. Lett.* **68**, 1022 (1996).
50. Y. Xia, M. Mrksich, E. Kim and G. M. Whitesides, *J. Am. Chem. Soc.* **117**, 9576 (1995).
51. C. Bauer and S. Dietrich, *Eur. Phys. J. B* **10**, 767 (1999).
52. J. O. Indekeu, *Physica A* **183**, 439 (1992).
53. I. Szleifer and B. Widom, *Mol. Phys.* **75**, 925 (1992).
54. H. Dobbs, *Langmuir* **15**, 2586 (1999).
55. H. Dobbs, *Physica A* **271**, 36 (1999).
56. S. Dietrich, in: *Phase Transitions and Critical Phenomena*, C. Domb and J. L. Lebowitz (Eds), Vol. 12, p. 1. Academic Press, London (1988).

## Contact angles on hydrophobic microparticles at water–air and water–hexadecane interfaces

GLEB E. YAKUBOV<sup>1,2</sup>, OLGA I. VINOGRADOVA<sup>1,2,\*</sup>  
and HANS-JÜRGEN BUTT<sup>3,†</sup>

<sup>1</sup>Max-Planck-Institute for Polymer Research, Postfach 3148, 55021 Mainz, Germany

<sup>2</sup>Laboratory of Physical Chemistry of Modified Surfaces, Institute of Physical Chemistry,  
Russian Academy of Sciences, 31 Leninsky Prospect, 117915 Moscow, Russia

<sup>3</sup>Institut für Physikalische Chemie, Universität Siegen, 57068 Siegen, Germany

**Abstract**—Advancing and receding contact angles on individual hydrophobic microspheres at the air–water and liquid–liquid, namely hexadecane–water, interfaces were determined. For this purpose, spherical silanated silica particles ( $R = 2.35\ \mu\text{m}$ ) and polystyrene particles of different radii ( $R = 1.80\text{--}4.38\ \mu\text{m}$ ) were attached to atomic force microscope (AFM) cantilevers. Polystyrene particles were sintered onto the AFM cantilevers to provide stability in organic solvent. Then the equilibrium position of the microsphere at the air–water interface of a drop or an air bubble was measured with an AFM-related set-up. From the equilibrium position the contact angles were calculated. Advancing and receding contact angles determined with silanated silica particles ( $\Theta_a = 97^\circ$  and  $\Theta_r = 81^\circ$ ) agreed roughly with contact angles measured on similarly prepared planar surfaces ( $\Theta_a = 95^\circ$  and  $\Theta_r = 83^\circ$ ). The apparent contact angles measured on polystyrene particles decreased with increasing particle size. This can be interpreted by assuming a negative line tension of the order of  $-0.3\ \mu\text{N}$ .

**Keywords:** Atomic force microscope; contact angle; flotation; line tension; particle; surface force.

### 1. INTRODUCTION

With the atomic force microscope (AFM), the topography of many surfaces can be imaged at high resolution in a vacuum, gas, or a liquid environment. In addition to imaging surfaces, it was soon realized that by measuring force vs. distance curves supplementary information about surface properties such as the charge density, the

---

\*Phone: 0049-6131-379162; Fax: 0049-6131-379340; E-mail: vinograd@mpip-mainz.mpg.de

†To whom correspondence should be addressed. Phone: 0049-271-7404125; Fax: 0049-271-7403198; E-mail: butt@chemie.uni-siegen.de

local elasticity, or the local surface energy could be obtained and thus the AFM has become an important tool in colloid science to measure surface forces (for reviews see refs [1, 2]). To determine surface forces, usually spherical particles of typically 1–10  $\mu\text{m}$  radius (microspheres) are glued onto tipless cantilevers. By using microspheres of defined radius instead of integrated sharp tips, the interacting geometry can be quantified more easily.

In a typical force experiment, a planar sample mounted onto a piezoelectric translator is moved towards the microsphere. Forces between the particle and the planar surface lead to a deflection of the cantilever. Multiplying the deflection of the cantilever  $\Delta z_c$  by its spring constant  $K$  gives the total force acting on the particle:  $F = K \cdot \Delta z_c$ . The separation  $d$  is calculated by adding the deflection to the position of the translator:  $d = \Delta z_c + z$ .

With this procedure, surface forces between solid surfaces are measured routinely. Much more difficult is the measurement of surface forces at soft surfaces such as the surface of a liquid or the interface between two liquids. Besides technical difficulties, there are principal problems. One problem is to extract the separation between the particle surface and the soft interface. Between hard solid surfaces, this separation can be calculated from the so-called ‘constant compliance’ region of the force curve. Once the tip is in contact with the sample, its separation no longer changes. Hence, any change in the position of the sample directly leads to a similar change in the cantilever deflection. This leads to a linear increase of the cantilever deflection with the sample position. This linear part of the force curve is attributed to zero separation. This is different for soft surfaces because in every part of a force curve the tip deforms the surface significantly and a change in the bubble or drop position does not lead to a similar change in the cantilever deflection. In addition, the tip might penetrate into the liquid–gas or liquid–liquid interface and a three-phase-contact (TPC) line might be established. Then one is dealing with a penetration distance rather than a separation.

Despite these difficulties, forces between microspheres and bubbles in water [3–9], water drops [3, 5], and oil drops in water [10, 11] have been accurately measured. Direct force measurements at liquid–gas and liquid–liquid interfaces are of both applied (flotation, recycling of paper, oil refinery) and fundamental interest.

In this paper, we describe the results of experiments with polystyrene and silanated silica particles. The particles were hydrophobic and had radii in the range of 1.80–4.38  $\mu\text{m}$ . We measured the force between these particles and (1) an air bubble in water, (2) a water drop in air, and (3) a water drop in hexadecane. Polystyrene particles were chosen because similarly made particles of different sizes could be obtained and polystyrene particles are often used in numerous colloid science applications. For comparison, experiments were performed with silanated silica particles.

As before, it turned out that the forces before and after TPC formation were completely different. Before a TPC is established, long-range forces such as, for example, the electrostatic double-layer force are acting. After a TPC has been

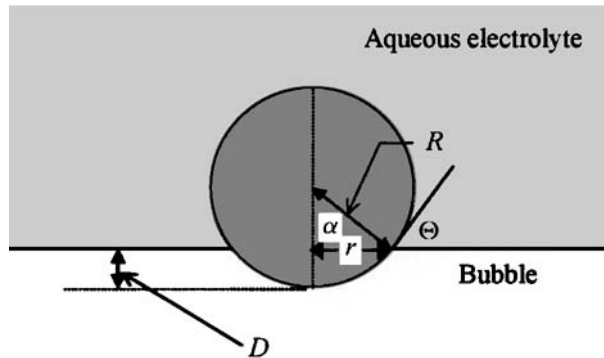


**Figure 1.** Schematic diagram of a spherical particle in TPC on the surface of a bubble in aqueous medium.

formed, the force is dominated by the capillary force, because the particle size is much smaller than the capillary length [12, 13]:

$$F_{\text{Cap}} = 2\pi R\gamma \cdot \sin \alpha \cdot \sin(\vartheta - \alpha), \quad (1)$$

where  $\gamma$  is the surface tension of the liquid,  $R$  is the particle radius, and  $\vartheta$  is the contact angle. The parameter  $\alpha$  describes the position of the particle in the interface (Fig. 1). The capillary force is zero for  $\alpha = \vartheta$ . This fact was used to determine the contact angle on individual microspheres. In accordance with the classical method of measuring contact angles on macroscopic spheres (called ‘sphere tensiometry’), we called this technique ‘microsphere tensiometry’ [5].

In this study, the contact angles on different hydrophobic particles at the air–water and hexadecane–water interfaces were analyzed. In particular, three questions were addressed: (1) What is the line tension on hydrophobic solids at the air–water–solid TPC? Below we obtain a relation between the apparent contact angle, the particle radius, and the line tension. It turns out that from a dependence of the apparent contact angle on the particle radius the line tension can be determined. Therefore we measured contact angles on polystyrene microspheres of different radii. (2) How large is the hysteresis between advancing and receding contact angles in microsphere tensiometry? A previous preliminary experiment indicated that the hysteresis was significantly smaller than on planar surfaces [5]. (3) Is it possible to determine the contact angles on individual particles at liquid–liquid interfaces with microsphere tensiometry?

## 2. MATERIALS AND METHODS

### 2.1. Particle preparation

Polystyrene spheres of 1.80, 3.15, and 4.38  $\mu\text{m}$  radius (Bangs Labs Inc., Fishers, IN, USA) were first rinsed with excessive amounts of water to remove adsorbed surfactants which were present to stabilize the polystyrene dispersion during

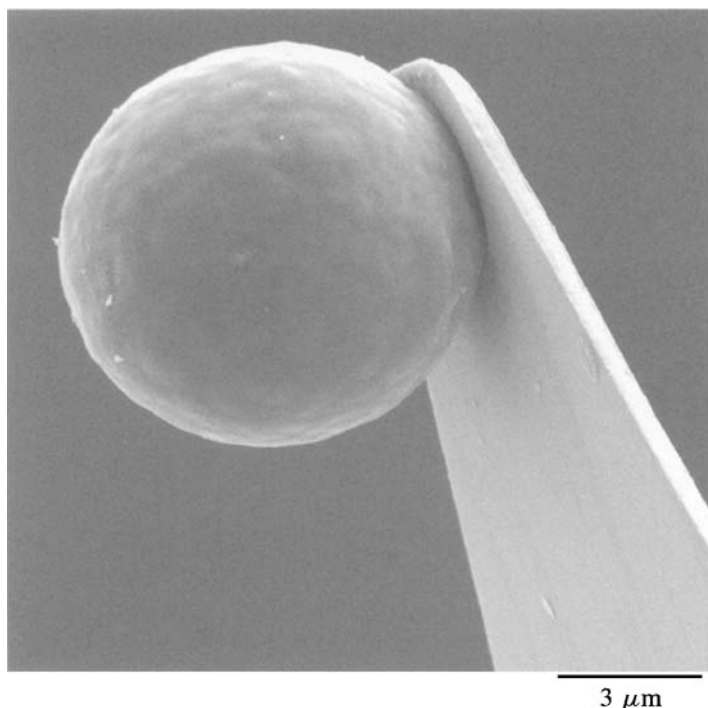


**Figure 2.** Typical scanning electron micrograph of a polystyrene particle of  $4.38\ \mu\text{m}$  radius sintered onto the end of an AFM cantilever. The particles were sputtered with gold.

synthesis. Therefore a suspension of the particles in the solution with the stabilizing surfactant was pushed through a nylon Millipore filter with a pore diameter of  $0.22\ \mu\text{m}$ . Water was then allowed to flow through the filter. After washing, the particles were removed from the filter onto a glass plate and dried in vacuum. In the last step, polystyrene particles were sintered or partially melted onto tipless cantilevers (Digital Instruments, Santa Barbara, CA, USA; V-shaped, 100 or  $200\ \mu\text{m}$  long,  $0.6\ \mu\text{m}$  thick, spring constants between 0.02 and  $0.3\ \text{N/m}$ ). The particles were placed at the right position of the cantilever. Then the cantilever was heated to  $120^\circ\text{C}$  for 45–240 s, depending on the particle size (Fig. 2) [14].

Silica spheres (Bangs Labs Inc., Fishers, IN, USA) of  $2.35\ \mu\text{m}$  radius were attached to tipless cantilevers by gluing them with a small amount of epoxy resin (Epikote 1004, Shell) as described before [9]. Then the particles were hydrophobized by exposing them to a vapor of 1,1,1,3,3,3-hexamethyldisilazane (Aldrich, Germany; 99.9%) for 5 h at  $70^\circ\text{C}$ .

The spring constant of each individual spring used was determined by moving it against a reference cantilever as described before [8]. The reference cantilever was calibrated by a method described by Cleveland *et al.* [15], by measuring its resonance frequency with attached spheres.



## 2.2. Liquids used

Water was purified using a commercial Milli-Q system containing ion exchange and charcoal stages. The deionized water had a conductivity less than  $0.1 \times 10^{-6}$  S/m and was filtered at  $0.22 \mu\text{m}$ . The Teflon cuvette was cleaned in concentrated hot nitric acid for several minutes, followed by thorough rinsing with high-purity water. Hexadecane (Aldrich, Germany; 99%, GC) was used without further purification.

## 2.3. Particle interaction apparatus (PIA)

The experimental set-up has been described in detail before [7] (Fig. 3). Briefly, cantilevers were fixed in a cantilever holder. An air bubble in water, a water drop in air, or a water drop in hexadecane (approximate diameter 1–2 mm) was placed onto the bottom of a Teflon cuvette with a pipette. Then the particle was positioned a few  $\mu\text{m}$  above the bubble (or drop) with a micrometer screw driven by a stepper motor (in height) and two micrometer screws of an  $X$ – $Y$  table (lateral position). This was done under optical control of a microscope with a long-distance lens (magnification 120) and a binocular. To measure the force vs. position curves, the cuvette with the bubble (or drop) was moved towards the particle with a  $15 \mu\text{m}$  range piezoelectric translator (Physics Instruments, Germany). This translator was equipped with integrated position sensors, which provided the position with an accuracy of 1 nm in closed-loop operation. During the movement, the deflection of the cantilever was measured with an optical lever technique. So the light from a laser diode (1.5 mW, 670 nm) was focused onto the back of the gold-coated cantilever. Via a mirror, the position of the reflected laser spot was measured with a position-sensitive device (United Detectors, UK; active area  $30 \times 5 \text{ mm}^2$ ).

When the force curves were taken, the typical driving speed was  $7 \mu\text{m/s}$ . Both the height position of the bubble or solid surface and the deflection of the cantilever were recorded with a digital oscilloscope (12-bit effective resolution). After transferring the data to a personal computer, the results were further analyzed. All experiments were done at room temperature without buffer. Hence, the pH was around pH 6.

## 2.4. Analysis of force curves

To be able to convert an output voltage of the position-sensitive device to a deflection in nm, force curves on a solid substrate were measured. When the tip is in contact with a hard solid substrate, any change in the height position is similar to a change in deflection. The result of a force measurement is a plot of the cantilever deflection  $\Delta z_c$  versus the height position of the piezo translator  $z$ . To obtain force vs. position curves,  $\Delta z_c$  was converted into a force according to  $F = K \cdot \Delta z_c$ .

## 2.5. Contact angle measurements on planar surfaces

On planar surfaces, contact angles were measured by optical observation of a sessile drop. The commercial set-up (Krüss, G10, Hamburg, Germany) was equipped with

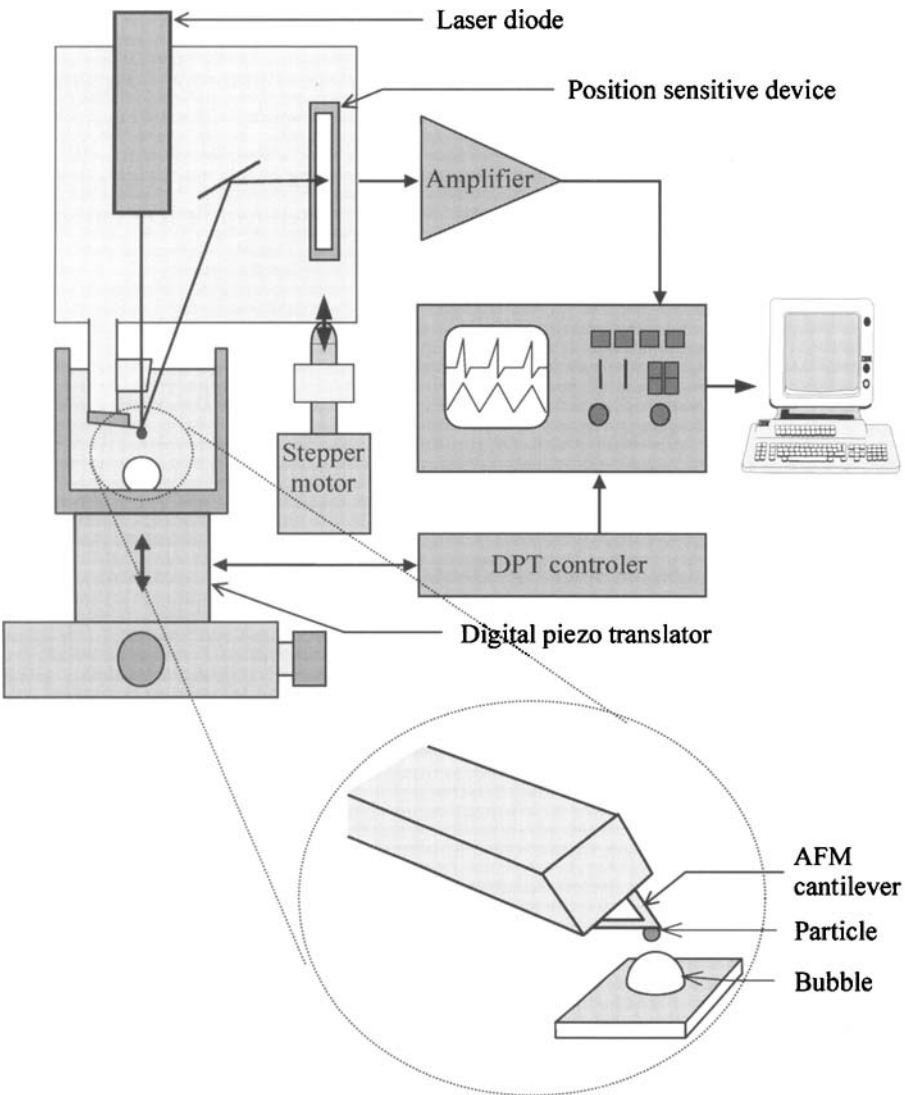


**Figure 3.** Schematic diagram of the particle interaction apparatus (PIA).

a stepper motor to drive the syringe which controls the drop volume. The estimated error is  $\approx 1^\circ$ .

**3. EXPERIMENTAL**

*3.1. Contact angle experiments*

Contact angle measurements are first described for the case of particle–bubble interaction. To measure the contact angle, the particle attached to a cantilever is

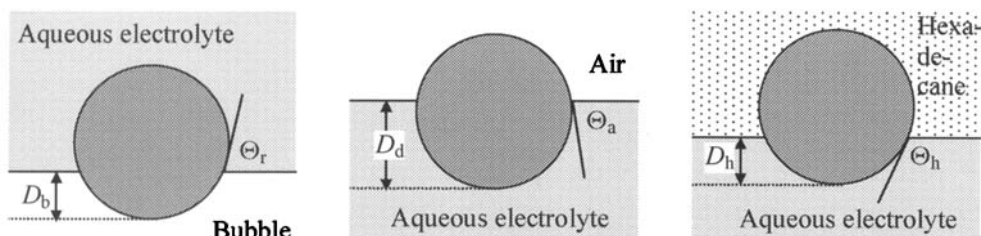


**Figure 4.** Schematic diagram showing the three types of contact angle measured.

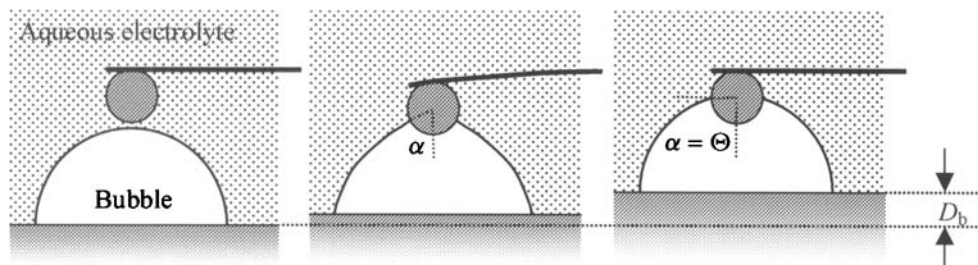


**Figure 5.** To measure the contact angle on an individual particle, a bubble is moved towards a particle. Before a TPC is established and in the absence of long-range forces, the cantilever is not deflected (left). After a TPC line has been formed, the bubble is deformed and the capillary force is acting on the particle. This leads to a deflection (middle). When the bubble is moved further towards the particle at some point, no force is acting on the cantilever (right). At this position, the bubble is again not significantly deformed. The difference in the sample height between the position just before a TPC is established and the zero-force position is the parameter  $D_b$ , which was used to calculate a value that we call the receding contact angle.

moved in an aqueous medium towards the bubble. When the particle touches the air–water interface, a three-phase contact (TPC) is formed and the capillary force pulls the particle into the bubble. When the bubble is moved further up at a certain position, no force is acting on the particle. This zero-force equilibrium position of the microsphere in the air–water interface is characterized by the penetration depth  $D_b$  (Fig. 4).  $D_b$  can be directly obtained from force vs. position curves without further analysis. It is the difference between the jump-in point and the zero-force position (Fig. 5). Then the contact angle was calculated from

$$\cos \Theta_r = \frac{R - D_b}{R}. \quad (2)$$

Since in the experiment the liquid is receding on the particle surface, we call the contact angle the apparent receding contact angle,  $\Theta_r$ . This apparent contact angle  $\Theta$  is not precisely equal to the contact angle  $\vartheta$  in equation (1). As will be discussed further, the apparent contact angle might be influenced by the line tension.

Apparent advancing contact angles on spherical particles,  $\Theta_a$ , were obtained from experiments with liquid drops (typical radius 1–2 mm). From the penetration depth of the particle into the zero-force position of the drop surface  $D_d$ , the advancing

contact angle was calculated according to

$$\cos \Theta_a = \frac{D_d - R}{R}. \quad (3)$$

In some cases, the liquid wetted the whole cantilever and not only the particle. This effect became more likely with decreasing contact angle. Practically, it limits the range accessible to contact angles above 40–50°. In other cases, only receding contact angles could be measured.

Contact angles on particles at the water–hexadecane interface were also measured. For that, a water drop of roughly 1–2 mm radius was placed with a pipette onto the bottom of the cuvette filled with hexadecane. From the distance between the particle jump-in position and the zero-force point  $D_h$ , the contact angle  $\Theta_h$  was calculated according to

$$\cos \Theta_h = \frac{D_h - R}{R}. \quad (4)$$

This is the advancing contact angle of water in hexadecane.

### 3.2. Line tension influence on the apparent contact angle

In the simple calculation given above, we considered only the capillary force. The capillary force is certainly the dominating force once a TPC line has formed. However, since the method is relatively sensitive, we also need to consider other contributions. The weight and buoyancy are negligible. Even for spheres of 5  $\mu\text{m}$  radius the weight does not exceed 0.01 nN or  $F/R = 0.002$  mN/m. We take into account two other factors: the line tension and the Laplace pressure inside the bubble (or drop).

The line tension  $\kappa$  is the energy required to form a unit length of TPC line. We use a simple model and assume that the line tension is constant and does not depend on the curvature of the particle. The energy of the whole TPC line is

$$E = \kappa 2\pi r = \kappa 2\pi R \cdot \sin \alpha. \quad (5)$$

The force caused by the line tension is given by

$$F_{\text{lt}} = \frac{dE}{dD} = \frac{dE}{d\alpha} \frac{d\alpha}{dD}. \quad (6)$$

Usually the force is the negative gradient of the potential energy. In this case, however, we use the positive derivative because increasing  $D$  goes in the negative direction. With  $D = R - R \cos \alpha$ , we obtain  $\frac{d\alpha}{dD} = \frac{1}{R \sin \alpha}$ . Differentiating  $E$  and inserting the expression for  $d\alpha/dD$  leads to

$$F_{\text{lt}} = 2\pi \kappa \cot \alpha. \quad (7)$$

In contrast to the capillary force, this does not depend on  $R$ .

The Laplace pressure inside the bubble (or drop) is given by  $p = 2\gamma/R_b$ , assuming that the bubble has a spherical shape of radius  $R_b$ . The Laplace pressure tends to push the particle out of the bubble. The result is an upward force of

$$F_{La} = p\pi r^2 = p\pi R^2 \sin^2 \alpha, \quad (8)$$

which we count as positive.

For the case of zero net force acting on the particle, the sum of all these forces is zero. The angle  $\alpha$  in this case is equal to  $\Theta$  and we have

$$2\pi R\gamma \sin \Theta \sin (\Theta - \vartheta) + p\pi R^2 \sin^2 \Theta + \kappa 2\pi \cot \Theta = 0. \quad (9)$$

The angle  $\Theta$  is the angle determined from the distances  $D_b$ ,  $D_d$ , or  $D_h$ . Now we substitute  $\Theta \equiv \vartheta + \varepsilon$ , where the angle  $\varepsilon$  describes the change in the zero-force position caused by the presence of a line tension and the Laplace pressure. This leads to

$$2R\gamma \sin \Theta \sin \varepsilon + pR^2 \sin^2 \Theta + 2\kappa \cot \Theta = 0. \quad (10)$$

From this equation and with an experimentally determined value of  $\Theta$ , we can calculate  $\varepsilon$  and the contact angle  $\vartheta = \Theta - \varepsilon$ . Equation (10) is, however, not an explicit expression for  $\vartheta$  and is inconvenient. Therefore it is instructive to consider two special cases.

*3.2.1. No Laplace pressure, only line tension.* In this case, we obtain

$$\sin \varepsilon = -\frac{\kappa}{R\gamma} \frac{\cos \Theta}{\sin^2 \Theta}. \quad (11)$$

The effect of the line tension depends on the ratio  $\kappa/R\gamma$  and the contact angle. Values for the line tension reported in the literature range from several  $-10^{-6}$  N to  $+10^{-6}$  N (see refs [16, 17] for reviews). For a contact angle  $\vartheta = 80^\circ$  and line tensions  $\kappa = -1, -0.2, 0.2$ , and  $1 \mu\text{N}$ , the apparent contact angles are plotted versus the particle radius in Fig. 6. The effect of the line tension increases with decreasing particle size. Positive line tensions decrease the apparent contact angle; negative line tensions increase it. For relatively high line tensions and particles below a certain critical size (for  $\kappa = 1 \mu\text{N}$ , this critical radius was  $2.7 \mu\text{m}$ ), no TPC line is formed [13, 18].

*3.2.2. No line tension, only Laplace pressure.* If the line tension is negligible, equation (10) can be simplified as:

$$\sin \varepsilon = -\frac{Rp}{2\gamma} \sin \Theta = -\frac{R}{R_b} \sin \Theta. \quad (12)$$

The correction depends on the ratio between the particle and the bubble (or drop) radii and on the contact angle. For a given bubble size, it increases linearly with the

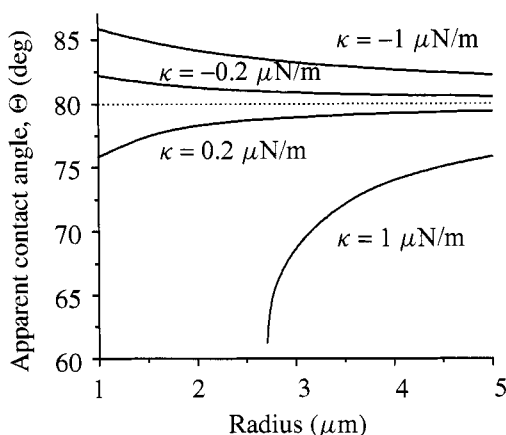


**Figure 6.** Apparent contact angle  $\Theta$  versus particle radius  $R$  for four different line tensions of  $-1$ ,  $-0.2$ ,  $0.2$ , and  $1 \mu\text{N}$ . The contact angle  $\vartheta$  was  $80^\circ$ . The results were calculated using equation (10).

particle radius. It does not depend on either the surface tension of the liquid or on the cross-sectional area.

For an *a priori* calculation of the expected change in apparent contact angle, we assume that  $|\varepsilon| \ll \vartheta$ . Then we can approximate  $\sin \varepsilon \approx -R/R_b \sin \vartheta$ . In our experiments, typical values are  $R = 3 \mu\text{m}$ ,  $R_b = 1 \text{ mm}$ , and  $\vartheta = 90^\circ$ . So we expect a correction to the contact angle of  $\varepsilon = -0.17^\circ$ , which we neglect.

Long-range forces might influence the contact angles obtained. In particle–bubble interaction, the electrostatic repulsion could prevent the particle from jumping into the bubble and hence could lead to a reduced  $D_b$  value. For particle–drop interaction, van der Waals attraction could lead to a jump-in before the particle actually touched the air–water interface. A larger value of  $D_d$  would be the consequence. Since electrostatic and van der Waals forces are still much shorter in range than the radius of the particle, this effect is negligible (for details see also refs [5, 9]). The error in the contact angle measurements on particles is approximately  $1^\circ$ .

## 4. RESULTS AND DISCUSSION

### 4.1. Force vs. position measurements at the air–water interface

A typical force vs. position curve measured between a polystyrene particle and an air bubble in an aqueous medium is shown in Fig. 7. At large distances, no interaction was observed. When the particle approached the air–water interface, a small repulsive, exponentially decayed component was usually observed. The same was observed with silanated silica particles. This is probably an electrostatic double-layer repulsion. As air bubbles bear a negative surface charge [19–22], the polystyrene surface also seems to be slightly negatively charged, or some submicroscopic bubbles are attached to it [23, 24].

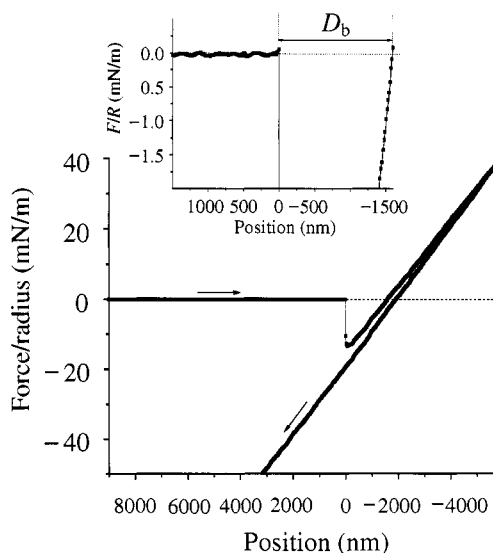


**Figure 7.** Force vs. position curve for the interaction measured between a polystyrene sphere ( $R = 4.38 \mu\text{m}$ ) and an air bubble in aqueous medium containing 1 mM KCl. The inset shows the part close to the jump-in in more detail.

After the repulsive barrier, the particle jumps into the air bubble and vice versa: the bubble snaps around the particle. When the position is decreased further at a certain point, no force is acting on the particle. The difference between the jump-in position and this zero-force position is  $D_b$  (Fig. 5).

#### 4.2. Contact angles at the air–water interface

Receding contact angles measured on silanated silica particles were highly reproducible and showed a variation of only  $\pm 1^\circ$  from particle to particle (Fig. 8). The average receding contact angle was  $\Theta_r = 81^\circ$ . This agrees with the receding contact angle of  $83^\circ$  measured on the similarly prepared planar surface.

Advancing contact angles on particles varied significantly more. Disregarding particle 4, the average advancing contact angle was  $\Theta_a = 97^\circ$ . This agrees with the advancing contact angle of  $95^\circ$  measured on the planar surface. The hysteresis observed was roughly the same both on planar surfaces ( $\Theta_a - \Theta_r = 12^\circ$ ) and on microparticles ( $\Theta_a - \Theta_r = 16^\circ$ ). This is in contrast to previous experiments, where we measured negligible hysteresis on silica particles ( $R = 2 \mu\text{m}$ ) silanated in an atmosphere of dichlorodimethylsilane ( $\Theta_a = \Theta_r = 101^\circ$ ).

In some cases, advancing contact angles were several tens of degrees *lower* than the average contact angle and even lower than the receding contact angle. This has been observed before [5]. One possible reason is a kinetic effect. When the particle jumps into the drop, the cantilever swings over its equilibrium position as observed before (Figs 9 and 10 of ref. [3]). There it might be trapped by a line-pinning effect. Such a vibration is damped out in experiments with a bubble. In

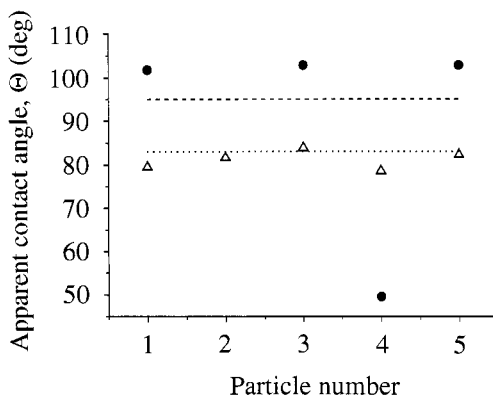


**Figure 8.** Apparent contact angles obtained with different silanated silica particles ( $R = 2.35 \mu\text{m}$ ) when interacting with a bubble (receding contact angle, open triangles) and a drop (advancing contact angle, circles). With silica particle 2, the advancing contact angles could not be measured because the whole cantilever was wetted by the liquid. The dotted and dashed lines show, respectively, the receding and the advancing contact angles measured on silanated silicon wafers. The results were obtained with pure water.

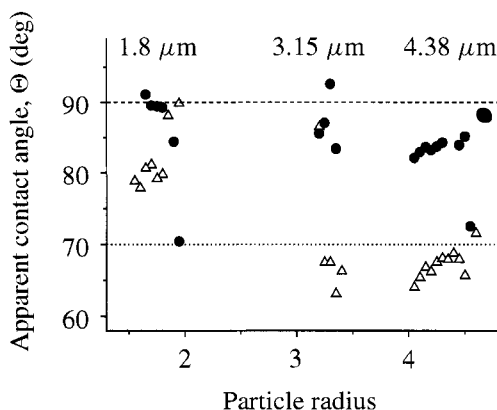


**Figure 9.** Apparent contact angles obtained with polystyrene particles of different radii when interacting with a bubble (receding contact angle, open triangles) and a drop (advancing contact angle, filled circles). The results are grouped with respect to the particle number, which is given according to the particle radius of the microspheres used. The dashed and dotted lines show, respectively, the advancing and the receding contact angles measured on a similar planar polystyrene surface. The results were obtained in pure water or in aqueous medium containing 1 mM KCl.

bubble experiments, the cantilever is surrounded by a liquid. This causes damping which is ten times higher than in air. Hence, in bubble experiments the movement of the particle and the cantilever is overcritically damped, while in the case of particle–drop experiments a vibration might occur. These vibrations cannot be observed in force vs. distance curves because they are too fast to be recorded.

Polystyrene particles showed a significantly higher heterogeneity and the contact angles depended on the pretreatment. Receding contact angles measured with



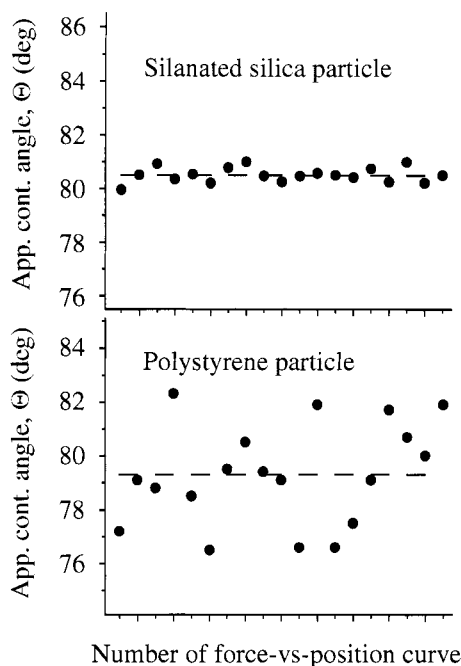


**Figure 10.** Apparent contact angles measured with a typical silanated silica particle and a polystyrene particle when interacting with a bubble obtained from subsequent force vs. position curves.

different polystyrene particles varied by  $\pm 4^\circ$  from particle to particle (Fig. 9). The average receding contact angles were  $\Theta_r = 81.9^\circ$ ,  $70.2^\circ$ , and  $67.3^\circ$  for particles of 1.8, 3.15, and  $4.38 \mu\text{m}$  radii, respectively. This agrees with the receding contact angle of  $70^\circ$  measured on the similarly prepared planar surface. The average advancing contact angles were  $\Theta_a = 88.7^\circ$ ,  $87.2^\circ$ , and  $84.5^\circ$ , respectively. These are slightly lower than the advancing contact angle of  $90^\circ$  measured on the planar surface. The hysteresis between the advancing and receding contact angles was  $7^\circ$ ,  $17^\circ$ , and  $17^\circ$ , respectively, which is again roughly the same as on planar surfaces ( $\Theta_a - \Theta_r = 20^\circ$ ).

The contact angles reported were obtained by measuring typically 15–20 force vs. position curves, extracting the  $D_b$  (or  $D_d$ ) values, averaging them, and using the average value to calculate the contact angle for a certain particle. In addition, it is instructive to use  $D_b$  (or  $D_d$ ) values for each approach and calculate the corresponding contact angle. In this way, we obtained a contact angle for each force vs. position curve. A representative set of contact angles obtained with a silanated silica particle and a polystyrene particle from subsequent force vs. position curves is shown in Fig. 10. Like the average contact angles, the contact angles obtained from individual force vs. position curves using polystyrene particles varied significantly more than the values obtained with silanated silica particles. This again reflects the heterogeneity of polystyrene particles.

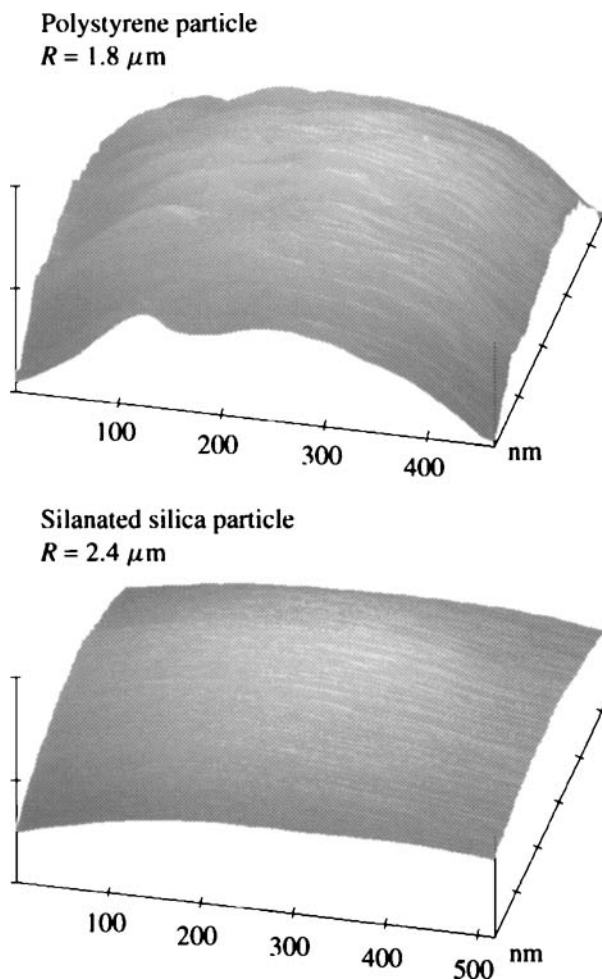


**Figure 11.** AFM images of the surface of a polystyrene particle ( $R = 1.80 \mu\text{m}$ ,  $z$ -scale  $20 \text{ nm/div}$ ) and a silanated silica particle ( $R = 2.35 \mu\text{m}$ ,  $z$ -scale  $15 \text{ nm/div}$ ). Images were taken in contact mode with standard silicon nitride cantilevers with integrated tips (Nanoscope 3, Digital Instruments, Santa Barbara, CA, USA) at a scan speed of  $5\text{--}10 \text{ Hz}$ .

A possible explanation for the large variation in contact angles obtained at different approaches is the high roughness of the polystyrene particles. The roughness (RMS) as determined from AFM images of polystyrene particles (Fig. 11) was  $3\text{--}5 \text{ nm}$  after subtracting the overall curvature. For silanated silica particles, the roughness was only  $1 \text{ nm}$ .

Both the receding and the advancing contact angles decreased with increasing radius (Fig. 12). This can formally be interpreted in terms of the existence of a negative effective or pseudo-line tension. For  $\Theta < 90^\circ$ , a negative line tension would lead to a larger penetration depth of a particle into a bubble,  $D_b$ , and to a smaller penetration depth of a particle into a drop,  $D_d$ . In both cases, the apparent

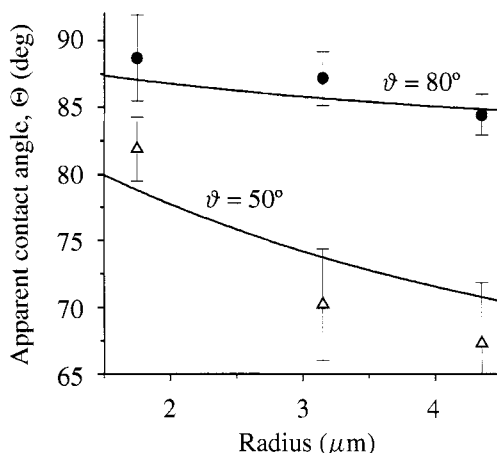


**Figure 12.** Mean apparent advancing (filled circles) and receding (open triangles) contact angles obtained with polystyrene particles vs. the particle radius. Error bars indicate the random error in the mean apparent contact angle. The continuous lines were calculated using equation (10) with a negative line tension of  $\kappa = -0.3 \mu\text{N}$  and contact angles  $\vartheta = 80^\circ$  and  $\vartheta = 50^\circ$ . The results were obtained with pure water or aqueous medium containing 1 mM KCl; no significant differences between these two electrolytes were observed.

contact angle increases. We could interpret our results by assuming a line tension of  $-0.3 \mu\text{N}$ , a receding contact angle (on a similar planar surface)  $\vartheta_r = 50^\circ$  and an advancing contact angle  $\vartheta_a = 80^\circ$ . The increase in the apparent contact angle caused by line tension is higher for small  $\vartheta$  and becomes smaller the closer the contact angle comes to  $90^\circ$ . At  $\vartheta = 90^\circ$ , line tension has no effect.

The values given for the contact angles on similar planar surfaces,  $\vartheta_a$  and  $\vartheta_r$ , and the line tension of polystyrene particles should not be overinterpreted. First, the values are not unique. The results can easily be fitted with other line tensions of the same order of magnitude as long as the contact angles are also changed appropriately. The results obtained with  $\kappa = -0.4 \mu\text{N}$ ,  $\Theta_a = 78^\circ$ , and  $\Theta_r = 40^\circ$  also agree with the apparent contact angles measured for different particle sizes. Second, the change in the contact angles could also be caused by different surface chemistry caused by differences in the particles' manufacturing processes.

#### 4.3. Interaction of polystyrene particles with a hexadecane–water interface

Experiments at the hexadecane–water interface could not be carried out with particles glued to cantilevers, because in hexadecane the glue swells or is even dissolved. To avoid this problem, polystyrene particles were partially melted onto tipless cantilevers. Meagher and Craig [25] melted pieces of polypropylene onto the ends of AFM cantilevers. They placed a polypropylene piece onto the end of the cantilever and heated it above the melting temperature. The polystyrene melted and formed a drop of spherical shape. The difference in our experiment is that we did not melt the particles; thus, the overall shape of the particles did not change.

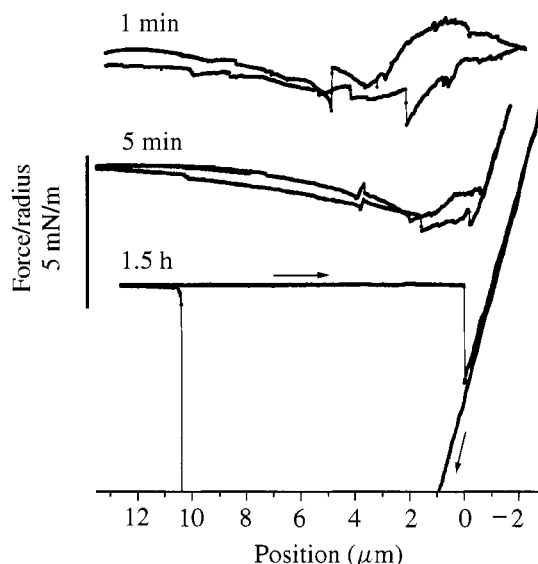


**Figure 13.** Force vs. position curves measured between a polystyrene sphere ( $R = 4.38 \mu\text{m}$ ) and a water drop containing 1 mM KCl in hexadecane. The three curves were taken at different times after injecting the water drop onto the bottom of the cuvette.

When a polystyrene particle approached a water drop in hexadecane, the force vs. position curves were qualitatively similar to the curves measured with a water drop in air. No long-range interaction was observed. As soon as the particle touched the hexadecane–water interface, it jumped into the drop.

When measuring the force between a water drop and a microsphere in hexadecane, we usually had to wait for 1–2 h until equilibrium was established (Fig. 13). The force vs. position curves measured before showed that no defined interface had been established. With increasing time, the force curves became more and more reproducible and the jump-in point became more and more defined. One possible explanation is a certain degree of swelling of the polystyrene in hexadecane.

The mean contact angle measured was  $145.3^\circ$ ; the average variation in the contact angle from particle to particle was  $\pm 2^\circ$ . This agrees with the advancing contact angle of  $150^\circ$  measured on a planar surface. A strict correlation was observed between the contact angles at the hexadecane–water interface and the receding contact angles measured on the same particles in air bubbles.

## 5. CONCLUSIONS

With the particle interaction apparatus (PIA), one is able to determine both advancing and receding contact angles on individual spherical microparticles with an accuracy of  $1^\circ$ . The interpretation of these contact angles is, however, different from the normal definition of contact angles on planar surfaces because they are determined from a position where no force is acting on the three-phase contact line. Polystyrene

particles showed a more complicated behavior than silanated silica particles. The *apparent* contact angle on the polystyrene particles used depended on the radius of the particle. This can formally be interpreted in terms of a negative pseudo-line tension, which is much greater than line tensions predicted theoretically. In addition, we demonstrated that with PIA it is possible to determine the contact angles on individual microspheres at liquid–liquid interfaces by microsphere tensiometry.

### Acknowledgements

We would like to thank M. Preuss and M. Ruppl, Universität Frankfurt, for providing scanning electron images. This work has been started at the University of Mainz. We acknowledge the financial support of the Alexander von Humboldt Foundation (O.I.V.) and the Deutsche Forschungsgemeinschaft under grant Bu 701/11 (G.E.Y.) within the priority program ‘Wetting and Structure Formation at Interfaces’.

### REFERENCES

1. H.-J. Butt, M. Jaschke and W. Ducker, *Bioelectrochem. Bioenerg.* **38**, 191 (1995).
2. B. Cappella and G. Dietler, *Surface Sci. Rep.* **34**, 1 (1999).
3. H.-J. Butt, *J. Colloid Interface Sci.* **166**, 109 (1994).
4. W. A. Ducker, Z. Xu and J. N. Israelachvili, *Langmuir* **10**, 3279 (1994).
5. S. Ecke, M. Preuss and H.-J. Butt, *J. Adhesion Sci. Technol.* **13**, 1181 (1999).
6. M. L. Fielden, R. A. Hayes and J. Ralston, *Langmuir* **12**, 3721 (1996).
7. M. Preuss and H.-J. Butt, *Langmuir* **14**, 3164 (1998).
8. M. Preuss and H.-J. Butt, *J. Colloid Interface Sci.* **208**, 468 (1998).
9. M. Preuss and H.-J. Butt, *Int. J. Miner. Process.* **56**, 99 (1999).
10. P. Mulvaney, J. M. Perera, S. Biggs, F. Grieser and G. W. Stevens, *J. Colloid Interface Sci.* **183**, 614 (1996).
11. B. A. Snyder, D. E. Aston and J. C. Berg, *Langmuir* **13**, 590 (1997).
12. A. V. Rapacchieta and A. W. Neumann, *J. Colloid Interface Sci.* **59**, 555 (1977).
13. A. Scheludko, B. V. Toshev and D. T. Bojadjiev, *J. Chem. Soc., Faraday Trans. 1* **72**, 2815 (1976).
14. M. E. Karaman, L. Meagher and R. M. Pashley, *Langmuir* **9**, 1220 (1993).
15. J. P. Cleveland, S. Manne, S. Bocek and P. K. Hansma, *Rev. Sci. Instrum.* **64**, 403 (1993).
16. J. Drelich, *Colloids Surfaces A* **116**, 43 (1996).
17. J. Gaydos and A. W. Neumann, in: *Applied Surface Thermodynamics*, A. W. Neumann and J. K. Spelt (Eds), p. 169. Marcel Dekker, New York (1996).
18. J. Mingins and A. Scheludko, *J. Chem. Soc., Faraday Trans. 1* **75**, 1 (1979).
19. S. Usui, H. Sasaki and H. Matsukawa, *J. Colloid Interface Sci.* **81**, 80 (1981).
20. P. Saulnier, J. Lachaise, G. Morel and A. Gracia, *J. Colloid Interface Sci.* **182**, 395 (1996).
21. H. J. Schulze and C. Cichos, *Z. Phys. Chem., Leipzig* **251**, 252 (1972).
22. R. H. Yoon and J. L. Yordan, *J. Colloid Interface Sci.* **113**, 430 (1986).
23. O. I. Vinogradova, N. F. Bunkin, N. V. Churaev, O. A. Kiseleva, A. V. Lobeyev and B. W. Ninham, *J. Colloid Interface Sci.* **173**, 443 (1995).
24. R. F. Considine, R. A. Hayes and R. G. Horn, *Langmuir* **15**, 1657 (1999).
25. L. Meagher and V. S. J. Craig, *Langmuir* **10**, 2736 (1994).

## Capillarity at the nanoscale: an AFM view

F. MUGELE\*, T. BECKER, R. NIKOPOULOS, M. KOHONEN  
and S. HERMINGHAUS

*Universität Ulm, Abteilung Angewandte Physik, D-89069 Ulm, Germany*

**Abstract**—We have used atomic force microscopy (AFM) to image liquid droplets on solid substrates. The technique is applied to determine the contact line tension. Compared to conventional optical contact angle measurements, the AFM extends the range of accessible drop sizes by three orders of magnitude. We analyze the global shape of the droplets and the local profiles in the vicinity of the contact line. These two approaches show that the optical measurement overestimates the line tension by approximately four orders of magnitude.

**Keywords:** Contact angle; wetting; line tension; atomic force microscopy; Young equation; interface potential.

### 1. INTRODUCTION

Since its invention in 1985 [1], atomic force microscopy (AFM) in a variety of operational modes (contact mode, non-contact mode, tapping mode, scanning polarization force microscopy) has become one of the most widely used experimental tools in surface physics and surface chemistry laboratories. Its unique lateral resolution has been used for characterization of surfaces in real space down to the atomic scale. In the context of adhesion and wetting, it is mainly used to measure forces, to measure the surface topography, and to characterize the quality and chemical composition of substrates with specifically-tailored wetting properties. Two specific operational modes of AFM, i.e. scanning polarization force microscopy (SPFM) [2] and tapping mode [3, 4], have been applied successfully to image not only the substrates, but also the topography of partially wetting liquid nanostructures. Both techniques have revealed details about the molecular forces governing the equilibrium shapes as well as the adsorption and spreading of liquids on a scale that was not amenable to conventional optical techniques.

---

\*To whom correspondence should be addressed. Phone: +49 731 502 2931. Fax: +49 731 502 2958. E-mail: [frieder.mugele@physik.uni-ulm.de](mailto:frieder.mugele@physik.uni-ulm.de)

One of the most heavily debated questions in the field of wetting deals with the influence of molecular and interfacial forces on the equilibrium contact angle  $\theta$  of a liquid droplet with a finite base radius  $R$  [5, 6]. The influence of the interfacial forces translates into an excess free energy of the three-phase contact line, the line tension  $\Gamma$ , which was calculated to be on the order of  $10^{-12}$  to  $10^{-10}$  J/m [7–9]. In the presence of a finite line tension, the contact angle of a liquid droplet depends on its size. In a large number of conventional contact angle goniometry experiments (or its automated version ‘axisymmetric drop shape analysis’ [10]), variations of  $\theta$  with  $R$  of the order of  $1^\circ$  have been reported for millimeter-sized droplets. These variations were interpreted in terms of a line tension of  $\Gamma \approx 10^{-5} \dots 10^{-6}$  J/m [5, 6, 10, 11], four to six orders larger than predicted on theoretical grounds. Recently, Law and coworkers [12] obtained a value of  $\Gamma \approx 10^{-10}$  J/m using optical interferometry. In a previous study, we used an AFM to investigate liquid droplets on patterned substrates [3, 4]. In that work, we extracted a line tension of the order  $10^{-10}$  J/m from variations of the local contact angle with the local curvature of the contact line. In the present study, we combine the conventional optical method of size-dependent contact angle goniometry on the millimeter scale with AFM measurements using micrometer-sized droplets on homogeneous substrates.

In addition to causing variations of the contact angle with droplet size, interfacial forces are also expected to induce deviations of the droplet profiles from the ideal spherical cap shape in the vicinity of the three-phase contact line. In the second part of the present contribution, we analyze individual AFM profiles and determine the upper limits on the magnitude of the interfacial forces and the line tension. From both types of analyses we obtain an upper limit of  $\Gamma \approx 10^{-10}$  J/m. In particular, we will show that values of  $\Gamma \approx 10^{-5} \dots 10^{-6}$  J/m, as quoted above, are incompatible with the high-resolution AFM measurements.

## 2. EXPERIMENTAL

For the experiments, we deposited droplets of hexaethylene glycol (HEG) on silanized silicon substrates. This system was chosen because HEG has a sufficiently low vapor pressure at room temperature to prevent any noticeable evaporation on the time scale of the experiments (several hours). Furthermore, it has a relatively high surface energy ( $\sigma_{lv} = 45$  mJ/m<sup>2</sup>), which allows for stable imaging conditions with AFM. Si substrates (purchased from Wacker) were used for their smoothness and chemical homogeneity. They were covered with a native oxide layer (thickness  $1 \text{ nm} < d_{\text{SiO}_2} < 2 \text{ nm}$ ). The substrates were ultrasonically-cleaned in ethanol and acetone and subsequently left overnight in an oxidizing solution (NoChromix™, GODAX Laboratories, Inc., Tacoma Park, MD, USA) to remove residual organic contaminants. Each step was followed by extensive rinsing in Millipore water. Homogeneous coverage of the samples with a molecularly-thin layer of phenyltrichlorosilane (PTCS) was obtained by exposing the substrates to a saturated vapor atmosphere for  $\approx 2$  h and subsequent ultrasonic cleaning in ethanol.

Optical contact angle measurements were performed with a commercial contact angle measurement system (OCA 15 plus, Dataphysics GmbH, Filderstadt, Germany) using the sessile drop method. Images of the droplets were recorded with a CCD-camera. The shape of the liquid–vapor interface (droplet contour) was determined by a computer program, which searches for the steepest intensity gradient in the images. Contact angles are obtained by fitting the droplet contour using both Laplace–Young and ellipsoidal fit functions.

To deposit the HEG droplets for the AFM measurements, we produced an aerosol in a closed container using a standard vaporizer (Fisher Scientific). The droplets were allowed to settle down on the substrate by gravity. This procedure leads to a distribution of droplets with typical diameters between 0.1 and 25  $\mu\text{m}$ . AFM experiments were performed in ambient conditions at a room temperature of  $\approx 22^\circ\text{C}$  and a relative humidity between 35 and 45%. Images were recorded with a commercial stand-alone AFM (Bioscope, Digital Instruments Co., Santa Barbara, CA, USA) operated in tapping mode. We used Si cantilevers (Nanosensors) with a typical resonance frequency of 300 kHz and a tip radius below 10 nm, as specified by the manufacturer. Before use, the tips were coated with a layer of a perfluorinated alkylsilane ((heptadecafluoro-1,1,2,2-tetrahydrodecyl)-dimethylmonochlorosilane; ABCR GmbH & Co. KG, Karlsruhe, Germany) from the gas phase, to improve the stability of the imaging conditions. Non-disturbing AFM imaging of liquids is a delicate process, which requires high stability of the instrument, low damping and suitable wetting properties of the liquid on the tip. We have described a detailed model of the imaging process in the previous issues of this journal [13, 14]. Briefly, it involves the formation and rupture of a small liquid neck in each oscillation cycle of the AFM cantilever. The presence of the neck leads to an additional intermittent attractive force close to the lower turning point of the cantilever oscillation. This force gives rise to the change in oscillation amplitude, which provides the error signal for the topography feedback loop. We estimate that the distortion of the liquid surface, which is associated with the liquid neck, is less than 5 nm [14].

### 3. MACROSCOPIC APPROACH

#### 3.1. Thermodynamic considerations

To a first approximation, the free energy of a liquid droplet residing on a solid substrate is given by the sum of the interfacial energies  $\sigma_{lv}$ ,  $\sigma_{sl}$ , and  $\sigma_{sv}$  of the liquid–vapor, solid–liquid, and solid–vapor interfaces, respectively, each weighted by the area of the respective interface. (We can neglect gravity, because we consider only droplets smaller than the capillary length.) Minimization of the free energy shows that the equilibrium shape of the droplet is a spherical cap and that the equilibrium contact angle  $\theta_Y$  is given by the Young equation:

$$\cos(\theta_Y) = (\sigma_{sv} - \sigma_{sl})/\sigma_{lv}. \quad (1)$$



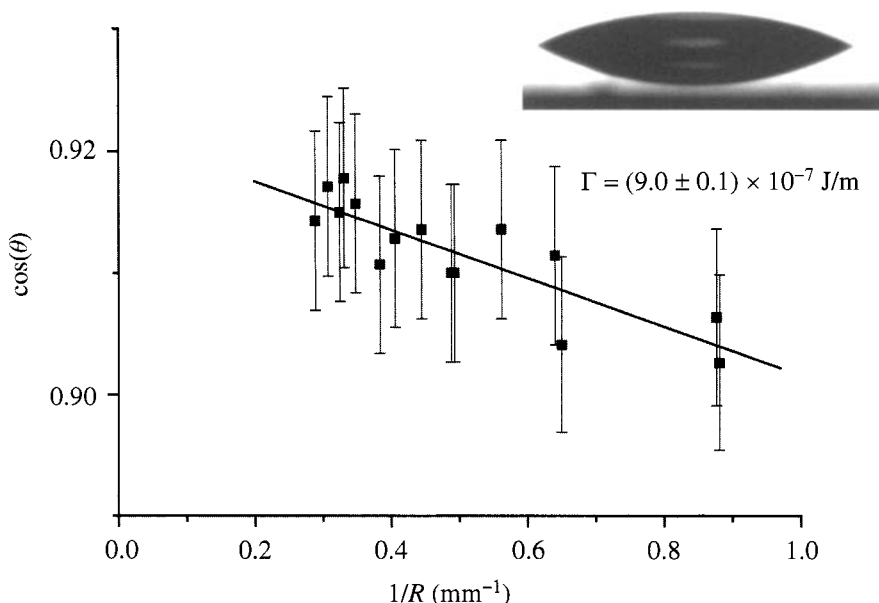


**Figure 1.** Optical contact angle measurements of HEG on coated Si. The cosine of the contact angle versus the inverse base radius is plotted. The solid line is a linear fit according to the modified Young equation. The inset shows a picture of a sessile drop taken with the CCD-camera of the contact angle measurement setup.

This approximation includes only the contributions of the two-phase interfaces to droplet energy. However, the molecules close to the perimeter of the droplet, i.e. close to the three-phase contact line, are influenced by both the solid–liquid and the liquid–vapor interfaces. Therefore, another contribution to the free energy of the droplet arises, which is given by the product of the length of the contact line and the line tension  $\Gamma$ . Taking this term into account, the equilibrium shape of the droplet is still a spherical cap, but now the equilibrium contact angle  $\theta(R)$  is given by the modified Young equation

$$\cos(\theta(R)) = \cos(\theta_Y) - \Gamma/(\sigma_{lv}R). \quad (2)$$

Hence the equilibrium contact angle is expected to increase (decrease) with decreasing drop size for a positive (negative)  $\Gamma$ . So far, we have introduced  $\Gamma$  as a purely phenomenological parameter. Its relation to interfacial forces will be discussed in detail below.

### 3.2. Optical measurements

The inset of Fig. 1 shows a picture of a typical droplet along with its mirror image in the substrate. Viewed from the top, it appears perfectly circular. We recorded a series of images of HEG droplets with various base radii between 1 and 3.5 mm. The droplet contour line was determined via the software, as mentioned in the

experimental section. Later, the contour line was fitted using the Laplace–Young fitting formula to determine the contact angle. The average contact angle is  $24^\circ$ . Within the range of drop sizes investigated, there is an apparent increase in contact angle of  $\approx 2^\circ$  with decreasing  $R$ . In the modified Young plot (Fig. 1) we obtain a linear correlation between the cosine of  $\theta$  and the inverse drop radius. At first glance, it seems natural to interpret the slope in this plot as a line tension of  $\Gamma = 9 \times 10^{-7}$  J/m. In this case, the extrapolated contact angle for infinitely large droplets is  $\theta_Y = \theta(R = \infty) = 22.9^\circ$ . The observed line tension is in qualitative agreement with other experiments using the same optical technique [10, 11]. However, we noticed a number of problems in the process of data recording and analyzing, which raise doubts about the accuracy of the result: the contact angle calculated for each specific droplet varied by  $\pm 1^\circ$ , depending on the setting of the zooms lens on the CCD camera and on the illumination. We also found that the Laplace–Young fitting produced a systematically increasing fitting error with decreasing drop size. For comparison, we analyzed the same images using ellipsoidal fits of the drop shape. The contact angles usually agreed with the Laplace–Young fits to within  $\pm 1^\circ$ , but the apparent line tension varied by more than one order of magnitude and sometimes even changed the sign. For these reasons, we conclude that the accuracy of both the data acquisition and analysis of this typical commercial contact angle setup are insufficient to analyze reliably the variations of the contact angle with drop size. Probably, some of the technical limitations can be improved in a specifically-optimized setup. However, the method will always be limited to droplet sizes of  $\approx 100 \mu\text{m}$  or larger. The most obvious way to test the reliability of the value of  $\Gamma = 9 \times 10^{-7}$  J/m, however, is to extrapolate the result to smaller drop sizes using equation (2). For instance, we would expect a contact angle of  $90^\circ$  for  $R = 22 \mu\text{m}$ . In contrast, for a value of  $\Gamma \approx 10^{-10}$  J/m, as predicted by theory, we obtain  $\theta(R = 22 \mu\text{m}) - \theta(R = \infty) = 0.05^\circ$ . While it is impossible to investigate droplets of this size with a conventional contact angle goniometry setup, it is very simple to distinguish between these two predictions using AFM.

### 3.3. AFM measurements

We produced micrometer-sized HEG droplets, as described above. Figure 2 shows an optical micrograph of a sample including the AFM cantilever. For the present experiments, we imaged a series of isolated droplets with base radii between  $0.38 \mu\text{m}$  and  $8 \mu\text{m}$ . The base radii of the droplets were obtained from circle fits to the perimeter of the droplet in the AFM images. Figure 3 shows an image of a particularly small droplet. A few local deformations of the contact line arise from the residual root mean square roughness of  $1 \text{ nm}$  of the substrate. The distortions in the contour lines reflect the noise in the measurement. The droplet has a spherical cap shape, as shown by the profile (open stars) in Fig. 4. Obviously, the contact angle is still finite for this sub-micrometer-sized droplet. In Fig. 4, we plot representative profiles for a series of droplets of varying size. In sharp contrast to the extrapolation using the optically-measured apparent line tension, qualitatively

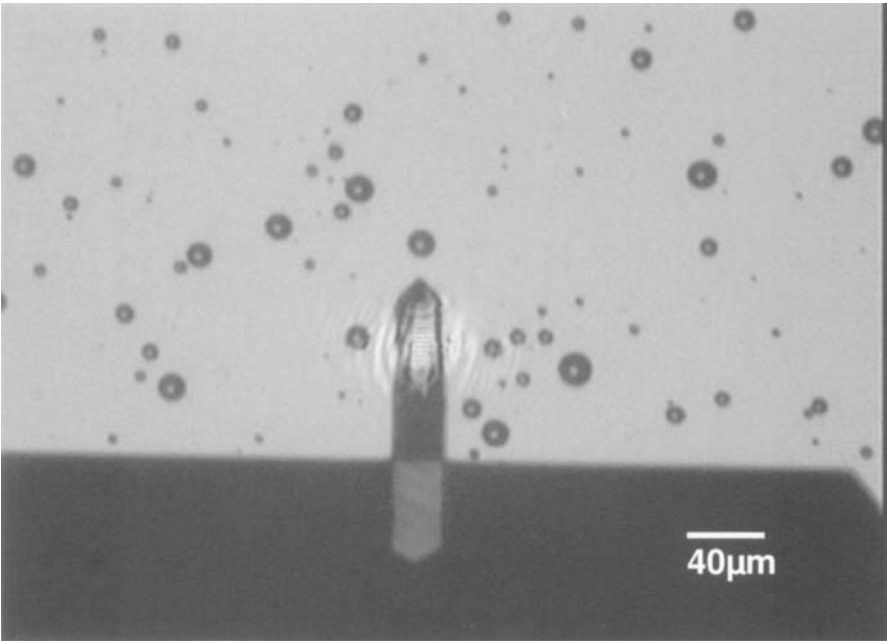


**Figure 2.** Optical microscope image of HEG droplets deposited from an aerosol and the AFM cantilever.

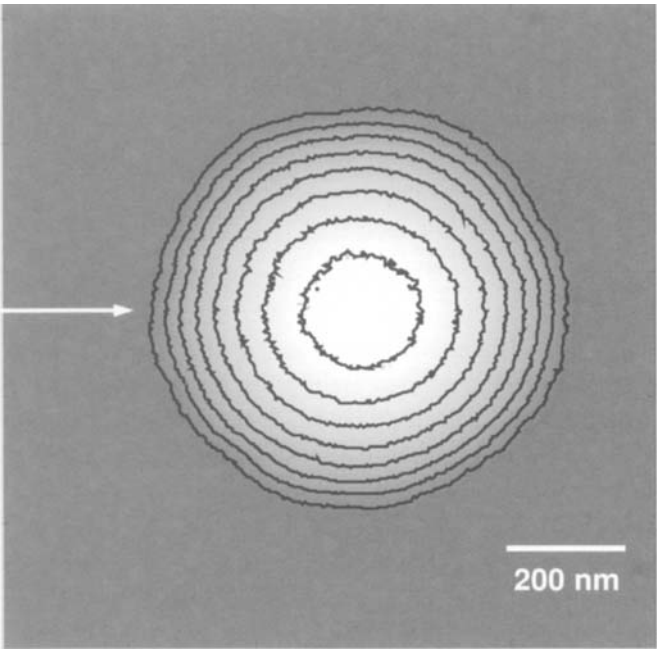


**Figure 3.** AFM image of an HEG droplet on PTCS-coated Si ( $R = 0.38\text{ }\mu\text{m}$ ;  $\theta = 24.4^\circ$ ). The contour lines are separated by 10 nm. The arrow indicates the position of the profile in Fig. 4.

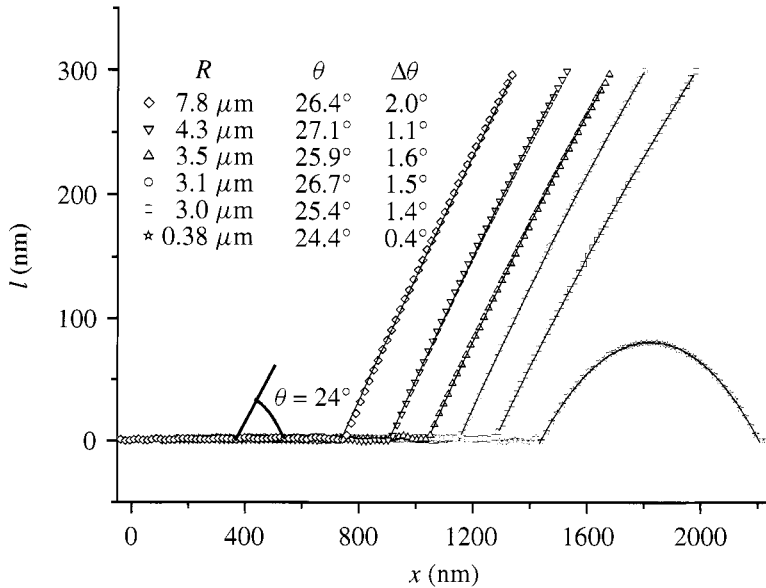


**Figure 4.** AFM profiles for a series of HEG droplets with different base radii. For clarity, only every second data point was plotted. The solid lines are spherical cap fits.

the same contact angle is obtained for all the droplets. The solid lines are spherical cap fits. For comparison, we also indicate the result of the optical measurement in the lower left corner.

The slope of individual profiles, as shown in Fig. 4, varies by  $\pm 2^\circ$  for a series of profiles taken at different positions along the contact line of the same droplet. To improve statistics, we average the contact angles obtained at each point of the contact line. In practice, this is achieved by extracting profiles locally perpendicular to the contact line at each point along the latter. The local contact angles are obtained from the slopes of parabolic fits to these profiles at their intersection with the substrate. For the fits, we excluded the region within 10 nm above the substrate to avoid any possible influence of interfacial force or other possible disturbances. The values for  $\theta$  given in Fig. 4 are obtained by averaging the local contact angles over each entire AFM image.

While the absolute accuracy of the contact angle measurements via the AFM is similar to the optical technique, the precision of the line tension measurement is improved by more than three orders of magnitude, as shown in the modified Young plot (Fig. 5). The open symbols are AFM results. The full square at  $1/R = 0$  represents the average of the optical contact angle data (Fig. 1). The dashed line extrapolates the optical results to smaller drop size. Obviously, the slope of the optical measurements is several orders of magnitude too big to account for the contact angles measured on the micrometer-sized droplets. Instead, a linear fit (solid line in Fig. 5) including all the data points yields a value of  $\Gamma = -(0.95 \pm 1.7) \times 10^{-10}$  J/m. Considering the error we cannot determine

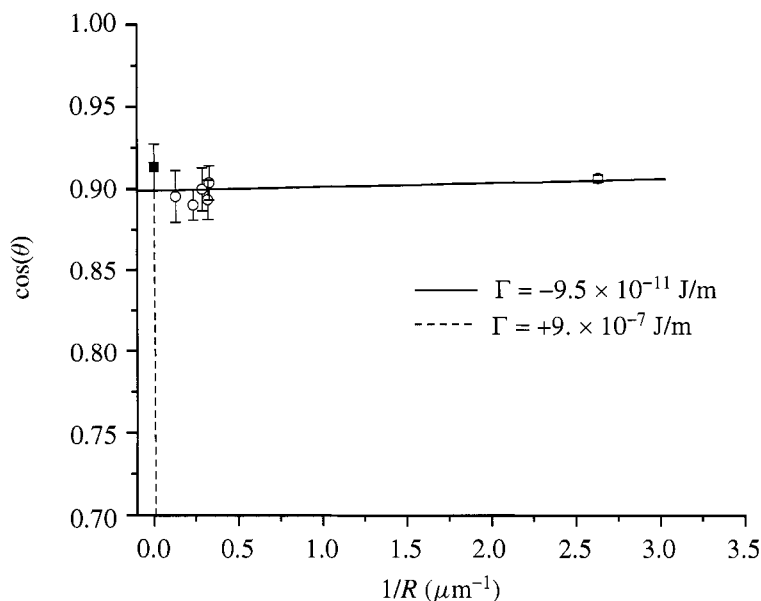


**Figure 5.** Cosine of contact angle versus the inverse base radius. Open circles are AFM data, the filled square represents the average of all the data points in Fig. 1. The dashed line is an extrapolation of the optical results to smaller drop size. The solid line is a fit through all the data points. The indicated values of  $\Gamma$  correspond to the slopes of the dashed and solid lines, respectively.

the sign of  $\Gamma$  from these measurements. The large error arises mainly from the deviation between the optical and the AFM measurements. We noticed that optical measurements on samples, which were exposed to the aerosol treatment in a closed container, produced  $\approx 2^\circ$  smaller values of  $\theta$  than the fresh samples used for the data presented in Fig. 1. Possibly, a microscopically thin layer of liquid covering the whole surface forms during the deposition process of the small droplets and reduces the solid–vapor interfacial energy. This effect would explain the minor deviations between optical and AFM measurements.

#### 4. MICROSCOPIC APPROACH

In Fig. 6a we plot a surface profile for a large droplet ( $R = 7.8 \mu\text{m}$ ) in the vicinity of the contact line. On the horizontal scale of this plot, the asymptotic spherical cap profile appears as a straight line. The experimental data closely follow this asymptotic reference profile. Systematic deviations between the measured profile and the reference profile are only observed within 20 nm of the substrate. The maximum height difference is approximately 5 nm. To understand the deviations, we have to consider the influence of the interfacial forces on the surface profiles. First, we note that the energy of a thin homogeneous film adsorbed onto a solid substrate depends on its thickness  $l$  [15]. The excess free energy per unit area of a film with thickness  $l$  (with respect to  $l = \infty$ ) is called the effective interface

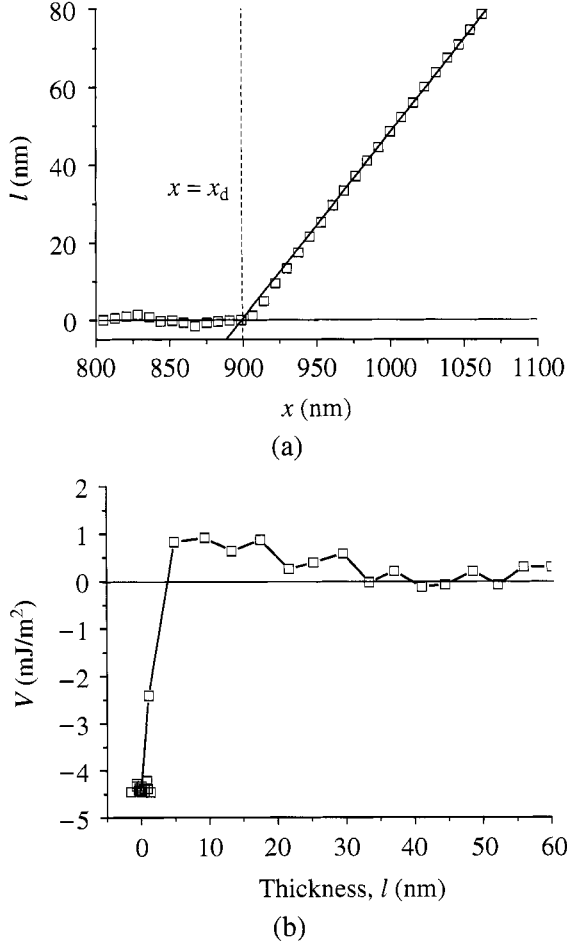


**Figure 6.** (a) Experimental AFM profile for a large HEG droplet ( $R = 7.8 \mu\text{m}$ ) close to the contact line.  $x_d$  indicates the intersection of the asymptotic profile (solid line) with the substrate. (b) Experimental effective interface potential  $V$  calculated from the experimental profile in (a).

potential  $V(l)$ . ( $V(l) \rightarrow 0$  for  $l \rightarrow \infty$ ). Its derivative leads to the interfacial forces or, more precisely, defines the disjoining pressure  $\Pi = -dV/dl$ . Close to the contact line, the local thickness  $l(x, y)$  is small and  $|V(l(x, y))|$  becomes noticeably larger than zero ( $x$  and  $y$  are the horizontal coordinates on the substrate). Hence, there is a contribution to the free energy of the whole droplet that depends on  $V$  and on the equilibrium shape of the surface profile within this range. The equation for the equilibrium profile is obtained by minimizing the free energy of the droplet. In the case of an axisymmetric drop, it reads [16, 17]

$$\sigma_{lv} \cdot \left( \frac{l''(r)}{(1 + l'(r)^2)^{3/2}} + \frac{l'(r)}{r(1 + l'(r)^2)^{1/2}} \right) = \frac{dV}{dl} + p_c. \quad (3)$$

Here,  $r$  is the radial coordinate and  $p_c = 2\sigma_{lv}/R_{3D}$  is the Laplace–pressure,  $R_{3D}$  is the radius of curvature of the liquid–vapor interface, primes denote the derivatives with respect to  $r$ . As we saw already in Fig. 6a, the average curvature of the liquid–vapor interface could be neglected in the vicinity of the contact line for sufficiently large droplets. In this case both  $p_c$  and the second term in the parentheses on the left-hand side of equation (3) can be omitted. We obtain the simplified one-dimensional analog of equation (3) [8]

$$\sigma_{lv} \cdot \frac{l''(x)}{(1 + l'(x)^2)^{3/2}} = \frac{dV}{dl}. \quad (4)$$

Here we replaced  $r$  by  $x$  to be consistent with our previous notation [4]. Now, we calculate the effective interface potential  $V$  by integrating equation (4) using the numerical derivatives  $l'(x)$  and  $l''(x)$  of the experimental profile  $l(x)$

$$V(l(x)) = \sigma_{lv} \int_{-\infty}^x l'(\tilde{x}) \frac{l''(\tilde{x})}{(1 + l'(\tilde{x})^2)^{3/2}} d\tilde{x} + \text{const.} \quad (5)$$

We choose the constant so as to obtain  $V \rightarrow 0$  for  $l \rightarrow \infty$ . The open symbols in Fig. 6b show the result. The zero position of the thickness scale was taken as the average substrate height far away from the droplet. Like any value of thickness quoted throughout this work, the thickness in this graph is relative to the unknown thickness  $l_0$  in that region. However,  $l_0$  is typically smaller than the roughness of the substrate, which gives rise to the scatter in the data points around  $l = 0$  in Fig. 6b. The curve in Fig. 6b meets two important requirements. First,  $V$  remains fairly constant at a large film thickness, which confirms that the approximations leading to equation (5) are fulfilled. Second, the depth of the minimum of  $V$  at  $l = l_0$  for a partially wetting liquid in thermodynamic equilibrium is given by  $\Delta V = V(\infty) - V(l_0) = \sigma_{lv} + \sigma_{sl} - \sigma_{sv} = \sigma_{lv}(1 - \cos(\theta_Y))$ . Using the asymptotic slope in Fig. 6a, we obtain  $\Delta V = 4.4 \text{ mJ/m}^2$ , in agreement with Fig. 6b. This second criterion can be used as an independent test to identify possible tip-induced distortions of the profile.

Once  $V$  is determined, we can calculate  $\Gamma$  within the framework of the interface displacement model [8]

$$\Gamma = \left\{ \int_{-\infty}^{\infty} dx V(l(x)) - \int_{-\infty}^{x_d} dx V(l_0) - \int_{x_d}^{\infty} dx V(\infty) \right\} + \left\{ \sigma_{lv} \cdot \int_{-\infty}^{\infty} dx [\sqrt{1 + l'(x)^2} - \sqrt{1 + a'(x)^2}] \right\}. \quad (6)$$

Here,  $x_d$  denotes the intersection between the asymptotic reference profile  $a(x)$  and  $l = l_0$ .  $a' = 0$  for  $x < x_d$  and  $a' = \tan \theta_Y$  for  $x > x_d$  is the slope of the reference profile. There are two contributions to  $\Gamma$ . The term in first set of brackets

arises directly from the interface potential  $V$ . The one in the second set of brackets arises from the additional liquid–vapor interfacial area that is created due to the (interface potential-induced) deformation of the profile. In both cases the respective contribution of the undisturbed profile in the absence of  $V$  is subtracted [18]. For the present data set, we obtain  $\Gamma = 1.7 \times 10^{-11}$  J/m. The absolute value is very sensitive to the contact angle of the reference profile. An error of  $\Delta\theta = 0.5^\circ$  leads to an uncertainty of  $\Delta\Gamma = \pm 3 \times 10^{-11}$  J/m. Comparing a series of randomly chosen profiles on the same droplet, we found variations of  $\Delta\Gamma = \pm 7 \times 10^{-11}$  J/m. Hence, we can give an upper limit of  $|\Gamma| = 10^{-10}$  J/m based on the profile analysis. Within the error,  $\Gamma$  could be either positive or negative.

To demonstrate that a value of  $\Gamma \gg 10^{-10}$  J/m is incompatible with the AFM profiles, we calculated surface profiles using a model function for the effective interface potential. As an example that mimics the partial-wetting situation of HEG on silanized Si, we used a repulsive (i.e. wetting) van der Waals contribution with a positive Hamaker constant  $A$  and an exponential short-range contribution with a prefactor  $C < 0$ .

$$V_{\text{model}}(l) = C \cdot \exp\left(-\frac{l}{\kappa}\right) + \frac{A}{12\pi(l + d_0)^2}. \quad (7)$$

We introduced a cutoff length  $d_0 = 0.1$  nm to prevent the divergence of the van der Waals term for  $l \rightarrow 0$ . We chose a decay length  $\kappa = 1.5$  nm and adjusted the value of  $C$  to match the experimental contact angle of  $24^\circ$ . The model function was inserted in equation (4) and the corresponding droplet profiles were computed numerically using a Runge–Kutta algorithm. To obtain profiles for various values of  $\Gamma$ , we varied  $A$  between  $10^{-19}$  and  $10^{-16}$  J. (For HEG on silanized Si, we expect  $A = 1.8 \times 10^{-19}$  J, based on the refractive indices.) For each value of  $A$ , we adjusted  $C$  to maintain the contact angle constant. The results are shown in Fig. 7 along with the corresponding values of  $\Gamma$ . As expected, the deviations from the asymptotic reference profile increase with increasing  $\Gamma$ . For  $\Gamma = 6.0 \times 10^{-10}$  J/m the distance between  $x_d$  and the intersection of the surface profile is  $\Delta x \approx 40$  nm. Such large deviations are clearly incompatible with the experimental profile. The exact values of both the line tension and  $\Delta x$  depend on the specific choice of the model function. Qualitatively, however, other model potentials that we used for comparison also produced values of  $\Delta x \gg 10$  nm whenever the parameters were adjusted to obtain  $|\Gamma| \gg 10^{-10}$  J/m.

While this result is consistent with the macroscopic approach, the calculated profile for  $A = 10^{-19}$  J does not fit the experimental data in Fig. 7. If van der Waals interactions were dominant in this system, we would expect deviations of the profile only for  $l < 5$  nm (see solid curve in Fig. 7). However, the HEG absorbs significant amounts of water under ambient conditions [19]. Thus the liquid is a two-component system that can display concentrations gradients in the vicinity of the liquid–solid interface. In this case, osmotic effects produce long-range profile distortions and a long-range effective interface potential. Given the poor control



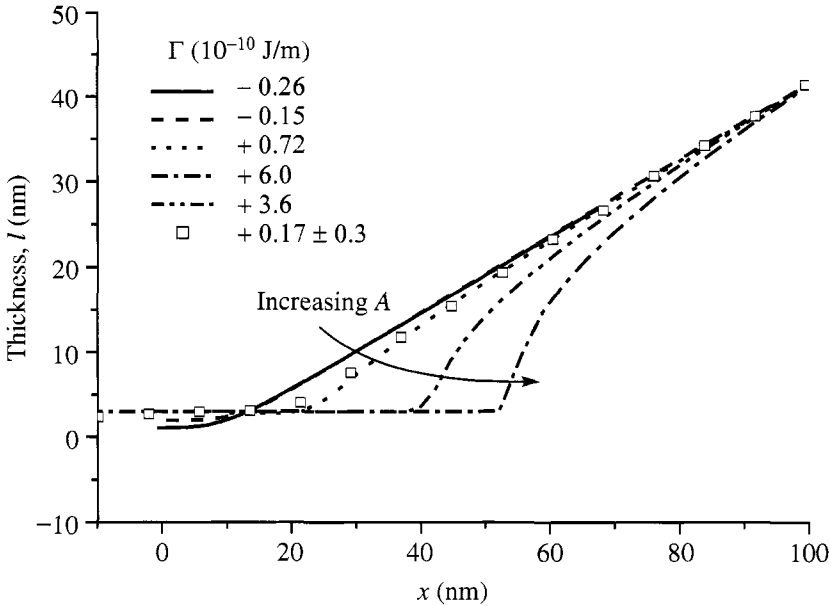


**Figure 7.** Equilibrium profiles (lines) calculated using equation (4) for the model interface potential (equation (7)) with a series of parameters  $A = 10, 100, 1000, 5000$ , and  $10\,000 \times 10^{-20}$  J corresponding to the indicated values of  $\Gamma$ .  $\Gamma$  increases in the same order as  $A$ . Open squares: experimental data (cf. Fig. 6a).

of these effects under ambient conditions, we do not attempt to fit or explain this aspect quantitatively.

## 5. DISCUSSION

In previous AFM measurements, we investigated droplets of HEG on substrates covered with a periodic pattern of hydrophilic and hydrophobic stripes [4]. This wettability pattern induced a modulation of the three-phase contact line along with a variation of the local contact angle. In those experiments, the line tension was calculated by analyzing the dependence of the local contact angle on the local curvature of the contact line. Equation (3) was interpreted in terms of a local balance of forces at the three-phase contact line. The line tension was obtained from slopes of the linear regions in the modified Young plot. This was an elegant way to cover a large range of curvature in a single measurement. With the present approach using homogeneous substrates, we need to image several droplets to obtain the same information. While this procedure is considerably more time consuming, the data analysis is more straightforward. First, it is technically simpler to determine the contact angle, because there are no variations of the local curvature of the contact line, which induce distortions of the profiles. Second, the interpretation of the results is simply a continuation of the macroscopic optical approach. Hence it

allows for a direct comparison to the optical measurements, as presented in Fig. 5. The discrepancy between the dashed line in this figure, which is based on the optical measurements alone, and the AFM results shows that it is not correct to interpret the trend in the optical measurements in terms of a line tension, as it appears in the modified Young equation. This conclusion is now obtained on the basis of the modified Young equation in its simplest form, without invoking its local interpretation where both  $\theta$  and the curvature depend on the position along the contact line.

In spite of this conclusion, the optical contact angle measurements clearly produced a trend in the contact angle with changing drop size. We already mentioned some of the technical problems in the data analysis that in our opinion cause the trend in the data. An alternative explanation, which was suggested in the literature, is the so-called pseudo-line tension. Small-scale heterogeneities on the substrate cause local deformations of the contact line and thereby increase the area of the liquid–vapor interface. The associated modulation of the interface decays exponentially with increasing distance from the contact line [20]. This increases the total surface energy depending on the amplitude and wavelength of the contact line roughness. From the roughness of the contact line in the AFM measurements we find an upper limit of  $\approx 20$  nm for the amplitude. The wavelength of the deformations is also  $\approx 20$  nm. For these values, we obtain an increase in capillary energy per wavelength, i.e. a pseudo-line tension, of the order  $10^{-9}$  J/m. This value is approximately three orders of magnitude smaller than the slope in Fig. 2. Hence, we have no explanation for this trend, except for the experimental problems discussed earlier.

## 6. CONCLUSIONS

The possibility to image liquid structures on the nanometer scale by an AFM extends the range of optical contact angle goniometry by three orders of magnitude. In this study, we have demonstrated the use of this new technique to determine the line tension of a liquid–solid–vapor three-phase contact line and have compared it to the conventional technique of optical contact angle measurements. The AFM measurements revealed that the strong drop size dependence of the contact angle, which is frequently observed in optical contact angle goniometry, is not caused by the line tension. This result is obtained directly in a macroscopic approach by analyzing the global shape of the liquid–vapor interface of micrometer-sized droplets. Furthermore, in the system investigated here, the specific long-range interfacial forces allow for a microscopic analysis of the force-induced distortions of the liquid–vapor interface in the immediate vicinity of the contact line. Their magnitude confirms the upper limit for the line tension of  $\Gamma \approx 10^{-10}$  J/m that was obtained from the global shape of the surface. We expect that similar results can be obtained for other organic liquids. Future experiments should also address questions related to substrate heterogeneities and contact angle hysteresis.

### Acknowledgements

We would like to thank the Deutsche Forschungsgemeinschaft (DFG) for financial support under Grant No. He 2016/5 within the Priority Program 'Wetting and Structure Formation at Interfaces'.

### REFERENCES

1. G. Binnig, C. Quate and C. Gerber, *Phys. Rev. Lett.* **56**, 930 (1986).
2. J. Hu, X. D. Xiao and M. Salmeron, *Appl. Phys. Lett.* **67**, 476 (1995); L. Xu, M. Salmeron and S. Bardon, *Phys. Rev. Lett.* **84**, 1519 (2000).
3. T. Pompe, A. Fery and S. Herminghaus, *Langmuir* **14**, 2585 (1998).
4. T. Pompe and S. Herminghaus, *Phys. Rev. Lett.* **85**, 1930 (2000).
5. J. Lyklema, *Fundamentals of Interface and Colloid science*, Vol. III. Academic Press, San Diego, CA (2000).
6. J. Drelich, *Colloids Surfaces A* **116**, 43 (1996).
7. J. S. Rowlinson and B. Widom, *Molecular Theory of Capillarity*. Clarendon, Oxford (1982).
8. J. O. Indekeu, *Physica A* **183**, 439 (1992).
9. C. Bauer and S. Dietrich, *Eur. Phys. J.* **B10**, 767 (1999).
10. A. Amirfazli, D. Y. Kwok, J. Gaydos and A. W. Neumann, *J. Colloid Interface Sci.* **205**, 1 (1998).
11. A. Amirfazli, S. Hänig, A. Müller and A. W. Neumann, *Langmuir* **16**, 2024 (2000); D. Duncan, D. Li, J. Gaydos and A. W. Neumann, *J. Colloid Interface Sci.* **169**, 256 (1995).
12. J. Y. Wang, S. Betelu and B. M. Law, *Phys. Rev. Lett.* **83**, 3677 (1999); J. Y. Wang, S. Betelu and B. M. Law, *Phys. Rev. E* **63**, 031601 (2001).
13. A. Fery, T. Pompe and S. Herminghaus, *J. Adhesion Sci. Technol.* **13**, 1071 (1999).
14. S. Herminghaus, T. Pompe and A. Fery, *J. Adhesion Sci. Technol.* **14**, 1767 (2000).
15. P. G. de Gennes, *Rev. Mod. Phys.* **57**, 827 (1985).
16. Y. Solomentsev and L. R. White, *J. Colloid Interface Sci.* **218**, 122 (1999).
17. E. K. Yeh, J. Newman and C. J. Radke, *Colloids Surfaces A* **156**, 137 (1999).
18. In principle, the relation between  $\Gamma$  and  $V$  and  $l(x)$  includes non-local contributions. However, a detailed comparison between non-local density functional calculations and the local approximation (equation (6)) showed that the non-local contributions were negligible in most practical cases, including our experiments [9].
19. Th. Richartz, J. Galle and G. Klose, *Chem. Phys. Lett.* **271**, 79 (1997).
20. J. F. Joanny and P. G. de Gennes, *J. Chem. Phys.* **81**, 552 (1984).

# Measurements of Colloidal Forces

## Surface forces between sphalerite and silica particles in aqueous solutions

ZHENGHE XU<sup>1,\*</sup>, RUAN CHI<sup>1</sup>, T. DIFEO<sup>2</sup> and J. A. FINCH<sup>2</sup>

<sup>1</sup> *Department of Chemical and Materials Engineering, University of Alberta, Edmonton, Alberta T6G 2G6, Canada*

<sup>2</sup> *Department of Mining and Metallurgical Engineering, McGill University, Montreal, Quebec H3A 2B2, Canada*

**Abstract**—Surface forces between a fractured sphalerite surface and a silica particle in supporting electrolyte solutions were measured using an atomic force microscope. Below pH 8, the long-range surface forces were found to be attractive, decreasing with increasing solution pH. The adhesion force varied from 18 mN/m at pH 4 to 7 mN/m at pH 8. At pH 10, an exponentially decayed repulsive force was measured and no adhesion was observed. The decay length was found to scale with the supporting electrolyte concentration. Although the repulsive force was reduced significantly when up to 0.5 mmol/l calcium ions were added, the surfaces remained non-adhering at contact. In contrast, an attractive force profile was obtained when 0.5 mmol/l cupric ions were added, accompanied by an adhesion force of 16 mN/m. In general, the measured force profile can be accounted for by considering classical van der Waals and electrical double-layer forces for constant surface charge density conditions. The measured force behavior correlates well with the observations in sphalerite–silica heterocoagulation tests.

**Keywords:** Surface forces; adhesion forces, DLVO theory; silica; sphalerite; heterocoagulation; flotation.

### 1. INTRODUCTION

Particle–particle interactions play an important role in a variety of industrial processes, including ceramic processing, powder technology, mineral flotation, pharmaceutical and food processing, and paint and ink formulations. In mineral flotation, for example, the attractive force between particles can be either beneficial or detrimental. For fine particle flotation, the homocoagulation of the targeted component is desirable as it improves the flotation rate of the component by increasing

---

\*To whom correspondence should be addressed. Phone: (780) 492-7667; Fax: (780) 492-2881; E-mail: zhenghe.xu@ualberta.ca

its apparent particle size. The heterocoagulation of dissimilar particles, on the other hand, is detrimental to the separation of the component [1], although this phenomenon has been used in carrier flotation to its advantage [2, 3]. In flotation, it is crucial to avoid heterocoagulation since at least two deleterious effects of fines can be seen: reduction in recovery and concentrate grade due to slime coatings and mechanical entrapment, respectively [4]. To obtain selective flotation, the separation and subsequent stabilization of individual components from composite aggregates have to be accomplished through controlling the physicochemical conditions of separation systems. Clearly, understanding and controlling the interaction forces among the particles in a processing environment are of vital importance.

The recent advances in modern instrumentation have propelled the research in surface force measurements by surface force apparatus (SFA) and atomic force microscope (AFM) [5]. The non-DLVO (Derjaguin–Landau–Verwey–Overbeek) colloidal forces, such as the hydration force, hydrophobic force, undulation force, protrusion forces, ion correlation forces, steric forces, and structural forces in non-aqueous systems, have been either experimentally confirmed or newly discovered [6]. For mineral processing applications, the colloidal forces involved have been measured for a range of mineral systems, such as silica–mica [7], silica–iron oxide [8], silica–alumina [9], silica–covellite [10], silica–zinc sulfide [11], zinc sulfide–zinc sulfide [12], and silica–air bubbles [13–15], to name a few. In the measurement of the colloidal forces between a silica particle and a synthetic zinc sulfide particle in aqueous supporting electrolyte solutions [11], the objective was to determine whether asymmetric oxide–sulfide interactions could be predicted from the knowledge of the symmetric systems. The limited data showed a monotonic repulsive force profile with no adhesion on separation in a 0.2 mmol KCl aqueous solution at pH 5.8. In this paper, we report the detailed force measurement with a fractured mineral sphalerite and a silica sphere in the context of selective sphalerite flotation. This work stems from the observed contamination of sphalerite concentrate by silica, if floated from a neutral pH slurry, but not from an alkaline slurry.

## 2. EXPERIMENTAL

### 2.1. Materials

Ultrahigh purity chemicals were used in this study. Potassium chloride (99.998%), sodium hydroxide (99.996%), calcium chloride (99.996%), hydrochloric acid (99.9999%), and cupric chloride (99.99%) were purchased from Alfa Aesar (USA) and used without further purification. The mineral sphalerite was purchased from Ward's Natural Science Establishment (Canada). It contained 68.26% Zn and 28.96% S with trace amounts of Fe (0.38%), Cu (0.063%), and Pb (0.012%). The sample was stored in a freezer at  $-4^{\circ}\text{C}$ . The silica sphere was from Polysciences, Inc. (Warrington, PA, USA) [16]. The water used in this study was prepared using an Elix-5 with a Millipore-UV plus unit (Millipore, Canada).

All the glassware was cleaned using a 10% sodium hydroxide aqueous solution with 5% (by volume) ethanol, and rinsed thoroughly with deionized water. The tools for assembling the AFM experiments and sample manipulation were cleaned with spectral grade chloroform, rinsed with ethanol (100%), and blow-dried with compressed nitrogen of ultrahigh purity.

## 2.2. Instrumentation and procedures

A Nanoscope E atomic force microscope (Digital Instruments, Santa Barbara, CA, USA) was used to measure the forces between the silica sphere and the fractured sphalerite in an aqueous medium. A detailed description of the working principles of the AFM for the colloidal force measurement is available in the literature [16–18]. In our experiments, a silica sphere was glued onto a short, thick AFM cantilever by means of a micro-manipulator viewed through an optical microscope. Effort was made to position the particle as close to the AFM tip as possible. A two-component epoxy, Master Bond Polymer (EP21LV, Master Bond, USA), was used as the adhesive. A typical micrograph of the glued silica particle onto a cantilever, obtained with a scanning electron microscope (SEM), is shown in Fig. 1. The

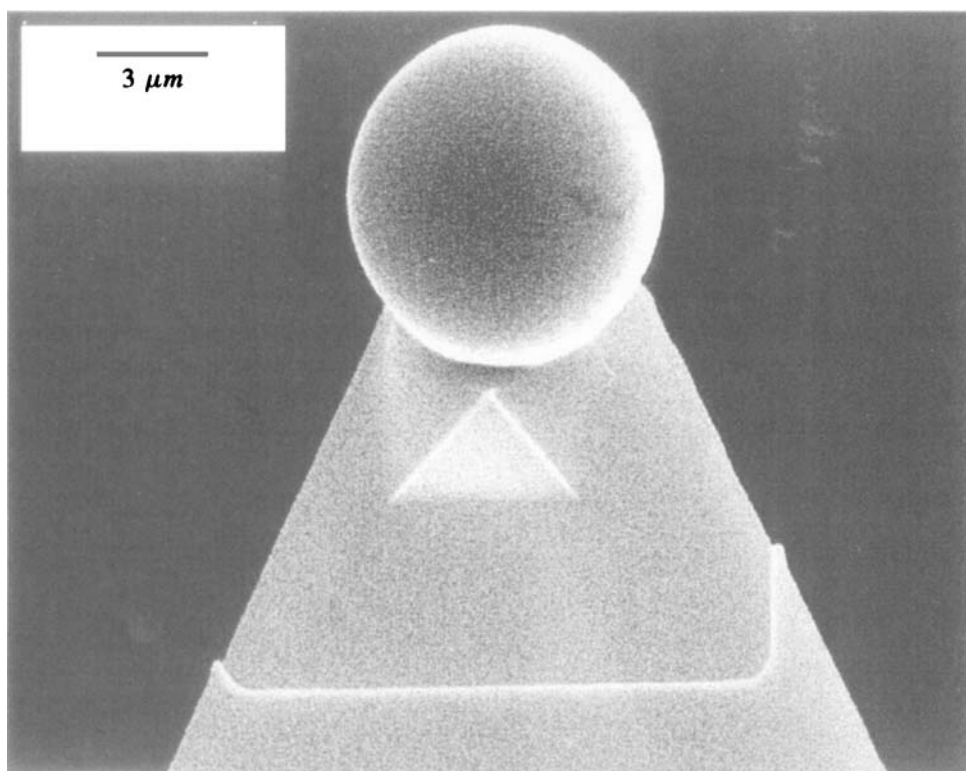


**Figure 1.** SEM micrograph of a 6- $\mu\text{m}$  silica sphere glued onto an AFM cantilever used in the colloidal force measurements.

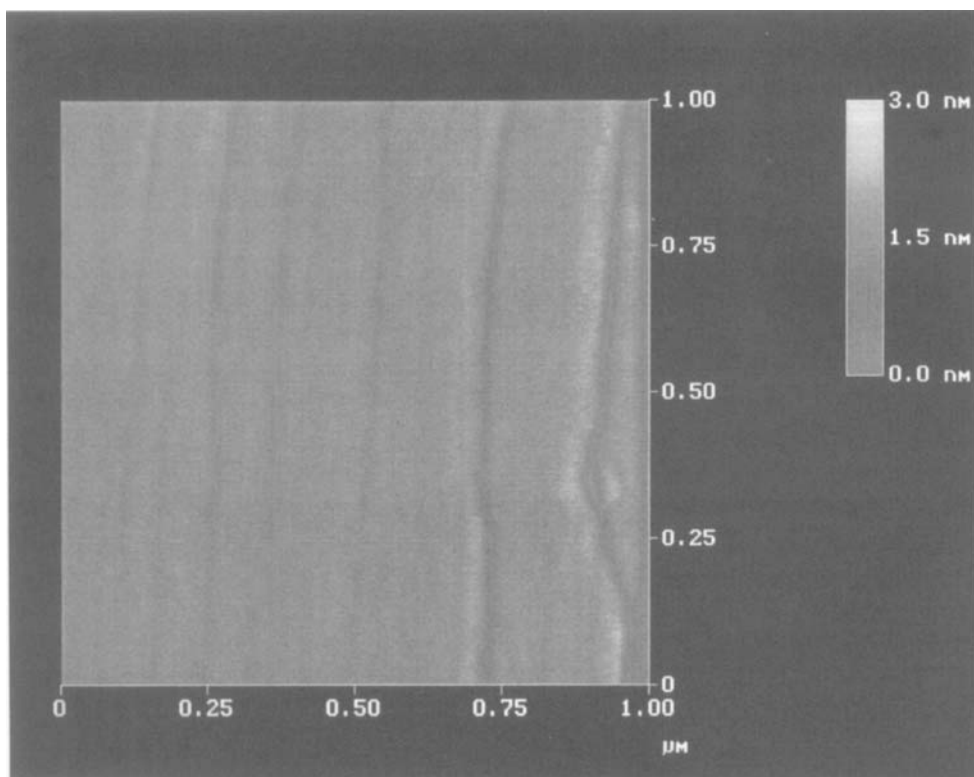


**Figure 2.** A typical AFM image of the fractured sphalerite surface obtained in air: contact mode AFM at a scan rate of 2.4 Hz.

spring constant of the cantilever (0.32 N/m) was calculated based on its geometry as determined from the SEM image [9]. The sphalerite was fractured immediately prior to the experiment. A carefully chosen grain of sphalerite was glued onto a freshly cleaved mica sheet with a flat fractured face exposed for testing. A typical AFM image of the fractured sphalerite surface is shown in Fig. 2. Attention was paid to the morphology of the surface and no attempt was made to obtain the atomic resolution images or surface crystalline characteristics. As shown in Fig. 2, over the  $1 \times 1 \mu\text{m}$  area imaged, a few steps of  $<0.5 \text{ nm}$  height were evident. With this scale of roughness, the fractured sphalerite surface can be considered smooth and suitable for AFM force measurement.

The apparatus was assembled under a horizontal laminar flow cabinet with zero count of particles greater than  $0.5 \mu\text{m}$ . The force measurements were performed with a fluid cell from Digital Instruments using freshly prepared solutions. Prior to the injection of the test solutions, the force was measured in air and a typical long-range attractive force profile was obtained. After the injection of the solution, the system was allowed to equilibrate for 15 min prior to the force run. A few force runs were performed under each test condition and only the representative force curves were analyzed using the established algorithm [16]. The measured forces ( $F$ ) were



normalized by the local radius of the silica sphere ( $R$ ) as  $F/R$  for comparison with the theory.

### 3. RESULTS

#### 3.1. Forces in KCl solutions

The surface forces between a silica sphere and a mineral sphalerite plate in 1 mmol/l electrolyte solution as a function of the solution pH are shown in Fig. 3. Under relatively acidic conditions of pH around 4, a long-range attractive force was measured. The two surfaces jumped into contact at a separation distance of *ca.* 30 nm. The range of the attractive force reduced as the solution pH was increased to 6, with a corresponding jump-in distance of 22 nm. With a further increase in solution pH to 8, a small energy barrier between the two surfaces appeared at a separation distance of around 14 nm. The interaction became repulsive all the way down to the 'contact' without adhesion on separation when the pH was 10. The observed force behavior appears to agree with the expectation of the electrostatic double-layer forces as the surface charge density of sphalerite is anticipated to change from positive to negative, while silica becomes progressively more negative with increasing solution pH, resulting in a stronger electrostatic double-layer repulsion at pH around 10. Corresponding adhesion force measurements showed a decrease

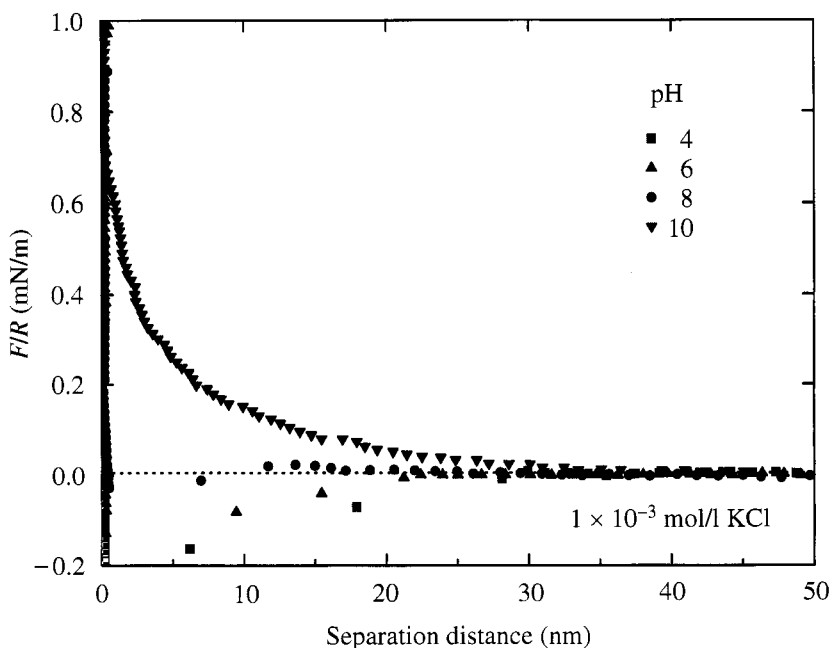


**Figure 3.** Measured forces between a silica sphere and a fractured sphalerite plate in 1 mmol/l KCl solution as a function of the solution pH.

in the adhesion force with increasing solution pH. At pH 4, the measured pull-off force was 18 mN/m, which reduced to 14 mN/m at pH 6 and 7 mN/m at pH 8. At pH 10, adhesion was not observed. It appears that under the limited forces that can be applied in AFM, a thin molecular dimension water film remained on the silica surface, due to its highly hydrophilic nature. This water film prevents intimate contact between the sphalerite and silica, at which the attractive van der Waals force would dominate. It is important to mention that a monotonic repulsive force was reported in an earlier study with a synthetic zinc sulfide and silica particles under similar conditions [11]. This apparent inconsistency may be attributed to the differences in the surface properties of the synthetic zinc sulfide and natural sphalerite. Different flotation responses of these two kinds of zinc sulfide were reported earlier [19]. It was reported that natural sphalerite particles are considerably more hydrophobic than synthetic zinc sulfide [20].

To confirm further whether the long-range repulsive forces did arise from the osmotic repulsion of overlapping electrical double layers, the forces were measured as a function of the electrolyte concentration. The results obtained at a solution pH of 10 are given in Fig. 4. Figure 4a shows that the range of the repulsive force reduced with increasing supporting electrolyte concentration. When plotted on a semi-log scale as shown in Fig. 4b, an almost linear relation is seen between the measured force and the separation distance, suggesting an exponential decay of the repulsive force with the separation distance. From the best fit of the curve, decay lengths of 9.4, 2.9, and 0.94 nm were obtained at KCl concentrations of  $10^{-3}$ ,  $10^{-2}$ , and  $10^{-1}$  mol/l, respectively. These values correspond well with the theoretically expected decay lengths of 9.6, 3.0, and 0.96 nm at corresponding electrolyte concentrations [6], suggesting that the overlap of the electrical double layers was responsible for the observed repulsive force in high pH solutions. It should be noted that even in 0.1 mol/l KCl solution, no adhesion force was measured, further confirming the existence of a thin molecular water layer at the 'contact' position.

### 3.2. Calcium effect

Since lime is often used as a pH modifier in sulfide flotation practice, the presence of calcium in the aqueous phase is anticipated to affect the interactions between the sphalerite and silica. The measured forces at pH 10 as a function of the calcium concentration are shown in Fig. 5a. Clearly, the addition of calcium ions reduced the long-range repulsive force. The detailed analysis showed that the reduction of the force could not be accounted for by the simple screening effect of increasing electrolyte concentration. Some degree of charge neutralization at the sphalerite and/or the silica surface appears to contribute to this reduction. It is interesting to note that at 0.5 mmol/l calcium, the force profile remains repulsive over the separation range measured. At this pH, no adhesion was measured on separation in the presence of up to 0.5 mmol/l calcium. This observation suggests that the two interacting surfaces retain surface charges of the same sign. These observations are consistent with earlier studies that showed minimal adsorption of calcium on silica

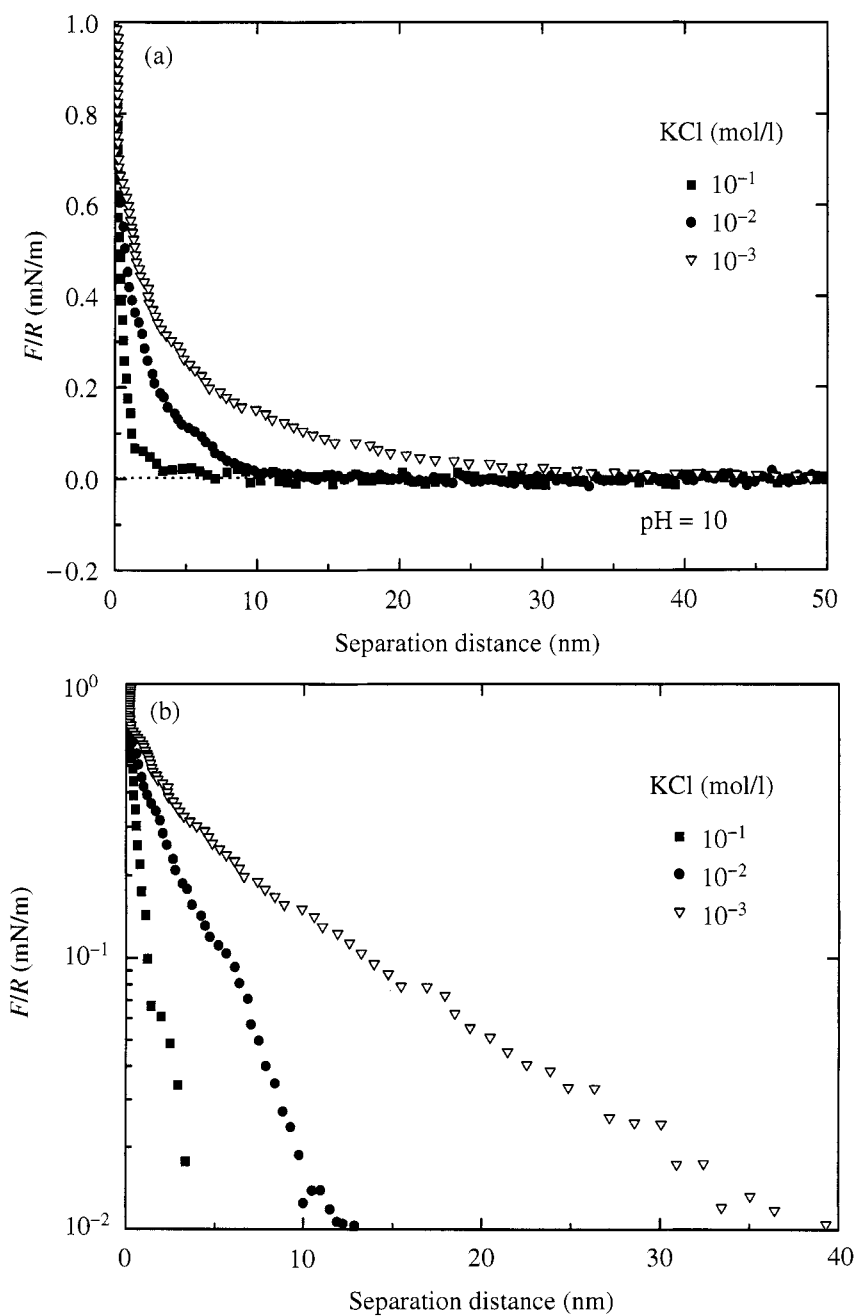


**Figure 4.** Measured forces between a silica sphere and a fractured sphalerite plate in KCl solution at pH 10: (a) linear scale plot; (b) semi-log scale plot to illustrate the electrolyte concentration dependence of the exponential decay of long-range repulsive forces.

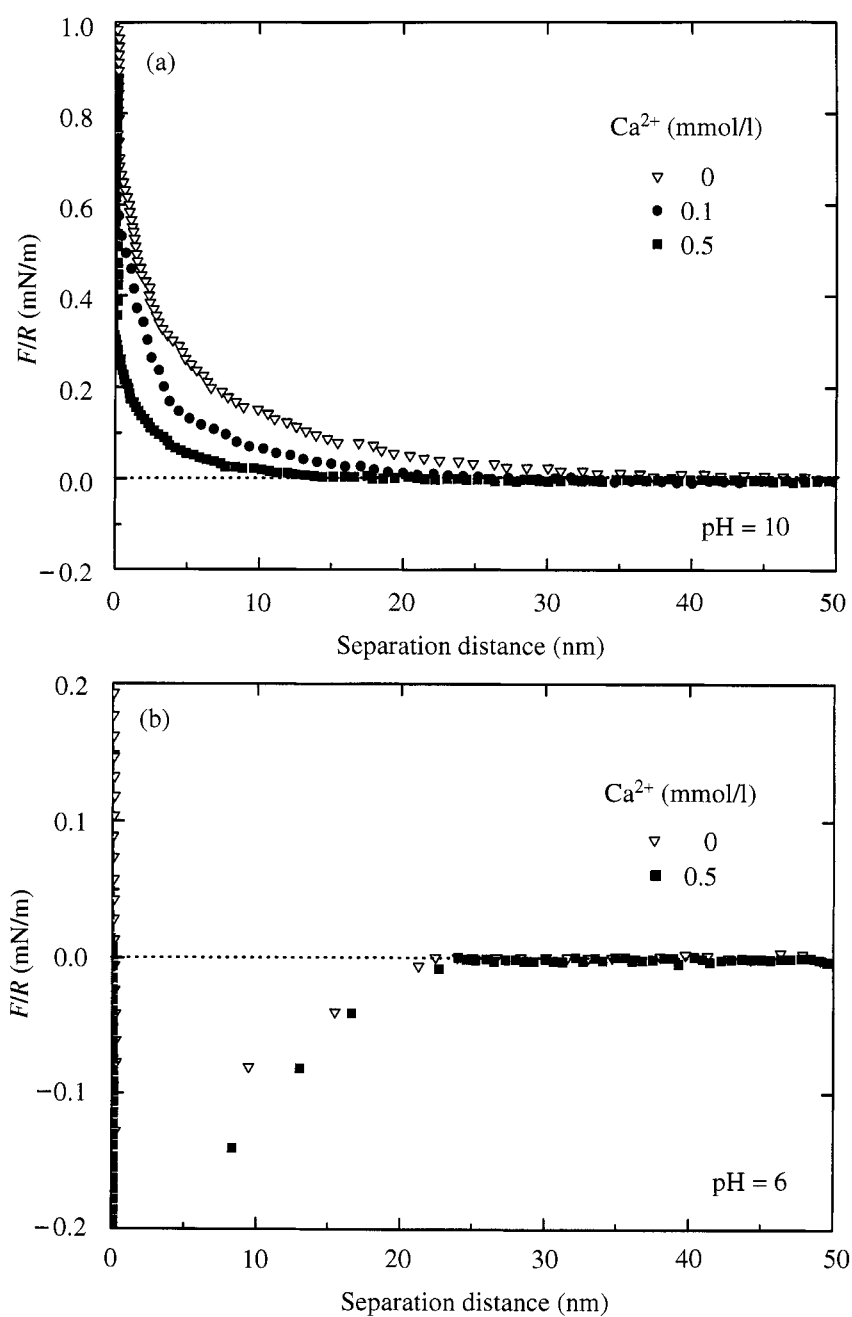


**Figure 5.** Effect of calcium ions on the forces between a silica sphere and a sphalerite surface in 1 mmol/l KCl solution: (a) at pH 10 and (b) at pH 6.

at pH below 10 [21]. The low adsorption density of calcium on silica below pH 10 was attributed to a low concentration of calcium monohydroxide cations ( $\text{CaOH}^+$ ), which are considered to be the species responsible for the specific adsorption of metal ions on various metal oxides. Similarly, the specific adsorption of calcium ions on oxidized sphalerite can be considered marginal. As a result, both the silica and the sphalerite surfaces remain negatively charged, resulting in an electrostatic double-layer repulsion. It should be mentioned that over the neutral pH range, the addition of calcium caused a marginal increase in the attractive forces with a slightly increased jump-in distance. At pH 6 as shown in Fig. 5b, for example, the jump-in distance increased from 22 nm to 25 nm with the addition of 0.5 mmol/l calcium. The observed increase in the attractive forces can be accounted for by an increased electrostatic double-layer attraction, as an increase in the positive surface potential of sphalerite upon the specific adsorption of calcium ions from association with surface sulfur species is anticipated [22], while the negative surface electric potential of silica is affected only marginally, due to the lack of specific adsorption of calcium at this pH [21].

### 3.3. Effect of cupric ion

Copper sulfate is typically used to activate the flotation of sphalerite in sulfide flotation practice. It is, therefore, interesting to study the effect of cupric ions on the interaction forces between sphalerite and silica. The forces measured in the presence of 0.5 mmol/l copper at pH 10 are shown in Fig. 6. For comparison, the force profiles of the silica interacting with the sphalerite in background electrolyte solutions with and without 0.5 mmol/l calcium addition are also included in this figure. Compared with calcium, cupric ions have a more pronounced effect on the interaction forces. In fact, the silica became attracted to sphalerite in 0.5 mmol/l cupric ion solution at this pH. The energy barrier was found to be negligible and the surfaces jumped into contact at a separation distance of 22 nm. An adhesion force of 16 mN/m was measured under these conditions. Unlike the calcium ions, cupric ions are known to chemisorb on sphalerite and replace the lattice zinc ions [23], resulting in a pseudo-covellite surface positively charged at pH around 10 [24]. The effect of cupric ions on the surface potential can be considered marginal as cupric ions at pH 10 are predominately in the form of  $\text{Cu}(\text{OH})_2(\text{s})$  or  $\text{HCuO}_2^-$ , which are incapable of specific adsorption on the silica surface [21]. However, whether the change of the interaction forces from repulsive to attractive by the addition of cupric ions is mainly due to the charge reversal on sphalerite or simply by the reduction of surface charge accompanied by an increased surface hydrophobicity on sphalerite cannot be distinguished. Nevertheless, the important message is that the presence of cupric ions is detrimental for the rejection of silica from the sphalerite concentrate, due to the anticipated heterocoagulation of the two. Clearly, in the presence of cupric ions, raising the slurry pH to 10 alone may not be sufficient to avoid the heterocoagulation of silica with sphalerite.

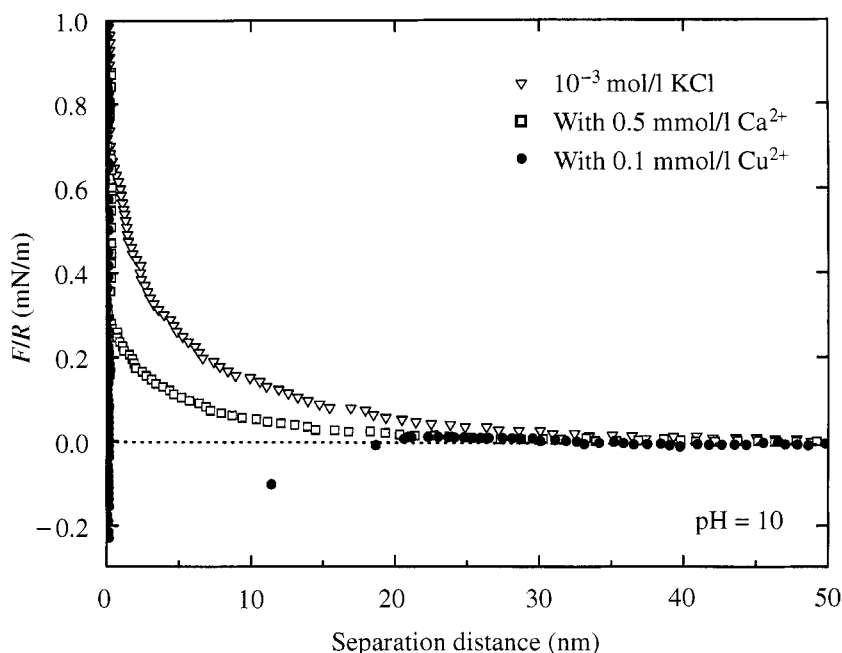


**Figure 6.** Effect of cupric ions on the forces between a silica sphere and a sphalerite surface in 1 mmol/l KCl solution at pH 10.

## 4. DISCUSSION

### 4.1. Theoretical considerations

To account quantitatively for the measured long-range repulsive forces at pH 10, for example, the electrostatic double-layer interaction energy was estimated by solving numerically the Poisson–Boltzmann equation using a previously developed algorithm [25]. Using the reported electrokinetic potential values of silica ( $-90$  mV) and sphalerite ( $-35$  mV) [11], the interaction energy was calculated for both constant surface potential ( $\psi$ ) and constant surface charge density ( $\sigma$ ) conditions. The results are given in Fig. 7, along with the experimentally measured force profile. A close match between the measured force profile and that calculated under the constant surface charge density condition confirms that the long-range repulsive force is indeed due to the overlap of electrical double layers around two interacting surfaces. More importantly, this comparison suggests that both surfaces maintained their original surface charge densities during their approach to each other. Similar observations were reported earlier [11, 12, 26].

Although the long-range repulsive forces measured at pH 10 with and without calcium addition can be attributed to the overlapping of the electrical double layers around the sphalerite and silica particles, the origin of the attractive force remains to be determined. For the present system (silica/water/sphalerite), a combined Hamaker constant ( $A_{132}$ ) of  $1 \times 10^{-20}$  J was calculated using the known

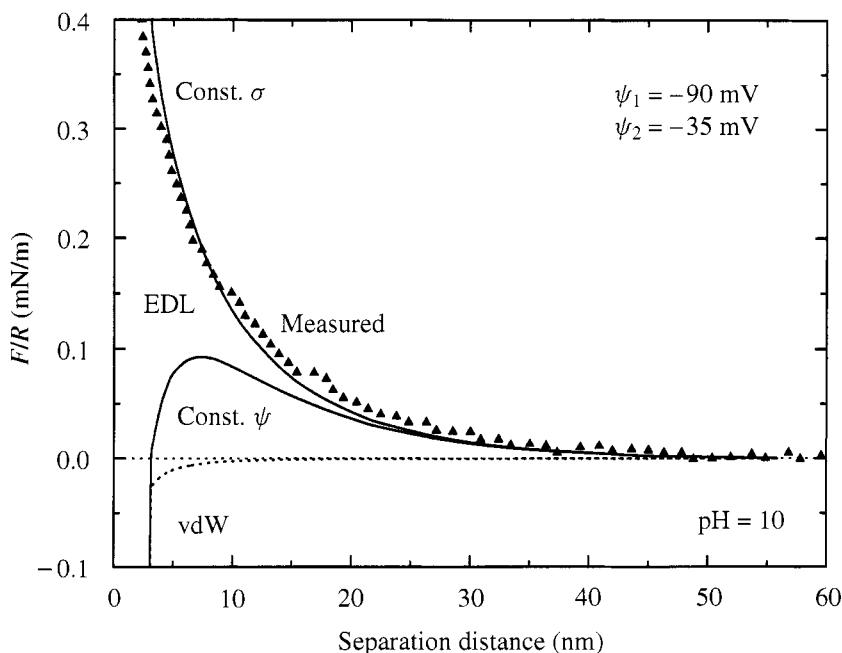


**Figure 7.** Comparison of the measured long-range repulsion in a 1 mmol/l KCl solution at pH 10 with that calculated from the DLVO theory using an exact numerical solution to the Poisson–Boltzmann equation. A Hamaker constant of  $1 \times 10^{-20}$  J and surface potentials of  $-90$  and  $-35$  mV for silica and sphalerite, respectively, were used in calculating the van der Waals and electrical double-layer forces.

Hamaker constants of  $1.97 \times 10^{-20}$  J for mica/water/ZnS [26],  $10 \times 10^{-20}$  J for mica/air/mica,  $6.5 \times 10^{-20}$  J for fused quartz, and  $3.7 \times 10^{-20}$  J for water [6]. With this Hamaker constant, the non-retarded van der Waals interaction energy ( $W_{\text{vdW}}$ ) was calculated using  $W_{\text{vdW}} = -A_{132}/12\pi D^2$ , where  $D$  is the separation distance. The calculated results given in Fig. 8 are compared with those measured at pH 4. Clearly, the measured attractive energy is much stronger with a longer interaction range than that predicted from the van der Waals forces. The implication here is that a non-van der Waals force dominates the attractive interaction energy.

One such attractive force could be from two overlapping electrical double layers of opposite charges. From the reported electrokinetic potential values, the interaction energy due to the overlap of electrical double layers was calculated using the constant surface charge density condition. The results given in Fig. 8 show a close match between the measured and calculated interaction energy profiles. The close agreement appears to suggest that the electrostatic attraction between the two surfaces carrying opposite surface charges is responsible for the measured attractive energy profile. The small difference between the predicted and the measured attraction could be attributed to the so-called ‘hydrophobic force’, although marginal. The sphalerite used in this work was found to be hydrophobic with a contact angle of  $68^\circ$  in 1 mmol/l KCl solution at pH 4. Similar contact angle

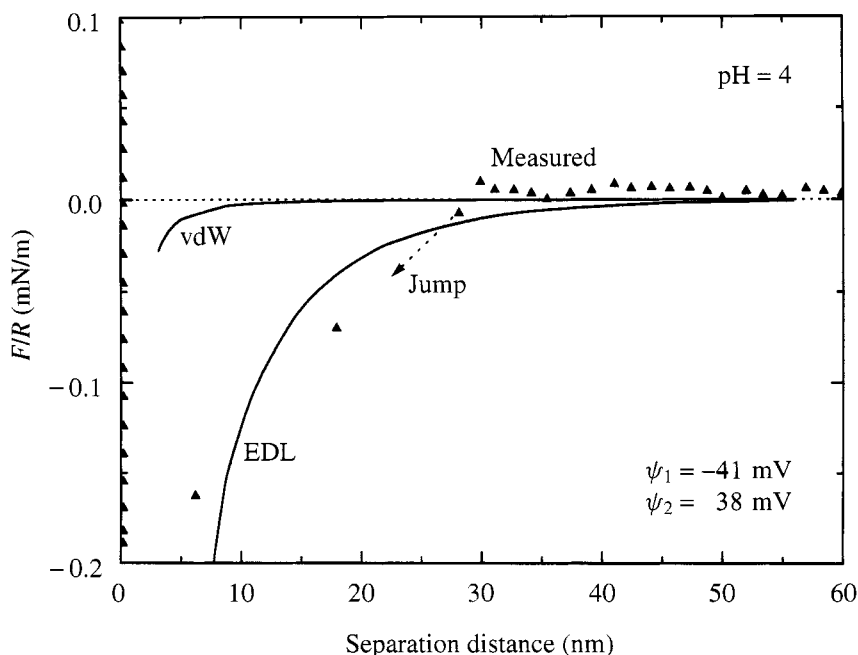


**Figure 8.** Comparison of the measured long-range attraction in a 1 mmol/l KCl solution at pH 4 with that calculated from the DLVO theory using an exact numerical solution to the Poisson–Boltzmann equation. A Hamaker constant of  $1 \times 10^{-20}$  J and surface potentials of  $-41$  and  $38$  mV for silica and sphalerite, respectively, were used in calculating the van der Waals and electrical double-layer forces.

values have been reported and the surface oxidation of sphalerite was believed to be responsible for this hydrophobicity [20]. A detailed analysis of the contributions from the hydrophobic force is beyond the scope of this paper and will be addressed elsewhere. Nevertheless, the general agreement between the measured force profiles and that predicted from the classical DLVO theory suggests that the stability of the system can be predicted from the electrokinetic data and readily controlled by changing the concentration of potential-determining ions such as zinc, copper or sulphate ions.

#### 4.2. Heterocoagulation

One of the objectives for measuring the surface forces between silica and sphalerite is to understand the cause of silica contamination in the sphalerite concentrate observed in mineral flotation practice. It was speculated that the heterocoagulation of silica with sphalerite was responsible for the observed concentrate contamination. The observed long-range attractive force and adhesion between sphalerite and silica over the pH range from 4 to 8 does indicate this possibility of contamination. To further confirm this possibility, coagulation tests were conducted. The visual observations are shown in Fig. 9. For a mixture of sphalerite and silica at 15:22 weight ratio and  $\sim 1\%$  total solids by weight, a clear supernatant was observed at pH



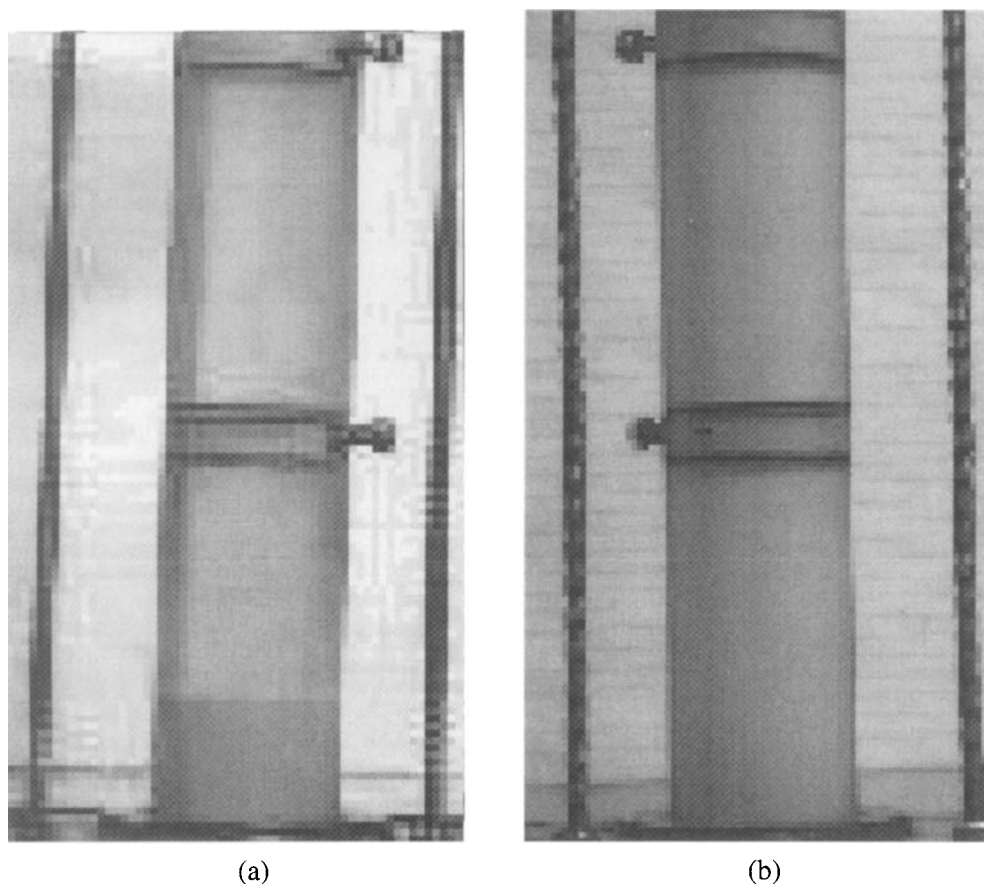


**Figure 9.** Visual observation on the heterocoagulation of silica with sphalerite: (a) the clear supernatant indicates heterocoagulation of silica with sphalerite at pH 7.1; (b) the opaque appearance (yellowish in color, not shown in the figure) indicates a stable suspension of silica and sphalerite at pH 10.6.

7.1, as shown in Fig. 9a. As the silica suspension itself is highly stable at this pH, the clear supernatant suggests the heterocoagulation of the two components. At pH 10.6, on the other hand, a stable yellowish suspension was observed, suggesting that both silica and sphalerite were in a dispersed state. These contrasting observations correspond well with the measured force profiles: an attractive force profile below pH 8 with a heterocoagulated system, and a repulsive force profile above pH 9 with a dispersed suspension. The visual observation combined with the results from the surface force measurements suggest that heterocoagulation between silica and sphalerite could be one of the causes of the silica contamination in the zinc concentrate floated under neutral pH conditions.

For most operations, flotation is carried out in alkaline pulps where heterocoagulation can be minimized. In this case, silica contamination is less of a problem. However, our study appears to suggest that the use of copper sulfate for activation

of sphalerite flotation is unfavorable for selective separation. The attractive force between silica and sphalerite would cause heterocoagulation of sphalerite with fine silica. To translate this knowledge into practice, the complex nature of flotation pulp chemistry needs to be considered. For example, the adsorption of an anionic collector, such as xanthate, is anticipated to neutralize the positive surface charge of copper-activated sphalerite and hence to minimize the electrostatic attraction. As a result, heterocoagulation may not be a significant issue under the hydrodynamic environment in flotation. Further study is needed to test this hypothesis.

## 5. CONCLUSIONS

1. The surface forces between a silica sphere and a fractured sphalerite surface in the supporting electrolyte solutions are attractive at pH below 8. Both the long-range attractive force and the adhesion force decrease with increasing solution pH.
2. At pH 10, a monotonic repulsive force is observed with no adhesion on separation. The repulsive force decays exponentially and the decay length scales with the electrolyte concentration.
3. The addition of calcium ions reduces the long-range repulsive force, with the surfaces remaining non-adhering at contact. The surface force becomes attractive upon the addition of cupric ions, with an adhesion contact being observed.
4. Both repulsive and attractive force profiles can be described by the classical DLVO theory with a constant surface charge density condition.
5. The measured force predicts the heterocoagulation of silica with sphalerite at pH below 8 but not at pH above 10, as confirmed experimentally.

## Acknowledgement

The financial support for this work provided by the Natural Sciences and Engineering Research Council of Canada (ZX) is greatly appreciated.

## REFERENCES

1. A. M. Gaudin, D. W. Fuerstenau and H. L. Miaw, *Can. Min. Metall. Bull.* **53**, 960 (1960).
2. F. A. Seeton, *Chem. Eng. News* **39**, 52 (1961).
3. E. W. Greene and B. J. Duke, *Trans. SME/AIME* **223**, 52 (1962).
4. D. W. Fuerstenau, in: *Fine Particle Processing*, P. Somasundaran (Ed.), pp. 669–705. SME, New York (1980).
5. P. M. Claesson, T. Ederth, V. Bergeron and M. W. Rutland, *Adv. Colloid Interface Sci.* **67**, 119 (1996).
6. J. N. Israelachvili, *Intermolecular and Surface Forces*, 2nd edn. Academic Press, New York (1990).

7. P. G. Hartley, I. Larson and P. J. Scales, *Langmuir* **13**, 2207 (1997).
8. G. Toikka, R. A. Hayes and J. Ralston, *J. Colloid Interface Sci.* **180**, 329 (1996).
9. S. Veeramasuneni, M. R. Yalamanchili and J. D. Miller, *J. Colloid Interface Sci.* **184**, 594 (1996).
10. R. H. Yoon and R. Pazhianur, *Colloids Surfaces A* **144**, 59 (1998).
11. R. Hayes and J. Ralston, *Colloids Surfaces A* **141**, 3 (1998).
12. T. H. Muster, G. T. Toikka, R. Hayes, C. Prestidge and J. Ralston, *Colloids Surfaces A* **104**, 203 (1996).
13. W. Ducker, Z. Xu and J. Israelachvili, *Langmuir* **10**, 3279 (1994).
14. H. J. Butt, *J. Colloid Interface Sci.* **166**, 109 (1994).
15. M. L. Fielden, R. A. Hayes and J. Ralston, *Langmuir* **12**, 3721 (1996).
16. W. Ducker, T. Senden and R. Pashley, *Langmuir* **8**, 1831 (1992).
17. Ya. Rabinovich and R. H. Yoon, *Langmuir* **10**, 1903 (1994).
18. J. Drelich, J. Nalaskowski, K. Y. Chee, S. Veeramasuneni and J. D. Miller, *Progress in Paper Recycling* **8**, 55 (1999).
19. S. R. Rao, J. A. Finch, Z. Zhou and Z. Xu, *Sep. Sci. Technol.* **33**, 819 (1998).
20. T. V. Subrahmanyam, C. A. Prestidge and J. Ralston, *Miner. Eng.* **9**, 727 (1996).
21. M. C. Fuerstenau and B. R. Palmer, in: *Flotation — A. M. Gaudin Memorial Volume*, M. C. Fuerstenau (Ed.), pp. 148–196. AIME, New York (1976).
22. J. D. G. Duran, M. C. Guindo, A. V. Delgado and F. Gonzalez-Caballero, *Langmuir* **11**, 3648 (1995).
23. T. W. Healy and M. S. Moignard, in: *Flotation — A. M. Gaudin Memorial Volume*, M. C. Fuerstenau (Ed.), pp. 275–297. AIME, New York (1976).
24. S. Acar and P. Somasundaran, *Miner. Eng.* **5**, 27 (1992).
25. A. Grabbe and R. Horn, *J. Colloid Interface Sci.* **157**, 375 (1993).
26. D. Atkins and R. Pashley, *Langmuir* **9**, 2232 (1993).

## **Long-range attractive forces and energy barriers in de-inking flotation: AFM studies of interactions between polyethylene and toner**

J. DRELICH<sup>1,\*</sup>, J. NALASKOWSKI<sup>2</sup>, A. GOSIEWSKA<sup>1</sup>, E. BEACH<sup>1</sup>  
and J. D. MILLER<sup>2</sup>

<sup>1</sup> *Department of Materials Science and Engineering, Michigan Technological University, Houghton, MI 49931, USA*

<sup>2</sup> *Department of Metallurgical Engineering, University of Utah, Salt Lake City, UT 84112, USA*

**Abstract**—The interfacial forces between a polyethylene particle and a toner substrate in alkaline aqueous solutions were studied using an atomic force microscope colloidal probe technique. Measurements were taken at pH 9 in water and solutions of  $5 \times 10^{-4}$  M  $\text{CaCl}_2$ ,  $1 \times 10^{-4}$  M Na oleate, and  $1 \times 10^{-4}$  M Na oleate plus  $5 \times 10^{-4}$  M  $\text{CaCl}_2$  in order to mimic the conditions present during de-inking flotation. A polyethylene particle was used to represent the air bubble. The observed interaction forces were described by the extended DLVO theory. An energetic barrier caused by electrical double-layer repulsion was observed in water and Na oleate solutions but was greatly diminished in  $\text{CaCl}_2$  solution. A long-range attractive force was found to be present in these systems and was described using a simple exponential function. The long-range attractive force was virtually the same in water and  $\text{CaCl}_2$  solution but decreased significantly in Na oleate solution because of the reduced hydrophobicity of the interacting surfaces caused by the adsorbed carboxylate layer. However, in the presence of oleate and calcium ions the observed attraction was even stronger and of longer range than in water and  $\text{CaCl}_2$  solutions. Moreover, no energetic barrier was observed. These results can be attributed to the presence of precipitated calcium oleates on the interacting surfaces.

**Keywords:** Atomic force microscopy; de-inking; flotation; hydrophobic forces; interfacial forces; surface chemistry; wastepaper.

### **1. INTRODUCTION**

Paper recycling requires the collection of wastepaper and the cleaning of cellulose fibers from ink and other additives introduced during paper production and printing

---

\*To whom correspondence should be addressed. Phone: (906)487-2932; Fax: (906)487-2934; E-mail: jwdrelic@mtu.edu

processes. The de-inking separation is accomplished through pulping, in the first step, and then screening, washing, flotation, and bleaching in the following steps [1]. The goal of pulping is to disintegrate the complex paper matrix and release cellulose fibers from the ink and mineral filler. The fiber is then recovered in a combination of separation steps. Ink particles (as well as hydrophobized mineral filler particles) can be successfully removed from the paper pulp by flotation. This is due to the 'natural' hydrophobicity of many inks and attractive interactions between air bubbles and ink particles. Although this general strategy was recognized a long time ago, probably at the beginning of paper recycling activities, no direct measurement of the forces involved between the particulates in de-inking flotation systems has been reported in the technical literature, mainly due to the lack of appropriate instrumentation. Several surface-chemistry laboratories using atomic force microscopy (AFM) are now studying this issue associated with de-inking flotation [2–4].

We recently adapted the AFM colloidal probe technique for the examination of interfacial interactions, which exist in paper pulp during its processing [2]. The AFM measurements are carried out in selected aqueous solutions of surfactants and inorganic salts and involve spherical hydrophobic particles of ink (toner) and polyethylene, which are glued to the AFM cantilever, and substrates such as ink, mineral, and cellulose fiber. Through continued AFM study, we expect to reach an understanding of the nature of the inter-particle forces involved in de-inking flotation systems. This paper summarizes part of the progress that has been made in our research program.

In this article, the interfacial forces measured between polyethylene particles and a toner substrate in water and aqueous solutions of sodium oleate and calcium chloride are presented. The toner was used as the real component of the paper de-inking flotation system. Polyethylene was used to represent an air bubble, in order to avoid the experimental and theoretical difficulties associated with the measurement of interfacial forces in three-phase systems involving elastic interface(s). There have been only a few attempts to measure the interfacial forces between the solid surface and gas bubble directly [5–8]. Most of the researchers studying the long-range interactions in several systems, including the particle flotation systems, have used an approach similar to ours and have glued hydrophobic polymers or hydrophobized inorganics as a probing tip to a cantilever [9–12].

A polyethylene particle was selected for the probe because of its relatively uniform, homogeneous, and hydrophobic surface. The hydrophobicity of polyethylene is less than that of air. For example, the interfacial tension between polyethylene and water is about 50 mN/m, whereas this value is about 72 mN/m for the water–air interface at room temperature. Also, a difference in molecular structure, at a sub-molecular level, can be expected for the adsorbed surfactant at the polyethylene–water interface compared with the adsorbed layer at the air–water interface. These differences, however, should not significantly affect the conclusions that have been reached in this paper.

We demonstrate that atomic force microscopy (AFM) is a powerful technique in probing long-range forces involved in the de-inking flotation system. As is shown in this paper, the magnitude of the interaction forces in the polyethylene–water–toner system depends on the solution chemistry. The forces can be increased as well as reduced, depending on the presence of dissolved species, carboxylate and calcium ions, in the solution.

## 2. EXPERIMENTAL

### 2.1. Materials and chemicals

Xerox Dry Ink Plus 5052/1050 composed of styrene/acrylate polymer, carbon black, amorphous silica, and zinc stearate was obtained from Xerox Corporation. A film of toner with a flat surface was prepared by melting it on the surface of smooth aluminum foil in a furnace at a temperature of 130–135°C. The surface root-mean-square roughness for such a prepared toner substrate was examined by AFM and was found to vary from 3 to 10 nm, depending on the surface location. The interfacial force measurements, described in the next part of the paper, were done on carefully selected surface locations of reduced roughness. The advancing water contact angle measured on such prepared toner substrates was 84–87°.

Low-density polyethylene powder (MW 1800 and melting point 117°C) was purchased from Scientific Polymer Products, Inc., and used to prepare spherical particles according to the procedure presented previously [13]. The polyethylene powder was suspended in glycerol, followed by heating. After reaching about 130°C, the suspension was stirred for 3–5 min and cooled down. Precipitated spherical particles were filtered and washed with water, as has been described in detail earlier [13]. Particles with a size from 8 to 15  $\mu\text{m}$  were used in the AFM study. The surface characterization of polyethylene particles prepared in this way has been presented previously [13].

Analytical grade sodium oleate and calcium chloride were purchased from Fisher Scientific. In all the experiments de-ionized water was used. Potassium hydroxide (Fisher Scientific) was used to adjust the pH of the solutions.

### 2.2. AFM measurements of the interfacial forces

The interfacial force measurements were performed using a Nanoscope E atomic force microscope from Digital Instruments, Inc. Polyethylene particles were glued to the AFM cantilevers by means of a micromanipulator and a CCD camera/monitor system. Single-beam silicon tipless cantilevers from Digital Instruments with a spring constant from about 18 to 30 N/m were used in this study. The spring constant ( $k$ ) of the cantilevers was calculated from the dimensions of the cantilever according to the formula

$$k = \frac{Eh^3(2a + w)}{12L^3}, \quad (1)$$

where  $a$  and  $w$  are the widths of the parallel sides of the trapezoid,  $h$  is the height of the trapezoid,  $L$  is the length of the cantilever measured from the base to the center of the glued particle, and  $E = 1.5 \times 10^{11}$  (N/m<sup>2</sup>) is the Young modulus of the cantilever.

The cantilevers were coated with a gold film (5–10 nm thick) before gluing the particle. This coating improved the reflectance of the laser beam from the surface of the cantilever during the AFM measurements.

The measurements were done in a fluid cell, provided by Digital Instruments, using freshly prepared solutions. The force values measured have been normalized with respect to the radius of the spherical particle. The diameter of the particle was determined from scanning electron microscopy (SEM) micrographs after completion of the interfacial force measurements. The SEM micrographs were also used to determine the dimensions of the AFM cantilevers.

### 2.3. Other measurements

Advancing contact angles were measured for gas bubbles attached to the flat surfaces of the toner and polyethylene substrates in water using a captive-bubble technique [14]. The substrate was melted on a glass slide and placed in a rectangular glass chamber on two stable supports with flat surfaces. The glass chamber was filled with an appropriate solution. A small air bubble was produced at the tip of a U-shaped needle using a microsyringe and this bubble was made to touch the substrate surface. Next, the size of the bubble was increased to approximately 60–70  $\mu\text{l}$ . Further, the base of the gas bubble was made to shrink by decreasing the volume of the bubble. The image of the bubble was captured by a Krüss Contact Angle Measurement System within 15–30 s. The advancing contact angle (measured through the aqueous phase) was determined based on the image analysis of the bubble. The advancing contact angles reported in this paper are for bubbles having a volume from about 20 to 40  $\mu\text{l}$ . No significant effect of the drop volume on the advancing contact angle was observed in this study.

Also, the same Krüss instrument was used to measure the surface tension of the solutions. The measurements were done using the pendant drop technique at room temperature.

## 3. RESULTS AND DISCUSSION

### 3.1. Reproducibility of $F/R$ vs. $H$ curves

The force versus separation distance ( $F/R$  vs.  $H$ ) curves recorded for the polyethylene particle–toner substrate system in water and aqueous solutions of sodium oleate and calcium chloride are shown in Figs 1–4. The measurements were repeated at several sites on the toner substrate in order to check the reproducibility of the AFM measurements. As shown in Figs 1–4, the experimental data are scattered,

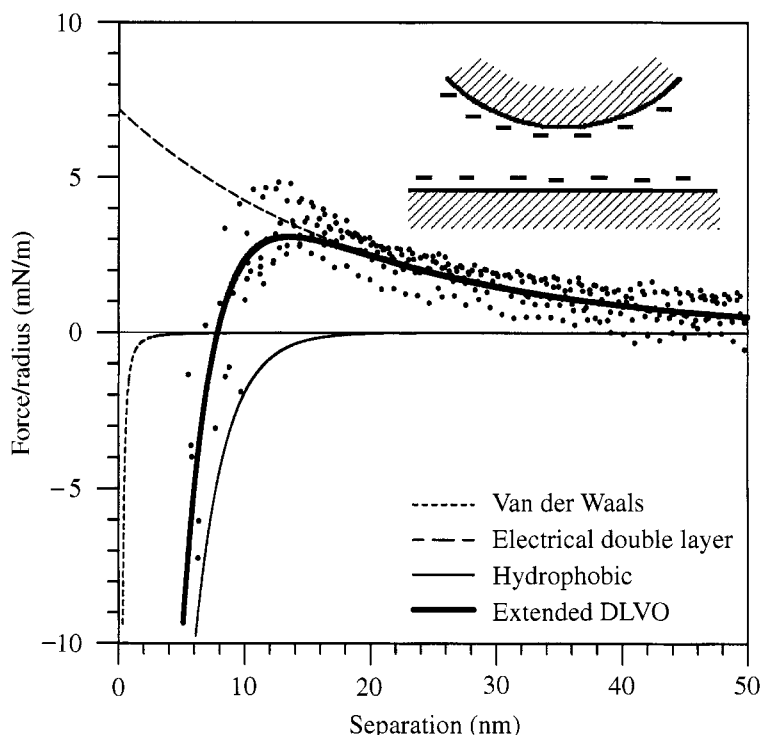


**Figure 1.** Normalized force versus separation distance curves for a polyethylene particle and toner substrate in water at pH 9 using the colloidal probe AFM technique. The lines show the theoretical curves calculated based on equations (4)–(7) and using the parameters given in Table 1. The inset shows the hypothetical state of interacting surfaces.

in some cases significantly. The scatter in the experimental results is quite a typical response in these measurements involving a toner and polyethylene, or any other hydrophobic substrate. We expect that such a limited reproducibility for the  $F/R$  vs.  $H$  curves is a result of solid surface imperfection, typical for many real solids commonly used in recent AFM studies. For example, polyethylene particles precipitated from a polyethylene-in-glycerol suspension and glued to AFM cantilevers sometimes reveal nanoscopic asperities at their surfaces [13]. Also, the SEM image of the surface of a melted toner substrate has revealed nano-irregularities [15]. Moreover, the toner used in this research was a polymeric material filled with carbon and silica particles and this mixture of components might be expected to result in a heterogeneous toner surface. Finally, heterogeneity of the polyethylene and toner surfaces could arise from non-uniform adsorption and precipitation of surface-active species from the solutions of sodium oleate and/or calcium chloride. Indeed, the largest scatter in the results was observed for the sodium oleate solution and especially for the mixture of sodium oleate and calcium chloride solutions, where precipitation of the calcium soap occurs.



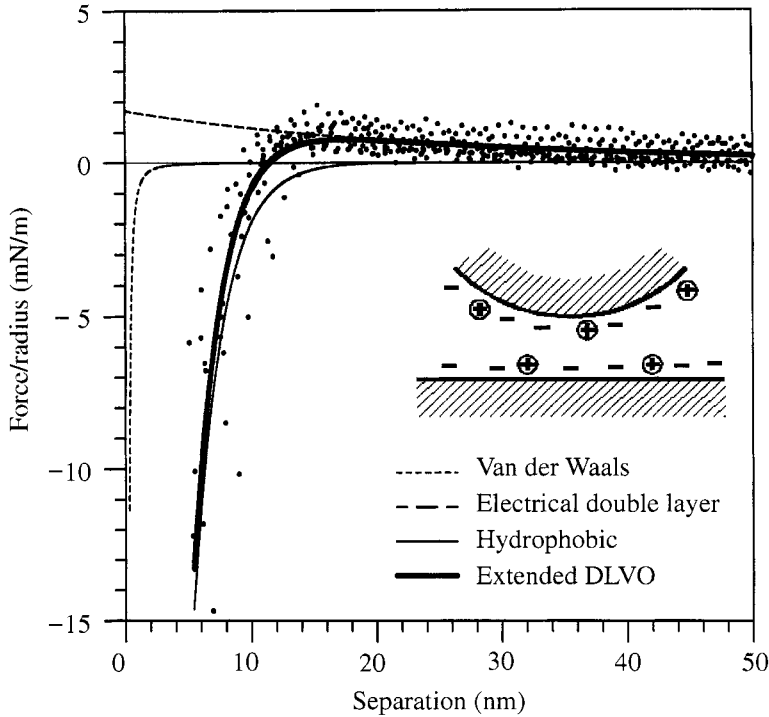


**Figure 2.** Normalized force versus separation distance curves for a polyethylene particle and toner substrate in 0.0005 M  $\text{CaCl}_2$  solution at pH 9 using the colloidal probe AFM technique. The lines show the theoretical curves calculated based on equations (4)–(7) and using the parameters given in Table 1. The inset shows the hypothetical state of interacting surfaces.

It should be noted here that there is always uncertainty in the point of zero separation distance in AFM measurements, especially if partially elastic polymeric surfaces are used, as in the present study. The deformation of the particle can cause a displacement in the separation distance in the force versus distance graph. The central displacement of the particle ( $\delta$ ) can be calculated using the JKR theory [16]:

$$\delta = \frac{a^2}{R} - \sqrt{4\pi W a \frac{(1 - \nu^2)}{E}}, \quad (2)$$

where

$$a^3 = \frac{3(1 - \nu^2)R}{2E} \left( P + 3\pi RW + \sqrt{6\pi RW P + (3\pi RW)^2} \right), \quad (3)$$

$R$  is the radius of the particle,  $W$  is the interfacial free energy per unit area for the adhering particle to a substrate,  $P$  is the load during the adhesion measurement,  $E$  is the Young modulus, and  $\nu$  is the Poisson ratio.

Assuming for our system the following parameters:  $E = 0.94$  GPa,  $\nu = 0.46$ ,  $P/R = 100$  mN/m,  $R = 5$   $\mu\text{m}$ , and  $W = 100$  mJ/m<sup>2</sup>, the central deformation of a polyethylene particle in water predicted by the JKR theory is about 25 nm for

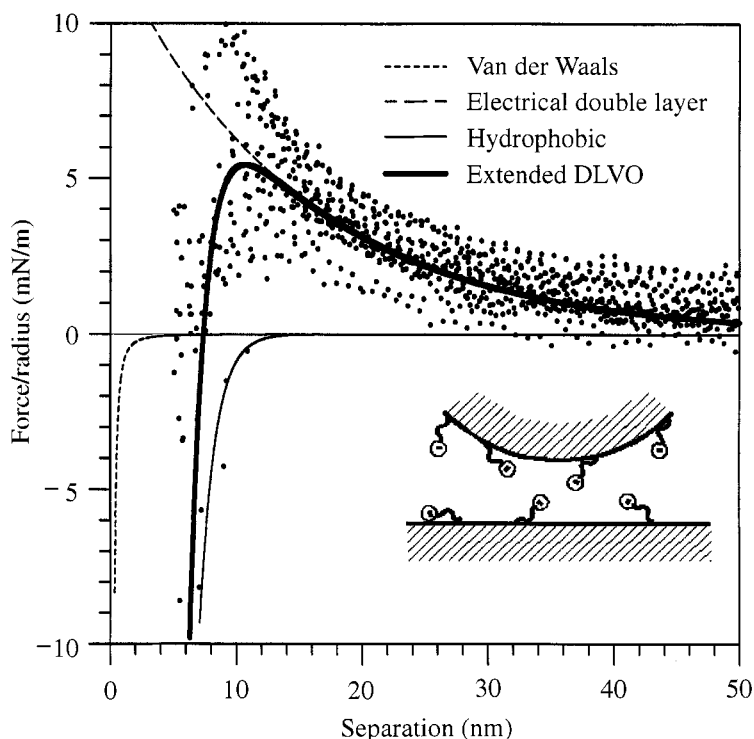


**Figure 3.** Normalized force versus separation distance curves for a polyethylene particle and toner substrate in 0.0001 M sodium oleate solution at pH 9 using the colloidal probe AFM technique. The lines show the theoretical curves calculated based on equations (4)–(7) and using the parameters given in Table 1. The inset shows the hypothetical state of interacting surfaces.

adhesion contact and about 7 nm for non-adhesion contact (when  $W = 0$ ). These values will vary if different parameters are used. For example, the Young modulus is from 0.2 to 1.1 GPa for polyethylene [17].

Schmitt *et al.* [18] estimated that the deformation of a polystyrene particle could be about 17 nm. Thus, the surface deformation effects might be significant in the AFM measurements. It should be recognized, however, that the JKR theory predicts the equilibrium deformation of the particle at infinite time. The AFM measurements usually take a fraction of a second. For example, we estimated that the time of contact between the polyethylene particle and the toner substrate was 0.1–0.2 s in our experiments. According to recent experimental work [18], the rest time of several seconds is required for a particle on the substrate to reach a level of deformation relevant to that predicted by the JKR model. It appears from these results [18] that particle deformation will be a fraction of this value for a contact time of 0.1–0.2 s. In view of this uncertainty, the exact degree of particle deformation during the AFM measurements still remains an unresolved problem. However, it appears to us based on the results and analysis provided by Schmitt *et al.* [18] that the deformation of the polyethylene particle should not exceed 1–4 nm.

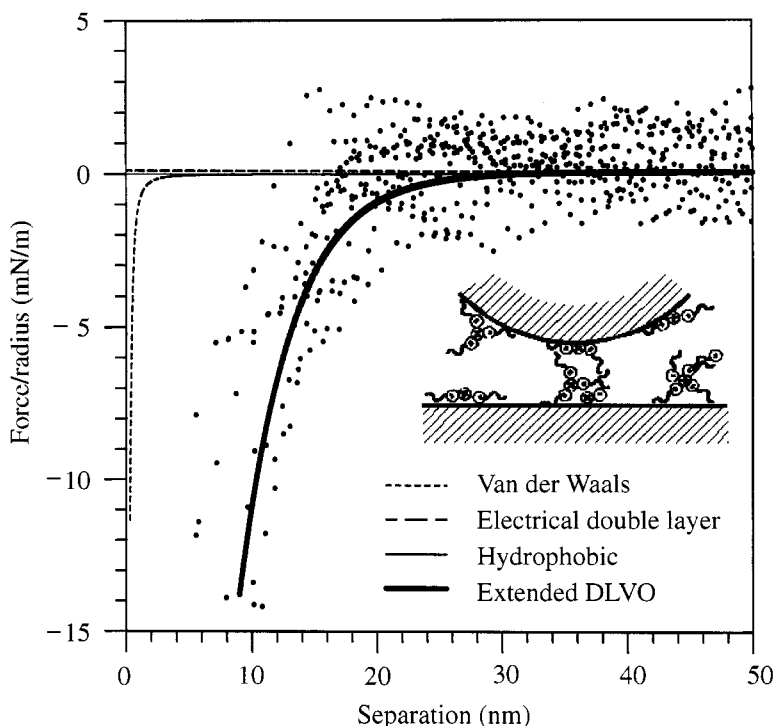


**Figure 4.** Normalized force versus separation distance curves for a polyethylene particle and toner substrate in a solution of 0.0001 M sodium oleate plus 0.0005 M  $\text{CaCl}_2$  at pH 9 using the colloidal probe AFM technique. The lines show the theoretical curves calculated based on equations (4)–(7) and using the parameters given in Table 1. The inset shows the hypothetical state of interacting surfaces.

This value is in the range of the scatter in the data presented in Figs 1–4. Thus, no correction for setting the point of zero separation was made in this paper and the raw AFM data are used in further discussion. Nevertheless, we agree with the suggestion of Schmitt *et al.* [18] that the serious problem of AFM measurements associated with particle deformation should receive more fundamental attention in future research. Such fundamental issues are, however, beyond the scope of this article, which discusses the application of AFM measurements in the analysis of de-inking flotation.

### 3.2. Interfacial forces

Since the aqueous systems examined included two hydrophobic substrates, polyethylene and toner, van der Waals interactions,  $(F/R)_{\text{vdW}}$ , electrical double-layer forces,  $(F/R)_{\text{EDL}}$ , and long-range (often attributed to ‘hydrophobic’ effects) forces,  $(F/R)_{\text{Hyd}}$ , should contribute to the total interaction involved between the polyethylene particle and toner substrate:

$$(F/R)_{\text{TOT}} = (F/R)_{\text{vdW}} + (F/R)_{\text{EDL}} + (F/R)_{\text{Hyd}}. \quad (4)$$

This combination of forces is also known as the extended DLVO theory. Both the van der Waals and the electrical double-layer forces are described by the DLVO theory; the 'hydrophobic' force is a new component of the DLVO theory introduced in recent years [19, 20]. Although the origins and magnitude of hydrophobic forces are still the subject of scientific dispute, these forces seem to be extremely important for the success of particle flotation [20].

We used the following equations to describe the forces [19, 20]:

- van der Waals force:

$$(F/R)_{\text{vdW}} = -\frac{A_{123}}{6H^2}; \quad (5)$$

- electrical double-layer force:

$$(F/R)_{\text{EDL}} = \frac{4\pi\sigma^2}{\varepsilon\varepsilon_0\kappa} e^{-\kappa H}; \quad (6)$$

- long-range attractive force:

$$(F/R)_{\text{Hyd}} = -C_0 e^{-H/D_0}; \quad (7)$$

where  $A_{123}$  is the Hamaker constant for the three-phase system (polyethylene–aqueous phase–toner system in this research);  $H$  is the distance between the surfaces (polyethylene particle and toner substrate in this study);  $\sigma$  is the mean surface charge density at the interface (average of surface charge at the surfaces of polyethylene and toner);  $1/\kappa$  is the Debye length;  $\varepsilon$  is the dielectric constant of the medium;  $\varepsilon_0$  is the permittivity of free space; and  $C_0$  and  $D_0$  are constants called the pre-exponential parameter and decay length, respectively.

The contribution of the van der Waals forces acting between the polyethylene and toner in water is significantly smaller than the electrical double-layer and hydrophobic forces. Using formula (8), we found that the Hamaker constant for the polyethylene–water–toner system was  $A_{123} = 6.13 \times 10^{-21}$  J,

$$A_{123} = (\sqrt{A_{11}} - \sqrt{A_{22}})(\sqrt{A_{33}} - \sqrt{A_{22}}), \quad (8)$$

where  $A_{11} = 8.43 \times 10^{-20}$  J is the Hamaker constant for polyethylene taken from ref. [21];  $A_{22} = 3.7 \times 10^{-20}$  J is the Hamaker constant for water [19]; and  $A_{33} = 6.5 \times 10^{-20}$  J [21] is the Hamaker constant for polystyrene that is assumed to be equal to the Hamaker constant for the toner (the major component of the toner is styrene/acrylate polymer and we assume that the Hamaker constant will not differ significantly from that for polystyrene).

The (repulsive) electrical double-layer forces were clearly visible in the  $F/R$  vs.  $H$  curves obtained for alkaline water (Fig. 1) and sodium oleate solution (Fig. 3), due to the exponential character of the  $F/R$  vs.  $H$  curves. In both systems, repulsive forces between polyethylene and toner were recorded at distances from about 10–12 nm to 50 nm. At shorter distances, in any solution (Figs 1–4) the repulsive electrical double-layer forces were overcome by stronger long-range

**Table 1.**

Theoretical and experimental parameters describing the experimental results and systems examined. See text for details

Solution <sup>a</sup>	$\sigma$ (mC/m <sup>2</sup> )	$1/\kappa$ (nm)	$C_0$ (mN/m)	$D_0$ (nm)	$\theta_A$ (toner) (degrees)	$\theta_A$ (PE) (degrees)	$\gamma_{LV}$ (mN/m)	$\Delta E$ (mJ/m <sup>2</sup> )
Water, pH 9.0 $\pm$ 0.1	4.7	19	−124	2.4	86	92	72	3.1
0.5 $\times 10^{-4}$ M CaCl <sub>2</sub> , pH 9.0 $\pm$ 0.1	2.0	25	−153	2.3	85	92	72	0.8
1 $\times 10^{-4}$ M Na oleate, pH 9.0 $\pm$ 0.1	7.2	14	−2992	1.2	79	83	45	5.5
1 $\times 10^{-4}$ M Na oleate plus 0.5 $\times 10^{-4}$ M CaCl <sub>2</sub> , pH 9.0 $\pm$ 0.1	0.3	92	−119	4.19	87	94	70	<0.1

<sup>a</sup>The concentration of 1  $\times 10^{-4}$  M sodium oleate is less than the solubility limit, whereas in the solution of 1  $\times 10^{-4}$  M Na oleate plus 0.5  $\times 10^{-4}$  M CaCl<sub>2</sub>, the calcium oleate forms precipitates [36].

attractive forces. This clearly indicates that competition between the repulsive electrical double-layer and long-range attractive forces is of primary importance to the success of de-inking flotation. The electrical double-layer component is presented in Figs 1–4. The parameters for the electrical double-layer force curve (mean surface charge and Debye length) were obtained by fitting equations (5) and (6) to the averaged experimental data. The parameters obtained from such fitting are presented in Table 1. These parameters are related to the ions present in the solution as well as adsorbed on the surface. Both interacting surfaces are negatively charged in alkaline water, due to the dissociation of ionic groups at the toner surface and the preferential adsorption of hydroxyl anions at the hydrophobic surfaces. The adsorption of calcium ions causes partial neutralization of the negative surface charge and a decrease of the mean surface charge density. The adsorption of dissociated oleate at the surface, through the hydrocarbon tail, results in an increase of the negative surface charge. A significant reduction in the surface charge density and the magnitude of electrostatic repulsion is observed in the presence of calcium oleate. We further discuss the electrical double-layer and long-range components of the polyethylene–water–toner interfacial forces in the following sections.

### 3.3. Long-range attractive forces

The long-range attractive forces have become the subject of intensive experimental and theoretical research in recent years [22–26]. The long-range component of the interaction forces in the examined systems was also calculated in this study by fitting equation (7) to the experimental values. The fitting was done in such a way that the sum of all force components (extended DLVO force) would fit the averaged experimental results. The obtained pre-exponential parameter ( $C_0$ ) and decay length ( $D_0$ ) of equation (7), describing the long-range attractive forces, are shown in Table 1.

The measurements of the long-range attractive forces in polyethylene–aqueous phase–toner systems have not been reported in the literature, so a direct justification of the results obtained cannot be provided. Nevertheless, the long-range attractive forces reported in this paper appear to be of similar magnitude and range to the hydrophobic forces measured between other dissimilar hydrophobic surfaces [22, 24, 27] having a similar degree of hydrophobicity, i.e. 80–95° for the advancing water contact angles. As shown in Figs 1–4, the long-range attractive forces were observed at distances from 10 to 35 nm. These long-range attractive forces appear to have a 10–20 nm shorter range than those discussed elsewhere [22, 24]. We do not have a clear explanation for this discrepancy; however, it should be noted that different ranges for long-range attractive interactions are reported in the literature for surfaces with similar water contact angles. Deformation of the particle during contact with the toner substrate, as discussed in the previous part of this paper, might be the reason for this discrepancy. It should also be emphasized that not only different solids were used in our study, but also these solid surfaces had a significantly different pattern of heterogeneity. Yoon and co-workers [22, 24]

used silica and glass covered by varying amounts of silane reagents, which usually form patches, non-uniformly distributed on the silanized surface, instead of a uniform molecular pattern [28–30]. This type of heterogeneity was not present in the systems studied in this program, although heterogeneities associated with the complex composition of the toner substrate were present in our system, as discussed in the previous section. In this regard, the fundamental conclusions from this applied research should be drawn with caution.

The parameter  $D_0$  (decay length), describing the long-range attractive forces, was used to analyze the differences between different solution chemistry conditions. The values of parameter  $D_0$  are shown in Table 1. It is evident that this parameter is affected by changes in the adsorbed species. The correlation between the decay length and changes in the measured contact angle further assures that the range of observed long-range forces is related to the hydrophobicity of the surfaces. There is only a small difference in the decay length between water and calcium chloride solution, which can be caused by the adsorption of calcium ions at the surfaces. In the presence of sodium oleate solution, the decay length drops to 1.2 nm and closely resembles the decay length for van der Waals forces. Oleate molecules probably adsorbed on both of the hydrophobic surfaces, polyethylene and toner, through the hydrocarbon chain and with the polar group (dissociated at pH 9) oriented towards the aqueous phase. The dissociated carboxylic acid groups reduce the hydrophobicity of the solid surface. The effect of adsorbed oleate molecules on the hydrophobicity of the toner and polyethylene surfaces is supported by the contact angle measurements (Table 1). As discussed previously, there is always uncertainty in the point of zero separation distance for AFM measurements. Due to this fact, sometimes it might be difficult to distinguish between van der Waals and short-range hydrophobic forces. However, in the presence of the sodium oleate and calcium chloride mixture, the decay length is twice as large as it was in water and the hydrophobic attraction is observed up to 35 nm. A slight increase in the water contact angle was also observed. This can be explained by the adsorption of strongly hydrophobic particles of calcium soap at the interacting surfaces.

### 3.4. Barriers against attachment of the toner to a gas bubble

As already discussed in the previous sections, the  $F/R$  vs.  $H$  experimental curves are the result of a combination of long-range attractive, repulsive electrical double-layer, and attractive van der Waals forces operating between the polyethylene particle and the toner substrate. Our major focus in this study is on the long-range attractive force. This force, we expect, often dominates in de-inking flotation systems whenever ink particles exhibit strong hydrophobic properties. Electrical double-layer forces might be, however, of larger magnitude than long-range attractive forces in many systems. Such cases were observed here for the water and sodium oleate solution. For example, Fig. 1 shows the  $F/R$  vs.  $H$  curves obtained for the polyethylene–water–toner system at pH 9. Strong repulsive forces are clearly present in this system at distances from about 10–12 nm to 50 nm. The

attachment of a polyethylene particle to the toner substrate in alkaline water will not occur spontaneously, as in other solutions (Figs 2 and 4). In order to initiate an attachment process, additional external energy must be provided that is at least equal in magnitude to the energy barrier associated with strong repulsive interactions. The consequence of the existence of such energetic barriers between a gas bubble and ink particles in a real de-inking flotation process is that the rate of flotation will be significantly reduced, or even eliminated. The extent of flotation reduction will depend on the internal energy available to the ink–water–bubble system (at a microscale).

The values of the energy barriers associated with the attachment of the model 'air bubble' to the toner ( $\Delta E = \Delta F/R_{\text{rep}}^{\text{max}}$ ) for the systems examined are listed in Table 1. The reported values are the maximum values from the fitted extended DLVO force curve and generally resemble the mean values for the energy barriers observed in the experimental force curves. As shown in Table 1, the anti-attachment barriers are only important in two systems: alkaline water and sodium oleate solution. Only a small energy barrier is observed in calcium chloride solutions. Practically no energy barrier was measured when a mixture of both calcium chloride and sodium oleate was considered. The appearance of energy barriers relates well to the mean surface charge obtained from the fitted electrical double-layer component of the total force. The surface charge is affected by species adsorbed at the surfaces. The preferential adsorption of calcium cations and calcium soap leads to a decrease in the surface charge, while the adsorption of oleate anions increases the negative charge at the surfaces. The increased surface charge results in a stronger electrical double-layer repulsion between the toner and polyethylene surfaces, and, consequently, a higher energy barrier is observed.

Finally, it is a common practice in a paper mill to use fatty acids as collectors and calcium ions as activators in the de-inking flotation [1, 31, 32]. The results presented in this paper clearly indicate that a combined role of the collector and activator results in an increase of the attractive forces between polyethylene and toner. We expect that this correlation will also apply to the gas bubble–toner particle and toner particle–toner particle systems in real de-inking flotation circuits. Importantly, the results of this study indicate that long-range forces seem to dominate and that energy barriers are eliminated in the solutions containing both carboxylic acid as collector and calcium ions as activators.

#### 4. CONCLUSIONS

Long-range attractive forces were measured between polyethylene and toner in aqueous solutions of sodium oleate and calcium chloride using atomic force microscopy. The empirical exponential function  $(F/R)_{\text{hyd}} = C_0 \exp(-H/D_0)$  was used to describe these long-range attractive forces.

The calculated decay length ( $D_0$ ) of the exponential function was found to vary from about 1.2 to 4.2 nm for the polyethylene–toner hydrophobic interactions



in alkaline aqueous solutions. The major increase in the  $D_0$  value was noted in solutions of precipitated calcium oleate, whereas the major decrease in the  $D_0$  value was reported in the alkaline solution of sodium oleate.

Energy barriers between polyethylene and the toner were observed in selected solutions and they were the result of repulsive electrical double-layer forces. In relation to de-inking flotation systems, the repulsive forces seem to be significant in low ionic strength solutions, which is generally not the case in paper recycling mills, where high ionic strength process water is used. This conclusion was also reached in previous AFM studies with tap water [33].

The results shown here (as well as those reported in previous papers [2, 33]) indicate that the range of long-range attractive force increases and the energy barrier decreases in the presence of calcium carboxylates. We expect the attractive forces between the toner and an air bubble in de-inking flotation to be enlarged in solutions of calcium carboxylates, which can partially explain the improved performance of de-inking flotation circuits using such solutions. However, agglomeration of ink particles through heterocoagulation, i.e. involving ink particles and calcium carboxylate precipitates, as recently discussed in the literature [34, 35], can be at least of equal importance for the success of de-inking flotation.

### Acknowledgement

The financial support from the US National Science Foundation (grant No. CTS-9618582) is greatly appreciated. We would like to thank Dr. Walter Milligan (Michigan Technological University) for deriving the spring constant equation for a trapezoidal beam. JD appreciates the assistance from K.-Y. Chee in an early stage of the manuscript preparation.

### REFERENCES

1. M. R. Doshi and J. M. Dyer (Eds), *Paper Recycling Challenge. Vol. II: Deinking and Bleaching*. Doshi & Associates, Appleton, WI (1997).
2. J. Drelich, J. Nalaskowski, K.-Y. Chee, S. Veeramasuneni and J. D. Miller, *Prog. Paper Recycl.* **8**, 55 (1999).
3. M. Rutland and R. J. Pugh, *Colloids Surfaces A* **125**, 33 (1997).
4. R. Chi, Z. Xu, T. DiFeo, J. A. Finch and J. L. Yordan, *J. Pulp Paper Sci.* (in press).
5. H.-J. Butt, *J. Colloid Interface Sci.* **166**, 109 (1994).
6. W. A. Ducker, Z. Xu and J. Israelachvili, *Langmuir* **10**, 3279 (1994).
7. M. L. Fielden, R. A. Hayes and J. Ralston, *Langmuir* **12**, 3721 (1996).
8. M. Preuss and H.-J. Butt, *Int. J. Miner. Process.* **56**, 99 (1999).
9. Ya. I. Rabinovich and R.-H. Yoon, *Langmuir* **10**, 1903 (1994).
10. L. Meagher and V. S. J. Craig, *Langmuir* **10**, 2736 (1994).
11. R. F. Considine, R. A. Hayes and R. G. Horn, *Langmuir* **15**, 1657 (1999).
12. N. Ishida, N. Kinoshita, M. Miyahara and K. Higashitani, *J. Colloid Interface Sci.* **216**, 387 (1999).
13. J. Nalaskowski, J. Drelich, J. Hupka and J. D. Miller, *J. Adhesion Sci. Technol.* **13**, 1 (1999).

14. J. Drelich, J. D. Miller and R. J. Good, *J. Colloid Interface Sci.* **179**, 37 (1996).
15. J. Drelich, J. Nalaskowski and J. D. Miller, *J. Colloid Interface Sci.* **201**, 253 (1998).
16. K. L. Johnson, K. Kendall and A. D. Roberts, *Proc. R. Soc. London, Ser. A* **324**, 301 (1971).
17. W. D. Callister, Jr., *Materials Science and Engineering: An Introduction*. John Wiley, New York (1997).
18. F.-J. Schmitt, T. Ederth, P. Weidenhammer, P. Claesson and H.-J. Jacobasch, *J. Adhesion Sci. Technol.* **13**, 79 (1999).
19. J. Israelachvili, *Intermolecular and Surface Forces*, 2nd edn. Academic Press, San Diego, CA (1992).
20. R.-H. Yoon and L. Mao, *J. Colloid Interface Sci.* **181**, 613 (1996).
21. A. W. Neumann, S. N. Omenyi and C. J. van Oss, *Colloid Polym. Sci.* **257**, 413 (1979).
22. Ya. I. Rabinovich and R.-H. Yoon, *Colloids Surfaces A* **93**, 263 (1994).
23. S. A. Ravishankar and R.-H. Yoon, *Miner. Metall. Process.* **14**, 10 (1997).
24. R.-H. Yoon, D. H. Flinn and Y. I. Rabinovich, *J. Colloid Interface Sci.* **185**, 363 (1997).
25. T. Ederth, P. Claesson and B. Liedberg, *Langmuir* **14**, 4782 (1998).
26. V. S. J. Craig, B. W. Ninham and R. M. Pashley, *Langmuir* **15**, 1562 (1999).
27. J. Nalaskowski, Ph.D. Dissertation, Technical University of Gdansk, Gdansk, Poland (1999).
28. J. Drelich and J. D. Miller, *Colloids Surfaces* **69**, 35 (1992).
29. R. Resch, M. Grasserbauer, G. Friedbacher, Th. Vallant, H. Brunner, U. Mayer and H. Hoffmann, *Appl. Surface Sci.* **140**, 168 (1999).
30. J. Nalaskowski, S. Veeramasesaneni, J. Hupka and J. D. Miller, *J. Adhesion Sci. Technol.* **13**, 1519 (1999).
31. A. Larsson, P. Stenius and L. Odberg, *Svensk Papperstid.* **87**, R158 (1984).
32. J. K. Borchardt, *Prog. Paper Recycl.* **2**, 47 (1993).
33. J. Pletka, A. Gosiewska, K.-Y. Chee, J. P. McGuire, J. Drelich and L. Groleau, *Prog. Paper Recycl.* **9**, 40 (2000).
34. D. Beneventi and B. Carre, *Prog. Paper Recycl.* **9**, 77 (2000).
35. M. A. D. Azevedo, J. Drelich and J. D. Miller, *J. Pulp Paper Sci.* **25**, 317 (1999).
36. M. L. Free and J. D. Miller, *Int. J. Miner. Process.* **48**, 197 (1996).

## Surface forces and characterization of glass surfaces bearing grafted polymers: solvent dependence

M. A. PLUNKETT, S. RÖDNER, L. BERGSTRÖM and M. W. RUTLAND\*

*Institute for Surface Chemistry, 114 86 Stockholm, Sweden and Department of Chemistry, Surface Chemistry, Royal Institute of Technology, 100 44 Stockholm, Sweden*

**Abstract**—The interactions between two glass surfaces bearing grafted polymer brushes of poly(12-hydroxystearic acid) (PHS) have been controlled by altering the solvent quality. The graft density was obtained through XPS and the solvent used was a mixture of ethanol and heptane, which was varied from good to poor solvency conditions by either a change of the relative concentrations of the two solvents, or by altering the temperature. The system is shown to be remarkably sensitive to the solvency conditions around the  $\theta$  position. It was also shown that hydrodynamic forces could be accurately and routinely accounted for in systems where the forces were monotonically repulsive.

**Keywords:** Surface forces; polyhydroxystearate;  $\theta$  temperature; steric force; segment–segment interaction; hydrodynamic force; mixed solvent; grafted polymer; XPS.

### 1. INTRODUCTION

The interactions between polymer bearing substrates are of interest due to their diverse applications as steric stabilizers and adhesion modifiers. The forces between such layers depend on the relative strength of the interactions between the polymer, the solvent and the surfaces. When one or more of these factors can be controlled, then the surface forces can be tuned. In general, most previous studies of the interactions of polymer coated surfaces have been performed in aqueous systems, though non-aqueous systems, which, in general, provide more possibilities for control of polymer–solvent interactions, are also of great technological importance. Steric stabilization is particularly important in non-aqueous media since electrostatic stabilization is ineffective under low dielectric constant conditions. An example of such a nonaqueous, sterically stabilized system is found in the ceramics industry, where electrophoretic deposition of nanoparticles requires a non-aqueous solvent [1, 2].

---

\*To whom correspondence should be addressed. Phone: +46 8 790 9900. Fax: +46 8 20 8998. E-mail: mark.rutland@surfchem.kth.se

In general, the solvent conditions for a surface grafted polymer (as well as a polymer in bulk solution) can be controlled by using a mixture of good and poor solvents. We note that there is not always a simple relationship between the solvent quality and the relative amounts of 'good' and 'poor' solvents. For example Petrovic *et al.* [3] have reported that the bulk swelling of poly(propylene glycol) crosslinked networks in a mixture of methanol and toluene has a maximum in a roughly 30:70 mixture of the solvents, rather than in either pure solvent. Furthermore, it is also normally expected that in a mixed solvent system, there is a preference for the good solvent to preferentially partition on the polymer [4]. This has been verified by small-angle neutron scattering experiments which not only show the collapse–stretching transition, but, also provided the graft concentration is high enough, show a preferential solvation of the polymer layer [5]. Nonetheless for miscible solvents, the degree of swelling of polymer brushes is, in general, dependent on the solvent composition in a straightforward manner [6].

A general introduction to the literature about forces between polymer coated surfaces can be obtained from, for example, the review articles by Patel and Tirrell [7], Luckham and Klein [8], and Milner [9]. Surface force experiments have previously been carried out on mixed solvent systems with adsorbed polymer layers by various groups [6, 10–13], and the range and magnitude of the surface forces were strongly affected by the solvent quality. A difficulty with using adsorbed polymers (which, in general, are preferred in applications due to the relative simplicity of the attachment step) is that the solvency conditions affect not only the polymer conformation, but also the grafted amount. In general, substrates which are convenient for surface force measurements are also difficult to graft polymers to, however when grafting is possible the polymer concentration is constant and conformational behaviour can be independently monitored (see e.g. [6, 14, 15] and references therein). Finally, the position of the hydrodynamic slip plane and the flow of solvent within polymer matrixes [8, 16–19] have been investigated for these types of systems.

The majority of previous work on PHS systems has been carried out on dispersed systems, for example by Napper [20] and others [21, 22]. In these cases the variations in the quality of the solvent have been used to alter the surface interactions and thus the colloidal behaviour. Surface force experiments in the good solvent regime have also been conducted on PHS by using an adsorbed comb polymer with PHS side-chains [23]. In this case the expected steric force was observed and the results correlated well with osmotic stress and rheology measurements. In addition, other work concerned with 2-dimensional ordering at the solvent–air interface has been reported [24]. Two-dimensional studies of PHS-coated silica particles (diameter  $\sim 2\ \mu\text{m}$ ), trapped at a solvent–air interface showed that the particles formed almost ordered arrays with a separation distance of several particle diameters. The conclusion was drawn that a long-range repulsive force was acting between the particles. However, the origin of this long-range repulsion was unclear since PHS is regarded as a non-charged polymer, thus excluding the possibility

of double-layer forces. Partly with a view to investigating this phenomenon we have studied the forces between two PHS-coated surfaces under good, bad, and  $\theta$  conditions.

In this study we have used the system of PHS terminally grafted onto glass in the presence of a mixed solvent of ethanol and heptane. This solvent system was chosen because it leads to  $\theta$  temperatures that lie within an accessible temperature range. A longer term goal of the study is to characterize a system where dynamic surface effects such as adhesion dependence on separation can be studied in terms of the viscoelasticity of the polymer film.

## 2. MATERIALS AND METHODS

The grafting of poly(12-hydroxystearic acid), (PHS), onto silica is a self-assembling, two-step process developed by Pathmamanoharan [25], using a silane functionalized polymer. The surfaces investigated were prepared from 2 mm borosilicate glass rods. The rods were cleaned with ethanol, dried with a gentle  $N_2$  flow and then flame-cleaned. The glass rods were then held in a butane–oxygen flame and melted to produce spheres of roughly 4 mm diameter. The glass spheres thus produced had very low surface roughness due to the high surface tension of molten glass [26].

The reaction between 3 g poly(12-hydroxystearic acid) (from ICI) and 0.5 ml of 3-Glycidioxypropyltrimethoxysilane (GPS, 98% from Aldrich) was allowed to take place in a reaction vessel under nitrogen with stirring at elevated temperature ( $125^\circ\text{C}$ ) and was catalyzed by  $10\ \mu\text{l}$  *N,N*-dimethyldodecylamine (97% from Aldrich) for 15 h. After cooling this mixture to room temperature, 100 ml of distilled toluene (p.a. Baker) was added. The freshly prepared glass spheres were then positioned in a Teflon-holder and immersed in functionalized PHS solution. The grafting of the PHS complex on the glass surfaces proceeded at room temperature under nitrogen for 48 h and was terminated by washing the spheres three times with freshly distilled toluene. The glass surfaces were then stored in toluene until use (maximum storage 1 week).

The force curves were determined using a bimorph surface force apparatus [27, 34] known as MASIF<sup>1</sup>, which works as follows. One surface is attached to a piezo-electric tube, which is used to control surface separation. The position of this surface is calibrated by a linear variable displacement transducer (LVDT). The other surface is attached to a force measuring bimorph, which on deflection produces an electrical charge, the magnitude of which can be used to obtain the force. During the course of the experiment the two surfaces are brought into a hard contact (or ‘constant compliance’ defined as the point at which no change in the

---

<sup>1</sup>MASIF (measurement and analysis of surface interaction forces), Australian Scientific Instruments, Canberra Australia (<http://www.anutech.com.au/asi/>).

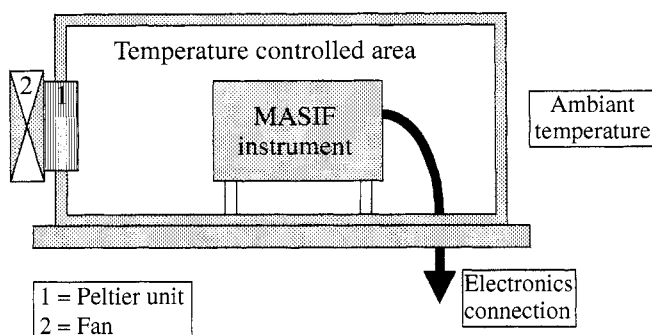


**Figure 1.** Schematic of the temperature control unit. The MASIF is contained within a temperature controlled space. The temperature is controlled by Peltier units (only one shown in schematic, real unit contains six Peltier units.)

surface separation is observed as the surfaces are pushed harder together) which is used to define zero separation. This position is, of course, not an absolute zero of surface separation since the hard wall does not necessarily occur at glass–glass contact, particularly with grafted polymer on the surface.

The measured forces are normalized by  $2\pi R$ , which is thus equivalent to the interaction energy between two flat surfaces according to the Derjaguin approximation [28]. In this case  $R$  is given by  $R = R_1 R_2 / (R_1 + R_2)$ , where  $R_1$  and  $R_2$  are the radii of the two surfaces. The normalization allows for direct comparison between different geometries since the dependence on radius is removed. The sensitivity of the normalized force ( $F/2\pi R$ ) is of the order of  $20 \mu\text{N/m}$  [26].

A major advantage of the MASIF instrument is its thermal control, obtained through the use of a commercially available control hood. In these experiments the temperature was varied between 21 and  $45^\circ\text{C}$  through the use of Peltier elements and fans (larger temperature spans are possible). To avoid vibrational noise, the control unit was shut off during measurement. This can lead to thermal drifts, though these are generally minor over the time scale of the measurement, typically around 1–2 min. To our knowledge, this is the first published work using the temperature control unit and it is schematically illustrated in Fig. 1.

All experiments were carried out using a mixture of ethanol (99.5%, Kemetyl) and distilled heptane (p.a. Merck). Ethanol acts as the flocculating agent for PHS whilst heptane is a good solvent. The solvent mixtures were prepared by mixing the pure solvents to the desired composition in a syringe, and then, after mounting of the surfaces, the solvent mixture was directly injected into the experimental cell. The cell was then allowed to equilibrate for 20 min to allow thermal equilibrium to be established and mixing currents to disappear.

Due to the fact that the surfaces are ramped together at constant approach speed, hydrodynamic forces are in some cases important. (In general in the MASIF the hydrodynamic force,  $F/2\pi R < 0.01 \text{ mN}$ .) This was accounted for by calculating the theoretical hydrodynamic force ( $F_H$ ), and subtracting it from the total force.

This has been achieved using the equation of Chan and Horn [29] who have solved the relevant hydrodynamic equations for the experimental geometry used in surface force measurements.

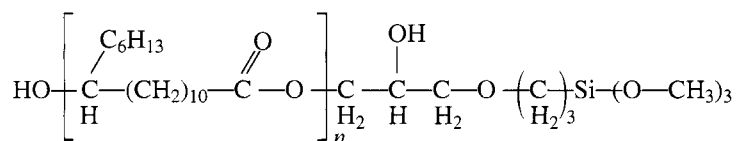
$$F_H = -\frac{6\pi\eta R^2}{D} \frac{dD}{dt}. \quad (1)$$

Where  $\eta$  is the viscosity,  $D$  is the separation between the two slip planes,  $dD/dt$  is the relative speed of approach of the two surfaces and  $R$  is the radius (previously defined). This is valid as long as the two radii used in the calculation of  $R$  are approximately the same, as is the case in the present set of experiments. Otherwise the  $R^2$  term in the hydrodynamics formula becomes more complicated as described by Chan and Horn [29].

The bulk viscosity values as measured by Shikhaliev *et al.* [30] for various temperatures and mixtures of ethanol and heptane were used at all separations regardless of possible variations due to confinement effects between the surfaces or within the polymer network. In these calculations the plane of no-slip is assumed to lie at the position of the hard wall, which is clearly an approximation. However, in practice, realistic variations in the placement of the slip plane make negligible difference to the calculated interaction. We note that although the top surface moves at a roughly constant speed, the deflection of the bimorph renders the speed of approach a function of the surface force, and thus of the separation. A repulsive force between the spheres leads to a decrease in approach speed as the separation diminishes. This causes the hydrodynamic force to become 'flatter' and thus reduces the importance of the placement of the slip plane. For attractive force runs, however, the location of the slip plane may become more important since the surfaces approach more rapidly at small separations.

## 2.1. Characterization of PHS

The polymer PHS after reaction with the anchoring silane has the following chemical structure,



The molecular weight averages  $M_w$ ,  $M_n$  and  $M_z$  of the polymer were determined by gel permeation chromatography to be 4795, 2870, and 7279 g/mol, respectively. This leads to a polydispersity of  $M_w/M_n = 1.67$ .

## 2.2. XPS analysis

X-ray photoelectron spectroscopy (XPS) was conducted using a Kratos Axis HS X-ray photoelectron spectrometer (Kratos Analytical, Manchester, UK). It was

used to obtain the atomic density of carbon at the silica surface, and hence to permit calculation of the amount of polymer grafted onto the surface and an approximation of the layer thickness in vacuum. Since the only available signals from the polymer are C and O and since the substrate is an oxidized silicon wafer, we are constrained to use the carbon signal. A certain amount of carbon contamination is always present, and this needs to be accounted for by considering the proportions of different carbon species (C1 aliphatic/C2 ether or alcohol/C4 esters or carboxylates) in the sample. The C4 signal was used as a fingerprint for the polymer, and the extra C2 signal was assigned to unreacted silanes. Finally, excess hydrocarbon was assumed to be the background contamination (which is usually of the order of about 5% for these measurements). The experiments were run at multiple take-off angles (90, 45, 30 and 20°) with an analysis area of around 1 mm<sup>2</sup>. The samples were analyzed in two ways. First, using a Mg K<sub>α</sub> X-ray source operated at 144 W (12 kV/12 mA) and for the high resolution carbon spectra a monochromator (Al K<sub>α</sub> X-ray source) operated at 300 W (15 kV/20 mA) was used. Detailed spectra for Si 2p, O 1s and C 1s were acquired with a pass energy of 80 eV (pass energy of 20 eV for high resolution carbon spectra). The elements present were first detected by wide scan spectra and then the relative surface compositions were obtained from quantification of subsequent detailed spectra. The sensitivity factors used were 0.27 for Si 2p, 0.66 for O 1s, and 0.25 for C 1s (supplied by Kratos). The grafted layer thickness and the grafted amount were calculated using the method described by Ernstsson *et al.* [31] as were values for photoelectron inelastic mean free paths ( $\lambda$ ) (equation (15) in that work).

### 2.3. Scaling theory

It is possible to fit interaction forces measured as a function of separation for steric interactions in good solvent using the scaling theory for polymer brushes derived by de Gennes [32, 33] as carried out, e.g. by Luckham and Klein [34].

$$W(D) = \frac{k_B T}{s^3} \left\{ \left[ \left( \frac{(2L_0)^{9/4}}{1.25 D^{5/4}} \right) + \left( \frac{D^{7/4}}{1.75 (2L_0)^{3/4}} \right) \right] - \left[ \left( \frac{2L_0}{1.25} \right) + \left( \frac{2L_0}{1.75} \right) \right] \right\}, \quad (2)$$

where  $s$  is the distance between the chain grafting points (assuming a square grafting lattice),  $2L_0$  is the initial interaction separation (contribution of  $L_0$  from each surface),  $D$  is the separation between the glass surfaces,  $k_B$  is the Boltzmann constant and  $T$  is the absolute temperature. The requirements for this treatment are strictly a large molecular weight, and a linear and monodisperse polymer brush. A problem arises in applying the scaling theory equations since the distance measured with the MASIF is not that between the glass surfaces but rather that between the compressed polymer layers. Whereas in the theory, zero separation corresponds to contact of the glass surfaces. Hence, in order to apply the theory, the unknown compressed layer thickness,  $\delta$  per surface, must be included as an extra fitting parameter. This was achieved by simply subtracting  $2\delta$  from the distances entered into equation (2).



For the brush model to be valid  $s < R_F$  (where  $R_F$  is the Flory radius). In this case  $R_F$  has not been experimentally measured but has been calculated from  $R_F = l \cdot N^{0.6}$  and using each polymer backbone unit (i.e. the methylene and the ether group) as the statistical unit ( $N$ ). The values obtained for the number average polymer mass is 3.6 nm, and for the molecular weight average polymer mass, 7.2 nm. It should be noted that the chain stiffness and the presence of side-chains (excluded volume effects) mean that  $R_F$  is underestimated in these calculations.

### 3. RESULTS

The results of the XPS analysis are summarized in Table 1. The higher signal intensities from the Mg/magnetic lens is generally considered to give the more accurate total C signal while the monochromator gives sufficient energy resolution to be able to distinguish the different carbon species. Thus the monochromator has been used to calculate ratios, while the Mg/magnetic lens has been used to obtain graft densities. Using the C4 as a 'fingerprint' for the polymer led to a calculated excess in both C1 and C2, indicating an additional species. The ratio of the C1 and C2 values is consistent with the ratio of the species in the silane monomer. Thus we can conclude that approximately two unreacted silane molecules appear to adsorb per grafted PHS polymer, based on the number average  $M_w$  of the polymer. (Any excess C1 signal beyond that calculated for unreacted silanes is consistent with the contamination levels measured on reference samples of the wafer.)

We note that the values obtained for the graft densities are not significantly affected by which XPS data set is used. Thus the value of 6.3 nm<sup>2</sup> for the area occupied per chain (or polymer molecule) on the surface (or  $s = 2.5$  nm where  $s$  is the separation between grafting points) calculated from the XPS results places this system in the brush regime. Note also that this calculation is based on the number average molecular weight which we deem to be the most appropriate for this calculation (the use of the weight average molecular mass,  $M_w$ , gives a

**Table 1.**  
XPS analysis

Analysis mode	Layer thickness
Angle resolved	8 Å
Single angle	Mean 16.2 Å S. D. 3.9 Å Mean 13.5 Å S. D. 3.9 Å
Detector	Surface density of ester groups (or monomer units)
Mg/magnet	Mean 1.6 nm <sup>-2</sup> S. D. 0.6 nm <sup>-2</sup>
Monochromator	Mean 1.6 nm <sup>-2</sup> S. D. 0.7 nm <sup>-2</sup>
Average area/polymer chain	6.3 nm <sup>2</sup>
Distance between graft points (s)	2.5 nm

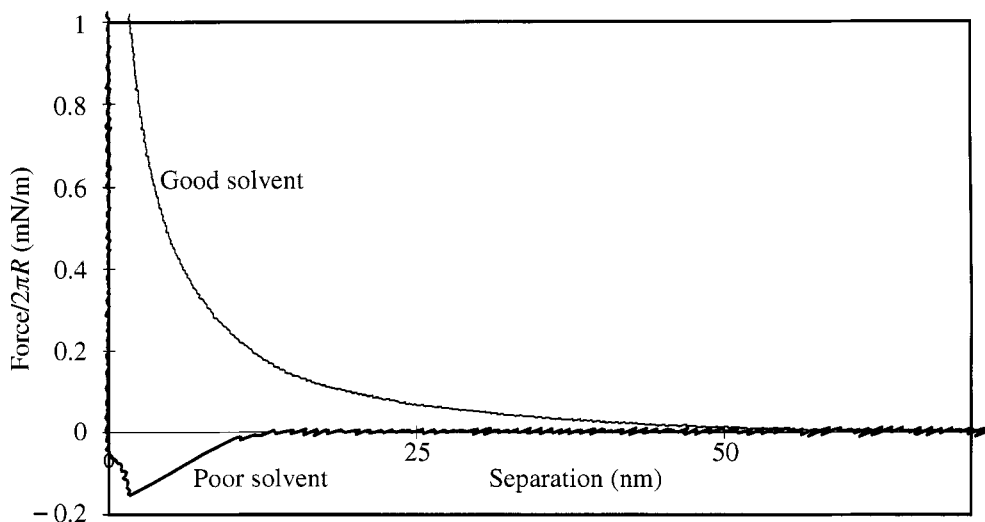


**Figure 2.** Force–distance profile between two PHS grafted glass surfaces in a mixed solvent of ethanol and heptane at 21°C, approach runs only. The profile is normalised as  $F/2\pi R$  vs separation to yield the interaction energy per unit area of flat surfaces. The upper (repulsive) curve represents the interaction in good solvent (40% ethanol) whilst the lower (attractive) curve represents poor solvent condition (43% ethanol).

value of 3.2 nm<sup>2</sup> which is also inside the brush regime for these molecules). It is worth mentioning in this context that the uncertainty in the graft density due to the polydispersity is far larger than any uncertainty in the XPS data.

The forces acting between the glass surfaces bearing grafted PHS layers were investigated as a function of solvent composition (heptane/ethanol) and temperature. In this solvent mixture heptane is a good solvent for PHS whereas ethanol is a poor solvent. Figure 2 shows the forces at 21°C for nominal concentrations of 40 and 43% ethanol (EtOH). In the upper curve (40% EtOH) the forces are purely repulsive and measurable at separations greater than 60 nm. The magnitude of the repulsion increases monotonically with decreasing separation and since the same force was observed on approach and separation, the adhesion between the surfaces was zero. Clearly these measurements are carried out under better than  $\theta$  conditions and the repulsion is due to steric confinement of the extended polymer chains. The forces are extremely sensitive to an increase in the ethanol content and change from repulsive to attractive when the ethanol content is increased to 43% (Fig. 2). The attraction becomes measurable at distances below 15 nm, and we conclude that the grafted polymers are now in a worse than  $\theta$  solvent. A jump into a small steric force barrier occurs from about 10 to around 1.5 nm, which is seen as a straight line in the force data presented in Fig. 2. The jump is the result of the spring instability, occurring due to the fact that the gradient of the force exceeds the spring constant, and the actual gradient of the attractive force is thus larger than indicated by the straight line in the figure [35]. The small steric repulsion just prior to contact is probably asso-

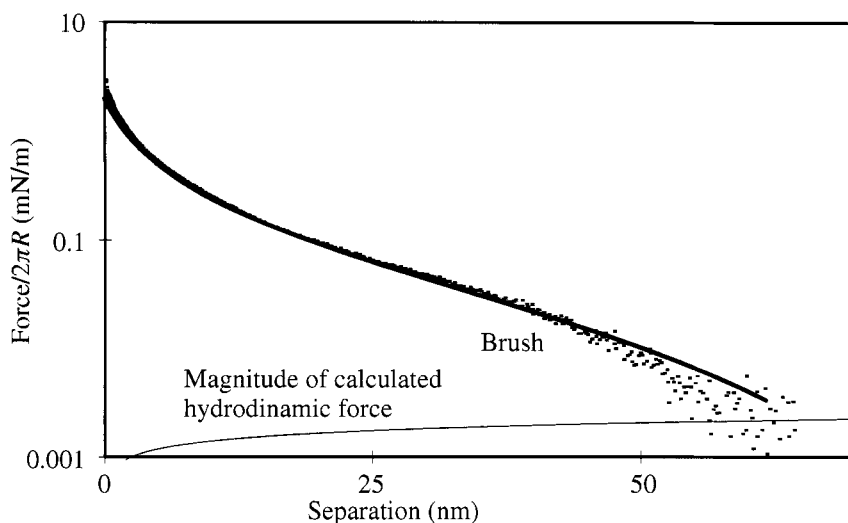


**Figure 3.** Force–distance profile for surfaces on approach in good solvent (40% ethanol) at 21°C. The data points (•) represent measured forces with the calculated hydrodynamic force removed, whilst the thicker curve represents a fit to scaling theory using the brush model ( $s = 1.35$  nm,  $\delta = 21.8$  nm,  $L_0 = 42$  nm). The bottom thin curve represents the calculated hydrodynamic force which is already removed from the data shown.

ciated with removal of some residual solvent from the polymer layer or restrictions in configurational entropy. Upon separation the surfaces adhered to each other very strongly with a normalized pull-off force of the order of 10 mN/m. Thus the properties of the polymer film have changed markedly over only a 3% change in solvent composition leading to a transition in the surface forces from entirely repulsive to almost uniformly attractive.

It should be noted that zero separation in each case is taken from the respective hard wall contacts, which do not necessarily correspond to the same compressed layer thickness since the solvent content of the compressed layer is likely to vary with the solvent composition. Thus, the curves are almost certainly offset from one another with respect to the contact position of the *glass* surfaces — the case of good solvent conditions is expected to have a larger offset in the measured zero position.

Both curves in Fig. 2 show the total measured force, including the hydrodynamic repulsion. In this case, however, the ‘hydrodynamic force’ is negligible in comparison to the total force. This is clearly illustrated in Fig. 3. Here the data from the better than  $\theta$  conditions in Fig. 2 are plotted after subtraction of the calculated hydrodynamic force — the calculated hydrodynamic force is shown in the same figure and is of considerably smaller magnitude for all separations less than 50 nm. (At higher separations the force is tending towards the resolution limit.) Here, of course, the hydrodynamic force assumes a laminar flow and there is no correction made for percolation of solvent through the overlapping brushes and is thus no more than indicative.

The steric repulsion in Fig. 3 is represented as individual data points both to distinguish the data from the fits and to indicate the resolution of the technique. The data are shown on a semi-log plot, in order to best display deviations of the theoretical fits from the data. Forces below  $4 \times 10^{-6}$  N/m are difficult to measure accurately as seen by the scatter in the data. While the branching, the polydispersity and the low molecular weight of the polymer strictly exclude the applicability of the existing scaling theories to describe the interactions, a crude attempt has nonetheless been made. The fit in Fig. 3 uses the scaling theory for polymer brushes in a good solvent (equation (2)) according to the theory of de Gennes [32, 33].

Clearly, the functional form of the measured force curve is well described by the scaling theory despite the fact that our grafted polymer does not meet the assumptions mentioned above. It is expected that the general appearance of the interaction should be the same, however the parameters obtained from the fit are not expected to be reliable. The following values for the parameters are obtained,  $s = 21.8$  nm,  $\delta = 1.35$  nm and  $L_0 = 42$  nm. The fact that  $s$ , the distance between the chain grafting points, lies well outside the brush range (and is very different from that obtained from XPS) demonstrates clearly that the scaling theory is totally inadequate to quantitatively describe the measured interactions in this case. We also note that the value of  $L_0$  is significantly larger than the contour length of a fully stretched chain based on both the average number of monomer units (18.5 nm) and the average molecular weight (29.5 nm). Given the polydispersity, however, this is not unexpected and reflects the fact that the longer chains dominate interactions at large separations.

We note in passing that, as a fitting exercise, the interactions can also be fitted with the scaling theory for mushroom adsorption [33] ( $s > R_F$ ). The fit returns the following values for the parameters,  $s = 2.88$  nm and  $\delta = 1.7$  nm. Remarkably (and presumably entirely coincidentally) the graft density obtained from the mushroom model is very close to that obtained from XPS measurements. The fact that both types of scaling theories return densities in completely inappropriate regimes underscores the fact that the scaling theory cannot be applied to our system.

An alternative to changing the solvent conditions in order to control the solvent quality is to vary the temperature. In the present case the solvent quality increases with increasing temperature and this was used to tune the interactions.

In Fig. 4 the data are shown for a new set of surfaces at an elevated temperature of 42°C and solvent mixture containing slightly more than 40% of ethanol. An attractive interaction is observed. The range of the attractive force and the depth of the minimum are both smaller than for the lower curve in Fig. 2 which we interpret as evidence that the system is closer to  $\theta$  conditions. There is also a small repulsion prior to the onset of the poor solvent induced attraction. As can be seen by the upper solid line in Fig. 4, which shows the calculated hydrodynamic force, this repulsion is entirely accounted for by hydrodynamics. The measured force, after subtracting the hydrodynamic interaction, is compared with the van der Waals force in the inset. The van der Waals force was calculated using a non-retarded Hamaker

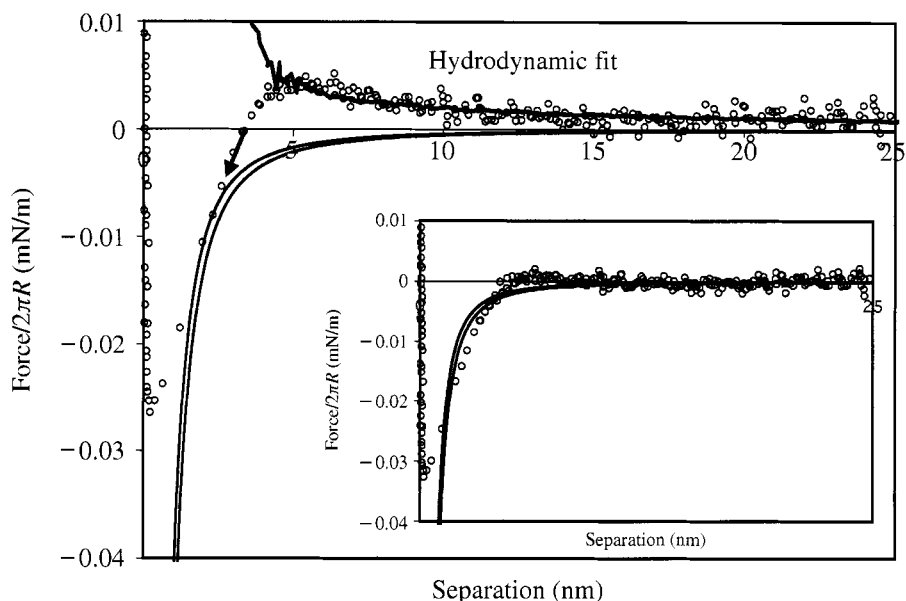


**Figure 4.** Force–distance profile for surfaces on approach in slightly poor solvent conditions (40% ethanol, 42°C). The data points ( $\circ$ ) are shown with a hydrodynamic fit (upper curve) whilst the two lower curves represent van der Waals fits with Hamaker constants of  $1.6 \times 10^{-21}$  J (left curve) and  $2.0 \times 10^{-21}$  J (right curve). The arrow represents the jump into contact of the surfaces. The inset shows the same van der Waals fits but the calculated hydrodynamic interaction has been removed from the data points.

constant ( $A$ ) which was calculated using an approximate solution to the Lifshitz theory derived, for example, by Israelachvili [36]. In these calculations the solvent dielectric constant and refractive index are needed. They were approximated by the arithmetic mean for heptane and ethanol, considering the solvent composition (40% ethanol). The dielectric properties of the glass surface coated with PHS were assumed to be equal to that of quartz (upper limit,  $A = 2.0 \times 10^{-21}$  J) or to that of octane (lower limit,  $A = 1.6 \times 10^{-21}$  J). Clearly, even though the range of the attraction is roughly consistent with that of a van der Waals force, the distance dependence is not. Hence, we conclude that segment–segment attractions between chains extending away from the surface make an important contribution to the measured attraction.

The data in Fig. 5 are obtained under identical experimental conditions as in Fig. 4, except for an increase in temperature of  $\sim 1^\circ\text{C}$  ( $42 \rightarrow 43^\circ\text{C}$ ). The main figure shows the total measured force, including any hydrodynamic contribution. The upper curve is that obtained from the approach run of the two surfaces whilst the lower curve is that obtained on separation. There is a clear hysteresis between approach and separation measurements. Such a hysteresis could be construed to be dependent on relaxation effects within the polymer layer. However, the inset shows the same data as in the main figure, with the calculated hydrodynamic contribution removed.

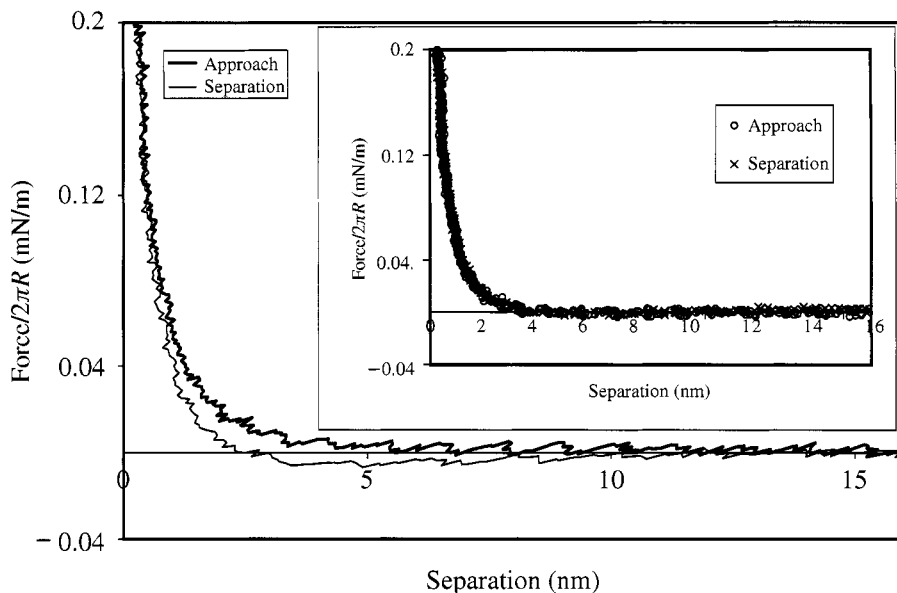


**Figure 5.** Approach (upper) and separation (lower) force–distance profiles at around the  $\theta$  position (40% ethanol, 43°C). The inset shows the same data with the calculated hydrodynamic contribution removed.

It is worth noting that the hydrodynamic contributions are opposite in sign between the approach and separation measurements and that the curves with hydrodynamic interaction removed lie on top of one another. Thus hydrodynamic considerations are sufficient to explain the entire hysteresis apparent in the main Fig. 5. We can thus conclude that the measurements have been carried out slowly enough to allow the polymer layer to adopt its equilibrium structure at each separation. The switch from attraction to repulsion when increasing the temperature by 1°C indicates that the system is very close to  $\theta$  conditions.

Once again, it is possible to fit the data from Fig. 5 to the theory of Dolan and Edwards [37] which is a scaling theory appropriate for  $\theta$  solvents. Two analytical expressions are obtained. The first is valid at short range whilst the second is valid at long range (both coinciding at intermediate ranges). Again, the current system is not suited to such treatment and convincing fits can be made, irrespective of the graft density used.

#### 4. DISCUSSION

Given the polydispersity of our polymer and the fact that the scaling theory has been shown to be inadequate for determining parameters such as layer thickness and graft density (we would have been unable to determine our grafting regime without the aid of the XPS analysis). While the relatively low signal intensity for the ester peaks (our fingerprint signal for the polymer) hinders a definitive absolute

value of the graft density, there is no doubt that the range of values obtained place our polymer surfaces in the brush regime irrespective of solvent conditions. This is important for understanding interactions in the poor solvent case as discussed later. To enable us to perform the XPS measurements on flat surfaces, the measurements were performed on oxidized silicon wafers rather than the glass spheres used in the force measurements. While the silanol group density on the two surfaces is expected to be slightly different [38], this density is much higher than the graft densities of the polymers.

The forces acting between glass surfaces coated by PHS in this mixed solvent system are evidently very sensitive to quite small changes in solvent composition and temperature. The  $\theta$  point, as determined from the force measurements in this study, can be compared with the results of Napper [20], who studied the flocculation of colloidal polymer particles stabilized by PHS. The PHS polymer in that case formed the non-adsorbing group of a diblock copolymer with a number average molecular weight of 1750 g/mol (for the PHS moiety). Napper showed that the critical solvent composition at which the system changed from stable to unstable occurred at higher ethanol concentrations with increasing temperature. The values reported by Napper were: 39.5% at 274 K, 50.5% at 297 K, and finally 58% at 313 K. Although the difference in  $\theta$  compositions is only  $\sim 10\%$  in terms of the ethanol concentration, this is still significant since only a 3% change in composition completely alters the system characteristics (Fig. 2). Although it is tempting to ascribe the differences to confinement effects in our case (lower curvature surfaces) the differences in molecular weights and grafting densities between the measurements make such comparisons difficult at best.

We now consider some other previous studies of relevance to the present investigation. Markovic *et al.* [21] used small angle neutron scattering (SANS) to study a comb polymer with PHS side-chains which adsorbed via the backbone, in dodecane solvent, and concluded that the PHS was fully extended. Doroszkowski and Lambourne [24], also adsorbed a PHS comb polymer to latex particles and used pressure–area isotherms to measure the repulsive steric interaction in heptane. From comparison with theory they determined that the PHS was fully extended in heptane, even for low polymer surface coverage. It is, however, noted that the size of the PHS side-chains used in the work of Doroszkowski and Lambourne [24] was around half the average number molecular weight of the grafted PHS chains used here. The previous observations of extended PHS chains are in good agreement with our observation that the onset of the interaction in better-than- $\theta$  solvents occurs at large separations compared to the polymer dimensions. The length of the fully stretched chain based on the average number of monomers is in fact around 18.5 nm (29.5 nm using the weight average molecular weight) whilst the onset of interaction corresponds to a brush length of 42 nm according to Fig. 3. Even though the fit tends to overestimate the force at large separation, the onset of the interaction clearly occurs at a separation much larger than that at which ‘number average’ chains could possibly interact. Thus we conclude that the long range interaction

is dominated by grafted chains that are considerably longer than the average. This is quite reasonable since 20% of the polymer (based on mass via gel permeation chromatography), when fully stretched, is longer than that needed to interact at the observed onset of interaction.

The force curves measured under worse-than- $\theta$  conditions (Figs 2 and 4) display a long-range attraction. We have already argued that this attraction is not consistent with a van der Waals force using any reasonable Hamaker constant — neither is the functional *form* of the attraction consistent with such an interaction. Hence, we have to consider other attractive force contributions such as bridging forces and polymer intersegment attraction. Intersegment attractions [36, 39, 40] are always present in worse-than- $\theta$  conditions as by definition the segment–segment interaction becomes more favourable than the segment–solvent interaction. This type of attraction has been studied by, for example, Hadziioannou *et al.* [40] where surface forces were investigated for adsorbed di-block copolymer polystyrene brushes in toluene and cyclohexane, above and below the  $\theta$  temperature. The results were qualitatively the same as observed here with an attractive force below the  $\theta$  temperature which could not be explained by invoking a Hamaker interaction. No bridging forces were observed; however, for the pure polystyrene case (adsorbed polystyrene homopolymer) [41], the adsorbed amount was a factor of three smaller and bridging occurred. This is a good demonstration that bridging forces cannot occur under high surface coverage conditions. (Bridging forces are distinguished from intersegment interactions by their range and magnitude and the fact that bridging forces can occur in good solvent conditions.)

The attraction observed in the present case can be explained by intersegment attraction, but let us also consider bridging as a possible mechanism. Bridging forces arise when the polymer has a preference for the substrate and the graft density is such that grafted molecules are able to adsorb onto the opposite surface. The fact that there is no hysteresis under  $\theta$  solvent conditions suggests that there is no polymer bridging in the present case. If bridging forces were present then these would not disappear under  $\theta$  conditions (or possibly even good solvent conditions) and hence some attraction would be expected prior to the steric repulsion [41, 42].

The lack of bridging is also consistent with other force measurements on PHS comb polymers [23] where bridging forces were not encountered. Bridging forces would also lead to some type of attraction in the case of colloidal suspensions, which is not seen [20–23]. Our XPS data indicate that we have a polymer brush and such a high graft density precludes the possibility of bridging in this case [7, 36, 42].

Modelling of interactions under poor solvent conditions is possible, though laborious. For example Ingersent *et al.* [43] modelled the interaction of polystyrene in cyclohexane (a poor solvent) adsorbed onto a mica surface. Measurements were performed in the SFA and comparisons made to the theory of Klein and Pincus [44], based on mean field approximations which were numerically solved. The results of the fits were qualitatively good, yet quantitatively only fair. We have, therefore, not attempted to perform similar calculations. However, we note that the force profile in



Fig. 4 is qualitatively consistent with the theory of Klein and Pincus [44]. The hump in the force curve seen in the lower curve in Fig. 2 during the last few nanometers before contact cannot be explained by the theory. The jump seen in this figure is of a large magnitude and thus the small apparent repulsion may be a dynamic effect since the surfaces move very rapidly during the jump. Changing to a stiffer spring would reduce the tendency for jumping, though at the same time it would reduce the sensitivity of the instrument. Since the forces in question are so small, this is impractical. Alternatively, the small hump may be part of a short range steric force due to loss of configurational entropy, or may even correspond to expulsion of solvent. It is not possible to distinguish between these explanations.

We have shown in Fig. 5 that the apparent hysteresis between approach and separation under close to  $\theta$  conditions is purely due to hydrodynamic interactions. When the forces are small hydrodynamic effects can be significant even at relatively low approach speeds and need to be routinely accounted for. Due to the  $R^2$  dependence of the force, the hydrodynamic interactions become more important in the MASIF than in the AFM — both of these techniques employ constant driving speeds. In the SFA, the approach is normally carried out in a step-wise fashion so the average approach speed is low. However, due to the larger radius in the SFA, care needs to be taken to allow sufficient time between measuring points if the equilibrium force curve is to be determined [45]. The agreement between approach and separation data in the inset of Fig. 5 shows just how accurately the interaction can be obtained assuming additivity of hydrodynamic and other force contributions. It also indicates that the hydrodynamic forces are accurately described by the simple treatment used here which assumes a laminar flow and a well-defined non-slip surface, despite the presence of a grafted polymer layer.

A further conclusion that can be drawn from the complete absence of hysteresis in Fig. 5 is that the relaxation time of the grafted layer is much shorter than the time scale of the measurement.

## 5. SUMMARY

The forces between grafted PHS layers have been shown to be extremely dependent on the solvent conditions. The MASIF instrument has proved particularly appropriate for this study since it has permitted both straightforward temperature control of the solvent conditions, as well as allowing grafting of the polymer onto the surface. This gives the decided advantage that the adsorbed amount remains unchanged during changes in solvent conditions and allows meaningful comparison of the forces under different conditions. A major disadvantage is, of course, the inability to measure the thickness of the compressed layer, which is important for estimating graft densities and to allow any theoretical fitting.

The force can equally easily be 'switched' from good to poor solvent conditions by temperature or solvent composition changes. In good solvent conditions the forces are long ranged repulsive as expected but cannot be sensibly fitted with

scaling theory since the PHS polymer fails to meet the requirements of such an application. Such a fit is an important possible means of obtaining a graft density, but since this avenue is closed, the XPS analysis of the surface proved vital for establishing the grafting regime. Despite the fact that the polymer does not particularly lend itself to XPS analysis either, the results were sufficiently clear to unambiguously establish the graft density as being in the brush regime.

We have identified a regime which we term 'close to  $\theta$ ' conditions. This was due to the dramatic decrease in the range and magnitude of the steric force in this regime compared to better than  $\theta$  conditions and the fact that only minute changes in the system were required to change the interaction to monotonically attractive. Simple hydrodynamics, which did not address percolation or plane of shear issues, was sufficient to completely remove the small hysteresis between approach and separation curves which indicates firstly that such a treatment was sufficient in this case and secondly that there were no viscoelastic effects in that regime.

The expected attractions were seen in bad solvent conditions and the magnitude of the attraction increased with decreasing solvent quality. We have thus now adequately characterised the normal forces and grafting behaviour to permit analysis of the complex dynamic adhesion behaviour which is described in an accompanying paper [46], and the frictional response of such systems, which we are now investigating.

### Acknowledgement

This work was supported by the SSF-program 'Colloid and Interface Technology'. Per Claesson is gratefully acknowledged for valuable discussions as is Marie Ernstsson for assistance with and discussion of the XPS measurements.

### REFERENCES

1. P. Sarker and P. S. Nicholson, *J. Am. Chem. Soc.* **79**, 1987 (1996).
2. M. S. J. Gani, *Ind. Ceram.* **14**, 163 (1994).
3. Z. S. Petrovic, W. J. Macknight, B. Koningsveld and K. Dusek, *Macromolecules* **20**, 1088 (1987).
4. A. Negadi, T. A. Vilgis and M. Benmouna, *Macromol. Theory Simul.* **9**, 628 (2000).
5. P. Auroy and L. Auvray, *Macromolecules* **25**, 4134 (1992).
6. A. Roters, M. Schimmel, J. Ruhe and D. Johannsmann, *Langmuir* **14**, 3999 (1998).
7. S. S. Patel and M. Tirrell, *Annu. Rev. Phys. Chem.* **40**, 597 (1989).
8. P. F. Luckham and J. Klein, *Adv. Colloid Interface Sci.* **73**, 1 (1997).
9. S. T. Milner, *Science* **251**, 905 (1991).
10. H. E. Johnson, H. W. Hu and S. Granick, *Macromolecules* **24**, 1859 (1991).
11. J. Marra and M. L. Hair, *Macromolecules* **21**, 2356 (1988).
12. J. Marra and M. L. Hair, *Colloids Surfaces* **34**, 215 (1988).
13. J. Marra and M. L. Hair, *Macromolecules* **21**, 2349 (1987).
14. R. R. Netz and D. Andelman, *Condens. Matter* **1** (2000).
15. J. Klein, *Coat. Chem. Acta* **63**, 441 (1990).
16. J. Israelachvili, *J. Colloid Interface Sci.* **110**, 263 (1986).

17. A. Dhinojwala and S. Granick, *Macromolecules* **30**, 1079 (1997).
18. J. Israelachvili, *Pure Appl. Chem.* **60**, 1473 (1988).
19. J. M. Georges, A. Tonck, J. L. Loubet, D. Mazuyer, E. Georges and F. Sidoroff, *J. Phys. II France* **6**, 57 (1996).
20. D. H. Napper, *Trans. Faraday Soc.* **64**, 1701 (1968).
21. I. Markovic, R. H. Otterwill and S. M. Underwood, *Langmuir* **2**, 625 (1986).
22. R. J. R. Cairns, R. H. Otterwill, D. W. J. Osmond and I. Wagstaff, *J. Colloid Interface Sci.* **54**, 45 (1976).
23. B. A. D. L. Costello, P. F. Luckham and T. F. Tadros, *Langmuir* **8**, 464 (1992).
24. A. Doroszowski and R. Lambourne, *J. Polym. Sci.: Part C* **253** (1971).
25. C. Pathmamanoharan, *Colloids Surfaces* **50**, 1 (1990).
26. T. Ederth, Novel surfaces for force measurements, PhD Thesis, Kungl Tekniska Högskolan, Stockholm (1999).
27. J. L. Parker, *Prog. Surf. Sci.* **47**, 205 (1994).
28. B. V. Derjaguin, *Kolloid Zeit.* **69**, 155 (1934).
29. D. Y. C. Chan and R. G. Horn, *J. Chem. Phys.* **83**, 5311 (1985).
30. Y. A. Shikhaliev, A. A. Mamedov and S. K. Khalilov, *Russ. J. Phys. Chem.* **48**, 1002 (1974).
31. M. Ernstsson, P. M. Claesson and S. Y. Shao, *Surf. Interface Anal.* **27**, 915 (1999).
32. P. G. de Gennes, *Macromolecules* **15**, 492 (1982).
33. P. G. de Gennes, *Adv. Colloid Interface Sci.* **27**, 189 (1987).
34. P. F. Luckham and J. Klein, *J. Chem. Soc. Faraday Trans.* **86**, 1363 (1990).
35. J. N. Israelachvili and B. W. Ninham, *J. Colloid Interface Sci.* **58**, 14 (1977).
36. J. Israelachvili, *Intermolecular & Surface Forces*. Academic Press, London (1997).
37. A. K. Dolan and S. F. Edwards, *Proc. R. Soc. Lond. A* **337**, 509 (1974).
38. M. W. Rutland, *Langmuir* **10**, 1110 (1994).
39. S. Biggs and A. D. Proud, *Langmuir* **13**, 7202 (1997).
40. G. Hadzioannou, S. Patel, S. Granick and M. Tirrell, *J. Am. Chem. Soc.* **108**, 2869 (1986).
41. J. Israelachvili, M. Tirrell, J. Klein and Y. Almog, *Macromolecules* **17**, 204 (1984).
42. J. Klein and P. Luckham, *Nature* **308**, 836 (1984).
43. K. Ingersent, J. Klein and P. Pincus, *Macromolecules* **19**, 1374 (1986).
44. J. Klein and P. A. Pincus, *Macromolecules* **15**, 1129 (1982).
45. M. W. Rutland and H. K. Christenson, *Langmuir* **6**, 1083 (1990).
46. M. A. Plunkett and M. W. Rutland, *J. Adhesion Sci. Technol.* **16**, 983 (2002).

# Adhesion Mapping and Surface Imaging

## **Design of a digitally controlled adhesion imaging mode using a scanning force microscope**

YI ZHANG, ANDRAS PUNGOR, GANGADHAR JOGIKALMATH  
and VLADIMIR HLADY\*

*Department of Bioengineering, University of Utah, Salt Lake City, UT 84112, USA*

**Abstract**—The design of a combined topography–adhesion–stiffness imaging mode in a scanning force microscope (SFM) based on a digital control system is presented. The digital control system provides for the flexibility in designing the shape of the loading–unloading force waveform and enables a fast rate (up to 1 kHz) of applying the loading–unloading waveform with a pre-defined maximum loading force. Furthermore, flexibility in optimizing the imaging conditions and analyzing the resulting force–displacement data is achieved. The limiting factor for the data acquisition speed appears to be the viscous drag of the working medium exerted onto the SFM cantilever. It is shown that subtracting a no-contact, zero-deflection baseline can compensate for the effects of the viscous drag. The performance of the digital adhesion mapping control system is illustrated by analyzing several different samples: a rigid silicon grid; a molecularly thin block copolymer film; and a thin, heterogeneous polymer film. The remaining problems are related to the cross-talk between the topography and stiffness-related slope.

**Keywords:** Adhesion; AFM; elasticity; pull-off force; SFM.

### **1. INTRODUCTION**

Various modes of scanning force microscopy (SFM) have been used in studies of surfaces and interfaces since the conception of SFM in the early 1980s [1–4]. An increasing number of SFM-based studies are being devoted to biological systems and biomaterials [5–12]. The spatially resolved information about materials surface energetics, topography, and mechanical properties such as compliance is available from local SFM force–displacement measurements (often referred to as ‘force curves’), i.e. from the local force interaction profiles between the SFM probe and a small area of the specimen [13]. The SFM technique can be used to

---

\*To whom correspondence should be addressed: Phone: 801-581-5042; Fax: 801-585-5151; E-mail: vladimir.hladky@m.cc.utah.edu

correlate the spatial distribution of these material properties with the material's biocompatibility, which ultimately depends on an intricate combination of surface energetics, topography, and mechanical properties.

Since force–displacement measurements can provide information about material properties, efforts have been made to record the spatial distribution of such properties. Typically, a sample is driven up and down in the  $z$ -direction while being scanned in a raster-like fashion in the  $x$ – $y$  plane and a force curve is obtained at each location. Sample properties such as the pull-off adhesion force and elasticity are then extracted from each force curve. The force curve analysis can be performed either on-line or off-line. In the so-called force volume mode, the whole three-dimensional (3-D) data set ( $x$ – $y$  position,  $z$ -displacement, and force) is stored and analyzed off-line [13]. This operation requires a large memory and the imaging speed is relatively slow: the maximum speed reported in the literature is 100 force curves per second [14]. Another way of recording the spatial distribution of material properties is to extract the desired parameters from the force curve by means of electronics hardware. Van der Werf *et al.* showed that with electronic hardware devices one could record 700 force curves per second [15]. Rosa-Zeiser *et al.* constructed the so-called pulsed force mode AFM [16], which simultaneously records adhesion, elasticity, and topography images. The force curve acquisition rate in the pulse force mode can be as high as 5 kHz. A hardware-based analysis system is not as flexible as a digital control system using a computer, and its use limits the analysis of force–displacement data.

In general, the pull-off adhesion force between the sample surface (subscript 1) and a spherical probe (subscript 2) in an aqueous medium (subscript 3),  $F_{132}$ , is related to the work of adhesion,  $W_{132}$ :

$$F_{132} = -1.5\pi R W_{132},$$

where  $R$  is the radius of the spherical probe [17]. In SFM adhesion experiments, the cantilever tip acts as an adhesion probe with an effective radius,  $R$ . The work of adhesion,  $W_{132}$ , depends on the interfacial energy between the sample and the SFM tip,  $\gamma_{12}$ ; the sample and the aqueous medium,  $\gamma_{13}$ ; and the SFM probe and the aqueous medium,  $\gamma_{23}$ , respectively:

$$W_{132} = -\gamma_{12} + \gamma_{13} + \gamma_{23}.$$

Using the combination of the pull-off force and contact angle measurements [recall that  $W_{mn} = \gamma_n(1 + \cos \theta)$ , where  $n$  stands for a liquid which shows a contact angle  $\theta$  on a solid  $m$ ], one can determine the work of adhesion (in vacuum) between the unknown sample and the SFM tip probe,  $W_{12}$ . Assuming that the contribution of the SFM probe surface energy to  $W_{12}$  remains unchanged, any variation of  $W_{12}$  can be assigned to the variation of the surface energy of the sample,  $\gamma_1$ .

We have recently utilized SFM mapping of the pull-off adhesion forces as a means to elucidate the two-dimensional (2-D) distribution of the interfacial energy of grafted poly(ethylene oxide) (PEO) chains and micrometer-sized oxidation patterns

on polystyrene [18, 19]. The analysis of the 2-D distribution of interfacial energies was performed using force volume mode imaging implemented in a commercial instrument (Topometrix). We found that the PEO-chain grafted surfaces contained sub-micrometer domains of higher interfacial energy in the PEO layer. It is not known whether these adhesion ‘hot’ spots are ubiquitous to all grafted layers, or they resulted because of a particularly non-uniform chemistry used to graft the PEO chains.

Our general aim is to measure the surface heterogeneity of a biomaterial and the length and time scale over which such heterogeneity exists. This information will be used in deciding whether a particular surface heterogeneity can be tolerated in a biomaterial application. In order to fulfil this aim, we needed highly resolved, spatial, and temporal information about the mechanical and energetic microheterogeneities of the biomaterial surface. The motivation for designing a new digitally controlled pull-off force imaging mode was two-fold:

- (1) The force volume imaging mode used in the past had a very low data acquisition speed. One spatial map with 50 by 50 pixel resolution and a 50 pN force resolution takes 1 h of imaging time. Furthermore, it provided no information on the local elasticity of the sample [18].
- (2) The pulsed force imaging mode [16], although much faster in data acquisition than the force volume imaging mode, is less flexible in the analysis of force–displacement measurements than a digitally controlled system.

In this paper, we introduce the design of a digital control system for adhesion and elasticity imaging, its interfacing with an SFM microscope, and illustrate its use under various experimental conditions with several different samples.

## 2. EXPERIMENTAL

In a typical recording of a force–displacement curve, one drives the  $z$ -piezo element up and down. When the  $z$ -piezo carries the SFM cantilever with a probe tip that makes contact with the sample surface, a deflection of the cantilever (i.e. force) is recorded by a quadrant, position-sensitive photodetector (PSD) as a function of the piezo displacement (hence the name ‘force–displacement curve’). The typical triangular  $z$ -piezo driving waveform and the output signal of the PSD (proportional to the cantilever deflection) are shown in Fig. 1. From the cantilever deflection signal one can calculate two parameters:

$$F_{\text{ad}} = K \Delta V_{\text{min}} = K(V_{\text{AN}} - V_{\text{min}})$$

and

$$F_{\text{max}} = K \Delta V_{\text{max}} = K(V_{\text{max}} - V_{\text{AN}}),$$

where  $F_{\text{ad}}$  is the pull-off adhesion force,  $F_{\text{max}}$  is the maximum loading force, and  $V_{\text{AN}}$  is the average signal when the SFM probe and the sample are not in contact.  $K$  is the conversion constant ratio between the actual force ( $F$ , in N) and the

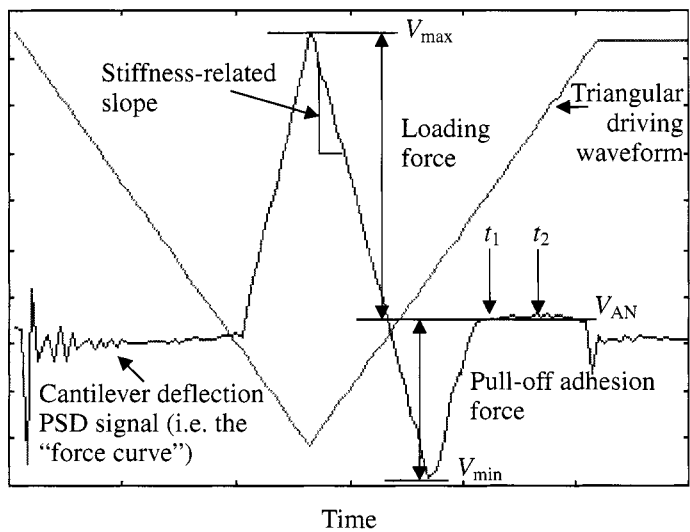


**Figure 1.** Cantilever deflection PSD signal during one cycle of *z*-piezo up–down movement driven by a triangular waveform.  $V_{AN}$  is the average voltage between  $t_1$  and  $t_2$  when the tip is not in contact with the sample surface. The values of  $\Delta V_{min}$  and  $\Delta V_{max}$  are indicated.

PSD signal ( $V$ , in V) ( $K = F/V$ ).  $K$  needs to be calibrated using the actual spring constant of the cantilever by measuring the force–displacement curve on a stiff sample [20]. The stiffness-related information about the sample (in units of force/length) is calculated from the unloading part of the force–displacement curve (Fig. 1).

2.1. Hardware design

The design of a digitally controlled pull-off force acquisition board was guided by two principles:

- (1) maintaining a constant load,  $F_{max}$ , in each cycle during the imaging of pull-off adhesion forces; and
- (2) achieving the fastest possible signal acquisition and on-line detection of  $F_{ad}$  and  $F_{max}$ .

A Nanoscope II AFM (Digital Instruments) was used as the basic SFM instrument. Adding new input and output ports to the Nanoscope control unit made the raw PSD signal and the high-voltage piezo drivers accessible. While the control unit of the Nanoscope II still controls the *x*–*y* scanning of the sample, a synchronized digital control board which regulates the *z*-piezo movement and collects the data from the PSD detector was added. The control process is shown in Fig. 2. The D/A converter of the board provides the waveform that drives the *z*-piezo up and down. The shape of the driving waveform can be chosen freely between triangular, sinusoidal or any other desired shape. After digitization of the PSD signal, the computer analyzes the waveform and calculates  $V_{max}$ ,  $V_{min}$ , and  $V_{AN}$ .  $\Delta V_{max}$  is then compared with a set-



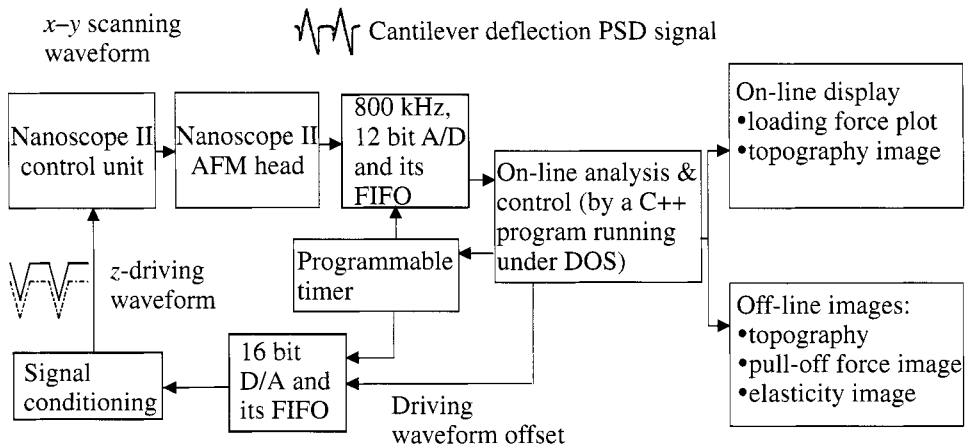


**Figure 2.** Block diagram of the digital control process.

point value and the difference signal is used to calculate the waveform offset that will compensate for the topographic variation and any baseline drift. Therefore, a negative feedback control loop is employed to keep the loading force constant. The data collected from the force curves are arranged and displayed to show either the topography or the pull-off adhesion force. The PSD signal is also stored for further off-line analysis.

There are two crucial points in the control process. First, the frequency of the loading force waveform needed to be synchronized with the  $x-y$  scanning rate. It also needed to be adjustable with a high accuracy to match the  $x-y$  scanning rate controlled by the Nanoscope II control unit. A programmable timer was used for this purpose. The second design problem was the feedback control of the maximum loading force,  $F_{\max}$ . In order to keep the parameter  $F_{\max}$  constant during each cycle, the data acquisition rate had to be fast enough to obtain the data required by the feedback algorithm. The typical error involved in keeping  $F_{\max}$  constant is related to the error in  $\Delta V_{\max}$ . The  $\Delta V_{\max}$  error for a flat surface is estimated to be below 0.1 V, which corresponds to a load variation of the order of 1 nN. In the case of a very rough surface, the parameters of the feedback algorithm including the  $x-y$  scan rate have to be adjusted for optimal compensation of the sample topography.

Large deflections of the cantilever can cause a non-linear PSD response. Both the contact and the adhesion parts of the force-displacement curve (Fig. 1) are checked for any non-linearity prior to the start of actual imaging. If non-linearity is present, a stiffer cantilever needs to be used.

The control board was designed to provide a continuous waveform with an adjustable offset. The output range of the D/A ( $\pm 10$  V) was further divided by 5 to match the input range of the Nanoscope II control unit's high-voltage piezo driver amplifier. The D/A resolution was set at 16 bits, to avoid any kind of resonance of the cantilever caused by the step function of the D/A converter. The effect of the driving waveform steps was reduced by using a low pass filter with an adjustable

cut-off frequency before the waveform was sent to the Nanoscope II input. The force curve frequency was set at 1 kHz. For accurate measurement of the detector signal, 200–300 sampling points per cycle were needed, which required that the minimum sampling frequency of the A/D converter be set at 300 kHz. The digital control board was developed for a PC system on an ISA BUS prototyping breadboard (JDR-PR10, JDR Microdevices). This board had a 16-bit layout with a buffered data and address bus together with a control for address decoding. The A/D channel was based on an ADS7810 (Burr-Brown), 800 kHz, 12-bit A/D converter. Considering the minimum sampling rate of 300 kHz, and the additional calculation and display time, a speed of 800 kHz was a reasonable choice. The input range of the A/D converter was  $\pm 10$  V. The output range of the detector signal was  $\pm 15$  V, so the PSD signal had to be adjusted to fit the input range of the A/D converter. For the D/A channel, we used a 16-bit DAC712 (Burr-Brown) converter. As both the A/D and the D/A signals have high speed, the amplifiers used on the board were selected to have wide bandwidth characteristics. Both A/D and D/A conversions were controlled by a programmable timer (8254, Intel). The base clock signal for the timer was derived from the computer's system clock. The A/D and D/A data were stored in the FIFO memories. This type of data storage provides for the possibility that the computer processor does the calculations and displays the results while the conversion is simultaneously taking place. The FIFO used (7202, IDT) had a  $1024 \times 9$ -bit memory. With a parallel connection, the two FIFO units covered the 16-bit length of the D/A and the 12-bit resolution of the A/D. The FIFO had status facts which gave information about the status of the memory, i.e. whether it was full, half-full, or empty.

## 2.2. Software design

The control software was compiled to run under DOS, which allowed for faster and more direct board control than under Windows. The essential components of the software included

- (a) hardware control: 8254 timer initialization, setting start and stop, reading from A/D FIFO, writing to D/A FIFO and interrupt handling;
- (b) feedback control of the loading force: generating the driving waveform, analysis of  $V_{\max}$ ,  $V_{AN}$ , and  $V_{\min}$ , and calculating the driving waveform offset to compensate for topography variation;
- (c) on-line display: plot of  $\Delta V_{\max}$  along the time scale and display of the image of  $\Delta V_{\min}$  (or topography-related waveform offset voltage);
- (d) user interface: adjusting the PID parameter of the feedback loop control, reporting errors, and storing data.

To achieve a high data acquisition rate, any on-line data handling and computation had to be as simple as possible. An integer form of data was used to speed up the calculation. Since the original data from the A/D and D/A converters had no higher resolution than 16 bits, a large part of the simple calculations could be done in an

integer mode. However, there was still some need for floating point manipulation such as in the PID feedback calculation, and in displaying the  $x-y$  plot of  $\Delta V_{\min}$  (or topography-related offset voltage). Furthermore, parameters such as the set-point of  $\Delta V_{\max}$ , the range of the  $z$ -driving waveform, and the PID parameters were all floating point numbers set by the user.

A user-friendly interface was created for entering the control parameters and displaying the results. The software program displayed the actual parameters on the screen. By entering new values, the user could change the parameters. The program also had a range check for the input parameters: they were accepted only if they were in the allowed range, otherwise the program signalled the user to re-enter the value. Once the parameters had been entered, the software program switched to its control function. The program then started the timer, which, in turn, generated the conversion frequency for the A/D and D/A converters. After reading the A/D FIFO, the new topographical offset was calculated and sent to the memory of the D/A converter. After every cycle, the program displayed a new data point on the  $V_{\max}(\text{time})$  plot and in the on-line image. The imaging process could be terminated at any time and the data and images stored.

The analysis of the adhesion and stiffness-related maps is typically performed off-line. For this report, the calibration of the adhesion and stiffness-related maps was performed using nominal cantilever spring constants provided by the manufacturer. Although the actual cantilever spring constant may vary from its nominal value by as much as  $\pm 50\%$ , this variation only affects the absolute magnitude of pull-off forces and not the relative adhesion map contrast.

### 2.3. Materials and methods

Thin dewetted polystyrene films were prepared by a spin-casting procedure: 0.1 ml of a 10 g/l solution of polystyrene ( $M_w = 28\,000$  Da, Aldrich) in toluene was spin-coated onto a glass coverslip at 4000 rpm for 2 min. The film thickness, as measured by ellipsometry, was approximately 100 nm. The film was annealed in vacuum at  $160^\circ\text{C}$  for 24 h. The block copolymer polystyrene-poly(ethylene oxide) film ( $M_{w,PS} = 12\,200$  Da,  $M_{w,PEO} = 23\,900$  Da, Polymer Source, Inc.) was first prepared as a monolayer on the air/water interface in a Langmuir trough. The film was compressed to a surface pressure of 10 mN/m before it was transferred to a silicon wafer using a horizontal transfer technique (Jogikalmath and Hlady, in preparation). The silicon wafer was first made hydrophobic using octadecyltrichlorosilane (OTS), using the following treatment: a clean silicon wafer was immersed in a 0.02% (v/v) solution of OTS in dicyclohexyl for 12 h, rinsed with chloroform, water, and then dried. All SFM imaging was performed in water using the Nanoscope II head, a fluid cell, and a  $10\ \mu\text{m}$   $x-y-z$  piezo scanner. The cantilevers with nominal spring constants of 0.1 and 0.5 N/m were from Park Scientific, Inc. The magnitudes of the pull-off adhesion force and the stiffness-related slope were calculated using the nominal spring constants of the cantilevers employed in the imaging experiments.

### 3. RESULTS AND DISCUSSION

#### 3.1. The role of the medium viscosity

The pull-off adhesion force, when measured in air, results from the capillary forces originating from a thin layer of water on the sample surface [21]. Because of that, it is recommended to map the pull-off forces in a liquid environment. Unfortunately, liquids have a much higher viscosity than air. When a cantilever moves through such media, its deflection is influenced not only by the interaction forces between the cantilever tip and the sample, but also by the viscous drag acting along the whole length of the cantilever. The drag affects the force measurements in two ways: (1) it lowers the resonance frequency of the cantilever, and (2) it modifies the deflection of the cantilever when it moves through the medium [22]. A traditional way to avoid the effect of the viscous drag on the cantilever resonance frequency is to work at a frequency much lower than the resonance frequency. Rosa-Zeiser *et al.* recommended that the force curve rate should be less than one-fifth of the cantilever resonance frequency [16]. However, a stiffer cantilever with a higher resonance frequency which would be suitable for faster imaging could compromise the resolution of the measured forces. Another approach to avoid the resonance is to drive the *z*-piezo by a sinusoidal waveform instead of the triangular wave [16]. Unlike the triangular driving waveform, a sinusoidal waveform has no high frequency components, so that one can work at higher force–displacement curve rates without irritating resonances.

The viscous drag affects the deflection of the cantilever moving through the medium in proportion to the cantilever velocity. This effect is easily seen in the case when the cantilever does not make any contact with the sample. In this case, while working in free space and far below the cantilever resonance, the cantilever deflection should be zero at all times. In a liquid, however, the shape of the no-contact, zero-deflection baseline will depend on the driving waveform (Fig. 3). For a sinusoidal waveform, the zero-deflection baseline will be another sinusoidal waveform with approximately 90° phase shift compared with the driving waveform (Fig. 3a). For a triangular driving waveform, the zero-deflection baseline will display baseline offsets between the loading and unloading parts of the waveform (Fig. 3b). The magnitude of the baseline offset (Fig. 3b) and the amplitude of the sinusoidal baseline (Fig. 3a) depend on the cantilever velocity (i.e. on the force–displacement curve rate). The faster the force curve rate, the larger the effect. In most experiments, for the loading part of the driving waveform the zero-deflection baseline is above the unloading part of the baseline. However, we have observed a positive offset in retraction in some cases. Namely, the effect is also affected by the location of the laser spot on the cantilever. The reason for the baseline offset in the case of a triangular driving waveform has been discussed by Hoh and Engel [23]. They also found the offset to be linear with the cantilever velocity and attributed the offset to the viscous drag. As viscous drag is linear with

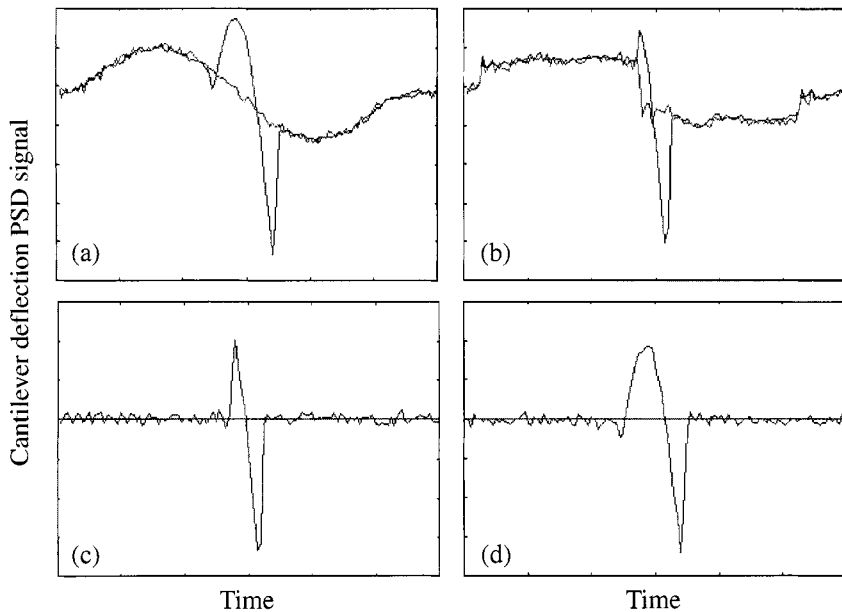


**Figure 3.** Effect of the medium viscous drag on the cantilever deflection. The no-contact, zero-deflection baseline is superimposed on a force–displacement curve measured at the same location of a polystyrene thin film using (a) a sinusoidal and (b) a triangular driving waveform in water. Subtraction of the zero-deflection baseline compensates for the viscous drag effects (c and d).

the object velocity at low speeds, the magnitude of the baseline offset is expected to be linear with the force curve rate.

As illustrated by Fig. 3, the baseline offsets can be quite large compared with the pull-off adhesion force. In order to measure the pull-off forces accurately, one has to compensate for this baseline offset. This is especially important for the sinusoidal driving waveforms, as the baseline is not constant along retraction. Using a digital control system, it is very easy to record the no-contact, zero-deflection baseline before each imaging experiment and subtract the baseline during the on-line analysis. The subtraction of the baseline is based on the assumption that the forces experienced in the tip–sample interactions and the viscous drag are additive. The compensation for the baseline offset in Figs 3a and 3b is shown in Figs 3c and 3d, respectively. After subtraction, the cantilever deflection signal in the no-contact region of the force–displacement curve is nearly constant, which indicates that the effect of viscous drag in the non-contact region is reproducible and repeatable. Since the  $\Delta V_{\min}$  values (which are proportional to the pull-off force) agreed with each other after subtraction of the zero-deflection baseline for the two different waveforms, we conclude that the assumption of the additivity of the pull-off forces and the viscous drag effect is quite reasonable (Figs 3c and 3d).

3.2. Adhesion dependence on loading force

In order to find the optimum conditions for pull-off force mapping, we also studied the relationship between the pull-off force and the maximum loading force. Figure 4 shows how the force–displacement curves measured between the silicon nitride tip and a polystyrene thin film in water change with increasing maximum loading force. The results indicate that a constant pull-off force is obtained once the loading force exceeds a certain critical value. We assume here that the effect observed is related to the viscoelasticity of polystyrene. A viscoelastic sample may not recover fully during the retraction part of the force–displacement cycle [22]. Thus, right at the pull-off event, the contact area between the tip and the sample will determine the effective radius of the tip,  $R$ . The higher the loading force, the larger the effective radius will be, resulting in a larger pull-off force. However, when the loading forces reach a certain critical magnitude, the contact area may not change very much. The observed loading force vs. pull-off force relationship indicates that one needs better control of the maximum load. If, for example, the maximum load changes due to topographic variations, the pull-off adhesion force will be affected even if there is no material difference; hence, cross-talk between the topography and adhesion will be present. Such cross-talk can be avoided by setting the set-point higher than the critical loading force. When measuring soft samples, one also needs to reduce the maximum load because higher loading forces may result in sample deterioration. In such cases, the only course left is to reduce the imaging speed, to make the feedback tighter on the maximum load.

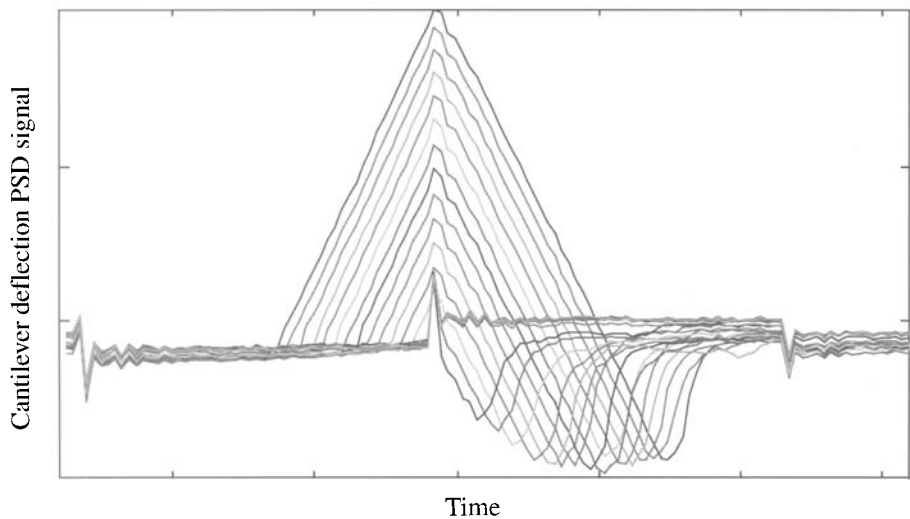


**Figure 4.** Effect of the maximum loading force on the force–displacement curve measured between the silicon nitride tip and a polystyrene thin film in water. The magnitude of the pull-off force approaches a constant value upon increasing the loading force.

### 3.3. Local stiffness

Indentation of the sample by the SFM tip at positive loading forces can be used to map the relative stiffness of the sample. In most cases, the slope of the force–displacement curve at positive loading forces varies with the displacement, as the indentation depth does not increase linearly with the loading force [20, 22]. The contact interactions between the tip and the sample are related to the viscoelastic characteristics of the tip and the sample, as well as to the tip geometry and the cantilever stiffness. We have developed a quantitative elasticity imaging technique based on a constant compliance feedback loop [24, 25]. Because of the need for a faster acquisition rate, in the present work we used a force–displacement slope at higher loading forces in the unloading part of the force curve to map the information about the relative sample stiffness (Fig. 1). At higher unloading forces, the slope is less affected by other events such as the jump-into-contact event (often due to the electrostatic interaction), or lateral displacement of the cantilever [23]. The slope, however, may be affected by strong adhesion forces that can ‘pin down’ the SFM tip and buckle the cantilever rather than deflect it [26].

Figure 5 shows the topography, pull-off adhesion force, and stiffness of a calibration silicon grid (Topometrix). The features seen in Fig. 5 are the 2  $\mu\text{m}$  diameter mesas etched in silicon. Topography, adhesion force, and stiffness-related slope images (100 by 100 pixels) were recorded simultaneously in an aqueous solution. The total imaging time was 50 s. The respective profiles of the three

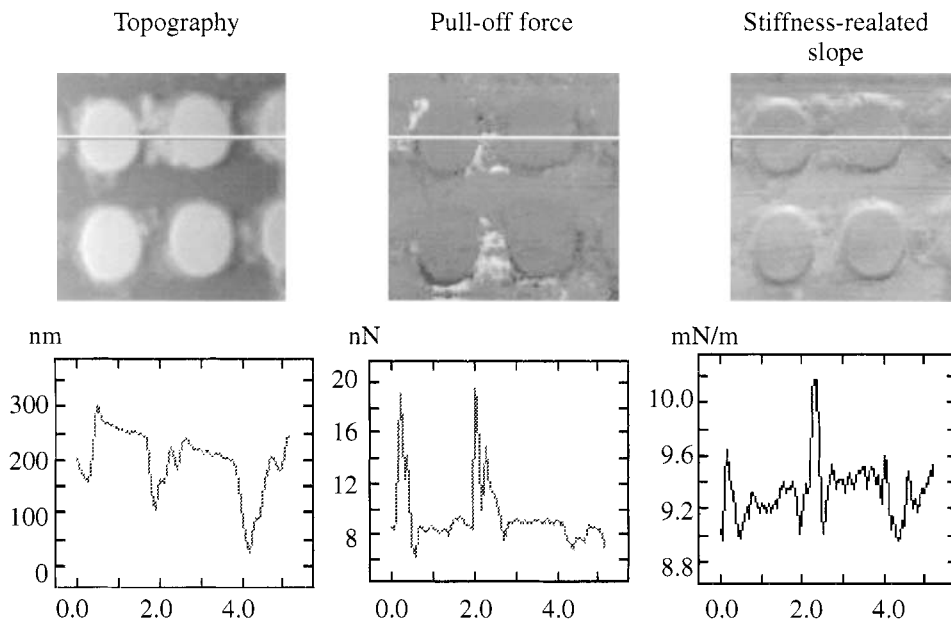


**Figure 5.** Topography, pull-off adhesion force, and stiffness-related slope maps (100 by 100 pixels) measured simultaneously on a silicon calibration grid (Topometrix) under aqueous solution. The force–displacement cycle rate was 200 Hz. The respective profiles are shown in the lower panels.

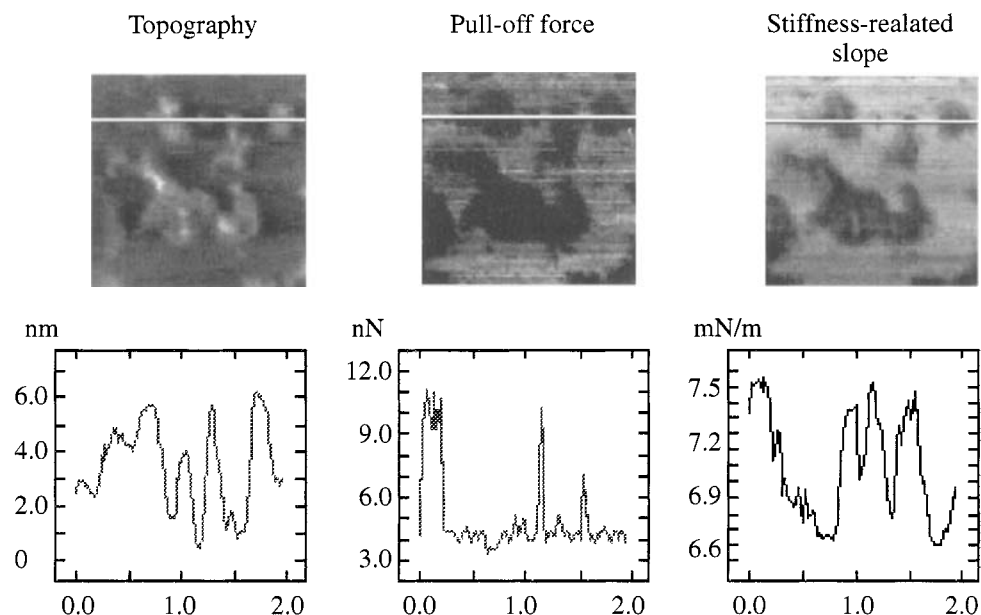


**Figure 6.** Topography, pull-off adhesion force, and stiffness-related slope maps (100 by 100 pixels) of a Langmuir–Blodgett film of polystyrene–poly(ethylene oxide) (PS–PEO) block copolymer on a hydrophobic silicon wafer. The force–displacement cycle rate was 200 Hz. The respective profiles are shown in the lower panels.

surface parameters are shown in the lower panels of Fig. 5: the variation in topography is quite distinct (features were  $0.16\ \mu\text{m}$  tall). The pull-off force map is rather flat with a mean pull-off force of approximately 8 nN. Areas of higher adhesion found in-between the mesas are assumed to originate from an unknown residue left on the surface after the lithographic process. The variation of the stiffness-related slope is, as expected, quite small: the map, however, shows a resemblance to the topography and the shadow-like enhancement effect in the slow scanning directions (normal to the profile shown in the lower panel).

Figure 6 shows a Langmuir–Blodgett film of polystyrene–poly(ethylene oxide) (PS–PEO) block copolymer transferred at a low surface pressure of 10 mN/m to a hydrophobic silicon wafer. The film, purposely transferred at low surface pressure, had an incomplete surface coverage: the transferred PS–PEO molecules were in island-like aggregates on the substrate. The respective profiles across the three images (100 by 100 pixels) are shown in the lower panels of Fig. 6. The three surface characteristics — topography, adhesion force, and elasticity — are displayed at 20 nm resolution. The topography map shows features of approximately 5 nm in height. The block copolymer dimension, based on the radii of gyration of PS and PEO chains, is around 9 nm (Jogikalmath and Hlady, in preparation). The pull-off force map shows higher adhesion on the hydrophobic silicon wafer (gray regions in the middle panel) and very low adhesion on the PS–PEO aggregates. The transferred PS–PEO islands are expected to have their PEO chains exposed



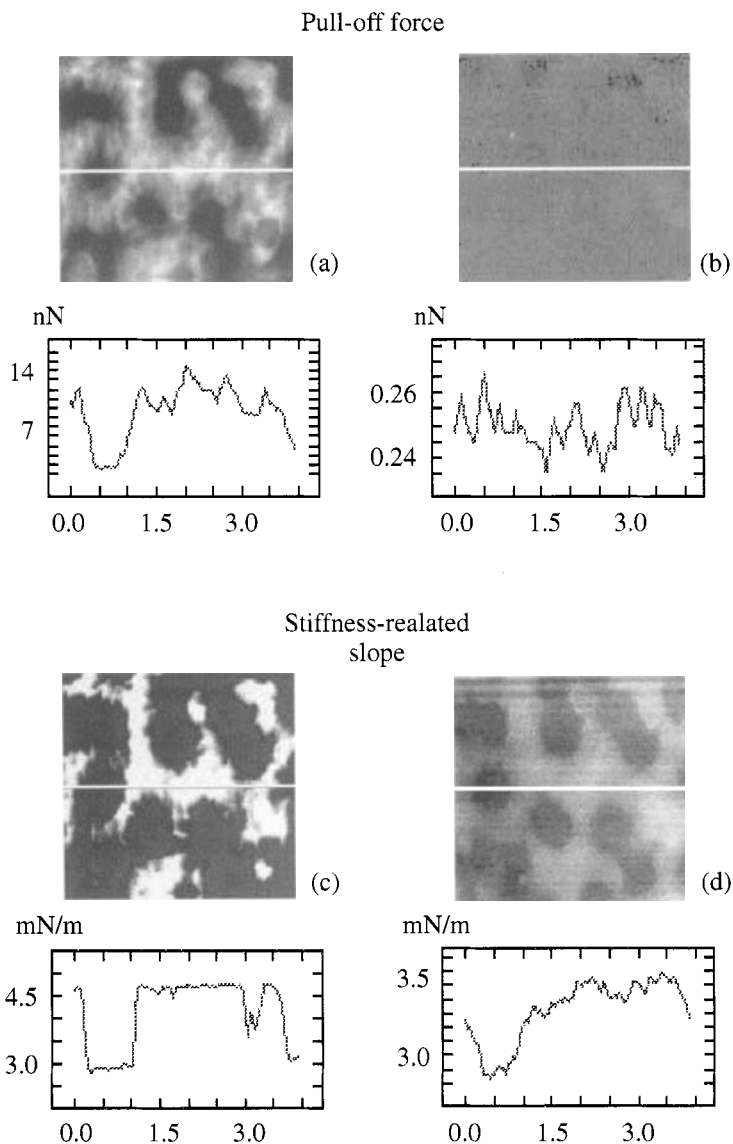


**Figure 7.** Pull-off adhesion force (a and b) and stiffness-related slope (c and d) maps (100 by 100 pixels) measured simultaneously on a thin, dewetted polystyrene film on a glass coverslip. The PS film was imaged under water (left panels) and under ethanol (right panels). The force–displacement cycle rate was 200 Hz. The respective profiles are shown in the plots below the images.

to the solution (dark regions in the middle panel). The stiffness-slope map shows a very small variation: the brighter regions of the uncoated hydrophobic silicon wafer indicate a stiffer material (right panel) than the PS–PEO islands. Such a small variation in stiffness is perhaps due to the very low thickness of the PS–PEO islands and the relatively large stiffness of the underlying substrate.

### 3.4. The role of different media on the pull-off forces of dewetted PS film

Figure 7 shows the maps of the pull-off adhesion force (upper panels, Figs 7a and 7b) and the stiffness-related slope (lower panels, Figs 7c and 7d) measured on a thin (approximately 100 nm thick) dewetted polystyrene (PS) film on a glass coverslip. The PS film was imaged under water (left panels) and under ethanol (right panels). The respective profiles are shown in the plots below the images. After spin-casting, the film was annealed above the polystyrene  $T_g$  temperature at 160°C for 24 h. During the annealing, the thin PS film dewets the glass coverslip surface because of its own surface tension and low interfacial energy. The pull-off force maps indicate a dramatic change in the adhesion upon replacement of water with ethanol: the adhesion force drops almost by two orders of magnitude and, under ethanol, becomes buried in the noise (the pull-off force noise level is approximately 20 pN). The stiffness-related images do not show the same dramatic changes upon changing the medium (Figs 7c and 7d). Furthermore, the contrast in the stiffness-related slope seems to be reversed: a higher stiffness is apparently found in the PS regions than in the glass coverslip. We are currently investigating several possible causes for this contrast reversal.

## 4. CONCLUSION

In this paper we have presented the design of a combined topography–adhesion–stiffness imaging mode in a scanning force microscope (SFM) based on a digital control system. The digital control system enabled us to define the shape of the loading–unloading force waveform and to achieve a fast rate (up to 1 kHz) of applying the loading–unloading waveform with a pre-defined maximum loading force. Furthermore, we achieved better flexibility in optimizing imaging conditions and analyzing the resulting force–displacement data. The limiting factor in the data acquisition speed appears to be the viscous drag of the working medium exerted onto the SFM cantilever. We showed that subtracting the no-contact, zero-deflection baseline could compensate for the effects of the viscous drag. The performance of the digital adhesion mapping control system was illustrated by analyzing several different samples: a rigid silicon grid, a molecularly thin block copolymer film, and a thin heterogeneous polymer film. The remaining problems that are currently under investigation are related to the cross-talk between the topography and the stiffness-related slope.

### Acknowledgements

This work was supported, in part, by NIH NHBLI grant HL44538 and by the Center for Biopolymers at Interfaces. We acknowledge the help in designing the control board provided by Dr. L. P. Sadwick.

## REFERENCES

1. P. K. Hansma, V. B. Elings, O. Marti and C. E. Bracker, *Science* **242**, 209–216 (1988).
2. D. Sarid, *Scanning Force Microscopy with Applications to Electric, Magnetic and Atomic Forces*. Oxford University Press, New York (1991).
3. R. Weisendanger, *Scanning Probe Microscopy and Spectroscopy*. Cambridge University Press, Cambridge (1994).
4. H. Takano, J. R. Kenseth, S.-S. Wong, J. C. O'Brien and M. D. Porter, *Chem. Rev.* **99**, 2845–2890 (1999).
5. M. Firtel and T. J. Beveridge, *Micron* **26**, 347–362 (1995).
6. C. A. Siedlecki, B. Lestini, K. Marchant-Kottke, S. Eppell, D. L. Wilson and R. E. Marchant, *Blood* **88**, 2939–2950 (1996).
7. R. Lal, *Scanning Microsc. Suppl.* **10**, 81–95 (1996).
8. H. G. Hansma, K. J. Kim, D. E. Laney, R. A. Garcia, M. Argaman, M. J. Allen and S. M. Parsons, *J. Struct. Biol.* **119**, 99–108 (1997).
9. E. A-Hassan, W. F. Heinz, M. D. Antonik, N. P. D'Costa, S. Nagaswaran, C.-A. Schoenenberger and J. H. Hoh, *Biophys. J.* **74**, 1564–1578 (1998).
10. S. N. Maganov and D. Reneker, *Annu. Rev. Mater. Sci.* **27**, 175–186 (1997).
11. C. A. Siedlecki and R. E. Marchant, *Biomaterials* **19**, 441–454 (1998).
12. A. Linder, U. Weiland and H. J. Apell, *J. Struct. Biol.* **126**, 16–26 (1999).
13. W. F. Heinz and J. H. Hoh, *Trends Biotechnol.* **4**, 143–150 (1999).
14. B. Cappella, P. Baschieri, C. Frediani, P. Miccoli and C. Ascoli, *Nanotechnology* **8**, 82–87 (1997).
15. K. O. van der Werf, C. A. J. Putman, B. G. de Grooth and J. Greve, *Appl. Phys. Lett.* **65**, 1195–1197 (1994).
16. A. Rosa-Zeiser, E. Weilandt, S. Hild and O. Marti, *Measurement Sci. Technol.* **8**, 1333–1338 (1997).
17. K. L. Johnson, K. Kendall and A. D. Roberts, *Proc. R. Soc. London, Ser. A* **324**, 310–313 (1971).
18. G. Jogikalmath, J. K. Stuart, A. Pungor and V. Hlady, *Colloids Surfaces A* **154**, 53–64 (1999).
19. C. C. Dupont-Gillain, B. Nysten, V. Hlady and P. G. Rouxhet, *J. Colloid Interface Sci.* **220**, 163–169 (2000).
20. B. Bhushan, in: *Handbook of Micro/Nanotribology*, 2nd edn, B. Bhushan (Ed.), pp. 3–80. CRC Press, Boca Raton, FL (1997).
21. J. Israelachvili, *Intermolecular and Surface Forces*. Academic Press, London (1991).
22. N. A. Burnham and A. J. Kulik, in: *Handbook of Micro/Nanotribology*, 2nd edn, B. Bhushan (Ed.), pp. 247–271. CRC Press, Boca Raton, FL (1997).
23. J. H. Hoh and A. Engel, *Langmuir* **9**, 3310–3312 (1993).
24. E. W. Stroup, A. Pungor and V. Hlady, *Ultramicroscopy* **66**, 237–249 (1995).
25. V. Hlady, A. Pungor and E. W. Stroup, US Patent 5,700,953 (1996).
26. J. K. Stuart and V. Hlady, *Langmuir* **11**, 1368–1374 (1995).

## Mapping of adhesion forces on soil minerals in air and water by atomic force spectroscopy (AFS)

F. L. LEITE<sup>1,2</sup>, A. RIUL, JR.<sup>3</sup> and P. S. P. HERRMANN<sup>1,\*</sup>

<sup>1</sup> *EMBRAPA Agricultural Instrumentation, Rua XV de Novembro 1452, CEP 13560-970, São Carlos, São Paulo, Brazil*

<sup>2</sup> *Instituto de Física de São Carlos, Universidade de São Paulo (USP), CEP 13560-970, São Carlos, São Paulo, Brazil*

<sup>3</sup> *Departamento de Física, Biologia e Química, FCT - Universidade Estadual Paulista (UNESP), CEP 19060-900, Presidente Prudente, São Paulo, Brazil*

**Abstract**—The adhesion force between an atomic force microscope (AFM) tip and sample surfaces, mica and quartz substrates, was measured in air and water. The force curves show that the adhesion has a strong dependence on both the surface roughness and the environmental conditions surrounding the sample. The variability of the adhesion force was examined in a series of measurements taken at the same point, as well as at different places on the sample surface. The adhesion maps obtained from the distribution of the measured forces indicated regions contaminated by either organic compounds or adsorbed water. Using simple mathematical expressions we could quantitatively predict the adhesion force behavior in both air and water. The experimental results are in good agreement with theoretical calculations, where the adhesion forces in air and water were mostly associated with capillary and van der Waals forces, respectively. A small long-range repulsive force is also observed in water due to the overlapping electrical double-layers formed on both the tip and sample surfaces.

**Keywords:** Atomic force spectroscopy; atomic force microscopy; adhesion forces; soil minerals.

### 1. INTRODUCTION

Atomic force microscopy [1] (AFM) is a powerful tool for the investigation of the surface morphology of polymers [2], biological materials [3], as well as in the study of magnetic [4], frictional [5] and adhesion forces [6–9] and surface charges [10] of solid materials. More recently, Atomic Force Spectroscopy (AFS) has been shown to be useful to measure the interaction force (e.g. adhesion force) and chemical properties of sample surfaces [11, 12]. Measurements of surface–surface

---

\*To whom correspondence should be addressed at EMBRAPA. Phone: (55-16) 274-2477. Fax: (55-16) 272-5958. E-mail: herrmann@cnpdia.embrapa.br

interactions at the nano-scale [13–15] are important because many materials have changed properties in this range [16–20]. Generally, in air the tip–sample surface interaction is a result of the superimposition of the van der Waals, electrostatic and capillary forces [11, 21]. On the other hand, two surfaces can interact in water through an electric double-layer, van der Waals and hydration forces [22].

Adsorbed water plays an important role in adhesion measurements, since it is responsible for the capillary force between the AFM tip and sample surface. In particular, with muscovite mica the adsorbed water is so strongly bound to the mica surface that it is impossible to remove it by simply ‘outgassing’ under UHV conditions or through a gentle heating of the sample [23]. Muscovite mica is ideal for studying a variety of surface phenomena since it is an aluminosilicate that can be easily cleaved yielding an atomically planar surface. It is well known that organic ions and simple compounds are picked up by clays (similarly to inorganic ions), and surface spectroscopy studies indicate the presence of carbon on the surface of air-cleaved mica [24]. The carbon is undoubtedly from organic origin, although there are evidences from surface reactivity with carbon dioxide [25]. Quartz, on the other hand, has a much rougher surface than mica, which is readily reflected in the force spectroscopy results.

The formation of a water film on the surface of materials, mainly on soil minerals, is an important feature because it is related to many physical, chemical and biological processes occurring in soils [26–28]. The investigation of capillary phenomenon by AFM represents a new way of characterizing the dynamics of aggregates. The tip/sample interaction in such different materials can be graphically represented by AFS [29, 30], which is used here to show how the adhesion (pull-off force) between the AFM tip and solid surfaces varies with both substrate morphology and the environment. Adhesion maps were used to illustrate sample regions that had been contaminated with organic compounds. This paper focuses on the importance of both the local curvature and contamination of the sample surface on adhesion measurements. In addition, we note that the force spectroscopy is a useful tool to observe the influence of repulsive forces acting in liquid media.

## 2. EXPERIMENTAL

Muscovite mica and quartz plates were used as samples. Mica can be easily cleaved in laboratory air to yield an atomically planar surface, as shown in Fig. 1 (surface roughness  $\approx 0.1$  nm). The mica used here was kindly donated by Dr. Jane Frommer from IBM Almaden Research Center (San Jose, CA, USA). This material is important for biological studies [30] and to investigate the fundamental principles of adhesion [31, 32], friction [33], vapor adsorption [34], contact angles [35], and surface forces involving gas, vapor and liquid systems [36, 37]. Quartz substrates were cleaned with a piranha solution as the surface cleaning agent, according to the experimental procedures described in Ref. [38].

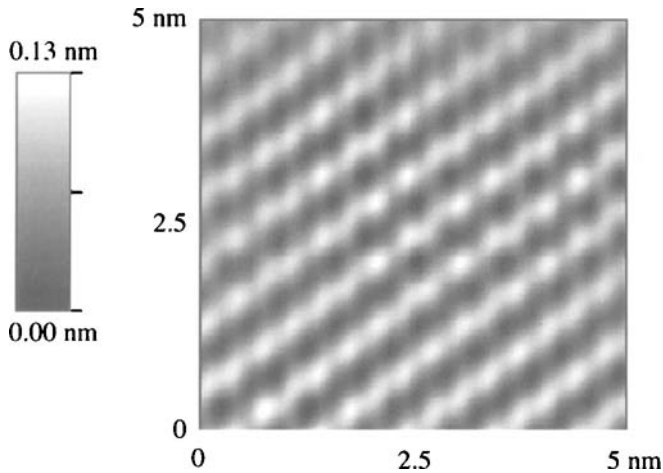


**Figure 1.** Topographic view, at the atomic level, of the mica muscovite surface showing the periodicity of the K atoms.

All measurements were carried out on a Topometrix TMX 2010 Discoverer Atomic Force Microscope, operating in contact mode. The cantilevers have a spring constant,  $k = 0.13 \pm 0.01$  N/m and tip curvature radius,  $R = 23 \pm 5$  nm. The values of length ( $L$ ), width ( $W$ ) and thickness ( $t$ ) of the cantilever and the tip radius (Fig. 2), were measured with a Philips model XL30-FEG Scanning Electron Microscope (SEM). The cantilever elastic constant was calculated using the following equation [39]:

$$k = EWt^3/4L^3, \quad (1)$$

where  $E$  (approx.  $7.3 \times 10^{10}$  N/m<sup>2</sup>) is the Young modulus of the cantilever material.

The piezoscanner is normally liable to display a behavior that departs from linearity between the force and the piezoscanner displacement. In order to check the accuracy of the measurements, subsidiary experiments were performed with a Topometrix standard grade silicon (Si) coated with quartz (average height: 24.0 nm and pitch: 15.0  $\mu$ m). The errors in length measurements were lower than those expected for the standard grade [40], being 2.5% and 0.1% for average height and pitch, respectively. The scanner used in the experiments has maximum scan ranges of 7  $\mu$ m in both  $x$  and  $y$  direction.

The force curves (cantilever deflection versus sample displacement) were obtained by measuring the vertical displacement of the sample — driven by the piezoscanner — and the deflection of the cantilever with respect to its position at rest. The curves were acquired in ambient conditions with  $47 \pm 3\%$  relative humidity and  $25 \pm 1^\circ\text{C}$  temperature. Adhesion forces were measured in Milli-Q<sup>®</sup> water with a special cell developed by Topometrix consisting of a glass support with two orifices for the inlet and outlet of liquids and an O-ring for sealing it. Force curves were digitally acquired at 100 points equally spaced from each other over the sample surface scanned area. Each force curve was comprised of a row of a maximum

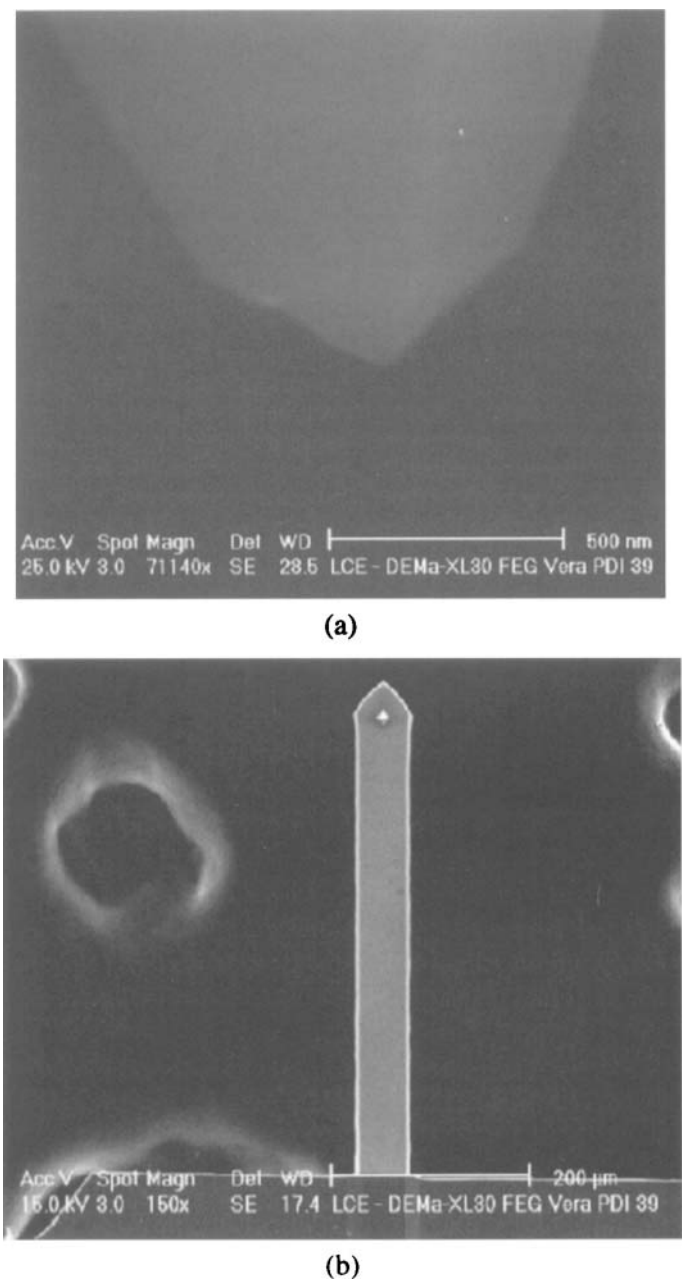


**Figure 2.** SEM micrographs of the silicon tip (a) and silicon cantilever (b) used.

250 data points acquired during the vertical movements of approach and retraction of the cantilever. Statistical software (StatSoft, 1999 version) was used to create the adhesion maps.

The adhesion forces on mica were examined by measuring the pull-off forces between the tip and the sample surface in the equipment calibration mode. All measurements were performed in both gas (air) and liquid (water) environments. The pull-off force detected at ambient conditions is comprised of both van der Waals and capillary forces. Since the effect from the capillary component is eliminated in water, the measured force in a liquid system is mainly attributed to the van der Waals interaction. Unfortunately, van der Waals forces are not the only forces in water. In the approach curve, just before the attractive van der Waals region, there is a repulsive force that raises the force curve over the zero line, which is the electric double-layer force, arising from charging of both sample and tip surfaces in liquids [41].

### 3. RESULTS AND DISCUSSION

Figure 3a shows typical force curves for mica in air. As the piezoscanner extends upward approaching the tip from 1 to 2, the tip is pulled down by the attractive force and jumps to contact with the surface at 2. As the piezoscanner continues to extend, the cantilever bends upward as the tip presses onto the surface. In this case, from 2 to 3, the slope of the force–distance curve provides information on the elasticity of the sample. When the tip reaches position 3, the piezoscanner retracts from the tip and the cantilever relaxes. As the sample continues to retract, the cantilever begins to bend downward, points 3 and 4, due to the adhesion force, until reaching the break point 4 at which the cantilever rebounds sharply upward to 5.

The adhesion force measured between points 4 and 5 can be expressed as:

$$F_{\text{adhes}} = k\delta_{\text{max}}, \quad (2)$$

where  $F_{\text{adhes}}$  is the adhesion force (nN),  $k$  and  $\delta_{\text{max}}$  are the elastic constant and the maximum deflection of the cantilever, respectively.

For mica (Fig. 3b), the force curves in water are similar to those in air, except that the noise in this case is much higher due to fluctuations in density and/or viscosity of the liquid and the piezoscanner approach speed [41]. This is indeed the reason why force curves cannot be obtained in some liquids. Besides, the adhesion force is much lower in a liquid, responsible for the behavior between points 4 and 5, as will be explained further.

Because the adhesion force is an important parameter for the surface properties of materials, we have investigated the accuracy of the measurements. Using equation (1) we estimated the adhesion forces from 30 measurements in air and water to be, respectively,  $30 \pm 3$  nN and  $12 \pm 1$  nN, showing that the environment has practically no effect on the data scatter. The 10% variation in the data obtained at the same point might be related to the fact that in 30 measurements the tip touches the sample surface at different points, within what we referred to as the critical variability radius,  $a_v$ . The definition of this critical variability radius is given in Fig. 4, where the dark circle below the tip corresponds to the tip–sample contact



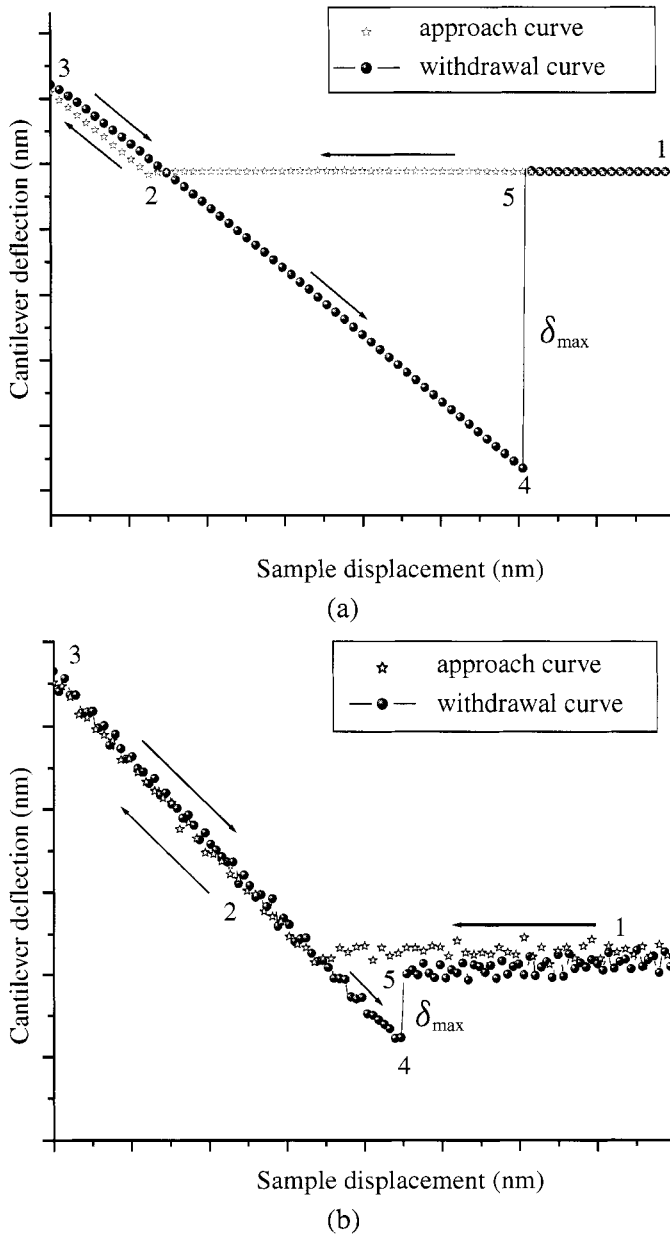


**Figure 3.** Typical force curves for mica in air (a) and in water (b).

area. The white circle corresponds to the maximum area of interaction between the tip and the sample surface ( $A_v = \pi a_v^2$ ) as the piezoscanner retracts and approaches in pull-off force measurements. This critical variability radius depends on the previous history of the piezoscanner (creep, non-linearity, hysteresis, age, etc.) and

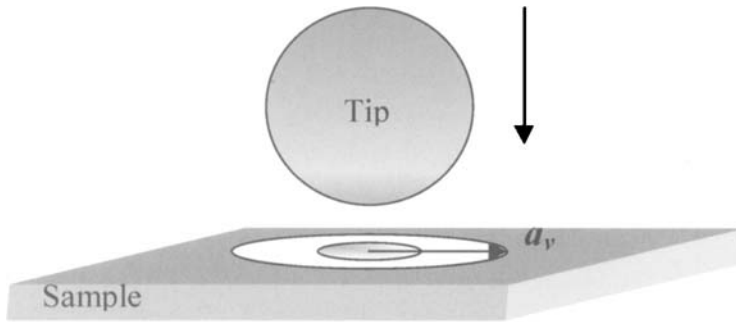


**Figure 4.** Critical variability radius,  $a_v$ , associated with the maximum variation of positioning of the piezoscanner in the measured force curves.

**Table 1.**

Average values of adhesion force to freshly cleaved mica in air and water and the variability associated with them

Points	Average value of the adhesion force $\bar{F}$ (nN)		Variability $\Delta \bar{F}$ (%)	
	Air	Water	Air	Water
1	$29 \pm 3$	$16 \pm 2$	10.3	12.5
2	$32 \pm 3$	$17 \pm 2$	9.4	11.8
3	$28 \pm 4$	$15 \pm 2$	14.3	13.3
4	$28 \pm 3$	$14 \pm 2$	10.7	14.2
5	$31 \pm 3$	$15 \pm 2$	9.7	13.3
Average value over 100 measurements	$25 \pm 4$	$12 \pm 2$	16.0	16.6

on the mechanical and electronic factors of the equipment such as vibration, thermal stability, feed-forward control and noise level (data not shown).

Figure 5a shows the topography of the muscovite mica freshly cleaved in air onto which force curve measurements were taken in five different regions. Figure 5b and 5c illustrates the corresponding adhesion map plots, in air and water, respectively. Each point represents 10 force curve measurements. In Fig. 5b and 5c the  $z$ -axis depicts the adhesion force magnitude while the  $xy$  plane corresponds to the sample surface. The variation in adhesion force,  $\bar{F}_{ad}$ , is given in Table 1, ranging from 9% to 14% depending on the region scanned during measurements in air or water. This confirms the statement in the previous paragraph that the environment has no significant effect on the adhesion variability. There is a 52% decrease in adhesion due to the meniscus removal, which is responsible for the capillary effect in the force curves in air. The adhesion shown in Fig. 5c is attributed mostly to van der Waals forces, while the capillary component dominates the adhesion forces in air (Fig. 5b).

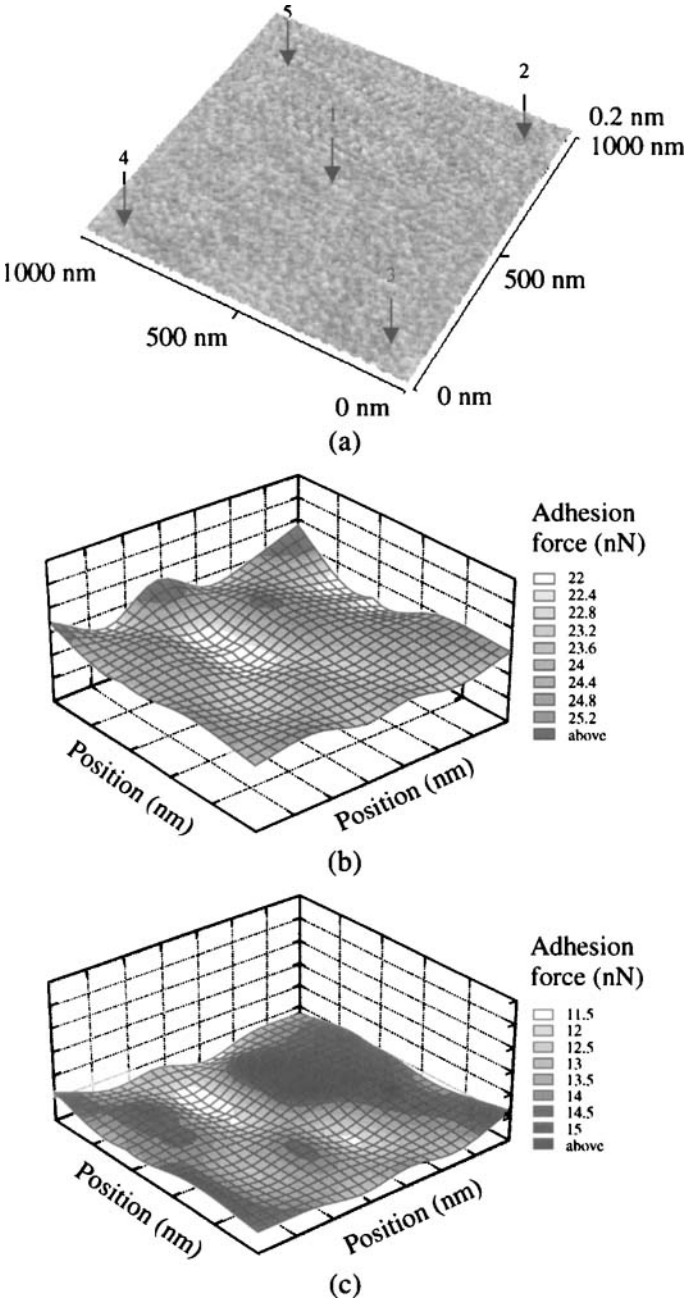
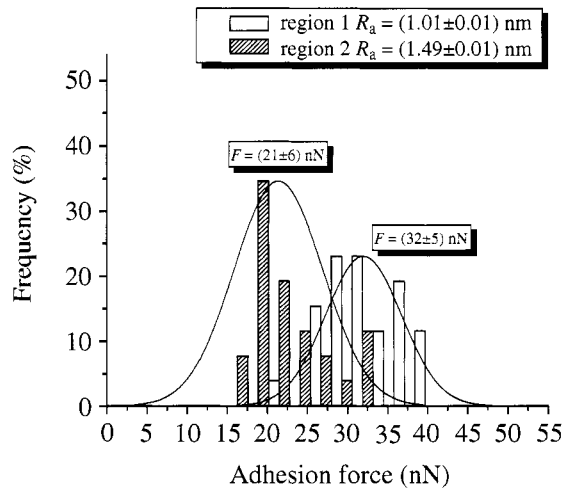
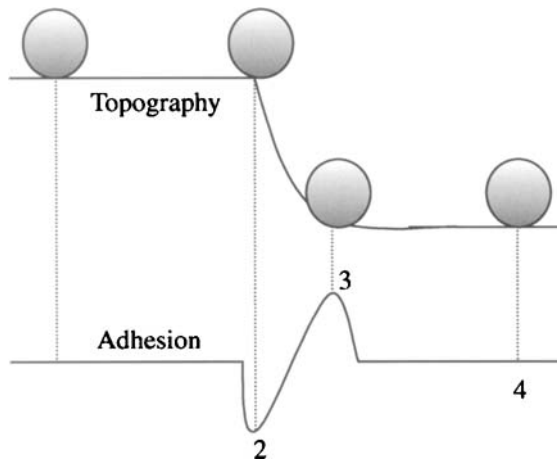


**Figure 5.** (a) Topographical image of the mica surface with a roughness of 0.1 nm. Adhesion map plots illustrating the variability of the adhesion forces onto mica in air (b) and water (c). The average adhesion forces were  $\bar{F} = (25 \pm 4)$  nN in air and  $\bar{F} = (12 \pm 1)$  nN in water. The black regions correspond to values up to 30% above the average adhesion.



(a)



(b)

**Figure 6.** (a) Histogram illustrating how the adhesion to quartz varies. (b) Schematic diagram showing the interaction between the AFM tip and the sample surface, and its influence on the magnitude of the measured adhesion force (adapted from Ref. [50]).

In order to confirm the importance of surface roughness, adhesion forces were measured on quartz samples, which had a higher surface roughness ( $\geq 1 \text{ nm}$ ) for a scanned area of  $1 \mu\text{m}^2$ . Such high value compared with that on mica leads to a larger variation in the adhesion force as the area is scanned, as shown in Fig. 6a. The adhesion force varied within 16% on smoother regions and 29% on rougher areas. The increased adhesion in smoother areas is consistent with the literature [42–45] as the surface properties at the nano-scale level, such as adhesion, are strongly influenced by the topography of the sample surface. Moreover, even a small surface roughness decreases significantly the adhesion force [46].

A commonly used representation of the tip/sample surface system is to consider the tip as a sphere of radius  $R$  and the sample surface as a plane [47, 48], as it was considered here. Figure 6b shows how the sample topography influences the adhesion force. The maximum adhesion force is reached when the tip is in region 3 where there is a larger contact area than those in regions 1 and 4, since a large part of the tip is in contact with the sample surface. The minimum adhesion force is measured in region 2 where the contact area is reduced and the effective bending is minimum. Therefore, adhesion maps are able to reveal differences in the topography of the samples. Willing *et al.* [49] studied adhesion based on the use of a colloidal probe in conjunction with the force-volume technique, where the spatial variation of the adhesion was visualized by analyzing the force-volume data with a software to create adhesion area maps.

Figure 7 shows three adhesion maps acquired in different regions of mica after 2 h of air exposure with constant humidity. The adhesion map in region A (Fig. 7a) indicates a decrease of approximately 33% in the adhesion force. The difference in roughness between regions A, B (Fig. 7b) and C (Fig. 7c) is small and, therefore, the maximum deviation in the adhesion force due to roughness should be smaller than 17% (regional variability, Table 1) for a mica sample. Thus, the 33% decrease in region A is assumed to arise from organic contamination, since the mica becomes hydrophobic after air exposure [50, 51]. The observed differences in force-curve measurements have been attributed to the adsorbed layer formed on mica surfaces cleaved in laboratory air. This adsorbed layer has often been referred to as 'organic', because of the presence of organic carbon detected by surface spectroscopic techniques such as SSIMS [52] and XPS [53]. The thickness and composition of this adsorbed layer on mica will vary depending on the laboratory atmosphere and the experimental procedures used.

The adhesion force is influenced by the sample conditions. Considering that part of this force is caused by adsorbed water, it is important to clarify the contamination effect in the pull-off force measurements. The presence of an organic contaminant layer onto a solid surface changes the contact angle, thus influencing the adsorption of a water layer over the sample surface. Consequently, changes in adhesion will be observed. The adhesion maps will show how the spatial variations of the sample–tip interactions depend on the surface conditions.

The regions B and C illustrated in Fig. 7, have a thin water layer, as will be shown later. The capillary force is given by [54]:

$$F_{\text{cap}}^{\text{air}} = 2\pi R\gamma_{\text{LV}}(\cos \theta_1 + \cos \theta_2), \quad (3)$$

where  $\gamma_{\text{LV}}$  is the liquid–vapor interfacial free energy,  $R$  is the radius of the AFM tip and  $\theta_1$  and  $\theta_2$  are the contact angles of water for the mica surface and the tip, respectively. For freshly cleaved mica, the water contact angle is  $\approx 0^\circ$  and for oxidized silicon tip (exposed to air) the contact angle is  $\approx 79^\circ$  (data not shown). Contact angle measurements were made with an optical microscope with a digital camera by measuring the angle between the surface and the tangent drawn on the

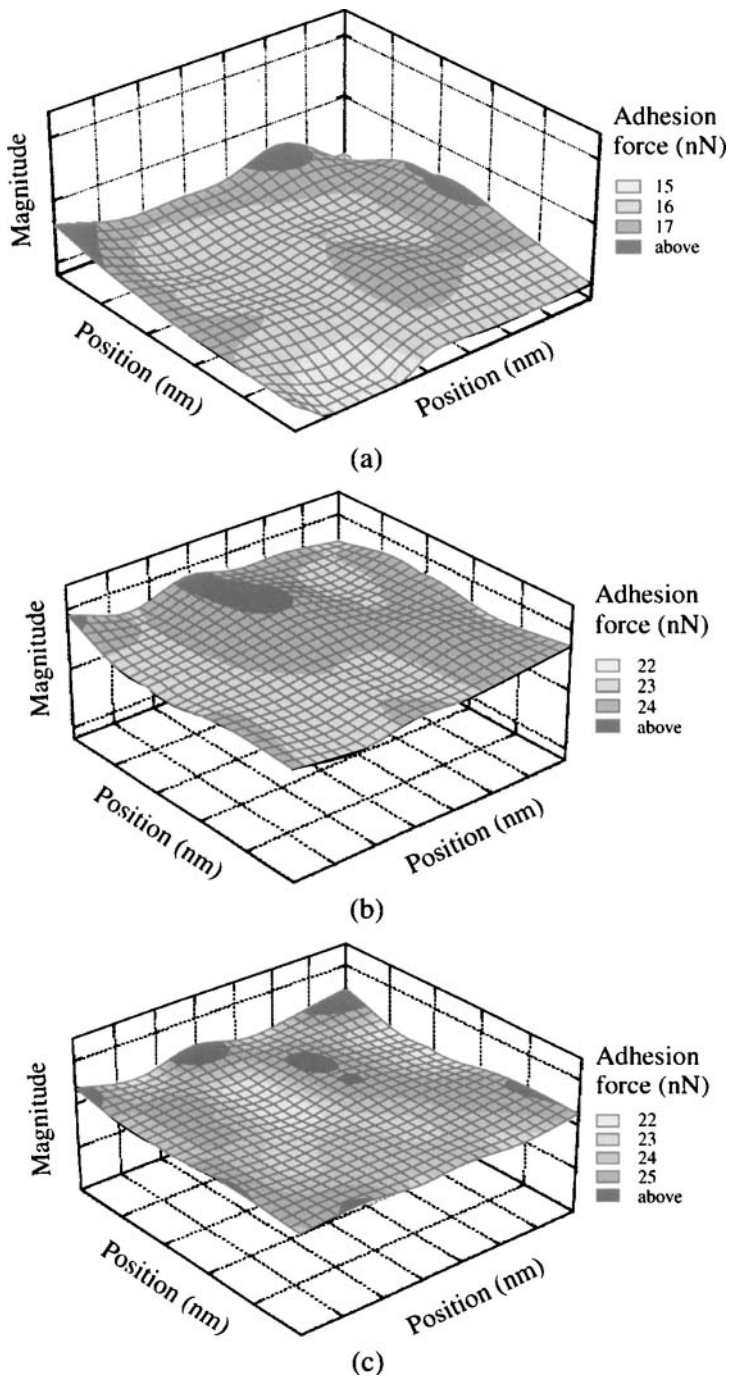


**Figure 7.** Adhesion maps onto mica: (a) region A ( $R = 1.3 \text{ \AA}$ ;  $\bar{F} = (16 \pm 3) \text{ nN}$ ), (b) region B ( $R = 1.1 \text{ \AA}$ ;  $\bar{F} = (23 \pm 3) \text{ nN}$ ); and (c) region C ( $R = 1.1 \text{ \AA}$ ;  $\bar{F} = (24 \pm 4) \text{ nN}$ ). Each adhesion map corresponds to a scanning area of  $1 \mu\text{m}^2$ . The black regions correspond to values up to 30% above the average adhesion.

water droplet image (five measurements were made on each surface of mica). The surface free energy of the adsorbed water layer is  $\gamma_v = 72.0 \text{ mJ/m}^2$ .

The resultant capillary adhesion force due to the presence of adsorbed water is  $15 \pm 3 \text{ nN}$ , from equation (3), with an estimated scatter of 20% due to errors in the measurements of contact angle and radius of curvature of the tip. This theoretical value is lower than that in Fig. 7 for regions B and C, because the contribution from van der Waals forces ( $F_{\text{vdW}}$ ) to adhesion was not taken into account in the theoretical calculation. The equation that relates the van der Waals forces (contact adhesion in the condensate,  $F_{\text{vdW}}$ ) and capillary forces is given by [32]:

$$F_{\text{adhes}}^{\text{air}} = 2\pi R\gamma_v(\cos\theta_1 + \cos\theta_2) + F_{\text{vdW}}, \quad (4)$$

where the second term on the right-hand side of equation (4) is the contact adhesion from the van der Waals forces [55]. One may eliminate capillary forces by measuring adhesion with both sample and AFM tip in the water, allowing one to estimate the contribution from the van der Waals forces only.

The force measured on the AFM cantilever in a liquid environment can be estimated using the Derjaguin–Muller–Toporov (DMT) [56] theory as:

$$F_{\text{vdW}}^{\text{water}} = 2\pi R\varpi_{132}, \quad (5)$$

where  $R$  is the AFM tip radius and  $\varpi_{132}$  is the work of adhesion per unit area between the AFM Si tip (subscript 2) and the sample surface (subscript 1) in a liquid environment (subscript 3). The DMT equation applies to rigid systems with low adhesion and small radii of curvature, but it can underestimate the true contact area. Equation (5) is correct for a spherical tip in contact with a planar surface, valid for long-ranged attraction around the periphery of the contact area, with the tip–sample geometry being constrained to remain Hertzian [57]. In other words, the DMT theory is the Hertzian theory with an offset due to surface forces, and no hysteresis between loading and unloading. However, Beach *et al.* [58] showed that the pull-off forces were not very sensitive to the maximum applied load suggesting that the use of continuum elastic contact mechanics in the analysis of measured force curves was not as straightforward as usually assumed in the literature. In our case, the work of adhesion (Si tip–water–mica) is  $\varpi_{132} = 0.11 \text{ J/m}^2$ , resulting in an adhesion force of  $16 \pm 2 \text{ nN}$  in water. From equation (4) it is possible to obtain the theoretical value of the adhesion force in air on freshly cleaved mica, which is  $31 \pm 5 \text{ nN}$ . The adhesion force results in air presented in Fig. 7b and 7c,  $F_{\text{adhes}} = 23 \pm 3$  and  $F_{\text{adhes}} = 24 \pm 4 \text{ nN}$ , respectively, demonstrate that the experimental data are consistent with the calculated values.

In order to separate the adhesion force fractions from each other, the pull-off forces were measured under two conditions in the same experimental assembly. Figure 8 shows a comparative plot between theoretical and experimental results in air and water. Histogram A shows a good agreement between the experimental pull-off forces in air and the theoretical results using equation (4), with the differences within the expected variation. This histogram represents the sum of the capillary

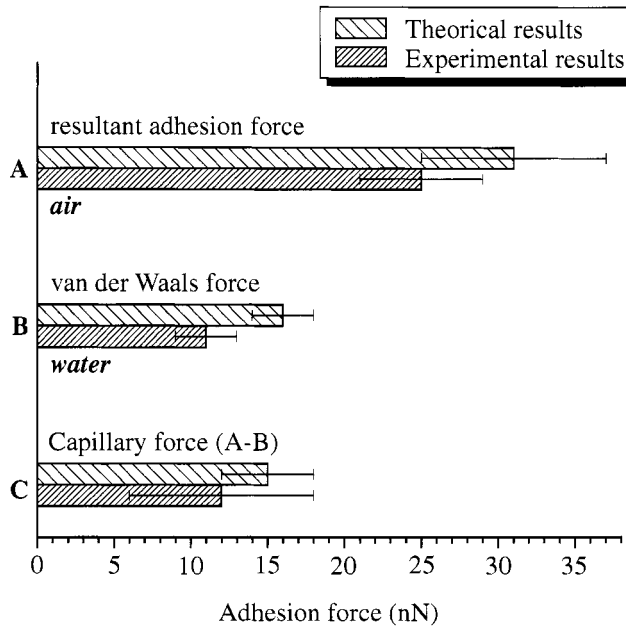


**Figure 8.** Histogram illustrating the theoretical and experimental variations of the adhesion force components in air and water.

and van der Waals interaction forces, i.e.  $F_{\text{adhes}}^{\text{air}} = F_{\text{cap}} + F_{\text{vdW}}$ . Histogram B shows the experimental and theoretical (equation (5)) results in water. It can be seen that the error bars do not overlap, indicating that the differences are no more than the 22% estimated error, confirming the existence of the repulsive force due to double layer. This histogram represents the adhesion effect caused mainly by the van der Waals interaction between the tip and the sample, i.e.  $F_{\text{adhes}}^{\text{water}} = F_{\text{vdW}}$ . Histogram C shows the capillary force component obtained from equation (3) and the difference between the experimental pull-off forces in air and water, i.e.  $F_{\text{adhes}}^{\text{air}} - F_{\text{adhes}}^{\text{water}} = F_{\text{cap}}$ .

The difference between the theoretical ( $16 \pm 2$  nN) and experimental ( $12 \pm 1$  nN) values for water, presented in Histogram B, comes from the repulsive forces between the tip and the mica surface. When immersed in a polar liquid medium like water, surface charges are induced on both the tip and the sample surface due to ionization, dissociation or spontaneous adsorption of charged species. To keep the electrical neutrality, opposite ionic species are held together closer to the tip/sample surface forming an electric double-layer. When mica is placed in water, the mechanism of the double-layer formation is attributed to the  $\text{K}^+$  dissolution, as well as ionic exchange between  $\text{K}^+$  and  $\text{H}_3\text{O}^+$  (or  $\text{H}^+$ ) [59]. The existence of the electrical double-layer is confirmed by the force curves, as shown in Fig. 9, where an upward trend appears before the attractive van der Waals interaction. Toikka *et al.* [60] showed that the double layer decreases the adhesion force, and that the apparent adhesion force depends on the pH of the solution. The authors confirmed



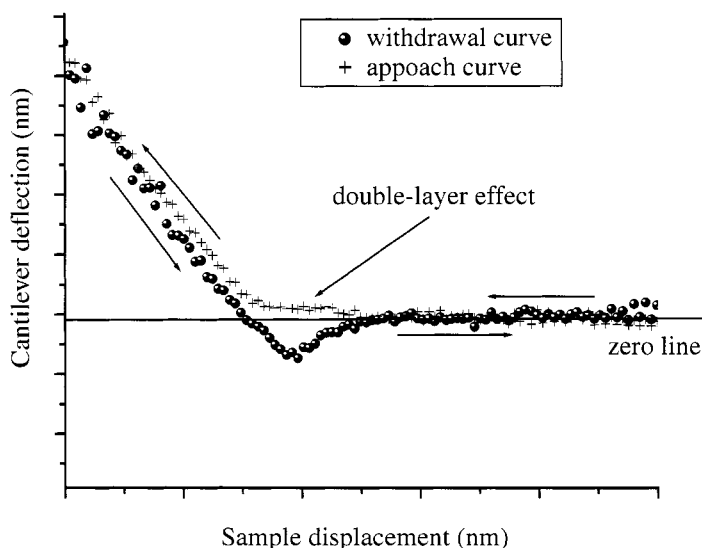


**Figure 9.** Typical force curve for mica under water. The upward trend pointed in the figure is indicative of the double-layer effect. The zero line represents that part the force curve in which the tip exerts no force on the sample, i.e. when the tip and sample are far apart, and the tip does not deflect.

the existence of this phenomenon by measuring adhesion forces in different pH solutions between an iron sample and silica colloidal probe.

The interaction between electric double-layers from different surfaces may be either attractive or repulsive, having different magnitudes, depending on the surface-charge properties of the tip and sample materials, concentration of ionic constituents, ionic strength, pH, and temperature. The effects of the electric double-layer forces on adhesion force measurements are only now beginning to be explored [60], and the results presented here might provide a better understanding on soil mineral interactions.

Adhesion maps obtained from force spectroscopy have shown clearly how surface contamination, roughness and the environmental conditions influence the adhesion forces. Little attention, however, is paid to the use of AFS for application in agricultural and colloidal science.

#### 4. CONCLUSIONS

The force curves obtained on some soil mineral particles (mica and quartz) show clearly that the adhesion force is sensitive to both the surface roughness and the environmental conditions.

The magnitude of adhesion depends on the roughness and local curvature of the sample surface, with a slight increase in the adhesion force in smoother regions. We have shown that adhesion forces estimated from several measurements taken at the

same place on the sample surface vary within 13% on mica and 29% on the much rougher quartz substrate.

The scatter in the measured curvature radius and elastic constant of the tip provides an error source to the adhesion force of typically 20% and 8%, respectively.

The adhesion maps made from hundreds of measurements at different points allow one to obtain information on heterogeneities in sample topography and on organic contamination. For example, carbon contamination on mica, possibly from human contact or carbon dioxide from air, affects the force curves. This was corroborated by the good agreement between the theoretical and experimental adhesion values obtained in both air and water. With the adhesion maps for samples in air and in water, a distinction can be made between capillary and van der Waals components of the adhesion force.

### Acknowledgements

The authors are grateful to CNPq, the nanobiotechnology network (CNPq/MCT) for the financial support and to Prof. Osvaldo N. Oliveira, Jr. for useful discussions and revision of this manuscript.

### REFERENCES

1. G. Binnig, C. F. Quate and Ch. Gerber, *Phys. Rev. Lett.* **56**, 930–933 (1986).
2. R. F. Lobo, M. A. Pereira-da-Silva, M. Raposo, R. M. Faria and O. N. Oliveira, Jr., *Nanotechnology* **14**, 101–108 (2003).
3. I. Penegar, C. Toque, S. D. A. Connell, J. R. Smith and S. A. Campbell, in: *Proceedings of the 10th International Congress on Marine Biofouling*, Melbourne, Australia (1999).
4. Y. Martin and H. K. Wickramasinghe, *Appl. Phys. Lett.* **50**, 1455–1457 (1987).
5. R. Erlandsson, G. Hadziioannou, C. M. Mate, G. M. McClelland and S. Chiang, *J. Chem. Phys.* **89**, 5190–5193 (1988).
6. C. Jacquot and J. Takadoum, *J. Adhesion Sci. Technol.* **15**, 681–687 (2001).
7. H. K. Christenson and P. M. Claesson, *Adv. Colloid Interface* **91**, 391–436 (2001).
8. L. H. G. Segeren, B. Siebum, F. G. Karssenberg, J. W. A. van den Berg and G. J. Vancso, *J. Adhesion Sci. Technol.* **16**, 793–828 (2002).
9. A. Ata, Y. Rabinovich and R. K. Singh, *J. Adhesion Sci. Technol.* **16**, 337–346 (2002).
10. C. Schonenberger and S. F. Alvarado, *Phys. Rev. Lett.* **65**, 3162–3164 (1990).
11. L. Sirghi, N. Nakagiri, K. Sugisaki, H. Sugimura and O. Takai, *Langmuir* **16**, 7796–7800 (2000).
12. A. Mendez-Vilas, M. L. Gonzalez-Martin, L. Labajos-Broncano and M. J. Nuevo, *J. Adhesion Sci. Technol.* **16**, 1737–1747 (2002).
13. S. Fujisawa, E. Kishi, Y. Sugawara and S. Morita, *Phys. Rev. B* **51**, 7849–7857 (1995).
14. D. M. Taylor, *Thin Solid Films* **331**, 1–7 (1998).
15. A. Torii, M. Sasaki, K. Hane and S. Okuma, *Sensors Actuators A Phys.* **40**, 71–76 (1994).
16. R. Garcia and R. Pérez, *Surf. Sci. Rep.* **47**, 197–301 (2002).
17. M. Binggeli and C. M. Mate, *J. Vac. Sci. Technol. B* **13**, 1312–1315 (1995).
18. M. Scherge, X. Li and J. A. Schaefer, *Tribol. Lett.* **6**, 215–220 (1999).
19. Q. Ouyang, K. Ishida and K. Okada, *Appl. Surf. Sci.* **169**, 644–648 (2001).
20. H. A. Mizes, K.-G. Loh, R. J. D. Miller, S. K. Ahuja and E. F. Grabowski, *Appl. Phys. Lett.* **59**, 2901–2903 (1991).

21. F. Mugele, T. Becker, R. Nikopoulos, M. Kohonen and S. Herminghaus, *J. Adhesion Sci. Technol.* **16**, 951–954 (2002).
22. L. Sirghi, N. Nakagiri, H. Sugimura and O. Takai, *Jpn. J. Appl. Phys.* **40**, 1420–1424 (2001).
23. H. K. Christenson, *J. Phys. Chem.* **97**, 12034–12041 (1993).
24. K. G. Bhattacharyya, *J. Electron Spectrosc. Relat. Phenom.* **63**, 289–306 (1993).
25. K. G. Bhattacharyya, *Langmuir* **5**, 1155–1162 (1989).
26. G. E. Brown, Jr., A. L. Foster and J. D. Ostergren, *Proc. Natl. Acad. Sci. USA* **96**, 3388–3395 (1999).
27. D. R. Nielsen, J. W. Hopmans and K. Reichardt, *Scale Dependence and Scale Invariance in Hydrology*. Cambridge University Press, Cambridge (1988).
28. R. Wiesendanger, *Scanning Probe Microscopy and Spectroscopy — Methods and Applications*. Cambridge University Press, Cambridge (1994).
29. G. A. Willing and R. D. Neuman, *Langmuir* **18**, 8370–8374 (2002).
30. H. H. P. Fang, K.-Y. Chan and L.-C. Xu, *J. Microbiol. Methods* **40**, 89–97 (2000).
31. R. G. Horn, J. N. Israelachvili and F. J. Pribac, *J. Colloid Interface Sci.* **115**, 480–492 (1987).
32. H. K. Christenson, *J. Colloid Interface Sci.* **121**, 170–178 (1988).
33. A. M. Homola, J. N. Israelachvili, M. L. Gee and P. M. McGuiggan, *Trans. ASME J. Tribology* **111**, 675–682 (1989).
34. D. Beaglehole and H. K. Christenson, *J. Phys. Chem.* **96**, 3395–3403 (1992).
35. J. Schultz, K. Tsutsumi and J.-B. Donnet, *J. Colloid Interface Sci.* **59**, 272–276 (1977).
36. J. N. Israelachvili, *Intermolecular and Surface Forces*, 2nd edn. Academic Press, New York, NY (1991).
37. H. K. Christenson, *J. Dispersion Sci. Technol.* **9**, 171–206 (1988).
38. C. E. Borato, P. S. P. Herrmann, L. A. Colnago, O. N. Oliveira and L. H. C. Mattoso, *Braz. J. Chem. Eng.* **14**, 367–373 (1997).
39. D. Tabor, *Gases, Liquids and Solids and Other States of Matter*, 3rd edn. Cambridge University Press, Cambridge (1991).
40. AFM Standard-B, P/N 10-10299, Topometrix. Maximum Deviation: average height = 8%; pitch = 2.5% (standard grade).
41. B. Cappella, P. Baschieri, C. Frediani, P. Miccoli and C. Ascoli, *IEEE Eng. Med. Biol.* **16**, 58–65 (1997).
42. T. Stifter, E. Weilandt, O. Marti and S. Hild, *Appl. Phys. A* **66**, S597–S605 (1998).
43. K. L. Johnson, *Tribology Int.* **31**, 413–418 (1998).
44. R. Jones, H. M. Pollock, J. A. S. Cleaver and C. S. Hodges, *Langmuir* **18**, 8045–8055 (2002).
45. E. R. Beach, G. W. Tormoen, J. Drelich and R. Han, *J. Colloid Interface Sci.* **247**, 84–89 (2002).
46. K. N. G. Fuller and D. Tabor, *Proc. R. Soc. London A* **345**, 327–342 (1975).
47. J. N. Israelachvili, *Surf. Sci. Rep.* **14**, 109–159 (1992).
48. T. Stifter, O. Marti and B. Bhushan, *Phys. Rev. B* **62**, 13667–13673 (2000).
49. G. A. Willing, T. H. Ibrahim, F. M. Etzler and R. D. Neuman, *J. Colloid Interface Sci.* **226**, 185–188 (2000).
50. B. Cappella and G. Dietler, *Surf. Sci. Rep.* **34**, 1–104 (1999).
51. J. Hu, X.-D. Xiao, D. F. Ogletree and M. Salmeron, *Surf. Sci.* **344**, 221–236 (1995).
52. M. G. Dowsett, R. M. King and E. H. C. Parker, *J. Vac. Sci. Technol.* **14**, 711–717 (1977).
53. L. Xu and M. Salmeron, *Langmuir* **14**, 5841–5844 (1998).
54. Y. Ando, *Wear* **238**, 12–19 (2000).
55. T. Eastman and D. M. Zhu, *Langmuir* **12**, 2859–2862 (1996).
56. B. V. Derjaguin, V. M. Muller and Yu. P. Toporov, *J. Colloid Interf. Sci.* **53**, 314–326 (1975).
57. J. Hertz, *Reine Angew. Math.* **92**, 156–171 (1881).
58. E. R. Beach, G. W. Tormoen and J. Drelich, *J. Adhesion Sci. Technol.* **16**, 845–868 (2002).
59. E. F. Souza, G. Ceotto and O. Teschke, *J. Mol. Catal. A* **167**, 235–243 (2001).
60. G. Toikka, R. A. Hayes and J. Ralston, *Langmuir* **12**, 3783–3788 (1996).

## The investigation of sized cellulose surfaces with scanning probe microscopy techniques

L. E. DICKSON<sup>1</sup> and J. C. BERG<sup>2,\*</sup>

<sup>1</sup> *Amgen, Inc., One Amgen Drive, Thousand Oaks, CA 91320, USA*

<sup>2</sup> *Department of Chemical Engineering, University of Washington, Seattle, WA 98195-1750, USA*

**Abstract**—Scanning probe microscopy techniques of lateral force microscopy, pull-off force measurement, and pulsed force mode adhesion imaging were employed to study the micro-scale surface chemistry of cellulose films hydrophobized by treatment with alkenyl succinic anhydride (ASA). Lateral force microscopy showed a monotonic decrease in surface frictional dissipation with increasing sizing level. The distributions of pull-off forces measured over a  $(1\ \mu\text{m})^2$  area showed a wide range of local adhesion values on all samples, yet disappearance of the highest adhesion sites with increasing level of sizing agent. The pulsed force mode results showed high-resolution adhesion images of cellulose that complemented the pull-off force distribution results. These results indicate that scanning probe microscopy techniques are able to detect the wettability heterogeneity of ASA-sized cellulose with nanometer resolution.

**Keywords:** Atomic force microscopy (AFM); hydrophobically modified cellulose; alkenyl succinic anhydride (ASA); sizing; wettability; adhesion.

### 1. INTRODUCTION

Fine printing technologies such as offset printing involve the transfer of small ink dots, of the order of 10–50  $\mu\text{m}$  in diameter, to a paper surface. Internal sizing agents, added to paper to impart resistance to liquid penetration, have a tremendous impact on the paper printability. While the surface topography of paper can be measured on the 10–50  $\mu\text{m}$  length scale, surface chemistry is measured by methods (such as the contact angle or penetration tests) which sample an area 10–100 times larger. In order to understand the relevance of micro-scale surface chemistry of a sheet to its final print quality, the measurement must be done on the micro-scale. Scanning probe microscopy (SPM) techniques are unique in their ability

---

\*To whom correspondence should be addressed. Phone: (206) 543-2029. Fax: (206) 543-3778.  
E-mail: berg@cheme.washington.edu

to measure topography, adhesion, friction, and other material properties of surfaces under ambient conditions on this length scale.

Scanning probe microscopes are a family of instruments for surface analysis that measure the force of interaction between a probe tip and a surface of interest, creating an areal map of surface properties from the atomic to micrometer level. Their advantages include the ability to ‘image’ surfaces in 3D, flexibility of the operating environment (ambient, liquid, vacuum), and the unprecedented ability to profile forces with pico-Newton resolution in a spatially resolved way. The atomic force microscope (AFM), invented in 1986 by Binnig, Quate, and Gerber, measures the forces experienced by the probe tip via the deflection of the flexible cantilever to which it is mounted [1]. The AFM provides unprecedented surface profilometry capability and measurement of nano-scale surface properties not measurable by any other technique. These capabilities make it an ideal tool for exploring the surface chemistry heterogeneity and micro-scale wettability of sized cellulose under ambient conditions.

### *1.1. Internal sizing — impact on wettability*

By means of physical or chemical interactions between their hydrophilic ends and the hydrophilic paper fiber surfaces, amphipathic sizing agents impart hydrophobicity by orienting their lipophilic tails away from the paper fiber surface, creating a low-energy surface which slows down wicking [2]. Synthetic ‘reactive’ sizing agents such as alkyl ketene dimer (AKD) or alkenyl succinic anhydride (ASA) chemisorb to the paper surface, forming stable chemical bonds. A homogeneous distribution of the sizing agent throughout the body of the sheet is imperative for consistency, but inter-fiber hydrogen bonding cannot be disrupted. For this reason, the sizing chemical used must have an appropriate balance between hydrophilic and lipophilic characters, and the sizing coverage should be uniformly distributed over the cellulose paper fiber surfaces. Despite the intuitiveness of these heuristics, the coverage and uniformity of these materials and the mechanism by which they alter wettability are generally not known.

It is widely known that ASA serves to hydrophobize the otherwise very hydrophilic cellulose surface of paper. The paper’s wettability — the tendency of a high surface tension liquid (such as water) to spread along the solid surface — is drastically altered by small adsorbed amounts of sizing agent. Recently, the wettability of highly sized pulp has been studied by dynamic contact angle measurements on single fibers [3]. The results indicated a direct correlation between sizing level and contact angle hysteresis (difference between the advancing and receding contact angles). In fact, cellulose filaments and unsized pulp fibers exhibit contact angle hysteresis even without the presence of a sizing agent [3–5]. Non-zero contact angle hysteresis constitutes a significant deviation from thermodynamic equilibrium and suggests surface chemical heterogeneity (generally, the advancing angle samples low-energy surface sites and the receding angle samples high-energy sites [6]). Although traditional wettability measurement techniques show extreme sensitivity

to low levels of adsorbed species at surfaces, they cannot elucidate the spatial distribution of these materials.

### 1.2. Scanning probe microscopy (SPM) studies of paper

Atomic force microscopy (AFM) has been employed in the study of pulp, paper, and wood products, though primarily as a tool for high-resolution profilometry [7, 8]. The regular, crystalline structure of cellulose microfibrils isolated from algae was imaged by AFM by Baker *et al.* [9]. The surface and cross-sections of black spruce wood fibers [10] and Kraft pulp fibers [11] were imaged in contact-mode AFM in both air and liquid. Bassemir *et al.* highlighted the utility of SPM techniques in investigating the roughness and morphological features of surfaces affecting print quality for graphic artists [12]. These studies have dealt with heterogeneity of paper surfaces that can be visualized by topographic mapping, not heterogeneity that is merely chemical in nature.

An attempt to study the molecular orientation and surface coverage of alkyl ketene dimer on eucalyptus fibers with SPM techniques was made by Kuys *et al.* [13]. Pursuing XPS and contact angle hysteresis data proposing a heterogeneous distribution of AKD on fiber surfaces, Kuys *et al.* sought to locate the expected hydrophobic and hydrophilic regions via lateral force microscopy (LFM) imaging and pull-off force measurements. Topography overshadowed any frictional differences in their lateral force results. A few pull-off force measurements were taken indicating some degree of surface energy heterogeneity, but no spatially resolved information about surface energy or hydrophilicity was obtained. Kuys *et al.* felt that there was considerable scope to continue the work with a model substrate (such as a cellulose film) to remove the topographic effects confounding the lateral force results.

Irvine *et al.* measured the adhesion energy distributions of sized and unsized papers via pull-off force measurements of local adhesion [14]. The force required to remove a 19  $\mu\text{m}$  polystyrene sphere (mounted onto the end of a cantilever) from the surface of paper sized with ASA between 0 and 5 lb/ton (0.515 g/kg) was recorded as a function of the position at 25 locations over a  $(100\ \mu\text{m})^2$  area. The results showed a wide distribution of local adhesion energies on all samples, but an increase in the preponderance of low local energies and a progressive elimination of the highest-energy sites with increasing sizing levels were observed. These promising results spurred the desire to obtain local adhesion data with an even greater lateral resolution and to verify that the measured adhesion was indeed chemical in nature and not dominated by surface topography.

### 1.3. Lateral force microscopy (LFM)

In LFM, a quad-cell position-sensitive photodetector monitors both the vertical and the torsional displacements of the cantilever as it is rastered back and forth across the surface, allowing simultaneous collection of topography and lateral force information [15]. The torsion, or twisting, of the cantilever arises from the lateral

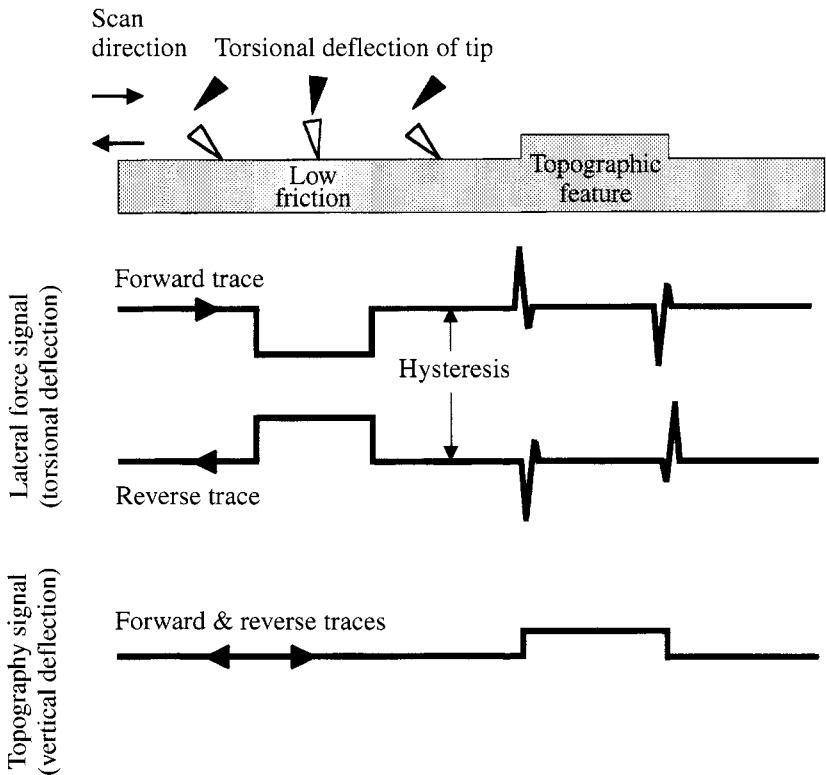


**Figure 1.** Diagram of the lateral force and topography signals for a cantilever tip interacting with a surface in the forward and reverse scan directions. On the left (top), a low-friction region is surrounded by a high friction material. On the right, a topographic feature impacts the lateral force signal.

forces experienced by the tip–sample contact during imaging and is influenced by surface friction, lubricity, adhesion, and capillary forces. The cantilever tip experiences lateral forces as it traverses changing slopes and edges in surface topography, so there is always a topographic element to LFM image contrast.

Whereas vertical deflection of the cantilever due to topography is the same irrespective of scan direction, the lateral force signal (torsional deflection) has the opposite sign in the forward and reverse scan directions (see Fig. 1 for an illustration). By subtracting the forward and reverse lateral force traces, a ‘lateral force hysteresis’ image is generated in which topographically induced signals are (roughly) cancelled out. As the magnitude of the lateral force hysteresis is proportional to the energy dissipation of the tip–surface contact, one would expect greater lateral force hysteresis on hydrophilic surfaces than hydrophobic ones, due to capillary forces exerted on the tip [16, 17].

#### 1.4. Pull-off force adhesion measurements

One of the great advantages of the atomic force microscope (AFM) is its ability to profile forces of interaction over very small areas. The cantilever tip can be used as a nanometer-scale adhesion tester by measuring the force required to remove it from intimate contact with a surface of interest. The Johnson–Kendall–Roberts (JKR) theory, developed from elastic contact theory, relates the pull-off force required to separate two bodies to the thermodynamic work of adhesion between them [18]. The pull-off force is thus proportional to local adhesion energy.

For pull-off measurements performed in air, the capillary forces exerted by adsorbed water complicate the interpretation of the pull-off force in terms of true surface energetics. When chemical heterogeneity influences the hydrophilicity of surfaces, adsorption of water on the surface will be affected and will alter the capillary force experienced by the AFM tip. We seek to exploit this feature of hydrophobically modified surfaces to monitor the micro-scale wettability of sized cellulose films. At present, pull-off forces must be measured at discrete points along the surface; therefore, adhesion information is obtained more slowly and with poorer spatial resolution than images of topography, etc. taken in standard SPM modes.

#### 1.5. Pulsed force mode

The need for the simultaneous acquisition of topography, adhesion, and compliance information was addressed by the development of ‘pulsed force mode’ (PFM) by Dr. Othmar Marti’s group in the Department of Experimental Physics, University of Ulm, Germany.<sup>1</sup> They developed an external controller and circuitry that could be added to a commercial AFM to perform these measurements simultaneously [19]. The cantilever is sinusoidally modulated at amplitudes from 10 to 500 nm and frequencies of 100 Hz to 5 kHz — well below the resonance frequency of commercial cantilevers. In the first cycle, the height of the surface is recorded. The cantilever then completes a force–distance profile by pressing the tip into contact with the sample and then reversing directions, causing a pull-off event. A ‘peak picker’ circuit allows the capture of the snap-in force, stiffness, maximum force (held constant at each point of measurement), and pull-off force at each point that the topography is known. In this way, only the pertinent information from the pull-off trace is stored, greatly increasing the acquisition rate and the number of samples that can be measured. A schematic diagram of the PFM’s modulated force–time (displacement) profile is shown in comparison with a standard pull-off force trace in Fig. 2. Because the tip is only in contact with the surface intermittently, the lateral resolution exceeds that of contact mode imaging.

In the present work, SPM techniques are employed to investigate the spatial wettability characteristics of a model cellulose film hydrophobized by treatment

---

<sup>1</sup> The PFM module is now available commercially from WITec GmbH, Ulm, Germany.



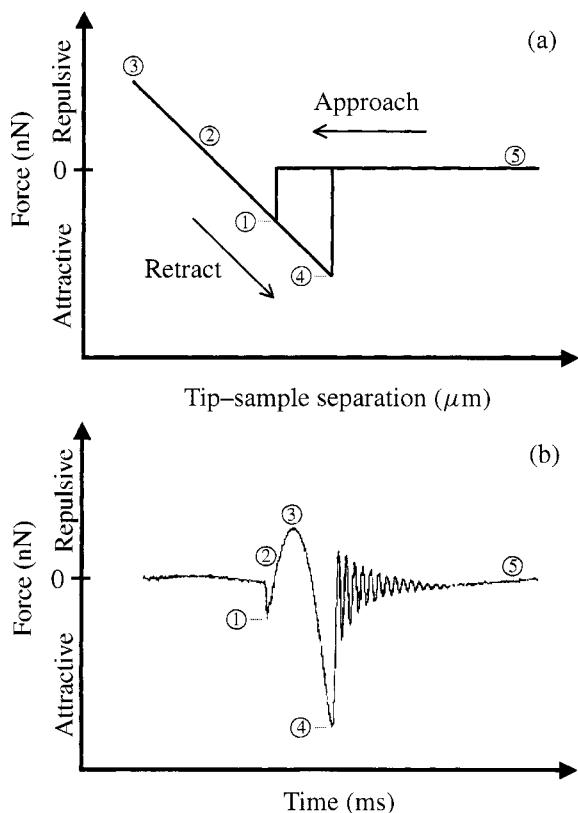


**Figure 2.** Comparison of (a) a standard force-displacement ( $z$ ) profile and (b) a pulsed force mode dynamic force-time profile, in which the displacement is varied over one cycle. Highlighted features of the curves correspond to (1) snap-in, (2) compliance or stiffness, (3) maximum applied force, (4) adhesion, and (5) zero net force baseline (where the tip and sample are out of contact).

with alkenyl succinic anhydride (ASA). The local variations in surface chemistry manifest themselves in surface friction and adhesion heterogeneity along the cellulose surfaces, so techniques specific to the monitoring of these properties are employed. LFM, pull-off force adhesion measurements, and PFM studies are carried out and the results compared with water contact angles measured on the same surfaces. By these measurements, we seek to understand the influence of ASA on the micro-scale chemistry of cellulose surfaces under ambient conditions.

## 2. MATERIALS AND METHODS

Regenerated cellulose films were prepared by deacetylation of cellulose acetate dip-cast films according to the procedure of Yu and Garnier (described elsewhere) [20]. To create uniform films, microscope slides that had been cleaned in an ethanolic potassium hydroxide solution were dipped into and removed from a 5% cellulose

acetate in acetone solution at a controlled rate of 40 mm/min by the dipping head of a Joyce-Loebl Langmuir Trough 4 unit. After 3 min of air drying, the films were immersed in a capped jar containing 0.5% sodium methoxide in methanol solution from Sigma (St. Louis, MO, USA) for 24 h. The films were rinsed with an excess of triply distilled water, then with methanol, and allowed to air-dry.

A prototype alkenyl succinic anhydride (ASA) wax from Nalco Chemical Co. (Naperville, IL, USA), used as received, was dissolved in toluene. Sizing solutions used in this work ranged from 0.4 to  $10^{-4}$ % by weight. The cellulose films were dipped in and out of the sizing solutions with the Joyce-Loebl instrument at 40 mm/min, cured for 15 min in a 60°C oven, and then subjected to 24 h of Soxhlet extraction with toluene to remove any unreacted or hydrolyzed ASA. Samples were stored in a desiccator until use.

Sessile drop goniometry was used to monitor the level of sizing on each film. A Ramé-Hart Model 100-00-115 goniometer (Mountain Lakes, NJ, USA) was used to record the initial (<5 s) contact angle of a 10  $\mu$ l drop of water on each film. Five measurements were taken per sample. Care was taken to avoid portions of the film used for contact angle measurements for subsequent AFM studies, as the films irreversibly swelled upon contact with excess water.

The samples were attached to magnetic steel discs using double-sided tape. These discs were mounted directly onto the end of the piezoelectric scanner (5  $\mu$ m or 100  $\mu$ m maximum  $x/y$  range) of a Park Scientific Instruments' AutoProbe CP (Sunnyvale, CA, USA). Lateral force microscopy (LFM) images ( $256 \times 256$  pixels) and force-distance profiles were taken using the AFM/LFM head. Low spring constant ( $k = 0.02$  N/m), sharp-tipped (tip radius,  $R \sim 20$  nm) silicon nitride cantilevers of rectangular cross-section were used for the lateral force imaging. Low set point forces (0.5–2.0 nN) and moderate scan rates (0.5–1 Hz) were used for the lateral force imaging to prevent damage to the soft cellulosic surfaces. Lateral force hysteresis images were computed by subtracting the reverse and forward LFM images point-by-point using Fortner Research's Transform 3.3 software (Sterling, VA, USA). Force-distance profiles were measured using moderately stiff silicon cantilevers with unmodified, sharp tips ( $k = 3.2$  N/m,  $R \sim 10$  nm), as they provided the best pull-off force resolution.

PFM imaging data were kindly provided by Dr. Sabine Hild at the University of Ulm, Germany. A sized cellulose film (water contact angle  $\sim 94^\circ$ ) and an unsized control (water contact angle  $\sim 33^\circ$ ) were prepared as above and sent to Dr. Hild. Images,  $400 \times 400$  pixels in size, were collected with a Topometrix Explorer equipped with a PFM module (controller and circuitry developed in their laboratory). Using a silicon nitride cantilever ( $k = 0.05$  N/m) modulated at 10 nm amplitude and 100 Hz, topography and adhesion images of a surface were obtained simultaneously. A threshold value of  $-2$  V was applied to the adhesion images (i.e. all values between  $-2$  and  $-10$  V appear black) in order to highlight the lowest energy (0 to  $-2$  V) sites. The compliance signal was not recorded for these measurements.

### 3. RESULTS AND DISCUSSION

#### 3.1. Lateral force microscopy

Lateral force hysteresis and topography images are shown for unsized (water contact angle  $31^\circ$ ) and intermediately sized (water contact angle  $65^\circ$ ) cellulose films in Fig. 3. The  $(50\ \mu\text{m})^2$  contact-mode topography images shown here are typical for these films. The films are relatively smooth and featureless with a root mean square (RMS) surface roughness of approximately 15 nm. A few asperities are visible on the surface, attributable to salt precipitates from the de-acetylation step. The surface energy heterogeneity suggested by dynamic contact angle studies on sized and unsized fibers [3] could manifest as high and low friction ‘patches’ on the surface. However, the absence of identifiable high and low friction regions in these

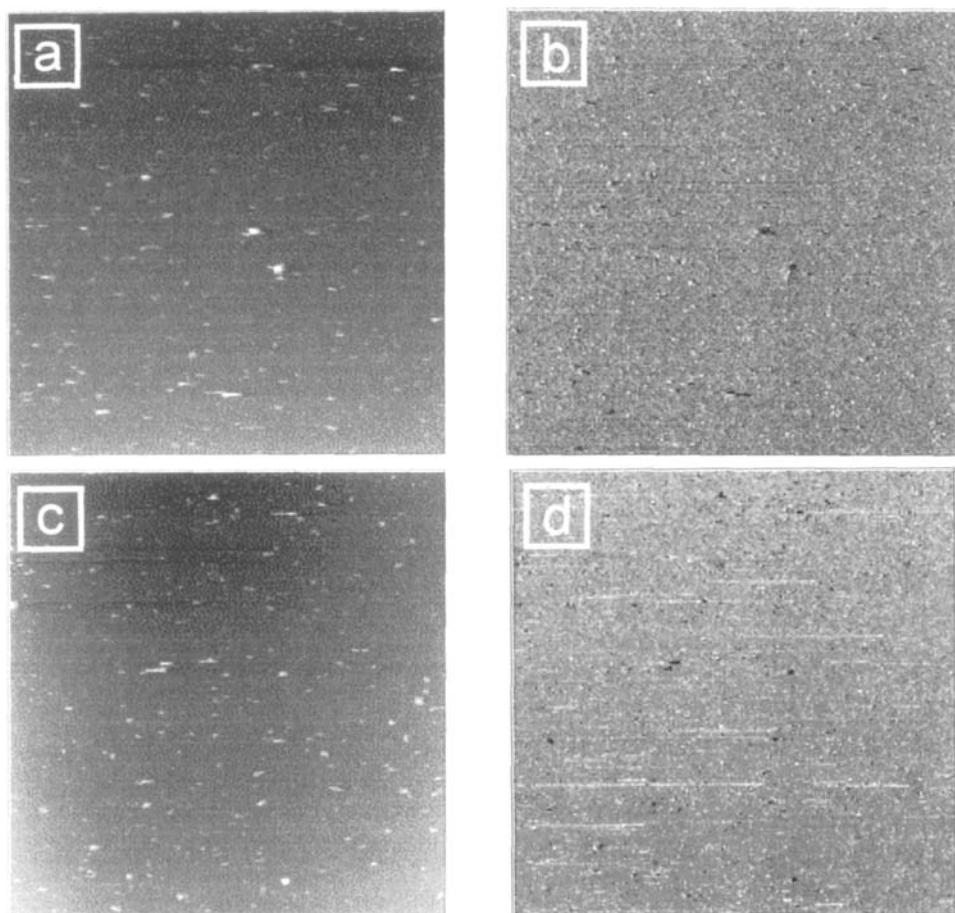


**Figure 3.** Topography and lateral force hysteresis images for sized and unsized cellulose films. Sized: (a) topography; (b) adhesion. Unsized: (c) topography; (d) adhesion. Image size:  $(50\ \mu\text{m})^2$ ; set point load: 0.5 nN; scan rate: 1 Hz.

images suggests that such domains are smaller than the resolution limit of the tip when imaging in the contact mode.

A typical friction loop taken over a single scan line for an unsized and a highly sized cellulose film is shown in Fig. 4. The magnitude of separation between the forward and reverse scan directions is much greater for the unsized sample than for the sized one, indicating greater energy dissipation and surface friction. The roughness of the individual scan lines indicates stick–slip behavior, due to the formation and rupture of contacts between the tip and sample during sliding. Due to the ubiquitous nature of adsorbed water when imaging in air, the distinct difference in absolute friction is primarily indicative of surface hydrophobicity differences, altering the capillary force experienced by the tip while imaging.

The average and standard deviations from  $(5\ \mu\text{m})^2$  whole lateral force hysteresis images of unsized, intermediately sized, and highly sized cellulose samples are plotted with equilibrium water contact angle data in Fig. 5. The data show a monotonic decrease in average surface dissipation with increased surface hydrophobicity.

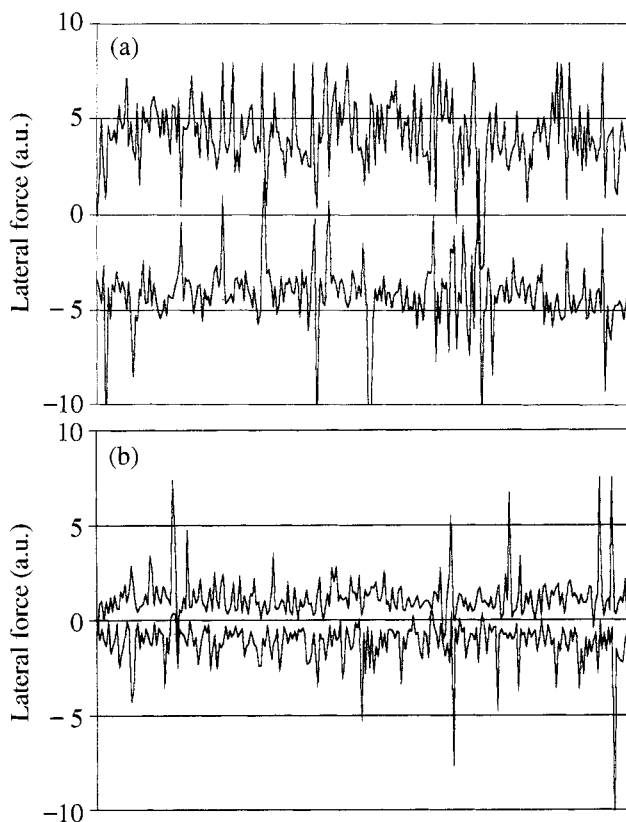


**Figure 4.** Lateral force traces in the forward (top) and reverse (bottom) scan directions for (a) unsized (water contact angle  $33^\circ$ ) and (b) sized cellulose (water contact angle  $96^\circ$ ). Scan size:  $50\ \mu\text{m}$ ; set point load: 2 nN; scan rate: 0.8 Hz.

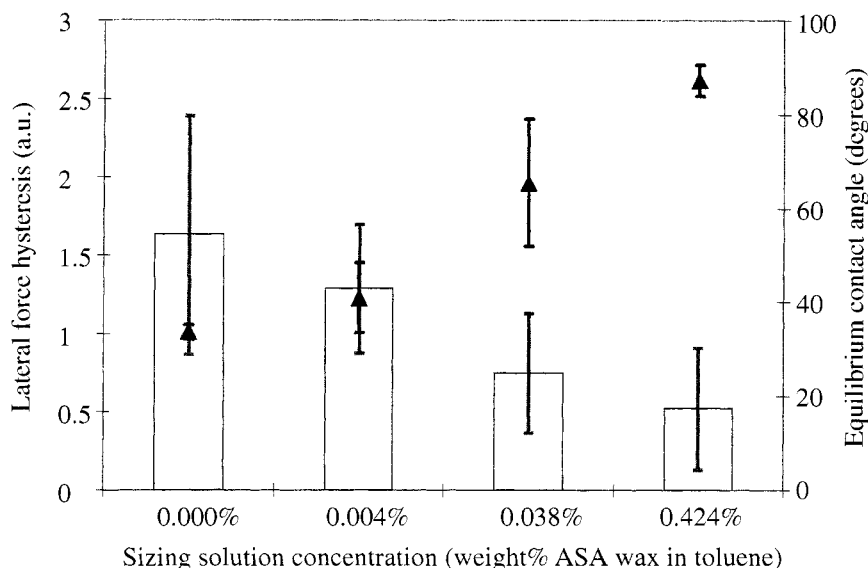


**Figure 5.** Mean lateral force hysteresis for whole images (bars, left axis) and corresponding mean equilibrium water contact angles (triangles, right axis) of unsized and sized cellulose. Image size:  $(5 \mu\text{m})^2$ ; set point load: 0.5 nN. (Error bars represent  $\pm$  one standard deviation.)

### 3.2. Pull-off force adhesion measurements

Pull-off forces measured at 48 equally spaced locations over a  $(1 \mu\text{m})^2$  area of unsized and sized cellulose surfaces are presented as discretized histograms in Fig. 6. The equilibrium contact angle of water with each sample is noted for each graph in the figure legend. A wide distribution of pull-off force magnitudes was measured on each sample, suggesting a range of local surface energies. It may be speculated that these differences are related to differences in the strength of the capillary forces: much higher on an unsized, hydrophilic cellulose surface than on an ASA-treated, hydrophobic surface. It is interesting to note the progressive elimination of the highest local pull-off forces with increasing hydrophobicity. These results are in agreement with the findings of Irvine *et al.*, who observed the same trends in pull-off force measurements between a  $19 \mu\text{m}$  polystyrene sphere and ASA-sized paper measured over a  $(100 \mu\text{m})^2$  area [14]. The observed size scale of the heterogeneity in the local adhesion force suggested that the surface energy heterogeneity of sized and unsized cellulose films was of the order of 10 nm.

The roughness on a surface of interest or probe tip leads to uncertainty in knowledge of the adhesion contact area between them and complicates the interpretation of measured pull-off forces. The  $(1 \mu\text{m})^2$  area on each film measured here was verified to be smooth by measurement of the topography in the contact mode done after the adhesion measurements. Topographic roughness is not expected to exert a significant impact on these adhesion measurements. Therefore, these pull-off force

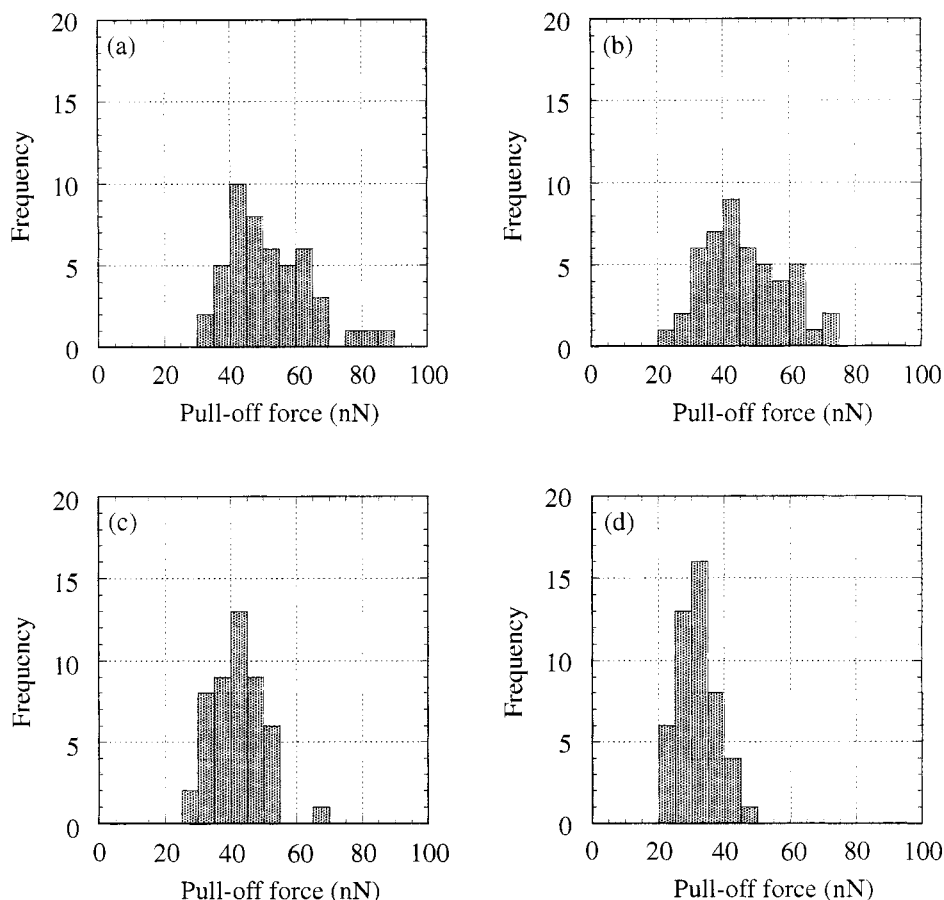


**Figure 6.** Frequency distributions of the pull-off forces measured with a sharp-tip silicon cantilever ( $k = 3.2 \text{ N/m}$ ,  $R = 10 \text{ nm}$ ). Forty-eight equally spaced measurements taken over  $(1 \mu\text{m})^2$  area. Samples sized with (a) 0%, (b) 0.004%, (c) 0.038%, and (d) 0.424% ASA in toluene by weight. The water contact angles determined independently for the four cases were (a)  $33^\circ$ , (b)  $40^\circ$ , (c)  $65^\circ$ , and (d)  $95^\circ$ .

measurements on sized and unsized cellulose films are indicative of heterogeneity in surface chemistry and wettability rather than gross topography.

### 3.3. Pulsed force mode (PFM)

Simultaneously collected topography and adhesion images obtained by PFM are shown for sized and unsized cellulose films in Fig. 7. Adhesion is measured in  $V$  (arbitrary units proportional to  $\text{nN}$ ), with dark representing high pull-off force values and light representing low pull-off force values. There is a distribution of adhesion values seen in both the sized and the unsized images, but the sized (more hydrophobic) sample has a higher number of low pull-off force sites than the unsized (more hydrophilic) sample, supporting previous pull-off force results. Unlike the

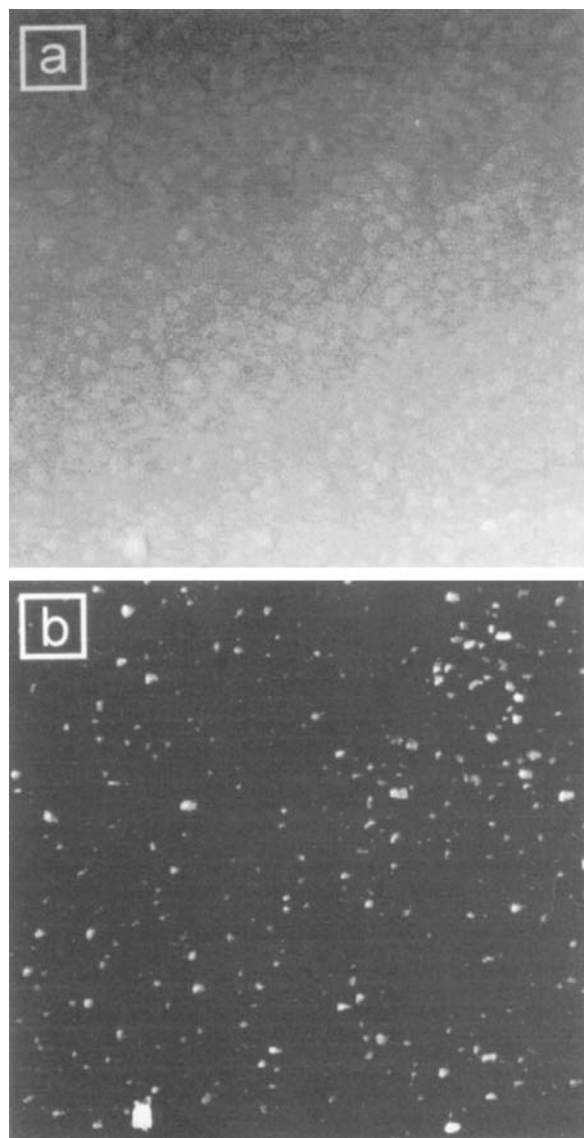


**Figure 7.** Pulsed force mode results. Topography and adhesion images taken simultaneously on unsized and sized cellulose films. Sized: (a) topography; (b) adhesion. Unsized: (c) topography; (d) adhesion. Image size:  $(2\ \mu\text{m})^2$ .

lateral force hysteresis images, features in the adhesion images do not appear to be related to surface topographic features. The low adhesion domains shown here appear to be of the order of 20–85 nm in size. Since these images were obtained under identical conditions on samples whose only differences were in sizing level, the local adhesion values are truly indicative of wettability changes and chemical heterogeneity. The distribution of ASA on the surface of the cellulose serves to

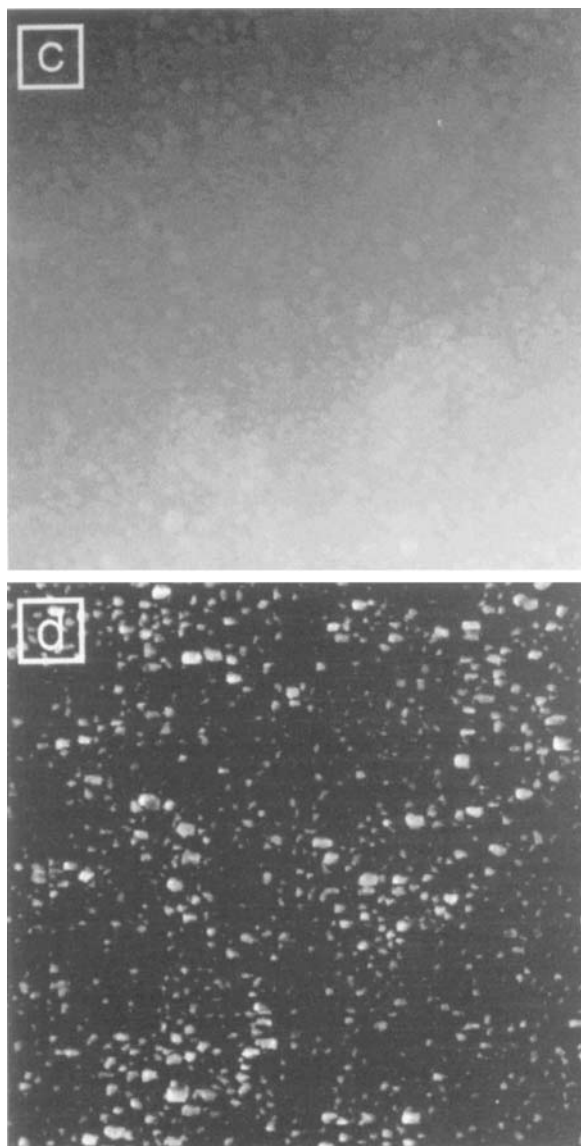


**Figure 7.** (Continued).

mask high-energy sites, creating a greater number of low-energy sites marked by low pull-off adhesion values.

#### **4. CONCLUSIONS**

Scanning probe microscopy techniques have been shown to be successful in highlighting adhesion differences due to ASA on the surface of cellulose. Sessile



drop contact angle measurements verified that low levels of ASA vastly altered the wettability of cellulose. Domains of high and low surface energies created by partial surface coverage by ASA were not spatially discernible by lateral force microscopy; however, dissipative differences between sized and unsized surfaces were highlighted by the torsional hysteresis of a scanning tip over the surfaces. Pull-off force measurements verified that the highest energy sites on cellulose were progressively eliminated as the sizing level was increased. The PFM results, where topography and adhesion are measured simultaneously, showed a greater number of low-energy sites on sized cellulose than on unsized samples. These results indicate that SPM techniques are able to spatially map the surface heterogeneity of ASA-sized cellulose with nanometer resolution.

### Acknowledgements

We gratefully acknowledge the financial support of the Weyerhaeuser Company, Tacoma, WA, USA. In addition, we thank Dr. Robert T. Hamilton (Weyerhaeuser Company), Dr. Gil Garnier (McGill University, Canada) and D. Eric Aston (University of Washington) for useful discussions, and Dr. Sabine Hild (University of Ulm, Germany) for providing the pulsed force mode measurements.

### REFERENCES

1. G. Binnig, C. F. Quate and C. Gerber, *Phys. Rev. Lett.* **56**, 930–933 (1986).
2. G. A. Smook, *Handbook for Pulp and Paper Technologists*, 2nd edn. Angus Wilde Publishers, Vancouver, BC, Canada (1992).
3. J. J. Krueger and K. T. Hodgson, *Tappi J.* **77**, 83–87 (1994).
4. O. N. Tretinnikov and Y. Ikada, *Langmuir* **10**, 1606–1614 (1994).
5. K. T. Hodgson and J. C. Berg, *Wood Fiber Sci.* **20**, 3–17 (1988).
6. P. G. de Gennes, *Rev. Mod. Phys.* **57**, 827–861 (1985).
7. S. J. Hanley and D. G. Gray, in: *Surface Analysis of Paper*, T. E. Connors and S. Banerjee (Eds), pp. 301–329. CRC Press, Boca Raton, FL (1995).
8. I. Duchesne and G. Daniel, *Nord. Pulp Paper Res. J.* **14**, 129–139 (1999).
9. A. A. Baker, W. Helbert, J. Sugiyama and M. J. Miles, *J. Struct. Biol.* **119**, 129–138 (1997).
10. S. J. Hanley and D. G. Gray, *Holzforschung* **48**, 29–34 (1994).
11. S. J. Hanley and D. G. Gray, *J. Pulp Paper Sci.* **25**, 196–200 (1999).
12. R. W. Bassemir, G. Costello and J. Parris, in: *TAGA (Technical Association of the Graphic Arts) Proceedings 1995*, Paris, pp. 876–893 (1995).
13. K. Kuys, Y. B. Truong and I. Parker, in: *Proceedings of the 51st Appita Annual General Conference* Vol. 1, pp. 21–28. Appita, Carlton, Australia (1997).
14. J. A. Irvine, D. E. Aston and J. C. Berg, *Tappi J.* **82**, 172–174 (1999).
15. R. Wiesendanger, in: *Scanning Probe Microscopy and Spectroscopy: Methods and Applications*, pp. 231–235. Cambridge University Press, Cambridge (1994).
16. R. M. Overney, E. Meyer, J. Frommer, D. Broderbeck, R. Lüthi, L. Howald, H.-J. Güntherhodt, M. Fujihara, H. Takano and Y. Gotoh, *Nature* **359**, 133–135 (1992).
17. J. Masai, T. Shibata-Seki, K. Sasaki, H. Murayama and K. Sano, *Thin Solid Films* **273**, 289–296 (1996).
18. K. L. Johnson, K. Kendall and A. D. Roberts, *Proc. R. Soc. London Ser. A* **324**, 301–313 (1971).

19. A. Rosa-Zeiser, E. Weilandt, S. Hild and O. Marti, *Measurement Sci. Technol.* **8**, 1333–1338 (1997).
20. L. Yu and G. Garnier, in: *Transactions of the 11th Fundamental Research Symposium*, C. F. Baker (Ed.), Vol. 2, pp. 1021–1045. Pira International, Surrey (1997).
21. K. L. Johnson, *Contact Mechanics*. Cambridge University Press, Cambridge (1987).

## **Atomic force microscopy, X-ray diffraction, X-ray photoelectron spectroscopy and thermal studies of the new melamine fiber**

R. S. RAJEEV<sup>1</sup>, S. K. DE<sup>1</sup>, ANIL K. BHOWMICK<sup>1,\*</sup>, BILL GONG<sup>2</sup>  
and S. BANDYOPADHYAY<sup>3</sup>,

<sup>1</sup> *Rubber Technology Centre, Indian Institute of Technology, Kharagpur-721302, India*

<sup>2</sup> *School of Chemistry, The University of New South Wales, Sydney-2052, Australia*

<sup>3</sup> *School of Materials Science and Engineering, The University of New South Wales, Sydney-2052, Australia*

**Abstract**—This paper reports the characterization of unaged and aged melamine fibers using various characterization techniques including atomic force microscopy (AFM), X-ray photoelectron spectroscopy (XPS), X-ray diffraction (XRD), scanning electron microscopy (SEM) and thermal analysis. Since melamine fiber is a relatively new fiber, very few studies on its characterization have been made. Morphological studies of the fiber surface using SEM display die lines running along the filament surface, which are characteristics of synthetic fibers and generally occur during spinning of the molten prepolymer through the spinnerets. AFM studies show that the surface of a melamine fiber filament contains a large number of hills and valleys, which are triangular in shape. AFM roughness analysis shows that melamine fiber surface is considerably rough which may aid in adhesion of the fiber with polymeric matrices. Ageing causes an increase in the surface roughness with simultaneous increase in the crystallinity of the fiber from 19.4% to 22.6%. In XPS studies, high concentrations of carbonyl and hydroxyl groups on the filament surface have been detected. Ageing causes a reduction in the hydroxyl group concentration and an increase in the carbonyl group concentration due to surface oxidation. The reduction in the surface hydroxyl groups due to ageing has also been detected in the Fourier-Transform infrared (FT-IR) spectra of the aged fibers. Thermogravimetric (TG) studies reveal a high thermal stability of the melamine fiber even in an oxidative environment such as air.

**Keywords:** Melamine fiber; ageing; morphology; atomic force microscopy; crystallinity; X-ray diffraction; X-ray photoelectron spectroscopy; thermal stability.

---

\*To whom correspondence should be addressed. Phone: 91-3222-83180. Fax: 91-3222-755303.  
E-mail: anilkb@rtc.iitkgp.ernet.in

## 1. INTRODUCTION

High performance fibers require specific properties. They usually have very high levels of at least one of the following properties; tensile strength, limiting oxygen index and chemical resistance. Melamine fiber is one of the latest high performance fibers [1]. This fiber is manufactured by BASF Corporation under the trade name Basofil. The Basofil offers high operating temperature and high limiting oxygen index and is typically used in high temperature applications such as in protective clothing and safety gloves. Because of its variable denier and staple length, low tensile strength and the difficulty in processing, melamine fibers are generally blended with other fibers such as aramid. Recently Rajeev *et al.* [2] have successfully incorporated melamine fibers in EPDM rubber matrix and have developed short fiber–rubber composites.

Since melamine fibers are relatively new, only a few reports are available regarding the characterization of these fibers. An understanding of the surface and the bulk properties of these fibers will help in the selection of a suitable matrix for the preparation of polymer-fiber composites based on melamine fiber. Information on the characterization of these fibers will also aid in adopting suitable techniques for modification of the fiber surface, which can improve the adhesion between the fiber and the matrix. Hopen [3] has reported the characterization of the melamine fiber using optical microscopy and FT-IR spectroscopy. The characterization of the microstructure of polymer fibers provides an insight into structure-property relationship of the fiber. Microscopy techniques are employed for the characterization of polymeric fibers to study features such as fiber shape, diameter, crystal size, voids and molecular orientation [4]. In order to understand the relation between the structure and properties of any polymeric material including fibers, their morphology should be clearly understood [5]. X-ray diffraction, optical microscopy, transmission electron microscopy and a range of other analytical tools are commonly employed to determine the structure of polymeric fibers. Lately, the AFM has become a widely accepted technique to study the surface morphology of fibers [6] and fiber-reinforced composites. Rajeev and coworkers [7] have employed tapping mode atomic force microscopy to detect the formation of an interphase between the fiber and the matrix in short melamine fiber reinforced EPDM rubber containing a dry bonding system. Microstructures of fibers based on polyethylene [8], polypropylene [9–12], polyimides [13] and aramids [14, 15] as well as carbon and graphite fibers [16, 17] have been investigated using AFM. Vanswijgenhoven *et al.* [18] have made a comparative study of the surface roughness of silicon carbide fibers using AFM and found that roughness amplitudes of different fiber grades exhibited considerable scatter. Techniques like X-ray diffraction (XRD), infra-red (IR) spectroscopy, electron spectroscopy for chemical analysis (ESCA or XPS), nuclear magnetic resonance (NMR) spectroscopy and thermal analysis in combination with microscopy techniques are useful in understanding the structure-property relationships of fibers. XPS is a very useful technique for detecting chemical structure changes on a fiber surface resulting from different surface

treatments [19–22]. Walterson [23] has studied the chemical composition of a carbon fiber surface using XPS and detected elements such as calcium, chlorine and silicone on the fiber surface along with carbon, nitrogen and oxygen. Recently, the degradation of melamine formaldehyde resin during XPS analysis has been investigated by Coullerez *et al.* [24]. Sellitti *et al.* [25] have characterized surfaces of carbon fibers by attenuated total reflection Fourier transform infrared spectroscopy. In order to study the surface characteristics of carbon fibers, Ishitani *et al.* [26] have employed Raman spectroscopy. This paper reports the characterization of melamine fiber using various analytical techniques including microscopy, spectroscopy and thermal analysis. It also reports the morphological and chemical changes that take place on the melamine fiber when it is aged in a circulating air oven for a prolonged period.

## 2. EXPERIMENTAL

### 2.1. Details of materials used

The melamine fiber used in the present study was supplied by BASF Corporation, Enka, NC, USA. The properties of the fiber are given in Table 1 [1]. Ageing of the fiber was done in a circulating air oven at 150°C for 7 days.

### 2.2. Scanning electron microscopy (SEM) studies

SEM photomicrographs of the unaged and aged fiber filaments were taken using JEOL JSM 5800 scanning electron microscope. The filaments were sputter coated with gold prior to the analysis.

**Table 1.**

Properties of melamine fiber [1]

Linear density (denier)	2.2
Tenacity (g/denier)	2.0
Elongation at break (%)	18.0
Tensile strength (MPa)	207
Tensile modulus (GPa)	6.9
Staple length (mm)	51
Diameter ( $\mu\text{m}$ )	12–18
Density (g/ml)	1.4
Moisture regain at 23°C and 65% relative humidity (%)	5
Limiting oxygen index (LOI)	32
Continuous use temperature (°C)	200
Maximum use temperature (°C)	260–370
Hot air shrinkage — 1 h at 200°C	<1%

### 2.3. Atomic force microscopy (AFM) studies

The AFM measurements were carried out in air at ambient conditions (25°C) with a Dimension 3000 Atomic Force Microscope, made by Digital Instruments Inc., Santa Barbara, CA, USA. The experiments were carried out in the tapping mode with constant amplitude, using microfabricated cantilevers. The scanning was done using etched silicon tip, square pyramid in shape, with a base dimension of approximately  $4\ \mu\text{m} \times 4\ \mu\text{m}$ . The characteristics of the probes were: spring constant ( $K$ ), 20–100 N/m; resonance frequency, 200–400 kHz; nominal tip radius of curvature, 5–10 nm; cantilever length, 125  $\mu\text{m}$ ; cantilever configuration, single beam; tip half angle, 18° side, 25° front and 10° back. All images contained 256 data points. Height and phase images were recorded simultaneously in each scanning. Images were analyzed using Nanoscope III image processing software. In AFM roughness analysis,  $R_q$  (i.e. the root mean square (RMS) average of the height deviations taken from a mean plane in the image) and  $R_a$  (i.e. the arithmetic average of the absolute values of the surface height deviations from the mean plane) were measured [27].

### 2.4. X-ray diffraction analysis

The X-ray diffraction patterns of the unaged and aged melamine fiber filaments were recorded with a Siemens X-ray Diffractometer (D 5000) using Cu  $K_\alpha$  radiation in the angular range ( $2\theta$ ) of 10–50° at an operating voltage of 30 kV and current 30 mA. In order to calculate the degree of crystallinity, the X-ray data were fitted using a Gaussian–Lorentzian function in the Microcal Origin software (version 5.0) and the areas under the crystalline and amorphous portions were determined. The degree of crystallinity ( $X_c$ ) was measured using the relation [28]

$$X_c = \frac{I_c}{I_a + I_c}, \quad (1)$$

where  $I_a$  and  $I_c$  are the integrated intensities corresponding to the amorphous and crystalline phases, respectively.  $2\theta$  values were reproducible within  $\pm 0.02^\circ$ . Crystallite size ( $P$ ), interchain distance ( $r$ ) and interplanar distance ( $d$ ) were calculated using the following equations [28]:

$$P = \frac{88.24}{\beta \cos \theta} \quad (\lambda = 1.54\ \text{\AA}), \quad (2)$$

$$r = \frac{5\lambda}{8 \sin \theta}, \quad (3)$$

$$d = \frac{\lambda}{2 \sin \theta}, \quad (4)$$

where  $\beta$  is the half-height width of the crystalline peak and  $\lambda$  is the wavelength of the X-ray radiation.

### 2.5. X-ray photoelectron spectroscopy (XPS) studies

The X-ray photoelectron spectroscopy (XPS) studies of the unaged and aged melamine fiber filaments were carried out using VG Scientific ESCALAB 220i-XL X-ray photoelectron spectrophotometer. The spectra were collected using monochromatic Al  $K_{\alpha}$  X-ray source of energy 1486 eV operated at 10 kV and 120 W with an emission current of 12 mA. Survey scans were recorded from 0 to 1200 eV. The working pressure in the instrument was  $2 \times 10^{-9}$  Torr and the photoelectron take-off angle was  $180^\circ$  with respect to the sample surface. The XPS data were fitted using a Gaussian–Lorentzian function. The different functional groups on the fiber surface were estimated from the respective areas of assumed Gaussian–Lorentzian curves using the equation [24]:

$$C_A = \frac{I_A/S_A}{\sum_{i=1}^n I_i/S_i}, \quad (5)$$

where  $n$  is the number of elements in the sample and  $C_A$  is the relative concentration of element A;  $I_A$  and  $I_i$  are the peak areas and  $S_A$  and  $S_i$  are the sensitivity factors which are used to normalize the intensities of the signals to give the atomic concentration of the elements.

### 2.6. Fourier-transform infrared (FT-IR) spectroscopy analysis

FT-IR spectroscopy analysis was carried out using Nicolet Nexus FT-IR spectrophotometer with DRIFTS (Diffuse Reflectance Infra-red Fourier Transform Spectroscopy) attachment operated in the absorption mode, in the wavenumber range of  $4000\text{--}400\text{ cm}^{-1}$  by mixing the fiber with the KBr powder. The concentration of the samples in the KBr was held constant to 0.7% (w/w) after a series of trial runs. The spectra were obtained using a resolution of  $4\text{ cm}^{-1}$  and averaged over 40 scans. A background spectrum obtained with pure KBr powder was subtracted from the acquired spectra in all the cases. A standard software (Omnic ESP, version 5.1) was used for data acquisition and analysis.

### 2.7. Thermal analysis

Thermogravimetric (TG) analyses of unaged and aged fibers were carried out under both argon and air atmospheres with a flow rate of 50 ml/min in a Setaram Labsys Thermal Analyzer (Caluire, France) using 10–12 mg samples taken in ceramic crucibles of approximately 4 mm diameter. The samples were purged for one hour in argon/air at ambient temperature and then heated to  $1200^\circ\text{C}$  at a heating rate of  $10^\circ\text{C}/\text{min}$ . The thermogravimetric and derivative thermogravimetric (DTG) curves were plotted using Setaram Setsoft Thermal Analysis software.

### 3. RESULTS AND DISCUSSION

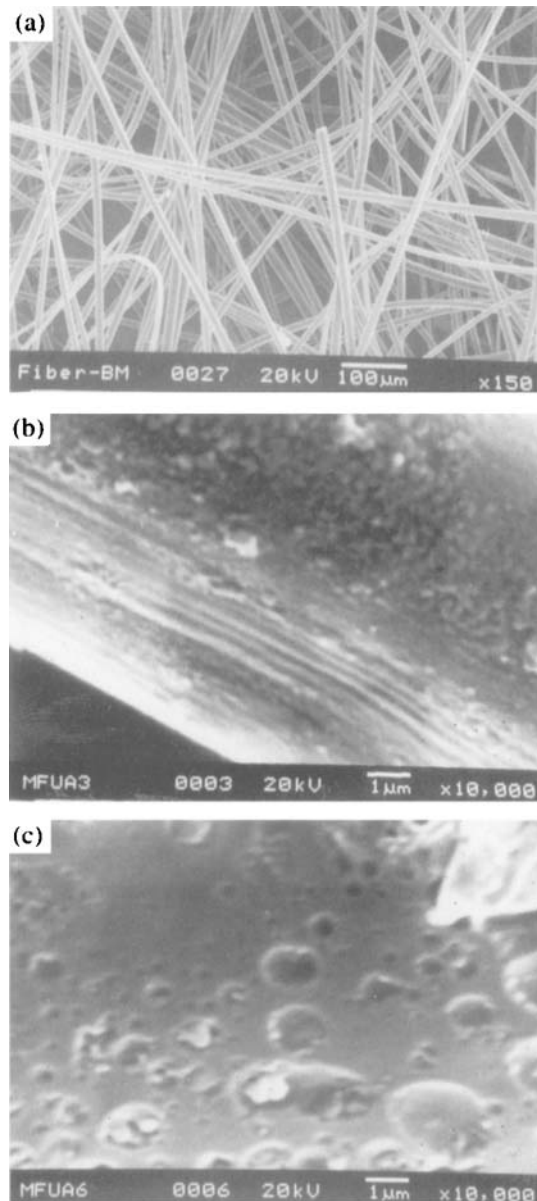
#### 3.1. Surface topography of melamine fiber

Figure 1a shows the SEM micrograph of the unaged melamine fiber at a magnification of 150. Melamine fiber available is in pulp form, which is a particular form of short fibers in which the filaments are of discontinuous length and narrow diameter compared to the conventional short fibers [2]. The filaments, which are in the entangled form, show a diameter variation from 14  $\mu\text{m}$  to 20  $\mu\text{m}$ . Figure 1b shows the SEM micrograph of the single melamine fiber filament. The filament surface contains striations, which are wavy in nature, running parallel to the horizontal axis of the filament. These striations are believed to be the die lines, which occur at the time of manufacturing of the filaments. These types of striation markings due to drawing are commonly observed on the surfaces of metallic filaments [29]. The filament also contains pits on the surface as shown in Fig. 1c. These pits are supposed to have occurred during the manufacturing of the fibers and may aid in better adhesion between the fiber and the matrix through mechanical interlocking. Figure 1d is the SEM micrograph of the end of a filament where it can be seen that the filaments do not have a circular crosssection. Rather, the cross section is flattened and bean shaped, which provides them a larger surface area, which is advantageous when melamine fibers are mixed with other fibers [3]. This type of crosssection may also cause improved adhesion with the matrix.

The height (left) and phase (right) AFM images of a typical unaged melamine fiber filament are shown in Fig. 2a. The height image is in a data scale of 1000 nm and the phase image is taken in a phase angle of  $50^\circ$ . The direction of the major fiber axis is shown with an arrow. The surface irregularities of the melamine fiber filament are visible in the height image, which shows that the fiber surface is composed of a large number of grains in different planes as well as grooves lying in a direction parallel to the horizontal axis of the filament. These grooves may be the die lines, as observed in the SEM image (Fig. 1b). Mainly three types of structures are evident in the phase image; long elongated grains having typical dimension 420 nm  $\times$  190 nm, grains having intermediate dimension of the order 260 nm  $\times$  150 nm and very small grains having dimension of the order 115 nm  $\times$  75 nm. The AFM section analysis of the height image in Fig. 2a is given in Fig. 2b. The figure shows that the grains on the filament surface are triangular in shape and are not lying in the same plane. Also, these grains are not equally spaced. The two prominent grooves shown in the section analysis (Fig. 2b) have widths 130 nm and 210 nm, which correspond to the width of a typical striation given in Fig. 1b. Therefore, the grooves observed in the AFM height image are the die lines on the fiber surface.

Figure 3a is the height image of the fiber filament at a data scale of 50 nm where the surface features are clearly visible as compared to the height image taken in a data scale of 1000 nm (Fig. 2a). The corresponding surface plot image in a data scale of 100 nm is given in Fig. 3b. The hills and valleys on the filament surface





**Figure 1.** SEM micrographs of: (a) unaged melamine fiber filaments at magnification 150 $\times$ ; (b) a single melamine fiber filament at magnification 10 000 $\times$ ; (c) the melamine fiber surface showing pits on the surface and (d) the end of a melamine fiber filament.

are evident in the surface plot image. Majority of hills are having sharp edges although hills with blunt edges are also visible. These observations are in line with the observations made in Fig. 2b. Therefore, it can be assumed that the grains found in the phase image of Fig. 2a are triangular in shape, formed by joining together of

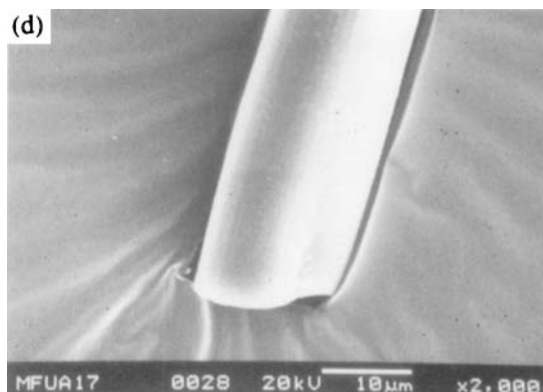


Figure 1. (Continued).

**Table 2.**

AFM roughness analysis parameters of unaged and aged melamine fibers

AFM roughness analysis parameters	Unaged fiber (nm)	Aged fiber (nm)
$R_q$	7.25	12.61
$R_a$	5.66	9.46

different platelets. In Fig. 3b, it can be observed that all the hills are not in the same plane and there is a distinct height variation between different hills.

The roughness analysis of the AFM height images of different fiber filaments shows that  $R_q$ , which is the root mean square (RMS) average of the height deviations taken from the mean plane, varies between 3.09 nm to 11.27 nm indicating that surface is not uniform among various filaments. The roughness analysis parameters of a typical unaged melamine fiber filament are given in Table 2. The surface roughness of melamine fiber filaments can enhance the adhesion between the fiber and the matrix.

The ageing of the filaments causes changes in the surface morphology. Figure 4 is the phase image of the aged melamine fiber filament. It can be seen that ageing causes the grains on the surface to fuse together to form clusters. The surface roughness is increased due to ageing. On comparing the roughness analysis of the unaged and aged fibers, it is found that the  $R_q$  value increases from 7.25 nm to 12.61 nm and  $R_a$  increases from 5.66 nm to 9.46 nm (Table 2). The changes in the surface profile due to ageing are also evident on comparing the section analysis of the unaged and aged fiber filaments, given in Figs 2b and 5, respectively. The changes on the fiber surface due to ageing may be due to the surface oxidation and removal of adsorbed water layer from the fiber surface, as explained later.

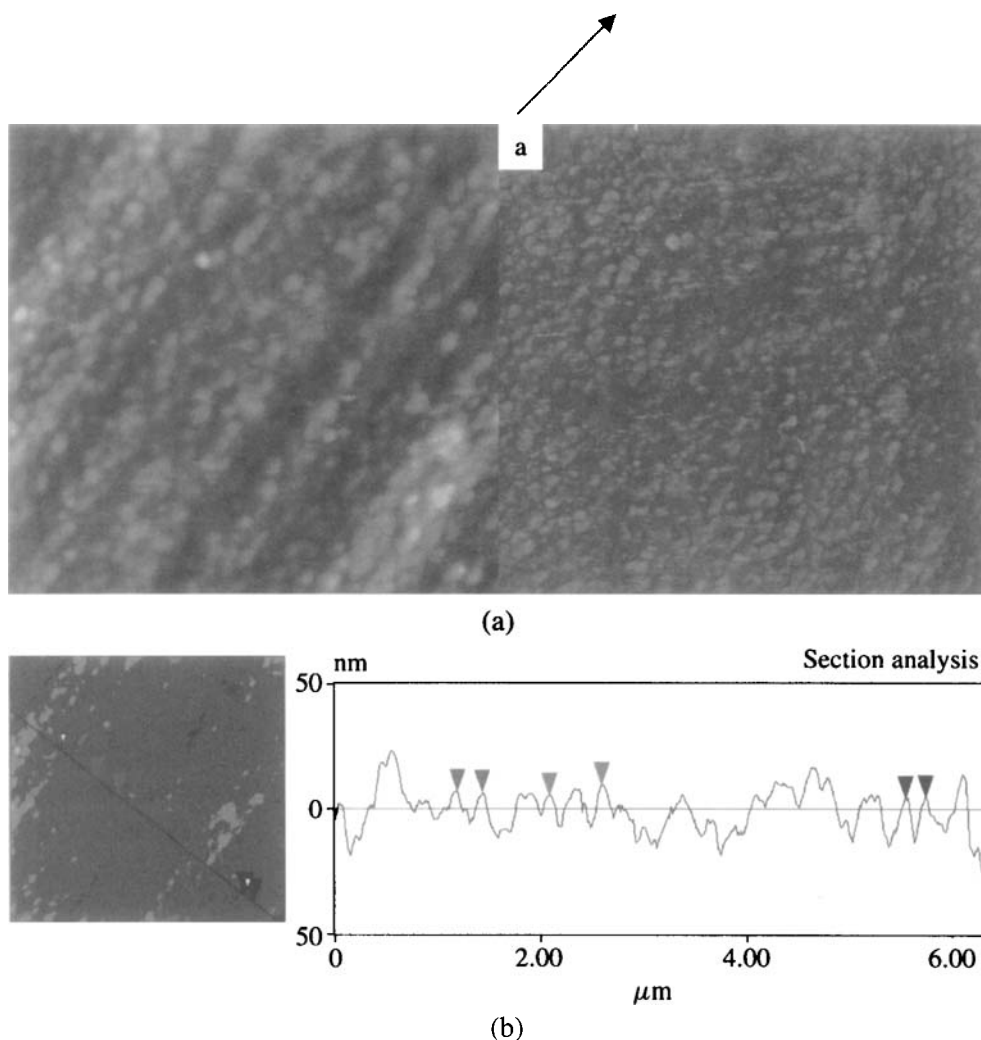


**Figure 2.** (a) Height (left) and phase (right) AFM images of the unaged melamine fiber filament in a scan area of  $5\ \mu\text{m} \times 5\ \mu\text{m}$ . Arrow indicates direction of major fiber axis; (b) AFM section analysis of the height image in Fig. 2a showing the triangular shaped grains on the fiber surface.

### 3.2. Crystallinity of melamine fiber

Figure 6 shows the X-ray diffraction spectra of unaged and aged melamine fiber. Melamine fiber is semi-crystalline, characterized by one sharp crystalline peak at an angle ( $\theta$ ) of  $14.5^\circ$  and the other 5 peaks having lower intensity at the angular ranges ( $\theta$ ) between  $17^\circ$  and  $25^\circ$ . The molecules are presumed to attain an ordered arrangement giving crystalline peaks at the time of spinning the prepolymer through the spinnerets [30]. The crystallite size, interchain distance and interplanar distance are calculated based on X-ray diffraction data with respect to the three most intense

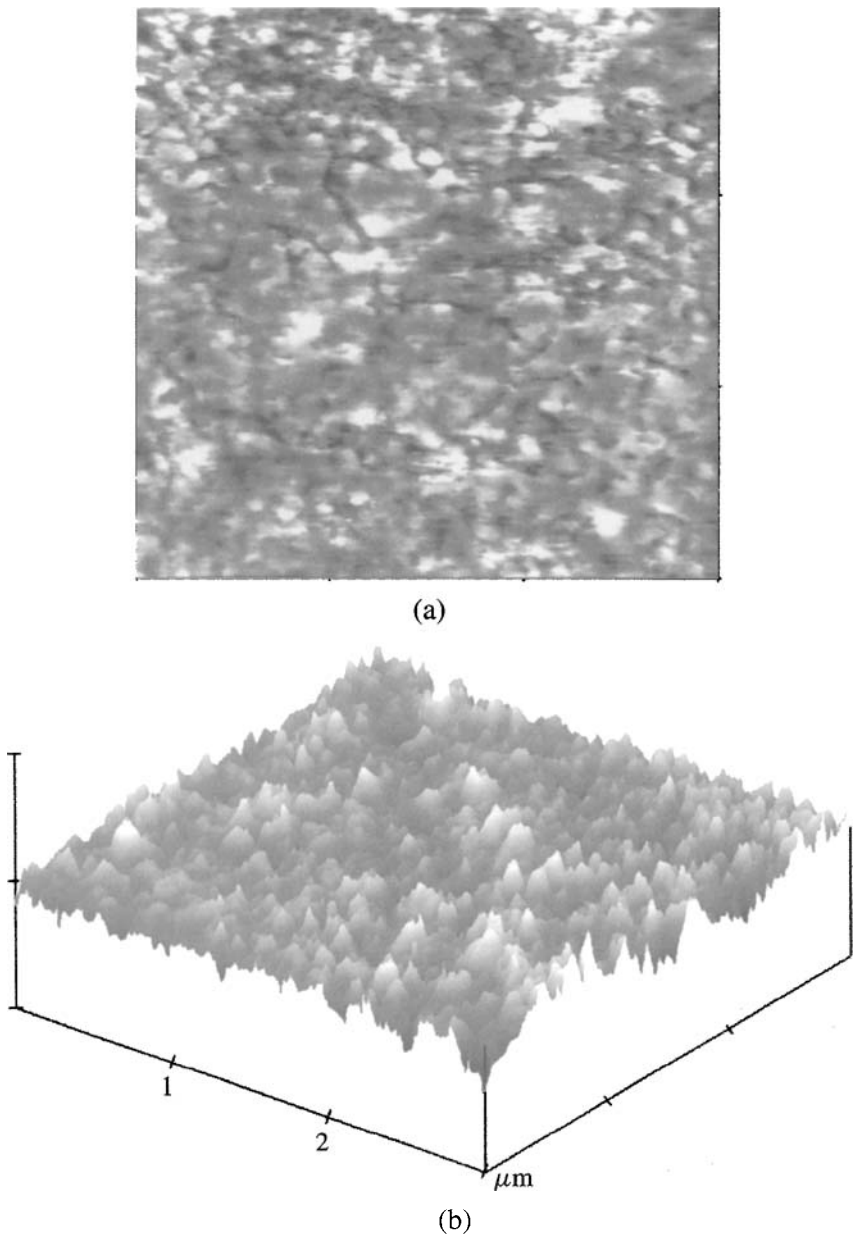


**Figure 3.** (a) AFM height image of the unaged melamine fiber filament in a data scale of 50 nm; (b) AFM surface plot image of the height image in Fig. 3a in a data scale of 100 nm.

crystalline peaks (denoted as 1, 2 and 3 in Fig. 6) for both unaged and aged melamine fibers and are given in Table 3.

The crystallinity of melamine fibers may be arising from the presence of ordered domains in the fiber. As pointed out by Young [5], there are chances of formation of

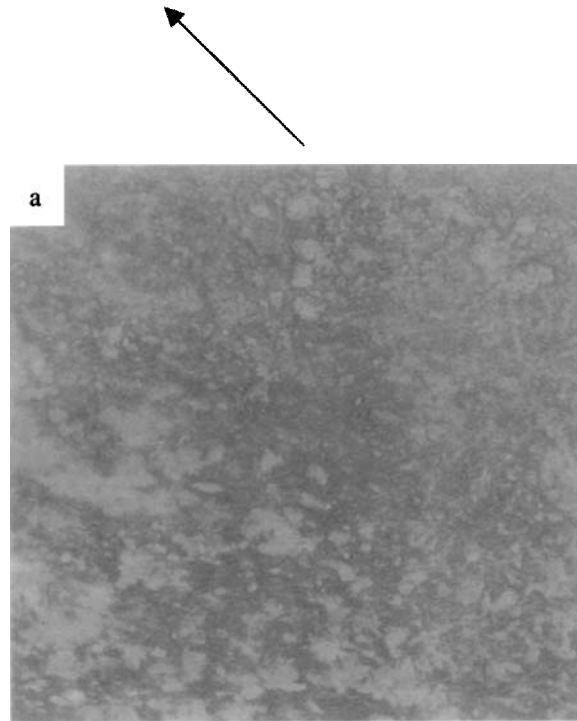


**Figure 4.** AFM phase image of the aged melamine fiber filament in a phase angle of  $60^\circ$ . Arrow indicates direction of major fiber axis.

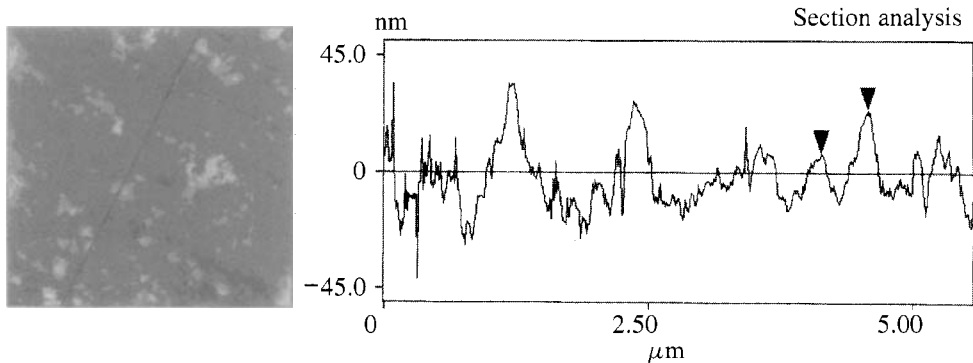


**Figure 5.** Section analysis of the height image of aged melamine fiber filament.

ordered domains in amorphous and semi-crystalline polymers. These domains are microscopic regions in which there is a certain amount of molecular order. A sharp intensity in the X-ray diffraction spectra of melamine fiber reveals that there is some degree of localized order arising presumably at the time of spinning of the fibers. Therefore, melamine fiber is considered to be consisting of coexisting crystalline and amorphous regions where the polymer chain is perfectly ordered over distances

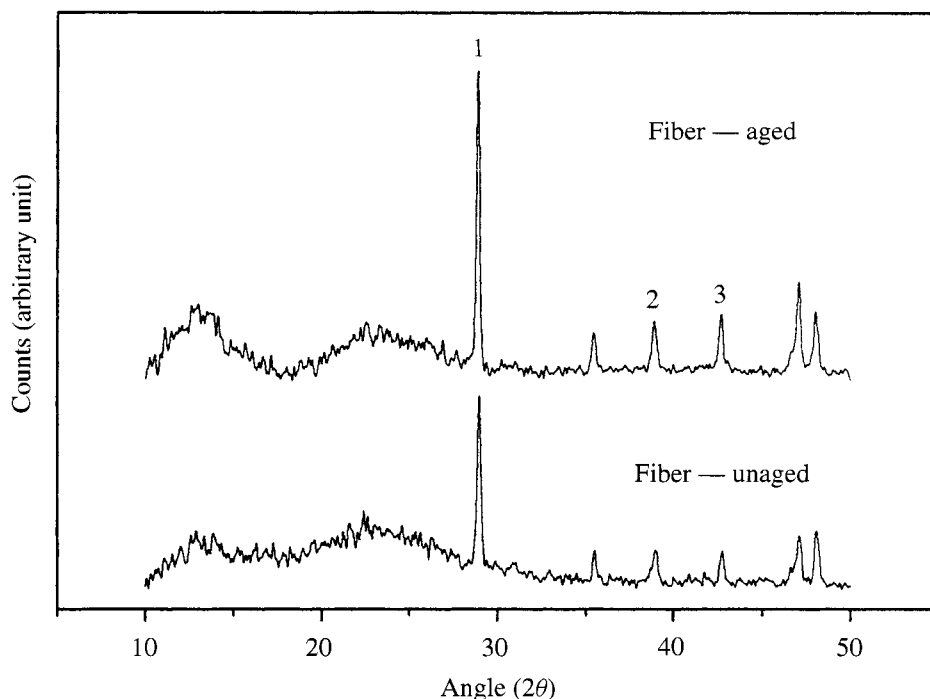


**Figure 6.** X-ray diffraction spectra of the unaged and aged melamine fiber filaments.

**Table 3.**

Parameters obtained from X-ray diffraction studies of unaged and aged fibers

Peaks	Peak angle ( $\theta$ )		Half height width ( $\beta$ )		Crystallite size ( $\text{\AA}$ )		Interchain distance ( $\text{\AA}$ )		Interplanar distance ( $\text{\AA}$ )		Crystallinity (%)	
	UA <sup>a</sup> A <sup>a</sup>		UA A		UA A		UA A		UA A		UA A	
1	14.5	14.4	0.24	0.20	382	451	3.85	3.86	3.08	3.09		
2	19.5	19.5	0.42	0.34	223	275	2.88	2.89	2.31	2.31	19.4	22.6
3	21.4	21.4	0.34	0.32	279	296	2.64	2.64	2.11	2.12		

<sup>a</sup> UA indicates unaged fiber and A indicates aged fiber. For peak numbers, see Fig. 6.

corresponding to the dimensions of the crystallites and at the same time polymer chains include disordered segments belonging to amorphous regions, as proposed by Herman *et al.* in the 'fringed micelle' model of partly crystalline polymers [31].

It can be seen from Fig. 6 that ageing causes an increase in the degree of crystallinity of the fibers from 19.4% to 22.6%. Ageing also produces an increase in the intensities of all the crystalline peaks. These changes suggest that ageing of melamine fiber at higher temperature for a prolonged period causes changes in the crystalline structure similar to that caused due to annealing of conventional polymeric fibers. Prolonged ageing at 150°C might have resulted in greater mobility of the molecules causing molecular rearrangement. There may be the possibility of

chain folding as well due to ageing, which may be the reason for the increased intensity of the crystalline peaks of the aged fibers, as suggested by Alexander [32]. On comparing the X-ray diffraction parameters of unaged and aged melamine fibers, given in Table 3, it can be seen that there is an increase in crystallite size due to ageing. Interchain distance and interplanar distance also increase marginally due to ageing, especially in the case of the sharp crystalline peak occurring at the peak angle ( $\theta$ )  $14.5^\circ$ . Increase in the crystallite size after ageing suggests the possibility of chain folding, which may be the reason for the sharper peaks in the XRD spectra of aged fibers. Thus, it can be assumed that there is some degree of molecular ordering due to ageing.

### 3.3. Surface composition of melamine fiber

The wide scan XPS spectra of the unaged and aged melamine fibers are given in Fig. 7. It can be seen that apart from the elements carbon, nitrogen and oxygen, which are the constituents of melamine formaldehyde polymer, the fiber surface also contains an appreciable amount of sodium along with a very low concentration of sulfur, chlorine and phosphorous. The presence of chlorine may be due to the contaminants on the fiber surface. The sodium and sulfur contributions probably come from processing operations. The main features on the fiber surface are  $C_{1s}$ ,  $O_{1s}$  and  $N_{1s}$  peaks. The relative percentage of carbon, nitrogen and oxygen on the

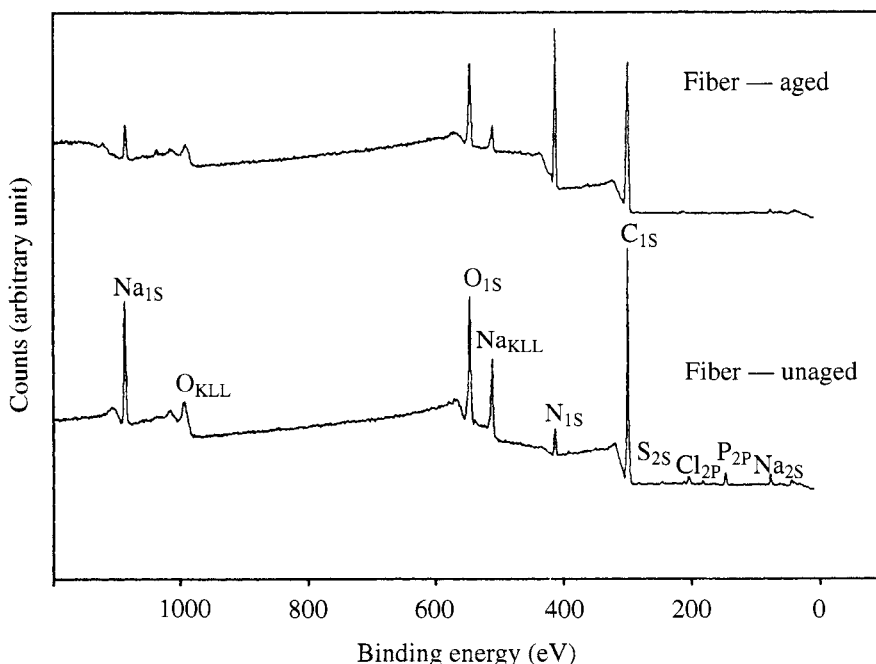


**Figure 7.** Wide scan XPS spectra of unaged and aged melamine fiber filaments.

**Table 4.**

XPS surface composition of unaged and aged melamine fibers

Core level and deconvoluted spectra	Unaged fiber			Aged fiber		
	Binding energy (eV)	% contribution of deconvoluted peaks	Relative percentage of elements	Binding energy (eV)	% contribution of deconvoluted peaks	Relative percentage of elements
C <sub>1s</sub>						
C <sub>1</sub>	288.7	3.6	75.2	288.8	10.6	61.0
C <sub>2</sub>	287.2	14.0		287.4	29.6	
C <sub>3</sub>	285.6	59.3		286.1	25.0	
C <sub>4</sub>	284.8	23.1		284.7	34.8	
O <sub>1s</sub>						
O <sub>1</sub>	533.8	40.4	4.7	534.5	18.4	27.1
O <sub>2</sub>	532.1	50.9		532.9	38.8	
O <sub>3</sub>	530.7	8.7		531.4	42.8	
N <sub>1s</sub>						
N <sub>1</sub>	399.9	46.7	20.1	400.0	34.6	11.9
N <sub>2</sub>	398.9	53.3		398.6	65.4	

fiber surface and the percentage contribution of deconvoluted peaks of each of the above elements are given in Table 4.

The C<sub>1s</sub> peak of the unaged melamine fiber is resolved into four peaks and are designated as C<sub>1</sub>, C<sub>2</sub>, C<sub>3</sub> and C<sub>4</sub> (Fig. 8a). These four different carbon atoms have binding energies 288.7, 287.2, 285.6 and 284.8 eV, respectively. The carbon atom having the highest binding energy among the four carbon atoms (C<sub>1</sub>) is assigned to the one attached to oxygen atom as C=O [33, 34]. These carbonyl groups are supposed to be formed by surface oxidation, which might have taken place during the manufacturing and processing of melamine fiber. As pointed out by Clark *et al.* [34], almost all commercially prepared polymer samples exhibit varying degrees of surface oxidation, which is not detected by other techniques. C<sub>2</sub>, with the binding energy of 287.2 represents carbon atoms which are present in the ring structure of melamine fiber [33], i.e. carbon atoms attached to two neighboring nitrogen atoms, as given in Scheme 1.

The deconvoluted peak C<sub>3</sub> with binding energy 285.6 eV has the largest relative concentration among the four types of carbon atoms on the surface, as shown in Table 4. The low binding energy of this carbon atom suggests that this carbon atom is attached to a hydroxyl group [35]. The presence of these hydroxyl groups can be attributed to two factors: melamine fiber surface contains a large number of methylol groups, which are formed during the manufacturing of these fibers. The first step in the preparation of melamine fiber is the reaction between melamine and formaldehyde in an aqueous solution to form methylol compounds as shown in Scheme 2, the step being called hydroxymethylation.



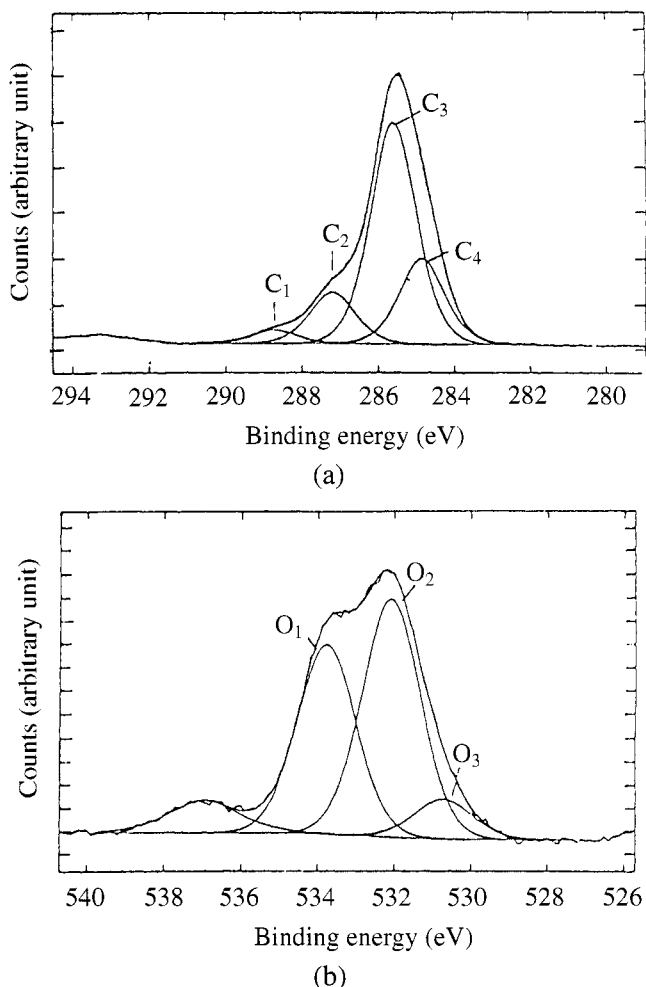


**Figure 8.** Deconvoluted XPS spectra of unaged melamine fiber: (a) C<sub>1</sub>S; (b) O<sub>1</sub>S and (c) N<sub>1</sub>S. See text for peak identification.

The reaction yields methylol melamine containing up to 6 methylol groups, which is shown in Scheme 3.

Therefore, it is likely that a large number of methylol groups are present on the fiber surface, which do not participate in the crosslinking reaction and contribute to deconvoluted peak C<sub>3</sub>. The presence of a large number of hydroxyl groups on the fiber surface may also be assigned to the adsorbed water molecules present on the fiber surface because of the hygroscopic nature of the fiber filaments.

The deconvoluted peak C<sub>4</sub> has the lowest binding energy typical of the carbon atom in a simple hydrocarbon chain as in polyethylene. It can be attributed to the carbon atoms in the CH<sub>2</sub> groups, which are formed during the condensation reaction between melamine and formaldehyde.

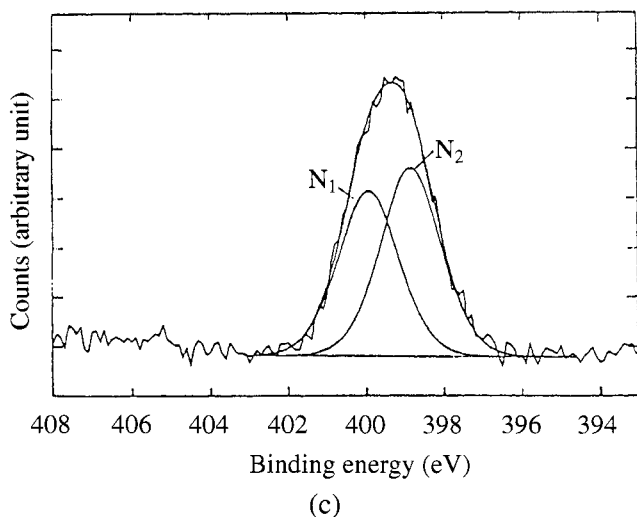
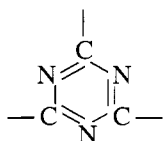
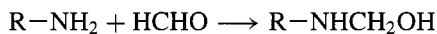


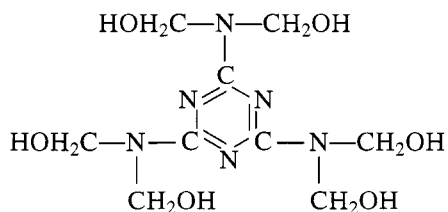
Figure 8. (Continued).



Scheme 1.



Scheme 2.



Scheme 3.

The oxygen spectrum is resolved into three peaks, which are shown in Fig. 8b. The three deconvoluted peaks are designated as O<sub>1</sub> (binding energy 533.8 eV), O<sub>2</sub> (binding energy 532.1 eV) and O<sub>3</sub> (binding energy 530.7 eV). The deconvoluted peak O<sub>1</sub> is due to the presence of water layer on the fiber surface [36]. The presence of the peak O<sub>2</sub>, which has the highest relative concentration among the three oxygen atoms present, can be attributed to the oxygen atoms in the methylol groups [37] on

the fiber surface as explained before. Deconvoluted peak O<sub>3</sub> is due to the presence of carbonyl groups on the fiber surface [38].

The results of the deconvolution of the nitrogen spectrum, given in Fig. 8c, show that there are two different types of nitrogen atoms on the melamine fiber surface. The chemical structure of melamine formaldehyde also suggests that there are two different types of nitrogen atoms in the polymer; one in the ring structure and the other in the out-of-ring segment that holds the methylol groups or crosslinks. N<sub>1</sub> (binding energy, 399.9 eV) is due to the nitrogen atoms which are attached to the electron withdrawing —CH<sub>2</sub>—O— group, and the other deconvoluted peak N<sub>2</sub> (binding energy 398.9 eV) is due to the nitrogen atoms which are present in the ring structure [39].

On comparing the relative concentrations of elements on the fiber surface before and after ageing (given in Table 4 and in Fig. 7), it can be seen that after ageing the relative concentration of nitrogen is reduced from 20% to 12% whereas that of oxygen is increased from 4.7% to 27.1%. The percentage contribution of the deconvoluted peak O<sub>1</sub> of the aged fiber, which is assumed to be due to the presence of adsorbed water layer on the fiber surface, is reduced from 40.4% to 18.4% after ageing due to reduced hydrophilicity. Thus it can be assumed that ageing causes less moisture uptake by the fiber filaments.

Ageing causes a substantial reduction in the methylol component on the fiber surface as evident from the reduced percentage contribution of the peak O<sub>2</sub> from 50.9% to 38.8%. This is possibly due to the fact that prolonged ageing causes conversion of some of the unreacted methylol groups to crosslinks and also chain extension. At the same time, additional carbonyl groups might have been formed due to further surface oxidation. This is evident from the increase in the percentage contribution of the deconvoluted peak O<sub>3</sub> from 8.7% to 42.8%. The reduction in the methylol group concentration causes reduced hydrophilicity, thus reducing the percentage contribution of the peak O<sub>1</sub> from 40.4% before ageing to 18.4% after ageing. The changes in the relative concentration of different carbon atoms due to ageing support the above observation. Percentage concentration of C<sub>1</sub>, which is the carbon atom in the carbonyl group, increases from 3.6% to 10.6% supporting the observation that more carbonyl groups are generated due to ageing. However, ageing does not cause significant shift of binding energies for the peaks corresponding to carbonyl group. Majumder and Bhowmick [40] have observed shifts in the binding energies of the peaks corresponding to carbonyl groups only under severe conditions in the case of electron beam modified EPDM rubber surface.

The decrease in the surface hydroxyl groups due to ageing is also evident from the FT-IR spectra of the unaged and aged fibers, shown in Fig. 9. Due to prolonged ageing, the intensities of the peaks in the region 3550–3220 cm<sup>-1</sup> due to —OH stretching vibrations and at 1375 cm<sup>-1</sup> due to —OH bending vibration are reduced. The carbonyl groups on the fiber surface are not clearly visible in the FT-IR spectra of both unaged and aged fibers. This is because the intensity of the peak in the

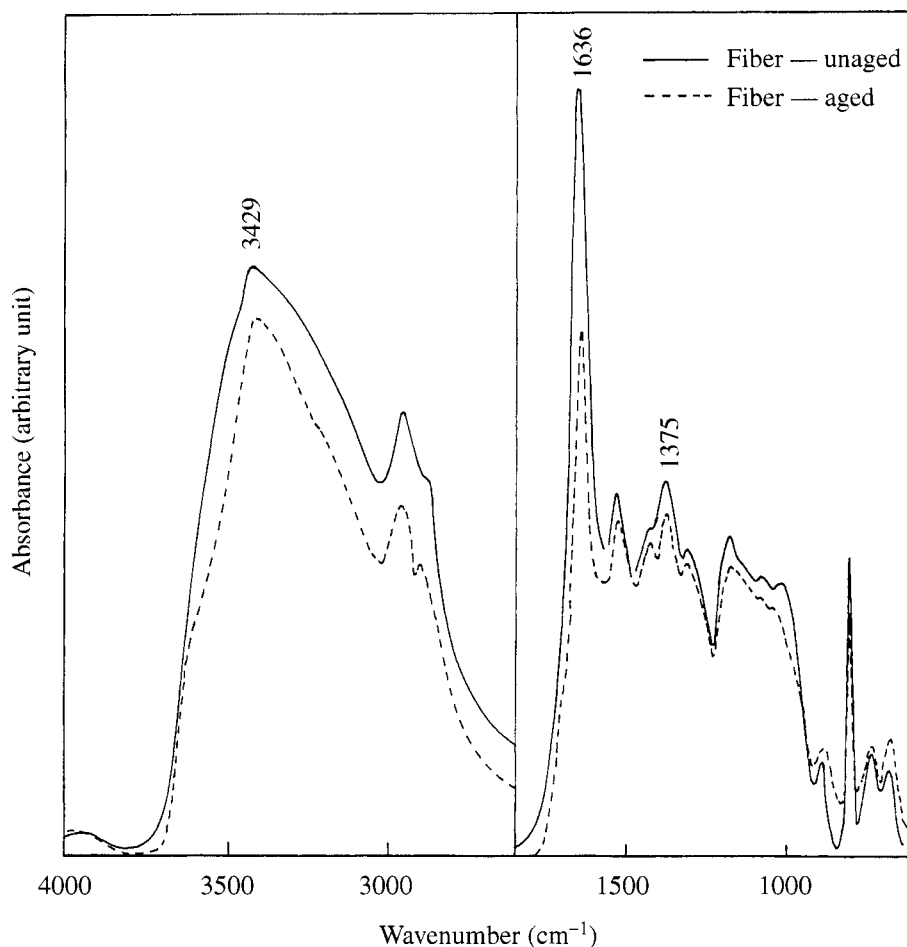


**Figure 9.** FT-IR spectra of the unaged and aged melamine fibers.

region  $1630\text{--}1640\text{ cm}^{-1}$  is masked by the intense absorption of the C—N linkage of the triazine ring.

### 3.4. Thermal stability of melamine fiber

Figure 10 shows the TG-DTG curves of unaged melamine fiber in argon and air and also the TG-DTG curve of the aged fiber in argon atmosphere. The degradation of melamine fiber both in argon as well as in air involves two major degradation steps apart from the small degradation steps, which are occurring at the early stages of degradation. These small degradation steps are mainly due to the release of  $\text{H}_2\text{O}$  and  $\text{CH}_3\text{OH}$  as detected by Devallencourt *et al.* [41], using FT-IR coupled with TG. The first major degradation step starts after  $350^\circ\text{C}$ , which is the fastest and the second step starts after  $390^\circ\text{C}$ . Table 5 lists the parameters  $T_d$  (the onset of degradation temperature),  $T_{dm}$  (the maximum degradation temperature) and

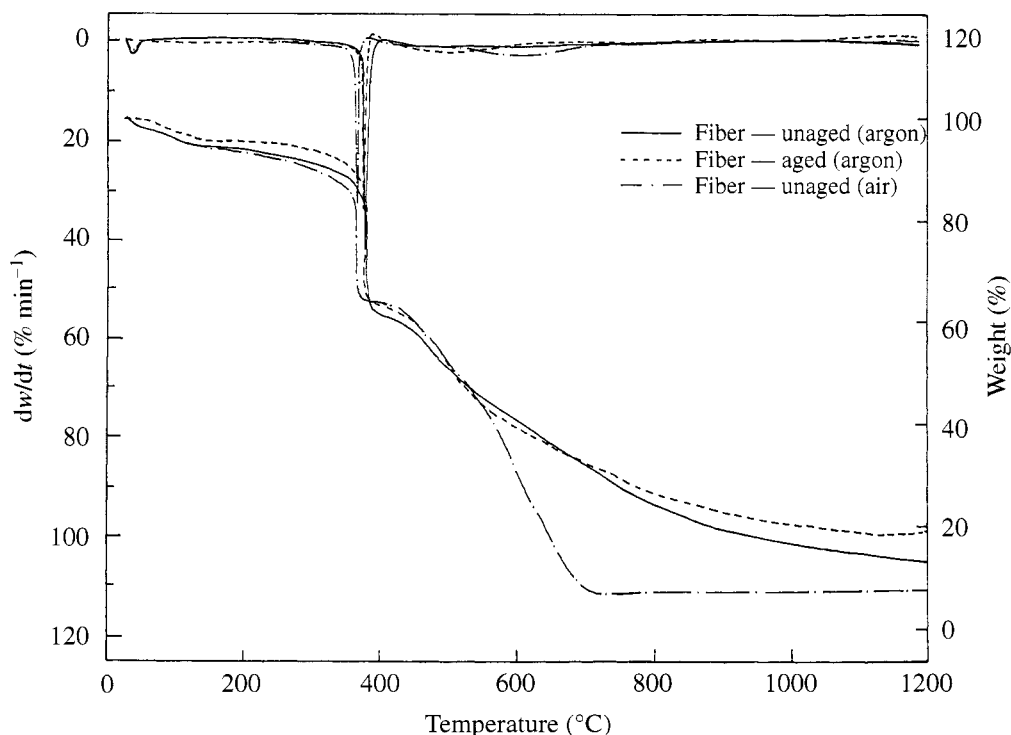


**Figure 10.** Dynamic TG-DTG curves of unaged and aged melamine fibers.

$(dw/dt)_m$  (the maximum rate of decomposition) for the first major degradation step. The table also contains the char yield at three different temperatures. From Fig. 10 and also from Table 5, on the basis of higher  $T_d$  and  $T_{dm}$ , it can be seen that the thermal stability of melamine fiber is slightly higher in an inert atmosphere like argon than in an oxidative atmosphere like air. This is because in air oxygen plays the role of a catalyst in accelerating the thermal degradation. The TG curves of the fibers, both in argon as well as in air, indicate that the degradation takes place in multiple steps. At the first major degradation temperature, there is a considerable weight loss and the DTG curve shows narrow and sharp peaks. This indicates that considerable molecular breakdown due to chain scission has taken place at the first major degradation step. Devallencourt *et al.* [41] identified the major degradation products of melamine formaldehyde resin using TG-DTG coupled with FT-IR. It can also be noted from the figure that degradation environment plays a significant role in the last degradation step. In air, degradation attains a plateau after 700°C; whereas in argon, degradation continues up to the end of the cycle. Char yield at both 800°C and 1200°C is higher in argon than that in air as shown in Table 5. The lower char yield in air may be attributed to the pyrolysis and combustion of the residual materials in the air and the formation of volatile char products due to the oxidation of char residues after the thermal decomposition [42].

**Table 5.**

Thermal degradation data of melamine fiber

Sample	Atmos- phere	$T_d^a$ (°C)	$T_{dm}^b$ (°C)	$(dw/dt)_m^c$ (% min <sup>-1</sup> )	Char yield	Char yield	Char yield
					(wt%) 400°C	(wt%) 800°C	(wt%) 1200°C
Fiber-unaged	Argon	376	379	48.3	62.5	24.6	11.6
Fiber-unaged	Air	362	367	47.5	65.8	7.5	7.5
Fiber-aged	Argon	374	379	48.3	63.8	26.7	19.2

<sup>a</sup> Onset of degradation temperature.<sup>b</sup> Maximum degradation temperature.<sup>c</sup> Maximum rate of decomposition.**Table 6.**

Decomposition temperature at various percentage weight losses

Sample	Atmos- phere	Decomposition temperature (°C) at various percentage weight loss							
		10	20	30	40	50	60	70	80
Fiber-unaged	Argon	346	376	382	439	512	603	721	885
Fiber-unaged	Air	312	361	364	458	515	563	600	639
Fiber-aged	Argon	364	374	376	455	506	582	739	1036

Ageing of the fibers does not affect  $T_d$ ,  $T_{dm}$  and  $(dw/dt)_m$ , but aged fibers produce a higher char residue. Also the initial minor degradation steps, found in the unaged fibers, are absent in the aged fibers, presumably due to the less hygroscopic nature of the aged fiber. The increased char yield of aged fibers makes them good ablative materials where a better char yield is desired to take up the high heat produced during ablation. Table 6 gives the decomposition temperature for various percent weight losses for the unaged and aged fibers. Table 6 clearly shows the high temperature stability of melamine fibers. Even after 300°C, only 10% weight loss takes place. The table also shows that initial 10% weight loss takes place at a higher temperature for aged fibers compared to that of unaged fibers in argon and also this temperature is the lowest for the fibers decomposed in air. It can also be noted that both the degradation environment and ageing play a major role in the decomposition behaviour of the fiber only after 50% weight loss. In the case of unaged fibers, 80% weight loss takes place at 885°C in argon, whereas in air, 80% weight loss takes place below 650°C. Thus the difference between the degradation processes in air and argon is evident only beyond 500°C. This means that the presence of oxygen in the air largely affects the last degradation step. For aged fibers, 80% weight loss takes place only beyond 1000°C in argon atmosphere whereas the same percent weight loss takes place at 885°C for the unaged fibers in the same atmosphere.

#### 4. CONCLUSIONS

1. AFM studies reveal that a melamine fiber filament surface consists of hills and valleys, hills being triangular in geometry. Roughness analysis of the fiber shows that there is considerable variation in surface roughness from filament to filament. The fiber surface also contains die lines occurring during the manufacturing of the fibers. Ageing of the fibers at 150°C for 7 days causes some changes in the surface features. Surface roughness of the filament increases due to ageing.
2. Melamine fibers are semicrystalline having percentage crystallinity of 19.4. Ageing increases the crystallinity from 19.4% to 22.6%.
3. X-ray photoelectron spectroscopy studies show that the fiber surface consists of a large number of both hydroxyl groups (due to the methylol compounds) and carbonyl groups (due to surface oxidation during manufacturing). Ageing causes a reduction in the hydroxyl groups and an increase in the carbonyl groups, showing that the fiber becomes less hygroscopic due to ageing. FT-IR studies confirm the reduction of surface hydroxyl groups due to ageing.
4. Thermal stability studies show that major degradation of melamine fibers takes place only beyond 300°C. There are mainly two major degradation steps in the decomposition of melamine fiber both in argon and in air. In argon, the degradation is slow and continues even beyond 1000°C; whereas, in air degradation attains a plateau after 700°C. Thermal analysis also shows that melamine fibers have a lower thermostability in an oxidative atmosphere than in an inert atmosphere. Ageing improves the char yield of the fibers, showing that the aged fibers are better ablative materials.

#### Acknowledgements

The authors thank M/s BASF South East Asia Pte Ltd., Singapore for the free supply of melamine fiber and the Indian Space Research Organization, Bangalore for sponsoring the project. One of the authors, R. S. Rajeev acknowledges the financial support provided by the Australia–India Council, Canberra, Australia for carrying out some of the experimental studies at the University of New South Wales, Sydney, Australia. Special thanks are due to Mr. Sergei Magonov, Digital Instruments, Santa Barbara, CA, USA for performing some of the AFM analyses.

#### REFERENCES

1. Technical literature, BASOFIL fiber, BASF Corporation, Enka, NC, USA (1999).
2. R. S. Rajeev, G. J. P. Kao, S. Bandyopadhyay, A. K. Bhowick and S. K. De, *Polym. Composites* **23**, 574 (2002).
3. T. J. Hoppen, *Microscope* **48**, 107 (2000).
4. L. C. Sawyer and T. D. Grubb, *Polymer Microscopy*. Chapman and Hall, London (1987).
5. R. J. Young, *Introduction to Polymers*. Chapman and Hall, London (1981).

6. V. V. Tsukruk, *Rubber Reviews* **20**, 430 (1997).
7. R. S. Rajeev, G. J. P. Kao, S. Bandyopadhyay, S. K. De and A. K. Bhowmick, *J. Mater. Sci.* **36**, 2621 (2001).
8. A. Wawkuszewski, H. J. Cantow and S. N. Magonov, *Polym. Bull.* **32**, 235 (1994).
9. J. Hautojarvi and A. J. Leijala, *J. Appl. Polym. Sci.* **74**, 1242 (1999).
10. A. De Rovere, R. L. Shambaugh and E. A. O'rear, *J. Appl. Polym. Sci.* **77**, 1921 (2000).
11. D. Snetivy and G. J. Vancso, *Polymer* **35**, 461 (1994).
12. K. D. Jandt, L. M. Eng, J. Peterman and H. Fuchs, *Polymer* **33**, 5531 (1992).
13. R. Patil, V. V. Tsukruk and D. H. Reneker, *Polym. Bull.* **29**, 557 (1992).
14. S. Rebouillat, J. C. M. Peng and J. B. Donnet, *Polymer* **40**, 7341 (1999).
15. S. F. Y. Li, A. J. McGhie and S. L. Tang, *J. Vac. Sci. Technol. A* **12**, 1891 (1994).
16. S. N. Magonov, A. Y. Gorenberg and H. J. Cantow, *Polym. Bull.* **28**, 577 (1992).
17. Y. Dzenis, D. H. Reneker, V. V. Tsukruk and R. Patil, *Composite Interfaces* **2**, 307 (1994).
18. E. Vanswijgenhoven, K. Lambrinou, M. Wevers and O. Van der Biest, *Composites Part A* **29A**, 1417 (1998).
19. A. Ishitani, *Carbon* **19**, 269 (1981).
20. C. Jones, *Carbon* **28**, 515 (1990).
21. P. Denison, F. R. Jones and J. F. Watts, *Surface Interface Anal.* **12**, 455 (1988).
22. F. Santiago, A. N. Mansour and R. N. Lee, *Surface Interface Anal.* **10**, 17 (1987).
23. K. Walterson, *Fiber Sci. Technol.* **17**, 289 (1982).
24. G. Coullerez, Y. Chevolot, D. Leonard, N. Xanthopoulos and H. J. Mathieu, *J. Surface Anal.* **5**, 235 (1999).
25. C. Sellitti, J. L. Koenig and H. Ishida, *Carbon* **28**, 221 (1990).
26. A. Ishitani, H. Ishida, G. Katagir and S. Tomita, in: *Composite interfaces*, H. Ishida and J. Koenig (Eds), p. 195. North-Holland, New York (1986).
27. "Nanoscope Command Reference Manual", Digital Instruments, Santa Barbara, CA, USA (1999).
28. S. Chattopadhyay, T. K. Chaki and A. K. Bhowmick, *Radiation. Phys. Chem.* **59**, 501 (2000).
29. K. K. Chawla, *Fibrous Materials*, Chapter 2. Cambridge University Press, Cambridge (1998).
30. Y. Nihongi and Y. Nobuo, US Patent No. 4,088,620 (1978).
31. K. Herman, O. Gerngross and W. Z. Abitz, *Physik. Chem.* **B10**, 371 (1930).
32. L. E. Alexander, *X-ray Diffraction Methods in Polymer Science*. Wiley Interscience, New York (1969).
33. L. N. Bui, M. Thompson, N. B. Mckeown, A. D. Romaschin and P. G. Kalman, *Analyst* **118**, 463 (1993).
34. D. T. Clark, A. Dilks, and H. R. Thomas, in: *Developments in Polymer Degradation — I*, N. Grassie (Ed.), Chapter 4. Applied Science Publishers, London (1977).
35. L. H. Peebles, *Carbon Fibers: Formation, Structure and Properties*, Chapter 7. CRC Press, Boca Raton, FL (1994).
36. B. Stypula and J. Stoch, *Corrosion Sci.* **36**, 2159 (1994).
37. A. M. Beccaria, G. Poggi and G. Castello, *Brit. Corrosion J.* **30**, 283 (1995).
38. S. Delpeux, F. Beguin Benoit, R. Erre, N. Manolova and I. Rashkov, *Eur. Polym. J.* **34**, 905 (1998).
39. L. T. Weng, C. Poleunis, P. Bertrand, V. Carlier, M. Sclavons, P. Franquinet and R. Legras, *J. Adhesion. Sci. Technol.* **9**, 859 (1995).
40. P. S. Majumder and A. K. Bhowmick, *Radiation Phys. Chem.* **53**, 63 (1998).
41. C. Devallencourt, J. M. Saiter, A. Fafet and E. Ubrich, *Thermochim. Acta* **259**, 143 (1995).
42. M. Rong and X. Li, *J. Appl. Polym. Sci.* **68**, 293 (1998).



## Morphology and elasticity of waterborne acrylic pressure-sensitive adhesives investigated with atomic force microscopy

J. MALLÉGOL<sup>1,\*</sup>, O. DUPONT<sup>2</sup> and J. L. KEDDIE<sup>1,†</sup>

<sup>1</sup> *Department of Physics, University of Surrey, Guildford GU2 7XH, UK*

<sup>2</sup> *UCB Chemicals, 33 Anderlechtstraat, B-1620 Drogenbos, Belgium*

**Abstract**—The morphology of pressure sensitive adhesives (PSAs), especially at the surface in contact with a release liner, is expected to have a dominant influence on the tack strength and energy in an application. We have used tapping-mode atomic force microscopy to determine the morphology at the surfaces of freshly-cast waterborne acrylic PSAs over lateral length scales of a few  $\mu\text{m}$ . We demonstrate that topographical features on silicone release liners can be used to pattern the PSA surface in contact with it. Control of the texture of a PSA surface can potentially be exploited to tailor its properties. Latex particle boundaries are much better defined at the air surface of the PSA in comparison to its back face. A series of experiments suggests that this difference results from the distribution of water-soluble species within the dry film. The pressures and processes involved in the transfer lamination process do not alter the PSA morphology. The first reported AFM images of the response of these materials to pressure and shear provide insight into the deformation mechanisms. Amplitude-distance curves on PSA surfaces show that there is a small decrease in tack and an increase in stiffness after ageing for 13 months.

**Keywords:** Acrylic; latex; pressure-sensitive adhesive; atomic force microscopy; indentation; roughness.

### 1. INTRODUCTION

Pressure-sensitive adhesives (PSAs) adhere quickly and firmly to a surface under the application of light pressure. They exhibit high adhesion strengths without necessarily any chemical bond formation at the interface [1]. PSAs are increasingly being used in more demanding applications that require enhanced performance

---

\*Current address: IRSID — Arcelor group, F-57283 Maizières-lès-Metz, France.

†To whom correspondence should be addressed. Phone: +44-1483-686803. Fax: +44-1483-686781. E-mail: j.keddie@surrey.ac.uk

characteristics [2]. Much progress has been made in understanding the mechanisms of tack and debonding in PSAs through a combination of modelling [3–6] and experiment [7–12]. This present work demonstrates a method to control the surface topography of a waterborne PSA. The topography and elasticity are then examined using atomic force microscopy. The relevance of this work will become clear in the following discussion.

Recent theoretical models [13, 14] and experimentation [15, 16] have shown that the surface roughness of the *adherend* (or probe surface) profoundly affects adhesion strength and tack energy. Likewise, the surface roughness of an *adhesive* is likely to influence the PSA performance in one or more ways: (1) decreasing the contact area between the adhesive and adherend; (2) creating interfacial microbubbles that provide suction; and (3) nucleating cavities in the de-bonding process. Each of these effects will be considered separately, although they are inter-related.

*Contact Area.* The tack energy of PSAs has been found experimentally to be proportional to the square of the *true* microscopic contact area with the adherend (as measured optically) [7]. In turn, the contact area is a function of the surface roughness of the adhesive, according to a recent model [3]. Other models have taken into account the effect of the surface roughness of the adherend in influencing the contact area with the adhesive [4].

*Microbubbles and suction.* A theory of tackiness developed by Gay and Leibler [5] assumes that the wavelengths of the roughness of the adhesive and adherend differ. When the two surfaces are placed in contact, two populations of microbubbles are created. It was proposed that these microbubbles produced suction that increased the tack energy and the force required to separate the two surfaces.

*Cavitation.* Probe tack tests have yielded great insight into the debonding mechanisms of PSAs. It has been clearly established that the formation of cavities at the interface, followed by fibrillation at higher nominal strains, is responsible for high tack energies [10]. Microbubbles at the interface, partially the result of adhesive roughness, are potential sites for cavity formation [5]. Internal interfaces in the film, resulting from poor particle coalescence, might serve as ‘weak points’ that determine the number of cavities that are formed [6].

In the case of waterborne (i.e. latex) PSAs, another factor must be considered. The presence of surfactants (and other low molecular-weight species) is likely to weaken the interface between the PSA and adherend and also might create nucleation sites for cavitation. Depending on the latex and surfactant types and the drying conditions, excess surfactant can be found at the PSA/air interface [17, 18] but also at the PSA/substrate interface [19, 20]. The presence of surfactant has been found to have a pronounced influence on the adhesion properties [21, 22]. Holl and co-workers [23] have shown that the interfacial effects resulting from the weak boundary layer of surfactant dominates the other effects influencing the adhesion properties. It is indeed noteworthy that surfactant is found at the locus of failure of the film [24].

Further development of PSAs requires an analytical technique able to probe the topography of the soft, tacky surfaces of PSAs. Optical microscopy can characterise surface features over length scales larger than the diffraction limit of light. But a technique to analyse the surface roughness of PSA surfaces and to characterise the surfactant distribution, at the nanometer scale, is also required. Detailed studies of adhesive roughness and topography are lacking in the literature.

Atomic force microscopy (AFM) has been extensively applied to many materials within the last decade, including latex films. However, in the field of PSAs, its use has been restricted by the problem of the AFM tip sticking to the adhesive surface and by deformation of the very soft surface by the tip. There are only a few reports of AFM applied to PSA surfaces [25–28]. Often AFM has been restricted to aged PSA surfaces that are less tacky and thus present less experimental difficulty [25, 26].

We have recently shown that it is possible to image latex PSA surfaces by using some rather extreme AFM tapping parameters [17]. In the present paper we demonstrate how AFM can be used as a characterization tool for PSA surfaces. Surface topography, the distribution of surfactant phases, and elasticity are all simply evaluated by this single technique. We provide the first AFM images showing the response of waterborne acrylic PSAs to pressure and shear.

## 2. MATERIALS AND METHODS

### 2.1. PSA characteristics

A model acrylic PSA latex (referred to in previous publications [17, 29] as PSA A) was investigated. The latex dispersion has a bimodal particle size distribution (average particle sizes of 180 nm and 350 nm) and a solids content of 60 wt%. It was prepared by standard semi-batch emulsion polymerization. The polymer is a random copolymer based on an acrylic ester, 2-ethylhexyl acrylate, which yields a soft and tacky material with a low glass transition temperature ( $T_g$ ). High  $T_g$  monomers (such as methyl methacrylate) are added in a smaller proportion to increase the  $T_g$ , in order to improve the cohesive strength as well as the peel and tack properties. A small amount of polar monomers (acrylic acid and methacrylic acid) are also copolymerised to improve adhesion to polar substrates and to provide sites for cross-linking reactions with other groups [13]. Dissolution of the latex polymer in organic solvent has revealed a low insoluble fraction, which indicates the presence of a significant amount of polymer chains with very high molecular weight and/or a partially cross-linked network. It is noteworthy that previous unpublished work in our laboratory has found that reducing the molecular weight did not enhance particle coalescence, as was observed by AFM. The  $T_g$  of the copolymer, as determined by DSC, is  $-45^\circ\text{C}$ . The loop-tack strength of the PSA film, determined according to Finat Test Method No. 9 (FTM9), is 512 N/m.

2.2. Preparation of samples

Films were cast onto silicone-coated release liners (30 cm × 20 cm) using a 40 μm hand-held bar coater. Both paper and polyester substrates were used. Hereafter, the release liners will therefore be referred to as silicone/paper and silicone/polyester. The films were dried under laminar air flow for 3 min on heated plates at 60°C in a controlled humidity chamber maintaining a relative humidity of 40%. (This drying temperature had been found to be the average temperature experienced by the latex on an industrial coater.) The dried films were about 20 μm thick.

PSAs laminates are usually manufactured via a lamination transfer process, which is illustrated in Fig. 1. First, the film is dried on a release liner (usually silicone/paper), then laminated on a facestock (paper or films of polymers such as poly(vinyl chloride), oriented polypropylene or poly(ethylene terephthalate)). In this work we have characterised both faces of the film: the PSA/silicone release liner face, which becomes the adherend contact face in an application, and the original top face that comes into contact with the facestock. Poly(vinyl chloride) sheets were used as the facestock in the transfer lamination process in the present work. Our sample preparation method replicated, as closely as possible, the transfer lamination process that is used in industrial production (Fig. 1). In some AFM experiments, the PSA was subjected to a pressure of  $3 \times 10^6$  Pa before analysis. The

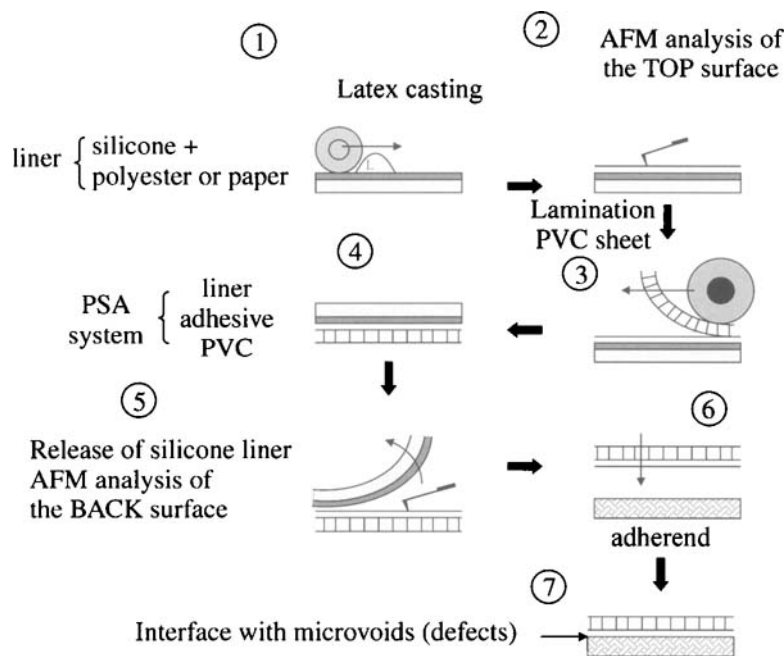


**Figure 1.** Schematic diagram showing the production of a PSA from the casting step and the transfer lamination process (Stages 1 to 4) to the end use (Stages 5 to 7). AFM analysis was performed at Stages 2 and 5.

surface of interest was placed in contact with a silicone release liner and compressed in a vise.

### 2.3. Atomic force microscopy of PSA surfaces

Small pieces (1 cm × 1 cm) of the cast PSA were cut from the large-area films and were analyzed with an atomic force microscope (Nanoscope IIIa, Digital Instruments, Santa Barbara, CA, USA) within three hours of casting. No significant evolution of the sample surface over a period of up to 12 h after casting was observed. All measurements used a silicon cantilever (NT-MDT, Moscow, Russia) equipped with an ultrasharp, conical silicon tip having a radius of curvature of about 10 nm. The nominal resonant frequency  $f_0$  of the cantilever is 320 kHz and its spring constant  $k$  is 48 N/m.

As indicated in Fig. 1, AFM analysis was performed on either the original interface with air (at Stage 2) or on the back face of the PSA after release of the silicone liner (at Stage 5). Images were recorded simultaneously in the topographic (height) mode and in the phase mode, with scan sizes ranging from 5  $\mu\text{m}$  to 30  $\mu\text{m}$ . The optimum method for obtaining images of latex PSA surfaces has been reported previously [17]. Parameters needed to describe the tapping conditions are the ‘free’ amplitude  $A_0$  and the setpoint value  $d_{sp}$ , which are defined in Fig. 2.

The high tack of the PSA surface makes it necessary to use high tapping amplitudes to impart enough energy to the tip to pull it off from the adhesive surface. The tip is prone to sticking to an adhesive surface when low tapping amplitudes are used. A high setpoint ratio is required to minimise indentation of the tip and thereby to reduce deformation of the soft surface. To obtain values of  $A_0$  and  $d_{sp}$  in metric units, a systematic calibration of the cantilever was obtained from amplitude-

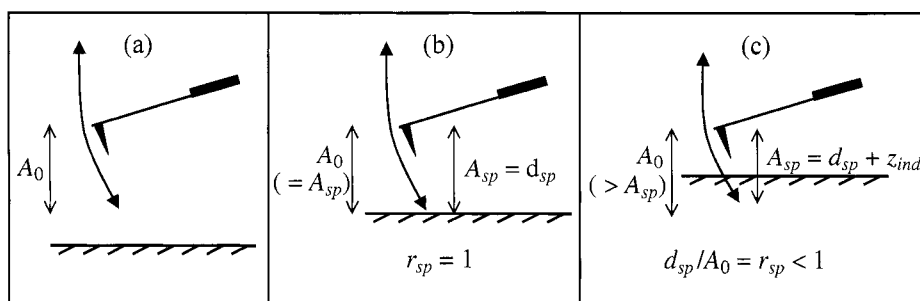


**Figure 2.** The free amplitude  $A_0$  is the oscillation amplitude of the cantilever when there is no interaction with the surface of the sample. The setpoint ratio  $r_{sp}$  for a soft surface has been defined as  $d_{sp}/A_0$ , where  $d_{sp}$ , the setpoint value, is the distance between the tip and the sample [17].  $A_{sp}$  is then the setpoint amplitude of the cantilever when it has been reduced by contact with the sample. (b) When the tip first comes into contact with the surface,  $A_{sp} = d_{sp}$  and  $r_{sp} = 1$ . (c) As the sample is raised up, the tip indents into the surface over a distance  $z_{ind}$ .  $A_{sp}$  is then equivalent to  $d_{sp}$  plus  $z_{ind}$  and  $r_{sp} < 1$ .

distance curves on a clean silicon wafer, assuming no deformation of the silicon surface and no bending of the cantilever during tapping [30].

All AFM images presented here have been obtained with nearly the same tapping conditions, as follows. The setpoint distance  $d_{sp}$  was between 90 and 100 nm for all measurements.  $A_0$  was typically 20 nm above the  $d_{sp}$  for the air surfaces of the PSAs and 30 to 40 nm above the  $d_{sp}$  for the face delaminated from the release liner. These tapping conditions ensure that the indentation of the AFM tip into the PSA surface is small enough to avoid significant distortion of the morphology. It is, however, important to realise that the surface is necessarily indented by contact with the AFM tip [17].

Amplitude-distance curves obtained with the AFM have been used to monitor the adhesion and mechanical properties of the surfaces. In an amplitude-distance curve, the variation of amplitude of the cantilever oscillation is monitored as a function of the scanner displacement as the sample surface is brought closer to the cantilever tip. When the tip is far from the sample surface, the amplitude of the cantilever oscillation is, by definition,  $A_0$ . When the tip enters into the range of interaction forces with the surface, there is usually a slight decrease in the free amplitude value and a phase shift in the oscillation. The contact point is defined as the start of the amplitude decrease.

Amplitude-distance curves were obtained from PSA surfaces using different  $A_0$  values (and hence different tapping energies). A qualitative comparison of fresh and aged PSA surfaces was made. The curves were repeated in five different areas [31], and examples presented here are representative of typical results. Amplitude-distance curves obtained from the PSA surface can also be used to evaluate the indentation depth of the tip into the PSA surface, as described elsewhere [17], and thereby can probe the surface hardness.

### 3. RESULTS AND DISCUSSION

This paper is divided into three inter-connected sections. The first section shows that surface features on the silicone substrate are permanently imprinted in the PSA cast on it. The second section compares the particle coalescence between the top and the back faces and considers the origin of the observed differences. The third section qualitatively explores whether the elasticity of the PSA surfaces evolves over time.

#### 3.1. *Imprinting of substrate patterns on the PSA surface*

We first consider the morphology of the surface of the silicone/polyester release liner. Figure 3 shows a large area AFM scan showing the topography of the silicone/polyester surface. Channels with a depth of about 80 nm and a width of 1–2  $\mu\text{m}$  are observed in topographical images. The pattern and the density of channels vary across the surface of the release liner. The channels are attributed to imperfections resulting from the silicone coating process. There is no evidence that the surface chemistry varies laterally across the channels.

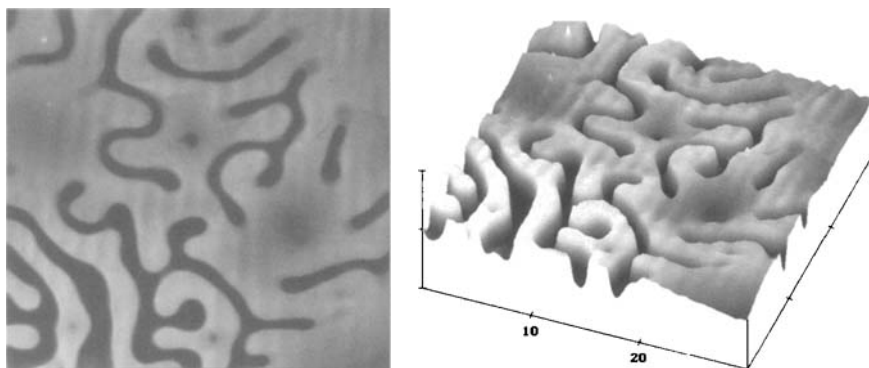


**Figure 3.** Top view (left) and 3D-view (right) of the irregular silicone/polyester substrate. Channels, with an average depth of 80 nm, are observed at the surface. Scan size:  $30\ \mu\text{m} \times 30\ \mu\text{m}$ ; height = 300 nm (left) and 200 nm per division (right).

We have discovered that this pattern of channels in the silicone/polyester release liner can be imprinted into the back face of a PSA film that is cast upon it. Figure 4 illustrates the effect as characterised by AFM. The top face of the PSA (obtained during Stage 2 of the process) has no dominant features except for the texture of the latex particles. The back face (obtained during Stage 5), by contrast, shows ridges with an appearance and dimensions that are comparable to the silicone/polyester surface. It is apparent that these ridges result from ‘moulding’ in the 80 nm deep silicone channels, but they are only about one-half the height expected if accurate replication had occurred. Hence, there is evidence for some relaxation or flow of the surface after delamination. The apparent differences between the topography of the channels and the moulded ridges, however, can also be partly attributed to deformation of the PSA induced by indentation of the AFM tip. In any case, the PSA surface does not fully flatten under the action of capillarity [32] when in contact with air, as would be expected for a strictly viscous liquid.

Replication of the release layer topography was likewise demonstrated with a silicone/paper substrate having greater roughness than in the silicone/polyester. Figure 5 shows the results. Ridges, up to 300 nm high, are observed in the substrate (Fig. 5A). This topography is replicated in the PSA surface that was delaminated from it (Fig. 5B), although the ridges are less than 200 nm in amplitude.

As already described in the Introduction, microbubbles might result from a difference in the length scales of roughness at an adhesive/adherend interface. It has been suggested that these bubbles create suction that can increase the adhesion strength [5]. On the other hand, excessive surface roughness of either the adhesive or adherend will limit the contact area at the interface, which can lower the adhesion strength and tack energy [3, 7]. Our results indicate that patterns on a silicone release layer could be used to tailor the surface topography of the PSA surface in order to impart the desired properties. Recent models of PSA adhesion specifically consider the roughness of the adhesive by describing it as cylindrical columns [3].

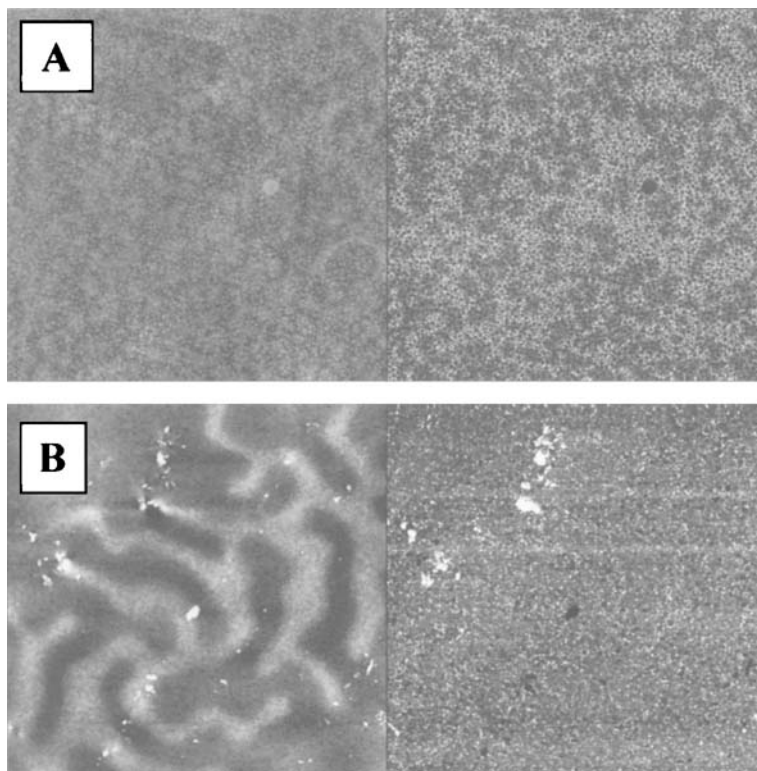


**Figure 4.** AFM images of the PSA showing the (A) top surface (Stage 2) (vertical scale: height = 50 nm; phase = 90 degrees) and the (B) back surface delaminated from the silicone/polyester release liner (Stage 5) (height = 100 nm; phase = 90 degrees). In both A and B, the height image is on the left, and the phase image is on the right. Scan size for both images is  $30\text{ }\mu\text{m} \times 30\text{ }\mu\text{m}$ . In 4B, features of the substrate are clearly apparent in the topographical image. The average height of the ridges is 40 nm. The distinct white spots are interpreted as dust contamination.

Patterns in the silicone release liner could be used to create any desired geometrical features at the optimum length scales.

### 3.2. Comparison of top and back PSA surfaces

Film morphology on a shorter length scale is considered next. Films usually appear flat over lateral distances of a few  $\mu\text{m}$ . Figure 6A is a representative image of the top surface of the PSA (Stage 2). Previous analysis has concluded that the particles near the air surface are flattened and cylindrical in shape [17]. Particle identity is clearly retained. The reason for this non-coalescence of particles has been previously attributed to the presence of the latex serum, containing surfactants and other low molecular weight species (mainly residues from the emulsion polymerisation) [29]. This liquid-like phase is rather uniformly distributed near the top surface, as can be observed in the larger area AFM images in Fig. 4A.



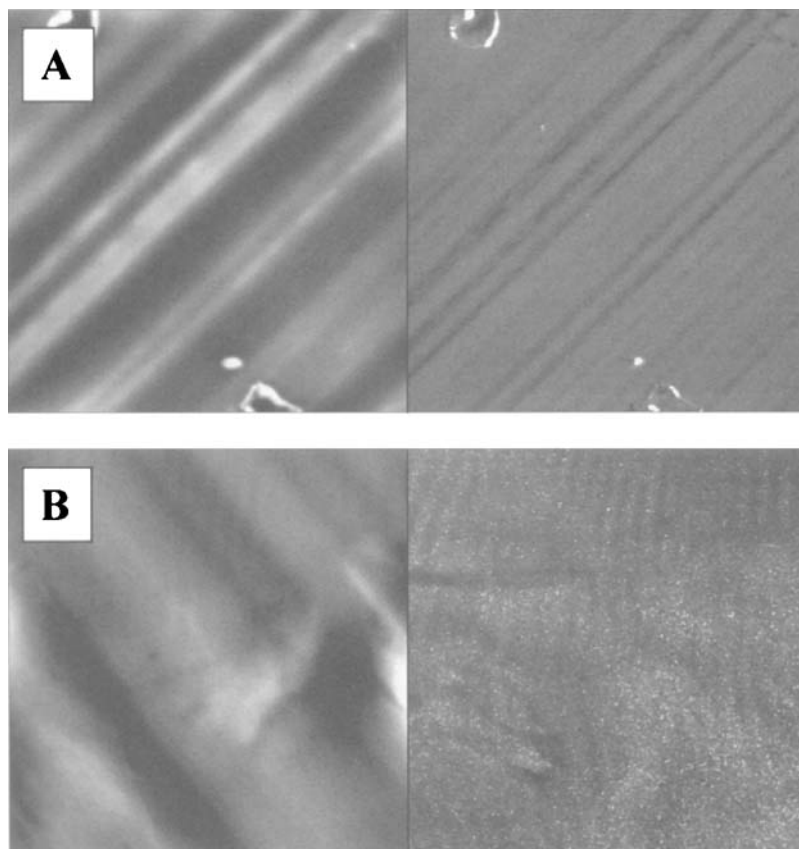


**Figure 5.** (A) AFM image of the silicone/paper release liner. (Vertical scale: height = 300 nm; phase = 50 degrees). (B) AFM image of the delaminated face of a PSA cast on the silicone/paper, 1 h after delamination (Stage 5). (Height = 200 nm, phase = 50 degrees). In both A and B, the height image is on the left, and the phase image is on the right. Scan size for all images:  $30\ \mu\text{m} \times 30\ \mu\text{m}$ .

In PSA technology, the film face in contact with the release liner during the transfer process is of great interest because it will be subsequently placed into contact with the adherend (Stage 6 in Fig. 1). Figure 6B shows such a surface after delamination from the release liner. We are not aware of any previous reports of an AFM image of the *back* face of a waterborne acrylic PSA. There is an obvious difference between this image of the back face in comparison to the top face (Fig. 6A).

Individual particles can be seen on the back face, especially in the phase image. The back surface is less regular and apparently rougher than the top surface. The dark areas in the height image and the bright regions in the phase image are interpreted as species formerly contained in the latex serum. This second phase is not uniformly distributed around the particles. Some aggregates have formed. In comparison to the top face, the particle boundaries are less well defined. At the back face, there appears to be less of the latex serum phase. This apparent difference in the latex serum concentration between top and back faces is currently

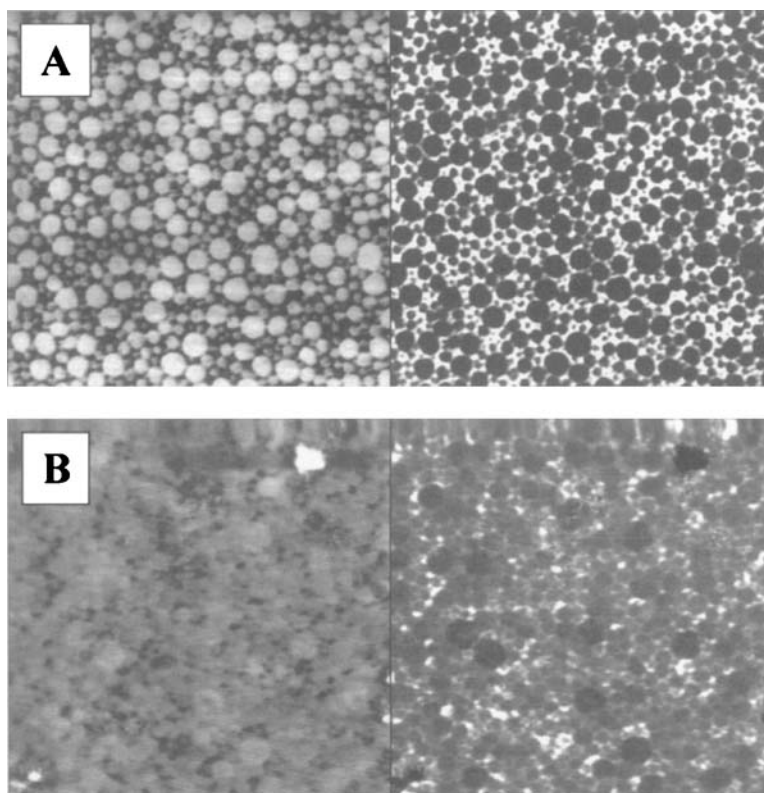


**Figure 6.** AFM images of (A) the top face of the PSA (Stage 2) and (B) the back face after delamination from a silicone/polyester release liner (Stage 5). (Vertical scale: height = 50 nm, phase = 90 degrees. Scan size:  $5\ \mu\text{m} \times 5\ \mu\text{m}$ .) In both A and B, the height image is on the left, and the phase image is on the right.

under investigation in our laboratory using complementary analytical techniques. The silicone/PSA interface probably has a low energy, which would not favor segregation of surfactant. The distribution of water-soluble species is probably influenced by the water concentration profiles during drying.

We now consider the reasons for the observed differences in morphology when comparing the back and top surfaces. These differences could be the result of one or more stages in the processing that are experienced by the back surface but not by the top face. The back face experiences contact with the silicone release liner during drying (Stage 1), the pressure applied with the rubber roll during the lamination of the PSA on the PVC sheet (Stage 3), prolonged contact with the silicone release liner (mainly Stage 4), and the operative forces during the delamination of the silicone liner (Stage 5). These factors will be considered in the following discussion.

First, experiments were conducted to explore the effect of pressure and delamination on the morphology and arrangement of particles, as a way to mimic the effects of delamination in Stage 5. A silicone/polyester sheet was applied to the top face of a PSA under slight pressure for two seconds and then removed. This procedure was

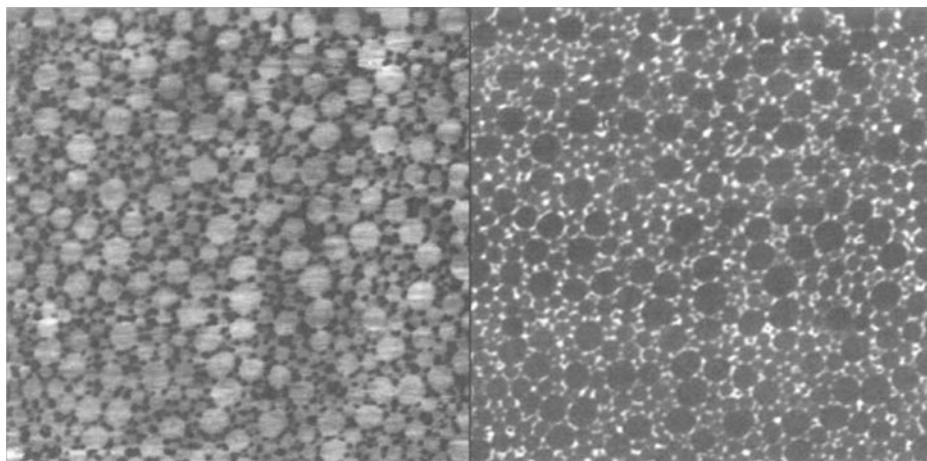


**Figure 7.** AFM images of the PSA top face that had been pressed lightly with a silicone/polyester sheet and left in contact for 4 h before delamination. (Scan size:  $5\ \mu\text{m} \times 5\ \mu\text{m}$ ; height = 50 nm, phase = 90 degrees). The height image is on the left, and the phase image is on the right.

repeated three times, and then the surface was analysed by AFM. Images obtained before and after this process appear very similar. The phase contrast is found to be slightly lower, but particle boundaries are still clearly defined, and there is nothing in common with what is observed at the back face. These simple experiments indicate that contact with a silicone surface, the application of light pressure, and de-lamination are not sufficient to disrupt the phase separating the particles at the top surface. It is not expected that these factors contribute strongly to the observed morphology at the delaminated back face (Fig. 6B).

A further experiment aimed to determine the effect of prolonged contact with a silicone surface on the particle morphology and arrangement of the top surface of the PSA. One might expect that a long contact time with silicone substrate could allow reorganisation of the surfactant phase and simultaneous particle coalescence. However, after the top face was placed in contact for four hours with a silicone/polyester release liner, there was no significant change in the appearance after delamination, as revealed in Fig. 7. Because the back faces in our experiments are usually analysed after less than two or three hours of lamination, we do not interpret the contact with the silicone liner as being related to the very different structure observed on the delaminated back face.

In another experiment, a silicone/polyester sheet was applied onto the top face of a PSA for 10 s under a high thumb-pressure that also induced shear forces. The silicone/polyester was then removed, and the PSA surface was immediately analysed with AFM. The start of the scan was delayed for four minutes after the removal of the silicone/polyester sheet while the AFM scanning parameters were being optimised. Two successive scans of the same area were performed and are shown in Fig. 8. The first scan was recorded, while moving from the top to the bottom (Fig. 8A), and ended 11 min after the silicone liner removal. The second

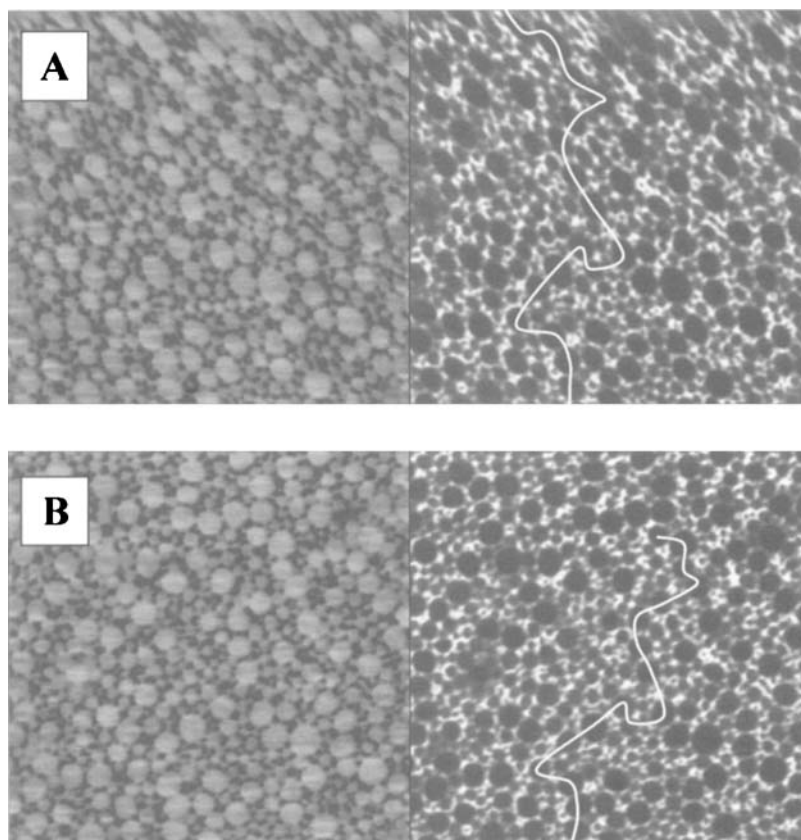


**Figure 8.** AFM images of the PSA top face after being pressed with silicone/polyester (under combined shear and pressure) (A) 4 min to 11 min after removal and (B) 11 min to 18 min after removal. After 12 min, the particles have returned to their original state. (Scan size:  $5\ \mu\text{m} \times 5\ \mu\text{m}$ ; height = 50 nm, phase = 90 degrees.) In both A and B, the height image is on the left, and the phase image is on the right.

scan was started immediately after, moving from the bottom to the top (Fig. 8B). The second scan finished 18 min after the silicone liner removal.

It can be observed in the first scan that particles are distorted from their circular shape by the shear stress that had been applied. As the scan progresses to the bottom of the image, the particles start to relax, and they appear less deformed. When the first scan is finished, the particles have almost completely relaxed, and so there is not much difference in the particle shape at the bottoms of the two images (Fig. 8A and B).

A white line has been drawn on the images as a guide to the eye to illustrate the consistency of the position of the particles in relation to each other. Elastic contraction of the surface, primarily in the direction running from the top to the bottom of the image, is vividly demonstrated. Comparison of Fig. 8B to images of the top surface after casting (Stage 2), such as in Fig. 6A, reveals that the surface is

not permanently altered by the application of pressure and shear forces great enough to deform the particles and to strain the film. The particles keep the same neighbors; they are displaced across the surface without changing their position in relation to each other. Apparently, stress is transmitted from one particle to another, but this stress does not disrupt the phase that surrounds the particles. Particle identity is retained.

These results provide convincing evidence that neither the pressure of the lamination process (Stage 3) nor the delamination of the silicone release liner (Stage 5) should alter the morphology of the back face. Instead, we propose that the differences observed between Figs 6A and 6B are due to differences in the distribution of the surfactant and other water-soluble species in the film that develop during film formation. In other work, we have shown that the surfactant phase at the top surface can stabilise particles against coalescence [29]. There appears to be less surfactant at the back face, and so there is a greater degree of coalescence. The reason for this difference in the surfactant distribution is currently under investigation in our laboratory.

In a similar experiment, the PSA surface was once again subjected to a shear force by a silicone sheet, but then the sheet was left in contact for 12 min before delamination. AFM analysis of the delaminated surface found no evidence for particle deformation or strain of the surface, as was the case in Fig. 8A when the surface was analysed shortly after delamination. We conclude that the PSA surface was initially deformed elastically during the application of the pressure and shear. During the storage, however, the PSA surface was able to relax to its original morphology by moving laterally along the silicone surface.

The elasticity and plasticity of the PSA surface was also examined on a larger length scale. The rough surface of a silicone/paper release liner (*cf.* Fig. 5A) was pressed onto the top of a PSA film using a vise. The high resulting pressure (*ca.* 3 MPa) was found to have a limited effect on the individual particles, with only some partial particle aggregation being observed. On larger length scales, there was no impression or indentation into the PSA surface from the topography of the silicone/paper substrate. The surface of the dry PSA behaved elastically and did not exhibit any plastic deformation.

### *3.3. Elasticity and tack of fresh and aged PSAs*

From a practical point of view, any stiffening of the PSA surfaces would have an impact on adhesion performance, particularly because it would inhibit the wetting of an adherend. In PSA films formed from rubber/tackifier blends cast from solution [33], stiffening was observed and was attributed to phase segregation during ageing. The phase separation also induced a loss of tack, which enabled the AFM analysis of the aged PSA films. In the acrylic latex PSA investigated here, there is no tackifying resin. Experiments were conducted to determine if the film properties at the surface were subject to change with ageing.

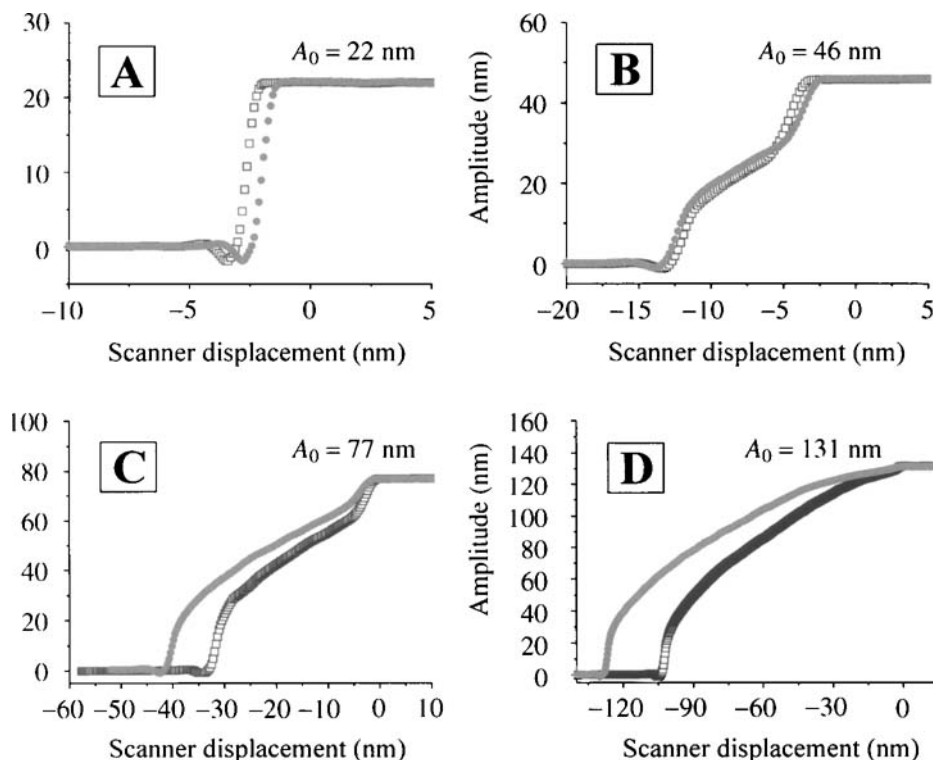


**Figure 9.** Comparison of indentation curves on the PSA's back surfaces of samples freshly cast (●) or aged 13 months (□), with four different free amplitudes: (A) 22 nm, (B) 46 nm, (C) 77 nm and (D) 131 nm. (The motion of the scanner moving upward is represented as moving from the right to the left in all figures.) A more complete description of the amplitude-distance curves can be found in Ref. [17].

We have noticed that the scanning conditions necessary to image *fresh* PSA films are not the same that are required for *aged* films. When the PSA is aged it requires lower tapping amplitudes, which suggests that it becomes stiffer and less tacky over time.

Amplitude-distance curves obtained from 13-month old PSA samples were compared to data obtained from freshly cast surfaces to explore whether there was any change in tack or stiffness with ageing. The analysis was performed on the back surfaces after delamination from the silicone release layer. The aged PSA was delaminated immediately before the AFM analysis to ensure that there was no surface contamination during the period of ageing, which would interfere with the measurements. The amplitude-distance curves for four different  $A_0$  are shown in Figs 9A–D.

When  $A_0 = 22$  nm, the tapping amplitude falls to zero shortly after contact between the tip and the surface. The amplitude for the fresh surface falls after a displacement that is about 1 nm less than found for the aged surface. This result indicates that the aged surface is slightly *less* tacky (as detected by the AFM tip).

With such a relatively low amplitude, the energy of the cantilever is quite low. Therefore, the attractive forces between the tip and the PSA surface are sufficient to trap the tip, causing the amplitude to fall to zero after a small displacement.

With  $A_0 = 46$  nm, there is similarly evidence that the aged surface is slightly less tacky, as indicated by the drop in amplitude on the fresh surface after a smaller displacement. Only small differences between the indentation into the fresh and aged surfaces are observed.

For the larger amplitudes ( $A_0$  of 77 nm and 131 nm), the energy of the cantilever is high enough to overcome the adhesion forces, and thus the amplitude does not drop abruptly after small displacements with the AFM tip being trapped on the surface. It then becomes possible to use the tip to indent into the surface to probe qualitatively the surface hardness. If a hard surface is moved toward the tip, then the amplitude would fall by the same distance as the displacement. The slope of the amplitude-distance curve consequently is unity for a hard surface. With a soft surface, the amplitude falls by an amount that is less than the distance of the scanner displacement. In Figs 9C and D, the amplitude decreases less with the scanner displacement for the fresh PSA in comparison to the aged PSA, which means that the indentation depth is greater in the fresh surface. This result suggests that there has been some stiffening in the aged PSA.

The information yielded by the amplitude-distance curves is then two-fold. There is a slight decrease in tackiness of the PSA during ageing, and it is accompanied by a slight stiffening of the surface. It is important, however, to note that the changes measured in these waterborne acrylic PSAs are very small. This result is in good agreement with the observation that the bulk properties of acrylic PSAs are stable over time.

Amplitude-distance curves provide a useful indication of the optimum tapping conditions for PSA surfaces. They allow the microscopist to define the zone of instability of the scanning parameters where the adhesion forces can provoke steep changes in amplitude. For example, with  $A_0 = 22$  nm, the amplitude falls to zero after a variation of only 1 nm! When  $A_0$  is small, there is a high sensitivity in the tip amplitude to a small scanner displacement, mainly because the energy of the oscillating tip is not high enough to overcome the adhesion forces. This is the reason why the use of a large  $A_0$  is necessary to image adhesive surfaces.

#### 4. SUMMARY

AFM is a powerful technique to characterise PSA surface topography and to reveal the extent of particle coalescence during film formation. We have discovered that corrugations on silicone substrates leave an imprint on the back face of PSA films, which persists over time and even after being compressed. Many applications of PSAs (labels, tapes, films) use a silicone-coated substrate as a release liner. Any defects or roughness transferred to the back face of a PSA film will be placed in contact with the adherend over the lifetime of the PSA. In turn, any interfacial voids

associated with the surface roughness are likely to influence the adhesion strength and the tack energy.

Particles are not coalesced at the top face of a waterborne, acrylic PSA. The particles are less distinct at the back face after delamination from the release liner. This different appearance of the back face can be attributed neither to the pressure during the lamination process nor to the removal of the silicone layer. It is very likely that the difference results from less surfactant (and other low molecular-weight species in the latex serum) being present at the back face.

The elasticity of the PSA surface has been demonstrated in a very visual manner. When subjected to a shear stress, the particles are distorted in shape, but they relax to their original shape within 12 min after release of the shear stress. The particles retain the same neighbors as they move laterally across the surface, during relaxation of the stress.

After ageing, PSA films do not lose their elastic properties. Only minor changes are detected in indentation curves after ageing PSAs for 13 months. Aged samples appear to be slightly less tacky and slightly stiffer than the fresh ones.

This work has illustrated that AFM provides numerous insights into the film formation and properties of PSA films. Further uses of AFM include the investigation of the influence of tackifiers on morphology and the origins of water whitening.

## REFERENCES

1. C. Creton, in: *Materials Science and Technology: A Comprehensive Treatment*, H. E. H. Meijer (Ed.), Vol. 18, p. 708. VCH, Weinheim, Germany (1997).
2. W. Brockmann and R. Hüther, *Int. J. Adhesion Adhesives* **16**, 81 (1996).
3. P. Tordjeman, E. Papon and J. J. Villenave, *J. Chem. Phys.* **113**, 10712 (2000).
4. C. Creton and L. Leibler, *J. Polym. Sci. B: Polym. Phys.* **34**, 345 (1996).
5. C. Gay and L. Leibler, *Phys. Rev. Lett.* **82**, 936 (1999).
6. I. Chikina and C. Gay, *Phys. Rev. Lett.* **85**, 4546 (2000).
7. P. Tordjeman, E. Papon, J.-J. Villenave, *J. Polym. Sci. Part B: Polym. Phys.* **38**, 1201 (2000).
8. A. Falsafi, M. Tirrell and A. V. Pocius, *Langmuir* **16**, 1816 (2000).
9. Y. Y. Lin, C.-Y. Hui and H. D. Conway, *J. Polym. Sci. B: Polym. Phys.* **38**, 2769 (2000).
10. H. Lakrout, P. Sergot and C. Creton, *J. Adhesion* **69**, 307 (1999).
11. T. Ondarcuhu, *J. de Physique II (France)* **7**, 1893 (1997).
12. A. J. Crosby and K. R. Shull, *J. Polym. Sci. B: Polym. Phys.* **37**, 3455 (1999).
13. D. Satas, in: *Handbook of Pressure Sensitive Adhesives*, 3rd edn, D. Satas (Ed.), Van Nostrand Reinhold, New York (1989).
14. B. N. J. Persson and E. Tosatti, *J. Chem. Phys.* **115**, 5597 (2001).
15. A. Chiche, P. Pareige and C. Creton, *C.R. Acad. Sci. Paris, t. I Série IV* **1**, 1197 (2000).
16. A. Zosel, *J. Adhesion Sci. Technol.* **11**, 1447 (1997).
17. J. Mallégol, O. Dupont and J. L. Keddie, *Langmuir* **17**, 7022 (2001).
18. A. Tzitzinou, P. M. Jenneson, A. S. Clough, J. L. Keddie, J. R. Lu, P. Zhdan, K. E. Treacher and R. Satguru, *Prog. Organic Coatings* **35**, 89 (1999).
19. M. W. Urban, *Prog. Organic Coatings* **32**, 215 (1997).
20. F. Belaroui, Y. Grohens, H. Boyer and Y. Holl, *Polymer* **41**, 7641 (2000).
21. J. Y. Charneau, P. A. Gerin, L. Vovelle, R. Schirrer and Y. Holl, *J. Adhesion Sci. Technol.* **13**, 203 (1999).



22. A. Zosel and B. Schuler, *J. Adhesion* **70**, 179 (1999).
23. P. A. Gerin, Y. Grohens, R. Schirrer and Y. Holl, *J. Adhesion Sci. Technol.* **13**, 217 (1999).
24. J. Y. Charneau, E. Kientz and Y. Holl, *Prog. Organic Coatings* **27**, 87 (1996).
25. A. Paiva, N. Sheller, M. D. Foster, A. J. Crosby and K.R. Schull, *Macromolecules* **33**, 1878 (2000).
26. A. Paiva and M. D. Foster, *ACS Polymer Preprints* **41**, 1433 (2000).
27. A. Doring, J. Stahr and S. Zollner, *Adhesives Age* **43** (9), 39 (2000).
28. A. G. Gilicinski, R. J. Haney, A. Famili and T. Mebrahtu, *J. Adhesive Sealant Counc.* **1**, 513 (1996).
29. J. Mallégo, O. Dupont, C. Jeynes, P. J. McDonald and J. L. Keddie, *Langmuir* **18**, 4478 (2002).
30. X. Chen, M. C. Davies, C. J. Roberts, S. J. B. Tendler, P. M. Williams, J. Davies, A. C. Dawkes and J. C. Edwards, *Ultramicroscopy* **75**, 171 (1998).
31. N. A. Burnham, R. J. Colton and H. M. Pollock, *Nanotechnology* **4**, 80 (1993).
32. S. E. Orchard, *Appl. Sci. Res. A* **11**, 451 (1962).
33. A. Paiva, N. Sheller, M. D. Foster, A. J. Crosby and K. R. Shull, *Macromolecules* **34**, 2269 (2001).

## **Relating material surface heterogeneity to protein adsorption: the effect of annealing of micro-contact-printed OTS patterns**

GERALD HODGKINSON and VLADIMIR HLADY \*

*Department of Bioengineering, 50 S. Central Campus Drive, Room 2480, University of Utah, Salt Lake City, UT 84112, USA*

**Abstract**—We have investigated the influence of micrometer- and sub-micrometer-scale surface heterogeneities in patterned octadecyltrichlorosilane (OTS) films on human serum albumin (HSA) adsorption and its spatial distribution. 5- $\mu\text{m}$ -wide OTS patterns were created on glass substrates by micro-contact printing and in some instances subsequent annealing was used to alter OTS molecule distribution within the patterns. Scanning force microscopy (SFM), advancing water contact angles and water vapor condensation figures were used to characterize the OTS films and to assess the nature of the heterogeneities within the various surface areas. High-resolution fluorescence microscopy was used to record images of fluorescently labeled albumin on OTS patterned films and fluorescence intensity was quantified and converted into the adsorbed amount. Adsorbed albumin was also characterized through SFM measurements. Combined SFM topography and lateral force microscopy (LFM) imaging revealed that micro-contact printing of OTS onto glass both replicated the stamp pattern and created small islands within the non-stamped regions between the patterns. The OTS coverage within stamped regions was not fully continuous but improved with subsequent annealing. Annealing also resulted in OTS island growth within the non-stamped regions and decreased average wettability on both the stamped and non-stamped areas. The extent of albumin adsorption was not proportional to OTS coverage, but correlated with the sub- $\mu\text{m}$  distribution of OTS chains. We inferred that the surface distribution of ligands such as OTS on a sub- $\mu\text{m}$  length scale determines the nature of albumin adsorption and its kinetics.

**Keywords:** Surface heterogeneity; micro-contact printing; force microscopy; albumin adsorption; fluorescence microscopy.

---

\*To whom correspondence should be addressed. Tel.: (1-801) 581-5042. E-mail: vladimir.hladý@m.cc.utah.edu

## 1. INTRODUCTION

Adsorption of proteins on biomaterials and model surfaces has been studied extensively in the past using a number of analytical techniques. A majority of these techniques, including ellipsometry, total internal reflection spectroscopy, surface plasmon resonance and Fourier transform infrared attenuated internal reflection, provided an averaged measure of protein adsorption on presumably uniform surfaces because of their inherent inability to spatially resolve the build-up of protein films at a sub-micrometer scale [1–4]. The majority of experiments conducted on protein adsorption to date fail to address the effects that adsorbent surface heterogeneities have on sub-micrometer scale protein 2D distribution in the adsorbed layer. To address this shortfall in the study of protein adsorption, scanning force microscopy (SFM) techniques, which provide nanometer-scale resolution surface information, have been used to investigate protein distribution on chemically heterogeneous substrates [5–8]. However, in order to resolve individual proteins, SFM requires ultra-flat substrates and has been shown to disrupt protein layers [6], especially in contact mode scanning. Similarly, scanning near-field optical microscopy, although it appears to be a promising method to monitor spatial protein distribution in protein layers [9], may also cause protein film damage. As a result of all these limitations, little has been done to show how micrometer and sub-micrometer substrate heterogeneities affect spatial and temporal protein adsorption patterns.

In the present study, we have combined SFM with high-resolution fluorescence microscopy (hrFM) to gain new information about adsorbent material heterogeneity effects on protein adsorption. Although limited by optical diffraction, hrFM can be used to monitor spatial and temporal protein adsorption on biomaterial surfaces both qualitatively and quantitatively [10–13].

In the past, self-assembled monolayers (SAMs) of organosilanes and alkanethiols have been frequently used as model surfaces to study the nature of protein adsorption on solid surfaces. The degree of organic molecules coverage on these surfaces and thus the surface wettability can be precisely controlled through a number of methods, as described in the literature [14, 15]. The hydrophobicity of SAMs has been known to control the amount of protein a modified substrate will adsorb [15, 16]. SAM substrates can be readily and reproducibly fabricated with single or multiple types of organic molecules. A variant of SAMs with spatially controlled hydrophobicity is the so-called ‘wettability gradient surface’ in which organic molecule coverage changes along one of the surface linear dimensions [17]. Using octadecyltrichlorosilane (OTS) wettability gradient surfaces, we have shown previously that albumin adsorption increases with increasing surface coverage of OTS up to a certain limit: any increase of OTS surface coverage above 42% neither affected albumin adsorbed amount nor its adsorption kinetics from a dilute albumin solution [17].

Micro-contact printing ( $\mu$ CP) is another well-known method to spatially control proteins on surfaces through creating SAM patterns [18–20].  $\mu$ CP methods have

been refined to enable the formation of well-defined sub-micrometer scale OTS features [21, 22] and the physical structure and organization of stamped OTS films have also been characterized [23–27].

The aim of this study was to investigate how heterogeneities and micro-gradients in a patterned OTS film directed the spatial distribution of adsorbed albumin. We used hrFM to monitor the course of human serum albumin adsorption on patterned OTS films with distinct differences in surface heterogeneities. The hrFM protein adsorption data were then matched and statistically correlated with the SFM-detected spatial distributions of OTS heterogeneity on the adsorbent material. Adsorbed albumin layers were also characterized with SFM techniques to confirm the results observed with hrFM measurements.

## 2. EXPERIMENTAL

### 2.1. Micro-contact printing

Poly(dimethylsiloxane) (PDMS) stamps and stamp pads were fabricated by curing Sylgard-184 (Dow Corning) prepolymer in silicon molds at an elevated temperature. The patterned mold used in these experiments consisted of a  $3 \times 3 \text{ mm}^2$  patterned area composed of  $5 \text{ }\mu\text{m}$  wide,  $1540 \text{ nm}$  high,  $3 \text{ mm}$  long mesas separated by  $5 \text{ }\mu\text{m}$  wide troughs (Mikromasch, Tallinn, Estonia). Planar silicon surfaces were used to fabricate featureless surface stamp pads. All molds and glass substrates used for OTS modification as well as glass surfaces used as controls were cleaned in a 'piranha' ( $\text{H}_2\text{O}_2/\text{H}_2\text{SO}_4$ , 1 : 2 (v/v)) mixture, rinsed several times with double-distilled deionized (DD) water, then dried with filtered nitrogen gas immediately prior to each OTS reaction. A scanning force microscope (Explorer, Topometrix) was used to verify the faithful reproduction of the silicone mold topography on the PDMS stamps. OTS-patterned surfaces were created by a stamp pad method as described previously [21]. Briefly,  $10 \text{ mM}$  OTS in anhydrous n-hexane (Sigma) was applied to a PDMS stamp pad and allowed to evaporate and absorb into the pad. The stamp pad was then dried for  $20 \text{ s}$  with a stream of filtered nitrogen. A stamp was brought into contact with the stamp pad for  $6 \text{ s}$  using a stepping motor stage to enable the transfer of OTS molecules and a portion of any remaining solvent to the stamp. The stamp was finally brought into contact with a pre-cleaned glass coverslip (thickness #1) for  $20 \text{ s}$ .

Upon stamping, the OTS patterned substrates were either immediately rinsed with hexane to remove any non-reacted OTS and then sonicated in an ethanol/DD water (1 : 1 (v/v)) mixture or first annealed followed by hexane rinsing and ethanol/water sonication step. The annealing step consisted of placing the OTS-patterned substrate into a covered glass dish in an oven (VWR) for  $20 \text{ s}$  where the glass dish surface temperature was  $122^\circ\text{C}$  and the oven air temperature was  $95^\circ\text{C}$ . Positive controls of both non-annealed and annealed OTS films were produced using smooth, planar stamps. Clean glass surfaces served as negative controls.

## 2.2. OTS pattern characterization

**2.2.1. Water contact angle.** Advancing water contact angles were measured on the OTS-patterned substrates and on all control surfaces with a goniometer (Rame-Hart, A-100) equipped with a video camera (XC-73, Sony) and a data acquisition system (Power Macintosh 7100 with LG-3 frame grabber and Image software, Scion) using the sessile drop method. The OTS-patterned substrates were positioned with the OTS bands facing either in parallel or perpendicular direction with respect to the goniometer's optical axis. A 0.25  $\mu\text{l}$  droplet of deionized and double-distilled water ( $\gamma = 72 \text{ mN/m}$  at  $20^\circ\text{C}$ ) was carefully placed with a microsyringe (Hamilton) on the surface and immediately measured. The procedure was repeated at least 10 times on each sample.

The Cassie equation [28] was used to find the average wettability and fraction of OTS coverage for both the stamped and non-stamped bands of the patterned samples and for the controls:

$$\cos \theta_{\text{adv}} = f \cos \theta_1 + (1 - f) \cos \theta_2, \quad (1)$$

where  $\theta_{\text{adv}}$  is the experimentally observed advancing water contact angle,  $f$  is a fraction of the OTS modified surface with characteristic contact angle,  $\theta_1$ , and  $\theta_2$  is the characteristic contact angle for an unmodified glass surface. The parameters required for solving the Cassie equation were obtained from the advancing water contact angles measured parallel ( $\theta_{\text{adv}\parallel}$ ) and perpendicular ( $\theta_{\text{adv}\perp}$ ) to the patterned OTS bands. A water contact angle of  $\theta_{\text{adv}} = 115^\circ$  was measured on a complete OTS monolayer and  $\theta_{\text{adv}} = 0^\circ$  on a cleaned glass surface. The OTS coverage in the stamped bands ( $f_{\text{OTS-st}}$ ) was calculated from:

$$f_{\text{OTS-st}} = \frac{\cos \theta_{\text{adv}\parallel} - \cos(0)}{\cos(115) - \cos(0)}. \quad (2)$$

An advancing water contact angle on the non-stamped bands ( $\theta_{\text{advnst}}$ ) was computed from:

$$\cos \theta_{\text{advnst}} = \left( \frac{\cos \theta_{\text{adv}\perp} - f_{\text{OTSsw}} \times \cos \theta_{\text{adv}\parallel}}{1 - f_{\text{OTSsw}}} \right), \quad (3)$$

where the fractional OTS band width,  $f_{\text{OTSsw}}$ , was found from AFM topographical images of the OTS patterns. The OTS coverage in the non-stamped bands ( $f_{\text{OTS-nst}}$ ) was then found as:

$$f_{\text{OTS-nst}} = \frac{\cos \theta_{\text{advnst}} - \cos(0)}{\cos(115) - \cos(0)}. \quad (4)$$

**2.2.2. Scanning force microscopy.** SFM cantilever tips (Veeco Metrology Group, 'Ultrasharp', nominal spring constant,  $k = 0.5 \text{ N/m}$ , gold-coated  $\text{S}_3\text{N}_4$ , V-shaped) were made hydrophobic using an adaptation of a previously described method [29]. Briefly, the probes were cleaned in an ice-chilled  $\text{H}_2\text{O}_2/\text{H}_2\text{SO}_4$  (1 : 2 (v/v)) solution for 2 min, then serially rinsed with the following three solvents in the order DD

water, ethanol and hexane. The chemical modification step was accomplished by placing the probes in a 10 mM OTS-hexane solution for 2 min followed by serial solvent rinsing in the order hexane, ethanol and DD water. The sessile drop method on the cantilever tip surface was used to verify the completion of the cleaning and OTS modification steps. The same SFM cantilever was used for all SFM measurements.

An SFM instrument (Explorer, Topometrix) was used to measure OTS and protein film topography using contact mode as well as to simultaneously map the friction forces using lateral force mode. Topometrix imaging software and SXM software (based on NIH Image software, S. Barrett, University of Liverpool) were subsequently used for image processing and to determine physical characteristics of the patterns such as film thickness, friction contrast and OTS island coverage within the non-stamped regions of the patterns. Best results were achieved by measuring OTS film topography and lateral force maps in air while adsorbed protein layers were measured in aqueous solution to avoid artifacts caused by drying the protein film.

*2.2.3. Condensation figures.* OTS-modified glass substrates were chilled and water vapor was quickly introduced to the substrate surfaces prior to taking bright field microscopy images using the microscope and CCD camera described in the FM measurements section below. Careful synchronization between water vapor introduction and image capture ensured imaging of surface-condensed water droplets within a fraction of a second of nucleation events.

### *2.3. Protein adsorption experiments*

*2.3.1. Protein labeling and purification.* Human serum albumin (HSA; ICN, Fraction V, fatty acid free) was conjugated with Alexa Fluor 488 (af488, Molecular Probes) and the resulting labeled protein (af488-HSA) was isolated through gel-permeation chromatography and further purified through extensive dialysis. Thin layer chromatography was used to verify the separation of free dye from the labeled protein. UV-Vis spectrophotometry was used to determine the degree of labeling and protein concentration in the final af488-HSA solution [1]. The degree of HSA labeling was 0.83 mol af488 per mol HSA. The final af488-HSA solution was then diluted to a concentration of 5  $\mu\text{g/ml}$  in 10 mM phosphate-buffered saline (PBS, pH 7.4, ionic strength 0.165 M). Aliquots of the 5  $\mu\text{g/ml}$  af488-HSA stock solution were stored in small vials at  $-20^\circ\text{C}$  and thawed immediately prior to each adsorption experiment. The same 5  $\mu\text{g/ml}$  af488-HSA stock solution was used for all adsorption experiments.

*2.3.2. Flow cell configuration.* The adsorption flow cell was designed to enable the flow of buffer and protein solutions across glass coverslip (thickness #1) surfaces while allowing real-time fluorescence imaging of protein adsorption on the OTS-modified glass coverslip surface facing the interior of the flow cell. The flow cell

consisted of two aluminum blocks, which were used to clamp the OTS-modified glass coverslip and a glass slide together separated by a 305- $\mu\text{m}$ -thick silicone rubber gasket. The flow cell was designed to have a microscope objective accessible opening on the side of the OTS-modified coverslip. The flow cell was placed on the stage of an upright fluorescence microscope (Nikon Eclipse E400) and a syringe-pump was used to flow solutions through the flow cell and into a collection reservoir.

**2.3.3. Adsorption experiment parameters.** A vial of 5  $\mu\text{g/ml}$  af488-HSA solution was allowed to reach room temperature and was filtered with a 0.22  $\mu\text{m}$  filter (Millipore) immediately before each adsorption experiment. The flow cell was initially filled with PBS and a dark count image was recorded of the sample surface. PBS in the inflow tubing was subsequently replaced with the af488-HSA solution immediately prior to beginning the adsorption experiment. Faster flow of protein solution and PBS were used during the first 30 s of adsorption and desorption processes to bring the solution to the observation area and thus limit the mixing and dilution effects. The flow was reduced to 0.1 ml/min thereafter. All experiments were conducted at room temperature.

**2.3.4. Fluorescence imaging.** Fluorescence images of adsorbed af488-HSA on the OTS-modified and clean coverslips were recorded using a 100 $\times$ , NA = 1.25, oil immersion objective (Leitz) in the epifluorescence configuration. A 12-bit Pelletier-cooled CCD camera (MicroMax, Princeton Instruments) was used to obtain high-resolution images of the adsorbed af488-HSA layer. Neutral density filters were employed to attenuate the excitation light in order to minimize photobleaching of the labeled protein and an exposure time of 4 s was used to reduce the effects of fluctuations in the excitation light source (75 W Xenon lamp) intensity and position over short time periods. A set of excitation band-pass, dichroic mirror and emission band-pass filters (Omega) was used to separate the excitation and emission photons.

## 2.4. Fluorescence image processing and analysis

Each fluorescence image was corrected for long-term variations in the excitation light intensity due to Xenon arc-lamp aging and changes in the microscope optical alignment, unevenness of the excitation illumination, and for fluorescence background originating from solution fluorescence, scattered light and electronic CCD readout noise according to the following equation:

$$I_{\text{Corr}}[x_i y_j] = k_{\text{LTVar}} \times \left\{ \left[ \frac{(I_{\text{Meas}}[x_i y_j] - I_{\text{Dark}}[x_i y_j])}{(I_{\text{FlatF}}[x_i y_j] - I_{\text{Dark}}[x_i y_j])} \times k_{\text{FlatF}} \right] - k_{\text{Backgr}} \right\}, \quad (5)$$

where  $I_{\text{Corr}}[x_i y_j]$  is the fluorescence image with the intensity corrected at any given pixel position,  $I_{\text{Meas}}[x_i y_j]$  is the recorded fluorescence image,  $I_{\text{Dark}}[x_i y_j]$  is the recorded dark count image,  $I_{\text{FlatF}}[x_i y_j]$  is the recorded flat-field fluorescence image  $k_{\text{LTVar}}$  is the correction factor for long-term variations in excitation light normalized

to the intensity of the background fluorescence caused by the af488-HSA solution in the flow cell under steady-state adsorption conditions,  $k_{\text{FlatF}}$  is the average pixel intensity of the flat-field image and  $k_{\text{Backgr}}$  is the average pixel intensity of the background protein solution fluorescence in the flow cell for the given experiment. Each flat-field fluorescence image was recorded using either a free af488 in PBS (for adsorption times less than 60 s) or a densely adsorbed layer of af488-HSA on a uniform OTS-treated glass coverslip (for adsorption times longer than 60 s), each taken immediately before the given experiment.

#### *2.4.1. Conversion of fluorescence intensity into adsorbed protein surface density.*

In fluorescence imaging of protein adsorption, the fluorescence intensity corrected at any given pixel position,  $I_{\text{Corr}}[x_i y_j]$ , is composed of the in-focus fluorescence emission from the adsorbed layer ( $I_{\text{Ads}}$ ) and the out-of-focus fluorescence emanating from the protein solution in the flow cell ( $I_{\text{Sol}}$ ). Since each of the two fluorescence contributions to the total fluorescence intensity can be separately determined in experiments and the concentration of the af488-HSA solution,  $c_{\text{Sol}}$ , is known, the surface concentration of surface bound af488-HSA,  $\Gamma_{\text{HSA}}$ , can, in principle, be calculated by finding the optical relationship between the two fluorescence components,  $I_{\text{Ads}}$  and  $I_{\text{Sol}}$ . The conversion from  $I_{\text{Ads}}$  and  $I_{\text{Sol}}$  to  $\Gamma_{\text{HSA}}$  used in this study paralleled the quantification of protein adsorbed amount in total internal fluorescence microscopy [30, 31] and will not be described in detail here (data not shown). The error in the measurement of the adsorbed HSA surface density was up to  $\pm 3.5\%$  (estimated from the standard deviations of protein fluorescence intensity measured within OTS bands). A linear relationship between the measured fluorescence intensity and the adsorbed HSA surface density was assumed. This assumption was based on the previous quantification of fluorescein-labeled HSA adsorption using radiography and mass-transfer limited adsorption process [17, 32]. Alexa Fluor 488 dye is both brighter and more photostable than fluorescein; consequently, its very low photobleaching and relatively large Stokes shift (21 nm), together with the low degree of protein labeling, ensured that the self-quenching and photobleaching of af488-HSA conjugate in the surface layer was minimal.

*2.4.2. Protein adsorption for SFM measurements.* OTS-patterned glass substrates and substrates with control surfaces were placed in an adsorption chamber containing PBS, which was then exchanged with filtered 5  $\mu\text{g}/\text{ml}$  af488-HSA solution. The samples were simultaneously incubated in af488-HSA for 90 min at room temperature then rinsed with and stored in PBS until analyzed.

### **3. RESULTS**

#### *3.1. OTS pattern characterization*

*3.1.1. SFM topographical imaging of OTS patterns and controls.* SFM images of the topography of various OTS patterned surfaces used in this study provided

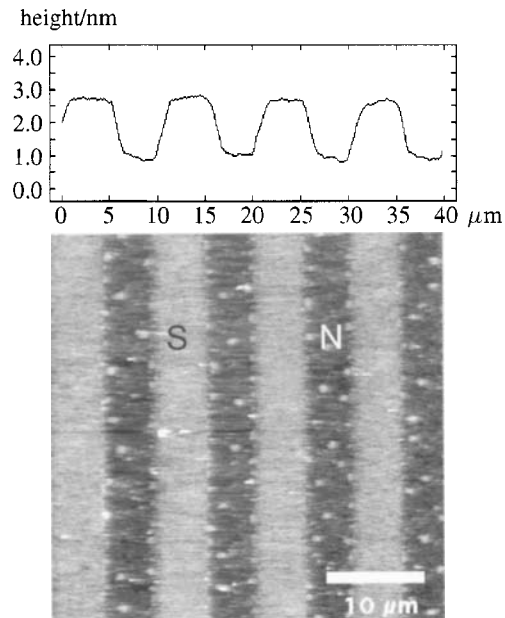


local information about OTS film thickness and distribution. Figure 1A and 1B displays the faithfulness of the reproduction of the OTS stamped pattern on the glass surfaces. Stamped bands in the non-annealed patterns (Fig. 1A) were  $5.37 \pm 0.38 \mu\text{m}$  wide, while the annealing step increased average stamped band width to  $5.92 \pm 0.3 \mu\text{m}$  (Fig. 1B). The average height of OTS patterns found in the stamped regions corresponded to a slightly less than reported monolayer thickness of 2.5 nm [23, 24], thus indicating that the stamped pattern might have been either compressed by the scanning SFM tip, or contained less than complete monolayer OTS coverage in these regions. Similarly to what was reported by others [23], the island formation within the non-stamped regions was also apparent and was found to increase with stamp contact time. Our initial hypothesis was that vapor phase transfer of OTS molecules from the stamp to the neighboring glass surface was responsible for the island formation. The contact time of 20 s was, therefore, selected to minimize island formation in non-stamped regions (Fig. 1). However, we also found that even with 20 s of stamp contact time a substantial quantity of non-reacted OTS remained in the stamped regions and that these molecules could: (a) either be quickly removed by solvent rinsing to produce a sharp step-function type of OTS pattern, or (b) be allowed to spread and react with the neighboring regions in a short annealing step. Using this second approach, we have combined  $\mu\text{CP}$  with a vapor diffusion-controlled silanization method [33], a combination that proved valuable in producing OTS films containing unique patterns of surface heterogeneities.

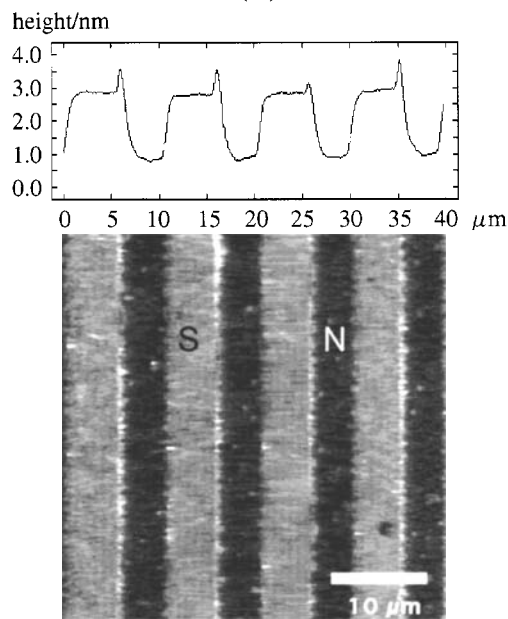
Migration of non-reacted OTS from the stamped regions could also occur by processes other than vapor phase transfer. For example, surface-diffusion could be responsible for the somewhat increased width of the stamped bands in annealed samples ( $5.37 \pm 0.38 \mu\text{m}$  for non-annealed pattern width vs.  $5.92 \pm 0.3 \mu\text{m}$  for annealed pattern) (Fig. 1). In some instances, the edges of the stamped bands in the annealed pattern are more than a monolayer thick, indicating that some piling up of the OTS molecules at the edges has occurred during the annealing step (Fig. 1B). Height profiles of the two patterns also demonstrate the existence of narrow OTS concentration gradients between stamped and non-stamped regions. A number of large OTS islands in the non-stamped bands in non-annealed samples (Fig. 1A) could also have been formed by the ejection of small amounts of OTS during the stamping process.

*3.1.2. Water contact angle measurements.* Figure 2 shows the top view of the water sessile drop edges on the OTS pattern. Water protrudes into the more hydrophilic bands and recedes from the more hydrophobic regions creating an undulating pattern of the drop edge perpendicular to the orientation of the OTS bands (Fig. 2A). The water drop edges positioned parallel to the OTS bands stop on the boundary of a hydrophobic band forming a straight drop edge (Fig. 2B).

Table 1 lists the measured water contact angles for the various areas on the OTS pattern and on controls as well as the calculated average OTS coverage for each area. Contact angles observed parallel to the stamped bands were used to calculate OTS



(A)



(B)

**Figure 1.** (A) SFM image of non-annealed OTS pattern topography. Brighter bands represent the stamped areas of the substrates (marked by an 'S') while non-stamped areas are darker (marked by an 'N'). An average height profile is presented in the panel above the image below. (B) SFM image of annealed OTS pattern topography. Brighter bands represent the stamped areas of the substrates (marked by an 'S') while non-stamped areas are darker (marked by an 'N'). An average height profile is presented in the panel above the image below.

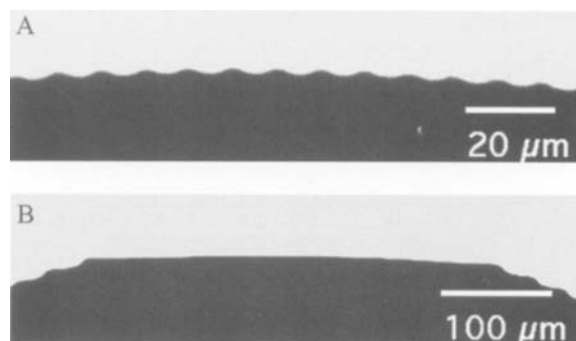


**Figure 2.** Top view of typical water-drop edges on OTS patterned substrates. (A) Water-drop edge positioned perpendicular to OTS bands reveals alternating hydrophobic and hydrophilic areas with a periodicity of approx. 10  $\mu\text{m}$ . (B) Water-drop edges positioned parallel to the OTS bands stop on one of the hydrophobic bands forming a straight drop edge.

**Table 1.**

Advancing water contact angles  $\pm 1$  standard deviation on stamped and non-stamped regions of the patterned substrates and on controls, and calculated OTS coverage within each specified area

	Non-annealed		Annealed		Non-annealed	Annealed	
	Stamped	Non-stamped	Stamped	Non-stamped	(Control)	Control	Glass
Contact angle ( $^{\circ}$ )	$67.4 \pm 2.1$	$37.3^a$	$94.6 \pm 2.3$	$49.8^a$	$67.5 \pm 1.5$	$94.2 \pm 1.9$	$0^b$
OTS coverage (%)	43.3	14.4	75.9	24.9	43.4	75.5	0

<sup>a</sup> Contact angle values calculated from experimental data using the Cassie equation (equation (1)).

<sup>b</sup> Glass coverslips completely wetted and so water contact angles could not be measured.

coverage within these regions according to equation (2). The measurements taken both parallel and perpendicular to the stamped bands were required to calculate these contact angles and the average OTS coverage within the non-stamped bands using equation (4). Due to the annealing process, the average OTS coverage increased from 43.2% to 75.9% in the stamped regions and from 14.4% to 24.9% within the non-stamped bands. There was good agreement between calculated OTS coverage for the stamped OTS areas and the OTS controls both before and after annealing treatment indicating that the methodology developed to compute each OTS coverage (i.e., use of equations (2)–(4)) was reliable.

**3.1.3. Condensation figures.** Water vapor condensation figures have been demonstrated as a convenient method to visualize local differences in substrate wettability [34]. Images of water vapor condensation figures on non-annealed and annealed stamped patterns revealed the nature of heterogeneity within the OTS films (Fig. 3). Water droplets, seen under bright field illumination as darker spots in Fig. 3, readily nucleated on cooled OTS patterned surfaces and initially began to grow on both the non-stamped and stamped bands of the non-annealed OTS pattern

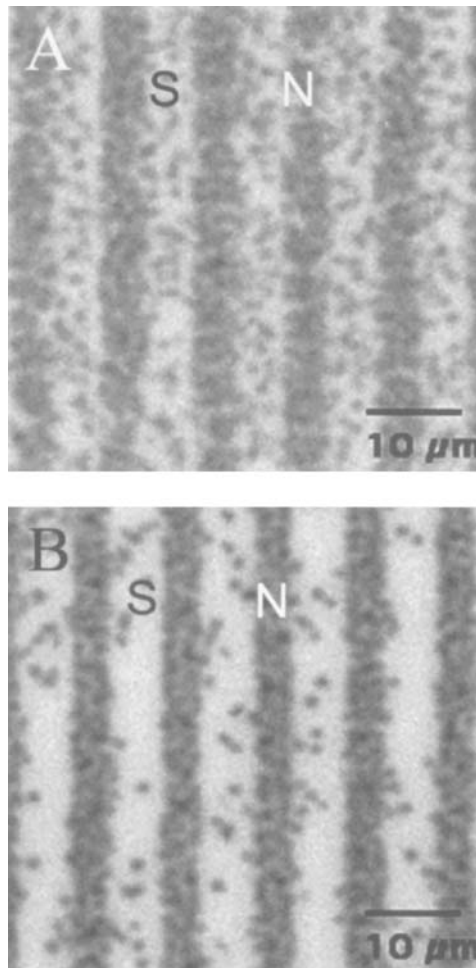


**Figure 3.** Water vapor condensation figures (water droplets appear as darker areas): S, stamped region; N, non-stamped region. (A) Non-annealed OTS pattern, (B) annealed OTS pattern. The lower contrast of the condensation image in the non-annealed pattern (A) is due to a lower density of nucleated droplets on the stamped OTS regions *versus* the non-stamped regions.

(Fig. 3A). The most visible difference between non-annealed and annealed stamped regions is that fewer droplets nucleated on the stamped OTS regions in the annealed sample. Assuming that the defects in the OTS-stamped regions served as droplet nucleation centers, we inferred that the OTS-stamped regions contained a smaller number of defects after the annealing process, while the non-stamped regions in both the non-annealed and annealed samples contained, overall, a larger number of nucleation sites.

*3.1.4. Lateral force microscopy imaging of OTS patterns and controls.* Lateral force microscopy (LFM) has been used in the past to visualize the extent of surface

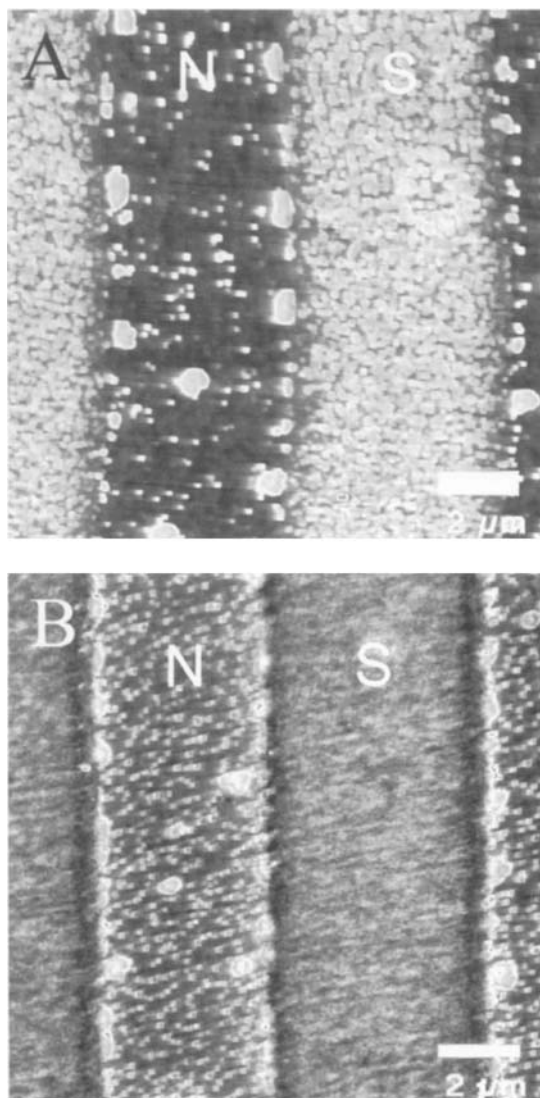


**Figure 4.** Lateral force microscopy images of OTS patterns: S, stamped, N, non-stamped regions. (A) Non-annealed pattern: the stamped areas are composed of many small islands and some islands exist in the non-stamped areas. (B) Annealed pattern: the stamped areas appear more continuous while considerable island formation has occurred within the non-stamped areas.

chemical heterogeneity that often eludes mere SFM topography imaging [5]. As evidenced in Fig. 4, LFM provided higher resolution images of the OTS patterns and associated microstructures than those found in SFM topography images (Fig. 1). The brighter regions in the LFM images in Fig. 4 corresponded to areas of higher OTS coverage. A collection of closely packed, nearly equiaxed islands was observed in the OTS-stamped regions in the non-annealed sample indicating that the

OTS reaction with glass during stamping proceeds through parallel nucleation and growth of many islands. A smaller number of similar size isolated islands was also found in the non-stamped regions. The annealing step appears to have coalesced the OTS island boundaries within the stamped regions but it also greatly increased the number of small OTS islands in the non-stamped bands (Fig. 4B). Interestingly, these islands did not grow in size upon annealing but remained similar in size to the islands found before the annealing process. A distinct, smaller population of larger OTS islands was found on both samples in the region between stamped and non-stamped bands. We conclude that the annealing process affected the extent of surface micro-heterogeneities on the stamped and non-stamped regions differently: it improved the uniformity of stamped OTS regions, while at the same time it decreased the uniformity in the non-stamped regions (Fig. 4A).

### 3.2. Albumin adsorption

Monitoring protein adsorption as a function of time through high-resolution fluorescence imaging provided information about how the adsorption process was affected by the micro-heterogeneities in the OTS layer. Figure 5 displays six snapshots of af488-HSA accumulation on the annealed and non-annealed OTS patterns at six different adsorption times, 1.5, 4, 10, 15, 30 and 90 min. Based on the hrFM images, we found that the adsorption of af488-HSA proceeded at a faster rate and reached steady state sooner on the OTS stamped regions than on the non-stamped regions for both the annealed and non-annealed OTS patterns. In the case of the non-annealed pattern (Fig. 5A), af488-HSA adsorbed at a higher surface density on the less wettable OTS-stamped areas:  $\Gamma_{\text{HSA}}$  was  $0.188 \mu\text{g}/\text{cm}^2$  on the areas with 43.3% average OTS coverage compared with  $\Gamma_{\text{HSA}} = 0.165 \mu\text{g}/\text{cm}^2$  on the non-stamped regions where average OTS coverage was 14.4%. Somewhat surprisingly, in the case of the annealed OTS pattern (Fig. 5B), protein adsorption was greater on the non-stamped regions than on the stamped regions, as indicated by the fluorescence image of the af488-HSA adsorbed layer at 90 min of adsorption. A higher surface density of af488-HSA,  $\Gamma_{\text{HSA}} = 0.220 \mu\text{g}/\text{cm}^2$ , was found on the less wettable, non-stamped regions, where average OTS coverage was 24.9%, than on the stamped bands where  $\Gamma_{\text{HSA}}$  was  $0.179 \mu\text{g}/\text{cm}^2$  (average OTS coverage 75.9%). The adsorption contrast between stamped and non-stamped bands for the annealed OTS pattern switched at about 12 minutes into the adsorption process.

Calculated af488-HSA coverage densities at 90 min of adsorption agree well with data published in the literature [17, 32, 35]. af488-HSA adsorption on the control OTS surfaces (i.e., on uniformly annealed and non-annealed OTS films on glass) were similar to those for the respective stamped areas of the OTS patterned surfaces, while the adsorbed amount of af488-HSA on the clean glass surface reached an average density of only  $0.057 \mu\text{g}/\text{cm}^2$  after 90 min of adsorption. Although each sample was subjected to 90 min of desorption by PBS buffer, only a small fraction of bound af488-HSA desorbed. The average desorbed amount for the OTS-modified substrates was 4% of the total adsorbed amount and was never greater than 6%

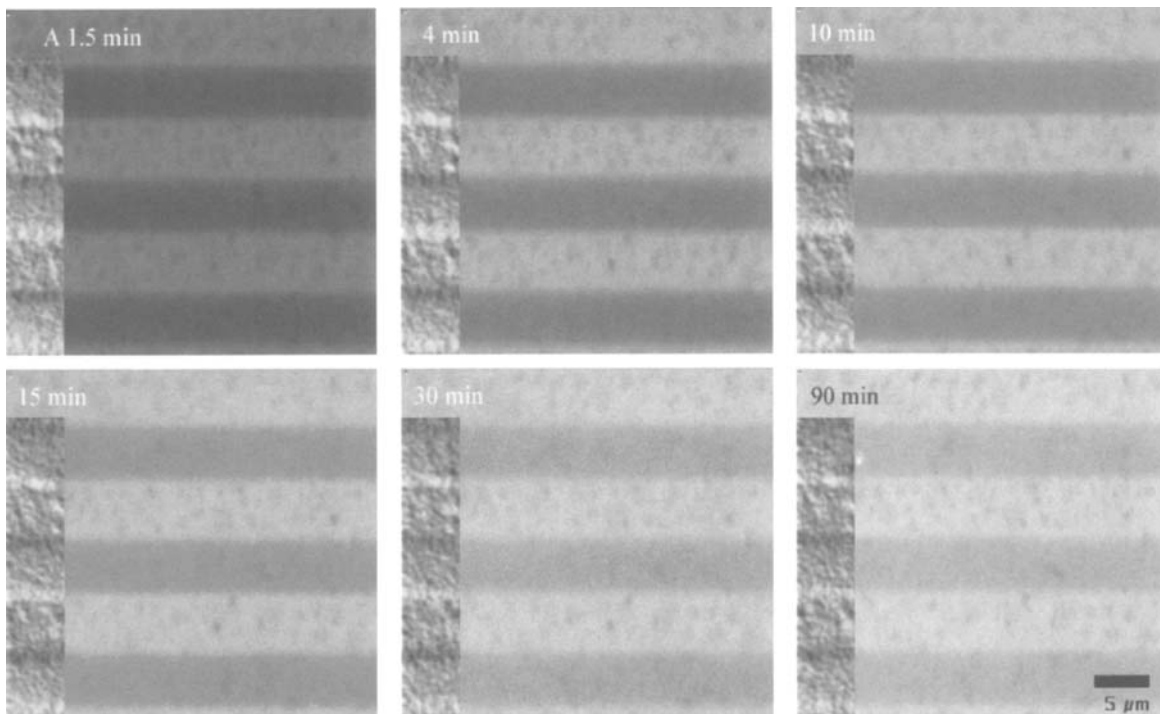


**Figure 5.** Time-course fluorescence images of af488-HSA adsorption on OTS patterns. All images have the same intensity scale, i.e., the intensity is proportional to af488-HSA adsorbed amount. Lower left section of each image was processed (bas-relief) to enhance the details of the af488-HSA distribution. (A) Non-annealed OTS pattern, as evidenced by changes in fluorescence intensity af488-HSA initially adsorbed more quickly on the OTS-stamped regions. Heterogeneities in the stamped OTS regions result in spatial irregularities in protein adsorption: darker spots within the OTS-stamped regions correspond to the level of af488-HSA adsorption, comparable to that found on the non-stamped areas. (B) Annealed OTS pattern: af488-HSA adsorbs faster on the OTS-stamped region edges and reaches steady-state fluorescence on the OTS-stamped areas within minutes. Adsorption proceeded more slowly on the non-stamped regions but the adsorbed amount eventually exceeded that in the OTS-stamped regions: the reversal in the band brightness was seen starting at 12 min of adsorption time. Darker spots within the non-stamped regions correspond to the af488-HSA adsorption on larger OTS islands, which was found to be comparable to the adsorbed amount found on the stamped areas.

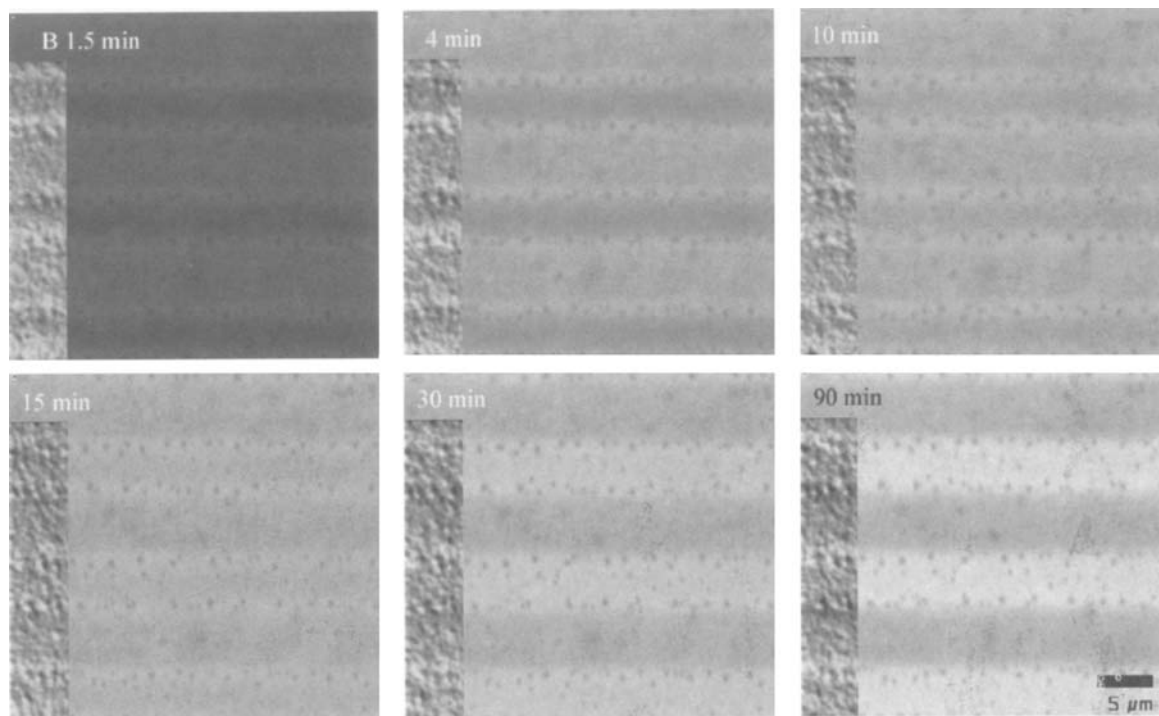


**Figure 5.** (Continued).



for any of the samples. The clean glass substrate experienced a 10% reduction in protein coverage after 90 min of PBS desorption.

### 3.3. Characterization of af488-HSA adsorption with SFM techniques

Topographical characteristics of all the samples were altered by af488-HSA adsorption. Figure 6 shows that af488-HSA adsorption on the non-annealed pattern increased the average height difference between the stamped and non-stamped bands from  $1.65 \pm 0.10$  to  $2.04 \pm 0.15$  nm, while on the annealed patterned surface the average height difference between stamped and non-stamped bands decreased from  $1.84 \pm 0.10$  to  $1.22 \pm 0.20$  nm after protein adsorption (Fig. 6A). The observed changes in the average height difference between stamped and non-stamped bands in the non-annealed and annealed patterns support the fluorescence data that protein preferentially adsorbed on the stamped areas in the non-annealed pattern and adsorbed in greater amounts on non-stamped areas in the annealed pattern. Interestingly, the adsorption process decreased the friction difference between the stamped and non-stamped bands in the non-annealed pattern indicating protein coverage in both areas, whereas little change in friction differences, if any, between the stamped and non-stamped bands was caused by HSA adsorption on the annealed pattern (Fig. 6B).

## 4. DISCUSSION

Based on OTS glass chemistry, we have fabricated and characterized model surface patterns designed to come in contact with complex biomacromolecules. Although the OTS patterns on these substrates appeared macroscopically homogeneous, they were found to contain chemical heterogeneities on a  $\mu\text{m}$  and sub- $\mu\text{m}$  scale in both stamped and non-stamped regions. The OTS stamped regions and defects therein, concentration gradients between stamped and non-stamped bands, and island formation in non-stamped regions all provide interesting features to facilitate the investigation of the effects of surface micro-heterogeneity on protein adsorption.

Macroscopic techniques, such as advancing water contact angles, are typically used to characterize surface wettability; but they sample large areas and provide only an average measure of surface coverage of hydrophobic moieties (Fig. 2). Similarly, water condensation images (Fig. 3), while convenient as a means to estimate the number of defects in the OTS patterns, are not only indirect but also difficult to standardize. Almost all OTS surface features, however, could be imaged on a sub- $\mu\text{m}$  scale using SFM. In particular, LFM has provided the highest resolution contrast in imaging OTS stamped regions, concentration gradients between stamped and non-stamped bands, defects in stamped bands and island formation in non-stamped regions (Fig. 4).

One aim of this study was to relate these small-scale surface heterogeneities with albumin adsorption. High-resolution fluorescence microscopy was selected as a

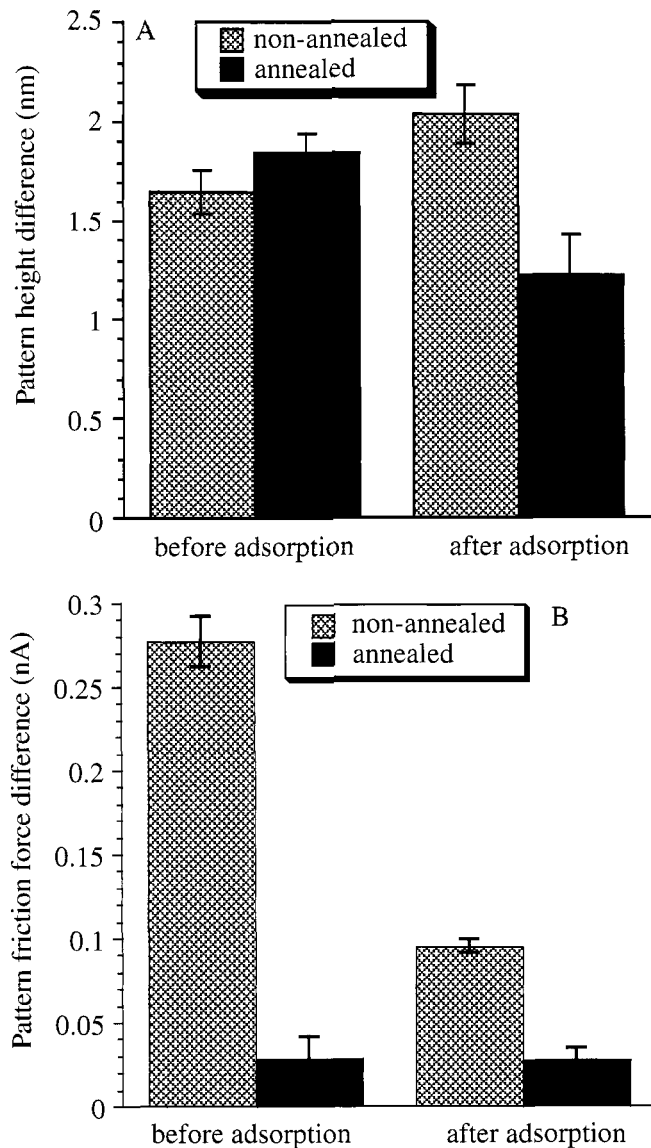


**Figure 6.** Average SFM parameters before and after HSA adsorption. (A) Average height differences between stamped and non-stamped bands before and after protein adsorption. (B) Average friction force difference between stamped and non-stamped bands before and after protein adsorption. The friction force is not calibrated and is presented in AFM photodetector current units (nA). Error bars are  $\pm 1$  standard deviation.

method to simultaneously monitor protein adsorption kinetics on OTS patterns, as well as to monitor protein spatial-temporal distributions on a  $\mu\text{m}$  and sub- $\mu\text{m}$  scale. But even in hrFM experiments, the adsorbed protein fluorescence is observed from many surface sites and is summed up to a composite fluorescence intensity

measured at each pixel of the image recording device (Fig. 5). Hence, the analysis of the effects of surface micro-heterogeneity on protein adsorption is limited by the optical resolution of the hrFM. Protein adsorption kinetics can provide some estimate of the energy distribution of binding sites available to the molecule being adsorbed. Namely, higher affinity surface sites are expected to fill up with bound proteins faster than lower affinity sites, although albumin adsorption was probably initially transport-limited due to relatively low protein solution concentration. As a result, a cluster of high-affinity sites will lead to a faster increase of fluorescence intensity and, conversely, clusters of low-affinity binding sites will bind proteins more slowly.

Although it has been shown in the past that HSA preferentially adsorbs on non-polar, hydrophobic surfaces [36–38], there is also strong evidence that HSA will bind more readily and strongly to binding sites containing both hydrophobic and hydrophilic moieties and boundaries than either to hydrophobic solids or to surfaces with densely-packed hydrophobic molecules. Namely, it has been shown that the wetting transition zone of a carefully prepared wettability gradient surface will adsorb more HSA than more hydrophobic portions of the gradient [17, 39]. It has also been shown that HSA molecules will preferentially adsorb on defect boundaries in organosilane films created on hydrophilic substrates [7, 8]. Golander *et al.* postulated that HSA preferentially adsorbed on areas of intermediate organosilane coverage because of the amphiphilic and deformable nature of the HSA molecule [39]. Several studies have also shown that organosilane films of intermediate coverage irreversibly bind HSA with a higher affinity than more hydrophobic or hydrophilic areas indicating more favorable interactions between the alkyl chains and the HSA molecules [38–40]. In fact, it has been shown that an HSA molecule possesses several fatty-acid-binding sites, which can interact with alkyl chains [41]. Petrash *et al.* further postulated that HSA preferentially binds to substrates containing less densely packed alkanesilanes and at film boundaries because the chains in these areas will have more freedom of movement which will enable an increased possibility for optimal interactions with HSA alkyl binding sites [40].

In the present study we observed the highest HSA adsorption on areas containing intermediate average OTS coverages of 24.9% (on non-stamped annealed bands,  $\Gamma_{\text{HSA}} = 0.220 \mu\text{g}/\text{cm}^2$ ) and 43.3% (on stamped non-annealed band,  $\Gamma_{\text{HSA}} = 0.188 \mu\text{g}/\text{cm}^2$ ) which corresponds well to previous findings [17]. The correlation between intermediate OTS coverage amounts and greater maximal HSA adsorption found in this study helps support evidence found by others [40] that greater adsorbed amounts may be due to surfaces where OTS molecules are less densely packed. The LFM maps (Fig. 4), however, provide more compelling evidence that increased HSA adsorption is not merely due to an average OTS packing, but rather to the surface heterogeneities present in the form of local OTS density distribution. In particular, HSA consistently adsorbed more readily on the non-stamped bands of the annealed patterns than on the stamped bands, despite the fact that the stamped

bands had an average OTS surface coverage nearly three times greater than the non-stamped bands. We conclude, therefore, that the surface micro-heterogeneities in the OTS films prepared in this study have a significant impact on protein adsorption and that areas of intermediate coverage facilitate increased HSA adsorption when compared to densely packed hydrophobic organosilane films. Three different effects of local OTS concentration are quite interesting: (1) within the stamped OTS bands in the non-annealed samples one finds areas of lower fluorescence intensity, i.e., local areas of low HSA adsorption (Fig. 5A), (2) HSA adsorption on the OTS concentration gradients in the annealed OTS patterns increases faster than the adsorption on the neighboring stamped and non-stamped regions (Fig. 5B) and (3) within the non-stamped regions in the annealed samples one also finds darker spots, indicating local areas of low HSA adsorption (Fig. 5B). While the darker spots within the OTS-stamped regions (case 1) correspond to the level of af488-HSA adsorption which is comparable to that found on the non-stamped areas, similar darker spots within the non-stamped regions (case 3) seem to correspond to the af488-HSA adsorption on larger OTS islands and at the adsorption level found on the stamped areas.

It has been shown by others that albumins denature to a greater extent on more hydrophobic surfaces [6, 42] and that initial binding rate increases with the ability of HSA to denature upon adsorption [43]. We postulate that strong hydrophobic interactions between a more densely-packed OTS region cause HSA molecules to denature upon adsorption in such a way that multiple surface binding sites are occupied. Because of the rapid depletion of these sites, one would expect to see albumin adsorption reach its steady state more quickly but at a lower adsorption level. We also postulate that areas containing mixed hydrophobic and hydrophilic sites bind protein at greater surface densities but more slowly due to the time required to find the best match between HSA alkyl binding sites and underlying substrate OTS chains. At very low OTS coverage, the OTS molecules are so distantly spaced that the number of OTS-HSA interactions is reduced so that adsorbed amount decreases with decreasing OTS coverage, i.e., with decreasing surface hydrophobicity.

## 5. CONCLUSIONS

In this study we have shown that high-resolution fluorescence microscopy is a viable technique to monitor protein adsorption and protein temporal-spatial changes down to a sub- $\mu\text{m}$  length and a second time scale. By correlating hrFM data with OTS pattern properties, such as SFM-determined lateral force and topography, we have shown that heterogeneities in OTS films existing on the  $\mu\text{m}$  and sub- $\mu\text{m}$  length scale have a significant effect on albumin adsorption kinetics, adsorbed amount, and its surface distribution. It is probable that the local OTS density distribution associated with heterogeneities found in the patterns created in this study and not

mere hydrophobicity effects provides a more accurate model to predict the nature and extent of HSA adsorption on various areas on these substrates.

## REFERENCES

1. V. Hlady, J. Buijs and H. P. Jennissen, *Methods Enzymol.* **309**, 402–429 (1999).
2. J. M. Brockman, B. P. Nelson and R. M. Corn, *Annu Rev. Phys. Chem.* **51**, 41–63 (2000).
3. P. Tengvall, I. Lundstrom and B. Liedberg, *Biomaterials* **19**, 407–422 (1998).
4. K. K. Chittur, *Biomaterials* **19**, 357–369 (1998).
5. T. C. Ta and M. T. McDermott, *Anal. Chem.* **72**, 2627–2634 (2000).
6. S. Ge, K. Kojio, A. Takahara and T. Kajiyama, *J. Biomater. Sci. Polymer Edn* **9**, 131–150 (1998).
7. C. H. Ho, D. W. Britt and V. Hlady, *J. Mol. Recogn.* **9**, 444–455 (1996).
8. J. Fang and C. M. Knobler, *Langmuir* **12**, 1368–1374 (1996).
9. R. Eckert, J. M. Freyland, H. Gersen, H. Heinzelmann, G. Schurmann, W. Noell, U. Staufer and N. F. De Rooij, *J. Microsc.* **202**, 7–11 (2001).
10. J. Wang, L. W. Ruddock and A. E. Cass, *Biosens. Bioelectr.* **9**, 647–655 (1994).
11. N. A. Alcantar, E. S. Aydil and J. N. Israelachvili, *J. Biomed. Mater. Res.* **51**, 343–351 (2000).
12. A. Fujimori, H. Naito and T. Miyazaki, *Artif. Organs* **22**, 1014–1017 (1998).
13. M. A. Model and K. E. Healy, *J. Biomed. Mater. Res.* **50**, 90–96 (2000).
14. A. Ulman, *J. Mater. Edn.* **11**, 207–280 (1991).
15. G. B. Sigal, M. Mrksich and G. M. Whitesides, *J. Am. Chem. Soc.* **120**, 3464–3473 (1998).
16. K. L. Prime and G. M. Whitesides, *Science* **252**, 1164–1167 (1991).
17. Y. S. Lin and V. Hlady, *Colloid. Surf. B: Biointerf.* **2**, 481–491 (1994).
18. R. S. Kane, S. Takayama, E. Ostuni, D. E. Ingber and G. M. Whitesides, *Biomaterials* **20**, 2363–2376 (1999).
19. R. Singhvi, A. Kumar, G. P. Lopez, G. N. Stephanopoulos, D. I. Wang, G. M. Whitesides and D. E. Ingber, *Science* **264**, 696–698 (1994).
20. M. Mrksich and G. M. Whitesides, *Annu. Rev. Biophys. Biomol. Struct.* **25**, 55–78 (1996).
21. T. Pompe, A. Fery and S. Herminghaus, *Langmuir* **15**, 2398–2401 (1999).
22. D. K. Schwartz, S. Steinberg, J. N. Israelachvili and J. A. Zasadzinski, *Phys. Rev. Lett.* **69**, 3354–3357 (1992).
23. N. L. Jeon, K. Finnie, K. Branshaw and R. Nuzzo, *Langmuir* **13**, 3382–3391 (1997).
24. A. G. Richter, C. Yu, A. Datta, J. Kmetko and P. Dutta, *Phys. Rev. E* **61**, 607–615 (2000).
25. S. R. Wasserman, G. M. Whitesides, I. M. Tidswell, B. M. Ocko, P. S. Pershan and J. D. Axe, *J. Am. Chem. Soc.* **111**, 5852–5861 (1989).
26. S. R. Cohen, R. Naaman and J. Sagiv, *J. Phys. Chem.* **90**, 3054–3056 (1986).
27. C. Y. Mildred, E. J. Kramer, R. Sharma, W. Zhao, M. H. Rafailovich, J. Sokolov and J. D. Brock, *Langmuir* **12**, 2747–2755 (1996).
28. A. B. D. Cassie, *Discuss. Faraday Soc.* **75**, 5041 (1952).
29. U. Srinivasan, M. R. Houston and R. T. Howe, *J. Microelectromech. Syst.* **7**, 252–260 (1998).
30. J. Buijs and V. Hlady, *J. Colloid Interf. Sci.* **190**, 171–181 (1997).
31. J. Buijs, D. W. Britt and V. Hlady, *Langmuir* **14**, 335–341 (1998).
32. V. Hlady and C. H. Ho, *Mater.-Wiss. Werkstofftech.* **32**, 185–192 (2001).
33. S. Daniel, M. K. Chaudhury and J. C. Chen, *Science* **291**, 633–636 (2001).
34. G. P. Lopez, H. A. Biebuyck, C. D. Frisbie and G. M. Whitesides, *Science* **260**, 647–649 (1993).
35. A. Baszkin and D. J. Lyman, *J. Biomed. Mater. Res.* **14**, 393–403 (1980).
36. P. van Dulm and W. Norde, *J. Colloid Interf. Sci.* **91**, 248–255 (1983).
37. S. L. Goodman, S. R. Simmons, S. L. Cooper and R. M. Albrecht, *J. Colloid Interf. Sci.* **132**, 561–570 (1990).

38. C. G. Golander and W. G. Pitt, *Biomaterials* **11**, 32–35 (1990).
39. C. G. Golander, Y. S. Lin, V. Hlady and J. D. Andrade, *Colloid. Surf.* **49**, 289–302 (1990).
40. S. Petrash, N. B. Sheller, W. Dando and M. D. Foster, *Langmuir* **13**, 1881–1883 (1997).
41. L. Boulkanz, C. Vidal-Madjar, N. Balcar and M. H. Baron, *J. Colloid Interf. Sci.* **188**, 58–67 (1997).
42. S. Noinville, M. Revault, M. H. Baron, A. Tiss, S. Yapoudjian, M. Ivanova and R. Verger, *Biophys. J.* **82**, 2709–2719 (2002).
43. W. G. Pitt, T. G. Grasel and S. L. Cooper, *Biomaterials* **9**, 36–46 (1988).

# Examination of Interphases and Nano-Indentation

## **Determining the interphase thickness and properties in polymer matrix composites using phase imaging atomic force microscopy and nanoindentation**

T. D. DOWNING<sup>1</sup>, R. KUMAR<sup>2</sup>, W. M. CROSS<sup>2</sup>, L. KJERENGSTROEN<sup>3</sup>  
and J. J. KELLAR<sup>1,\*</sup>

<sup>1</sup> *Department of Materials and Metallurgical Engineering, South Dakota School of Mines and Technology, Rapid City, South Dakota 57701, USA*

<sup>2</sup> *Materials Engineering and Science Program, South Dakota School of Mines and Technology, Rapid City, South Dakota 57701, USA*

<sup>3</sup> *Department of Mechanical Engineering, South Dakota School of Mines and Technology, Rapid City, South Dakota 57701, USA*

**Abstract**—In polymer matrix composites, the interface between the reinforcing phase and the bulk phase is paramount to the overall performance of the composite as a structural material. This interface is now thought to be a distinct, three-dimensional phase surrounding the reinforcing phase called the interphase. The developments of the atomic force microscope and nanoindentation devices have facilitated the investigation of the interphase. Previously, force modulation atomic force microscopy (AFM) and nanoindentation were the primary methods used to determine the size of the interphase and its stiffness relative to the bulk phase. The present investigation utilized phase imaging AFM and nanoindentation to examine the interphase in a glass fiber-reinforced epoxy matrix composite. Nanoindentation experiments indicated that the relatively stiff fiber might have caused a gradient in the modulus across the interphase region. Specifically, the modulus next to the fiber approached that of the fiber and decreased to that of the bulk polymer as the distance away from the fiber increased. Once the fiber was removed by chemical etching, this gradient reversed itself; hence, nanoindentation, due to the fiber bias, was not found to be adequate for measuring actual interphase properties. It was found that phase imaging AFM was a highly useful tool for probing the interphase, because it involves much lower interaction forces between the probe and the sample than force modulation or nanoindentation. The interphase in the model composite investigated was found to be softer than the bulk phase with a thickness of 2.4–2.9  $\mu\text{m}$ , and was independent of fiber silane pretreatment, for silane pretreatments between 0.1% and 5.0% (initial aqueous concentration).

**Keywords:** Interphase; polymer matrix composites; atomic force microscopy (AFM); phase imaging; nanoindentation.

---

\*To whom correspondence should be addressed. Phone: (605) 394-2343; Fax: (605) 394-3360; E-mail: [jkellar@silver.sdsmt.edu](mailto:jkellar@silver.sdsmt.edu)



## 1. INTRODUCTION

In polymer matrix composites (PMCs), the region separating the bulk polymer from the fibrous reinforcement is of utmost importance to load transfer. This region was originally dubbed an *interface*, but is now most often viewed to be an *interphase* because of its three-dimensional, heterogeneous nature [1, 2]. This is not to say that it is a distinct phase, as the interphase does not have a clear boundary. It is more accurately viewed as a transition region that possesses neither the properties of the fiber nor those of the matrix. Consequently, the mechanical properties of the interphase are of interest. This paper discusses methods used in these analyses and a new approach to measuring the size and relative mechanical properties of the interphase.

Researchers have hypothesized that the interphase has distinct mechanical properties from those of the reinforcing phase or the bulk polymer. For example, an interphase that is softer than the surrounding polymer would result in lower overall stiffness and strength, but greater resistance to fracture [2, 3]. The deformable layer theory describes this type of interphase [4]. On the other hand, an interphase that is stiffer than the surrounding polymer would give the composite less fracture resistance but make it very strong and stiff [5]. This type of interphase is described by the restrained layer theory [6]. It is conceivable that the nature of the interphase would vary with the specific composite system (e.g. carbon fiber versus glass fiber).

The existence of an interphase in PMCs had long been speculated before the advent of techniques that could probe on the scale necessary to show its existence. The interphase is generally thought to be very thin (less than 5  $\mu\text{m}$ ), with the differences in properties between the bulk polymer and the interphase very subtle. The thickness and property gradients within the interphase region have been the focus of increasing research efforts during recent years. These efforts have been heightened by the advent of scanning probe microscopy, which has the ability to probe materials, and presumably the interphase, on the nanometer scale.

In 1990, Williams *et al.* [3] estimated the thickness of the interphase in a carbon fiber/epoxy system to be 500 nm. Williams *et al.*'s approach involved a micro-pullout method to estimate interphase thickness. In 1997, VanLandingham *et al.* used an atomic force microscopy (AFM) nanoindentation technique to determine the thickness of the interphase in a copolymer to be 3  $\mu\text{m}$  [7]. In 1998, Munz *et al.*, using force modulation AFM, determined the interphase in a carbon fiber/epoxy system to be 20–80 nm thick [8]. Also in 1998, Mai *et al.* observed the interphase in a glass fiber/epoxy composite using force modulation AFM to be 1–3  $\mu\text{m}$  [9]. In 1999, Bogetti *et al.* found the interphase in a carbon fiber/epoxy system to be 3 nm [10]. A summary of these findings, along with the system and technique used, appears in Table 1. Also shown in Table 1 is the relative hardness of the interphase compared with the bulk polymer (if determined).

As can be seen in Table 1, the primary methods for measuring interphase characteristics have been AFM force modulation and various forms of nanoindentation. Force modulation involves moving the atomic force microscope tip across a sample

**Table 1.**

Summary of previous findings on interphase thickness and properties in various PMCs

Investigators	Polymer system (method)	Interphase thickness; hardness relative to bulk polymer
Munz <i>et al.</i> [8]	Carbon fiber in epoxy (AFM force modulation)	20–80 nm est.; hardness not reported
Bogetti <i>et al.</i> [10]	Carbon fiber in epoxy (finite element analysis of AFM nanoindentation)	0.003 $\mu\text{m}$ ; softer
Williams <i>et al.</i> [3]	Carbon fiber in epoxy (nanoindentation and micro-pullout debonding)	500 nm est.; softer
VanLandingham <i>et al.</i> [7]	Epoxy and polysulphone (AFM nanoindentation)	3 $\mu\text{m}$ ; harder
Winter and Houston [11]	Glass fiber in epoxy (nanoindentation/interfacial force microscopy)	8 $\mu\text{m}$ ; softer initially, then harder than bulk
Mai <i>et al.</i> [9]	Glass fiber in epoxy (AFM force modulation)	1–3 $\mu\text{m}$ ; ductile in sized fibers, brittle in unsized

in contact mode while the force between the tip and the sample is modulated using a piezoelectric element in the tip holder [12]. Nanoindentation utilizes the same principle as microindentation (or microhardness testing). The difference is that in nanoindentation the probe and loads are much smaller so as to produce indents a few micrometers to a few hundred nanometers in size. Nanoindentation is performed either with an indenter probe on the end of a capacitive load sensor or by a diamond AFM probe affixed to a stiff, stainless steel cantilever.

Reviewing the material in Table 1, it appears that the interphase in carbon fiber systems appears to be thinner than in glass fiber systems and the interphase generally tends to be softer than the surrounding polymer. Also, surface treatment of the fibers is rarely reported. This paper will focus on nanoindentation and a phase imaging technique, the use of which in interphase analysis has not been reported. Phase imaging is similar to force modulation except that Tapping Mode<sup>TM</sup> is used rather than contact mode.

In Tapping Mode<sup>TM</sup>, the AFM tip is oscillated at its resonant frequency and the tip briefly and lightly impacts the sample surface during each oscillatory cycle [13]. This is advantageous in probing soft materials, such as polymers, because the tip-sample interactions are much less damaging than in force modulation or nanoindentation. Phase imaging measures the changes in the phase lag of the oscillation frequency when the AFM tip interacts with areas of differing mechanical

**Table 2.**  
Materials used in this research

Constituent	Product	Manufacturer	Comment
Fiber	25 $\mu\text{m}$ diameter, optical grade $\text{SiO}_2$	Dolan-Jenner	Optical fiber approximating fiberglass reinforcement
Matrix material	EPON 828	Shell Chemical	Commercially used polymer
Curing agent	Nadic methyl anhydride (NMA)	Aldrich Chemical	
Initiator	Imidazole	Avocado Research	0.5% concentration
Surface treatment	$\gamma$ -Aminopropyl- triethoxysilane ( $\gamma$ -APS)	Aldrich Chemical	0.0%, 0.1%, 1.0%, and 5.0% concentrations

properties, and is an extremely sensitive method for differentiating surface features of differing stiffness [12]. For example, a softer material will lead to a greater phase shift and appear bright in the phase image [14]. The phase image would, in the case of a softer interphase, show a bright area surrounding the reinforcing phase. The size of this bright area would then indicate the size of the interphase. Conversely, an area adjacent to the fiber that is darker than the surrounding matrix would indicate a harder, stiffer interphase. However, some care must be exercised in the interpretation of data between different materials as the phase lag may depend on the contact mechanics of the tip–sample interaction.

**2. EXPERIMENTAL**

The choice of materials for this research was made to integrate all areas of investigation within our research group. The integrated effort includes various analytical techniques and encompasses multiple scales, namely molecular, nanometer, and micrometer. Evanescent wave spectroscopy using optical glass fibers has been used to give molecular level information concerning PMC interphase chemistry [15, 16]. Similarly, microbead-debonding tests have been used to measure microscopic level mechanical properties [17, 18]. Taking these other areas of investigation into account, Table 2 shows the constituents of the fiber/matrix system used in this research.

Each sample was initially prepared by fiber surface treatment followed by polymer curing. The curing agent chosen was NMA with 0.5% imidazole initiator (see Table 2). The fiber bundles used with the epoxy system were immersed in an aqueous solution of  $\gamma$ -aminopropyltrimethoxysilane ( $\gamma$ -APS) at room temperature for 1 h. The fiber bundles were then dried at 115°C for 1 h and cooled to 93°C. Treated fibers were next placed in a 100 : 90 EPON 828–NMA mixture along with

## Roughness Analysis

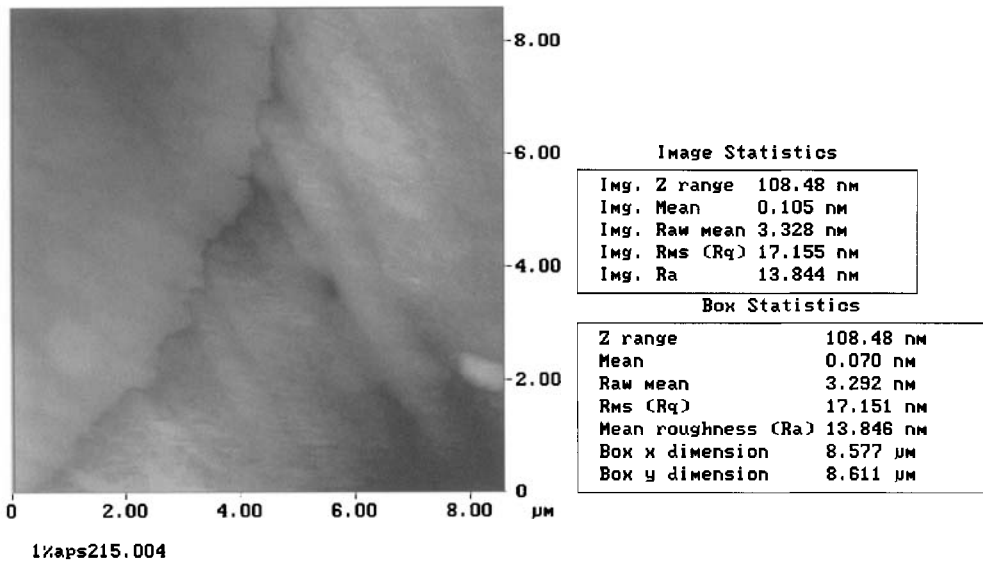


**Figure 1.** AFM roughness analysis of a 1% silane sample.

0.5% imidazole initiator. The mixture was contained in an insulated aluminum cell and maintained at 93°C using a Harrick Scientific temperature controller. After 1 h the temperature was increased over a period of 10 min to 115°C and the sample was allowed to cure overnight [16].

Subsequently, the samples were prepared for AFM and nanoindentation analyses. The sample preparation was as follows. The original specimens were donut-shaped with the fibers running circumferentially about the center. The ‘donut’ was then cut along a diameter. A small section, approximately 3 cm in width, was then cut from one of the half-donut pieces. The small section was then shaped into a 2 cm cube using a circular diamond wafering blade. The resulting cube had fibers running along the upright axis perpendicular to the top and bottom faces. The cube was then affixed to a stainless steel disc, or puck, such that the fibers ran perpendicular to the puck.

Next, the top face of the sample was polished using suspended alumina particles on a standard polishing wheel. Polishing was performed stepwise starting with 1  $\mu\text{m}$  alumina particles (Buehler Scientific), then 0.3  $\mu\text{m}$  particles, and finally 0.05  $\mu\text{m}$  particles. The top face of the sample was then cleaned in an ultrasonic bath consisting of three parts water to one part isopropyl alcohol [8]. After the sample was dried, it was then ready for analysis.

The surface of a typical sample had a vertical range of 100–200 nm with an RMS roughness ( $R_q$ ) of 15–20 nm and a mean roughness ( $R_a$ ) of 10–20 nm. Figure 1

shows a roughness analysis of an AFM height image of a typical sample using a Digital Instruments Nanoscope IIIa Multi-Mode AFM. The fiber appears on the left-hand side of the image. Some scoring in the polymer matrix (right-hand side) due to polishing can be seen.

The polished sample was then analyzed using phase imaging in Tapping Mode<sup>TM</sup> [13, 14]. Areas adjacent to a fiber, yet sufficiently away (approximately 20  $\mu\text{m}$ ) from another fiber were selected so as to prevent the influence of interphase overlap. The drive frequency of the cantilever was chosen such that the tip-sample forces were minimized. This was achieved by setting the drive frequency at the low end of the second free resonant frequency [19]. Other settings, such as feedback set point and oscillation amplitude, were kept constant from one sample to the next.

For nanoindentation experiments, the near-fiber region was located and imaged using scanning force microscopy (SFM) available with the Digital Instruments Nanoscope IIIa Multi-Mode AFM. To avoid erroneous results due to rough topography, the surface to be indented was checked for flatness, with a maximum permissible topographical variation of 5 nm.

Nanoindentations were performed using a Hysitron Triboscope<sup>TM</sup> Nanomechanical Test Instrument running parallel to the AFM. The standard indenting procedure prescribed by Hysitron Inc. [20] was adopted for performing nanoindentations. A peak load of 120  $\mu\text{N}$  at a loading rate of 40  $\mu\text{N/s}$  was used. SFM images of indents and their load-displacement curves were stored in the Hysitron sensor program for future analysis.

After initial nanoindentation, the samples were leached with concentrated hydrofluoric acid for 5 min to remove the fibers. Each sample surface was repolished and nanoindentations were performed on the same region to see the change in nanomechanical properties in the near-fiber region in the absence of fibers. The nanoindenting procedure and parameters were kept the same as those used for samples with fibers. Figure 2 shows the images before and after leaching fibers from the sample.

### 3. RESULTS

Nanoindentation experiments next to the fiber resulted in a gradient in the reduced modulus. Specifically, as shown in Fig. 3A, the reduced modulus varied between  $\sim 35$  and  $\sim 5$  GPa at a distance of about 1.5  $\mu\text{m}$  away from the fiber, after which the modulus value seemed to be close to that of the bulk matrix. However, after the fiber was removed by chemical etching, this gradient in the modulus was reversed, as shown in Fig. 3B. A similarly shaped curve was observed for every fiber studied, although the maximum value obtained varied. Also, the bulk value of  $\sim 5$  GPa was constant in all tests.

Figure 4 shows a representative phase image from one of the samples. The interphase thickness was determined by a statistical analysis of the phase image data. Each phase image was taken apart line-by-line and averaged to produce a

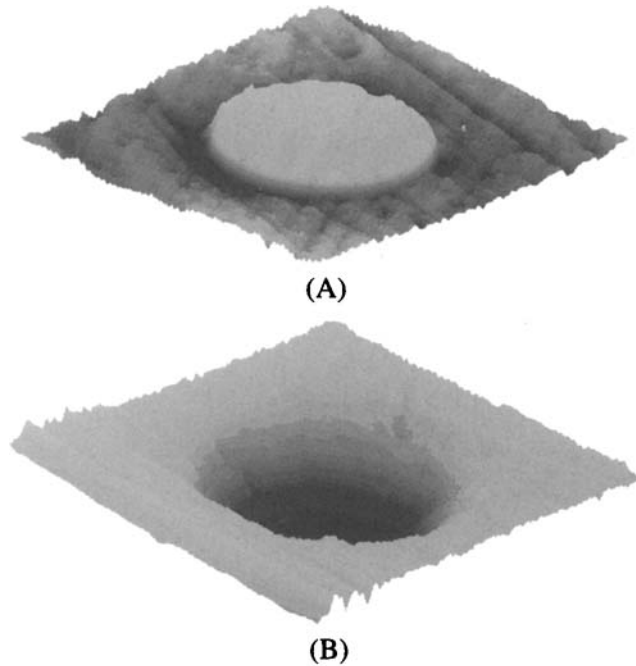


**Figure 2.** (A) AFM image of the composite surface in the presence of a glass fiber. The scan size of the image is 53.20  $\mu\text{m}$ . (B) AFM image of the composite surface in the absence of a glass fiber. The scan size of the image is 51.29  $\mu\text{m}$ .

**Table 3.**  
Interphase thickness determined by phase imaging

$\gamma$ -APS concentration (%)	Average interphase thickness of each fiber scanned ( $\mu\text{m}$ )
0.0	No successful trials
0.1	2.2, 2.1, 2.9, 2.8, 2.5, 2.7, 2.6, 2.5, 2.8, 2.7, 2.1, 3.0, 2.7, 2.4, 2.4
1.0	2.3, 2.6, 2.8, 3.1, 2.5, 2.4, 2.3, 2.2, 2.5, 2.7, 3.0, 2.8, 2.6, 2.7, 2.6
5.0	2.8, 2.9, 3.2, 3.3, 2.6, 2.7, 2.7, 2.8, 2.5, 3.1, 2.3, 2.9, 2.9, 2.5, 2.3

single line representing the mean scan line. This mean line showed the property gradient between the fiber and the bulk polymer. The thickness of the interphase is the distance from the fiber where the property gradient decayed 90%, or 10% of its initial value. In Fig. 4, the position of the three sets of pointers indicates the 100% (right pointer) and 10% (left pointer) values of the gradient. Table 3 shows the phase imaging results of each sample with different  $\gamma$ -APS fiber pretreatments.

The sample with no  $\gamma$ -APS pretreatment did not yield any phase imaging results because the fibers debonded each time the sample surface was prepared, creating a chasm between the fiber and the interphase that was too deep to probe with the AFM. This was due to the fact that the surface treatment promotes adhesion between

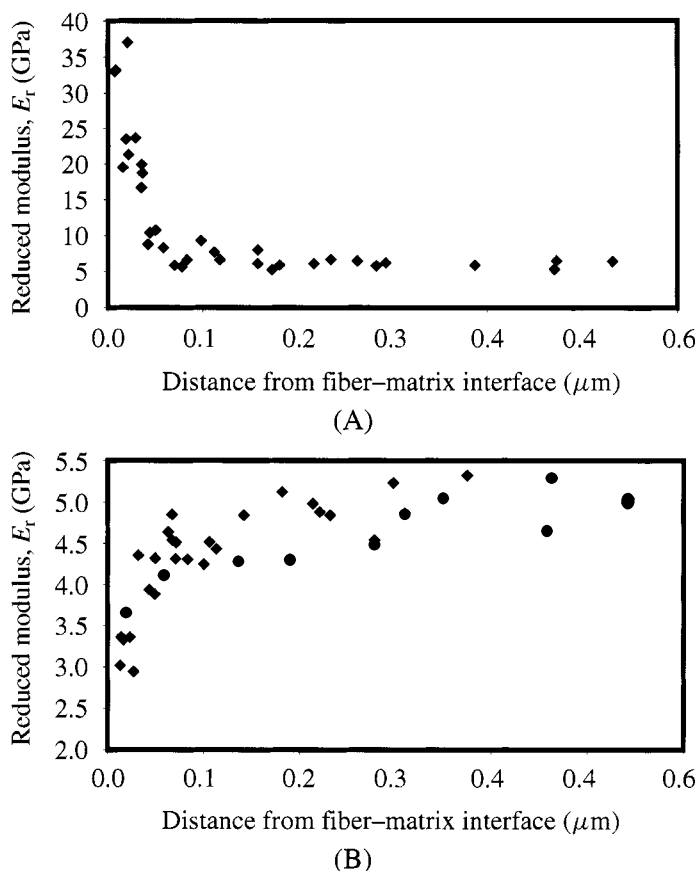


**Figure 3.** (A) Reduced modulus of the matrix next to the fiber, in the presence of a fiber. The reduced modulus varied between  $\sim 35$  and 5 GPa at a distance of about  $1.5 \mu\text{m}$ . (B) Reduced modulus of the matrix next to the fiber, in the absence of a fiber. The reduced modulus varied between  $\sim 3$  and 5 GPa at a distance of about  $1.5 \mu\text{m}$  away from the original fiber volume. Results for 1 wt%  $\gamma$ -APS surface-treated fiber.

the fiber and epoxy, and since no  $\gamma$ -APS was used with this sample, the fibers did not bond well to the epoxy.

The interphase thickness in this system was found to vary between  $2.4$  and  $2.9 \mu\text{m}$  (95% confidence). Furthermore, it was found that this interphase thickness did not vary with the silane concentration pretreatment, when this pretreatment was used. The dark area on the right of the phase image shown in Fig. 4 is the fiber. The bright area to the left of the fiber is the interphase, which then transitions into the darker bulk material. Because the interphase is brighter than the bulk material, it is relatively softer, as described previously. Figure 4 also shows the thickness of the interphase. The distance between the three sets of pointers is shown to the right of the image. As can be seen in this example, the thickness of the interphase ranges from  $2.3$  to  $2.4 \mu\text{m}$ .

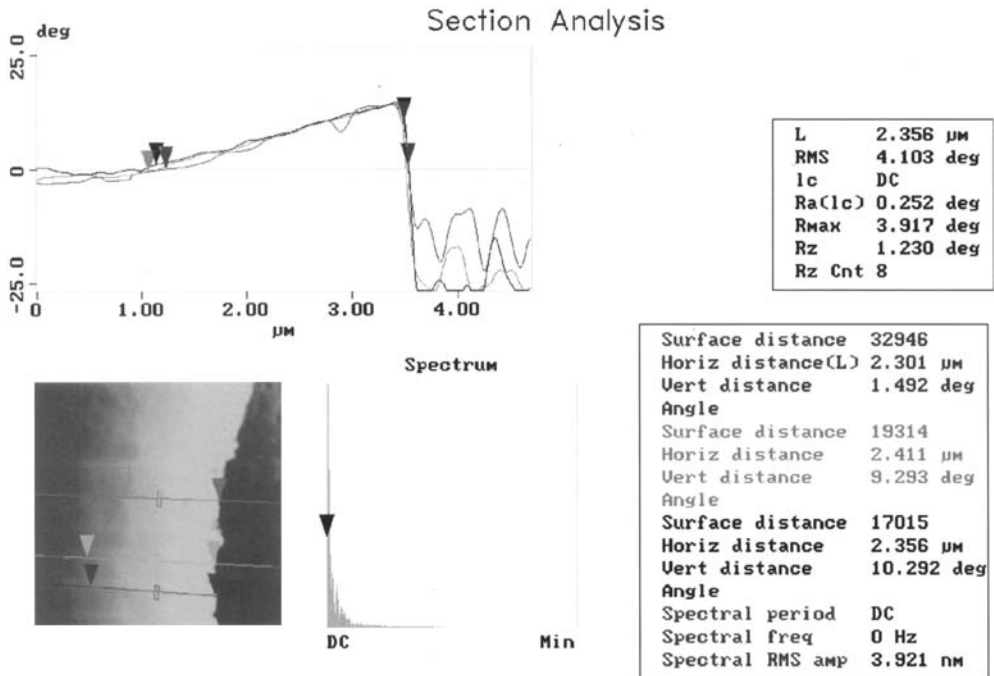


**Figure 4.** Section analysis of phase image showing interphase size and gradient.

#### 4. DISCUSSION

A possible effect of the fiber on the interphase measurements was seen by nanoindentation. This fiber effect manifests itself as an increase in the effective modulus when the nanoindentations are made within 1 μm of the fiber. In other words, despite the extremely low load (120 μN) used with nanoindentation measurements, the presence or absence of the fiber influenced the reduced modulus values that resulted within 1 μm of the fiber. Our research group is currently performing other analyses, including finite element analysis, to model the effect of fiber proximity. Phase imaging of the samples on which nanoindentation was conducted indicates that the interphase thickness is 2.4–2.9 μm and that the interphase is softer than the bulk polymer matrix. Neither of these effects was observed in the nanoindentation data. With the fiber present, a stiffer interphase was found within 1 μm of the fiber and no difference between the fiber and the matrix was found. The first effect has been attributed to a fiber bias, as described previously. The second effect is most likely due to the relatively small differences between the properties of the interphase and matrix making their differentiation difficult. These effects indicate that, for the system studied in this work, a 120 μN load does not provide sufficient sensitivity for the resolution of the interphase properties.

Consequently, the approach to determining the thickness and relative stiffness of the interphase via phase imaging appears to be an improvement over nanoindentation. The advantage of phase imaging over current nanoindentation techniques



is the ability to probe a soft sample using very small loads. It has been estimated that tapping mode contact forces between the tip and the sample surface is of the order of 100–150 nN [19]. This makes phase imaging much more sensitive to local variation in surface stiffness, much more so than nanoindentation where loads are between 50 and 150  $\mu$ N.

Phase imaging also proved a much better method of analysis than force modulation for this system. Force modulation was attempted but the resultant images provided an extremely low contrast when compared with phase imaging. This low contrast is thought to occur because the AFM probe is not in constant contact with the sample surface in phase imaging, whereas in force modulation the probe is dragged along the sample surface. This creates high lateral forces that degrade the sample significantly, resulting in a lower contrast.

As mentioned earlier, the phase imaging results suggest that the interphase thickness does not change appreciably with the silane concentration. These results can be interpreted in terms of the possible methods by which the interphase forms. Furthermore, the coating of fibers with silane coupling agents is not a very well understood phenomenon. Current understanding suggests that such silane coatings have three layers [21]: a surface bonded layer whose structure depends on the type of substrate and the conditions under which adsorption occurred. This surface bonded layer is attached to a chemisorbed multilayer whose structure is fairly compact near the surface and becomes less compact as the distance from the surface increases. Finally, the outermost layer is a physically bonded layer which is composed of silane oligomers which are only weakly bonded to the silane, which is chemisorbed to the surface. The relative abundance of each of these phases depends on the surface chemistry of the fiber and on the solution concentration. At 5% silane in solution, relatively more physisorbed silane is expected to be present on the fiber than when 1% silane is in solution. At 0.1% silane, little or perhaps no physisorbed silane is expected.

Two hypotheses for the same interphase thickness can then be envisioned. First, the physisorbed silane may be soluble in the epoxy resin. This would cause all surfaces to exhibit a nearly identical chemisorbed silane surface to the polymer. Alternatively, the chemical differences between the physisorbed layer and the chemisorbed layer are extremely small, thus causing the polymer to 'see' essentially the same surface in all cases. Previous research on coupling agent reaction chemistry in our group has indicated that only a little of the adsorbed silane leaves the surface upon exposure to epoxy polymer [22]. This seems to indicate that the alternative explanation may be more likely.

In either case, the important factor is the chemical nature of the surface. In many cases, the interphase forms due to preferential adsorption of one component (usually the amine curing agent) with respect to the other components of the polymer. Thus, if essentially identical surfaces are exposed to the polymer, equal thickness interphases should result. This assumes that the interphase is much thicker than the thickness of the adsorbed layer. A good test of this hypothesis would be to

measure via phase imaging the interphase thickness in the absence of adsorbed silane. Unfortunately, we were unable to complete these experiments in time for this paper, due to debonding of the fiber from the matrix during sample preparation.

The preferential adsorption of one component of the polymer is also thought to be responsible for the softness of the interphase. VanLandingham *et al.* [23] showed that altering the stoichiometry of epoxy resulted in an alteration of the network formed during curing. Specifically, the epoxies contained a harder phase and a softer phase. For amine-rich epoxy, which may be similar to the interphase, a greater amount of the softer phase was observed compared with stoichiometric (bulk) epoxy.

## 5. CONCLUSIONS

A possible fiber effect was found on nanoindentation measurements in the near-fiber region. This was shown by nanoindentation measurements with and without the fiber present. Under these conditions, the gradient in the modulus was seen to reverse itself. AFM phase imaging is a good tool for measuring the thickness and relative stiffness of the interphase in PMCs. Specifically, due to the extremely low loads involved with phase imaging, any fiber bias effect found with nanoindentation can be minimized. For the PMC system investigated, phase imaging found the interphase to be 2.4–2.9  $\mu\text{m}$  thick, with the interphase being softer than the bulk matrix. Also, the interphase size was found to be independent of the fiber silane pretreatment. Future work will incorporate finite element analysis with nanoindentation and AFM phase imaging. It is felt that this combined analytical/experimental approach will lead to an improved understanding of the role of the interphase in PMC performance.

## Acknowledgements

We would like to thank Farrah Johnson for sample preparation. This research was made possible by grants from the National Science Foundation (CMS-9453467 and DMR-9724532).

## REFERENCES

1. L. H. Sharpe, *J. Adhesion* **4**, 51 (1972).
2. L. T. Drzal, in: *Epoxy Resins and Composites II*, K. Dusek (Ed.), pp. 3–32. Springer-Verlag (1986).
3. J. G. Williams, M. E. Donnellan, M. R. James and W. L. Morris, *Mater. Sci. Eng. A* **126**, 305 (1990).
4. E. P. Plueddemann, *Silane Coupling Agents*, 2nd edn. Plenum Press, New York (1991).
5. M. R. Piggott, *Mater. Res. Soc. Symp. Proc.* **170**, 265 (1990).
6. C. A. Kimins and J. Roteman, *J. Polym. Sci. A* **527** (1963).

7. M. R. VanLandingham, S. H. McKnight, G. R. Palmese, J. R. Elings, X. Huang, T. A. Bogetti, R. F. Eduljee and J. W. Gillespie, Jr., *J. Adhesion* **64**, 31–59 (1997).
8. M. Munz, H. Sturm, E. Schulz and G. Hinrichsen, *Composites Part A* **29A**, 1251–1259 (1998).
9. K. Mai, E. Mäder and M. Mühle, *Composites Part A* **29A**, 1111–1119 (1998).
10. T. A. Bogetti, T. Wang, M. R. VanLandingham and J. W. Gillespie, Jr., *Composites Part A* **30A**, 85–94 (1999).
11. R. M. Winter and J. E. Houston, in: *Proceedings of the SEM Spring Conference on Experimental and Applied Mechanics*, pp. 355–358. Society for Experimental Mechanics (1998).
12. S. N. Magonov and D. H. Reneker, *Annu. Rev. Mater. Sci.* **27**, 175–222 (1997).
13. N. A. Burnham, O. P. Behrend, F. Oulevey, G. Gremaud, P. J. Gallo, D. Gourdon, E. Dupas, A. J. Kulik, H. M. Pollock and G. A. D. Briggs, *Nanotechnology* **8**, 67–75 (1997).
14. M. H. Whangbo, S. N. Magonov and H. Bengel, *Probe Microsc.* **1**, 23–42 (1997).
15. F. Johnson, M. Connell, E. Duke, W. Cross and J. Kellar, *Appl. Spectrosc.* **52**, 1126 (1998).
16. F. J. Johnson, W. M. Cross, D. A. Boyles and J. J. Kellar, *Composites Part A* **31**, 959 (2000).
17. L. L. Qian, F. A. Bruce, J. J. Kellar and R. M. Winter, *Measurement Sci. Technol.* **6**, 1009–1015 (1995).
18. W. M. Cross, L. Kjerengtroen, R. M. Winter, W. Jiang, W. Fan and J. J. Kellar, in: *Materials for the New Millennium: ASCE 1996 Materials Engineering Conference*, K. Chong (Ed.), Vol. 1, pp. 356–365. ASCE, Washington, DC (1996).
19. J. P. Spatz, S. Sheiko, M. Müller, R. G. Winkler, P. Reineker and O. Marti, *Nanotechnology* **6**, 40–44 (1995).
20. Hysitron Inc., *Triboscope Nanomechanical Test System, Setup and Operation Guide* (1996).
21. R. N. Rothon, in: *Particulate-Filled Polymer Composites*, R. Rothon (Ed.), Ch. 4, pp. 140–146. Longman Scientific and Technical, UK (1995).
22. M. E. Connell, W. M. Cross, T. G. Snyder, R. M. Winter and J. J. Kellar, *Composites Part A* **29A**, 495–502 (1998).
23. M. R. VanLandingham, R. F. Eduljee and J. W. Gillespie, Jr., *J. Appl. Polym. Sci.* **71**, 699–712 (1999).

## Use of an atomic force microscope to measure surface deformations in polymeric systems

MICHAEL C. ROGGEMANN<sup>1</sup> and JOHN G. WILLIAMS<sup>2,\*</sup>

<sup>1</sup> *Department of Electrical Engineering, Michigan Technological University, Houghton, MI 49931, USA*

<sup>2</sup> *Department of Chemistry, Michigan Technological University, Houghton, MI 49931, USA*

**Abstract**—An atomic force microscope is used to image an unstressed sample which is subsequently stressed and re-imaged. An image analysis program is described which allows mapping of surface deformations from the images.

In order to show the scope of the present analysis of deformation in plastics, three load conditions showing deformation in a glassy plastic have been selected. In the first a simple tensile load is applied and the image is obtained at low magnification. These images show the general, homogeneous deformation expected with a general elongation in the load direction, an obvious Poisson contraction in the surface plane normal to the load direction and some slight suggestion of Poisson contraction in the through-thickness direction. This loading configuration is intended to reproduce the predicted deformations to illustrate the applicability of the method under simple load conditions. The second loading condition, of a tensile specimen containing a hole, is intended to illustrate the applicability of the system to more complex loading conditions where stress concentrations modify the deformation pattern. The third loading condition is around the tip of a crack propagating in a predictable way in a standard fracture toughness specimen. These images are intended to show the usefulness of the method in characterizing deformations in a complex stress field during failure of the material.

*Keywords:* AFM; polymers; deformation.

### 1. INTRODUCTION

In order to characterize material behavior of complex systems, a knowledge of the elastic modulus is essential. For many systems the modulus has been shown to vary on a very fine scale such as in the interphase between the fiber and the matrix in traditional composites [1] and between the adherend and adhesive in a bonded joint [2]. In these regions, material properties change on the spatial scale of a

---

\*To whom correspondence should be addressed. Phone: (906) 487-2491. Fax: (906) 487-2061. E-mail: jgwillia@mtu.edu

few tenths of a micrometer to a few micrometers. In order to determine and map modulus variations such as these, knowledge of the local stresses and strains is needed at an appropriate scale. For example, in adhesive joints, researchers often postulate the presence of an interfacial region with different mechanical properties from the bulk adhesive. A knowledge of the displacements near the interface that occur on loading an adhesive joint would supply direct evidence for modulus variations in this region.

### *1.1. Microscopy of polymers*

Optical, electron, and atomic force microscopies have been used to characterize surfaces of polymers.

Optical resolution is suitable for analysis of materials down to about 10  $\mu\text{m}$ . Analysis of stereomicrographs can be used to provide surface maps from optical images [3], but phase-microscopy could also be used. Optical equipment can give detailed image of the average stress through a transparent polymeric sample using polarized light and stress-optical procedures [4].

Scanning electron microscopy can be used to provide information on the surface topography of material samples. This has been used for analysis of crack growth in metallic materials [5] and for analysis of deformation around fibers in plastic matrix composites [1, 6]. This technique is complex and can give rise to artifacts [1].

Atomic force microscopy is well suited to analysis of surface deformations in materials. It has high  $X$ ,  $Y$ , and  $Z$  resolution. This paper describes development of image analysis algorithms to map surface displacements induced in polymeric systems by the application of loads.

## **2. EXPERIMENTAL**

### *2.1. Materials and sample preparation*

The materials used were based on an epoxy resin (Epon 825 supplied by Shell Chemical Corp.) cured with a proprietary amine (Jeffamine D230 supplied by Texaco Corp.). The amine is identified as an amine terminated polyoxypropylene which was stated to have an approximate molecular weight of 230. For the tensile sample with hole, the epoxy matrix was used directly. For the simple tensile and cracked samples, the epoxy system was modified by the addition of 10 wt% of a carboxyl terminated polybutadiene polymer (Hycar 1300). The resin, curing agent, and additives were mixed in stoichiometric proportions by hand and then agitated the mix in an ultrasonic bath for about 1 min to ensure homogenization [7]. The mix was then centrifuged to remove entrapped air, poured into molds and cured at 60°C for several hours.

Tensile samples were cast into micro-tensile molds which produced samples about 50 mm long with a 25-mm waist section, 5 mm across and 1 mm thick. Sample

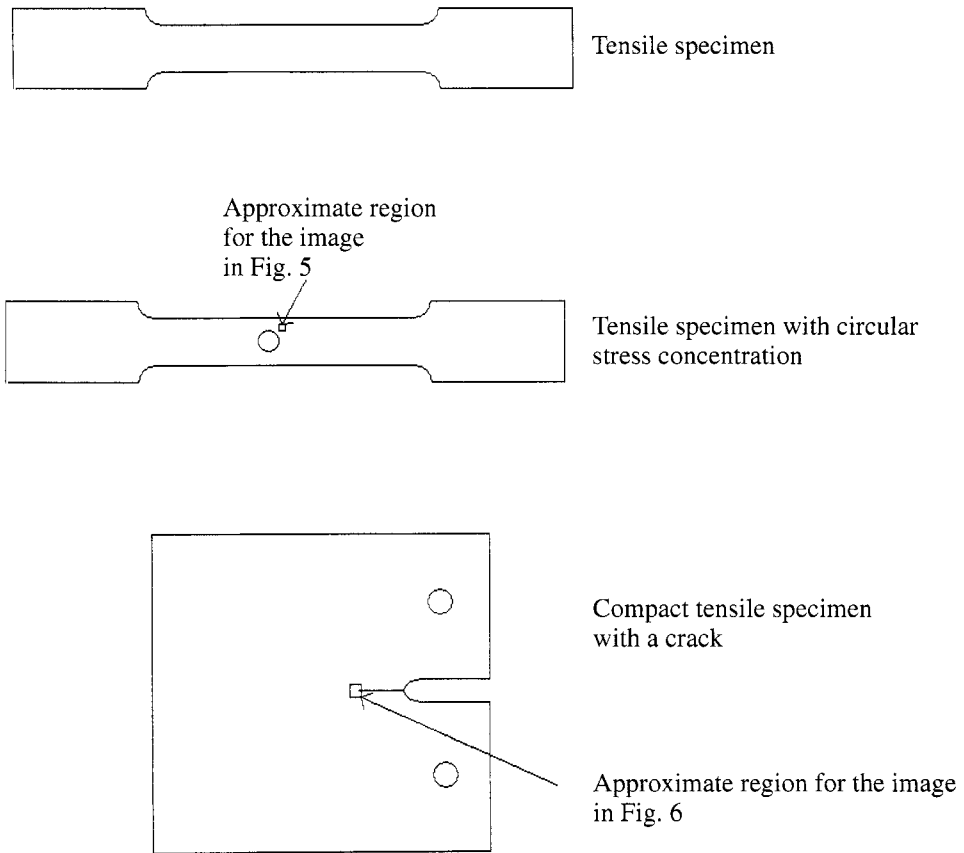


**Figure 1.** Schematic representation of the sample configurations used. The tensile specimens are about 40 mm long and about  $4 \times 1$  mm cross section in the waist region. The hole giving the stress concentration in the second sample is slightly under 1 mm diameter. The compact tensile samples are about 10 mm square and 1 mm thick. The sample is notched and a short crack initiated in the notch using a razor blade as a wedge.

dimensions were approximately those suggested by ASTM 1708. The compact tensile specimens were cast as sheets between glass plates with silicone rubber spacers which were cut into rectangular samples. The final dimensions were 12 mm square and 1 mm thick. The process used for initiating a sharp crack in the specimen is described in ASTM D5045. Following this method, a notch was cut into the sample using a jeweller's hacksaw and a sharp crack tip was initiated by tapping a precooled razor blade into the notch of the sample, cooled in liquid nitrogen. Specimen configurations are shown in Fig. 1.

In all cases, the samples were polished using carborundum paper from 240 grit down to 1200 grit on a Buehler roll polishing table and then on a Buehler rotating polishing station using alumina grit from 5 to  $0.05 \mu\text{m}$ . The samples were cleaned in an ultrasonic bath. The samples were then coated with a film of carbon using

standard vacuum coating techniques. Although samples without carbon could be imaged, the carbon reduced problems associated with build-up of static charge and added fine structure to the image at the submicrometer level. The tensile sample with the hole was polished and coated after drilling a single 1-mm diameter hole approximately in the center of a standard tensile dogbone. The compact tensile specimen was polished and coated after the crack had been initiated.

## 2.2. Atomic force microscopy measurements

A Topometrix Acurex IIL AFM was used to generate the surface topographic images. The samples were held in a straining stage which was bolted to the stage of the AFM. The standard specimen chuck had the capability to move the straining stage in the  $X-Y$  directions or to rotate it. After positioning the sample under the microscope probe, the sample stage was locked in place using vacuum clamps. The stage was fitted with open jaw grips for the miniature tensile dogbone samples or a pin jaw for the miniature compact tensile specimens. In general, the samples were imaged in an unstressed state and were then deformed and images of the deformed specimens were taken under load. The straining stage incorporated a load cell with a load capacity of 100 kg. The load cell output was recorded on a PC. A mechanical dial gage was used to measure the overall crosshead displacement. The load cell was calibrated with dead weights before use and the dial gage was read directly.

The AFM images were recorded in non-contact mode in which the tip vibrates close to its natural resonant frequency. The control mechanism adjusts the height of the tip above the surface to maintain a constant amplitude of vibration. The image is generated using the position of the tip relative to the surface as the tip is moved across the surface.

The measurement of surface deformations reported here requires collecting two images of essentially the same area differing in the applied load. Although the software used to analyze the deformation included a procedure to register the two image areas, it was found that the precision was improved if the overlap area between the images was maximized. The load could not be changed on the specimen while the probe was in contact with the surface as any  $Z$  movement would have resulted in damage to the probe. With care, however, the general area close to the end of a fiducial mark could be imaged, using the lowest magnification of the instrument (100  $\mu\text{m}$  square). Local features visible in this image would generally allow a 50- $\mu\text{m}$  square viewing area to be selected that was the same, within the required precision, each time the surface was imaged. Images were collected with image areas down to about 5  $\mu\text{m}$  square but at higher magnifications the features on the images became difficult for the software to detect reliably and the deformation data were lost in noise. Future work will address methods for optimizing the size of surface features to allow images to be resolved at higher magnifications.

Generally, two images were recorded at each load condition and the Topometrix software package was used to flatten and rescale the images. The algorithm used was a second-order plane correction which was used to minimize the effect of

the curvature in the path of the probe tip during collection of the image on this instrument. The files were exported in ASCII format into the analysis software (MATLAB Version 5.1).

The Topometrix software package passes the image to the MATLAB software as two matrices. Both matrices are square with the number of rows and columns equal to the resolution selected during imaging. In this case the resolution was 300 pixels. Each cell contains a number which is a quantitative assessment of an image property measured by the Topometrix program. The height data used for this work were derived from the voltage supplied to the piezo-crystal linearized by internal calibration of the voltage applied to the Z-piezoelement as a function of tip position in the Z-axis.

The program to derive the deformation data from the selected images is described in detail below. In this program, the first image, after optimum registration with the second image, is divided into a number of test areas. For example, in the simple tensile load case shown below, the test area was  $10 \times 10$  pixels. The outside rows and columns are removed as the edge-areas in the deformed image in two of the dimensions will typically lie outside the reference test area. This leads to a random match which obscures the precision of the remaining matches.

The search area is restricted to reduce computational time and to reduce the probability of a match between random areas giving a chance correlation higher than the real match due to the statistical nature of the correlation. A high value for this variable usually results in a large number of random, large displacements, while a low number limits the size of the largest displacement that can be found equal to the value of the input number in pixels. If the real displacement is larger than this value, the program will find a random match. Some optimization of the data can be obtained by trying different values for this constant.

Displacements, such as those shown in Fig. 2, are found from the  $X$  and  $Y$  coordinates necessary to register the test area in the two images. The program also produces output such as is shown in Fig. 3. This output image includes thumbnail images of the two areas after superposition, a plot of the maximum correlation coefficient (scaled to lie between zero and one) as a function of  $X$ ,  $Y$  position of each element and three 3D curves illustrating the variation of the  $X$ ,  $Y$ , and  $Z$  displacements with the position of the test region in the first image.

### 2.3. Image processing

In image processing the correlation,  $\Gamma(\Delta\vec{x})$ , between two continuous images  $i_1(\vec{x})$  and  $i_2(\vec{x})$ , where  $\vec{x}$  is a two-dimensional spatial location in the image, is given by equation (1):

$$\Gamma(\Delta\vec{x}) = \int d^2\vec{x} i_1(\vec{x}) i_2(\vec{x} + \Delta\vec{x}), \quad (1)$$

where  $\Delta\vec{x}$  is a shift variable, and the integration is taken over all space. For the simple case where  $i_2(\vec{x})$  is simply a shifted version of  $i_1(\vec{x})$ , i.e. if  $i_2(\vec{x}) =$



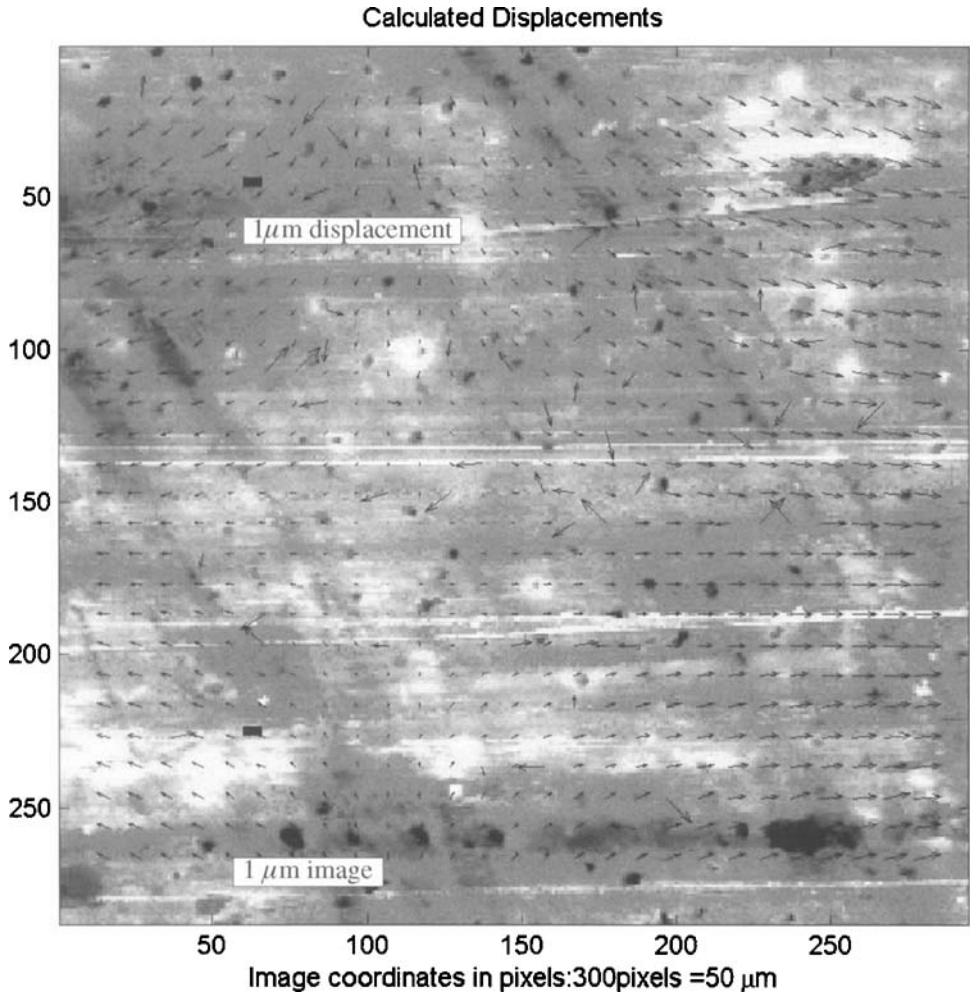


**Figure 2.** Calculated displacements for a tensile sample superimposed on the image of the unstrained sample. Loading on the sample is described in the text but the tensile load is applied in the horizontal direction.

$i_1(\vec{x} - \Delta\vec{x}_1)$ , it is easy to show that  $\Gamma(\Delta\vec{x})$  takes its maximum value for the shift  $\Delta\vec{x} = \Delta\vec{x}_1$ , and that  $\Gamma(\Delta\vec{x}) > 0$ . Conversely, in the limiting case where  $i_1(\vec{x})$  and  $i_2(\vec{x})$  consist entirely of zero-mean, uncorrelated noise,  $\Gamma(\Delta\vec{x}) = 0$ . It is also possible for  $\Gamma(\Delta\vec{x}) < 0$ , in which case  $i_1(\vec{x})$  and  $i_2(\vec{x})$  are said to be ‘anticorrelated’, but as will become apparent later in the paper, this case is of no interest in the present application. When  $i_2(\vec{x})$  is similar, but not identical to  $i_1(\vec{x})$ ,  $\Gamma(\Delta\vec{x})$  still typically (except in a few degenerate cases) takes on some maximum positive value, though the maximum value is generally less than the maximum mentioned above for the case where  $i_1(\vec{x})$  and  $i_2(\vec{x})$  are shifted versions of each other. This maximum in  $\Gamma(\Delta\vec{x})$  occurs at the shift for which  $i_1(\vec{x})$  and  $i_2(\vec{x})$  match to the largest extent

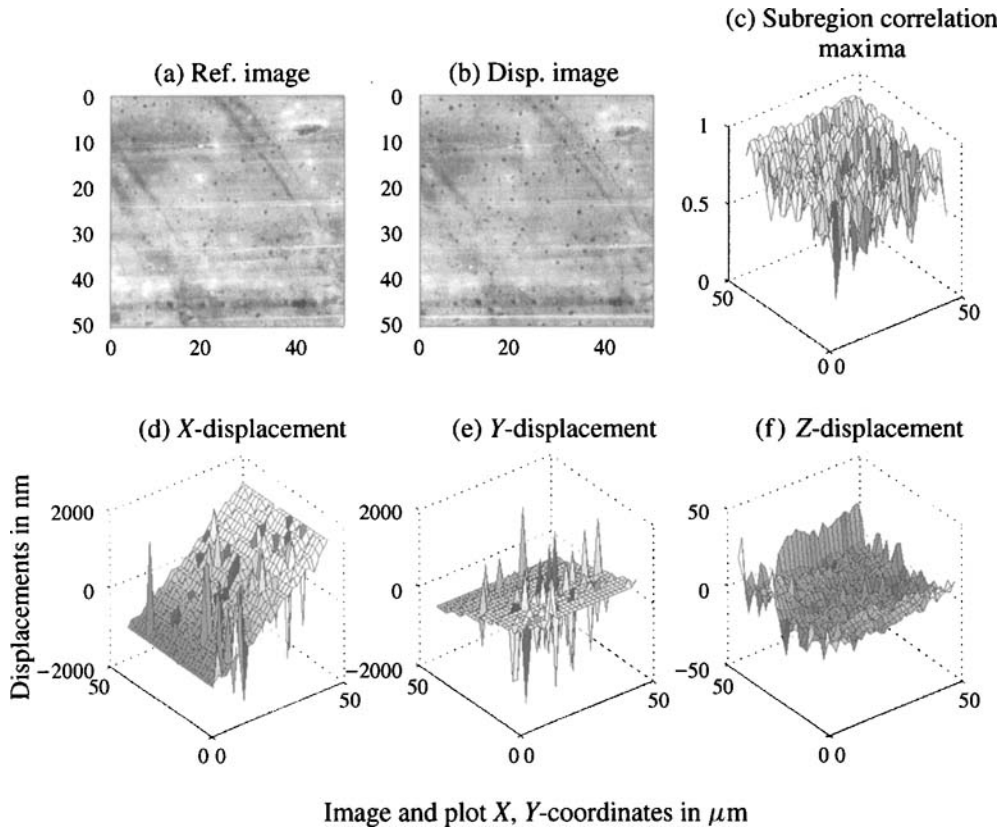


**Figure 3.** Summary output from the analysis program for the image of the simple tensile specimen shown in Fig. 2. The two images (a) and (b) represent the unstrained and strained images after global superposing and trimming of unmatched areas. Image (c) shows the maximum correlation obtained for each area. Images (d)–(f) show the displacements in the  $X$ -,  $Y$ -, and  $Z$ -directions, respectively, over the image area.

possible. Because of these properties of the correlation function, correlations are widely used in image and signal processing, and in automatic pattern recognition to measure the similarity between an unknown input image and a set of prestored template, or reference images. In fact, the so-called ‘matched filter’ widely used in signal and image processing is based on a Fourier-domain implementation of this idea. Because variations in the magnitude of  $i_1(\vec{x})$  or  $i_2(\vec{x})$ , and measurement noise corruption could change the maximum value of  $\Gamma(\Delta\vec{x})$ , a normalized version of  $\Gamma(\Delta\vec{x})$  is generally used in practice. This normalized version is given in continuous space by equation (2):

$$\gamma(\Delta\vec{x}) = \frac{\int d^2\vec{x} i_1(\vec{x}) i_2(\vec{x} + \Delta\vec{x})}{\left[ \int d^2\vec{x} (i_1(\vec{x}))^2 \times \int d^2\vec{x} (i_2(\vec{x}))^2 \right]^{1/2}}, \quad (2)$$

so that when  $i_2(\vec{x}) = i_1(\vec{x} - \Delta\vec{x}_1)$ ,  $\gamma(\Delta\vec{x})$  takes its maximum value of unity at the shift  $\Delta\vec{x} = \Delta\vec{x}_1$ . Real digital images, such as the AFM images discussed here, are discretely sampled in space, and exist only on a defined set of two-dimensional points in an image. The representation of the discrete image corresponding to the continuous image  $i_1(\vec{x})$  with the notation  $i_1(m, n)$ , where  $(m, n)$  is a two-dimensional location in the image array, and the discrete version of  $i_2(\vec{x})$  are defined similarly. The discrete, normalized correlation of two images  $i_1(m, n)$  and  $i_2(m, n)$  is defined similarly to the continuous normalized correlation given in equation (2), and is given by equation (3):

$$\gamma(\Delta m, \Delta n) = \frac{\sum_{m,n} i_1(m, n) i_2(m + \Delta m, n + \Delta n)}{\left[ \sum_{m,n} (i_1(m, n))^2 \times \sum_{m,n} (i_2(m, n))^2 \right]^{1/2}}, \quad (3)$$

where  $(\Delta m, \Delta n)$  is the discrete shift. In the case of AFM images, it is in practice very difficult to reproduce the same reference plane from measurement to measurement. The result is that if a sample is measured with the AFM, removed from the AFM, and then reinserted and remeasured, then  $i_1(\vec{x})$  and  $i_2(\vec{x})$  would generally differ from each other by a small constant. A specialized form of  $\gamma(\Delta m, \Delta n)$  is computed in this case by using spatial mean-removed versions of  $i_1(m, n)$  and  $i_2(m, n)$  in equation (3), where the mean-removed versions are represented by  $i_1^{\text{mr}}(m, n)$  and  $i_2^{\text{mr}}(m, n)$ , respectively. Hence, the actual form of the normalized discrete correlation used here is obtained by substituting  $i_1^{\text{mr}}(m, n)$  and  $i_2^{\text{mr}}(m, n)$  for  $i_1(m, n)$  and  $i_2(m, n)$  in equation (3).

In implementing a practical calculation of  $\gamma(\Delta m, \Delta n)$  care must be taken to account for the fact that if  $i_1^{\text{mr}}(m, n)$  has  $N_1 \times M_1$  pixels, and  $i_2^{\text{mr}}(m, n)$  has  $N_2 \times M_2$  pixels, then  $\gamma(\Delta m, \Delta n)$  has  $(N_1 + N_2 - 1) \times (M_1 + M_2 - 1)$  pixels. Approaches for managing this problem typically involve zero-padding the data into a larger array or, as done here, selecting subframes of the original data to process, and restricting the range of shifts examined. Henceforth, only with the discrete normalized correlation  $\gamma(\Delta m, \Delta n)$  is considered.

The image processing algorithm described in the next section is based on the assumption that on a small spatial scale the surface elements of the polymer sample simply move as a result of the applied stress, and do not change significantly in any other way. This assumption allows an algorithm to be developed which seeks the 'new' location of the surface element in the image taken after the stress was applied. The new location of the surface element is estimated using a processing technique based on the discrete normalized correlation given in equation (3). With these preliminaries, the algorithm is now described in detail.

## 2.4. Algorithm description

The algorithm for detecting the stress-induced displacements of polymer surfaces using automatic computer processing of pairs of AFM images has six steps, which are given below:

- (1) Measure a reference image  $i_R(x)$  of the region of the sample which is of interest.
- (2) Apply a mechanical stress to the polymer, and measure the deformed image,  $i_D(x)$ . The goal is to have  $i_R(x)$  and  $i_D(x)$  coincide spatially to the largest extent possible, though perfect realization of this goal is impossible in practice.
- (3) Calculate  $\gamma^n(\Delta x)$  for the whole images  $i_R(x)$  and  $i_D(x)$  and search the resulting array for the shift  $\Delta x_R$  which maximizes  $\gamma^n(\Delta x)$ . The shift  $\Delta x_R$  corresponds to the macroscopic misregistration of the regions of interest in  $i_R(x)$  and  $i_D(x)$  resulting from the inability to perfectly select the exact same regions in the reference and deformed images.
- (4) Macroscopic registration is accomplished by shifting the image  $i_D(x)$  by the amount  $-\Delta x_R$ , and selecting the overlapping portions of both images.
- (5) Finally, the reference image  $i_R(x)$  is separated into a number of small, non-overlapping regions, and the discrete, normalized correlation is computed for each of the possible shifts in a larger search region within  $i_D(x)$ . The search region is generally centered on the location of the subregion extracted from  $i_R(x)$ . The shift which maximizes  $\gamma^n(\Delta x)$  is taken as the stress-induced displacement of the surface element in  $i_R(x)$  being processed.
- (6) Relevant information is stored for quantitative analysis and presented for visualization.

## 3. RESULTS

Table 1 shows the experimental configurations used to load the samples and to record the images for the three experimental load configurations.

**Table 1.**

Load configuration		Simple tension	Tension with stress concentration	Crack propagation
Resin system	Units	Rubber toughened epoxy	Unmodified epoxy	Rubber toughened epoxy
Applied load	N			3
Calculated stress	MPa	8.6	5.7	
Crosshead movement	mm		0.38	<0.5
Calculated strain	%	0.016		
Image size	pixels	50 × 50	20 × 20	50 × 50
Resolution	pixels	300	300	300
Test area	pixels	10 × 10	10 × 10	10 × 10
Search range	pixels	±10	±10	±10

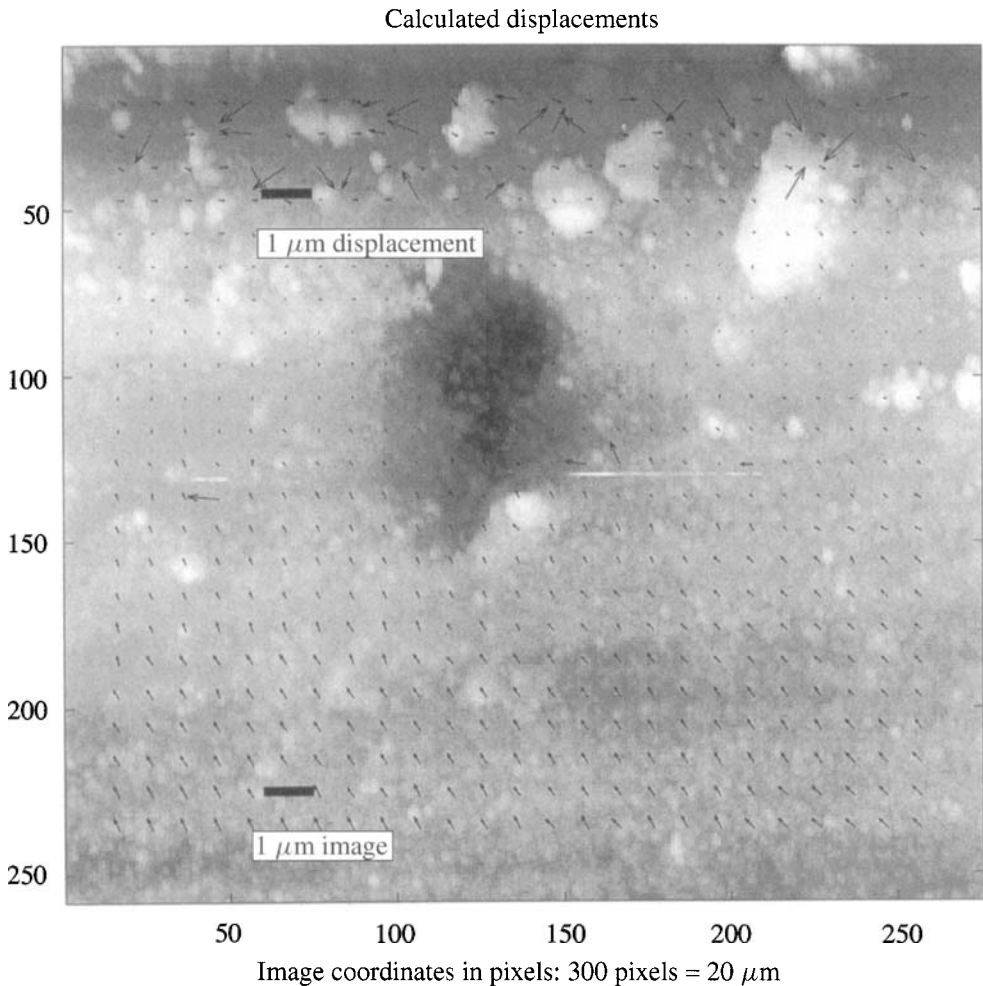


**Figure 4.** Calculated displacements for a tensile sample with stress concentration superimposed on the image of the unstressed sample. Tensile loading was applied in the horizontal direction. The area imaged is such that the edge of the hole cannot be seen but the general direction is to the top-right corner of the image. A dust particle obscures part of the image.

In the first example, the specimen is loaded in simple tension. Figure 2 shows the  $X$ ,  $Y$  displacements resulting from processing this pair of images and Fig. 3 shows the detail computer output image corresponding to Fig. 2. The surface deformations found for the second load case, i.e. for the tensile sample with a stress concentration, are shown in Fig. 4 and those for the third example, the cracked sample, are shown in Fig. 5. For the first two examples, the displacements in the  $Z$ -direction are observed to be uniform over the sample and no significant change in the deformation can be detected. In the third case, the variation of the  $Z$  displacement over the image is significant and Fig. 6 shows a representation of the  $Z$  displacement data.

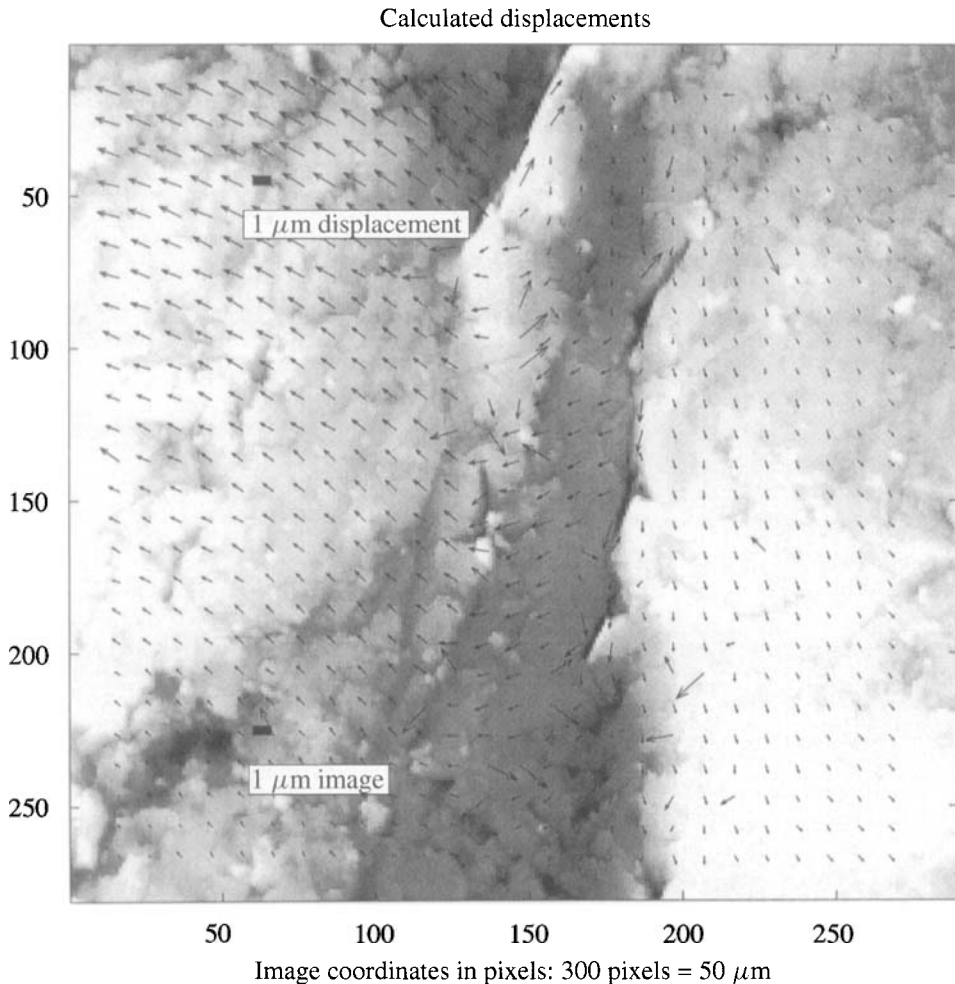


**Figure 5.** Calculated displacements for a cracked sample superimposed on the image of the unstressed sample. The tip of the crack can be seen in the top, center of the image. The tensile load causing the crack to propagate is applied in the horizontal direction.

## 4. DISCUSSION

### 4.1. Interpretation of the displacements

Interpretation of the surface displacements can be difficult. The process of developing the images has caused a considerable amount of averaging of the data in an effort to reduce the effect of misalignment of the two images, curvature due to the geometry of the movement of the cantilever (which is constrained to move in an arc) and massive movements of the sample during loading and unloading. This means that the  $X$  and  $Y$  displacements are referred to an arbitrary zero.

## Z-deformation for the cracked specimen

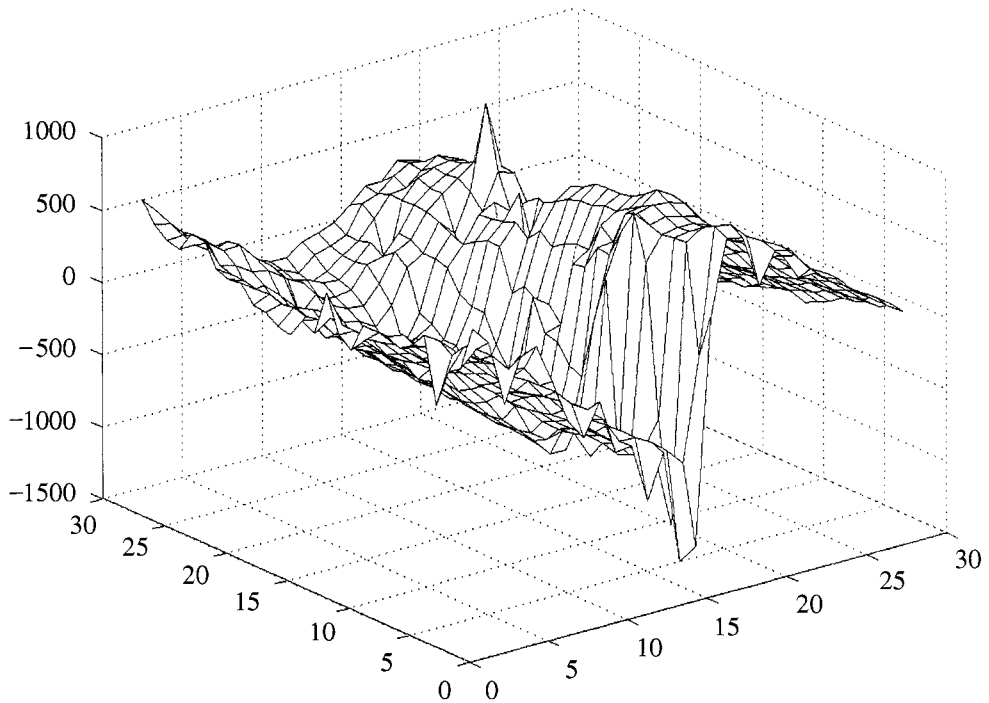


**Figure 6.** A three-dimensional representation of the Z-displacement data for the cracked sample. The image is rotated 180° compared to Fig. 5. The X and Y coordinates are the test area numbers (thirty areas represents 50  $\mu\text{m}$ ). The Z coordinate is in nm. The crack tip can be seen in the center of the front edge of the image. A large Z displacement associated with the crack tip can be seen.

*4.1.1. Tensile/compressive and shear strains.* The in-plane displacements can be converted to relative strains by differentiating the displacements:

$$\varepsilon_x = \frac{\partial u}{\partial x}, \quad (4)$$

$$\varepsilon_y = \frac{\partial v}{\partial y}, \quad (5)$$

$$\varepsilon_{x,y} = \frac{\partial u}{\partial y} + \frac{\partial v}{\partial x}, \quad (6)$$

where  $\varepsilon_x$  and  $\varepsilon_y$  are the tensile components of the deformation in the X (column) and Y (row) directions and  $\varepsilon_{x,y}$  is the shear strain in the X, Y (image) plane and  $u$  is the X displacement in the load (X) or column direction and  $v$  is the displacement in the Y or row direction. For the present experiments the deformation appears uniform between pixels and the differential terms can be replaced by discrete differences between adjacent cells in the matrix. If the displacement vectors, shown by arrows in Figs 2, 4, and 5, vary in a uniform way across the surface of the sample, as may

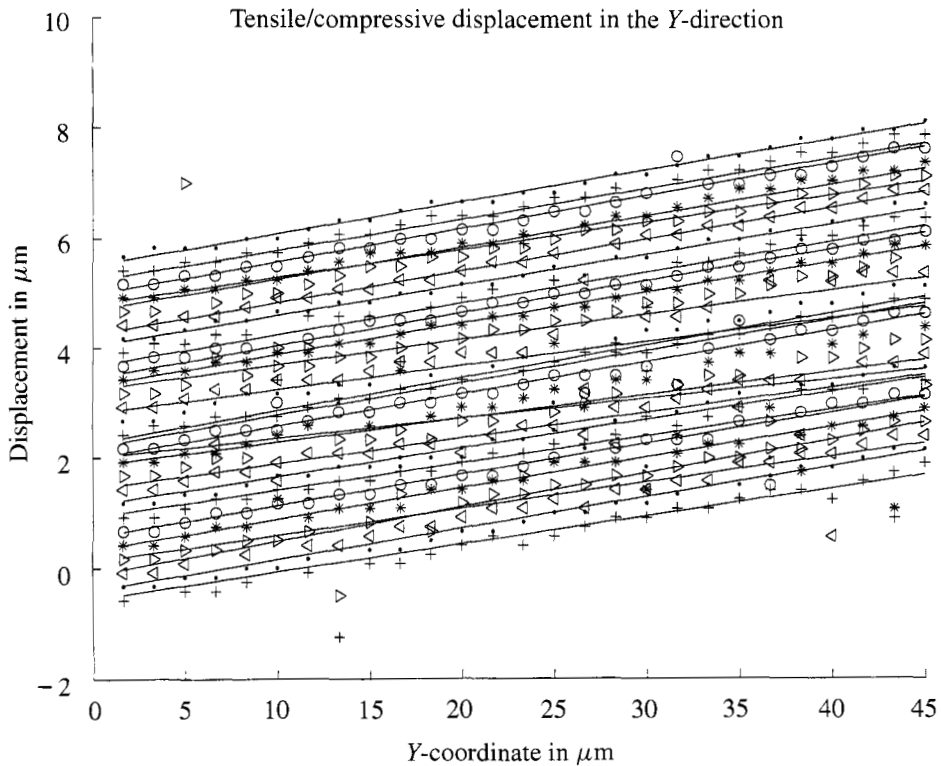


**Figure 7.** The tensile/compressive displacements plotted as a function of the  $Y$  coordinate of the image for each horizontal row of image areas. Data for successive traverses across the image are displaced by five pixels (approximately  $0.15 \mu\text{m}$ ) vertically. Linear regression lines for each traverse are shown. The local strain can be obtained by differentiating the displacements so the average strain across the sample is the slope of the regression line. Data are from the tensile sample for which the displacement data are shown in Fig. 2.

be seen in Figs 2 and 4, the data can be interpreted in terms of a uniform strain in the sample. This may be found by fitting a least squares regression line to the calculated deformation estimates on a column by column or row by row basis. The slopes of these regression lines are then estimates of the mean strains in each column or row according to equations (4)–(6). Figure 7 shows variation of the  $Y$ -displacement data plotted as a function of the  $Y$  coordinate of the test area in the original image. Regression lines have been fitted to each. It can be seen that the  $Y$ -displacement data can be described as linear in the  $Y$ -coordinate and the slope is an estimate of the strain in the  $Y$ -direction. Similar plots as suggested by equations (5) and (6) also show similar linear displacements and Fig. 8 shows estimates of the strain in the  $X$  and  $Y$  directions and the two components of the shear strain as a function of the row or column number for which they were obtained. It can be seen that the strain in the  $X$ -direction is constant, as a function of the column number, with a mean value of  $0.039 \mu\text{m}/\mu\text{m}$ , that the strain in the  $Y$ -direction is constant, as a function of row



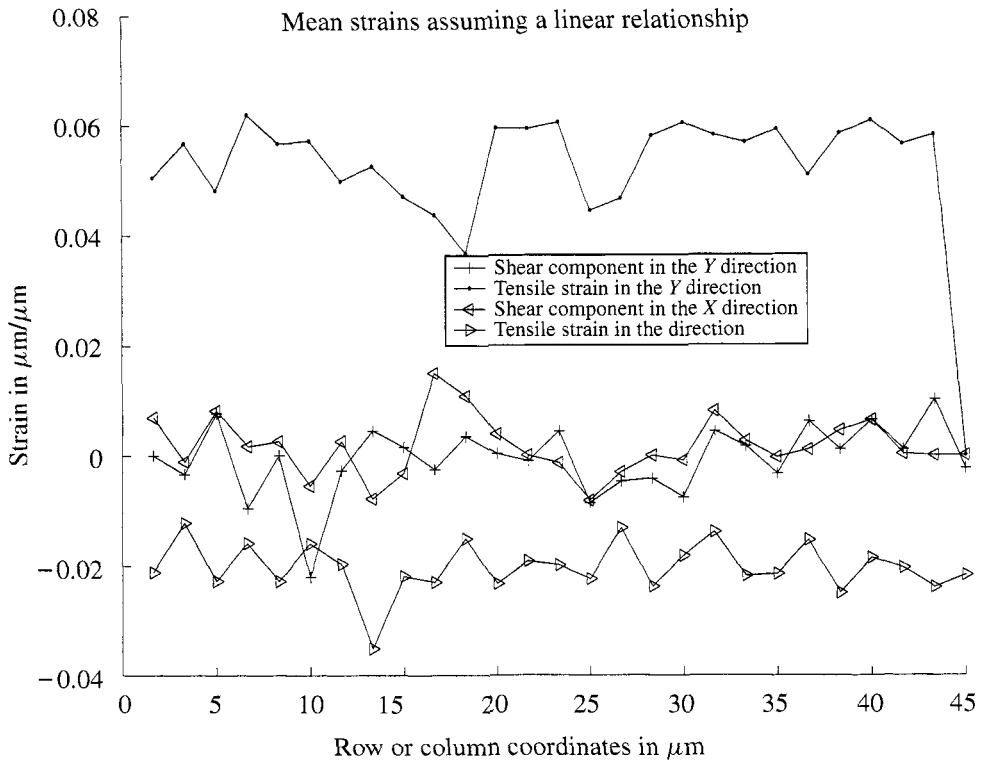


**Figure 8.** The average strain as estimated from the slope of the regression lines shown in Fig. 7 and for similar plots for the tensile displacements and the shear displacement components plotted as a function of the row or column coordinates for which they were measured. Data are from the tensile sample for which the displacement data are shown in Fig. 2.

number, with a mean value of  $-0.02 \mu\text{m}/\mu\text{m}$  and that both shear components are equal to zero.

For the second example, a similar analysis shows that the tensile stress is apparently low and significant shear strains are observed but that the strains are not uniform across the sample. A more complex analysis would be needed to describe the distribution of strain across the sample surface quantitatively. Analysis of the data for the third example will be the subject of a subsequent publication. The strains vary across the sample in a complex way perhaps indicating the presence of complex geometry associated with crack propagation as is seen in similar studies in metallic samples [5].

#### 4.2. Out-of-plane data

The best estimate for the  $Z$  displacement is found from the difference in mean values of all points in the matrix representing the test area from the first image with the mean values of all points in the matrix representing the registered area in the second

image. This procedure is complicated by the image handling prior to analysis. Most images are smoothed using a general quadratic expression to produce images with features defined in a similar way in both images and to remove the apparent curvature introduced by the way in which the scan head is moved in an arc during image capture. In most examples, any  $Z$  displacement which also has a form which may be described as a power-law expression in  $X$  and  $Y$  will be removed or modified by the smoothing program. If this is not done, the images will reflect global height changes caused by slight rotations of the sample during imaging. Significant  $Z$  displacements will only be observed if they vary over an area significantly smaller than the overall image. Further studies will be needed to derive displacements in the  $Z$ -direction for samples with uniform deformation across the sample such as in the samples with a tensile load and with a stress concentration.

Inspection of Fig. 5 shows that the deformation seen in the system with a crack is not uniform. Around the crack tip, the local components of the displacements are high but away from the tip they are low. As the displacements are not uniform, it is not statistically valid, in this case, to calculate the mean strains from a linear displacement model. However, for this system the  $Z$ -displacement is also non-uniform and displacements in local areas are high as seen in Fig. 6. One side of the crack tip has been displaced in the  $Z$ -direction compared to the other side. In the image some significant displacement can be seen toward the top-right corner of the image. This could be caused by a local deformation such as a shear-band near the surface of the sample.

## 5. CONCLUSIONS

This report has shown some success in development of a process to calculate displacements and strains from atomic force microscope images. The samples studied showed that the displacements and strains determined were consistent with bulk deformation analysis for these simple samples at the relatively low magnifications used in this study.

### *Acknowledgements*

The authors wish to gratefully acknowledge funding for the purchase of the atomic force microscope from the US Army through Grant DAAG55-97-1-0084 and for research funding from the National Science Foundation through Grant DMR-9972941.

## REFERENCES

1. J. G. Williams, M. E. Donnellan, M. R. James and W. L. Morris, *Mater. Sci. Eng.* **A126**, 305–312 (1990).

2. Committee Report, Reliability of Adhesive Bonds in Severe Environments, National Materials Advisory Board, National Research Council, NMAB-422, December 1, 1984, p. 31 quoted from R. F. Wegman, *Surface Preparation Techniques for Adhesive Bonding*, p. 4. Noyes Publications (1989).
3. T. C. Chu, W. F. Ranson, M. A. Sutton and W. H. Peters, *Exp. Mech.* **25**, 232–244 (1985).
4. D. M. Schuster and E. Scala, in: *Fundamental Aspects of Fiber Reinforced Composites*, R. T. Schwartz and H. S. Schwartz (Eds), pp. 45–62. Wiley, New York (1968).
5. D. R. Williams, D. L. Davidson and J. Lankford, *Exp. Mech.* **20**, 134–139 (1980).
6. W. L. Morris, R. V. Inman and B. N. Cox, *J. Mater. Sci.* **24**, 199 (1989).
7. J. P. Bell, *J. Appl. Polym. Sci.* **27**, 3503–3510 (1982).

## **Studies of the interphase in epoxy–aluminum joints using nano-indentation and atomic force microscopy**

FUPING LI<sup>1</sup>, JOHN G. WILLIAMS<sup>1,\*</sup>, BURHANETTIN S. ALTAN<sup>2</sup>,  
IBRAHIM MISKIOGLU<sup>2</sup> and ROBERT L. WHIPPLE<sup>2</sup>

<sup>1</sup> *Department of Chemistry, Michigan Technological University, Houghton, MI 49931, USA*

<sup>2</sup> *Department of Mechanical Engineering — Engineering Mechanics, Michigan Technological University, Houghton, MI 49931, USA*

**Abstract**—The interfacial region in an epoxy–aluminum joint has been investigated using a nano-indenter and an atomic force microscope (AFM). The stiffening effect in a soft layer resulting from the restriction of the neighboring harder phase was studied. It is proposed that the region where the indent in the softer material is modified by the harder material can be used to define the indent affected zone (IAZ). The results showed that IAZ was larger than the size of the contact impression of the indentation and increased with increasing indent depth.

**Keywords:** Adhesive; interphase; nano-indenter; AFM.

### **1. INTRODUCTION**

It is well accepted that the properties of the interfacial region between two bonded materials have a significant influence on the behavior and performance of the material system. The term ‘interphase’ was first introduced by Sharpe [1] to describe the transition region between the adhesive and the adherend in adhesive joints and between the fiber and the matrix in composites. The interphase includes the two-dimensional interface zone [2] and the three-dimensional transition region, which is usually non-uniform, contains a property gradient and has an ill-defined boundary [3].

Attempts have been made to develop techniques to characterize the interphase region in bonded material systems [4, 5]. Techniques, such as atomic force microscopy (AFM), micro-indentation, and dynamic mechanical analysis (DMA)

---

\*To whom correspondence should be addressed. Phone: (906) 487-2491. Fax: (906) 487-2061.  
E-mail: jgwillia@mtu.edu

have been used to study the properties of the interphase. Techniques, such as X-ray photoelectron spectroscopy (XPS), secondary ion mass spectrometry (SIMS), and Auger electron spectroscopy (AES), are generally used to study the chemical constitution of the interphase.

The details of the properties and nature of the interphase remain a concern although many studies have been reported. The relatively small size of the interphase and the difficulty of analyzing stresses and strains in the region have hindered development of adequate models for the interphase [6, 7].

The micro-indentation test is a method used for the estimation and mapping of the mechanical properties, including modulus and hardness, on a sub-micrometer scale. Nano- and micro-indenters have been developed to measure load and displacement as an indenter is forced into the surface of a material. The indentation load–displacement data obtained can be used to calculate the mechanical properties of the material tested using different models. Williams *et al.* [6] have used a nano-indenter to measure the modulus near the fiber in an epoxy/graphite composite. The results suggested that the modulus of the material surrounding the fiber was affected by two competing phenomena: a chemical and a mechanical effect. The latter is caused by the presence of the stiff fiber adjacent to the soft material, which contributes to the measurement of an apparent high modulus.

AFM is used as a nanoscale profilometer for measuring the topography of materials through interaction of the probe and the sample surface. AFM instruments have also been used as nano-indenters to map hardness and modulus on a nanoscale. In one such study, VanLandingham *et al.* [7] studied the interphase between fibers and an epoxy matrix in composite systems using AFM indentation as a function of temperature. They suggested that the stiffening effect caused by the restriction imposed by the fiber on the adjacent matrix material would limit the capabilities of this technique for measuring the interphase properties directly. However, their studies showed that this technique was effective in evaluating such a system provided that the moduli of the two materials were similar.

Downing *et al.* [8] reported studies on glass fiber–epoxy systems using a nano-indenter. Their results indicated that the high modulus fiber had a direct effect on the measurement of the properties of the interphase. They concluded that nano-indentation was not an effective method for measuring actual interphase properties. They recommended using phase imaging AFM for the study of the interphase.

Kim *et al.* [9] used a nano-indenter to study the interphase in silane treated glass fiber–epoxy composites. They reported finding a gradient in the modulus measured by their instrument between the fiber and the bulk matrix. They suggested that this gradient reflected properties of the interphase and that the size of the interphase could be estimated by directly measuring the distance between the low and high plateau moduli in the curve of modulus as a function of the indent position.

To date, most studies have concentrated on fiber–matrix systems. Little attention has been given to the interphase in metal bonded systems. Bentadjine *et al.* [10] reported studies on interphase formation using an epoxy diamine adhesive and an

aluminum substrate. They found that the glass transition temperature ( $T_g$ ) of the adhesive depended on the thickness of the adhesive layer. They suggested this was due to reaction of the adhesive with the hydrated metallic oxide layer and that this resulted in the formation of the interphase in their system.

In this investigation, a nano-indenter and AFM were used to study the interphase in epoxy–aluminum joints. The aim was to develop a technique to determine the magnitude of the mechanical interaction between the adherend and the adhesive and to understand the nature of the interphase in a typical bonded material system.

## 2. EXPERIMENTAL

### 2.1. Materials

The resin used in this work was an epoxy resin (DER-331, supplied by Dow Chemical Company) cured with an amine terminated poly(propylene glycol) (Jeffamine D230, supplied by Texaco Co.). The resin and the curing agent were mixed in a stoichiometric ratio and the mixture was stirred thoroughly and then placed in an ultrasonic vibration bath for three minutes to ensure complete mixing. The mixture was centrifuged to eliminate air bubbles [11]. The aluminum used was an unidentified commercial aluminum alloy (Steel Works Inc., Denver, CO, USA) in the form of 75 mm × 25 mm × 3 mm strips. The aluminum strips were degreased using acetone, and polished by using a sequence of alumina slurries with the sizes from 5 to 0.05  $\mu\text{m}$ . This gave a surface roughness of approximately 50 nm as determined from an AFM topographic image. After polishing, the strips were degreased again using acetone. Two aluminum strips were bonded using the adhesive and copper shims to control the adhesive thickness. The adhesive thickness of the sample was 0.30 mm. Samples were cured at  $80 \pm 2^\circ\text{C}$  for 2 h. After cure, the samples were cut using a Buehler low-speed diamond sectioning saw, to obtain thin sections of the bonded system. Samples were approximately 10 mm thick and 25 mm long. The cut surfaces containing the bond were then polished using the same procedures as before to ensure that the surface of the section was smooth with a surface roughness about 50 nm as measured using the AFM in imaging mode. Tabor [12] has suggested that the roughness of the surface of the sample has no effect on the result if the indentation depths are much greater than the surface roughness. For small indentations, however, such as in the present work, the surface roughness of the sample can be critical to the quantitative measurement of properties, because roughness affects the contact area in a variety of ways [13].

Reference marks were scribed across the specimen to easily locate the images both in the indenter as well as in the AFM.

### 2.2. Indentation measurements

Indentation was performed using a Nano-indenter XP (MTS Systems Corporation). The resolution in measuring the load and indenter displacement with the standard

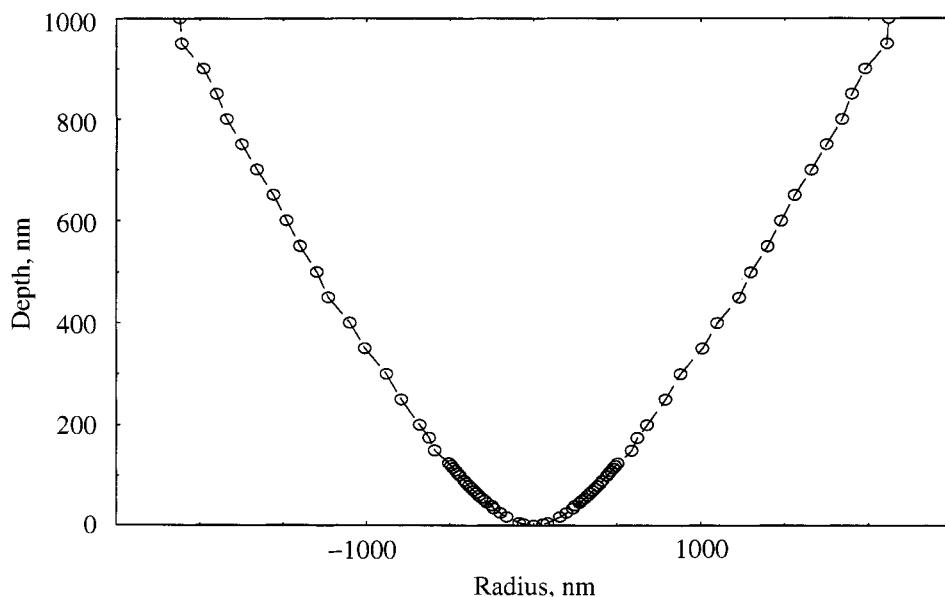


**Figure 1.** The profile of the conical tip used in the nano-indenter.

XP head is 50 nN and 0.01 nm, respectively [14, 15]. A conical tip with the profile shown as Fig. 1 was used (this profile was obtained from the SEM image supplied by the manufacturer).

For each test, indents were made from the bulk aluminum into the bulk adhesive. The indenter was programmed to carry out a large number of indents (typically 150) to a controlled depth and indentation rate, each indent being separated by a constant distance which was selected depending on the indent depth. The deeper the indentation, the larger the area affected by the indent, and hence the larger the spacing required to avoid interference between adjacent indents. For 600 nm depth indentation used in this paper, a 3.6- $\mu\text{m}$  space was adopted. In order to make more indentations in the region of interest, indentations were made across the interface at an angle of about 85° and several rows of indentations were made for each sample.

### 2.3. Image acquisition

Contact mode AFM was used to image the topography of the sample surface. Images were acquired as soon as possible after completion of the indentation run to minimize recovery due to relaxation. The images were obtained with a 100- $\mu\text{m}$  scan range at a scan rate of 50  $\mu\text{m/s}$  with a nominal contact force of 0.0 mN. The resolution was set to 300 pixels per side. An image of a series of indents across an aluminum–epoxy interphase obtained by the AFM is shown in Fig. 2. The AFM image was used to determine the distance of each indent from the aluminum/epoxy interface and to determine the profile of the indent. In order to increase precision, the Topometrix software was used to zoom into each indent to

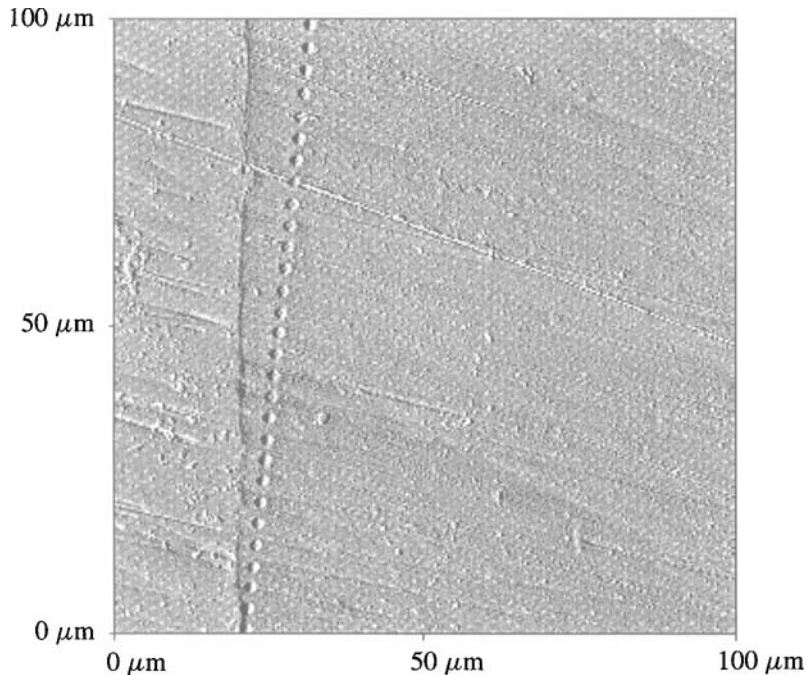


**Figure 2.** An AFM micrograph of a part of a series of indents near the interface. The left is the aluminum phase and right is the epoxy phase. The vertical line in the image is the interface between the two phases and the angle of the indents relative to the interface is about  $85^\circ$ .

produce a topographical image as shown in Fig. 3. A profile was measured along a line through the center of the indent, normal to the apparent interface. Such a profile is shown in Fig. 4.

### 3. RESULTS

#### *3.1. Measurement of the distance from the indent to the interface*

The distance of the indents from the interface was measured, initially, using indent profiles such as shown in Fig. 4. The edge here was first defined as the point where the Z-profile showed an appreciable change from the average profile across the aluminum. This point is labeled as 'Interface' in Fig. 4. This point is not a precise definition of the position of the interface because the height change between the aluminum and the epoxy adhesive is an artifact of the polishing method. A more precise definition of the position of the interface was obtained by examination of the variation of apparent modulus, as defined in the nano-indenter software, as a function of indent depth. This estimate of the elastic modulus is obtained by superimposing a sinusoidal oscillating force on the load applied by the indenter. The amplitude of this oscillating force is small enough that it does not affect the deformation process significantly. The displacement resulting from the oscillating



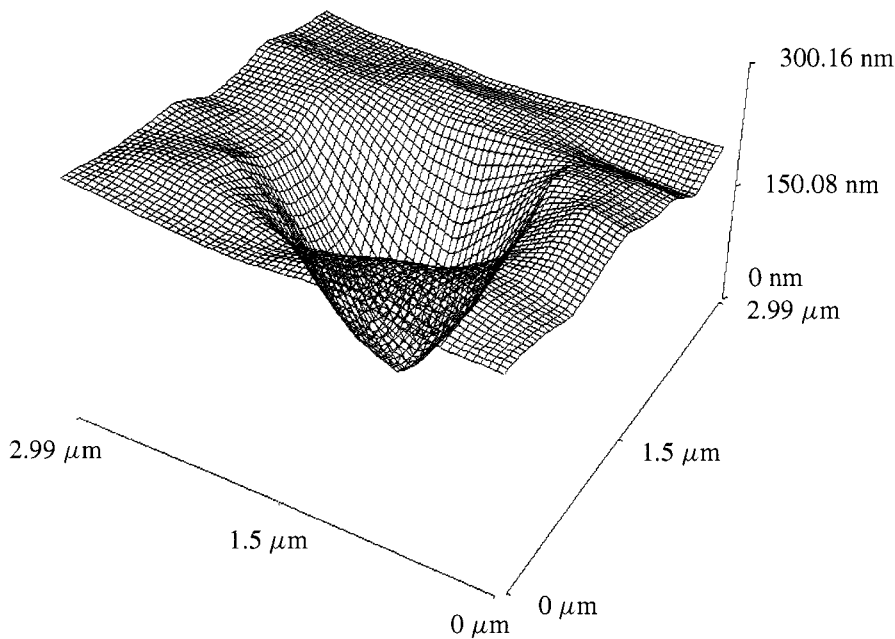


**Figure 3.** AFM topography of an indent in the adhesive near the epoxy/aluminum interface shown in Fig. 2.

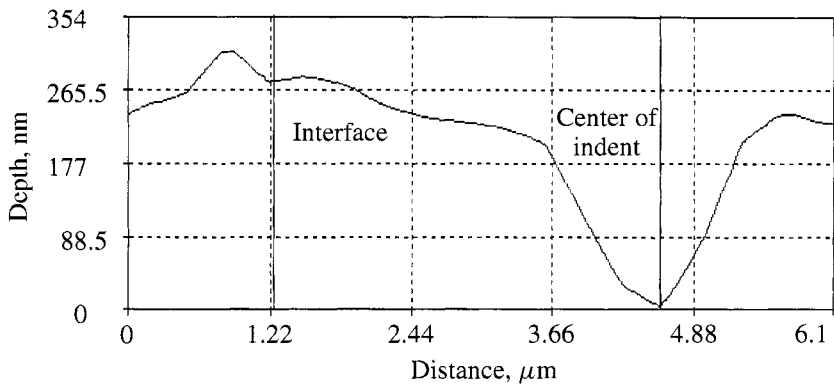


**Figure 4.** Profile of the indent in the adhesive shown in Fig. 3.

force is also sinusoidal in nature but out of phase with the force. The phase and amplitude of the displacement response are then used to evaluate the materials' properties. Further details are given in Ref. [14]. Figure 5 shows the variation of apparent modulus at a specified indent depth as a function of the apparent distance from the interface, as defined above. It can be seen that all the curves for the apparent modulus crossover at one point at about  $-0.2\text{ }\mu\text{m}$  on the X-axis. For indents in the aluminum, close to the interface, as the indent depth increases, the load carried by the aluminum is transferred to the softer resin. This causes the

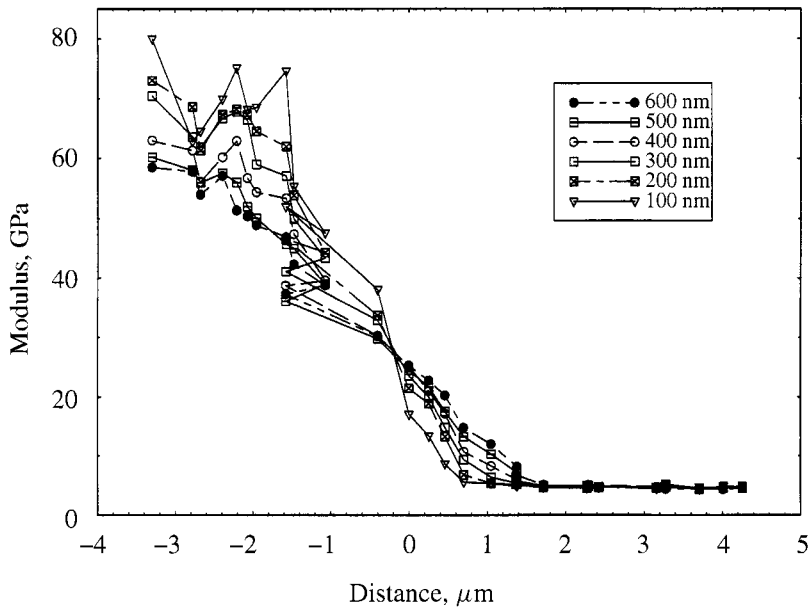


**Figure 5.** Variation of the apparent modulus with the distance from the interface for indents at fixed depth. The depths are indicated in the inset box.

apparent modulus to decrease. Similarly, an indent in the resin near the interface shows an apparent increase in modulus as load is transferred increasingly to the aluminum. It is observed that modulus vs distance plots for different indentation depths intersect at a common point. For all the data used in this work, the distance from the interface is calculated by subtracting  $0.2 \mu\text{m}$  from the apparent interface distance as defined from the image profile.

As the indenter was forced into the surfaces of materials studied, the load–displacement relationships were recorded. Such data can be used to determine mechanical properties. The two mechanical properties most frequently measured are the elastic modulus and the hardness. Different analysis techniques have been proposed for determining the modulus and hardness. With the method proposed by Oliver and Pharr [14], the modulus can be measured to within 5%. However, none of the present methods considers the effects of non-homogeneous materials. A load–displacement curve for an indentation in the adhesive phase is shown in Fig. 6.

During indentations in materials containing more than one phase, it is not yet possible to determine the modulus or hardness of either material. Two factors inhibit the interpretation of load/displacement curves in terms of mechanical properties of the materials under test. The relative load carried by each phase is unknown and must be determined based on a model for the system. In addition, the load is largely carried by the stiffer component and this makes it very difficult to identify small variations in the softer component. Any model for the system under test will need

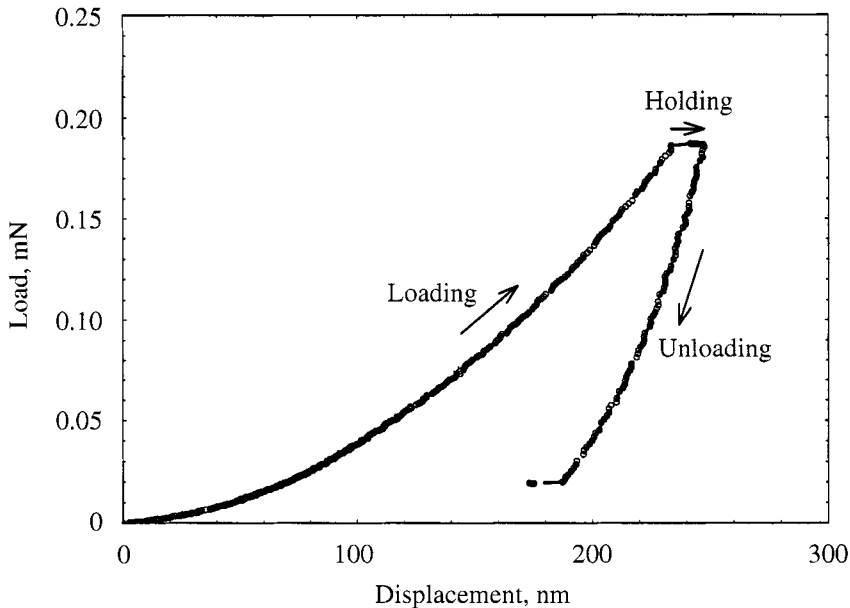


**Figure 6.** A load–displacement curve showing the displacement during loading and unloading for a typical indentation in the adhesive phase. The hold time is not measured but was typically about 60 s.

to know the area under the indenter. This requires an accurate knowledge of the tip profile. However, profiles of the indents such as shown in Fig. 4 suggest that plastic deformation has caused the formation of a raised lip around the indent which increases the actual area under load by an indeterminate amount. In view of these problems, we limit our discussion of the deformation process to the experimental load and indentation depths as indicated by the nano-indenter software.

### 3.2. Determination of the dimensions of the indent affected zone

The problems of interpretation of the relationship between indentation load and depth for homogeneous materials have been reviewed [16, 17]. Two extreme models have been postulated to describe the plastic flow of materials during indentation. In the first, the material which is displaced by the volume of the indenter flows in a direction roughly normal to the indentation direction at essentially constant volume. In the second, material flow is basically in the same direction as the indenter movement and the volume is absorbed by compressive yielding under the indenter. In the present experiments, all indents in the aluminum, the epoxy, or near the interface showed the presence of a lip of the material surrounding the indent as shown in Fig. 4. We interpret this as suggesting that the first model predominates during our experiments. Our analysis of the indent process, for this work, looks at the surface effects around the indent and does not give information concerning the effects of the indent on material below the indenter. In particular, we address the problem of experimentally determining how far from the indenter can a separate

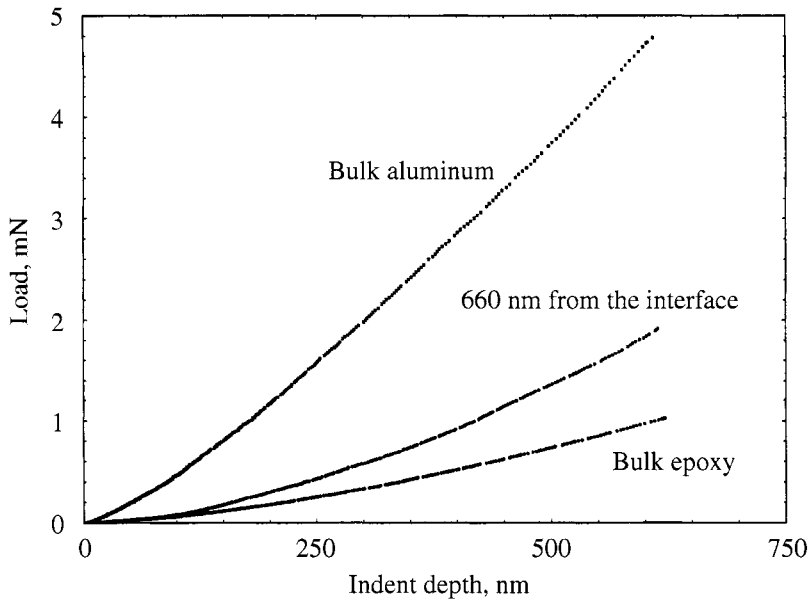


**Figure 7.** Typical load–displacement curves for indentations in the bulk aluminum, in the adhesive and near the interface.

phase be and not affect the indentation process. We call this zone the indent affected zone (IAZ). As the indenter we use is conical we will associate the radius of the indenter at the substrate surface with the radius of the surface projection of the IAZ ( $R_{IAZ}$ ).

The material will flow as the indenter is forced into the material [18]. The region affected by the indentation is not just the size of the contact impression but is larger due to plastic yielding in the surrounding area. Two major effects may influence the load vs indent depth response during an indentation in the adhesive near the interface. If the distance between the center of the indenter and the relatively rigid adherend were small compared to the maximum indenter radius, the indenter would also come in contact with the adherend as the indentation depth increased. When contact with the adherend occurs, then a sharp increase in the slope of the load vs indent depth plot is expected. A similar behavior occurs even if the indenter in the close proximity of the interface does not come in contact with the adherend, but stiffening occurs due to the interaction of the plastic zone around the indenter with the adherend. Figure 7 shows load–depth curves for indents in the aluminum, in the epoxy adhesive well away from the interface and an indent in the adhesive 660 nm from the interface. It can be seen that there is no abrupt change in the slope of the indent curve anywhere on the curve, which could be taken as an indication of the start of the surface projection of the IAZ.

A clearer indication of the point at which the interface first has an effect on the indentation process is seen in the load–indentation curves. The nano-indenter software supplies a curve of indent load as a function of indent depth, as shown

in Fig. 7. We redraw these curves to show the load at a selected indent depth as a function of the nominal distance from the interface. Figure 8 shows a series of such curves. For each selected indent depth, the load at the selected depth is approximately constant when the indent is carried out in the adhesive at a point remote from the interface. As the interface is approached, at some critical distance, the load at the selected depth starts to increase. We suggest using this critical distance to define the surface radius of the IAZ. Figure 9 shows the determination of the critical distance from the interface. For points remote from the interface, we fit a line parallel to the X-axis. For points closer to the interface, we fit a linear curve to define the general shape of the indentation curve. The critical distance is given by the intersection of these constructed lines. Figure 10 shows estimates of the critical distance (IAZ) as a function of the indent depth and Fig. 11 shows the IAZ as a function of the projected radius of the indenter tip as estimated using Fig. 1. It can be seen that the critical distance depends on the indent depth and increases with indent depth. In order to determine reproducibility, we repolished the surface and repeated the test. Both runs are included in Figs 10 and 11.

From Fig. 8, it can be seen that the data with indent depth 50 nm or less are scattered and show no obvious gradient, which prevents estimation of the critical point. This is due to such factors as the surface roughness and variation in the shape of the tip. This result agrees with Baker’s conclusion that ‘quantitative interpretation of the data becomes rapidly more difficult for indentations below about 100 nm deep (loads of about 1 mN)’ [13].

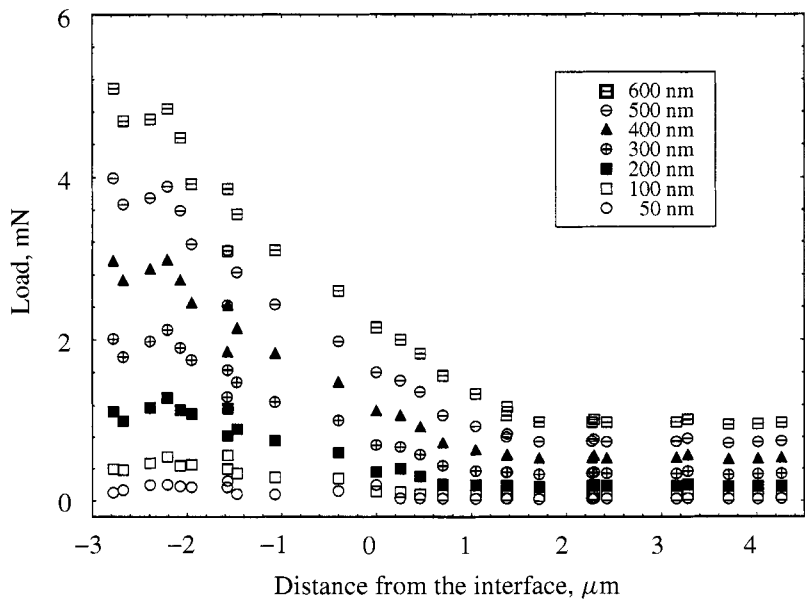


**Figure 8.** Variation of the load at constant indent depth with distance from the interface. The depths are indicated in the inset box.

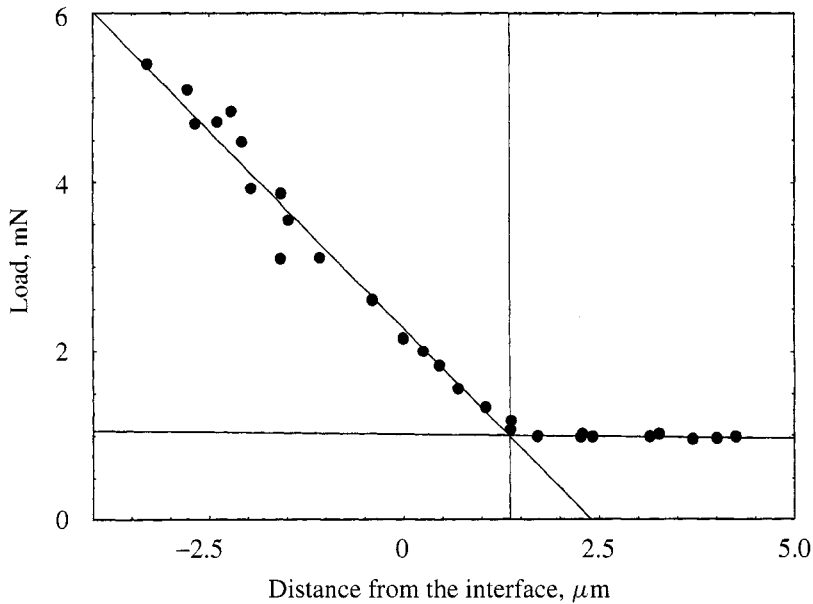


**Figure 9.** Illustration of the process for determining the position of the edge of the indent affected zone. Two straight lines are drawn through the data near to the interface and remote from the interface and the intersection is taken to define the edge of the indent affected zone. The data shown are at an indentation depth of 400 nm.

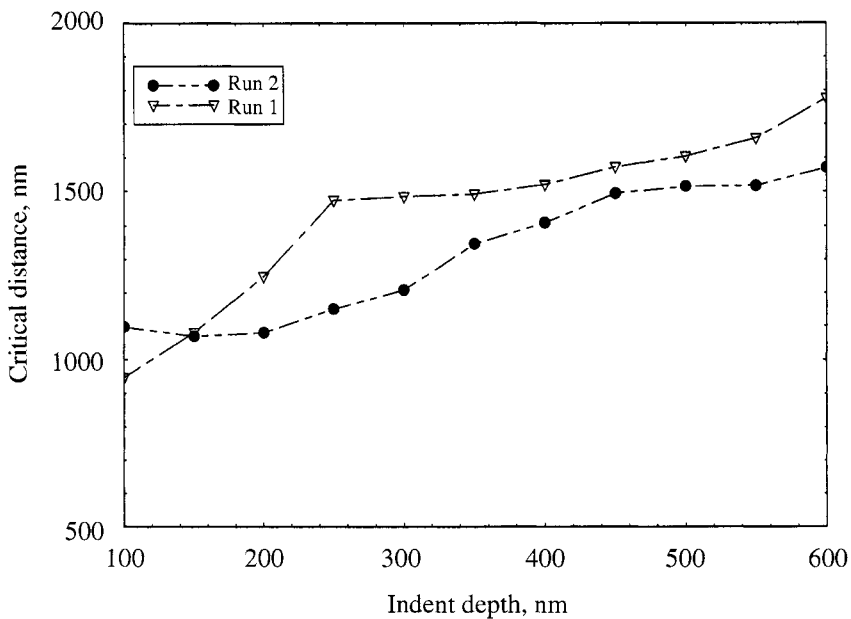


**Figure 10.** The critical distance as a function of the indent depth.

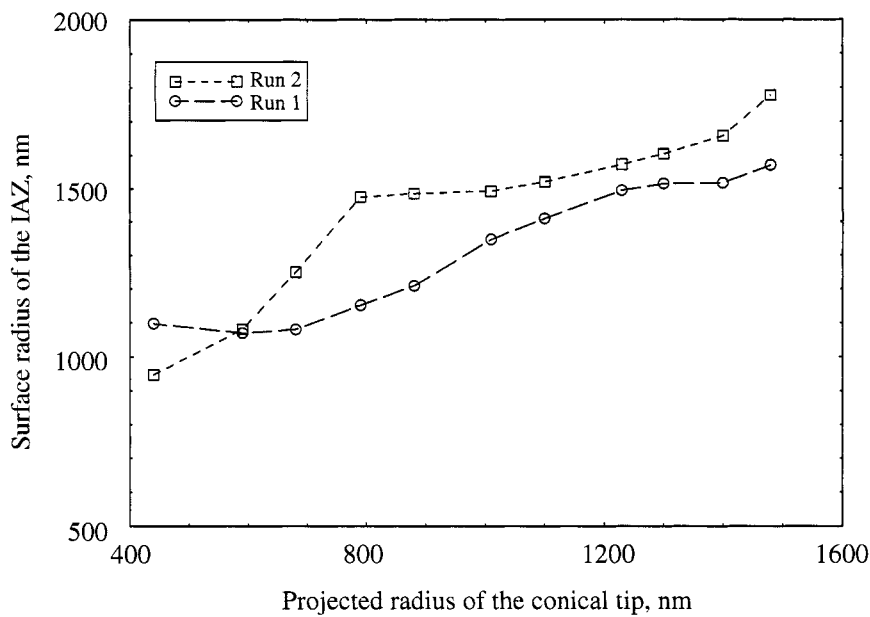


**Figure 11.** Variation of the surface radius of the indent affected zone (IAZ) as a function of the projected radius of the indenter.

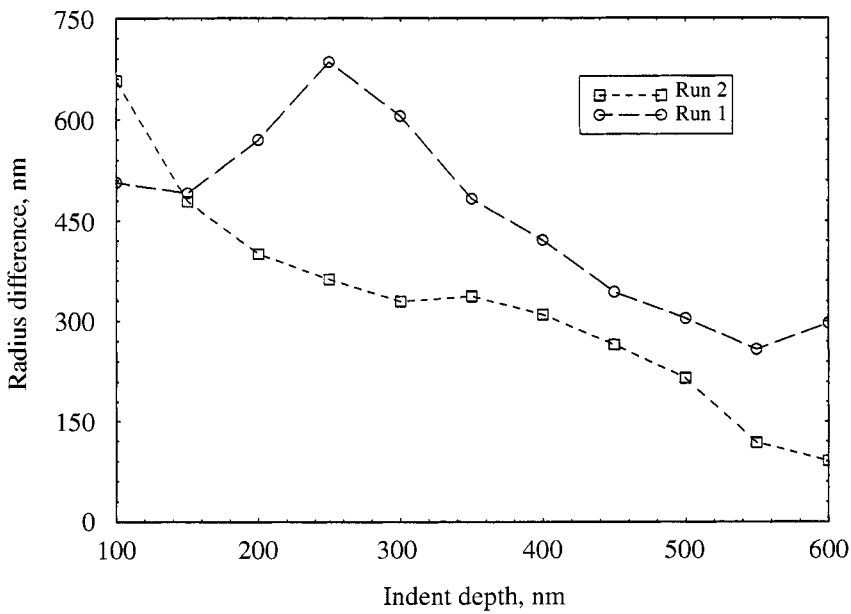


**Figure 12.** A plot of the difference between the surface radius of the IAZ and the projected tip radius as a function of indent depth.

Previous workers [9] have suggested that curves such as these indicate the presence of an interphase. We disagree with this interpretation and we suggest that this is a natural effect of the interaction of the tip and the interface. It is possible that information could be extracted from the way the critical distance varies with the distance from the interface. Figure 12 shows a plot of the difference between surface radius of the IAZ and the tip radius at the surface. As can be seen, the curve is always positive showing that the IAZ is always larger than the radius of the tip at the surface. This suggests that the appropriate model for the indentations should include a significant amount of plastic flow. Two curves are shown to illustrate the variability between runs. The sample was repolished between runs.

It can be seen that the IAZ is generally greater than the tip area at the surface. This is consistent with previous observations that considerable plastic flow is occurring beyond the tip area. It can be seen from Fig. 12, however, that the difference between the IAZ radius and the projected radius is decreasing for larger indents. It is not clear why this should be so.

### *3.3. Profiles of indents and indenter tip*

As the indenter is being forced into the surface of a material, the displacement of the indenter causes both elastic and plastic deformations in the indented material. On the assumption that the elastic deformation can be totally recovered and the plastic deformation is permanent, only the latter will be left after the indenter is unloaded. By measuring the shape of the residual indent in comparison with that of the indenter tip, the plastic deformation can be estimated and hence the elastic deformation can be determined. For dissimilar materials, it can be expected that the ratios of the elastic and plastic deformations should be different. Actually, this ratio will vary with the indent depth. But there will be no problem for comparing and analyzing the ratios of different materials if the same indent depth is used.

The profiles of the indents at different locations of the systems studied are shown in Fig. 13, with indents in the bulk Al and epoxy phases and an indent just in the interfacial region.

The reason for the asymmetry of the profile of indent in the interfacial region is related to the relative moduli and elastic properties of the aluminum and epoxy materials. The aluminum shows very little elastic recovery (20%), but the epoxy shows a much larger elastic recovery (60%). Deformation recovery in the epoxy near the aluminum is lower and is restricted by the aluminum, which has a much higher modulus than the epoxy. Further from the actual aluminum/epoxy interface, the effect of the aluminum is reduced until a point at which the influence of the aluminum is no longer detectable. In Fig. 13, it can be seen that the actual interface is at about 150 nm from the center of the indent position. The epoxy near the interface recovers to the same extent as the bulk material at about 640 nm far from the interface. This suggests that the range over which the aluminum affects the epoxy during elastic recovery is about 490 nm. The difference in the maximum deformations in aluminum and epoxy is about 210 nm. From Fig. 12, we see that



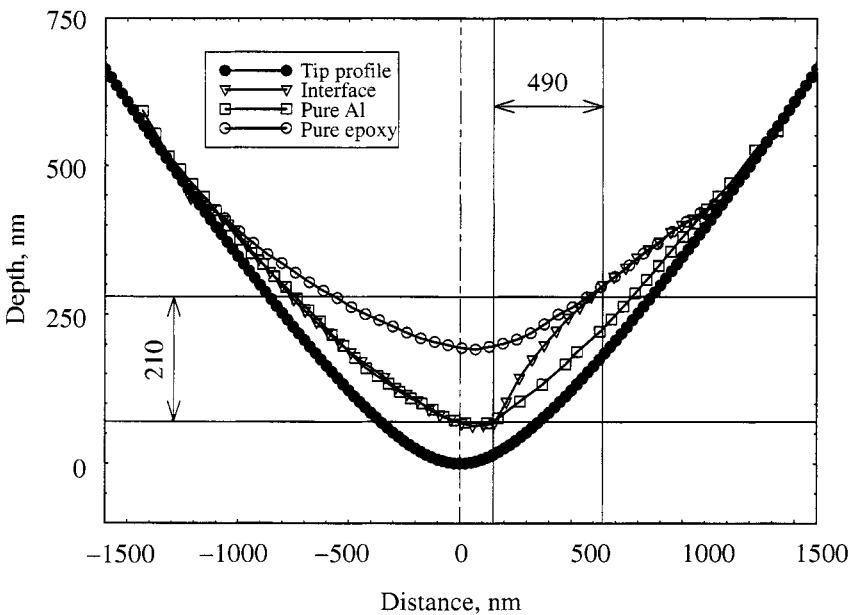


**Figure 13.** Plots of three indent profiles in the aluminum, the epoxy and near the interface compared to the tip profile, determined to an indentation depth of 600 nm. The aluminum phase is to the left side of the plot.

for an indent depth of 210 nm, the difference between the indentation affected zone and projected radius of the indenter should be about 420 nm which is similar to the 490 nm zone estimated from the recovery profile.

From Fig. 13, it can also be seen that the diameter of the plastic deformation in the sample surface formed by the indentation using the conical tip is almost the same as the tip profile at that depth. This suggests that in the surface plane, the elastic recovery was quite small.

4. CONCLUSIONS

A method employing a nano-indenter and an AFM for the characterization of the interface/interphase in epoxy–aluminum bond has been presented in this paper. The method used has been shown to be effective in studying the mechanical properties of the interphase region on a sub-micrometer scale. We report a process for determining the distance from the indenter at which the effect of the indentation can just be detected which we define as the border of the indent affected zone (IAZ). The IAZ is significantly larger than the surface radius of the indenter, and it increases with the indent depth, which suggests that considerable plastic flow is occurring during the indentation process. For our system, the initial results suggest that the difference between the surface radius of the IAZ and the surface radius of

the indenter is greater nearer the interface than further away which may indicate the presence of an interphase.

The profiles of the indents in the bulk phases and very near the interface also indicate that the IAZ is larger than the indenter radius. The magnitude of this effect is of the same order as that obtained from the load–displacement data.

### Acknowledgements

The authors wish to gratefully acknowledge funding for the purchase of the atomic force microscope from the US Army through Grant DAAG55-97-1-0084 and for the purchase of the nano-indenter from the National Science Foundation through Grant CMS-9977462.

### REFERENCES

1. L. H. Sharpe, *J. Adhesion* **4**, 51 (1972).
2. P. J. Herrera-Franco and L. T. Drzal, *Composites* **23**, 2–27 (1992).
3. J. G. Williams, M. R. James and W. L. Morris, *Composites* **25**, 757–762 (1993).
4. K. Jayaraman, K. L. Reifsnider and R. E. Swain, *Composite Technol. Res.* **15**, 3–13 (1993).
5. B. K. Fink and R. L. McCullough, *Composites: Part A* **30**, 1–2 (1999).
6. J. G. Williams, M. E. Donnellan, M. R. James and W. L. Morris, *Mater. Sci. Eng. A* **126**, 305–312 (1990).
7. M. R. VanLandingham, R. R. Dagastine, R. F. Eduljee, R. L. McCullough and J. W. Gillespie, Jr., *Composites: Part A* **30**, 75–83 (1999).
8. T. D. Downing, R. Kumar, W. M. Cross, L. Kjerengtroen and J. J. Kellar, *J. Adhesion Sci. Technol.* **14**, 1801–1812 (2000).
9. J. K. Kim, M. L. Sham and J. Wu, *Composites: Part A* **32**, 607–618 (2001).
10. S. Bentadjine, A. A. Roche and J. Bouchet, in: *Adhesion Aspects of Thin Films*, K. L. Mittal (Ed.), Vol. 1, pp. 239–260. VSP, Zeist, The Netherlands (2001).
11. J. P. Bell, *J. Appl. Polym. Sci.* **27**, 3503–3511 (1982).
12. D. Tabor, *The Hardness of Metals*. Oxford University Press, Oxford (1951).
13. S. P. Baker, *Thin Solid Films* **308–309**, 289–296 (1997).
14. W. C. Oliver and G. M. Pharr, *J. Mater. Res.* **7**, 1564–1583 (1992).
15. W. C. Oliver, *MRS Bull.* **11** (5), 15–19 (1986).
16. H. E. Boyer, in: *Hardness Testing*, pp. 4–11. ASM Intl, Metals Park, OH (1987).
17. D. Kramer, H. Huang, M. Kriese, J. Robach, J. Nelson, A. Wright, D. Bahr and W. W. Gerberich, *Acta Materialia* **47**, 333–343 (1999).
18. J. Woigard and J.-C. Dargenton, *J. Mater. Res.* **12**, 2455–2458 (1997).

## Interphase variation in silane-treated glass-fiber-reinforced epoxy composites

C. GRISWOLD<sup>1,\*</sup>, W. M. CROSS<sup>1</sup>, L. KJERENGSTROEN<sup>2</sup>  
and J. J. KELLAR<sup>3,†</sup>

<sup>1</sup> *Materials Engineering and Science Program, South Dakota School of Mines and Technology,  
501 E. St. Joseph Street, Rapid City, SD 57701, USA*

<sup>2</sup> *Department of Mechanical Engineering, South Dakota School of Mines and Technology,  
501 E. St. Joseph Street, Rapid City, SD 57701, USA*

<sup>3</sup> *Department of Materials and Metallurgical Engineering, South Dakota School of Mines and  
Technology, 501 E. St. Joseph Street, Rapid City, SD 57701, USA*

**Abstract**—The interphase region of an epoxy/glass fiber model composite was examined by atomic force microscopy phase imaging (AFM-PI) and nanoindentation. The interphase thickness was determined by AFM-PI as a function of  $\gamma$ -aminopropyl silane coupling agent concentration. With no silane, no measurable interphase was observed. With adsorption from 5 wt% solution, the observed interphase was  $888 \pm 30.3$  nm thick. Coupling agent adsorption was also performed from 0.1, 1 and 3 wt% silane solutions. The interphase thickness was found to increase with increasing silane solution concentration from 110 to 210 to 375 nm, respectively. Nanoindentation of these same interphases showed that only the 3 wt% and 5 wt% interphases were sufficiently thick enough to not include a significant fiber bias effect. For these two interphases, the indentation depths in the interphase were 8.3% and 42% greater, respectively, than the indentation depth in the matrix.

**Keywords:** Phase imaging; nanoindentation; polymer matrix composite; interphase; silane-coupling agent.

### 1. INTRODUCTION

The interphase in polymer matrix composite (PMC) materials was postulated in the mid-1970s by Sharpe [1] and has received considerable research attention over the past 15–20 years [2–21]. The interphase region is thought to be extremely

---

\*Present address: Boeing M&P Engineering, 5301 Bolsa Avenue, Huntington Beach, CA 92647, USA.

†To whom correspondence should be addressed. Tel.: (1-605) 394-2343. Fax: (1-605) 394-3369. E-mail: Jon.Kellar@sdsmt.edu

important to PMCs due to its position between the bulk reinforcing fiber and the bulk matrix, and is critical for the transfer of load between the matrix and fiber. The size, properties and effects of the interphase are, in general, quite system-dependent. For instance, interphases between 3 nm and 3  $\mu\text{m}$  in thickness, and both more or less stiff than the surrounding matrix have been found in different systems [12].

In this work, the interphase in a glass-fiber epoxy system has been studied by a combined atomic force microscopy phase imaging (AFM-PI) and nanoindentation approach. The primary goal was to determine the effect of different levels of silane coupling agent surface treatment on the interphase formed. In order to determine these effects,  $\gamma$ -aminopropyltrimethoxysilane (APS) was adsorbed onto glass fibers from 0, 0.1, 1.0, 3.0 and 5.0 wt% aqueous solutions. The surface-treated fibers were then embedded into a Hysol 608<sup>®</sup> polymer matrix and prepared for subsequent interphase analysis.

## 2. EXPERIMENTAL

The experimental procedures followed are described below and can be divided into two primary areas: composite fabrication and AFM sample preparation.

### 2.1. Composite fabrication

To fabricate the composite samples, three steps were needed: fiber cleaning, silane adsorption and fiber encasement.

**2.1.1. Fiber cleaning.** Optical glass fibers (Dolan-Jenner, Lawrence, MA, USA) were used to create AFM samples [9, 10, 13, 19]. The fibers were first cleaned of surface contaminants. Surface contaminants may include any debris from handling the fibers, but, most often, the main contaminant on the fiber is a sizing. The sizing's chemical make-up is usually proprietary, and it was removed, prior to silane coupling agent adsorption to obtain a known surface treatment.

Fiber cleaning was accomplished by first cutting a group of fibers to a length of approximately 6 inches. This length of fiber was then placed in a radio-frequency, oxygen plasma asher (Plasma Prep II, SPI, West Chester, PA, USA) for approximately 24 h to remove the sizing.

**2.1.2. Silane adsorption.** After the fibers were cleaned, approximately 200 fibers for each silane concentration used were selected. APS was adsorbed on the fibers from an aqueous solution at the natural pH of the APS solution. Next, fibers were placed in a drying oven at 100°C to drive off excess water and to promote polymerization of adsorbed silane layers.

**2.1.3. Fiber encasement in Hysol 608<sup>®</sup>.** Once the fibers were removed from the drying oven, they were immediately encased in Hysol 608<sup>®</sup>. The two components

of Hysol 608<sup>®</sup>, resin and hardener, were mixed by weight percent in accordance with Loctite specifications and allowed to cure for 24 h [22].

## 2.2. AFM sample fabrication

To obtain AFM phase imaging and nanoindentation results, three steps were followed: microtoming, phase imaging set-up and nanoindentation set-up.

**2.2.1. Microtoming.** Effective study of the interphase region by high-resolution microscopy requires minimal height differences between the interphase, matrix and fiber regions. Optimally, the surface should be free of any debris and chemical and mechanical alterations.

Conventional polishing techniques and chemical etching were rejected because they may cause physical or chemical alteration of the surface. Instead, microtoming was chosen as the method for preparing very flat samples. The microtoming method was chosen because little alteration of the surface should occur and minimal debris is left behind. Finally, microtoming yields very little surface height variation between composite constituents.

Microtoming requires a surface that can be easily cut and one that corresponds to the width of the microtome blade; therefore, the procedure outlined by Micro Star Technologies to obtain suitable surfaces was followed [23]. The microtome process may leave some debris behind on the surface, such as fiber and matrix particles. Therefore, microtomed samples were cleaned for approximately 15 min in an ultrasonic bath with a 50/50 mixture of distilled water and isopropyl alcohol.

**2.2.2. Phase imaging set-up.** A Nano Scope IIIa manufactured by Digital Instruments was used to implement phase imaging. After a Veeco NanoProbe (FESP) was inserted into the tip holder, tuning of the nano-probe was executed. The drive frequency, after tip-sample engagement, was corrected due to damping effects. This step ensures that the resulting phase shift of the phase signal shown during scanning is correct. Other parameters, such as the integral and proportional gains were optimized. Once scanning parameters were optimized, the area between the fiber and matrix was scanned. Light tapping was implemented first to view 'true topography' of an area. True topography describes an area that appears to have topography on scope mode, but will have no indication of phase shift on the phase imaging scope mode, as shown in Fig. 1. Once a suitable area was found, hard tapping was implemented to distinctly reveal the interphase.

During light tapping mode extreme height variations were not observed between the interphase regions and the matrix material regions. However, height variations of approximately 20 nm between the fiber and interphase regions were observed. Consequently, steps were taken during scanning to eliminate artifacts.

Phase imaging was performed in a multitude of directions with respect to the fiber. However, most scans were completed where the fast scan axis of the probe

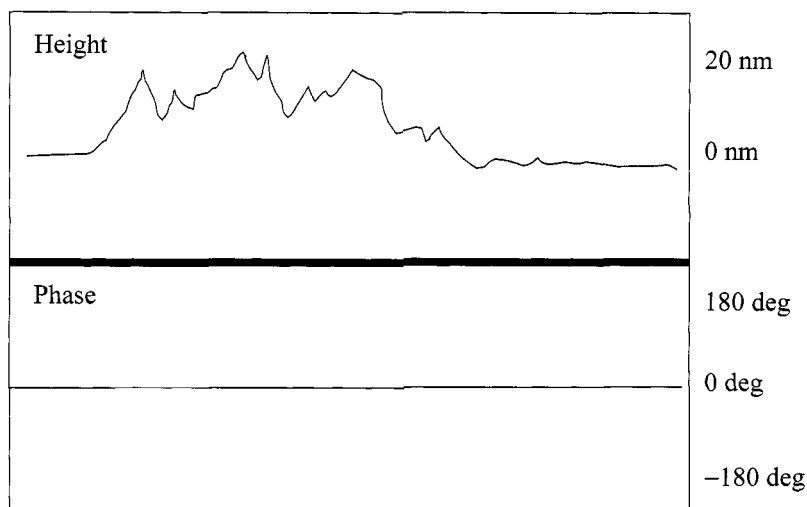


**Figure 1.** Schematic representation of true topography in which the height image shows variation but the phase image does not.

was perpendicular to the fiber surface (fiber–matrix interface), as the small area of fiber examined during AFM-PI generally showed a linear fiber surface. This allowed similar images to be collected for many samples. Because the scan axis was perpendicular to the fiber, jumping of the probe from fiber to interphase may occur if the scan rate was too high and, in turn, result in invalid measurements. Therefore, a slow scan rate, less than 1 Hz, was implemented to avoid erroneous measurements of the interphase due to skipping of the probe.

**2.2.3. Nanoindentation set-up.** After the interphase region was located and its width determined by phase imaging, an AFM-based, diamond-tipped nanoindenter supplied by Digital Instruments was used to scan the regions in tapping mode. As the scan was generated, topography data were collected, which allowed an optimal region for indenting to be found. The best-suited region was chosen based on topography. Pits, voids, debris and, most importantly, debonding, could be seen on the microscope camera screen. Debonding appeared as a black ring around the fiber. Areas exhibiting these defects were avoided. Once the area was selected, light tapping was performed to analyze the area of interest with respect to true topography.

Once the best-suited region for nanoindenting was found, this region was centered in the scanning window and the nanoindenting software initiated, in accordance with reference manual, Nano-indentation and Nano-scratching with SPMs for NanoScope<sup>TM</sup> Version 4.32 Software [24].

Input parameters were adjusted until approximately 16  $\mu\text{N}$  would be applied to the executed indents. The force was calculated from equation (1).

$$\text{Force (N)} = \text{Spring constant} \left( \frac{\text{N}}{\text{m}} \right) \times \text{Trigger threshold (V)} \\ \times \text{Sensitivity} \left( \frac{\text{nm}}{\text{V}} \right) \times \text{units conversion factor.} \quad (1)$$

The force is a set parameter in this case, because the target for indenting was approximately 16  $\mu\text{N}$ . The spring constant was measured by Digital Instruments to be 199 N/m. The sensitivity factor was determined from performing calibration indents on an infinitely hard surface, such as sapphire, and collecting deflection data. The data was analyzed by methods described in Nano-indentation and Nano-scratching with SPMs for NanoScope Version 4.32 Software support note manual and the sensitivity factor was measured to be approximately 83 nm/V [24]. The units conversion factor provides a balance of units to the overall equation and its value is  $1 \times 10^{-9}$  m/nm. Therefore, the only factor unknown was the trigger voltage, determined from equation (1), and its value was typically 1 to 1.2 V.

By selecting the array mode, multiple indents could be made on a sample with the same parameters. This matrix style of indents was chosen because the probe would indent into the fiber, interphase and matrix within a short time span. Force–deflection curves were captured at the time of each indent, so analysis of the indents could be performed at a later time. Next, tapping mode was reinitiated to collect a topography image of the indents. This allowed for the verification of the placement of the indents. Figure 2 shows indents executed in a  $10 \times 5$  array. Indent number 1 is in the upper right-hand corner (62.5 nm), while indent 50 is in the lower left-hand corner (8.0 nm).

### 3. RESULTS AND DISCUSSION

Both phase imaging and nanoindentation were performed on all samples. However, after the interphase thickness was determined, several of the surface treatments gave interphases so thin that reliable nanoindentation results (i.e., those without a fiber bias effect [25]) could not be obtained. The phase imaging results will be given first, followed by the relevant nanoindentation results.

#### 3.1. Phase imaging results

Figures 3–5 show representative images of the interphase region for 0, 1 and 3% silane surface treatments as revealed by AFM-PI. For all the samples studied, the interphase thickness was determined with at least 10 measurements on three different fibers to determine the statistical distribution of the interphase thickness. Table 1 contains the interphase thickness data. From Table 1, the interphase thickness clearly increases with increasing level of surface treatment. Furthermore,

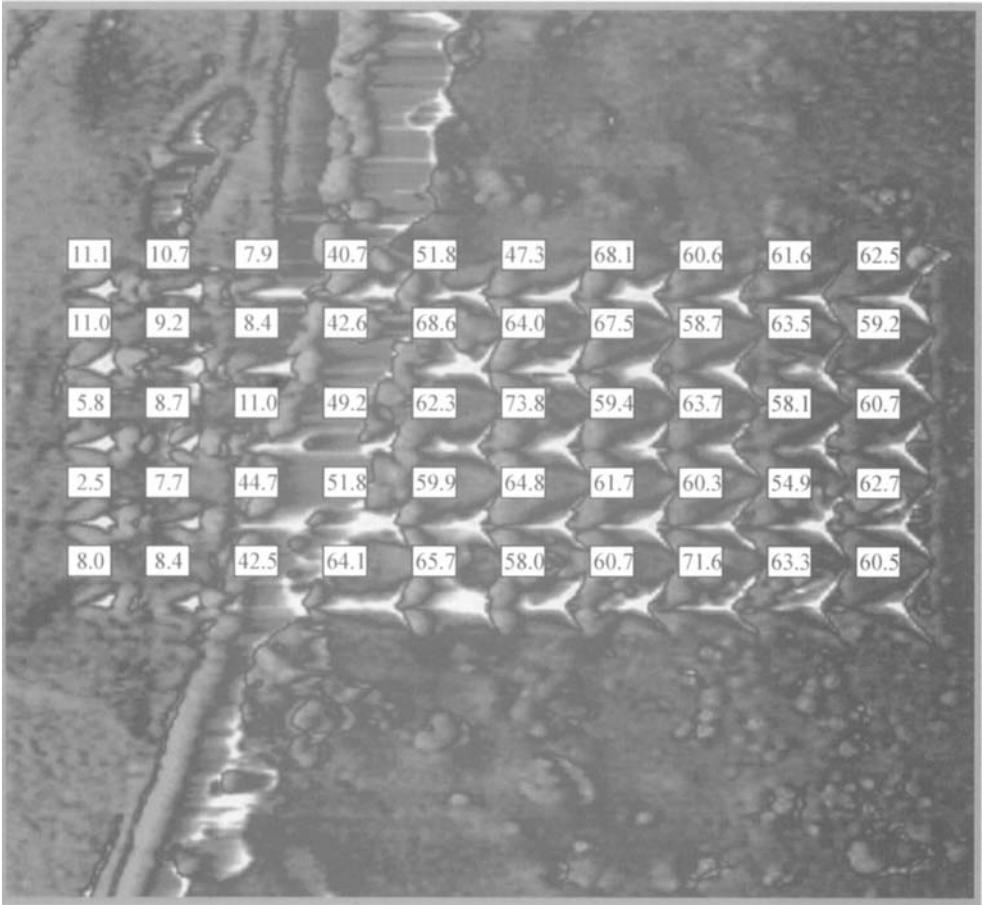


**Figure 2.** Indentations in a 0.1% silane-treated sample by AFM phase imaging. The depth of each indent in nanometers is listed above each indent. The fiber is to the left, matrix to the right and the interphase is green.

**Table 1.**  
Interphase thickness data summary

Silane	Resulting interphase mean width (nm) at 95% confidence
Zero	0
0.1% $\gamma$ -APS	110 $\pm$ 8.5
1.0% $\gamma$ -APS	210 $\pm$ 7.7
3.0% $\gamma$ -APS	375 $\pm$ 9.7
5.0% $\gamma$ -APS	888 $\pm$ 30.3

the coefficient of variation for the data sets in which an interphase was found are all less than 8% and usually less than 4%, showing the extremely good reproducibility of interphase measurements.



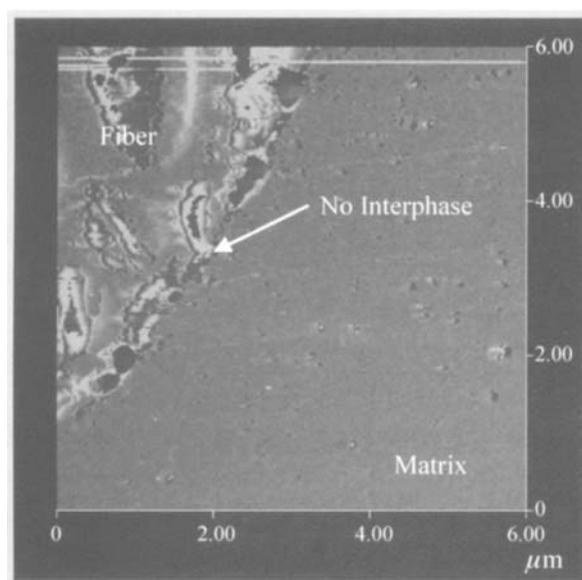


**Figure 3.** 0% APS silane AFM phase image.

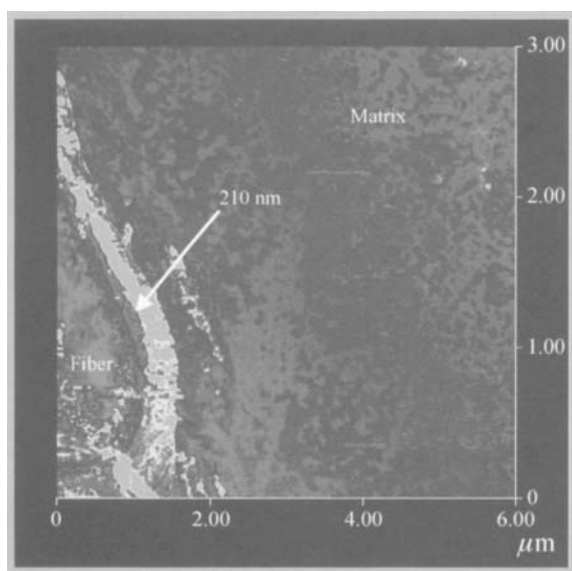


**Figure 4.** 1.0% APS silane phase image.

In addition to the thickness measurement, AFM-PI can also give an indication whether the interphase region is more or less stiff than the surrounding matrix.

In Figs 4 and 5 (phase images) an interphase region is clearly visible. The interphase regions are different in color, primarily for reasons of discernability between the different samples. A softer interphase alters the phase image by

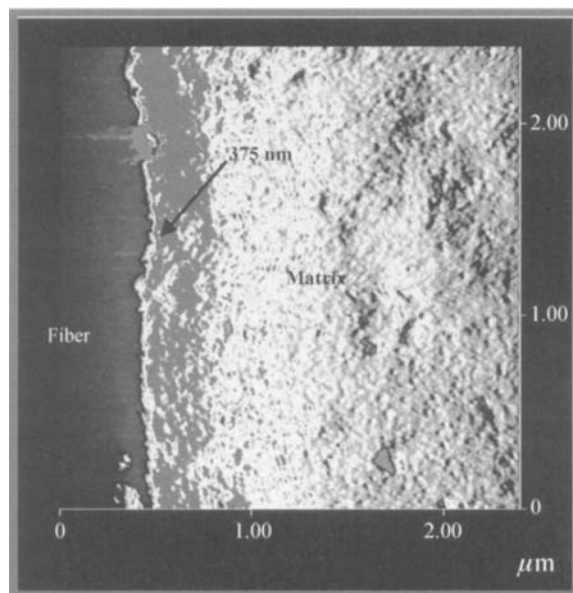


**Figure 5.** 3.0% APS silane phase image.

increasing the damping of the drive frequency of the probe, and thus, alters the phase difference by a certain degree. All of the interphase regions damped the drive frequency, which caused a shift in the phase data. The feedback controls of the AFM try to keep the probe at constant amplitude; therefore, a higher frequency, which corresponds to a higher energy, is needed to drive the probe. The shift to a higher frequency is observed on the phase data scope mode as a shift down of the line on the digital oscilloscope compared to the line of the matrix material. If the color scale is in its standard mode of 2 in software version 4.32r3 for Nano Scope IIIa, this shift is observed as a dark area. Therefore, all the interphase regions observed were softer than the surrounding matrix, as they appeared as darker areas or lower areas on the  $z$  scale compared to the bulk matrix.

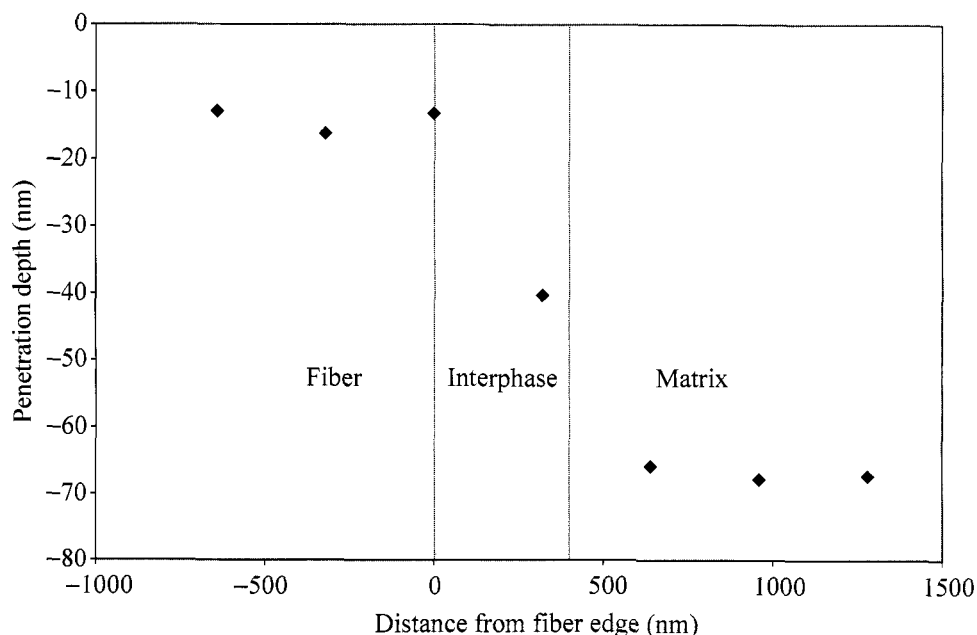
### 3.2. Nanoindentation results

Figure 2 shows a representative sample of indents near a fiber with the corresponding indentation depths. Nanoindentation was performed on the 0%, 0.1% and 1.0% APS samples; however, the indents made into the area where the measured interphase was located contained fiber bias effects. This was most apparent in the 0% and 0.1% samples. For example, the 0% APS sample did not yield a clearly evident interphase; therefore, the indents made near the fiber with a  $16\ \mu\text{N}$  load should have had the same penetration depth as those in the matrix. However, as the indents progressed near the fiber, this penetration depth decreased. This phenomenon is also apparent in the 0.1% and 1.0% APS samples that had a measurable interphase. The percent difference between the indentation depths in the interphase and matrix

of the 0.1% sample is  $-7.6\%$ . Ultimately, this signifies that the softer interphase, as viewed by phase imaging, was manifesting as a stiffer body when mechanically analyzed by nanoindentation. This conclusion contradicted what was found previously through phase imaging and is most likely due to fiber bias effects. The 1.0% APS sample yielded a percent difference of  $6.6\%$ . This positive value signifies that the interphase indents had a deeper penetration depth than those made into the matrix, and agrees with the qualitative measurements from AFM-PI. However, the interphase indents may have been compromised by fiber bias effects, similar to the effect found for the 0% and 0.1% APS samples. Also, prior work in our research group [25] showed that, for nanoindentation near glass fibers, there was a linear increase in the indentation modulus as a function of distance from the fiber surface. Extrapolating Kumar's data [25] to  $16\text{ }\mu\text{N}$  indicates that fiber bias effects would decrease the indentation depth approximately 53% at 110 nm, 46% at 210 nm, 33% decrease for 375 nm and 17% decrease for 888 nm.

**3.2.1. 3.0% APS.** The  $10 \times 5$  arrays of indents that were executed under the  $16\text{ }\mu\text{N}$  load produced an average penetration depth of  $65 \pm 2\text{ nm}$  for the interphase region and  $60 \pm 0.5\text{ nm}$  for the matrix area. Figure 6 shows the indents as average penetration depths for the 3.0% APS sample.

**3.2.2. 5.0% APS.** A set of indents were performed on the 5.0% APS samples. The average penetration depth for a  $16\text{ }\mu\text{N}$  load for the interphase was  $60 \pm 10\text{ nm}$ .



**Figure 6.** Average penetration depths of the 3.0% APS indents.

The average penetration depth for the matrix material was  $42 \pm 10$  nm under the same load. Figure 7 shows the indents as average penetration depths for the 5.0% APS sample.

Table 2 shows a summary of the nanoindentation data that was collected for the 3.0% and 5.0% APS samples. An increase in differences between the penetration in the interphase versus penetration in the matrix occurs as the percent of silane is increased. In order to better comprehend the data, the interphase indent depths were 'normalized' to the matrix indent depth. Using the estimation of bias effect given above [25], the interphase indent depths are estimated to be 62% (3 wt% silane) and 72% (5 wt% silane) greater than the matrix indent depths and in good agreement with each other. While the matrix indent penetration depth should be the same for all the samples, this was, however, not the case and is attributed mostly due to variability in the AFM software such as deflection sensitivity, *z*-piezo travel, period of execution and sample surface differences.

The findings presented here indicate that the width of the interphase is affected by the amount of silane bonded to the fiber. Greater amounts of silane were expected to yield larger interphase regions, because the higher solution concentrations of silane should result in more physisorbed material that could diffuse into the matrix material [5, 8]. However, the above statement should be tempered with the reality that the adsorption density of the silane on the glass fibers does not necessarily directly correlate to the initial silane solution concentration of the aqueous bath [26].

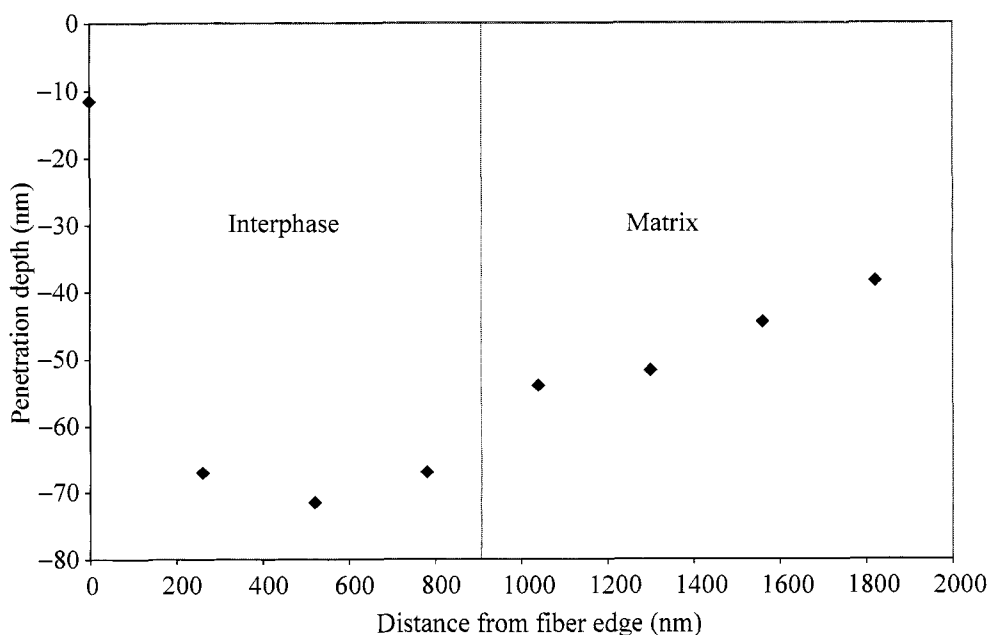


**Figure 7.** Average penetration depths of the 5.0%  $\gamma$ -APS indents.

**Table 2.**

Nanoindentation results summary

Silane concentration (%)	Average interphase penetration depth (nm)	Average matrix penetration depth (nm)	% difference (interphase–matrix)/matrix	Load ( $\mu\text{N}$ )
3.0	$65 \pm 2$	$60 \pm 1$	8.33	16
5.0	$60 \pm 5$	$42 \pm 5$	42.86	16

The nanoindentation results support the idea of the presence of a bonded network of silane molecules, as well as help determine the reduced modulus of the interphase. The indentations made into the interphase regions were expected to be deeper than those in the matrix under the same load, because the matrix is stiffer than the interphase.

The 3% and 5% silane-treated samples followed the expected outcome of having larger penetration depths in the interphase region when compared to the matrix indents. Table 2 indicates that the relative difference in penetration depths of the indents made into the interphase and matrix increases with increasing silane concentration. The indents that were made into the larger interphase regions were easier to place in the interphase, because there was more interphase area to access. The larger area also allowed the indents to be placed such that fiber bias effects would not greatly affect lateral displacement. To even further limit the effects of the fiber on the indents, loads less than 16  $\mu\text{N}$  could be used [15].

The interphase regions that correspond to the different silane percent treatments may not have the same elasticity, because the different amounts of silane may affect the curing of the interphase [9, 10, 13, 19]. Specifically, these works indicate that the silane surface treatment inhibits the curing of the epoxy around the fiber reinforcement, and reactions between the organo-functional portion of the silane molecule and the matrix occur [9, 10, 13, 19]. Also, in the study by Connell *et al.* [10] no diffusion of coupling agent away from the fiber surface was detected, supporting the possibility that interphase formation was greatly dependent on the surface treatment/matrix interface. An obvious increase in penetration depth is observed with increasing silane concentration in the current work. The increasing trend in penetration depth may have been observed, because the greater amount surface treatment led to a relatively less curing of the epoxy in the interphase.

In general, the properties of the silane layers are not the sole contributor of the formation of the interphase. However, the silane layer, through its ability to react with the epoxy, does affect the curing of the epoxy matrix and may be an important contributor to the formation of the interphase region.

#### 4. CONCLUSIONS

Varying the amount of silane coupling agent affected the interphase thickness. AFM-PI was used to locate and then image the interphase region. Specifically, as the

silane concentration increased, the interphase thickness increased from 0 nm at 0% APS to 888 nm at 5.0% APS, and the interphase was less stiff than the surrounding matrix or adjacent fiber.

Nanoindentation tests revealed that the percent difference of the penetration depth in the interphase compared to the epoxy matrix increased from 8.33% at 3.0% APS to 42.86% at 5.0% APS. Fiber bias effects were observed for lesser silane concentration treatments, leading to spurious nanoindentation data.

## REFERENCES

1. L. H. Sharpe, *J. Adhesion* **4**, 51 (1972).
2. L. T. Drzal, *Vacuum* **41**, 1615 (1990).
3. H. Al-Mousawi, E. K. Drown and L. T. Drzal, *Polym. Compos.* **14**, 195 (1993).
4. G. R. Palmese, R. L. McCullough and N. R. Sottos, *J. Adhesion* **52**, 101 (1995).
5. R. Rothon, *Particulate-Filled Polymer Composites*. Longman Scientific & Technical, Harlow (1995).
6. F. R. Jones, *Key Eng. Mater.* **116/117**, 41 (1996).
7. S. Cossins, M. Connell, B. Cross, R. Winter and J. Kellar, *Appl. Spectrosc.* **50**, 900 (1996).
8. J. Kim and Y. Mai, *Engineering Interfaces in Fiber Reinforced Composites*. Elsevier, Amsterdam (1998).
9. F. J. Johnson, M. E. Connell, E. F. Duke, W. M. Cross and J. J. Kellar, *Appl. Spectrosc.* **52**, 1126 (1998).
10. M. Connell, W. Cross, T. Snyder, R. Winter and J. Kellar, *Composites Part A* **29A**, 495 (1998).
11. M. R. VanLandingham, R. F. Eduljee and J. W. Gillespie, Jr., *J. Appl. Polym. Sci.* **71**, 699 (1999).
12. T. Downing, R. Kumar, W. Cross, L. Kjerengtroen and J. Kellar, *J. Adhesion Sci. Technol.* **14**, 1801 (2000).
13. F. Johnson, W. Cross, D. Boyles and J. Kellar, *Composites Part A* **31A**, 959 (2000).
14. E. Mader, K. Mai and E. Pisanova, *Comp. Interf.* **7**, 133 (2000).
15. E. Mader and S. Gao, *J. Adhesion Sci. Technol.* **15**, 1015 (2001).
16. M. Tanoglu, S. Ziaee, S. H. McKnight, G. R. Palmese and J. W. Gillespie, Jr., *J. Mater. Sci.* **36**, 3041 (2001).
17. M. Tanoglu, S. H. McKnight, G. R. Palmese and J. W. Gillespie, Jr., *Polym. Compos.* **22**, 621 (2001).
18. A. Hodzic, S. Kalyanasundaram, J. K. Kim, A. E. Lowe and Z. H. Stachurski, *Micron* **32**, 765–775 (2001).
19. W. Cross, F. Johnson, J. Mathison, C. Griswold and J. J. Kellar, *J. Adhesion* **78**, 571 (2002).
20. M. G. Todd and F. G. Shi, *J. Appl. Phys.* **94**, 4551 (2003).
21. J.-K. Kim and A. Hodzic, *J. Adhesion* **79**, 383 (2003).
22. Loctite, Product Description Sheet Hysol® Product 608 (2001). Accessible online at <http://tds.loctite.com/tds5/docs/HYSA608-EN.PDF>.
23. *Diamond Knives Manual*. Micro Star Technologies, Huntsville, TX (2004).
24. *Nanoindentation and Nanoscratching with SPMs for NanoScope™ Version 4.32 Software*. Digital Instruments, Santa Barbara, CA (1998).
25. R. Kumar, W. M. Cross, L. Kjerengtroen and J. J. Kellar, *Composite Interfaces* **11**, 431 (2004).
26. N. Nishiyama, R. Shick, K. Horie and H. Ishida, in: *Controlled Interphases in Composite Materials*, H. Ishida (Ed.), pp. 707–713. Elsevier Science, New York, NY (1990).

## Characterization of the interphase in epoxy/aluminum bonds using atomic force microscopy and a nano-indenter

JOHN G. WILLIAMS<sup>1,\*</sup>, FUPING LI<sup>1</sup> and IBRAHIM MISKIOGLU<sup>2</sup>

<sup>1</sup> *Department of Chemistry, Michigan Technological University, Houghton, MI 49931, USA*

<sup>2</sup> *Department of Mechanical Engineering-Engineering Mechanics,  
Michigan Technological University, Houghton, MI 49931, USA*

**Abstract**—It is believed that a transition region may exist between the bulk adhesive and the adherend, which would play an important role in the performance of the joint. Epoxy/aluminum joints were studied using a nano-indenter and an atomic force microscope (AFM). Some samples were based on direct bonding of aluminum specimens with the epoxy adhesive and some used aluminum samples pre-coated with a softer epoxy system to simulate a soft interphase. The topography of indented samples was measured using AFM and the image was used to define the indentation positions. Results were interpreted in terms of three types of interactions of the indenter with the sample in the interface region: (a) direct contact of the indenter with both phases during indentation, (b) contact of the indenter with a single phase but for which the indentation response was directly affected by the adjacent phase and (c) contact with a modified resin phase near the interface the: ‘interphase’. The importance of sample surface preparation was also studied. Results showed that polishing the surface often resulted in formation of ridges and troughs near the interface which resulted in artifacts, which could be interpreted as indicating the presence of a soft interphase.

**Keywords:** Interphase; adhesive; indentation; AFM.

### 1. INTRODUCTION

It has been well accepted that an interphase, which may exist between the adherend and bulk adhesive in an adhesively-bonded joint, would play an important role in the performance of a bonded joint. The interphase would have properties different from those of the bulk adhesive. It may be formed spontaneously between the adherend and adhesive or may be intentionally introduced, for example, by using a surface pretreatment or through the use of coupling agents.

---

\*To whom correspondence should be addressed. Tel.: 1-906-487-2491. Fax: 1-906-487-2061.  
E-mail: jgwillia@mtu.edu

In this paper, the term 'interface' is defined as the surface formed between the aluminum adherend and the epoxy adhesive. This surface is two-dimensional in that it has no thickness, but is three-dimensional in that it follows the topography of the surface. The term 'interphase' includes the region starting with the interface and extending into the epoxy adhesive in which the adhesive has different properties from those of the bulk adhesive. We associate a dimension or thickness of the interphase with the distance from the interface to the point at which the adhesive properties are indistinguishable from those of the bulk adhesive. This thickness cannot be precisely defined and is dependent on the sensitivity of the technique used to define the properties of the adhesive.

Compositional differences have been reported across interphases from studies using a variety of techniques. Such differences could result from preferential adsorption of the curing agent onto the metal or metal oxide surface [1] and reaction between the adsorbed curing agent and polar groups on the substrate surface [2, 3], or due to the formation of organo-metallic complexes [4] of metal ions dissolved from the adherend which diffuse into the adhesive [5].

Experimental evidence for compositional differences in adhesive joints suggests that an interphase may exist, but its thickness is still difficult to define. Most of the research concerned with the thickness of the interphase has concentrated on a boundary formed during manufacture of organic matrix composites using thermoplastic and thermosetting polymers and a variety of fibers. Estimates of the thickness of the interphase in composites have suggested sizes from a few nanometers to a fraction of a micrometer [6–11]. Although the chemistry causing the formation of the interphase must be sensitive to the composition of the fiber and the matrix, it is possible that the thickness of the interphase may be similar in both composites and adhesive joints. A recent report by Roche *et al.* [4] suggested that the interphase thickness in an epoxy/aluminum joint might be between 200  $\mu\text{m}$  to 400  $\mu\text{m}$ . Our previous work showed that the formation of such a thick interphase might be caused by the evaporation of the curing agent during cure, and the effect was not observed when the adhesive was sandwiched between two aluminum adherends (data not shown).

In this paper, we report studies on epoxy aluminum joints. A nano-indenter was used to make a series of indentations in the interfacial region and an atomic force microscope was used to define the positions of the indentations with respect to the interface and to define the indentation profile. Joints studied included some samples in which the aluminum was pre-coated with a softer epoxy resin system to simulate a soft interphase.

## 2. EXPERIMENTAL

### 2.1. Materials

The resin used in this work was an epoxy resin (DER-331, supplied by Dow Chemical) cured with three amine-terminated poly(propylene glycol)s (Jeffamine



D230, Jeffamine D400 and Jeffamine 2000, supplied by Texaco). The Jeffamine D230 was used at the stoichiometric mixing ratio of 32.5 parts per hundred parts of resin (measured by weight and abbreviated 'phr'), the Jeffamine D400 was used at 60 phr and the Jeffamine D2000 was used at 288 phr. One sample was prepared using 2-ethyl-4-methylimidazole (EMI-24), also supplied by Texaco, as a catalytic curing agent. The mixing ratio was 5 phr. The resin and the curing agent were mixed and the mixture was stirred thoroughly and then placed in an ultrasonic bath for 3 min to ensure complete mixing [12]. The mixture was centrifuged to eliminate air bubbles. The aluminum used was commercial aluminum alloy 2024-T4 (Alcoa) in the form of  $65 \times 30 \times 3$  mm strips. The strips were ultrasonically degreased in acetone, and polished using a sequence of alumina slurries with sizes from  $5 \mu\text{m}$  to  $0.05 \mu\text{m}$ . This gave a surface roughness of approximately 50 nm as determined from an AFM topographic image. After polishing, the strips were ultrasonically degreased again in acetone, and stored in acetone for up to 20 min before being bonded with the epoxy adhesive. Two aluminum strips were bonded with the adhesive using copper shims to control the adhesive thickness. The adhesive thicknesses of the samples were about 0.30 mm. Samples were cured at  $80 \pm 2^\circ\text{C}$  for 2 h. Previous work [13] had shown that this cure cycle was sufficient for the amine-cured systems to achieve full cure, as indicated by the glass transition temperature. After cure, the samples were cut using a Buehler low-speed diamond-sectioning saw to obtain sections of the bonded system. Samples were approximately  $10 \times 30 \times 3$  mm. The cut surfaces containing the bond were then polished using the same procedures as before to ensure that the surface of the section was smooth with a surface roughness about 50 nm as measured using the AFM in the imaging mode. For most samples, the surface near the interface(s) was checked to ensure that no polishing troughs with height or depth greater than 50 nm were present.

Reference marks were scribed across the specimen to easily ensure that the AFM image included the region in which the indentations were made.

For some specimens, an artificial interphase was produced. The interphase was formed by coating the aluminum surface with a system based on epoxy resin cured with Jeffamine D400 or a blend of equal weights of Jeffamine D400 and Jeffamine D2000. The modulus of the coating system was significantly lower than that of the adhesive system based on Jeffamine D230. The soft layers were cured using the same cure cycle as for the adhesive. During the course of the indentation experiments, the modulus of the materials could be estimated from the indentations in regions distant from the interface. Table 1 shows the estimated moduli for the aluminum and the epoxy systems used.

For one sample, the layer was quite thick and the thickness of the layer was measured to be  $15 \pm 1 \mu\text{m}$  using a Vector TX1 ultrasonic thickness gage supplied by NDT Instruments. For the second sample with an artificial interphase, the epoxy system was dissolved in acetone to give a solution of about 5% solids and this was used to coat the adherend surface. After flashing off the solvent the residual film was

**Table 1.**  
Properties of materials

Material	Modulus (GPa)	Glass transition temperature (°C) [13]
Aluminum	85	—
Epoxy/Jeffamine D230	5.3	80
Epoxy/Jeffamine D400	4.9	40
Epoxy/Jeffamine D400 + D2000	2.2	near room temperature
Epoxy/2-ethyl-4-methylimidazole	approx. 6	—

too thin to be measured using the ultrasonic thickness gage (less than 1  $\mu\text{m}$ ). After cure of the soft layer for all cases, a bond was formed with a normally prepared aluminum adherend and with the adhesive based on Jeffamine D230.

2.2. Indentation measurements

Indentation was performed using a conical tip in a Nano-indenter XP (MTS Systems). The resolutions in measuring the loads and indenter displacements with the standard XP head are 50 nN and 0.01 nm, respectively [14, 15]. For each test, indentations were made from the bulk aluminum into the bulk adhesive. The indenter was programmed to carry out a large number of indentations (typically 150) to a controlled depth and at a controlled indentation rate, each indentation being separated by a constant distance which was dependent on the indentation depth. The deeper the indentation, the larger the area affected by the indentation, and hence the larger the spacing required to avoid interference between adjacent indentations. For maximum indentation depths of 600 nm used in this study, a 3.6  $\mu\text{m}$  space was adopted. In order to make more indentations in the region of interest, indentations were made across the interphase at an angle of about 85° and several rows of indentations were made for each sample.

2.3. Acquisition of AFM images

Atomic force microscopy (AFM) images were acquired using a Topometrix Acurex II microscope. Contact mode AFM was used to image the topography of the sample surface. Images were acquired as soon as possible after completion of the indentation run to minimize recovery due to relaxation. The images were obtained with a 100  $\mu\text{m}$  scan range at a scan rate of 50  $\mu\text{m/s}$  with a nominal contact force of 0.0 mN. The resolution was set to produce an image with 1000 pixels per side. The AFM image was used to estimate the approximate distance of each indentation from the epoxy/aluminum interface and to determine the profile of the indentation.

2.4. Interactions between the indenter and the adhesive, adherend and interphase

The nano-indenter generates data in the form of tables and plots showing the variation of the indentation load as a function of the indentation depth. For

homogeneous materials, this can be interpreted in terms of hardness and elastic modulus of the material but the models used for the analysis are not appropriate for interphase studies. When the indenter tip is close to the boundary between different materials with widely different mechanical properties, three distinct interactions affect the load/indentation relationship.

*2.4.1. Direct contact between the indenter and the two phases.* If the indenter tip radius at maximum indentation depth is greater than the distance from the tip to the interface, the indentation will start in one material but, at some point in the indentation process, direct physical contact will be made with the second material. For example, if the indentation starts in the soft adhesive the load/indentation depth plot has a relatively low gradient indicative of the soft matrix. At some point during the indentation process, the indenter will make contact with the adherend. The slope of the load/indentation depth plot will then start to increase indicative of an increasing apparent hardness of the composite material as the load is carried to an increasing extent by the harder adherend. We term these interactions ‘contact interactions’.

*2.4.2. Non-contact interactions between the indenter and the two phases.* On a more subtle level, elastic forces associated with the compression zone of the material in direct contact with the indenter will be transmitted by shear stresses into nearby material which will deform in the same direction as the directly compressed material, although to a lesser extent, as the distance from the direct compression zone of the indenter increases. In addition, as plastic deformation of the material under the indenter occurs, plastic flow will result in material build-up around the indenter and this ‘pile-up’ of material will change the indentation process. For example, as the material builds up around the indenter, the area of the indenter in contact with the adhesive will be increased. The angle between the indenter and the adhesive surface will also change. We term these interactions ‘composite interactions’.

*2.4.3. Interphase interactions.* Neither of the above two effects is related to the possible presence of a volume of material near the interface with different mechanical properties from the bulk adhesive. We refer to any interaction solely due to a local variation of material near the interface an ‘interphase interaction’.

In an earlier work [16], we have suggested a process for presenting the indentation data in such a way as to simplify interpretation. This work extends this process to improve interpretation of indentation data near the interface in terms of the three interactions described above.

## *2.5. Data processing*

The experimental data obtained are a series of load/indention curves obtained during a series of indentations made at different distances from the interface. Figure 1

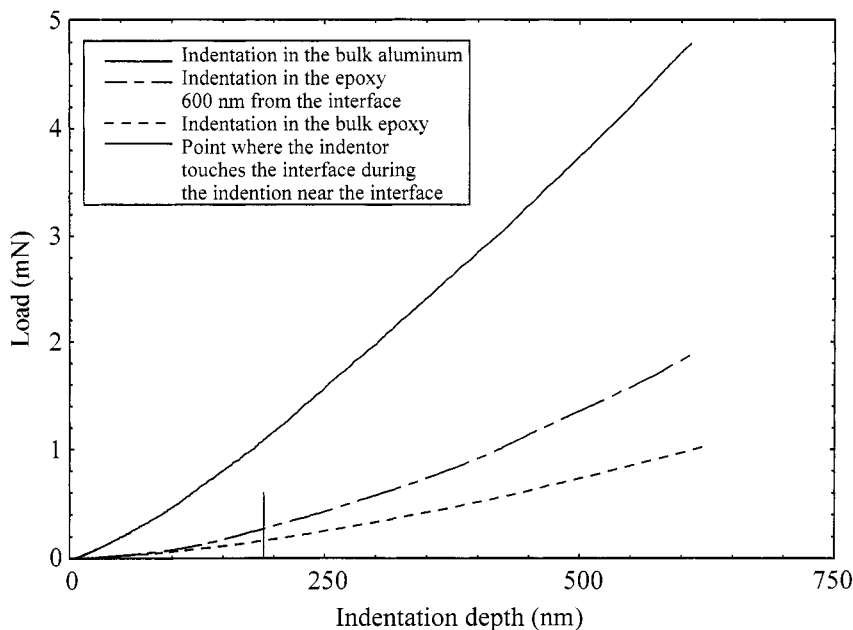


**Figure 1.** Typical load/indentation depth curves for a sample without an artificial interphase. The indenter has a radius of 660 nm at a depth of 190 nm and this depth is marked by a short vertical line.

shows a typical set of data for load as a function of indentation depth for an indentation at a fixed distance from the interface.

*2.5.1. Estimation of the distance of the indentation from the interface.* The first major experimental problem is to define the precise distance of the indentation from the interface. In our earlier work [16], we reported a method of defining the position of the interface using atomic force microscope images of the indentations in the interface region. The AFM software can be used to obtain a height profile through the indentation at right angles to the interface. Figure 2 shows an AFM image of a part of a typical set of indentations and a typical profile. The profiles usually show some sort of height change at the interface, but the height change cannot be interpreted in terms of the exact position of the interface. Initially, we measure the distance from the apparent line formed by the start of the ‘pile-up’ effect of the polishing process at the interface on the aluminum side of the bond as indicated in Fig. 2. How this relates to the distance from the interface will be discussed in more detail below. This distance will be used as a rough, preliminary estimate of the distance of the indentation from the interface. One of the data files generated by the nano-indenter is a material modulus for the sample calculated from the amount of deformation recovered when the load is momentarily reduced. As the calculation is based on an analysis of the deformation assuming the material to be homogeneous, we refer to such a modulus as a pseudo-modulus. The data table outputted by the instrument gives the pseudo-modulus at indentation depths selected

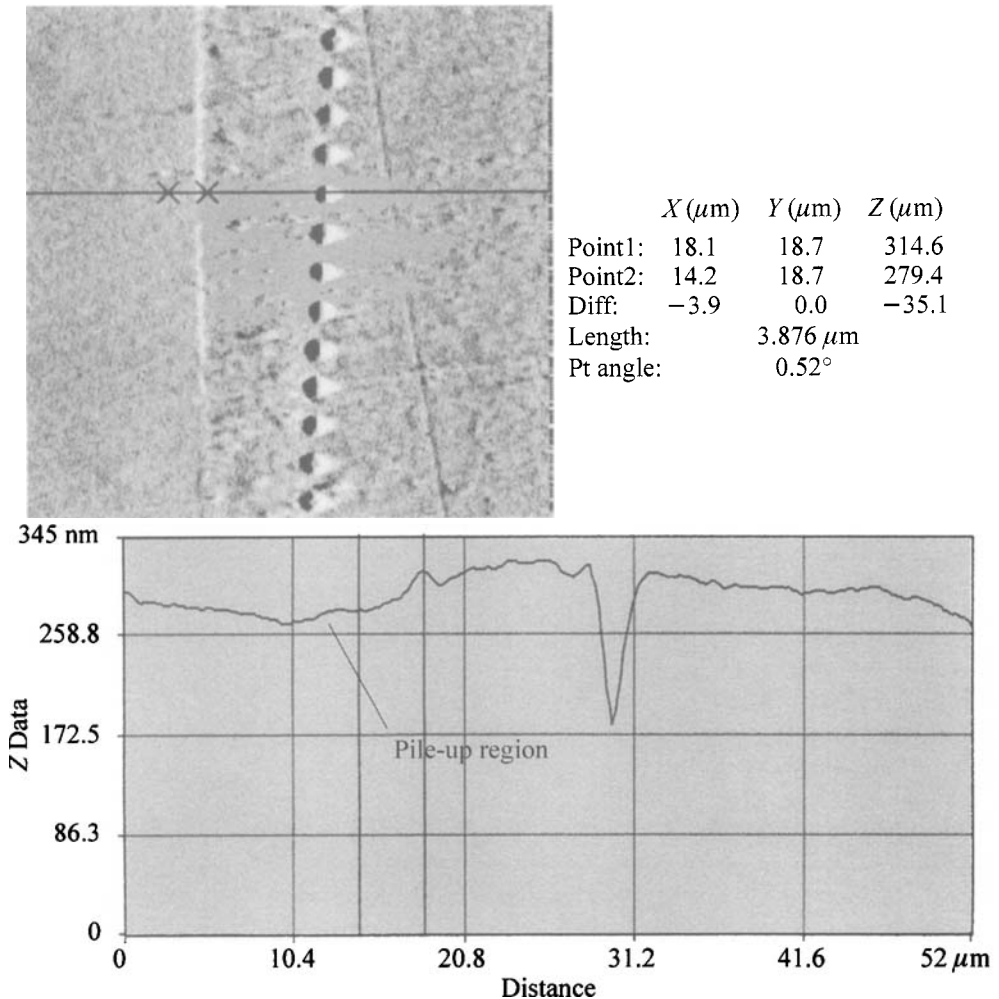


**Figure 2.** An AFM image of a typical set of indents across an interface is shown in the upper portion of this figure. The aluminum phase is on the left. The lower image shows a profile across the interface taken as indicated in the micrograph. The pile-up region is indicated on the traverse. The cross-marks on the image correspond to the vertical lines on the profile.

by the instrument and the related load. We interpolate the modulus to give values associated with particular indentation depths we select. This interpolation process is discussed below.

A plot of the interpolated, pseudo-modulus as a function of this estimate of the distance from the interface at fixed indentation depths was constructed such as shown in Fig. 3. In Fig. 3, a point where the pseudo-modulus is independent of indentation depth can be seen where plots at different indentation depths crossover. This is associated with the point where the indenter is very close to the interface. If the indenter tip starts the indentation exactly on the interface and if the interface

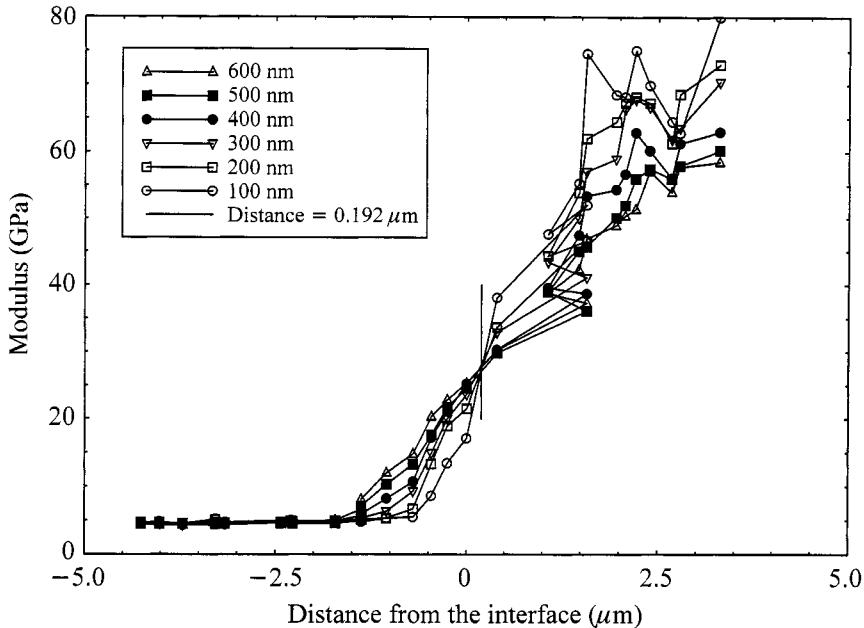


**Figure 3.** A typical plot of modulus against distance from the interface as defined from the profile of the section. The vertical line is drawn through the point where the modulus is independent of the indentation depth. This point is  $0.192 \mu\text{m}$  from the position of the interface as estimated using the section profile.

continues directly below the indenter tip, as the indentation depth increases half of the indentation will remain in both the adhesive and the adherend. For any other indentation not exactly on the interface, as the indentation depth increases the fraction of the indentation volume associated with either the adherend or the adhesive will change as the indenter is not symmetric about the indentation axis. Consequently, the point where the curves cross-over can be taken to be an improved estimate of the position of the interface. Subsequent plots are corrected to use distances referred to this point as the interface. The precision of this process is estimated to be of the order of  $\pm 0.5 \mu\text{m}$ . This estimate will be shown below to be insufficiently accurate to be used in estimating the thickness of any possible interphase and a further correction will be derived.

**2.5.2. Presentation of the data.** Essentially, the indentation experiments provide information about the relationship between three variables: load at an indentation depth for an indentation at a distance from the interface. The indentations shown in Fig. 1 are typical of indentations in the bulk aluminum, near the interface and in the bulk adhesive (in Fig. 1, the vertical line at an indentation depth of  $190 \mu\text{m}$  marks the point where the indenter first makes contact with the interface as determined using methods described below). Although there is a perceptible change in the rate of change of curvature of the load/indentation depth curve for the indentation near

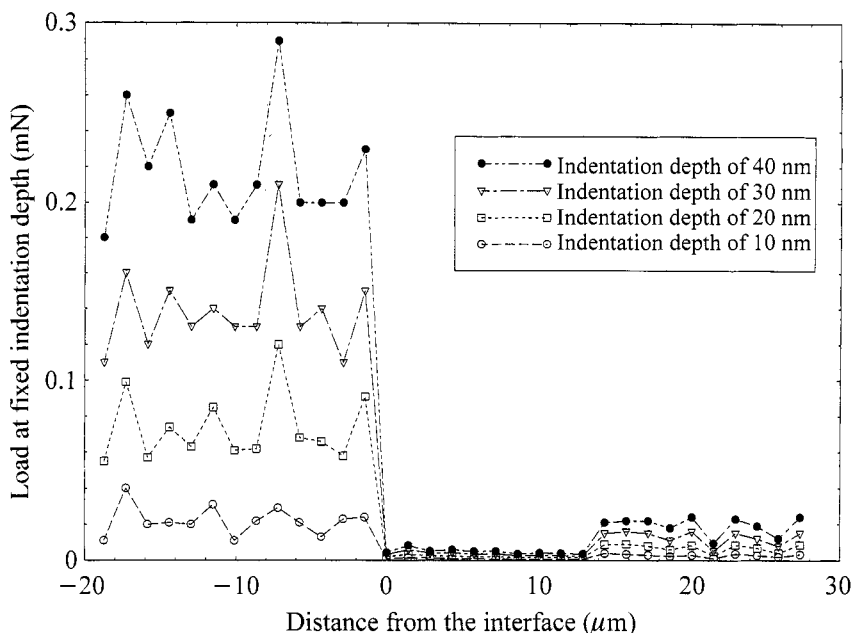


**Figure 4.** Plot of the load at fixed indentation depth as a function of distance from the interface corrected using the modulus/distance data. The sample has a soft artificial interphase of thickness about 15  $\mu\text{m}$ . Data are shown for very small indentation depths of 10–40 nm. Data at depths up to 600 nm showed similar trends.

the interface, it is not easy to use this curve to define this point as the change is very subtle. We suggest that it is easier to interpret the experimental data if the results are presented in terms of either the variation of the load required to obtain an indentation of a given depth, as a function of distance from the interface, as described in our earlier work [16], or as the variation of the indentation depth at a fixed load, as a function of the distance from the interface. Both presentations require the data to be interpolated between data points from the original load/indentation depth tables.

We used two processes to interpolate data. Initially, we visually interpolated values from the indentation tables. This is reasonably precise as the points taken during the indentation experiment are very closely spaced. However, this is a very time consuming process. In order to reduce the effort and improve the accuracy of the interpolation, a ninth-order polynomial was used to fit the load/indentation depth data. Two different polynomials were needed. One polynomial giving the load as a function of indentation depth was used to calculate the loads at specific indentation depths. The second gave the indentation depth as a function of the load and was used to calculate the indentation depths at specific loads. The data can then be presented as a table of triads of load/indentation depth/distance from the interface which can be presented in three dimensions or as plots of load at a fixed indentation depth as a function of distance from the interface or as indentation depths at a fixed load as a function of distance from the interface. Figure 4 shows

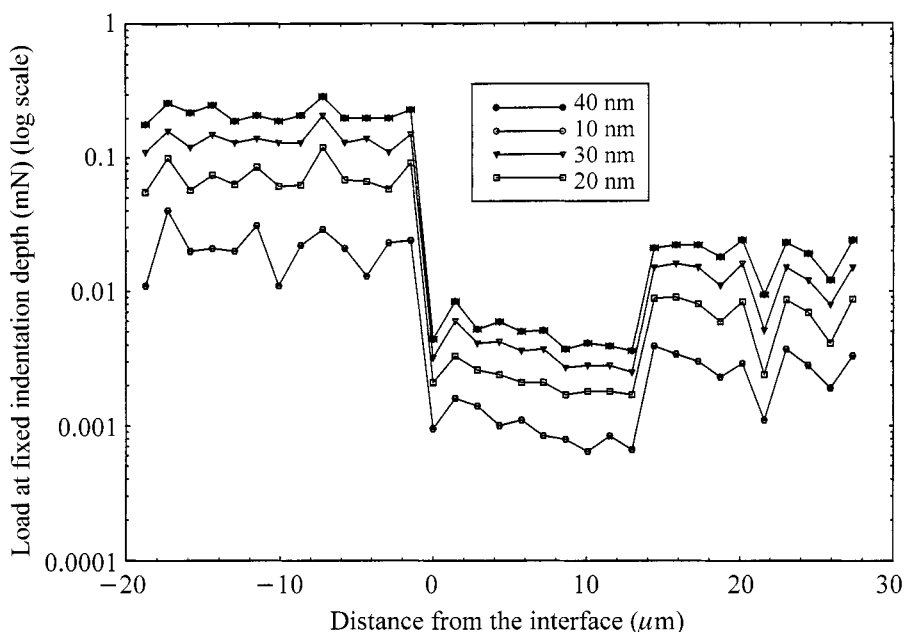


**Figure 5.** Data from Fig. 4 plotted on a semi-log scale.

a plot of load at fixed indentation depth as a function of corrected distance to the interface. It can be seen that for a system containing aluminum and epoxy adhesive, the load axis covers a range of several decades (0.03 to 0.0005 mN). As the majority of this work is focused on possible interphases formed in the soft epoxy material, the presence of the very stiff aluminum forces the load scale to be very coarse and it is difficult to see any detail in the variation of the load in the epoxy region. We have found it more useful to present the data as the logarithm of the load as a function of the distance from the interface as shown in Fig. 5. It should be noted that the sample used to produce Figs 4 and 5 had a significant polishing trough (see below). The data presented in the form of indentation depth at fixed load as a function of distance from the interface as a semi-log format are illustrated in Fig. 6 for several indentation loads. These curves are presented in semi-log format for the same reasons as for Fig. 5.

**2.5.3. Superposition of the indenter tip profile on the figures.** Interpretation of curves such as in Figs 5 and 6 is much easier if information on the tip profile can be included so that the relative positions of the edge of the indenter and the interface can be estimated.

For load/distance curves such as shown in Fig. 5, this can be done by including a bar in the  $x$  plane on each point with a length equal to the diameter of the profile at the indentation depth of the point. As each curve is at the same indentation depth, the bars are of equal length on a given curve but increase between curves as the indentation depth increases.



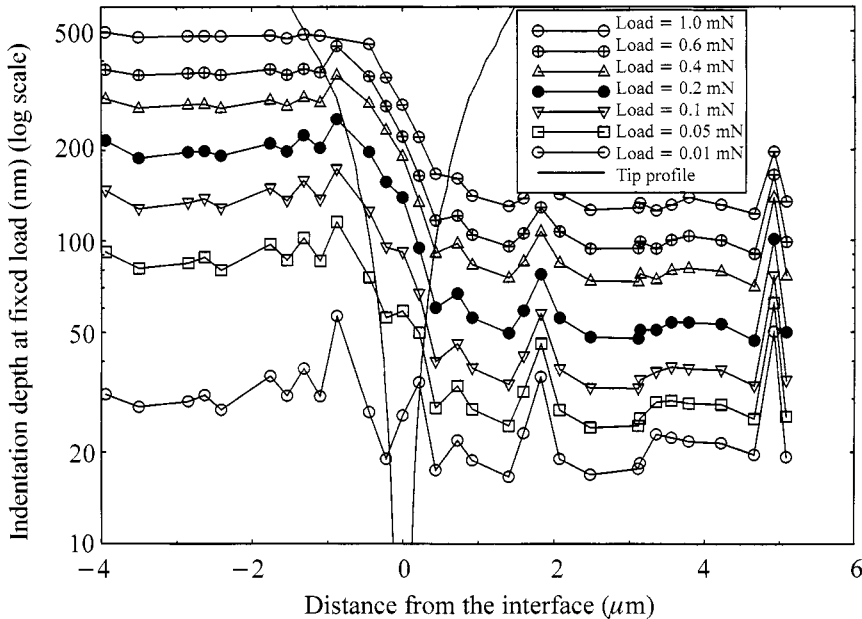


**Figure 6.** Plots of the depth at fixed indentation load as a function of the distance from the interface on a semi-log scale. Data are given for depths at loads from 0.01 to 1.0 mN. The tip profile is plotted on the same axes. The sample, in this case, had a very thin (less than  $1\ \mu\text{m}$ ) artificial interphase based on the EMI-24 cured system and the adhesive was based on the D230 system.

For the indentation depth/distance curves such as shown in Fig. 6, the tip profile can be plotted directly as the  $x$ -axis is directly related to the tip width at any indentation depth and the  $y$ -axis is the indentation depth.

### 3. RESULTS AND DISCUSSION

During the experimental work done, it became apparent that reproducibility of data was a serious problem. Curves taken from a similar sequence of indentations at a different point on the surface or on the surface following re-polishing, or from new samples with similar preparations, often showed different features. In particular, samples often showed apparent troughs in the load at fixed depth/distance plots used to calculate the radius of the indentation affected zone (IAZ) as reported earlier [17]. It was apparent that the points showing the most variability were the points in the adhesive close to the interface. Estimation of the radius of the IAZ is sensitive to these points. It became apparent that the precision of the estimation of the radius was about  $\pm 0.2\ \mu\text{m}$ . Most estimates of the radius of the IAZ were equal to the indenter tip radius at that indentation depth.

A second problem was seen on examination of plots of the load at fixed depth/distance curves. Many curves showed minima in the loads near the interface which suggested the presence of a soft interphase. This observation would be very

significant but repeated samples did not show this feature with any consistency. It was concluded that it was an artifact of sample preparation, probably associated with the surface polishing procedure.

### *3.1. Artifacts due to polishing defects*

As described above, all samples were polished flat before testing in the nano-indenter. A flat surface across the bond is critical to the characterization of the interphase between the adherend and adhesive using indentation and topography methods. For example, uneven boundaries across the bond or between the fiber and matrix in a composite can result in artifacts which can lead to possible misinterpretation of variations in indentation properties as evidence of the presence of an interphase [15].

For indentation studies, a rough surface may also result in artifacts. Figure 5 shows the indentation load as a function of the corrected distance from the interface for the system with a thick artificial soft interphase. Figure 5 shows plots at a series of indentation depths of 10, 20, 30 and 40 nm. Similar data are obtained at all depths up to the maximum depth of 600 nm used in this study. The figure shows indents starting in the bulk aluminum on the left side of the plot, the transition into the soft interphase at the interface and the soft interphase extending out to about 15  $\mu\text{m}$  (consistent with the measured thickness of the interphase), a transition into the bulk adhesive up to about 20  $\mu\text{m}$  and finally the bulk adhesive on the right side of the plot. The regions of all plots showing rapid changes in the indentation load with indentation position near 0  $\mu\text{m}$  and near 20  $\mu\text{m}$  we associate with direct physical contact of the indenter with the second phase as described below. Two significant regions can be seen in the thick, soft interphase. The first observation is the general slow decrease of indentation load with indentation position across most of the soft interphase and the second are the regions from about 0–1  $\mu\text{m}$  and from about 12–20  $\mu\text{m}$  from the aluminum epoxy interface where the data suggest that the observed load goes through a minimum with indentation position. This could be interpreted as due to the presence of a thin, soft interphase between the layers. We suggest that this is an artifact introduced by a change in profile of the polished surface. Figure 7 shows a surface profile through this region as a plot of relative surface height as a function of distance from the approximate interface. This image includes the permanent deformation from two previous indents from earlier runs on the same sample. Included in the image is a profile of the indenter tip from geometry data supplied by the manufacturer superimposed on the profile at an arbitrary position. The image shows that the polishing process for this sample left a trough about 5  $\mu\text{m}$  deep and about 10  $\mu\text{m}$  across at this point. Indents carried out in the flat regions on either side of the trough can be interpreted as experiencing the load applied to the indenter as being transferred approximately to the area of the indenter as estimated from a section through the indenter at the indent depth. This load results in the measured indent depth. The indent on the right side of the profile in Fig. 7 would be typical. Indentations carried out on the sides of the trough, however, experience, at

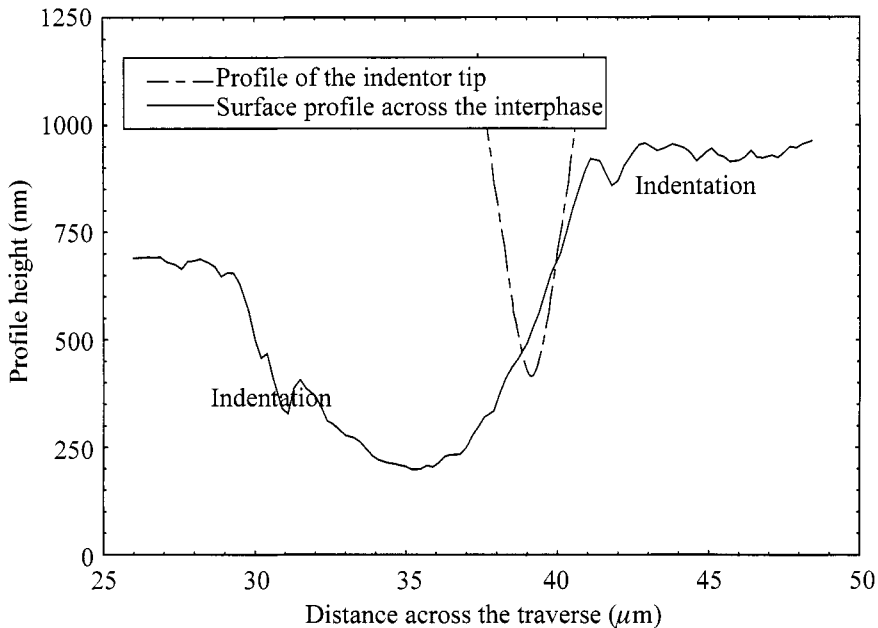


**Figure 7.** A profile of a section of the sample with an artificial soft interphase with thickness about 15  $\mu\text{m}$ . The polishing procedure used in preparation of this specimen has left a trough in the soft interphase near the interface between the two epoxy phases. The profile includes two indents from two separate indentation experiments. A profile of the indenter tip is included at an arbitrary position.

least for the initial part of the indentation, a much larger area as the section through the tip is taken at an oblique angle to the tip axis. While the load is the same, the increased area implies that the stress is lower and, hence, the indentation depth would decrease. We suggest that the apparent minimum in the load/distance curve is an artifact due to the presence of a polishing trough near the interface between adhesive and soft, artificial interface. It is significant, we believe, that the depths of the minima shown in Fig. 5 increase as the indentation depth decreases and, at the larger indentation depths, the minima disappear. Improved polishing removed this artifact, as seen in later figures, and all further samples were imaged to ascertain that any troughs near interfaces were less than 50 nm deep and the majority of the data used to define interphase properties were for indentations 50 nm or greater. The limitation to 50 nm minimum indentation depth also reduces the possibility that polishing might induce structural changes in the surface [18].

### 3.2. Detection of direct contact during indentation

The use of plots of indentation depth at constant load as a function of distance from the interface makes it easy to determine if and when the indenter makes contact with the second phase. Figure 6 shows such a plot for the system based on aluminum bonded with epoxy-Jeffamine D230. We interpret this figure as illustrating that the rapid change in depth at a fixed load near the interface is almost entirely due to the

occurrence of direct contact of the indenter with the two phases. The depth at a fixed load is constant for each indentation in the aluminum (right-hand side of Fig. 6) until the indenter touches the epoxy as illustrated by the superimposed image of the indenter. The indent depth increases rapidly as the indenter is moved closer to the interface and onto the epoxy side. For most indent loads, after the indenter no longer touches the aluminum, the indent depth again becomes constant. From the plots indicating the effects of high loads, it might appear that the load becomes constant even though the indenter should still be in contact with the aluminum. Study of AFM images for indentations made very close to the interface on the epoxy side shows that the residual indentation for two or three indentations is very asymmetric, suggesting that the tip has moved sideways into the epoxy during the indentation process. Figure 8 shows such a profile.

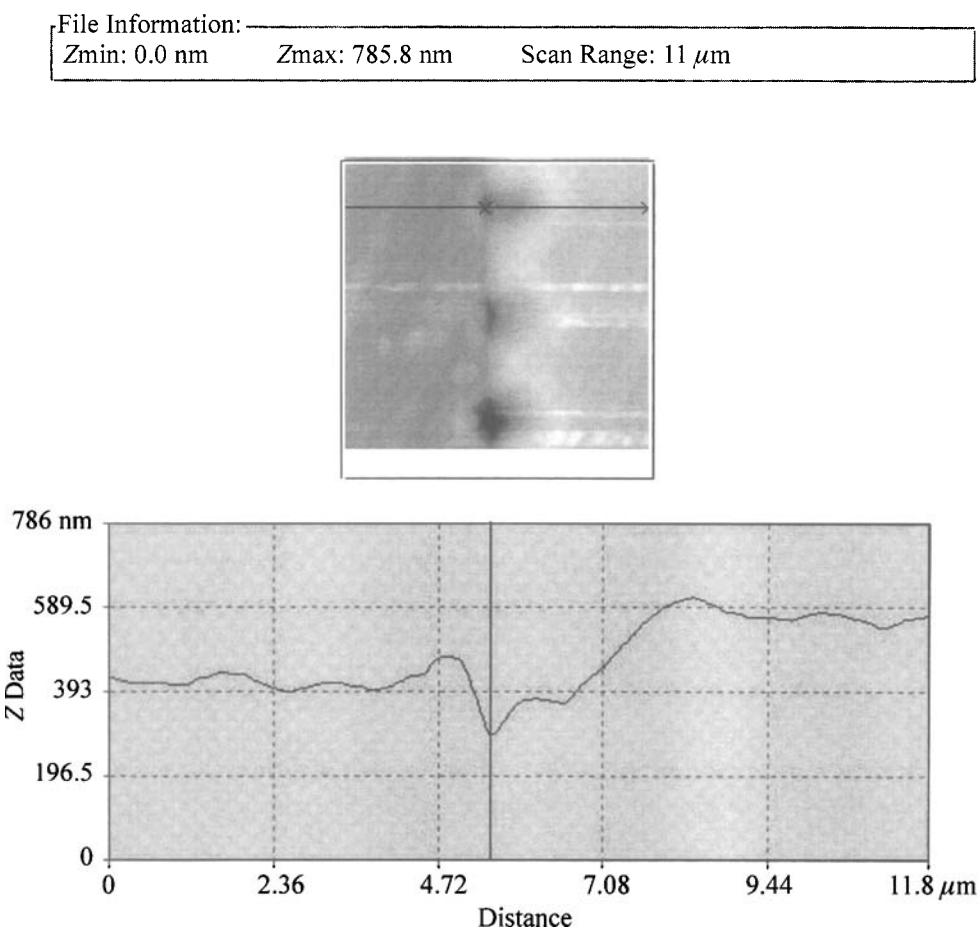


**Figure 8.** Image of a section of the interphase (upper image) and a profile through the section. The profile shows distortion due to movement of the indenter. The horizontal line through the section shows where the profile was taken. The sample is the same sample as was used to obtain the data shown in Fig. 6.

### 3.3. Detection of the composite interaction during indentation

The most direct evidence for a stiffening effect of the rigid material near a softer material during the indentation process can be seen in Figs 4 and 5. In this sample a thick soft interphase of epoxy resin cured with a blend of Jeffamine D2000 and D400 was coated onto the aluminum to give a 15  $\mu\text{m}$  artificial interphase. As this layer is much thicker than the diameter of the indenter at maximum indentation depth, the artificial interphase is easily seen as a region of low modulus, low load at fixed indentation depth and high indentation depth at fixed load. Examination of the Figs 4 and 5 show that the pseudo-modulus is not constant across the sample. Although Figs 4 and 5 show data for a sample which had the polishing artifact near the interface between the two epoxy materials, all plots of indentations in the samples with a thick soft interphase showed the same trend across the whole interphase. The same effect is seen at all indentation depths up to 600 nm. We interpret this as evidence for a reinforcing effect of the much more rigid aluminum and the relatively rigid epoxy cured with Jeffamine D230 which was used as adhesive. As the interphase is traversed the sample detects relatively more of one stiffening agent than the other and, hence, appears to become softer as the epoxy adhesive side is approached.

This suggests that in this case, the composite effect can be seen over the full width of the interphase (15  $\mu\text{m}$ ).

Figure 6 also shows data which might suggest that the epoxy material is stiffened by the aluminum for up to 2  $\mu\text{m}$  from the interface. The region in which the load at constant indentation depth is constant for the indents in the aluminum remain constant right up to the point where the indenter touches the epoxy resin. On the epoxy side, however, the epoxy gets progressively softer as the distance from the interface increases even after the indenter no longer touches the aluminum. It does not become constant until about 2  $\mu\text{m}$  from the interface.

It should be noted that a soft interphase would give a similar result to that shown here and there is no easy way to distinguish the two effects conclusively.

### 3.4. Detection of a soft interphase

In order to see if nano-indentation was capable of detecting a soft interphase, systems were prepared with artificial soft interphases by using coatings of epoxy resin cured with higher molecular weight amines which give cured systems with lower moduli. One system was based on pure resin/curing agent as the coating and gave an interphase of about 15  $\mu\text{m}$  thickness. The second used a dilute solution of the curing system which gave a coating thickness below the measuring capability of the ultrasonic thickness gauge (less than 1  $\mu\text{m}$ ). Figures 4 and 5 above show a region from the interface to a distance about 14  $\mu\text{m}$  from the interface where the load at fixed indentation depth is lower than both in the aluminum or in the epoxy adhesive. We interpret this as indicating the presence of the thick artificial soft interphase. For the thin interphase, however, the film sometimes indicated the

presence of a soft interphase by the appearance of one or two points with a low load at fixed indentation depth but sometimes did not. We suspect that the reason for the inconsistent results was that the thickness of the interphase was comparable to the distance between adjacent indents. When data from several traverses of the interphase were plotted together, the data showed too much scatter to allow interpretation. We believe that the scatter was caused by a lack of precision in defining the exact position of the interface for different traverses. In order for data from several runs to be presented together, a process had to be developed that was consistent with the abilities of the instrument and that would allow direct comparison of data from several traverses of the interphase on the same system.

Comparison of several runs suggested that the general shape of the curves was the same but that they appeared shifted along the  $x$ -axis which shows the distance from the interface. A shift in this axis would imply that the position of the interface had not been defined identically for each sample. Figures 9 and 10 show data from four traverses of the interphase for the sample with a thin, soft interphase of thickness less than  $1\ \mu\text{m}$ . Each curve has been shifted to place the point of inflection of each of the four runs at the point where the distance axis is zero. The shift was determined for each run using the data for the lowest indent depth and the same

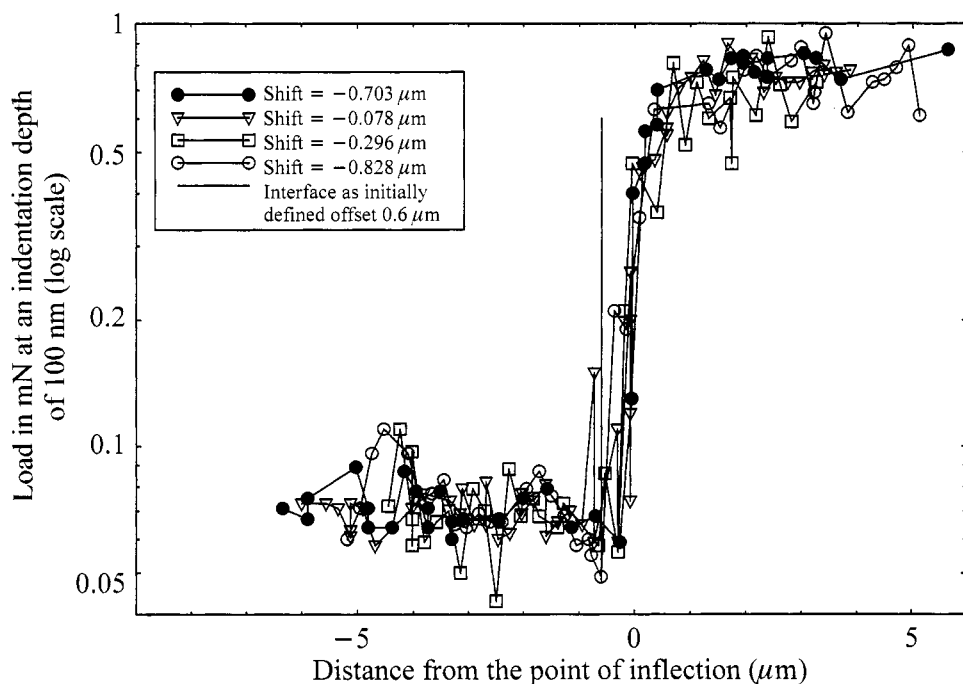


**Figure 9.** Plots of the load at 100 nm indentation depth for the system with a thin artificial interface. The curves have been shifted horizontally to make the point of inflection appear at zero  $x$  displacement. The indicated interface is offset from the true interface by about  $-0.6\ \mu\text{m}$ . The data are shown for two runs each on two separate samples.

shift was applied to the second data set at the higher indent depth. Figures 11 and 12 show similar plots of data for four curves for a sample without the artificial interphase. The shift represents a change in the definition of the origin for the  $x$ -axis which is no longer zero at the interface; however, it makes the shift much easier and is more repeatable. The interface lies near the point where the distance axis equals  $-0.60 \mu\text{m}$ . The shifts required are shown in Table 2. The relative shifts along the distance axis are similar to the precision of the definition of the placement of the interface as defined from the pseudo-modulus/indent depth curves described above so this process reflects a refinement of the definition of the relative position of the interface.

The four runs for each system used two separate samples for each condition and each sample was measured twice: once as described above and then the sample was re-polished to expose new surface and was then measured again.

The data for the system with the soft interphase suggest that there is a region in the epoxy, close to the interface, that has a significantly lower indent at fixed load. This would suggest an interphase with a lower modulus and with a thickness around  $1 \mu\text{m}$ . For the systems without an artificial interphase, the curves show a much less marked region with a few samples, suggesting a layer with a smaller modulus difference and with a lower probability of being detected. We interpret these data as suggesting that it may be possible to detect the presence of a soft interphase, such as the artificial interphase used in these experiments but an interphase with a modulus 20% lower than the bulk with a thickness of the order of  $1 \mu\text{m}$  is very close to the detection limit using the processes developed in this study.

Although the interface is a two-dimensional surface it has a shape in three dimensions due to the initial roughness of the polished aluminum surface. It is possible that the indentation process could be affected by the three-dimensional characteristics of the interface immediately below the surface of the sample. The surface is polished to give a roughness of about  $50 \text{ nm}$  as measured from an AFM image. The profile of the interface at the surface suggests that the interface is undulating with a wavelength of fractions of a micrometer and an average amplitude

**Table 2.**

Shifts required for superposition of the inflection point at distance = 0 in Figs 9–12

System	Run	Shift ( $\mu\text{m}$ )
Aluminum/epoxy-Jeffamine D400/epoxy-Jeffamine D230/aluminum	1	-0.828
	2	-0.296
	3	-0.078
	4	-0.703
Aluminum/epoxy-Jeffamine D230/aluminum	1	-0.354
	2	-0.385
	3	+0.104
	4	-0.156

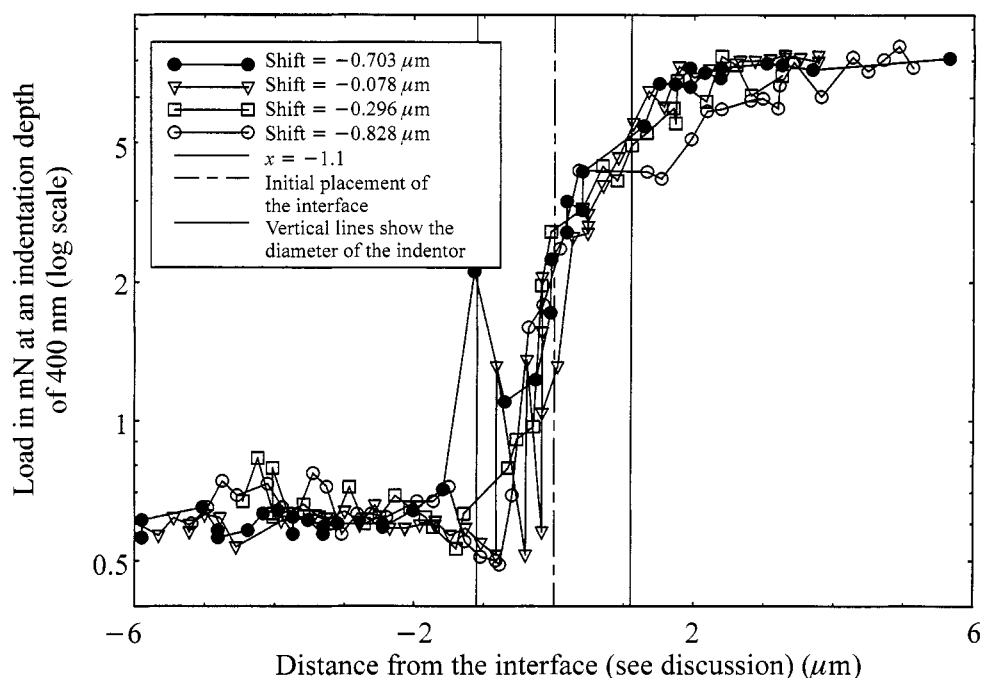


**Figure 10.** Plots of the load at 400 nm indentation depth for the system with a thin artificial interface. The indicated interface is offset from the true interface by about  $-0.6 \mu\text{m}$ . The data are shown for two runs each on two separate samples. This figure includes an indication of the width of the indenter as two vertical lines on each side of the apparent interface, indicating the indenter radius at 400 nm depth.

of  $0.05 \mu\text{m}$ . It is probable that the same applies to a profile taken at right angles to the exposed surface. Underneath the exposed plane of the sample, therefore, the surface is likely either protruding into the path of the indenter or tilting away with equal probability. Any protrusion into the path of the indenter will have a significant effect in reinforcing the system while a small undercut would have little effect. In addition, there are always only one or two indents made close to the interface. The net result is that it is possible that observation of a modified interphase may not be possible in every run.

Superimposed on this possibility is the problem described above in that roughness of the surface near the interface can produce artifacts which look suggestive of a soft interphase.

We suggest that the information shown here is consistent with the possibility that Figs 9 and 10 are showing the effect of an interphase of lower modulus than the adhesive and with a thickness around one micrometer. Even more cautiously, the sporadic occurrence of slight minima near the interface in Figs 11 and 12 suggests that a similar but thinner interphase could exist in this system as well.

In order to produce more definitive data, using nano-indentation and AFM, procedures must be developed to improve the collection of data for indentations



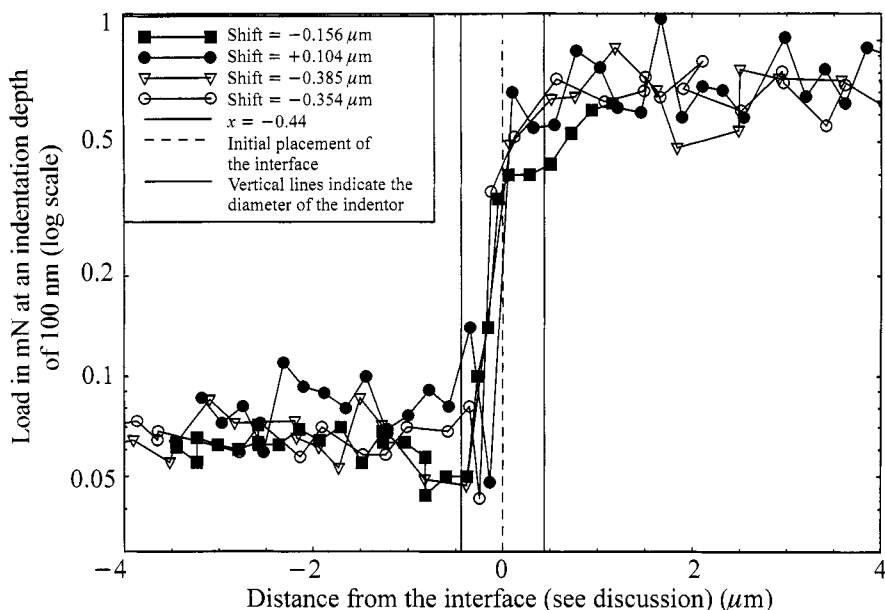


**Figure 11.** Plots of load at 100 nm indentation depth for the system without an artificial interface. The data are shown for two runs each on two separate samples. This figure includes an indication of the width of the indenter as two vertical lines on each side of the apparent interface, indicating the indenter radius at 100 nm depth.

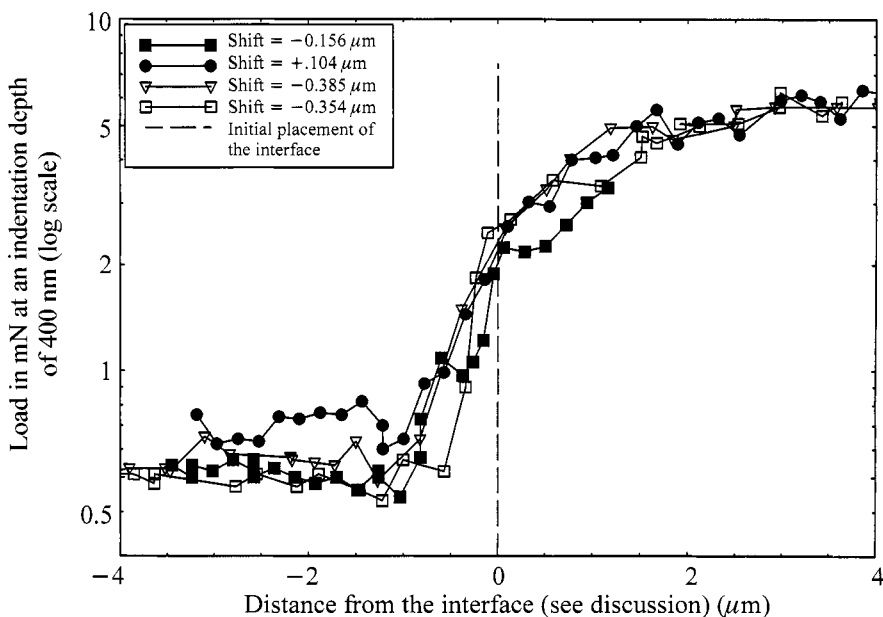


**Figure 12.** Plots of load at 400 nm indentation depth for the system without an artificial interface. The data are shown for two runs each on two separate samples.

within a micrometer of the interface which would allow statistical interpretation of experimental evidence.

#### 4. CONCLUSIONS

This paper describes the results of a study of the interface in aluminum-epoxy resin joints using nano-indentation and AFM imaging.

The results are interpreted in terms of three interactions between the indenter and the material:

- (a) A 'direct' interaction when the indenter hits the second phase during the indentation.
- (b) A 'composite' interaction when the properties of the phase being indented are directly modified by the adjacent phase which is not in contact with the indenter.
- (c) An 'interphase' interaction when one or more of the phases in the interface region have different properties from the bulk materials and the change in properties affect the indentation.

By using a sample with a thin, soft layer placed on the aluminum and cured before formation of the bonded joint, it was shown that indentation data could be used to indicate the presence of a soft interphase. This process, however, is inconsistent and may fail to show the presence of the interphase. Surface preparation of the section of the joint prior to carrying out the indentation process can give rise to artifacts with very similar properties.

In spite of the problems of interpretation of nano-indentation results in two-phase media, some suggestion of the possible presence of a soft, thin interphase in a normal epoxy/aluminum joint was shown.

#### REFERENCES

1. F. Fondéur and J. L. Koenig, *Appl. Spectros.* **47**, 1–6 (1992).
2. R. G. Dillingham and F. J. Boerio, *J. Adhesion* **24**, 315–319 (1987).
3. H. Kollek, *Int. J. Adhesion Adhesives* **5**, 75–85 (1985).
4. A. A. Roche, J. Bouchet and S. Bentadjine, *Int. J. Adhesion Adhesives* **22**, 431–441 (2002).
5. S. Maeda, T. Assai, S. Fujii, Y. Nomura and A. Nomoke, *Polym. Sci. Eng.* **58**, 32–36 (1988).
6. J. G. Williams, M. E. Donnellan, M. R. James and W. L. Morris, *Mater. Sci. Eng. A* **126**, 305–312 (1990).
7. M. Munz, H. Sturm, E. Schulz and G. Hinrichsen, *Composites Part A* **29**, 1251–1259 (1998).
8. T. A. Bogetti, T. Wang, M. R. VanLandingham and J. W. Gillespie, Jr, *Composites Part A* **30**, 85–94 (1999).
9. S. Gao and E. Mäder, *Composites Part A* **33**, 559–576 (2002).
10. K. Mai, E. Mäder and M. Muhle, *Composites Part A* **29**, 1111–1119 (1998).
11. T. D. Downing, R. Kumar, W. M. Cross, L. Kjerengtroen and J. J. Kellar, *J. Adhesion Sci. Technol.* **14**, 1801–1812 (2000).
12. M. L. Huang and J. G. Williams, *Macromolecules* **27**, 7423–7428 (1994).

13. J. P. Bell, *J. Appl. Polym. Sci.* **27**, 3503–3511 (1982).
14. W. C. Oliver and G. M. Pharr, *J. Mater. Res.* **7**, 1564–1583 (1992).
15. W. C. Oliver, *MRS Bull.* **11**, 15–19 (1986).
16. F. Li, J. G. Williams, B. S. Altan, I. Mishioglu and R. L. Whipple, *J. Adhesion Sci. Technol.* **16**, 935–949 (2002).
17. S. P. Baker, *Thin Solid Films* **308-309**, 289–296 (1997).
18. J. E. Houston and R. M. Winter, *Polymer Prep.* **41** (5), 1454–1455 (2000)

## **Stiffness and adhesion characterization of nanolithographed poly(methyl methacrylate) by means of force–displacement curves**

B. CAPPELLA \*, H. STURM and E. SCHULZ

*Federal Institute of Materials Research (BAM), Lab. VI.2, Unter den Eichen 87,  
D-12200 Berlin, Germany*

**Abstract**—Poly(methyl methacrylate) (PMMA) surfaces have been modified by dynamic plowing lithography. The resulting modified structures, presenting regions of different densities and stiffnesses, have been studied by force–displacement curves. The elasto-plastic response, the stiffness, and the adhesion of the modified samples have been characterized. Force–displacement curves are able to distinguish between unmodified PMMA and two different structures resulting from the lithography, i.e. compressed PMMA and low density PMMA. In particular, the low density regions are made up of cluster-like globular particles, whose elasto-plastic response and adhesion are measured and whose contribution to the total elasto-plastic response and to the adhesion has been studied in detail.

**Keywords:** AFM; lithography; force–displacement curves; stiffness; adhesion; elasto-plastic response.

### **1. INTRODUCTION**

In the last few years there has been a considerable interest in methods aimed to modify surfaces taking advantage of the atomic force microscopy's (AFM) capability of directly machining the sample surface. This can be achieved in two ways: static plowing and dynamic plowing. In static plowing [1–3], AFM is employed in contact mode to pattern a single poly(methyl methacrylate) (PMMA) layer and subsequently use it as an etch mask. This technique presents some drawbacks. It has been shown that, while engraving a line into the resist by static plowing, torsion of the cantilever may lead to edge irregularities [4]. Additionally, depending on the local stiffness of the sample and/or of the cantilever, while

---

\*To whom correspondence should be addressed. Fax: (49) (30) 8104 1627.

imaging the surface before or after the modification, further modifications may take place due to dragging of the surface.

By dynamic plowing lithography (DPL) [5–8] the surface is modified by indenting it with a vibrating tip using Tapping Mode AFM. This lithography technique is nearly free from problems due to cantilever torsion. Furthermore, the successive imaging of the modified surface does not lead to any further modification. Despite the great advantages of this technique, little work has been done to understand its principles and to improve its performance.

In particular, it has been shown [9] that the indentation of the tip in a rapid intermittent contact produces not only holes, but also regions surrounding the carved holes, called ‘border walls’. Except for small modulation amplitudes and/or small scanning speeds, the volume of these border walls is always much larger than the volume of the holes. This means that the density of the material in these border walls must be considerably smaller than the density of the material in the unmodified film. Further changes in the physico-chemical properties of the modified material cannot be excluded.

Force–displacement curves [10] are likely to give insights into the mechanical behaviour and the physico-chemical properties of lithographed PMMA. This is important not only to understand the composition of the modified films, but also to emphasize the possibilities of sample analysis by means of this technique and to show the capability of AFM force–displacement curves to evidence slight differences in the physico-chemical properties between very similar materials. As a matter of fact, so far force–displacement curves have been employed to characterize only elastic samples. In this domain, the AFM has proved to be a leading tool in the study of the stiffness of samples on a local micrometric scale (see Ref. [11] and references therein), even if some instrumental [11] and theoretical [12] problems limit its use to the comparison of materials with different stiffnesses and make impossible, with the exception of some trivial cases, an absolute determination of the Young moduli. On the other hand, there has been very little work on samples with plastic response. The lack of a theory, the presence of viscoelastic effects [13] and some instrumental difficulties have limited the work in this field.

In this study we have employed force–displacement curves for the investigation of the mechanical and physico-chemical properties of PMMA, previously modified by means of DPL. We have shown the possibility of distinguishing between the elasto-plastic responses of regions of different densities, to study the fine structure of the plastic response of low density areas, and to gain some insights into the interplay between plastic deformation and adhesion.

## 2. EXPERIMENTAL

The AFM used in our experiments is comprised of a commercial microscope head (Topometrix TMX 2000 Explorer, Santa Clara, CA, USA), a piezoelectric scanning table (P-517.2CL, Physik Instrumente GmbH & Co., Waldbronn, Germany) for XY

scanning, and a Z-piezoactuator (P-753.11C, Physik Instrumente GmbH & Co., Waldbronn, Germany) for Z positioning. Both the XY table and the Z-piezoactuator are equipped with integrated capacitive displacement sensors. The maximum scan range of the scanning table is  $250 \times 250 \mu\text{m}^2$ . The maximum Z-range is  $12 \mu\text{m}$ .

The experimental set-up for DPL has been discussed in a previous article [8]. During DPL the microscope is operated in Tapping Mode. In Tapping Mode, the cantilever driven by a dither piezoactuator vibrates near its resonance frequency and, since the oscillation amplitude depends on the distance between the cantilever and the sample, a feedback loop keeps the vibration amplitude constant by changing the extension of the Z-piezoactuator, i.e. the distance between the sample surface and the cantilever. The topography of the sample is reconstructed from the changes in the Z-piezoactuator extension. In order to carve the sample surface, the modulation amplitude applied to the dither piezoactuator driving the cantilever oscillations is suddenly increased (within  $100 \mu\text{s}$ ). The complex response of the cantilever has been analysed in Ref. [8]. Here we can say for simplicity sake that when the amplitude is increased, the sample is further approached to the tip and the tip is likely to indent the sample surface, leading to elastic and plastic deformations.

The same program has been used to perform lithography and to acquire force–displacement curves. The scanning method, employed for the acquisition of force–displacement curves is described in detail in Ref. [14]. At the beginning the tip is away from the sample at a height  $z_0$ , then the sample is approached until the force exerted on the tip reaches a pre-assigned value  $F_{\text{max}}$ . The corresponding height  $z(F_{\text{max}})$  and the deflections in the last  $N_z$  approaching points are stored. The distance between two subsequent points is  $\delta z$ . Then the sample is retracted for a distance  $\Delta z = N_z \delta z$  and the deflections in the next  $N_z$  withdrawing points are stored. After this, the sample is retracted further for a short distance, in order to avoid the vertical distance between the cantilever and the subsequent XY point being less than  $\Delta z$ . This process is repeated on  $N_x N_y$  points all over the scanned area. A three-dimensional matrix of  $(2N_z + 1)N_x N_y$  data points is stored. The columns  $d_{ijz}$  are the force–displacement curves, the first plane  $d_{xy0}$  is the topography, containing the heights  $z(F_{\text{max}})$ , and the subsequent planes are the force slices  $d_{xyk}$ , containing the deflection of the cantilever at a distance  $k\delta z$  from  $z(F_{\text{max}})$ .

The PMMA films were prepared by depositing droplets of a solution of 10 g of PMMA (Röhm GmbH, type 7N,  $M_w \cong 120 \text{ kD}$ ) in 15 g of acetone on a glass slide and letting the acetone slowly evaporate. Only the side previously in contact with the glass was used in the following experiments. The PMMA sample thickness was about 1 mm.

Commercially-available cantilevers (Pointprobe NCL, Nanosensors, Wetzlar-Blankenfeld, Germany) with length  $L = 225 \mu\text{m}$ , width  $W = 38 \mu\text{m}$ , thickness  $T = 7 \mu\text{m}$ , resonance frequency  $F = 156 \text{ kHz}$ , and spring constant  $k_c = 30 \text{ N/m}$  were used. Unless otherwise specified, all experiments were performed at room temperature in air.

3. RESULTS AND DISCUSSION

Figure 1 shows a lithographed  $7 \times 7 \mu\text{m}^2$  PMMA surface, where sixteen rectangles have been carved. The structure of such rectangles, carved by means of DPL, has been described in details in a previous article [9]. The rectangles have been written as a sequence of overlapping holes. When the tip carves a hole a certain quantity of material is accumulated around the hole forming a border wall. The position of such a border wall depends on the particular tip employed for carving, whereas the ratio of the positive volume  $V_{\text{pos}}$ , i.e. the volume of the border wall, to the negative volume  $V_{\text{neg}}$ , i.e. the volume of the hole, depends on the modulation amplitude used to carve the holes and on the scanning speed. The experiments discussed in Ref. [4] show that the material forming the border walls cannot be simply the bulk material carved out of the holes, because  $V_{\text{pos}}$  is in most cases much bigger than  $V_{\text{neg}}$  (except for small writing amplitudes and/or small scanning speeds). So one must admit, that the indentation of a rapidly oscillating tip gives rise to some density changes and maybe physico-chemical changes of PMMA.

When the holes overlap, some of the material in the border walls of the single holes is carried out of the rectangles by the tip. The material carried out of the

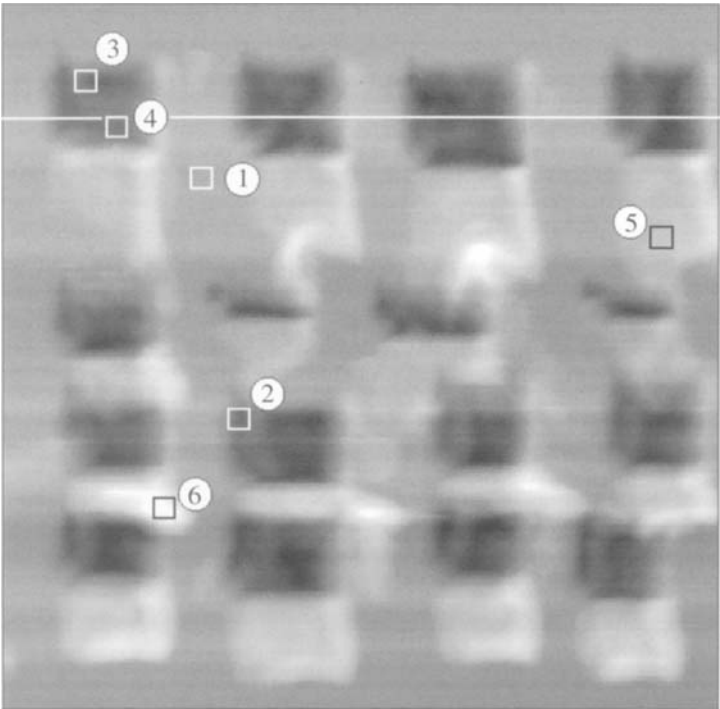


**Figure 1.** Topography evaluated from force–displacement curves ( $7 \times 7 \mu\text{m}^2$ ;  $200 \times 200$  pixel;  $\Delta Z$  400 nm) of a PMMA sample, where sixteen rectangles have been previously carved by means of DPL. The little squares numbered 1 to 6 indicate the position of the force-displacement curves shown in Fig. 2. The white line is the line where the hysteresis presented in Fig. 3 has been calculated.

rectangles is accumulated in two large border walls outside the rectangles, a short border wall on the right and a tall border wall at the bottom. Part of the material is left inside the rectangle, so that the whole surface of the rectangles is covered with residues of the border walls of the single holes, i.e. with material of the border walls of the single holes that has not been carried out of the rectangles. Only the first vertical line on the left and the last horizontal line at the bottom are free from residues of the border walls [9]. Such residues of the border walls cannot always be seen clearly in the force–displacement curves topography, but they are evident in tapping mode topographies (not shown).

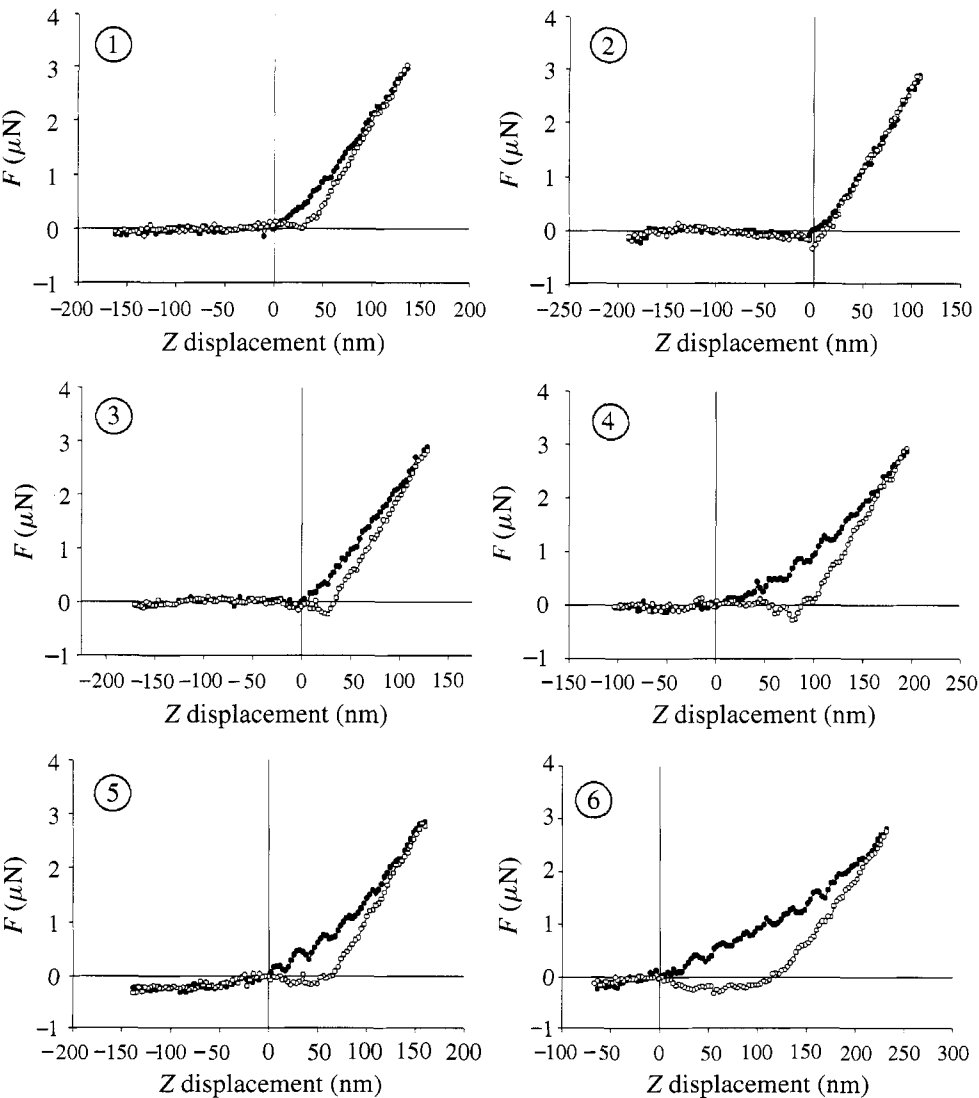
A characterization of such structured samples by means of force–displacement curves can provide some insights into the structure and into the mechanical and physico-chemical properties of the material forming the border walls.

Figure 2 shows six typical force–displacement curves at different locations on the lithographed PMMA. The numbers correspond to the squares indicated in Fig. 1. Approach (withdrawal) curves are plotted with full (open) circles. All plots have the same  $XY$  range. The nominal value of the spring constant  $k_c$  given by Nanosensors, i.e.  $k_c = 30 \text{ N/m}$ , has been used to calculate the forces.

The first curve (1) was acquired on unmodified PMMA. The most important feature is the hysteresis between the contact lines. This hysteresis is due to the plastic deformation of the sample (discussed in [10, 15]). It is useful to compare this curve with the second curve (2), acquired at the left end of a rectangle, i.e. where no residues of the border walls are present. In this curve, no hysteresis is present. This means that the behaviour of the sample is that of an ideally elastic sample. An ideally elastic sample, even if it undergoes a deformation during the approach, regains its shape step by step during the withdrawal, so that the loading and unloading curves, i.e. the approach and withdrawal contact lines, overlap. On the other hand, if a sample is unable to regain its shape, at a given displacement the unload forces are smaller than the load forces. Hence, the first derivative of the force, i.e. the slope of the contact line, is larger for the withdrawal curve than for the approach curve. The distance between the two intercepts of the tangents to the initial portions of contact lines with the zero axes, called ‘zero load plastic indentation’, gives the penetration depth of the tip into the sample.

Unmodified PMMA is compressed by the tip during the loading curve, whereas the PMMA at the left end of the rectangles, already compressed during DPL, cannot undergo a further plastic deformation. Force–displacement curves are able to sense the difference in density between the two regions. The compression, and hence the hysteresis, becomes larger on the residues of the border walls inside the rectangles (curves 3 and 4), or on the short border walls outside the rectangles (curve 5). Finally, on tall border walls outside the rectangles (curve 6), the hysteresis is very much larger than in the other cases. This means that the rapid intermittent contact during DPL produces low-density PMMA, that is successively accumulated in the border walls.





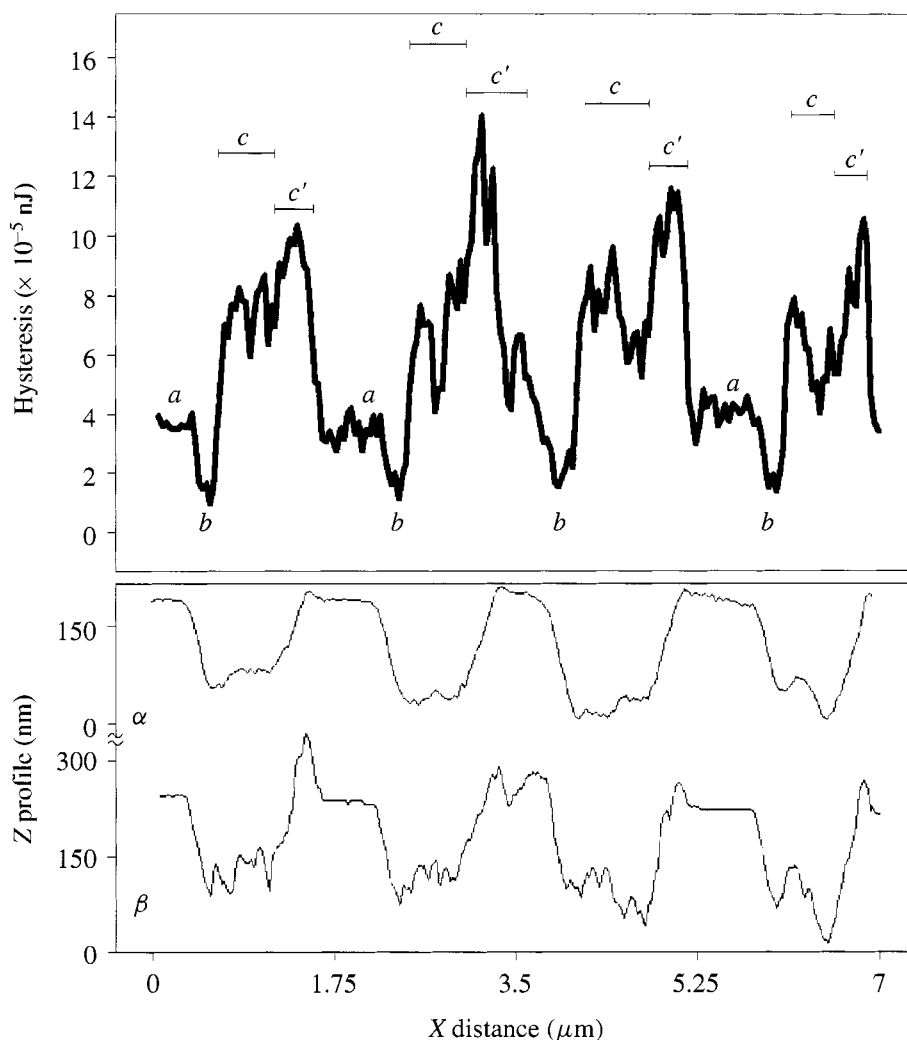
**Figure 2.** Six force–displacement curves on lithographed PMMA. Numbers correspond to the positions shown in Fig. 1. Curves with full (open) circles are the approach (withdrawal) curves. Hysteresis has its minimum on compressed PMMA (curve 2) and its maximum on the high border walls below the rectangles (curve 6).

Also the curvature of the loading curve is an indication of the presence of a compressible material. In particular, the last three curves in Fig. 2 (curves 4–6) can be fitted with a function of the form  $F = F_0 + az^2$  without any linear term, whereas the first three curves in Fig. 2 (curves 1–3) can be fitted only with a linear term. This means that, when the tip is placed on the residues of the border walls inside the rectangles or on the border walls outside the rectangles, it pushes at the

beginning on a soft material that becomes stiffer and stiffer as the tip compresses it. Consequently, the slope of the loading curve goes from 0 (very soft material) to  $k_c$  (very stiff material). In the fourth and fifth curves only the end of the loading curve has a slope equal to  $k_c$ , i.e. only after the compression the sample is much stiffer than the tip. Such a degree of compression cannot be reached on tall border walls. In the curves on tall border walls, e.g. number 6, the slope is always smaller than  $k_c$ , also at the very end of the loading curve (maximum slope: 93% of  $k_c$ ). The degree of compression, and hence the possibility to reach the maximum slope  $k_c$ , depends on  $F_{\max}$ . If  $F_{\max}$  is larger the high border walls can also be fully compressed, and the slope will reach its maximum value  $k_c$ .

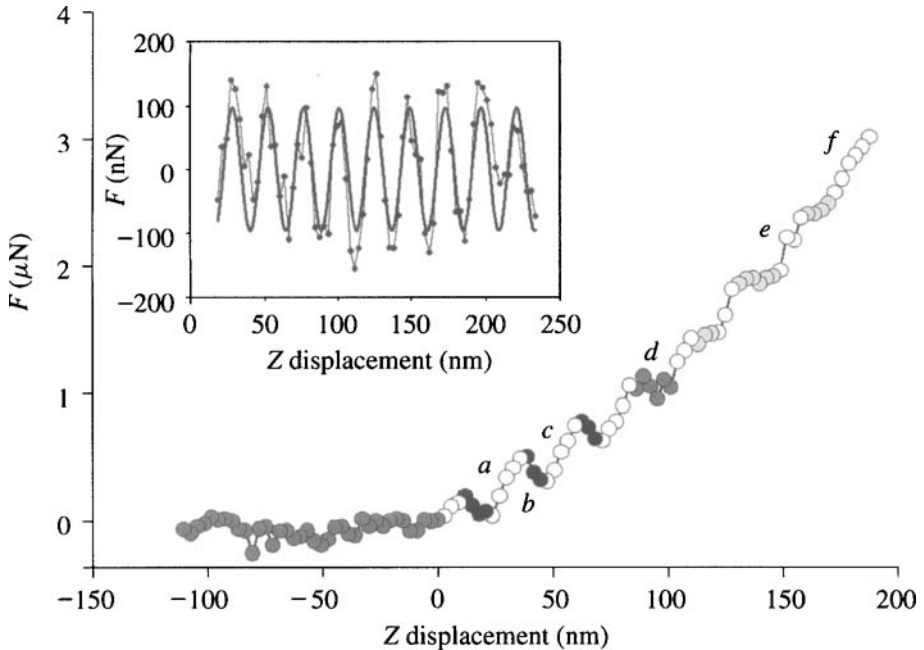
The unloading curve always has (except in the sixth curve) a slope equal to  $k_c$ . This means that the low density material (residues of the border walls inside the rectangles or small border walls outside the rectangles) has been completely compressed, or in other words that the low density material has been completely indented and a hole has been carved. Hence, the tip has gone through the low-density material, that has a fully plastic response, and has reached the underlying unmodified PMMA, having a quite fully elastic response. Therefore, in all curves except the sixth, two parts of the contact region can be distinguished: a part with hysteresis, corresponding to the indentation of the low density material and showing a plastic response, and a part without hysteresis, corresponding to the contact with the unmodified PMMA and showing an elastic response. Only in the sixth curve the PMMA cannot be fully compressed, due to its large height, and the material shows an elasto-plastic response. Of course we could have reached a fully elastic regime with a higher force, i.e. by pushing further and compressing further the PMMA in the tall border walls.

Figure 3 shows the hysteresis  $H$  in force–displacement curves along the white line of Fig. 1. The hysteresis has been calculated as the area between the approach and the withdrawal curves. Also the  $Z$  profiles obtained from the force–displacement curves topography ( $\alpha$ ) and from the Tapping Mode topography ( $\beta$ ) are shown. Four different regions can be distinguished: the unmodified PMMA (a) with  $H \cong 4 \times 10^{-5}$  nJ, the compressed region at the left end of the rectangles (b) with  $H \cong 1 \times 10^{-5}$  nJ, the residues of the border walls inside the rectangles (c) with  $6 \times 10^{-5} < H < 8 \times 10^{-5}$  nJ, and the small border walls outside the rectangles (c') with  $8 \times 10^{-5} < H < 14 \times 10^{-5}$  nJ. Note that in the region (c'), i.e. on the border walls outside the rectangles, the hysteresis is larger than in region (c) because the PMMA under the border walls has not been compressed. The values of  $H$ , and also the variations inside the region (c), are in agreement with the Tapping Mode topography. It is now possible to understand why the residues of the border walls inside the squares cannot be seen in force–displacement curves based topography, particularly when they are rather small: when  $z(F_{\max})$  is acquired, the low-density PMMA forming such residues has already been compressed and flattened. The same dependence of the hysteresis on the presence of border walls and compressed regions has been measured in water.



**Figure 3.** Hysteresis  $H$  and  $Z$  profiles along the white line of Fig. 1. The first  $Z$  profile ( $\alpha$ ) has been obtained from the force–displacement curves topography and the second ( $\beta$ ) from the Tapping Mode topography. Letters indicate four different regions: unmodified PMMA (a), with  $H \cong 4 \times 10^{-5}$  nJ; compressed PMMA (b), with  $H \cong 1 \times 10^{-5}$  nJ; residues of border walls inside the rectangles (c), with  $6 \times 10^{-5} < H < 8 \times 10^{-5}$  nJ; and short border walls at the right of the rectangles ( $c'$ ), with  $8 \times 10^{-5} < H < 14 \times 10^{-5}$  nJ.

Several approach curves present a periodic curve superimposed on the contact line. Such ‘oscillations’ of the loading force have been evidenced in the curve in Fig. 4. After the points on the zero line (dark grey circles) there is a small region where the force increases. All these regions with a positive force gradient ( $dF/dZ \cong k_c$ ) are shown with white circles. The first three regions with a positive gradient are followed by three intervals with negative gradient (black circles), the



**Figure 4.** A force–displacement approach curve on the residues of the border walls inside the first rectangle. A periodic curve superimposed on the contact line can be seen. Open circles correspond to intervals where the first derivative of the force is greater than  $k_c$ , light grey points to intervals where the first derivative of the force is about  $k_c$ , dark grey points to intervals where the first derivative of the force is close to 0, and black points to intervals where the first derivative of the force is negative. The letters refer to the model shown in Fig. 5. The inset shows the oscillations around the approach contact line values of another force–displacement curve. The oscillations have been evidenced by subtracting a quadratic fit from the experimental curve. The period of the oscillation is 24 nm; the amplitude is about 200 nN.

fourth is followed by an interval with zero gradient (dark grey circles), and the last three are followed by intervals where the gradient is also positive, but smaller (light grey circles). The inset in Fig. 4 shows a loading curve acquired on a tall border wall, in which the quadratic fit has been subtracted from the curve. The curve can be fitted with a function of the form

$$F = a \sin\left(\frac{2\pi z}{b} + \phi\right),$$

with  $b = 24.1 \pm 0.1$  nm and  $a = 200 \pm 30$  nN.

The letters on the curve in Fig. 4 correspond to the simple model illustrated in Fig. 5. The border wall can be seen as a pile of globular PMMA cluster-like structures. At the beginning of the loading phase, the tip pushes on one of these globular structures, and the force increases (a). On the top of the border wall, since they are not surrounded by other globular structures and/or by the substrate, the globular structures are likely to be removed without being deformed or compressed.

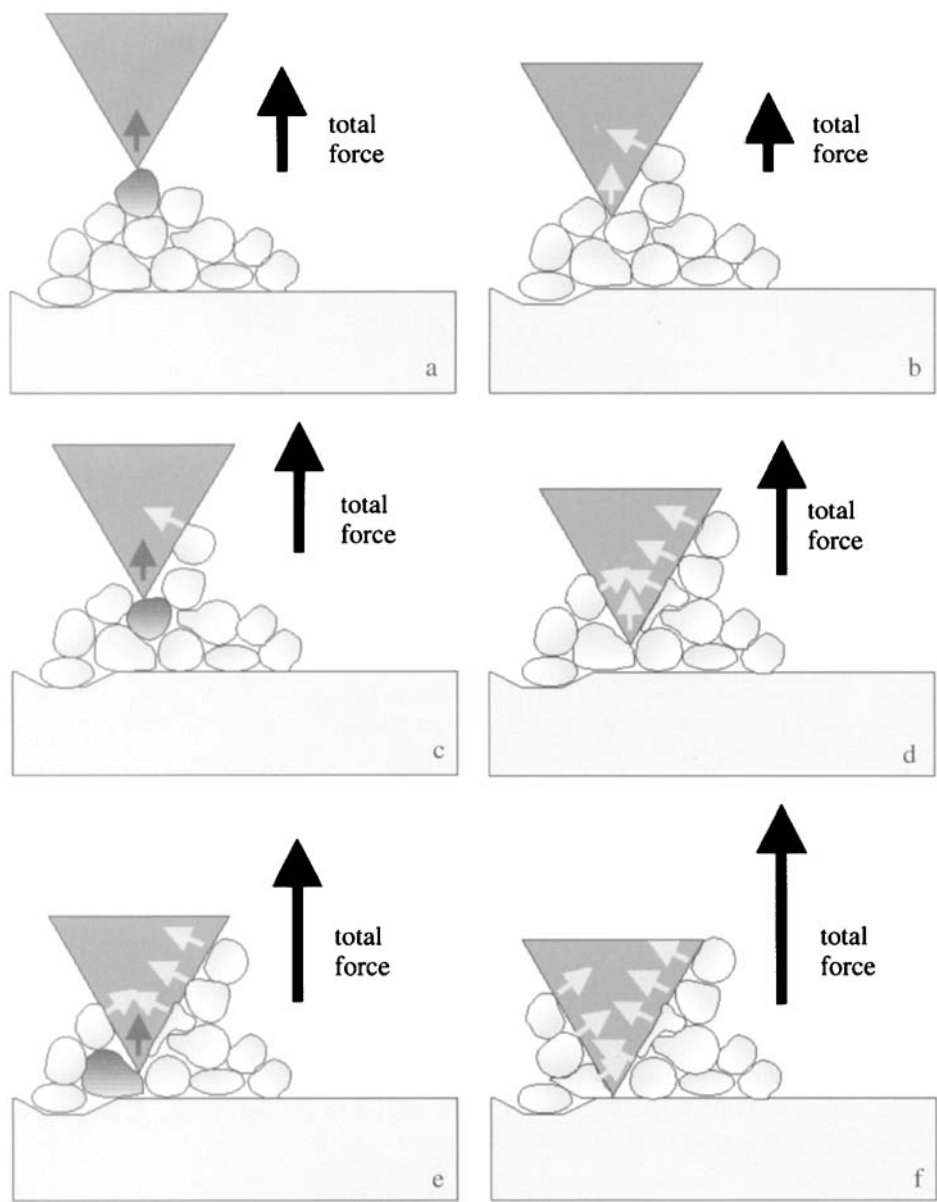


**Figure 5.** Model of the periodic dependence of the stiffness on the distance, when force–displacement curves are acquired on border walls outside the rectangles or on residues of the border walls inside the rectangle. The letters refer to Fig. 4. The globular structures represent the particles, on which the tip is pushing. Arrows indicate the force exerted on the tip.

Once this first globular structure (particle) has been removed, the force decreases (b), until the tip meets another particle. This process is repeated several times (c, e). Since the tip penetrates further into the border wall and the pushed particle is surrounded by other particles and is eventually in contact with the bulk PMMA, the

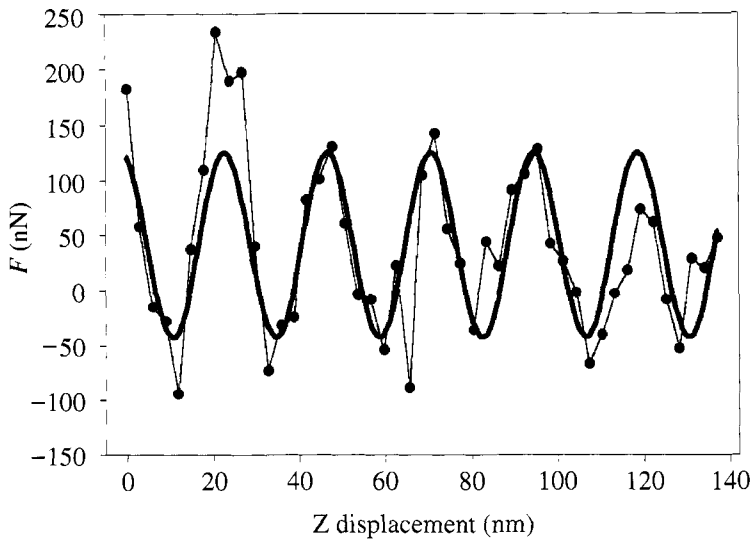


**Figure 6.** Periodic dependence of the stiffness on the distance along the withdrawal contact line. The period of the oscillation is 24 nm; the amplitude is about 150 nN. The oscillations around the withdrawal contact line values have been obtained by subtracting a linear fit from the experimental curve. The curve has then been fitted to a sinusoidal function.

successive particles are probably compressed and deformed. Eventually, after some cycles, the force after the removing/compressing of one particle, i.e. the sum of the forces exerted by all particles in contact with the tip when they are not pushed, may stay constant (d) or increase. When all particles have been removed and no compression is possible any longer the sample becomes much stiffer than the tip (f). The two contributions to the increase of the slope, i.e. of the stiffness, are: (a) the presence of an increasing number of globular structures exerting a certain small force on the tip; and (b) the effect of the 'bulk' structure beneath the border wall. The period of the oscillations shown in the inset of Fig. 4 is not determined by the distance, but by the force. This means that the force increases until it reaches a certain threshold value, i.e. the force at which a globular mass can be moved and eventually deformed. Since the force and the displacement are proportional, this engenders a spatial periodicity.

Also withdrawal curves on high border walls show a periodic curve superimposed on the unloading curve. A periodic curve obtained by subtracting a linear fit from an unloading curve is shown in Fig. 6. Such a periodic dependence is not present in all curves showing a periodic curve superimposed on the approach curves (for example, it is present in the fourth curve of Fig. 2, but not in the fifth). The period of the cycles is the same and the amplitude is similar. A simple model can be imagined also for the withdrawal. At the beginning of the withdrawal curve (that is, near the maximum force), the compressed particles can partially regain their shape as the pushing force of the tip decreases. As the tip is retracted further, the slightly compressed particles on the surface regain their position, attempting to close up

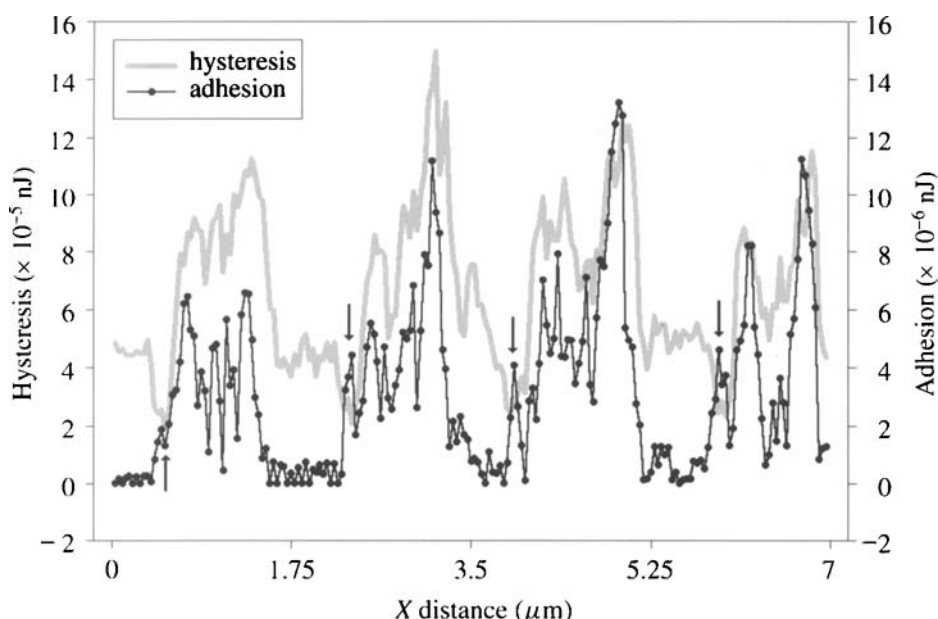


**Figure 7.** Adhesion along the white line of Fig. 1. Also the hysteresis of Fig. 3 (grey line) is reported for comparison. Arrows mark the regions of compressed PMMA.

the ‘hole’ left by the retracting tip. By doing this, they follow the retracting tip, exerting an adhesion force, until they detach, because the adhesion with the other PMMA particles becomes larger than the adhesion with the tip. Sometimes the last cycles in the retracting curve are missing, because the particles on the top of the border wall have been definitely removed. When the periodic curve is present only in the approach curve, and not in the withdrawal curve, it is evident that all particles have been strongly compressed and/or removed during the approach, so that they cannot regain their position.

Figure 7 shows the adhesion along the white line in Fig. 1. The grey line is a plot of the hysteresis, already shown in Fig. 3. It is evident that hysteresis and adhesion are correlated. On unmodified PMMA the adhesion is practically zero. On compressed PMMA (regions marked with an arrow) the adhesion is larger, but this is likely to be due to a cross-talk with topography: when the tip is placed near an edge, the sides of the tip are also in contact with the sample and the adhesion increases because it is proportional to the contact area [16]. In any case, the increase of adhesion inside or outside the rectangles cannot be due to a cross-talk with topography. It is rather due to the fact that the tip has penetrated into the PMMA and has carved a hole, modifying the surface topography. As already said, during the retraction, the globular particles that have been removed and/or deformed regain their position and/or their shape. The first globular particles on the surface, i.e. the first particles which have been removed, are likely to follow the tip during the withdrawal, thus exerting an adhesion force.

#### 4. CONCLUSIONS

PMMA lithographed by Dynamic Plowing Lithography has been investigated with AFM force–displacement curves. This turns out to be important not only to understand the mechanical and physico-chemical changes induced by DPL, but also to prove the capability of force–displacement curves for sensing and measuring particularly small differences in stiffness and adhesion.

Three different kinds of PMMA have been distinguished: unmodified PMMA; compressed PMMA; and low-density PMMA. Both elasto-plastic response and adhesion are found to be discriminating factors. In particular, a model has been presented in which the low-density PMMA is made up of cluster-like particles, whose contribution to the total elasto-plastic response and to the total adhesion can be singled out by means of force–distance curves. This model has been confirmed by experimental data.

#### REFERENCES

1. P. Pingue, M. Lazzarino, F. Beltram, C. Cecconi, P. Baschieri, C. Frediani and C. Ascoli, *J. Vac. Sci. Technol. B* **15**, 1398–1401 (1997).
2. R. Magno and B. R. Bennett, *Appl. Phys. Lett.* **70**, 1855–1857 (1997).
3. S. Miyake, *Appl. Phys. Lett.* **67**, 2925–2927, (1995).
4. V. Bouchiat and D. Esteve, *Appl. Phys. Lett.* **69**, 3098–3100 (1996).
5. B. Klehn and U. Kunze, *J. Appl. Phys.* **85**, 3897–3903 (1999).
6. S. Skaberna, M. Versen, B. Klehn, U. Kunze, D. Reuter and A. D. Weck, *Ultramicroscopy* **82**, 153–157 (2000).
7. M. Wendel, H. Lorenz and J. P. Kotthaus, *Appl. Phys. Lett.* **67**, 3732–3734 (1995).
8. M. Heyde, K. Rademann, B. Cappella, M. Geuss, H. Sturm, T. Spangenberg and H. Niehus, *Rev. Sci. Instrum.* **72**, 136–141 (2001).
9. B. Cappella and H. Sturm, *Acta Microscopica* **10**, 8–15 (2001).
10. B. Cappella and G. Dietler, *Surf. Sci. Rep.* **34**, (1–3), 1–104 (1999).
11. J. Domke and M. Radmacher, *Langmuir* **14**, 3320–3325 (1998).
12. D. Maugis, *J. Colloid Interface Sci.* **150**, 243–269 (1992).
13. J. P. Aimé, Z. Elkaakour, C. Odin, T. Bouhacina, D. Michel, J. Curely and A. Dautant, *J. Appl. Phys.* **76**, 754–762 (1994).
14. B. Cappella, P. Baschieri, C. Frediani, P. Miccoli and C. Ascoli, *Nanotechnology* **8** (2), 82–87 (1997).
15. N. A. Burnham and R. J. Colton, *J. Vac. Sci. Technol. A* **7**, 2548–2556 (1989).
16. H. A. Mizes, K.-G. Loh, R. J. D. Miller, S. K. Ahuja and E. F. Grabowski, *Appl. Phys. Lett.* **59**, 2901–2903 (1991).